MOLECULAR BEAM EPITAXY 1996

Proceedings of the Ninth International Conference on Molecular Beam Epitaxy

Malibu, California, USA, 5–9 August 1996

Part 1
Sections I–VIII

Edited by:

Y.-C. Kao

North-Holland

MOLECULAR BEAM EPITAXY 1996

PROCEEDINGS OF THE NINTH INTERNATIONAL CONFERENCE ON
MOLECULAR BEAM EPITAXY
MALIBU, CALIFORNIA, USA, 5–9 AUGUST 1996

PART 1
Sections I–VIII

Edited by:
Y.-C. Kao
Texas Instruments, USA

DTIC QUALITY INSPECTED 2

ELSEVIER

Amsterdam – Lausanne – New York – Oxford – Shannon – Tokyo

19970815 028

Copyright © 1997 Elsevier Science B.V. All rights reserved

This journal and the individual contributions contained in it are protected by the copyright of Elsevier Science B.V., and the following terms and conditions apply to their use:
Photocopying
Single photocopies of single articles may be made for personal use as allowed by national copyright laws. Permission of the Publisher and payment of a fee is required for all other photocopying, including multiple or systematic copying, copying for advertising or promotional purposes, resale, and all forms of document delivery. Special rates are available for educational institutions that wish to make photocopies for non-profit educational classroom use.
In the USA, users may clear permissions and make payment through the Copyright Clearance Center Inc., 222 Rosewood Drive, Danvers, MA 01923, USA. In the UK, users may clear permissions and make payment through the Copyright Licensing Agency Rapid Clearance Service (CLARCS), 90 Tottenham Court Road, London W1P 0LP, UK. In other countries where a local copyright clearance centre exists, please contact it for information on required permissions and payments.
Derivative works
Subscribers may reproduce tables of contents or prepare lists of articles including abstracts for internal circulation within their institutions.
Permission of the Publisher is required for resale or distribution outside the institution.
Permission of the Publisher is required for all other derivative works, including compilations and translations.
Electronic storage
Permission of the Publisher is required to store electronically any material contained in this journal, including any article or part of an article.
Contact the Publisher at the address indicated.
Except as outlined above, no part of this publication may be reproduced, stored in a retrieval system or transmitted in any form or by any means, electronic, mechanical, photocopying, recording or otherwise, without prior written permission of the Publisher.

No responsibility is assumed by the Publisher for any injury and/or damage to persons or property as a matter of products liability, negligence or otherwise, or from any use or operation of any methods, products, instructions or ideas contained in the material herein. Although all advertising material is expected to conform to ethical (medical) standards, inclusion in this publication does not constitute a guarantee or endorsement of the quality or value of such product or of the claims made of it by its manufacturer.

⊗ The paper used in this publication meets the requirements of ANSI/NISO Z39.48-1992 (Permanence of Paper)

Reprinted From:
JOURNAL OF CRYSTAL GROWTH 175/176 (1997) Part 1

The Manuscripts of the Proceedings were
received by the Publisher: mid-September 1996/late-January 1997

PRINTED IN THE NETHERLANDS

NINTH INTERNATIONAL CONFERENCE ON MOLECULAR BEAM EPITAXY
Malibu, California, USA, August 5–9, 1996

Conference Chairman

K.L. Wang, University of California, Los Angeles

Technical Program Committee

D.C. Streit (Chair), TRW
A. Brown, Georgia Tech
K.Y. Cheng, University of Illinois
K. Eberl, Max-Planck Institute
C.T. Foxon, University of Nottingham
T. Fujii, Fujitsu Laboratories
R.L. Gunshor, Purdue University
J.S. Harris, Stanford University
Pin Ho, Lockheed-Martin
Y. Horikoshi, NTT Research Laboratories
Y.-C. Kao (Proceedings Editor), Texas Instruments
M.-Y. Kong, Chinese Academy of Sciences
D. Mars, Hewlett-Packard Laboratories
J. Massies, CNRS
Y. Shiraki, University of Tokyo
A.J. Springthorpe, Bell-Northern
B.G. Streetman, University of Texas, Austin
W.T. Tsang, Lucent Technologies
Ch. Tu, University of California, San Diego
W.I. Wang, Columbia University
O.K. Wu, Hughes Research Laboratories

Organizing Committee

O.K. Wu (Chair), Hughes Research Laboratories
J. Arias, Rockwell
Ping Chen, University of Southern California
D. Chow, Hughes Research Laboratories
R. Dawson, Sandia National Laboratories
A. Gossard, Univeristy of California, Santa Barbara
F. Grunthaner, JPL
D.E. Grider (Co-Chair), Hughes Research Laboratories
J.E. Jensen, Hughes Research Laboratories
L. Kolodziejski, MIT
H. Lee, University of California, Irvine
P. Gillis, University of California, Los Angeles
C. Wood, University of Maryland
Yong Zhang, Hughes Research Laboratories

International Advisory Committee

B.G. Streetman (Chair), University of Texas, Austin
P. Bhattacharya, University of Michigan
L.L. Chang, Hong Kong University
A.Y. Cho, Lucent Technologies
L. Esaki, Tsukuba University
J.P. Faurie, CNRS
S. Gonda, Osaka University
K.-F. Huang, National Chiao Tung University
D. Houghton, NRC
E. Kasper, University of Stuttgart
B.A. Joyce, University of London
H. Kroemer, University of California, Santa Barbara
A.-Z. Li, Chinese Academy of Sciences
Th.G. McGill, Cal Tech
J. Miller, Hewlett-Packard Laboratories
L.T. Nuyen, PicoGiga
E.H.C. Parker, University of Warwick
M. Pessa, Tempera University
K.H. Ploog, Paul-Drude Institute
H. Sakaki, University of Tokyo
J.F. Schetzina, North Carolina State University
K.L. Wang, University of California, Los Angeles
G. Weimann, Walter-Schottky Institute

Acknowledgments

Financial support from the following agencies is gratefully acknowledged:

Air Force Office of Scientific Research (AFOSR)
Army Research Office (ARO)
Office of Naval Research (ONR)
National Science Foundation (NSF)
Defense Advanced Research Projects Agency (DARPA)

Exhibitors

ADDON Creative Epitaxy Equipment
Advanced Ceramics Corporation
American Xtal Technology (AXT)
ASTeX/Applied Science Tech.
Bede Scientific, Inc.
Charles Evans & Associates
CI Systems, Inc.
CVD Products, Inc.
DCA Instruments
D&T International Company
EPI MBE Products Group
Fisons Instruments/VG Semicon
Granville-Phillips Company
Johnson Matthey
MCP Wafer Technology
NIMTEC Inc./Japan Energy
OS Technology
Oxford Applied Research
Pacific Lightwave
Riber Division/Instruments SA, Inc.
Shin-etsu Chemical
Staib Instruments, Inc.
Sumitomo Electric (SEMIA, Inc.)
Surface/Interface, Inc.
SVT Associates, Inc.
SVT/EPI MBE Group
Thermionics Laboratory, Inc.
United Mineral & Chemical Corp.
Universal Systems of Tokyo
Varian Vacuum Products
VSI Vacuum Science
VTS J. Schwarz GmbH
Woolam Company

Preface

This issue of the Journal of Crystal Growth contains the papers presented at the 9th International Conference on Molecular Beam Epitaxy (MBE-IX), held at the Pepperdine University campus in Malibu, California, USA, from August 5th to 9th, 1996. This biennial conference has been held among Europe, Japan and United States. Previous conferences were held in Osaka, Japan (1994), Schwäbisch Gmünd, Germany (1992), La Jolla, USA (1990), Sapporo, Japan (1988), York, UK (1986), San Fransisco, USA (1984), Tokyo, Japan (1982), and Paris, France (1978).

MBE-IX was well attended with over 450 attendees coming from 27 countries, among them, 193 from overseas. Besides, 33 commercial vendors participated in an equipment and product exhibit.

In MBE-IX, 265 papers, including 14 invited talks, were selected from 400 abstract submissions. The percentage of papers being selected is the lowest as compared to previous International MBE conferences, indicating strong interest and growth in MBE development. MBE is now of fundamental importance in the creation of advanced new materials and device structures for electronics, optoelectronics, and photonics applications. MBE has progressed to the point that it is now an important tool for both research and production applications. The scope of the conference covered the entire spectrum of MBE technology, from material aspects to device applications. Topics include MBE technology and growth for III–V, II–VI compounds, group-IV elements and alloys; nitrides and antimonides, quantum dots, wires, and wells; in situ monitoring, control, processing, and characterization; gas-source MBE including MOMBE and CBE; and both electrical- and optical-based device applications. A plenary session was held on Applications and future directions of MBE materials to overview and evaluate several MBE-based system insertion and applications.

The MBE-IX committee would like to acknowledge various US federal agencies for their financial support of the conference. The committee also would like to thank Mrs. Ronda Grider and her enthusiastic and able staff for arranging facilities, room and board services, and for running the conference smoothly. The program committee is grateful to the session chairpersons for their excellent handling of the sessions.

About 88% of the 265 papers presented at the conference are included in this volume, resulting in a fairly thick proceedings. The editor would like to thank all the referees for their assistance in producing this volume and acknowledge the invaluable help of Dr. David Grider of Hughes Research Laboratories and Anita Koch and the staff of North-Holland/Elsevier Science.

Yung-Chung Kao

Contents

Preface ix

SECTION I. MBE TECHNOLOGY AND APPLICATIONS

Applications of MBE grown PHEMTs
J.V. DiLorenzo, B. Lauterwasser and M.P. Zaitlin 1
Millimeterwave and digital applications of InP-based MBE grown HEMTs and HBTs
P. Greiling 8
Mass production of InAs Hall elements by MBE
I. Shibasaki 13
High power mid-infrared quantum cascade lasers with a molecular beam epitaxy grown InP cladding operating above room temperature
J. Faist, F. Capasso, C. Sirtori, D.L. Sivco, J.N. Baillargeon, A.L. Hutchinson, S.-N.G. Chu and A.Y. Cho 22
Progress and prospect of group-III nitride semiconductors
I. Akasaki and H. Amano 29
Solid-source MBE for growth of laser diode materials
M. Toivonen, P. Savolainen, H. Asonen and M. Pessa 37
Low threshold 1.3 μm InAsP/GaInAsP lasers grown by solid-source molecular beam epitaxy
C.C. Wamsley, M.W. Koch and G.W. Wicks 42
Solid source MBE growth and regrowth of 1.55 μm wavelength GaInAsP/InP ridge lasers
F.G. Johnson, O. King, F. Seiferth, S. Horst, D.R. Stone, R.D. Whaley, M. Dagenais and Y.J. Chen 46
Virtual control simulator for closed-loop epitaxial growth
J.J. Zhou, Y. Li, D. Pacheco, H.P. Lee and X. Liu 52
Sensor controlled linear motion oven (S-LIMO) for group III flux operation
P.P. Chow, K.R. Evans, A.J. SpringThorpe, P. Fisher, J.J. Klaassen, A. Wowchak and J. Van Hove 61
Improved MBE-grown GaAs using a novel, high-capacity Ga effusion cell
R.N. Sacks, P. Colombo, G.A. Patterson and K.A. Stair 66

SECTION II. NITRIDES

Growth of GaN, InGaN, and AlGaN films and quantum well structures by molecular beam epitaxy
M.A.L. Johnson, W.C. Hughes, W.H. Rowland, Jr., J.W. Cook, Jr., J.F. Schetzina, M. Leonard, H.S. Kong, J.A. Edmond and J. Zavada 72
Optimization of AlGaN films grown by RF atomic nitrogen plasma using in-situ cathodoluminescence
J.M. Van Hove, P.P. Chow, A.M. Wowchak, J.J. Klaassen, M.F. Rosamond and D.R. Croswell 79
Er doping of III-nitrides during growth by metalorganic molecular beam epitaxy
J.D. MacKenzie, C.R. Abernathy, S.J. Pearton, U. Hömmerich, X. Wu, R.N. Schwartz, R.G. Wilson and J.M. Zavada 84
Growth kinetics of GaN grown by gas-source molecular beam epitaxy
J.R. Jenny, R. Kaspi and K.R. Evans 89
Stability of surface reconstructions on hexagonal GaN grown by molecular beam epitaxy
P. Hacke, G. Feuillet, H. Okumura and S. Yoshida 94
Growth and p-type doping of GaN on c-plane sapphire by nitrogen plasma-assisted molecular beam epitaxy
M.C. Yoo, M.Y. Park, S.K. Kang, H.D. Cho and J.W. Lee 100
Surface crystal-structure of a GaN film as an in situ mask using MOMBE
S. Yoshida and M. Sasaki 107
Cathodoluminescence of GaN films grown under Ga and N rich conditions by radio-frequency-molecular beam epitaxy
S.H. Cho, U. Tanaka, T. Maruyama, K. Akimoto, H. Okumura and S. Yoshida 112
Studies of GaN layers grown on sapphire using an RF-source
T.G. Andersson, K. Nozawa and Y. Horikoshi 117
Blue and green electroluminescence from GaN/InGaN heterostructures
R. Averbeck, H. Tews, A. Graber and H. Riechert 122
Zinc blende GaN grown by radio frequency plasma assisted molecular beam epitaxy
H.D. Cho, N.H. Ko, S.H. Park, T.W. Kang, J.W. Han, K.S. Eom, S.H. Won and K.S. Jung 125

Initial growth stage of GaN on Si substrate by alternating source supply using dimethyl-hydrazine
A. Hashimoto, Y. Aiba, T. Motizuki, M. Ohkubo and A. Yamamoto 129
Relation between surface reconstruction transitions and growth kinetics of zincblende (0 0 1) GaN
O. Brandt, H. Yang, A. Yamada and K.H. Ploog 134
Gas source molecular beam epitaxy of cubic GaN/GaAs (0 0 1) using hydrazine
S.A. Nikishin, G.A. Seryogin, H. Temkin, V.G. Antipov, S.S. Ruvimov and A.V. Merkulov 139
N incorporation in GaN_xP_{1-x} and InN_xP_{1-x} using a RF N plasma source
W.G. Bi and C.W. Tu 145
Gas source MBE growth of GaN rich side of $GaN_{1-x}P_x$ using ion-removed ECR radical cell
K. Iwata, H. Asahi, K. Asami and S. Gonda 150

SECTION III. III–V MATERIALS: GROWTH KINETICS AND DOPING

Laterally nonuniform Ga segregation at GaAs/AlGaAs interfaces during MBE growth
W. Braun, A. Trampert, L. Däweritz and K.H. Ploog 156
Suppression of AlGaAs/GaAs superlattice intermixing by p-type doping
K. Muraki and Y. Horikoshi 162
InAs/GaAs in-plane strained superlattices grown on slightly misoriented (1 1 0) InP substrates by molecular beam epitaxy
Y. Nakata, O. Ueda, Y. Nishikawa, S. Muto and N. Yokoyama 168
Surface reconstruction and morphology evolution in highly strained InAs epilayer growth on GaAs(0 0 1) surface
Q. Xue, T. Ogino, H. Kiyama, Y. Hasegawa and T. Sakurai 174
Real space imaging of GaAs/AlAs (0 0 1) heterointerfaces
J. Behrend, M. Wassermeier, W. Braun, P. Krispin and K.H. Ploog 178
Control of chemical composition and band gap energy in $Ga_xIn_{1-x-y}Al_yAs$ on InP during molecular beam epitaxy
J.M. Schneider, J.-T. Pietralla and H. Heinecke 184
Properties of InAs thin films grown on (1 0 0)-oriented GaAs substrate with various tilted angles and directions of misorientation
M. Yamamoto, T. Iwabuchi, T. Ito, T. Yoshida, T. Isoya and I. Shibasaki 191
Low temperature (LT) and stoichiometric low temperature (SLT) MBE GaAs and related compounds: improved structural, electrical and optical properties
M. Missous and S. O'Hagan 197
Growth dynamics of InGaAs/GaAs by MBE
F. Fournier, R.A. Metzger, A. Doolittle, A.S. Brown, C. Carter-Coman, N.M. Jokerst and R. Bicknell-Tassius 203
A Monte Carlo study of gallium desorption kinetics during MBE of (1 0 0)-GaAs/AlGaAs heterostructures
K. Mahalingam, D.L. Dorsey, K.R. Evans and R. Venkatasubramanian 211
Re-entrant behavior of 2D to 3D morphology change and 3D island lateral size equalization via mass exchange in Stranski–Krastanow growth: InAs on GaAs(0 0 1)
T.R. Ramachandran, R. Heitz, N.P. Kobayashi, A. Kalburge, W. Yu, P. Chen and A. Madhukar 216
Heuristic rules for group IV dopant site selection in III–V compounds
R. Venkatasubramanian, D.L. Dorsey and K. Mahalingam 224
Surface segregation of Si in δ-doped $In_{0.53}Ga_{0.47}As$ grown by molecular beam epitaxy
B. Vögele, C.R. Stanley, E. Skuras, A.R. Long and E.A. Johnson 229
Two-dimensional limitations when increasing the Si-concentration from δ-doping to thin Si-layers in GaAs
J.V. Thordson, T.G. Andersson, G. Swenson and U. Södervall 234
Determination of $Al_xGa_{(1-x)}As$ composition: the MBE perspective
Z.R. Wasilewski, M.M. Dion, D.J. Lockwood, P. Poole, R.W. Streater and A.J. SpringThorpe 238

SECTION IV. IN SITU MONITORING AND CONTROL

Monitoring Ga and In desorption and In surface segregation during MBE using atomic absorption
A. Jackson, P. Pinsukanjana, L. Coldren and A. Gossard 244
Simultaneous in situ measurement of substrate temperature and layer thickness using diffuse reflectance spectroscopy (DRS) during molecular beam epitaxy
Y. Li, J.J. Zhou, P. Thompson, D. Pacheco, D.L. Sato, O. Arain and H.P. Lee 250
Application of pyrometric interferometry to the in situ monitoring of $In_{0.52}Al_{0.48}As$, $In_{0.53}Ga_{0.47}As$, and quaternary alloy growth on InP substrates
R.M. Sieg, R.N. Sacks and S.A. Ringel 256

Use of optical fiber pyrometry in molecular beam epitaxy
K.G. Eyink, J.K. Patterson, S.J. Adams, T.W. Haas and W.V. Lampert 262
Measurement of MBE substrate temperature by photoluminescence
Y. Takahira and H. Okamoto 267
Effect of substrate thickness, back surface texture, reflectivity, and thin film interference on optical band-gap thermometry
S.R. Johnson and T. Tiedje 273
Real time in-situ thickness control of Fabry–Perot cavities in MBE by 44 and 88 wavelength ellipsometry
C.H. Kuo, M.D. Boonzaayer, M.F. DeHerrera, D.K. Schroder, G.N. Maracas and B. Johs 281
Two-dimensional to one-dimensional mode change in GaAs molecular beam epitaxy revealed by in situ scanning electron microscopy
N. Inoue, Y. Kawamura, Y. Homma, J. Osaka, T. Araki and T. Ito 286
In situ observation of MEE GaAs growth using scanning electron microscopy
Y. Homma, H. Yamaguchi and Y. Horikoshi 292
A new in situ III–V surface characterization technique: chemical modulation spectroscopy
P.A. Postigo, T. Utzmeier, G. Armelles and F. Briones 298
Electronic properties of monolayer steps on GaAs (0 0 1) surfaces studied by scanning tunneling microscopy
K. Kanisawa, H. Yamaguchi and Y. Horikoshi 304
Evolution of short- and long-range order during Si incorporation on GaAs(0 0 1) observed by RAS and RHEED during MBE
L. Däweritz, K. Stahrenberg, P. Schützendübe, J.-T. Zettler, W. Richter and K.H. Ploog 310
A RHEED and STM study of Sb-rich AlSb and GaSb (0 0 1) surface reconstructions
P.M. Thibado, B.R. Bennett, B.V. Shanabrook and L.J. Whitman 317
Effects of morphology on photoemission oscillation measurements during growth of resonant tunneling devices
J.J. Zinck and D.H. Chow 323
Reflectivity difference spectroscopy study of thin film ZnSe grown on GaAs by molecular beam epitaxy
C.C. Kim, Y.P. Chen, M. Daraselia, S. Sivananthan, S.-C.Y. Tsen and D.J. Smith 328
Real-time monitoring of RHEED using machine vision techniques
R.F. Kromann, R.N. Bicknell-Tassius, A.S. Brown, J.F. Dorsey, K. Lee and G. May 334
In-situ BEEM study of interfacial dislocations and point defects
H. von Känel, T. Meyer and H. Sirringhaus 340
In situ STM characterisation of Ga^+ focused ion beam interactions with MBE grown GaAs(1 0 0)
S.J. Brown, P.D. Rose, E.H. Linfield, D.A. Ritchie, V. Drouot and G.A.C. Jones 346

SECTION V. VERTICAL CAVITY SURFACE EMITTING LASERS GROWTH

MBE growth of highly reproducible VCSELs
Y.M. Houng and M.R.T. Tan 352
Fabrication of InGaAs vertical-cavity surface-emitting lasers by molecular beam epitaxy on (4 1 1)A GaAs substrates and its room-temperature operation
Y. Hanamaki, T. Takeuchi, N. Ogasawara and Y. Shiraki 359
Growth of vertical cavity surface emitting laser material on (3 1 1)B GaAs by MBE
D.E. Mars, S.J. Rosner, Y. Kaneko, S. Nakagawa, T. Takeuchi and N. Yamada 365
Molecular beam epitaxy of AlGaAsSb system for 1.55 μm Bragg mirrors
J.C. Harmand, A. Kohl, M. Juhel and G. Le Roux 372
Carbon delta doping in chemical beam epitaxy using CBr_4
T.B. Joyce, T.J. Bullough, T. Farrell, B.R. Davidson, D.E. Sykes and A. Chew 377
Strain compensation in highly carbon doped GaAs/AlAs distributed Bragg reflectors
A. Mazuelas, R. Hey, M. Wassermeier and H. T. Grahn 383

SECTION VI. IN SITU PROCESSING: ETCHING AND REGROWTH

Improving the etched/regrown GaAs interface by in-situ etching using tris-dimethylaminoarsenic
N.Y. Li, Y.M. Hsin, P.M. Asbeck and C.W. Tu 387
Analysis of in-situ etched and regrown AlInAs/GaInAs interfaces
P. Chavarkar, D.S.L. Mui, T. Strand, L.A. Coldren and U.K. Mishra 393

Selective area epitaxy of GaAs using very low energy Ga^+ focused ion beam deposition combined with molecular beam epitaxial growth
H.E. Beere, J.H. Thompson, G.A.C. Jones and D.A. Ritchie 398
Selective area chemical beam epitaxial regrowth of Si-doped GaAs by using silicon tetraiodide for field effect transistor application
S. Izumi, Y. Yamamoto, T. Kunii, S. Miyakuni, N. Hayafuji, K. Sato and M. Otsubo 404
MBE regrowth on AlGaInAs DFB gratings using in-situ hydrogen radical cleaning
H. Künzel, J. Böttcher, A. Hase, H.-J. Hensel, K. Janiak, G. Urmann and A. Paraskevopoulos 411
Hydrogen radical surface cleaning of GaAs for MBE regrowth
T.M. Burke, E.H. Linfield, D.A. Ritchie, M. Pepper and J.H. Burroughes 416
Novel $Ga_2O_3(Gd_2O_3)$ passivation techniques to produce low D_{it} oxide-GaAs interfaces
M. Hong, J.P. Mannaerts, J.E. Bower , J. Kwo, M. Passlack, W-Y. Hwang and L.W. Tu 422
Iodine-assisted molecular beam epitaxy
M. Micovic, D. Lubyshev, W.Z. Cai, F. Flack, R.W. Streater, A.J. SpringThorpe and D.L. Miller 428
Passivation of misfit dislocations by atomic hydrogen irradiation in lattice-mismatched heteroepitaxy
M. Yokozeki, H. Yonezu, T. Tsuji and N. Ohshima 435
Formation of an n-GaAs/n-GaAs regrowth interface without carrier depletion using electron cyclotron resonance hydrogen plasma
T. Niwa, N. Furuhata and T. Maeda 441
High-temperature surface cleaning of AlGaAs without As flux for MBE regrowth
K. Iizuka, K. Matsumaru, T. Suzuki, Y. Takahira, T. Nishioka and H. Okamoto 447

SECTION VII. GROUP IV MATERIALS: Si, SiGe, AND SiC

Fabrication and band alignment of pseudomorphic $Si_{1-y}C_y$, $Si_{1-x-y}Ge_xC_y$ and coupled $Si_{1-y}C_y/Si_{1-x-y}Ge_xC_y$ quantum well structures on Si substrates
K. Brunner, W. Winter, K. Eberl, N.Y. Jin-Phillipp and F. Phillipp 451
MBE growth and structural characterization of $Si_{1-y}C_y/Si_{1-x}Ge_x$ superlattices
S. Zerlauth, J. Stangl, A.A. Darhuber, V. Holý, G. Bauer and F. Schäffler 459
Why is a quantum-confined Stark shift absent in type-I strained $Si_{1-x}Ge_x$/Si symmetric quantum wells?
Y. Miyake, J.Y. Kim, Y. Shiraki and S. Fukatsu 465
Sidewall faceting and inter-facet mass transport in selectively grown epitaxial layers on SiO_2-masked Si(1 1 0) substrates
Q. Xiang, S. Li, D. Wang, K. Sakamoto, K.L. Wang, G. U'Ren and M. Goorsky 469
Enhancement of substitutional carbon incorporation in hydrogen-mediated pseudomorphic growth of strained alloy layers on Si(0 0 1)
G. Lippert, P. Zaumseil, H.J. Osten and M. Kim 473
New hydrogen desorption kinetics from vicinal Si(0 0 1) surfaces observed by reflectance anisotropy spectroscopy
J. Zhang, A.K. Lees, A.G. Taylor, M.H. Xie, B.A. Joyce, Z. Sobiesierksi and D.I. Westwood 477
Reduction of SiGe heterointerface mixing by atomic hydrogen irradiation during molecular beam epitaxy and its mechanism
K. Nakagawa, Y. Kimura and M. Miyao 481
Control of composition and crystallinity in the molecular beam epitaxy of strain-compensated $Si_{1-x-y}Ge_xC_y$ alloys on Si
E.T. Croke, A.T. Hunter, C.C. Ahn, T. Laursen, D. Chandrasekhar, A.E. Bair, D.J. Smith and J.W. Mayer 486
Stratified suspension of highly ordered Si nanoparticles in SiO_2 created by Si MBE with oxygen co-implantation
Y. Ishikawa, N. Shibata and S. Fukatsu 493
Characterization of mismatched SiGe grown on low temperature Si buffer layers by molecular beam epitaxy
K.K. Linder, F.C. Zhang , J.-S. Rieh and P. Bhattacharya 499
Hybrid MBE growth and mobility limiting factors of *n*-channel Si/SiGe modulation-doped systems
A. Yutani and Y. Shiraki 504
Effect of Hydrogen on the growth kinetics of Si(0 0 1) during GSMBE from disilane
K. Mizushima, D.D. Vvedensky, P. Šmilauer, A. Zangwill, J. Zhang and B.A. Joyce 509
Visible light emission from MBD-grown Si/SiO_2 superlattices
S.V. Novikov, J. Sinkkonen, O. Kilpelä and S.V. Gastev 514
Luminescence study on Ge islands as stressors on $Si_{1-x}Ge_x$/Si quantum well
E.S. Kim, N. Usami, H. Sunamura, S. Fukatsu and Y. Shiraki 519
The growth and luminescence of SiGe dots
H. Chen, X.G. Xie, W.Q. Cheng, Q. Huang and J.M. Zhou 524

Characterization of homoepitaxial SiC layers
J. Schmitt, T. Troffer, K. Christiansen, M. Schadt, S. Christiansen, R. Helbig, G. Pensl and H.P. Strunk 528

SECTION VIII. II–VI MATERIALS

II–VI light-emitting devices based on beryllium chalcogenides
F. Fischer, G. Landwehr, Th. Litz, H.J. Lugauer, U. Zehnder, Th. Gerhard, W. Ossau and A. Waag 532
Molecular beam epitaxial growth of lattice-matched $Zn_xCd_yMg_{1-x-y}Se$ quaternaries on InP substrates
L. Zeng, A. Cavus, B.X. Yang, M.C. Tamargo, N. Bambha, A. Gray and F. Semendy 541
Surface preparation of ZnSe substrates for MBE growth of II–VI light emitters
W.C. Hughes, C. Boney, M.A.L. Johnson, J.W. Cook, Jr. and J.F. Schetzina 546
Reduction of extended defects in II–VI blue–green laser diodes
T.B. Ng, C.C. Chu, J. Han, G.C. Hua, R.L. Gunshor, E. Ho, E.L. Warlick, L.A. Kolodziejski and A.V. Nurmikko 552
Optimized growth of lattice-matched ZnCdSe epilayers on InP substrates
A. Cavus, L. Zeng, B.X. Yang , N. Dai, M.C. Tamargo, N. Bambha and F. Semendy 558
Reducing the defect density in MBE-ZnSe/III–V heterostructures
E.L. Warlick, E. Ho, G.S. Petrich and L.A. Kolodziejski 564
Investigation of the structural properties of MBE grown ZnSe/GaAs heterostructures
I. Hernández-Calderón, E. López-Luna, J. Luyo, M. Meléndez-Lira, O. de Melo, P. Díaz, L. Hernández, J. Fuentes, R. León and H. Sitter 571
ZnSe homoepitaxial growth on solid-phase recrystallized substrates
E. Tournié, P. Brunet, C. Ongaretto, C. Morhain, J.-P. Faurie, R. Triboulet and J.O. Ndap 577
MBE growth of n-type ZnSe and ZnS using ethylchloride as a dopant
T. Yasuda, B.-P. Zhang and Y. Segawa 583
Growth mechanism of II–VI compound semiconductors by molecular beam epitaxy
H. Okuyama, T. Kawasumi, A. Ishibashi and M. Ikeda 587
Hydrogen sulfide treatment of GaAs substrate and its effects on initial stage of ZnSe growth
J. Suda, R. Tokutome, Y. Kawakami, Sz. Fujita and Sg. Fujita 593
Homogeneous and δ-doped ZnS:Mn grown by MBE
S. Schön, M. Chaichimansour, W. Park, T. Yang, B.K. Wagner and C.J. Summers 598
Electrical characterization of engineered ZnSe–GaAs heterojunction diodes
M. Lazzeri, V. Pellegrini, F. Beltram, M. Lazzarino, J.J. Paggel, L. Sorba, S. Rubini, A. Bonanni and A. Franciosi 603
Molecular beam epitaxial growth of ZnSe(1 1 1) films on GaAs(1 1 1)B substrates and nitrogen doping
N. Matsumura, T. Matsuoka, H. Shimakawa and J. Saraie 608
Molecular beam epitaxial growth of ZnSe on GaAs substrates: influence of precursors on interface quality
C.C. Kim, Y.P. Chen, S. Sivananthan, S.-C.Y. Tsen and D.J. Smith 613
p-Type doping of beryllium chalcogenides grown by molecular beam epitaxy
H.-J. Lugauer, Th. Litz, F. Fischer, A. Waag, T. Gerhard, U. Zehnder, W. Ossau and G. Landwehr 619
Molecular beam epitaxy of BeTe on vicinal Si(1 0 0) Surfaces
X. Zhou, S. Jiang and W.P. Kirk 624
Blue-light emission from ZnSTe-based EL devices
I.K. Sou, J. Mao, Z. Ma, W.S. Chen, Z. Yang, K.S. Wong and G.K.L. Wong 632
Room-temperature continuous-wave operation of ZnSe-based blue–green laser diode grown by molecular beam epitaxy
Moon-Deock Kim, Bong-Jin Kim, Min-Hyon Jeon, Jeong-Keun Ji, Sang-Dong Lee, Eun-Soon Oh, Jin-Suck Kim, Hae-Sung Park and Tae-Il Kim 637
Growth and characterization of lattice-matched HgSe
L. Parthier, H. Wißmann, S. Luther, G. Machel, M. Schmidbauer, R. Köhler and M. von Ortenberg 642
p-Type doping with arsenic in (2 1 1)B HgCdTe grown by MBE
P.S. Wijewarnasuriya, F. Aqariden, C.H. Grein, J.P. Faurie and S. Sivananthan 647
High performance HgCdTe two-color infrared detectors grown by molecular beam epitaxy
R.D. Rajavel, D.M. Jamba, O.K. Wu, J.E. Jensen, J.A. Wilson, E.A. Patten, K. Kosai, P. Goetz, G.R. Chapman and W.A. Radford 653
Ellipsometric analysis of CdZnTe preparation for HgCdTe MBE growth
J.D. Benson, A.B. Cornfeld, M. Martinka, J.H. Dinan, B. Johs, P. He and J.A. Woollam 659
Molecular beam epitaxial growth of the CdMnTe/CdTe superlattices on (100) GaAs substrates
M. Yano, K. Koike, T. Furushou and T. Yodo 665

Elastic and plastic deformation in low mismatched $Cd_xHg_{1-x}Te/Cd_{1-y}Zn_yTe$
T. Colin, T. Skauli and S. Løvold 670
A study of MBE growth and thermal annealing of p-type long wavelength HgCdTe
L. He, J.R. Yang, S.L. Wang, S.P. Guo, M.F. Yu, X.Q. Chen, W.Z. Fang, Y.M. Qiao, Q.Y. Zhang, R.J. Ding and T.L. Xin 677
Nitrogen doping of Te-based II–VI compounds
S. Tatarenko, T. Baron, A. Arnoult, J. Cibert, M. Grün, A. Haury, Y. Merle d'Aubigné, A. Wasiela and K. Saminadayar 682

SECTION IX. QUANTUM DOTS

Low-threshold injection lasers based on vertically coupled quantum dots
V.M. Ustinov, A.Yu. Egorov, A.R. Kovsh, A.E. Zhukov, M.V. Maximov, A.F. Tsatsul'nikov, N.Yu. Gordeev, S.V. Zaitsev, Yu.M. Shernyakov, N.A. Bert, P.S. Kop'ev, Zh.I. Alferov, N.N. Ledentsov, J. Böhrer, D. Bimberg, A.O. Kosogov, P. Werner and U. Gösele 689
Overgrowth of InGaAs quantum dots formed by alternating molecular beam epitaxy
R.P. Mirin, J.P. Ibbetson, J.E. Bowers and A.C. Gossard 696
Self-assembling InP quantum dots for red lasers
K. Eberl, A. Kurtenbach, M. Zundel, J.Y. Jin-Phillipp, F. Phillipp, A. Moritz, R. Wirth and A. Hangleiter 702
Increased size uniformity through vertical quantum dot columns
G.S. Solomon, S. Komarov, J.S. Harris, Jr. and Y. Yamamoto 707
Self-assembled structures of closely stacked InAs islands grown on GaAs by molecular beam epitaxy
Y. Nakata, Y. Sugiyama, T. Futatsugi and N. Yokoyama 713
Room temperature luminescence from self-organized $In_xGa_{1-x}As/GaAs$ ($0.35 < x < 0.45$) quantum dots with high size uniformity
K. Kamath, P. Bhattacharya and J. Phillips 720
Growth and characterization of self-organized InSb quantum dots and quantum dashes
T. Utzmeier, J. Tamayo, P.A. Postigo, R. García and F. Briones 725
MBE growth of novel GaAs/n-AlGaAs field-effect transistor structures with embedded InAs quantum traps and their transport characteristics
G. Yusa and H. Sakaki 730
In situ RHEED control of direct MBE growth of Ge quantum dots on Si (0 0 1)
V.A. Markov, A.I. Nikiforov and O.P. Pchelyakov 736
Growth controlled fabrication and cathodoluminescence study of 3D confined GaAs volumes on non-planar patterned GaAs(0 0 1) substrates
A. Konkar, H.T. Lin, D.H. Rich, P. Chen and A. Madhukar 741
Manipulating InAs island sizes with chemical beam epitaxy growth on GaAs patterns
M.S. Miller, L. Landin, S. Jeppesen, A. Petersson, I. Maximov, B. Kowalski and L. Samuelson 747
Self-organized quantum dot structures in strained $(GaP)_n(InP)_m$ short period superlattices grown on GaAs (N 1 1) by gas-source MBE
S.J. Kim, H. Asahi, M. Takemoto, K. Asami, J.H. Noh and S. Gonda 754
Intersubband absorption from $In_{0.26}Ga_{0.74}As/GaAs$ quantum dot superlattice
D. Pan, Y.P. Zeng, J.M. Li, C.H. Zhang, M.Y. Kong, H.M. Wang, C.Y. Wang and J. Wu 760
Molecular-beam epitaxy of self-assembled InAs quantum dots on non-(1 0 0) oriented GaAs
P.P. González-Borrero, E. Marega, Jr., D.I. Lubyshev, E. Petitprez and P. Basmaji 765
InAs/GaAs self-assembled quantum dots grown by ALMBE and MBE
A. Bosacchi, P. Frigeri, S. Franchi, P. Allegri and V. Avanzini 771
Formation of self-organized $In_{0.5}Ga_{0.5}As$ quantum dots on GaAs by molecular beam epitaxy
Jen-Inn Chyi, Tzer-En Nee, Ching-Ting Lee, Jia-Lin Shieh and Jen-Wei Pan 777
MBE growth and magnetotunnelling transport properties of a single GaAs/AlAs/GaAs barrier incorporating InAs quantum dots
M. Henini, I.E. Itskevich, T. Ihn, P. Moriarty, A. Nogaret, P.H. Beton, L. Eaves, P.C. Main, J.R. Middleton and J.S. Chauhan 782

SECTION X. QUANTUM WIRES

Selective MBE growth of GaAs wire and dot structures using atomic hydrogens and their electronic properties
T. Noda, Y. Nagamune, Y. Ohno, S. Koshiba and H. Sakaki 787

Molecular beam epitaxial growth of InGaAs/InGaAsP quantum wires on V-grooved InP substrates with (1 1 1) sidewalls
J. Wang, D.A. Thompson, B.J. Robinson and J.G. Simmons 793
Vertically stacked quantum wires fabricated by an in situ processing technique
M. López-López and T. Ishikawa 799
UHV-AFM study of MBE-grown 10 nm scale ridge quantum wires
S. Koshiba, I. Tanaka, Y. Nakamura, I. Kamiya, T. Someya, T. Ngo and H. Sakaki 804
Improved optical qualities of GaAs/$Al_{0.3}Ga_{0.7}As$ tilted T-shaped quantum wires fabricated by glancing-angle molecular beam epitaxy
N. Tomita, T. Kishi, K. Takekawa, K. Fujita, T. Watanabe, A. Adachi, S. Shimomura and S. Hiyamizu 809
High-density GaAs/$(GaAs)_2(AlAs)_2$ quantum wires naturally formed on (7 7 5)B-oriented GaAs substrates by molecular beam epitaxy
M. Higashiwaki, M. Yamamoto, S. Shimomura, A. Adachi and S. Hiyamizu 814
Growth of GaInAsP quantum wire heterostructures using the strain-induced lateral-layer ordering process
A.M. Moy, A.C. Chen, K.Y. Cheng, L.J. Chou and K.C. Hsieh 819

SECTION XI. ANTIMONIDE MATERIALS

MBE growth of high-power InAsSb/InAlAsSb quantum-well diode lasers emitting at 3.5 μm
G.W. Turner, M.J. Manfra, H.K. Choi and M.K. Connors 825
Microstructural properties of InAs/$InAs_xSb_{1-x}$ superlattices and $InAs_xSb_{1-x}$ ordered alloys grown by modulated molecular beam epitaxy
Y.-H. Zhang, A. Lew, E. Yu and Y. Chen 833
Sb-surface segregation and the control of compositional abruptness at the GaAsSb/GaAs interface
R. Kaspi and K.R. Evans 838
MBE growth of Si-doped InAlAsSb layers lattice-matched with InAs
M. Kudo and T. Mishima 844
Molecular beam epitaxial growth of GaInSbBi for infrared detector applications
Q. Du, J. Alperin and W.I. Wang 849
Large mismatch heteroepitaxy of InSb on Si(1 1 1) substrates using CaF_2 buffer layers
W.K. Liu, X.M. Fang, J. Winesett, W. Ma, X. Zhang, M.B. Santos and P.J. McCann 853
Indium antimonide doped with manganese grown by molecular beam epitaxy
D.L. Partin, J. Heremans and C.M. Thrush 860
Molecular beam epitaxial growth of high electron mobility InAs/AlGaAsSb deep quantum well structures
N. Kuze, H. Goto, M. Matsui, I. Shibasaki and H. Sakaki 868
MBE growth and characterization of high-quality GaInAsSb/AlGaAsSb strained multiple quantum well structures
A.Z. Li, Y. Zhao, Y.L. Zheng , G.T. Chen, G.P. Ru, W.Z. Shen and J.Q. Zhong 873
MBE growth of GaInAsSb p/n junction diodes for thermophotovoltaic applications
P.N. Uppal, G. Charache, P. Baldasaro, B. Campbell, S. Loughin, S. Svensson and D. Gill 877
Molecular-beam-epitaxial growth of $Ga_{1-x}In_xSb$ on GaAs substrates
J.H. Roslund, O. Zsebők, G. Swenson and T.G. Andersson 883
Stranski–Krastanov growth of InSb, GaSb, and AlSb on GaAs: structure of the wetting layers
B.R. Bennett, B.V. Shanabrook, P.M. Thibado, L.J. Whitman and R. Magno 888
Buffer-dependent mobility and morphology of InAs/(Al,Ga)Sb quantum wells
M. Thomas, H.-R. Blank, K.C. Wong and H. Kroemer 894

SECTION XII. DEVICES: ELECTRICAL-BASED

Molecular beam epitaxy of vertically compact $Al_xGa_{1-x}As$/GaAs laser-HEMT structures for monolithic integration
A. Gaymann, J. Schaub, W. Bronner, N. Grün, J. Hornung and K. Köhler 898
MBE growth of quaternary InGaAlAs layers in InGaAs/InAlAs HBTs to improve device performance
T.R. Block, J. Cowles, L. Tran, M. Wojtowicz, A.K. Oki and D.C. Streit 903
Improved hole transport properties of highly strained $In_{0.35}Ga_{0.65}As$ channel double-modulation-doped structures grown by MBE on GaAs
M. Kudo, H. Matsumoto, T. Tanimoto, T. Mishima and I. Ohbu 910
MBE growth of double-sided doped InAlAs/InGaAs HEMTs with an InAs layer inserted in the channel
M. Sexl, G. Böhm, D. Xu, H. Heiß, S. Kraus, G. Tränkle and G. Weimann 915

Resonant tunnelling of holes in double barrier heterostructures grown by MBE on (1 1 0) oriented GaAs substrates
M. Henini, R.K. Hayden, T. Takamasu, N. Miura, L. Eaves and G. Hill 919
GaAs/AlAs resonant tunneling diodes with super-flat interfaces grown on (4 1 1)A GaAs substrates by MBE
K. Shinohara, K. Kasahara, S. Shimomura, A. Adachi, N. Sano and S. Hiyamizu 924
Photoluminescence characterization of MBE grown AlGaAs/InGaAs/GaAs pseudomorphic HEMTs
M. Wojtowicz, D. Pascua, A.-C. Han, T.R. Block and D.C. Streit 930

SECTION XIII. DEVICES: OPTICAL-BASED

Multispectral InGaAs/GaAs/AlGaAs laser arrays by MBE growth on patterned substrates
K. Kamath, P. Bhattacharya and J. Singh 935
MBE growth of high-quality InP for GaInAs/InP heterostructures using incongruent evaporation of GaP
H. Künzel, J. Böttcher, P. Harde and R. Maessen 940
Gas-source molecular beam epitaxial growth of low threshold current 1.3 μm InAsP/InGaAsP lasers
P. Thiagarajan, G.E. Giudice, H. Temkin and G.Y. Robinson 945
High temperature (Ga)InAsP/high band gap GaInAsP barriers 1.3 μm SL-MQW lasers grown by gas source MBE
Ph. Pagnod-Rossiaux, F. Gaborit, N. Tscherptner, L. Roux, C. Starck and B. Fernier 948
MBE grown mid-infrared type-II quantum-well lasers
C.-H. Lin, S.J. Murry, D. Zhang, P.C. Chang, Y. Zhou, S.S. Pei, J.I. Malin, C.L. Felix, J.R. Meyer, C.A. Hoffman and J.F. Pinto 955
Waveguide modulator structures with soft optical confinement grown by the epitaxial shadow mask (ESM) MBE-technique
S. Malzer, W. Geißelbrecht, U. Hilburger, M. Kneissl, P. Kiesel, R. Mayer and G.H. Döhler 960
The growth and characterization of two new P-type compressively strained layer InGaAs/AlGaAs/GaAs quantum well infrared photodetectors for mid- and long-wavelength infrared detection
J. Chu, S.S. Li and P. Ho 964
Large array of GaAs modulators and detectors flip-chip solder bonded to silicon CMOS using InGaP as the selective etch stop for GaAs substrate removal
J.M. Kuo, Y.C. Wang, K.W. Goossen, L.M.F. Chirovsky, S.P. Hui, B.T. Tseng, J. Walker, A.L. Lentine, R.E. Leibenguth, G. Livescu, W.Y. Jan, J.E. Cunningham, L.A. D'Asaro, A. Ron, D. Dahringer, D. Kossives, D.D. Bacon, R.L. Morrison, R.A. Novotny, D.B. Buchholz and W.E. Mayo 971
Molecular beam epitaxy of strain-compensated InGaAs/GaAsP quantum-well intersubband photodetectors
K. Bacher, S. Massie and M. Seaford 977
MBE growth and characterization of doped multiple quantum well avalanche photodiodes
H.M. Menkara, R.N. Bicknell-Tassius, R. Benz, II, and C.J. Summers 983
Low dark current AlGaInAs/InP waveguide photodiodes using hybrid MBE and MOCVD growth
K. Nishikata, H. Shimizu, K. Hiraiwa, S. Yoshida, N. Yamanaka, M. Irikawa and A. Kasukawa 990
Improved electroabsorption properties in 1.3 μm MQW waveguide modulators by a modified doping profile
X.B. Mei, K.K. Loi, W.S.C. Chang and C.W. Tu 994
Investigation of Si-doped p-type AlGaAs/GaAs, AlGaAs/InGaAs quantum well infrared photodetectors and multiquantum wells grown on (3 1 1)A GaAs
A. Chin, C.C. Liao, J. Chu and S.S. Li 999
808 nm high-power laser grown by MBE through the control of Be diffusion and use of superlattice
Donghai Zhu, Zhanguo Wang, Jiben Liang, Bo Xu, Zhanping Zhu, Jun Zhang, Qian Gong and Shengying Li 1004

SECTION XIV. HETEROEPITAXY: METAMORPHIC, MAGNETIC, AND OTHER MATERIALS

Continuously graded buffers for InGaAs/GaAs structures grown on GaAs
A. Bosacchi, A.C. De Riccardis, P. Frigeri, S. Franchi, C. Ferrari, S. Gennari, L. Lazzarini, L. Nasi, G. Salviati, A.V. Drigo and F. Romanato 1009
Molecular beam epitaxy growth and characterization of $In_xGa_{1-x}As$ ($0.57 \leqslant x \leqslant 1$) on GaAs using InAlAs graded buffer
S.M. Wang, C. Karlsson, N. Rorsman, M. Bergh, E. Olsson, T.G. Andersson and H. Zirath 1016
Improved nucleation and spiral growth of PbTe on BaF_2 (1 1 1)
A.Y. Ueta, G. Springholz and G. Bauer 1022
Molecular beam epitaxy of $Al_{0.48}In_{0.52}As/Ga_{0.47}In_{0.53}As$ heterostructures on metamorphic $Al_xGa_yIn_{1-x-y}As$ buffer layers
M. Haupt, K. Köhler, P. Ganser, S. Müller and W. Rothemund 1028
Incorporation of As_2 in $InAs_xP_{1-x}$ and its application to $InAs_xP_{1-x}$/InP quantum well structures
M. Hopkinson and J.P.R. David 1033

Growth of abrupt GaAs/Ge heterointerfaces by atomic hydrogen-assisted molecular beam epitaxy
Y. Okada, J.S. Harris, Jr., A. Sutoh and M. Kawabe 1039
Growth and characterization of In_2Se_3 epitaxial films by molecular beam epitaxy
T. Okamoto, A. Yamada and M. Konagai 1045
Effects of strain on the growth and properties of $CuInSe_2$ epitaxial films
S. Niki, P.J. Fons, H. Shibata, T. Kurafuji, A. Yamada, Y. Okada, H. Oyanagi, W.G. Bi and C.W. Tu 1051
MBE growth of $PbSe/CaF_2/Si(1\ 1\ 1)$ heterostructures
P.J. McCann, X.M. Fang, W.K. Liu, B.N. Strecker and M.B. Santos 1057
(GaMn)As:GaAs-based III–V diluted magnetic semiconductors grown by molecular beam epitaxy
T. Hayashi, M. Tanaka, T. Nishinaga, H. Shimada, H. Tsuchiya and Y. Otuka 1063
Epitaxy of (Ga, Mn)As, a new diluted magnetic semiconductor based on GaAs
A. Shen, H. Ohno, F. Matsukura, Y. Sugawara, N. Akiba, T. Kuroiwa, A. Oiwa, A. Endo, S. Katsumoto and Y. Iye 1069

SECTION XV. MBE GROWTH ON VICINAL SUBSTRATES

Growth parameter dependence of step patterns in AlGaAs molecular beam epitaxy on vicinal GaAs(1 1 0) inclined toward (1 1 1)A
S. Hasegawa, K. Sato, S. Torii and H. Nakashima 1075
Effects of tensile strain and substrate off-orientation on the growth of GaInAs/InP multiple quantum well structures by CBE
T. Marschner, R.T.H. Rongen, M.R. Leys, F.D. Tichelaar, H. Vonk and J.H. Wolter 1081
Organized growth of GaAs/AlAs lateral superlattices on vicinal surfaces: where are the limits?
F. Laruelle, F. Lelarge, Z.Z. Wang, T. Mélin, A. Cavanna and B. Etienne 1087
Formation of multi-atomic steps and novel n-AlGaAs/GaAs heterojunctions on vicinal (1 1 1)B substrates by MBE and anisotropic transport of 2D electrons
Y. Nakamura, S. Koshiba and H. Sakaki 1092
MBE growth of two-dimensional electron gases on (110) GaAs
C.B. Sørensen, H. Gislason and J.M. Hvam 1097
The building up of terrace periodicity by MBE growth on (0 0 1) GaAs vicinal surfaces
F. Lelarge, Z.Z. Wang, A. Cavanna, F. Laruelle and B. Etienne 1102
Photoluminescence investigation of p-type Si-doped AlGaAs grown by molecular beam epitaxy on (1 1 1)A, (2 1 1)A and (3 1 1)A GaAs surfaces
M. Henini, N. Galbiati, E. Grilli, M. Guzzi and L. Pavesi 1108
Patterned growth on GaAs (3 1 1)A substrates
R. Nötzel, J. Menniger, M. Ramsteiner, A. Trampert, H.-P. Schönherr, L. Däweritz and K.H. Ploog 1114

SECTION XVI. SINGLE AND MULTIPLE QUANTUM WELLS

Strain-balanced AlGaInAs/InP heterostructures with up to 50 QWs by MBE
H. Hillmer, R. Lösch and W. Schlapp 1120
New route to reduce ionized impurity scattering in modulation-doped GaAs quantum wells
R. Hey, K.-J. Friedland, H. Kostial, R. Klann and H.K. Ploog 1126
The growth of AlGaAs–InGaAs quantum-well structures by molecular beam epitaxy: observation of critical interdependent effects utilizing the design of experiments approach
R.N. Bicknell-Tassius, K. Lee, A.S. Brown, G. Dagnall and G. May 1131
MBE growth and physics of strongly coupled p-type double quantum wells showing correlated $\nu = 1$ quantum Hall state
M. Henini, R.J. Hyndman, T. Ihn, B.L. Gallagher, T.J. Foster, J.S. Chauhan and J.R. Middleton 1138
Photoluminescence study of Si/SiGe multiple quantum wells grown by MBE
D. Grützmacher, R. Hartmann, E. Müller, U. Gennser and A. Dommann 1144
Photoluminescence spectra of shadow masked multiple quantum wells
S. Sopitpan, P. Cheewatas, S. Thainoi, S. Ratanathammaphan and S. Panyakeow 1152
Radiative decay in type-II GaP/AlP/GaP quantum wells
S. Nagao, K. Fujii, T. Fujimori, H. Gotoh, H. Ito and F. Minami 1157
Temperature-insensitive photoluminescence above 300 K in strained $Ga_xIn_{1-x}As$ multiple quantum wire heterostructures
D.E. Wohlert, S.T. Chou and K.Y. Cheng 1162

Growth-mode-induced surface morphology and its relation to optical properties of GaAs single quantum wells
R. Hey, I. Gorbunova, M. Ramsteiner, M. Wassermeier, L. Däweritz and K.H. Ploog 1167
Photoluminescence of low-temperature AlGaAs/GaAs multiple quantum wells
W. Feng, F. Chen, Q. Huang and J.M. Zhou 1173

SECTION XVII. GAS SOURCE MBE: MOMBE AND CBE

Surface chemistry during metalorganic molecular beam epitaxy studied by pulsed molecular beam scattering
M. Sasaki and S. Yoshida 1178
Lateral coupling of InP/GaInAsP/InP structures by selective area MOMBE
M. Wachter, U. Schöffel, M. Schier and H. Heinecke 1186
New semiconductors TlInGaP and their gas source MBE growth
H. Asahi, M. Fushida, K. Yamamoto, K. Iwata, H. Koh, K. Asami, S. Gonda and K. Oe 1195
CBE of 1.55 μm (GaIn)(AsP) lasers for monolithic integration
A. Nutsch, B. Torabi, H. Kratzer, G. Tränkle and G. Weimann 1200
MOMBE growth of highly tensile-strained InGaAsP MQWs and their applications to 1.3-μm wavelength low threshold current lasers
H. Sugiura, M. Ogasawara, M. Mitsuhara, N. Yamamoto and M. Itoh 1205
Growth and transformation of ultra-thin InAs/InP layers obtained by chemical beam epitaxy
N. Lebouché-Girard, A. Rudra and E. Kapon 1210
Transient surface states during the CBE growth of GaAs
T. Farrell, D. Hill, T.B. Joyce, T.J. Bullough and P. Weightman 1217
Be redistribution in InGaAs and InP grown by gas source molecular beam epitaxy
T. Mozume and K. Hosomi 1223
Growth temperature-dependent conduction-type inversion of C-doped InGaAs grown by chemical beam epitaxy
Jeong-Rae Ro, Sung-Bock Kim, Seong-Ju Park and El-Hang Lee 1231
Selective area etching of III–V semiconductors using TDMAAs and TDMASb in metalorganic molecular beam epitaxy chamber
K. Yamamoto, H. Asahi, T. Hayashi, K. Hidaka and S. Gonda 1236
Indium surface segregation during chemical beam epitaxy of $Ga_{1-x}In_xAs$/GaAs and $Ga_{1-x}In_xP$/GaAs heterostructures
M. Mesrine, J. Massies, C. Deparis, N. Grandjean, E. Vanelle and M. Leroux 1242
Full gaseous source growth of separate confinement MQW 1.55 μm laser structures in a production MOMBE
M. Popp, H. Heinecke, H. Baumeister and E. Veuhoff 1247
GSMBE growth and characterization of $In_xGa_{1-x}As$/InP strained-layer MQWs in a P-i-N Configuration
Wang Xiaoliang, Sun Dianzhao, Kong Meiying, Hou Xun, Zeng Yiping 1254
Symmetric triangular-barrier optoelectronic switch (S-TOPS) by gas source MBE
H. Sakata, Y. Nagao and Y. Matsushima 1259
Chemical beam epitaxy growth of tensile-strained GaAsP/GaAlAs quantum well heterostructures for laser application
J.Ch. Garcia, A. Lebkiri, A. Fily, Ph. Collot, J. Massies and M. Leroux 1265

SECTION XVIII. MBE GROWTH CHARACTERIZATION AND ANALYSIS

Contamination in molecular beam epitaxy: the role of arsenic drag effect
Z.R. Wasilewski, S.J. Rolfe and R.A. Wilson 1270
Photoluminescence and X-ray characterization of relaxed $Si_{1-x}Ge_x$ alloys grown on silicon on insulator (SOI) and implanted SOI substrates
M.A. Chu, M.O. Tanner, F. Huang, K.L. Wang, G.G. Chu and M.S. Goorsky 1278
Modulated-beam studies of the layer-by-layer etching of GaAs(0 0 1) using $AsBr_3$: identification of the reaction mechanism
J. Zhang, O.P. Naji, P. Steans, P. Tejedor, T. Kaneko, T.S. Jones and B.A. Joyce 1284
Morphology of MBE grown InAs films studied by atomic force microscope
Y. Wang, Y.N. Sheng, W. Ge, J. Wang, L.L. Chang, J. Xie, J. Ma and J. Xu 1289
Luminescence anomaly in band gap tailored $In_{0.53}(Ga_xAl_{1-x})_{0.47}As$ quaternary alloy grown by molecular beam epitaxy
A. Ramam and S.J. Chua 1294
Full wafer optical characterisation of resonant tunnelling structures using photoluminescence excitation spectroscopy
P.D. Buckle, P. Dawson, M. Missous and W.S. Truscott 1299

Scanning tunneling spectroscopy and first-principles investigation on GaAs(0 0 1)(2 × 6)-S surface formed by molecular beam epitaxy
S. Tsukamoto, T. Ohno and N. Koguchi 1303

Does scanning tunnelling microscopy provide a realistic picture of the step array of vicinal GaAs(0 0 1) surfaces grown at high temperature?
L. Däweritz, H. Nörenberg, P. Schützendübe and K.H. Ploog 1309

Substrate temperature change in III–V molecular beam epitaxy
K.R. Evans, J.E. Ehret, C.R. Jones and R. Kaspi 1316

Author index 1321

Subject index 1341

ELSEVIER

Journal of Crystal Growth 175/176 (1997) 1–7

JOURNAL OF CRYSTAL GROWTH

Applications of MBE grown PHEMTs

J.V. DiLorenzo, B. Lauterwasser, M.P. Zaitlin*

Raytheon Company, Advanced Device Center, 362 Lowell Street, Andover, Massachuseets 01810, USA

Abstract

In the last decade pseudomorphic high electron mobility transistors (PHEMTs) have gone from a laboratory curiosity with unique low-noise performance to a high-volume commercial product for a variety of power and low-noise applications. At Raytheon Microelectronics, we currently use several thousand 4 in PHEMT wafers per year and expect this quantity to grow rapidly in the next few years. We describe a variety of PHEMT circuits for military, space, and commercial applications.

PACS: 89.20. + a; 85.30.Tv; 85.40.Gn

Keywords: PHEMT; MBE; Applications

1. Introduction

The pseudomorphic high electron mobility transistor (PHEMT) was widely recognized as an excellent low-noise amplifier shortly after its invention. Since the early 1990s, modifications of material structure and device geometry have resulted in the demonstration of outstanding PHEMT power performance as well, and PHEMT technology is now used in a wide variety of military, space, and commercial applications. The PHEMT's combination of low noise, high power, high efficiency, and good linearity along with its ability to deliver outstanding performance over a wide range of bias conditions have made it the device of choice for a host of RF front-end applications including phased array radar, satellite communications, wireless LAN, cellular phone, and personal communications (PCS) type systems. PHEMTs are capable of operating well into the millimeter wave frequency range with excellent power and efficiency.

From the very beginning, the development and subsequent growth of PHEMT technology has depended on molecular beam epitaxy (MBE) to provide the critical III–V heterostructures on which PHEMT operation is based. Although numerous attempts have been made to grow PHEMT layers using other epitaxial growth techniques, none have ultimately been as successful as MBE. The growing

* Corresponding author. Fax: + 1 508 470 9345; e-mail: mark_p_zaitlin@raytheon.com.

0022-0248/97/$17.00 Copyright © 1997 Elsevier Science B.V. All rights reserved
PII S0022-0248(96)01224-9

use of PHEMT technology in real world systems has both motivated and been dependent upon the development of production worthy MBE systems. Multiwafer MBE reactors capable of automated operation and high up-time are essential to the cost-effective manufacture of PHEMT devices and systems. Continuous improvement in growth control, uniformity, and machine reliability are the major challenges facing today's MBE system manufacturers.

2. MBE at Raytheon Microelectronics

PHEMTs are the workhorses for microwave circuits at Raytheon Microelectronics (formerly the Advanced Device Center) for both low noise and power applications. These transistors are fabricated with 4-in MBE grown material obtained from a combination of commercial vendors and Raytheon internal MBE systems.

Raytheon Microelectronics currently has two production MBE systems for growing PHEMT wafers. These are a Riber 49 capable of growing three 4-in wafers and a Riber 48 capable of single wafer (4-in) growth shown in Fig. 1. An upgrade is planned for both machines to enable them to achieve growth of four 4-in wafers. Both machines are fully automated allowing cost-effective 24 h operation with only 1 and a half shifts manned. Growth continues over weekends with only 1 person present for one shift each day.

At high volumes the wafer cost of MBE growth becomes comparable to ion-implanted GaAs for MESFETs, but with the superior performance advantages of PHEMTs. An estimate of the cost scaling for 4-in PHEMT wafers grown in a multiwafer MBE machine is shown in Fig. 2. This estimate assumes

- New MBE plus installation cost of $2.5 M with 5 year depreciation.

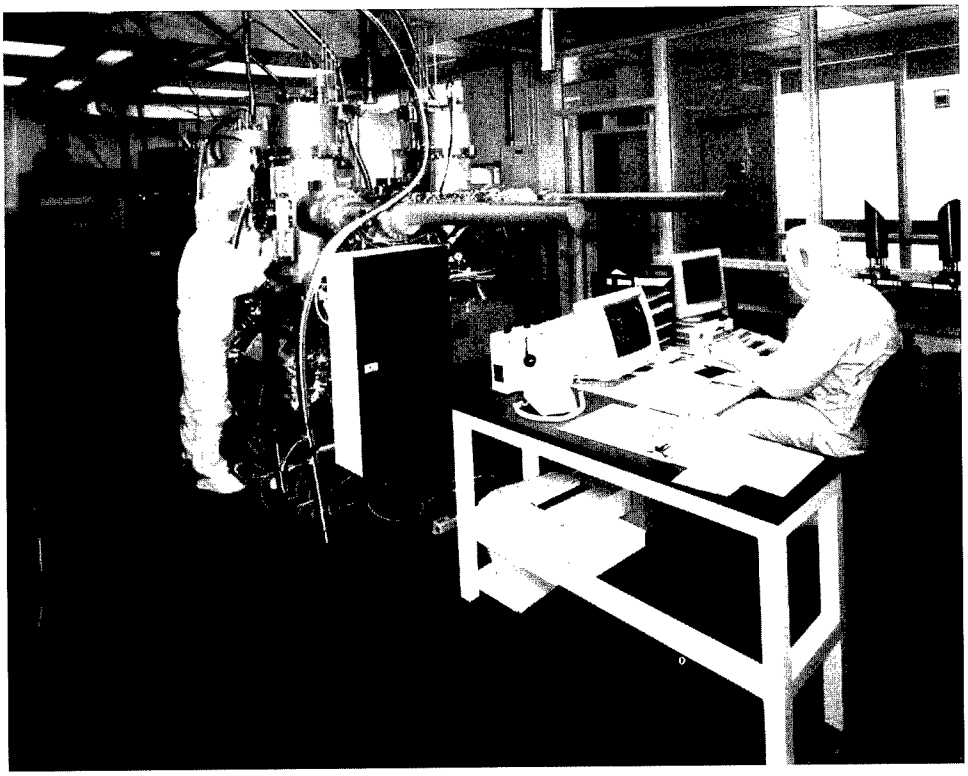

Fig. 1. Raytheon production MBE machines.

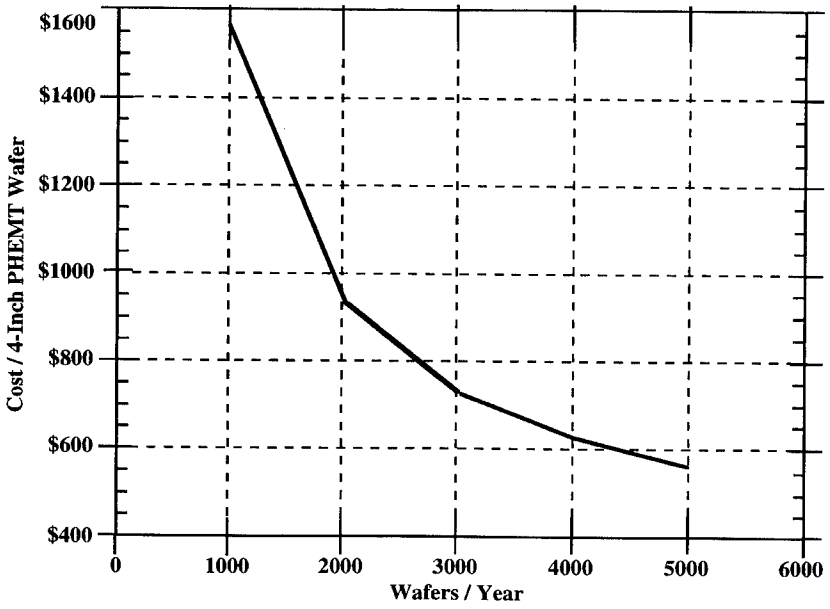

Fig. 2. Estimated PHEMT growth cost from one multi-wafer MBE machine.

- Substrate plus material cost of $250 per 4-in wafer.
- Labor, facilities, repair and other yearly costs of $1.5 M.
- An 80% yield.

At 5000 wafers per year from a single machine, the estimated cost per wafer is roughly twice the substrate plus material cost making it quite competitive with ion-implanted material.

3. PHEMT wafer projections

The rapidly expanding microwave market, particularly the area of wireless communications has increased the demand for GaAs based components. At Raytheon Microelectronics this corresponds to a large increase in the projected number of 4-in PHEMT wafers required. This is seen in Fig. 3 showing the normalized PHEMT wafer requirements for the next few years. Although, current use is quite significant, numbering in the thousands of wafers per year, a near step function increase is anticipated for next year reaching into the tens of thousands of wafers per year.

Almost all of this expected increase comes from cellular and PCS based products in the commercial area as shown in the breakdown of 1997 projected PHEMT usage (Fig. 4). With Space and Military applications remaining nearly constant almost 90% of the PHEMT requirements fall in the

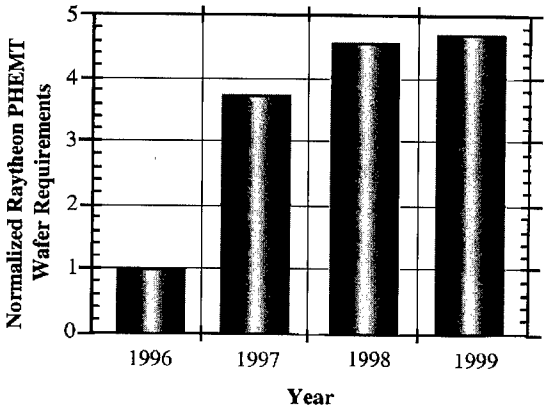

Fig. 3. Projected MBE PHEMT wafer requirements at Raytheon.

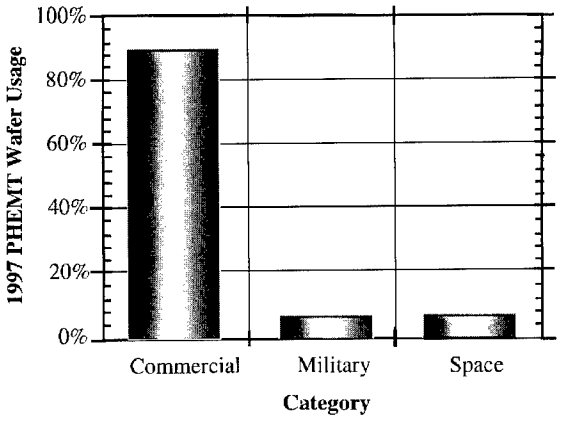

Fig. 4. Division of projected PHEMT wafer usage.

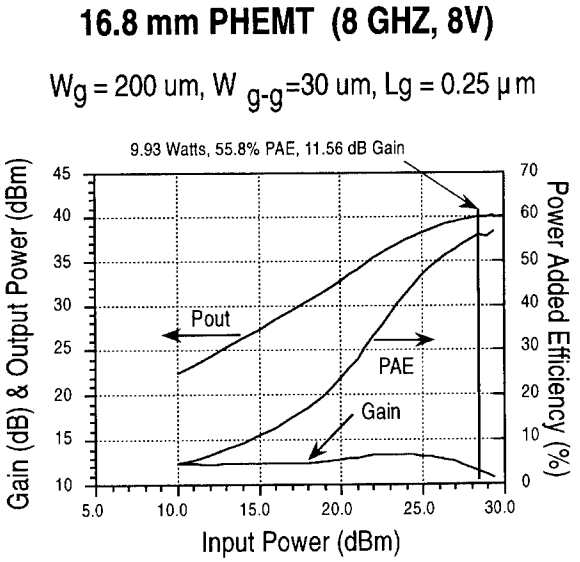

Fig. 5. Power performance from a 16.8 mm PHEMT at 8 GHz.

commercial area and almost all of those are for cellular and PCS based products.

To meet this challenging ramp up of PHEMT wafer requirements Raytheon plans to:

(1) Upgrade our current Riber production MBEs to accommodate four 4-in wafers.

(2) Purchase additional MBE production systems. We are currently planning on adding two more systems on line.

(3) Continue and even accelerate our purchases of PHEMT material from outside vendors. Raytheon is currently purchasing significant fractions of the PHEMT output of several different suppliers.

Switching to 6-in wafers is unlikely within the next few years. From the point of view of growth, multiwafer MBE systems which can simultaneously grow four 4-in wafers could only grow a single 6-in wafer, which translates into a reduction in area of ~44%. Replacement of foundry processing equipment would be an additional expense.

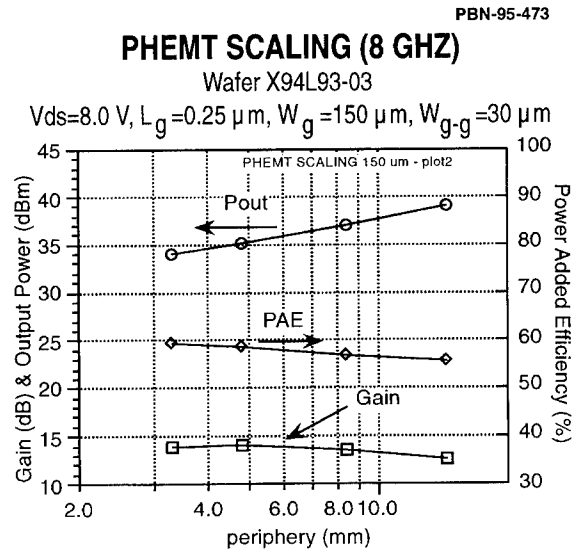

Fig. 6. Scaling of power PHEMTs at 8 GHz.

4. PHEMT power performance

PHEMTS are being used in a growing number of military and commercial systems because of their outstanding microwave performance characteristics. Fig. 5 shows power, gain, and efficiency curves for a 16.8 mm PHEMT device measured at 8 GHz. Nearly 10 W of output power is achieved with 56% power-added efficiency. Fig. 6 demonstrates that PHEMTs maintain consistent gain and efficiency over a wide range of device periphery. PHEMTs also provide excellent linearity over a range of bias and drive conditions, a characteristic which is critical to the use of PHEMT technology

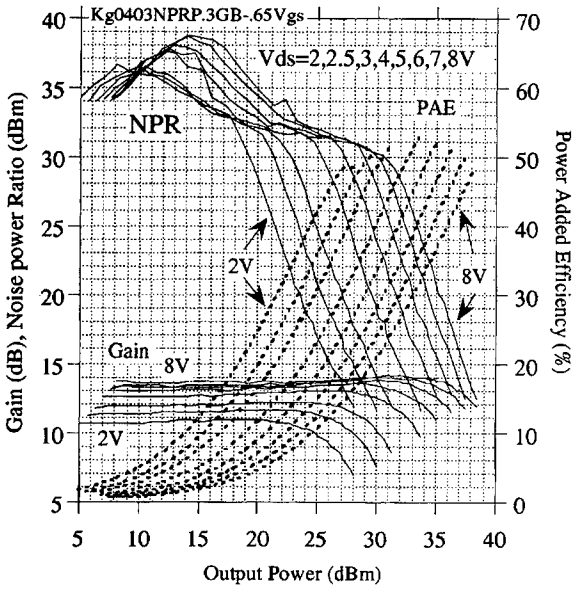

Fig. 7. Noise–power ratio (NPR) performance for a PHEMT over a wide-range of bias conditions.

in commercial space based communications systems. Fig. 7 shows the gain, efficiency, and the noise–power ratio (NPR) of a PHEMT device for drain voltages ranging from 2 to 8 V, while Fig. 8 shows adjacent channel power ratio (ACPR) for a PHEMT cellular phone power amplifier.

5. Military applications of PHEMT technology

A number of phased array radar systems have been or are being developed to address requirements for advanced guidance, tracking, and communications capabilities for the US Department of Defence. These systems essentially consist of arrays of fixed radiating elements each of which is connected to a solid state microwave transmit/receive (T/R) module. The largest such system built to date is the Army's THAAD Radar which is the radar component of the theater high altitude area defence system. Each THAAD Radar system requires 25 344 X-band T/R modules and over 200 000

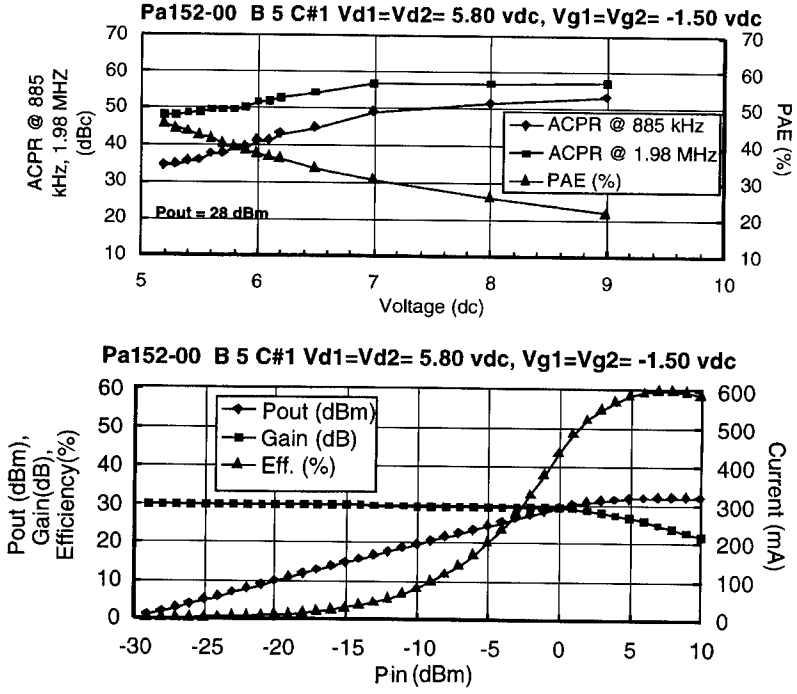

Fig. 8. PHEMT CDMA cellular amplifier performance.

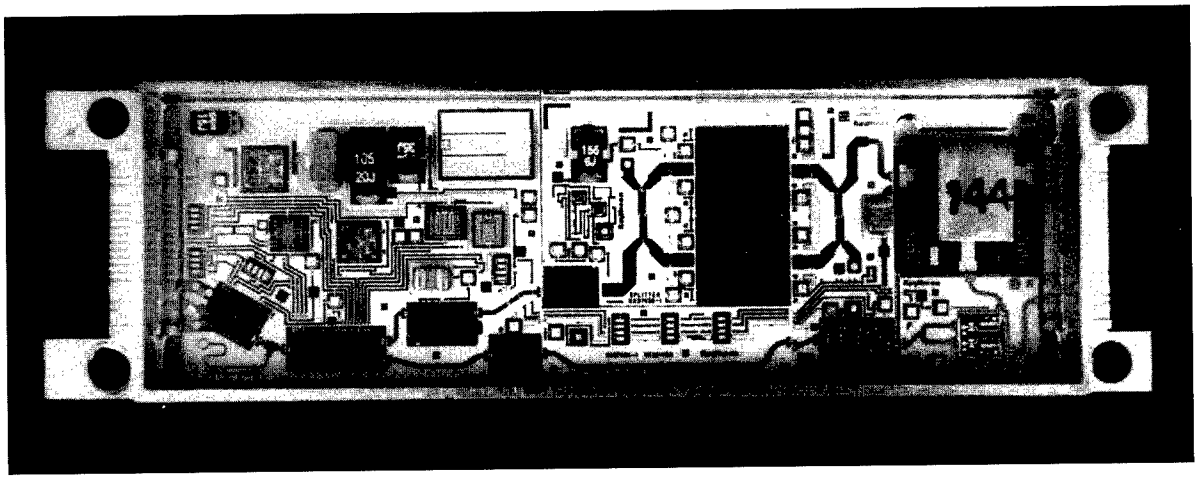

Fig. 9. THAAD radar T/R module.

GaAs MMICs. A photograph of a THAAD Radar T/R module is shown in Fig. 9. Raytheon has built two full-size arrays and one half-size array of the THAAD Radar system for the demonstration/validation phase of the THAAD program using MESFET technology. In order to increase the range and sensitivity of the THAAD Radar, and thus the effectiveness of the THAAD system, without sacrificing efficiency, future systems are expected to be built using PHEMT technology for the power and low-noise amplifier MMICs. A total of 14 additional radars are planned, which translates to well over a million PHEMT circuits.

In another example of a military phased array antenna system, Raytheon is developing a C-band module, which will be used for airborne communications as part of the cooperative engagement capability (CEC) program. The result of this program will be a fully integrated battlefield response capability such that each individual threat is addressed by the most appropriate unit (i.e., the nearest or most appropriately armed plane, ship, or ground unit). PHEMTs were chosen for the use in the multi-watt C-band module because their ability to produce high output power density and high gain with low-power consumption mean that chips can be made smaller, and thus modules can be made smaller and lighter, with PHEMTs than with MESFETs.

Increasingly, military operations rely on an advanced communications capability. The MILSTAR system is a tri-service satellite based worldwide communications system which allows ground based, ship based, and airborne personnel to communicate via secure voice and data transmissions. Various types of terminals are integrated into the MILSTAR system. One of the land based terminals being developed for the Army is known as the secure, mobile, anti-jam, reliable, tactical terminal, or SMART-T. This terminal, which mounts to a humvee-type vehicle, requires microwave transmit modules capable of output power in excess of 10 watts at Q-band. PHEMT technology, utilizing sub-quarter micron gate length devices, is capable of providing the high powers and high efficiencies needed to support this level of module performance at millimeter wave frequencies.

6. Space-based applications of PHEMT technology

The capability of PHEMT devices to deliver high power and high efficiency with excellent reliability make them ideal candidates for space based systems, where small size, light weight, and minimum DC power consumption are essential. Furthermore, PHEMT devices maintain excellent power performance over a wide range of input power and

bias conditions which makes it possible to operate in both a very linear regime without unduly sacrificing performance and to operate in both full-power and reduced-power modes. These capabilities are critical for the operation of several commercial space based communications systems currently under development. One such system is Loral's Globalstar™ satellite system, which uses S-band modules for the transmit antenna and L-band modules for the receive antenna. In transmit, the system operates with an 8 V bias on the power amplifier MMIC for full-power transmission but backs off to only a 2 V bias on the power amp during periods of reduced system usage. It is the ability of the PHEMT to operate with very high and very stable gain at very-low quiescent currents over such a large range of bias voltages, which gives the device its decisive edge over the MESFET for space-based communication applications.

Another such system is the IRIDIUM® system, which consists of a constellation of 66 low earth orbit satellites. Each IRIDIUM® satellite carries three main mission antenna panels containing an array of L-band T/R modules. A total of 24 354 modules will be required for the initial system deployment. The high-power PHEMT amplifiers in the Iridium module are operated in a Doherty amplifier configuration which produces very stable noise–power ratio over a large range of input power.

7. Commercial applications of PHEMT technology

One of the fastest growing segments of the commercial microwave market is in RF front-ends for cellular phone systems. In the infancy of transistor radios, the number of transistors was a key selling point. In today's cellular phones, except for "talk-time", technology is not advertised. In order to sell in this competitive market place, performance to specification must be demonstrated, while maintaining low cost. PHEMT technology provides the user excellent performance while maintaining low costs. One of the unique properties that sets PHEMT technology above MESFETs or silicon transistors is the gain at a low quiescent bias. In a typical cellular phone, 5-stages of silicon transistors or 3-stages of MESFETs are required to provide the same gain as a 2-stage PHEMT. The PHEMT bias point is similar to a Class-AB PA. This bias point is typically associated with nonlinear or saturated power amplifiers. However by providing harmonic terminations, high-linearity performance can be achieved. Raytheon's commercially available 4.8 V dual mode power amplifier (RMPA-0911-53) provides 60% power-added efficiency (PAE) at saturated power (32 dBm) and achieves 40% PAE at 28 dBm in linear operation with 38 dBc adjacent-channel power and 50 dBc alternate-channel power levels. These measurements were made without changing the bias voltage or loads to obtain optimum performance.

Another high-growth commercial market is the wireless local area network (WLAN) market. Wireless LAN systems allow portable or desktop computers to communicate with one another, with peripheral devices such as printers or plotters, or with a building's hard-wired ethernet backbone without the need for connecting cables or wires.

8. Conclusions

MBE Grown PHEMTs have demonstrated performance advantages of Si transistors over GaAs MESFETs and are now being introduced into a wide variety of commercial, space, and military systems. PHEMTs have matured from the development stage into high-volume production and their use is expected to accelerate in the coming years. The challenge of MBE system manufacturers will be to combine close control of material characteristics with high throughput to keep costs competitive.

ELSEVIER

Journal of Crystal Growth 175/176 (1997) 8–12

JOURNAL OF CRYSTAL GROWTH

Millimeterwave and digital applications of InP-based MBE grown HEMTs and HBTs

Paul Greiling

Hughes Research Laboratories, 3011 Malibu Canyon Road, Malibu, California 90265, USA

Abstract

Microwave and millimeterwave devices grown by MBE have significantly advanced the state of the art for RF device performance with respect to noise figure, power output, power added efficiency and extended the clock frequency of digital circuits into the millimeterwave regime. Ober the last 10–15 years, military systems have greatly benefited from the superior performance of MBE grown devices. In order to have a similar impact on the commercial marketplace, MBE growers will have to focus their efforts on a different set of performance criteria; i.e. cost, uniformity and reproducibility. This paper discusses outstanding performance achieved by MBE grown devices and outlines the criteria for commercial applications.

Keywords: HEMT; HBT; InP; SiGe; GaAs; T/R modules

The growth of semiconductor device layers by MBE has allowed device designers to develop bandgap engineered, low noise HEMTs, high power and power added efficiency HEMTs and HBTs, and high speed digital/analog HBT ICs with an order of magnitude performance improvement over standard Si CMOS, Si bipolar transistors or GaAs MESFETs. The superior performance of MBE grown, heterojunction devices has motivated the analysis, development and optimization of Si, GaAs and InP-based HBT and HEMT technologies for military systems such as radar's, communications, EW or smart munitions. The generic transceiver for all these applications is shown in Fig. 1 in which MBE grown devices such as GaAs- and InP-based HEMTs and HBTs as well as SiGe HBTs provide a significant performance improvement for each of the components in the transceiver. The transition of these technologies to commercial applications is dependent on different criteria, i.e. cost and time-to-market, rather than performance at an affordable cost as for military applications.

Si bipolar ICs offer a 25 GHz device technology, with practical operation up to 5 GHz. GaAs MESFETs with half micron gates offer a 40 GHz technology, with effective operation up to 20 GHz. In contrast, MBE grown, heterojunction devices curently being developed, such SiGe, GaAs and InP-based HBTs and GaAs and InP-based HEMTs, offer a greater than 100 GHz device technology with operation extending well into the millimeterwave frequency range.

0022-0248/97/$17.00 Copyright © 1997 Published by Elsevier Science B.V. All rights reserved
PII S0022-0248(96)01225-0

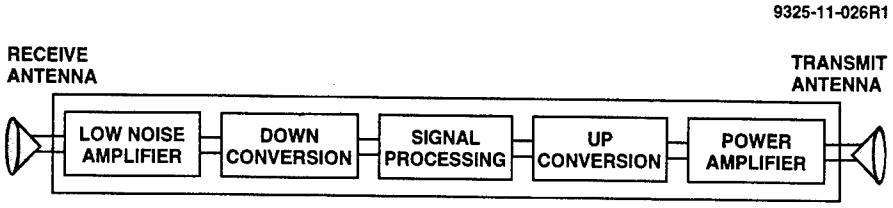

Fig. 1. Generic microwave/millimeterwave transceiver.

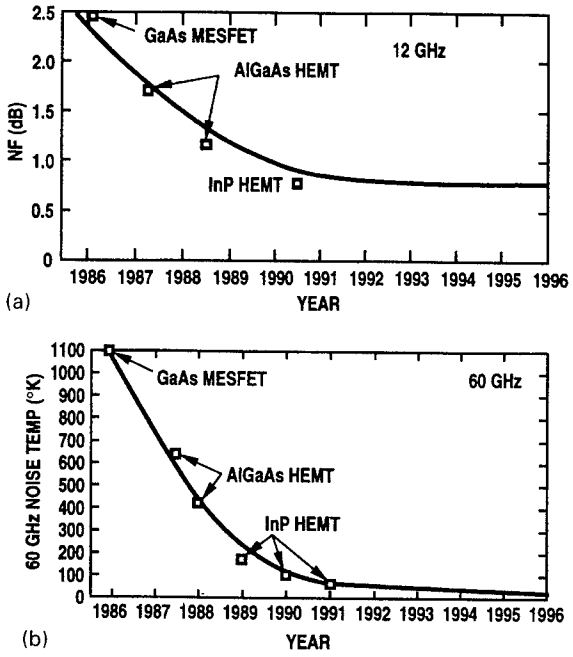

Fig. 2. (a) X-band state-of-the-art low noise MMIC performance versus time; (b) V-band state-of-the-art noise temperature versus time.

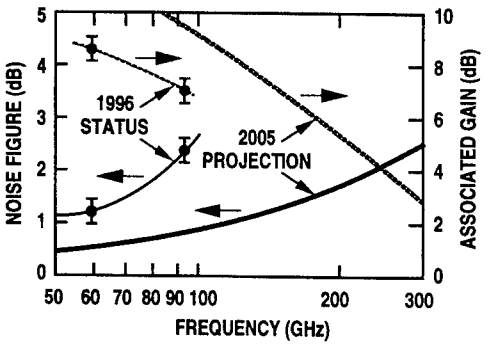

Fig. 3. Projected low noise performance for Sb-based HEMTs.

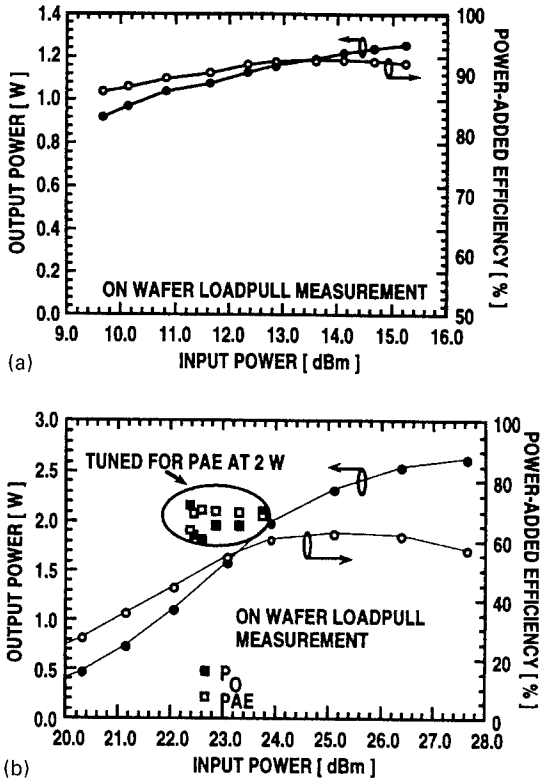

Fig. 4. (a) InP-based HBT S-band performance; (b) InP-based HBT X-band performance.

The next generation of phased-array radar systems will require reduced weight, volume and enhanced power/efficiency performance parameters to fulfil military needs. Operating frequencies extend from the ultra-high frequency (UHF) through microwave to millimeterwave spectrums. GaAs MESFET technology has evolved to the point that it is approaching its perceived ultimate performance limits. In response to advanced radar performance requirements, technology efforts are being

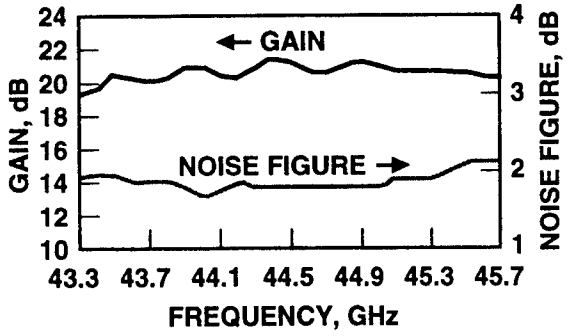

Fig. 5. InP-based Q-band 3-stage low noise MMIC amplifier performance.

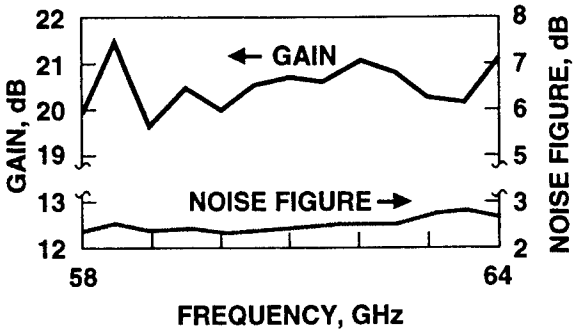

Fig. 6. InP-based V-band 3-stage low noise MMIC amplifier performance.

pushed toward devices which can yield T/R modules with octave bandwidths, noise figures under 2 dB, output power of 20 W and power added efficiencies greater than 30%. Today, low noise MMIC amplifiers have demostrated noise figures as low as 0.5 dB at X-band and noise temperatures below 100 K at V-band as shown in Fig. 2a and Fig. 2b. Future reductions in noise figure at X-band or even V-band will only be small. Therefore future work on low noise devices will be to extend the frequency of operation to the sub-millimeterwave region as shown in Fig. 3 for the projected low noise device performance for Sb-based HEMTs. The area in which new materials systems and better device structures can make a significant contribution is in power and power added efficiency. Today, a 10 W X-band power amplifier incorporating GaAs-based PHEMT exists. The next generation

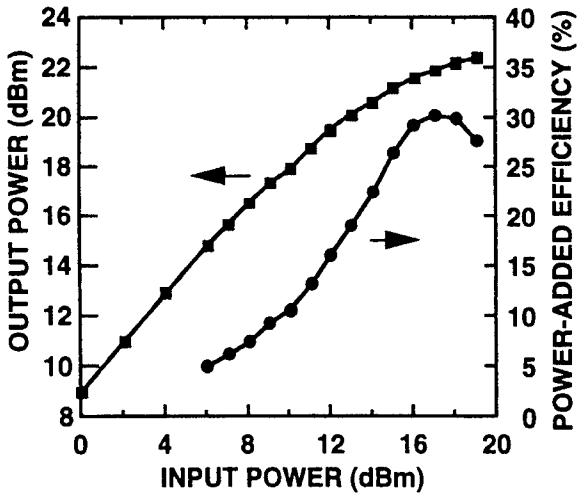

Fig. 7. InP-based V-band power amplifier.

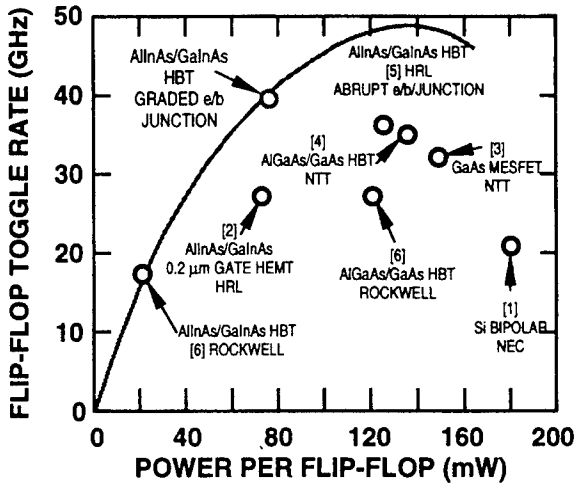

Fig. 8. HBT IC high frequency performance.

power device will be the InP-based HBT as demonstrated by the excellent results shown in Fig. 4a and Fig. 4b [1, 2]. Coming along in the next five years will be the GaN MODFET with a potential for very high breakdown voltages and therefore high power. Radar systems incorporating these new technologies will offer enhanced power-aperture products, wider bandwidths, reduced prime power consumption, and improved reliability.

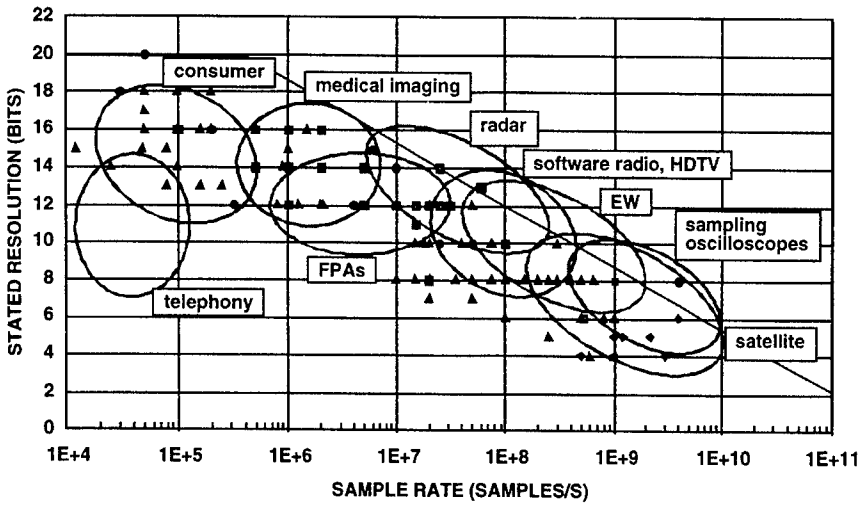

Fig. 9. State-of-the-art A/D converter performance.

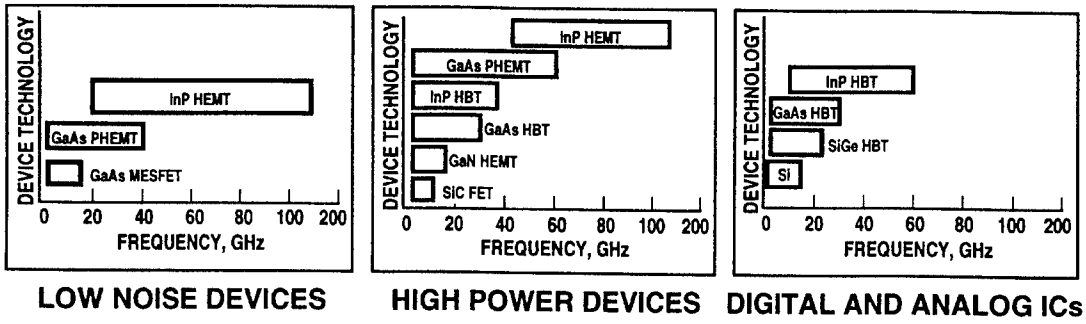

Fig. 10. Device technology versus application.

Satellite communication systems are moving to higher frequencies for more bandwidth, resulting in a need for heterojunction devices to meet the performance requirements. For satellite communications, device performance, i.e., noise figure, power added efficiency and reliability, is all-important. Systems are being developed requiring devices operating from X through V band. Low noise devices with less than 0.3 dB NF at X band rising with frequency to less than 1 dB NF @ V-band and SSPAs with 20 W and 40% PAE at Ku band and 1 W and 30% at V-band are also needed. Shown in Fig. 5 and Fig. 6 [3] are the plots of the noise figure and gain of a Q- and V- band InP-based low noise MMIC amplifier showing outstanding performance. Fig. 7 [4] shows a 60 GHz InP-based HEMT power amplifier with 160 mW of power and 30% PAE. With the exploding market for data/voice/video communication, future satellites will require on-board, high performance signal processing with 40 GBPS or greater capacity. The InP-based HBT has demonstrated digital ICs operating at 39.5 GHz (Fig. 8 [5]) with the potential of 80 GHz digital dividers. Finally, devices for satellite applications must have a MTTF of greater than 10^7 h at operating temperature. These performance requiremetns are helping expand the envelope of performance for MBE grown heterojunction device technologies.

For both radar and satellite systems as well as EW applications, designers want to digitize the signal as close to the front end as possible. This is

Table 1
Transceiver performance parameters versus application

	Radar/EW	Satellite comm.	Wireless	Automotive
Frequency	2–18 GHz BW	L thru V-bands	Ku, K&V-bands	K&W-bands
Low noise amplifier	< 2 dB nf over entire band	0.15 dB nf @ C-band 1.5 dB nf at V-band	< 3 dB NF	< 5 dB NF
Power amplifier	20–50 W with > 30% PAE/module	60–100 W, > 60% PAE at C 5 W, > 30% PAE @ V	1–3 W Po	< 10 mW Po
Cost goal	Affordable cost	Performance	$50–$100/MMIC	< $50/CHIP SET
Critical issues	Power output A/D converter	Power added efficiency A/D converter	Time-to-market cost	Cost, Cost, Cost!

driving the development of a 100 GHz or greater IC technology for A/D converters, synthesizers, MUX/DEMUXs, DDSs, and PRNs. Requirements for A/D converters with 16 bits @ 100–200 MHz and up to 10–12 bits @ 10 GHz are appearing for advanced radars and EW systems. A summary of state-of-the-art performance for A/D converters is shown in Fig. 9 [6]. In order to improve the performance of A/D converters, both device technology as well as circuit design must be enhanced. Synthesizers and DDS operating in the 5–20 GHz frequency range are being designed for the next generation of satellite systems. These needs are encouraging the development of an MBE grown heterojunction IC technology with f_T and f_{MAX} well above 100 GHz and a speed power product in the 10–30 femtojoules.

Initially the emphasis has been on MBE grown heterojunction device and IC performance for military systems with cost a secondary consideration. Today, performance at an affordable cost, utilizing a dual-use industrial base, governs both R&D investment and procurement. In the future, the cost-driven, commercial markets of automotive collision warning radars, personnel communication systems, and digital radios will determine the direction of millimeterwave device and IC R&D. Fig. 10 shows the device technology of choice for low noise, power and digital/analog IC applications whereas Table 1 lists the critical performance parameters and technology issues for each transceiver market. Note that for low noise amplifier applications, the performance is achievable but the cost needs to be reduced. For several applications, high power device and A/D converter technologies needs improvement. In all cases, reduced cost is a must. Thus researchers in MBE technology must be cognizant of the change in the marketplace from devices and ICs with higher frequencies of operation, lower noise figure, higher power output, higher power added efficiencies, wider bandwidths and higher dynamic range to larger wafers, uniformity across the wafer and from wafer-to-wafer, reproducibility from wafer-to-wafer, and lower growth costs/wafer in order to meet the demands of the marketplace.

References

[1] C. Nguyen, et al., Proc IEDM (1995) 799.
[2] C. Nguyen, et al., Presented at the Heterostructure Workshop, Sapporo, Japan (1996).
[3] L. Tran, et al., IEEE MMT-S Dig. (1996) 9.
[4] M. Matloubian, private communication.
[5] J. Jensen, et al., GaAs IC Symp. Dig. (1992) 101.
[6] R. Walden, GaAs IC Symp. Dig. (1994) 217.

ELSEVIER

Journal of Crystal Growth 175/176 (1997) 13–21

JOURNAL OF CRYSTAL GROWTH

Mass production of InAs Hall elements by MBE

Ichiro Shibasaki

Corporate Research and Development Administration (Fuji), Asahi Chemical Industry Co., Ltd., 2-1 Samejima, Fuji-city, Shizuoka 416, Japan

Abstract

Hall elements as mass production magnetic sensors are a new application area for thin film technology such as vacuum deposition and MBE. Highly sensitive InSb thin film Hall elements formed by vacuum deposition are often applied as magnetic field sensors for small DC brushless motors used in electronic equipment. InAs Hall elements developed and produced by MBE have high sensitivity and stability over a wide temperature range and have potential for the present and future applications required by many electronic systems. Here, we review the recent status of applications, production, and the good characteristics of InAs Hall elements for use as magnetic sensors. Our production MBE system has confirmed the feasibility of high yield, mass production of thin film InAs Hall elements.

Keywords: InSb Hall element; InAs Hall element; Mass production MBE; InAs quantum well

1. Introduction

Recently, there has been a strong demand for Hall elements in the field of electronic equipment such as video cassette recorders (VCRs), personal computers with floppy disk drives (FDDs), compact disk read-only memory (CD-ROM) drives, and other electronic systems where Hall elements are mainly used as magnetic sensors in the brushless motors of these devices.

For these applications, we developed highly sensitive InSb thin film Hall elements fabricated by vacuum deposition [1]. About 800 million of these InSb Hall elements were produced and sold commercially in 1995, which covers approximately 70% of the world market. Moreover, many new future applications of contactless sensors that are Hall elements for magnetic field sensing are expected because these sensors can detect static magnetic fields as well as variable magnetic fields.

These new applications require high reliability and an operation range extending from low temperatures far below 0°C to high temperatures far above 100°C. For example, Hall elements used for automotive sensors in the engine compartment require stable operation at 150°C, and recent applications for current sensors require stable sensing of very weak magnetic fields. The Hall elements must have high sensitivity and low noise properties.

The only problem with InSb Hall elements is that their narrow operation temperature range, which is restricted to near room temperature, is not sufficient for some of these new applications. Commercially available GaAs Hall elements fabricated by ion-implantation are stable at higher temperatures. However, they, too, cannot be used for some

0022-0248/97/$17.00 Copyright © Elsevier Science B.V. All rights reserved
PII S0022-0248(96)00924-4

of those new applications because of lower sensitivity to magnetic fields and an offset drift that arises at low temperatures below 0°C.

The MBE grown 0.5 μm thick InAs that is lightly doped with Si, without any intermediate layer on GaAs (100) substrate, shows stable temperature properties and a high electron mobility of $\sim 10\,000\ cm^2/V \cdot s$. We used this InAs thin film to develop a new InAs Hall element that has a wider range of operation temperature than InSb Hall elements as well as about 50% higher sensitivity than the GaAs Hall elements [2, 3]. Moreover, this Hall element has high stability for pulse voltage noise, low offset drift, and low $1/f$ noise properties, all of which are excellent properties for sensing weak magnetic fields.

For mass production of this InAs Hall element, we designed a production MBE system with a multi-wafer substrate holder that has a large growth area (a substrate holder with twelve 2-in. wafers).

Under standard production growth conditions, a high yield of more than 98% was obtained for production of InAs thin films by MBE and also high device yield for InAs Hall elements. Furthermore, since the start of production, 5 million of these MBE Hall elements have already been applied as magnetic sensors in practical devices (DC current sensors, brushless motors, etc.).

However, InAs thin films grown directly on GaAs have not shown the high electron mobility observed in bulk InAs single crystals. To obtain a higher electron mobility, the use of an InAs deep quantum well (DQW) structure is investigated. DQWs were grown by using undoped insulating layers lattice matched to InAs (i.e. AlGaAsSb(35 nm)/InAs(15 nm)/AlGaAsSb(600 nm)/GaAs). This DQW has a high room temperature electron mobility of $20\,000–32\,000\ cm^2/V \cdot s$. The typical Hall output voltage of this DQW Hall element is 300 mV/(0.05 T · 6 V) (high sensitivity) and the temperature dependence of the Hall output voltage is very small over a wide temperature range. InAs DQW Hall elements hold promise as future magnetic sensors, and we confirmed that DQW can also be produced in a large growth area MBE system or multi-wafer MBE system, which opens up a new DQW production technology.

2. Highly sensitive InSb Hall elements and their problems

In the early stages, InSb Hall elements were fabricated mainly from thin single crystal InSb. That type of Hall element was an expensive device and not suitable for mass production. There existed a strong need for low price, low cost and mass production Hall elements with high sensitivity to magnetic fields for use in consumer electronic systems.

For this purpose, we developed highly sensitive InSb thin film Hall elements with a novel high sensitivity structure and a mass production process for them. This Hall element opened up a new area for brushless DC motor technology and later resulted in large scale application of Hall elements as magnetic sensors in small DC brushless motors [1, 4].

Novel production technology for InSb polycrystal thin films with high electron mobility of more than $20\,000–30\,000\ cm^2/V \cdot s$ and 0.8 μm thick on thin mica substrates (1st row of Table 1) was established by multi-source vacuum deposition with time dependent (variable) substrate heating similar to MBE.

For the InSb thin films formed by vacuum deposition, we found some new important properties. The temperature dependencies of the Hall coefficients and conductivity were similar to those of single crystal InSb. However, the electron mobility had a very small temperature dependence near room temperature, differently from the single crystal InSb. This is because InSb thin film formed on thin mica substrate by vacuum deposition is polycrystalline. This is a very important property which has led to the discovery of a new driving method

Table 1
Properties of InSb and InAs thin films and InAs DQW

	Dopant	Electron mobility μ_H ($cm^2/V \cdot s$)	Electron density n ($\times 10^{16}\ cm^{-3}$)	Thickness d (μm)
InSb	None	20 000–30 000	2	0.8
InAs	Si	11 000	8	0.5
DQW	None	20 000–32 000	50	0.015

with small temperature dependence of Hall output voltage for the practical thin film InSb Hall elements fabricated by vacuum deposition.

A high sensitivity device structure of the InSb thin film Hall element was established. InSb thin film removed from thin mica substrate used for the magnetically sensitive portion of the Hall element was sandwiched between a ferrite substrate and a small ferrite chip. This structure amplifies the magnetic field in the gap between the ferrite substrate and chip by a factor of about 3–6 compared to the original magnetic field applied to Hall element. Therefore, since the InSb thin film in the gap experiences the amplified magnetic field, the Hall elements have ultra-high sensitivity to the magnetic field. This special structure is shown in Fig. 1. The first row of Table 2 shows typical characteristics of InSb high sensitive Hall elements for commercial products.

A new driving method was developed for the high sensitivity Hall elements. Since our Hall element has high input resistance of around 350 Ω, the thin film InSb Hall element is stable under a limited input voltage and is driven at constant voltage, which has never been realized for conventional crystalline single InSb Hall elements. This constant voltage driving results in the Hall output voltage of our highly sensitive InSb Hall elements having a very small or stable temperature dependence near room temperature, the same as for electron mobility. This new driving technique reduces the temperature coefficient of the Hall output voltage from -2.0%/deg to ± 0.1–0.2%/deg near room temperature. This is one of the most important practical merits of our highly sensitive InSb thin film Hall elements, and it is now a standard driving method. These Hall elements have ultra-high sensitivity to magnetic fields, practical reliability, and allow many kinds of small package designs that are good for applications.

The first practical application of our highly sensitive Hall element was the magnetic sensor for music record player motors. This first application confirmed our Hall element as a practical magnetic sensor for brushless motors. Since that application, our Hall elements have been mass produced and have served in many applications. Recent major applications include DC brushless motors or Hall

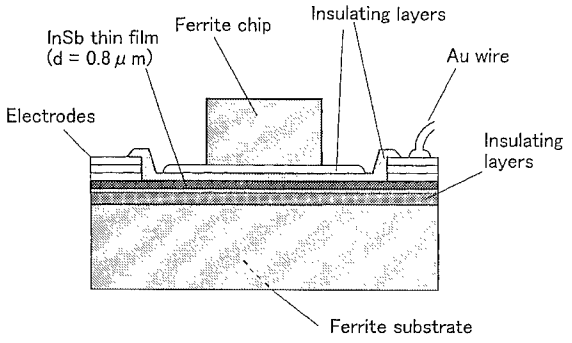

Fig. 1. The highly sensitive InSb Hall element (cross-section).

Table 2
Characteristics of InSb, InAs, and InAs DQW Hall elements

	Driving voltage V_{in} (V)	Hall output voltage V_H (mV) ($B = 0.05$ T)	Offset voltage V_u (mV) ($B = 0$ T)	Resistance R_{in} (Ω)
InSb	1	150–320	$< \pm 7$	240–550
InAs	6	100	$< \pm 16$	400
DQW	6	250–300	$< \pm 16$	700

motors used in VCRs, FDD motors, CD-ROM drive motors of personal computers, and similar electrical equipment. In 1995, more than 800 million of these InSb thin film Hall elements were produced by vacuum deposition and used in many kinds of applications (mainly magnetic sensors for DC Brussels motors).

Some problems relating to these Hall elements should be discussed. The success of these Hall elements as magnetic sensors lead to many new applications for Hall elements incorporating the functions of contactless sensing and static magnetic field sensing. These new applications impose more severe operation conditions on the Hall elements. A typical new application is automotive sensors in the engine compartment or outside the body frame. These applications require a wide operation temperature range of from -40°C to 150°C.

The only problem with the InSb Hall elements is a narrow operation temperature range, such as

from -10°C to 100°C. This is because of the large temperature coefficient for input resistance of -2.0%/deg. This operation range is not sufficient for some of the new applications. However, there is strong demand for Hall elements with high sensitivity and wide operation range for recent applications such as current sensors, automotive sensors, industrial sensors, and so on. Our aim in research on new Hall elements is to suit those new applications.

3. MBE growth of InAs thin films for Hall elements and their production MBE system

Single-crystal InAs has a high electron mobility of more than 30 000 $cm^2/V \cdot s$. The InAs thin films grown by MBE also has a high electron mobility and has a wider band gap energy than InSb. Thus, it is one promising material for use in Hall elements that are both highly sensitive and stable over a wide temperature range as practical magnetic sensors [3–5]. To reduce the temperature dependence of Hall output voltage for InAs Hall elements at higher temperatures, n-type impurity doping of InAs was effective (This is also valid for a InSb Hall element) [6]. Thus, InAs was Si doped during MBE growth.

A 0.5 μm thick InAs thin film doped with a suitable amount of Si and grown directly on GaAs(1 0 0) substrate shows a high electron mobility of $\sim 10\,000$ $cm^2/V \cdot s$. The electron mobility and resistivity of this thin film show very little temperature dependence over a wide temperature range. Using this InAs thin film, we developed InAs Hall elements having about 50% higher sensitivity than GaAs Hall elements and a wider operation temperature range than InSb Hall elements. The Hall output voltage of this element has good linearity in magnetic field as well as other very good properties as magnetic sensors [2, 3].

3.1. Preparation of production MBE system

For mass production of InAs Hall elements, we designed a production MBE system with three chambers and a large growth area or multi-wafer holder having throughput of more than 100 million Hall elements per year. The most important issue in designing production MBE systems is the engineering of a mass production system. Many problems special to production systems have arisen. For example, easy maintenance is very important in a production system.

Some features of our production MBE system with three chambers are listed below.

(1) A large vertical growth chamber with 1 100 mm diameter;

(2) A wafer holder with twelve 2-in. substrates (large growth area);

(3) Thickness uniformity design and substrate rotation system;

(4) 10 source ports with large diameter flanges;

(5) Specially designed Knudsen cells with large capacity (from 100 to 300 cc or more);

(6) Stable substrate heating system in growth chamber;

(7) Entry chamber with 11-wafer holder;

(8) Wafer holder transfer system employing magnetic coupling;

(9) Simple operation;

(10) Easy, automated operation;

(11) High throughput.

The purpose of the large diameter chamber is to reduce warm up of the inner surface of the chamber caused by strong radiation from the substrate heater during operation. Other important points considered in designing the system are reducing power consumption in the vacuum chamber for reducing undesired out gassing from the chamber wall and inner housing during operation, to reduce thermal interaction between source and substrate by radiation from sources, and stable substrate and source heater control. Reducing liquid nitrogen consumption is also very important for low product cost.

3.2. Growth conditions and throughput for production MBE system

We found standard growth conditions for InAs thin film with Si-doping on GaAs substrates [5]. Growth time of within 1 h was established. Simple estimation of the production capacity of our MBE system is more than 100 million Hall effect devices per year. This value is sufficient for mass production of Hall elements.

4. Production MBE growth of InAs thin films and fabrication of InAs Hall elements

4.1. MBE growth

We have grown Si doped InAs thin films (0.5 μm on GaAs (1 0 0) substrate (2° off) without an intermediate buffer layer by MBE [2, 7]. There is a well-known large lattice mismatch between InAs and GaAs about (7.2%). However, we found optimized growth conditions for InAs thin films with no such trouble for Hall element application. This InAs thin film has a two layered structure with respect to electron mobility in the growth direction. The layer farthest from the substrate interface has a higher electron mobility and is doped with Si donor atoms to obtain a high electron mobility [3, 5].

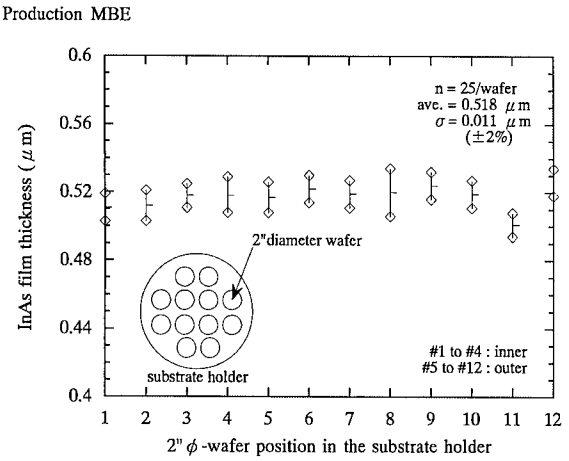

Fig. 2. Uniformity of InAs thin film fabricated by production MBE (film thickness).

4.2. Uniformity in electrical properties of InAs thin film fabricated by production MBE

Fig. 2 shows the thickness uniformity of Si doped InAs thin films grown on semi-insulating GaAs substrates by the production MBE system. Fig. 3 shows the uniformity of the electron mobility and sheet resistance. The values are sufficient for high yield of Hall effect device. Twelve InAs thin films grown on GaAs substrates by production MBE are shown in Fig. 4. We have obtained 95% yield with the MBE operation within suitable specifications restricted according to device characteristics. We experienced good reproducibility with the production MBE system. Moreover, whatever problems we experienced for thin films grown by MBE, the MBE system always had corresponding problems. This is the most beautiful and reliable point ever experienced in vacuum deposition. This means MBE is suitable as a production system.

4.3. Fabrication of InAs Hall elements

We have designed practical Hall elements which use 0.5 μm thick InAs thin films grown directly on (1 0 0) GaAs substrate. The standard electron density and mobility of InAs thin film are $8 \times 10^{16}/cm^3$ and 11 000 $cm^2/V \cdot s$, respectively (2nd row of Table 1). InAs thin films are processed to form Hall elements by a specially developed wafer process and assembled in a commercial mass production line. This Hall element has a 0.36 mm^2 chip size. The fabrication process is shown in Fig. 5. An average yield of more than 96% for Hall element chips on wafer has been achieved for the wafer process. The InAs Hall element chip bonded on a lead island is shown in Fig. 6. The final product is also shown in Fig. 7.

4.4. Typical characteristics of mass production InAs Hall elements

The typical Hall output voltage (or sensitivity) of this Hall element in magnetic field is 100 mV/(6 V × 0.05 T). This is tabulated in the second row of Table 2 and is compared to the values for other Hall elements. The temperature dependence of Hall output voltage for a wide temperature range and sensitivity is shown and compared with various other kinds of Hall elements in Fig. 8.

This InAs Hall element has no problem at lower temperature where InSb Hall elements and GaAs Hall elements sometimes have suffered problems resulting from their material properties. Since the input resistance of this InAs Hall element does not change much with temperature, practical application in a wide temperature range is possible. The range depends on the electron density in the active

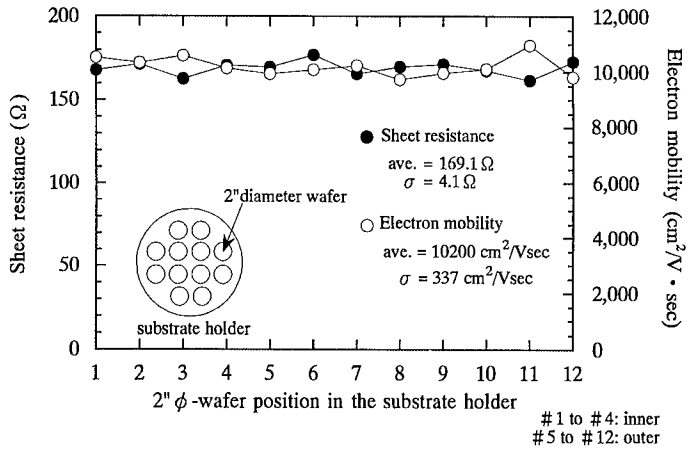

Fig. 3. Uniformity of InAs thin film fabricated by production MBE (sheet resistance and electron mobility).

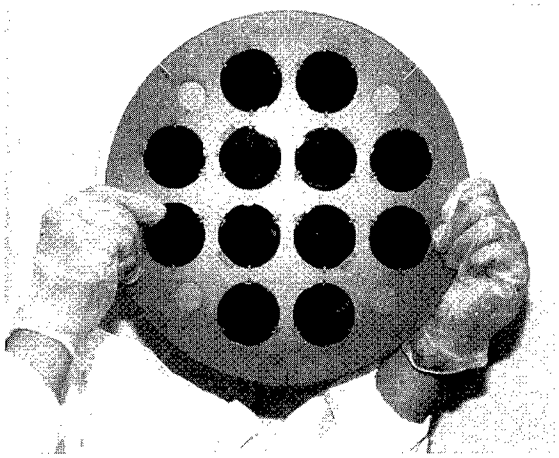

Fig. 4. Photograph of 12 InAs thin films grown on GaAs 2 in. wafers by production MBE.

layer [5]. The Hall element chip size and sometimes the package, etc., are also important factors affecting the operation temperature range. The higher operation temperature (near 150°C) required by automotive sensors in engine the compartment would be attainable by optimizing element design. These are important factors in determining the maximum rating of practical Hall elements. A small package suitable for small DC motors is possible.

Strong stability against pulse voltage noise and very low offset voltage drift are observed. Very low $1/f$ noise is also a feature of this Hall element. Low noise detection of very weak magnetic fields required by current sensor applications may be possible. Minimum magnetic field sensitivity of 0.003 mT was measured for MBE InAs Hall elements with a heavy Si doping (electron density of $5 \times 10^{17}/\text{cm}^3$) and 0.05 mT was measured for GaAs Hall elements. This small minimum detection level is very important for current sensor applications. Moreover, the Hall output voltage and input resistance of this heavily doped InAs Hall element have very small, nearly zero, temperature dependence over a very wide temperature range (from -40 to 160°C). These fine properties are all good for current sensor applications, magnetic field measurement and other applications as a contactless sensor [4, 5]. These new features of InAs Hall elements will be suitable for new future applications.

5. InAs deep quantum wells and application to Hall elements

To realize even higher sensitivity for InAs Hall elements, a even higher electron mobility and higher sheet resistance is required for the InAs active layer. This means that an ultra-thin InAs active layer with a higher electron mobility is required. A InAs thin film 0.5 μm thick, grown directly on GaAs has lower electron mobility than bulk InAs

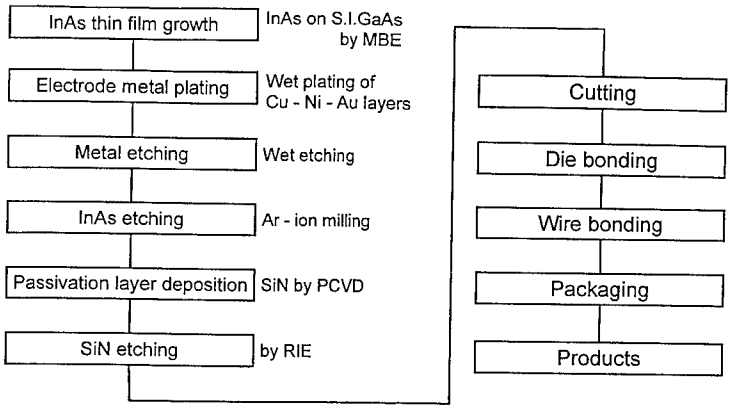

Fig. 5. Fabrication process of InAs Hall elements.

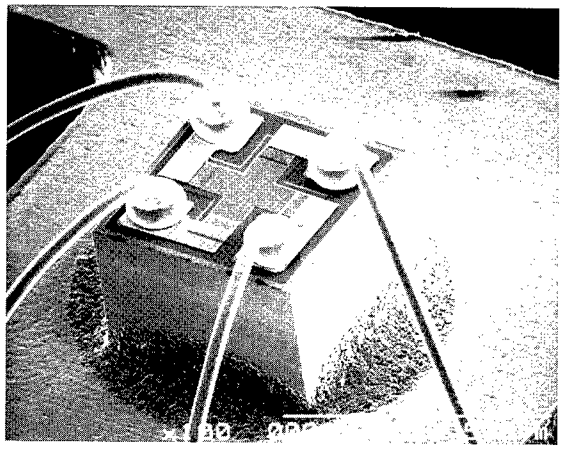

Fig. 6. Photograph of InAs Hall element chip.

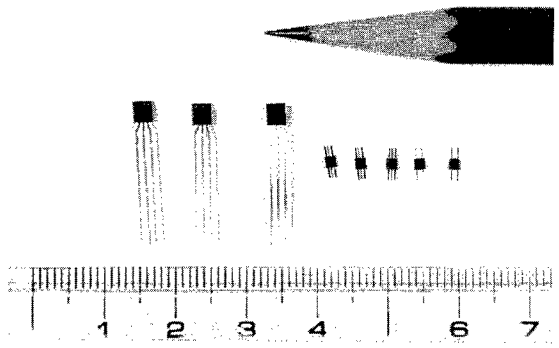

Fig. 7. Photograph of InAs Hall elements fabricated by production MBE.

single crystal because of the large lattice mismatch ($\sim 7\%$) between InAs and GaAs. To obtain a higher electron mobility, InAs deep quantum well structures (DQW) have been studied and grown by using a special insulating layer that is lattice matched to InAs by MBE [8–10].

We found a new insulating layer of quaternary material with Sb that has the same lattice constant as InAs and has a large band gap energy of about 1.0 eV a suitable composition that works well as a high potential barrier to form the InAs quantum well. For instance, $Al_xGa_{1-x}As_ySb_{1-y}$ ($0 \leqslant x \leqslant 1$, $0 \leqslant y \leqslant 1$) is a suitable composition range. This layer absorbs many kinds of defects produced by lattice mismatch between the GaAs substrate and the InAs. Moreover, these defects are electrically inactive and the layer acts as an insulating layer, pinning electrically active defects. By using this insulating layer, we can make rather deep quantum wells with a conductive InAs channel layer having a high electron mobility. The typical InAs DQW Hall element structure is shown in Fig. 9. An InAs well of a thickness of 15 nm was used and a structure comprising of GaAsSb(5 nm)/AlGaAsSb(35 nm)/InAs(15 nm)/AlGaAsSb(600 nm)/GaAs was grown by MBE. The DQW had a high electron mobility of 20 000–32 000 $cm^2/V \cdot s$ (row 3 of Table 1) [11, 12]. The typical Hall output voltage from this DQW was 300 mV/(0.05 T · 6 V) (row 3 of Table 2). The InAs DQW Hall element had a high sensitivity and its temperature dependence was very small compared to other kinds of Hall elements (Fig. 8).

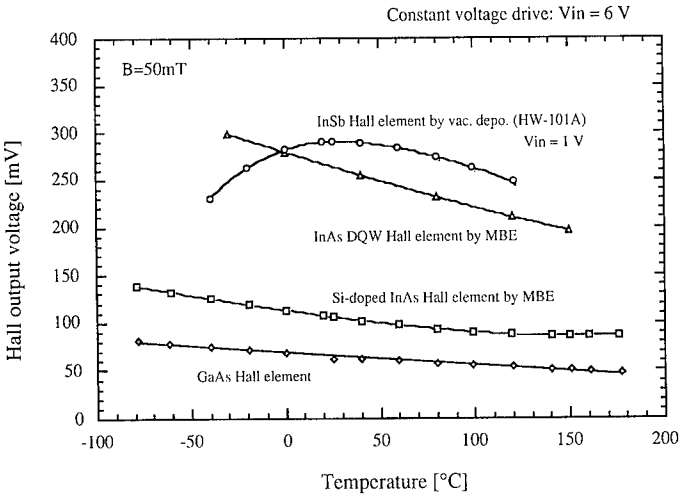

Fig. 8. Temperature dependence of Hall output voltage for various kinds of Hall elements.

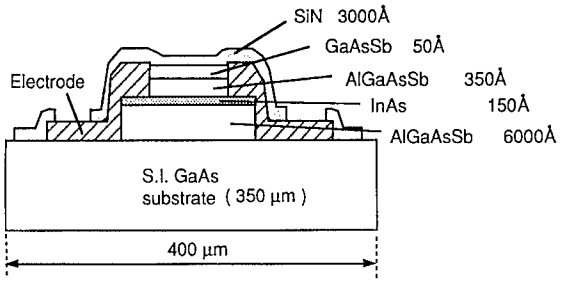

Fig. 9. InAs DQW Hall element (cross-section).

InAs DQW Hall elements hold promise as future magnetic sensors. The InAs DQW is grown uniformly by MBE using a multi-wafer holder with a rotation mechanism. The average electron mobility and sheet carrier density for four 2-in. wafers on one substrate holder grown by MBE are $24\,050 \pm 180\ \mathrm{cm^2/V \cdot s}$ and $(0.568 \pm 0.008) \times 10^{12}/\mathrm{cm^2}$, respectively. We believe InAs DQW Hall elements having high sensitivity and stability in a wide temperature range will be produced by this production MBE in the future. The InAs DQW is applicable to many kinds of sensors and electronic devices. Therefore, MBE technology would be applied to the mass production of many kinds of electronic and sensing devices.

6. Conclusions

The Hall element as a magnetic sensor has established a major application area for III–V compound semiconductor thin films. A production MBE system was designed and applied to produce InAs Hall elements. The high sensitivity and wide operation temperature range characteristics required for future applications of Hall elements were demonstrated in the InAs Hall elements fabricated by MBE. Moreover, many good characteristics for applications have been shown for InAs Hall elements. MBE technology has been shown to have great potential for production of Hall elements. InAs Hall elements fabricated by MBE will open new areas of application for magnetic sensors and will contribute to the advancement of electronic systems with its contactless sensing function.

References

[1] I. Shibasaki, The 8th Sensors Symp. C3-1, Tech. Dig. (IEE, Tokyo, 1989) p. 211.
[2] I. Shibasaki, Y. Kanayama, T. Ito, F. Ichimori, T. Yoshida, K. Nagase and K. Harada, 1991 Int. Conf. on Solid-State Sensors and Actuators (Transducers, '91), Dig. Tech. Papers (IEEE, USA, 1991) p. 1068.
[3] Y. Kanayama, K. Nagase, S. Muramatsu, A. Ichii, T. Iwabuchi, T. Yoshida, F. Ichimori, T. Ito and I. Shibasaki,

Proc. 4th Int. Symp. on Micro Machine and Human Science (1993) p. 165.
[4] I. Shibasaki, IEEE Lasers and Electro-Optics Society 1995 Annual Meeting, Conf. Proc., Vol. 1 (1995) p. 85.
[5] T. Iwabuchi, T. Ito, M. Yamamoto, K. Sako, Y. Kanayama, K. Nagase, T. Yoshida, F. Ichimori and I. Shibasaki, J. Crystal Growth 150 (1995) 1302.
[6] I. Shibasaki, T. Kajino and K. Tajika, Japan patent P1598818 (Application: July 13, 1982).
[7] M. Yamamoto, T. Iwabuchi, T. Ito, T. Yoshida, H. Imai, T. Isoya and I. Shibasaki, J. Crystal Growth 175/176 (1997) 191.
[8] K. Nagase, S. Muramatsu, N. Kuze, A. Ichii, I. Shibasaki and K. Mori, The 7th Int. Conf. on Solid-State Sensors and Actuators (Transducers '93) D12-07, Dig. Tech. Papers, Late News (IEE, Tokyo, 1993) p. 32.
[9] N. Kuze, K. Nagase, S. Muramatsu, S. Miya, T. Iwabuchi, A. Ichii and I. Shibasaki, J. Crystal Growth 150 (1995) 1307.
[10] S. Miya, S. Muramatsu, N. Kuze, K. Nagase, T. Iwabuchi, A. Ichii, M. Ozaki and I. Shibasaki, J. Electron. Mater. 25 (1996) 415.
[11] N. Kuze, H. Goto, S. Miya, S. Muramatsu, M. Matsui and I. Shibasaki, Material Research Symp. Proc., Vol. 399, Boston, 1995 (Material Research Society, Evolution of Epitaxial Structure and Morphology, 1996) p. 165.
[12] N. Kuze, H. Goto, M. Matsui, I. Shibasaki and H. Sakaki, J. Crystal Growth 175/176 (1997) 868.

ELSEVIER

Journal of Crystal Growth 175/176 (1997) 22–28

JOURNAL OF CRYSTAL GROWTH

High power mid-infrared quantum cascade lasers with a molecular beam epitaxy grown InP cladding operating above room temperature

Jérôme Faist*, Federico Capasso, Carlo Sirtori, Deborah L. Sivco, James N. Baillargeon, Albert L. Hutchinson, Sung-Nee G. Chu, Alfred Y. Cho

Bell Laboratories, Lucent Technologies, Murray Hill, New Jersey 07974, USA

Abstract

A new quantum cascade laser is reported with very high performance at high temperatures. These high performances are obtained by a design combining low doping, a funnel injector and a three well vertical transition active region. A molecular beam epitaxy grown InP top cladding layer is also used to optimize heat transport. Peak pulsed optical power of 200 mW and average power of 6 mW are obtained at 300 K and at a wavelength $\lambda = 5.2$ μm. The devices operate also in continuous wave up to 140 K with 2 mW of optical power.

The quantum cascade (QC) laser [1] is a new optical source in which one type of carrier, typically electrons, cascading down an electronic staircase, make transitions between energy levels created by quantum confinement. This source has the unique feature of having its emission wavelength entirely controlled by its geometry (i.e., the layer thickness) and not by the material's bandgap. In practice, this wavelength taylorability is limited on the short wavelength side to a photon energy of a fraction (typically ~60%) of the relevant band discontinuity, and on the long wavelength side by the absorption by the restrahlen band or by the free carriers. As an example, structures based on InGaAs/AlInAs lattice matched to InP (conduction band discontinuity of 0.52 eV) were designed and operated between 4.3 and 11.2 μm wavelengths [1–6]. In the quantum cascade laser, the main non-radiative channel is optical phonon emission rather than the Auger effect [1]. This fact, along with the atomic-like joint density of state of the intersubband transition, are the reasons for the low-temperature dependence of its threshold current (large T_0) and its operation at high temperatures above room temperature [6]. On the contrary, lead-salt lasers [7], III–V-based antimonide interband lasers [8], or even interband lasers based on type II transitions [9–11] are strongly limited by Auger scattering and therefore have to operate at lower temperatures (typically $T < 220$ K). The quantum cascade laser is thus a promising new source for

* Corresponding author.

0022-0248/97/$17.00 Copyright © 1997 Elsevier Science B.V. All rights reserved
PII S0022-0248(96)00868-8

environmental sensing, industrial process monitoring, medical, law enforcement and military applications.

The active region of our GaInAs/AlInAs heterostructure is grown lattice-matched to a n^+ InP substrate by molecular beam epitaxy (MBE) and consists of 25 stages. As shown in Fig. 1, each stage comprises a three quantum-well active region and a superlattice injection/relaxation region. As in previous structures [1–6], the active region is engineered so that at the threshold field (76 kV/cm), the ground states of the 4.7 and 4.0 nm thick quantum wells in the active region have anticrossed to achieve an energy separation approximately resonant with the optical phonon energy ($\sim$34 meV). As a result, we obtain a short (τ_2–τ_{21} = 0.4 ps) lifetime of the $n = 2$ state. The electron scattering time from level 3 to level 2 is longer since it involves optical phonon emission associated with a large momentum transfer (τ_{32} = 2.1 ps). The resulting lifetime of level 3 is $\tau_3 = (\tau_{31}^{-1} + \tau_{32}^{-1})^{-1} = 1.3$ ps.

Compared with previous lasers based on a *vertical* transition [2], i.e. characterized by a strong overlap of the upper- and lower-state wave functions of the lasing transition, this new design has an additional 0.9 nm thick GaInAs quantum well coupled to the active region by a 1.5 nm barrier which selectively enhances the amplitude of the wave function of level 3 in the 5.0 nm injection barrier (see Fig. 1) [6]. This maximizes the injection efficiency by increasing the overlap between the $n = 3$ wave function and the ground-state wave function ***g*** of the injector while reducing that of the latter with the $n = 2$ and $n = 1$ states. This minimizes injection into these states by elastic or inelastic scattering [2]. However, in contrast to QC structures based on a diagonal transition [1], the presence of this additional 0.9 nm well does not reduce the oscillator strength of the lasing transition (z_{32} = 1.6 nm).

The chirped superlattice of the relaxation/injection region acts as a Bragg reflector to suppress the escape of electrons from the $n = 3$ excited state into the continuum while allowing their extraction from the lower state ($n = 1$) into the miniband of the relaxation region [2]. The width of this "miniband" decreases towards the 5.0 nm injection barrier to minimize injection into the active region of electrons thermally excited to higher states of the miniband (Fig. 1). This has the effect of funneling electrons into the ground state ***g*** of the relaxation/injection region.

For best high-temperature performance, the energy difference Δ between the quasi-Fermi-energy

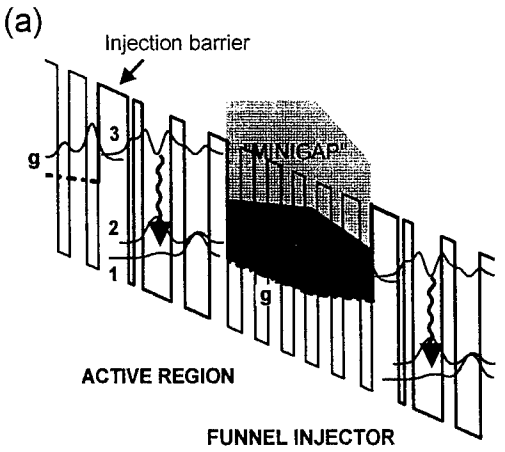

(b)

InGaAs	$n = 1\times10^{20}$cm^{-3}	10nm
graded	$n = 7\times10^{18}$	30
	$n = 7\times10^{18}$	1200
AlInAs	3×10^{17}	700
	2×10^{17}	600
graded	$n = 2\times10^{17}$	30
InGaAs	$n = 1\times10^{17}$	300
Active region (25x)		1200
InGaAs	$n = 1\times10^{17}$	300
graded	$n = 2\times10^{17}$	25
InP	$n = 1\times10^{18}$	

(c)

	$n = 7\times10^{18}$cm^{-3}	1300nm
InP	2×10^{17}	1500
	5×10^{17}	20
graded	$n = 2\times10^{17}$	30
InGaAs	$n = 1\times10^{17}$	400
Active region (25x)		1200
InGaAs	$n = 1\times10^{17}$	400
graded	$n = 2\times10^{17}$	25
InP	$n = 2\times10^{17}$	

Fig. 1. (a) Schematic conduction band diagram of a portion of the active region of the structure under positive bias condition and an electric field of 7.6×10^4 V/cm. The wavy line indicates the transition responsible for laser action. The moduli squared of the relevant wave functions are shown. The layer sequence of one period of the $Al_{0.48}In_{0.52}As/Ga_{0.47}In_{0.53}As$ structure, in nanometers, left to right and starting from the injection barrier is (5.0/0.9), (1.5/4.7), (2.2/4.0), (3.0/2.3), (2.3/2.2), (2.2/2.0), (2.0/2.0), (2.3/1.9), (2.8/1.9). The structures are left undoped, with the exception of layers number 14–16 for sample D-2122 and 11–13 for sample D-2160 which are n-type doped with Si to $N_d = 2\times10^{17}$ cm^{-3}. (b) Layer structure of the waveguide of the reference sample D-2160. (c) Layer structure of the waveguide of the sample D-2122. The dashed line indicates the interface where the growth was interrupted.

in the ground state of the injector g and the lowest state ($n = 2$) of the lasing transition (see Fig. 1) is designed to be relatively large ($\Delta \sim 110$ meV) and the sheet density of the n-type doped injection region is kept to a low value ($n_g = 1.2 \times 10^{11}$ cm^{-2}), to minimize the number of electron thermally activated from the injector into level 2 [2].

Ternary materials such as AlInAs have a thermal resistance 15–20 times larger than binaries such as InP. We compared devices with two different optical waveguide designs. The reference sample (D-2160), grown in one step, uses a top AlInAs cladding similar to the one of previous QC lasers (see Fig. 1b). In the second device (D-2122), as shown in Fig. 1c, the first MBE growth is stopped after the growth of the core of the waveguide is completed. The sample is then arsenic-capped and transferred in a second MBE chamber fitted with a phosphorus solid source [11]. There, the arsenic is thermally desorbed under UHV condition and the growth of a InP cladding is immediately started.

A transmission electron microscope (TEM) micrograph of a cross section of a few periods of the active region of structure D-2122 is displayed in Fig. 2. The InGaAs material is the lighter and the AlInAs the darker shade of gray. This picture clearly shows that the interfaces are very sharp and flat. As an example, the 0.9 nm well is clearly visible and its thickness constant across the 8 periods of the structure that are displayed. In general, the measured thickness agree with the intended ones within the accuracy ($\pm 5\%$) of the TEM instrument. TEM cross-sections showing the active region and part of the waveguide region are compared in Fig. 3 for the structures with AlInAs (Sample D2160) and InP (sample D2122) claddings. These pictures demonstrate clearly that the InP/GaInAs interface resulting from the regrowth of the InP in sample D2122 is sharp and free of defects.

Devices from wafer D-2122 were processed into circular mesas of 200 μm diameter to study their temperature-dependent electroluminescence. The luminescence intensity normalized to the low temperature value, shown in the inset of Fig. 4, decreases slightly with increasing temperature. Its temperature dependence (solid line) was calculated by considering that the non-radiative scattering rate is proportional to $(2n + 1)$, where n is the Bose–Einstein factor associated with optical phonons and taking the phonon energy $\hbar\omega_{lo} = 34$ meV. The good agreement with the measurements is indicative that optical phonon scattering is the main non-radiative channel. The electroluminescence spectra were measured with a Fourier-transform infrared spectrometer using a step scan and lock-in detection technique. As shown in Fig. 4, the full-width-at-half-maximum (FWHM) of the luminescence spectrum increases from 16 meV at 10 K to 28 meV at 300 K. This relatively narrow line width indicates that the small 0.9 nm well does not increase significantly the broadening of the lasing transition [12].

Fig. 2. Transmission electron micrograph of seven period of the active region of sample D2122. The white bands are the InGaAs alloy layers, the white ones the AlInAs alloy. The largest dark band is the AlInAs injection barrier. The bottom of the picture corresponds to the substrate side. Left-to-right layer sequence on Fig. 1 corresponds to top-to-bottom on this figure.

The laser samples were processed into mesa etched ridge waveguides of width 8–14 μm [2]. The

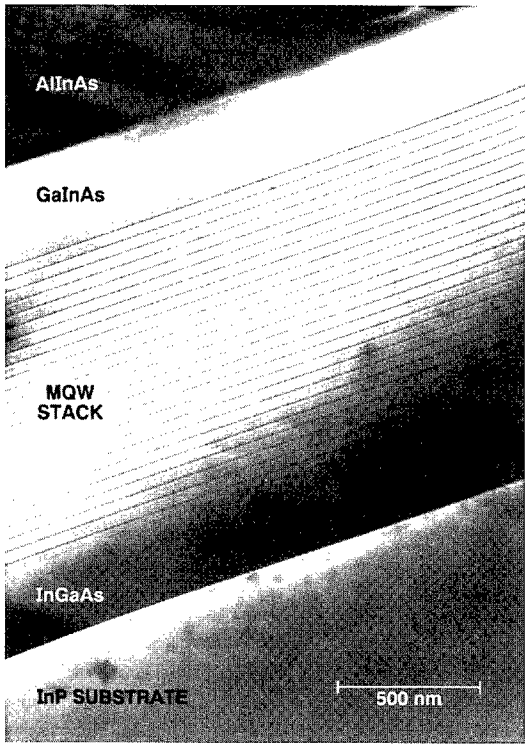

(a)

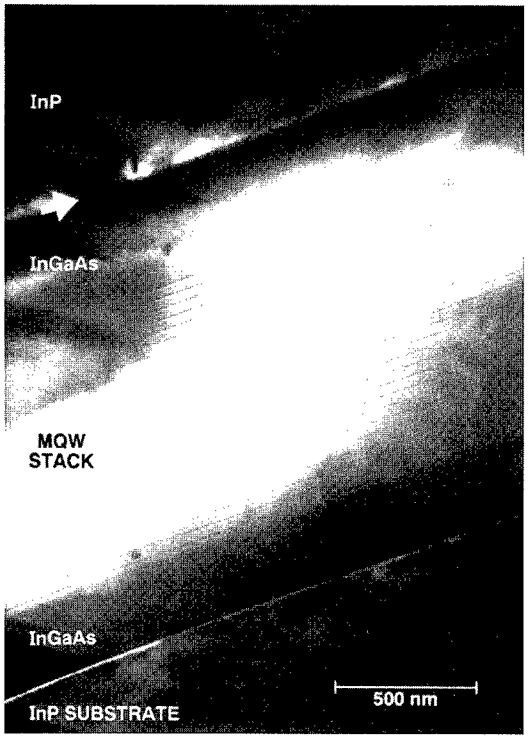

(b)

Fig. 3. (a) Transmission electron micrograph of the center of the waveguide of sample D2160. The 25 periods of the active region multilayer are clearly visible, cladded by the InGaAs layers. The InP substrate is visible on the bottom of the picture and the AlInAs cladding on the top. (b) Same micrograph, made on sample D2122. The interface between the first growth of the InGaAs/AlInAs stack and the InP regrowth is shown with an arrow. The regrowth process is free from visible dislocations or defects, as shown in this picture.

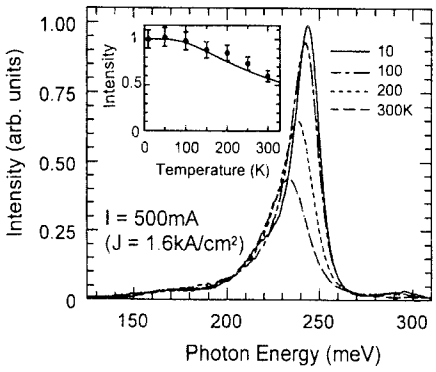

Fig. 4. Intersubband electroluminescence spectrum of device D-2122 at increasing temperatures. Inset: normalized luminescence intensity as a function of temperature. The intensity is linear with current. The solid line is the theoretical prediction for optical phonons emission.

lasers are cleaved in 3 mm long bars and the facets left uncoated. They are then mounted epilayer up on the temperature-controlled (10–320 K) cold head of a He flow cryostat. These devices were driven by 50 ns current pulses with a 4.5 kHz repetition rate. Fig. 5 shows the optical power versus drive current from a single facet of the InP cladded sample D-2122 obtained using $f/0.8$ optics and a calibrated, room temperature HgCdTe detector. Maximum peak output powers of about 200 mW at 300 K and 100 mW at 320 K are obtained. The differential slope efficiency, $dP/dI = 106$ mW/A at 300 K and 78 mW/A at 320 K, is only slightly less than one-half of its low-temperature value ($dP/dI = 250$ mW/A). In comparison, at $T = 300$ K, sample D-2160 (AlInAs cladding) exhibits about

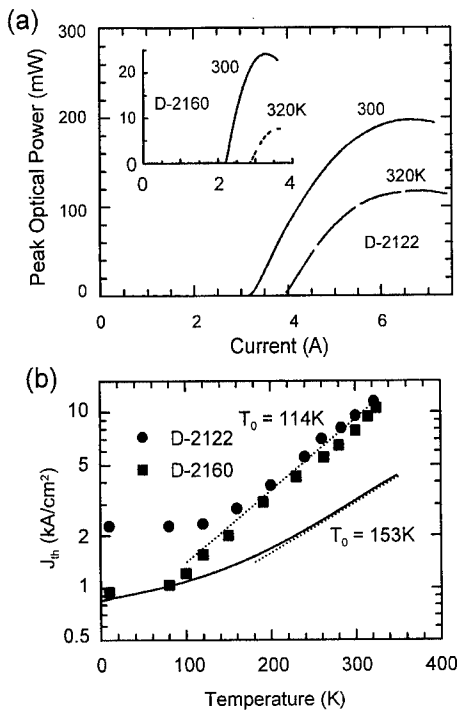

Fig. 5. (a) Collected pulsed optical power from a single facet versus injection current for heat sink temperatures of $T = 300$ K and $T = 320$ K and for the InP cladded sample D-2122 (14 μm × 2.9 mm). The collection efficiency is estimated to be $\eta = 70\%$. Inset: Same characteristics, but for sample D-2160 (9 μm × 3 mm). (b) Threshold current density in pulsed operation for both samples as a function of temperature. The solid line is the theoretical prediction. The dotted lines indicate the range over which the T_0 parameter is derived.

one-tenth of the power levels and slope efficiencies. We attribute this difference, which appears only above $T \sim 200$ K, to the enhanced heat removal during the pulse by the top InP cladding as compared to the AlInAs cladding.

In Fig. 5b, the threshold current density J_{th} is plotted as a function of temperature for both samples D-2160 and D-2122. At $T = 300$ K, the threshold current densities are very similar for both samples and are about 8–10 kA/cm^2. Between ~ 160 K and 320 K, the data can be described by the usual exponential behavior $J \sim \exp(T/T_0)$ with an average $T_0 = 114$ K. This value is much larger than the one obtained for interband lead-salt or III–V antimonide lasers [6–10] ($T_0 \sim 20$–45 K). On the same graph, we also plot the computed threshold current density J_{th} given by the following equation

$$J_{th} = \frac{1}{\tau_3(1 - \tau_2/\tau_{32})} \times \left[\frac{\varepsilon_0 n L_p \lambda(2\gamma_{32})}{4\pi q \Gamma_p N_p z_{32}^2}(\alpha_m + \alpha_w) + q n_2^{therm}\right]. \quad (1)$$

To describe the finite-temperature behavior, we added to the threshold current density J_{th}, [2] a term due to the thermal population n_2^{therm} of the state $n = 2$, which is included in our model by an activated behavior $n_2^{therm} = n_g \exp(-\Delta/kT)$. We also assumed that the lifetimes τ_i, limited by optical phonon emission, decrease with temperature according to the Bose–Einstein factor as discussed above for the case of the electroluminescence. In this expression, $\alpha_m = -\ln(R)/L_{cav} = 4.5$ cm^{-1} are the mirror losses (for $L_{cav} = 3$ mm), $\alpha_w = 10$ cm^{-1} are the waveguide losses, extrapolated from an analysis of the subthreshold luminescence [3], $\lambda = 5.2$ μm is the emission wavelength, $L_P = 45$ nm is the length of each stage, $\Gamma_p = 0.022$ is the overlap between the mode and one period of the structure, $N_p = 25$ is the number of periods, $n = 3.22$ is the mode refractive index, ε_0 the vacuum permittivity, and q the electron charge. We assumed that the gain has a broadening $2\gamma_{32}$ given by the experimental FWHM of the luminescence displayed in Fig. 4. We obtain a relatively good agreement at low temperature especially for device D-2160. However, our model predicts a larger T_0 of 153 K. Hot electron effects which translate into a higher population of state $n = 2$ are the most probable explanation for this discrepancy.

The devices were also tested at room temperature in pulsed mode with a relatively large (3.3%) duty cycle. The pulse length was 50 ns and the repetition rate 670 kHz. The light was collected by a non-imaging energy concentrator and its average intensity measured by a broad-band laser power meter. As shown in Fig. 6 the high peak power observed in sample D-2122 translates into an average power in the 2–10 mW range. Continuous wave (cw) operation of these devices is shown in Fig. 7. The devices operate cw up to 140 K for sample D2122 and 121 K for sample D-2160 with tens of

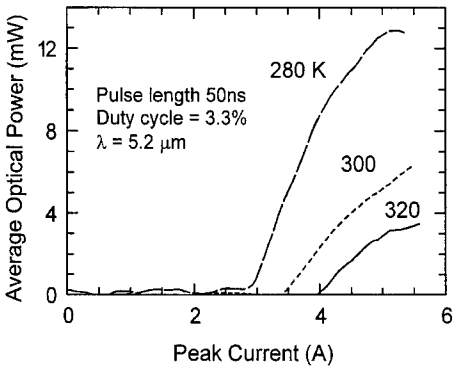

Fig. 6. Average power as a function of current for sample D-2122 (14 μm × 3 mm) for various temperatures.

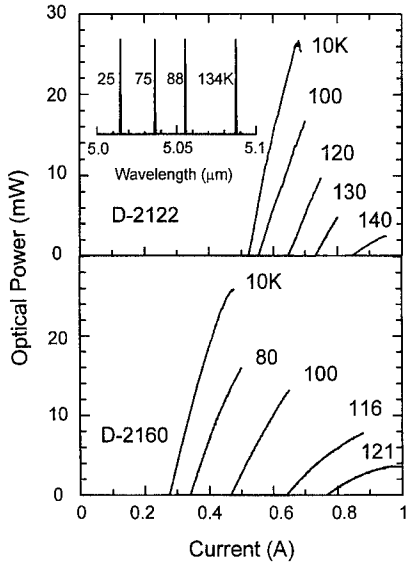

Fig. 7. Continuous optical output power from a single facet versus injection current for various heat sink temperatures. (a) sample D-2122 (7 μm × 2.9 mm). (b) sample D-2160 (9 μm × 3 mm). Single mode high-resolution spectra are shown in the inset. The side-mode suppression ratio is 20 dB.

miliwatts of optical power from one facet. For sample D2122, the measured slope efficiency at $T = 10$ K is $dP/dI = 213$ mW/A per facet, close to the value obtained in pulse operation ($dP/dI = 250$ mW/A). It corresponds to a differential quantum efficiency per period $\eta_d = 7 \times 10^{-2}$ when corrected for the collection efficiency of 0.5. The expression for η_d reads

$$\eta_d = \frac{1}{2}\frac{\alpha_m}{\alpha_m + \alpha_w}\left(1 - \frac{\tau_2}{\tau_{32}}\right), \quad (2)$$

which yields $\eta_d = 0.125$, a little less than twice the measured value. We also observed experimentally that the measured slope efficiency η_d of devices with a cavity length reduced from 3 mm down to 1.5 mm is almost constant (the increase is less than 10%). In contrast, Eq. (2) predicts an increase of η_d by a factor of 1.5 for the same cavity length reduction. These discrepancies are well explained by spatial hole burning effects, not taken into account in our model. The differential slope efficiency in continuous wave decreases from $dP/dI = 213$ mW/A at $T = 10$ K to 130 mW/A at $T = 100$ K and to 28 mW/A at $T = 140$ K. The decrease in slope efficiency with increasing temperature is mostly due to self-heating effects [3].

As shown in the inset of Fig. 7 for sample D-2122, single-mode operation is obtain over a wide range of temperature and currents between 5.015 μm (25 K) and 5.088 μm (134 K). This wavelength tuning of about 30 cm^{-1} is larger than the one previously reported [3] and is completely due to heating effects.

In conclusion, we have shown that QC lasers are able to perform with very high performances in pulsed mode at room temperature and above. The average power level obtained at room temperature (~5 mW) is sufficient for most sensing applications. These devices also operate in continuous wave with miliwatts of single-mode power up to a temperature of 140 K.

References

[1] J. Faist, F. Capasso, D.L. Sivco, C. Sirtori, A.L. Hutchinson and A.Y. Cho, Science 264 (1994) 553.
[2] J. Faist, F. Capasso, C. Sirtori, D.L. Sivco, A.L. Hutchinson and A.Y. Cho, Appl. Phys. Lett. 66 (1995) 538.
[3] J. Faist, F. Capasso, C. Sirtori, D.L. Sivco, A.L. Hutchinson and A.Y. Cho, Appl. Phys. Lett. 67 (1995) 3057.
[4] C. Sirtori, J. Faist, F. Capasso, D.L. Sivco, A.L. Hutchinson and A.Y. Cho, Appl. Phys. Lett. 66 (1995) 3242; C. Sirtori, J. Faist, F. Capasso, D.L. Sivco, A.L. Hutchinson and A.Y. Cho, Appl. Phys. Lett. 68 (1996) 1745.

[5] C. Sirtori, J. Faist, F. Capasso, D.L. Sivco, A.L. Hutchinson and A.Y. Cho, Appl. Phys. Lett. (1996), in press.
[6] J. Faist, F. Capasso, C. Sirtori, D.L. Sivco, A.L. Hutchinson and A.Y. Cho, Electron. Lett. 32 (1996) 560; J. Faist, F. Capasso, C. Sirtori, D.L. Sivco, J.N. Baillargeon, A.L. Hutchinson, S.N.G. Chu and A.Y. Cho, Appl. Phys. Lett. 26 (1996) 3680.
[7] Z. Shi, M. Tacke, A. Lambrecht and H. Böttner, Appl. Phys. Lett. 66 (1995) 2537.
[8] H.K. Choi, G.W. Turner and H.Q. Le, Appl. Phys. Lett. 66 (1995) 3543.
[9] D.H. Chow, R.H. Miles, T.C. Hasenberg, A.R. Kost, Y.-H. Zhang, H.L. Dunlap and L. West, Appl. Phys. Lett. 67 (1995) 3700.
[10] J.R. Meyer, I. Vurgaftman, R.Q. Yang and L.R. Ram-Mohan, Electron. Lett. 32 (1996) 45.
[11] Y.P. Yakovlev, K.D. Moiseev, M.P. Mikhailova, O.G. Ershov and G.G. Zegra, Conf. on Laser and Electro-Optics CLEO'96, 2–7 June (1996), Paper $CTuO_2$.
[12] J.N. Baillargeon, A.Y. Cho, F.A. Thiel and R.J. Fischer, Appl. Phys. Lett. 65 (1994) 207.

ELSEVIER

Journal of Crystal Growth 175/176 (1997) 29–36

JOURNAL OF CRYSTAL GROWTH

Progress and prospect of group-III nitride semiconductors

Isamu Akasaki*, Hiroshi Amano

Department of Electrical and Electronic Engineering, Meijo University, 1-501 Shiogama-guchi, Tempaku-ku, Nagoya 468, Japan

Abstract

Recent progress of crystal growth, conductivity control of group-III nitrides, has enabled us to produce high-performance short wavelength light-emitting diodes. Room temperature operation of nitride-based laser diodes has also been realized. Still, much further advances are required in many areas of materials science and device fabrication of the nitrides.

Keywords: Gruop-III nitrides; OMVPE; MBE; Low-temperature buffer; Conductivity control; LEDs; Lasers

1. Introduction

The group-III nitrides with the exception of BN, that is wurtzite polytypes of AlN, GaN, InN and their alloy AlGaInN, have the direct transition type band structures with band-gap energies ranging 1.9 eV for InN, 3.4 eV for GaN and 6.2 eV for AlN at room temperature. Moreover, due to the strong bond between nitrogen and each group-III atom, they are chemically and physically stable. Furthermore, GaN has high thermal conductivity and high electron saturation velocity. Therefore, they are one of the most promising materials for applications to short wavelength light emitters, such as light-emitting diodes (LEDs) and laser diodes (LDs) in the green to ultraviolet (UV) regions, as well as high-temperature electronic devices.

To realize such new devices, it is essential to grow high-quality nitride single crystals and to control their electrical conductivity. During the last two decades before 1985, much pioneering work has been done for GaN from the fundamental point of view and for practical use by many researchers. Unfortunately, however, it is fairly difficult to grow large-size bulk GaN crystals because equilibrium vapor pressure of nitrogen at the growth temperature is extremely high compared to those of phosphorous, arsenic, and antimony, in other III–V compounds. Besides, it had been quite difficult to grow high-quality epitaxial nitride films with a flat surface free of cracks. This is caused by the lack of substrate materials with lattice constants and thermal expansion coefficients close to those of GaN and the nitride alloys. Moreover, it has been well known that undoped GaN is strongly n-type with

*Corresponding author. Fax: +81 52 832 1244; e-mail: akasaki@meijo-u.ac.jp.

0022-0248/97/$17.00 Copyright © 1997 Elsevier Science B.V. All rights reserved
PII S0022-0248(96)00946-3

high residual electron concentrations and p-type GaN and GaN p–n junctions had not been realized until recently. These problems had prevented the fabrication of GaN-based devices for a long time.

Recent developments of the growth technology and of the basic understanding of the growth mechanism for the heteroepitaxial growth of GaN on highly mismatched substrates (e.g. sapphire) have enabled us to grow very high quality thin GaN [1, 2], AlGaN [3], GaInN [4, 5] films and their heterostructures [6, 7] with specular surfaces free of cracks. In addition, the mechanism of impurity incorporation and its activation in nitrides has been developed step by step. Conductivity control of both n-type [8] and p-type nitrides [9, 10] has also been achieved. Furthermore, optical and carrier confinement have been achieved by using heterostructures, and the emission wavelength has been controlled by the use of alloys as the active layer [11]. These achievements as well as the earlier discovery of impurities, which form very efficient blue luminescence centers in the nitrides [12], have led to the fabrication of high-brightness UV/blue, bluish-green, green and yellow LEDs with efficiencies in excess of 1% [11, 13–15]. Today, the GaN-based blue LED is commercially available. The brightness and the efficiency of these devices are comparable to the GaAlAs-based red LEDs and the AlGaInP-based orange to yellow LEDs. Room temperature operation of a nitride-based violet laser diode (LD) [16] and UV LD [17] has been realized. A nitride-based high-speed modulation doped field effect transistor (MODFET) using two-dimensional electron gas (2DEG) has been also developed [18].

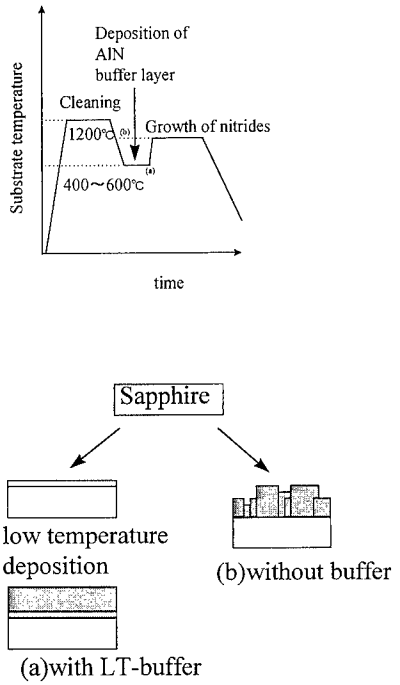

Fig. 1. Timing chart and the model for the growth of GaN by OMVPE with (a) and without (b) the LT-buffer layer.

2. Recent progress of crystal growth of nitrides

2.1. Low-temperature buffer layer method

A great advance in crystal growth by organometallic vapor phase epitaxy (OMVPE) was achieved by Amano et al. in 1986 [1]. They proposed the use of a low-temperature deposited (LT) buffer layer. Fig. 1 illustrates the growth process with (a) and without (b) the LT-buffer layer. We [19, 20] elucidated the growth mode and the role of the buffer layer in detail. Three-dimensional growth dominates when the GaN is grown directly on the sapphire substrate, while quasi-two-dimensional growth dominates when GaN is grown with the LT-buffer layer. As a natural consequence, all results, that are surface morphology, X-ray rocking curve, photoluminescence properties, electrical properties as well as cross-sectional transmission electron microscopy showed clearly that not only the crystalline quality, but also the luminescence as well as electrical properties, have been dramatically improved simultaneously using the LT-buffer layer method. It should be stressed that such high-quality GaN layers can be realized that are thin enough to avoid generating cracks. The essential role of the LT-buffer layer were found to be both the supply of high-density nucleation centers having the same orientation as the substrate and the promotion of the lateral growth of epitaxial film due

to the decrease in interfacial free energy between the epitaxial film and the substrate. The effectiveness of the LT-buffer layer method on the improvement of the crystalline quality of the nitride alloys such as AlGaN and GaInN was also proved. This buffer layer method was followed by Nakamura, who used a LT-GaN buffer layer in 1991 [2].

Today, these low-temperature AlN or GaN buffer layers are indispensable and standard for the growth of GaN and nitride alloys on sapphire substrates by OMVPE.

2.2. Preparation of layered structures

Control of thickness and alloy composition is an important issue for the fabrication of efficient light emitters and high-performance transistors, because ternary compounds such as AlGaN and GaInN are lattice-mismatched systems. Fig. 2 shows a cross-sectional transmission electron micrograph of a five well GaInN/GaN multi-quantum well (MQW) structure sandwiched between AlGaN layers, which were grown on sapphire substrates using the LT-buffer layer [21]. Dislocation density threading the MQW was found to be of the order of 10^8 cm^{-2} [22]. It is suggested that these dislocations are not electrically inactive in the nitrides [23]. Fig. 3 shows the $2\theta/\theta$ mode profile from a GaInN/GaN multi-layered structure having six pairs of GaInN and GaN layers sandwiched between AlGaN layers [22]. The experimental result agrees the calculated

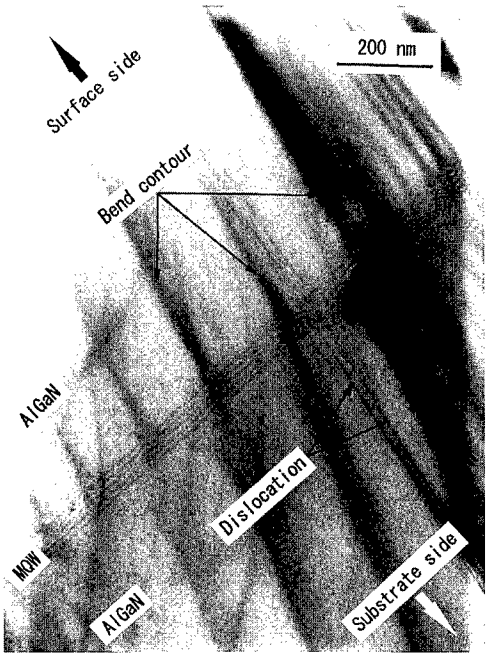

Fig. 2. Cross-sectional transmission electron micrograph of AlGaN/(GaInN/GaN)$_5$/AlGaN/LT-buffer/ sapphire.

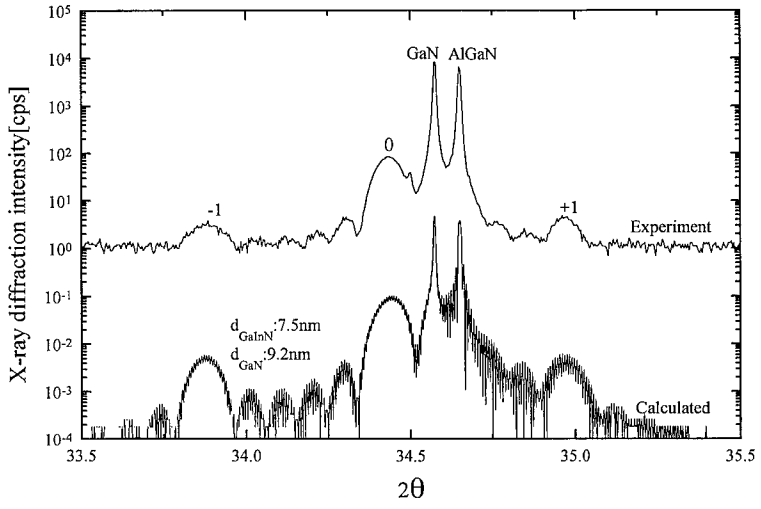

Fig. 3. High-resolution X-ray diffraction ($2\theta/\theta$ scan profile) of (GaInN/GaN)$_6$MQW/GaN/LT-buffer /sapphire structure.

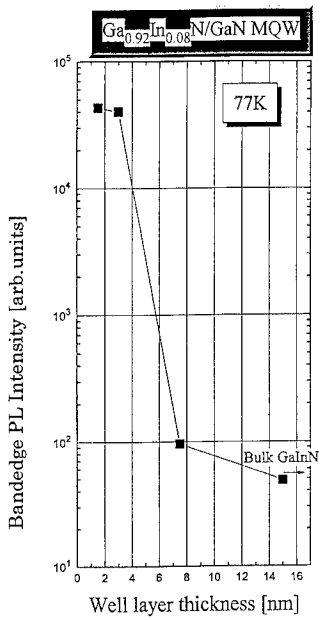

Fig. 4. Dependence of band-edge photoluminescence intensity on GaInN well layer thickness.

result obtained using kinematical theory. Four fringes can be clearly observed between the zeroth and first-order peaks of the MQW, which indicates that the interface is smooth and that the thickness and the alloy composition are well controlled. Akasaki et al. [22] showed that the band edge photoluminescence intensity increases with the decrease of the well thickness. The intensity of MQW with the thickness smaller than 2.5 nm is about 1.5 (at room temperature) or 3 (at 77 K, Fig. 4) orders of magnitude higher than those of bulk GaInN. In 1995, Nakamura et al. [14, 24] showed efficient blue, green and yellow LEDs fabricated using very thin GaInN quantum well active layers. Burm et al. reported GaN-based MODFET with transconductance of 40 mS/mm, f_T of 21.4 GHz and f_{max} of 77.5 GHz (with 0.25 μm long gate), respectively [18]. The MODFET structure consisting of a 75 Å GaN channel, 50 Å $Al_{0.16}Ga_{0.84}N$ spacer, 20 Å Si-doped charge supply layer, 130 Å $Al_{0.16}Ga_{0.84}N$ barrier and 60 Å $Al_{0.06}Ga_{0.94}N$ cap layer, was grown by OMVPE on sapphire substrate using the LT-AlN buffer layer.

3. Achievement of conductivity control

3.1. n-Type conductivity

In 1986, Sayyah et al. studied Si doping of GaN and AlGaN [25]. They reported that SiH_4 was harmful to the growth of GaN and AlGaN and did not affect the conductivity of the film. Nominally undoped GaN grown by OMVPE using the LT-buffer method is generally highly resistive, due to the reduced concentration of residual donors. Therefore, in order to obtain low-resistive n-type GaN, doping with a donor impurity is necessary. In 1990, Amano and Akasaki [8] and Murakami et al. [26] showed that SiH_4 is suitable for Si doping during OMVPE growth of GaN and AlGaN using the LT-buffer method and that Si behaves as a donor. They also showed that the cathodoluminescence intensity increases with increasing Si concentration in n-type GaN and AlGaN. The electron concentration at room temperature can be controlled from the undoped level to levels of more than 10^{19} cm^{-3}. The incorporation rate of Si in GaN does not strongly depend on the substrate temperature. Therefore, it is possible to control the concentration of Si in GaN by changing the flow rate of the precursor, either SiH_4 or Si_2H_6.

Today, Si doping in OMVPE growth with the LT-buffer layer is widely adopted for the conductivity control of the n-type nitrides, GaN, AlGaN and GaInN.

3.2. p-Type conductivity

So far, many groups attempted to produce p-type GaN. No group, however, succeeded in making it until 1989. Good controllability of Mg concentration during OMVPE growth of GaN was reported [27] by using bis-cyclopentadienylmagnesium (Cp_2Mg) as the Mg precursor. The added Mg was mostly inactive as-grown. In 1989, a low-energy electron beam irradiation (LEEBI) treatment was used to activate the Mg to yield p-type GaN and p–n junction type LEDs, for the first time by us [9]. Free-hole concentration at room temperature of about 2×10^{17} cm^{-3} was achieved at that time. Today, hole concentration at room temperature of about 2×10^{18} cm^{-3} is achieved. In 1991,

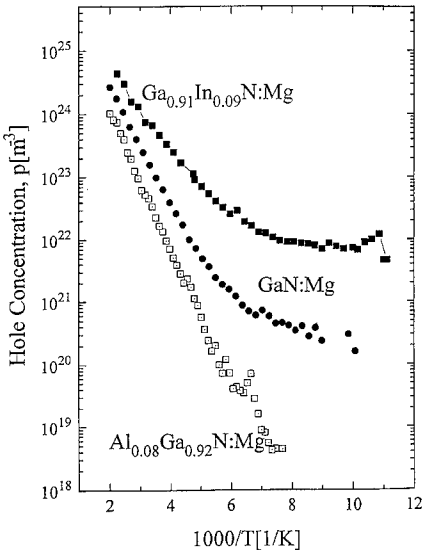

Fig. 5. Temperature dependence of the hole concentration of $Al_{0.08}Ga_{0.92}N$: Mg, GaN : Mg and $Ga_{0.91}In_{0.09}N$: Mg.

p-type AlGaN was obtained in the same manner [28]. Later, Nakamura et al. [10] achieved p-type GaN by thermal annealing in a hydrogen-free atmosphere. They showed that Mg is passivated by hydrogen in the as-grown state. The reduction of hydrogen passivation is the dominant process required to activate the Mg when ammonia is used as the nitrogen source [29]. Fig. 5 shows the temperature dependence of the hole concentration of Mg-doped $Al_{0.08}Ga_{0.92}N$, GaN and $Ga_{0.91}In_{0.09}N$. Contrary to the case for Si, the activation energy of Mg was found to depend on the alloy composition.

At present, in OMVPE, all the p-type GaN and group-III nitride alloys are prepared by Mg doping using Mg-precursors such as Cp_2Mg, followed by the LEEBI treatment or thermal annealing in a hydrogen-free atmosphere.

4. Brief history of the stimulated emission from nitrides

The first stimulated emission and laser action by optical pumping was reported by Dingle et al. in 1971 [30]. The temperature was 2 K. Cingolani et al. in 1986 reported high temperature stimulated emission up to 120 K [31]. They also reported an electron–hole plasma model as the mechanism of the stimulated emission in GaN. In 1990, Amano et al. [32] reported the first room temperature stimulated emission by optical pumping using high-quality GaN epitaxial layers grown with the LT-buffer layer. They also pointed out that by use of heterostructures, reduction of threshold power was possible. This is due to the well-known effect of carrier and optical confinement by the heterostructure. Khan et al. reported in 1991 [33] the first surface mode stimulated emission by optical pumping. Kim et al. [34] observed optical gain from AlGaN/GaN double heterostructures (DH) by optical pumping at room temperature. In 1995, a threshold power for stimulated emission by optical pumping of 27 kW/cm^2 was- reported by Akasaki et al. [22], which is the lowest to date and corresponds to 7.4 kA/cm^2 for current injection. The achievement of stimulated emission with low threshold by optical pumping and high-performance LEDs mentioned above, both strongly suggest the possibility of the realization of nitride-based LDs. Akasaki et al. in 1995 [35] observed the onset of stimulated emission by current injection for the first time. In late 1995 and the early 1996, Nakamura et al. fabricated the first nitride-based LD [16]. The structure is basically a separate confinement heterostructure (SCH). The active layer is a MQW having the number of well layers. GaN and AlGaN were used as the waveguide and cladding layers, respectively.

Fig. 6 [17] shows the emission spectra at the current density of 3.0 kA/cm^2 (Fig. 6a) and 1.5 kA/cm^2 (Fig. 6b) from one side edge of a device having a very thin GaInN quantum well with thickness of 1.5 nm. Strong and very narrow emission is clearly observed when current density exceeds 2.9 kA/cm^2, which is much higher than that expected from theoretical calculation [36]. Fig. 7 shows the calculated result of the dependence of the threshold current density (J_{th}) of the nitride-based MQW on the number of GaInN well layers in the active layer. In this calculation, wurtzite dipole matrix element was used [37]. Effective masses of electron and hole in the well layer were assumed to be $0.2m_0$ and $0.8m_0$, respectively. As shown in the

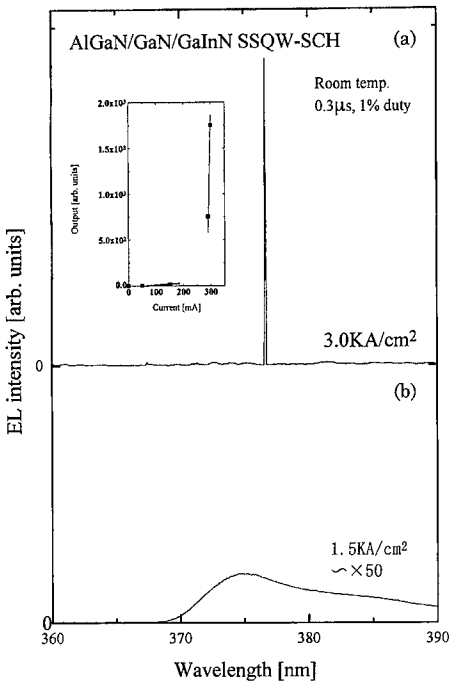

Fig. 6. Emission spectra above (a) and below (b) threshold current density (J_{th}) from the device having very thin quantum well. Inset shows I–L (current–light output) characteristic of the device.

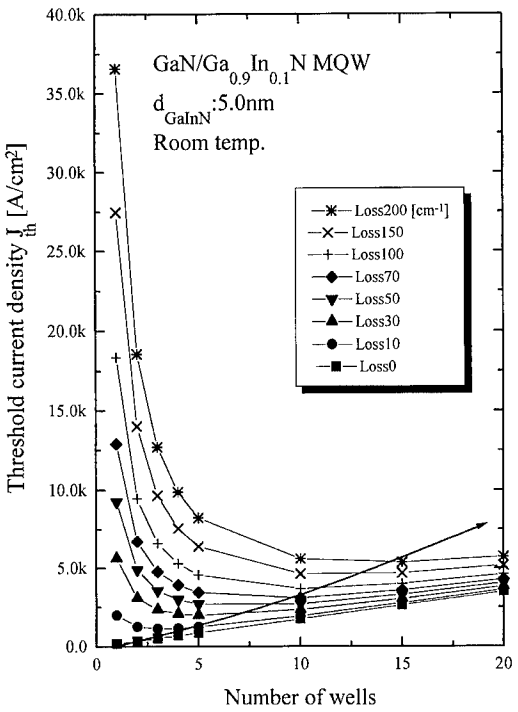

Fig. 7. Estimated threshold current density (J_{th}) of nitride-based MQW as a function of the number of GaInN quantum well layers in the active layer.

figure, if the total loss (= propagation loss + mirror loss) is negligibly small, J_{th} increases with the increase of number of quantum wells. However, if the total loss is not negligible, there are optimum numbers of quantum wells in order to achieve the lowest J_{th}. Therefore, to reduce J_{th}, it is necessary to decrease the loss as well as to optimize the device structure.

5. Future prospect of group-III nitrides

Until recently, hexagonal nitrides, grown by OMVPE on sapphire substrates, have been mostly used in devices mentioned above. In addition to hexagonal nitrides, cubic nitrides and so-called III–V nitrides, which include GaNAs, GaNP, AlNSiC and other materials containing nitrogen as one of the major constituents, are attracting the attention by many researchers.

On the other hand, various kinds of substrates such as Si, GaAs, SiC, ZnO, MgO, $MgAl_2O_4$ and $NdGaO_3$, which have less-mismatched and/or electrically conductive substrates, are being used for a variety of reasons. Some of them can be cleaved easily. This leads to the possibility of fabricating a good cavity mirror.

Nowadays, nitride people are employing OMVPE as well as several kinds of growth methods such as molecular beam epitaxy (MBE), hydride vapor phase epitaxy (HVPE), etc.

Recently, we have developed high-quality GaN and $Ga_{1-x}In_xN$ ($x < 0.2$) by RF-plasma-assisted MBE, which show intense near-band-edge photoluminescence at room temperature. A DH of p-GaN : Mg/n-GaInN/n-GaN has also been grown. Both n-GaN and n-GaInN were nominally undoped, while p-GaN was doped with Mg with a hole concentration of about $1.2 \times 10^{19}\,cm^{-3}$ at room temperature. No special postgrowth

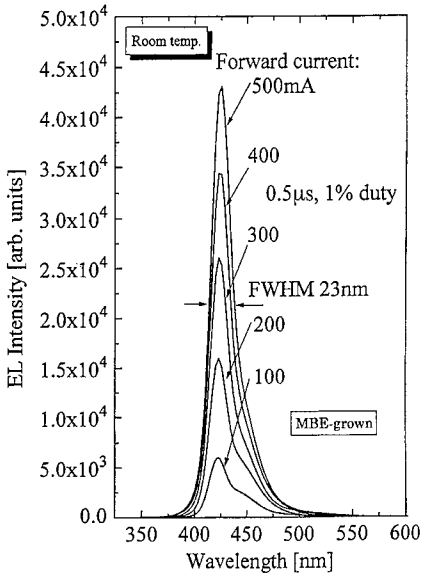

Fig. 8. EL spectra from p-GaN : Mg/$Ga_{0.8}In_{0.2}N$/n-GaN DH structure grown by MBE on GaN substrate with different forward currents at room temperature.

treatment was carried out. Fig. 8 shows electroluminescence (EL) spectra from p-GaN : Mg/$Ga_{0.8}In_{0.2}N$/n-GaN DH grown by MBE on a GaN subatrate, which was grown on sapphire C-face by OMVPE using the LT-AlN buffer layer. Intense violet emission originates in near-band-edge emission in the GaInN layer is clearly observed. The EL efficiency was about 0.3%, which is lower than those of OMVPE-grown LED by a factor of five to ten. This may be due to unoptimized device structure and impurity concentration [38].

At present, the band-edge photoluminescence intensities of undoped GaN and GaInN grown by MBE on GaN/the LT-AlN buffer/sapphire substrates are comparable to those of OMVPE.

On the contrary to OMVPE-grown GaN doped with Mg, the photoluminescence spectrum from MBE-grown GaN doped with Mg does not show so-called violet-blue emission due to Mg-related deep levels, but donor–acceptor (Mg) like violet emission. This is one of features of Mg-doped GaN grown by MBE.

Another advantage of using MBE growth over OMVPE growth of GaN is the capability in obtaining higher hole concentrations (e.g. 2×10^{19} cm^{-3}) than those (e.g. 5×10^{18} cm^{-3}) by OMVPE, without any special treatment after growth [39].

On the other hand, the growth rate of MBE is 0.2–0.8 μm/h typically, which is smaller than that of OMVPE by a factor of five to ten.

Less-strained or strain-free nitride films are being prepared by the use of homoepitaxial growth on GaN substrate, which has been already successfully grown by HVPE [40]. Selective area growth and several kinds of etching of nitrides are being studied for the fabrication of desirable device structures, such as the optical cavity, waveguide structure and low-dimensional structures.

6. Summary

In conclusion, an accumulation of a large quantity of outstanding work, in particular, in the areas of crystal growth and conductivity control has led to the commercialization of bright blue LEDs and the realization of LDs based on the nitrides. The performance of these nitride-based light emitters is still progressing at present. However, much further improvements of crystalline quality and conductivity, in particular, p-type conductivity are required for the realization of nitride-based high-performance LDs and FETs.

In addition to the OMVPE technology, therefore, the MBE technology will acquire a greater importance in future.

Acknowledgements

The authors are greatly indebted to the following collaborators who have made major contributions to this work: M. Koike, N. Shibata, T. Tanaka, L.F. Eastman, B. Monemar, I. Suemune and their groups. This work was supported partly by the Ministry of Education, Science, Sports and Culture of Japan (High-Tech Research Center Project and contract nos. 06452114, 07505012 and 07650025), Japan Society for the Promotion of Science ("Research for the Future" Program) and Daiko Foundation.

References

[1] H. Amano, N. Sawaki, I. Akasaki and Y. Toyoda, Appl. Phys. Lett. 48 (1986) 353.
[2] S. Nakamura, Jpn. J. Appl. Phys. 30 (1991) L1705.
[3] Y. Koide, H. Itoh, N. Sawaki and I. Akasaki, J. Electrochem. Soc. 133 (1986) 1956.
[4] N. Yoshimoto, T. Matsuoka, T. Sasaki and A. Katsui, Appl. Phys. Lett. 59 (1991) 2251.
[5] S. Nakamura and T. Mukai, Jpn. J. Appl. Phys. 31 (1992) L1457.
[6] K. Itoh, T. Kawamoto, H. Amano, K. Hiramatsu and I. Akasaki, Jpn. J. Appl. Phys. 30 (1991) 1924.
[7] S. Nakamura, M. Senoh and T. Mukai, Jpn. J. Appl. Phys. 32 (1993) L8.
[8] H. Amano and I. Akasaki, Mater Res. Soc. Ext. Abs. EA-21 (1990) 165.
[9] H. Amano, M. Kito, K. Hiramatsu and I. Akasaki, Jpn. J. Appl. Phys. 28 (1989) L2112.
[10] S. Nakamura, M. Senoh and T. Mukai, Jpn. J. Appl. Phys. 30 (1991) L1708.
[11] S. Nakamura, T. Mukai and M. Senoh, Appl. Phys. Lett. 64 (1994) 1687.
[12] J.I. Pankove, E.A. Miller, D. Richman and J.E. Berkeyheiser, J. Lumin. 4 (1971) 63.
[13] I. Akasaki, H. Amano, K. Itoh, N. Koide and K. Manabe, Inst. Phys. Conf. Ser. 129 (1992) 851.
[14] S. Nakamura, M. Senoh, N. Iwasa and S. Nagahama, Jpn. J. Appl. Phys. 34 (1995) L797.
[15] M. Koike, N. Shibata, S. Yamasaki, S. Nagai, S. Asami, H. Kato, N. Koide, H. Amano and I. Akasaki, Mater. Res. Soc. Symp. Proc. 395 (1996) 889.
[16] S. Nakamura, M. Senoh, S. Nagahama, N. Iwasa, T. Yamada, T. Matsushita, H. Kiyoku and Y. Sugimoto, Jpn. J. Appl. Phys. 35 (1996) L74.
[17] I. Akasaki, S. Sota, H. Sakai, T. Tanaka, M. Koike and H. Amano, Electron. Lett. 32 (1996) 1105.
[18] J. Burm, W.J. Schaff, L.F. Eastman, H. Amano and I. Akasaki, Appl. Phys. Lett. 68 (1996) 2849.
[19] I. Akasaki, H. Amano, Y. Koide, K. Hiramatsu and N. Sawaki, J. Crystal Growth 98 (1989) 209.
[20] K. Hiramatsu, S. Itoh, H. Amano, I. Akasaki, N. Kuwano, T. Shiraishi and K. Oki, J. Crystal Growth 115 (1991) 628.
[21] I. Akasaki and H. Amano, Inst. Phys. Conf. Ser. 145 (1995) 19.
[22] I. Akasaki, H. Amano and I. Suemune, Proc. Int. Conf. on Silicon Carbide and Related Mater. (1995) p. 7.
[23] F.A. Ponce, B.S. Krusor, J.S. Major, Jr., W.E. Plano and D.F. Welch, Appl. Phys. Lett. 67 (1995) 410.
[24] S. Nakamura, M. Senoh, N. Iwasa and S. Nagahama, Appl. Phys. Lett. 67 (1995) 1868.
[25] K. Sayyah, B.C. Chung and M. Gershenzon, J. Crystal Growth 77 (1986) 424.
[26] H. Murakami, T. Asahi, H. Amano, K. Hiramatsu, N. Sawaki and I. Akasaki, J. Crystal Growth 115 (1991) 648.
[27] H. Amano, M. Kitoh, K. Hiramatsu and I. Akasaki, J. Electrochem. Soc. 137 (1990) 1639.
[28] I. Akasaki and H. Amano, Mater. Res. Soc. Symp. Proc. 242 (1992) 383.
[29] S. Nakamura, N. Iwasa, M. Senoh and T. Mukai, Jpn. J. Appl. Phys. 31 (1992) 1258.
[30] R. Dingle, K.L. Shaklee, R.F. Reheny and R.B. Zetterstrom, Appl. Phys. Lett. 19 (1971) 5.
[31] R. Cingolani, M. Ferrara and M. Lugara, Solid State Commun. 60 (1986) 705.
[32] H. Amano, T. Asahi and I. Akasaki, Jpn. J. Appl. Phys. 29 (1990) L205.
[33] M.A. Khan, D.T. Olson, J.M. Van Hove and J.N. Kuznia, Appl. Phys. Lett. 58 (1991) 1515.
[34] S.T. Kim, H. Amano, I. Akasaki and N. Koide, Appl. Phys. Lett. 64 (1994) 1535.
[35] I. Akasaki, H. Amano, S. Sota, H. Sakai, T. Tanaka and M. Koike, Jpn. J. Appl. Phys. 34 (1995) L1517.
[36] I. Akasaki, S. Sota, H. Sakai and H. Amano, Ext. Abs. 1996 Int. Conf. Solid State Devices & Mater. (1996) p. 65.
[37] S. Kamiyama, K. Ohnaka, M. Suzuki and T. Uenoyama, Jpn. J. Appl. Phys. 34 (1995) L821.
[38] H. Sakai, T. Koide, H. Suzuki, M. Yamaguchi, S. Yamasaki, M. Koike, H. Amano and I. Akasaki, Jpn. J. Appl. Phys. 34 (1995) L1429.
[39] H. Amano, H. Sakai, S. Sota, T. Tanaka and I. Akasaki, Proc. Int. Symp. Blue Laser and LEDs (1996) p. 259.
[40] T. Detchprohm, H. Amano, K. Hiramatsu and I. Akasaki, Appl. Phys. Lett. 61 (1992) 2688.

ELSEVIER

Journal of Crystal Growth 175/176 (1997) 37–41

JOURNAL OF CRYSTAL GROWTH

Solid-source MBE for growth of laser diode materials

Mika Toivonen[a,*], Pekka Savolainen[a], Harry Asonen[b], Markus Pessa[a]

[a] *Tampere University of Technology, Department of Physics, P.O. Box 692, FIN-33101 Tampere, Finland*
[b] *TUTCORE Ltd., P.O. Box 48, FIN-33721 Tampere, Finland*

Abstract

We report on the growth of $Ga_xIn_{1-x}As_yP_{1-y}$ and $(Al_xGa_{1-x})_{0.51}In_{0.49}P$ thin films and related laser diode structures by solid-source molecular beam epitaxy, using valved cracking cells as sources of group-V fluxes. As shown here, high-quality materials, including strained-layer quantum well lasers for a large range of wavelengths from 0.68 to 1.69 μm, can be grown in a reproducible way. The performance characteristics of the fabricated lasers are comparable to those obtained by using other growth methods.

1. Introduction

Epitaxial $Ga_xIn_{1-x}As_yP_{1-y}$ compound semiconductors, lattice-matched to InP or GaAs substrates, are basic materials for laser diodes which emit at the wavelengths (λ) from 1.1 to 1.65 μm or from 0.8 to 1.1 μm, respectively. Wide-gap $(Al_xGa_{1-x})_yIn_{1-y}P$ lattice-matched to GaAs is another basic material for lasers, particularly at $0.63\ \mu m < \lambda < 0.69\ \mu m$.

Thin-film growth methods, such as metal-organic chemical vapour deposition (MOCVD), chemical beam epitaxy (CBE), and gas-source molecular beam epitaxy (GSMBE) are employed for preparing $Ga_xIn_{1-x}As_yP_{1-y}$ and $(Al_xGa_{1-x})_yIn_{1-y}P$ and related device structures. All these methods need toxic hydrides (AsH_3 and PH_3) as group-V sources to grow state-of-the-art materials. Apparently, there is a desire for a toxic-gas-free growth method that would be safe and simple to use. Such a technique now exists. It is a variant of MBE, a so-called solid-source MBE (SSMBE), which requires no hydrides.

The key components of SSMBE are valved cracking cells loaded with elemental solid arsenic and phosphorus. These cells produce stable and reproducible group-V fluxes [1]. Optical, electrical, and structural properties of $Ga_xIn_{1-x}As_yP_{1-y}$ and $(Al_xGa_{1-x})_yIn_{1-y}P$ are as good as those obtained by MOCVD, CBE, or GSMBE [1, 2]. Arsenide/phosphide heterostructures with abrupt interfaces [3] and many different lasers have also been grown by SSMBE, notably $\lambda \approx 1.3\ \mu m$ GaInAsP/InP multi-quantum well (MQW) lasers [4], 0.98 μm GaInAs/GaInP single-QW (SQW) lasers [5], and 0.68 μm GaInP/AlGaInP SQW lasers [6], all exhibiting very good performance characteristics.

In this paper, we describe SSMBE growth of $Ga_xIn_{1-x}As_yP_{1-y}$ and $(Al_xGa_{1-x})_yIn_{1-y}P$, lattice-matched to InP and GaAs. We also examine laser

* Corresponding author. Fax: + 358 3 3652600; e-mail: toivonen@ee.tut.fi.

0022-0248/97/$17.00 Copyright © 1997 Elsevier Science B.V. All rights reserved
PII S0022-0248(96)00828-7

diodes grown by this method to further assess the material quality.

2. Experimental procedure

Our SSMBE reactor uses valved cracking cells for both arsenic and phosphorus [5]. The chamber is evacuated by a 500 l/s ion-pump which keeps the idling pressure at about 2×10^{-10} mbar. The group-III elements and dopants are evaporated from conventional effusion cells.

The phosphorus cell consists of three separately heated zones: a red phosphorus oven, a white phosphorus reservoir, and a high-temperature cracking head. The cell is loaded with 7 N red phosphorus. This three-zone source eliminates the problems caused by pressure bursts and flux instabilities which are usually encountered with conventional effusion cells or with earlier two-zone valved sources, typical of arsenic cracking cells [7, 8]. Our arsenic cell is loaded with 7N5 solid arsenic.

In the three-zone phosphorus cell, the P_2 flux is produced from P_4 molecules which are provided by a white phosphorus charge generated prior to growth by sublimating red phosphorus at $\sim 400°C$ for a few hours. We could grow about 1.2 mm of phosphides with 150 g of red phosphorus. This is consistent with other reports where the consumption rate of phosphorus has been found to be about 0.09 g/μm of InP [9].

The P_2 and As_2 fluxes could be measured with an ionisation gauge. This was possible even though the background pressure tended to complicate accurate measurements. For example, when growing $\lambda_g = 1.1$ μm GaInAsP beam equivalent pressures (BEP) of 1.1×10^{-5} and 2.2×10^{-6} mbar were used for the P_2 and As_2 fluxes, respectively. The P_2 and As_2 fluxes were adjusted with the aid of automated valve positioners which allowed a rapid flux change needed for growth of heterostructures.

3. Results and discussion

3.1. Growth of GaInAsP

We prepared $Ga_xIn_{1-x}As_yP_{1-y}$ layers lattice-matched to InP for $1.1\ \mu m < \lambda_g < 1.55\ \mu m$. Growth of the $\lambda_g \approx 1.3$ μm layers was the most difficult. The difficulties were practically the same as those encountered in GSMBE growth [10, 11] and SSMBE growth of this semiconductor [12]. We found that the growth was unstable and yielded rough surfaces with poor optical and structural quality when the growth rate was 1 μm/h and the substrate temperature 490°C. When the growth rate was increased to 2 μm/h, the quality of layers became much better in every respect. One may interpret these problems in preparing $Ga_xIn_{1-x}As_yP_{1-y}$ at $\lambda_g \approx 1.3$ μm as due to an occurrence of a miscibility gap [11]. However, high-quality GaInAsP-on-InP at $\lambda_g \approx 1.3$ μm can still be grown if compressive strain in GaInAsP is introduced or if the growth conditions are chosen to be far from thermodynamic equilibrium [10].

SSMBE growth of GaInAsP of $\lambda_g = 1.1$ μm and $\lambda_g = 1.55$ μm, lattice-matched to InP, was rather straightforward and produced films with a high crystalline and optical quality.

Growth of $Ga_xIn_{1-x}As_yP_{1-y}$ lattice-matched to GaAs for $0.65\ \mu m < \lambda_g < 0.85\ \mu m$ was also studied. The main goal of this work part was to prepare GaInAsP waveguide material for 0.98 μm quantum well lasers.

We made test growths for $Ga_xIn_{1-x}As_yP_{1-y}$, prior to growing devices, to adjust the valve positions properly for desired compositions. We observed that the reproducibility of the group-V composition was good. For example, in one of our test series four 1 μm thick GaInAsP ($\lambda_g \approx 1.55$ μm) films were grown on successive days with the same pre-set values of the valve controller each day for both As_2 and P_2 fluxes. The variations in lattice constant remained within ± 200 ppm in this test.

Another point to bring up about these experiments is that the incorporation behaviour of As_2 and P_2 produced from the valved cracking cells is practically the same as that of As_2 and P_2 produced from hydride sources in the presence of hydrogen in GSMBE [11]. Arsenic always incorporates preferentially. The incorporation efficiencies of phosphorus and arsenic depend on the growth rate and relative concentration of In and Ga in the alloy. In general, the incorporation of phosphorus increases with increasing substrate temperature.

$Ga_xIn_{1-x}As_yP_{1-y}$ on InP and GaAs was characterised by double crystal X-ray diffraction (DCXRD), room temperature (RT) PL, and van der Pauw Hall measurements. The full width at half maximum (FWHM) of the DCXRD rocking curves of $Ga_xIn_{1-x}As_yP_{1-y}$ were about 30–35 arcsec for all the films studied. For comparison, the FWHM of the substrate was 20–25 arcsec (see the inset of Fig. 1).

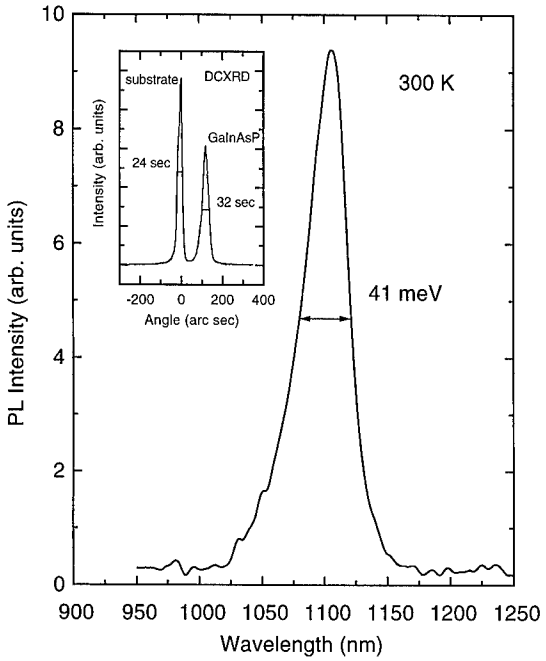

Fig. 1. Room temperature PL spectrum for a 1 μm thick GaInAsP ($\lambda_g = 1.1$ μm) layer. The inset shows the DCXD spectrum for the same sample. The lattice mismatch between the substrate and the layer is − 400 ppm.

As an example of the electrical properties of our GaInAsP films, Table 1 lists Hall data for a number of 2 μm thick GaInAsP ($\lambda_g = 1.1$ μm) samples. It shows that all the films are of high electrical quality even if their growth conditions were not precisely optimised. They also exhibited good RT PL spectra, yielding intensive PL peaks with 38 meV < FWHM < 46 meV. Fig. 1 shows an example of a RT PL spectrum for a 1 μm thick GaInAsP ($\lambda_g = 1.1$ μm) film.

To conclude, the structural, optical, and electrical characteristics of $Ga_xIn_{1-x}As_yP_{1-y}$ films deposited onto InP and GaAs substrates, as found in this work, are comparable to those earlier reported by our group using the GSMBE [13, 14] and to those reported by AT&T Bell Laboratories using SSMBE [1, 12].

3.2. Growth of AlGaInP

A number of $(Al_xGa_{1-x})_{0.51}In_{0.49}P$ samples were grown with x varying from 0 to 1 in anticipation of the growth of visible laser structures on GaAs. Device quality AlGaInP layers were prepared using a growth rate of 2 μm/h and a BEP of 2×10^{-5} mbar at 510°C. Narrow DCXRD line widths of ~ 25 arcsec (substrate 20 s) were routinely obtained across the whole composition range. Dopant concentrations of ~ 10^{18} cm^{-3} were readily achievable for both n-type and p-type samples.

3.3. Growth of laser diodes

We grew laser structures for emission at 0.68 μm < λ < 1.69 μm. The active regions of the lasers contained strained layers of single quantum

Table 1
Hall data of 2 μm thick GaInAsP ($\lambda_g = 1.1$ μm) layers grown on 'epi-ready' (1 0 0) InP substrates at 480°C

Sample	$n(p)_{300\ K}$ (cm^{-3})	$\mu_{300\ K}$ ($cm^2/V \cdot s$)	$n(p)_{77\ K}$ (cm^{-3})	$\mu_{77\ K}$ ($cm^2/V \cdot s$)
Undoped	-3.97×10^{15}	3900	-2.10×10^{15}	22610
n1	-2.10×10^{17}	3110	-1.92×20^{17}	4320
n2	-1.85×10^{18}	2220	-1.82×10^{18}	2490
p1	2.23×10^{17}	38	1.44×10^{17}	60
p2	2.72×10^{18}	41	2.03×10^{18}	51

wells or multi-quantum wells. The growth parameters were determined by growing a series of test samples which had similar active regions to those of the lasers of interest. RT PL and DCXRD were measured from these multi-layer structures.

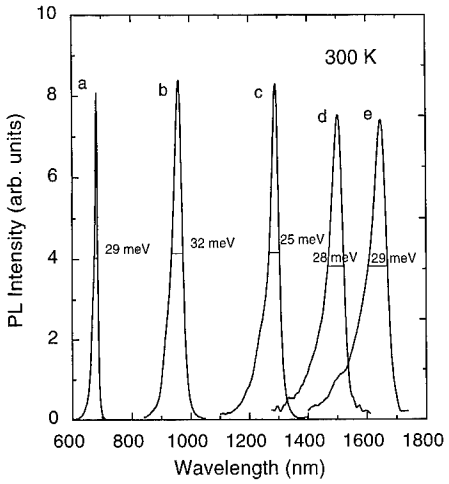

Fig. 2. Room temperature PL spectra from SSMBE grown QW structures containing (a) a compressively strained GaInP QW sandwiched between AlGaInP waveguide and cladding layers on GaAs, (b) a compressively strained InGaAs QW surrounded by quaternary InGaAsP waveguides and InGaP claddings on GaAs, (c, d) five compressively strained GaInAsP QWs separated by lattice-matched GaInAsP barriers and surrounded by GaInAsP waveguides and InP cladding regions on InP.

It was found that the PL line width and intensity closely correlated with the characteristics of the corresponding lasers. Fig. 2 shows RT PL spectra for some of the test samples over the entire range of wavelengths studied. As may be seen, the samples exhibit narrow line widths indicating the presence of high-quality QW structures. Interestingly, the samples with five $Ga_xIn_{1-x}As_yP_{1-y}$ quantum wells (Samples c, d, and e in Fig. 2) have small RT PL FWHM's of 25–29 meV, suggesting that the arsenic mole fraction in the MQW stacks remained nearly constant despite many rapid valve opening and closing operations accomplished during growth. A good emission wavelength accuracy, $\Delta\lambda \leqslant 10$ nm, was obtained quite readily and reproducibly for all the targeted wavelengths.

3.4. Characteristics of laser diodes

Broad-area lasers and ridge waveguide lasers were processed from the grown structures by means of standard photo-lithographic methods. Table 2 summarises the key features of the broad-area lasers, see also Refs. [4, 5, 15–17] for more details of some of the lasers.

The characteristics of our 0.905, 0.980, 1.3, and 1.55 μm lasers grown by SSMBE are comparable to those of state-of-the-art devices of similar structures

Table 2
Characteristics of SSMBE-grown lasers; λ is the emission wavelength, J_{th} is the threshold current density, $J_{th,\infty}$ is the threshold current density extrapolated to the infinite cavity length, T_0 is the characteristic temperature, $\theta_\perp$ is the FWHM angle of the perpendicular far-field, η_i is the internal quantum efficiency, η_d is the total differential efficiency and α_i is the internal loss

Structure	QW No.	λ (nm)	J_{th} (A/cm^2) at L (μm)	$J_{th,\infty}$ (A/cm^2)	T_0 (K)	FF, $\theta_\perp$ (deg)	η_i^c (%)	η_d (%)	α_i^c (cm^{-1})
GaInP/AlGaInP [15]	1	680	500 at 1250	175	90,[a] 130[b]	43	–	74	–
InGaAsP/InGaAsP/ InGaP	2	905	250 at 1000	180	100–150	29	–	> 82	–
InGaAs/InGaAsP/ InGaP [5]	1	980	172 at 1540	60	150–250	26	98.2	> 90	1.8
InGaAsP/InP [4]	5	1300–1350	400 at 1600	305	65	44	93	63	10.7
InAsP/InGaP/InP[d] [16]	10	1350	1150 at 1600	870	100	28	66	59	6.4
InGaAsP/InP [17]	5	1500–1570	387 at 1440	310	66.5	50	64	54	10.7
InGaAsP/InP	5	1665–1690	430 at 1540	340	59	45–50	–	> 35	–

[a] $T_0 = 90$ K between 20–80°C.
[b] $T_0 = 130$ K between 20–50°C.
[c] η_i and α_i are determined at 20°C.
[d] Strain compensated structure.

grown by other methods. Very low threshold currents down to 18 mA for $5 \times 300\ \mu m^2$ as-cleaved ridge waveguide 1.3 and 1.55 μm devices were obtained, and the threshold current densities extrapolated to infinite cavity length yielded values around 300 A/cm^2.

In particular, the ridge waveguide 0.98 μm lasers, our most thoroughly studied devices, exhibited excellent characteristics. With long cavities, 1.6 mm, and AR/HR mirror coatings these lasers launched cw output powers up to 260 mW in stable, kink-free, single-mode operation with a slope efficiency of over 0.9 W/A. The maximum thermally saturated power was 550 mW. Reliability tests have been going on for over 11 000 h at 125 mW and 8000 h at 150 mW in an automated constant power mode at room temperature. Until now, no degradation has been observed.

4. Conclusions

We have studied the growth of laser diode materials employing valved cracking cells as sources of group-V fluxes. High quality $Ga_xIn_{1-x}As_yP_{1-y}$ and $(Al_xGa_{1-x})_{0.51}In_{0.49}P$ films were prepared with an anticipation of laser diode growth. The incorporation behaviour of P and As was found to be very similar to what we have observed for GSMBE.

Several strained-layer QW laser diodes having emission wavelengths between 0.68 and 1.69 μm were also fabricated. The characteristics of these lasers were found to be fully comparable to those of the similar devices grown by other methods. Our results demonstrate that the novel valved cracking technology has made it possible to grow high quality laser diodes from visible to infrared region using only solid sources.

Acknowledgements

This work was supported, in part, by the Academy of Finland (Projects: EPIMATTER and SSMBE) and the Technology Development Centre (Project: SSMBE).

References

[1] J.N. Baillargeon, A.Y. Cho, F.A. Thiel, R.J. Fischer, P.J. Pearah and K.Y. Cheng, Appl. Phys. Lett. 65 (1994) 207.
[2] D.J. Mowbray, O.P. Kowalski, M. Hopkinson, M.S. Skolnick and J.P.R. David, Appl. Phys. Lett. 65 (1994) 213.
[3] F.G. Johnson, G.W. Wicks, R.E. Viturro and R. LaForce, J. Vac. Sci. Technol. B 11 (1993) 823.
[4] M. Toivonen, P. Savolainen, H. Asonen and R. Murison, Jpn. J. Appl. Phys. 35 (1996) L634.
[5] M. Toivonen, M. Jalonen, A. Salokatve, J. Näppi, P. Savolainen, M. Pessa and H. Asonen, Appl. Phys. Lett. 67 (1995) 2332.
[6] K. Tappura, J. Aarik and M. Pessa, IEEE Photonics Technol. Lett. 8 (1996) 319.
[7] J.N. Baillargeon, A.Y. Cho and R.J. Fischer, J. Vac. Sci. Technol. B 13 (1995) 64.
[8] W.E. Hoke, D.G. Weir, P.J. Lemonias, H.T. Hendriks, G.S. Jackson and P. Colombo, J. Vac. Sci. Technol. B 13 (1995) 733.
[9] J.N. Baillargeon, A.Y. Cho, R.J. Fischer, P.J. Pearah and K.Y. Cheng, J. Vac. Sci. Technol. B 12 (1994) 1106.
[10] K. Tappura and H. Asonen, J. Crystal Growth 110 (1993) 217.
[11] M. Pessa, K. Tappura and A. Ovtchinnikov, Thin Solid Films 267 (1995) 99.
[12] J.N. Baillargeon, A.Y. Cho and K.Y. Cheng, J. Appl. Phys. 79 (1996) 7652.
[13] K. Tappura, J. Appl. Phys. 74 (1993) 4565.
[14] G. Zhang, Appl. Phys. Lett. 63 (1993) 1128.
[15] M. Toivonen, P. Savolainen and M. Pessa, Semicond. Sci. Technol. 11 (1996) 1923.
[16] M. Toivonen, P. Savolainen, H. Asonen and R. Murison, J. Vac. Sci. Technol. B 14 (1996) 1736.
[17] P. Savolainen, M. Toivonen, H. Asonen and R. Murison, Jpn. J. Appl. Phys. 35 (1996) L900.

ELSEVIER

Journal of Crystal Growth 175/176 (1997) 42–45

JOURNAL OF CRYSTAL GROWTH

Low threshold 1.3 μm InAsP/GaInAsP lasers grown by solid-source molecular beam epitaxy

C.C. Wamsley*, M.W. Koch, G.W. Wicks

The Institute of Optics, University of Rochester, Rochester, New York 14627, USA

Abstract

A threshold current density of 270 A/cm^2 has been measured for 2 mm long InAsP/GaInAsP broad area lasers grown by solid source molecular beam epitaxy. To date, these are the lowest reported threshold current density 1.3 μm lasers by any type of MBE growth technique. An optimum growth temperature of 465°C was determined for InAsP by maximizing the photoluminescence intensity from a test structure modeled after the laser core, and a room-temperature photoluminescence line width of 18 meV was measured on an actual laser growth.

Keywords: Semiconductor lasers; Multiple quantum wells; SSMBE

1. Introduction

Low threshold current 1.3 μm lasers operating at elevated temperatures and high output powers are desired for many different fiber optic applications. Low threshold operation is desired to reduce power requirements as well as chirp and the line width enhancement factor of directly modulated lasers. Poor high-temperature characteristics currently force the utilization of thermoelectric coolers which increases costs and raises lifetime concerns. To meet this need, strained GaInAs, GaInAsP, and InAsP lasers have been studied using many different epitaxial growth techniques [1–4]. Benefits of strained-layer lasers include lower threshold currents and higher differential gain. Strain helps by altering the valence band structure which reduces the density of states that are involved in the lasing transition, thus lowering the threshold current [5, 6]. The altered valence band-band structure also suppresses Auger recombination and intervalance band absorption [6]. InAsP/InP has the added benefit of a large conduction band offset, $\Delta E_c = 0.7\,\Delta E_g$ [7], as compared to GaInAs/InP or GaInAsP/InP, $\Delta E_c = 0.4\,\Delta E_g$ [8, 9]. The larger conduction band offset more tightly confines carriers to the quantum wells, reducing carrier loss, especially at higher operating temperatures. Due to the large strain, approximately 1.5%, utilized in 1.3 μm InAsP/GaInAsP lasers, only a few quantum wells can be grown before exceeding the pseudomorphic critical thickness. However, the

* Corresponding author.

0022-0248/97/$17.00 Copyright © 1997 Elsevier Science B.V. All rights reserved
PII S0022-0248(96)00949-9

characteristic temperature, T_0 increases with well number, so to achieve better high-temperature operation, more wells are desired [10]. To overcome critical thickness concerns, strain-compensated devices containing barriers and wells of opposite strain have been investigated [11, 12], but will not be discussed here. In this paper we report on the growth and characterization of 1.3 μm compressively strained InAsP/GaInAsP MQW lasers grown by solid-source molecular beam epitaxy.

2. Experimental procedure

The MBE system used in this work is a turbomolecular pumped Riber 32P. A liquid-nitrogen (LN_2)-cooled trap, located in the foreline between the turbomolecular pump and the roughing pump, is used to capture phosphorus before it enters the roughing pump. The LN_2-cooled trap can be isolated and separated from the machine under a nitrogen atmosphere for cleaning in a fume hood. Standard effusion cells were used for the group III materials and EPI MBE Products Group valved group V sources produced the arsenic, As_4, and phosphorus, P_2, beams. The arsenic source is a single-oven-valved cracker source [13]. The phosphorus source is a dual-oven-valved cracker source designed to operate with pregenerated white phosphorus [14, 15]. Because of the low sublimation coefficient of red phosphorus, a source operating with red phosphorus will exhibit large flux transients [16]. White phosphorus has a much higher sublimation coefficient, and can produce a stable and controllable phosphorus beam [16, 17]. Heating the red phosphorus at 400°C for 4 h with the valve closed creates enough white phosphorus for about 15 μm of phosphide growth at a beam equivalent pressure of 1×10^{-5} Torr [18].

The SCH-MQW laser structure consisted of 1 μm thick n (Si $\sim 1 \times 10^{18}$ cm^{-3}) and p (Be $\sim 5 \times 10^{17}$ cm^{-3}) doped InP clads, the undoped active region, and a 0.1 μm p^+ (Be $\sim 1 \times 10^{19}$ cm^{-3}) GaInAsP cap. The active region consisted of three 41 Å InAsP strained quantum wells separated by 200 Å lattice-matched GaInAsP barriers sandwiched between 1500 Å GaInAsP confinement regions. All GaInAsP material had a emission wavelength of 1.1 μm. The barrier and well compositions were chosen so that no growth stops or cell temperature changes were necessary. At the start of the quantum well regions, the gallium was shuttered closed and the arsenic valve opened to get the desired InAsP emission. This allowed the gallium and indium cell temperatures to remain fixed throughout the growth at the fluxes needed to grow the desired GaInAsP quaternary. In the AlGaAs/GaAs material system, it has been shown that substrates misoriented towards the (1 1 1)A direction produce better quality material [19]. To investigate this concept in the InP material system, lasers were grown on pieces of (1 0 0) exact and (1 0 0) misoriented 4° towards (1 1 1)A n-type InP substrates bonded with indium to 2 in silicon wafers.

3. Results and discussion

The optimum growth temperature for the InAsP lasers was 465°C as determined in a photoluminescence (PL) study using the active region described above as the test structure. Substrate temperatures were measured using a thermocouple suspended behind the substrate and calibrated using the congruent sublimation temperature of GaAs. No temperature changes were made during the growth of any of the samples. Fig. 1 shows the influence of substrate temperature on the PL intensity. Typical room temperature PL FWHM line widths of the InAsP quantum well test structure were around 25 meV, indicative of the high-quality material and abrupt interfaces produced by SSMBE. After removal of the upper clad and cap layers by wet chemical etching, a very low room-temperature PL FWHM line width of 18 meV was measured on a laser (Fig. 2) and is among the best reported to date for InAsP quantum wells [1, 20]. The PL study also demonstrated that samples grown on the misoriented substrate consistently exhibited lower PL intensities and poorer surface quality.

Fifty micron wide, broad-area lasers were fabricated from both exact and misoriented samples grown at the same time. Testing was made under pulsed conditions with the devices placed n-side

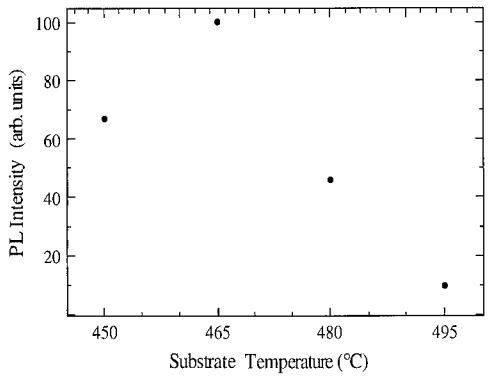

Fig. 1. PL intensity versus substrate temperature for InAsP/GaInAsP test structure.

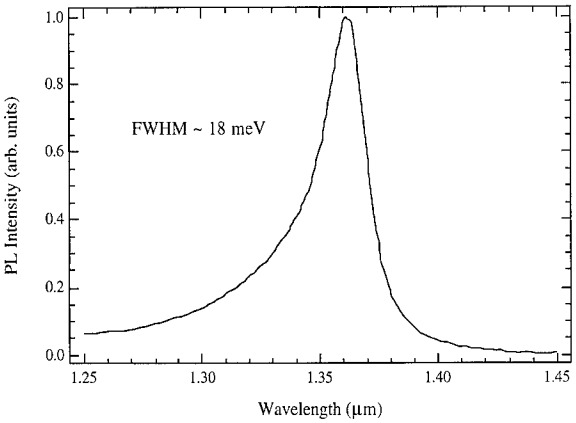

Fig. 2. Room-temperature PL spectra of InAsP/GaInAsP MQW laser on (1 0 0) exact substrate.

down on a copper block. Fig. 3 shows the threshold current density versus inverse cavity length for both orientations. A low threshold current density value of 290 A/cm^2 was achieved on 1 mm exact devices and 270 A/cm^2 was achieved on 2 mm misoriented devices. To our knowledge, these are the lowest reported threshold current densities for 1.3 μm broad-area lasers grown by any type of MBE growth technique. Extrapolation to infinite cavity lengths yield threshold current densities of 220 A/cm^2 for the misoriented material and 170 A/cm^2 for the exact material. Calibrated light versus intensity (L–I) measurements were taken to determine the internal quantum efficiency and the

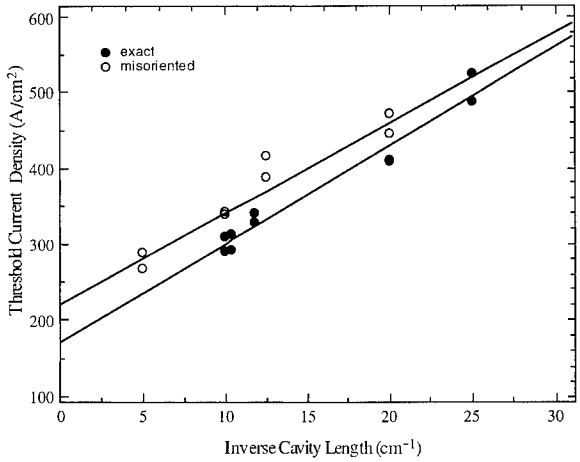

Fig. 3. Threshold current density versus inverse cavity length for InAsP/GaInAsP MQW lasers.

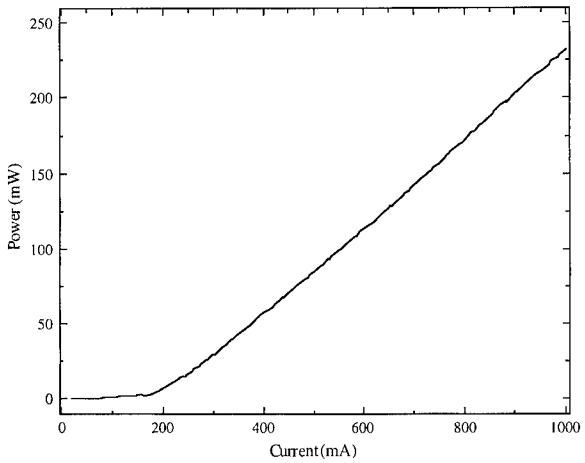

Fig. 4. L–I curve for a 1 mm InAsP/GaInAsP MQW laser on (1 0 0) exact substrate.

internal loss of the devices. A typical L–I curve is shown in Fig. 4 for a 1 mm device. From the slope efficiencies of the L–I curves and the threshold current densities, average internal quantum efficiency and internal loss values of $\eta_i \sim 64\%$ and $\alpha_i \sim 7\ \mathrm{cm}^{-1}$, and $\eta_i \sim 60\%$ and $\alpha_i \sim 5.5\ \mathrm{cm}^{-1}$ were determined for the exact and misoriented material, respectively. The characteristic temperatures T_0, as determined from a threshold current versus

temperature plot were around 51°C and 40°C for the exact and misoriented material, respectively. Since the structure was not optimized for carrier confinement and contained only three narrow wells, the low characteristic temperatures are not unexpected. The substrate orientation dependence is still being investigated.

4. Summary

To summarize, the lowest threshold current density 1.3 μm lasers grown by MBE have been demonstrated. A threshold current density of 270 A/cm^2, measured on a 2 mm broad area device, and a room-temperature PL FWHM line width of 18 meV clearly illustrate the effectiveness of the solid-source molecular beam epitaxial growth technique for growing high quality semiconductor devices.

References

[1] M. Yamamoto, N. Yamamoto and J. Nakano, IEEE J. Quantum Electron. QE-30 (1994) 554.
[2] P. Thiagarajan, A.A. Bernussi, H. Temkin, G.Y. Robinson, A.M. Sergent and R.A. Logan, Appl. Phys. Lett. 67 (1995) 3676.
[3] M. Toivonen, P. Savolainen, H. Asonen and R. Murison, Jpn. J. Appl. Phys. 35 (1996) L634.
[4] H. Sugiura, M. Itoh, N. Yamamoto, M. Ogasawara, K. Kishi and Y. Kondo, Appl. Phys. Lett. 68 (1996) 3213.
[5] E. Yablonovitch and E.O. Kane, J. Lightwave Technol. LT-4 (1986) 504.
[6] A.R. Adams, Electron. Lett. 22 (1986) 249.
[7] R.P. Schneider, Jr. and B.W. Wessels, J. Electron. Mater. 20 (1991) 1117.
[8] R.E. Cavicchi, D.V. Lang, D. Gershoni, A.M. Sergent, J.M. Vandenberg, S.N.G. Chu and M.B. Panish, Appl. Phys. Lett. 54 (1989) 739.
[9] E.A. Montie, P.J.A. Thijs and G.W. 't Hooft, Appl. Phys. Lett. 53 (1988) 1611.
[10] T. Namegaya, N. Matsumoto, N. Yamanaka, N. Iwai, H. Nakayama and A. Kasukawa, IEEE J. Quantum Electron. QE-30 (1994) 578.
[11] A. Ougazzaden, A. Mircea and C. Kazmierski, Electron. Lett. 31 (1995) 803.
[12] A. Kasukawa, N. Yokouchi, N. Yamanaka and N. Iwai, Electron. Lett. 31 (1995) 1749.
[13] D.L. Miller, S.S. Bose and G.J. Sullivan, J. Vac. Sci. Technol. B 8 (1990) 311.
[14] G.W. Wicks, M.W. Koch, J.A. Varriano, F.G. Johnson, C.R. Wie, H.M. Kim and P. Colombo, Appl. Phys. Lett. 59 (1991) 342.
[15] M.L. Dotor, D. Golmayo and F. Briones, J. Crystal Growth 127 (1993) 619.
[16] F.G. Johnson and C.E.C. Wood, J. Appl. Phys. 78 (1995) 1664.
[17] G.W. Wicks, M.W. Koch, F.G. Johnson, J.A. Varriano, G.E. Kohnke and P. Colombo, J. Vac. Sci. Technol. B 12 (1994) 1119.
[18] C.C. Wamsley, M.W. Koch and G.W. Wicks, J. Vac. Sci. Technol. B 14 (1996) 2322.
[19] R.K. Tsui, J.A. Curless, G.D. Kramer, M.D. Peffley and G.W. Wicks, J. Appl. Phys. 59 (1986) 1508.
[20] H. Sugiura, M. Mitsuhara, H. Oohashi, T. Hirono and K. Nakashima, J. Crystal Growth 147 (1995) 1.

ELSEVIER

Journal of Crystal Growth 175/176 (1997) 46–51

JOURNAL OF CRYSTAL GROWTH

Solid source MBE growth and regrowth of 1.55 μm wavelength GaInAsP/InP ridge lasers

F.G. Johnson[a,*], O. King[a], F. Seiferth[a], S. Horst[a], D.R. Stone[a], R.D. Whaley[b], M. Dagenais[b], Y.J. Chen[c]

[a] *Laboratory for Physical Sciences, University of Maryland, College Park, Maryland 20740, USA*
[b] *Department of Electrical Engineering, University of Maryland, College Park, Maryland 20742, USA*
[c] *Department of Electrical Engineering, University of Maryland, Baltimore, Maryland 21228, USA*

Abstract

We report on the solid source molecular beam epitaxial growth of $Ga_xIn_{(1-x)}As_yP_{(1-y)}$ and its application to separate confinement heterostructure laser diodes operating at 1.55 μm. High-quality quaternary films were grown reproducibly with a band gap wavelength of 1.3 μm. Separate confinement heterostructure laser diodes operating at 1.55 μm were produced with active regions containing four $Ga_{0.47}In_{0.53}As$, $Ga_{0.27}In_{0.73}As_{0.8}P_{0.2}$, or $InAs_{0.6}P_{0.4}$ quantum wells. Broad area laser threshold current densities were as low as 275 A/cm^2 and equal the best results reported for similar devices grown by other techniques. Ridge lasers were fabricated with threshold currents of 20 mA and external quantum efficiencies of 0.21 mW/mA per facet. Specular InP was regrown over etched ridges and was used to produce buried ridge laser diodes.

1. Introduction

Fiber optic communication systems rely heavily on $InP/Ga_xIn_{(1-x)}As_yP_{(1-y)}$ materials to provide light emission at 1.3 and 1.55 μm. Subsequent to liquid phase epitaxy (LPE) [1], solid source molecular beam epitaxy (MBE) was one of the first to grow $Ga_xIn_{(1-x)}As/InP$ [2] and $Ga_xIn_{(1-x)}As_yP_{(1-y)}/InP$ [3] double heterostructure lasers. Since then, gas source molecular beam epitaxy (GSMBE) [4], chemical beam epitaxy (CBE) [5], and metalorganic vapor phase epitaxy (MOVPE) [6, 7] have all been used to grow high-quality separate confinement heterostructure (SCH) lasers operating at 1.55 μm. However, these multi-quantum well SCH laser structures were difficult to reproduce using solid source MBE and conventional effusion cells, because they required the ability to adjust the As_2 and P_2 fluxes accurately and quickly.

The introduction of valved, cracking effusion cells to supply As_2 [8] and P_2 [9] fluxes from solid sources allowed for the precise control of group-V fluxes during MBE. MBE has since been used to grow arsenide/phosphide heterostructures with

* Corresponding author. Fax: +1 301 935 6723; e-mail: fred@lps.umd.edu.

0022-0248/97/$17.00 Copyright © 1997 Elsevier Science B.V. All rights reserved
PII S0022-0248(96)00878-0

abrupt interfaces [10] and $Ga_xIn_{(1-x)}As_yP_{(1-y)}$ films lattice matched to InP [11]. These advances led to the development of quaternary containing 1.35 μm [12] and 1.55 μm [13] SCH laser diodes grown by solid source MBE that had threshold current densities comparable to devices grown by other techniques. In this paper, we report on the quality and reproducibility of solid source MBE grown $Ga_xIn_{(1-x)}As_yP_{(1-y)}$ films ($\lambda \approx$ 1.3 μm) and SCH lasers with $Ga_{0.47}In_{0.53}As$, $Ga_{0.27}In_{0.73}As_{0.8}P_{0.2}$, and $InAs_{0.6}P_{0.4}$ quantum wells ($\lambda \approx 1.55$ μm).

2. Experiment

The laser diodes in this study were grown over a period of several months in a conventional MBE machine on 2″ sulfur-doped (100) InP substrates misoriented by 4 degrees towards (111)A. The substrate temperature during growth was 475°C, which was approximately 25°C below the observed oxide desorption temperature. Gallium, indium, silicon, and beryllium fluxes were supplied from effusion cells containing elemental sources. The growth rates were 1.3 monolayers/s for InP, corresponding to a beam equivalent pressure (BEP) of 4.1×10^{-6} mbar, and 1.8 monolayers/s for $Ga_xIn_{(1-x)}As_yP_{(1-y)}$, corresponding to an added gallium BEP of 6.4×10^{-7} mbar. Two independent, valved effusion cells were used to supply As_4 ($T_{cracker} = 500$°C) and P_2 ($T_{cracker} = 1000$°C) fluxes. One cell contained elemental arsenic, and the other was loaded with elemental red phosphorus. Because of the low sublimation coefficient of red phosphorus [14], a portion was converted to white phosphorus before growth [15].

3. Results and discussion

In this paper, lattice matched $Ga_{0.27}In_{0.73}As_{0.58}P_{0.42}$ with a band gap wavelength near 1.3 μm is used to construct the core of SCH laser diodes. In conjunction with the growth of various laser structures, eight quaternary films were grown over a period of several months to monitor the flux calibration and material quality. The group-V fluxes were set before each growth by adjusting the valve positions on the group-V sources to obtain ion gauge BEP's of 1.7×10^{-5} (P_2) and 1.3×10^{-5} (As_4) mbar. The group-V to group-III atomic flux ratio can be calculated from the BEP's [16, 17] and was found to be 14 : 1.

The resulting film compositions were determined by analyzing the photoluminescence (PL) and X-ray diffraction spectra [25]. The lattice mismatch, $(\Delta a/a)$, for the eight $Ga_{0.27}In_{0.73}As_{0.58}P_{0.42}$ samples varied within ± 0.0005, corresponding to a change in arsenic mole fraction of less than ± 0.015. This reproducibility is comparable to the accuracy of the ion gauge BEP measurements. The atomic incorporation efficiency of arsenic relative to phosphorus was calculated from the BEP's and the film composition and was found to be 9 : 1. As a result, only the accuracy of the arsenic BEP measurement is significant in determining the film composition. The arsenic BEP was set between 1.25 and 1.35×10^{-5} mbar before each growth. This variation in arsenic BEP corresponds to a change in arsenic mole fraction of ± 0.01 and accounts for most of the experimental variability in quaternary composition. At lower group-V to group-III atomic flux ratios, the incorporation efficiencies of phosphorus and arsenic become more similar, and small variations in both fluxes will effect the film composition.

Theory predicts a miscibility gap for $Ga_xIn_{(1-x)}As_yP_{(1-y)}$ grown at typical MBE growth temperatures, particularly for alloys with a band gap wavelength near 1.3 μm [18]. GSMBE grown $Ga_xIn_{(1-x)}As_yP_{(1-y)}$ films with $y \approx 0.5$–0.9 show spinodal-like decomposition that degrades the surface morphology and broadens PL and X-ray diffraction peak line widths [19]. This decomposition could, however, be mitigated somewhat by increasing the group-V to group-III flux ratio, which serves to reduce surface adatom diffusion during growth [19]. As the group-V to group-III flux ratio is further increased, however, the morphology again degrades due to the large amounts of hydrogen present in the GSMBE growth zone [20]. By switching to solid sources, this limitation on the group-V fluxes can be avoided.

The PL and symmetric (004) double-crystal X-ray diffraction spectra from $Ga_{0.27}In_{0.73}As_{0.58}$

$P_{0.42}$ films grown by solid source MBE are shown in Fig. 1a and Fig. 1b, respectively. The films had a specular surface morphology. The room temperature PL peak line width of 42 meV is similar to the 45 meV line width predicted by theory [21]. In the X-ray diffraction spectrum, the higher intensity peak is from the InP. The lower intensity peak comes from the 0.7 μm quaternary film and has a full width at half maximum (FWHM) line width of 27 arcsec. This line width is equal to that predicted by a dynamical simulation [22] of a fully disordered 0.7 μm thick $Ga_{0.27}In_{0.73}As_{0.58}P_{0.42}$ alloy. These line widths and morphology results show that it is possible to choose solid source MBE growth conditions such that the degradation normally associated with spinodal-like decomposition of quaternary alloys with band gap wavelengths near 1.3 μm is avoided.

Three different SCH laser diode structures were grown and characterized. Except for the quantum wells, the basic structure and growth conditions were similar for all three. This structure consisted of a 1 μm Si-doped (5×10^{17}) InP buffer layer, an 0.24 μm unintentionally doped symmetric core region containing $Ga_{0.27}In_{0.73}As_{0.58}P_{0.42}$ and four quantum wells, a 1.5 μm Be-doped (6×10^{17}) InP upper cladding layer, and a 0.2 μm Be-doped (1×10^{19}) $Ga_{0.47}In_{0.53}As$ cap. The quantum wells were chosen to vary the amount of compressive strain while maintaining laser emission near 1.55 μm. They were either 65 Å $Ga_{0.47}In_{0.53}As$ ($\varepsilon = 0.0\%$), 105 Å $Ga_{0.27}In_{0.73}As_{0.8}P_{0.2}$ ($\varepsilon = 0.7\%$), or 95 Å $InAs_{0.6}P_{0.4}$ ($\varepsilon = 1.9\%$) quantum wells separated by 125, 100, or 110 Å barriers, respectively. A 10 s growth interruption was inserted at each interface that required a change in group-V composition. In addition, a 150 Å $Ga_{0.27}In_{0.73}As_{0.58}P_{0.42}$ etch stop layer was inserted in the upper clad of the growths used to make ridge lasers to improve the process yield.

For similar SCH laser diodes grown by MOVPE, it is common to include an undoped InP layer after the core. Zinc is typically used as the p-type dopant and is known to diffuse during MOVPE [23]. Secondary ion mass spectrometry was performed on a SCH laser diode structure with $Ga_{0.47}In_{0.53}As$ quantum wells to check the doping profiles in our laser diodes. Both the Si and Be doping profiles dropped abruptly at the corresponding InP to $Ga_{0.27}In_{0.73}As_{0.58}P_{0.42}$ interface. Both were lower by more than a factor of 25 in the active region as compared to the doping density in the cladding layers.

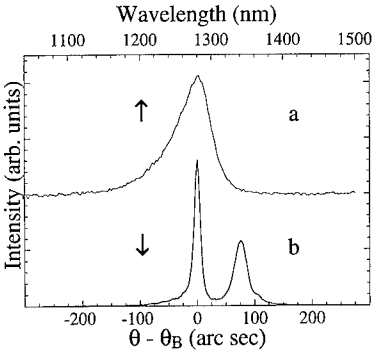

Fig. 1. (a) Photoluminescence and (b) X-ray diffraction spectra from $Ga_{0.27}In_{0.73}As_{0.58}P_{0.42}$ films grown on InP.

The three different SCH laser structures were characterized using PL and X-ray diffraction before processing. All three types displayed relatively narrow PL peaks near 1.55 μm at room temperature (FWHM 22–28 meV) and 1.44 μm at 15 K (FWHM 6–7 meV). In addition, the reproducibility of the peak wavelength was quite good. The SCH laser structure containing four 105 Å $Ga_{0.27}In_{0.73}As_{0.8}P_{0.2}$ ($\varepsilon = 0.7\%$) quantum wells was grown 11 times over a period of several months, and the wavelength of the room temperature PL peak varied within a 42 nm range between 1.535 and 1.577 μm. This variation is equivalent to an arsenic mole fraction variation of ± 0.01 and is again comparable to the accuracy at which we can determine the group-V BEP. The X-ray diffraction spectra of the laser structures show a single peak corresponding to the InP substrate and cladding layers as well as several superlattice satellite peaks corresponding to the periodicity associated with the four quantum wells in the core. The (004) symmetric double-crystal diffraction spectrum from the laser diode structure with four 95 Å $InAs_{0.6}P_{0.4}$ quantum wells is shown in Fig. 2.

Broad area laser diodes with uncoated, cleaved facets were fabricated from the three types of SCH laser structures described above. The p-contacts

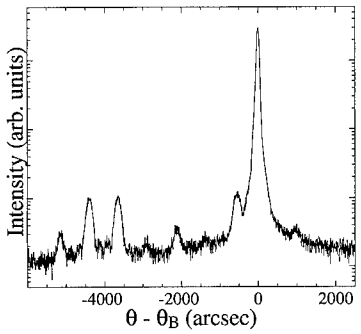

Fig. 2. Symmetric (004) X-ray diffraction spectrum from a SCH with four $InAs_{0.6}P_{0.4}$ quantum wells.

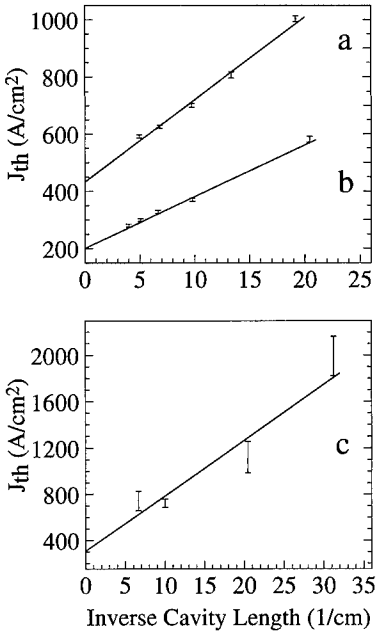

Fig. 3. Plot of threshold current density versus inverse cavity length for broad area SCH laser diodes with four (a) 0.0%, (b) 0.7%, and (c) 1.9% compressively strained quantum wells.

were 100 μm wide, and the $Ga_{0.47}In_{0.53}As$ cap layers were selectively removed in between the individual devices to achieve electrical isolation. Threshold current densities were determined using the p-contact dimensions; no correction was made for current spreading.

Plots of threshold current density, J_{th}, versus inverse length are shown in Fig. 3a, Fig. 3b, and Fig. 3c for laser diodes containing quantum wells with 0.0%, + 0.7%, and + 1.9% compressive strain, respectively. Four to eight devices of each length were measured, and device variation is represented by the height of the error bars. For the laser diodes with four unstrained 65 Å $Ga_{0.47}In_{0.53}As$ quantum wells, the lowest measured J_{th} value was 580 A/cm^2. The extrapolated transparency current density, J_o, was 432 A/cm^2. These J_{th} values are comparable to results in the literature of 500–700 A/cm^2 for similar unstrained laser diodes [1, 5, 7]. The measured internal quantum efficiency ($\eta_i = 0.75$), characteristic temperature ($T_o = 55$ K), and internal loss ($\alpha = 20\ cm^{-1}$), are also typical for these devices. The laser diodes containing four strained 105 Å $Ga_{0.27}In_{0.73}As_{0.8}P_{0.2}$ ($\varepsilon = + 0.7\%$) quantum wells had a J_{th} as low as 275 A/cm^2, and a J_o of 200 A/cm^2 (50 A/cm^2 per well). These results are comparable to the best J_{th} reports in the literature (268–324 A/cm^2) from any growth technique for similar four quantum well devices [6, 7].

It has been shown that increasing the compressive strain in the quantum well reduces J_{th} for SCH lasers by reducing the nonradiative recombination rate [6, 7]. A third SCH laser structure was grown by solid source MBE with four $InAs_{0.6}P_{0.4}$ quantum wells to achieve a compressive strain of + 1.9% while maintaining an emission wavelength of 1.55 μm. A ternary quantum well should be less susceptible to the decomposition problems sometimes seen in quaternary films since the composition lies well away from the miscibility gap [19]. In addition, variations in the group-III flux over time or across the wafer will not affect the alloy composition of the well.

The J_{th} values from broad area lasers made from this material are shown in Fig. 3c. The results are not as good as results from the lasers grown with quantum wells of lower strain. Furthermore, there was a large variation in J_{th} between diodes of the same length, as seen by the increased height of the error bars. Low-temperature cathodoluminescence showed the existence of dark, parallel lines running in the plane of the quantum well. Given the

magnitude of the strain and the thickness of the quantum wells, it is not surprising to find the film partially relaxed. It is interesting to note, however, that the PL intensity and linewidths did not vary significantly from the results of the other two laser diode structures in this study. In addition, there was no obvious degradation of the InP peak linewidth in the X-ray diffraction spectrum, Fig. 2. It may still be possible to use this highly strained $InAs_{0.6}P_{0.4}$ layer in the active region of these devices. If a tensile strained quaternary were used in the core to partially compensate for the high compressive strain of the wells, it may be possible to avoid relaxation and achieve better device performance.

Ridge lasers were fabricated from the laser diode material with + 0.7% strained quantum wells. The ridge dimensions were 4.5 μm × 500 μm, and the cladding on either side of the ridge was removed to leave a residual layer thickness of 0.35 μm. The facets were formed by cleaving and were uncoated. After depositing a layer of Si_3N_4, a window was opened on the ridge to deposit a Ti/Pt/Au contact. The lasers were single mode, and a plot of the light intensity versus injected current is shown in Fig. 4. Threshold currents were 20 mA and the external quantum efficiency was 0.21 mW/mA per facet.

Several attempts were made to produce buried ridge lasers using solid source MBE. For ridges defined by deep reactive ion etching (> 1.7 μm), the regrown InP had poor morphology and voids near the active region. A technique used to produce buried ridge lasers using GSMBE was more successful [24]. First, the active region was grown and capped with a 0.1 μm layer of InP. The sample was then removed from the MBE chamber, and shallow, nearly vertical ridges (0.8 μm) were defined by reactive ion etching (RIE). Next, the InP cladding layer, doped 2×10^{18} p-type, and a $Ga_{0.47}In_{0.53}As$ cap were regrown over the ridges. The regrown film had a good surface morphology, and no voids were seen in cross-sectional secondary electron microscopy (SEM) images. The threshold currents varied between 34 and 68 mA for these devices, which is higher than the results discussed above from similar ridge devices fabricated without regrowth. Future results should improve by treating the surface before regrowth to remove any damage, by optimizing the contact width and alignment, and by utilizing proton implantation to reduce current spreading.

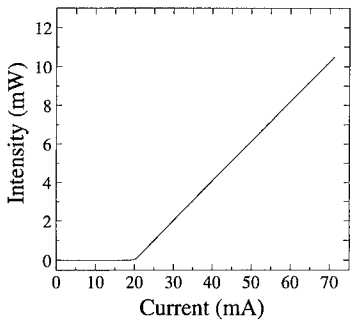

Fig. 4. Plot of light intensity versus current for a ridge laser diode.

4. Conclusion

We have shown that solid source MBE can be used to produce high-quality SCH laser diodes for 1.55 μm wavelength applications. Quaternary compositions and laser diode emission wavelengths are reproducible using an ion gauge to adjust the group-V beam equivalent pressures before growth. Quaternary films with band gap wavelengths near 1.3 μm did not show degradation normally associated with the miscibility gap for these alloys. Broad area and ridge laser results are comparable to the best results for similar devices grown using other growth techniques. We have also shown that solid source MBE is a viable technique for producing buried ridge lasers. However, improvements must be made in order to match the results from other growth techniques.

Acknowledgements

The authors wish to thank W.T. Beard, T.L. Filemyr, J. Fitz, K. Mobarhan, and R.A. Wilson for useful discussions and technical assistance.

References

[1] J.J. Hsieh, Appl. Phys. Lett. 28 (1976) 283.
[2] B.I. Miller, J.H. McFee, R.J. Martin and P.K. Tien, Appl. Phys. Lett. 33 (1978) 44.
[3] W.T. Tsang, F.K. Reinhart and J.A. Ditzenberger, Electron. Lett. 18 (1982) 785.
[4] C. Starck, J.Y. Emery, R.J. Simes, M. Matabon, L. Goldstien and J. Barrau, J. Crystal Growth 120 (1992) 180.
[5] W.T. Tsang, F.S. Choa, M.C. Wu, Y.K. Chen, A.M. Sergent and P.F. Sciortino, Jr., Appl. Phys. Lett. 58 (1991) 2610.
[6] P.J.A. Thijs, L.F. Tiemeijer, P.I. Kuindersama, J.J.M. Binsma and T. Van Dongen, IEEE J. Quantum Electron. 27 (1991) 1426.
[7] J.S. Osinski, P. Grodzinski, Y. Zou and P.D. Dapkus, IEEE J. Quantum Electron. 29 (1993) 1576.
[8] D.L. Miller, S.S. Bose and G.J. Sullivan, J. Vac. Sci. Technol. B 8 (1990) 311.
[9] G.W. Wicks, M.W. Koch, J.A. Varriano, F.G. Johnson, C.R. Wie, H.M. Kim and P. Colombo, Appl. Phys. Lett. 59 (1991) 342.
[10] F.G. Johnson, G.E. Kohnke and G.W. Wicks, Mater. Res. Soc. Symp. Proc. 324 (1994) 279.
[11] J.N. Baillargeon, A.Y. Cho, F.A. Thiel, R.J. Fischer, P.J. Pearah and K.Y. Cheng, Appl. Phys. Lett. 65 (1994) 207.
[12] M. Toivonen, A. Salokatve, M. Jalonen, J. Nappi, H. Asonen, M. Pessa and R. Murison, Electron. Lett. 31 (1995) 797.
[13] F.G. Johnson, O. King, F. Seiferth, D.R. Stone, R.D. Whaley, M. Dagenais and Y.J. Chen, J. Vac. Sci. Technol. B 14 (1996) 2753.
[14] F.G. Johnson and C.E.C. Wood, J. Appl. Phys. 78 (1995) 1664.
[15] W.E. Hoke, D.G. Weir, P.J. Lemonias, H.T. Hendriks, G.S. Jackson and P. Colombo, J. Vac. Sci. Technol. B 13 (1995) 733.
[16] J. Jeans, Kinetic Theory of Gases (Cambridge University Press, London, 1940) ch. 3, p. 59.
[17] T.A. Flaim and P.D. Ownby, J. Vac. Sci. Technol. 8 (1971) 661.
[18] K. Onabe, Jpn. J. Appl. Phys. 21 (1982) 797.
[19] R.R. LaPierre, T. Okada, B.J. Robinson, D.A. Thomson and G.C. Weatherly, J. Crystal Growth 155 (1995) 1.
[20] H. Asonen, K. Rakennus, K. Tappura, M. Hovinen and M. Pessa, J. Crystal Growth 105 (1992) 101.
[21] A. Suzuki, H. Kyuragi, S. Matsumura and H. Matsunami, Jpn. J. Appl. Phys. 19 (1980) L207.
[22] Bede Scientific, Computer code RADS (Bede Scientific, Durham, 1993).
[23] C. Blaauw, F.R. Shepherd and D. Eger, J. Appl. Phys. 66 (1989) 605.
[24] D. Bonnevie, F. Poingt, L. Le Gouezigou, A. Guichardon, A. Accard, R. Simes, B. Fernier and L. Goldstein, J. Crystal Growth 127 (1993) 5.
[25] M. Razeghi, The MOCVD Challenge, Vol. 1 (Hilger, Philadelphia, 1989).

ELSEVIER

Journal of Crystal Growth 175/176 (1997) 52–60

JOURNAL OF CRYSTAL GROWTH

Virtual control simulator for closed-loop epitaxial growth

J.J. Zhou[a,*], Y. Li[a], D. Pacheco[a], H.P. Lee[a], X. Liu[b]

[a] *Department of Electrical and Computer Engineering, University of California, Irvine, California 92715, USA*
[b] *Department of Electronic Engineering, Tsinghua University, Beijing, People's Republic of China*

Abstract

We report the use of a virtual control simulator for analyzing the behavior of a closed-loop molecular beam epitaxy system based on in situ narrow-band pyrometric interferometry and single-wavelength laser reflectance monitoring. Specific case studies include thickness control of GaAs/AlAs distributed Bragg reflectors and continuous growth rate estimation of GaAs/AlAs calibration structures. In both cases, the control simulator provides valuable insight on the design of the control system prior to its actual implementation.

PACS: 81.15.Hi; 81.05.Ea; 71.55.Eq

Keywords: Growth rate; MBE; Simulation; DBR

1. Introduction

Recent progress in sensor and integrated sensor technology [1, 2] together with ever declining computational overhead has stimulated interest towards a closed-loop molecular beam epitaxy (MBE) system. To date normal incidence optical reflectance [3, 4] and pyrometric interferometry [5] are already being used routinely for growth calibrations and closed-loop control for vertical cavity surface emitting lasers (VCSELs) structures in both metal organic chemical vapor deposition (MOCVD) and MBE systems. While the necessary sensor technology has advanced considerably, relatively little work has been directed on the study of control methodology. Given the complexity involved in the design process, the need for the control simulator grew out of our own practical experience in implementing a closed-loop MBE system. Such a simulator can be used not only for the verification of control codes, but also allows the users to examine the behavior of a control scheme under likely systematic and random perturbations generally encountered in actual experimentation. The advance knowledge gained from the simulation studies enables the users to establish realistic specifications and performance expectation of the control system prior to actual implementation. In this article, we describe a prototype control simulator based on in situ narrow-band pyrometric

* Corresponding author. Fax: +1 714 824 3732; e-mail: jzhou@ece.uci.edu.

0022-0248/97/$17.00 Copyright © 1997 Elsevier Science B.V. All rights reserved
PII S0022-0248(96)01223-7

interferometry (PI) and single-wavelength laser reflectance (LR) implemented for MBE growth.

2. Basic approach

We have adopted a model-reference scheme for closed-loop control of MBE growth. The schematics of the control system for AlAs/GaAs DBR structures and growth rate estimation on GaAs/AlAs calibration structures are shown in Fig. 1a and Fig. 1b, respectively. The execution of the control system is described as follows: An intended target structure is specified in terms of successive marker layers having a thickness of ζ_i and a complex refractive index $n_i(\lambda_m, T_s) - j\kappa_i(\lambda_m, T_s)$, where T_s is the growth temperature and λ_m is the monitoring wavelength. The evolution of the reference signal versus thickness z_n for the jth layer depends on the preceding structure and is calculated based on the physical model of the monitored process, i.e. $X_j(z_n) = g(T_s, n_i, \kappa_i, \zeta_i, z_n)$, $i \in \{1, j-1\}$. Once $X(z_n)$ is obtained, it is low-pass-filtered and processed into a continuous reference "signal phase," $\Theta_r(z_n)$, by means of a least-squares phase extraction (LSPE) method. A detailed description of the LSPE method has been published elsewhere [6]. A reference phase list, $\Theta_r(\zeta_i)$, is stored at pre-determined marker points ζ_i. For the closed-loop growth control, the monitored data of the test sample $Y_e(t_n)$ is processed into $\theta_e(z_n)$ in a similar way. However, since $Y_e(t_n)$ is observed in the time domain, an additional step is required to convert $Y_e(t_n)$ to its corresponding thickness representation (i.e. $Y_e(t_n) \rightarrow Y_e(z_n)$). This is achieved by interpolating neighboring $Y_e(t_n)$ using an estimated growth rate g_{est}. The value of g_{est} is initially provided by the user, but in principle can be updated during the monitoring process as more accurate values are being obtained. When $\theta_e(z_n)$ is equal to $\Theta_r(\zeta_i)$, the control system interprets that the growth has reached the ith marker point and actuates the shutters if a change of material layer is called for.

The performance of the control system is dictated by how close $X(z_n)$ is matched to $Y(z_n)$. To optimize the design of the control system, it is highly desirable to examine the impact of the systematic drift between $X(z_n)$ and $Y(z_n)$ on the overall performance of the control system. This, however, is nearly impossible to examine experimentally due to the multitude of variables involved in the monitoring process and the enormous time and cost such experiments will take. Instead, we use a virtual control simulator to investigate the impact of the uncertainties in the parameters involved in the control process. The schematics of the control simulator used in this study is identical to Fig. 1. However, the $Y_e(t_n)$ from an actual test sample is replaced by $Y_{sim}(t_n)$ generated by a growth/sensor simulator. The growth/sensor simulator calculates the sensor signal at a growth rate g_{sim} using the same equation as the one used for the reference signal but using different parameters, i.e. $Y_j(t_n) = g(T'_s, n'_i, \kappa'_i, \ell'_i, z_n = g^*_{sim} t_n)$, $i \in \{1, j-1\}$. When $\theta_{sim}(\ell'_i)$ is equal to $\Theta_r(\zeta_i)$, the simulated growth is said to have reached a layer thickness ℓ'_i. At this point, a command is sent to the growth/sensor simulator to generate a new sensor signal for a new marker layer. The objective of this study is to examine the layer thickness, ℓ'_i, retrieved from the control simulator relative to the target values (ζ_i) when the parameters (n'_i, κ'_i, T'_s, etc.) used in the growth/sensor simulator are deviated from those used for calculating the reference signal (n_i, κ_i, T_s, etc.). In this way, the influence of systematic errors intrinsic to the control system can be evaluated in a self-consistent way without carrying out the actual experimentation.

3. Case studies and discussion

In this section, the use of the virtual simulator is illustrated for (a) closed-loop growth of a 15 pair AlAs/GaAs DBR structures (monitored using PI) and (b) continuous extraction of growth rates for a GaAs/AlAs calibration structure (using both PI and LR). Both monitoring techniques have been extensively studied for MBE growth. Unless stated otherwise, the monitoring wavelength, λ_m, for PI measurement and LR is set at 1048 ($\Delta\lambda_m$ of 60 nm) and 650 nm, respectively.

3.1. Closed-loop control of DBR mirrors

For the 15 pair $\lambda/4$ AlAs/GaAs DBR structures, each marker layer ζ_i is chosen at the end of the

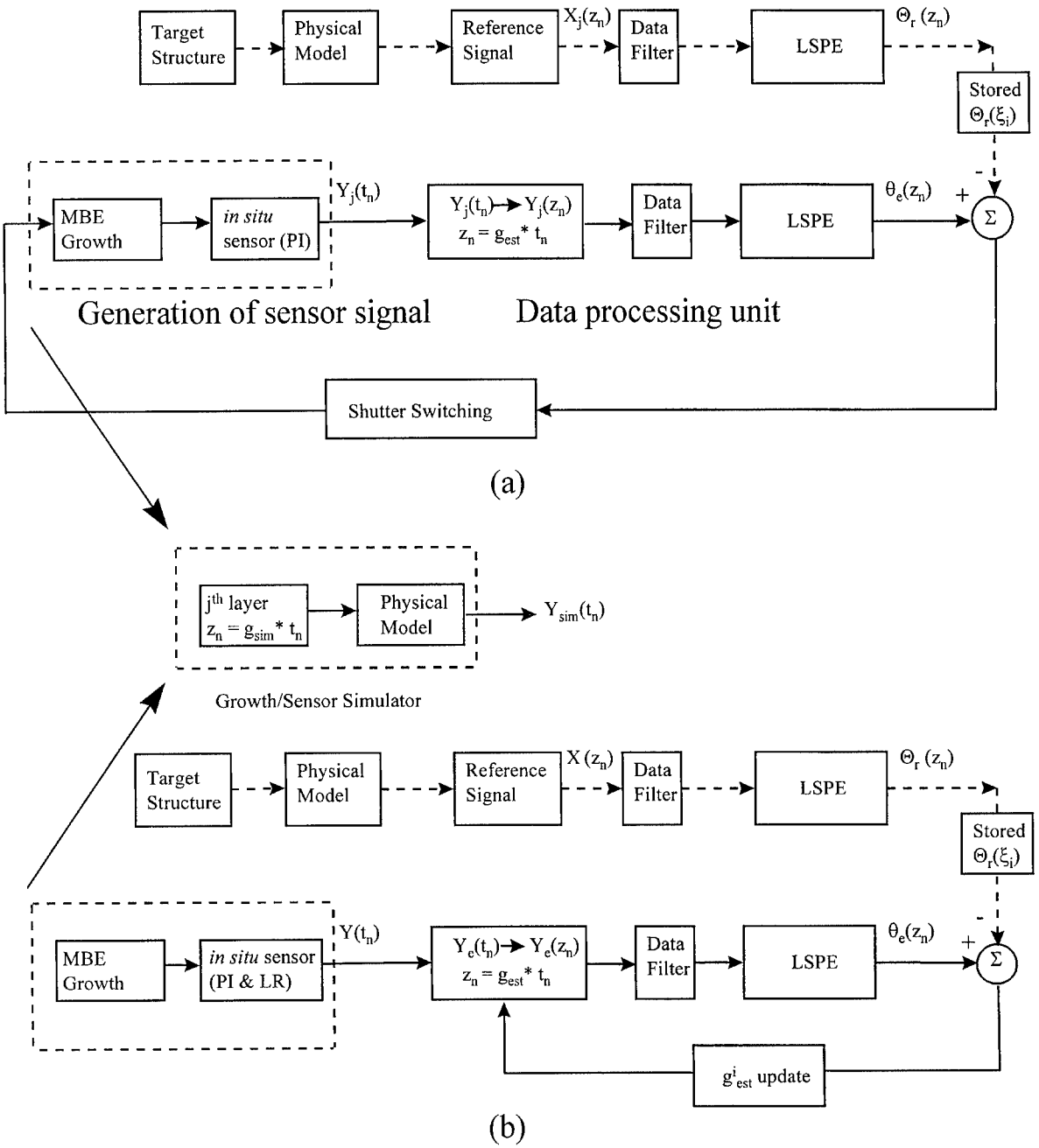

Fig. 1. The schematics of the model-reference control system for (a) thickness control of a 15 pair AlAs/GaAs DBR structure, and (b) growth rate estimation of a GaAs/AlAs calibration structure. The pre-calculated signal and the real-time monitored signal are represented by dashed and solid lines, respectively. For the control simulator, the actual growth and the in situ sensor are replaced by a single growth/sensor simulator.

material layer. The performance of the control system is analyzed in terms of the ℓ'_i retrieved from the control simulator and the spectrum of the optical reflectance of the entire retrieved DBR structure. A major difficulty in the calculation of the reference signal arises from the drift of T_s during MBE growth which causes an intensity modulation of the oscillatory PI signals. A steady drop of T_s has been inferred from previous PI measurements during the growth of AlAs/GaAs DBR structures. This is attributed to a steady increase of the overall sample emissivity [7]. However, accurate modeling of T_s is rather difficult to obtain because of the complexity of the heat transfer process involved. The impact of temperature drift on the performance of the control system is investigated using the control simulator. Here, we assume a constant T_s (Fig. 2a) throughout the entire growth in calculating the reference signal, $X(z_n)$ (Fig. 2b). A slow-varying $T'_s(t_n)$ (Fig. 2c) that changes from 600 to 560°C during the course of the growth is introduced by the sensor/control simulator. The simulated sensor signal $Y_{sim}(t_n)$ and the resulting ℓ'_i retrieved from the control simulator are shown in Fig. 2d and Fig. 2e, respectively. Reflectance spectra of the retrieved and the target structures are also shown in Fig. 2f. The simulator shows a 2 nm blue shift in the peak reflectance wavelength (as well as the phase of the reflection coefficient) for the reference structure. To isolate the impact of T_s, we have set n'_i, κ'_i and g_{est} equal to n_i, κ_i, and g_{sim} for all layers in the calculation of $Y_{sim}(t_n)$.

A second source of error for the closed-loop control system arises from the uncertainty of the optical constants used in calculating the reference signal. Fig. 3a and Fig. 3b show the retrieved layer thickness when the refractive indices, n, of both AlAs and GaAs used in the sensor simulator are either 3% larger or smaller than the corresponding values used in the reference signal calculation. As in the previous case, we have set κ'_i, T'_s and g_{est} equal to κ_i, T_s, and g_{sim} for all layers in the calculation of $Y_{sim}(t_n)$. The reflectance spectra of the retrieved and target structures are also shown in Fig. 3c and Fig. 3d, respectively. Wavelength shifts, $\Delta\lambda_{peak}$, in the peak reflectance and phase of the reflection coefficient of -41 and $+39$ nm are observed for each case.

A third concern in the design of the control system arises from the imprecision in the estimated growth rate g_{est} used in the data processing unit (initially provided by the users) relative to the actual growth rate. We examine this problem by introducing a difference between g_{sim} and g_{est} in the control simulator. The results are shown in Fig. 4a and Fig. 4b for monitoring wavelengths of 1048 and 940 nm, respectively. In both cases, the values for g_{est} is 15% larger than that of the g_{sim}. The corresponding simulated PI signals and reflectance spectra of the retrieved DBR structure are shown in Fig. 4c–Fig. 4f, respectively. The $\Delta\lambda_{peak}$ of $+1$ and -10 nm are observed in each case. The results highlight the impact of monitoring wavelength relative to the target DBR structure. In addition, it should be noted that g_{est} can be updated iteratively at the end of each marker layer during the course of the growth (i.e., using a variable of g^i_{est}). This issue will be discussed in greater detail in the next section.

In all the above studies, we have observed a highly desirable self-compensating mechanism at work. While the thickness of individual sublayer (GaAs or AlAs) may deviate from the target value, the control simulator has a tendency to conserve the overall optical phase $(k_0 n_1 \ell_1 + k_0 n_2 \ell_2)$ of individual DBR pairs. This tends to preserve the overall periodicity of the DRS structure and reduce the $\Delta\lambda_{peak}$. This self-compensating mechanism has also been observed experimentally [6].

3.2. Continuous growth rate monitoring

We have recently extended the model-reference scheme for continuous growth rate estimation of GaAs and AlAs layers using both PI and LR monitoring [8]. The experiments were conducted on GaAs/AlAs calibration samples in which each material layer is divided into evenly spaced marker points. The reference phase list, $\Theta_r(z_i)$, provides a thickness versus signal-phase calibration. The quasi-instantaneous growth rates are determined from the time interval when θ_e reaches successive marker points. Each newly determined growth rate, g^i_{est}, is then updated in the data processing unit for subsequent calculation of $\theta_e(z_n)$. The schematic of the growth estimation process is shown in Fig. 1b.

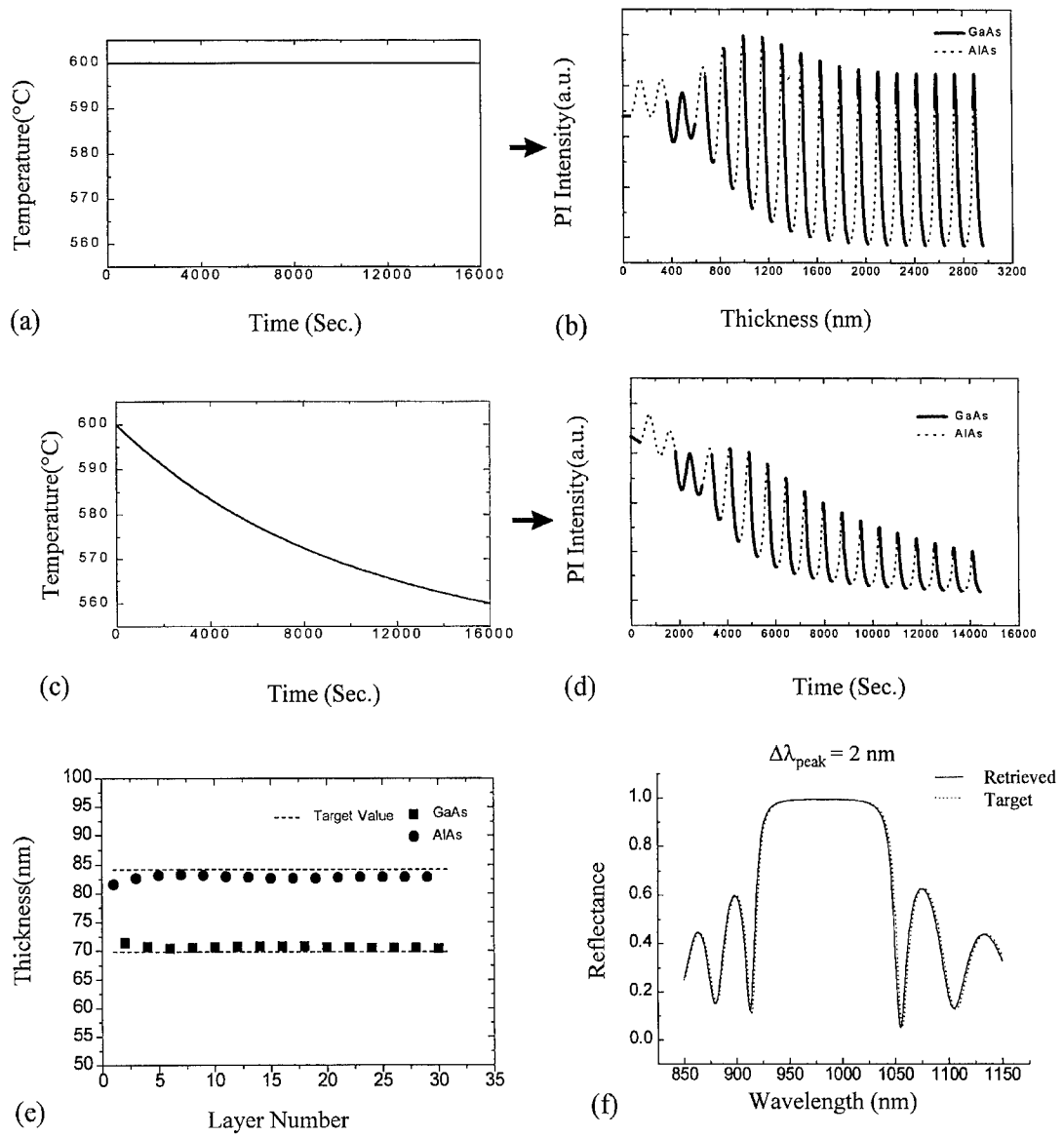

Fig. 2. (a) and (b) show the substrate temperature and the reference signal of the target DBR structure. (c) and (d) show the evolution of the substrate temperature used in the growth/sensor simulator and the resulting monitoring signal $Y(t_n)$. (e) plots the layer thickness retrieved from the control simulator, along with the target values (84.2 nm for AlAs and 69.8 nm for GaAs). The reflectance of the retrieved and target DBR structures are shown in (f). A deviation in the peak of the DBR structure ($\Delta\lambda_{peak}$) of 2 nm is noted. The phase of the reflection coefficient exhibits similar shift.

Using this method, the minimum thickness resolution of the estimated growth rate is set by the marker spacing. Ideally, the marker space should be chosen as small as possible, so as to achieve a continuous growth rate estimation. However, when the marker spacing becomes too small, "local" fluctuations between Θ_r and θ_e cause severe errors in the estimated growth rate. The control

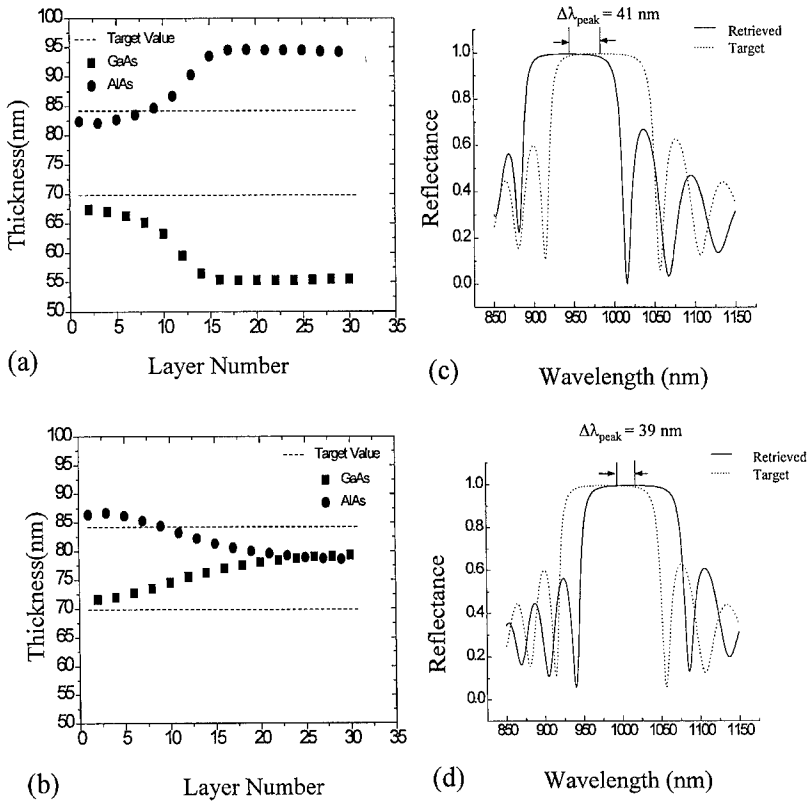

Fig. 3. Plots of retrieved layer thickness ((a) and (b)) and the corresponding reflectance spectrum ((c) and (d)) of the DBR structures due to the uncertainty of the refractive indices. In (a) the refractive indices of both GaAs and AlAs used in growth/sensor simulator are 3% higher than the corresponding values used for calculation of reference signal (3.71 for GaAs and 3.0 for AlAs). This results in a $\Delta\lambda_{peak}$ of −41 nm (blue shift). In (b) the refractive indices of both GaAs and AlAs used in sensor simulator are 3% lower than the corresponding values used for calculation of reference signal. This results in a $\Delta\lambda_{peak}$ of 39 nm. Refractive indices of 3.71 and 3.0 are used for GaAs and AlAs at growth temperature of 600°C, respectively.

simulator is used to determine the minimum allowable marker spacing in this method. The simulation results are shown in Fig. 5a for marker spacing between 15 and 45 nm. A constant g_{sim} of 0.2 nm/s is used for both the AlAs and GaAs layers. The values of g^i_{est} coverage to within 1.25% of g_{sim} after a thickness of 60 nm even though the initial estimate g^0_{est} is off by as much as 10%. Next, we examine the convergence of g^i_{est} on g^0_{est} using the control simulator. The results are shown in Fig. 5b for AlAs layer. With a marker spacing of 30 nm and an initial g^0_{est} that deviates from g_{sim} by as much as 20%, the simulated g^i_{est} converges to within 2.5% of g_{sim} after a thickness of 60 nm. Based on the simulation results, experimental studies were carries out monitoring using both PI and LR on GaAs/AlAs calibration structures. Highly accurate growth rate estimation (error < 1.5%, as calibrated using post-growth spectral ellipsometry) was achieved for both AlAs and GaAs layers by this method using a marker spacing of 30 nm. The details of the work are reported elsewhere [8].

The control simulator is also used to evaluate the performance of the growth rate estimation process under dynamic condition. To do so, we vary g_{sim} of GaAs both linearly and abruptly in the

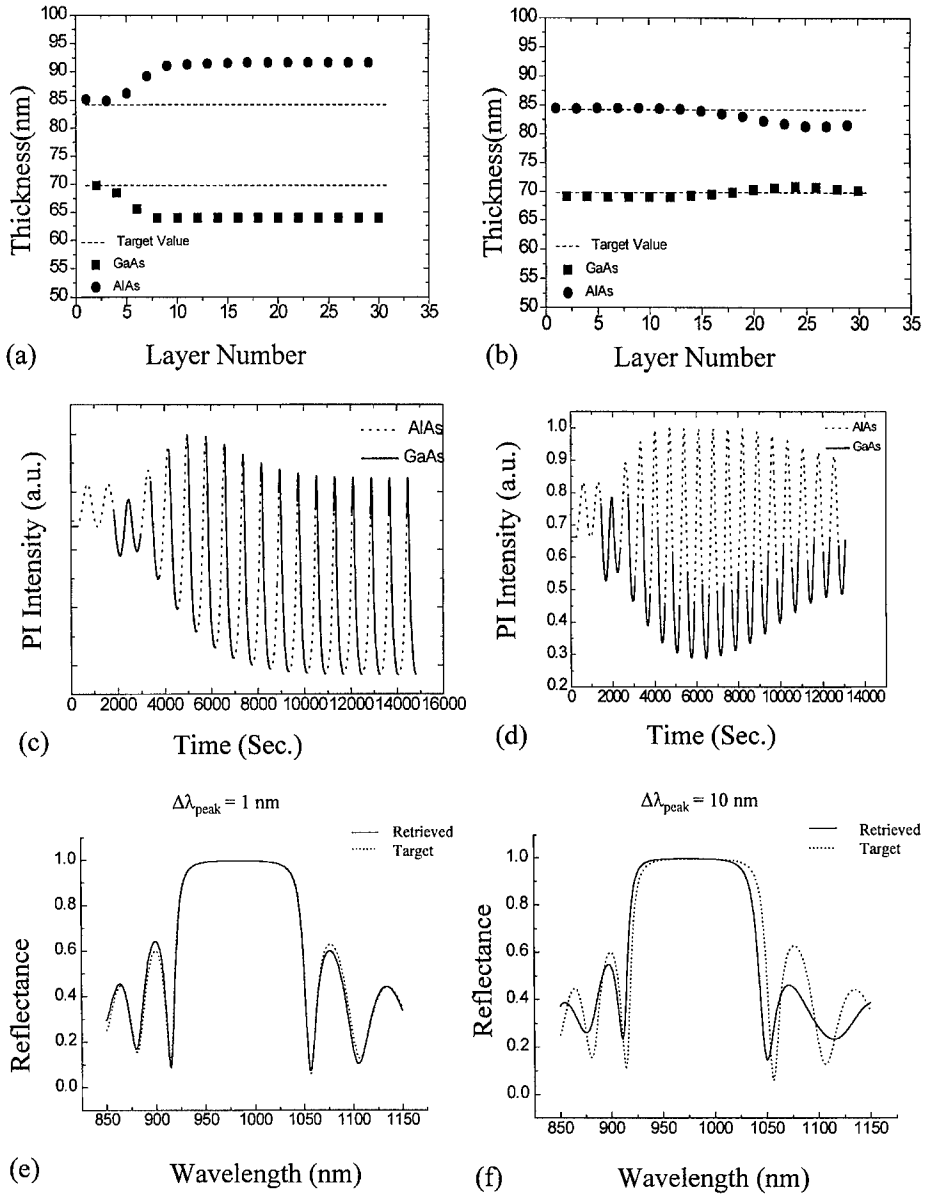

Fig. 4. Plot of retrieved layer thickness ((a) and (b)) and the corresponding PI signal ((c) and (d)), reflectance spectrum ((e) and (f)) of the DBR structures due to the uncertainty in the estimated growth rate using two different monitoring wavelength of (a) 1048 nm and (b) 940 nm, respectively. The corresponding $\Delta\lambda_{peak}$ are 1 and 10 nm for (a) and (b), respectively. In both cases, g_{est} (estimated values) of 0.23 nm/s are used, which is 15% higher than 0.2 nm/s used for g_{sim} (simulator). The influence of the monitoring wavelength is clearly evident.

growth/sensor simulator as shown in Fig. 6a and Fig. 6b, respectively. In both the cases, the simulated results show that continuous tracking of the growth rate (within 2% of g_{sim}) is possible for a marker spacing of 30 nm. An actual experimentation was carried out on a GaAs/AlAs calibration. In this experiment, the GaAs growth rates were varied from steady-state values of 0.225–0.266 nm/s

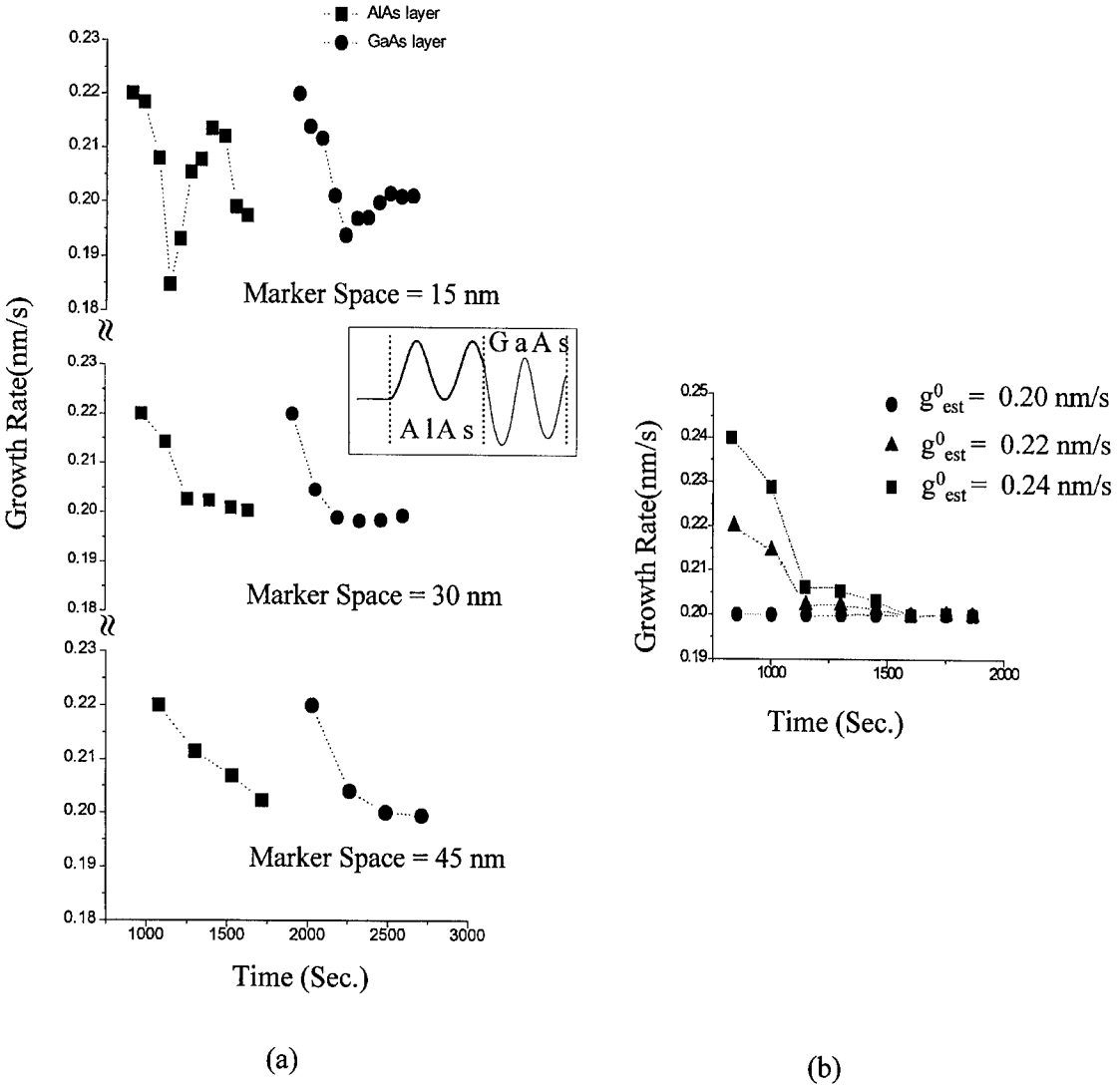

Fig. 5. Part (a) plots the convergence of g^i_{est} from the control simulator for both AlAs and GaAs layers for marker spacing of 15, 30 and 45 nm using a constant g_{sim} of 0.2 nm/s and an initial g^0_{est} of 0.22 nm/s. Part (b) shows the convergence of g^i_{est} on the AlAs layer for initial estimates, g^0_{est}, of 0.2, 0.22 and 0.24 nm/s, respectively. The PI monitoring signal is also shown in the inset of the figure.

abruptly by changing the temperature setting of the Ga Knudsen cell. These preset growth rate have been well calibrated using post-growth ellipsomtry. The estimated g^i_{est} are shown in Fig. 6c. The average values for g^i_{est} are found to be 0.223 and 0.262 nm/s, respectively. The accuracy level achieved in the experimental growth rate estimation is extremely close to that obtained from the simulation studies. A more detailed report on growth rate estimation experiment will be discussed in a later publication.

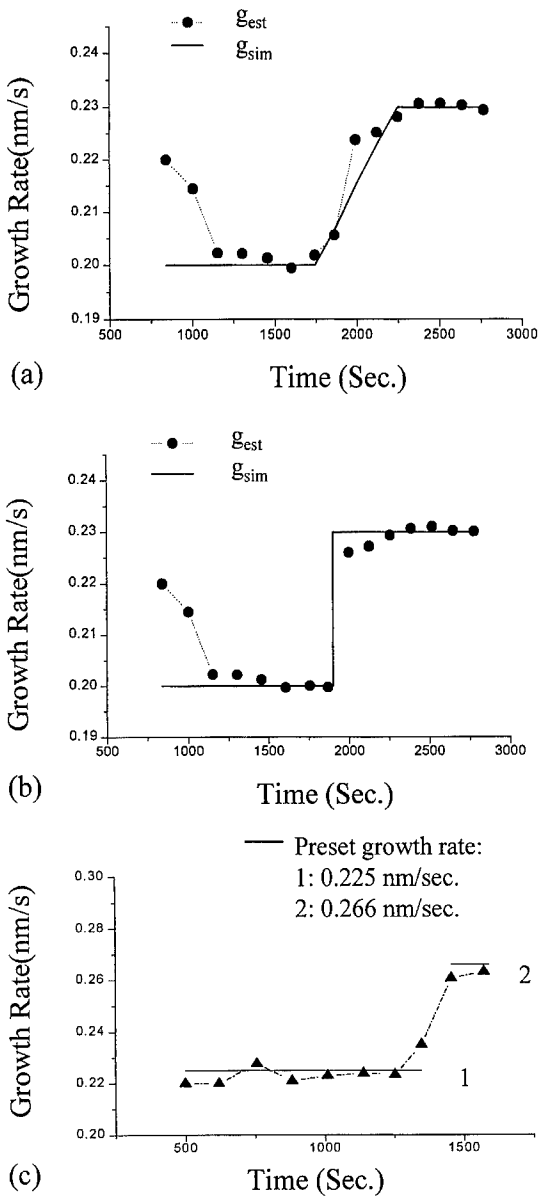

Fig. 6. Estimated growth rates from the control simulator under dynamic conditions in which g_{sim} is varied (a) linearly (over a span of 400 s) and (b) abruptly from 0.20 and 0.23 nm/s. Part (c) shows the g^{i}_{est} extracted from an actual experimental measurement. The accuracy level achieved in the experimental growth rate estimation is comparable to that obtained from simulation.

4. Summary

In summary, we have discussed the essential functions of a sensor simulator in evaluating the performance of a model-reference control system. In both the applications we have studied, the control simulator provided useful insight in analyzing the influence of systematic error intrinsic to the control system. Although all studies presented here are based on the model-reference scheme, we believe that the application of control simulator can be extended for the comparative studies of control algorithms as well.

Acknowledgements

The project was supported by the Irvine Research Fellowship.

References

[1] J.A. Roth, presented at 9th Int. Conf. on Molecular Beam Epitaxy Pepperdine University Malibu, California, 5–9 August (1996).
[2] Y. Li, J.J. Zhou, P. Thompson, D.L. Sato and H.P. Lee, presented at 9th Int. Conf. on Molecular Beam Epitaxy, Pepperdine University Malibu, California, 5–9 August (1996).
[3] G.S. Li, W. Yuen, K. Toh, L.E. Eng and C.J. Chang-Hasnain, IEEE Photon. Tech. Lett. 7 (1995) 971.
[4] H.Q. Hou, H.C. Chui, K.D. Choquette, B.E. Hammons and W. Breiland, IEEE Photon. Tech. Lett. 8 (1996) 1285.
[5] Y.M. Houng, M.R.T. Tou, B.W. Liang, S.Y. Wang and D.E. Mars, J. Vac. Sci. Technol. B 12 (1994) 1221.
[6] X. Liu, E. Ranalli and H.P. Lee, IEEE Photon. Tech. Lett. 8 (1996) 340.
[7] H.P. Lee, Y. Li, D.L. Sato and J.J. Zhou, J. Vac. Sci. Technol. B 14 (1996) 2151; Y.M. Houng, Hewlett Packard Laboratory, private communication.
[8] J.J. Zhou, Y. Li, P. Thompson, R. Chu, H.P. Lee, Y.C. Kao and F.G. Celii, presented at the 38th TMS Electron. Mater. Conf. University of California Santa Barbara, 26–28 June (1996), J. Electron. Mater., accepted.

ELSEVIER

Journal of Crystal Growth 175/176 (1997) 61–65

JOURNAL OF CRYSTAL GROWTH

Sensor controlled linear motion oven (S-LIMO) for group III flux operation

P.P. Chow[a,*], K.R. Evans[b,1], A.J. SpringThorpe[c], P. Fisher[a], J.J. Klaassen[a], A. Wowchak[a], J. Van Hove[a]

[a] *SVT Associates, 7620 Executive Drive, Eden Prairie, Minnesota 55344, USA*
[b] *Avionics Directorate, Wright Laboratory, Wright- Patterson Air Force Base, Ohio 45433-7323, USA*
[c] *Nortel Technology, Advanced Technology Laboratory, P.O. Box 3511, Station C, Ontario, Canada,* K1Y 4H7

Abstract

A linear motion Ga source has been constructed and tested for smooth flux variation. The beam flux can be monitored by sensors such as atomic absorption, RHEED, and pyrometric interferometry. We demonstrated stable and reproducible operation of the source using sensor feedback. Constant layer composition can be maintained despite Ga thermal desorption at high temperatures. Arbitrary composition profile can be easily achieved for band gap engineering.

1. Introduction

In solid source MBE the source is usually temperature stabilized to supply a constant beam flux. When composition change is desired the growth process must be interrupted for the cell temperature to reach a new set point. The temperature response of the source however is often slow, and the flux change cannot be made smoothly and reproducibly. Here we suggest that a different approach to achieving smooth group III flux variation is to employ the linear motion oven (LIMO) concept [1]. By coupling the source to a linear drive mechanism its distance to the substrate can be varied, producing desired flux changes. The change in flux can be approximated by an inverse power relationship. If the melt in the crucible is situated at a distance D from the substrate surface and the cell is moved by an amount Z, then the flux J can be expressed as $J = A(D + Z)^{-n}\,\mathrm{cm}^{-2}\,\mathrm{s}^{-1}$. Here A is a material constant and n varies around 2 depending on cell geometry. If it can be measured by a sensor in real time then the desired flux change can be controlled precisely. Moving the cell also provides the flexibility of improving film uniformity as well as elimination of flux transient by avoiding thermal perturbance due to the shutter action.

There are many band gap-engineered devices that require controlled composition or dopant changes. For example, continuously graded index

* Corresponding author. Fax: +1 612 934 2737; e-mail: chowx005@tc.umn.edu.

[1] Present address: Semiconductor Laser International, 421 E. Main Street, Endicott, New York 13760, USA.

0022-0248/97/$17.00 Copyright © 1997 Published by Elsevier Science B.V. All rights reserved
PII S0022-0248(96)00872-X

confinement layers have been suggested to reduce resistance in a Vertical Cavity Surface Emitting Laser (VCSEL). Another example is graded base, or base to emitter or collector junction in a hetero-junction bipolar transistor (HBT). In practice, it would also be convenient to be able to fine-tune the Group III flux ratio quickly for precision lattice matching adjustment. Here we demonstrate the concept for fabricating the key components of the Fabry–Perot emission region of a SEL structure. It consists of quantum wells, graded index layers and cavity matching regions. Operation of the LIMO-cell can be tailored for such structures.

2. Source operation

A linear motion source [2] was used for testing in a SVT Associates MBE growth chamber equipped with several monitoring instruments including reflection high-energy electron diffraction (RHEED), atomic absorption (AA), ellipsometer, reflection mode mass spectrometer, and pyrometric interferometer (PI). The flux can be precisely regulated using feedback from a combination of these sensors. A LabView software program compares the sensor feedback to a reference signal and sends an output to a stepping motor on the LIMO-cell. The amount of the source motion, if needed, is determined from the established calibration runs. In the case of RHEED the growth rate was first determined by a fast fourier transform routine, also written in LabView, from the intensity oscillation before being compared to the intended growth rate.

Fig. 1 shows the aluminum flux variation, measured by the AA technique, as the source is moved. Here the aluminum melt was maintained at a constant temperature so the absorption change was due to the flux variation from the motion of the cell. As expected, the flux has an inverse power relationship to the sensor distance. Similar dependence was obtained by RHEED oscillation to measure the actual growth rate change as a function of cell position. Before growth experiments these measurements have been carried out for both the Al and Ga sources so that the flux to source position relationship is individually established.

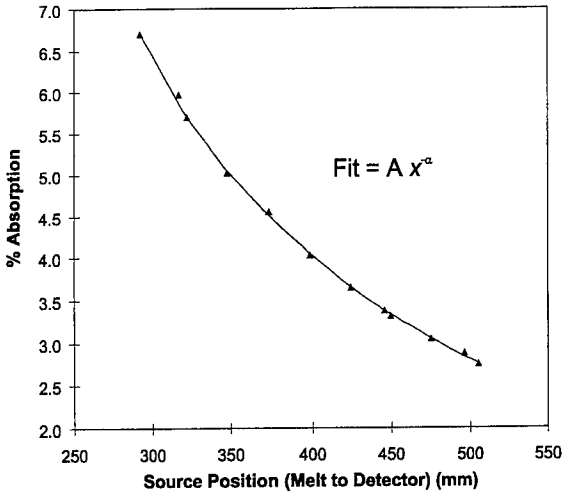

Fig. 1. Atomic absorption measurement of the aluminum flux as function of melt to sensor distance.

3. Growth results

3.1. AlGaAs layer composition

To grow high optical quality AlGaAs, high substrate temperature is required at which Ga desorption becomes significant. Although the Ga loss can be compensated by providing excess Ga flux, precision control is difficult as it depends critically on the wafer temperature. We first evaluate the Ga loss at elevated temperatures by the so-called reverse RHEED oscillation [3] technique. The measurement is displayed in Fig. 2 where in the region marked A it shows the normal intensity oscillation as the layer was being deposited. The shutter was then closed, and the intensity recovered and started to oscillate again as a result of Ga atoms leaving the surface. Such desorption occurs layer by layer giving rise to the periodic variation in RHEED intensity. The net Ga loss may be estimated by comparing the two rates. Similar oscillation was observed for AlGaAs. Having demonstrated that the Ga loss is significant at these growth temperatures we undertook to quantify the amount required for constant composition AlGaAs growth.

A series of AlGaAs layers was grown at increasingly higher substrate temperatures. The nominal

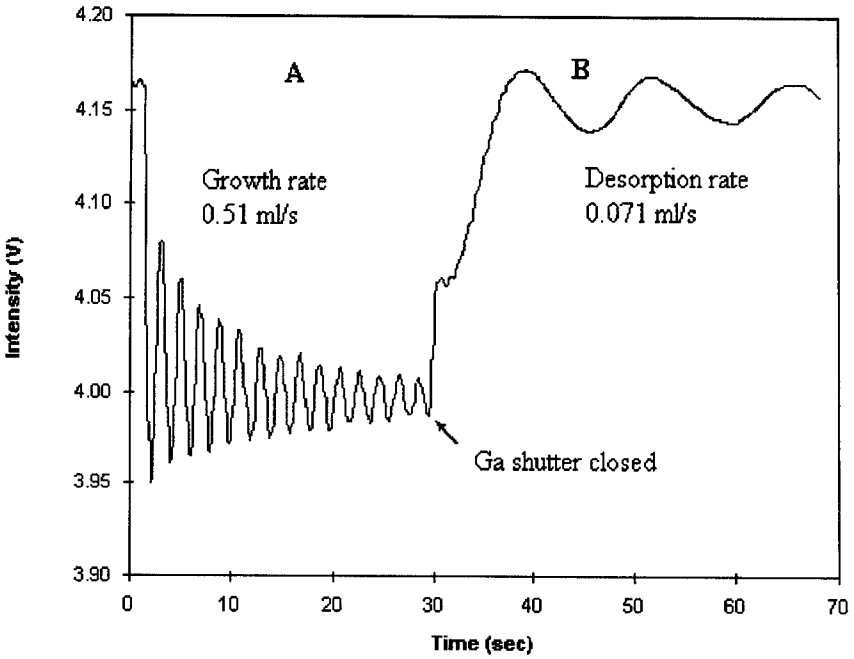

Fig. 2. RHEED oscillation showing GaAs growth (A) and Ga desorption (B) rates.

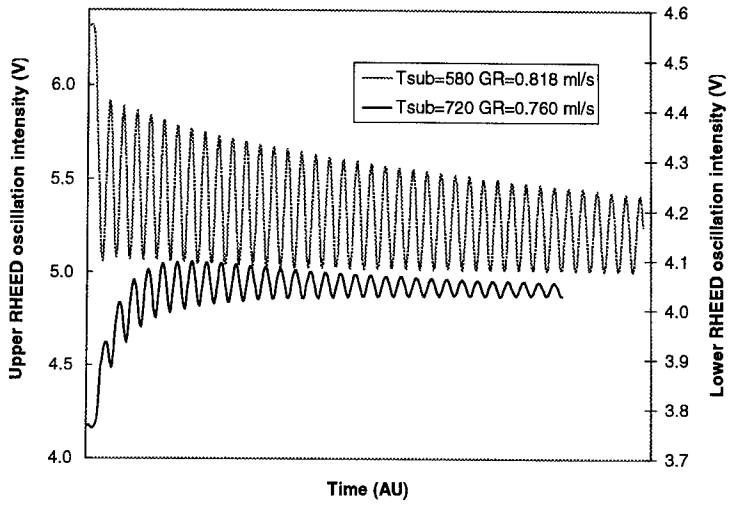

Fig. 3. RHEED oscillation during growth of $Al_{0.3}Ga_{0.7}As$ at 580°C (upper trace and left-hand side scale), and 720°C (lower trace and the right-hand scale). The difference of growth rate is due to Ga loss at high temperature.

aluminum composition was always kept at 30%. Since there is no Al evaporation from the surface, any observed change in the growth rate must be due to the Ga loss. This is apparent in the RHEED oscillation data shown in Fig. 3. The upper trace was done at 580°C where no Ga loss occurs and the lower trace shows decrease in growth rate from the Ga loss at 720°C. This observation suggests

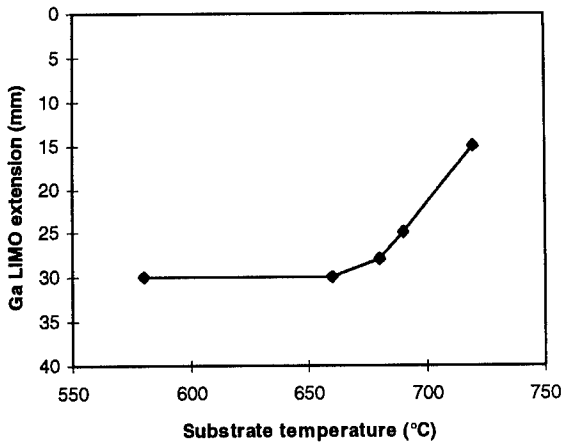

Fig. 4. Ga LIMO position required for complete Ga compensation during growth at each substrate temperature, as determined from RHEED oscillation.

a method to keep AlGaAs growth composition constant at 720°C is to move the LIMO-cell forward while monitoring the RHEED. The proper growth position for the cell would be where the growth rate returns to the set value which in this case is same as the upper trace oscillation. From this series of experiments one can map out the required Ga compensation at different growth temperatures. Fig. 4 presents the cell position versus the substrate temperature for Ga compensation at high growth temperatures for growing constant composition $Al_{0.3}Ga_{0.7}As$. Note that at 680°C the Ga desorption starts to become discernable, and the cell was then moved to make up the loss. Increasingly higher Ga flux is necessary to maintain constant composition as the temperature is raised. The fraction of Ga compensation obtained in this fashion agrees very well with earlier reverse oscillation data shown in Fig. 3. We maintain that the LIMO-cell is capable of effecting on-demand flux adjustments given the proper real-time sensing input.

3.2. *Variable composition structure*

The Fabry–Perot cavity contains an active quantum well region consisting of AlGaAs layers of different compositions. Although such structures may sometimes be made by simple shuttering, more complex structures, of arbitrary composition variation for example, may be better accomplished by the proposed technique. For high optical quality it is desirable to grow the structure at above 680°C where Ga loss from the layer is significant. Here we used the real time feedback to compensate for the loss by moving the source to a new location. For demonstration we have made a multi-layered sample consisting of five 150 Å thick $Al_{0.15}Ga_{85}As$ quantum wells and 500 Å of $Al_{0.3}Ga_{0.7}As$ barrier layers, by repeatedly moving the source between two calibrated positions. SIMS depth profiling of the structure clearly resolved the well and barrier separation. It showed good reproducibility of the Al flux variation within the instrument resolution.

3.3. *AlGaAs optical constant measurement*

For optimizing VCSEL design and performance it is helpful to know the optical properties of the layers at the growth temperature. Although in situ ellipsometry measurements have been carried out, previously the AlGaAs composition was difficult to be closely controlled. By overcoming the problem of composition control at high growth temperatures the measured optical constants become more meaningful. Here they are measured optically by the pyrometric interferometry (PI) technique [4] which also measures the growth temperature and layer thickness. Briefly, the method analyzes the interference patterns of the thermal radiation from the substrate. The thermal emission is reflected and refracted at the interfaces of the growing layer, changing the emissivity ε as a function of layer thickness d. By measuring the reflectivity from a known light emitter at the wavelength of interest, one can compute the emissivity directly by assuming energy conservation (reflection and absorption equal to unity) and the Kirchhoff's law. In this case a normal incidence LED at 950 nm was employed and its reflectivity from the wafer was used to compute the emissivity of the sample. In addition to the wafer temperature, the reflectivity of a growing $Al_{0.3}Ga_{0.7}As$ was continuously monitored as shown in Fig. 5 to obtain the optical thickness of the thin film. Knowing both the physical and optical film thickness precisely, by RHEED and PI, respectively, allowed us to obtain the optical

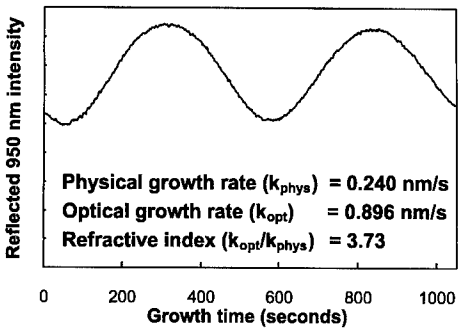

Fig. 5. PI reflectivity monitoring for optical thickness measurement.

constants of a particular AlGaAs composition at the growth temperature. In this case the refractive index is determined to be 3.73 for $Al_{0.3}Ga_{0.7}As$ at 660°C. Combining these in situ techniques therefore allows all the experimental parameters to be measured precisely, yielding valuable information which would otherwise be less meaningful.

4. Conclusion

A linear motion source is for the first time implemented for MBE growth. Using RHEED oscillation we demonstrated that the flux may be fine-tuned by sensor feedback. RHEED was selected because of its sensitivity to the the layer surface and familiarity to the MBE practitioners, other in situ measures would be just as effective if layer information could be obtained in real time. Components of a Fabry–Perot cavity structure were used as a demonstration but the technique should find use in many other applications where lattice matching and smooth composition variation are critical. The linear motion source therefore provides an effective way of precision MBE fabrication of multilayer structures.

Acknowledgements

We wish to thank David Reich and Dan Croswell for invaluable technical support.

References

[1] C.R. Jones, D.L. Beasley, E.N. Taylor, K.R. Evans and J.S. Solomon, J. Vac. Sci. Technol. B 13 (1995) 739.
[2] Model No. Limo-4.5-4, SVT Associates, 7620 Executive Dr. MN 55344
[3] J.M. Van Hove and P.I. Cohen, Appl. Phys. Lett. 47 (1995) 726.
[4] F.G. Böbel, H. Möller, A. Wowchak, B. Hertl, J. Van Hove, L.A. Chow and P.P. Chow, J. Vac. Sci. Technol. B 12 (1994) 1207.

ELSEVIER

Journal of Crystal Growth 175/176 (1997) 66–71

JOURNAL OF CRYSTAL GROWTH

Improved MBE-grown GaAs using a novel, high-capacity Ga effusion cell

R.N. Sacks[a,*], P. Colombo[b], George A. Patterson[c], Kathleen A. Stair[d]

[a] *Department of Electrical Engineering, Ohio State University, 2015 Neil Avenue, Columbus, Ohio 43210, USA*
[b] *EPI MBE Products, St. Paul, Minnesota 55110, USA*
[c] *Hewlett-Packard, Microwave Technology Division, Santa Rosa, California 95403, USA*
[d] *Materials Research Center, Northwestern University, Evanston, Illinois 60208, USA*

Abstract

A novel PBN crucible has allowed the design of a new high-capacity Ga source incorporating a unique heat shielding cap. The extra heat shielding at the front of the source allows hot lip operation with considerably lower power than for previous designs, thus completely eliminating Ga droplets without an inordinately high heat load. Compared with another high-capacity, low-flux transient cell (an EPI 125DF), the new source operated with significantly less power and produced lower defect densities. Specifically, defect densities of 22–27 defects/cm^2 for ~ 1 μm thick GaAs layers have been obtained with the new source, compared with 88–92 defects/cm^2 from the 125DF. In addition, an 18.7 μm thick GaAs layer grown with the new cell had only 277 defects/cm^2. The new source also produced GaAs with low background doping ($< 2 \times 10^{13}$/cm^3), low total trap density ($< 2.0 \times 10^{12}$/cm^3), and good uniformity over a 3 in diameter wafer (center-to-edge decrease in GaAs thickness of $\sim 2.2\%$). It also exhibited low flux transients ($< 2\%$) and low-long term drift.

Keywords: Molecular beam epitaxy; Gallium arsenide

1. Introduction

While significant progress in Ga sources for molecular beam epitaxy (MBE) has been made in recent years, there still remains room for improvement. The properties of greatest interest for Ga sources are oval defect density, stability (shutter transients and long-term drift), uniformity, background doping, and capacity. To date, no single design has succeeded in optimizing all of these parameters at once, and there remains room for improvement in each individual figure of merit. At present, there are two Ga source designs in greatest use, having some points in common. Both incorporate two independently controlled heater windings (filaments) to allow the tip to be run hotter than the bottom. This has been shown to greatly

* Corresponding author. Fax: +1 614 2927596; e-mail: sacks@ee.eng.ohio-state.edu.

0022-0248/97/$17.00 Copyright © 1997 Elsevier Science B.V. All rights reserved
PII S0022-0248(96)01025-1

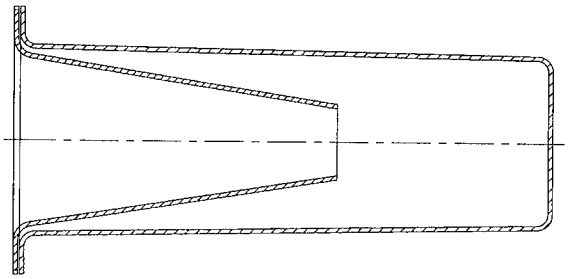

Fig. 1. EPI 125DF crucible with conical insert. The main crucible length is 108 mm. The insert length is 50 mm, and the diameters of the bottom and top orifices are 15 mm and 36 mm.

decrease the number of source-generated oval defects compared to single winding sources by reducing or eliminating Ga droplets which build up at a cooler tip [1]. Both designs also produce good uniformities and low background doping. The difference is in the trade-off of defect density, stability, and capacity. One design has a single, conical crucible and has produced very low defect densities, but is susceptible to shutter transients, has higher than desirable long-term drift due to Ga melt depletion, and is not optimized for capacity. The other design has a straight walled crucible and a conical insert, open at the top and bottom, as exemplified by the EPI 125DF, and shown schematically in Fig. 1. This type has virtually no shutter transient, greatly reduced long-term drift, and high capacity, but produces somewhat higher defect densities than the conical cell. The motivation for this work was to produce a source that would not only eliminate the deficiencies of these two cell designs while maintaining their benefits, but also improve overall performance, especially with regard to further reduction of defect density and long-term drift.

The starting point for this study was the 125DF source described above. The only drawback to this design compared to the conical crucible is the higher defect density, which has two probable causes. The first involves the higher power needed by the tip heater winding to keep the conical insert hot enough to remain free of Ga droplets. This is both because the insert is isolated from the windings by the straight-walled crucible, and because it is further from the windings due to its taper. The higher power may produce a higher flux of impurities outgassing either from the furnace itself or from the nearby cryoshroud walls which act as nucleation centers for defect formation. It has been shown previously that chemical impurities such as C [2], GaO [3], and S [4] can promote defect formation. The other possible cause is impurities (most likely GaO), becoming trapped in the "corner" defined by the insert and the crucible wall and continuing to evolve slowly and generate defects. Attempts have been made to reduce the thermal loading of the tip by using furnaces with high-density tip heater windings, and by replacing the pyrolytic boron nitride (PBN) insert with one made of PBN-encapsulated pyrolytic graphite (PG), since PG is a better thermal absorber than PBN. While these have reduced defects from the 125DF source, the cell is still at a slight disadvantage compared to the conical crucible cell. In addition, it would be desirable to reduce long-term drift even further, and to increase ultimate capacity.

The enabling technology for this study was the development of a means for producing PBN crucibles with "reverse tapers" or "necks" [5]. This allowed the fabrication of a one-piece crucible which combines the benefits of both the straight-walled main body and the conical insert. The crucible is cylindrical in overall shape, but necks down to a small orifice with a short cone. This design also allowed the incorporation of a unique heat-shielding cap at the front of the cell, with the intention of making the cell more thermally efficient and allowing the tip to be held considerably hotter than the body without radiating large amounts of heat to the surroundings. The cell is also equipped with two heater windings and two thermocouples ("tip" and "primary"), with the tip heater filament being a high-density winding. This cell has been called the EPI SUMO, and is illustrated in Fig. 2. Compared to the 125DF, the fact that there is no conical insert means that heating of the tip should take less power, and any possibility of impurities being trapped in a "corner" would be eliminated, both of which should help in reducing defect densities. Concerning capacity, the 125DF can be filled with $\sim$ 125 g of Ga, while the SUMO can be loaded with $\sim$ 300 g of Ga, with the potential for expansion to even larger size.

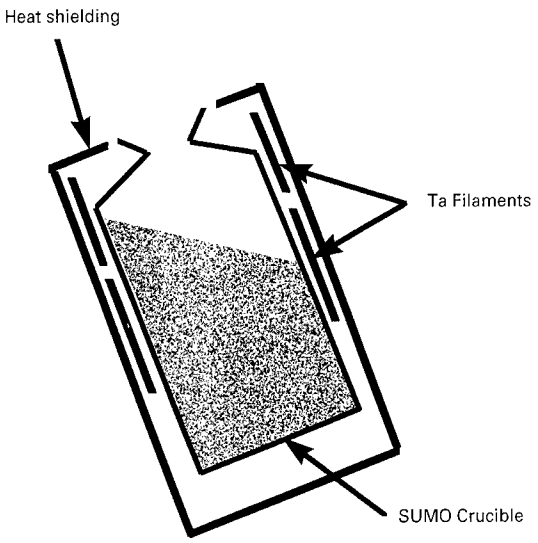

Fig. 2. Schematic of SUMO source. The crucible length is 95 mm, and the orifice size is 16 mm.

2. Experimental procedure

Growths were performed in a Varian GEN II with 3″ diameter wafer capability. Initially, the SUMO source was tested side-by-side with a 125DF source equipped with a PBN-encapsulated PG conical insert and a high-density tip heater filament. The two furnaces occupied equivalent positions on the source flange, the two most upward looking. Both sources were on 3 in long extension nipples, as were all other sources on the growth chamber, giving a normal source-to-substrate spacing of ~ 7.2 in. Both sources have two thermocouples, a "primary" which is a band thermocouple in contact with the crucible about halfway up, and a "tip" thermocouple which is not in contact with the crucible and is located at the mouth of the source. Heating and temperature control was achieved by using the primary thermocouple only for feed-back control to a Eurotherm 818 P-I-D controller connected to a "power splitter" power supply. The power splitter allows the user to adjust the fraction of total power going to the primary and tip heater windings. A second round of tests was performed with the SUMO as the only Ga source, mounted on a 5 in long, water-cooled extension nipple (the 3 in nipples mentioned above had no cooling). For all growths reported below, the substrate temperature was 600°C as measured by an IRCON V-series GaAs specific pyrometer, and As_2 from a valved As cracking source was used. For initial trial of the SUMO, it was loaded with only 50 g of Ga, but this was later increased to 150 g and then 200 g. The results reported below showed no dependence on the initial fill level. Substrate rotations of 6–10 RPM were used.

Flux transients were measured with an ion gauge in the substrate growth position. The output of the gauge controller was relayed through an A/D board and monitored on a computer to allow flux measurements to three significant figures. The error of this technique is no greater than 2%.

Uniformity was tested by growing a 20-period AlAs(160 Å)/GaAs(56 Å) multiple quantum well (MQW) structure on 3″ (75 mm) diameter wafers. Layer thickness variations across the wafers were then measured with photoluminescence (PL) mapping. The scanning PL system used has been described elsewhere [6]. The GaAs thickness variation of the most uniform wafer grown with the SUMO cell was confirmed using reflectometry on an 18.7 μm thick GaAs layer grown on top of a 200 Å AlAs "reflection" layer.

To test defect densities, we grew modulation doped field effect transistors (MODFETs) with a 1 μm GaAs buffer, and total thickness of 1.1 μm on 2″ diameter substrates taken from the same boule. The GaAs growth rate for all runs was 1.05 μm/h. The effect of varying the amount of power to the cell tips was studied by performing growths with the cells operating between 85% and 100% of total power to the tip filament. Defect densities were measured with a Tencor Surfscan 6200 set to count all defects larger than 1.28 μm.

Background doping was estimated with capacitance–voltage (C–V) measurements on a 17.8 μm thick nominally undoped GaAs layer grown on a semi-insulating substrate at 600°C and close to minimum As flux. Trap concentrations were measured with deep level transient spectroscopy (DLTS) on a P^+–N junction also grown at 600°C and close to minimum As flux, where the

N-GaAs layer was doped at $1 \times 10^{15}/cm^3$. Mobilities were measured on Hall samples fabricated from some of the MODFET structures grown for the defect density measurements.

3. Results and discussion

3.1. Flux transients

Any flux transients for both sources were unmeasurable with our technique ($< 2\%$).

3.2. Temperatures and power consumption

Table. 1 shows the tip and primary thermocouple temperatures as a function of percent total power to the tip for the both cells operating at a GaAs growth rate of 1 μm/h. Also shown is the power consumption for both cells with 100% power to the tip. One important point to note is that when comparing the same power ratios, the SUMO cell always maintains a considerably greater difference in the tip vs. the primary temperature than the 125DF, which should help to keep the lip of the cell free of Ga droplets. A second point is that, as expected, the power consumption of the SUMO is considerably less than the 125DF ($\sim 57\%$ for 100% tip power), which should reduce thermal loading of the surroundings.

3.3. Uniformity

PL wafer maps showed that the variation in quantum well (QW) thickness is axially symmetric, as expected. All thickness variations given below are relative to the thickness at the wafer center. While the 125DF (on its usual 3 in long extension nipple) produced GaAs thickness decreases of $\sim 1\%$ at 25 mm out from the center, and $\sim 2.2\%$ at 33 mm out, the SUMO cell on the initial 3 in long extension nipple gave thickness drops at those same radial distances of $\sim 3\%$ and $\sim 5\%$ respectively. Putting the SUMO cell on a 5 in long extension nipple (i.e., moving it back from the substrate by an additional 2 in) resulted in GaAs uniformities at least as good as from the 125DF. This is illustrated in Fig. 3, which shows the variation of room temperature QW PL energy with distance from the wafer center for the 125DF cell and for the SUMO on the 5 in nipple. This high uniformity was confirmed by reflectometry on an 18.7 μm thick GaAs layer grown with the SUMO on the 5 in nipple.

3.4. Visible defects

The SUMO cell produced consistently lower defect densities than the 125DF, as illustrated in

Table 1
Temperatures, power consumption, and defect densities at a GaAs growth rate of 1 μm/h

Source	Total power to tip (%)	Primary (°C)	Tip (°C)	Δ tip–primary (°C)	Power (W)	Total defects/ cm^2	Approx. weeks since last vent
125DF	85	1095	1191	96		155	16
125DF	90	1107	1217	110		95	4
125DF	100	1105	1235	130	380	90 ± 2^a	4
SUMO	85	987	1155	168		137	4
SUMO	90	993	1185	192		63	4
SUMO	100	978	1199	222	210	36 ± 2^a	4
SUMO[b]	100	986	1220	234	209	53 ± 5^a	2
SUMO[b]	100	993	1236	243	220	24 ± 2^a	12

[a] Average of two growths.[b] On 5" water-cooled nipple.

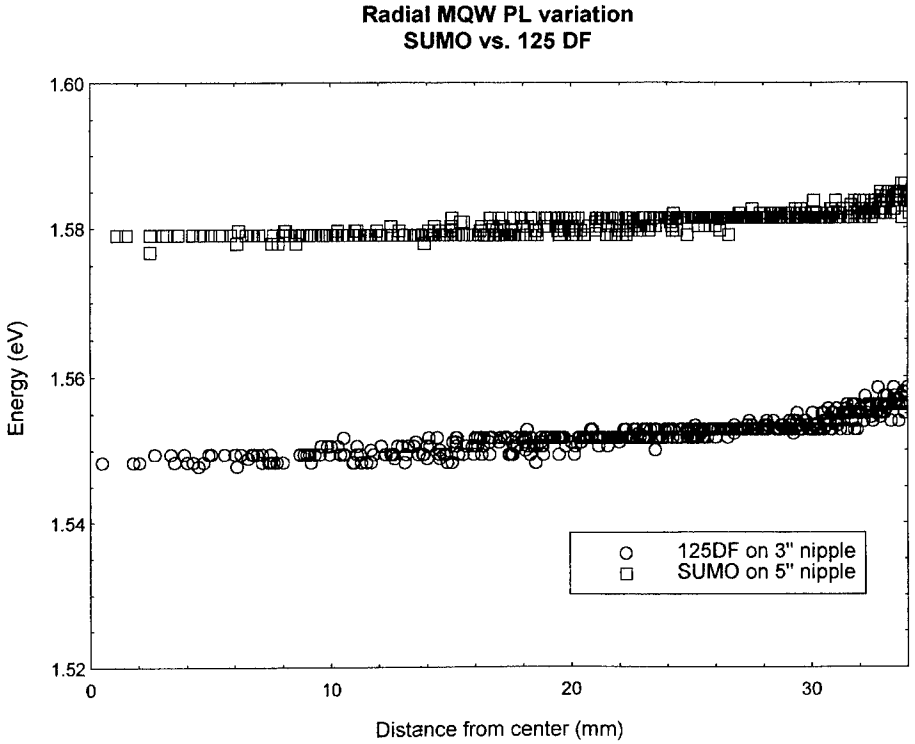

Fig. 3. Variation of QW room temperature PL energy with distance from 3 in diameter wafer center for the 125DF and the SUMO cell mounted on 5 in long extension nipple. The actual QW thicknesses are slightly different for each sample: 53 Å for the SUMO-grown and 59 Å for the 125DF-grown.

Table 1. For both sources, defect densities decreased with increased power to the tip, consistent with reduced tip Ga droplets. This is in contrast to an earlier study on a different cell design which used stacked disk inserts [7] and required relatively high temperatures and powers compared to the 125DF. For that cell defect density actually increased with increasing tip power, presumably due to excess radiated heat generating impurities from the surroundings which overwhelmed any benefit from droplet reduction. While the best result achieved with the 125DF was 90 defects/cm^2, the best results with the SUMO were 36 defects/cm^2, when it was mounted on the 3 in long, uncooled extension nipple and 24 defects/cm^2 when it was mounted on the 5 in long, water-cooled nipple. It is not entirely clear whether the improvement from 36 to 24 defects/cm^2 was due to the water cooling or the fact that the growth chamber had been under vacuum longer (12 weeks vs. 4 weeks) when the better results were generated. However, an indication that the water cooling was playing an important role is that growths done only 2 weeks after the SUMO was installed on the 5 in nipple produced relatively low defect densities of 53 defects/cm^2.

3.5. Electrical material quality

C–V measurement of a 17.8 μm thick nominally undoped GaAs layer grown with the SUMO cell on a semi-insulating substrate showed the layer to be fully depleted, implying a background doping $< 2 \times 10^{13}$/cm^3. DLTS measurements of a P^+–N junction, where the N-GaAs layer was doped at

$1 \times 10^{15}/cm^3$ gave total trap concentrations of $1.5–2.0 \times 10^{12}/cm^3$. Hall measurements on MODFET"s have yielded 77 K mobilities of 132 000 cm^2/Vs for $n_s = 4 \times 10^{11}/cm^2$. All of the above taken together indicate good to excellent electrical quality for GaAs grown with the SUMO cell.

4. Summary

A new high-capacity group III source incorporating a novel crucible and unique heat shielding cap has been evaluated with respect to power consumption, flux transient, visible defect density, layer uniformity, and electrical material quality. Results in all these categories were good to excellent, and in particular, the new cell produced much lower defect densities compared to the older design high capacity, low transient cell. The new cell also has more than double the Ga capacity of the old design.

Acknowledgements

The authors wish to thank A.J. SpringThorpe of Bell-Northern Research for reflectometry and some Surfscan measurements, and R.M. Sieg of Ohio State University (E.E. Dept.) for the help with some of the growths.

References

[1] D.G. Schlom, W.S. Lee, T. Ma and J.S. Harris, Jr., J. Vac. Sci. Technol. B 7 (1989) 296.
[2] M. Bafleur, A. Munoz-Yague and A. Rocher, J. Crystal Growth 59 (1982) 531.
[3] Y.G. Chai and R. Chow, Appl. Phys. Lett. 38 (1981) 796.
[4] Y.G. Chai, Y.-C. Pao and T. Hierl, Appl. Phys. Lett. 47 (1985) 1327.
[5] CVD Products, Inc., Hudson, New Hampshire, USA.
[6] A.L. Moretti, F.A. Chambers, G.P. Devane and F.A. Kish, IEEE J. Quantum Electron. 25 (1989) 1018.
[7] R.N. Sacks, G.A. Patterson and K.A. Stair, J. Vac. Sci. Technol. B 14 (1996) 2187.

ELSEVIER

Journal of Crystal Growth 175/176 (1997) 72–78

JOURNAL OF CRYSTAL GROWTH

Growth of GaN, InGaN, and AlGaN films and quantum well structures by molecular beam epitaxy

M.A.L. Johnson[a], W.C. Hughes[a], W.H. Rowland, Jr.[a], J.W. Cook, Jr.[a], J.F. Schetzina[a,*], M. Leonard[b], H.S. Kong[b], J.A. Edmond[b], J. Zavada[c]

[a] *Department of Physics, North Carolina State University, P.O. Box 8202, Raleigh, North Carolina 27695-8202, USA*
[b] *Cree Research, Inc., 2810 Meridian Parkway, Durham, North Carolina 27713, USA*
[c] *US Army Research Office, Research Triangle Park, North Carolina 27709-2211, USA*

Abstract

GaN, AlGaN and InGaN films have been grown by molecular beam epitaxy (MBE) using RF plasma sources for the generation of active nitrogen. These films have been deposited homoepitaxially onto GaN/SiC substrates and heteroepitaxially onto $LiGaO_2$ substrates. $LiGaO_2$ is an ordered and closely-lattice-matched orthorhombic variant of the wurtzite crystal structure of GaN. A low-temperature AlN buffer layer is necessary in order to nucleate GaN on $LiGaO_2$. Thick GaN and AlGaN layers may then be grown once deposition is initiated. InGaN has been grown by MBE at mole fractions of up to 20% as a quantum well between GaN cladding layers. The indium containing structures were deposited onto GaN/SiC substrates to focus the development effort on the InGaN growth process rather than on heteroepitaxial nucleation. A modulated beam technique, with alternating short periods of (In, Ga)N and (Ga)N, was used to grow high-quality InGaN. The modulated beam limits the nucleation of metal droplets on the growth surface, which form due to thermodynamic limitations. A narrow PL dominated by band edge luminescence at 421 nm results from this growth technique. Growth of GaN at high temperatures is also reported.

1. Introduction

The III–V nitride semiconductor materials have undergone a tremendous expansion of research and development activity in the past three years. By tailoring of the Al(Ga, In)N alloy composition, the band gap of these materials range from 6.2 eV for AlN, through 3.4 eV for GaN, to 1.9 eV for InN [1]. The use of these direct band gap semiconductors for optoelectronic applications has led to the introduction of commercially available blue and green light emitting diodes (LEDs) as well as the recent demonstrations of laser diodes fabricated from III–V nitride heterostructures [2].

Although, all of the commercial nitride LEDs have been prepared by metalorganic vapor phase epitaxy (MOVPE), MBE growth of nitrides has also been expanded rapidly during the past three years. Several issues need to be addressed for the successful growth of III–V nitride materials by

* Corresponding author. Fax: +1 919 5157667; e-mail: jan_schetzina@ncsu.edu.

0022-0248/97/$17.00 Copyright © 1997 Elsevier Science B.V. All rights reserved
PII S0022-0248(96)01019-6

MBE: the development of effective 'active' nitrogen sources for growth of nitrides by MBE at reasonable growth rates; the evaluation of possible substrates for nitride film deposition; the effective control of AlGaN and InGaN alloy compositions in multilayered structures for visible light emitter applications; and the development of a doping technology, particularly for p-type doping of AlGaN, GaN and eventually InGaN.

At North Carolina State University (NCSU), we have used RF plasma sources to generate active nitrogen for III–V nitride film deposition by molecular beam epitaxy (MBE). Optical emission spectroscopy has shown RF plasma sources to be effective in the generation of both atomic nitrogen and first-positive series excited molecular species (3.9 eV binding energy) which are essential for MBE growth of nitrides [3, 4].

Our previous work at NCSU has focused on the MBE growth of GaN and AlGaN materials and multilayered structures on GaN/SiC substrates [5, 6]. The GaN/SiC substrate that we employ consists of a 1–3 μm thick buffer layer of GaN deposited by MOVPE on an underlying 6H–SiC substrate at Cree Research, Inc. The dislocation density near the surface of the GaN/SiC substrate is about 10^8 per cm^2. The GaN/SiC substrate provides a homoepitaxial surface for GaN deposition by MBE. This allows us to evaluate the MBE growth process itself and circumvents the problems associated with low-temperature heteroepitaxial nucleation on grossly mismatched substrates such as sapphire or SiC. Additionally, the n-type GaN/SiC substrates employed are electrically conducting and thus provide the means for a backside contact in the development of optoelectronic devices such as LEDs or lasers.

With the successful development of AlGaN and GaN growth on GaN/SiC substrates, we are now also evaluating heteroepitaxial deposition of GaN and AlGaN on bulk $LiGaO_2$ substrates. The crystal structure of $LiGaO_2$ is orthorhombic and is an ordered variant of the GaN wurtzite, with oxygen occupying the anion sites and lithium and gallium occupying alternating layers of the cation sites [7]. As shown in Fig. 1, the {0 0 1} plane of $LiGaO_2$ possesses an underlying hexagonal symmetry which should be suitable for growth of the (0 0 0 1) basal plane of hexagonal GaN. Crystal ordering results in a slight distortion of the bond angles of $LiGaO_2$ from the perfect hexagonal structure. However, the equivalent average basal plane lattice constant of $LiGaO_2$ (a_{ave} = 3.152 Å) is closely lattice-matched to that of GaN (a = 3.189 Å) [2, 7]. We have found that heteroepitaxy of GaN on $LiGaO_2$ by MBE requires the use of a low-temperature AlN buffer layer for nucleation. Similar buffer layers have been reported for the heteroepitaxial growth of GaN on sapphire [8, 9].

We have also extended the homoepitaxial approach of MBE growth on GaN/SiC substrates to the study of InGaN growth. The band gap energy of InGaN spans the entire range of visible wavelengths from blue at 400 nm to red at 650 nm with

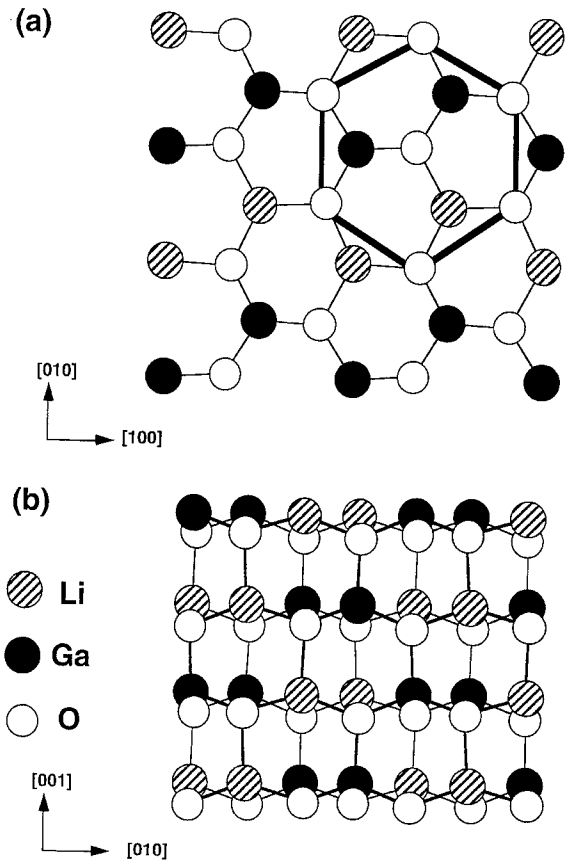

Fig. 1. Crystal structure of (a) $LiGaO_2$ c-plane and (b) $LiGaO_2$ a-plane.

increasing indium mole fraction [1]. As a result, growth of high-quality InGaN is critical for the successful fabrication of visible optoelectronic devices.

InGaN deposition is complicated by thermodynamic instability of InN. At typical MBE nitride growth temperatures of 800°C, the equilibrium vapor pressure of nitrogen over InN is greater than 1×10^{-4} Torr [10]. This is a higher pressure than the beam equivalent pressure of the incident source fluxes. As a result, InN will tend to dissociate faster than it can be deposited under these conditions. As a solid solution, the vapor pressure of nitrogen over InGaN should be much lower than InN. However, previous studies of high-temperature MOVPE growth of InGaN have shown that any segregation of InN on the growing crystal surface will result in the sublimation of nitrogen and condensation of indium droplets [11, 12]. In Fig. 2, the competing pathways between InGaN incorporation and indium droplet formation are shown schematically. Once indium droplets are formed, they act to getter the incoming indium flux so that appreciable indium incorporation within the growing InGaN film is very small. Increasing the indium flux can produce InGaN with even less indium incorporation.

Growth kinetics play a vital role in controlling InGaN film quality by determining the preference between InGaN incorporation and indium segregation. One approach is to deposit InGaN at a lower substrate-temperature, thereby reducing the InN dissociation rate. The reduction in substrate temperature comes with a corresponding loss of crystal quality rendering this material unsatisfactory for device applications [12]. To overcome these limitations, high indium to gallium source ratios and atomic layer epitaxy approaches have been used in MOVPE growth of InGaN by several groups [11–14]. In this study, we report the deposition of InGaN by a migration-enhanced modulated-beam deposition technique which suppresses the formation of indium droplets. Using this approach, InGaN layers having indium up to 20% have been successfully prepared by MBE.

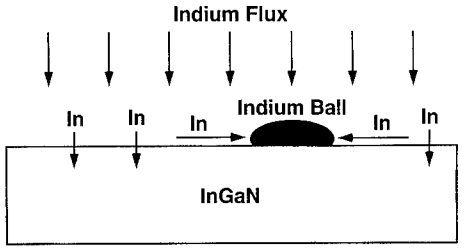

Fig. 2. Illustration of InGaN growth segregation model. The dual In incorporation results in the formation of In balls.

2. Experimental details

III–V nitride films were grown using a modified EPI Inc. model 930 MBE system. The main growth chamber has ports for up to ten sources, including the capability of simultaneously operating multiple RF plasma sources. A Boralectric substrate filament provides substrate heating for wafers up to 75 mm in diameter to over 1000°C, as monitored by an external optical pyrometer. All critical MBE growth functions are computer controlled. An ion gauge, which can be extended to a point immediately in front of the substrate, is used to measure the various source fluxes prior to MBE film growth.

High-purity gallium (7N), aluminum (6N+) and indium (7N) were used in standard effusion cells. VLSI grade (5N5) nitrogen was passed through the RF sources to generate the 'active' nitrogen species used for nitride film growth. Nitrogen plasma sources obtained from Oxford Instruments, SVT Associates, and EPI, Inc. were employed during various stages of this study. Optical emission spectroscopy indicated that all of these sources generated a significant fraction of atomic and first positive excited molecular nitrogen appropriate for MBE growth [5]. The RF plasma sources were mounted on 4.5 in. UHV flanges and each had a water-cooled RF coil surrounding a pyrolytic boron nitride reaction tube. An inductively coupled plasma was generated within the PBN tube and injected through an aperture into the MBE chamber. The RF sources had external matching networks which were connected to power supplies capable of delivering up to 600 W at 13.56 MHz. Most of the nitride films prepared during the present study were grown using plasma source pressures of 5×10^{-5} Torr

(estimated to correspond to nitrogen gas flow rates of several sccm) and plasma source powers of 400 W. A flux of 2×10^{-7} Torr for gallium resulted in a typical GaN growth rate of 0.2 μm/h.

A separate vacuum chamber was used for plasma cleaning of the substrates prior to nitride film growth. A hydrogen/helium gas mixture fed through an ASTeX ECR source was employed in the cleaning chamber and provided an excellent method for removing surface contaminants such as oxygen and carbon. A third chamber equipped with an Auger spectrometer was used to evaluate the surfaces before and after the cleaning process and after MBE film growth. All three vacuum chambers were connected via a UHV transfer tube which allowed critical preparation and growth steps to be performed without exposing the substrates to air.

The MBE-grown films were characterized by means of in-situ reflection high-energy electron diffraction (RHEED), Nomarski interference contrast microscopy, variable temperature photoluminescence (PL), and double-crystal X-ray diffraction. The X-ray rocking curves were obtained using a Blake Industries double-crystal diffractometer and Cu K_α X-rays. The double-crystal unit was operated in a standard fashion with the detector fully-open (no aperture) for rocking curve measurements. The PL measurements were obtained using a 15 mW HeCd laser for excitation and an EG&G Princeton Applied Research monochromator equipped with interchangable 150, 600, 2400 g/mm gratings and a cooled 700 pixel diode–array detector. The spectrometer was calibrated using the known atomic emission lines from a mercury lamp.

3. Results and discussion

3.1. Growth of GaN and AlGaN/GaN quantum wells on $LiGaO_2$ substrates

Fig. 3a shows a double-crystal X-ray rocking curve obtained for a representative $LiGaO_2$ substrate. It is seen that the full-width at half-maximum (FWHM) of the equivalent (0 0 0 2) diffraction peak is only 18 arcsec, which is indicative of very excellent crystal quality.

In order to nucleate GaN on $LiGaO_2$, a thin AlN buffer layer was initially deposited on the $LiGaO_2$ substrate at 600°C for 5 min. The temperature was then increased to 800°C, while the AlN deposition continued for an additional 5 min. Following this, GaN film growth was initiated. Fig. 3b shows a representative X-ray rocking curve with a full-width at half-maximum (FWHM) of 103 arcsec for GaN on $LiGaO_2$. RHEED patterns observed during growth were consistent with epitaxial deposition and display mixed 2D and 3D growth mode characteristics. A thick GaN buffer layer, up to 3.25 μm total, was also grown using the low-temperature AlN nucleation layer.

Without an AlN nucleation buffer layer, the overlying GaN epilayers tend to crack and delaminate from the $LiGaO_2$ substrate after growth. With the low-temperature AlN buffer layer, clear and

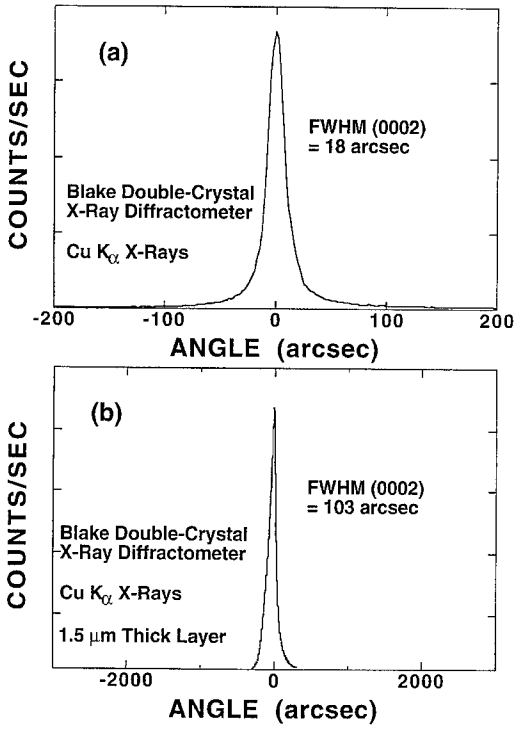

Fig. 3. X-ray of (a) $LiGaO_2$ before growth and (b) GaN on $LiGaO_2$.

specular epitaxial films result. We believe that this AlN buffer layer provides a nucleation layer for growth of GaN upon heating to 800°C, similar to the approach employed by others for growth of GaN on sapphire [1]. However, we feel that the low-temperature buffer on $LiGaO_2$ is always necessary to cap the surface of the substrate thus preventing surface sublimation. This interpretation is consistent with observed changes in the RHEED patterns of $LiGaO_2$ wafers heated to 800°C which show a deterioration with time indicative of surface roughening due to sublimation of the substrate surface. Thus, it would appear that $LiGaO_2$ may not be stable enough to serve as a substrate for MOVPE growth of III–V nitrides, which is currently performed at 1050°C.

The structure for the AlGaN/GaN multilayer film grown on $LiGaO_2$ was a 1 μm thick GaN buffer layer, with a 5 period structure containing 50 Å GaN wells and 100 Å AlGaN barriers grown on top of the buffer. The nominal AlGaN composition was 8% to 10%. Separate 500 Å thick layers of AlGaN precede and follow the 5 period structure. Fig. 4 shows a room-temperature PL spectrum obtained for an AlGaN/GaN multilayer structure grown by this technique. It is seen that the spectrum is dominated by a strong peak at 3.460 eV, presumably emitting from recombination in the GaN wells shifted somewhat to higher energy because of quantum confinement. The peak at 3.63 eV comes from the AlGaN cladding layers and corresponds to an aluminum mole fraction of 8%, assuming Vegard's law for this alloy.

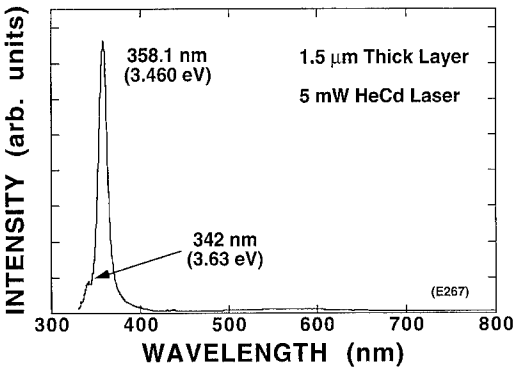

Fig. 4. Room temperature PL of AlGaN/GaN multiquantum well structure on $LiGaO_2$.

3.2. Growth of GaN/InGaN structures on GaN/SiC substrates

The test structure for the InGaN MBE growths, deposited on MOVPE GaN/SiC substrates, was a 1500 Å GaN buffer layer followed by a thin (50–200 Å) undoped InGaN layer and capped with a 500 Å GaN layer. Two different growth techniques were tested for the InGaN deposition: A continuous deposition of InGaN at the desired flux ratio or a InGaN modulated beam deposition in 10 s alternating sequences of (In, Ga)N and (Ga)N. The purpose of the intermittent GaN layer in the modulated beam approach is to stabilize the InGaN growing surface prior to the nucleation of indium droplets on the growth surface. At a nominal growth rate of 1500 Å/h, this sequence corresponds to alternating 4 Å thick layers of InGaN and GaN. An indium to gallium flux ratio of 1:2 was measured by the ion gauge flux monitor prior to growth.

The continuously deposited InGaN resulted in poor material quality, characterized by a PL signal indicating band edge GaN at 3.41 eV and significant deep level emissions in the range of 2.0–2.4 eV as shown in Fig. 5a. Additionally, in some thicker films, metal droplets were observed on the surface following growth. By comparison, the modulated beam technique resulted in a significantly improved strong band edge PL peak emitted from the InGaN quantum well at room temperature and 77 K as shown in Fig. 5b and Fig. 5c, respectively.

To examine the influence of substrate temperature during InGaN growth, the temperature was adjusted by decreasing it during the last five minutes prior to initiation of the InGaN deposition. The substrate temperature was subsequently increased back to the original GaN deposition temperature of 780°C one minute after completion of the InGaN film growth. No growth interruption was used during temperature adjustments. A streaky RHEED pattern, characteristic of two-dimensional epitaxial deposition, was observed throughout the InGaN film growth. The highest indium incorporation was observed for InGaN

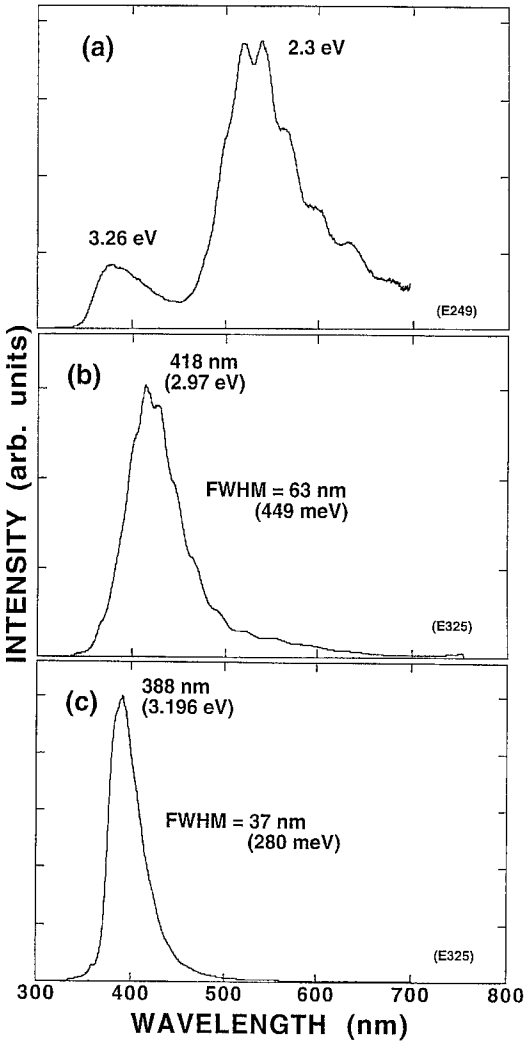

Fig. 5. InGaN grown by (a) continuous MBE deposition PL at 295 K, (b) migration-enhanced modulated-beam MBE deposition PL at 295 K and (c) migration-enhanced modulated-beam MBE deposition PL at 77 K.

grown by the modulated beam technique with a substrate setpoint of 600°C which resulted in an InGaN film which displayed a PL peak centered at 421 nm. This emission wavelength corresponds to an indium incorporation of about 20% when a band bowing parameter of 1.0 eV is used as has been previously reported for the InGaN material system [1].

3.3. MBE growth of GaN at high temperatures

By using two RF plasma sources simultaneously we have been able to double the supply of active nitrogen for MBE film growth of nitrides. As a consequence, we have obtained growth rates for GaN and AlGaN films of up to 0.8 μm/h for MBE film growth at 800°C. Perhaps more significantly, by increasing the flux of active nitrogen at the substrate via the two-source technique, we have been able to achieve MBE growth of GaN at 900°C for the first time with growth rates of 0.2–0.3 μm/h. Fig. 6 shows PL emission spectra obtained for a 1 μm thick undoped GaN film grown at 900°C onto a GaN/SiC substrate. As seen from Fig. 6a, the PL spectrum at room temperature consists of a single sharp peak at 3.409 eV having a FWHM = 36 meV. No significant deep level emission in the yellow–green 2.2 eV defect band range is present in the spectrum. Fig. 6b shows a 4.2 K high resolution

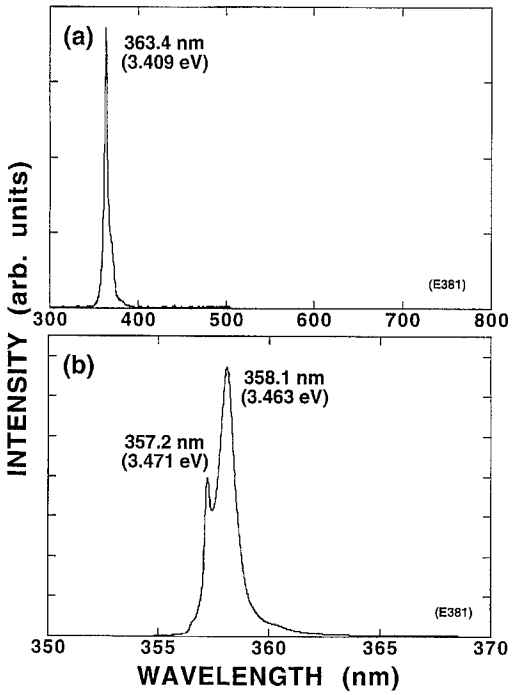

Fig. 6. GaN grown at 900°C with two plasma sources: (a) PL of GaN at room temperature and (b) high resolution PL of GaN at 4.2 K.

PL spectrum obtained for this GaN sample. The spectrum consists of two sharp excitonic peaks at 3.463 and 3.471 eV, respectively. No measurable deep level PL emission was found for this sample at 4.2 K. *C–V* measurements for this undoped GaN sample indicated that the layer was n-type with N_d–N_a $\sim 5 \times 10^{16}$ per cm^3. This low background doping level, which results because there is sufficient active nitrogen present during MBE film growth, implies that controlled substitutional doping of GaN may be possible at very high growth temperatures ($\sim$900°C or higher). Such studies are underway at NCSU and will be reported at a later date.

4. Summary and conclusions

MBE has been used to deposit GaN, AlGaN and InGaN films. Single or multiple RF plasma sources have been used to generate ample active nitrogen required for MBE growth at nitrides at typical MBE growth rates (0.2–0.8 μm/h). Using this process, GaN and AlGaN films were deposited on $LiGaO_2$ substrates. A thin low-temperature AlN buffer layer was necessary to nucleate nitride growth on $LiGaO_2$.

A modulated beam technique was successfully used to deposit InGaN on GaN/SiC by MBE at up to 20% mol fraction indium. This technique resulted in strong band edge PL at 421 nm. With the modulated beam technique, the growth of high-quality InGaN by MBE for optoelectronic applications has been demonstrated.

Acknowledgements

The authors wish to thank J. Matthews of NCSU for his assistance in substrate preparation, X-ray diffraction measurements and MBE system maintenance.

References

[1] S. Strite and H. Morkoç, J. Vac. Sci. Technol. B 10 (1992) 1237.
[2] S. Nakamura, M. Senoh, S. Nagahama, N. Iwasa, T. Yamada, T. Matsushita, H. Kiyoku and Y. Sugimoto, Jpn. J. Appl. Phys. 35 (1996) L74.
[3] W.E. Hoke, P.J. Lemonias and D.G. Weir, J. Crystal Growth 111 (1991) 1024.
[4] R.P. Vaudo, Z. Yu, J.W. Cook, Jr. and J.F. Schetzina, Opt. Lett. 66 (1995) 268.
[5] W.C. Hughes, W.H. Rowland, Jr., M.A.L. Johnson, Sz. Fujita, J.W. Cook, Jr., J.F. Schetzina, J. Ren and J.A. Edmond, J. Vac. Sci. Technol. B 13 (1995) 1571.
[6] M.A.L. Johnson, Sz. Fujita, W.H. Rowland, Jr., K.A. Bowers, W.C. Hughes, Y.W. He, N.A. El-Masry, J.W. Cook, Jr., J.F. Schetzina, J. Ren and J.A. Edmond, J. Vac. Sci. Technol. B 14 (1996) 2349.
[7] M. Marezio, Acta. Cryst. 18 (1965) 481.
[8] I. Akasaki, H. Amano, Y. Koide, K. Hiramatsu and N. Sawaki, J. Crystal Growth 98 (1989) 209.
[9] S. Yoshida, S. Misawa and S. Gonda, Appl. Phys. Lett. 42 (1983) 427.
[10] R.D. Jones, PhD Thesis, Rensselaer Polytechnic Institute (1986).
[11] M. Shimizu, K. Hiramatsu and N. Sawaki, J. Crystal Growth 145 (1994) 209.
[12] S. Bedair, Mater. Res. Soc. Symp. Proc. 331 (1996) 561.
[13] N. Yoshimoto, T. Matsuoka, T. Sasaki and A. Katsui, Appl. Phys. Lett. 59 (18) (1991) 2251.
[14] S. Nakamura and T. Mukai, Jpn. J. Appl. Phys. 31 (1992) L1457.

ELSEVIER

Journal of Crystal Growth 175/176 (1997) 79–83

JOURNAL OF CRYSTAL GROWTH

Optimization of AlGaN films grown by RF atomic nitrogen plasma using in-situ cathodoluminescence

J.M. Van Hove*, P.P. Chow, A.M. Wowchak, J.J. Klaassen, M.F. Rosamond, D.R. Croswell

SVT Associates, 7620 Executive Drive, Eden Prairie, Minnesota 55344, USA

Abstract

In-situ cathodoluminescence (CL) is presented as a technique for determining film composition, optical quality, doping levels, and temperature of MBE grown group III nitride films. Excitation of the films is done with either the Auger or RHEED electron gun operating between 1 and 10 keV. The CL emission is monitored using a 3 nm resolution monochromator. Optimization of the GaN growth process using a RF atomic nitrogen plasma source is discussed using in-situ cathodoluminescence to reduce the "yellow" defect level present in GaN. Composition and quality of $Al_xGa_{1-x}N$ films are shown to be quickly determined from the peak position and width. This is extremely useful in the nitride system where reflection high-energy electron diffraction (RHEED) oscillations are not routinely observed. Measurement of the substrate temperature during GaN growth is demonstrated by monitoring the shift in band edge position with temperature. p-type doping and MQW levels observed by CL are shown to allow quick optimization of device and material properties.

1. Introduction

Interest in the group III (Al, Ga, In) nitrides and their ternary and quartenary alloys has increased dramatically with the recent progress in developing blue semiconductor lasers. Other devices such as high temperature, high power electronics and solar blind UV detectors are being developed in this wide band gap material system. While much of the growth of group III nitrides has been done with metal-organic chemical vapor deposition (MOCVD), recent progress has been made in molecular beam epitaxy (MBE) of these materials. The advancement of MBE in nitride growth is due in part to the improvement of nitrogen sources. The demonstration of 1 μm/h growth rates using both RF atomic nitrogen plasma sources and NH_3 injectors has allowed MBE grown material to achieve comparable quality to MOCVD material [1].

One advantage MBE has over other growth techniques is the ability to monitor the growth process in-situ. Reflection high-energy electron diffraction (RHEED) is now a commonly used in-situ technique for calibration of composition and

* Corresponding author. Fax: +1 612 934 2737; e-mail: jvanhove@svta.com.

0022-0248/97/$17.00 Copyright © 1997 Elsevier Science B.V. All rights reserved
PII S0022-0248(97)00869-X

growth rates for most III–V materials. Unfortunately, RHEED oscillations have only been observed under limited conditions for nitride growth. This makes film composition difficult to determine quickly in-situ. In this work, we present the use of in-situ cathodoluminescence (CL) for determining film composition, optical quality, doping levels and temperature of AlGaN films.

Cathodoluminescence is an optical technique which uses an electron beam to excite the film. The resulting emission provides material information similar to that obtained by photoluminescence, such as the position of the band edge and the mid gap energy levels [2]. This technique has been used by Rouleau and Park to monitor in-situ the blue/green CL emission from MBE-grown ZnSe films [3]. A significant advantage of in-situ CL is that it can be accomplished using a standard RHEED gun present in most MBE systems. Dispersion of the RHEED streak fluorescence through a simple monochromator /detector allows the band gap of the deposited material to be determined. From this measurement, the composition of $Al_xGa_{1-x}N$ and $In_xGa_{1-x}N$ films can be determined. The substrate temperature, a critical yet often poorly determined parameter, can be measured from the band gap shift with temperature. This is especially useful for group III nitrides grown on transparent sapphire as interference from the substrate heater hinders pyrometer measurements. The optical quality of the deposited film can also be evaluated from the FWHM of the band-edge emission, and qualitative assessment of the doping level can be made from the structure of the CL emission.

2. Experimental procedure

Fig. 1 shows a schematic of the in-situ cathodoluminescence setup used in the MBE growth chamber [4]. A collimator lens mounted on a retractable bellows stage is brought in close proximity to the epi-wafer surface for quick in-situ analysis and can be withdrawn behind the cryo panels for protection during material deposition. CL excitation is done with the RHEED electron gun at 10 keV while still observing the RHEED pattern. The emitted light was measured with a $\frac{1}{8}$ m (3 nm resolution) monochromator and PMT detector. A similar CL setup equipped with a fixed lens system is used with the Auger electron gun in the MBE analysis chamber

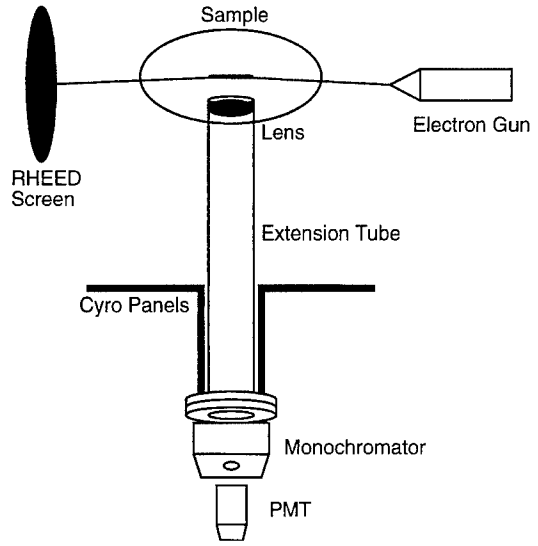

Fig. 1. In-situ CL setup used in the MBE growth chamber. A moveable stage allows the lens assembly to be brought close to the RHEED streak. CL excitation is done with the RHEED electron gun at 10 keV while observing the RHEED pattern. The emitted light is measured with a 3 nm resolution monochromator and PMT detector. A similar fixed lens system was used in the preparation chamber with the Auger electron gun used to excite the film.

An atomic RF plasma source developed specifically for the growth of MBE nitride was used for this work and has been described previously [5]. The basic concept is to create a plasma of nitrogen with the use of a RF field. RF energy (200–550 W) is fed into the gun through a water-cooled copper coil. A pyrolitic boron nitride (PBN) tube with a changeable nozzle is centered between the RF coils. Nitrogen is introduced to the tube with a leak valve and a plasma is created within the tube. Flow rates of 2–3 sccm of nitrogen is enough to produce growth rates around 1 μm/h. Elemental Ga and Al supplied from effusion cells were used for the group III elements. Mg doping was done using a conventional effusion cell while Si doping was done using a compact e-beam source. Sapphire (0 0 0 1) was used as the substrate with a low-temperature AlN buffer layer grown prior to GaN deposition.

Growth temperatures ranged between 750 and 900°C and a Ga-rich III–V flux ratio was used. X-ray diffraction taken from a 1 μm thick GaN on AlN/sapphire substrate using this technique shows a (0 0 0 2) diffraction peak with a full-width half-maximum of 39 arcsec which is comparable to the best MOCVD X-ray results [6].

3. Results and discussion

Fig. 2 shows the CL spectrum from a 1 μm thick layer of GaN on sapphire. These scans were taken at a beam voltage of 4 keV in the analysis chamber of the MBE system. The CL intensity is plotted on a log scale to highlight the yellow emission level which is present in most GaN films [7]. The log scale reveals considerable information lost in traditional linear plots. Fig. 2A shows the room temperature CL emission from an unintentionally doped n-type 10^{16} cm^{-3} GaN film. This film shows very little yellow emission around 550 nm and has a sharp band edge peak with a FWHM of 66 meV. Fig. 2B shows the room-temperature CL spectrum from a GaN film deposited under non-ideal conditions. The extremely large yellow emission peak centered around 550 nm is possibly due to the presence of oxygen and carbon in the GaN film. Similar yellow emission levels are observed under low growth temperatures, high N/Ga flux ratios, and on poor quality AlN buffer layers. Using the in-situ CL scans, both the yellow defect emission level and the FWHM of the GaN band edge can be measured quickly and growth conditions can subsequently be adjusted.

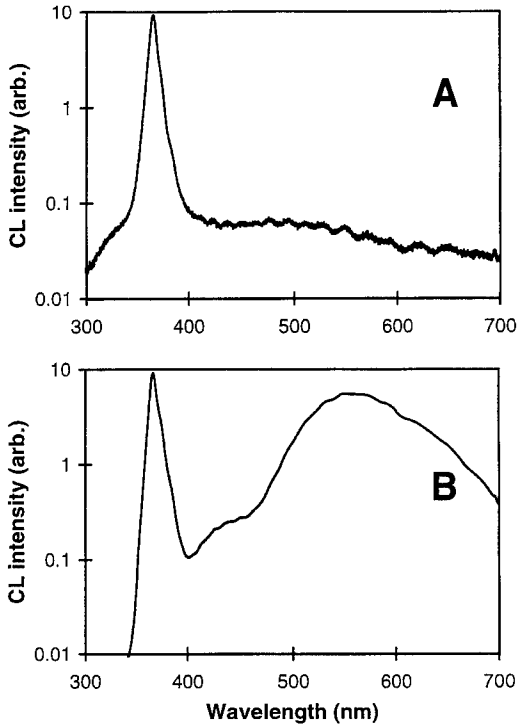

Fig. 2. In-situ CL spectrum from 1 μm of GaN on sapphire taken after growth at two different growth conditions. The CL intensity is plotted on a log scale to highlight the yellow emission level. (A) Room temperature CL emission from n-type 10^{16} cm^{-3} GaN showing very little yellow emission at 550 nm. The FWHM of the band edge peak is 66 meV. (B) Room temperature CL from GaN deposited in an unoptimized MBE system. Extremely intense yellow emission centered around 550 nm is observed. The yellow defect emission level and the FWHM of the GaN band edge can be measured in-situ and growth conditions adjusted.

The in-situ CL scans are extremely useful for optimizing Mg doped p-type GaN. MBE grown Mg doped films are p-type as grown, but control of the doping level remains a problem for GaN film growth. This is due in part to the low sticking coefficient of Mg at the growth temperature used. Fig. 3 shows a CL spectrum from a 1 μm thick layer of Mg-doped p-type GaN on sapphire. The CL intensity is plotted on a log scale. The Hall carrier concentration of this film was measured to be 10^{18} cm^{-3} but the incorporated Mg is expected to be much higher. The band edge emission is still present, but is now considerably broadened by the heavy Mg level (compared with the undoped GaN CL shown in Fig. 2A). At higher doping levels, the band-edge peak is replaced by a strong peak centered around 390–400 nm. This is in contrast to MOCVD grown p-type GaN which shows an emission level centered around 425–450 nm [8]. Fig. 3 also shows a sharp emission peak at 694 nm due to UV excitation of the Cr^{3+} impurity in the sapphire.

A major advantage of in-situ CL is in determining the composition of AlGaN films by measuring the band gap of the deposited material. From this measurement, the Al content can be determined [9]. Fig. 4 shows the CL spectrum from a multiple quantum well sample deposited on a $Al_{0.15}$

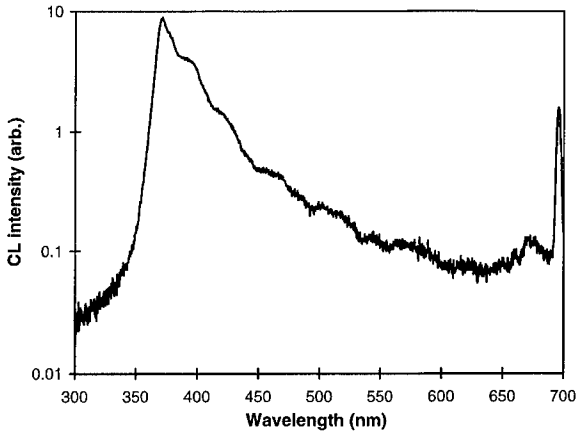

Fig. 3. In-situ CL spectrum from 1 μm of Mg-doped p-type GaN on sapphire. The CL intensity is plotted on a log scale. Hall carrier concentration of this film was 10^{18} cm^{-3}. The band edge emission is broadened by the heavy Mg level when compared to the undoped GaN CL shown in Fig. 2A. Emission from Cr^{3+} in the sapphire substrate is observed at 694 nm due to strong UV excitation of the substrate from the p-type film.

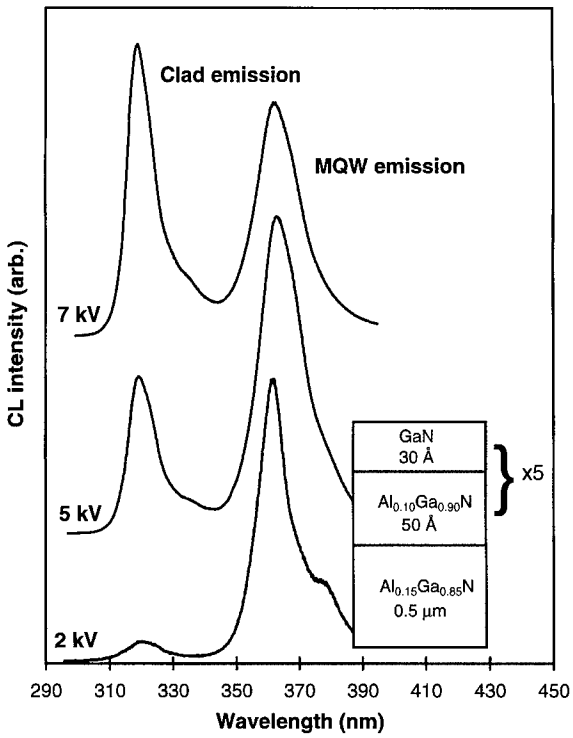

Fig. 4. In-situ CL spectrum from a multiple quantum well sample deposited on to a $Al_{0.15}$ $Ga_{0.85}N$ clad layer on sapphire. The CL intensity is plotted on a linear scale. The MQW region consisted of 5 repeats 50 Å of $Al_{0.10}$ $Ga_{0.90}N$ barriers and 30 Å GaN wells. Emission is clearly observed from the quantum well region around 358 nm and from the clad layer at 320 nm. The 10% barrier level is weakly observed around 335 nm. The CL spectra are taken at three different electron voltages to demonstrate CL's ability to depth profile a structure. At higher beam voltages, the lower clad emission becomes dominant.

$Ga_{0.85}N$ clad layer on sapphire. The CL intensity is plotted on a linear scale. The MQW region consisted of 5 repeats of 50 Å $Al_{0.10}$ $Ga_{0.90}$ N barriers and 30 Å GaN wells. Emission from the quantum well region is clearly observed at 358 nm and from the clad layer at 320 nm. The 10% barrier level is weakly observed around 335 nm. Emission has been observed from Al_x Ga_{1-x} N for $x = 0$–1. CL is extremely useful for scanning high Al content films where deep UV lasers are costly for PL measurements. The CL spectra are shown at three different electron beam voltages to demonstrate CL's ability to depth profile a structure. At higher beam voltages, the lower clad emission becomes dominant due to the increased penetration of the electron beam and the thickness of the clad layer.

Measurement of the substrate temperature for GaN growth is particularly difficult due to the transparency of sapphire from the IR to the UV. This is compounded by the lack of any well-defined change in the RHEED pattern after oxide removal for calibration of an optical pyrometer. Fig. 5 shows the CL spectrum from a 1 μm thick layer of GaN on sapphire as a function of growth temperature. These scans were taken in the growth chamber with the RHEED electron gun at 10 keV. The CL intensity is plotted on a linear scale. The figure shows the band edge peak as the substrate temperature is increased. The temperature is determined from the known shift in the energy gap with temperature [10, 11]. Considerable broadening of the peak is observed at higher temperatures, but the intensity of the CL emission dropped only a factor of three from room temperature to 500°C. Above this temperature, the UV peak position was not determined due to overlapping emission from the substrate heater filaments. Improvements minimizing this interference will allow measurement of the absolute substrate temperature during the growth at 800°C.

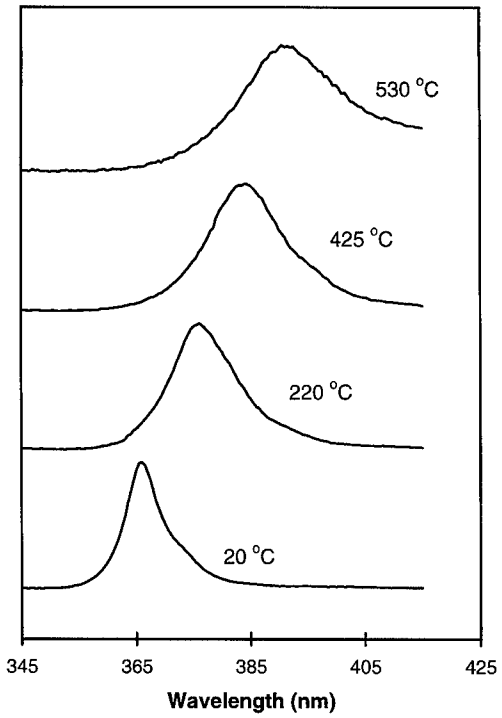

Fig. 5. In-situ CL spectrum from 1 μm of GaN on sapphire as a function of growth temperature. The CL intensity is plotted on a linear scale. The temperature given is based on the band edge position versus temperature from Refs. [9, 10]. Measurement of the temperature during growth at 800°C should be possible with an improved substrate holder to reduce light from the heater filaments.

4. Summary

Reliable analysis techniques are necessary for the continued advancement of group III nitride technology. In-situ CL is presented as a valuable technique for determining film composition, optical quality, doping levels, and temperature of MBE-grown nitride films. It is a straightforward technique which utilizes existing RHEED and/or Auger equipment for a new purpose, and can be readily retrofitted to older MBE systems.

Acknowledgements

This work was supported in part by NASA Contract NAS5-38054 (D.A. Mott), BMDO Contract NOOO14-96-C-0251, monitored by C. Wood ONR, and BMDO Contract DASG60-96-C-0120, monitored by M. McCurry, Army Space Command.

References

[1] J.M. Van Hove, G. Carpenter, E. Nelson, A. Wowchak and P.P Chow, J. Crystal Growth 164 (1996) 154.
[2] B.G. Yacobi and D.B. Holt, J. Appl. Phys. 59 (1986) R1.
[3] C.M. Rouleau and R. M Park, Appl. Phys. Lett. 60 (1992) 2723.
[4] SVT Associates Model LMCL3, Patent disclosure filed.
[5] J.M. Van Hove, G.J. Cosimini, E. Nelson, A.M. Wowchak and P. P Chow, J. Crystal Growth 150 (1995) 908.
[6] K. Doverspike, L.B. Rowland, D.K. Gaskill and J.A. Freitas, Jr., J. Electron. Mater. 24 (1995) 269.
[7] J. Neugebauer and C.G. Van de Walle, Appl. Phys. Lett. 69 (1996) 503.
[8] I. Akasaki, H. Amano, M. Kito and K. Hiramatsu, J. Lumin. 48/49 (1991) 666.
[9] S. Yoshida, S. Misawa and S. Gonda, J. Appl. Phys. 53 (1982) 6844.
[10] J.I. Pankove, J.E. Berkeyheiser, H.P. Maruska and J. Wittke, Solid State Commun. 8 (1970) 1051.
[11] B. Monemar, Phys. Rev. B 10 (1974) 676.

ELSEVIER

Journal of Crystal Growth 175/176 (1997) 84–88

JOURNAL OF CRYSTAL GROWTH

Er doping of III-nitrides during growth by metalorganic molecular beam epitaxy

J.D. MacKenzie[a,*], C.R. Abernathy[a], S.J. Pearton[a], U. Hömmerich[b], X. Wu[b], R.N. Schwartz[c], R.G. Wilson[c], J.M. Zavada[d]

[a] *Department of Materials Science and Engineering, University of Florida, Gainesville, Florida 32611, USA*
[b] *Department of Physics Research Center for Optical Physics, Hampton University, Hampton, Virginia 23668, USA*
[c] *Hughes Research Laboratory, Malibu, California 90265, USA*
[d] *US Army Research Office, Research Triangle Park, North Carolina 27709, USA*

Abstract

Solid source Er doping of AlN and GaN during growth by plasma-assisted metalorganic molecular beam epitaxy (MOMBE) with an Er effusion source has resulted in AlN : Er and GaN : Er exhibiting room-temperature 1.54 μm photoluminescence (PL). The luminescence detected in the AlN : Er samples was orders of magnitude greater in intensity than that from ion-implanted material and represents the first demonstration of strong emission from rare-earth doped, epitaxial III-nitrides doped during growth. The effects of growth temperature on Er incorporation and segregation behavior have also been examined. PL studies, including room temperature and thermal quenching experiments have been conducted showing a reduction in PL intensity of approximately a factor of two between 15 K and room temperature for strongly luminescent AlN : Er. Preliminary results from GaN : Er indicated that thermal quenching is considerably greater in this material than in AlN : Er.

PACS: 78.55.Cr; 71.55.Eq; 71.20.Eh; 71.20.Nr

1. Introduction

Optical communications systems based on a 1.54 μm signal carrier exploit the intrinsic attenuation loss minima of silica fibers to achieve efficient, long distance signal transmission. High gain lasers and detectors based on the InGaAsP system were developed in order to take advantage of these optimum wavelength regimes. However, systems based on narrow-gap InGaAsP active components suffer from poor wavelength temperature stability, and the need for inefficient and expensive repeater stations based on electro-optical detection and regeneration. Optical amplification systems achieving gain through stimulated emission from optically pumped rare-earth ions have also been developed. These systems, known as rare-earth doped fiber

* Corresponding author.

0022-0248/97/$17.00 Copyright © 1997 Elsevier Science B.V. All rights reserved
PII S0022-0248(96)00925-6

amplifiers, do not suffer from the temperature stability problems of semiconductor systems based on band-edge emission. However, the extensive pumping systems required in these systems can be expensive and large. These drawbacks stimulated the development of optoelectronic components based on Er doping of Si [1, 2] and III–V materials [3–5].

Ideally, Er^{3+} transitions near 1.54 μm could be exploited in wide bandgap semiconductor optoelectronics. Since the optical transitions of interest are decoupled from valence interactions, the emission from the rare earths would not be subject to the shifts in performance observed with conventional, temperature-sensitive optoelectronics. Trends observed for Er incorporation in other semiconductor materials have indicated a significant increase in PL with increasing band gap [6]. Concurrent with this trend, it has also been suggested that the electronic environment provided by more ionic semiconductor hosts enhances the inner 4f shell Er^{3+} transitions responsible for the desired optical emission [7]. Upon co-implantation of Er and O, Fl and other species into Si, substantial increases in 1.54 μm PL have been reported [8, 9]. It has been theorized that the presence of ionic species alter the local field environment of the Er^{3+} ions enhancing the optical activity. Expanding on these premises, wide band-gap, ionic compound semiconductors including II–VI materials, as well as the III-nitrides show significant promise as hosts for rare-earth dopants. The structural and thermal stability of GaN and AlN make them particularly attractive for reliable, long service-life applications.

Luminescence from Er implanted into the nitrides was first observed by Wilson et al. [10]. 1.54 μm PL attributed to transitions between Er^{3+} $^4I_{13/2}$ and $^4I_{15/2}$ levels was observed in ion implanted GaN and AlN. However, Er luminescence from the AlN was seen only at low temperatures. Developing on this work, we have demonstrated solid source Er doping of AlN and GaN during growth by metalorganic molecular beam epitaxy (MOMBE). Doping during growth can be a more flexible technique than ion implantation for many growth applications due to the absence of ion damage, unlimited layer thickness, and better doping profile control.

2. Experimental procedure

Films were grown by MOMBE in an INTEVAC Gas Source Gen II on In-mounted (0 0 0 1) Al_2O_3 and semi-insulating GaAs. The films were preceded by a low temperature AlN buffer (T_g 425°C). Dimethylethylamine alane (DMEAA) and triethyl gallium (TEGa) provided the group III fluxes. Reactive nitrogen for the growth of AlN was provided by a Wavemat MPDR 610 electron cyclotron resonance (ECR) plasma source with an Al_2O_3 plasma chamber. Further details of the AlN growth technique employed here have been presented previously [11]. An SVT RF plasma source with a pBN chamber was used to deposit the GaN films. A shuttered effusion oven charged with 4 N Er was used for doping. Er incorporation was profiled by secondary ion mass spectrometry (SIMS). Al, N, and O levels were also monitored. Room- and low-temperature photoluminescence was used to evaluate 1.54 μm luminescence. For the AlN : Er thermal quenching measurements, Er^{3+} PL was excited using the 488 nm line of an Ar ion laser and measured with a liquid-nitrogen cooled Ge detector. An optical parametric oscillator pumped by a Q-switched Nd : YAG laser was the excitation source used for the GaN : Er PL experiments. A He refrigerator capable of reaching temperatures as low as 12 K was used to cool the sample. The surface morphology of the nitride films was characterized by scanning electron microscopy (SEM) using a JEOL 35CF. Crystallinity was quantified by 5 crystal high-resolution X-ray diffraction with a Philips MRD system. Surface composition was analyzed with Perkin-Elmer Auger electron spectroscopy (AES) apparatus.

3. Results and discussion

Doping concentrations from 3×10^{17} to 2×10^{21} cm^{-3}, as determined by SIMS, were achieved for cell temperatures ranging from 955°C to 1343°C. An Arrhenius-like thermal activation energy of approximately 4.0 eV was fit to the observed incorporation behavior which is comparable to the corresponding $\sim$ 3.0 eV activation energy for the vapor

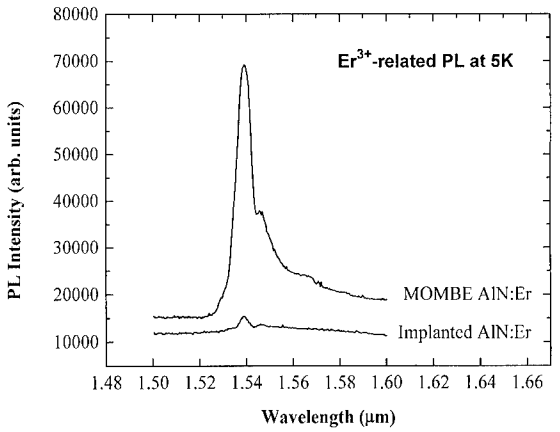

Fig. 1. Comparison of 5 K Photoluminescence spectra of AlN : Er samples doped by implantation and during growth.

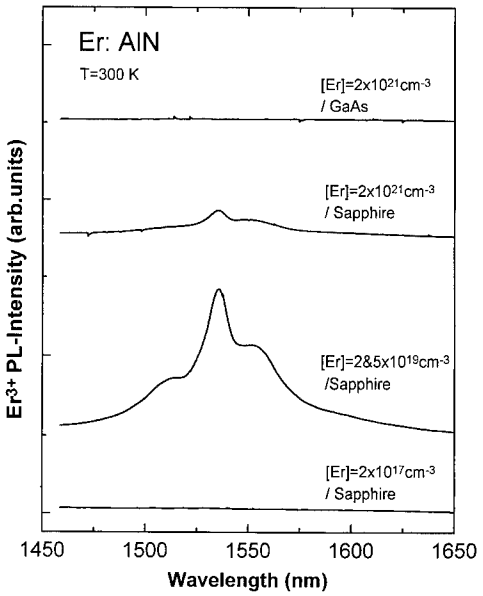

Fig. 2. Room temperature photoluminescence spectra from AlN : Er films grown on GaAs and Al_2O_3 at several Er compositions.

pressure of Er in this temperature range. Strong 1.54 μm Er^{3+} photoluminescence was observed in AlN : Er doped to levels $\geqslant 3\times10^{18}$ cm^{-3}. The 5 K PL intensities ($\lambda_{pump} = 458$ nm) from these films were nearly two orders of magnitude greater than those observed in AlN implanted with Er to similar levels (Fig. 1). AlN : Er films deposited on GaAs showed considerably weaker PL at low temperatures than AlN : Er grown on Al_2O_3. No 1.54 μm signal was detected at room temperature for AlN : Er/GaAs (Fig. 2). AlN : Er/Al_2O_3 samples doped $2–5\times10^{19}$ cm^{-3} showed considerably stronger 1.54 μm PL signal than samples doped 2×10^{21} cm^{-3} in Fig. 2. However, the actual thickness of the Er-doped layer was approximately a factor of four less for the more heavily doped sample. Adjusting for this, the normalized PL intensity is similar for both doping levels suggesting that the luminescence saturates at high doping levels. High resolution X-ray diffraction rocking curves for the AlN : Er on GaAs were very diffuse while considerably stronger peaks with half-widths of 6100′ and 6800′ were observed for samples grown on sapphire with [Er] of 3×10^{17} and 2×10^{21} cm^{-3}, respectively. This indicates that AlN structural quality has a significant effect on the optical activity of Er^{3+} and that increasing [Er] adversely affects crystallinity. Oxygen backgrounds of $\sim 2\times10^{20}$ cm^{-3} were observed in all AlN samples. Sputtering of oxygen from the alumina ECR plasma cup is believed to be the source of this oxygen. A number of researchers have observed an increase in luminescence attributed to local ionic ligand field effects induced by O and other electronegative species in Si [12, 13] and III–V materials[14]. 1.54 μm emission, though somewhat weaker, was observed for the first time in solid source-doped GaN : Er ($T_{Er} \sim 1110$°C) deposited using the BN-chamber RF plasma source. The line shape of the 1.54 μm emission at 13 K shown in Fig. 3 is similar to that of AlN : Er grown by MOMBE.

Thermal quenching experiments indicated that 488 nm-pumped Er^{3+}-related PL quenches by approximately a factor of two between 15 and 300 K for AlN : Er doped $2–5\times10^{19}$ cm^{-3}. The quenching behavior of MOMBE-derived AlN : Er compares favorably with that of other semiconductor hosts (Fig. 4). Dramatically, less quenching was observed for AlN : Er than has been reported for Si or GaAs [6]. Thermal quenching of Er^{3+} has been attributed to various quenching mechanisms

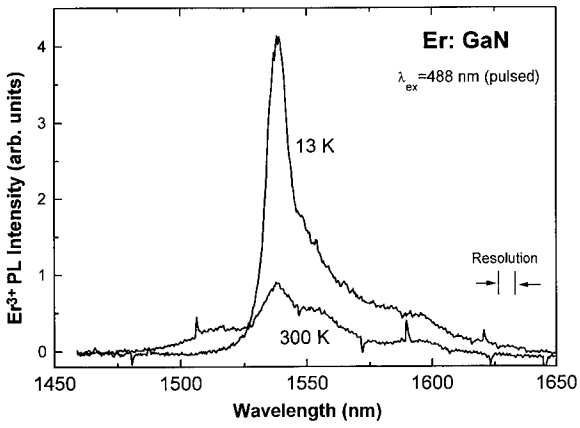

Fig. 3. Room temperature and 13 K photoluminescence from solid-source Er doped GaN.

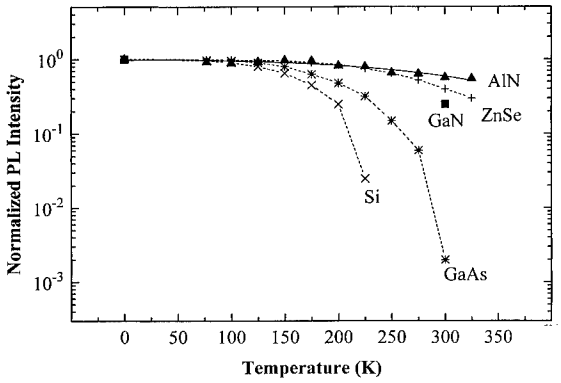

Fig. 4. PL thermal quenching of Er^{3+}-related PL for solid-source doped AlN : Er compared to Er implanted Si, GaAs, and ZnSe [6].

including de-excitation by delocalization and loss of excited state electrons to the conduction band and cooperative upconversion [8, 15]. Further experimentation is required to elucidate this effect. Preliminary pulsed excitation results showed a more substantial reduction in PL intensity from GaN : Er at higher temperatures.

Rounded surface features, observed on AlN : Er by SEM, increased in size from $\sim$ 1–2 μm (T_{cell} 955°C) to $\sim$ 3–5 μm (T_{cell} 1343°C). Fig. 4 compares the surfaces of undoped AlN, AlN : Er

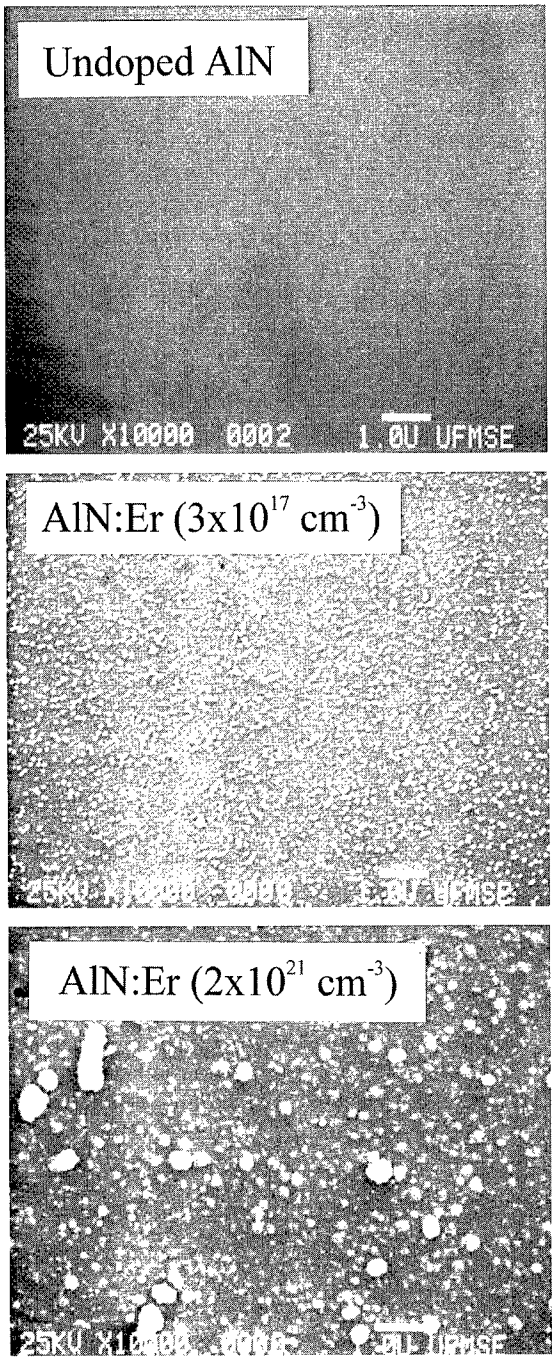

Fig. 5. Scanning electron micrographs (1000X) of AlN : (from top to bottom) undoped, [Er] $\sim 3\times10^{17}\,cm^{-3}$, and [Er] $\sim 2\times10^{21}\,cm^{-3}$.

(3×10^{17} cm^{-3}, and AlN : Er (2×10^{21} cm^{-3}). Auger electron analysis indicates that the surface features present in these SEM micrographs are not Er droplets. This is also supported by the absence of an [Er] surface spike during dynamic SIMS profiling. The effect of growth temperature on the sticking coefficient of Er was also investigated with SIMS. A film stack consisting of three layers of AlN : Er, each $\sim$ 1000 Å, grown at 800°C, 600°C, and 500°C, and separated by 500 Å of undoped AlN was deposited on Al_2O_3. The stack was capped with $\sim$ 1000 Å of undoped AlN (see Fig. 5). A constant Er cell temperature of 1090°C was maintained for all three layers. The Er concentration fell by nearly a factor of 2 as the growth temperature was reduced from 800°C to 500°C. This behavior suggests that solubility effects may limit the incorporation efficiency. The absence of [Er] accumulation at the surface or other profile features indicates that Er does not segregate strongly during growth.

In summary, AlN : Er and GaN : Er films exhibiting room temperature PL have been grown by MOMBE. Low-temperature PL intensity was more than two orders of magnitude higher in AlN : Er/Al_2O_3 films than in implanted AlN. Low temperature 1.54 μm PL was less intense for AlN : Er samples grown on GaAs than for those grown on Al_2O_3, indicating that structural quality has a considerable effect on optical activity. Er appears to impact structural quality as indicated by a coarsening in surface features and a degradation in crystallinity with increasing [Er]. A slight reduction in incorporation efficiency was observed at lower growth temperatures. Thermal quenching experiments showed a $\sim$ 50% reduction in PL signal from AlN : Er between 15 and 300 K demonstrating a substantially higher-temperature limit than conventional III–V materials [2, 16] and Si [2]. These results demonstrate the potential for rare-earth luminescence in group III nitrides grown by MOMBE.

Acknowledgements

This work has been supported in part by ARO-ASSERT Grant DAAH04-95-1-0196. We would also like to acknowledge the support of the staff of the MICROFABRITECH facility at the University of Florida.

References

[1] F.Y.G. Ren, J. Michel, Q. Sun-paduano, B. Zheng, H. Kitagawa, D.C. Jacobson, J.M. Poate and L.C. Kimmerling, MRS Symp. Proc. 301 (1993) 125.
[2] G. Franzo, F. Priolo, S. Coffa, A. Polman and A. Carnera, Nucl. Instrum. Methods B 96 (1995) 374.
[3] J. Nakata, M. Taniguchi and K. Takahei, Appl. Phys. Lett. 61 (1992) 2665.
[4] A.J. Neuhalfen and B.W. Wessels, Appl. Phys. Lett. 59 (1991) 2317.
[5] J.M. Redwing, T.F. Kuech, D.C. Jordon, B.A. Vararstra and S.S. Lau, J. Appl. Phys. 76 (1994) 1585.
[6] P.N. Favennec, H. L'Haridon, D. Moutonnet and Y.L. Guillo, Electron. Lett. 25 (1989) 718.
[7] J.M. Zavada and Dahua Zhang, Solid State Electron. 38 (1995) 1285.
[8] S. Coffa, F. Priolo, G. Franzo, V. Bellani, A. Carnera and C. Spinella, Phys. Rev. B 48 (1994) 11782.
[9] J. Michel, J.L. Benton, R.I. Ferranta, D.C. Jacobson, D.J. Eaglesham, E.A. Fitzgerald, Y.H. Xie, J.M. Poate and L.C. Kimmerling, J. Appl. Phys. 70 (1991) 2672.
[10] R.G. Wilson, R.N. Schwartz, C.R. Abernathy, S.J. Pearton, N. Newman, M. Rubin, T. Fu and J.M. Zavada, Appl. Phys. Lett. 65 (1994) 992.
[11] J.D. MacKenzie, C.R. Abernathy, S.J. Pearton, V. Krishnamoorthy, S. Bharatan, K.S. Jones and R.G. Wilson, Appl. Phys. Lett. 67 (1995) 253.
[12] P.N. Favennec, H. L'Haridon, D. Moutonnet, M. Salvi and M. Gauneau, Jpn. J. Appl. Phys. 29 (1990) L524.
[13] J. Michel, J.L. Benton, R.F. Ferrante, D.C. Jacobson, D.J. Eaglesham, E.A. Fitzgerald, Y. Xie, J.M. Poate and L.C. Kimmerling, J. Appl. Phys. 70 (1991) 2672.
[14] J.E. Colon, D.W. Elsaesser, Y.K. Yeo, R.L. Hengehold and G.S. Pomrenke, MRS Symp. Proc. 301 (1993) 169.
[15] G.N. van den Hoven, PhD Thesis, University of Utrecht, The Netherlands (1996).
[16] A.J. Neuhalfen and B. Wessels, Appl. Phys. Lett. 59 (1991) 2317.

ELSEVIER

Journal of Crystal Growth 175/176 (1997) 89–93

JOURNAL OF CRYSTAL GROWTH

Growth kinetics of GaN grown by gas-source molecular beam epitaxy

J.R. Jenny[a,*], R. Kaspi[b], K.R. Evans[a,1]

[a] *Wright Laboratory (WL/AADP), Wright-Patterson Air Force Base, Ohio 45433-7323, USA*
[b] *University Research Center, Wright State University, Dayton, Ohio 45435, USA*

Abstract

We report on the incorporation kinetics of gallium during gas-source molecular beam epitaxy (GSMBE) of GaN using elemental Ga and NH_3 gas as source materials. Desorption mass spectrometry (DMS) is used to perform in situ quantitative measurements of GaN formation, Ga desorption and Ga surface accumulation during growth. The rate of formation of GaN is reported as a function of incident Ga flux (0.1–0.75 ML/s) and incident NH_3 flux ($1–300 \times 10^{-7}$ Torr beam-equivalent pressure) at a constant growth temperature of 725°C. Three distinct growth regimes are observed: (1) GaN is formed where all of the incident Ga flux is consumed, (2) part of the incident Ga is consumed to form GaN while the excess is desorbed from the surface, and (3) GaN formation coexists with desorption and surface accumulation of Ga. It is generally observed that the Ga surface accumulation is inhibited by increasing the rate of incidence of NH_3 and/or by decreasing the rate of incidence of Ga at this temperature. In addition, the order of the reaction between Ga and NH_3 is determined to be unity, supporting the validity of the $Ga + NH_3 \rightarrow GaN + \frac{3}{2} H_2$ reaction.

PACS: 68.55.Bd; 68.10.Jy

Keywords: Growth kinetics; GaN; GSMBE; NH_3

1. Introduction

Due to their wide, direct band gap [1], a large number of potential applications for semiconductor heterostructures containing high-quality III-N layers have been identified [2–4]. Despite the large effort expended in recent years, many fundamental growth-related problems remain unsolved. The kinetics of GaN formation, for example, is not yet well understood. It is imperative, however, that growth conditions during epitaxy be well-identified and reproducible in order for efficient growth optimization to take place. To date, only a few studies have addressed III-N growth kinetics [5, 6] using gas-source molecular beam epitaxy (GSMBE). It

* Corresponding author.
[1] Present address: Semiconductor Laser International, 421 E. Main St. Endicott, New York 13760, USA.

0022-0248/97/$17.00 Copyright © 1997 Elsevier Science B.V. All rights reserved
PII S0022-0248(96)01020-2

was observed that when Ga reacts with ammonia (NH_3) to form GaN, either Ga desorption or Ga surface accumulation or both are likely to occur, and that this results in incorporation ratio (defined as the portion of the Ga flux that incorporates into the film as GaN) considerably less than unity. In this paper, we use GSMBE to deposit GaN layers while we systematically examine the Ga incorporation ratio σ(Ga) within a large parameter space defined by the incident NH_3 and elemental Ga fluxes at a fixed growth temperature. We employ desorption mass spectrometry (DMS) as an in situ tool to delineate different growth regimes and measure σ(Ga) under a variety of incident fluxes. This is accomplished by using DMS to observe the onset of the accumulating component of the incident Ga flux, and to quantify both the desorbing and accumulating component of the incident Ga flux in order to extract the rate of GaN formation.

2. Experimental procedure

GaN layers were deposited on 2 in diameter sapphire wafers oriented in the (0 0 0 1) direction in a Varian-360 MBE chamber modified to accommodate NH_3 gas. Elemental Ga was evaporated using a conventional effusion cell. The substrates were In-bonded onto the Mo block and the temperature was monitored by an optical pyrometer mounted on an effusion cell port. The growth chamber was evacuated using a 2400 l/s oil diffusion pump equipped with a liquid-nitrogen baffle which is optically opaque. Incident Ga fluxes were calibrated using reflection high-energy electron diffraction (RHEED) during GaAs growth and converted to units of ML/s of GaN growth. The incident NH_3 fluxes were varied manually through a leak valve located adjacent to the chamber, and measured in situ using a nude ion gauge which is rotated into position.

Ga desorption was monitored by a quadrupole mass spectrometer (QMS) which is mounted onto the central port on the source flange, in direct line-of-sight of the wafer. The line-of-sight of the QMS is limited to approximately the central half of the wafer area, as previously described elsewhere [7]. The housing containing the QMS was differentially pumped using a 60 l/s turbomolecular pump. For Ga desorption measurements, the QMS was tuned to mass/charge $=69$ amu/e, and was operated in a constant mass mode while data were transferred to a personal computer for real time and post growth analysis.

The incident Ga flux J_i(Ga) was varied between 0.1 and 0.86 ML/s, while the incident NH_3 flux $J_i(NH_3)$ was varied between 1×10^{-7} and 3×10^{-5} Torr beam-equivalent pressure (BEP). The substrate temperature was held constant at 725°C.

Sapphire substrates were initially outgassed at $T=725$°C, and were nitridized with $J_i(NH_3)=5\times10^{-5}$ Torr BEP for 5 min. Approximately, 100 monolayers of AlN were deposited in each case as a buffer between the GaN film and the substrate. A thick GaN was then deposited as a template for desorption experiments. The GaN film surfaces during experiments exhibited sharp streaky RHEED patterns with well-defined half order reconstruction lines, indicative of a relatively smooth surface.

3. Measurement of GaN formation rates

When Ga and NH_3 are coincident on the substrate surface and σ(Ga) is near unity, no significant desorption signal is expected to be measured by the QMS. However, when σ(Ga) <1 then a QMS Ga signal is expected. Moreover, when growth with σ(Ga) proceeds without significant Ga surface accumulation, the QMS Ga signal is expected to be closely associated with the opening and closing of the Ga shutter. This is because the GaN surface is stable at $T=725$°C, and Ga desorption from the surface is not expected after the incident J_i(Ga) is terminated and the surface quickly reaches its equilibrium surface stoichiometry. For example, when GaN growth using J_i(Ga) $=0.1$ ML/s at $T=725$°C is terminated, the QMS Ga signal is observed to decay rapidly to zero, exhibiting a single time constant as dictated by first-order surface kinetics. Data marked 'b' through 'g' in Fig. 1 demonstrate this as $J_i(NH_3)$ varies from 2.3×10^{-7} to 2.04×10^{-6} Torr, respectively.

In contrast to this, Ga accumulation during growth results in Ga desorption, J_d(Ga), which

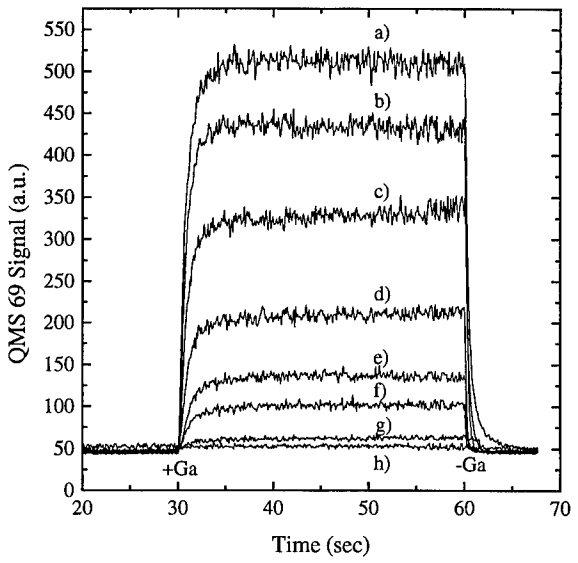

Fig. 1. Ga desorption (at 725°C) versus time (J_i(Ga) = 0.1 ML/s) for the following $J_i(NH_3)$ ($\times 10^{-7}$ Torr, BEP): (a) 0, (b) 2.3, (c) 4.9, (d) 8.4, (e) 11.0, (f) 14.0, (g) 20.4, and (h) 81.6.

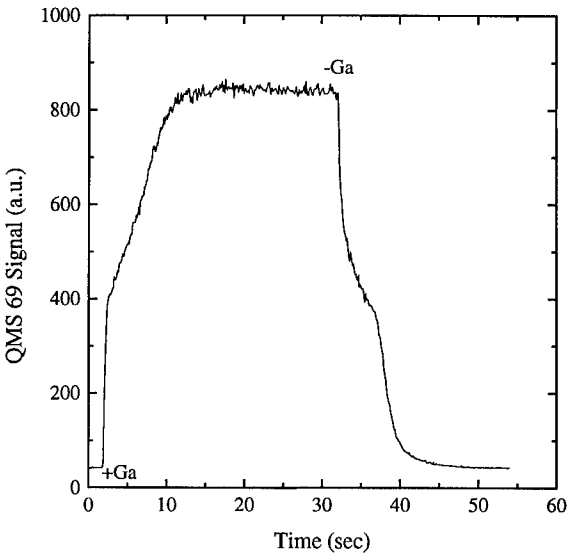

Fig. 2. Ga desorption (725°C, J_i(Ga) = 0.57 ML/s, and $J_i(NH_3)$ = 0 Torr BEP)versus time in a island growth regime. The difference in the curve shape from Fig. 1 is indicative of Ga accumulation on the GaN surface.

does not rapidly decay to zero when GaN growth is terminated. This is because Ga pools which form on the surface are not stable at $T = 725$°C, and will continue to lose Ga through desorption until they are depleted. An example of this is shown in Fig. 2 where J_i(Ga) of 0.57 ML/s was directed onto the GaN surface without an accompanying ammonia flux. It is clearly observed that the rise and decay of QMS 69 signal is not described by a single exponential, but rather exhibit an additional feature as a result of surface Ga accumulation. As expected, Ga desorption persists even after the Ga shutter is closed, for nearly 20 s in the case of data shown in Fig. 2, until the accumulated Ga is depleted. The main utility of observing this feature is that the growth conditions required to cause the onset of Ga accumulation can be easily determined in this manner. Note that even small amounts of Ga accumulation during deposition becomes evident as the decay signal is mathematically analyzed. Another utility of this feature is that it yields a quantitative measure of the amount of Ga accumulated during growth. This is achieved by quantifying excess Ga desorption after the Ga shutter is closed by the proper calibration of the QMS Ga signal. QMS Ga signal calibration is easily achieved by desorbing a known incident Ga flux in its entirety at an elevated temperature where J_i(Ga) = J_d(Ga). An example of this is shown in data marked 'a' in Fig. 1.

The rate of formation of GaN at steady state, thus σ(Ga), can be obtained in one of the two methods. In the case when no Ga accumulation occurs, σ(Ga) is given directly by $1 - J_d(Ga)/J_i(Ga)$. When Ga accumulation occurs, σ(Ga) can be computed by quantifying the Ga accumulation by extracting the rate of Ga accumulation based on the duration of the Ga shutter opening, and determining an effective J_i(Ga) with which to calculate σ(Ga).

Note that the amount of Ga accumulation during growth is occasionally observed to reach a constant value and coexist with GaN formation. Data shown in Fig. 2, for example, indicate that the Ga desorption rate is constant after the initial rise, and we observe that the amount of excess Ga desorption after growth is terminated is often independent of the duration of film growth. Despite the fact that

growth with Ga accumulation is of limited value to the grower, the extraction of σ(Ga) at these conditions can give additional insight into GaN growth kinetics.

4. Results and discussion

Investigation of desorption spectra and σ(Ga) measurements were used to identify and delineate the three distinct growth regimes: (1) GaN formation only, (2) GaN formation and Ga desorption, and (3) GaN formation, Ga desorption, and Ga accumulation. Measured values of σ(Ga) as a function of J_i(Ga) and $J_i(NH_3)$ are shown in Fig. 3, which depicts an isothermal growth phase diagram at $T = 725°C$.

It was observed that for J_i(Ga) $< \sim 0.25$ ML/s, σ(Ga) increased with increasing $J_i(NH_3)$, and that the entire 0–1 range of σ(Ga) could be achieved without Ga accumulation at $T = 725°C$. For example, for J_i(Ga) = 0.23 ML/s, σ(Ga) was observed to increase from 0.1 to ~ 1 as $J_i(NH_3)$ was increased from 2.3×10^{-7} to 2.1×10^{-6} Torr BEP. In this range, the Ga desorption flux observed

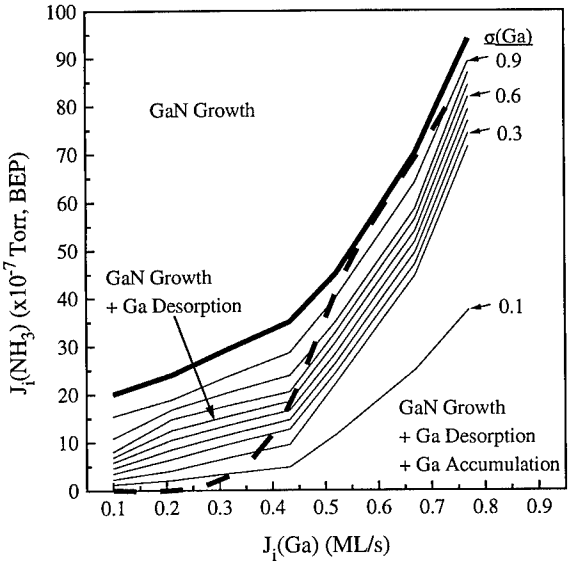

Fig. 3. Plot of Ga incorporation ratio, σ(Ga), contours as a function of Ga and NH_3 fluxes. Labeled in the figure are the three primary regimes for Ga adatoms.

at steady state, J_d(Ga), is equivalent to J_i(Ga) (1–σ(Ga)). For $J_i(NH_3)$ above 2.1×10^{-6}, J_d(Ga) is zero and growth takes place in a regime where all Ga forms GaN (labeled 'GaN Growth').

For $\sim 0.25 < J_i$(Ga) $< \sim 0.55$ ML/s, it was observed that Ga accumulation occurs alongside GaN growth and Ga desorption at low $J_i(NH_3)$, but is suppressed at intermediate values of $J_i(NH_3)$. For example, for J_i(Ga) $< \sim 0.49$ ML/s, Ga accumulation was observed using $J_i(NH_3) \sim 1.6 \times 10^{-6}$ Torr BEP, but was eliminated for $J_i(NH_3) \sim 2.1 \times 10^{-6}$ Torr BEP.

For J_i(Ga) $> \sim 0.55$ ML/s, it was observed that large ammonia fluxes are required to suppress Ga accumulation, and that the minimum $J_i(NH_3)$ values required for suppression of Ga accumulation are also the minimum values to achieve σ(Ga) ~ 1.

These observations suggest a surface kinetic equilibrium driven by the surface lifetime of Ga adatoms. Their average surface lifetime at a given temperature is reduced by the availability of NH_3 for reaction, and by the presence of Ga pools which act as Ga adatom sinks. The growth phase diagram can be interpreted as the competition between the three processes which consume the Ga adatom (reaction, desorption, accumulation). In the 'GaN growth' regime, reaction rate with ammonia is dominant in reducing the surface lifetime over others. In the 'GaN growth + Ga desorption' regime the reduced availability of reactive NH_3 results in a larger Ga adatom surface lifetime whereby a portion of the Ga adatom population can thermally desorb. In the 'GaN growth + Ga desorption + Ga accumulation' regime, the Ga surface lifetimes are primarily limited by Ga accumulation as inter-island distances become smaller than the average surface diffusion lengths. It is likely that much of the Ga desorption flux in this regime originates from accumulated Ga on the surface.

The formation of GaN is thought to proceed according to the following relationship:

$$Ga + NH_3 \rightarrow GaN + \tfrac{3}{2}H_2 \quad (1)$$

and the kinetic equation is given by

$$d(GaN)/dt = (NH_3)(Ga) \quad (2)$$

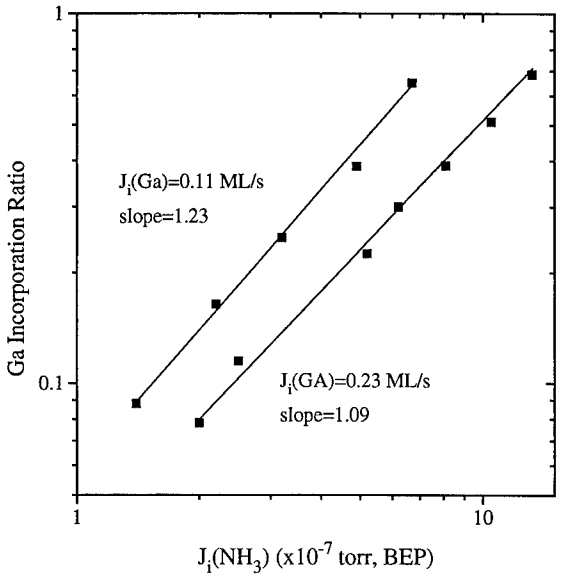

Fig. 4. Law of mass action for GaN formation at 725°C. Slopes near unity indicate that Eq. (1) is representative of processes in effect at interface (e.g. in low Ga flux regime).

and if, Δt = constant = 30 s and (Ga) = constant,

$$(\mathrm{GaN}) \propto (\sigma(\mathrm{Ga})) \propto (\mathrm{NH_3})^n, \quad n = 1. \tag{3}$$

Eq. (3) implies that when $J_i(\mathrm{Ga})$ is constant, the rate of GaN formation, $\sigma(\mathrm{Ga})$, is proportional to $J_i(\mathrm{NH_3})$ for the above chemical reaction to be valid. In Fig. 4, $\sigma(\mathrm{Ga})$ is shown as a function of $J_i(\mathrm{NH_3}) = 0.11$ and 0.23 ML/s. In the figure, both slopes are near unity which indicates that Eq. (1) is a correct description of the reaction at these Ga fluxes.

5. Conclusions

A broad study of the effect of Ga and NH_3 on the incorporation of Ga into GaN films grown by MBE was conducted. An isothermal plot was produced which sheds light upon the nature of the incorporation of Ga in the regime of NH_3 fluxes from 1 to 100×10^{-7} Torr and for Ga fluxes from 0.11 to 0.86 ML/s. The plot can be broken into three regimes. The first is where there exists only GaN growth. This occurs at all Ga fluxes studied, but only at the higher NH_3 fluxes. Second, there is a region where competition for the Ga adatom exists between the formation of GaN and the Ga desorption. This occurs at low Ga and low NH_3 fluxes. Finally, at high Ga and low NH_3 fluxes, a competition between Ga accumulation, Ga desorption, and GaN formation occurs. Due to the heavy saturation of Ga in the form of Ga pools, this competition is not desired for the growth of device quality GaN layers.[8]

Acknowledgements

The authors thank C.R. Jones and C. Litton for technical support. R.K. was supported by US Air Force Contract #F33615-95-C-1765. J.R.J. was supported by a National Research Council fellowship. This work was partially supported by the US Air Force Office of Scientific Research (AFOSR).

References

[1] M.E. Lin, S. Strite and H. Morkoç, in: The Encyclopedia of Advanced Materials, Eds. D. Bloor et al. (Pergamon, Oxford, 1994) pp. 79–86.
[2] S. Strite and H. Morkoç, J. Vac. Sci. Technol. B 10 (1992) 1237.
[3] H. Morkoç et al., J. Appl. Phys. Rev. 76 (1994) 1363.
[4] R.F. Davis, Proc. IEEE 79 (1991) 702.
[5] C.T. Foxon et al., J. Vac. Sci. Technol. B 14 (1996) 2346.
[6] C.R. Jones, T. Lei, R. Kaspi and K.R. Evans, Proc. 1995 Materials Research Society (Materials Research Society, Boston, MA, 1996).
[7] K.R. Evans, R. Kaspi, C.R. Jones, R.E. Sherriff, V. Jogai and D.C. Reynolds, J. Crystal Growth 127 (1993) 523.
[8] R. Kaspi and K.R. Evans, Proc. 1992 Materials Research Society (Materials Research Society, Boston, MA, 1993).

ELSEVIER

Journal of Crystal Growth 175/176 (1997) 94–99

JOURNAL OF CRYSTAL GROWTH

Stability of surface reconstructions on hexagonal GaN grown by molecular beam epitaxy

P. Hacke[1], G. Feuillet[2], H. Okumura, S. Yoshida

Electrotechnical Laboratory, 1-1-4 Umezono, Tsukuba 305, Japan

Abstract

Control of the reversible transformation between the (2×2) surface reconstruction and the unreconstructed (1×1) surface of hexagonal-phase GaN during growth by molecular beam epitaxy is examined with respect to substrate temperature, gallium flux, nitrogen flow rate, nitrogen plasma cell power and system pressure. The transition is considered to occur at a particular surface stoichiometry which depends on the net arrival rate of reactant species at the growth surface. The (2×2) surface reconstruction as observed by RHEED is stable under a nitrogen environment, whereas the disappearance of the half-order reconstruction occurs during Ga-rich growth yielding a (1×1) RHEED pattern and eventual accumulation of metallic Ga on the growth surface. Based on these observations, a model describing the flux balance at the transition stoichiometry is developed. It is shown to be useful for estimating the concentration of active nitrogen species available, determining the interdependence of growth parameters, and optimizing growth conditions.

PACS: 68.55.Bd; 68.35.Md; 61.14. – x

Keywords: MBE; GaN; RHEED; Reconstructions

1. Introduction

Molecular beam epitaxy (MBE) is a promising method for fabrication of GaN-based heterostructure devices where high purity and precise control of layer thickness are required. Light emitting diodes and transistors using MBE-grown GaN layers have already been reported [1, 2]. While GaN-based devices fabricated by metalorganic vapor-phase epitaxy (MOVPE) have been commercialized [3], MBE technique, despite its potential advantages, has not yet been proven to reproducibly yield high-quality GaN layers for commercial purposes. Encouraging reports of MBE-grown GaN films with high carrier mobility exist [4], but there remain problems such as poor surface morphology and ion damage from plasma cells used to excite molecular nitrogen [5]. Studies to determine the influence of growth parameters such as stoichiometry, temperature, and plasma conditions on the resulting film quality have been reported

[1] E-mail: evehp@etl.go.jp.

[2] On leave from: Commissariat à L'Energie Atomique, Centre de Grenoble, 17 rue des martyrs, F-38054 Grenoble Cedex 9, France. E-mail: feuille@drfmc.ceng.cea.fr.

0022-0248/97/$17.00 Copyright © 1997 Elsevier Science B.V. All rights reserved
PII S0022-0248(96)01174-8

[6–8], but the interdependency of parameters is rather complicated; each parameter is often varied independently to determine the optimum growth conditions.

The (2 × 2) reconstruction has been previously observed and demonstrated to correspond to a stable growth front for achieving good quality epitaxial GaN layers by MBE [9–11]. The appearance of this and other reconstructions on the surface of GaN during various stages of MBE growth, with discussion on their possible origins, has also been documented [10, 11].

We have found the (2 × 2) reconstruction to be a useful reference point for the stoichiometry of the GaN surface during growth by MBE [12, 13]. During growth, the (2 × 2) reconstruction was observed to exist on smooth growth surfaces free of excess Ga. The fading of the (2 × 2) reconstruction as observed by RHEED occurs when the Ga concentration on the surface is increased. When the surface Ga is increased beyond a certain amount, the half-order reconstruction is no longer visible and a (1 × 1) RHEED pattern is obtained. This transition can be induced by increasing the oncoming Ga flux or by decreasing the growth surface temperature, thereby increasing the sticking coefficient of Ga on the surface. It was found that growing in the (2 × 2) reconstruction regime near the transition yields favorable epitaxial film quality [13].

In this work, the transition between the (1 × 1) and the (2 × 2)-reconstructed surface observed by RHEED is used as a reference point for a certain surface stoichiometry to examine the interdependency of substrate temperature, gallium flux, nitrogen flow rate, nitrogen plasma cell power, and system pressure. With this reference point, the observed relationship between the growth parameters is used to model the stoichiometric balance and arrival rates of the reacting species at the surface.

2. Experimental procedure

A standard MBE apparatus equipped with RHEED was used for growth. Reactive nitrogen species were generated by an Astex electron cyclotron resonance (ECR) cell operated at 40 W (unless otherwise stated). No energetic ion removing grid or magnet was used. The flux from the Ga effusion cell arriving at the substrate was calibrated as a function of Ga cell temperature using RHEED oscillations on GaAs in combination with a Bayard–Alpert ion guage. Sample temperature was measured with a thermocouple placed behind the substrate. Growth was carried out homoepitaxially on 3 μm thick GaN layers grown by metalorganic vapor-phase epitaxy (MOVPE) on (0 0 0 1) sapphire to ease nucleation, eliminate interface strain and defects associated with substrate lattice mismatch. Substrates were cleaned sequentially in hot aqua-regia, degreasing solvents, concentrated hydrofluoric acid and finally rinsed in propanol. The substrate was introduced into the chamber and degassed at 400°C for 1 h. The characteristic (2 × 2) RHEED pattern could often be distinguished at this stage if the GaN substrate surface was smooth and properly cleaned. After nitrogen gas was flowed into the chamber, the substrate was heated to the growth temperature. No particular high-temperature thermal cleaning or surface nitridization step was employed prior to beginning of growth. A range of growth conditions was examined as described in detail in the discussion below.

3. Results and discussion

It is found that the transition for the (2 × 2)–(1 × 1) RHEED pattern follows a curve on a plot of substrate temperature vs. Ga flux as in Fig. 1. For a given nitrogen flow rate and plasma cell power, shifting growth conditions slightly to the upper left of a curve (i.e., higher Ga flux or lower substrate temperature) yields a surface that is (1 × 1), whereas to the lower right of a curve (i.e. lower Ga flux or higher substrate temperature) gives the conditions where the (2 × 2) reconstructions can be seen.

The transition from the surface which displays the (2 × 2) reconstruction to that which is unreconstructed is believed to correspond to a unique stoichiometric ratio of atoms on the surface. This stoichiometry is expected to be the same for any combination of growth parameters at which the transition is observed and, therefore, used as a

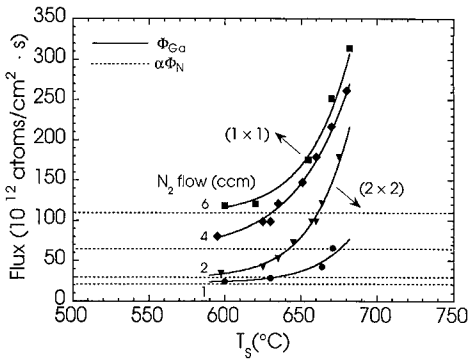

Fig. 1. Plot of Ga flux Φ_{Ga} vs. substrate temperature T_s showing the transition curves between (2 × 2) reconstructed and unreconstructed surfaces for differing nitrogen flow rates. The dotted lines at the base of each curve denote $\alpha\Phi_N$, the nitrogen flux participating in growth.

reference point by which the interdependency of growth parameters can be determined.

During growth, some flux ratio of reactive nitrogen atoms Φ_N to gallium atoms Φ_{Ga} arriving at the surface is necessary to maintain the surface stoichiometry corresponding to the reconstruction transition. In the case of low temperatures where Ga reevaporation from the growth surface is negligible, the ratio is written as $\alpha\Phi_N = \Phi_{Ga}$. For the present analysis, α is assumed to be temperature independent. At higher growth temperatures, it is seen that an exponentially higher amount of oncoming Ga flux is required to maintain the surface at the transition stoichiometry. This extra Ga is required to compensate for the reevaporation of Ga from the surface as the substrate temperature is increased. The transition curves in Fig. 1 are displaced upward with increasing nitrogen flow rate, indicating that the active nitrogen increases with the nitrogen flow rate. It is shown below that this displacement is approximately linear with nitrogen passing through the cell.

The form of the transition curves can be interpreted as a sum of a constant and an exponential,

$$\Phi_{Ga} = \alpha\Phi_N + A \exp(-E_a/kT_s). \quad (1)$$

The desorption of Ga from the growth surface at temperature T_s is a thermally activated process given by the term $A \exp(-E_a/kT_s)$ with activation energy E_a and preexponential A, which is assumed constant. Fitting the data in Fig. 1 with Eq. (1), a typical activation energy function for the Ga reevaporation is $6.5 \times 10^{28} \exp(-2.76/kT_s)$, where Boltzmann's constant k has units eV/K and the uncertainty in the activation energy is about 0.4 eV [13]. The activation energy we observe for the desorption compares reasonably with 2.8 eV, that of evaporation of metallic Ga [14]. This indicates that we are observing the desorption of excess Ga from the GaN surface rather than thermal decomposition of the crystal, which is expected to have a significantly higher activation energy.

By Eq. (1), the number of Ga atoms participating in growth per unit time and surface area, $\Phi_{Ga} - A \exp(-E_a/kT_s)$, is equal to $\alpha\Phi_N$. Therefore, the value of $\alpha\Phi_N$ obtained as a result of the curve-fitting procedure is the nitrogen flux participating in growth if a perfect lattice stoichiometry is assumed. The values of $\alpha\Phi_N$ determined for the different flow rates are shown by the dotted lines at the base of each curve in Fig. 1. Knowing the net deposition rate of species on the sample surface, the GaN growth rate can then be calculated [13].

The ability to describe successfully the data in Fig. 1 in terms of only $\alpha\Phi_N$ and the net Ga flux attests to the validity of the model and the associated assumptions. Within the range of conditions under consideration, it is apparently unnecessary to account for desorption of nitrogen to explain the data.

Although there is some uncertainty in the activation energy E_a due to difficulties in accurate and consistent surface temperature measurement from sample to sample where variations in thermal conduction around the substrate and thermocouple exist, the repeatability of points on a transition curve for a given sample is good to within a variation of about 2°C in Ga cell and substrate temperature indicating that the transition curves of the (2 × 2) reconstruction are a good reference for growth.

When films are grown for extended periods beyond the transition curve where the (2 × 2) reconstruction pattern cannot be seen because of excess Ga, dimming of the fundamental RHEED diffraction rods also occurs. In this case, returning to the transition conditions does not immediately yield

the reappearance of the reconstructions. Growth in the Ga rich side of the transition curve is found to eventually cause excess Ga droplet formation over the GaN surface. The stationary nature of the transition conditions is forfeited until accumulated Ga is reevaporated. For a given reactive nitrogen supply, the transition curve approximately corresponds to the conditions of maximum growth rate achievable without development of Ga droplets. A stable growth front can be maintained for many hours with almost no adjustments to the growth parameters at the transition stoichiometry. In the extremes, mobility of the growth species may be reduced at temperatures less than $\sim 575°C$ and three-dimensional growth can take place. At high temperatures above $\sim 750°C$, some blurring of the RHEED pattern is observed which may be due to degeneration of the surface. However, within the range of conditions shown in Fig. 1, the curves demonstrate a broad range of interdependent growth parameters which yield a given surface stoichiometry for stable growth.

When the substrate temperature is held constant during growth, the exponential term in Eq. (1) corresponding to the reevaporation of Ga from the surface is constant. At transition conditions, the effect of a growth condition change can be measured in terms of the Ga flux required to keep the growth surface at the transition stoichiometry. With Eq. (1), the active nitrogen participating growth $\alpha\Phi_N$, and a general measure of the active nitrogen flux available can be obtained as a function of various growth and system parameters. By this means, the relationship between active nitrogen species participating in growth and the nitrogen flow rate was determined. While Fig. 1 shows the upward displacement of the transition curves for four nitrogen flow rates, a more detailed examination of this increase was done on a single sample surface at constant temperature, plasma power and system pressure. The system pressure was monitored with an ion guage placed near the sample and maintained by adjusting the valve to the pumping system. Fig. 2 shows that the Ga flux needed to maintain the surface at the transition stoichiometry increases approximately linearly with nitrogen flow rate between 3 and 9 ccm. By Eq. (1), the nitrogen participating in growth is also

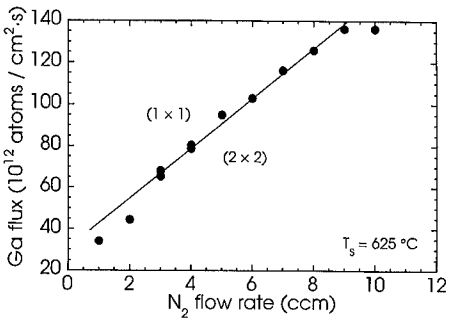

Fig. 2. The transition between the (2×2) and (1×1) surface examined as a function of nitrogen flow rate. It is found that the Ga flux to maintain the growth surface at the transition stoichiometry is approximately linear with nitrogen flow rate between 3 and 9 ccm, indicating that the active nitrogen supply participating in growth is also linearly related to nitrogen flow rate through the plasma cell.

increasing linearly. It can therefore be concluded that the active nitrogen available, and consequently, the growth rate can be increased linearly with nitrogen flow rate within this range. Interpolating the line to the y-axis where the nitrogen supply is zero, $\Phi_{Ga} = A\exp(-E_a/kT_s)$ by Eq. (1). At this condition, no growth is expected and the arriving Ga flux must be equal to reevaporating Ga to maintain the surface at the transition stoichiometry. The activation-energy function for surface Ga reevaporation given above gives 21.3×10^{12} at/cm^2 s at $T_s = 625°C$, corresponding reasonably to the value of 30×10^{12} at/cm^2 s obtained at the y-intercept in Fig. 2.

Using the transition surface stoichiometry as a reference point for the determination of the active nitrogen species participating in growth, the plasma power was varied and the Ga flux required to obtain the (2×2)–(1×1) RHEED transition was sought. Fig. 3 shows the transition curve for two nitrogen flow rates. In both cases, it is found that the amount of available nitrogen for growth increases with plasma power to approximately 40 W, then saturates. It is seen that increasing plasma power beyond a certain point provides no additional active nitrogen, and consequently, no increased growth rate.

Although these particular results are probably characteristic of the present plasma source and

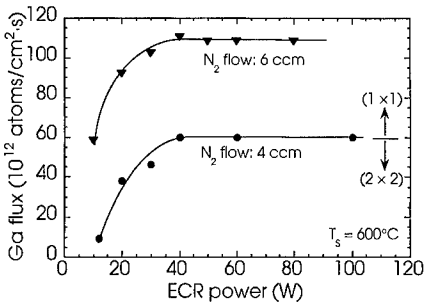

Fig. 3. The transition between the (2 × 2) and (1 × 1) surface examined as a function of plasma excitation power. For two nitrogen flow rates, it is found that the Ga flux to maintain the growth surface at the transition stoichiometry increases as the power is increased to ~ 40 W, but the transition curve is flat for greater excitation power. This indicates that the active nitrogen supply increases for powers up to 40 W, then saturates.

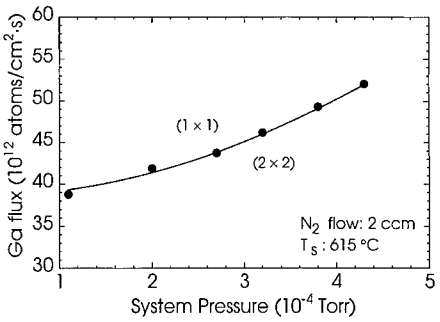

Fig. 4. The reconstruction transition curve plotted as Ga flux vs. chamber pressure, for the determination of the relative arrival rates of species at the growth surface as the mean free path is reduced. For a constant nitrogen flow rate, it is seen that the Ga flux from the cell must be increased to maintain the surface at the (2 × 2)–(1 × 1) transition stoichiometry. It is believed that there are more Ga collisions taking place because the Ga cell is placed almost two times further away from the substrate than the nitrogen plasma cell exit; the Ga flux must thus be increased to compensate.

system geometry, it is nevertheless a test to determine the active nitrogen flux available which can be applied in any system. Although information about nitrogen species has been obtained using optical emission spectra (for example, Refs. [15, 16]) or mass spectroscopy (for example, Ref. [16]) the present method can be used on any MBE system equipped with RHEED. A further benefit is that no assumptions need to be made with regard to the efficiency of reaction of the various excited nitrogen species, since, in the RHEED surface analysis, the nitrogen species participating in growth is being measured directly.

The transformation between the (2 × 2) and the (1 × 1) RHEED pattern was examined as a function of system pressure to determine the influence of pressure on the growth stoichiometry. Fig. 4 shows the transition as a function of pressure obtained using a constant nitrogen flow rate of 2 ccm and substrate temperature of 615°C. It can be seen that an increasing amount of Ga supply is required to maintain the surface stoichiometry corresponding to the reconstruction transition as the pressure is increased; it appears that the increased background pressure causes more blocking of the Ga from the cell relative to the nitrogen supply that is maintained constant. A possible explanation for the behavior observed in Fig. 4 is that in the present system, the exit aperture of the nitrogen cell is significantly closer to the substrate than the Ga melt in the Knudsen cell; the distance between the Ga cell and the substrate is 20 cm, whereas the distance between the nitrogen cell and the substrate is 11.5 cm. Because the Ga source is almost twice as far from the substrate, it is expected that the Ga is more susceptible to the influence of the decrease in the mean free path associated with the pressure increase. In order to compensate, the Ga flux from the cell must be increased to maintain the surface at the transition stoichiometry.

4. Conclusion

Transition curves delimiting the (2 × 2) reconstruction regime were characterized and shown to be a reference for a particular growth surface stoichiometry which can be used for observing the interdependency of growth parameters. The transformation from a (2 × 2)-reconstructed surface to that which gives a (1 × 1) RHEED pattern was shown to occur because of excess Ga on the surface. For a given reactive nitrogen supply, the transition curve approximately corresponds to the conditions of maximum growth rate achievable without development of Ga droplets on the surface. The displacement of the transition curves show how growth rate

can be scaled with nitrogen supply, and the influence of nitrogen plasma cell power and background pressure on the arrival rates of growth species. The (1×1)–(2×2) reconstruction transition provides a means for in situ monitoring of the stoichiometry on the sample surface.

Acknowledgements

We are indebted to Y. Iyechika of Sumitomo Chemical Co. Ltd. for valuable discussions and providing MOVPE-GaN substrates, K. Ohta for GaAs RHEED oscillation data, and H. Okushi for his support and encouragement. P.H. and G.F. are Science and Technology Agency Fellows.

References

[1] R.J. Molnar, R. Singh and T.D. Moustakas, Appl. Phys. Lett. 66 (1995) 268.
[2] J. Pankove, S.S. Chang, H.C. Lee, R.J. Molnar, T.D. Moustakas and B. Van Zeghbroeck, Technical Digest – International Electron Devices Meeting 1994, 94CH35706 (IEEE, Piscataway, 1994) p. 389.
[3] S. Nakamura, M. Senoh and T. Mukai, Jpn. J. Appl. Phys. 32 (1993) L8..
[4] M.E. Lin, B. Sverdlov, G.L. Zhou and H. Morkoç, Appl. Phys. Lett. 62 (1993) 3479.
[5] H. Morkoç, A. Botchkarev, A. Salvador and B. Sverdlov, J. Crystal Growth 150 (1995) 887.
[6] T.D. Moustakas, T. Lei and R.J. Molnar, Physica B 185 (1993) 36.
[7] S.H. Cho, H. Sakamoto, K Akimoto, Y. Okada and M. Kawabe, Jpn. J. Appl. Phys. 34 (1995) L236.
[8] R.J. Molnar and T.D. Moustakas, J. Appl. Phys. 76 (1994) 4587.
[9] M.E. Lin, S. Strite, A. Agarwal, A. Salvador, G.L. Zhou, N. Teraguchi, A. Rockett and H. Morkoç, Appl. Phys. Lett. 62 (1993) 702.
[10] W.C. Hughes, W.H. Rowland, Jr., M.A.L. Johnson, S. Fujita, J.W. Cook, J.F. Schetzina, J. Ren and J.A. Edmond, J. Vac. Sci. Technol. B 13 (1995) 1571.
[11] K. Iwata, H. Asahi, S.J. Yu, K. Asami, H. Fujita, M. Fushida and S. Gonda, Jpn. J. Appl. Phys. 35 (1996) L289.
[12] G. Feuillet, P. Hacke, H. Okumura and S. Yoshida, Int. Symp. on Blue Laser and Light Emitting Diodes, March 5–7 (1996), LN-4.
[13] P. Hacke, G. Feuillet, H. Okumura and S. Yoshida, Appl. Phys. Lett. 69 (1996) 2507.
[14] Determined from R.E. Honig and D.A. Kramer, RCA Review 30 (1969) 285.
[15] C.T. Foxon, T.S. Cheng, S.V. Novikov, D.E. Lacklison, L.C. Jenkins, D. Johnson, J.W. Orton, S.E. Hooper, N. Baba-Ali, T.L. Tansley and V.V. Tret'yakov, J. Crystal Growth 150 (1995) 892.
[16] S.H. Cho, U. Tanaka, K. Hata, T. Maruyama and K. Akimoto, in: Proc. Int. Symp. on Blue Laser and Light Emitting Diodes (Ohmsha, Tokyo, 1996) p. 500.

ELSEVIER

Journal of Crystal Growth 175/176 (1997) 100–106

JOURNAL OF CRYSTAL GROWTH

Growth and p-type doping of GaN on c-plane sapphire by nitrogen plasma-assisted molecular beam epitaxy

Myung C. Yoo*, M.Y. Park, S.K. Kang, H.D. Cho, J.W. Lee

Photonics Semiconductor Laboratory, Samsung Advanced Institute of Technology, P.O. Box 111, Suwon 440-600, South Korea

Abstract

Effect of III/V ratio on the quality of GaN epilayers has been investigated. GaN films were grown on the c-plane of sapphire by using radio frequency (RF) nitrogen plasma-assisted molecular beam epitaxy (MBE). A home-made III–V nitride MBE system consisted of an inductively coupled RF nitrogen plasma source and solid source effusion cells were used to grow GaN films. The results of reflection high energy electron beam diffraction (RHEED) and double crystal X-ray diffraction indicate that crystal quality of GaN epilayers is strongly dependent on the Ga flux. Room temperature photoluminescence spectrum of undoped GaN epilayer is peaked at 3.39 eV and no discernible yellow luminescence resulting from ion damages are observed. Effect of Mg flux on the carrier concentration of p-GaN have also been investigated. Fairly uniform p-doping concentration as high as $5.33 \times 10^{18}/\text{cm}^3$ throughout the GaN crystal were obtained. The sample grown with $T_{\text{Ga}} = 900°\text{C}$ and $T_{\text{Mg}} = 130°\text{C}$ exhibits very streaky RHEED patterns and the highest p-type doping concentration.

Keywords: GaN; MBE; p-Doping

1. Introduction

Recent advancement in the growth techniques of III–V nitride semiconductors which include metalorganic chemical vapor deposition (MOCVD) and molecular beam epitaxy (MBE) has resulted in the commercialization of GaN-based blue/green light emitting diodes (LEDs) [1, 2] and successful demonstration of current-injection blue/purple lasing under pulsed mode [3, 4]. MOCVD has been a choice of growth method for fabricating GaN-based LEDs and laser diode since the growth rate of the MOCVD process is faster than that of MBE due to high atomic nitrogen incorporation with Ga [5]. As a result, most research groups working on the GaN-based material growth have concentrated on the MOCVD. However, the turn-on voltage of the Nichia's MOCVD-grown laser diode is 28 V due to high contact resistance of p-GaN layer [4]. This is mainly attributed to the low p-doping concentration, in the range of mid 10^{17} to low $10^{18}/\text{cm}^3$, in the MOCVD process.

* Corresponding author. Fax: + 82 331 280 9357; e-mail: mcyoo@saitgw.sait.samsung.co.kr.

0022-0248/97/$17.00 Copyright © 1997 Published by Elsevier Science B.V. All rights reserved
PII S0022-0248(96)01226-2

Meanwhile, MBE has recently been utilized using conventional III–V MBE systems equipped with either electron cyclon resonance (ECR) or radio frequency (RF)-plasma sources for supplying atomic nitrogen. The main advantages of MBE over MOCVD for GaN growth are (a) low temperature growth, (b) precise control of thickness and composition, (c) high p-type doping concentration [6, 7], (d) free of post-growth annealing process for p-type conductivity [7], and (e) in situ characterization capability. Despite these advantages, however, slow growth rate of MBE, typically 0.1–0.15 μm/h, is the main disadvantage compared with other growth techniques [8].

Nevertheless, in order to realize the continuous wave lasing of GaN-based blue laser diode, it is essential to reduce p-type contact resistance by increasing the p-type doping concentration and enhance the optical gain by fine control of active layer thickness and composition at low temperature. In this respect, MBE is considered as a viable growth method to meet those requirements. This is evidenced by Akasaki et al. who have demonstrated ultraviolet lasing (316 nm) under pulsed mode by using GaN/GaInN ultra thin multilayers grown with RF-plasma assisted MBE on MOCVD-grown GaN [9, 10].

In this work, we have investigated growth and doping of GaN epilayers by using RF plasma-assisted MBE (PAMBE). The main objective of this work is to study the effect of Ga and Mg flux on the optical, electrical and structural properties of epitaxial GaN thin films. The major characterization tools used for this study were reflection high energy electron beam diffraction (RHEED) and double crystal X-ray diffraction (DXRD), photoluminescence (PL), Van der Pauw–Hall effect measurement, and secondary ion mass spectrometry (SIMS).

2. Experimental procedure

A schematic of the MBE system specifically designed and constructed for the growth of high-quality III-nitride epitaxial thin films is shown in Fig. 1. The MBE system is capable of growing up to twelve 3 in wafers continuously without breaking vacuum. In order to obtain a high growth rate and to provide flexibility in gas use, a 600 W inductively coupled RF nitrogen plasma source and 2200 ℓ/s corrosion resistant turbomolecular pump were employed. We obtained a growth rate of up to 0.6 μm/h without significantly deteriorating the film quality. Effusion cells which include Ga, Al, In and Si, Mg dopant cells from EPI MBE Products Group were used to supply highly uniform molecular beam fluxes. The lowest pressure obtained was 4×10^{-11} Torr by using turbomolecular pump and 400 ℓ/s ion/Ti sublimation pumps.

c-Plane (0 0 0 1) sapphire wafers were used as a substrate. Prior to growth, sapphire substrates were degreased in organic solvents and etched in a 3 : 1 solution of H_2SO_4 and H_3PO_4 at 170°C. In the growth chamber, the substrates were subjected to thermal desorption at 850°C for 30 min followed by nitridation using nitrogen plasma source for 20 min to form a thin AlN prelayer. After that, 20 nm thick AlN buffer layers were grown at 500°C. High purity N_2 (6N) was further cleaned using a nitrogen purifier (ASA Getters Inc.) and supplied into the RF plasma source. In-growth doping was done using high purity Si (6N) and Mg (6N) as n- and p-type dopants, respectively. For n-type doping, Si cell temperature was set at 1070°C while Mg cell temperatures were varied from 120 to 190°C in order to study the Mg flux effect on the p-doping of the GaN epilayers. Detailed experimental set up and procedures can be found elsewhere [11, 12].

In situ characterizations were carried out using 15 kV RHEED (Staib Instruments Inc., Model EK-15-RMG) and 200 amu quadrupole mass spectrometer (Balzers, Model 100 MA) to monitor the surface structure of films grown during GaN growth and atomic nitrogen flux, respectively. Crystal quality of the grown samples were measured by DXRD (Bede Scientific Inc., Model FR 590) at 35 kV and 35 mA. Room temperature PL were performed using 325 nm He–Cd laser at 1.6 mW power with GaAs PM-tube detector. Van der Pauw–Hall measurements were used to determine the carrier concentrations and Hall mobility of grown GaN samples. Finally, Mg doping profile in the GaN crystal were characterized using Cameca ims 5f SIMS system.

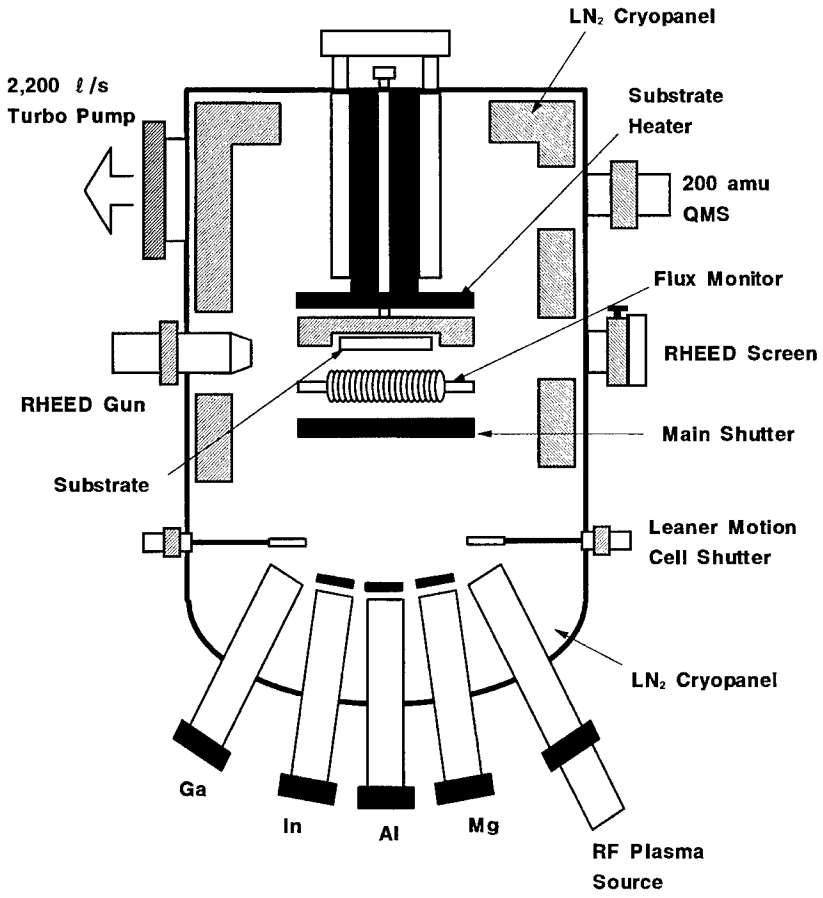

Fig. 1. A schematic of MBE system specifically designed and constructed for the growth of high-quality III-nitride epitaxial thin films.

3. Results and discussion

In Fig. 2, RHEED patterns of 0.2 μm-thick GaN epilayers taken at [11–20] azimutal are shown as a function of Ga temperature. In order to study the effect of III–V flux ratio on the crystal quality, Ga temperatures were varied from 900 to 915°C while substrate temperature and nitrogen plasma source conditions were fixed at 750°C and 400 W RF power with 2 sccm N_2 flow rate, respectively. The background pressure during GaN growth was typically 4.5×10^{-5} Torr at 2 sccm N_2 flow rate. The growth rates of GaN films shown in the Fig. 2 were in the range of 80–150 nm/h depending on the Ga temperature. From the figures, it is clearly seen that the RHEED pattern is getting more streaky and sharper with decreasing Ga temperature. The most streaky RHEED pattern is obtained for the sample grown with Ga temperature at 900°C. It is considered that slow growth rate of the sample grown at low Ga temperature also results in better film quality.

Ga flux effect on the GaN crystal quality is further investigated by determining full width at half maximum (FWHM) of X-ray rocking curve. Fig. 3 shows the variation of FWHM values as a function of Ga cell temperature. The lowest FWHM of the GaN film shown in Fig. 3 is 460 arcsec for the 0.3 μm-thick sample grown with $T_{Ga} = 900$°C. The FWHM value increases from 460 to 1200 arcsec as the Ga temperature raises from 900 to 915°C. Judging from the RHEED and

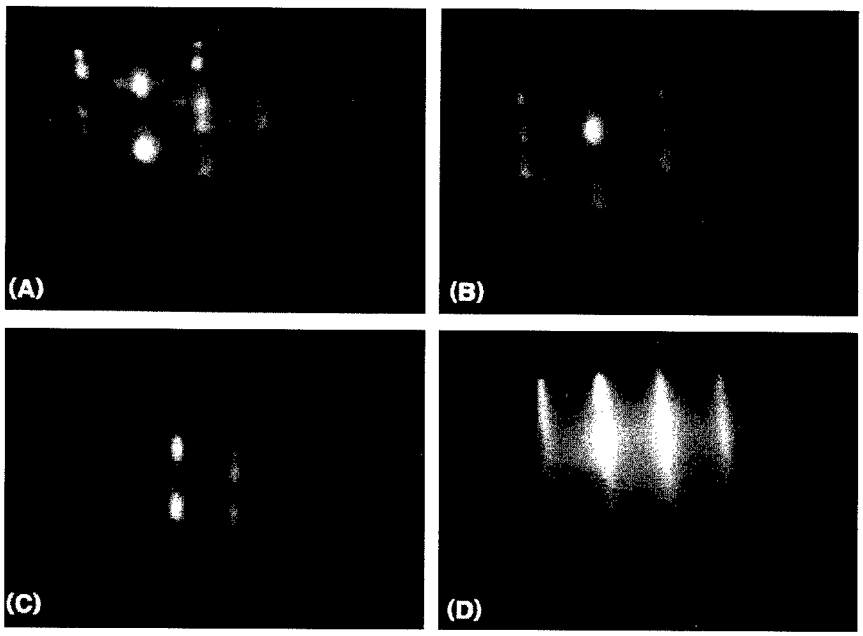

Fig. 2. RHEED patterns of 0.2 μm thick undoped GaN epilayers taken at [11–20] azimutal as a function of Ga temperature: A) T_{Ga} = 915°C, B) T_{Ga} = 910°C, C) T_{Ga} = 905°C, and D) T_{Ga} = 900°C, at a fixed nitrogen flux (400 W RF power, 2 sccm N_2 flow) and substrate temperature (T_s = 750°C).

DXRD results, it is concluded that crystal quality of GaN epilayers is strongly dependent on the Ga flux. As far as the structural property of GaN epilayer is concerned, the DXRD results are consistent with that of RHEED.

Effect of Ga flux on the optical property of undoped GaN films were investigated using PL. In Fig. 4, room temperature PL spectra of undoped GaN samples are shown as a function of Ga temperature. At room temperature, fairly strong exciton peaks were observed at 3.39 eV for all samples indicating that the grown GaN thin films are of an optically high quality. FWHM of exciton peaks for these undoped GaN samples are varied from 185.5 to 263 meV. The samples grown with Ga temperatures at either 900 or 915°C exhibit narrower FWHM than those at other Ga temperatures. From the results of RHEED, DXRD, and PL of undoped GaN samples, it seems like that there are no close relationships between structural property and optical property of GaN films. In particular, however, it is important to note that no discernible yellow emissions are observed in our PAMBE-grown GaN epilayers although PL measurements were carried out at room temperature while it is usual in the MOCVD-grown GaN films [13]. This means that there are no detectable impurities from source materials or defects generated by energetic nitrogen ions from RF nitrogen source.

In-growth doping of n-GaN and p-GaN, have been carried out using solid source Si and Mg as n-type and p-type dopant, respectively. Silicon dopant cell temperature was set at 1070°C for all n-GaN growth samples. The resulting n-type doping concentration was measured to be 3–5 × $10^{18}/cm^3$ by Van der Pauw–Hall measurement. In order to study the effect of Mg flux on the doping concentration of p-GaN, Mg cell temperatures were varied from 120 to 190°C at a fixed substrate temperature and nitrogen flux. Fig. 5 shows series of RHEED patterns for 1.0 μm-thick p-GaN samples as a function of Mg flux. Comparing with undoped GaN samples shown in Fig. 2, in general, RHEED patterns are streaky since these p-doped GaN samples were grown at relatively lower Ga temperatures, i.e. slower growth rate.

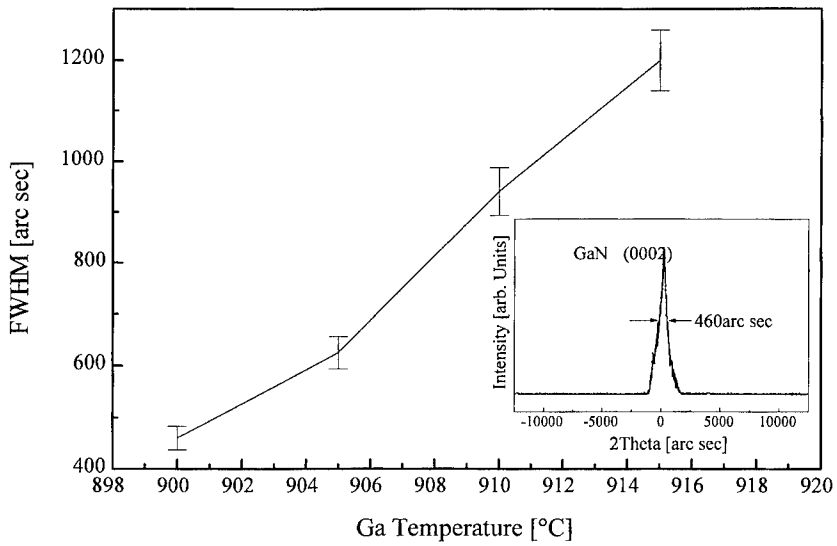

Fig. 3. FWHM of X-ray rocking curve for 0.3 μm thick undoped GaN films as a function of Ga temperature; substrate temperature and nitrogen flux were same as indicated in Fig. 2 (inset shows a representative X-ray rocking curve of the sample grown with $T_{Ga} = 900°C$).

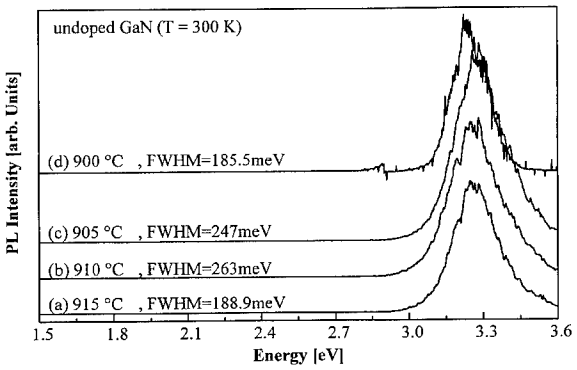

Fig. 4. Room temperature PL spectra of undoped GaN films grown with different Ga temperatures at a fixed substrate temperature (750°C) and nitrogen flux (400 W RF power, 2 sccm N_2 flow); (a) 915°C, (b) 910°C, (c) 905°C, and (d) 900°C.

From the figures, the best RHEED pattern can be obtained for the sample grown with $T_{Ga} = 900°C$ and $T_{Mg} = 130°C$ [Fig. 2b]. With increasing or decreasing Mg flux, the RHEED patterns turn spotty. Particularly, the RHEED pattern of the sample doped with $T_{Mg} = 120°C$ looks very hazy and amorphous. According to our RHEED study, maintaining the optimum flux ratio between Ga and Mg is necessary to grow atomically flat surface of GaN epilayers. In naked eye inspections, we were able to observe a transparent appearance for the sample grown with $T_{Ga} = 900°C$ and $T_{Mg} = 130°C$. Otherwise, the samples grown with either higher or lower Mg flux appear to be yellow.

Results from Van der Pauw–Hall measurements of p-doped GaN samples are listed in Table 1. We obtained a p-type carrier concentration of GaN as high as $5.33 \times 10^{18}\ cm^{-3}$ by PAMBE without post-growth annealing treatment. p-Type carrier concentration of sample 2 increases by two orders of magnitude compared with sample 1 as Mg temperature increases from 120 to 130°C, which is equivalent to the Mg flux increment by 13.5 times. However, further increase in Mg flux eventually reduces p-type carrier concentration. When the Mg atoms are introduced into the GaN above the solubility limit, excess Mg atoms cannot take a substitutional site of the GaN crystal. As a result, these interstitial atoms are acting as donors rather than as acceptors; hence, these excess Mg atoms deteriorate the conduction process of the p-type material. According to the RHEED analysis and Hall effect measurements, it is found that there is a close relationship between surface flatness and p-type

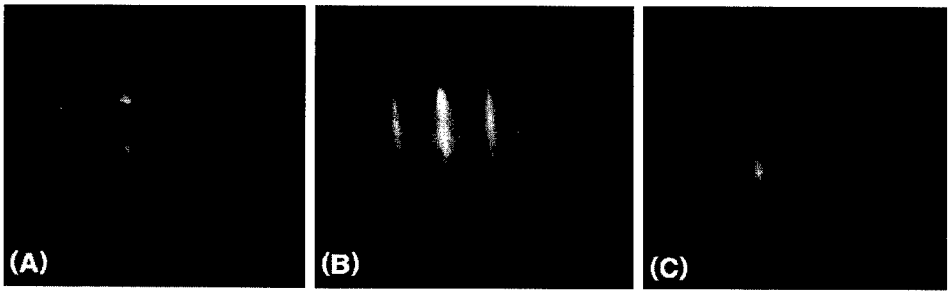

Fig. 5. RHEED patterns of 1.0 μm thick p-doped GaN epilayers taken at [11–20] azimutal as a function of Mg temperature: (A) $T_{Mg} = 120°C$, (B) $T_{Mg} = 130°C$, (C) $T_{Mg} = 190°C$, at a fixed Ga flux ($T_{Ga} = 900°C$) and nitrogen flux (400 W RF power, 2 sccm N_2 flow).

Table 1
Van der Pauw–Hall measurement results of p-doped GaN samples at a fixed substrate temperature and nitrogen flux

Sample number	T_{Ga} (°C)/flux (Torr)	T_{Mg} (°C)/flux (Torr)	Film thickness (μm)	Mobility ($cm^2/V \cdot s$)	Carrier concentration (cm^{-3})
1	$900/9.1 \times 10^{-5}$	$120/8.1 \times 10^{-11}$	1.08	347	3.80×10^{16}
2	$890/7.0 \times 10^{-5}$	$130/1.1 \times 10^{-9}$	0.80	1.31	4.00×10^{18}
3	$900/9.1 \times 10^{-5}$	$130/1.1 \times 10^{-9}$	0.71	4.19	5.33×10^{18}
4	$900/9.1 \times 10^{-5}$	$190/2.2 \times 10^{-8}$	1.16	147	5.65×10^{17}

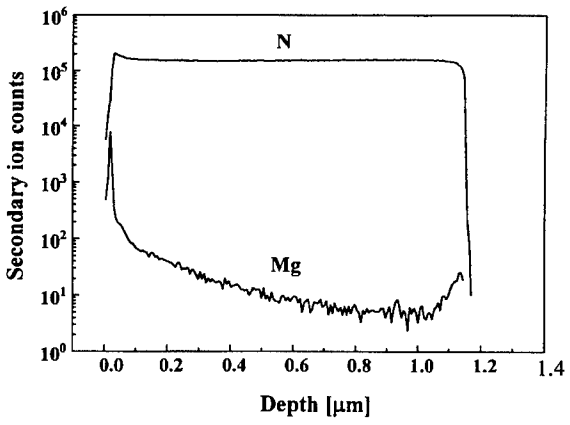

Fig. 6. SIMS depth profile of the 1.0 μm thick Mg doped GaN epilayer grown with $T_{Mg} = 130°C$ and $T_{Ga} = 900°C$.

doping concentration of GaN epilayer in the PAMBE-growth. In Fig. 6, SIMS depth profiles of Mg in the GaN films grown at $T_{Ga} = 900°C$ and $T_{Mg} = 130°C$ are shown. The Mg concentration profile is fairly uniform and no indication of surface segregation is observed in the GaN crystal.

4. Conclusions

Effect of III/V ratio on the quality of GaN epilayers have been investigated. The results of RHEED and double crystal X-ray diffraction indicate that crystal quality of GaN epilayers is strongly dependent on the Ga flux. Room temperature PL spectrum of undoped GaN epilayer is peaked at 3.39 eV and no discernible yellow emissions resulting from ion damages are observed. Effect of Mg flux on the carrier concentration of p-GaN have also been investigated. Fairly uniform p-type doping concentration as high as $5.33 \times 10^{18}/cm^3$ were obtained. The sample grown with $T_{Ga} = 900°C$ and $T_{Mg} = 130°C$ exhibits very streaky RHEED patterns and the highest p-type doping concentra-

tion. According to the RHEED analysis and Hall measurement, we found that optimal Ga and Mg flux ratio should be maintained at a constant nitrogen flux to grow highly doped p-GaN.

References

[1] S. Nakamura, M. Senoh, N. Iwasa and S. Nagahama, Jpn. J. Appl. Phys. 34 (1995) L797.
[2] S. Nakamura, M. Senoh, N. Iwasa, S. Nagahama, T. Yamada and T. Mukai, Jpn. J. Appl. Phys. 34 (1995) L1332.
[3] S. Nakamura, M. Senoh, S. Nagahama, N. Iwasa, T. Yamada, T. Matsushita, H. Kiyoku and Y. Sugimoto, Jpn. J. Appl. Phys. 35 (1996) L74.
[4] S. Nakamura, M. Senoh, S. Nagahama, N. Iwasa, T. Yamada, T. Matsushita, H. Kiyoku and Y. Sugimoto, Appl. Phys. Lett. 68 (1996) 2105.
[5] H. Morkoc, S. Strite, G. Gao, M. Lin, B. Sverdlov and M. Burns, J. Appl. Phys. 76 (1994) 1363.
[6] J.M. Myoung, C.K. Kim, K.H. Shim, O.V. Gluschenkov, K. Kim and M.C. Yoo, Proc. 1996 Mater. Res. Soc. Spring Meeting, to be published.
[7] R.J. Molnar, R. Singh and T.D. Moustakas, Appl. Phys. Lett. 66 (1995) 268.
[8] M. Johnson, S. Fujita, W. Rowland, W. Hughes, Y.H. He, N. El-Masry, J. Cook and J. Schetzina, J. Electron. Mater. 25 (1996) 793.
[9] I. Akasaki and H. Amano, Proc. Int. Symp. on Blue Laser and Light Emitting Diodes, Chiba Univ., Japan, 11 (1996).
[10] I. Akasaki, S. Sota, H. Sakai, T. Tanaka, M. Loike and M. Amano, Electron. Lett. 32 (1996) 1105.
[11] M.C. Yoo, T.I. Kim, K. Kim, K.H. Shim and J.T. Verdeyen, Opt. Quantum Electron. 27 (1995) 427.
[12] K. Kim, M.C. Yoo, K.H. Shim and J.T. Verdeyen, J. Vac. Sci. Technol. B 11 (1994) 1942.
[13] W. Shan, T. Schmidt, X. Yang, J.J. Song and B. Goldenberg, J. Appl. Phys. 79 (1996) 3691.

ELSEVIER

Journal of Crystal Growth 175/176 (1997) 107–111

JOURNAL OF CRYSTAL GROWTH

Surface crystal-structure of a GaN film as an in situ mask using MOMBE

Seikoh Yoshida[a,*], Masahiro Sasaki[b]

[a] *The Furukawa Electric Co., Ltd., Yokohama R&D Laboratories, 2-4-3 Okano, Nishi-ku, Yokohama 220, Japan*
[b] *Institute of Applied Physics, University of Tsukuba, 1-1-1 Tennohdai, Tsukuba, Ibaraki 305, Japan*

Abstract

We have studied an atomically thin GaN film as a mask for the in situ selective-area growth (SAG) of GaAs (1 1 1)B using metalorganic molecular beam epitaxy (MOMBE). We examined atomically thin GaN film formed on GaAs (1 1 1)B in order to investigate whether GaN can be used as a mask for an in situ process or not. It was found that the GaAs growth-suppression effect of a specific GaN surface showing a streaky RHEED pattern corresponding to a flat single crystal is highest, while those of other GaN surfaces are lower. This behavior is similar to that observed for a GaAs (1 0 0) substrate.

1. Introduction

In situ selective-area growth (SAG), in which all of the related processes, including mask formation, patterning, growth and mask removal, are performed in an ultra-high vacuum (UHV) system, is an important technique for making a fine structure [1–5]. The development of mask materials to fulfill the in situ process conditions is required to realize in situ SAG. We have already reported that the GaAs growth selectivity as a mask of a cubic GaN surface on a GaAs (1 0 0) substrate using metalorganic molecular beam epitaxy (MOMBE) strongly depends on the GaN formation conditions (substrate temperatures and source-gas pressures), and that only a single crystalline and flat GaN surface has high selectivity as a mask [5]. However, it has not yet been clarified whether or not GaN formed on a GaAs (1 1 1)B substrate has high selectivity for GaAs deposition. It has also been reported that metalorganic gases are difficult to decompose on an As-rich GaAs (1 1 1)B surface [6]. It is necessary to obtain a GaAs (1 1 1)B surface in order to form an atomically thin GaN with a flat surface on the GaAs (1 1 1)B substrate.

In this paper we report on the growth condition of GaAs (1 1 1)B with a smooth surface and the formation condition of atomically controlled GaN on the surface. Moreover, in order to determine the factor related to an excellent mask for GaAs SAG, we also investigated the relation between the crystal structure and the GaAs growth-suppression effect of the mask material.

* Corresponding author. Fax: +81 45 322 6961; e-mail: seikoh@yokoken.furukawa.co.jp.

0022-0248/97/$17.00 Copyright © 1997 Elsevier Science B.V. All rights reserved
PII S0022-0248(96)00918-9

2. Experimental procedure

We used an MOMBE apparatus. A cryoshrouded quadrupole mass spectrometer (QMS) and a reflection high-energy electron-diffraction (RHEED) apparatus were positioned in this chamber. Nozzles for introducing trimethylgallium (TMG) as a Ga source gas, dimethylhydrazine (DMHy, $((CH_3)_2NNH_2)$) [7–10] as a nitrogen source gas, and trisdimethylaminoarsine (TDMAAs, $As(N(CH_3)_2)_3$) as an arsenic source gas [11, 12], as well as a Knudsen effusion cell for a solid As source, were also placed in this chamber.

We first investigated the condition to obtain a flat GaAs (1 1 1)B surface under the different surface cleaning and growth conditions. After that, GaN formation was carried out on the smooth GaAs (1 1 1)B surface at various substrate temperatures. In order to investigate the GaAs growth selectivity of the formed GaN surfaces, we measured the growth-suppression periods (GSPs) for GaAs on GaN surfaces formed under various conditions by using RHEED when the surfaces were simultaneously exposed to TMG and As_4 at 430°C [10]. This GSP is defined as a time when any change of the RHEED pattern began to occur due to the GaAs deposition. The reactions of TMG on GaN surfaces were investigated using QMS and RHEED apparatus. The surface morphologies were observed by a Nomarski microscope.

3. Results and discussion

In order to form an atomically thin GaN film as a mask on a GaAs (1 1 1)B substrate, the GaAs (1 1 1)B surface must be flat before GaN formation on the surface. GaAs native oxide was first thermally removed at 610°C under an As ambient and then, a GaAs (1 1 1)B epitaxial layer was grown in the temperature range of 540–580°C. Beam equivalent pressures of TMG and As_4 are 1.0×10^{-7} and 1.5×10^{-6} Torr, respectively. The growth rate of GaAs (1 1 1)B epitaxial layer was less than $\frac{1}{5}$ compared with that of GaAs (1 0 0), and the distinct RHEED pattern gradually became weak as GaAs growth was proceeded. We confirmed from the observation of surface morfology by a Nomarski microscope that pyramidal hillocks with triangular or hexagonal shapes were formed on the GaAs (1 1 1)B surface before growth, and that the surface become to be roughened after growth. It is conjectured that when the native oxide on the GaAs (1 1 1)B substrate was thermally removed, the surface was roughened; this surface roughness was not improved even though a thick GaAs epitaxial layer was grown on the rough surface. It was thus difficult to obtain an epitaxial layer of GaAs (1 1 1)B with a flat surface under the above-mentioned flux conditions of TMG and As_4.

We used TDMAAs for removing the native oxide and cleaning the surface of GaAs (1 1 1)B, since TDMAAs was effective for the removal of native oxide on the GaAs (1 0 0) substrate [11]. When the GaAs (1 1 1)B surface was exposed to TDMAAs (1.0×10^{-7} Torr) at substrate temperatures of 450–470°C for 30 min, the RHEED pattern changed from a hallow one to a streaky one showing (2×2) As-stabilized structure (Fig. 1), resulting in removing the native oxide on the surface. While the RHEED patterns did not change when the native oxide on the substrate surface was exposed to TDMAAs below 440°C, and therefore, the native oxide was not removed. It was found from a Nomarski observation that the surface after cleaning was flat. After the surface cleaning of GaAs (1 1 1)B, about 100 Å-thick GaAs epitaxial layer was grown on the surface using TMG (1.5×10^{-7} Torr) and TDMAAs (1.0×10^{-7} Torr) at 500°C for 1 h, and we confirmed that the surface after growth was also smooth by the Nomarski observation. It was thus confirmed that a GaAs (1 1 1)B epitaxial layer with a smooth surface can be easily grown by using TDMAAs instead of As_4.

GaN formation was carried out on GaAs (1 1 1)B substrates with a smooth surface. Atomically thin GaN of about 5 monolayers was formed on a GaAs (1 1 1)B epitaxial layer at different substrate temperatures using a constant DMHy pressure (6×10^{-6} Torr). In the case of substrate temperatures below 600°C, RHEED pattern did not show GaN and only GaAs RHEED pattern was observed. That is, no GaN film was formed on the GaAs (1 1 1)B substrate. At 600–610°C, the GaAs RHEED spots became weak and the RHEED spots showing a hexagonal GaN began to appear after

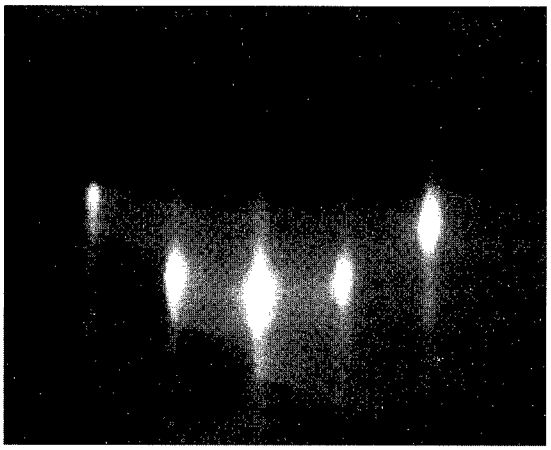

Fig. 1. RHEED pattern showing a (2 × 2) structure of GaAs (1 1 1)B.

Fig. 2. GaN RHEED pattern formed on GaAs (1 1 1)B substrate at substrate temperatures of 600–610°C.

DMHy exposure for 15 min. The RHEED pattern became a mixture of streaky GaN spots and a fuzzy ring pattern after DMHy exposure for 25 min (Fig. 2). Using a Nomarski microscope, we observed that the GaN surface was roughened, containing pyramidal hillocks with various triangular or hexagonal shapes. When the GaN surface was simultaneously exposed to TMG and As_4 at 430°C for 10 min, the RHEED pattern began to show polycrystalline GaAs, deposited on the surface. That is, the GaAs growth-suppression period (GSP) of this surface was 10 min.

In the case of 620–630°C, a GaN film showing a distinct streaky RHEED pattern was formed on GaAs (1 1 1)B substrate after DMHy exposure for 15 min (Fig. 3). Although we observed using a Nomarski microscope that the GaN surface was still roughened, and pyramidal hillocks with triangular shapes were existed, the streaky RHEED pattern showed that the flatness of the GaN surface was atomically improved compared with other formed GaN surfaces. The GaAs GSP on the surface was more than 2 h under the above-mentioned conditions. That is, it was found that the GaAs growth suppression effect on the surface is very large, and that this surface has a high selectivity as a mask for GaAs selective growth.

At substrate temperatures above 640°C, the RHEED pattern of GaN also showed a mixed

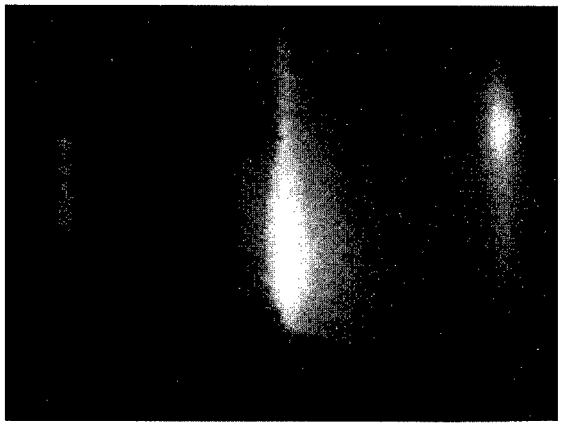

Fig. 3. GaN RHEED pattern formed on GaAs (1 1 1)B substrate at substrate temperatures of 620–630°C.

pattern of streaky spots and fuzzy rings. We observed using a Nomarski microscope that this surface was rough. That is, it was found that this surface is not single crystal from the partial ring pattern. This is considered to be as follows. The substrate surface became rough before GaN formation, since the substrate temperature was too high and the arsenic desorption from the substrate occurred due to no arsenic supply. As a result, it is considered that various GaN nucleations occurred

on the rough surface under DMHy exposure. Therefore, a single crystal of GaN with a smooth surface could not be obtained at a comparatively high substrate temperature, such as 640°C under a constant DMHy pressure (6×10^{-6} Torr). We also confirmed that the GaAs GSP of this surface was 30 min under the above-mentioned conditions. That is, the growth selectivity to GaAs on this surface is low.

Tables 1 and 2 show GSPs of variously formed GaNs as well as surface crystal structures of GaN in the case of GaAs (1 0 0) and GaAs (1 1 1)B substrates, respectively. The crystal-structure of GaN formed on the GaAs (1 1 1)B substrate shows a hexagonal structure from RHEED pattern and X-ray diffraction, although that of GaN on the GaAs (1 0 0) has a cubic structure or a cubic and hexagonal mixed structure [10]. In the case of GaN on GaAs (1 1 1)B, a weak streaky image of the RHEED pattern remains even though the surface partially became polycrystalline following the surface roughness. We found using a Nomarski microscope that there were pyramidal hillocks on the GaN surface showing a weak streaky and partial ring RHEED pattern, while the GaN surface showing a distinct streaky pattern was very smooth. Using a Nomarski microscope, it was found that the regular pyramidal hillocks are partially ordered on the surface. That is, the regular facet faces are partially formed on the hillock surfaces. We consider that these regular facets give streaky spots of RHEED. It is also considered that when GaAs (1 1 1)B substrate surface was roughened following arsenic dissociation due to no arsenic supply during GaN formation, regular facet faces were easy to form on the roughened surface. Therefore, in order to obtain a GaN surface giving the longest GaAs GSP, the RHEED image of GaN with a flat surface is required to be a distinct streaky pattern without any weak streaky image or ring image in the case of using a GaAs (1 11)B substrate.

Table 1
Growth suppression periods (GSPs) on the GaN mask with RHEED images showing various surface structures on GaAs (1 0 0) substrate

RHEED image	Crystal structure	GSP
Fuzzy	Amorphous	< 10 min
Spotty	Cubic and hexagonal	30 min
Spotty	Cubic	1 h
Streaky	Cubic	> 3 h
Ring	Polycrystalline	30 min

Table 2
Growth suppression periods (GSPs) on the GaN mask with RHEED images showing various surface structures on GaAs (1 1 1)B substrate

RHEED image	Crystal structure	GSP
Distinct streaky	Hexagonal	> 2 h
Streaky spots and fuzzy ring	Hexagonal and polycrystalline	30 min

On the other hand, in the case of using GaAs (1 0 0) substrate, when the GaN formation conditions were changed, the RHEED image was variously changed following the formation conditions, compared with that of GaN on GaAs (1 1 1)B, as shown in Tables 1 and 2. For example, if a substrate surface was roughened during GaN formation, the RHEED image showed a polycrystalline ring, and no streaky pattern of GaN was observed on the GaAs (1 0 0) substrate. This result differs from that of the case of GaAs (1 1 1)B substrate. It is considered that regular facet faces are more difficult to form on the roughening surface of GaAs (1 0 0) compared with the case of GaAs (1 1 1)B, since GaAs (1 0 0) surface was more roughened than that of GaAs (1 1 1)B in the same formation condition of GaN.

It was also proved that the suppression effect for GaAs deposition on the GaN surface became larger with the improvement of single crystallization and surface flatness. That is, the GSPs of the surfaces of amorphous or polycrystalline GaN film on the GaAs (1 0 0) substrate were short and the GSP of a single GaN with a smooth surface was longest (Table 1). Not all of the formed GaN surfaces act as a mask for GaAs SAG, but that only a single-crystalline GaN surface showing a streaky RHEED pattern has the highest GaAs growth-suppression effect.

On the basis of these results, it was found that both atomically thin cubic and hexagonal GaN

films with a smooth surface showing a streaky RHEED pattern have the longest GaAs GSP. We recently found from the result of a QMS analysis using pulsed TMG scattering that although a single GaN surface with a smooth surface has a deep precursor state giving a long resident time of TMG during scattering, TMG desorbs on the surface without any decomposition [13]. However, the GaAs growth-suppression mechanism on a GaN surface has not yet been clarified in detail, although we recognize from the result of a QMS analysis that it is important for TMG not to react with the GaN surface in order to become a good mask for GaAs SAG. We believe that the GaAs growth suppression-effect of GaN become higher when GaN is a single crystal with high quality and the surface-structure becomes stable, since TMG decomposition on a GaAs surface with a well-defined (2×4) structure having high stability is suppressed according to QMS analysis [14].

4. Summary

Atomically thin GaN film formation was carried out on GaAs (1 1 1)B using MOMBE in order to investigate the surface crystal-structure of GaN as a mask for an in situ process. We found that the GaAs growth-suppression effect of a GaN surface showing a streaky RHEED pattern corresponding to flat and single GaN formed on a GaAs (1 1 1)B substrate is highest when the GaN surface was exposed to TMG and As_4, while GaN surfaces showing other RHEED patterns have a short GSPs to GaAs deposition on the surface. As a result, a single GaN film showing a streaky RHEED pattern formed on a GaAs (1 1 1)B as well as a GaAs (1 0 0) substrate has the highest growth selectivity to GaAs deposition as a mask on the surface at 430°C.

Acknowledgements

This work was carried out at Optoelectronics Technology Research Laboratory (OTL). The authors would like to thank Dr. M. Tamura, Dr. Y. Katayama, and Dr. I. Hayashi for their helpful discussions and continuous encouragement.

References

[1] M. Taneya, Y. Sugimoto, H. Hidaka and K. Akita, Jpn. J. Appl. Phys. 28 (1989) L515.
[2] K. Akita, M. Taneya, Y. Sugimoto and Y. Katayama, J. Vac. Sci. Technol. B 7 (1989) 1471.
[3] S. Yoshida and M. Sasaki, J. Crystal Growth 133 (1993) 540.
[4] S. Yoshida, M. Sasaki, in: Proc. 19th Int. Symp. on GaAs and Related Compounds, Karuizawa, Japan, 1992, Inst. Phys. Conf. Ser. 129, Eds. T. Ikegami, F. Hasegawa and Y. Takeda (Institute of Physics, London, 1993) p. 49.
[5] S. Yoshida, M. Sasaki and H. Kawanishi, J. Crystal Growth 136 (1994) 37.
[6] Y. Ohki, Y. Hiratani and M. Sasaki, Appl. Phys. Lett. 59 (1991) 2538.
[7] H. Okumura, S. Misawa and S. Yoshida, Appl. Phys. Lett. 59 (1991) 1058.
[8] H. Okumura, S. Yoshida, S. Misawa and E. Sakuma, J. Crystal Growth 120 (1992) 114.
[9] S. Strite, J. Ruan, Z. Li, A. Salvador, H. Chen, David J. Smith, W.J. Choyke and H. Morkoc, J. Vac. Sci. Technol. B9 (1991) 1924.
[10] S. Yoshida and M. Sasaki, Appl. Surf. Sci. 82/83 (1994) 28.
[11] S. Yoshida and M. Sasaki, J. Crystal Growth 150 (1995) 557.
[12] S. Yoshida and M. Sasaki, J. Crystal Growth 151 (1995) 220.
[13] M. Sasaki and S. Yoshida, unpublished.
[14] M. Sasaki and S. Yoshida, J. Vac. Sci. Technol. B 10 (1992) 1720.

ELSEVIER

Journal of Crystal Growth 175/176 (1997) 112–116

JOURNAL OF CRYSTAL GROWTH

Cathodoluminescence of GaN films grown under Ga and N rich conditions by radio-frequency-molecular beam epitaxy

Sung Hwan Cho[a,*], Uitsu Tanaka[a], Takahiro Maruyama[a], Katsuhiro Akimoto[a], Hajime Okumura[b], Sadafumi Yoshida[b]

[a] *Institute of Materials Science, University of Tsukuba, 1-1-1 Tennodai, Tsukuba, Ibaraki 305, Japan*
[b] *Electrotechnical Laboratory, 1-1-4 Umezono, Tsukuba, Ibaraki 305, Japan*

Abstract

Cathodoluminescence (CL) topographs were taken at room temperature at 364 nm on undoped GaN films grown by plasma-enhanced molecular beam epitaxy at various V/III ratios. The CL topographs were compared with scanning electron microscope (SEM) images. The CL topograph was found to be significantly influenced by the V/III ratio during growth. For GaN films grown at low V/III ratio, spatially nonuniform luminescence intensity was observed. This nonuniformity in luminescence may be due to the local variation of stoichiometry of GaN induced by Ga microsegregation. At nitrogen-rich condition, almost flat surfaces in SEM image were observed and the uniform intensity of luminescence was obtained by CL topograph. Thus, the nitrogen-rich condition is favourable to get structually and optically uniform films.

PACS: 78.60.H; 68.55.B

Keywords: Cathodoluminescence; GaN; Microsegregation

1. Introduction

Gallium nitride is of great interest because of its potential as a material for the development of light-emitting diodes (LEDs) and laser diodes (LDs) in the blue and ultraviolet spectral region [1], and the investigation on the growth methods and properties of GaN-based materials is currently a subject of much interest [2–7]. Though high-efficiency blue LEDs have been successfully fabricated by metalorganic chemical vapor deposition [8], plasma-enhanced molecular beam epitaxy (MBE) is regarded as an another candidate for growing GaN since it is easy to grow p-type material without any post growth treatment [9]. The luminescent properties are important for the

* Corresponding author. Fax: + 81 298 55 7440; e-mail: akimoto@esys.tsukuba.ac.jp

0022-0248/97/$17.00 Copyright © 1997 Elsevier Science B.V. All rights reserved
PII S0022-0248(96)00865-2

operation of high-efficiency light-emitting devices and there are some reports on photoluminescence properties of MBE-grown GaN [10, 11]. However, the GaN films grown on (0 0 0 1) sapphire contains a high density of dislocations, stacking faults and columnar structure [12, 13] so it is necessary to clarify the spatial dependence of the luminescence. Cathodoluminescence (CL) is a powerful tool to study the spatial dependence in relation to the emission wavelength and intensity.

In this paper the CL topograph of GaN films grown on (0 0 0 1) sapphire substrates under various V/III ratio was studied in relation to the scanning electron microscope (SEM) image.

2. Experimental procedure

GaN films were epitaxially grown on *c*-plane sapphire substrates by MBE using a conventional Knudsen effusion cell for gallium and a radio-frequency plasma gun purchased from Eiko Engineering Co. for nitrogen activation. The growth chamber was evacuated by one turbomolecular pump of 600 l/s and the base pressure is typically 7×10^{-8} Pa [14]. The nitrogen flow rate was controlled using a mass flow controller. The substrates were chemically treated by general method [15] and prior to the growth of GaN, the substrate surface was exposed to the nitrogen plasma for 20 min at 670°C to form a thin AlN layer. Then, the GaN films were grown with a substrate temperature of 700°C, RF plasma power of 150 W, and Ga-cell temperature of 975°C. The nitrogen flow rate was varied from 0.4 to 5 sccm. The growth rate for the nitrogen flow rate more than 1 sccm was 0.2 μm/h.

A streaky pattern was observed by reflection high-energy electron diffraction during growth for the samples grown under relatively higher nitrogen flow rate, and the (0 0 0 2) X-ray diffraction peak was observed with the full-width at half-maximum of 10 min by θ–2θ mode. The CL measurements were performed in a SIMADZU EPMA-8705 system at 300 K. All samples used in this study showed near-band edge emission at 364 nm and fairly weak deep level emission in the CL spectra, so the CL topographs were studied only at 364 nm.

3. Results and discussion

Fig. 1a shows a SEM image of undoped GaN grown under gallium-rich condition with the nitrogen flow rate of 0.4 sccm. Metallic structures with a diameter of about 4–5 μm are observed and the fact that these mound can be etched away in an HCl solution provides evidence of Ga droplets.

Fig. 1b shows a CL topograph at 364 nm corresponding to the area of the SEM image. The dark spots in the CL topograph which indicate no CL emission correspond to the Ga-droplets. In close vicinity to the Ga droplet, strong band edge

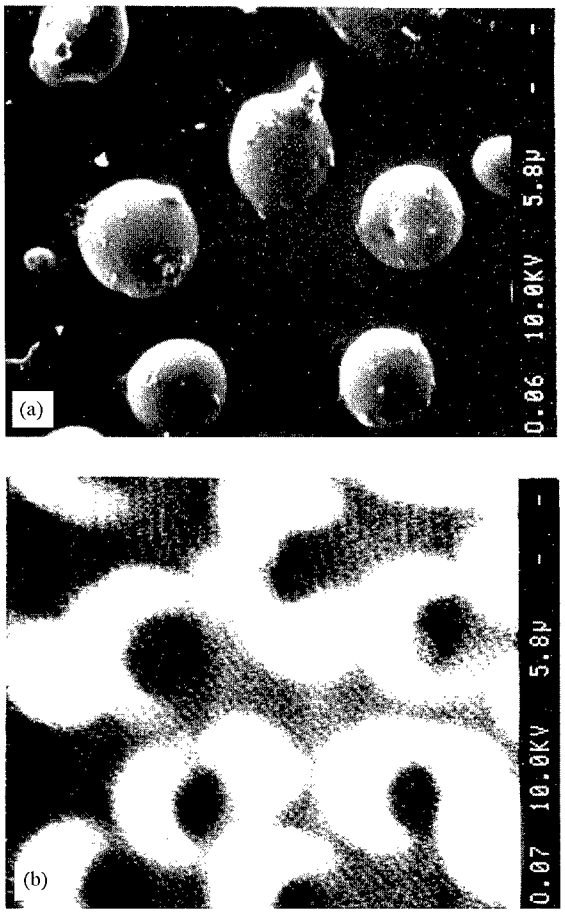

Fig. 1. SEM image of GaN film grown at nitrogen flow rate of 0.4 sccm (a) and CL topograph at 364 nm corresponding to the area of SEM image (b).

emission corresponding to the white area in Fig. 1b was observed. The gray region in Fig. 1b is GaN with weaker band edge intensity. The cause of the nonuniformity of the edge emission may be due to the variation of stoichiometry of GaN. That is, Ga-rich GaN may be grown in close vicinity of the Ga droplet due to Ga diffusion or migration, resulting a formation of N vacancies. The N vacancy is believed to act as a shallow donor. Generally, the luminescence efficiency is proportional to the carrier concentration. Therefore, it is resonable to conclude that the nonuniform CL topograph is due to variations in stoichiometry.

To investigate the properties of the place where the Ga droplets are formed, the GaN film grown under gallium-rich condition was dipped in HCl to remove Ga-droplets. Then, the GaN film was etched in a solution of $NaOH : H_2O_2$. Fig. 2 shows an SEM image of GaN surface which was etched in $NaOH : H_2O : H_2O_2$ (5 : 20 : 5) solution for 30 min with irradiating ultraviolet light from D_2 lamp to the sample surface during etching. The etching rate was about 1 μm/h at room temperature. The dark spots (indicated by a white arrow in Fig. 2) show the trace of Ga-droplets after etching, and etch pits are observed in each dark spot. That is, the Ga-droplets are formed around the etch pits. It is thought that the etch pits are formed by an accelerated etching at chemically weak bonded region such as grain boundary or dislocation. This result shows that the excess atoms may migrate and gather around dislocations or grain boundary.

When the nitrogen flow rate was increased to 1 sccm, the Ga-droplets disappeared in the SEM image; however, the microstructures-like fibroid pattern with the diameter of about 2–5 μm microstructure are observed as shown in Fig. 3a. These microstructures were widely distributed over the GaN surface.

Fig. 3b shows a CL topograph at 364 nm for the same area as shown in Fig. 3a. The microstructures show high intensity of the edge emission. The GaN surface still shows a spatial difference of

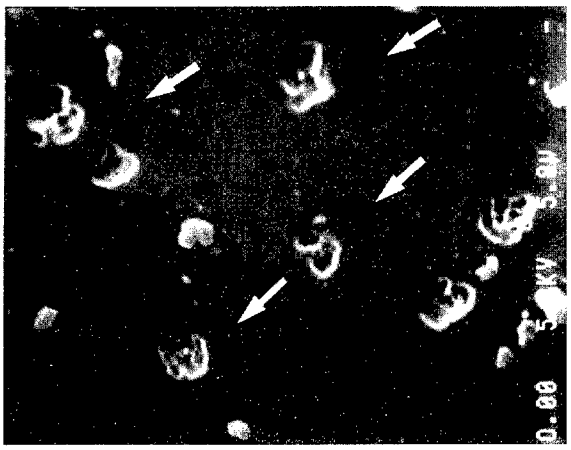

Fig. 2. SEM image of GaN surface etched by $NaOH + H_2O_2$ solution.

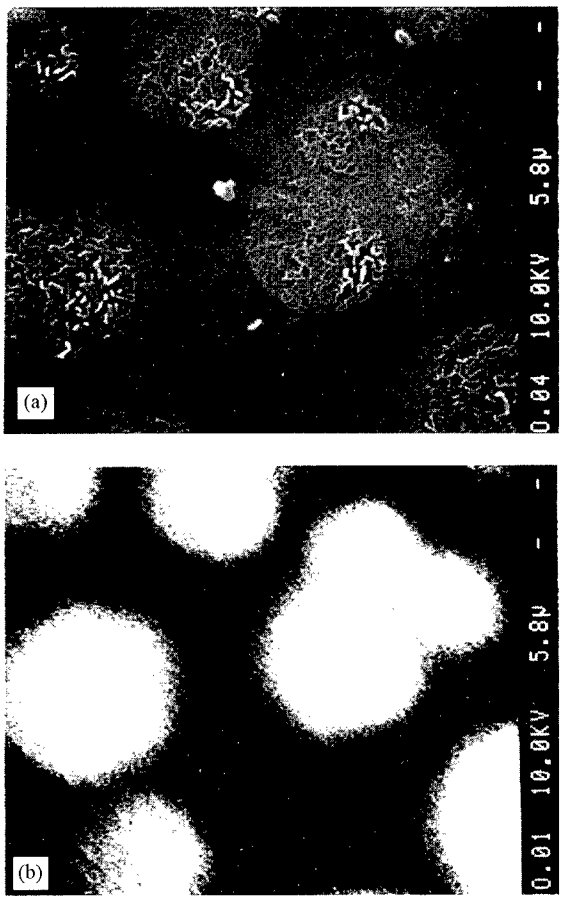

Fig. 3. SEM image of GaN film grown at nitrogen flow rate of 1 sccm (a) and CL topograph at 364 nm corresponding to the area of SEM image (b).

luminescence intensity. The details of the microstructure is not clarified yet; however, the cause of the formation of the microstructure may be supposed to be due to Ga microsegregation. Excess Ga atoms may be trapped at dislocation or grain boundary where the lattice is strained, and the strained region may expand to a distance of a few μm from the dislocation core or grain boundary. Thus, Ga-rich GaN may be grown around dislocation or grain boundary, resulting in the formation of nonuniform CL topograph.

When the nitrogen flow rate increased up to 2 sccm, the microstructures disappeared from the GaN surface, and a faint pattern-like island was observed as shown in Fig. 4a. Though, the CL topograph still shows nonuniformity as shown in Fig. 4b, the bright patch pattern in CL topograph does not to the island pattern. The cause of this nonuniformity of the CL topograph may be a segregation of very small Ga-clusters which hardly affect the crystal structure or surface morphology. The bright area may correspond to a Ga-rich crystal region, and Ga-clusters may gather at the strained area as discussed above. If the cause of the nonuniformity of the CL topograph is due to local variations of stoichiometry induced by Ga

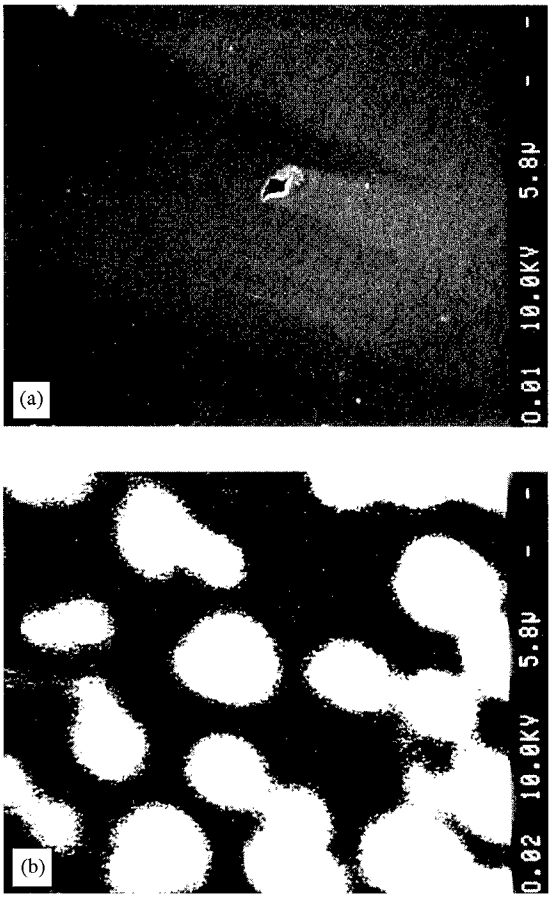

Fig. 4. SEM image of GaN film grown at nitrogen flow rate of 2 sccm (a) and CL topograph at 364 nm corresponding to the area of SEM image (b).

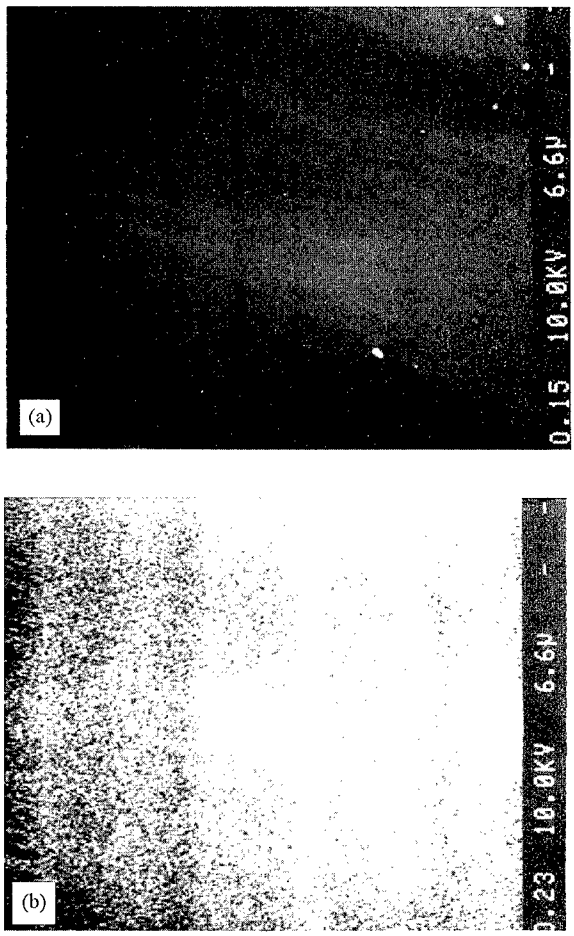

Fig. 5. SEM image of GaN film grown at nitrogen flow rate of 5 sccm (a) and CL topograph at 364 nm corresponding to the area of SEM image (b).

microclusters trapped near the dislocation or grain boundary, the density of the bright spots in the CL topograph may roughly agree with the etch pit density. The density of the bright spot in Fig. 4b is $\sim 10^6/cm^2$, and the average etch pit density of GaN grown under the similar conditions is about $\sim 10^7/cm^2$ [16]. Therefore, it may be possible to think that the cause of the nonuniformity in CL topograph relates with dislocation or grain boundaries.

When the nitrogen flow rate was 5 sccm, the surface morphology was fairly improved and the CL topograph became uniform as shown in Fig. 5a and Fig. 5b. It should be noted that the nitrogen-rich growth condition is favourable to get structurally and optically uniform films.

4. Summary

CL topographs were taken at room temperature at 364 nm from GaN films grown under various V/III ratio and compared with SEM images. The CL topograph was found to be significantly influenced by the V/III ratio during growth. In the GaN films grown under the Ga-rich condition, Ga-droplets were observed by SEM and the intensity of CL from GaN surface in close vicinity to the Ga droplet was strong. With increasing V/III ratio, flat and smooth surfaces were obtained; however, CL topograph showed a patch pattern with a diameter of 2–3 μm. At N-rich condition, the surface morphology was improved and the CL topograph became uniform. The cause of the nonuniform CL topographs may be due to a local variation of stoichiometry induced by Ga droplets or Ga micro-segregation.

References

[1] H. Amano, K. Hiramatsu, M. Kito, N. Sawaki and I. Akasaki, J. Crystal Growth 93 (1988) 379.
[2] F.A. Ponce, B.S. Krusor, J.S. Major, Jr., W.E. Plano and D.F. Welch, Appl. Phys. Lett. 67 (1995) 41.
[3] W.R.L. Lambrecht, B. Segall, J. Rife, W.R. Hunter and D.K. Wickenden, Phys. Rev. B 51 (1995) 13516.
[4] C.H. Hong, D. Pavlidis, S.W. Brown and S.C. Rand, J. Appl. Phys. 77 (1995) 1705.
[5] H. Nakayama, P. Hacke, M.R.H. Kahn, T. Detchprohm, K. Hiramatsu and N. Sawaki, Jpn. J. Appl. Phys. 35 (1996) L282.
[6] Q. Zhu, A. Botchkarev, W. Kim, O. Aktas, A. Salvador, B. Sverdlov, H. Morkoc, S.C.Y. Tsen and D.J. Smith, Appl. Phys. Lett. 68 (1996) 1141.
[7] S.J. Pearton, J.W. Lee and C. Yuan, Appl. Phys. Lett. 68 (1996) 2690.
[8] S. Nakamura, T. Mukai and M. Senoh, Appl. Phys. Lett. 64 (1994) 1678.
[9] T.D. Moustakas and R.J. Molnar, Mater. Res. Soc. Conf. Proc. 281 (1993) 753.
[10] S.H. Cho, T. Maruyama and K. Akimoto, Jpn. J. Appl. Phys. 34 (1995) L1575.
[11] R. Singh, R.J. Molnar, M.S. Unlu and T.D. Moustakas, Appl. Phys. Lett. 64 (1994) 336.
[12] W. Qian, M. Skowronski, M. Degraef, K. Doverspike, L.B. Rowland and D.K. Gaskill, Appl. Phys. Lett. 66 (1995) 1252.
[13] F.A. Ponce, D.P. Bour, W. Gotz and P.J. Wright, Appl. Phys. Lett. 68 (1996) 57.
[14] S.H. Cho, U. Tanaka, K. Hata, T. Maruyama and K. Akimoto, Jpn. J. Appl. Phys. 35 (1996) L644.
[15] S.H. Cho, H. Sakamoto, K. Akimoto, Y. Okada and M. Kawabe, Jpn. J. Appl. Phys. 34 (1995) L236.
[16] S.H. Cho, K. Hata, T. Maruyama and K. Akimoto, J. Crystal Growth 173 (1997) 260.

ELSEVIER

Journal of Crystal Growth 175/176 (1997) 117–121

JOURNAL OF CRYSTAL GROWTH

Studies of GaN layers grown on sapphire using an RF-source

T.G. Andersson[1,*], K. Nozawa, Y. Horikoshi[2]

NTT Basic Research Laboratories, 3-1 Morinosato, Atsugi-shi, Kanagawa 243-1, Japan

Abstract

We have studied the relation between MBE growth parameters and film quality after growth of GaN on the *c*-plane of sapphire using a conventional Ga-source and an RF-source for the excitation of N_2. The growth rate was varied using Ga-flux, determined by RHEED oscillations on GaAs, $r_{GaAs} = 0.1$–0.8 μm/h. The N_2-flux was 0.5–1.5 sccm. Most layers of GaN were grown at 760°C as measured by a pyrometer, while higher temperatures were utilised to determine the dismissal of growth. The RF-power and AlN buffer layer parameters were kept constant. The GaN-thicknesses were 0.2–1 μm/h. For low growth rates of ~50 nm/h, there was a preferential growth of microcrystals in the growth direction which therefore overemphasised the measured film thickness. No film could be grown above 800°C as the desorption rate was too high. For a GaN growth rate of 300 nm/h the sticking coefficient was ~85%. By varying the Ga- and N_2-fluxes it was evident that the film quality, as provided by the photoluminescence spectra, strongly depended on the growth parameters. Photoluminescence peak intensities generally improved with film thickness below 1 μm. In 1 μm thick films, we observed excitonic related peaks close to the band gap as well as peaks 50–60 meV below due to the presence of defects or impurities. We found a strong correlation between growth parameters and optimum growth and therefore the highest layer quality could be obtained only when all parameters were carefully optimised.

1. Introduction

Technical and scientific interests in GaN-based materials is very strong, especially after the recent demonstrations [1] of electrically stimulated emission from GaN in the blue and UV regions of visible light. Studying the detailed growth of GaN and its effect on the material properties is therefore important to understand the conditions for preparing high-quality materials. While there is substantial information about growth by metal organic vapor phase epitaxy (MOVPE), less is known about molecular beam epitaxy (MBE) growth of GaN on sapphire using a radiofrequency (RF) source [2]. Comparing with homoepitaxial MBE-GaAs there are more parameters that influence the GaN-growth. The most important might be the lack of a suitable substrate that match the GaN lattice constant. Sapphire with ~8% lattice mismatch to GaN has shown to provide good wurtzite crystal quality in terms of X-ray diffraction [3]. Depending on the substrate, epitaxial layers can be

* Corresponding author.

[1] Present address: Department of Physics, Chalmers University of Technology and Göteborg University, S-412 96 Göteborg, Sweden. E-mail: f4bta@fy.chalmers.se.

[2] Present address: Department of Electrical Engineering, Waseda University, Japan.

0022-0248/97/$17.00 Copyright © 1997 Published by Elsevier Science B.V. All rights reserved
PII S0022-0248(96)01221-3

made either in zinc blende (after growth on semiconductors) or wurtzite structure (growth on Al_2O_3 or SiC). The latter introduces $\sim$0.2 eV larger [4] band gap than zinc blende and its valence band is split into three subbands.

The GaN growth process in a molecular beam epitaxy system, using a Ga-furnace and an RF-source for nitrogen dissociation, resembles that of solid-source GaAs. In principle, the growth rate is controlled by the Ga-flux and there is Ga-desorption at high substrate temperatures. For vacuum deposition, including MBE, relatively low growth temperatures, below $\sim$800°C, have been reported [5], while VPE methods typically grow at 1000°C and above to generate high-quality layers. Such temperatures provide some difficulty in MBE due to Ga-desorption which increases with growth temperature above $\sim$650°C. This can be compensated by increasing the Ga-flux (and consequently N_2-flux). So far there is no universal relationship available of the MBE-growth parameters in order to obtain optimum material quality. In this work we have studied the growth of GaN on sapphire (0 0 0 1) at growth rates from 50 to 400 nm/h, and in a medium range of growth temperatures, T_g = 600–800°C. In addition, we varied Ga- and N_2-flux at the constant growth temperature of T_g = 760°C, to quantify the sticking coefficient and to investigate their influence on the shape of the photoluminescence (PL) spectra.

2. Experimental procedure

The material was grown in an MBE-system used for combined GaN and GaAs growth. This enabled the easy control of the Ga flux by RHEED oscillation measurements which provided the Ga-flux in terms of the GaAs(0 0 1) growth rate, r_{Ga}^{GaAs}. This is a convenient reference, especially if the GaN material is not homogeneous. Because of the crystallographic difference between GaAs zinc blende and GaN wurtzite structures, respectively, this rate is about 90% higher than that of GaN, r_{Ga}^{GaN}, for a constant Ga-flux. The nitrogen source was a commercial one (Oxford Instruments SAE 25M) supplied by dry N_2-gas vapourised from liquid nitrogen.

Sapphire substrates were mounted In-free and their backside had a pre-deposited thin layer of Mo facing the substrate heater filaments. We used the pyrometer temperature as the growth temperature T_g. Since the desired temperature for GaN growth is generally higher than that of GaAs, a high thermal load is dispatched into the growth chamber. Due to excess radiation from the substrate holder there could also be a large difference between the growth temperature and the thermocouple temperature T_{TC} behind the substrate. At T_g = 760°C we found T_{TC} was 800°C. Comparing our data to earlier published work introduces uncertainties, since in some cases there is no distinction reported between T_{TC} and T_g. Before growth, the substrate was thermally annealed under UHV-conditions.

The actual growth of GaN was carried out after a short nitridation of the substrate surface at 400°C followed by the deposition of a thin 25 + 25 nm thick AlN buffer layer grown in a two-step process at 400 and 500°C, respectively. In the nitridation, active nitrogen species react with surface atoms which on the sapphire replace the surface oxygen with nitrogen [7]. Strictly speaking the AlN layer consists of two structural parts: a thin layer ($\sim$5 nm) given by the initial nucleation and a thicker part having crystallites with their (0 0 0 1)-axis parallel to the sapphire (0 0 0 1) axis [6]. The detailed role of the buffer layer is unclear. In strongly lattice-mismatched systems its presence is necessary for growth of high-quality materials [8]. Part of the substrate surface was masked in order to measure the film thickness after growth. A turbomolecular pump kept the N_2-pressure at about $(2–6) \times 10^{-5}$ Torr for an N_2-flux of 0.5–1.5 sccm for an RF-power of 300 W. The GaN layers were inspected by optical microscopy, thicknesses were measured by a surface profiler, the structure by X-ray diffraction, surface morphology by SEM and AFM and the optical quality was studied by PL at 300 and 9 K using a He–Cd laser.

3. Results and discussion

3.1. Growth rate

Growth rate data are shown in Fig. 1 for N_2-flux of 0.5 sccm. In general, the GaN growth rate

r_{Ga}^{GaN} was considerably lower than that of GaAs and also below the expected, $r_{Ga}^{GaN} = 0.53 r_{Ga}^{GaAs}$ for Al_2O_3(0 0 0 1) and GaAs(0 0 1), respectively. The factor of 0.53 comes from the crystallographic difference between the zinc blende and wurtzite structures. At a very low growth rate, $r_{Ga}^{GaAs} = 0.1$ μm/h, the value of r_{Ga}^{GaN} was ~50% higher than expected for the wurtzite structure. Micrographs by SEM and AFM on ~200 nm thick films showed GaN microcrystallites with sizes from ~30 to 300 nm. Increasing r_{Ga}^{GaAs} to the interval 0.2–0.5 μm/h the GaN growth rate was found to be 45% of r_{Ga}^{GaAs} indicating an apparent sticking coefficient of ~85%; see Fig. 1. In this case the growth on the buffer layer is characterised by truncated pyramidal mesas seen in SEM and AFM as well by other investigations [9]. The fact that the dependence is linear above 0.2 μm/h suggests a fairly homogeneous growth, also supported by SEM measurements. The value of r_{Ga}^{GaN} saturates for $r_{Ga}^{GaAs} > 0.5$ μm/h because of saturation in nitrogen-over-gallium supply.

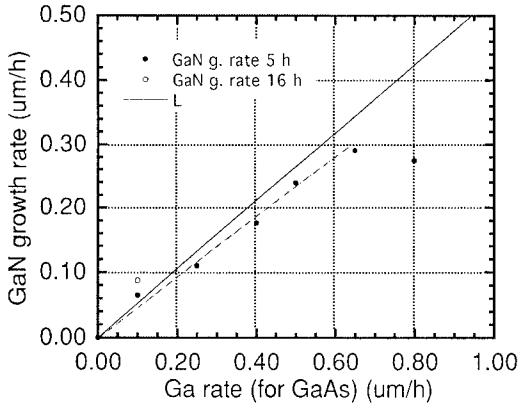

Fig. 1. The growth rate of GaN on sapphire (0 0 0 1) as a function of the growth rate on GaAs(0 0 1) using the same Ga-source temperature and calibrated by RHEED oscillations. Thicknesses were measured by a surface profiler. A separate study on the lateral film inhomogeneity was made indicating less than 7% maximum error from middle of film to one corner.

3.2. Growth temperature

In the second series, the effect of the growth temperature was addressed. No clear dependence of r_{Ga}^{GaN} on growth temperature could be established for $r_{Ga}^{GaAs} = 0.1$ μm/h in the range 700–780°C, but a reduction at 800°C. Growth during 5 h provided layer thicknesses of approximately 300 nm. The X-ray analysis, *θ–2θ*, showed improved material quality with temperature as the FWHM of the GaN peak decreased from approximately 100 arcmin at $T_g = 600$°C to around 60 arcmin at 730–790°C, while the buffer layer AlN peak width decreased from 100 arcmin at 730°C to 20 arcmin at 815°C. The peak widths are relatively large since the layers are thin. The most important information, however, is the clear trend of reduction in peak width with temperature. The GaN growth rate was drastically reduced for growth temperatures above 800°C due to Ga desorption and only the AlN-peak was detected. Growth at 740°C gave the best film in terms of PL-intensity. Thus, for the given growth parameters, it was an optimum growth temperature where the decline in PL-emission above 785°C might be an effect of Ga-desorption or reduction of III/V-ratio. One conclusion is that the growth parameters are interrelated such that the parameter window for best material quality is quite narrow.

3.3. Influence of Ga-rate and N_2-flux on PL-emission

In this series, 0.2–1 μm thick layers were grown and T_g was 760°C, i.e. well below the rapid reduction of sticking at 800°C. The growth rate and N_2-flux were varied while the other growth parameters were constant. In general, the PL-emission at ~2.2 eV, involving deep levels, was typically very low for the measurement temperature, 9 K. In the near band gap region, five different peaks were observed from 3.24 to 3.475 eV, with relative peak intensity depending on growth parameters. For film thicknesses 200–300 nm, a peak at 3.42 eV possibly related to defects, usually dominated the intensity of the exciton related peak at 3.475 eV. Increasing the growth rate or the layer thickness improved the excitonic recombination. The PL emission from two layers with similar thickness, ~1 μm, but grown at different rates, $r_{Ga}^{GaAs} = 0.1$ and 0.4 μm/h, respectively is presented in Fig. 2. As shown, there are one or two exciton related peaks

at 3.472 and 3.475 eV, respectively and one or several peaks 50–200 meV below the band gap energy which are associated with structural defects, donor-valence band recombination (D^0, h^+) and recombinations including shallow acceptors [10, 11]. The lower growth rate provided a higher intensity and the high energy peak at 3.475 eV. Increasing the rate reduced the overall PL-intensity and shifted the peak somewhat to 3.472 eV. Both peaks have been observed simultaneously in layers grown above 0.4 μm/h. In Fig. 2 the FWHM is 27 meV for 3.424 eV and 13 meV for 3.475 meV, while the best value observed was ~3 meV. The origin of the highest energy peaks is not the A- and B-exciton recombinations [12] shifted due to strain [13], since there was no indication of shift between different layers and not with thickness. It is more likely that the 3.475 eV peak is the neutral-donor-bound exciton (D^0, X), also called the I_2-line [14–16]. The origin of the corresponding line for higher growth rate I_x (shifted relative to I_2) is not known. It can be related to a structural defect or incorporation of As (or another unintentional impurity) in the GaN layers since its intensity increases with growth rate. The relative intensity between I_x and I_2 is always less than 2 as I_2 is usually a shoulder on the high-energy side when I_x is dominating. As shown in Fig. 2 there is also another peak, 50–60 meV below I_x and I_2, respectively, which we denote as a "defect" peak. The ratio between them and the I-peaks depends on the growth parameters. We used this ratio as a fingerprint of the material quality. This is quantified in Fig. 3 by plotting the ratio between the near band gap peaks at 3.472–3.475 eV and the intensity of the largest observed "defect" peak, I_{ex}/I_{def}. Some variation from position-to-position was observed but much less than previously reported [2]. As shown, this ratio varied strongly with growth rate (despite the increasing film thickness at the used constant growth time). The film thickness increased with growth rate from ~ 265 nm to 2.1 μm. The corresponding increase in PL-emission with growth rate reflects improvement in film quality with film thickness only up to 0.4 μm/h (~1 μm). The decline for higher rates is the lack of N* species limiting the growth rate and creating N-vacancies in the layer. To confirm this a similar study was made with N_2-flow rate as a parameter keeping the other parameters constant. This is shown in Fig. 4 for the highest growth rate used in Fig. 3. The quality improves with N_2-flow and eventually decline for excess supply of nitrogen.

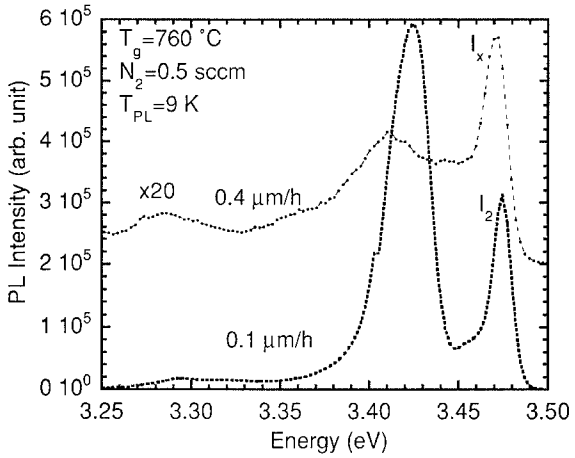

Fig. 2. The photoluminescence spectra from two ~1 μm thick layers grown at different growth rates but otherwise similar growth parameters as indicated in the text. The spectra shift of peak positions depending on the growth rate.

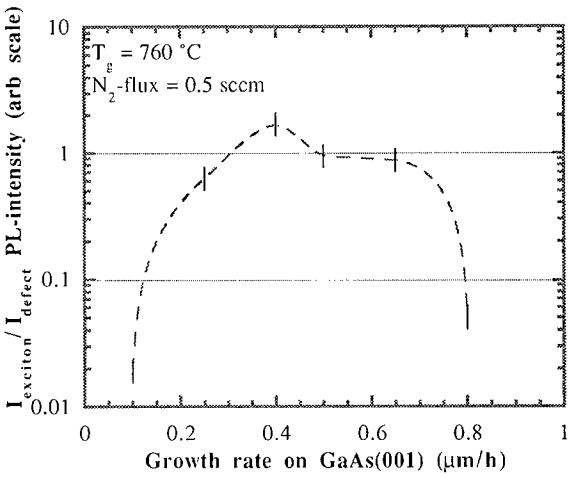

Fig. 3. The relative PL-intensities between an exciton related peak and a defect related peak, I_{ex}/I_{def} (see text for details) as a function of the Ga-flux (represented by GaAs growth rate from RHEED oscillations). The growth temperature was 760°C and the nitrogen flux 0.5 sccm. The best band-gap-related PL emission is obtained for an equivalent GaAs growth rate of 0.4–0.65 μm/h.

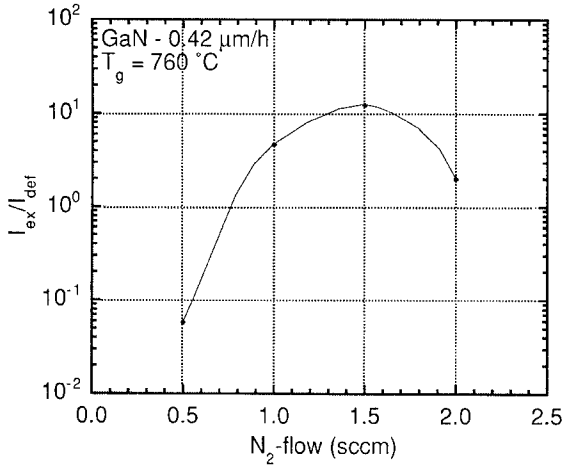

Fig. 4. The relative PL-intensities, I_{ex}/I_{def} (as in Fig. 3), as a function of the N_2-flux for $T_g = 760°C$ and $r_{Ga}^{GaAs} = 0.8$ μm/h (GaN growth rate is 0.42 μm/h). The best film quality (i.e. best PL conditions) is obtained for an N_2-flux of 1.5 sccm.

The results of Figs. 3 and 4 support the previous conclusion on the relatively strong interrelation of the growth parameters.

In summary, we studied MBE-growth of thin GaN films on sapphire substrates using the Ga-flux from the homoepitaxial GaAs RHEED oscillations as a reference. X-ray and photoluminescence measurements were made. We related variations in PL-spectra to growth parameters represented by growth temperature, growth rate and gallium/nitrogen supply. The X-ray peak widths from the GaN and the AlN buffer layer were very sensitive to growth temperature. We believe that high-quality layers can be made only within a quite narrow "parameter window" of growth parameters.

Acknowledgements

We acknowledge valuable discussions with F. Scholz and Y. Hirayama.

References

[1] S. Nakamura, M. Senoh, S. Nagahama, N. Iwasa, T. Yamada, T. Matsushita, H. Kiyoku and Y. Sugimoto, Jpn. J. Appl. Phys. 35 (1996) L74.
[2] C. Trager-Cowan, K.P. O'Donnell, S.E. Hooper and C.T. Foxon, Appl. Phys. Lett. 68 (1996) 355.
[3] T. Sasaki and S. Zembutsu, J. Appl. Phys. 61 (1987) 2533.
[4] D.E. Lacklison, J.W. Orton, I. Harrison, T.S. Chen, L.L. Jenkins, C.T. Foxon and S.E. Hooper, J. Appl. Phys. 78 (1995) 1838.
[5] R.C. Powell, N.-E. Lee, Y.-W. Kim and J.E. Greene, J. Appl. Phys. 73 (1993) 189.
[6] I. Akasaki, H. Amano, Y. Koide, K. Hiramatsu and N. Sawaki, J. Crystal Growth 98 (1989) 209.
[7] K. Uchida, A. Watanabe, F. Yano, M. Kouguchi, T. Tanaka and S. Minagawa, J. Appl. Phys. 79 (1996) 3487.
[8] K. Hiramatsu, S. Itoh, H. Amano, I. Akasaki, N. Kuwano, T. Shiaishi and K. Oki, J. Crystal Growth 115 (1991) 628.
[9] W. Kim, Ö. Aktas, A.E. Botchkarev, A. Salvador, S.N. Mohammad and H. Morkoc, J. Appl. Phys. 79 (1996) 7657.
[10] S. Strite and H. Morkoc, J. Vac. Sci. Technol. B 10 (1992) 1237.
[11] G.D. Chen, M. Smith, J.Y. Lin, H.X. Jiang, A. Salvador, B.N. Sverdlov, A. Botchkarev and H. Morkoc, J. Appl. Phys. 79 (1995) 2675.
[12] B. Monemar, Late News Abstract at TWN 95 (Topical Workshop on III–V Nitrides) Nagoya, 1995.
[13] K. Nozawa and Y. Horikoshi, Jpn. J. Appl. Phys. 32 (1993) 628.
[14] M. Illegems, R. Dingle and R.A. Logan, J. Appl. Phys. 43 (1972) 3797.
[15] J.I. Pankove, Mater. Res. Soc. Symp. Proc. 97 (1987) 409.
[16] G.D. Chen, M. Smith, J.Y. Lin, H.X. Jiang, M. Asif Khan and J.C. Sun, Appl. Phys. Lett. 67 (1995) 1653.

ELSEVIER

Journal of Crystal Growth 175/176 (1997) 122–124

JOURNAL OF CRYSTAL GROWTH

Blue and green electroluminescence from GaN/InGaN heterostructures

R. Averbeck*, H. Tews, A. Graber, H. Riechert

Siemens AG, Corporate Research and Development, D-81730 Munich, Germany

Abstract

GaN/InGaN pn-junctions were grown by molecular beam epitaxy. Depending on the In content bright blue (470 nm) or green (513 nm) electroluminescence was observed at room temperature.

PACS: 42.80; 73.40.L; 68.55; 78.60.F

All commercially available GaN based light emitting diodes (LEDs) are presently fabricated by metalorganic vapour phase epitaxy [1, 2]. Up to now only GaN homojunctions [3] or parts of an LED structure [4] have been grown by molecular beam epitaxy (MBE). Our paper presents the first report of bright blue and green electroluminescence from GaN/InGaN heterostructures grown entirely by MBE.

GaN and InGaN layers were grown by MBE on *c*-plane oriented sapphire substrates using elemental sources for Ga and In and an RF plasma source for nitrogen. All layer sequences were started with a thin GaN buffer layer grown at 800°C. The growth temperatures of GaN and InGaN were 720°C and 700°C, respectively. We realized InGaN layers with In contents exceeding 40%, as determined by X-ray diffraction. Nominally undoped GaN layers show room temperature hall mobilites of over 250 $cm^2/(V\,s)$ and an electron density of about $2 \times 10^{17}\ cm^{-3}$. Conventional effusion cells with Si and Mg were used for n- and p-type doping. No annealing or other treatment was required to activate the dopants. As-grown GaN : Mg yields a hole concentration of $2.5 \times 10^{17}\ cm^{-3}$ at a hole mobility of 10 $cm^2/(V\,s)$.

Fig. 1 shows the LED test structure used for this study. It consists of 1000 nm GaN : Si followed by 30 nm of undoped InGaN and 200 nm GaN : Mg. Circular Ti/Au contacts with 200 μm diameter were evaporated onto the wafer after growth. Applying a DC voltage between two contacts yields a symmetric *I-V*-curve of two pn-junctions with opposite polarity connected in series. At voltages below 5 V no significant current is measured due to the high sheet resistivity of the thin GaN : Mg

* Corresponding author.

0022-0248/97/$17.00 Copyright © 1997 Elsevier Science B.V. All rights reserved
PII S0022-0248(96)01009-3

layer. At voltages above 10 V leakage through the reverse biased diode leads to a superlinear increase of the current and electroluminescence is observed under the contact of the forward biased diode.

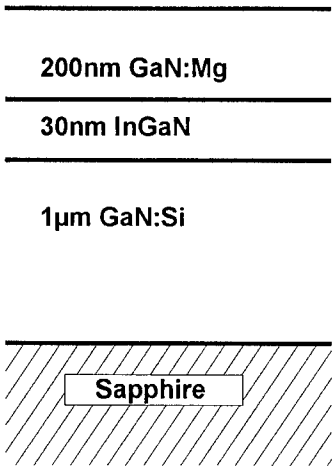

Fig. 1. Layer sequence of the LED test structure used in this study.

Fig. 2 presents the electroluminescence spectrum of an LED test structure with an In content of 27% according to X-ray diffraction. It was taken at a current of 20 mA at room temperature. Intensive blue light is observed, visible even during daylight. The peak position of 470 nm (2.64 eV) coincides with the photoluminescence signal. From the measured In content of 27% one would expect a bandgap of 2.80 eV [1] showing that an approximately 160 meV deep level is involved in the optical transition. This may be due to Mg impurities since Mg is used for the p-type doping [5]. The electroluminescence spectrum displayed in Fig. 3 was taken from a sample with an In content of 40%. The emission wavelength of 513 nm (2.42 eV) yields bright green light. The peak position is also in accordance with photoluminescence measurements and lies about 160 meV below the expected bandgap of 2.58 eV [1].

In conclusion we have shown that MBE is a viable technique to grow GaN/InGaN heterostructures for LED applications. High In incorporation due to low growth temperatures and efficient p-type doping without post growth treatment are clear advantages compared to currently used growth techniques.

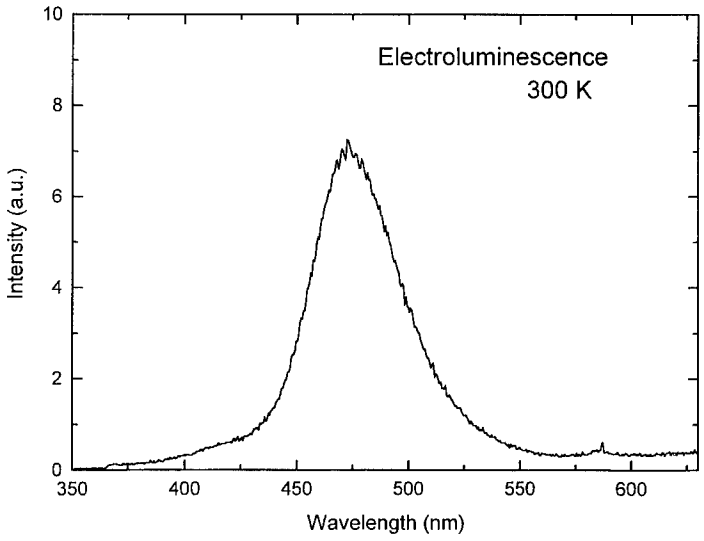

Fig. 2. Blue electroluminescence from a GaN/$In_{0.27}Ga_{0.73}N$ pn-structure at room temperature.

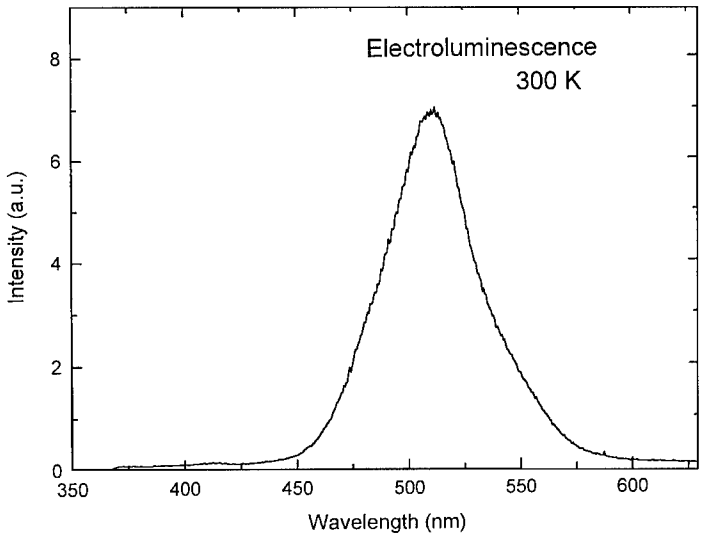

Fig. 3. Green electroluminescence from a GaN/$In_{0.40}Ga_{0.60}N$ pn-structure at room temperature.

References

[1] S. Nakamura, J. Vac. Sci. Technol. A 13 (1995) 705.
[2] Cree Research Inc., V.A. Dmitriev, reported at the 1st European GaN workshop, Rigi, Switzerland (1996), unpublished.
[3] R.J. Molnar, R. Singh and T.D. Moustakas, Appl. Phys. Lett. 66 (1995) 268.
[4] H. Sakai, T. Koide, H. Suzuki, M. Yamaguchi, S. Yamasaki, M. Koike, H. Amano and I. Akasaki, Jpn. J. Appl. Phys. 34 (1995) 1429.
[5] W. Götz, N.M. Johnson, J. Walker, D.P. Bour, H. Amano and I. Akasaki, Appl. Phys. Lett. 67 (1995) 2666.

ELSEVIER

Journal of Crystal Growth 175/176 (1997) 125–128

JOURNAL OF CRYSTAL GROWTH

Zinc blende GaN grown by radio frequency plasma assisted molecular beam epitaxy

H.D. Cho[a], N.H. Ko[a], S.H. Park[a], T.W. Kang[a,*], J.W. Han[b], K.S. Eom[c], S.H. Won[d], K.S. Jung[d]

[a] *Department of Physics, Dongguk University, 3-26 Pil-Dong, Chung-Ku, Seoul 100-715, South Korea*
[b] *Department of Physics, Sejong University, 98 Gunja-Dong, Kwangjin-Ku, Seoul 449-701, South Korea*
[c] *Uiduck University, San 50 Yugeom, Kangdong, Kyungju, Kyungbuk, South Korea*
[d] *Department of Electronic Engineering, Kyunghee University, 1 Seocheon-Ri, Kiheung Eup, Yongin-Kun, Kyungki-Do 499-701, South Korea*

Abstract

We investigate the influence of nitridation on the growth of GaN films. We present undoped α- and β-GaN on 3C-SiC coated Si (0 0 1) with and without nitridation, respectively, using radio frequency plasma assisted molecular beam epitaxy. In the case without nitridation, the RHEED (2 × 2) streak pattern at both [1 0 0] and [1 1 0] azimuths shows that the high-quality zinc blende GaN films are grown. The X-ray diffraction (XRD) shows that (0 0 2) zinc blende GaN is observed at $2\theta = 39.53°$. At 10 K, PL of the zinc blende GaN is dominated by band edge emission at 3.362 eV. On the other hand, α-GaN films are obtained it nitridation that exhibit the (0 0 0 2) wurtzite GaN peak at 34.25° in the XRD measurement.

1. Introduction

Recently, interest in the group-III nitride semiconductors has increased because of their potential for the development of light-emitting devices in the visible and UV spectral regions, high-temperature electronics and high power microwave devices. Bulk single crystals or wafers are not yet available and the choice of adequate substrates for heteroepitaxy has been a nontrivial problem for experimentalists. Al_2O_3 is commonly used but its large misfit with respect to GaN (14–16%) has been a limiting factor in the quality of the grown epilayers. There have been several reports that the nitridation plays an important role in the growth of GaN on Al_2O_3 substrates. Most of films had a wurtzite phase [1–3]. However, growing zinc blende GaN for LD fabrication is of interest and there have been reports using 3C-SiC substrates for the growth of zinc blende GaN [4–9]. The equilibrium crystal structure for III–V nitrides is the wurtzite structure while GaN and InN have been observed to have the zinc blende structure when grown on a cubic substrate. Cubic GaN has been grown on (0 0 1) GaAs, 3C-SiC, MgO, and (0 0 1) Si [10]. Therefore, in this study before growing GaN on 3C-SiC-coated Si (0 0 1), we investigated how the

* Corresponding author.

0022-0248/97/$17.00 Copyright © 1997 Elsevier Science B.V. All rights reserved
PII S0022-0248(96)00864-0

nitridation has an influence on the growth of GaN films. As a result, we report undoped wurtzite and zinc blende GaN on 3C-SiC-coated Si (0 0 1) with and without nitridation, respectively, using molecular beam epitaxy (MBE) equipped with a reactive nitrogen ion source operated at 13.56 MHz.

2. Experimental procedure

The growth studies were carried out on 3C-SiC coated Si (0 0 1) substrates. By using a RF plasma discharge, nitrogen free radical source, we obtained α- and β-GaN epilayers with and without nitridation, respectively. The β-SiC-coated Si substrates employed in this study were etched in a HF solution and once in the growth chamber were heated to 750°C for about 10 min to desorb the oxide layers. A two-stage growth process was employed in which growth was initiated at a substrate temperature of 530°C and then the temperature was increased to 600°C. A forward RF plasma power of 180–200 W was supplied to the RF plasma discharge, nitrogen free radical source, and the background nitrogen partial pressure in the MBE growth chamber was 5×10^{-4} Torr. GaN films were grown on 3C-SiC substrates at about 600°C. Prior to the film growth, the substrate surfaces were exposed to an activated nitrogen beam for 7–10 min to be completely covered with nitridated layers, and then GaN was grown with a Ga molecular beam from an effusion cell and an activated nitrogen beam from RF plasma source. During the growth, the surfaces were monitored by in-situ reflection high-energy electron diffraction (RHEED) with a 30 keV beam. The crystallinity of the GaN epilayers obtained was characterized by X-ray diffraction (XRD). Photoluminescence (PL) measurements were carried out at 10K using a 325 nm line of a He–Cd laser, model IKI 3552R-G.

3. Results and discussion

The resulting RHEED pattern on the β-SiC-coated Si (0 0 1) substrate showed Kikuchi lines indicative of the good crystalline quality of the substrate in the [1 1 0] azimuth after the surface pretreatment at 750°C. A streaky, unconstructed pattern was observed. When β-GaN films were grown on 3C-SiC as the buffer layer at 530°C, immediately the streaky β-SiC pattern was replaced by the spotty pattern. But as the growth temperature was increased to 600°C, one-half-order diffraction lines appeared in both the [1 1 0] and [1 0 0] azimuths, indicative of the occurrence of streaky (2×2) surface reconstruction. The RHEED pattern recorded in both the [1 1 0] and [1 0 0] azimuths showed that zinc blende GaN without nitridation was grown with the atomically smooth

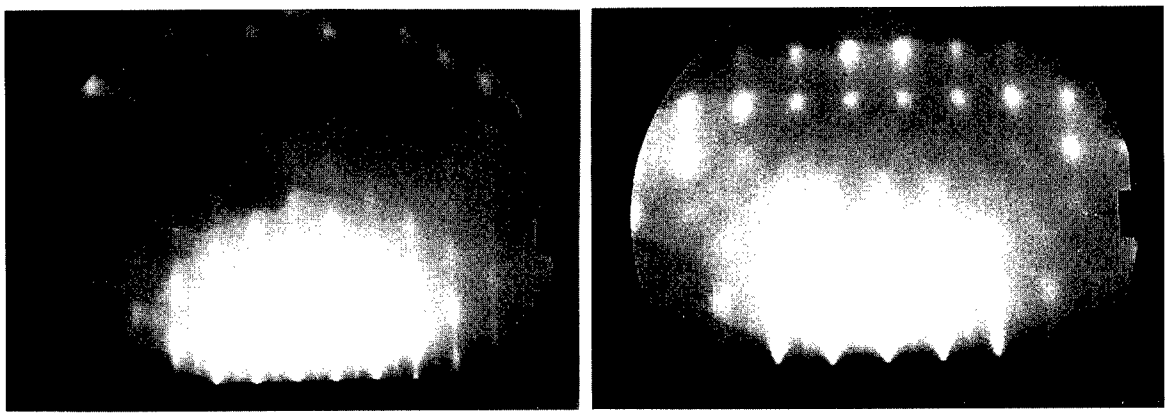

Fig. 1. RHEED patterns of β-GaN grown on 3C-SiC at 600°C: (a) [1 1 0], (b) [1 0 0].

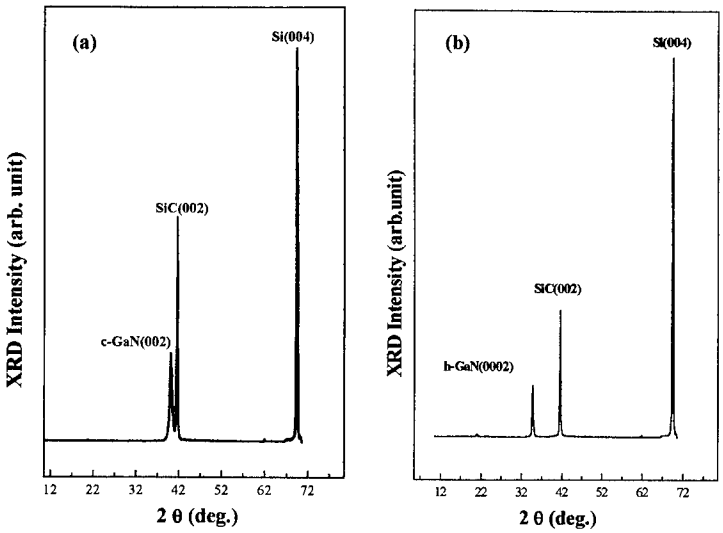

Fig. 2. X-ray diffraction of GaN grown on 3C-SiC at 600°C with and without nitridation.

and flat surface nature (Fig. 1a and Fig. 1b). The structural evidence for the growth of α- and β-GaN was confirmed by means of X-ray diffraction (XRD). The typical diffraction spectrum recorded from two different samples are illustrated in Fig. 2a and Fig. 2b. As can be seen from the Fig. 2a only a peak associated with (0 0 2) zinc blende GaN reflection at about $2\theta = 40°$ in the non-nitrided film is evident in the spectrum. A reflection from hexagonal GaN was not observed. It could be confirmed that the above XRD data together with RHEED during growth indicated the GaN films to be purely zinc blende. In the case of GaN grown with nitridation, Fig. 2b showed that hexagonal GaN (0 0 0 2) peak at around 34° can be observed. The low temperature (10 K) PL spectra of non-nitrided zinc blende GaN film revealed near band edge emission at 3.362 eV (a), as shown in Fig. 3 in which has been attributed to an intrinsic/bound excitons and 3.311 eV (b) was associated with a donor–acceptor pair recombination [11]. Zinov'ev et al. have reported that ~3.25 eV (c) is attributed to radiative impurity-related transition ($E_{e\text{-}h}$) [12]. Also, based on the optical data for β-GaN from Okumura et al., we believe that 3.182 eV (d) is attributed to the emission related with impurity level [7].

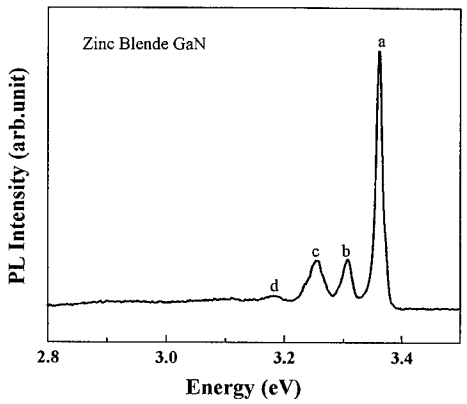

Fig. 3. PL spectra of β-GaN measured at 10 K.

4. Conclusions

We presented the α- and β-GaN films grown on 3C-SiC coated Si (0 0 1) substrates with and without nitridation, respectively, by molecular beam epitaxy (MBE) using radio frequency plasma discharge, nitrogen free radical source. The XRD peak of α- and β-GaN films was observed at approximately 34° and 40° with and without nitridation, repectively. 10 K PL spectra showed that β-GaN

film without nitridation revealed near band edge emission at 3.362 eV. Further investigation for the α-GaN films according to the nitridation will be studied.

Acknowledgements

This work was supported in part by the Korea Science and Engineering Foundation through the SPRC at Junbuk National University in 1996.

References

[1] D.E. Lacklison, J.W. Orton, I. Harrison, T.S. Cheng, L.C. Jenkins, L.C. Foxon and S.E. Hooper, J. Appl. Phys. 78 (1995) 1838.
[2] T. Sasaki and T. Matsuoka, J. Appl. Phys. 64 (1988) 4531.
[3] Z. Sitar, L.L. Smith and R.F. Davis, J. Crystal Growth 141 (1994) 11.
[4] M.J. Paisley and R.F. Davis, J. Vac. Sci. Technol. A 11 (1993) 18.
[5] J.G. Kim, A.C. Frenkel, H. Liu and R.M. Park, Appl. Phys. Lett. 65 (1994) 91.
[6] H. Liu, A.C. Frenkel, J.G. Kim and R.M. Park, J. Appl. Phys. 74 (1993) 6124.
[7] H. Okumura, S. Yoshida and T. Okashisa, Appl. Phys. Lett. 64 (1994) 2997.
[8] M.J. Paisley, Z. Sitar, J.B. Posthill and R.F. Davis, J. Vac. Sci. Technol. A 7 (1989) 701.
[9] H. Okumura, S. Misawa, T. Okahisa and S. Yoshida, J. Crystal Growth 136 (1994) 1361.
[10] S. Strite and H. Morkoc, J. Vac. Sci. Technol. B 10 (1992) 1237.
[11] C.H. Hong, D. Pavlidis, S.W. Brown and S.C. Rand, J. Appl. Phys. 77 (1995) 1705.
[12] N.N. Zinov'ev, A.V. Andrianov, B.Y. Averbukh, I.D. Yaroshetskii, T.S. Cheng, L.C. Jenkins, S.E. Hooper, C.T. Foxon and J.W. Orton, Semicond. Sci. Technol. 10 (1995) 1117.

ELSEVIER

Journal of Crystal Growth 175/176 (1997) 129–133

JOURNAL OF CRYSTAL GROWTH

Initial growth stage of GaN on Si substrate by alternating source supply using dimethyl-hydrazine

Akihiro Hashimoto*, Yoshitaka Aiba, Takanori Motizuki, Mitugu Ohkubo, Akio Yamamoto

Department of Electrical and Electronics Engineering, Fukui University, Bunkyo 3-9-1, Fukui 910, Japan

Abstract

Alternating source supply mehtod of Ga and N sources is proposed to control the initial nitridation stages for the direct growth of GaN on Si. The initial growth stages under the alternating source supply are characterized by the X-ray photoelectron spectroscopy and the atomic force microscope. A suppression effect for the nitridation of Si surface by an excess Ga supply is investigated. The systematic analysis of the spectra shows that the Ga atoms play an important role in both the removal of Si native oxides and the suppression of the nitridation during the initial growth stages. The atomic force microscopic images show that the surface morphologies depend on the substrate temperature of the initial growth stages. The surface morphology of the sample grown at 500°C is smoother than the one grown at 600°C. This implies that there is a possibility to realize the growth conditions for the pseudo Stranski–Krastanov growth mode without Si nitridation at the initial stages in a low temperature region in the alternating source supply method for the direct growth of III–V nitrides on Si.

PACS: 81.15.Hi

Keywords: Initial growth stage; GaN on Si; Alternating source supply; Dimethyl-hydrazine

1. Introduction

Growth of III–V nitride compound semiconductors onto a Si substrate offers a very attractive potential to the future of optoelectronic devices in silicon-based integrated circuits such as optoelectronics integrated circuits (OEIC) [1]. Recently, we have succeeded in the growth of InN single crystal layers on Si (1 1 1) substrates by metal organic chemical vapor deposition (MOCVD) using a GaAs intermediate layer grown by molecular beam epitaxy (MBE) [2]. However, the direct growth of III–V nitrides onto the Si substrate is desirable from the viewpoint of device applications, if it is possible to obtain high crystal quality films. However, there are some problems to be solved in the direct growth of III–V nitrides onto the Si substrates. Especially, it is pointed out that the

* Corresponding author.

0022-0248/97/$17.00 Copyright © 1997 Elsevier Science B.V. All rights reserved
PII S0022-0248(96)00979-7

initial nitridation of the Si surfaces would prevent the following epitaxy after the initial stages from obtaining high quality III–V nitrides on Si [3]. It is well known in the case of other III–V compound semiconductors such as GaAs on Si substrates that the initial growth stage plays an important role in the following growth process and the crystal quality [4]. Therefore, it is essential to control the nitridation in the initial stages to obtain the high quality III–V nitride films directly grown on the Si substrates. There are some techniques to control the initial nitridation of Si and/or the growth stages such as using the low temperature GaN buffer layer proposed by Lei et al. [1]. However, the nitridation during the initial low temperature buffer layer growth is not yet fully understood. Recently, Uchida et al. revealed by the atomic force microscopic (AFM) observations that the initial nitridation proccess of the α-Al_2O_3 consists of three stages and that the initial nirtidation stage also play an important role in obtaining the high quality films even on the α-Al_2O_3 substrates that have been considered to have rather stable surface structure [5]. As the clean Si surface made in ultra-high vacuum conditions maybe more reactive than the α-Al_2O_3 surface, it becomes necessary to find out the control parameters in the initial stages to obtain a high crystal quality film on a Si substrate. In this paper, we propose the alternating source supply method using Ga and dimethyl hydrazine (DMHy) to control the initial nitridation process of the Si substrates.

2. Experimental procedure

Nitridation experiments were carried out by the metal organic molecular beam epitaxial (MOMBE) system using trimethyl gallium (TMG) and DMHy. Si (1 1 1) wafers, on which are deposited about 0.5 μm Si buffer layers in an Si-MBE system annealing at 1000°C after the Si depositions, were used as the substrates after the conventional HF etching to remove the native oxide. The beam-equivalent pressure of the DMHy gas was 2×10^{-6} Torr and it was sufficiently high for the nitridation of the GaAs substrates in our system. Alternating source supply at the first step of the growth was maintained by using the Ga sources and the DMHy by shutter and valve controls. In the present work, the Ga source TMG was supplied at 500°C to the Si substrates and the total amounts of supplied Ga at the first step were varied from 1 to 10 monolayers (ML) to investigate the effects of the initial supplied Ga atoms for the nitridation process by the DMHy. Typical initial nitridations by the DMHy was peformed for 2 min with 2 min time interval after the Ga supply. Some samples consisted of thin GaN growth layers of 40 ML thickness obtained by the simultaneous supply of TMG and DMHy for 20 min after the initial stages. The temperature dependence of the initial nitridations was also investigated at 500°C and 600°C.

X-ray photoelectron spectroscopic (XPS) measurements by using Al $K\alpha_{1,2}$ monochromatized radiation were carried out to characterize the initial nitridation processes by the alternating source supply method. We scaned the regions of Si_{2p}, C_{1s}, N_{1s}, O_{1s} and Ga_{2p} levels in the XPS measurements. The atomic force microscopic (AFM) observations in atmosphere were also performed by the contact mode to investigate the surface morphologies of the grown films. Scan area and force reference in the AFM observations were about 1000 nm × 1000 nm and -0.087×10^{-9} N, respectively.

3. Results and discussion

Fig. 1 shows the Si_{2p} XPS spectra corresponding to (a) Si substrate just after the HF etching, (b) Si substrate exposed by DMHy beam and (c) Si substrate exposed by DMHy beam after 1 ML TMG supply, respectively. The peaks at 99, 102 and 103.4 eV correspond to Si–Si, Si–N and Si–O bonds, respectively. It can be easily seen in Fig. 1b that there is a strong peak compared with Fig. 1a at about 103 eV which is between the Si–N and the Si–O bonds. This peak may be due to the coupling of the contributions from the Si–N bonds formed by the DMHy exposure for 2 min and from the Si–O bonds of the native Si oxide formed during the sample preparations such as mounting on the Mo blocks for the MOMBE system. Because the N_{1s} signal at 398 eV can also be observed in the

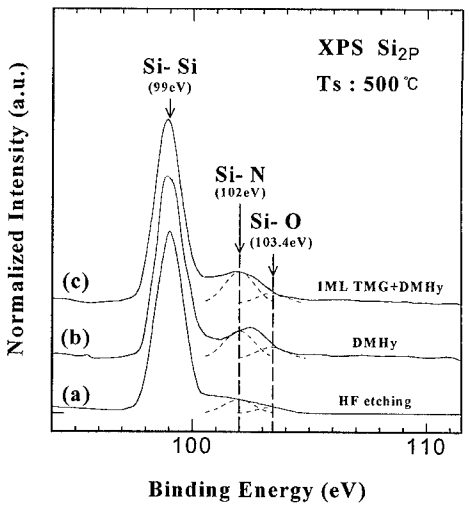

Fig. 1. Typical Si_{2p} XPS spectra from (a) Si substrate just after the HF etching, (b) Si substrate exposed by the DMHy for 2 min, and (c) Si substrate exposed by the DMHy for 2 min after the 1 ML TMG supplying with 2 min time interval, respectively.

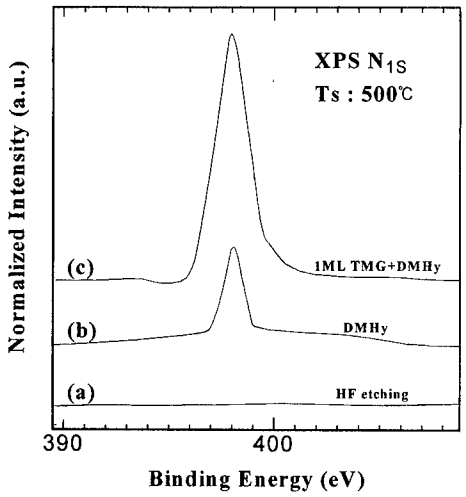

Fig. 2. Typical N_{1s} XPS spectra from (a) Si substrate just after the HF etching, (b) Si substrate exposured by the DMHy for 2 min, and (c) Si substrate exposured by the DMHy for 2 min after the 1 ML TMG supplying with 2 min time interval, respectively.

wide-scaned XPS spectra, this result indicates that the Si surface is partially covered with the Si–N bonds. However, whenever 1 ML TMG is supplied before the DMHy supply, there is a peak shift from 103 eV in Fig. 1b to 102 eV as shown in Fig. 1c and, therefore, the Si–N signal intensity increases remarkably in contrast with the decrease of the Si–O peak intensities. The result can also be confirmed by the N_{1s} XPS spectra as shown in Fig. 2. Remarkable increase of the N_{1s} peak intensity can be easily observed in comparison with Fig. 2b and Fig. 2c. The results indicate that the increases of the Si–N peak intensities are due to the removal effect of the native oxide layers by the Ga irradiation as the following chemical reactions [6]:

$$SiO_2 + 4Ga = Si + 2Ga_2O, \quad (1a)$$

$$SiO_2 + 2Ga = SiO + Ga_2O, \quad (1b)$$

and are due to the progress of nitridation of the clean Si surfaces. The above chemical reactions are also supported by the fact that any XPS signal of Ga_{2p} was not observed in the case shown in Fig. 1c in spite of 1 ML TMG supply. Therefore, it is suggested that the excess Ga irradiations such as 10 ML Ga supply is necessary to form the clean Si surface without the nitridations.

In the case of 10 ML Ga supply, the apparent decrease of Si–N peak intensities were observed with vanishing of the Si–O peaks as shown in Fig. 3b and Fig. 3c, in spite of additional 40 ML GaN growth after the initial stages, as compared with Fig. 3a. For the substrate temperature of 600°C as shown in Fig. 3c, the Si–N peak intensity decreases to the considerably low signal level compared to the case of the substrate temperature of 500°C shown in Fig. 3b. The temperature dependent suppression effect of nitridation may be due to the nature of the excess Ga atoms and their oxides such as the diffusion length of excess Ga atoms and the removal rate of the native oxide layers related with some complicated processes of evaporation of oxide materials. At any rate, these results indicate that both the existence of the excess Ga atoms on the Si surfaces and the substrate temperature in the alternating source supply method play an essential role in the suppression of the nitridation of the initial growth stages.

Fig. 4 shows the relative peak intensity ratios of $I_{Si\text{–}N}/I_{Si\text{–}Si}$ and $I_{Si\text{–}O}/I_{Si\text{–}Si}$ with the error bars in the XPS measurements of the present work. Because

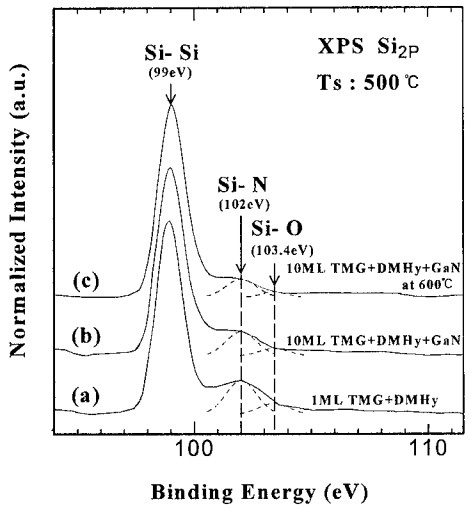

Fig. 3. Typical Si_{2p} XPS spectra from Si substrates exposured by the DMHy for 2 min after (a) 1 ML and (b) 10 ML TMG supplying at 500°C and after (c) 10 ML TMG supplying at 600°C, respectively, with 2 min time interval.

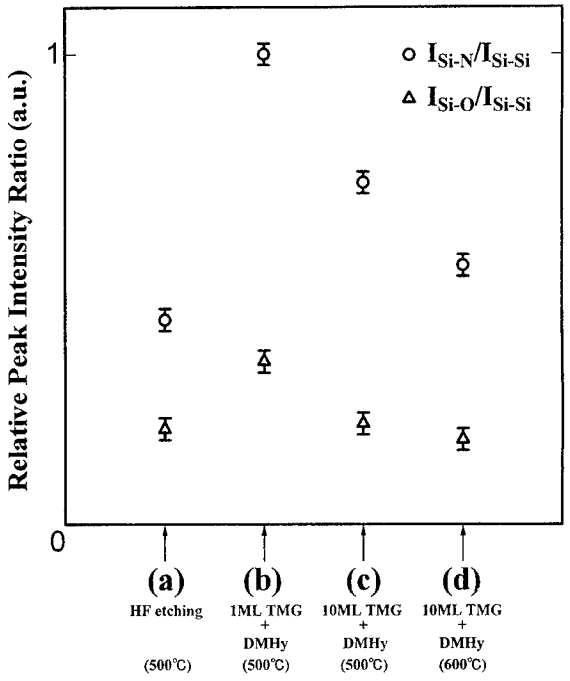

Fig. 4. Two kinds of ratio of the XPS relative peak intensities, $I_{Si\ O}/I_{Si\ Si}$ and $I_{Si\text{-}N}/I_{Si\ Si}$, for various initial conditions.

there is no N_{1s} peak in the XPS spectrum in the case of Si substrate just after the HF etching as shown in Fig. 2a, the relative peak intensity ratio of $I_{Si\text{-}N}/I_{Si\text{-}Si}$ for (a) HF etching should be considered as the background level by the contributions of the oxide materials such as $Si\text{–}O_x$ in the native oxide layer [7]. It is easy to see again that the excess Ga atoms play an important role in both the removal of the Si native oxide and the suppression of the Si nitride formations during the initial growth stages. However, it is worth while to notice that there is a capable Si–N related intensity difference between the case (a) as the background level and the case (d) in Fig. 4. This difference maybe due to some features of the interfacial atomic structures between Si and GaN such as Si/N/Ga and/or more complicated atomic arrangements, if the removal of native oxide by the excess Ga atoms is complete.

Fig. 5 shows the AFM images for the samples of 10 ML Ga supplying at (a) 500°C and (b) 600°C, respectively, together with the roughness along the diagonal lines from upper left-hand side to lower right-hand side in each AFM solid image. The AFM images show the small islands due to the GaN thin layers of about 40 ML equivalent thickness grown in the Volmer–Weber (V–M) growth mode. The surface morphology and the island density grown at 500°C is smoother and lower than for the one grown at 600°C. The average island diameters and heights are about 27 and 0.40 nm with $\sigma = 0.06$ nm for the case of (a) and are about 40 and 0.82 nm with $\sigma = 0.07$ nm for the case of (b), where σ is the standard deviation of island heights. The results imply that the surface morphology depends on the substrate temperature at the initial stages. Because the misfit of the GaN and Si (~17%) is a little larger than the critical value of 14% which is the border line between the Stranski–Krastanov (S–K) growth mode and the V–W growth mode, the smoother surface morphology in Fig. 5a implies that there might be a room for a possibility to control the V–M growth mode to the pseudo-S–K growth mode without Si nitridation in a low temperature region in the alternating source supply method by investigating the optimum growth conditions for the initial growth stage.

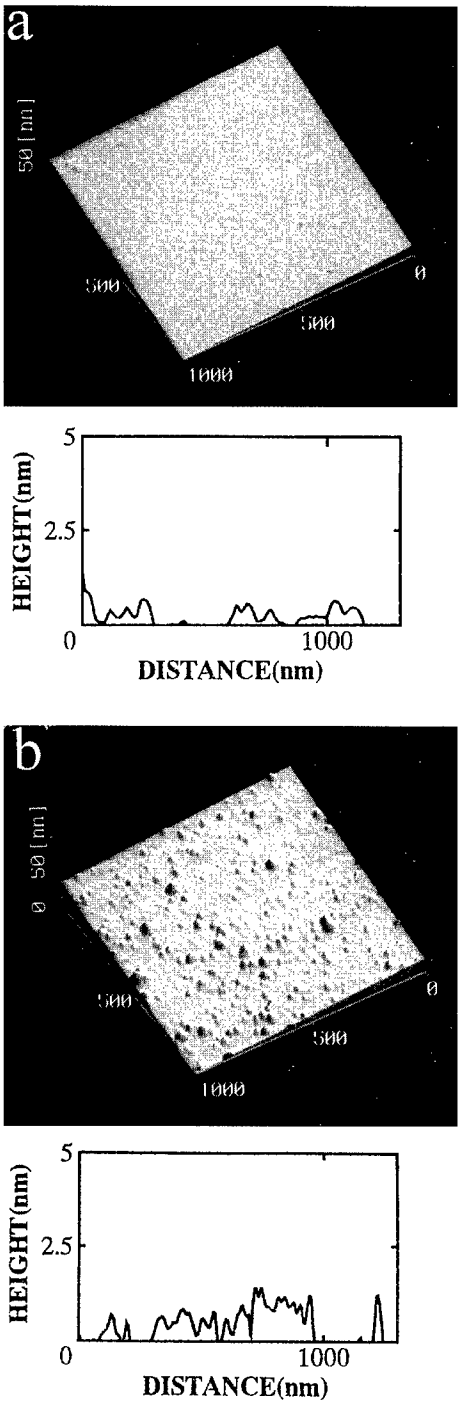

Fig. 5. The AFM images for the samples in the cases of 10 ML Ga supplying at (a) 500°C and (b) 600°C, respectively, together with the roughness along the diagonal lines from upper left-hand side to lower right-hand side in each AFM solid image.

4. Conclusions

In conclusion, the alternating source supply of Ga and DMHy to control the initial nitridation process were proposed. The analysis of the XPS spectra and the AFM images showed that the Ga atoms play an important role in both the removal of the Si native oxide and the suppression of the Si nitride formations during the initial growth stages. The results also imply that there is a possibility of the pseudo-S–K growth mode without nitridations by optimizing the growth conditions in the low temperature region in the alternating source supply method. It is expected that the alternating source supply method in the initial growth stage is an useful one to grow the excellent lattice-mismatched heteroepitaxial layers of III–V nitrides onto the Si substrates.

Acknowledgements

The authors wish to express their appreciation to Dr. Seiko Yoshida for his help and fruitful discussions and Dr. Susumu Yonezawa for his help in the AFM measurements. This work was supported by a Grant-in-Aid for Scientific Research by The Japanease Ministry of Education, Science and Culture.

References

[1] T. Lei, M. Fanciulli, R.J. Molnar, T.D. Moustakas, R.J. Graham and J. Scanlon, Appl. Phys. Lett. 59 (1991) 944.
[2] A. Yamamoto, Y. Yamauchi, M. Ohkubo and A. Hashimoto, Abstracts of the Topical Workshop on III–V Nitrides (1995) B9.
[3] A. Yamamoto, M. Tsujino, M. Ohkubo and A. Hashimoto, J. Crystal Growth 137 (1994) 415.
[4] A. Hashimoto, N. Sugiyama and M. Tamura, Jpn. J Appl. Phys. 30 (1991) 3755.
[5] K. Uchida, A. Watanaeb, F. Yano, T. Tanaka and S. Minagawa, Abstracts of the Topical Workshop on III–V Nitrides (1995) B2.
[6] S. Wright and H. Kroemer, Appl. Phys. Lett. 36 (1980) 210.
[7] J.S. Johannessen, W.E. Spicer and Y.E. Strausser, J. Appl. Phys. 47 (1976) 3028.

ELSEVIER

Journal of Crystal Growth 175/176 (1997) 134–138

JOURNAL OF CRYSTAL GROWTH

Relation between surface reconstruction transitions and growth kinetics of zincblende (0 0 1) GaN

Oliver Brandt*, Hui Yang[1], Akira Yamada[2], Klaus H. Ploog

Paul-Drude-Institut für Festkörperelektronik, Hausvogteiplatz 5–7, D-10117 Berlin, Germany

Abstract

We study the relation between surface reconstruction transitions and surface kinetics for cubic GaN grown by plasma-assisted molecular beam epitaxy on (0 0 1) GaAs. Reflection high-energy electron diffraction is used to monitor the transient behavior of the surface reconstruction upon the pulsed supply of either Ga or N at a given substrate temperature. A quantitative analysis of the dynamics of the surface reconstruction transitions yields the desorption fluxes of Ga and N. The exceptionally high thermal stability of the (2×2)-reconstructed surface in vacuum is examined by ab initio total-energy calculations.

The growth behavior of crystals is, in general, determined by both bulk thermodynamics and surface kinetics. However, for nonequilibrium conditions such as established during molecular beam epitaxy (MBE) or metal organic vapor phase epitaxy (MOVPE), surface kinetics plays a major and often dominating role for growth. The reason for this fact is that the surface constitutes a two-dimensional phase in its own right which has properties much distinct from the underlying bulk phase [1–4]. It is this surface phase which is responsible for the growth kinetics of the material [5].

In a previous work, we reported the observation of three distinct surface phases of cubic GaN(0 0 1), namely, a N terminated (1×1), and Ga terminated (2×2) and c(2×2) reconstructed surfaces [6]. In vacuum, either surface was observed to relax towards the (2×2) reconstructed surface, which was found to be stable up to temperatures as high as 700°C. From the experimentally determined Ga coverages and reconstruction symmetries, simple surface structure models were constructed. The (2×2) reconstruction was described as being formed by Ga dimer rows along the [1 1 0] direction which are separated by one missing dimer row. Filling of the missing dimer rows at the center positions of the four adjacent Ga dimers corresponds at full monolayer coverage to the c(2×2)

* Corresponding author.

[1] Present address: National Research Center for Optoelectronic Technology (NCOT), Institute of Semiconductors, Chinese Academy of Science, P.O. Box 912, Beijing 100083, People's Republic of China.

[2] Present address: Tokyo Institute of Technology, 2-12-1 O-okayama, Meguro-ku, Tokyo 152, Japan.

0022-0248/97/$17.00 Copyright © 1997 Elsevier Science B.V. All rights reserved
PII S0022-0248(96)00980-3

reconstruction. Note that both of these reconstruction models are spanned up by chemically identical basic units, namely, the Ga dimers. The high stability of the (2×2) surface with respect to the $c(2\times2)$ reconstruction has thus remained an open question.

In this work, we study the surface reconstruction transitions of cubic GaN both experimentally and theoretically. The transition dynamics is monitored under isothermal conditions by in situ reflection high-energy electron-diffraction (RHEED). We compare these experiments to simulations using a kinetic model which describes the reconstruction transitions in terms of the initial adsorption, diffusion, and subsequent evaporation of the respective surface species. Finally, we employ ab initio total-energy calculations in order to understand these transitions on an atomistic level.

The GaN film used for this investigation is prepared on an exactly (0 0 1)-oriented GaAs substrate by MBE using a high voltage ($\simeq 1.5$ kV) plasma glow-discharge N source. The growth procedure follows that described in Ref. [6]. Surface reconstructions are monitored in situ by RHEED, using an incident angle of 3° and an acceleration voltage of 15 kV. The RHEED intensity is detected by a CCD camera and analyzed by an image processing system. The temperatures quoted in this paper are thermocouple readings following a three-point calibration [7]. The Ga flux is determined by RHEED intensity oscillations during GaAs buffer layer growth under N_2 background pressure. The N flux is obtained via *ex situ* measurements of the thickness of films grown under Ga rich conditions [8].

Total energies and forces are calculated within the local density approximation for supercell structures representing the reconstructed GaN surfaces. We employ Perdew and Zunger's [9] parametrization of the exchange-correlation energy and norm-conserving pseudopotentials of the Kleinman–Bylander form tabulated by Stumpf et al. [10]. The pseudo wave functions are expanded in terms of a plane-wave basis set corresponding to a kinetic-energy cutoff of 30 Ry. Two special $\boldsymbol{k}$ points are used to sample the primitive surface Brillouin zone. The atomic positions in the top three layers are relaxed until the calculated forces are smaller than 0.15 eV/(1x1).

An impinging flux of either Ga or N onto the (2×2) surface leads to a transition to a $c(2\times2)$ or a (1x1) reconstruction, respectively. Measuring the intensity of the half-order reconstruction streak along a $\langle 1\,1\,0\rangle$ azimuth allows us to record this phenomenon in real time. Figs. 1 and 2 show selected examples of such time scans upon the pulsed supply of 1 ML N (Fig. 1) and 0.5 ML Ga (Fig. 2) for two different temperatures. The maximum intensity corresponds in each case to that of the (2×2) reconstruction, while the intensity drop is associated to the transition towards either the (1×1) or $c(2\times2)$ reconstructed surfaces (The former surface remains stationary for any amount of N supplied in excess of 1 ML). It is obvious from these experiments that the half-order streak first vanishes upon the impinging flux of both N and Ga, but recovers in a finite time once the supply has ceased. Note that the recovery time is substantially shorter at higher temperature. The simplest explanation for this effect consists in the initial adsorption of either N or Ga, thus forming surface phases distinct in coverage and symmetry from the (2×2) surface phase, followed by the isothermal desorption of the species building up these phases.

Assuming that these reconstruction transitions are caused by adsorption, diffusion and desorption

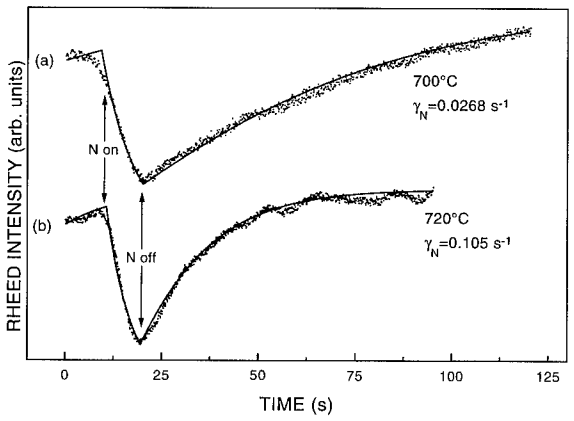

Fig. 1. RHEED intensity transient upon a 1.0 monolayer N dose at (a) 700°C and (b) 720°C. Solid squares represent experimental data, and solid lines show the best fit of our model. The time interval of N supply is indicated in the figure, as well as the desorption rates deduced from the fits.

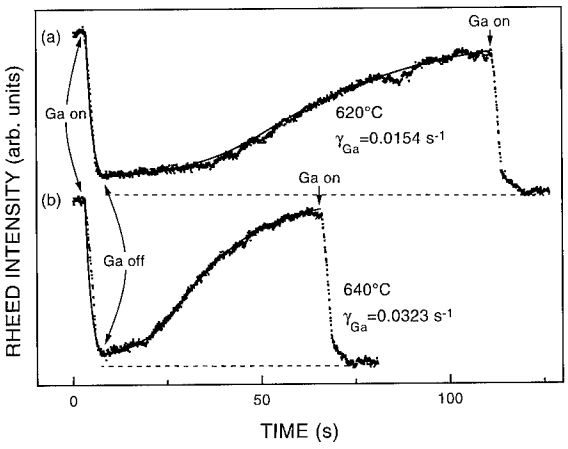

Fig. 2. RHEED intensity transient upon a 0.5 monolayer Ga dose at (a) 620°C and (b) 640°C. Solid squares represent experimental data, and solid lines show the best fit of our model. The dashed lines show the zero level which is defined by the half-order beam intensity equaling the background intensity. The time intervals of Ga supply are indicated in the figure, as well as the desorption rates deduced from the fits.

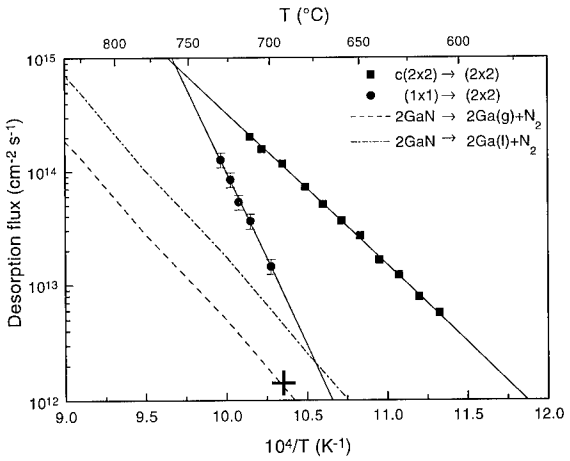

Fig. 3. Arrhenius representation of the N and Ga desorption fluxes. The points are experimental data. The cross marks the lower limit for the stability of the (2×2) reconstructed surface. The solid lines are least-square fits of single exponentials to our data. The dashed and dash-dotted lines represent the data of Refs. [11, 12] for the free surface evaporation of GaN. For the Ga and N desorption flux, the fits result in Arrhenius parameters $\ln Z_0$ and E_a ($\ln Z = \ln Z_0 - E_a/k_B T$) of 64.5 ± 0.6 and 2.69 ± 0.05 eV and 102 ± 2 and 6.1 ± 2 eV, respectively.

of the corresponding surface species, we next apply a phenomenological model for the surface kinetics of GaN for its quantitative analysis. This model, which is discussed in more detail in Ref. [7], accounts for adsorption and desorption of both Ga and N as well as for the formation of excess Ga, which eventually will form droplets, and for GaN growth in the case of the simultaneous presence of Ga and N. Simulations based on this model are shown in Figs. 1 and 2 together with the corresponding experimental data, the latter of which were normalized to one with the zero level defined by the simultaneously recorded background intensity. Since these RHEED transients are actually a measure of the isothermal desorption rate as a function of coverage, the good agreement of the experimental and simulated transients reveals that desorption of both N and Ga is a *first-order* process.

Fig. 3 shows the desorption fluxes derived from our simulations in an Arrhenius representation. The volatility of both Ga and N related surface phases is, in the investigated temperature range, on the same order of magnitude as that observed for the free evaporation of bulk GaN. The stability of all surface phases is many orders of magnitude higher than expected under equilibrium conditions, showing that in all cases desorption is greatly kinetically hindered. Interestingly, at temperatures below 760°C, Ga is the more volatile species at the growth front rather than N.

Next, we discuss the results of ab initio calculations on the stability of the Ga terminated surfaces observed experimentally. The $c(2 \times 2)$ is found to be indeed the most stable surface in the Ga rich limit. For this surface, the orbitals of N atoms are filled with the valence electrons of Ga adatoms, for which the dangling bonds of Ga adatoms are compensated by dimerization, thus resulting in the stabilization of the surface. In contrast, if Ga adatoms form dimers on the half-covered (2×2) surface, unoccupied dangling bonds of N atoms are formed because of the electron deficit [-2e per(2×2) unit cell] of this surface. It thus seems that dimerization is electrostatically unfavorable in this case. In fact, the total energy of undimerized surfaces with 0.5 ML Ga coverage is found to be close to the experimentally observed (2×2) phase.

However, care must be exercised when comparing these results to our experimental findings. It is by no means obvious that our kinetic experiments probe the ground state of the system. Kinetic barriers which inhibit further transformation of the surface into an energetically more favorable phase cannot be ruled out. In fact, the transition observed may be understood to result from dimer desorption alone, and does not involve the dissociation of dimers nor their migration. When focusing on the atomic configuration of the two surface phases involved in this transition, we find that the electron deficit of the (2×2) phase causes a strong relaxation of Ga dimers towards the surface. As shown in the electron density plots in Fig. 4, the distance between the topmost Ga dimers and the second nitrogen plane is 0.66 and 1.16 Å for the (2×2) and the $c(2 \times 2)$ surface, respectively. This difference makes the two surface under consideration distinguishable on an atomic level, and is the key for the understanding of their different stability. For simulating the dynamics of the surface during desorption, we move a single Ga dimer step by step toward the vacuum region from its stable site (with all other atoms fixed at their initial stable sites). The calculated results are summarized in Fig. 5. It is found that the energy required to remove a Ga dimer from the (2×2) surface is higher than that required for a Ga dimer on the $c(2 \times 2)$ surface.

Microscopically, the transition from the $c(2 \times 2)$ and (2×2) surfaces may thus be understood in terms of a dynamical desorption-and-stabilization model. Upon the desorption of a Ga dimer from the $c(2 \times 2)$ surface, the four neighboring Ga-dimers will relax toward the surface resulting in the local stabilization of the (2×2) unit cell. Subsequent desorption of Ga dimers will occur at the second-nearest neighbors sites, and so on, resulting in the spontaneous phase transition from the $c(2 \times 2)$ to the (2×2) surface.

In conclusion, our study has an important consequence for the growth of cubic GaN. Under Ga rich $[c(2 \times 2)]$ growth conditions, the surface stoichiometry during growth is severely influenced by Ga desorption. This phenomenon intricates the

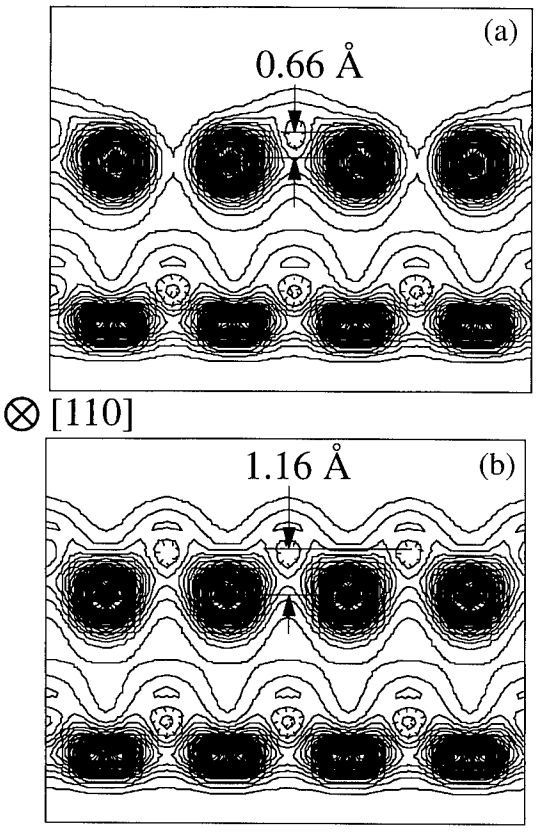

Fig. 4. Electron density maps in [1 1 0] projection of the (a) (2×2) and (b) $c(2 \times 2)$ surfaces.

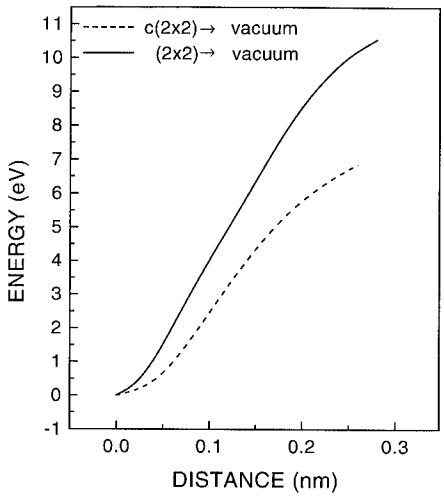

Fig. 5. Energy differences for the movement of a Ga dimer away from its stable site on the $c(2 \times 2)$ and (2×2) surfaces.

growth of single-phase cubic GaN films where the slightest deviation from the optimum surface stoichiometry induces the nucleation of the hexagonal phase [6]. However, Ga desorption does not take place at MBE temperatures when stoichiometry is adjusted such that the surface reconstructs in the (2×2) phase. Experiments following these considerations indeed result in a much improved reproducibility in the growth of single-phase cubic GaN.

Acknowledgements

Financial support of this work by the Bundesministerium für Bildung und Forschung (BMBF) of the Federal Republic of Germany is gratefully acknowledged.

References

[1] J.M. Moison, C. Guille and M. Bensoussan, Phys. Rev. Lett. 58 (1987) 2555.
[2] M. Copel, M.C. Reuter, E. Kaxiras and R.M. Tromp, Phys. Rev. Lett. 63 (1989) 632.
[3] F.K. LeGoues, V.P. Kesan, S.S. Iyer, J. Tersoff and R. Tromp, Phys. Rev. Lett. 64 (1990) 2038.
[4] H. Yamaguchi and Y. Horikoshi, Phys. Rev. B 51 (1995) 9836.
[5] E. Tournié, A. Trampert and K.H. Ploog, Europhys. Lett. 25 (1995) 663.
[6] O. Brandt, H. Yang, B. Jenichen, Y. Suzuki, L. Däweritz and K.H. Ploog, Phys. Rev. B 52 (1995) R2253.
[7] O. Brandt, H. Yang and K.H. Ploog, Phys. Rev. B, to be published.
[8] H. Yang, O. Brandt and K.H. Ploog, J. Electron. Mater., to be published. The values resulting from these measurements are in excellent agreement with the N flux derived from the *in situ* experiments presented in this paper.
[9] J.P. Perdew and A. Zunger, Phys. Rev. B 23 (1981) 5048.
[10] R. Stumpf, X. Gonze and M. Scheffler, Fritz-Haber-Institut Research Report No.1, April 1990, unpublished.
[11] R. Groh, G. Gerey, L. Bartha and J.I. Pankove, Phys. Stat. Sol (A) 26 (1974) 353.
[12] Z.A. Munir and A.W. Searcy, J. Chem. Phys. 42 (1965) 4223.

ELSEVIER

Journal of Crystal Growth 175/176 (1997) 139–144

JOURNAL OF CRYSTAL GROWTH

Gas source molecular beam epitaxy of cubic GaN/GaAs (0 0 1) using hydrazine

S.A. Nikishin[a,*,1], G.A. Seryogin[a], H. Temkin[a], V.G. Antipov[b], S.S. Ruvimov[b], A.V. Merkulov[b]

[a] *Electrical Engineering Department, Colorado State University, Ft. Collins, Colorado 80523, USA*
[b] *A.F. Ioffe Institute, 26 Politechnicheskaya, St. Petersburg 194021, Russian Federation*

Abstract

Growth nucleation and evolution of morphology of GaN on (0 0 1) GaAs is investigated as a function of the N_2H_4/Ga flux ratio. The use of hydrazine allows us to reach high flux ratios without causing any damage to the epitaxial layer. Epitaxial GaN is purely cubic but shows growth anisotropy dependent on the flux ratio. GaN layers grown at low flux ratios shows three-dimensional nucleation and no preferential island orientation. With higher flux ratios the nucleation rate increases, the surface becomes smoother, and the growth anisotropy markedly increases. The growth morphology reflects the surface anisotropy of the underlying GaAs substrate. Cathodoluminescence measurements show that the exciton recombination is the dominant light emission mechanism at 300 and 77 K.

Growth of cubic GaN (β-GaN) on (0 0 1) oriented GaAs substrates has been reported by a number of research groups [1–7]. One of the more compelling reasons for investigating β-GaN is the possibility of reaching very high p-type doping levels [4]. It is well known that in order to control p-type doping of GaN in molecular beam epitaxy (MBE) the density of N-related vacancies, resulting from the relatively low N pressure, must be carefully controlled. Since in most cases atomic nitrogen is produced by plasma assisted sources, high N fluxes result only in sample degradation through ion damage. In plasma assisted MBE nucleation of GaN on GaAs is very sensitive to the concentration of native defects at the surface [7]. A detailed understanding of the growth nucleation of GaN/GaAs is also needed in order to obtain growth of mixed III–V - nitride compounds which are of considerable technological interest [8].

In this work, we report on the growth of GaN on (0 0 1) GaAs by gas-source molecular beam epitaxy (GSMBE) with hydrazine (N_2H_4) as a source of nitrogen. The high reactivity of N_2H_4 provides an attractive alternative to plasma-derived atomic N or NH_3 in epitaxial growth of GaN [1, 6]. We show that large N_2H_4/Ga flux ratios are possible

* Corresponding author. Fax: + 1 970 491 8186; e-mail: sergei@lance.colostate.edu.

[1] Permanent address: A.F. Ioffe Institute, 26 Politechnicheskaya, St.Petersburg 194021, Russian Federation.

0022-0248/97/$17.00 Copyright © 1997 Elsevier Science B.V. All rights reserved
PII S0022-0248(96)00981-5

without any danger of surface damage to GaAs. At the initial stages of growth, the flux of active N is shown to control the island size and the film morphology.

The growth experiments were carried out in a custom designed MBE apparatus described previously [6], on nominally (0 0 1) oriented epi-ready GaAs substrates. The native oxide layer was removed by annealing at 550–650°C ramp under hydrazine flux. The surface nitridation of GaAs commenced at this step, as evidenced by a change in the reflection high-energy electron diffraction (RHEED) pattern. In all the growth experiments the sample was held at a constant temperature of 550°C. The flux of hydrazine was controlled with a precision leak valve and the flux was calibrated with an Bayard–Alpert ion gauge. The flux calibration was carried out without liquid nitrogen in the cryopanels of the growth chamber. The hydrazine flux varied from 4.1×10^{15} to as high as 1.1×10^{17} at/cm^2 s. The Ga flux was calibrated in the growth of GaAs and then held constant. However, in the growth of GaN the effective Ga flux may vary from 1.2×10^{14} to 6×10^{13} at/cm^2 s, as inferred from decreased growth rates at high hydrazine fluxes. This is in good agreement with previous work [7]. We were thus able to obtain a very wide range of N_2H_4/Ga flux ratios. At high flux range the growth is clearly controlled by the Ga flux. However, it is possible that the group III-active nitrogen flux ratio becomes less then unity at the lowest hydrazine fluxes.

The initial stages of growth were monitored with RHEED in [1 1 0] and [$\bar{1}$ 1 0] azimuths. At a submonolayer coverage we were able to observe, at the same time, reflections from the substrate and the film. The GaAs reflections disappear after deposition of the first one or two monolayers of GaN, implying a complete surface coverage. This is consistent with the transmission electron microscopy (TEM) results discussed below. Since the processes of nitridation and oxide removal occur simultaneously, the surface reconstruction of GaAs is complex and the detailed surface structure is difficult to determine. However, the initial RHEED pattern is consistent with islanding on the scale of less than ~ 100 nm. Fig. 1 shows RHEED patterns obtained after about 10 nm of growth. The RHEED

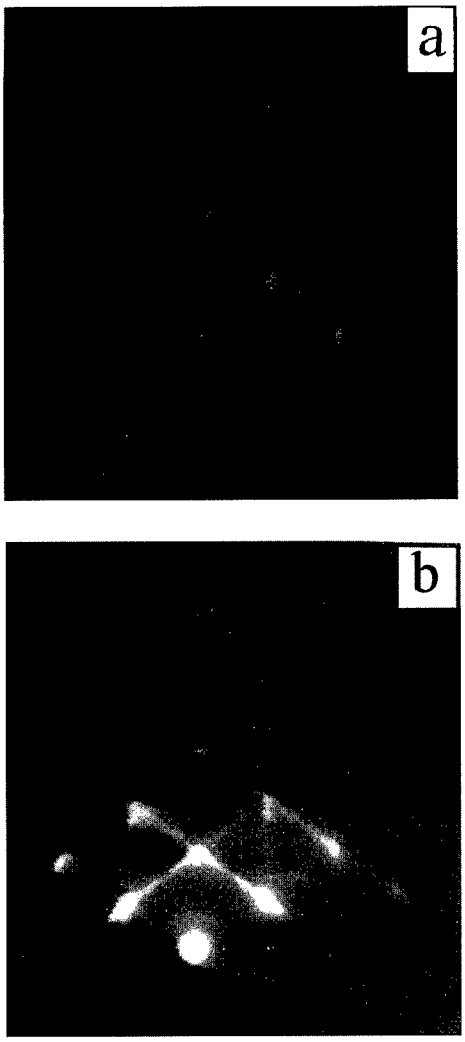

Fig. 1. RHEED data obtained after approximately 10 nm of β-GaN/GaAs (0 0 1) growth. Panels (a) and (b) show the [$\bar{1}$ 1 0] and [1 1 0] azimuths, respectively

data shows that GaN nucleates, at the earliest stages, in the cubic phase, even in the absence of As overpressure [7]. The cubic nature of the film is confirmed by low-energy electron diffraction (LEED, Fig. 2). At the growth temperature used here the RHEED pattern suggests that the initial growth is three-dimensional, for all hydrazine fluxes used here. Two-dimensional growth is not observed, even in samples as thick as 100 nm. In addition, comparison between RHEED patterns

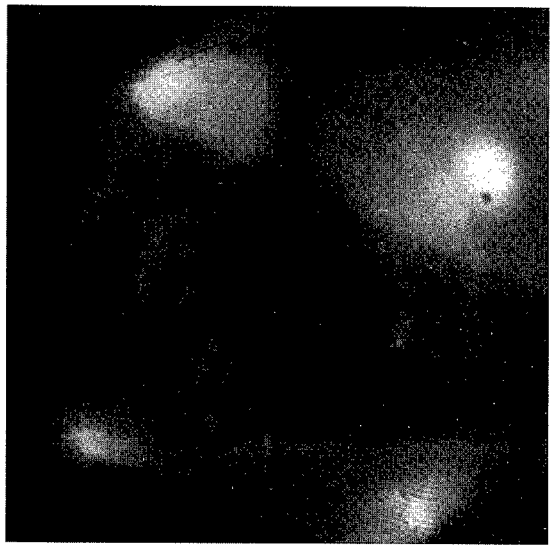

Fig. 2. LEED data obtained after approximately 10 nm of β-GaN/GaAs (0 0 1) growth. Electron energy $\sim$ 48 eV.

imaged in two orthogonal azimuth directions shows that the growth must be highly anisotropic, and oriented preferentially along the [$\bar{1}$ 1 0] direction.

Additional, quantitative, information on the growth anisotropy and its correlation with the N_2H_4/Ga flux ratios can be obtained from the ex situ atomic force microscopy (AFM) measurements. Representative AFM images obtained on $\sim$ 150 nm thick samples of β-GaN are shown in Fig. 3. The surface morphology is strongly dependent on the N_2H_4/Ga flux ratio. The film grown at a low flux ratio, illustrated in Fig. 3a, consists of loosely fitting islands smaller than 100 nm, without a clearly defined orientation. The maximum height of crystallites is also $\sim$ 100 nm. This film is thus quite rough, with the root-mean-square (RMS) roughness of 14 nm. Its appearance is similar to that reported by Yang et al. [7] for growth under, what we consider, low nitrogen flux. With increasing hydrazine flux the films become much more dense and oriented. The average island size in the [$\bar{1}$ 1 0] direction increases, Fig. 3b and Fig. 3c, resulting in very pronounced island anisotropy. The rectangular islands disappear completely under the highest fluxes. The film becomes much

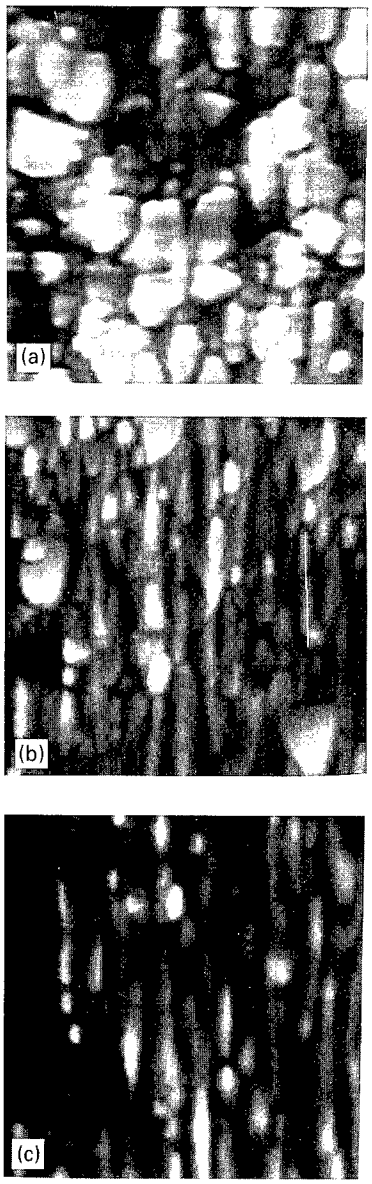

Fig. 3. Atomic force microscopy. AFM images of $\sim$ 150 nm thick GaN layers grown at different flux ratios N_2H_4/Ga: (a) $\sim 7 \times 10^1$; (b) $\sim 4 \times 10^2$; and (c) $\sim 1 \times 10^3$. The islands are aligned along the [$\bar{1}$ 1 0]direction. The gray scale changes from 100 nm in panel (a) to 50 nm in panel (b), and 30 nm in panel (c). Each panel represents an area of 1×1 μm^2.

smoother and at the highest N_2H_4/Ga flux ratios the RMS surface roughness decreases to 1.8 nm. The RMS roughness of 0.5 nm was obtained by Yang et al. [7] under As stabilized growth.

A flat interface between GaAs and GaN is obtained only for high N_2H_4/Ga flux ratios, as ascertained from SIMS profiling (Fig. 4) carried out on samples grown with high and low flux ratios. The depth resolution of this measurement is $\sim$10 nm. Since the SIMS profile is averaged over an area of $200 \times 200\ \mu m^2$, the GaN/GaAs interface in the sample grown with a low hydrazine flux appears graded, as judged by the As trace. High fluxes result in apparently abrupt interfaces. While some As out-diffusion may be present, the width of the SIMS interface in samples grown under low hydrazine fluxes is exaggerated by averaging over a large area of a rough sample (Fig. 4b). However, SIMS results strongly suggest that the film roughness observed in the AFM measurements arises, to a large extent, from the interface roughness.

The details of the interface roughness were investigated using transmission electron microscopy (TEM). A TEM cross-section of a 100 nm thick GaN layer and its interface with the GaAs substrate is shown in Fig. 5. The image is oriented along the [$\bar{1}$ 1 0] plane. The sample was grown under an intermediate hydrazine flux, N_2H_4/Ga $\sim 4 \times 10^2$. In some areas, the interface between GaN and GaAs indeed appears rough. In these areas the peak-to-valley excursions in the interface roughness are on the order of $\sim$ 10 nm. This is in very good agreement with the AFM data obtained on the surface of GaN. The epitaxial layer thus largely mimics the interface morphology. It appears that the surface roughness originates at the oxide removal-nitridation stage. Similar surfaces are observed when the oxides of GaAs are thermally removed in the absence of a protective As flux. The contribution of the nitridation process to the surface roughness thus appears quite minor. Indeed, when the As beam is used at the oxide removal stage the surface is smooth and a (2×4) RHEED surface structure is observed. This is an important point, since all the stacking faults visible in the TEM cross section originate at kinks in the interface. Similar conclusion was reached by Strite et al. [2].

The TEM cross-section of Fig. 5 also shows a thin, less than three monolayers, interfacial layer. Since it shows a TEM contrast different from that of the substrate or the epitaxial layer, its chemical composition is also likely to be different. While our growth temperature is relatively low the long growth times, about 1 h, make the As out-diffusion possible. However, the TEM microdiffraction pattern (Fig. 6) shows purely cubic GaN on (0 0 1) GaAs.

The cathodoluminescence spectra were measured at temperatures of 300 and 80 K. In the room-temperature spectra the ultraviolet band dominated with a maximum at 393 nm (3.16 eV) and half-width of 52 nm (0.42 eV). We believe this band represents bound exciton recombination [6, 11]. The broad "defect" band also had observed

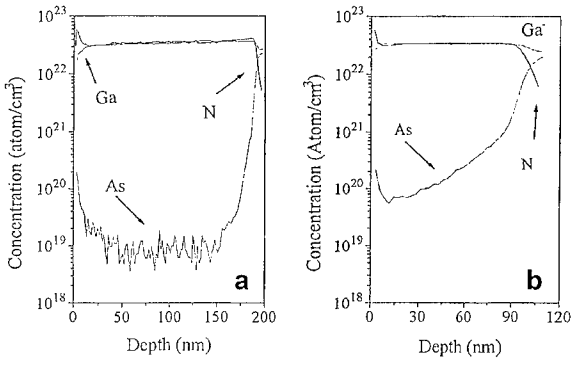

Fig. 4. SIMS profiles for samples of β-GaN/GaAs (001): (a) $\sim$180 nm thick, RMS $\sim$1.8 nm, (N_2H_4/Ga) $\sim$ 700; (b) $\sim$100 nm thick, RMS $\sim$11.4 nm, (N_2H_4/Ga) $\sim$70.

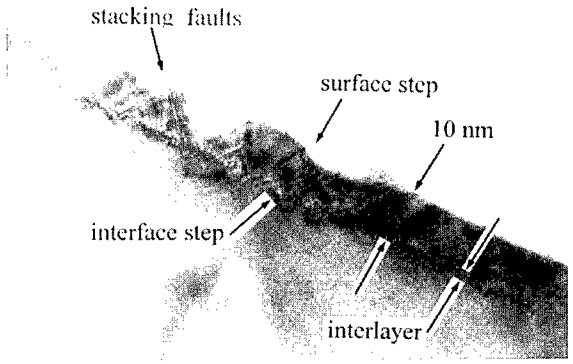

Fig. 5. High-resolution TEM cross-section of a $\sim$100 nm thick layer of GaN grown on (0 0 1) GaAs under an intermediate flux ratio. The cross-section is in the [$\bar{1}$ 1 0] direction. The surface morphology replicates the interface roughness.

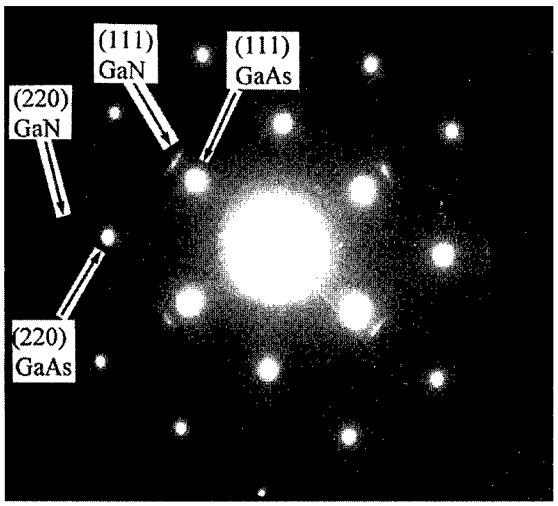

Fig. 6. TEM microdiffraction pattern for β-GaN/GaAs (0 0 1) showing cubic GaN structure.

with a maximum roughly in the range 600 nm. When the samples were cooled to 80 K we observed a narrowing of the main band to 0.36 eV and a shift of 0.07 eV toward shorter wavelengths, in agreement with the temperature dependence of width of band gap for cubic GaN [6]. The best luminescence properties of cubic GaN layers were obtained at the highest N_2H_4/Ga flux ratios.

There are two interesting findings in the growth experiments described here. First, we observe purely cubic GaN growth on (0 0 1) oriented GaAs. This growth is obtained in the absence of As flux in a chamber with very low As background pressure. Previous reports on this subject indicated that high As background pressure is needed in order to promote nucleation of cubic GaN [7]. Second, we find very strong dependence of the nucleation rate and layer morphology on the N_2H_4/Ga flux ratio. At very low flux ratios the GaN layers are very rough and the growth morphology clearly indicates three-dimensional nucleation. With higher flux ratios the nucleation rate increases, the surface becomes significantly smoother, and the growth anisotropy markedly increases [10]. The layer quality clearly improves at higher N_2H_4/Ga flux ratios.

In heteroepitaxy, the layer morphology reflects both the nucleation rate and the diffusion length. At growth conditions leading to high diffusion lengths, such as high-temperature or low-group V fluxes, the effective nucleation rate will be low and three-dimensional island growth will result. Conversely, when the diffusion length is low, the effective nucleation rate is expected to be high and the growth will proceed through the formation of smaller islands with relatively high density. This effect is clearly observed here, with the GaN nucleation rate increasing with increasing N_2H_4/Ga flux ratios.

The resulting change in the growth anisotropy is more complicated. At low fluxes the film appears poorly ordered and isotropic. It is far from clear that this morphology represents intrinsic growth of GaN/GaAs. It may be, for instance, an artifact of incomplete surface nitridation and the resulting non-uniform growth nucleation. The effects of nitridation, with the initial surface roughening, and the growth itself are difficult to separate. In general, the morphology of III–V compounds is expected to show some degree of anisotropy, reflecting the anisotropy of surface diffusion lengths [9]. On vicinal substrates surface anisotropy can arise from interactions with surface steps. On nominal surfaces, diffusion length of Ga on (1 0 0) GaAs differs by factors of 3–4 between the [$\bar{1}$ 1 0] and [1 1 0] directions. If the surface anisotropy is maintained in the growth of GaN, we would expect the type of surfaces observed here under high fluxes of hydrazine.

Acknowledgements

The authors affiliated to the Ioffe Institute's acknowledge financial support from Russian State Program "Surface atomic structures" (project N95-2.21). Work at Colorado State University is supported by ONR (N0014-93-0003). We would like to thank A. Osinsky for help with the AFM measurements and A.S. Zubrilov and D.V. Tsvetkov for the cathodoluminescence measurements.

References

[1] M. Mizuta, S. Fujieda, Y. Matsumoto and T. Kawamura, Jpn. J. Appl. Phys. 25 (1986) L945.

[2] S. Strite, J. Ruan, Z. Li, A. Salvador, H. Chen, D.J. Smith, W.J. Choyke and H. Morkoc, J. Vac. Sci. Technol. B 9 (1991) 1924.
[3] H. Okumura, S. Misawa and S. Yoshida, Appl. Phys. Lett. 59 (1991) 1058.
[4] M.E. Lin, G. Xue, G.L. Zhou, J.E. Greene and H. Morkoc, Appl. Phys. Lett. 63 (1993) 932.
[5] T.S. Cheng, L.C. Jenkins, S.E. Hooper, C.T. Foxon, J.W. Orton and D.E. Lacklison, Appl. Phys. Lett. 66 (1995) 1509.
[6] V.G. Antipov, A.S. Zubrilov, A.V. Merkulov, S.A. Nikishin, A.A. Sitnikova, M.V. Stepanov, S.I. Troshkov, V.P. Ulin and N.N. Faleev, Semiconductors (Russia) 29 (1995) 946.
[7] H. Yang, O. Brandt, M. Wassermeier, H.P. Schonherr and K.H. Ploog, Appl. Phys. Lett. 68 (1996) 244.
[8] F.G. McIntosh, K.S. Boutros, J.C. Roberts, S.M. Bedair, E.L. Piner and N.A. El-Masry, Appl. Phys. Lett. 68 (1996) 40.
[9] M.A. Cotta, R.A. Hamm, T.W. Staley, S.N.G. Chu, L.R. Harriott, M.B. Panish and H. Temkin, Phys. Rev. Lett. 70 (1993) 4106.
[10] S.A. Nikishin, V.G. Antipov, S.S. Ruvimov, G.A. Seryogin and H. Temkin, Appl. Phys. Lett. 69 (1996) 3227.
[11] J.N. Kuznia, J.W. Wang, Q.C. Chen, S. Krishnakutty, M. Asif Khan, T. George and J. Frietas, Jr., Appl. Phys. Lett. 65 (1994) 2407.

ELSEVIER

Journal of Crystal Growth 175/176 (1997) 145–149

JOURNAL OF CRYSTAL GROWTH

N incorporation in GaN_xP_{1-x} and InN_xP_{1-x} using a RF N plasma source

W.G. Bi*, C.W. Tu

Department of Electrical and Computer Engineering, University of California, San Diego, La Jolla, California 92093-0407, USA

Abstract

We report a study of N incorporation behavior into GaP and InP as a function of growth conditions. With increasing N_2 flow-rate fraction (N_2 flow rate over total group-V gas flow rate), the N composition increases up to a point but then saturates. This might be due to the small solubility of N in these materials or the leveling off of the active N species at higher N_2 flow rate. At a fixed N_2 flow-rate fraction, the higher the growth temperature T_s is, the less N can be incorporated, which results from the lowering of the sticking coefficient of nitrogen at higher T_s. Although the general trend of the growth condition dependence is the same for N incorporation in InP and GaP, the amount of N that can be incorporated is quite different. With GaP, N as high as 16% can be obtained, while with InP, only less than 1% can be incorporated. This is considered to be due to the very high equilibrium vapor pressure of N_2 over InN compared to that over GaN.

1. Introduction

As we know, integrating III–V compounds with Si has been a dream for more than a decade. However, as the materials investigated in the past all have lattice constants larger than that of Si, a large number of dislocations were generated in these III–V epilayers due to the large lattice mismatch (and mismatch in thermal expansion coefficients) and, consequently, became one of the main obstacles hindering the realization of this dream [1–3]. Recently, with the emergence of III-N [4–7], there is a considerable interest in synthesizing materials that can be lattice-matched to Si [8–17]. Since Si sits between nitrides and arsenides or phosphides, it is quite possible to combine nitride with arsenide or phosphide to form a direct-band material that is lattice-matched to Si. For example, with 2%, 20%, and 49% N, respectively, GaN_xP_{1-x}, GaN_xAs_{1-x}, and InN_xP_{1-x} all can lattice-match to Si. However, due to the large miscibility gap, the N composition is limited. For example, according to the delta lattice parameter model [18], the interaction parameter Ω is 28 900 cal/mol for the GaN–GaP system, from which a miscibility gap extending from $x = 3 \times 10^{-7}$ to 0.9999997 at 700°C has been predicted. Furthermore, experimental studies on this material so far also indicate that only a small amount of N can be incorporated in GaP. Li et al. [19] achieved 0.08% N in GaN_xP_{1-x} using chemical beam epitaxy (CBE) with co-injected

* Corresponding author.

0022-0248/97/$17.00 Copyright © 1997 Elsevier Science B.V. All rights reserved
PII S0022-0248(96)00812-3

TBP and NH_3, Miyoshi et al. [20] obtained 4% N in GaN_xP_{1-x} using metalorganic vapor phase epitaxy (MOVPE) with dimethylhydrazine (DMHy) as the N source, while Baillargeon et al. [9, 10] reported up to 7.6% N incorporation in GaP grown by MBE using dissociated NH_3 as N source, which is the highest N composition ever reported. Recent calculations [21] based on thermodynamic considerations show that due to the strong force constant for Ga compounds, the solubility of N in GaAs and GaP is very small. However, as the force constant is very weak for In compounds, a much higher N incorporation in InAs and InP is expected. This raises hopes that InNP might be a suitable candidate that can be grown lattice-matched to Si. To our knowledge, no work on the N incorporation in InP has been reported. In this paper we report our investigation of N incorporation behavior in InP and GaP, and we try to clarify the factors determining the N incorporation in III–V binaries.

2. Experimental procedure

The growth apparatus used in this work is a modified Varian Gen-II MBE system equipped with two 2200 l/s cryopumps. Ultra-high purity N_2 was injected through a N radical beam source (Oxford Applied Research Model MPD21) operated at a radio frequency (RF) of 13.56 MHz to generate active N species. The RF power used was 300 W. GaNP and InNP samples were grown on undoped (1 0 0) GaP substrates and on semi-insulating (1 0 0) InP substrates, respectively. Pure elemental Ga was used as the group-III source, and thermally cracked phosphine was used as the group-V source. The film thickness was 0.5 μm. The growth temperature was varied from 500 to 600°C for GaNP and from 310 to 420°C for InNP. After thermal cleaning of the GaP substrate at 650°C (or InP substrate at 460°C) under a P_2 flux to remove surface oxide layers, a 0.1 μm thick GaP (or InP) layer was grown as a buffer layer. Then the substrate temperature was lowered to the growth temperature, and the ignition of the N plasma was attempted. The initial N_2 flow rate was set at 3 sccm in order to strike a plasma, and the background pressure was 5×10^{-5} Torr. During growth, the background pressure was around $1.5–3 \times 10^{-5}$ Torr depending on the N_2 flow rate used (0.54–2.1 sccm). High-resolution X-ray rocking curve (XRC) measurements were performed using a Philips X-ray diffractometer. The current and voltage of the X-ray generator were 20 mA and 35 kV, respectively, and the $Cu_{\alpha 1}$ line was used. The N composition in GaNP and InNP was determined from (5 1 1) asymmetric reflections to take into account the strain-induced lattice constant change of the GaN_xP_{1-x} and InN_xP_{1-x} films [22].

3. Results and discussion

Fig. 1 shows N composition in GaN_xP_{1-x} versus N_2 flow rate fraction. The PH_3 flow rate used was 1.68 sccm for all samples. The growth rate, R_g was 0.9 ML/s for samples represented by open squares and 0.78 ML/s for those by solid squares. From the figure we can see that N incorporation is higher for higher R_g. A similar phenomena has been observed by Miyoshi et al. [20]. The reason for this is not quite clear at the moment. It might be due to the far-more-away-from-thermoequilibrium growth conditions when R_g is higher [20].

Note also in Fig. 1 that the N composition in GaN_xP_{1-x} is generally different from that in the vapor phase. With increasing the N_2 flow rate fraction, the N composition increases almost linearly up to a point, and then seems to level off. This

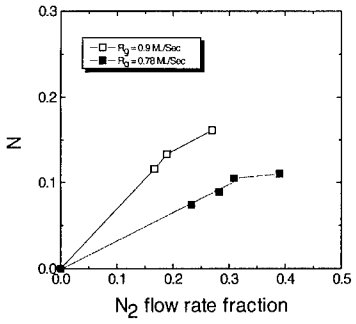

Fig. 1. N composition in GaN_xP_{1-x} versus N_2 flow rate fraction (the N_2 flow rate over the total group-V flow rate). The growth rate was 0.9 ML/s for samples represented by open squares and 0.78 ML/s for those by solid squares.

phenomena is different from arsenide/phosphide mixed group-V compounds like $InAs_xP_{1-x}$ or $GaAs_xP_{1-x}$ [23], where no saturation was observed. It is thought to be due to either the small solubility of N in GaP or the plasma source used. As has been reported [18], due to the differences in lattice structure (GaN: wurtzite, GaP: zincblende) and in lattice constant (~20%) between GaN and GaP, an extremely large miscibility gap extending from $x = 3 \times 10^{-7}$ to 0.9999997 at 700°C is expected for GaN_xP_{1-x} [18]. This large miscibility gap will be the main obstacle preventing the successful growth of this material. One thing worth noting is that although such a big miscibility gap exists for GaN_xP_{1-x}, we have achieved a N incorporation as high as 16% using GSMBE and RF N plasma source. We believe this is the highest N incorporated in GaP ever reported. This is due to the non-equilibrium growth technique we used.

Another possible reason for the saturation behavior of N incorporation in GaP in Fig. 1 might be due to the plasma source used. Fig. 2 shows the square root of the optical emission intensity I of the plasma source as a function of N_2 flow rate. As I is proportional to the square of the ground-state atomic nitrogen concentration [24, 25], the saturation of the square root of I at higher N_2 flow rate in Fig. 2 indicates the leveling off of the active N species, i.e., at a fixed RF power, the active N species increase with increasing N_2 flow rate and then tend to level off. This is because when the N_2 flow rate is small, the applied RF power is large enough to activate a large fraction of the N_2 supplied, i.e., the N_2 is almost completely activated. However, as the N_2 flow rate increases further, the RF power may not be enough to dissociate as large a fraction of the N_2 supplied, and only part of the N_2 will be activated. This will lead to a saturation of the active N species at high N_2 flow rate as seen in Fig. 2. Considering the fact that the N incorporation coefficient will not change with N_2 flow rate, the saturation of the activated N species will limit further incorporation of N in GaN_xP_{1-x}.

The temperature dependence of the N composition in GaN_xP_{1-x} is shown in Fig. 3. Increasing growth temperature will result in less N incorporated into GaP. For example, the N composition is reduced from 0.16 to 0.045 when the substrate temperature is increased from 500 to 600°C. Similar behavior has been observed by Miyoshi et al. [20]. This decreasing N incorporation with increasing growth temperature might be due to the lowering of the sticking coefficient of nitrogen or to the enhanced kinetics of $N + N = N_2$ on the surface, i.e., reassociation followed by desorption at higher T_s.

Fig. 4 shows the N composition in InN_xP_{1-x} as a function of the N_2 flow rate fraction at different growth temperatures. The growth rate is 0.9 ML/s. As can be seen here, the N composition in InN_xP_{1-x} shows the same trend as that observed for GaN_xP_{1-x}, but the N composition that can be

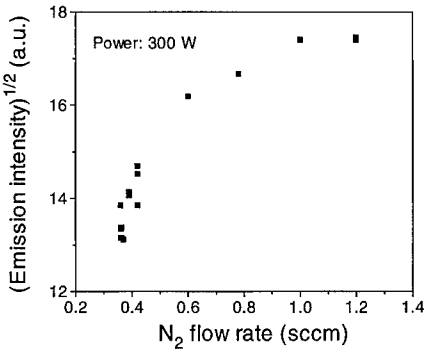

Fig. 2. Square root of the optical emission intensity of the plasma source as a function of N_2 flow rate at a RF power of 300 W.

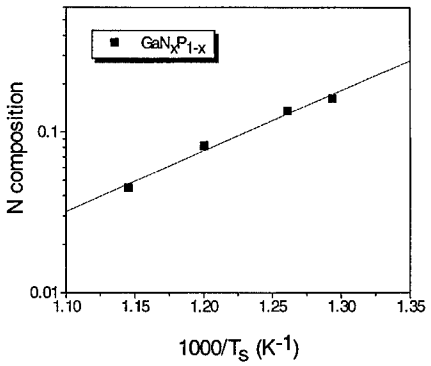

Fig. 3. Arrhenius plot of the N composition in GaN_xP_{1-x} at constant N_2 and PH_3 fluxes and 300 W RF power.

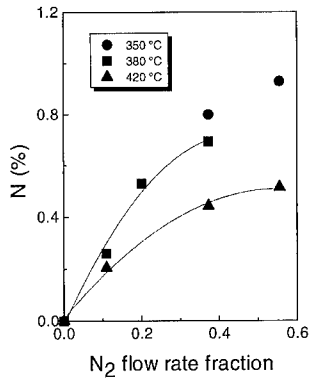

Fig. 4. N composition in InN_xP_{1-x} as a function of the N_2 flow rate fraction at different growth temperatures.

incorporated is much smaller than that in GaP. For GaN_xP_{1-x}, N as high as 16% has been obtained, while for InN_xP_{1-x}, only 0.93% N is achieved. This is different from the thermodynamic considerations where orders of higher magnitude of N solubility in InP than in GaP is expected [21]. This might be due to the very high equilibrium vapor pressure of N_2 over InN compared to that over GaN [26, 27]. As we know, in crystal growth in the vapor phase, a key factor is that the components are supplied at pressures higher than the equilibrium vapor pressure. Because of the very high vapor pressure of N_2 over InN, it is expected that an extremely large number of active N species is needed in order to achieve a higher N incorporation in InP. However, the saturation of the N plasma source at high N_2 flow rates limits the N composition in InP. As far as N incorporation in GaP is concerned, because of the much lower equilibrium vapor pressure of N_2 over GaN compared with that over InN, the active N species generated by the plasma source might be still enough for the growth of GaNP with higher N composition, consequently much more N incorporation in GaP than in InP can be obtained.

4. Summary

In summary, we have studied the behavior of incorporating N into GaP and InP using a RF N plasma source. The N composition increases slowly with increasing the N_2 flow rate, and then saturates after a certain point as a result of the leveling off of the N_2 plasma source at high N_2 flow rates and the small solubility of N. Lowering the growth temperature is effective in incorporating more N in GaP and InP. Although thermodynamic considerations predict a much higher N incorporation in InP than in GaP, due to the very high N_2 equilibrium vapor pressure over InN, it is very difficult to incorporate N into InP. Less than 1% N has been obtained so far. Further incorporation of N in InP needs modification of the N plasma source by using a larger beam exit aperture or trying other growth techniques where the amount of N_2 that can be supplied is not limited by the background pressure. On the other hand, for N incorporation in GaP, a much higher N concentration, up to 16%, has been incorporated as a result of the much lower N_2 equilibrium vapor pressure over GaN compared to that over InN and the non-equilibrium MBE growth technique used.

Acknowledgements

We would like to thank Texas Instruments System Component Laboratory for the support of this work.

References

[1] M. Umeno, T. Jimbo and T. Soga, J. Crystal Growth 98 (1989) 188.
[2] Y. Kohama, Y. Kadota and Y. Ohmachi, Jpn. J. Appl. Phys. Lett. 28 (1989) 1337.
[3] S.F. Fang, K. Adomi, S. Iyer, H. Morkoc, H. Zabel, C. Choi and N. Otsuka, J. Appl. Phys. 68 (1990) R31, and references therein.
[4] S. Nakamura, M. Senoh, S. Nagahama, N. Iwasa, T. Yamada, T. Matsushita, H. Kiyoku and Y. Sugimoto, Jpn. J. Appl. Phys. 35 (1996) L74.
[5] S. Strite and H. Morkoc, J. Vac. Sci. Technol. B 10 (1992) 1237.
[6] S. Nakamura, T. Mukai and X. Senoh, Appl. Phys. Lett. 64 (1994) 1687.
[7] R.F. Davis, Proc. IEEE 79 (1991) 702.
[8] X. Liu, M.E. Pistol, L. Samuelson, S. Schwetlick and W. Seifert, Appl. Phys. Lett. 56 (1990) 1451.
[9] M. Weyers, M. Sato and H. Ando, Jpn. J. Appl. Phys. 31 (1992) L853.

[10] M. Weyers and M. Sato, Appl. Phys. Lett. 62 (1993) 1396.
[11] M. Kondow, K. Uomi, T. Kitatani, S. Watahiki and Y. Yazawa, J. Crystal Growth 164 (1996) 175.
[12] J.N. Baillargeon, K.Y. Cheng, G.E. Holfler, P.J. Pearah and K.C. Hsieh, Appl. Phys. Lett. 60 (1992) 2540.
[13] J.N. Baillargeon, P.J. Pearah, K.Y. Cheng, G.E. Holfler and K.C. Hsieh, J. Vac. Sci. Technol. B 10 (1992) 829.
[14] X. Liu, S.G. Bishop, J.N. Baillargeon and K.Y. Cheng, Appl. Phys. Lett. 63 (1993) 208.
[15] W.G. Bi and C.W. Tu, Appl. Phys. Lett. 69 (1996) 3710.
[16] M. Kondow, K. Uomi, K. Hosomi and T. Mozume, Jpn. J. Appl. Phys. 33 (1994) L1056.
[17] M. Sato, J. Crystal Growth 145 (1994) 99.
[18] G.B. Stringfellow, J. Crystal Growth 27 (1974) 21.
[19] N.Y. Li, W.S. Wong, D.H. Tomich, H.K. Dong and C.W. Tu, J. Crystal Growth 164 (1996) 180.
[20] S. Miyoshi, H. Yaguchi, K. Onabe and R. Ito, Appl. Phys. Lett. 63 (1993) 3506.
[21] Y.C. Kao, T.P.E. Broekaet, H.Y. Liu, S. Tang, I.H. Ho and G.B. Stringfellow, Mater. Res. Soc. Symp. Proc. 423 (1996) 335.
[22] W.G. Bi, F. Deng, S.S. Lau and C.W. Tu, J. Vac. Sci. Technol. B 13 (1995) 754.
[23] H.Q. Hou and C.W. Tu, J. Electron. Mater. 21 (1992) 137.
[24] J. Berkowitz, W.A. Chupka and G.B. Kistiakowsky, J. Chem. Phys. 25 (1956) 457.
[25] A.N. Wright and C.A. Winkler, Active Nitrogen (Academic Press, New York, 1968).
[26] J.B. Macchesney, P.M. Bridenbaugh and P.B. O'Connor, Mater. Res. Bull. 5 (1970) 783.
[27] T. Matsuoka, J. Crystal Growth 124 (1992) 433.

ELSEVIER

Journal of Crystal Growth 175/176 (1997) 150–155

JOURNAL OF CRYSTAL GROWTH

Gas source MBE growth of GaN rich side of $GaN_{1-x}P_x$ using ion-removed ECR radical cell

K. Iwata, H. Asahi*, K. Asami, S. Gonda

The Institute of Scientific and Industrial Research, Osaka University, 8-1 Mihogaoka, Ibaraki, Osaka 567, Japan

Abstract

GaN-rich side of $GaN_{1-x}P_x$ alloy are grown on (0 0 0 1) sapphire substrates by electron cyclotron resonance molecular beam epitaxy (ECR-MBE) using an ion removed ECR radical cell after the growth of high-quality GaN layers. $GaN_{1-x}P_x$ exhibits potentially large variation of band-gap energy with P composition due to its large bowing. Maximum P composition of $x = 0.015$ is obtained. However, at the growth condition of high PH_3 flow rate, phase separation into GaN-rich $GaN_{1-x}P_x$ and GaP-rich $GaP_{1-y}N_y$ is observed. Near band edge excitonic photoluminescence (PL) peak from GaN-rich side of $GaN_{1-x}P_x$ layers shows large red shift with P composition. It suggests that the direct band edge of GaNP alloy shows large bowing.

PACS: 68.55.Bd; 78.55.Cr

Keywords: GaN; GaNP; Gas source MBE; ECR radical cell; Band gap narrowing; Phase separation

1. Introduction

III–V nitride compound semiconductors are attracting attention due to their applications in optical devices. Recently, it was proved that wide-band gap III–V nitrides are suitable to fabricate blue–green light emitting diodes and a room temperature pulsed operation of violet laser diodes was demonstrated [1]. This material system has a potential of a wide wavelength range of optical devices from ultra-violet to longer than 2 μm by adding As or P due to the large bowing of band gap energy. The study of GaP : N was started since the discovery of the isoelectronic trap in 1965 [2]. The content of nitrogen in GaP had been increasing by the improvement of crystal growth techniques [3]. When the content y of $GaP_{1-y}N_y$ reached 0.02–0.03, red shift of emission spectra was observed and it was explained as a band gap narrowing due to a large bowing parameter of GaP–GaN material system [4]. Until now, several authors reported the growth of GaP-rich or GaAs-rich side of GaPN or GaAsN [3–7]. However, there are no report on the GaN-rich side of $GaN_{1-x}P_x$ or $GaN_{1-x}As_x$ compound semiconductors except for Igarashi [8]. He reported only the growth of GaNP by halide vapor phase epitaxy and no data for band

* Corresponding author. E-mail: asahi@sanken.osaka-u.ac.jp

0022-0248/97/$17.00 Copyright © 1997 Elsevier Science B.V. All rights reserved
PII S0022-0248(96)00926-8

gap energy was reported. Hereafter, we call GaP rich $GaP_{1-y}N_y$ as GaPN and GaN rich $GaN_{1-x}P_x$ as GaNP for simplicity. In this paper, we report the gas source MBE growth of GaN-rich side of GaNP and their band gap variation with P composition. GaN-rich side of GaNP was grown on (0 0 0 1) sapphire substrate using ion-removed ECR (electron cyclotron resonance) radical cell after the growth of high quality GaN layer [9].

2. Experimental procedure

GaN-rich side of GaNP layers were grown in a gas source MBE system. The growth chamber was evacuated by an oil diffusion pump with a liquid nitrogen trap. Elemental gallium (Ga), and ECR plasma-enhanced nitrogen (N_2) and thermally cracked PH_3 were used as group III and group V sources, respectively. The substrate used was (0 0 0 1) sapphire. The substrate surface was chemically etched with a hot solution of HCl: $H_3PO_4 = 3:1$ and was thermally cleaned at 800°C for 10 min without plasma-enhanced nitrogen irradiation and for 3 min under plasma-enhanced nitrogen irradiation in the gas source MBE growth chamber just before growth.

In order to minimize ion damage during film growth, we used the ion-removed ECR plasma cell [10–13]. Two magnets for ion removal are located in parallel at the exit of the ECR liner. The magnetic field is perpendicular to the cell axis. The ion-removal efficiency of the ion-removed ECR plasma cell was measured as a function of nitrogen N_2 flow rate using a Faraday cup and it was more than 99% [10].

Low-temperature GaN buffer layer was grown at 400°C and the thickness was 1.2 nm. On this low-temperature GaN buffer layer, GaN layer was grown at 750°C. The substrate temperature was measured by an infrared optical pyrometer calibrated at the melting point of InSb (525°C). The growth rate was 0.3 μm/h with a N_2 flow rate of 1.5 SCCM. The Ga flux was 1.0×10^{-7} Torr.

During the high-temperature growth of GaN, RHEED (reflection high-energy electron diffraction) pattern revealed streaky x2 reconstructed surface as shown in Fig. 1a. On the GaN layer, GaNP

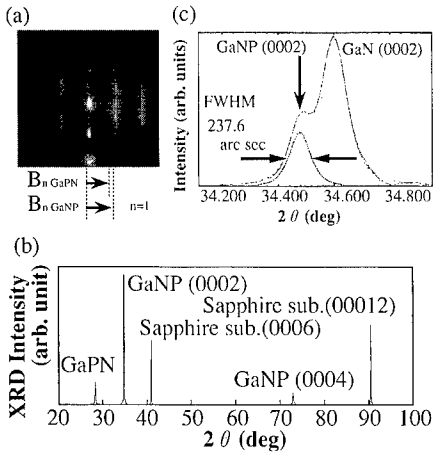

Fig. 1. (a) RHEED pattern during the growth of GaNP (PH_3 = 1.0 SCCM). Diffractions from both GaNP (GaN-rich side of $GaN_{1-x}P_x$) and GaPN (GaP-rich side of $GaP_{1-y}N_y$) spacing are observed during growth. (b) XRD rocking curve from GaNP on sapphire substrate for the same sample. (c) XRD rocking curve around GaN (0 0 0 2) angle.

was grown by adding PH_3 flow. The flow rate of PH_3 ranged from 0.1 to 1.0 SCCM and the PH_3 cracking temperature was 750°C.

Crystalline quality was determined by RHEED and XRD (X-ray diffraction) using Cu K_{α_1} radiation. PL (photoluminescence) measurement was conducted at 77 K and room temperature using a He–Cd laser (325 nm, 19 mW) as an excitation source.

The PL spectrum from the GaN layer grown by this MBE system under optimized growth condition always showed no deep emission and quite strong excitonic emission intensity. It was also observed that the FWHM (full width at half maximum) of excitonic emission peak at 77 K was as narrow as 29 meV [10].

3. Results and discussion

3.1. GaNP growth on sapphire substrate

GaN-rich side of GaNP (thickness: 0.6 μm) was grown after the high temperature growth of GaN layer (thickness: 0.3 μm) on sapphire substrate.

In situ RHEED observation was carried out. During the growth of GaN layer, x2 RHEED patterns were observed [10]. The x2 pattern changed to x1 pattern when GaNP alloy growth was started [9]. During the growth of GaNP layer, RHEED exhibits x1 streak pattern. When the PH_3 flow rate was low (0.1, 0.3 and 0.5 SCCM), the x1 streak pattern was kept during this alloy growth. However, when the PH_3 flow rate was high (1.0 SCCM), the weak spotty pattern which indicated another interplanar spacing appeared in addition to the GaN strong streak pattern as shown in Fig. 1a. It suggests the existence of two different interplanar spacing during GaNP growth. From measurement of B_{ny} (weak spotty pattern) and $B_{n\mathrm{GaNP}}$ (strong streak pattern), the interplanar spacing ratio d_y/d_{GaNP} is given by

$$\frac{d_y}{d_{\mathrm{GaNP}}} = \frac{n/B_{ny}}{n/B_{n\mathrm{GaNP}}} = 1.208,$$

where $B_n = k\cos\Theta_0 - k\cos\Theta$, $k = 1/\Gamma$, Γ is the wavelength of the incident electron beam, n is an order of interference, Θ_0 and Θ are incident and scattered angles of the electron beam of RHEED, respectively, and $B_n = n/d$. This value is close to the bond length ratio of 1.2137 between GaP and GaN. It is considered that the difference between 1.2137 and 1.208 is due to the interplanar spacing difference between GaP and GaP-rich side of GaPN. Observation of both the GaN-rich side of GaNP and GaP-rich side of GaPN pattern indicates that the GaPN grain occurred on the growing surface under the condition of PH_3 flow rate of 1.0 SCCM.

Fig. 1b shows X-ray diffraction rocking curve for the GaNP on sapphire substrate for the high PH_3 flow rate of 1.0 SCCM. A clear peak around $2\theta_y = 28.369°$ with FWHM value of 248 arcsec was observed. The interplanar spacing ratio between this peak and GaN (0 0 0 2) peak around $2\theta_{\mathrm{GaN}} = 34.569°$ is given by

$$\frac{d_y}{d_{\mathrm{GaN}}} = \frac{\lambda \sin^{-1}\theta_y}{\lambda \sin^{-1}\theta_{\mathrm{GaN}}} = 1.2125,$$

where λ is the X-ray wavelength, θ is the Bragg angle for the (0 0 0 2) diffraction. The bond length ratio between GaP and GaN is 1.2137. These two values are quite similar although there is only 0.12% difference between these two values. This difference is due to the interplanar spacing difference between GaP and GaP-rich side of GaPN, since it is considered that the clear peak around $2\theta_y = 28.369°$ comes from the GaP-rich side of GaPN (0 0 0 2) diffraction. Furthermore, the difference shows that the N composition y of the GaP-rich side of $GaP_{1-y}N_y$ is 0.006. The bond length ratio between GaPN (GaP-rich GaPN) and GaNP (GaN-rich GaNP) is 1.2083 which was determined from interplanar spacing between $GaP_{0.984}N_{0.006}$ and $GaN_{0.985}P_{0.015}$ measured by XRD and this value is very close to 1.208 which was determined by RHEED pattern observation. We considered that GaNP is hexagonal because P composition is small, but GaPN is not known. The (0 0 0 4) peak is very weak but it is possible to observed when the X-ray power is increased.

Therefore, it is concluded that the phase separation occurred in the GaNP layer grown with the PH_3 flow rate of 1.0 SCCM. The phase separation was also observed for the GaNP layer grown with the PH_3 flow rate of 0.5 SCCM. However, another GaNP layers grown with smaller PH_3 flow rates of 0.1 and 0.3 SCCM did not show the XRD peak around $2\theta_y = 28.369°$.

Fig. 1c shows the X-ray diffraction rocking curve around GaN (0 0 0 2) angle for the GaNP layer grown with the PH_3 flow rate of 1.0 SCCM. The anglar step when we did X-ray θ–2θ diffraction is 0.002° and it is considered that the resolution is enough to determine the P composition. Two peaks are observed at 2θ angles of 34.569° and 34.457°. It is considered that the former peak comes from GaN buffer layer and the latter from GaNP alloy layer. So the sample grown with PH_3 = 1.0 SCCM is phase-separated into $GaP_{0.984}N_{0.006}$ and $GaN_{0.985}P_{0.015}$. The P composition x of $GaN_{1-x}P_x$ is only 1.5%, despite the high PH_3 flow rate of 1.0 SCCM. It seems that the P composition of 1.5% is upper limit of the growth of GaN-rich side of GaNP on sapphire substrate under the present growth condition. The FWHM of GaNP (0 0 0 2) peak is 237.6 arcsec, which was as narrow as that of GaN (0 0 0 2).

Fig. 2 shows the relation between the composition x of $GaN_{1-x}P_x$ layer and PH_3 flow rate. We

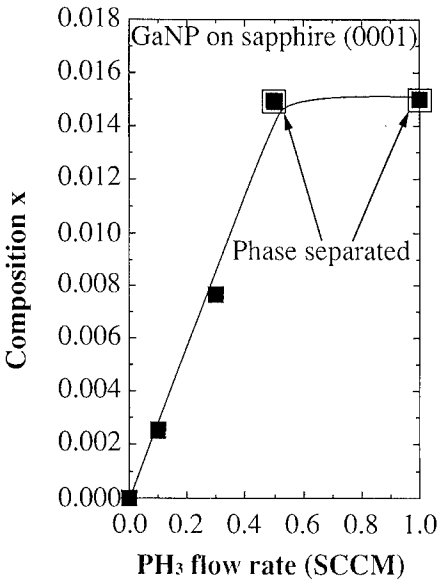

Fig. 2. P composition variation with PH_3 flow rate for the GaN-rich side of GaNP alloys.

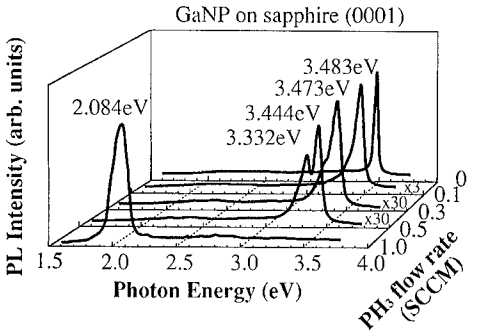

Fig. 3. 77 K PL spectra from the GaNP (PH_3 = 0, 0.1, 0.3, 0.5, 1.0 SCCM) grown on sapphire (0 0 0 1).

have obtained P compositions $x = 0.0026$, 0.0077, 0.015 of $GaN_{1-x}P_x$ layers for the PH_3 flow rate of 0.1, 0.3, 0.5 SCCM, respectively. However, when the PH_3 flow rate was 1.0 SCCM, the saturation of P composition x was observed as shown in Fig. 2. It is considered to be due to the phase separation (miscibility gap) of this alloy system.

3.2. Red shift of PL peak of GaNP

We clearly observed the PL spectra from all of GaNP layers grown here are shown in Fig. 3. The PL spectrum from the GaNP layer grown with PH_3 flow rate of 1.0 SCCM was dominated by the PL emission from the above-mentioned phase separated $GaP_{1-y}N_y$ ($y = 0.006$) region. The PL spectrum was very similar to that reported by Baillargeon et al. [4] and the comparison gives 0.01 as a N composition y of the $GaP_{1-y}N_y$ region. This value shows fairly good agreement with the above-mentioned result of $y = 0.006$ from the XRD measurement.

The PL spectra from the other GaNP layers (PH_3 flow rate = 0.1, 0.3 and 0.5 SCCM) in Fig. 3 shows a clear emission peak from alloy layer and no deep emission at around 2.2 eV. The PL spectrum from phase separated sample with $PH_3 = 0.5$ SCCM shows that the $GaN_{1-x}P_x$ ($x = 0.015$) (direct-band) have much stronger PL than $GaP_{1-y}N_y$ ($y = 0.006$) (indirect-band). Each emission peak from alloy layer shows a shift toward lower energy with increasing P concentration. We observed RT PL and these RT profiles show red shift like 77K one at the lower energy side.

Fig. 4 shows the plot of 77K PL peak energy versus P composition x of $GaN_{1-x}P_x$. We observed experimentally large energy shift toward lower energy in the GaN-side of GaN–GaP alloy material system for the first time.

The closed square data point in Fig. 4 shows the plot of 77 K PL peak energy versus P composition x of $GaN_{1-x}P_x$. Compared with the line with no bowing, large peak energy shift is clear as can be seen in Fig. 4. It is considered that the large energy shift is due to the large bowing parameter of GaN–GaP alloy material system compared with other III–V compound semiconductors.

This alloy has a small lattice mismatch to GaN layer and the accommodation coefficient is given by

$$\frac{\Delta a_{\text{measured}}}{a_{\text{sub}}} = \left(1 + \frac{2v}{1-v} + \frac{8v\ t_{\text{epi}}}{1 - vt_{\text{sub}}}\right)\frac{\Delta a_{\text{epi}}}{a_{\text{sub}}},$$

where $\Delta a_{\text{epi}} = a_{\text{epi}} - a_{\text{sub}}$, t is a layer thickness and v is the Poisson's ratio. We used GaN Poisson's

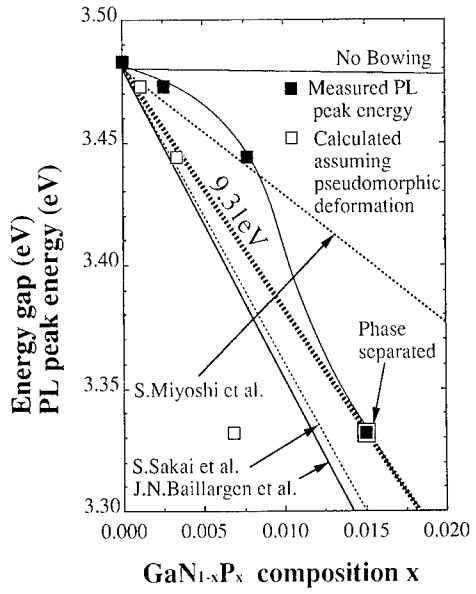

Fig. 4. PL peak energy at 77 K versus P composition x for grown $GaN_{1-x}P_x$. The closed and open square data points are plots without and with accommodation of elastic strain at GaNP and GaN interface. Theoretically calculated data are also plotted along with the curve with no bowing.

ratio of $v_{<0001>} = 0.38$ [12]. These results are shown by the open square data points in Fig. 4. This calculation was done assuming that the GaNP alloy layer is grown under the complete pseudomorphic condition. In the case of $GaN_{1-x}P_x$ ($x = 0.015$), we observed phase separation by XRD and it considered that the strain relaxation occurred completely. So, the strain accommodated red shift profile shows the bold dashed line in Fig. 4.

The gradient of theoretically calculated band gap energy curve for the GaN–GaP alloy material system is also plotted in Fig. 4 [4, 13, 14]. In this figure, only the gradient is compared, and the absolute band gap energy value is not taken into account. It seems that the gradient of the present work generally agrees with those of Baillargen et al. [4] and Sakai et al. [15]. We estimated the bowing parameter from the dielectric theory of electronegativity developed by Van Vechten [15] and obtained it as 9.31 eV.

4. Conclusions

We have grown the GaN-rich side of $GaN_{1-x}P_x$ layers on (0 0 0 1) sapphire substrate with high temperature GaN buffer layer by gas source MBE using ion-removed ECR radical cell for the nitrogen source. The use of ion-removed ECR radical cell made it possible to grow high quality GaN. The maximum P composition x of $GaN_{1-x}P_x$ was 0.015 and phase separation into GaN rich GaNP and GaP-rich GaPN was observed for the high PH_3 flow rate growth condition. Large red shift of the PL peak was observed from $GaN_{1-x}P_x$ ($x = 0.0026$, 0.0077 and 0.015). The gradient of these red shifts agreed with those reported by the theoretical calculation for GaNP alloy. Nevertheless, we have experimentally observed, for the first time, the large red shift indicating large bowing parameter in this alloy system.

Acknowledgements

The authors would like to express their thanks to the Material Analysis Center of ISIR for the X-ray diffraction measurements. This work is supported in part by the Murata Science Foundation. K.I. acknowledges a support from the Japan Society for the Promotion of Science for Young Scientists.

References

[1] S. Nakamura, M. Senoh, S. Nagahama, N. Iwasa, T. Yamada, T. Matsushita, H. Kiyoku and Y. Sugimoto, Jpn. J. Appl. Phys. 35 (1996) L74.
[2] D.G. Thomas, J.J. Hopfield and C.J. Frosch, Phys. Rev. Lett. 15 (1965) 857.
[3] J.N. Baillargeon, K.Y. Cheng, S.L. Jackson and G.E. Stillman, Appl. Phys. Lett. 69 (1991) 8025.
[4] J.N. Baillargeon, K.Y. Cheng, G.E. Hofler, P.J. Pearah and K.C. Hsieh, Appl. Phys. Lett. 60 (1992) 2540.
[5] M. Weyers, M. Sato and H. Ando, Jpn. J. Appl. Phys. 31 (1992) L853.
[6] S. Miyoshi, H. Yaguchi, K. Onabe, R. Ito and Y. Shiraki, Appl. Phys. Lett. 63 (1993) 3506.
[7] M. Kondow, K. Uomi, K. Hosomi and T. Mozume, Jpn. J. Appl. Phys. 33 (1994) L1056.
[8] O. Igarashi, Jpn. J. Appl. Phys. 31 (1992) 3791.

[9] K. Iwata, H. Asahi, K. Asami and S. Gonda, Jpn. J. Appl. Phys. 35 (1996) 41635.
[10] K. Iwata, H. Asahi, S.J. Yu, K. Asami, H. Fujita, M. Fushida and S. Gonda, Jpn. J. Appl. Phys. 35 (1996) L289.
[11] K. Iwata, H. Asahi, S.J. Yu, M. Fushida, K. Asami and S. Gonda, in: Topical Workshop on III–V Nitrides, Nagoya, Japan, September 1995, Abstracts, H-1.
[12] T. Detchprohm, K. Hiramatsu, K. Itoh and I. Akasaki, Jpn. J. Appl. Phys. 31 (1992) L1454.
[13] S. Miyoshi and K. Onabe, in: Topical Workshop on III–V Nitrides, Nagoya, Japan, September 1995, Abstracts, P-1.
[14] S. Sakai, Y. Ueta and Y. Terauchi, Jpn. J. Appl. Phys. 32 (1993) 4413.
[15] J.A. Van Vechten, Phys. Rev. 182 (1969) 891.

ELSEVIER

Journal of Crystal Growth 175/176 (1997) 156–161

JOURNAL OF CRYSTAL GROWTH

Laterally nonuniform Ga segregation at GaAs/AlGaAs interfaces during MBE growth

W. Braun*, A. Trampert, L. Däweritz, K.H. Ploog

Paul-Drude-Institut für Festkörperelektronik, Hausvogteiplatz 5–7, D-10117 Berlin, Germany

Abstract

We have studied the Ga segregation at the normal GaAs/$Al_xGa_{1-x}As$ interface by a new in situ electron diffraction technique during molecular beam epitaxy and by ex situ transmission electron microscopy. We find Ga segregating up to 20 crystal planes when depositing AlAs on GaAs. The measurements indicate an anisotropic in-plane structure of this interface with elongated $Al_xGa_{1-x}As$ regions extending along [$\bar{1}$ 1 0]. The inverted interface is abrupt with a measurement error of less than one bilayer. Our findings provide new insight into both the mechanism of RHEED intensity oscillations as well as the segregation process.

1. Introduction

GaAs–$Al_xGa_{1-x}As$ heterojunctions are widely considered as prototype heterointerfaces in terms of abruptness and structural perfection as well as regarding their potential for electronic band-gap engineering in advanced devices. However, it has been known for quite some time that there is a strong asymmetry between the normal ($Al_xGa_{1-x}As$-on-GaAs) and inverted (GaAs-on-$Al_xGa_{1-x}As$) interfaces regarding their structural [1] and electronic [2] properties.

In this paper we directly demonstrate the segregation of Ga many lattice planes into the overgrowing AlAs (0 0 1). In addition, this Ga segregation exhibits a strongly anisotropic in-plane structure which we directly monitor by reconstruction-induced phase shifts (RIPS) of reflection high-energy electron diffraction (RHEED) intensity oscillations during molecular beam epitaxy (MBE) growth of the interfaces. No measurable segregation is found at the GaAs-on-AlAs (0 0 1) interface. These results are confirmed by high-resolution transmission electron microscopy (HRTEM) along [1 1 0] and [$\bar{1}$ 1 0]. The existence of a lateral structure demonstrates the need for a three-dimensional treatment of the segregation problem. At the same time, the experiments indicate that the Ga segregation is not kinetically limited. In addition, our findings reveal a new understanding of RHEED intensity oscillations and demonstrate the general applicability of this method to monitor the formation of heterointerface in real-time on an atomic scale.

* Corresponding author. fax: +49 30 20377 201; e-mail: braun@pdi.wias-berlin.de; www: http://pdi1.wias-berlin.de/~braun.

0022-0248/97/$17.00 Copyright © 1997 Elsevier Science B.V. All rights reserved
PII S0022-0248(96)00817-2

2. Experiment

We deposited GaAs and $Al_xGa_{1-x}As$ by MBE on GaAs (0 0 1) substrates in a continuous series of 30 s growth pulses separated by 30 s growth interruptions. The deposition rate was typically 0.2 nm/s. The 20 keV electron beam impinged at angles ranging from 0.2 to 1.5° along a high-symmetry azimuth and the resulting intensity oscillations were recorded at different positions of the diffraction pattern. Throughout the growth sequence, the diffraction conditions were kept constant. This procedure eliminated diffraction-related effects like the dependence of the oscillation phase on electron beam incidence angle [3]. The growth sequence was designed to contain both homoepitaxial and heteroepitaxial pulse successions so that all four possibilities, GaAs on GaAs, $Al_xGa_{1-x}As$ on GaAs, $Al_xGa_{1-x}As$ on $Al_xGa_{1-x}As$ and GaAs on $Al_xGa_{1-x}As$, were present. The curves were then superimposed with respect to the onset of growth by means of the shutter actuation signal.

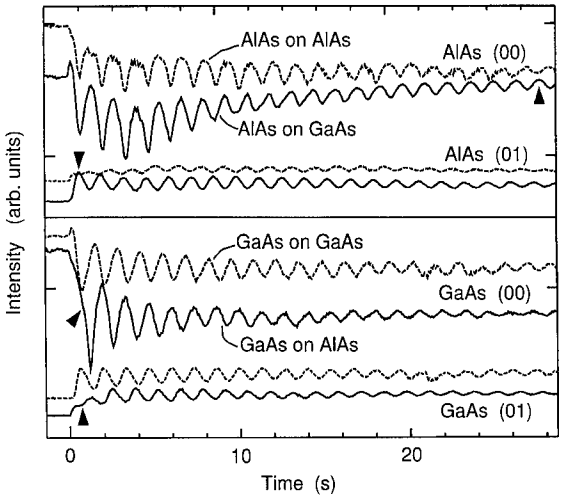

Fig. 1. Synchronized RHEED intensity oscillations from AlAs/GaAs and GaAs/AlAs interfaces recorded with an incidence angle of 0.35°. For all 4 pairs of traces, the broken line is the homoepitaxial reference and the solid line represents the signal from heterointerface formation. The {0 1} intensities can only be measured outside the Laue circle at these low angles. The electron energy was 20 keV with the beam directed along the [$\bar{1}$ 1 0] azimuth. The growth rates were 0.2 nm/s at a sample temperature of 584°C, and the As_4 beam equivalent pressure was 3.2×10^{-3} Pa.

3. Results and discussion

A comparison of heteroepitaxial and homoepitaxial RHEED intensity trace pairs for both GaAs and AlAs is shown in Fig. 1. After a certain transition distance, marked by the arrows, the oscillations from heterointerface formation are shifted with respect to the homoepitaxial reference oscillations. This phase shift is opposite in direction, but of the same magnitude for normal and inverted heterointerfaces. Far from the heterointerface, it assumes the same saturation value for the specular spot and the {0 1} reflections. The transition distance to achieve the final value of the phase shift is, however, strongly different on different reflections, as marked by the arrows. It takes up to 20 oscillations at the specular spot position in the [$\bar{1}$ 1 0] azimuth, whereas the phase shift is completed typically during the first oscillation along other azimuths or at positions in the diffraction pattern different from the specular spot. The very short transition distance observed at the inverted interface implies that the sampling depth of the oscillating part of the RHEED signal is less than the 0.28 nm (0 0 2) lattice plane spacing, denoted in the following as one layer. If it were larger, an abrupt interface gradually crossing the sampled volume would produce a gradually varying signal with a minimum transition distance equal to the probing depth. As we will show, the observed phase shift phenomena are closely connected to the surface reconstruction. We therefore call this class of effects the reconstruction-induced phase shifts (RIPS) of RHEED intensity oscillations [4].

From such experiments as we have performed with different growth and diffraction conditions, we deduce that the saturation value of the RIPS is *independent of diffraction conditions* like the beam incidence angle, but rather depends on the two surface reconstructions before and after interface formation. We therefore conclude that the RIPS saturation value cannot be a diffraction phenomenon. Instead, it is linked to the difference in group III element content of the two surface reconstructions.

Since growth is performed with As overpressure, the As supply is not rate-limiting. Instead, the constant group III flux during deposition defines the time-axis of the RHEED oscillations. For homoepitaxy, the deposition of group III elements equal to the group III content of n bulk layers advances the growth front by n layers. However, the reconstructed layers at the surface may contain incomplete group III sublattices. If the reconstruction changes during growth, group III material is consumed or released in the transition, resulting in a shift of the remaining oscillations. Interpreting the phase shift in this way, we identify it with the loss or gain of the group III elements between the two surface reconstructions. This conclusion imposes relative constraints on different possible structure models. In our case, GaAs exhibits the $\beta(2\times4)$ RHEED pattern using the Farrell–Palmstrøm terminology [5] and AlAs shows the $c(4\times4)$ pattern. From the phase shift we, therefore, conclude that the surface structures producing these patterns differ by half a (0 0 2) layer of Ga or Al.

The phase shift between GaAs and AlAs implies chemical sensitivity of the oscillation phase that should allow us to determine the surface composition during growth. We, therefore, replaced AlAs in our pulse sequence by $Al_xGa_{1-x}As$ with varying x and obtained the curves shown in Fig. 2. The inverted interface was chosen because the rapid phase shift there increases the measurement accuracy. As in Fig. 1, the broken lines represent the homoepitaxial reference oscillations. The RIPS saturates at the same value for both the specular spot and the (01) reflection. The relationship between phase shift and composition obtained from the RIPS is plotted in the lower part of the figure. This dependence relates a given value of the oscillation phase to a certain surface composition. From the signal obtained on the specular spot at the normal interface along $[\bar{1}\,1\,0]$, we thus deduce strong segregation at the normal interface. The shift on the $\{0\,1\}$ streaks of the same measurement, however, is immediate, indicating that at this point in the diffraction pattern, no segregation is detected. The surface material composition as a function of the deposited AlAs layers is plotted in Fig. 3 for both reflections.

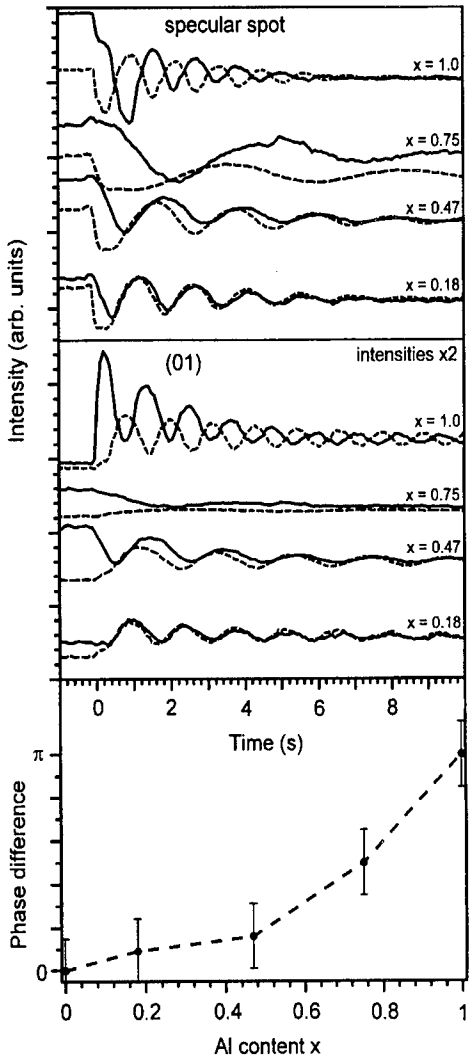

Fig. 2. Relationship between alloy composition x and phase shift. The AlAs was replaced by $Al_xGa_{1-x}As$ in measurements using growth conditions similar to Fig. 1. The resulting dependence is plotted in the lower part of the figure. Shown are the curves for GaAs on GaAs (broken lines) and GaAs on $Al_xGa_{1-x}As$ (solid lines) at the inverted interface.

This contradiction between the two results obtained from different locations of the diffraction pattern is resolved by taking into account the surface morphology of the GaAs surface and the special scattering geometry of RHEED. Because of the small probing depth of the RHEED electrons, the signal is very sensitive to disorder in the

topmost crystal layer. Information from disordered surface regions is detected at or near the specular spot, which would be the only peak in the diffraction pattern of a perfectly amorphous 2D structure. The ordered regions with complete lateral symmetry contribute to all scattering orders. The surface of $\beta(2\times4)$-reconstructed GaAs (0 0 1) exhibits an anisotropic morphology [6], leading to long and relatively straight step edges along [$\bar{1}$ 1 0]. This suggests that the disordered regions we monitor on the specular spot can be identified as steps on the surface. If the RHEED beam is parallel to these step edges, it can sensitively accumulate the signal. We therefore expect an enhanced sensitivity of the specular spot signal regarding the structure of steps along [$\bar{1}$ 1 0]. This finding is supported by the fact that on the specular spot along the [1 1 0], the RIPS saturates immediately [7]. In this direction, the step edges on the surface are bent and ragged.

This real-space sensitivity of RHEED leads us to conclude that segregation is a predominantly step-mediated process that is suppressed on the flat surface regions. The different binding energies of terrace and step atoms facilitate exchange reactions at steps. This argument still holds during growth in the limit of layer-by-layer growth, which corresponds to the case of weakly damped RHEED oscillations. Then, a step present on the surface prior to growth remains roughly at the same lateral position after the deposition of one bilayer. The step region therefore propagates in growth direction while serving as a continuous source of exchange reactions in the segregation process. The smaller-scale islands causing the oscillations during deposition nucleate on the terraces where no Ga atoms are released from the complete underlying plane, and therefore no segregation is observed in higher diffraction orders.

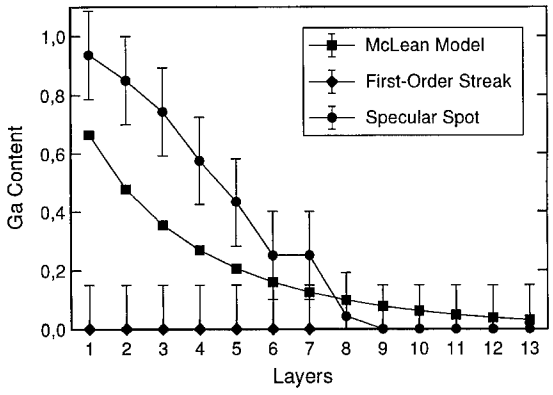

Fig. 3. Surface alloy composition determined with the relation of Fig. 2 at the specular spot position, the first-order diffraction streak and the theoretical curve using the McLean model with the parameters of Ref. [10].

Current RHEED theory does not yet allow the treatment of realistic stepped surfaces [8]. We therefore cannot determine the quantitative fraction of the segregating and nonsegregating regions on the surface directly from the diffraction pattern. Repetition of the RIPS experiment along the [1 1 0] azimuth shows an immediately saturating shift on both streaks within the measurement accuracy [7], indicating that the fraction of segregation areas is small. A laterally homogeneous segregation profile is modeled for the GaAs–AlAs materials system using McLean's formula [9]

$$\ln\left(\frac{x_b}{1-x_b}\right)=\frac{E_s}{kT}+\ln\left(\frac{x_s}{1-x_s}\right),$$

where x_s and x_b denote the surface and bulk compositions, E_s the segregation energy, and thermal equilibrium between the surface layer and bulk material is assumed. Using parameters deduced from in situ electron spectroscopy experiments [10], the curve plotted in Fig. 3 is obtained. The experimental values obtained from the specular spot signal indicate a nonexponential segregation that would produce an approximately constant (top hat) concentration profile if it were homogeneous across the surface. The signal from the first-order spot indicates no segregation. These three results are consistent if the area of the intermixed region makes up only part of the surface area, while its material composition remains Ga-rich with an almost constant composition. We, therefore, expect to obtain segregation in elongated regions that follow the [$\bar{1}$ 1 0] direction.

The HRTEM micrographs shown in Fig. 4 were taken along the extremal directions of the surface anisotropy. Along [$\bar{1}$ 1 0] laterally separated segregation regions are visible at the normal interface. Since the sample thickness corresponds to roughly

80 {1 1 0} crystal planes, this finding implies a high degree of order along the beam direction. In the perpendicular [1 1 0] direction, the segregation regions are projected along their narrow direction, leading to a broad, featureless band. No segregation, as expected from the RHEED experiments, is seen at the normal heterointerface. The extent of the transition regions is marked by grey bars to the side. Assuming a step as the source of segregation, the small lateral separation of the segregation regions might be due to kinks in the step edge that typically shift the step by four lattice constants, the periodicity of the $\beta(2\times4)$ reconstruction in this direction.

The assumption of a thermal equlibrium in the McLean model requires that this equilibrium is approached faster than the typical time-scales involved in the growth process. We investigated the kinetics of the segregation by varying the AlAs growth rate in experiments otherwise similar to the one shown in Fig. 1. The measured transition distances of the phase shift were 13 ± 2, 15 ± 2 and 16 ± 2 layers for growth rates of 0.13, 0.17 and 2.1 nm/s and otherwise identical growth and diffraction conditions. This approximately constant transition distance indicates that the exchange process is not kinetically limited. Instead, we can conclude that segregation takes place in a local equilibrium situation close to the step edges.

4. Conclusions

In summary, we have shown that the difference of the reconstruction-induced phase shifts of

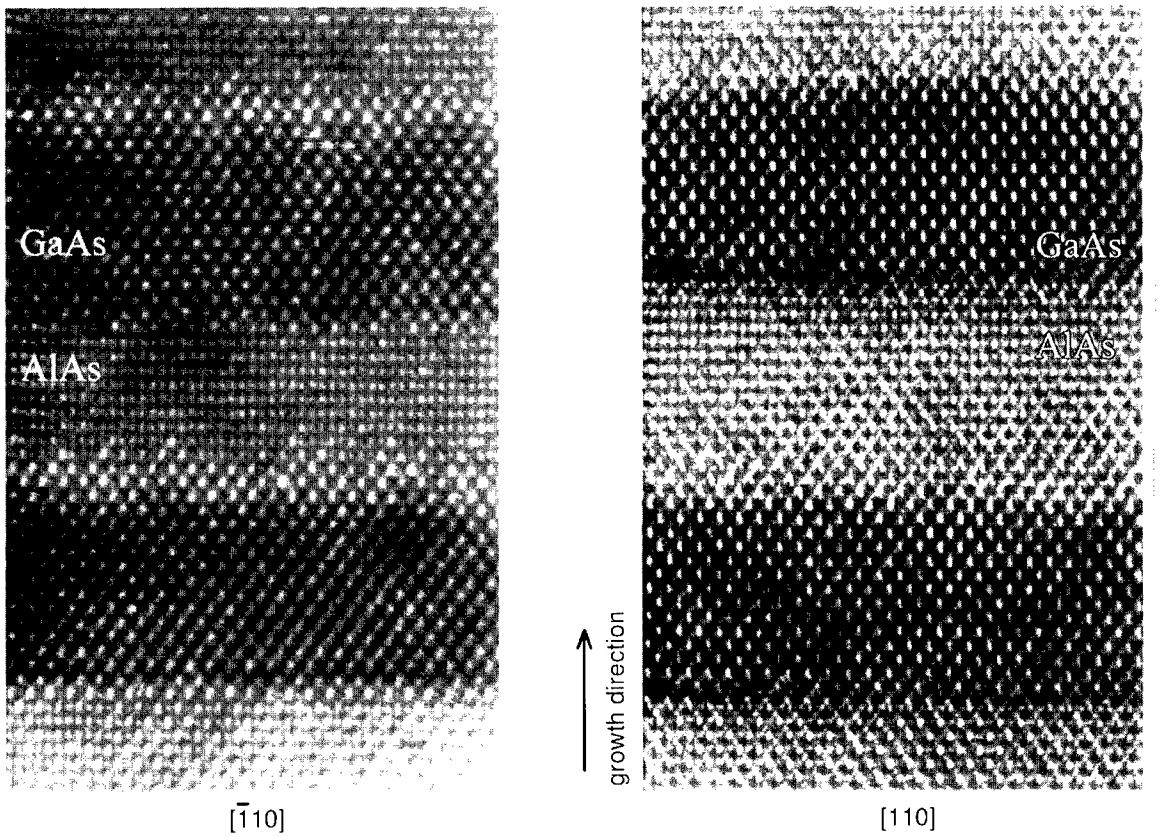

Fig. 4. HRTEM micrographs along two azimuths of a nominal 14 layer/14 layer GaAs/AlAs superlattice. The growth conditions for the sample were similar to those detailed in Fig. 1. The electron energy was 400 keV.

RHEED oscillations at specular and nonspecular positions can be explained by the morphological sensitivity of RHEED. We discovered strong laterally anisotropic Ga segregation for MBE growth of AlAs on GaAs, whereas no segregation is present for deposition of GaAs on AlAs. The measurement method relies only on the surface reconstruction difference and the presence of RHEED intensity oscillations. It should therefore be applicable to any materials system that meets these two requirements.

Acknowledgements

The authors gratefully acknowledge the support of the Deutsche Forschungsgemeinschaft (Sonderforschungsbereich 296) and thank Oliver Brandt for helpful discussions.

References

[1] G.S. Spencer, J. Menéndez, L.N. Pfeiffer and K.W. West, Phys. Rev. B 52 (1995) 8205; B. Etienne and F. Laruelle, J. Crystal Growth 127 (1993) 1056; R. Kohleick, A. Förster and H. Lüth, Phys. Rev. B 48 (1993) 15 138; B. Jusserand and F. Mollot, Appl. Phys. Lett. 61 (1992) 423.

[2] See, e.g.: L.N. Pfeiffer, K.W. West, H.L. Störmer and K.W. Baldwin, Appl. Phys. Lett. 55 (1989) 1888; T. Saku, Y. Hirayama and Y. Horikoshi, Jpn. J. Appl. Phys. 30 (1991) 902; T. Sajoto, M. Santos, J.J. Heremans, M. Shayegan, M. Heilblum, M.V. Weckwerth and U. Meirav, Appl. Phys. Lett. 54 (1989) 840.

[3] J. Zhang, J.H. Neave, P.J. Dobson and B.A. Joyce, Appl. Phys. A 42 (1987) 317.

[4] W. Braun and K. Ploog, Appl. Phys. A 60 (1995) 441.

[5] H.H. Farrell and C.J. Palmstrøm, J. Vac. Sci. Technol. B 8 (1990) 903.

[6] E.J. Heller and M.G. Lagally, Appl. Phys. Lett. 60 (1992) 2675; J. Sudijono, M.D. Johnson, M.B. Elowitz, C.W. Snyder and B.G. Orr, Surf. Sci. 280 (1993) 247.

[7] W. Braun and K.H. Ploog, J. Appl. Phys. 75 (1994) 1993.

[8] For some recent work on the GaAs (0 0 1) surface, see: Y. Ma, S. Lordi, P.K. Larsen and J.A. Eades, Surf. Sci 289 (1993) 47; J.M. McCoy, U. Korte, P.A. Maksym and G. Meyer-Ehmsen, Phys. Rev. B 48 (1993) 4721.

[9] D. McLean, Grain Boundaries in Metals (Clarendon, Oxford, 1957) ch. 5, p. 118.

[10] J.M. Moison, C. Guille, F. Houzay, F. Barthe and M. Van Rompay, Phys. Rev. B 40 (1989) 6149.

ELSEVIER

Journal of Crystal Growth 175/176 (1997) 162–167

JOURNAL OF CRYSTAL GROWTH

Suppression of AlGaAs/GaAs superlattice intermixing by p-type doping

K. Muraki*, Y. Horikoshi[1]

NTT Basic Research Laboratories, 3-1 Morinosato-Wakamiya, Atsugi, Kanagawa 243-01, Japan

Abstract

We report a systematic investigation of the effect of n- and p-type doping on the AlGaAs/GaAs superlattice (SL) intermixing using photoluminescence. We find that the SL intermixing is not only enhanced by Si doping but also suppressed by Be doping. Although previous models have suggested the contribution of triply negatively charged Ga vacancies, V_{Ga}^{3-}, in n-type and intrinsic materials and of doubly positively charged Ga interstitials, I_{Ga}^{2+}, in p-type materials, we find that at 900°C the Al–Ga interdiffusion is mediated by singly negatively charged Ga vacancies, V_{Ga}^{-}, in both p- and n-type materials for $n < 1 \times 10^{18}$ cm^{-3}. These results are shown to be explained consistently in terms of the Fermi-level effect. Our results demonstrate that the thermal stability of AlGaAs/GaAs heterostructures can be controlled, i.e., weakened or strengthened, by appropriate tuning of the Fermi level.

1. Introduction

The atomic diffusion in GaAs and associated III–V compound semiconductors is affected by various parameters such as the Fermi level and/or the stoichiometry of the crystal. Presently, it is considered that the column-III atom diffusion in GaAs is mediated by triply negatively charged Ga vacancies, V_{Ga}^{3-}, in n-type and intrinsic materials, and by doubly positively charged Ga interstitials, I_{Ga}^{2+}, in p-type materials [1]. The contribution of charged species to the atomic diffusion manifests itself as a diffusion coefficient strongly dependent on the Fermi level of the crystal, the so-called "Fermi-level effect". For instance, n-type impurities such as Si, Sn, or Te doped either in situ or after growth enhance the Al–Ga interdiffusion, causing significant superlattice (SL) disordering during post-growth annealing.

As for p-type impurities, it is known that the post-growth in-diffusion or implantation of Zn or Be gives rise to significant layer disordering, as a result of the combined effects of the Fermi level and the non-equilibrium defects created through the dopant diffusion. That is, p-type doping increases the I_{Ga}^{2+} concentration via the Fermi-level effect, and the dopant diffusion via the kick-out mechanism creates I_{Ga}^{2+} in excess of its thermal equilibrium concentration. On the other hand, different results have been reported for grown-in

* Corresponding author. Fax: + 81 462 40 4727; e-mail: muraki@will.brl.ntt.jp.

[1] Present address: Faculty of Science and Engineering, Waseda University, 3-4-1 Okubo, Shinjuku, Tokyo 169, Japan.

0022-0248/97/$17.00 Copyright © 1997 Elsevier Science B.V. All rights reserved
PII S0022-0248(96)00928-1

p-type impurities. Deppe et al. [2] have reported that Mg doping at 8×10^{18} cm^{-3} enhances the SL disordering, whereas Guido et al. have reported that carbon doping retards the SL intermixing [3]. On the other hand, Kawabe et al. [4] and Kamata et al. [5] have observed no significant effect of Be doping for concentrations below 4×10^{19} cm^{-3}. These discrepancies can be due partly to the limited resolution of the methods used to probe the SL disordering. These authors used transmission electron microscopy [2, 3], Auger electron spectroscopy [4], secondary-ion mass spectrometry (SIMS) [5], which are rather insensitive to small amount of SL intermixing. Also, different annealing conditions used, i.e., the As pressure or the surface protection techniques, can be responsible for the discrepancies.

In this work, we present a systematic study of the effect of Si and Be doping on the AlGaAs/GaAs SL intermixing. To study the SL intermixing, we employ photoluminescence (PL), which is more sensitive to the Al–Ga interdiffusion than those methods used in the previous studies. Arsenic-pressure dependent experiments have also been carried out to identify the defects involved in the diffusion process. We find that in the As-rich condition the SL intermixing is not only enhanced by n-type doping but also suppressed by p-type doping. These results are shown to be explained consistently in terms of the Fermi-level effect.

2. Experimental procedure

Samples studied are $Al_xGa_{1-x}As/GaAs$ ($x = 0.34$) SL structures grown at 580°C on undoped semi-insulating GaAs (0 0 1) substrates by molecular-beam epitaxy. Twenty periods of SL layers consisting of 10-nm $Al_xGa_{1-x}As$ and 10-nm GaAs were grown on a 0.2-μm thick GaAs buffer layer, capped with a 0.1-μm thick GaAs layer. The whole epitaxial layers including the top and bottom GaAs layers as well as the SL layers were doped throughout either with Si or Be [6]. Two different doping levels, 3×10^{17} and 7×10^{17} cm^{-3}, were employed for both Si and Be.

The samples were annealed at 800–950°C for 1 h in sealed quartz ampoules evacuated to 2×10^{-6} Torr. For the As-pressure dependent experiments, small pieces of solid As (6N) were enclosed in each ampoule to produce desired As overpressure during the annealing. We have also carried out the annealing without excess As. Even without As, the sample surface remained specular even after annealing up to 950°C.

Photoluminescence was measured at 9 K with an Ar^+-ion laser as the excitation light source. The Al–Ga interdiffusion coefficient was calculated from the photoluminescence peak energy shift caused by the thermal annealing. In this approach, the diffusion coefficients in the range from 5×10^{-19} to 5×10^{-17} cm^2/s can be determined with reasonable accuracy for an annealing duration of 1 h.

3. Results and discussions

First, we will describe the results obtained for annealing without excess As. In Fig. 1, the PL spectra of differently doped SL's taken on the as-grown samples and those annealed at 900°C without As are shown as dashed and solid lines, respectively. For clarity, the PL intensities are normalized by their peak values. After the annealing, the PL peaks shift toward higher energies, as a consequence of the Al–Ga interdiffusion at the heterointerfaces and the resultant smearing of the SL potentials. It is seen that the peak shift is increased by Si doping relative to the undoped sample, and the peak shift further increases with increasing Si concentration, indicating that the Al–Ga interdiffusion is enhanced by Si doping.

On the other hand, the Be-doped SL's show small peak shift, even smaller than that of the undoped SL. Furthermore, the peak shift decreases further with increasing Be concentration. This result clearly shows that the Al–Ga interdiffusion is suppressed by Be doping. As shown later, similar results have been obtained for the annealing at 800–950°C without excess As. In a previous study, Kawabe et al. reported that the co-doping of Be with Si cancels the Si-induced disordering enhancement when the Be concentration is higher than that of Si [4]. The present result is significant in that the interdiffusion is further decreased relative to the

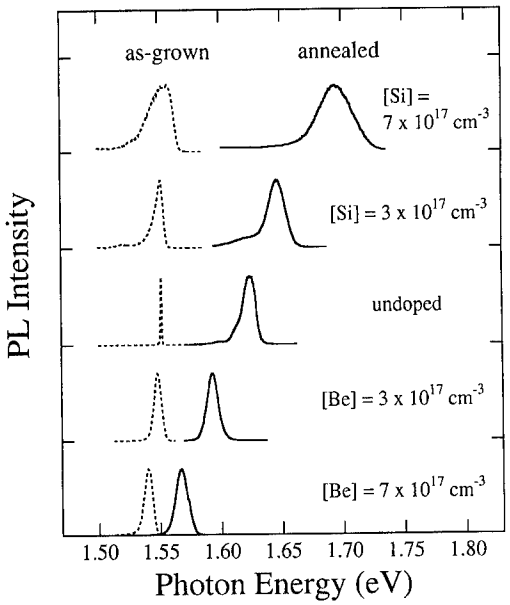

Fig. 1. 9 K PL spectra of differently doped SL's, taken on as-grown samples (dashed lines) and those annealed at 900°C without As (solid lines).

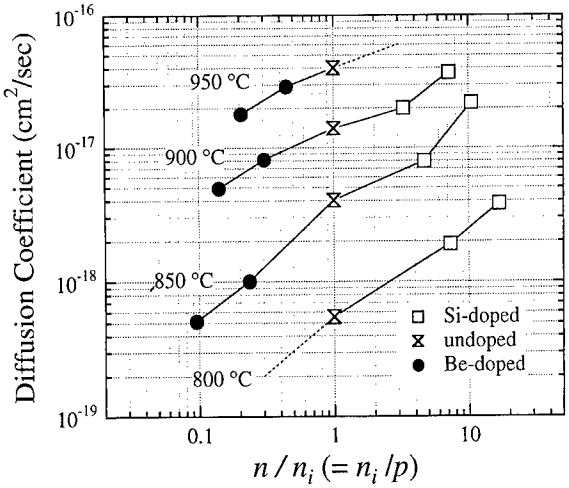

Fig. 2. Al–Ga interdiffusion coefficient for annealing without As plotted as a function of n/n_i.

undoped case. Our result agrees with the report by Guido et al. [3], in that the p-type doping retards the SL intermixing. Although they attributed the retarded intermixing to local atomic interaction specific to carbon, the present result suggests that the suppression of interdiffusion is not specific to carbon, but a rather common feature of grown-in p-type impurities.

We have calculated the Al–Ga interdiffusion coefficient from the PL peak energy shift caused by the SL intermixing. The Schrödinger equation has been numerically solved to obtain the energy levels in the diffused SL potentials. In the calculations, the band-bending effect due to the charge transfer from the $Al_xGa_{1-x}As$ layers to the GaAs layers was ignored [7]. For each sample, the PL peak energy shift measured from its as-grown position has been compared with the calculation to determine the diffusion coefficient.

Fig. 2 displays the Al–Ga interdiffusion coefficients calculated from the PL data of Fig. 1, together with the results for 800, 850, and 950°C. The data are shown only for those in the range from 5×10^{-19} to 5×10^{-17} cm^2/s. The horizontal axis, $n/n_i(=n_i/p)$, is the electron concentration n normalized by the intrinsic carrier concentration n_i at each annealing temperature (n_i normalized by the hole concentration p) [8]. Note that n/n_i is related to the Fermi level E_F through the following equation

$$n/n_i = \exp[(E_F - E_i)/k_BT], \tag{1}$$

where E_i is the Fermi level of intrinsic crystal, k_B is the Boltzmann constant, and T is the temperature. Thus, it is understood that $n/n_i > 1$, $n/n_i = 1$, and $n/n_i < 1$ correspond to n-type, intrinsic, and p-type materials, respectively.

By plotting the diffusion coefficient as a function of n/n_i, it is clear that the diffusion coefficient varies continuously from p-type through intrinsic to n-type region at each temperature. This suggests that the observed enhancement/suppression of the interdiffusion should be explained in a unified manner, i.e., by a single mechanism that depends solely on the Fermi level rather than the chemical species of the dopant. Let us assume that the diffusion is dominated by acceptor-like defects trapping m extra electrons, X^{m-}. According to the model of the Fermi-level effect [1], the thermal equilibrium concentration of X^{m-} depends on n/n_i as

$$[X^{m-}] \propto (n/n_i)^m = (n_i/p)^m = \exp[m(E_F - E_i)/k_BT]. \tag{2}$$

The Be-doping induced suppression of the interdiffusion is explained in terms of Eq. (2) as follows. The Be doping lowers the Fermi level and decreases the electron concentration, thereby decreasing the thermal equilibrium concentration of X^{m-}. It is also important to note in Eq. (2) that the power index m to n/n_i represents the number of extra electrons trapped by the defect. In Fig. 2, the relationship between the diffusion coefficient and n/n_i is seen to be almost linear [9]. Hence, we can say that the defect dominating the interdiffusion is an acceptor-like defect trapping one extra electron.

In order to identify the defects involved in the interdiffusion, we have studied the As-pressure dependence of the interdiffusion at 900°C. The results are shown in Fig. 3, in which the PL energies of SLs annealed with excess As are plotted as a function of the As_4 pressure. The horizontal bars on the left side represent the energy positions of each SL for the annealing without As. Note that their horizontal positions are arbitrary. It is seen that the undoped and Be-doped SLs show a consistent upward shift of the PL energies with increasing As_4 pressure. On the other hand, the Si-doped samples exhibit different behavior. The PL energy of the

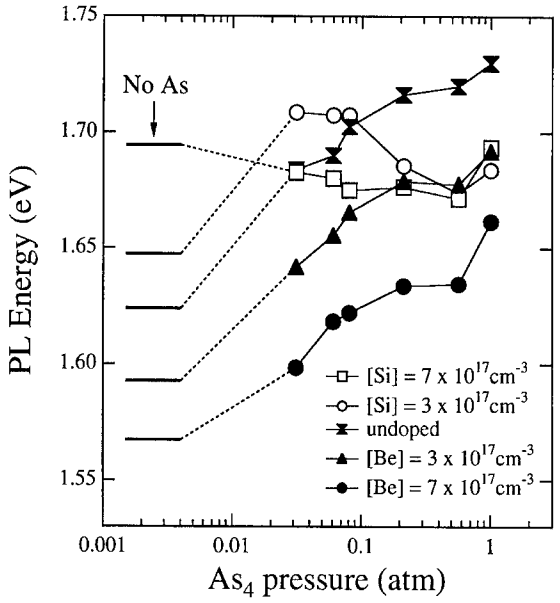

Fig. 3. PL energies of annealed SL's (900°C, with excess As) as a function of As_4 pressure during the annealing. The horizontal bars represent the PL energies for annealing without As.

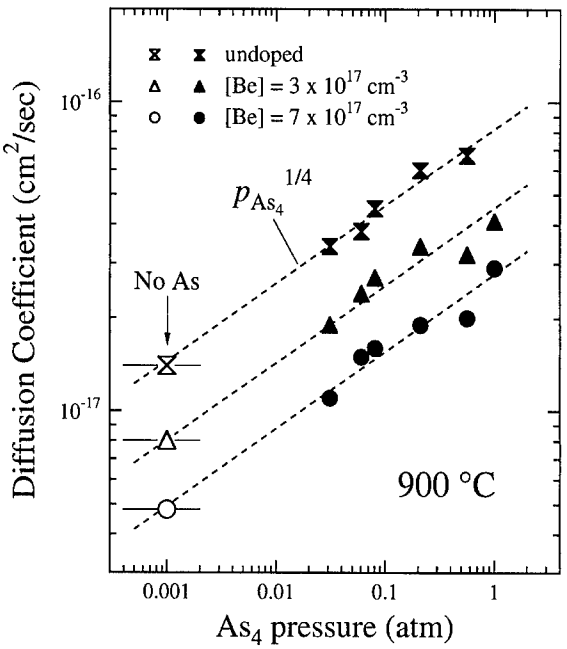

Fig. 4. Al–Ga interdiffusion coefficient at 900°C as a function of As_4 pressure. The solid and open symbols represent the data for annealing with and without As, respectively.

[Si] = 3×10^{17} cm^{-3} SL first increases and then falls off above the As_4 pressure of 0.2 atm. We note, however, that for the As_4 pressures above 0.2 atm the PL is dominated by a broad feature on the low-energy side of the band-edge transition. We ascribe this feature to some deep centers created by the thermal annealing. Similarly, we suspect that the PL of the [Si] = 7×10^{17} cm^{-3} SL annealed with excess As is due to some deep centers rather than the band-edge transition.

In Fig. 4, the Al–Ga interdiffusion coefficient calculated from the PL data of Fig. 3 are shown as solid symbols. The data are shown only for the undoped and Be-doped samples for the reason mentioned above. It is seen that the diffusion coefficient increases in proportion to $P_{As_4}^{1/4}$ in the whole pressure range from 0.03 to 1.0 atm. The power index of $\frac{1}{4}$ stems from the fact that the GaAs surface is interacting with As tetrameters in the vapor phase via the interaction

$$\tfrac{1}{4}As_4(g) \leftrightarrow As_{As} + V_{Ga}. \quad (3)$$

The consistent increase of the diffusion coefficient with the As_4 pressure demonstrates that at 900°C the diffusion is governed by Ga vacancies.

Also included in Fig. 4 are the data for annealing without As, which are shown as open symbols. Their horizontal positions are chosen in such a way that the data line up on the $P_{As_4}^{1/4}$ curves extrapolated from the data with known As_4 pressure. As seen in the figure, good agreement is obtained for both undoped and Be-doped samples by assuming an As_4 pressure of 0.001 atm. This result demonstrates that at 900°C the diffusion is dominated by Ga vacancies even for the annealing without As. On the other hand, when the temperature was reduced to 800°C, the diffusion coefficient exhibited "V-shaped" dependencies on the As pressures similar to those reported in Refs. [10, 11], indicating that both vacancy and interstitial contribute to the diffusion at 800°C. However, the results were rather complicated; different As pressure dependencies were observed for different doping. Hence, we will not discuss the results at 800°C further.

Combining the above two results, the As-pressure dependence and the Fermi-level dependence, we can conclude that at 900°C the Al–Ga interdiffusion is governed by Ga vacancy trapping one extra electron, V_{Ga}^{-}, in both n- and p-type materials. The present conclusion contradicts with the previous model that the column-III atom diffusion is governed by V_{Ga}^{3-} in n-type and intrinsic materials and by I_{Ga}^{2+} in p-type materials. The contribution of V_{Ga}^{3-} is based on the SIMS data of Mei et al. [12], in which the Al–Ga interdiffusion was observed to increase in proportion to $(n/n_i)^3$ [1]. In our previous SIMS study [13], however, we have reported that at 900°C the third-power law dependence occurs only for $[Si] > 10^{18}$ cm^{-3}, and the dependence was found to be much weaker for $[Si] < 10^{18}$ cm^{-3}, consistent with the present PL results. Thus, we speculate that the Ga vacancy changes its charge state with the Fermi level, the dominant charge state being V_{Ga}^{3-} for $n > 10^{18}$ cm^{-3} and V_{Ga}^{-} for $n < 10^{18}$ cm^{-3} at 900°C. This speculation is consistent with the theoretical calculation by Baraff and Schlüter that the lowest-energy charge state of Ga vacancy changes with the Fermi level [14].

Finally, the contribution of I_{Ga} has not been addressed in this study, since we focused on the diffusion at 900°C, where the vacancy mechanism dominates over the interstitial mechanism. Further investigation at lower temperatures, where the interstitial mechanism comes into play, is needed to clarify the contribution of I_{Ga}.

4. Conclusions

We have carried out a systematic study of the effect of n- and p-type doping on the Al–Ga interdiffusion. We find that in the As-rich condition the Al–Ga interdiffusion is not only enhanced by n-type doping but also suppressed by p-type doping. These results have been explained consistently in terms of the Fermi-level effect. From the observed dependence on the As pressure and the Fermi level, the defects dominating the Al–Ga interdiffusion at 900°C are determined to be Ga vacancies trapping one extra electron, V_{Ga}^{-}, in both p- and n-type materials for $n < 10^{18}$ cm^{-3}. Our results demonstrate that the thermal stability of AlGaAs/GaAs heterostructures can be controlled, weakened or strengthened, by appropriate tuning of the Fermi level.

Acknowledgements

The authors would like to thank Mr. S. Miyashita for the sample growth, Dr. M. Uematsu for experimental advice, and Dr. Y. Hirayama for fruitful discussions and continuous encouragement.

References

[1] T. Y. Tan, U. Gösele and S. Yu, Crit. Rev. Solid State Mater. Sci. 17 (1991) 47, and references therein.
[2] D.G. Deppe, N. Holonyak, Jr., W.E. Plano, V.M. Robbins, J.M. Dallesasse, K.C. Hsieh and J.E. Baker, J. Appl. Phys. 64 (1988) 1838.
[3] L.J. Guido, B.T. Cunningham, D.W. Nam, K.C. Hsieh, W.E. Plano, J.S. Major, Jr., E.J. Vesely, A.R. Sugg, N. Holonyak, Jr. and G.E. Stillman, J. Appl. Phys. 67 (1990) 2179.
[4] M. Kawabe, N. Shimizu, F. Hasegawa and Y. Nannichi, Appl. Phys. Lett. 46 (1985) 849.
[5] N. Kamata, K. Kobayashi, K. Endo, T. Suzuki and A. Misu, Jpn. J. Appl. Phys. 26 (1987) 1092.

[6] The top GaAs layer was employed to avoid the influence of the surface depletion.
[7] We have also carried out self-consistent calculations to find that the effect of the band-bending on the PL energy is negligibly small.
[8] The intrinsic carrier concentration was calculated to be 4.2×10^{16}, 6.7×10^{16}, 1.0×10^{17} and $1.5\times10^{17}\,cm^{-3}$ for 800, 850, 900, and 950°C, respectively.
[9] In reality, the dependence is sublinear. This is partly because the carrier concentration is decreased by the thermal annealing. Typically, the carrier concentration of n-type samples dropped to half of the initial values.
[10] L.J. Guido, N. Holonyak, Jr. and K.C. Hsieh, Inst. Phys. Conf. Ser. 96 (1988) 353.
[11] A. Furuya, O. Wada, A. Takamori and H. Hashimoto, Jpn. J. Appl. Phys. 26 (1987) L926.
[12] P. Mei, H.W. Yoon, T. Venkatesan, S.A. Schwarz and J.P. Harbison, Appl. Phys. Lett. 50 (1987) 1823.
[13] K. Muraki and Y. Horikoshi, in: Proc. 22nd Int. Symp. on Compound Semiconductors, Cheju, Korea (1995) (Inst. Phys. Conf. Ser. 145 (1996) 547).
[14] G.A. Baraff and M. Schlüter, Phys. Rev. Lett. 55 (1985) 1327.

ELSEVIER

Journal of Crystal Growth 175/176 (1997) 168–173

JOURNAL OF CRYSTAL GROWTH

InAs/GaAs in-plane strained superlattices grown on slightly misoriented (1 1 0) InP substrates by molecular beam epitaxy

Yoshiaki Nakata*, Osamu Ueda, Yuji Nishikawa, Shunichi Muto[1], Naoki Yokoyama

Fujitsu Laboratories Ltd., 10-1 Morinosato-Wakamiya, Atsugi 243-01, Japan

Abstract

InAs/GaAs in-plane strained superlattices (IPSSLs) were grown by molecular beam epitaxy. The substrates used were misoriented (1 1 0) InP tilted in the [0 0 $\bar{1}$] direction. We grew alternately half monolayers of InAs and GaAs while keeping the periodic single monolayer steps. The obtained structures were evaluated by transmission electron microscopy (TEM) and photoluminescence (PL) measurements. The TEM images revealed that the laterally periodic structures were formed almost in the [0 0 1] direction. The lateral period corresponded to the mean terrace width of the substrate. The PL peak energy obtained at 77 K was 0.77 eV, which was 40 meV lower than those of homogeneous InGaAs alloys. From the estimation of the transition energy dependence of $In_{1-x}Ga_xAs/In_xGa_{1-x}As$ strained superlattices on the mixing ratio x, we deduced that the obtained IPSSL was composed of $In_{0.74}Ga_{0.26}As/In_{0.26}Ga_{0.74}As$. This composition was consistent with the measurement by energy-dispersive X-ray microanalysis.

1. Introduction

Low-dimensional carrier-confined nano-structures such as quantum wires and dots are of great interest in high-performance electronic and photonic device applications. For fabricating these structures, methods involving lithography and etching, selective or ridge growth on patterned substrates, and self-organization phenomena in epitaxial growth have been proposed and studied extensively. Among these methods, growth of laterally periodic structures by growing alternately fractional monolayers of constituent materials via step flow growth on misoriented substrates [1] is the most important technique for direct formation of high-density quantum wires and quantum dot array structures. So far, GaAs/Al(Ga)As [1–8] and GaSb/Al(Ga)Sb [9–11] laterally periodic structures (i.e. in-plane superlattices (IPSLs)) have been grown on misoriented (0 0 1) GaAs and GaSb substrates by molecular beam epitaxy (MBE) and metalorganic chemical vapor deposition (MOCVD). The most serious problem in preparing these structures is that the composition difference between the barriers and the wells is far smaller (about 0.1 or 0.2) than ideal [9, 12–14]. Although the transmission electron microscopy (TEM) or X-ray diffraction (XRD) revealed the formation of laterally periodic

* Corresponding author. Fax: +81 462 50 8844; e-mail: nakata@qed.flab.fujitsu.co.jp.

[1] Present address: Faculty of Engineering, Hokkaido Univ., Sapporo, Japan.

0022-0248/97/$17.00 Copyright © 1997 Elsevier Science B.V. All rights reserved
PII S0022-0248(96)00826-3

structures with the same period as the mean terrace width of the substrates, the photoluminescence (PL) indicated small lateral composition modulation and poor lateral carrier confinement. Most studies, however, have been limited to lattice matched systems. Highly strained systems have hardly been studied.

On the other hand, the self-organized lateral composition modulations along the [1 1 0] direction, called strain-induced lateral-layer ordering (SILO), has been observed in highly strained $(GaP)_n/(InP)_m$ and $(GaAs)_n/(InAs)_m$ short period superlattices on exactly oriented (0 0 1) substrates [15–17]. The generation mechanism for SILO has not been completely understood at present, but it is obvious that a self-organizing phenomena caused by strain induces lateral composition modulations. If such a self-organizing phenomena can be managed in the growth technique using step flow growth, composition modulation should be greatly improved.

Recently, we demonstrated the growth of InGaAs/InAlAs IPSLs on misoriented (1 1 0) InP substrates [18–21]. TEM and PL showed that InGaAs/InAlAs IPSLs were indeed grown, but InAlGaAs alloy regions still existed. In this paper, we describe the MBE growth and structural features of InAs/GaAs in-plane strained superlattices (IPSSLs) grown on misoriented (1 1 0) InP substrates.

2. Growth of InAs/GaAs IPSSL

The substrates used were misoriented (1 1 0) InP tilted in the [0 0 $\bar{1}$] direction. On these substrates, single and double monolayer steps of (1 1 $\bar{1}$) B terminated with group V atoms were ordered according to the growth condition [18, 20–22]. Before growth, the substrates were thermally cleaned at approximately 570°C for 30 s under an As pressure of 1.4×10^{-5} Torr. InAs/GaAs IPSSLs were grown by conventional MBE. The shutter sequence for the IPSSL growth are shown in Fig. 1a. We alternately grew half-monolayers of InAs and GaAs, keeping regular arrays of single monolayer steps. A schematic diagram of the IPSSL structure expected for an ideal growth is shown in Fig. 1b. InAs/GaAs laterally periodic structures with the period of the

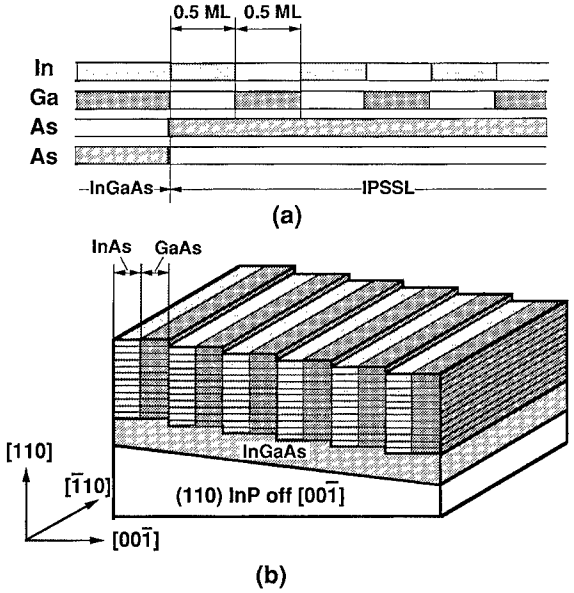

Fig. 1. (a) Shutter sequence for InAs/GaAs IPSSL growth. (b) Schematic diagram of the ideal IPSSL structure.

mean terrace width of the substrates should be grown. The growth rate of InAs and GaAs were about 95 and 83 nm/h, respectively. For one half-monolayer growth, the time required is 3.9 s for InAs and 4.5 s for GaAs. The growth temperature used was about 470°C and was measured with a calibrated pyrometer. The As pressure used for IPSSL growth was 4.3×10^{-6} Torr, and was 1.0×10^{-5} Torr for InGaAs and InAlAs growth. They were measured using an ion gauge at the substrate position. We changed the As pressure at the interfaces without growth interruption by switching two As cells kept at these pressures. The growth condition mentioned above was chosen for forming single monolayer step ordering.

Fig. 2a and Fig. 2c are the reflection high-energy electron diffraction (RHEED) patterns obtained for the growth of (a) an InGaAs buffer layer and alternate half monolayers of (b) InAs and (c) GaAs on a 3° tilted substrate. The electron beam incidence was parallel to the step edge ([$\bar{1}$ 1 0] azimuth). In every pattern, split spots showing single monolayer step ordering were clearly observed. Step ordering was kept even when growing InAs and GaAs alternately.

Fig. 2. RHEED patterns when growing (a) InGaAs buffer layer, and growing alternate half monolayers of (b) InAs and (c) GaAs on a substrate 3° tilted in the [0 0 $\bar{1}$] direction.

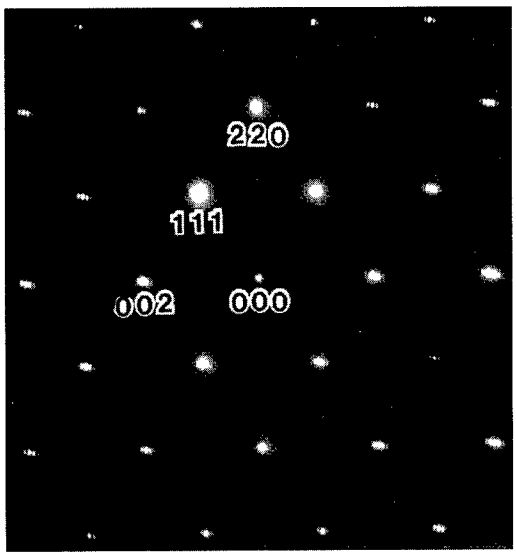

Fig. 3. ($\bar{1}$ 1 0) cross-sectional TED pattern of the IPSSL grown on a substrate 1.5° tilted in the [0 0 $\bar{1}$] direction.

3. Evaluation of InAs/GaAs IPSSL

3.1. Structural features

In order to clarify the structural features, we characterized obtained structures by TEM. Fig. 3 is a ($\bar{1}$ 1 0) cross-sectional transmission electron diffraction (TED) pattern obtained from the IPSSL grown on a 1.5° tilted substrate with an 8 nm wide mean terrace width. Extra spots are clearly observable. These extra spots are symmetric relative to the fundamental spots, aligned almost in the [0 0 1] direction. They reflected long lateral periodicity in the [0 0 1] direction. Positions of these spots were about $h, k, l \pm n/13.5$ where h, k, l are either all even or all odd, and n is an integer, indicating that the lateral period corresponded to 8 nm, which is equal to the mean terrace width of the substrate.

Fig. 4a is a ($\bar{1}$ 1 0) cross-sectional TEM dark field image. This IPSSL structure was grown on a 1.2° tilted substrate with a mean terrace width of 10 nm. The laterally periodic structure composed of the bright and dark contrasts start just after the InGaAs buffer layer. The periodic direction is almost in the [0 0 1] direction. The average period is approximately 10 nm, which is equal to the terrace width. In-plane distribution of IPSSL formation was evaluated by the plan-view TEM. Fig. 4b shows the dark field TEM image from the (1 1 0) plan view. The IPSSL was found to be formed almost along the [$\bar{1}$ 1 0] direction. The lateral interfaces were seen to be extended fairly straight over several microns. However, slight undulation of the periodic contrasts and partial disordering are also observed. These may be attributed to both slight variation of growth rate and fluctuation of terrace width during growth.

The composition distribution was analyzed by energy-dispersive X-ray microanalysis (EDX) integrated in a field emission-type scanning transmission microscope (FE-STEM). In this system, the spatial resolution of this analysis can be about 1 nm since the electron beam was focused to about 1 nm diameter. Fig. 5 shows the ($\bar{1}$ 1 0) cross-sectional profiles of In and Ga atoms and the corresponding FE-STEM image. The IPSSL was grown on a 1.2°

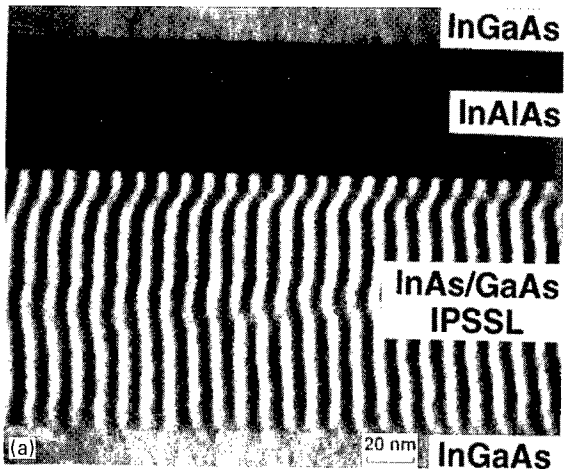

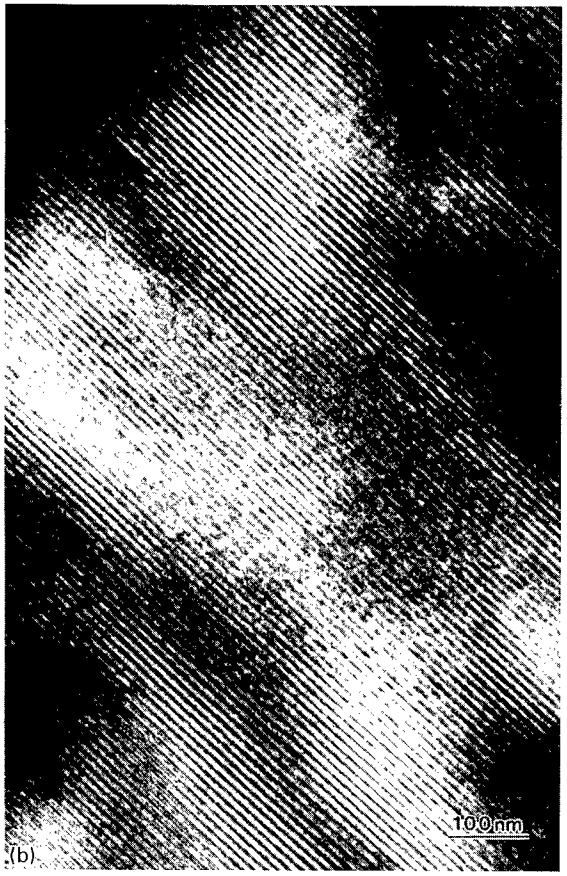

Fig. 4. (a) ($\bar{1}$ 1 0) cross-sectional TEM dark field image of the IPSSL grown on a substrate 1.2° tilted in the [0 0 $\bar{1}$] direction. (b) (1 1 0) plan view of TEM dark field image.

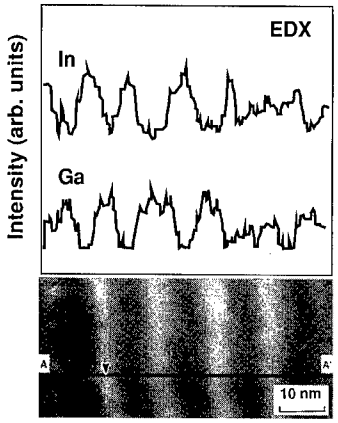

Fig. 5. Spatial distribution of In and Ga atoms measured by EDX and a corresponding FE-STEM image.

tilted substrate. The profiles of In and Ga concentrations oscillate almost complementary to each other. The atomic ratio of In, Ga and As at the position indicated with an arrow is about 12 : 38 : 50. Therefore, InAs and GaAs mixed slightly with each other and resulted in the growth of $In_{0.24}Ga_{0.76}As$ alloy.

3.2. PL properties

The 77 K PL spectrum of the IPSSL grown on a 1.2° tilted substrate is shown in Fig. 6. The schematic diagram of the cross-sectional structure is also shown in the inset. A 100 nm thick IPSSL and a 200 nm thick InGaAs alloy lattice-matched to InP were grown on an InGaAs/InAlAs buffer layer. The vertical dimension of the IPSSL (100 nm) will not influence the transition energy. Therefore, the quantization due to the confinement of the carriers in the [0 0 1] direction would dominate the transition energy. The obtained spectrum has two peaks. One is at 0.81 eV and the other is at 0.77 eV. Since there is no peak at energy lower than 0.8 eV for the InGaAs alloy, the peak at 0.77 eV (1.61 μm) corresponds to the IPSSL. The full-width at half-maximum (FWHM) of the IPSSL is about 27 meV. This is slightly broader than for the InGaAs alloy, but much narrower than 47 meV of the InGaAs/InAlAs IPSL [18]. The size fluctuations were fairly suppressed compared to InGaAs/InAlAs

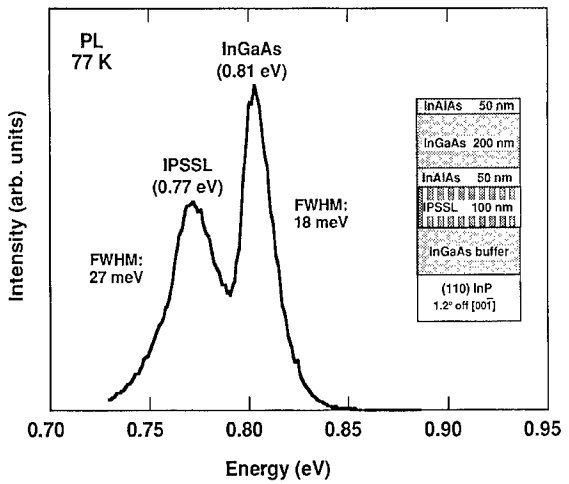

Fig. 6. PL spectrum of the IPSSL grown on a substrate 1.2° tilted in the [0 0 $\bar{1}$] direction.

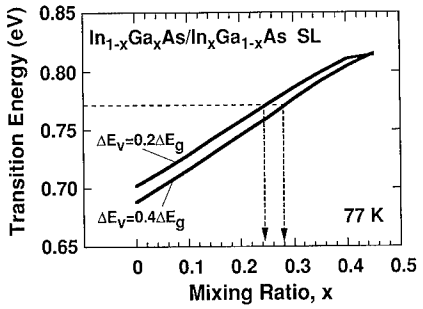

Fig. 7. Calculated transition energy of $In_{1-x}Ga_xAs/In_xGa_{1-x}As$ superlattices.

IPSL. In order to estimate the composition of the IPSSL, we calculated the transition energy for the $In_{1-x}Ga_xAs$(5 nm)/In_xGa_{1-x} As (5 nm) superlattices using nearest-neighbor sp^3*s tight-binding approximation [23, 24]. We took into account the strain effect using the strain Hamiltonian [25]. The details of our calculation method have been shown elsewhere [26]. Fig. 7 shows the calculated transition energy as a function of the mixing ratio, x. In this calculation, we assumed that for valence band edge discontinuity, $\Delta E_v = (0.3 \pm 0.1)\Delta E_g$ ($\Delta E_g = E_g(In_{1-x}Ga_xAs) - E_g(In_xGa_{1-x}As)$). The obtained PL peak energy of 0.77 eV agreed well when $x = 0.26 \pm 0.02$, showing that the IPSSL is composed of $In_{0.74}Ga_{0.26}As$ and $In_{0.26}Ga_{0.74}As$. This is consistent with the measurements by EDX of Fig. 5. The composition difference, Δx, is as large as 0.48, which is the highest value, to our knowledge, ever reported for IPSLs. These results indicate the potential of our method for fabricating as-grown quantum wires which emits light with practical wavelengths of about 1.3 and 1.5 μm.

4. Summary

InAs/GaAs IPSSLs were grown on misoriented (1 1 0) InP substrates by MBE. The TEM images indicated formation of laterally periodic structure with the period of the mean terrace width of the substrates. From a comparison of obtained PL peak energy with calculated transition energy for the $In_{1-x}Ga_xAs/In_xGa_{1-x}As$ superlattice, we deduced that our IPSSL structure was composed of $In_{0.74}Ga_{0.26}As/In_{0.26}Ga_{0.74}As$. This composition was consistent with the measurements by EDX.

Acknowledgements

We would like to thank K. Nakajima, T. Nakamura and H. Ishikawa for their encouragement throughout this work.

References

[1] P.M. Petroff, A.C. Gossard and W. Wiegmann, Appl. Phys. Lett. 45 (1984) 620.
[2] J.M. Gaines, P.M. Petroff, H. Kroemer, R.J. Simes, R.S. Geels and J.H. English, J. Vac. Sci. Technol. B 6 (1988) 1378.
[3] M. Tsuchiya, J.M. Gaines, R.H. Yan, R.J. Simes, P.O. Holts, L.A. Coldren and P.M. Petroff, Phys. Rev. Lett. 23 (1989) 466.
[4] S.A. Chalmers, A.C. Gossard, A.L. Weisenhorn, S.A.C. Gould, B. Drake and P.K. Hansma, Appl. Phys. Lett. 55 (1989) 2491; P.M. Petroff, A.C. Gossard and W. Wiegmann, Appl. Phys. Lett. 45 (1984) 620.
[5] T. Fukui and H. Saito, Appl. Phys. Lett. 50 (1987) 824.
[6] T. Fukui and H. Saito, J. Vac. Sci. Technol. B 6 (1988) 1373.
[7] T. Fukui, H. Saito and Y. Tokura, Appl. Phys. Lett. 55 (1989) 1958.

[8] T. Fukui and H. Saito, Jpn. J. Appl. Phys. 29 (1990) L731.
[9] S.A. Chalmers, H. Kroemer and A.C. Gossard, Appl. Phys. Lett. 57 (1990) 1751.
[10] S.A. Chalmers, H. Weman, J.C. Yi, H. Kroemer, J.L. Merz and N. Dagli, Appl. Phys. Lett. 60 (1992) 1676.
[11] K.C. Wong, M. Krishnamurthy, B. Brar and J.C. Yi, Appl. Phys. Lett. 63 (1993) 1211.
[12] M.S. Miller, H. Weman, C.E. Pryor, M. Krishnamurthy, P.M. Petroff, H. Kroemer and J.L. Merz, Phys. Rev. Lett. 23 (1992) 3464.
[13] H. Kanbe, A. Chavez-Pirson, H. Ando and T. Fukui, Appl. Phys. Lett. 58 (1991) 2969.
[14] M. Kasu, H. Ando, H. Saito and T. Fukui, Appl. Phys. Lett. 59 (1991) 301.
[15] K. Hsieh, J.N. Baillargeon and K.Y. Cheng, Appl. Phys. Lett. 57 (1990) 2244.
[16] K.Y. Cheng, K.C. Hsieh and J.N. Baillargeon, Appl. Phys. Lett. 60 (1992) 2892.
[17] S.T. Chou, K.C. Hsieh, K.Y. Cheng and L.J. Chou, J. Vac. Sci. Technol. B13 (1995) 650.
[18] Y. Nakata, O. Ueda, A. Tackeuchi, S. Nakamura, M. Yamaguchi and S. Muto, J. Crystal Growth 150 (1995) 341.
[19] O. Ueda, Y. Nakata, A. Tackeuchi, S. Nakamura and S. Muto, J. Crystal Growth 150 (1995) 346.
[20] Y. Nakata, in: Proc. 7th Int. Conf. on InP and Related Compounds, Sapporo (1995) p. 751.
[21] Y. Nakata, O. Ueda and S. Muto, in: Proc. 7th Int. Conf. on InP and Related Compounds, Sapporo (1995) p. 165.
[22] Y. Nakata, O. Ueda, T. Inata, S. Nakamura, M. Yamaguchi, S. Sasa and S. Muto, in: Proc. 19th Int. Symp. on GaAs and Related Compounds, Karuizawa, 1992, Inst. Phys. Conf. Ser., Vol. 129, Eds. T. Ikegami, H. Hasegawa and Y. Takeda (Institute of Physics, Bristol, 1993) p. 435.
[23] J.C. Slater and G.F. Koster, Phys. Rev. 94 (1954) 1498.
[24] P. Vogl, H.P. Hjalmarson and J.D. Dow, J. Phys. Chem. Solids. 44 (1983) 365.
[25] F.H. Pollak and M. Cardona, Phys. Rev. 172 (1968) 816.
[26] Y. Nishikawa, Y. Nakata, A. Tackeuchi, S. Muto and O. Wada, Jpn. J. Appl. Phys. 34 (1995) L915.

ELSEVIER

Journal of Crystal Growth 175/176 (1997) 174–177

JOURNAL OF CRYSTAL GROWTH

Surface reconstruction and morphology evolution in highly strained InAs epilayer growth on GaAs(0 0 1) surface

Q. Xue*, T. Ogino, H. Kiyama, Y. Hasegawa, T. Sakurai

Institute for Materials Research (IMR), Tohoku University, Sendai 980-77, Japan

Abstract

Novel planar growth of highly strained heterostructure of InAs/GaAs(0 0 1) by molecular beam epitaxy (MBE) has been studied by an in situ scanning tunneling microscope (STM) and reflection high-energy electron diffraction (RHEED). It is found that deposition of submonolayer indium on the GaAs As-rich 2×4 substrate produces a new 4×2 reconstruction, and a novel layer-by-layer growth of multilayers of InAs can be achieved when the growing front displays this 4×2 symmetry. Here, we will discuss the atomic structure of the 4×2 reconstruction, based on the voltage-dependent high-resolution STM images. In addition, a new strain relaxation mechanism – domain wall structure, in terms of the present novel planar growth mode, will also be addressed.

PACS: 61.16.Di; 61.14.Hg; 68.55.Bd

Keywords: STM; MBE; InAs; GaAS; Layer-by-layer growth

1. Introduction

As a model system for molecular beam epitaxy (MBE) growth of the heterostructure based on III–V compound semiconductors, InAs on GaAs(0 0 1) continues to attract attention because of its potential applications in optoelectronic materials and devices. The accumulated epitaxial strain energy arising from large lattice mismatch (7.2%) between InAs and GaAs drives the system to a quick 3D islanding from the initial layer-by-layer mode with a critical thickness of ~ 2 ML under standard MBE growth conditions. The formation of these islands has been shown to be "self-assembled" both spatially and vertically, which provides an alternative for fabrication of three-dimensional confined nanostructures with unusual optical and transport properties. However, for quantum well structure where electrons are confined only in one direction, one would always expect layer-by-layer growth and both morphologically and compositionally abrupt interfaces [1–8].

Molecular beam epitaxy (MBE) growth is inherently a nonequilibrium process and the morphology of a growing film and its evolution strongly depend on kinetics. Previous studies have shown that under In-rich growth condition, usual

* Corresponding author. E-mail: xue@apfim.imr.tohoku.ac.jp.

0022-0248/97/$17.00 Copyright © 1997 Published by Elsevier Science B.V. All rights reserved
PII S0022-0248(96)01235-3

3D islanding can be significantly surpressed and basically a 2D growth was observed for multilayer materials [1–4]. In this work, we investigated the evolution of surface morphology and structure as a function of the III/V flux ratio and epilayer thickness of InAs in the novel layer-by-layer growth of InAs on the GaAs(0 0 1) substrate, by using an in situ MBE–STM system. Here we will demonstrate that deposition of appropriate amount of In on the GaAs–As-rich substrate could result in a new In-rich 4×2 structure, and it is found to play an important role for the progressive growth of high-quality strained InAs epilayer.

2. Experimental procedure

Details of sample preparation by MBE can be found elsewhere [9]. The buffer layer was grown on nominally flat GaAs(0 0 1) substrate at 580°C, 3×10^{-6} Torr As_4 pressure, and growth rate of 0.5 μm/h. The STM image of as-quenched surface of the substrate grown under these conditions show a very defined 2×4 reconstruction [9]. Indium was deposited on the 2×4 surface from an In Knudsen cell in the MBE chamber with a base pressure of 1×10^{-10} Torr. During deposition, the substrate was kept at 450°C. The In flux was calibrated by reflection high-energy electron diffraction (RHEED) intensity oscillation in a separate experiment. The 4×2 phase was prerpared by migration enhanced epitaxy (MEE) with As_4/In flux ratio of 3–5 at 450°C. All STM images were recorded at room temperature with a constant current of 40 pA. After STM imaging, the samples were further examined by LEED in the STM chamber and RHEED in the MBE chamber to confirm the long-range ordering of the surface as established by STM.

3. Results and discussion

Shown in Fig. 1 are the high-resolution STM images of the 4×2 surface. The images (a) and (b) were taken at negative bias (at -2.2 and -1.6 V, respectively) on the samples, corresponding to electronic tunneling from the filled states of the sample surface to the tip. Filled states image consists of bright straight lines running along the [1 1 0]

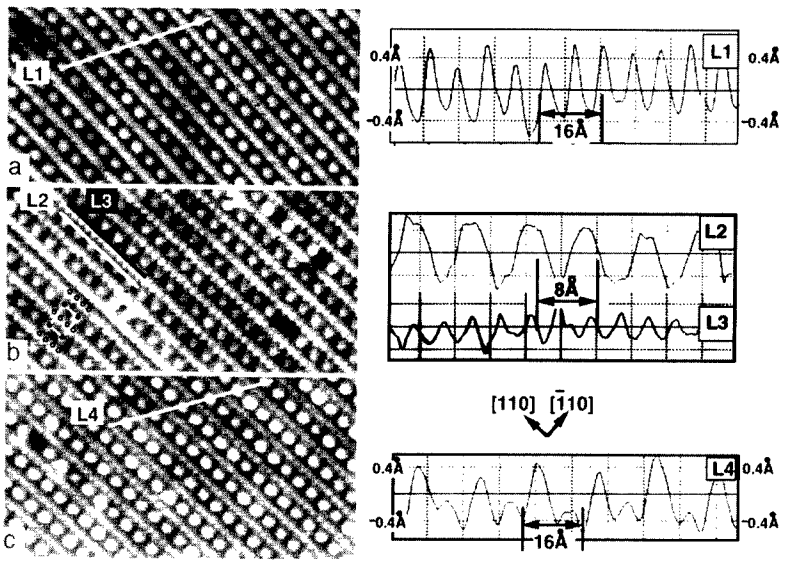

Fig. 1. The high-resolution STM images of newly formed In-rich 4×2 reconstruction: (a) filled states at -2.2 V, (b) filled states at 1.6 V and (c) empty states at $+2.5$ V. The corresponding cross-section profiles are displayed in the right panels of the images. In (b), a 4×2 unit cell is highlighted by a white rectangle.

direction and separated uniformly by 16 Å along the direction ([$\bar{1}$ 1 0]) perpendicular to the line, revealing the 4× periodicity of the surface in the [$\bar{1}$ 1 0] direction. Sandwiched in between the lines are regular humps. The distance between the neighboring humps along the [1 1 0] direction is determined to be 8.0 Å, corresponding to the 2× periodicity of the surface. The 4× and 2× periodicities of the surface can be further identified by the line plots L1 and L2, respectively, as shown in the right panels of Fig. 1a and Fig. 1b. Since the 2× direction agrees with the In-dimerization direction, we are able to immediately assign the individual hump to be tunneling from In (dimer). Furthermore, we observe a distinct 1× periodicity along the line with decreasing bias voltage, which is more clearly revealed by the line plot L3 of Fig. 1b. The small humps forming the 1× periodicity always straddle the larger 2× humps along the [1 1 0] direction, which are highlighted by empty and solid circles, respectively, together with a 4×2 unit cell in Fig. 1b. These observations safely exclude the possibility of the surface to be the homoepitaxially grown InAs(0 0 1) 4×2 surface [10, 11]. According to the line plot L1, there is no measurable contrast for the hump and line features.

We have successfully obtained the empty states image of the surface, which is shown in Fig. 1c. At a glance, the overall surface structure is basically identical to that shown in the filled stated image Fig. 1a or Fig. 1b. However, the contrast has completely reversed; the individual humps now are imaged more brightly than the straight lines. The corresponding line plot L4 indicates an average contrast difference of 0.5 Å for the hump and line related features. Based on these observations, we assign the individual humps tunneling from the first-layer In dimers, and the lines from the second layer As, and propose a tentative model for this new reconstruction in Fig. 2.

According to this model, the two-fold periodicity is due to the dimerization of the newly deposited In adatoms in the [1 1 0] direction, the missing In-dimer gives rise to the 4× periodicity along another ([$\bar{1}$ 1 0]) direction. The exposed As atoms in the missing dimer rows dimerize and their regular arrangement explains the observed 1× periodicity along the line. The model abides with the electron

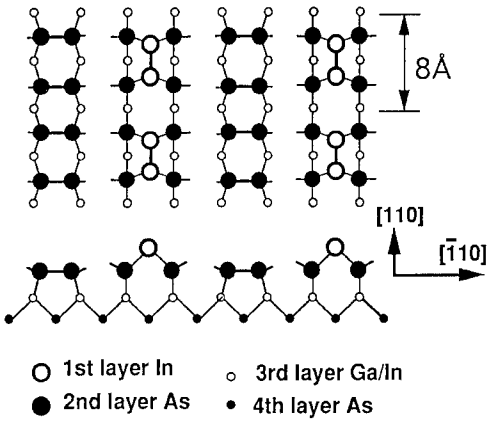

Fig. 2. Proposed ball-to-stick model for the 4 × 2 reconstruction in this study. According to this model, the 2× hump (larger) and the 1× hump (smaller) seen in Fig. 1b are assigned as a first-layer In dimer and a second-layer As dimer, respectively.

counting model and insures that all As dangling bonds are fully filled with two electron and all In dangling bonds are empty (thus, leaves no net charge on the surface) [12], establishing a stable semiconducting surface. The model produces a surface In coverage of 0.33 ML, which gives a reasonable consistency with the experimental parameter used. Considering that the empty (filled) states are preferentially concentrated on group III (V) sites, the observed contrast reversion from the filled to empty states images can be understood by the different levels of the As lone-pair dangling bonds and In dimer-bonding orbitals which are located in the valence and conducting bands, respectively [12–14].

When the substrate is wetted with this 4×2 structure, the progressive InAs multilayer can be grown two-dimensionally under a very strict and simple criterion: the In/As flux ratio, growth temperature must be chosen so that the growing front could reproduce the 4×2 symmetry. To demonstrate the layer-by-layer growth, in Fig. 3, we show surface morphology after a deposition of 13 ML (note that the critical thickness is only ~2 ML for the system). The 3D islanding in the normal Stranski–Krastanov mode is clearly suppressed to a large extent, only four levels (every level corresponds to approximately 2.95 Å, slightly larger than

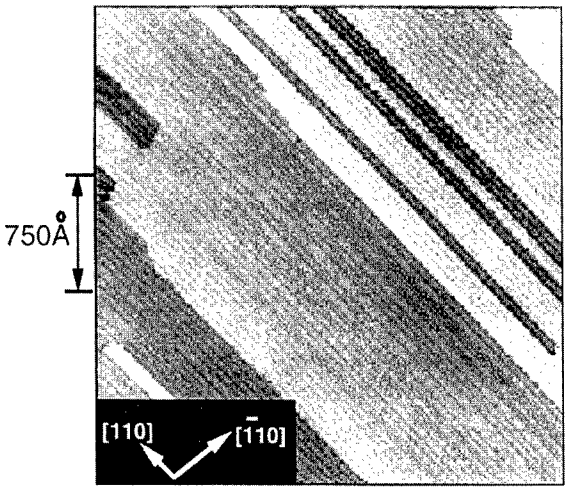

Fig. 3. An overview of the surface morphology after 13 ML InAs epilayer was deposited on the GaAs(0 0 1)–As-2 × 4 surface under In-rich condition. The image was recorded at negative bias voltage (−2.5 V) on the sample.

the bilayer step height (2.8 Å) of the bulk GaAs) are seen over an area of 2300 × 3000 Å, clearly proving a 2D planar growth in the present case. Since the use of migration-enhanced epitaxy and In-rich growth condition assure enough adatom diffusion, the change in growth mode is obviously not a result of kinetic limitation. If it is the case, it should cause an earlier transition to 3D. We, therefore, agree with Snyder et al. that the 2D growth mode observed presently is due to an increasing surface tension [3]. Because no stacking-fault dislocation and other defects have been observed at this stage, a natural question is, how the strain accumulated in the 2D epilayer relaxes. To answer this, let us go back to the STM image (Fig. 3). If we study the structure carefully, it is found that although the surface maintains an overall 4 × 2 symmetry, but in detail it is modulated with characteristic dark lines, namely, domain walls, at which the As-row separation takes a special value of $2 \times N$ ($N = 3, 4, \cdots$). This feature is actually very similar the $2 \times N$ structure on the strained Ge/Si interface and the vacancy defect lines induced by Ni contamination on the Si(0 0 1)-2 × 1 surface [15–17], which has been attributed to the surface strain relaxation. Therefore, this observation indicates a new strain relief mechanism, and its details will be discussed elsewhere [18].

4. Conclusion

In summary, the initial stage of growth of InAs/GaAs(0 0 1) heterostructure has been investigated by in situ STM. A new 4 × 2 surface reconstruction has been established. This structure plays a significant role – as a template – in the layer-by-layer growth of high-quality InAs/GaAs interface. A new strain relief phenomenon – the domain wall formation – facilitating the novel 2D growth, was observed and discussed.

References

[1] W.J. Schaffer et al., J. Vac. Sci. Technol. B 1 (1983) 688.
[2] E. Tournie, et al., Appl. Phys. Lett. 60 (1992) 2877; Europhys. Lett. 25 (1994) 663.
[3] C.W. Snyder et al., Appl. Phys. Lett. 62 (1993) 46.
[4] M.Y. Yen et al., Surf. Sci. 174 (1986) 606.
[5] V. Bressler et al., Phys. Rev. Lett. 74 (1995) 3209.
[6] Snyder et al., Phys. Rev. B 46 (1992) 9551.
[7] Snyder et al., Phys. Rev. Lett. 66 (1991) 3032.
[8] D.J. Eaglesham and M. Cerullo, Phys. Rev. Lett. 64 (1990) 1943.
[9] Hashizume, et al., Phys. Rev. Lett. 73 (1994) 2208; Phys. Rev. B 51 (1995) 4200.
[10] H. Yamaguchi and Y. Horokoshi, Jpn. J. Appl. Phys. 33 (1994) L1423.
[11] S. Ohkouchi and I. Tanaka, Appl. Phys. Lett. 59 (1991) 1588.
[12] W.A. Harrison, J. Vac. Sci. Technol. 16 (1979) 1492; H.H. Farrell, et al., J. Vac. Sci. Technol. B 5 (1984) 1482; M.D. Pashley, Phys. Rev. B 40 (1990) 10481.
[13] T.-C. Chang and D.E. Aspnes, Phys. Rev. B 41 (1990) 12002; D.E. Aspnes, et al., Phys. Rev. Lett. 64 (1990) 192.
[14] Q.K. Xue et al., Phys. Rev. Lett. 73 (1995) 3177.
[15] Y.W. Mo and M.G. Lagally, J. Crystal Growth 111 (1991) 876.
[16] R. Butz and S. Kampers, Appl. Phys. Lett. 61 (1992) 1307.
[17] H.J.W. Zandvliet et al., Phys. Rev. Lett. 75 (1995) 3890.
[18] Q.K. Xue, Y. Hasegawa and T. Sakurai, Nature, to be published.

ELSEVIER

Journal of Crystal Growth 175/176 (1997) 178–183

JOURNAL OF CRYSTAL GROWTH

Real space imaging of GaAs/AlAs (0 0 1) heterointerfaces

J. Behrend*, M. Wassermeier, W. Braun, P. Krispin, K.H. Ploog

Paul-Drude-Institut für Festkörperelektronik, Hausvogteiplatz 5–7, D-10117 Berlin, Germany

Abstract

We have studied the interface formation in molecular beam epitaxial (MBE) grown GaAs/AlAs (0 0 1) heterostructures using scanning tunneling microscopy in ultrahigh vacuum (UHV-STM) and reflection high-energy electron diffraction (RHEED). High-resolution STM images reveal at the normal interface an indistinct compositional profile due to a strong Ga segregation into the AlAs layer. For the abruptly formed inverted interface the STM images indicate the incorporation of intrinsic point defects at the interface plane. Large-scale STM scans of both interface configurations and of the as-grown AlAs (0 0 1) surface show that the morphological differences are less important as expected. Therefore, we propose that the defect incorporation contributes considerably to the asymmetry in the electronic properties of the two different interface types.

PACS: 68.35.Fx; 68.55.Bd; 68.55.Ln; 73.20.Hb; 73.61.Ey; 87.64.Dz

1. Introduction

The investigation of the interface structure of $GaAs/Al_xGa_{1-x}As$ heterostructures has played a major role in the progress of advanced device concepts, since this material system is commonly used as a model for fundamental studies and for commercial applications [1]. In particular, the study of the complicated interplay between the growth conditions, the actual interface structure and the resulting electronic properties has remained a central issue of molecular beam epitaxy (MBE) research [2].

Until present, the asymmetry in the compositional profile and the electron mobility of the normal interface (AlAs on GaAs) and the inverted interface (GaAs on AlAs) are rather unclear. In DC transport measurements the Si migration during growth towards the inverted interface [3] and the enhanced interface roughness due to the AlAs growth [4, 5] were found to be the dominant electron mobility degrading effects.

By probing the cleaved edge of a $GaAs/Al_xGa_{1-x}As$ ($x = 0.3$) heterostructure with scanning tunneling microscopy (STM) a demixing of both, GaAs and AlAs in the $Al_xGa_{1-x}As$ regions with a typical modulation length scale of 2 nm was found [6, 7]. This modulation is also present at the interfaces, causing an interface roughness of the same magnitude.

* Corresponding author. E-mail: behrend@pdi.wias-berlin.de.

0022-0248/97/$17.00 Copyright © 1997 Elsevier Science B.V. All rights reserved
PII S0022-0248(96)01178-5

The spectral signature of optical techniques such as photoluminescence spectroscopy (PL) indicate discrete thickness variations for GaAs/AlAs quantum wells on a lateral scale, larger (resulting in peak splitting) or smaller (leading to broadened peaks) than the exciton diameter due to the averaging effect of the exciton wave function over these small size roughnesses [8].

In order to clarify this issue, it would be very useful to obtain planar real-space images of the as-grown surfaces. In this paper we report the first STM results of the as-grown AlAs(0 0 1) surface and intermediate stages of the formation of the normal and inverted interfaces in the GaAs/AlAs system.

2. Experimental procedure

The experiments were carried out in a combined MBE–STM system which allows STM imaging in ultrahigh vacuum (UHV) immediately after growth or surface preparation. (0 0 1)-oriented epi-ready n-type GaAs wafers were used as a substrate material. The buffer layer of 100 nm thick GaAs was grown at 580°C under an As_4 flux of 3×10^{-6} Torr and Si-doped with $2 \times 10^{18}\,cm^{-3}$. These growth conditions were optimized for the preparation of a smooth As-rich surface with a well-ordered (2×4) reconstruction.

The different stages of formation of the normal interface were realized by deposition of AlAs at a growth temperature of 610°C onto the initial GaAs surface with varying layer thicknesses between 1 and 10 ML. To achieve the initial stage of the inverted interface configuration 1 ML GaAs was grown on 50 ML AlAs at a temperature of 600°C. The growth rate was varied between 0.1 and 0.3 ML/s depending on the deposited layer thickness.

During growth, the sample surfaces were monitored using reflection high-energy electron diffraction (RHEED). To avoid any influence of compensating surface defects due to the Si-doping, the last 15 ML below the surface of all structures were grown undoped. After growth, the samples were cooled to room temperature using an optimized quenching procedure such that the RHEED pattern remained unchanged during the whole process.

One important experimental issue for the STM imaging of highly reacting surfaces is the sample handling under UHV. To accomplish the lowest possible contamination level, the sample transfer into the STM chamber of the UHV system was performed at pressures below 8×10^{-11} Torr in a time of about 2 min. The pressure in the STM chamber itself was better than 1×10^{-11} Torr, which allowed tunneling experiments for about 5 h without noticeable oxidation even of pure AlAs. Filled state STM images were collected with an electron-bombarded tungsten tip using voltages of about 3 V at tunneling currents of 300–700 pA.

3. Results and discussion

The formation of the normal interface starts from the As-rich (2×4) reconstructed GaAs(0 0 1) surface shown in Fig. 1a. Before any AlAs is deposited the reconstruction of this initial surface is well ordered. The unit meshes contain two As dimers and two missing dimers forming straight rows along the $[\bar{1}\ 1\ 0]$ direction. Small holes in the terraces formed by missing unit meshes and steps caused by a slight unintentional miscut of the substrate are the main intrinsic growth defects of this surface structure. The high order observed in the STM image agrees very well with the RHEED pattern also shown in Fig. 1a which exhibits well-defined and symmetric spots on a bright Laue circle in the $4 \times$ direction.

The normal interface formation is distinguished by a continuous change of the reconstruction. During the AlAs growth the symmetry of the RHEED pattern changes from the (2×4) GaAs to a diffuse (2×3) intrinsic to the AlAs. This process is concluded after 6–10 AlAs ML. The STM image of this stage of the normal interface formation is shown in Fig. 1b and reveals a large amount of kinks which are created in the As dimer rows disturbing the order of the (2×4) reconstruction gradually. With respect to the initial surface, in particular at step edges, the As coverage is reduced exposing the second Al and/or Ga layer. At this stage of the normal interface formation the (2×4) symmetry of the RHEED pattern still remains but becomes

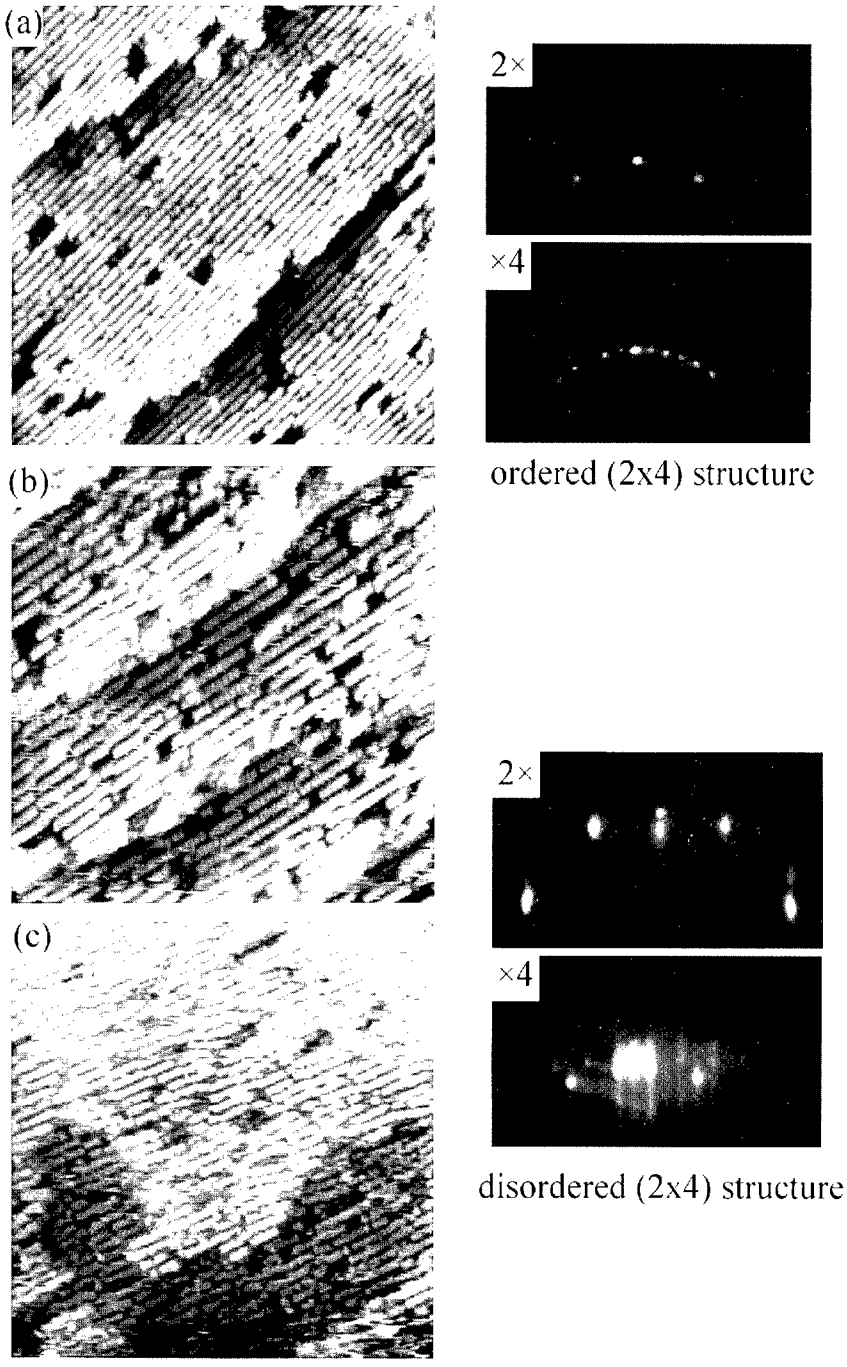

Fig. 1. High resolution $40 \times 40\ nm^2$ large STM images and the corresponding RHEED pattern showing the initial GaAs(0 0 1) surface (a), the normal interface after the deposition of 10 ML of AlAs on GaAs (b) and the inverted interface after the growth of 1 ML GaAs on AlAs (c).

streaky, the Laue circle disappears and the half-order spot of the $\times 4$ direction is very weak or vanishes (see Fig. 1b and Fig. 1c). This finding is correlated to the disordered As missing dimer row structure in the STM data.

The observed slow transient from the GaAs (2×4) to the AlAs (2×3) reconstruction at the normal interface is related to a strong Ga segregation into the AlAs in agreement with an investigation of this process by reflection difference spectroscopy [9]. This finding was also deduced from phase shift measurements of the RHEED intensity oscillations during the initial stage of the interface formation [10]. As a consequence, the STM images after AlAs deposition between 1 and 10 ML show the structure of an $Al_xGa_{1-x}As$ surface alloy with a large x value instead of an intrinsically reconstructed AlAs layer.

In contrast to the behavior at the normal interface, the inverted interface configuration formes very rapidly. Already after the deposition of 2 ML of GaAs on the AlAs, the phase transition of the reconstruction is complete. From this the absence of segregation and intermixing is concluded leading to a sharp compositional profile at the inverted interface. The RHEED pattern abruptly changes from the (2×3) to a clear (2×4) symmetry with the characteristic weak half-order spot. The pattern looks very similar to the one that was present after AlAs deposition during the formation of the normal GaAs/AlAs interface, indicating a disordered (2×4) reconstruction. The high-resolution STM image in Fig. 1c showing the inverted interface after the deposition of 1 ML GaAs confirms this expectation. A high degree of disorder introduced by kink formation and a decreased As coverage is visible on the surface. In contrast to the normal interface, the kink density is remarkably higher.

In the case of Si doping, the kink formation is attributed to the creation of compensating surface defects due to the added n-type dopants to keep the Fermi level at mid-gap [11]. This explanation does not seem to be reasonable for the incorporation of an isoelectronic species like Al in GaAs. From recent DLTS measurements, however, it is known that during AlAs growth negatively charged intrinsic point defects identified as As vacancies are created at the surface [12]. From the corresponding defect levels electrons can be released. Therefore, we conclude that AlAs deposition on the GaAs(0 0 1) surface will produce compensating surface defects in response to electronic states, which originate from As vacancies inherent to the AlAs growth. The incorporation of the defect layer at the inverted AlAs/GaAs interface plane during its abrupt formation may contribute to the asymmetry in the electronic properties between both interface types.

This conclusion is supported by surprisingly smooth morphology of the as-grown AlAs(0 0 1) surface which is evident from the large-scale STM images of Fig. 2a–Fig. 2c. The imaged surface represents a steady-state structure during 2D nucleated AlAs growth with a typical length scale of about 30 nm and a large degree of anisotropy along the $[\bar{1}\,1\,0]$ direction. It exhibits monolayer high steps and islands arranged similar to the GaAs(0 0 1) surface grown without annealing [13]. The images show three different surface areas of the same 50 ML thick AlAs layer and compare the main morphological features with the size of an average exciton diameter (marked in the pictures by a ring). Almost defect-free terraces larger than the exciton diameter dominate the STM image of Fig. 2a. However, the terrace width can also be shrinked to dimensions below the exciton size due to step bunching as shown in Fig. 2b. In addition, small islands on and/or holes in the terraces comparable to the exciton diameter were found to be present in Fig. 2c. The step edges are very rough and show a pronounced meandering. In contrast to the as-grown GaAs(0 0 1) surface, however, the difference in roughness between A-type and B-type steps is less important on the AlAs(0 0 1) surface.

As the large-scale STM scans in Fig. 3 from the stage directly after the interface formation show, this relatively smooth morphology is preserved at the inverted interface.

4. Summary

With respect to the average exciton diameter the morphological differences between both interface types in GaAs/AlAs heterostructures are less important than expected and thus cannot alone

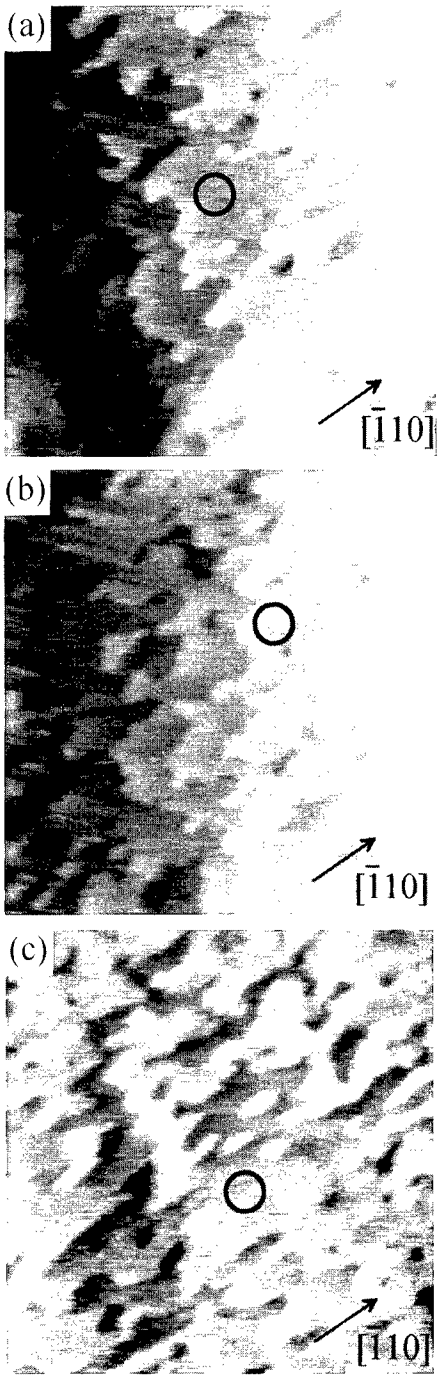

Fig. 2. $400 \times 400\,nm^2$ large STM scans revealing the morphological properties of a 50 ML thick as-grown AlAs(0 0 1) layer. The rings mark an average exciton diameter for comparison.

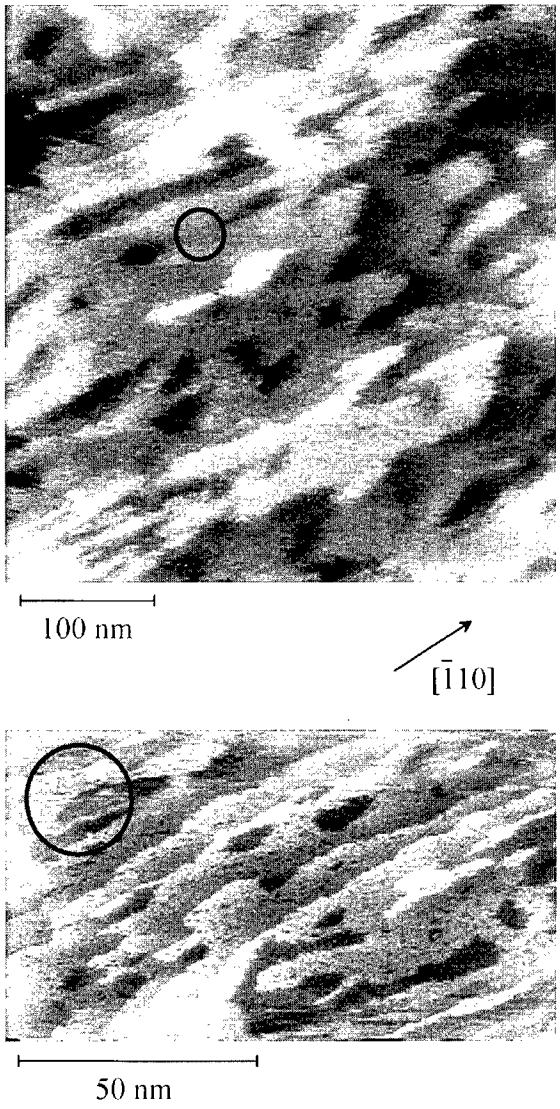

Fig. 3. Large scale STM scans of the inverted interface after the deposition of 1 ML of GaAs on a 50 ML thick AlAs layer. The rings mark an average exciton diameter for comparison.

explain the asymmetry in electronic properties. Instead, the creation of intrinsic point defects at the growing AlAs surface may play an important role. In contrast to the normal interface, the kink density at the inverted interface is remarkably higher indicating a high intrinsic point defect density at the growing AlAs surface. These defects are burried at the inverted interface plane due to the abrupt phase

transition of the reconstruction from (2×3) to (2×4) and the absence of segregation or intermixing. From this we can conclude that in addition to the previously reported Si migration effect, the incorporation of intrinsic point defects plays an important role in reducing the electron mobility in two-dimensional electron gas heterojunctions at the inverted interface.

References

[1] C. Weißbuch, J. Crystal Growth 127 (1993) 742.
[2] T. Sajoto, M. Santos, J.J. Heremans and M. Shayegan, Appl. Phys. Lett 54 (1989) 840.
[3] L. Pfeiffer, E.F. Schubert, K.W. West and C.W. Magee, Appl. Phys. Lett. 58 (1991) 2258.
[4] L. Pfeiffer, K.W. West, H.L. Störmer and K.W. Baldwin, Appl. Phys. Lett. 55 (1989) 1888.
[5] T. Saku, Y. Hirayama and Y. Horikoshi, Jpn. J. Appl. Phys. 30 (1991) 902.
[6] M.B. Johnson, U. Maier, H.P. Meier and H.W.M. Salemink, Appl. Phys. Lett. 63 (1993) 1273.
[7] O. Albrektsen, H.P. Meier, D.J. Arent and H.W.M. Salemink, Appl. Phys. Lett. 62 (1993) 2105.
[8] B. Orschel, G. Oelgart, R. Houdré, M. Proctor and F.K. Reinhardt, Appl. Phys. Lett. 62 (1993) 843.
[9] M. Wassermeier, I. Kamiya, D.E. Aspnes, L.T. Florez, J.P. Harbison and P.M. Petroff, J. Vac. Sci. Technol. B 9 (1991) 2263.
[10] W. Braun and K.H. Ploog, J. Appl. Phys. 75 (1994) 1993; Appl. Phys. A 60 (1995) 441.
[11] M.D. Pashley, K.W. Haberern, R.M. Feenstra and P.D. Kirchner, Phys. Rev. B 48 (1993) 4612.
[12] P. Krispin, R. Hey and H. Kostial, J. Appl. Phys. 77 (1995) 5773.
[13] J. Sudijono, M.D. Johnson, M.B. Elowitz, C.W. Snyder and B.G. Orr, Surf. Sci. 280 (1993) 247.

ELSEVIER

Journal of Crystal Growth 175/176 (1997) 184–190

JOURNAL OF CRYSTAL GROWTH

Control of chemical composition and band gap energy in $Ga_xIn_{1-x-y}Al_yAs$ on InP during molecular beam epitaxy

J.M. Schneider, J.-T. Pietralla, H. Heinecke*

Department of Semiconductor Physics, University of Ulm, Albert-Einstein-Allee 45, D-89069 Ulm, Germany

Abstract

The growth of $Ga_xIn_{1-x-y}Al_yAs$, lattice matched with respect to InP, by molecular beam epitaxy (MBE) is investigated. To achieve a precise prediction over the chemical composition, the quaternary layers were produced by the simultaneous growth of the ternaries $Ga_{0.47}In_{0.53}As$ and $Al_{0.48}In_{0.53}As$. The aluminium content y of the quaternary layer is independently preset by the ternary growth rates. The quaternary samples were characterized by X-ray diffraction as well as by low-temperature (4.2 K) and room-temperature (RT) photoluminescence (PL). At both temperatures, we found a linear dependence of the energy at maximum PL intensity on the aluminium content y in the quaternary layer. The calculated linear fit for the quaternary data points corresponds closely with the linear interpolation between our $Ga_{0.47}In_{0.53}As$ and $Al_{0.48}In_{0.52}As$ data. These results enabled the determination of the equation system, giving the composition x, y of $Ga_xIn_{1-x-y}Al_yAs$ as a function of the measured lattice mismatch $\Delta d/d$ and PL.

PACS: 78.66.Fd; 81.15.Hi; 81.10.Aj

Keywords: Molecular beam epitaxy; GaInAlAs; Quaternary material; Band gap energy; Growth kinetics

1. Introduction

$Ga_xIn_{1-x-y}Al_yAs$ is an attractive material for photonic device applications. For band gap engineering of heterostructures in the material system InP/GaInAs/AlInAs/GaInAlAs the precise knowledge of the dependence of the band gap energy E_G on the material composition is required. For the analysis of $Ga_xIn_{1-x-y}Al_yAs$ layers generally *both* techniques, X-ray diffraction and PL, are used to evaluate the composition x and y. For the same reason the precise relationship of the composition x, y as the function of the lattice mismatch $\Delta d/d$ and PL is mandatory. Nevertheless, there still exists a significant scatter in the data of E_G on the material composition for both the quaternary and ternary materials. For $Ga_xIn_{1-x-y}Al_yAs$,

* Corresponding author. Fax: + 49 731 502 6106; e-mail: heinecke@sunrise.e-technik.uni-ulm.de.

0022-0248/97/$17.00 Copyright © 1997 Elsevier Science B.V. All rights reserved
PII S0022-0248(96)01209-2

lattice matched to InP, a bowing relationship for E_G with rising aluminium content y is observed both at RT and at 4.2 K (e.g. see Refs. [1, 2]). Others found a linear interpolation between $Ga_{0.47}In_{0.53}As$ and $Al_{0.48}In_{0.52}As$ with rising y (e.g. see Refs. [3, 4]). Even for the band-gap energy of the ternary compounds $Ga_{0.47}In_{0.53}As$ (e.g. see Refs. [5, 6]) and $Al_{0.48}In_{0.52}As$ (e.g. see Refs. [7, 8]) various data are reported. Therefore, there is a need to produce $Ga_xIn_{1-x-y}Al_yAs$ reference samples with a well-known and defined chemical composition by high-precision MBE and then to evaluate the band gap energy by PL. From the measured results of X-ray and PL on ternary layers and on the quaternary reference layers, grown as mixtures of the ternaries and lattice matched to InP, we deduced an equation system for the precise evaluation of the composition x, y of $Ga_xIn_{1-x-y}Al_yAs$ as a function of the lattice mismatch $\Delta d/d$ and PL.

2. Experiment

2.1. Experimental procedure

The precise adjustment of all group III material fluxes (Al, Ga, In) is mandatory to achieve a reproducible composition in the resulting ternary or quaternary layers on InP. Therefore, material fluxes were determined by a high-precision output current measurement of the flux ion gauge using a high-precision electrometer amplifier [9]. For the simultaneous growth of the ternary compounds $Ga_xIn_{1-x}As$ and $Al_yIn_{1-y}As$ the growth chamber is equipped with two In cells, one Ga and one Al cell.

The layers were grown in a solid-source MBE (Riber 32 P) on (1 0 0) oriented Fe-doped InP substrates. The substrates were organically cleaned, etched and thermally pretreated [9]. The ternary and quaternary layers were grown using As_4 (standard effusion cell), maintaining a growth temperature between 505 and 525°C below the indium desorption regime.

In the first step the ternary compounds $Ga_{0.47}In_{0.53}As$ and $Al_{0.48}In_{0.52}As$ were independently grown on InP with growth rates r_1 and r_2, respectively. The precisely adjusted ratio of the growth rates is used to predict the chemical composition of the corresponding $Ga_xIn_{1-x-y}Al_yAs$ layer which is produced by the simultaneous growth (superposition) of these ternaries:

$$x = 0.47r_1/(r_1 + r_2), \quad y = 0.48r_2/(r_1 + r_2). \tag{1}$$

The linear superposition of the ternary growth rates holds true as long as the growth temperature is chosen below the indium desorption region, where the sticking coefficient of all group III atoms is assumed to be equal to one. The lattice mismatch $\Delta d/d$ of all quaternary layers were kept within $-7 \times 10^{-4} < \Delta d/d < 5 \times 10^{-4}$.

2.2. Characterization

The growth rates were precisely determined by the measurement of the layer thicknesses (± 25 nm) and the period of the growth run. The layered structures were masked by stripes of photoresist and then selectively etched down to the InP substrate in a 3 : 1 : 1 mixture of $H_2SO_4 : H_2O_2 : H_2O$. After removal of the photoresist the thicknesses of the remaining layer ridges were measured by an alpha-step measurement. The InAs mole fraction of the ternary layers were determined by X-ray diffraction. For quaternary layers, X-ray diffraction was used only to control the superposition of the ternary results. PL measurements at RT and at 4.2 K were carried out using a standard PL configuration [9].

3. Results and discussion

3.1. $Ga_{0.47-y}In_{0.53}Al_yAs$ reference layers, lattice matched to InP

In Fig. 1, the X-ray measurements of the ternary compounds $Ga_{0.47}In_{0.53}As$ and $Al_{0.48}In_{0.52}As$ and of a quaternary $Ga_{0.23}In_{0.53}Al_{0.24}As$ layer are shown. The ternaries were independently grown before the quaternary layer with growth rates $r_1 = 0.68$ μm/h and $r_2 = 0.67$ μm/h, respectively. The quaternary layer is then the result of the simultaneous growth of both the ternaries. It is obvious that the superposition of the ternaries with $\Delta d/d = 8.3 \times 10^{-5}$ and -9.0×10^{-5}, respectively, yields the lattice mismatch $\Delta d/d = 2.0 \times 10^{-4}$ of the quaternary layer within the limits of reproducibilty ($\pm 2.5 \times 10^{-4}$). We also checked the superposition of the growth rates. The sum of the ternary growth rates ($r_1 + r_2 = 1.35$ μm/h) corresponds to the growth rate of the quaternary material ($r = 1.36$ μm/h). For all samples we found the equation r_1 (GaInAs) + r_2 (AlInAs) = r (GaInAlAs) to be valid within experimental error ($\Delta r = \pm 0.03$ μm/h).

Several quaternary sample series with different aluminium content y have been produced by varying the ratio r_1/r_2 of the ternary growth rates and applying the growth procedure described above. The aluminium content y of each set of samples is listed in Table 1 which is calculated from the ratio r_1/r_2 via Eq. (1). The accuracy of the calculated aluminium content is given in column 2. This maximum error is estimated from the precision of the thickness measurements. The adjustment of the group III material fluxes (see Section 2.1) enables a high degree of reproducibilty of material composition. The variation of the lattice mismatch $\Delta d/d$ within a number of samples which were grown in successive growth runs including successive cell calibration is kept within $\pm 2.5 \times 10^{-4}$, maintaining identical growth temperatures (see column 4, except for $y = 23.8\%$,

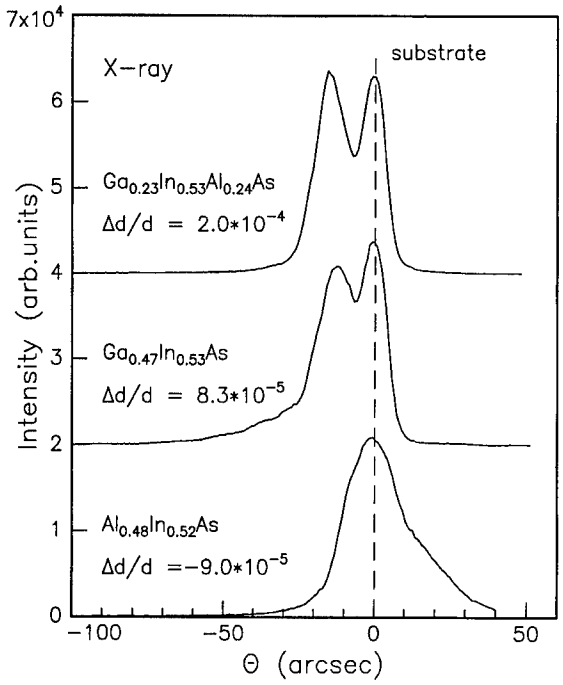

Fig. 1. X-ray measurements of $Ga_{0.47}In_{0.53}As$, $Al_{0.48}In_{0.52}As$ and $Ga_{0.23}In_{0.53}Al_{0.24}As$. The quaternary layer is grown by the superposition of both ternary material fluxes.

Table 1
Data of sets of $Ga_{0.47-y}In_{0.53}Al_yAs$ reference layers with the aluminium content y as a parameter

Ratio r_1/r_2	Aluminium content y (%)	Number of samples	$\Delta d/d$ ($\times 10^{-4}$)	E_{PL} (meV)	
				RT	4.2 K
10.63	4.1(± 0.014)	2	− 3.8↔ − 3.7	804–807	868–870
2.56	13.3(± 0.014)	5	0.5↔3.1	930–934	1000–1003
1.01	23.8(± 0.011)	6	− 5.2↔3.9	1100–1113	1167–1180
0.97	24.2(± 0.014)	4	− 6.9↔ − 4.6	1101–1113	1164–1177
0.15	40.4(± 0.014)	2	1.7↔5.1	1342–1356	1421

Note: y is calculated from the ratio of the ternary growth rates r_1/r_2 via Eq. (1).

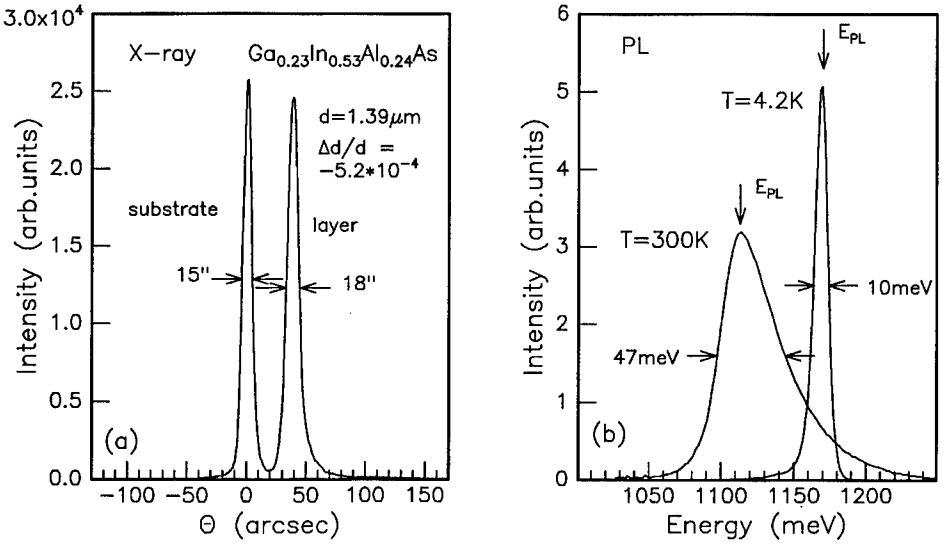

Fig. 2. (a) X-ray measurement and (b) corresponding PL spectrum at RT and at 4.2 K of $Ga_{0.23}In_{0.53}Al_{0.24}As$/InP. The arrows mark the energy position at maximum PL intensity (E_{PL}).

505°C < T_{growth} < 525°C). The energy at maximum PL intensity E_{PL} varied not more than ±7 meV at RT and at 4.2 K (columns 5 and 6).

The X-ray diffraction curve of an 1.39 μm thick $Ga_{0.23}In_{0.53}Al_{0.24}As$ layer on InP is presented in Fig. 2a which shows almost equal intensities for layer and substrate peak. The layer full-width at half-maximum (FWHM) of 18.4 arcsec is very close to the theoretical limit of 16.6 arcsec for an 1.39 μm thick sample [10]. Therefore, a high crystalline quality of the quaternary material as well as a high degree of control over the material composition in the growth direction is achieved. Fig. 2b presents the corresponding PL spectrum for the $Ga_{0.23}In_{0.53}Al_{0.24}As$ layer, both at RT and at 4.2 K. The FWHM of 10 meV at 4.2 K is intermediate between the FWHM found for the ternaries (typically 2–3 meV for $Ga_{0.47}In_{0.53}As$ and 12–20 meV for $Al_{0.48}In_{0.52}As$).

In Fig. 3 the measured E_{PL} at RT vs. the aluminium content y in the quaternary layer calculated from the ternary growth rates (see Eq. (1)) is shown. In addition, our results on optimized $Ga_{0.47}In_{0.53}As$ (755 meV)

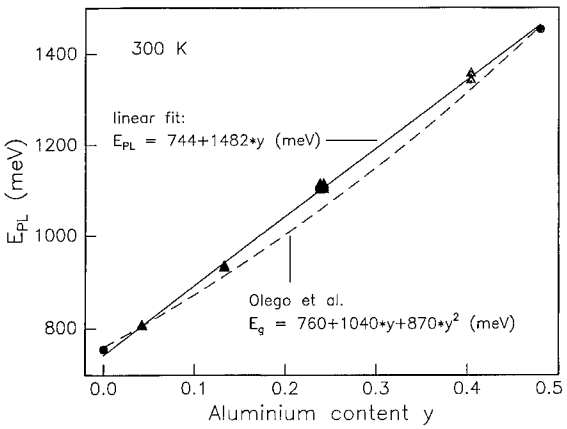

Fig. 3. Energy at maximum PL intensity E_{PL} at RT plotted vs. the aluminium content y. Solid line: linear fit; dashed line: $E_G(y)$ found by Olego et al. [1].

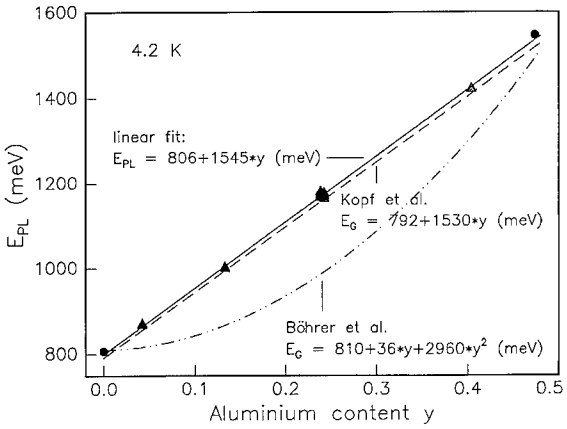

Fig. 4. Energy at maximum PL intensity E_{PL} at 4.2 K plotted vs. the aluminium content y. Solid line: linear fit; dashed line: $E_G(y)$ found by Kopf et al. [3]; dashed-dotted line: $E_G(y)$ found by Böhrer et al. [2].

and $Al_{0.48}In_{0.52}As$ (1453 meV) are included. These ternary layers were grown with similar growth rates compared to the quaternary layers ($\approx$1.2–1.4 μm/h) [9, 11]. We find a linear relationship between E_{PL} and the aluminium content y. Moreover, this linear relationship is almost identical with the linear interpolation between our results on the ternaries $Ga_{0.47}In_{0.53}As$ and $Al_{0.48}In_{0.52}As$. The analytical expression of the linear relationship at RT is given by

$$E_{PL}(y) = 744 + 1482y \quad \text{(meV)}, \tag{2}$$

which is similar to that found by Kopf et al. [3]: $E_G(y) = 752 + 1453y$ (meV). The dashed line in Fig. 3 presents the relationship given by Olego et al. [1] which has a more pronounced bowing for intermediate aluminium contents y. From our data such a bowing behaviour can be excluded.

The results at 4.2 K are presented in Fig. 4. As for RT, we find at 4.2 K a linear relationship between E_{PL} and the aluminium content y in the quaternary layer. Again the linear relationship is almost identical with the linear interpolation between our data of the optimized ternaries $Ga_{0.47}In_{0.53}As$ (807 meV) and $Al_{0.48}In_{0.52}As$ (1546 meV). The analytical expression at 4.2 K is given by

$$E_{PL}(y) = 806 + 1545y \quad \text{(meV)}. \tag{3}$$

In contrast to RT where the relationship found by Kopf et al. is similar to Eq. (2), at 4.2 K our relationship shows a systematic shift of about 15 meV towards higher energies. Böhrer et al. reported a relationship for $E_G(y)$ with a dominant quadratic term in y. It is believed that the bowing is mainly caused by alloy disorder [2].

3.2. Evaluation routine for the composition of $Ga_xIn_{1-x-y}Al_yAs$

The data from the preceding section allow for setting up an equation system for the evaluation of the composition x, y of the quaternary layer as dependent on E_{PL} (RT and 4.2 K) and the lattice mismatch $\Delta d/d$. The two central equations are

$$\Delta d/d_{exp.} = \frac{1}{P(x,y)} \frac{(1-x-y)a_{InAs} + xa_{GaAs} + ya_{AlAs} - a_{InP}}{a_{InP}}, \tag{4}$$

$$E_{PL,exp.} = (1-x-y)A + xB + yC, \tag{5}$$

where $\Delta d/d_{exp.}$ is the lattice mismatch measured by X-ray diffraction, a_x are the lattice constants of InAs, GaAs, AlAs and InP (see Table 2), $E_{PL,exp.}$ is the measured energy at maximum PL intensity and A, B and C are fit parameters which cannot be deduced from literature due to the scatter of data mentioned in the introduction. Based on the results of Section 3.1 we evaluated these fit parameters which are listed in Table 2 for RT and 4.2 K. In Eq. (4), $P(x, y)$ is the elastic response of the lattice depending on the composition and is approximated by a linear interpolation between the binary compounds:

$$P(x,y) = \frac{C_{11}(x,y)}{C_{11}(x,y) + 2C_{12}(x,y)} \text{ with } C_{ij}(x,y) = (1-x-y)C_{ij,InAs} + xC_{ij,GaAs} + yC_{ij,AlAs}, \tag{6}$$

where $C_{ij,x}$ are the elastic moduli of the binary compounds (see Ref. [12]).

An approximation for $P(x, y)$ is given by $P \approx 0.5$ for a lattice mismatch $\Delta d/d \leqslant \pm 5 \times 10^{-3}$. The error $\Delta(x, y)$ made for x and y is less than ± 0.0004. For this case the equation system can be resolved for x

Table 2
Fit parameters A, B and C at RT and at 4.2 K

	A (meV)	B (meV)	C (meV)	a_{InP} (Å)	a_{InAs} (Å)	a_{GaAs} (Å)	a_{AlAs} (Å)
RT	324 ± 8	1221 ± 8	2693 ± 8	5.8688 [13]	6.0584 [13]	5.6532 [13]	5.6611 [13]
4.2 K	302 ± 5	1385 ± 5	$2923 + 10/-5$	5.8658 [9]	6.0537 [9]	5.6478 [9]	5.6571[a]

Note: These parameters for Eqs. (5), (7) and (8) are fit to the results of Section 3.1. Lattice constants a_x for the binary compounds at RT and at 4.2 K.

[a] Calculated, see Ref. [9].

and y as follows:

$$y = \frac{0.5a_{\mathrm{InP}}\Delta d/d_{\mathrm{exp.}} - [(a_{\mathrm{GaAs}} - a_{\mathrm{InAs}})(E_{\mathrm{PL,\,exp.}} - A)]/(B - A) - a_{\mathrm{InAs}} + a_{\mathrm{InP}}}{[(a_{\mathrm{GaAs}} - a_{\mathrm{InAs}})(A - C)]/(B - A) + a_{\mathrm{AlAs}} - a_{\mathrm{InAs}}}, \tag{7}$$

$$x = \frac{E_{\mathrm{PL,exp.}} - A + (A - C)y}{B - A}. \tag{8}$$

Using Eqs. (7) and (8) yields the composition x, y of a $Ga_xIn_{1-x-y}Al_yAs$ layer as a function of the measured data E_{PL} and $\Delta d/d$ as required for standard analytical routines.

4. Conclusions

We have grown $Ga_{0.47-y}In_{0.53}Al_yAs$ reference samples on InP with a well-defined chemical composition calculated only from the ternary growth rates. PL measurements were performed to evaluate the fundamental relationship between the band gap energy and the composition. We deduced a reliable evaluation routine for the composition x, y of $Ga_xIn_{1-x-y}Al_yAs$ as a function of X-ray and PL data. These results form a solid basis for the material growth in device applications as well as for the analysis of quaternary layers. The knowledge of the band gap energy as a function of the material composition enables precise band gap engineering for photonic devices composed of heterostructures of the InP/GaInAlAs material system.

References

[1] D. Olego, T.Y. Chang, E. Silberg, E.A. Caridi and A. Pinczuk, Appl. Phys. Lett. 41 (1982) 476.
[2] J. Böhrer, A. Krost and D.B. Bimberg, Appl. Phys. Lett. 63 (1993) 1918.
[3] R.F. Kopf, H.P. Wei, A.P. Perley and G. Livescu, Appl. Phys. Lett. 60 (1992) 2386.
[4] T. Fujii, Y. Nakata, Y. Sugiyama and S. Hiyamizu, Jpn. J. Appl. Phys. 25 (1986) L254.
[5] P.W. Yu, C.K. Peng and H. Morkoç, J. Appl. Phys. 65 (1989) 2427.
[6] V. Swaminathan, R.A. Stall, A.T. Macrander and R.J. Wunder, J. Vac. Sci. Technol. B 3 (1985) 1631.
[7] I.T. Ferguson, T.S. Cheng, C.M. Sotomayor Torres and R. Murray, J. Vac. Sci. Technol. B 12 (1994) 1319.
[8] B. Wakefield, M.A.G. Halliwell, T. Kerr, D.A. Andrews, G.J. Davies and D.R. Wood, Appl. Phys. Lett. 44 (1984) 341.
[9] M. Popp, M. Schiefele, M. Hurich, M. Wachter, J.M. Schneider, B. Marheineke and H. Heinecke, J. Crystal Growth 150 (1995) 528.
[10] H. Hillmer, R. Lösch, W. Schlapp and A. Pöcker, J. Crystal Growth 146 (1995) 159.
[11] J.M. Schneider, M. Popp, M. Schiefele, J.-T. Pietralla and H. Heinecke, Proc. Eur. MBE VIII, 22–24 March Granada, Spain (1995) p. 65.
[12] Landolt-Börnstein, Semiconductors: Physics of Group IV Elements and III–V Compounds, New Series III, Vol. 17a (Springer, Berlin, 1982).
[13] O. Madelung, Data in Science and Technology (Semiconductors) (Springer, Berlin, 1991).

ELSEVIER

Journal of Crystal Growth 175/176 (1997) 191–196

JOURNAL OF CRYSTAL GROWTH

Properties of InAs thin films grown on (1 0 0)-oriented GaAs substrate with various tilted angles and directions of misorientation

Masaki Yamamoto[a,*], Tatsuro Iwabuchi[a], Takashi Ito[a], Takashi Yoshida[a], Toshiro Isoya[a], Ichiro Shibasaki[b]

[a] *Asahi Kasei Electronics Co., Ltd., 2-1 Samejima, Fuji City, Shizuoka 416, Japan*
[b] *Asahi Chemical Industry Co., Ltd., 2-1 Samejima, Fuji City, Shizuoka 416, Japan*

Abstract

We studied the dependence of the surface morphology and the sheet carrier density of InAs thin films epitaxially grown on (1 0 0)-oriented GaAs substrate with various misorientations of tilt directions and angles of tilt. We also studied the relation between the directions of tilt and the device properties of Hall elements fabricated from InAs thin films grown on GaAs substrates. With a misorientation of 2°, we found a strong dependence of the offset voltage on the direction of tilt of the GaAs substrate. We applied these results to the fabrication of practical InAs Hall elements by molecular beam epitaxy. These Hall elements are now commercially available as magnetic sensors. Over five million Hall elements have been applied to current sensors and brushless motors in electronic appliances.

Keywords: InAs Hall element; InAs on GaAs; Thin film; MBE; InAs morphology on GaAs

1. Introduction

A strong demand for Hall elements has arisen in the field of electronic appliances such as video cassette recorders (VCRs), floppy disk drives (FDDs), and compact disk read-only memory (CD-ROM) drives. Hall elements are used mainly for brushless motors in such equipment. Worldwide, over 1000 million Hall elements are produced in 1995. The Hall element is one of the largest applications of compound semiconductors. Over 70% of Hall elements produced are made of InSb thin film grown on a mica substrate by vacuum deposition [1]. The remainder are mainly GaAs Hall elements fabricated by ion implantation.

InSb Hall elements have an advantage of high sensitivity to the magnetic field, but show less temperature stability. On the other hand, GaAs Hall elements have low sensitivity, but can be used in a wide temperature range [2, 3]. Therefore, it is highly desirable to produce Hall elements that offer both high sensitivity and excellent temperature stability. We have researched and developed a new type of Hall element that consists of InAs thin film

* Corresponding author. Fax: + 81 545 62 3419; e-mail: a9111034@ut.asahi-kasei.co.jp.

0022-0248/97/$17.00 Copyright © 1997 Elsevier Science B.V. All rights reserved
PII S0022-0248(96)00956-6

grown on GaAs substrates by MBE [4–6]. InAs has higher electron mobility than GaAs and a wider energy gap than InSb. InAs thin films are grown on semi-insulating GaAs substrate by molecular-beam epitaxy (MBE). Toward production of InAs Hall elements in large quantities, we have designed a production-scale MBE system that affords high throughput and good uniformity. We have also discovered that Si-doped InAs thin films have both high electron mobility and excellent temperature stability. Si-doped InAs thin film grown on GaAs substrate at a thickness of 0.5 μm has an electron mobility of about 12 000 $cm^2/(V\,s)$. At an electron density of 8×10^{16} cm^{-3} or higher, the temperature coefficient of the sheet resistance is 0.05%/°C around room temperature and the sheet resistance at 125°C is still higher than that at room temperature. By processing this InAs thin film into Hall elements, we developed practical Hall elements that have high sensitivity. Our Si-doped InAs Hall elements perform well and can be operated in a wide temperature range [7].

Offset voltage is also important for Hall elements. In order to reduce the offset voltage in production, we studied and detected an effect of direction and angle of misorientation of the GaAs substrate.

In this paper, we report on our study of the dependence of the surface morphology, and of the sheet carrier density of InAs thin films epitaxially grown on (1 0 0)-oriented GaAs substrate on various directions and angles of tilt misoriented. We found the strong relation between the directions of tilt and one of the device properties, i.e., the offset voltage of Hall elements fabricated from InAs thin films grown on GaAs substrates.

2. InAs thin film grown on GaAs substrate with various misoriented angles and directions of tilt

InAs thin films were grown on semi-insulating Horizontal Bridgman type (1 0 0)-oriented GaAs substrate with 2° misorientation using various directions of tilt, as shown in Fig. 1, namely, tilted toward [0 $\bar{1}$ 0] (called A-direction in Fig. 1), toward [0 $\bar{1}$ $\bar{1}$] (E-direction), toward [0 0 $\bar{1}$] (D-direction), and toward [0 1 $\bar{1}$] (H-direction), all under the same conditions of MBE growth. The substrate temperature was around 480°C and the growth rate was approximately 1.0 μm/h. Nomarski interference microscope photographs of the surface morphology of the InAs thin films are shown in Fig. 2. As shown in the figure, the structures of the surface morphology of InAs thin films depend on the directions of tilt of the (1 0 0)-oriented GaAs substrates. The surface morphology at 2° misorientation is different between two similar directions, such as between the A-direction (tilted toward [0 $\bar{1}$ 0]) and the D-direction (tilted toward [0 0 $\bar{1}$]). These two right angle directions are identical in the absence of misorientation.

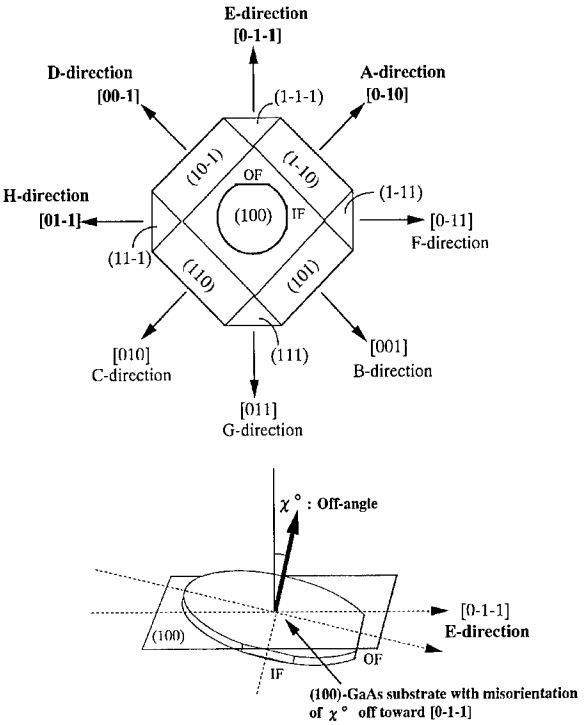

Fig. 1. The various directions of tilt of the misorientation. Directions shown in boldface (A, D, E, H) are those used in this study.

Fig. 3 shows Nomarski interference microscope photographs of the surface morphology of InAs thin films grown on (1 0 0)-oriented GaAs substrate with 1°, 2°, 3°, and 4° misorientation tilted toward [0 0 $\bar{1}$] (D-direction) under the same conditions of MBE growth. As can be seen, the more tilted is the

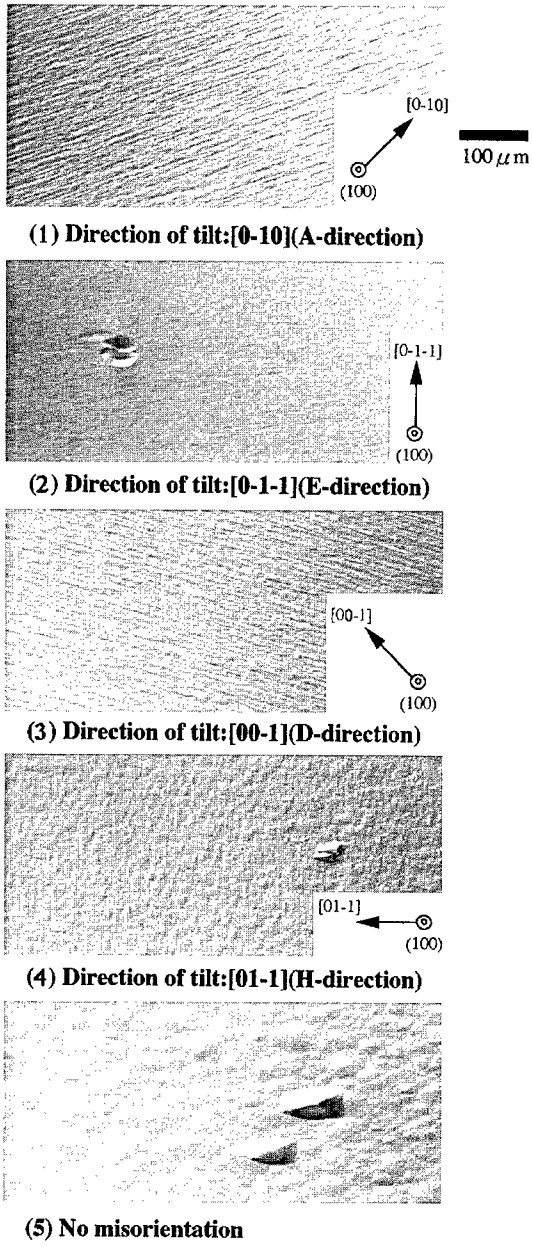

Fig. 2. Nomarski interference microscope photographs of the surface morphologies of Si-doped InAs thin films grown on (1 0 0)-oriented GaAs with various directions of tilt: (1) toward [0 $\bar{1}$ 0], (2) toward [0 $\bar{1}$ $\bar{1}$], (3) toward [0 0 $\bar{1}$], (4) toward [0 1 $\bar{1}$], and (5) no misorientation. Arrows indicate directions of tilt.

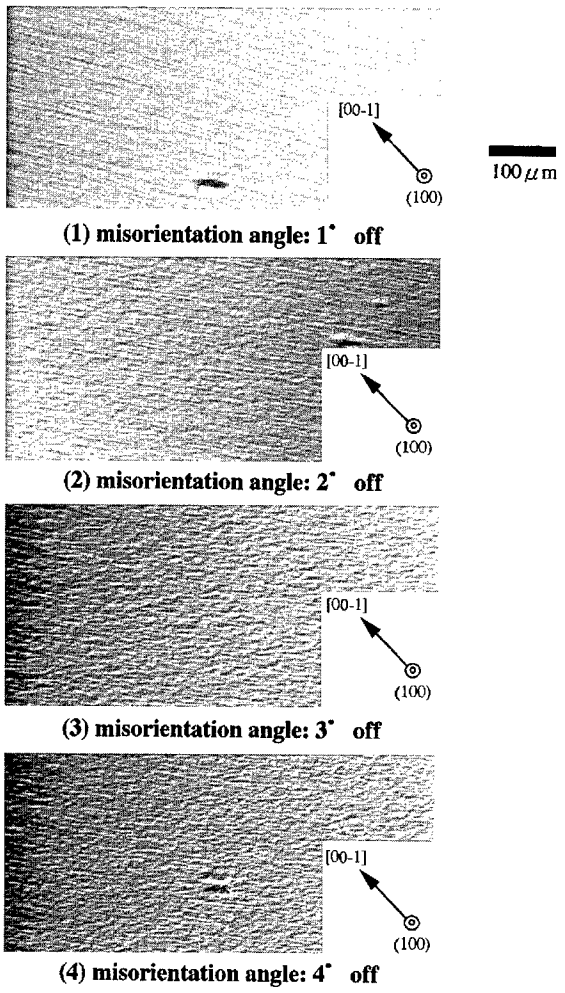

Fig. 3. Nomarski interference microscope photographs of the surface morphologies of Si-doped InAs thin films grown on (1 0 0)-oriented GaAs tilted toward [0 0 $\bar{1}$] (D-direction) with various misorientation angles: (1) 1°, (2) 2°, (3) 3° and (4) 4°. Arrow indicates direction of tilt.

angle of misorientation, the rougher is the surface morphology of the InAs thin films. The surface morphology of InAs thin films is not changed for Si-doping into InAs during MBE for the above-stated growth conditions.

Fig. 4 shows a relation between the sheet carrier density of the Si-doped InAs thin film grown on (1 0 0)-oriented GaAs substrate at a misorientation of 2° and directions of tilt. Undoped InAs thin films

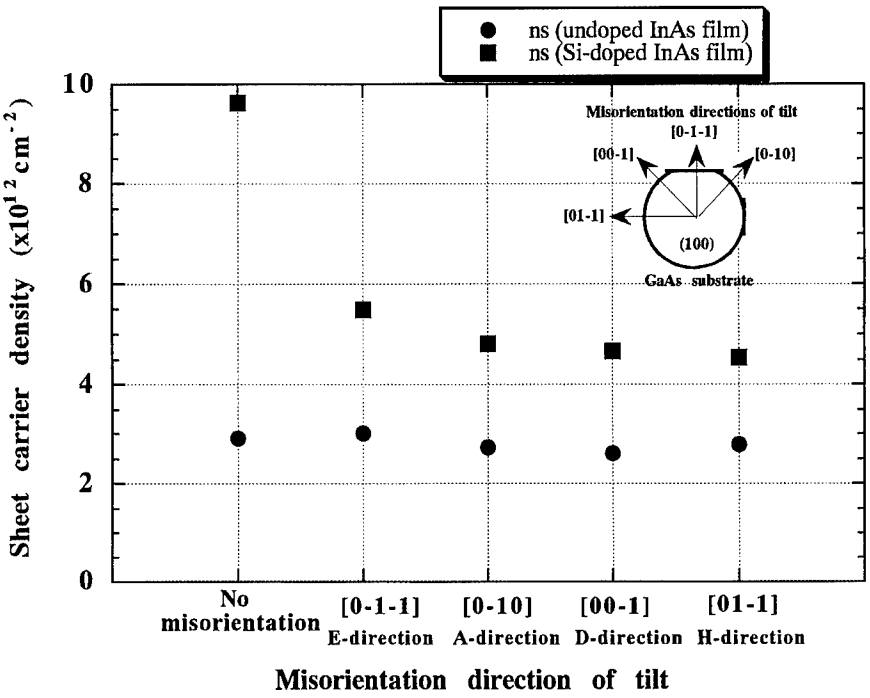

Fig. 4. Sheet carrier density of InAs thin films grown by MBE on GaAs substrates at 2° misorientation with various directions of tilt.

have nearly the same sheet carrier density for all directions and no misorientation. The sheet carrier (electron) density is almost the same at a misorientation of 2° with various directions of tilt (E, A, D and H directions) for Si-doped InAs thin films. The Si-doped InAs thin film grown on (1 0 0)-oriented GaAs substrate with no misorientation has the largest sheet carrier (electron) density.

Fig. 5 shows the sheet carrier density of the InAs thin film grown on (1 0 0)-oriented GaAs substrate tilted toward [0 0 $\bar{1}$] (D-direction) versus tilted angle of misorientation. For Si-doped InAs thin films, the more tilted is the angle of misorientation, less dense is the sheet carrier density of the InAs thin film. The InAs thin film grown on (1 0 0)-oriented GaAs substrate with no misorientation has the largest electron density. In case of undoped InAs thin films, no difference of sheet carrier density is observed for various tilt angles and no misorientation.

3. Offset voltage of InAs Hall element

The Si-doped thin InAs films grown on GaAs substrates by MBE were processed into practical Hall elements by the standard production process shown in Fig. 6. The structure of the practical Hall element fabricated is the symmetrical cross pattern, is shown in Fig. 7.

Table 1 shows the difference in properties of the offset voltage of Hall elements fabricated from the Si-doped InAs thin films grown on (1 0 0)-oriented GaAs substrate with the various directions of tilt shown in Fig. 1. The offset voltage depends largely on the direction of tilt. The smallest offset voltage good for production was observed for InAs Hall elements for the (1 0 0)-oriented GaAs substrate tilted toward [0 $\bar{1}$ $\bar{1}$] (the E-direction).

We studied the origin for the difference in the offset voltage. It could be either the anisotropy of etching of InAs thin film or the intrinsic character of the InAs thin film. Our standard production

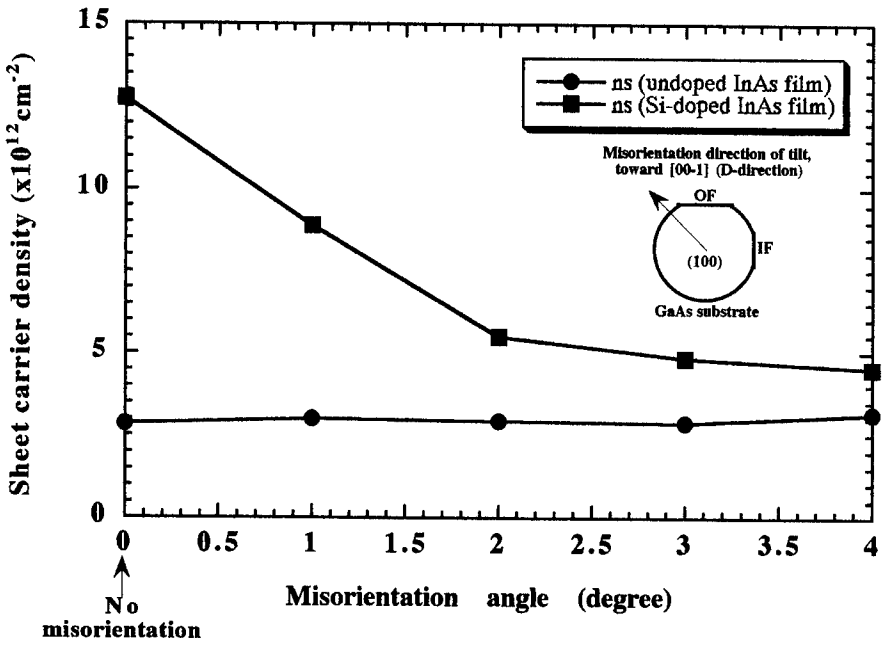

Fig. 5. Sheet carrier density of InAs thin films grown on GaAs substrates at 2° misorientation with various angles of tilt, and tilted toward [0 0 $\bar{1}$] (D-direction).

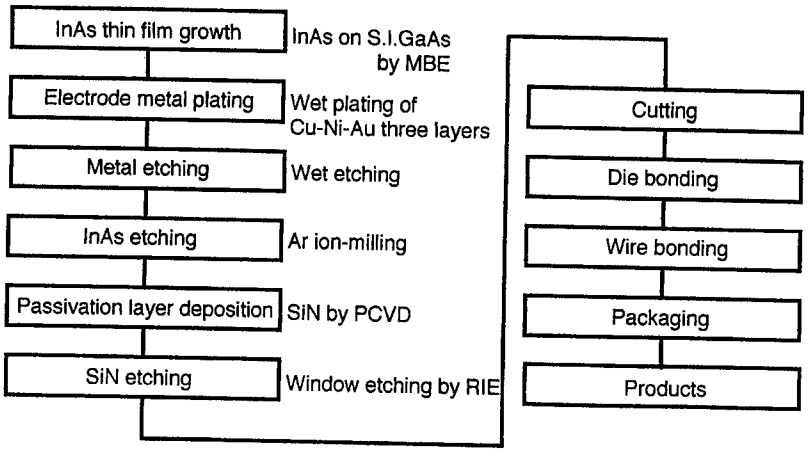

Fig. 6. Fabrication process of the InAs Hall element.

process uses both wet chemical etching and Ar ion-milling in etching for the patterning of the InAs thin film. Thus, to investigate the etching process' dependence of the off-set voltage, we fabricated the Hall elements for both processes with only wet chemical etching and only Ar-ion milling, which is a more isotropic etching than wet chemical etching. The results are also shown in Table 1. There is no difference in the tendency of the offset voltage between our production process, wet etching process

Table 1
Offset voltage of Hall elements fabricated by various wafer processes from Si-doped InAs thin films grown on (1 0 0)-oriented GaAs substrates with various directions of tilt

Misorientation direction of tilt	Offset voltage V_u Ave. $\pm \sigma$ (mV/V_{in} = 3 V)		
	Production process	Dry etching process by ion-milling	Wet etching process
[0 $\bar{1}$ 0] (A-direction)	-5.20 ± 0.96	-3.34 ± 1.28	-3.43 ± 1.68
[0 0$\bar{1}$] (D-direction)	5.55 ± 0.99	1.62 ± 1.39	1.83 ± 1.35
[0 $\bar{1}$ $\bar{1}$] (E-direction)	-0.03 ± 0.68	0.25 ± 1.49	0.86 ± 1.22
[0 1 $\bar{1}$] (H-direction)	0.01 ± 1.28	0.26 ± 1.08	-0.10 ± 1.05
No misorientation	-0.12 ± 1.58	0.36 ± 2.47	0.08 ± 2.09

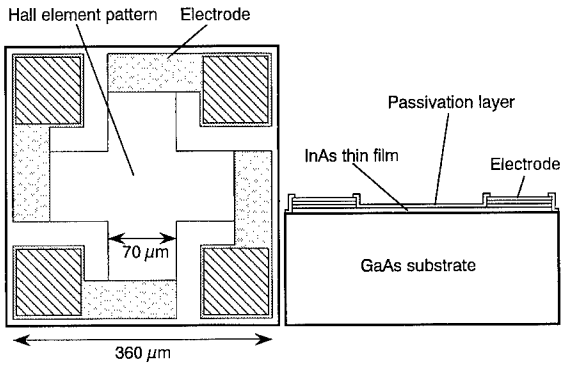

Fig. 7. Structure of the InAs Hall element chip.

and the ion-milling process. Therefore, the difference in properties of the offset voltage of Hall elements fabricated from InAs thin films grown on (1 0 0)-oriented GaAs substrate with various directions of tilt is attributed mainly to the crystalline character of the InAs thin film.

4. Conclusions

We found a strong dependence of the offset voltage on the directions of tilt of the GaAs substrate at 2° misorientation. As a result, Hall elements fabricated from InAs thin films grown on (1 0 0)-oriented GaAs substrate at 2° misorientation tilted toward [0 $\bar{1}$ $\bar{1}$] have the smallest offset voltage. This observed property is important in fabricating practical InAs Hall elements. These results were applied to the fabrication of practical InAs Hall elements by MBE.

Our InAs Hall element is a promising device that opens up new areas for magnetic field sensor applications.

Acknowledgements

The authors would like to thank Dr. H. Imai and Mr. K. Komatsu for their aid in this research.

References

[1] I. Shibasaki, The 8th Sensor Symp. C3-1, Tech. Dig. (IEE, Tokyo, 1989) p. 211.
[2] A. Hohjoh, S. Tanaka and I. Kuru, Jpn. J. Appl. Phys. 15 (1976) 261.
[3] H. Tanone, T. Tsurushima and S. Kataoka, IEEE Trans. Electron Dev. ED-27 (1980) 1188.
[4] I. Shibasaki, Y. Kanayama, K. Nagase, T. Ito, F. Ichimori, T. Yoshida and K. Harada, The 10th Sensor Symp. C2-2, Tech. Dig. (IEE, Tokyo, 1991) p. 113.
[5] I. Shibasaki, Y. Kanayama, T. Ito, F. Ichimori, T. Yoshida, K. Nagase and K. Harada, 1991 Int. Conf. on Solid-State Sensor and Actuators (Transducers '91), Dig. Tech. (IEEE, USA, 1991) p. 1069.
[6] Y. Kanayama, K. Nagase, S. Muramatsu, A. Ichi, N. Kuze, T. Iwabuchi, F. Ichimori, T. Yoshida, T. Ito and I. Shibasaki, in: Proc. 4th Int. Symp. on Micro Machine and Human Science (1993) p. 165.
[7] T. Iwabuchi, T. Ito, M. Yammamoto, K. Sako, Y. Kanayama, K. Nagase, T. Yoshida, F. Ichimori and I. Shibasaki, J. Crystal Growth 150 (1995) 1302.

ELSEVIER

Journal of Crystal Growth 175/176 (1997) 197–202

JOURNAL OF CRYSTAL GROWTH

Low temperature (LT) and stoichiometric low temperature (SLT) MBE GaAs and related compounds: improved structural, electrical and optical properties

M. Missous*, S. O'Hagan

Department of Electrical Engineering and Electronics, UMIST, P.O. Box 88, Manchester M60 1QD, UK

Abstract

GaAs and related materials grown at 200–300°C under normal, group V-rich growth conditions are highly non-stoichiometric with excess group V concentrations of up to 10^{21} cm^{-3}. The material properties are, therefore, defect controlled. Here we further our previous studies of low-temperature grown GaAs to show that doping with Si or Be at concentrations at or greater than 10^{19} cm^{-3} reduces the excess As related defect concentration by more than an order of magnitude, not only on GaAs(1 0 0) but also on GaAs(3 1 1)A and GaAs(3 1 1)B surfaces, compared to undoped material grown under identical conditions. Furthermore, we show that by careful control of the As : Ga flux ratio at low temperature, stoichiometric low-temperature (SLT) conditions may be achieved which can be used to grow GaAs, AlGaAs and other III–V compounds of electrical and optical performance comparable to material grown at high temperatures. SLT quantum well (QW) structures of AlGaAs/GaAs and SLT QW and two-dimensional electron gas (2DEG) structures of InAlAs/InGaAs, lattice matched to InP, are used to demonstrate the excellent quality material achievable and how it may be applied to optical and electrical devices. The work illustrates the wide range of material benefits which can be attained in the low-temperature growth regime.

1. Introduction

Much interest in III–V compounds grown by molecular beam epitaxy (MBE) at low substrate temperature (200–300°C) has arisen due to the non-stoichiometry of materials grown under high group V overpressure [1]. In GaAs, for example, excess As concentrations of 10^{20}–10^{21} cm^{-3} result in low minority carrier lifetime [2], a shifted Fermi level compared to S.I. GaAs [3] and, after thermal annealing, high resistivity [2]. These properties are exploited in such applications as GaAs MESFET buffer layers [2], non-alloyed ohmic contact formation [4] and fast photoconductive switching [5].

Technological advantages also arise from the ability to grow high electrical and optical quality GaAs at low temperature, including increased free

* Corresponding author. Fax: + 44 161 2004770.

0022-0248/97/$17.00 Copyright © 1997 Elsevier Science B.V. All rights reserved
PII S0022-0248(96)00958-X

carrier concentration [6], reduced outdiffusion of impurities from heavily doped device regions e.g. heterojunction bipolar transistor (HBT) bases [7] and low resistivity non-alloyed ohmic contacting [8]. The high defect count of low-temperature GaAs grown under normal growth conditions – the source of its value in the applications mentioned above – proves seriously detrimental when doping the material [9, 10].

We have shown previously that non-stoichiometry is not an intrinsic property of low-temperature (LT) GaAs. It is controllable by heavy doping [11] and careful tailoring of growth conditions to produce a stoichiometric low-temperature (SLT) compound [12]. Here we extend our work on GaAs(1 0 0) [11] to (3 1 1)A and B surfaces, demonstrating that the suppression of excess As incorporation by heavy doping is also active on these surfaces. We also describe how achieving SLT conditions has allowed low temperature growth of improved quality, quantum well (QW) and 2 dimensional electron gas (2DEG) structures.

2. Experimental procedure

The MBE growth techniques are detailed elsewhere [13]. Unless otherwise stated, the samples were grown at a nominal substrate temperature of 250°C. For comparative studies of (1 0 0), (3 1 1)A and (3 1 1)B surfaces, substrates of each type were loaded simultaneously in a multiple 2″ wafer holder to ensure identical conditions, and an As : Ga beam equivalent pressure (BEP) ratio of greater than 4 was used to ensure excess As conditions. Intended doping concentrations were [Si] = 1×10^{19} cm^{-3} and [Be] = 1.5×10^{19} cm^{-3}. QW and 2DEG samples, on the other hand, were grown under stoichiometric conditions as was evidenced by RHEED intensity oscillations observed during the growth [12].

Crystalline quality was investigated by double crystal X-ray diffraction (DCXD). The Hall effect was used for electrical characterisation, and neutral As antisite concentration was measured using near band edge infra-red (NBEIR) absorption. Finally, photoluminescence (PL) measurements probed the optical performance of QW structures.

3. The effect of dopants on (1 0 0), (3 1 1)A and (3 1 1)B surfaces

Fig. 1a–Fig. 1c show the DCXD rocking curves of undoped, Si- and Be-doped (1 0 0), (3 1 1)A and (3 1 1)B samples, respectively. The undoped epilayer lattices are clearly expanded compared to the SI GaAs substrates, as reported for (1 0 0) [1] and (3 1 1)B [14] material. The peak separation of 60 arcsec in the undoped (1 0 0) curve agrees well with what we usually measure for a nominal substrate temperature of 250°C using a valved cracker As_2 source. Evidently, across all the surfaces, doping with Si and Be at this concentration reduces the lattice parameter of the epilayers compared to undoped layers grown under identical conditions. In the Si (1 0 0) and (3 1 1)A, and the Be (1 0 0) and (3 1 1)A cases, only a single diffraction peak

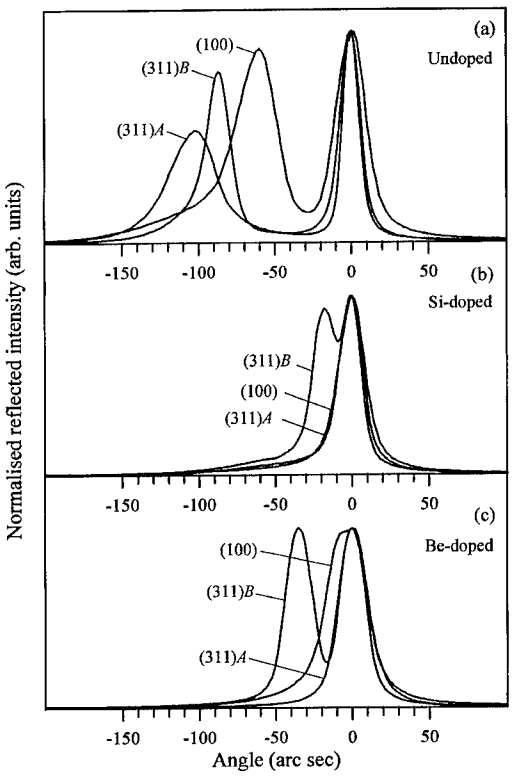

Fig. 1. DCXD rocking curves of GaAs(1 0 0), (3 1 1)A and (3 1 1)B epilayers grown at 250°C (a) undoped, (b) doped with [Si] = 1×10^{19} cm^{-3} and (c) doped with [Be] = 1.5×10^{19} cm^{-3}.

appears although the FWHM of the peak in the Be (1 0 0) curve is broader (32 arcsec) than that of the Be (3 1 1)A, Si (1 0 0) and Si (3 1 1)A curves (20–22 arcsec). We believe that heavy doping reduces excess As concentration to a level below the limit detectable by DCXD ($\sim 1-2\times10^{19}$ cm^{-3}), on the (3 1 1)A and B surfaces as well as on (1 0 0) surfaces [11].

The relative total excess As concentration, estimated from the diffraction peak separation, correlates with the neutral As antisite concentration ([As_{Ga}]°), measured by NBEIR absorption and presented in Fig. 2. The highest concentration is seen in the undoped samples, reducing by a factor of 2–8 with Be doping, and a factor of 5–10 with Si doping.

Table 1 shows 300 K and 77 K carrier concentration and mobility in the layers. In the undoped (3 1 1)A and B samples, low mobility is indicative of hopping conduction in the As_{Ga} defect band, a well established phenomenon in undoped LT-GaAs [15]. The undoped (1 0 0) sample mobility is much higher, however, most likely reflecting the contribution of the SI GaAs substrate to conduction within the structure [16] and less conduction in the epilayer as a lower antisite concentration reduces hopping probability. All the Si-doped layers show n-type conductivity, with carrier concentration and mobility reducing with increasing excess As concentration as estimated from the IR absorption results. The mobilities measured, although low, are reasonable for strongly compensated, heavily

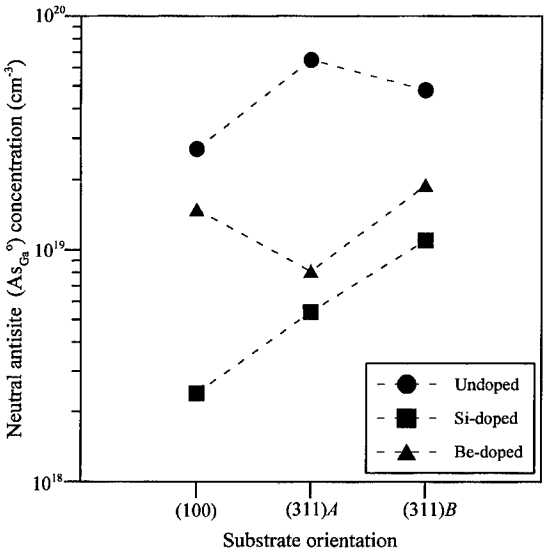

Fig. 2. NBEIR absorption spectra of GaAs(1 0 0), (3 1 1)A and (3 1 1)B epilayers grown at 250°C undoped, doped with [Si] = 1×10^{19} cm^{-3} and doped with [Be] = 1.5×10^{19} cm^{-3}. Note the dashed lines are added only as a guide to the eye.

Table 1
Free carrier concentration and mobility in undoped, Si-doped and Be-doped samples grown on (1 0 0), (3 1 1)A and (3 1 1)B substrates, measured using the Hall effect

Sample	300 K		77 K	
	n[p] (cm^{-3})	$\mu_{n[p]}$ (cm^2/V·s)	n[p] (cm^{-3})	$\mu_{n[p]}$ (cm^2/V·s)
Undoped				
(1 0 0)	2.5×10^{11}	2042	–	–
(3 1 1)A	4.9×10^{15}	19	–	–
(3 1 1)B	5.8×10^{14}	29	–	–
Si-doped				
(1 0 0)	2.7×10^{18}	489	3×10^{18}	426
(3 1 1)A	8.5×10^{17}	173	1×10^{18}	81
(3 1 1)B	3.3×10^{16}	227	1.8×10^{16}	81
Be-doped				
(1 0 0)	1.2×10^{14}	173	1.1×10^{11}	1477
(3 1 1)A	[1.4×10^{15}]	[308]	–	–
(3 1 1)B	1.7×10^{16}	4	–	–

Note that where the material appeared p-type, the values are in square brackets.

doped n-type material and are in close agreement with previous measurements on low-temperature grown, highly Si-doped GaAs [11]. This suggests that *band* conductivity is the dominant process in the Si-doped layers, with any hopping contribution removed by the reduced antisite concentration.

Si is an amphoteric impurity in GaAs and forms either an acceptor [17] or a donor [18, 19] on the (3 1 1)A face depending on growth conditions. On (3 1 1)A substrates and (3 1 1)A facets etched into (1 0 0) substrates, both GaAs and AlGaAs became n-type for V/III flux ratios $\geqslant 3$ and substrate temperature $\leqslant 450°$ [18, 19], both of which conditions are satisfied here. Be atoms, however, should all assume Ga lattice sites. We note that the Be acceptors are much more heavily compensated than the Si donors, most probably due to a greater abundance of compensating As_{Ga} donors [10], than V_{Ga} acceptors [9]. It should be noted that the measurements on the Be (1 0 0) and Be (3 1 1)A samples are probably unreliable due to surface and interface depletion of the heavily compensated epilayer [20]. n-type conductivity with low mobility in the Be (3 1 1)B sample could indicate hopping conduction, as the absorption results do yield a high $[As_{Ga}]^{\circ}$ in the layer.

In summary, simultaneous growth of GaAs on (1 0 0), (3 1 1)A and (3 1 1)B surfaces at 250°C under As-rich conditions, has shown that doping with Be or Si in concentrations at or greater than $1 \times 10^{19} cm^{-3}$ significantly reduces the amount of excess As incorporated into all surface orientations compared to undoped layers grown under identical conditions. The relative efficiency of the suppression mechanism on the different orientations will be discussed elsewhere [21].

The nature of the suppression mechanism is not known, however possible explanations, namely radiative heating by the hot dopant cell, especially the Si source, and the effect of the dopant itself on the lattice parameter, have been previously addressed and discounted [22].

4. Stoichiometric low temperature (SLT) grown device structures

Despite the effects mentioned above, the electrical and optical performance [11] is still heavily degraded. To improve doped and undoped material quality, a further 3–4 orders of magnitude of excess As concentration must be removed. This requires careful control of the Group III and Group V fluxes to produce a stoichiometric compound. We have shown that under SLT conditions: (i) layers are closely lattice matched to their substrates [13], (ii) high electrical and optical quality doped epitaxial layers can be grown [11] and (iii) undoped GaAs and AlGaAs exhibit RHEED intensity oscillations during growth [12]. We now show that active structures and devices can be produced in this manner. Fig. 3a and Fig. 3b show the 6 K PL spectra of two QW samples grown under SLT conditions. The first structure uses $Al_{0.4}Ga_{0.6}As$/GaAs and has 3 wells of thickness 40, 80 and 120 Å, respectively, grown at nominally 250°C. The second uses $In_{0.53}Al_{0.47}As/In_{0.52}Ga_{0.48}As$, lattice matched to InP, with well widths of 50, 100 and 200 Å, grown at 200°C. In the AlGaAs/GaAs sample, the wells of 80 and 120 Å thickness exhibit radiative transitions of a line width comparable to that seen in high-temperature grown QW samples

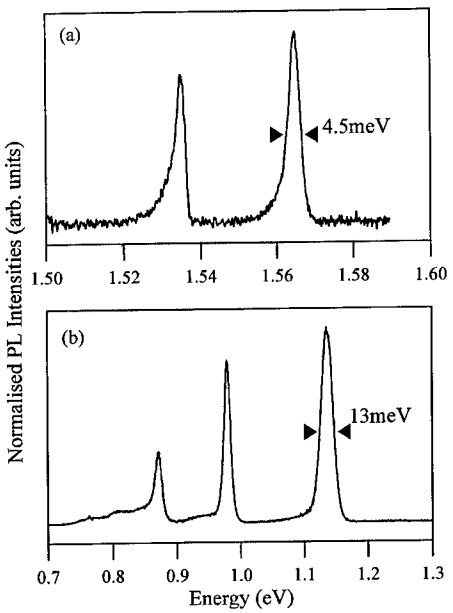

Fig. 3. 6K PL spectra of (a) a 250°C grown $Al_{04}Ga_{0.6}As$/ GaAs QW structure and (b) a 200°C grown $In_{0.53}Al_{0.47}As/In_{0.52}Ga_{0.48}As$ QW structure, lattice matched to InP.

of the same structure. The PL intensity is significantly impaired, however it should be noted that the III/V flux ratio was optimised for SLT growth of AlGaAs and, without a second Ga or As source, could not be changed readily to the conditions required for GaAs without growth interruption. There is, therefore, excess As in the structure – as proven by the observation of As precipitates by transmission electron microscopy of the structure after annealing at 600°C (to be detailed separately) – but in insufficient concentration to obliterate the luminescence completely. We believe emission intensity would be improved with the MBE system configured to optimise SLT conditions in GaAs and AlGaAs. The InAlAs/InGaAs sample shows stronger PL intensity probably due to the In–As bond being weaker than the Ga–As or Al–As bonds [23], thereby allowing SLT conditions to be more readily achieved. From this we surmise that it is possible to tailor growth conditions to produce optically active SLT structures in a number of III–V material systems.

Finally, modified two-dimensional electron gas (2DEG) structures were grown at 200°C, using $In_{0.53}Al_{0.47}As/In_{0.52}Ga_{0.48}As$ lattice matched to InP, under a range of V/III flux ratios. The InGaAs channel was 1 μm thick, thicker than the more usual 500 Å or less used in high electron mobility transistor (HEMT) structures. Fig. 4 illustrates the improvement seen in sheet carrier concentration and mobility in the two-dimensional electron gas (2DEG) structure as SLT (flux ratio = 1) conditions are approached. Measurements on a 500°C grown control sample are shown by way of comparison. Under SLT conditions, the 77 K carrier density and mobility almost reach the 1.5×10^{12} cm^{-2} and 60,000 $cm^2/V \cdot s$ figures, respectively, measured in the control sample. The higher charge density measured in the SLT structure at 300 K most likely arises from the thicker than normal channel mentioned above.

Our work clearly shows that the achievement of SLT conditions in the growth of a number of III–V compounds allows the successful production of good electrical and optical device quality structures at substrate temperatures as low as 200–250°C. It follows that growth conditions can be successfully used in the 'defect engineering' of MBE structures

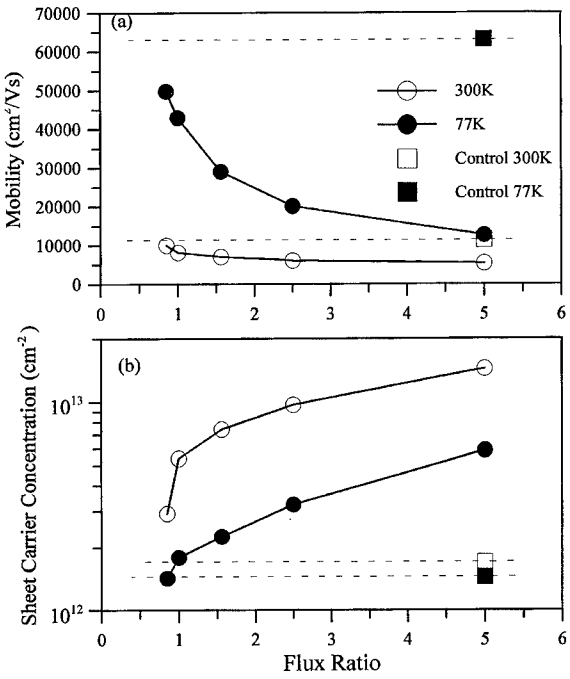

Fig. 4. (a) electron mobility and (b) sheet carrier concentration in a 200°C grown $In_{0.53}Al_{0.47}As/In_{0.52}Ga_{0.48}As$ 2DEG structure. The dashed lines are included only as a guide to the eye.

to exploit the diverse technological advantages of highly defective, 'classic LT' material through to the benefits of high-quality SLT materials.

5. Conclusion

Comparative studies have been performed on undoped and heavily Si and Be doped GaAs epilayers, simultaneously grown (1 0 0), (3 1 1)A and (3 1 1)B substrates at low temperature, under As-rich conditions. The results indicate that the dopant acts to suppress the incorporation of excess As into the higher index surfaces in the same way as has already been reported for the (1 0 0) face [11]. All Si-doped material exhibits n-type band conductivity rather than the hopping seen in undoped layers. Be doped layers are more heavily compensated but still show a sizeable reduction in excess As concentration.

Secondly, SLT conditions can be achieved by careful manipulation of the growth variables, to allow growth of a wide range of excellent electrical and optical device quality structures across a number of III–V material systems. A combination of doping and careful growth control can now be used to exploit all the beneficial aspects of MBE growth performed at low substrate temperature.

Acknowledgements

We would like to acknowledge Dr. P. Buckle and Dr. J. Hartung for their help with the PL measurements. This work was supported by the UK Engineering and Physical Sciences Research Council.

References

[1] M. Kaminska, E.R. Weber, Z. Liliental-Weber, R. Leon and Z. Rek, J. Vac. Sci. Technol. B 7 (1989) 710.
[2] F.W. Smith, A.R. Calawa, C-L. Chen, M.J. Manfra and L.J. Mahoney, IEEE Electron Devices Lett. 9 (1988) 77.
[3] D. C Look, J.T. Grant and J.R. Sizelove, Appl. Phys. Lett. 61 (1992) 1329.
[4] M.P. Paktar, T.P. Chin, J.M. Woodall, M.S. Lundstrom and M.R. Melloch, Appl. Phys. Lett. 66 (1995) 1412.
[5] J.F. Whitaker, Mater. Sci. Eng. B 22 (1993) 9.
[6] M. Ramsteiner, J. Wagner, J.P. Silviera and F. Briones, Inst. Phys. Conf. Ser., Vol. 112 (1990) p. 85.
[7] K. Zhang, S.S. Bose and D.L. Miller, J. Electron. Mater. 21 (1992) 187.
[8] P.D. Kirchner, T.N. Jackson, G.D. Pettit and J.M. Woodall, Appl. Phys. Lett. 47 (1985) 26.
[9] S.A. McQuaid, R.C. Newman, M. Missous and S. O'Hagan, Appl. Phys. Lett. 61 (1992) 3008.
[10] D.E. Bliss, W. Walukiewicz, J.W. Ager, E.E. Haller, K.T. Chan and S. Tanigawa, J. Appl. Phys. 71 (1992) 1699.
[11] S.P. O'Hagan and M. Missous, J. Appl. Phys. 75 (1994) 7835.
[12] M. Missous, J. Appl. Phys. 78 (1995) 4467.
[13] M. Missous and S.P. O'Hagan, J. Appl. Phys. 75 (1994) 3396.
[14] T.M. Cheng, C.Y. Chang and J.H. Huang, Appl. Phys. Lett. 66 (1995) 55.
[15] D.C. Look, D.C. Walters, M. Mier, M.O. Manasreh, J.R. Sizelove, C.E. Stutz and K.R. Evans, Phys. Rev. B 42 (1990) 3578.
[16] D.C. Look, G.D. Robinson, J.R. Sizelove and C.E. Stutz, Proc. 7th Conf. on Semi-insulating III–V Materials, Ixtapa (1992) p. 141.
[17] W.I. Wang, E.E. Mendez, T.S. Kuan and E. Esaki, Appl. Phys. Lett. 47 (1985) 826.
[18] W.Q. Li, P.K. Bhattacharyya, S.H. Kwok and R. Merlin, J. Appl. Phys. 72 (1992) 3129.
[19] H.P. Meier, R.F. Broom, P.W. Epperlein, E. van Gieson, C. Harder, H. Jäckel, W. Walter and D.J. Webb, J. Vac. Sci. Technol. B 6 (1988) 692.
[20] A. Chandra, C.E.C. Wood, D.W. Woodward and L.F. Eastman, Solid State Electron. 22 (1979) 645.
[21] S. P. O'Hagan and M. Missous, to be published.
[22] S.P. O'Hagan, M. Missous, A. Mottram and A.C. Wright, J. Appl. Phys. 79 (1996) 8384.
[23] H. Morkoc, J. Drommond and R. Fischer, J. Electrochem. Soc. 129 (1982) 824.

ELSEVIER

Journal of Crystal Growth 175/176 (1997) 203–210

JOURNAL OF CRYSTAL GROWTH

Growth dynamics of InGaAs/GaAs by MBE

Françoise Fournier[a,*], Robert A. Metzger[a], Alan Doolittle[a], April S. Brown[a], Carrie Carter-Coman[a], Nan Marie Jokerst[a], Robert Bicknell-Tassius[b]

[a] *School of Electrical and Computer Engineering, Microelectronics Research Center, Georgia Institute of Technology, Atlanta, Georgia 30332-0269, USA*

[b] *Georgia Tech Research Institute, Georgia Institute of Technology, Atlanta, Georgia 30332-0269, USA*

Abstract

The growth dynamics of the InGaAs/GaAs system have been investigated by desorption mass spectrometry (DMS). Indium desorption spectra indicate the presence of one or two desorption mechanisms depending on the V/III beam equivalent pressure ratio. The activation energy associated with one of the desorption processes is found to be 1.3 eV and independent of V/III ratio and arsenic species. Analysis of the decay curve allows the calculation of the indium surface population during growth. This population is compared for the different growth conditions investigated. Indium incorporation coefficient curves as a function of substrate temperature are presented. Indium incorporation is found to be enhanced using high V/III ratio and the arsenic dimer, As_2.

1. Introduction

The large band gap and lattice constant difference between GaAs and InAs makes the InGaAs/GaAs system of technical interest for electronic and optical applications. In addition, growth kinetic processes which depend on strain enable the production of quantum-confined structures and can be exploited by varying the indium composition of the InGaAs alloy. Several studies have shown that the dynamics during the growth of InGaAs are complex [1], particularly at temperatures where indium desorption, segregation and incorporation are all important. A good understanding of the surface cation kinetics and the influence of growth parameters on indium incorporation are necessary in order to adequately control the growth of InGaAs.

Another motivation for the study of InGaAs growth dynamics is to enable the full understanding and exploitation of the strain modulated epitaxy (SME) approach [2, 3]. This new technology utilizes thin compliant substrates which are bottom-patterned. The pattern in the compliant bonded substrate modulates the growing overlayer to substrate thickness ratio. The strain at the surface of the growing film, which depends on this ratio, is thus laterally controlled. Thus, one aspect of this study was to measure the dependence of InGaAs growth dynamics on strain. Some previous

* Corresponding author. Fax: + 1 404 894 5028; e-mail: fournier@prodiga.mirc.gatech.edu.

0022-0248/97/$17.00 Copyright © 1997 Published by Elsevier Science B.V. All rights reserved
PII S0022-0248(96)00888-3

reports [4, 5] have shown that the activation energy for desorption has a significant strain dependence. In order to fully exploit indium kinetics in SME, we need to understand the relations existing between strain and surface mechanisms, such as segregation, desorption and migration for the InGaAs/GaAs system.

By repositioning the mass spectrometer in a direct line of sight with the growing surface, several authors [5, 6] have shown that desorption mass spectrometry (DMS) is a useful in situ surface characterization tool. We report in this paper the result of an extensive DMS study during the growth of InGaAs on GaAs.

2. Experimental procedure

A UTI mass spectrometer, tuned on the charge to mass peak ratio 115 of indium was positioned in line-of-sight to the substrate holder via an aperatured nipple. Substrate temperatures were measured by a thermocouple in direct contact to the back of the substrate holder. Oxide desorption was monitored by RHEED and the thermocouple reading was calibrated by assigment of the observed oxide desorption temperature to 580°C. (1 0 0)-oriented GaAs substrates were mounted on an indium-free holder. An EPI arsenic cracker was used to produce fluxes of both arsenic tetramers and dimers. For the desorption spectra recorded in presence of As_2, the temperature of the arsenic cracker was increased to 900°C but the temperature of the evaporator was kept constant to 335°C. Thus, only the As_2 and As_4 molecular fluxes were modified but the arsenic flux was not changed.

The growth experiment was repeated as a function of substrate temperature (510–630°C), indium composition (5–21%), InGaAs growth rate (0.43–0.912 μm/h), V/III beam equivalent pressure ratio (17 : 1, 36 : 1), measured with As_4 and arsenic species. After substrate oxide removal, a 1200 Å GaAs buffer layer was deposited at 580°C. The substrate temperature was then lowered to the first temperature of the investigated range, 510°C, and $In_xGa_{1-x}As$ was grown for 25 s (approximately, 63 Å of $In_{0.21}Ga_{0.79}As$ in the case of 21% In). During the InGaAs deposition, the substrate was not rotated, and the mass spectrometer desorption signal, which was assumed to be directly proportional to the indium desorbed flux, $F_D(In)$, was recorded for further data analysis. We reference the mass spectrometer signal of 3.485×10^{-11} A to an incident indium flux of $F_i = 0.192$ μm/h. After deposition of the InGaAs layer and a return to zero for the mass spectrometer desorption signal, the substrate temperature was raised to 580°C, and a 600 Å GaAs layer was grown, in order to smooth the surface and bury the preceding InGaAs layer. A new set of measurements was then taken at the next highest InGaAs growth temperature.

3. Results and discussions

The desorption spectra (indium desorption as a function of time during InGaAs growth) were recorded for different growth temperatures and growth conditions (Fig. 1 shows desorption spectra for growth with As_4). Each desorption spectrum has the same profile as described by Evans [5]; an exponential rise at growth initiation ($t = 0$), followed by the realization of a steady-state signal. The amplitude of the steady-state signal increases with increasing substrate temperature. Upon termination of the InGaAs growth ($t = 25$ s), the desorption signal drops back to zero with a time constant which depends on the growth conditions. For low substrate temperatures (510–520°C), no detectable mass spectrometer signal was recorded. The indium desorption signal begins to appear around 530°C. The data presented (see Fig. 1) were obtained with GaAs and InGaAs growth rates of 0.714 and 0.912 μm/h, respectively. The indium composition was approximately 21%. Fig. 1a shows data for growth under a low V/III (17 : 1) ratio, while Fig. 1b shows data obtained for growth with a higher V/III ratio (36 : 1). The shape of these two sets of desorption spectra is quite different. The series of curves at low V/III ratio is square-shaped, and we can define two desorption mechanisms in the decay curve, with two different rate constants K_{d1} and K_{d2}. In the case of the higher V/III ratio, the shape is more rounded, and the decay curve can be modeled by a single desorption mechanism. These two sets of measurements were repeated using

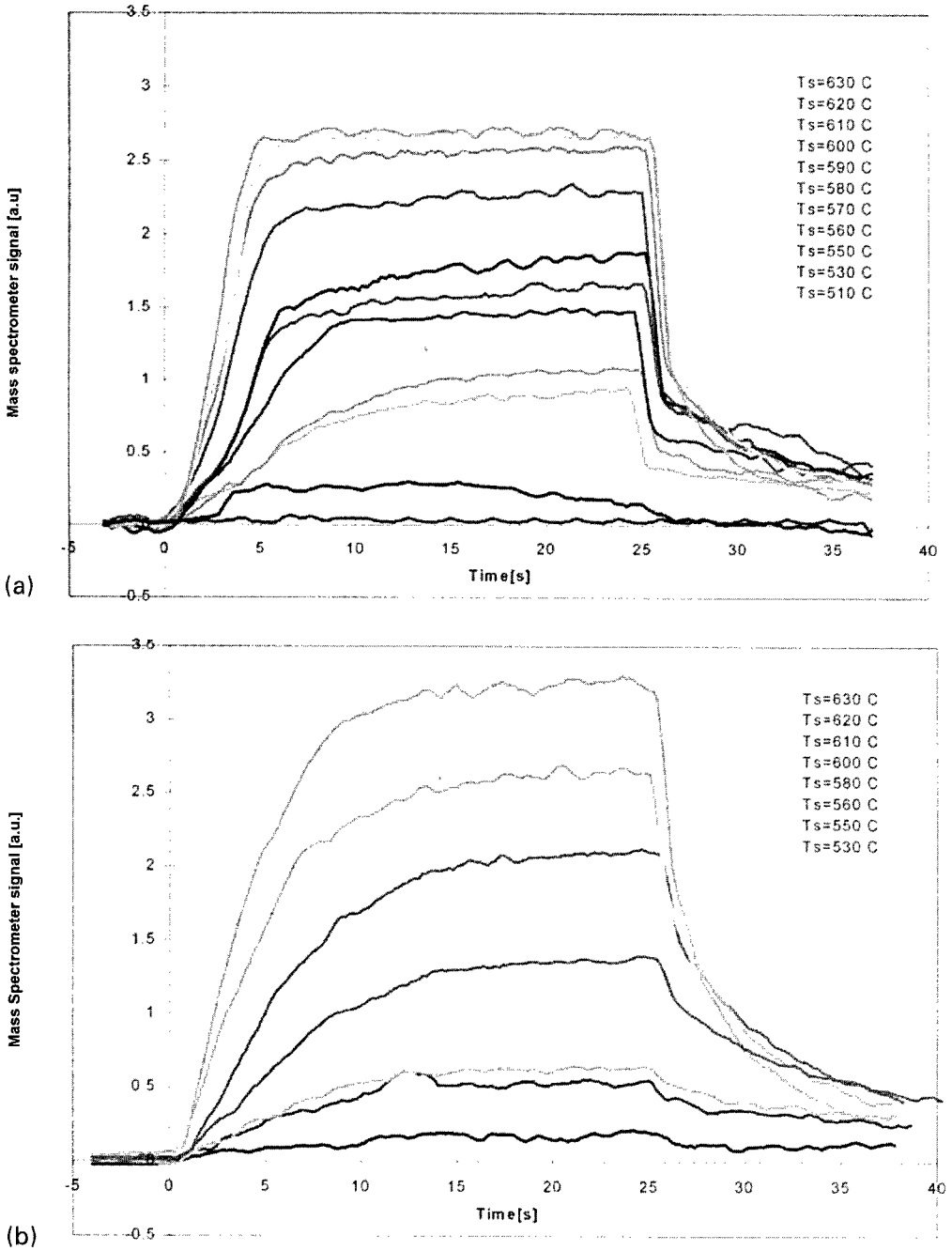

Fig. 1. Series of desorption spectra as a function of substrate temperature during growth of $In_{0.21}Ga_{0.79}As$ on GaAs MBE, in the presence of As_4, for low V/III ratio ($\sim$ 17 : 1) (a) and high V/III ratio ($\sim$ 36 : 1) (b). (a) presents two desorption mechanisms while (b) only shows one mechanism.

the dimer As_2, with the same dependence on V/III ratio observed. Other studies report data which may appear similar but are interpreted differently from the data in this study. Evans et al. [7] observe two desorption phenomena for InAs deposited on GaAs. They attribute the lowest-temperature desorption mechanism (620°C) to indium desorption from a segregated surface layer, and the higher-temperature desorption (700°C) to indium evolving from the lattice. The two mechanisms observed in our data occur at temperatures less than 640°C. Kao et al. [8] in their DMS analysis of InGaAs growth, observed two separable signals in their decay curve. They associated one part of the signal to desorption, while the other part was interpreted as indium reflection due to the observed insensitivity of the signal to substrate temperature.

In our case, below 530°C, no measurable desorbed signal is noted in the presence of an open or closed indium shutter. For temperatures above 610°C, we observed a saturation of the steady-state amplitude (see Fig. 1a). The saturation amplitude is dependent on the V/III ratio. In the presence of higher V/III ratio, the saturation appears at a temperature greater than 630°C. For high V/III ratio and high temperatures we note similar behaviour for the growth of InGaAs utilizing As_2.

In order to extract more information from the mass desorption spectra, we utilize a general equation describing the indium surface population during growth. By analogy to the dopant incorporation model presented by Wood and Joyce [9], we can write the temporal variation of the indium surface population, N_s, as

$$dN_S(\mathrm{In})/dt = F_i - K_d(N_S(\mathrm{In}))^p - K_I(N_S(\mathrm{In}))^q, \quad (1)$$

where F_i is the incident indium flux in atoms/cm^2, the second term defines the indium desorbed flux, $F_D(\mathrm{In})$, and the final term represents the incorporation flux, $F_I(\mathrm{In})$. K_d and K_I are, respectively, the desorption and incorporation rate contants. The units of K depend on the reaction order. Finally, p and q are, respectively, the desorption and incorporation order. In the case of several desorption mechanisms different K_d need to be defined. In the case of two mechanisms, the K expressions can be written as a function of activation energy and substrate temperature, as follows:

$$K_{d1} = K_{d10} \exp(-E_{A1}/kT), \quad (2)$$

$$K_{d2} = K_{d20} \exp(-E_{A2}/kT). \quad (3)$$

In order to take into account the two separate desorption mechanisms which clearly appear in our desorption spectra, we have introduced two terms in the desorption part of Eq. (1), each related to one desorption phenomenon and each with an associated activation energy, E_{A1} and E_{A2}. We assume that E_{A1} corresponds to the desorption activation energy of an indium segregated layer, which does not appear in the presence of a high V/III ratio. E_{A2} represents the desorption activation energy for indium atoms from a more tightly bound state.

The initial rise in signal apparent in the desorption spectra corresponds to the creation of an indium surface population. During the establishment of this population, indium incorporation, segregation and desorption are present. This situation can be described by Eq. (1). When the steady state is reached ($dN_S(\mathrm{In})/dt = 0$), Eq. (1) gives: $F_i = K_d(N_S(\mathrm{In}))^p + K_I(N_S(\mathrm{In}))^q$.

The transient rise and saturation characteristics of the desorption spectra are difficult to analyse because the creation of an indium surface population, as well as incorporation and desorption, are all taking place simultaneously.

Upon termination of growth, the analysis is made easier due to the presence of a single surface process: desorption. The fit of the decay curve allows us to determine the desorption rate, K_{d2}, as a function of substrate temperature. Because of the sharp variation present in the first part of the decay curve, no data fit was obtained in this region; thus, we were unable to extract information about the desorption rate, K_{d1} associated with the first mechanism. An Arrhenius plot of the K_{d2} gives the next activation energy associated with the second desorption process, E_{A2}. We found an average value of 1.3 eV for E_{A2}, which agrees well with the previous values [10–12] reported for indium desorption. We find that the value of E_{A2} seems to be relatively independent of the V/III ratio and arsenic species.

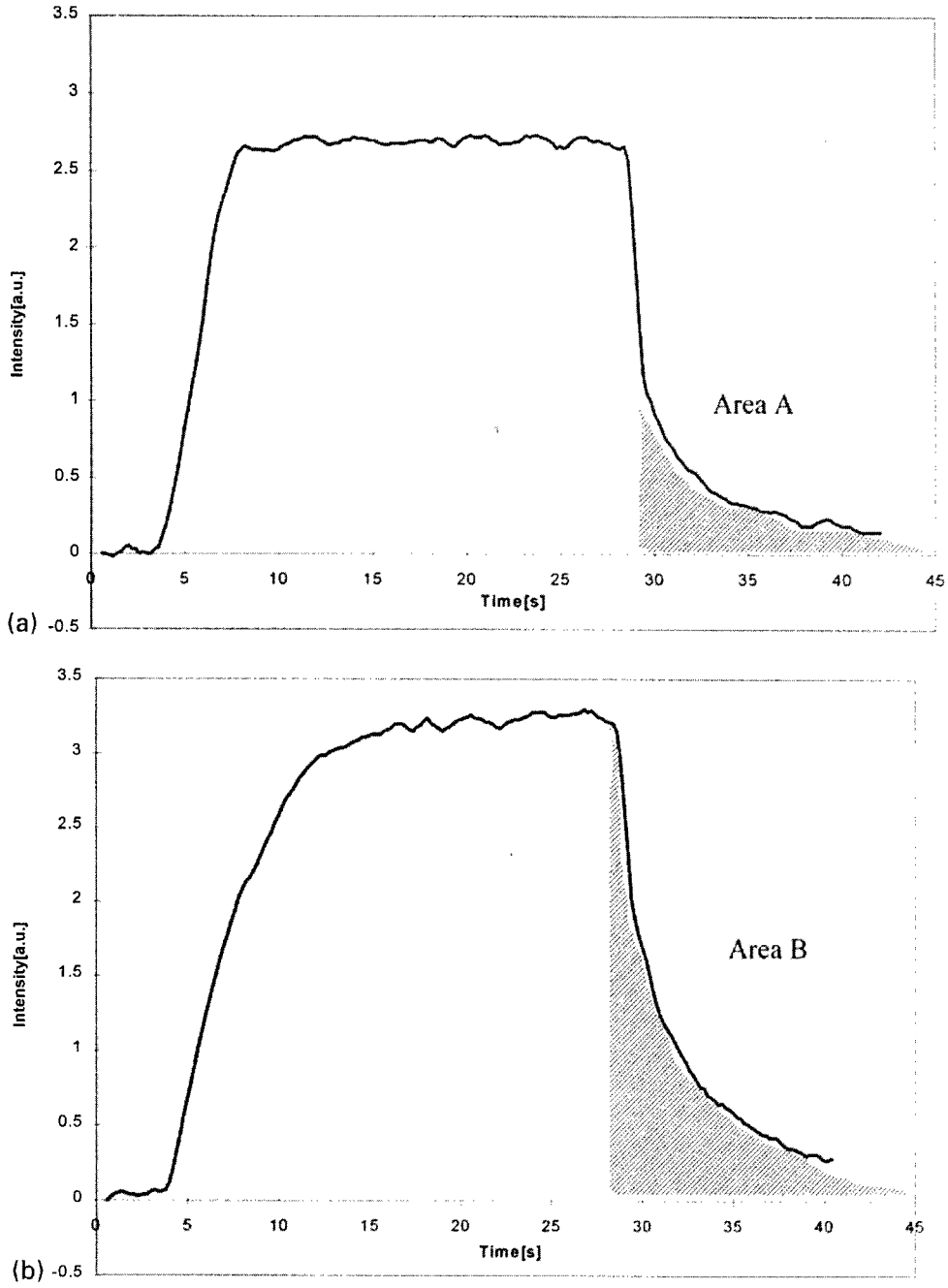

Fig. 2. Desorption spectra for $T = 630°C$, the indium percentage and InGaAs growth rate are, respectively, 21% and 0.912 μm/h. The arsenic tetramer, As_4, is used. Area A (a) and B (b) are proportional to the indium surface population from the most tightly bound state. (a,b) correspond to a low V/III ratio ($\sim 17:1$) and higher V/III ratio ($\sim 36:1$).

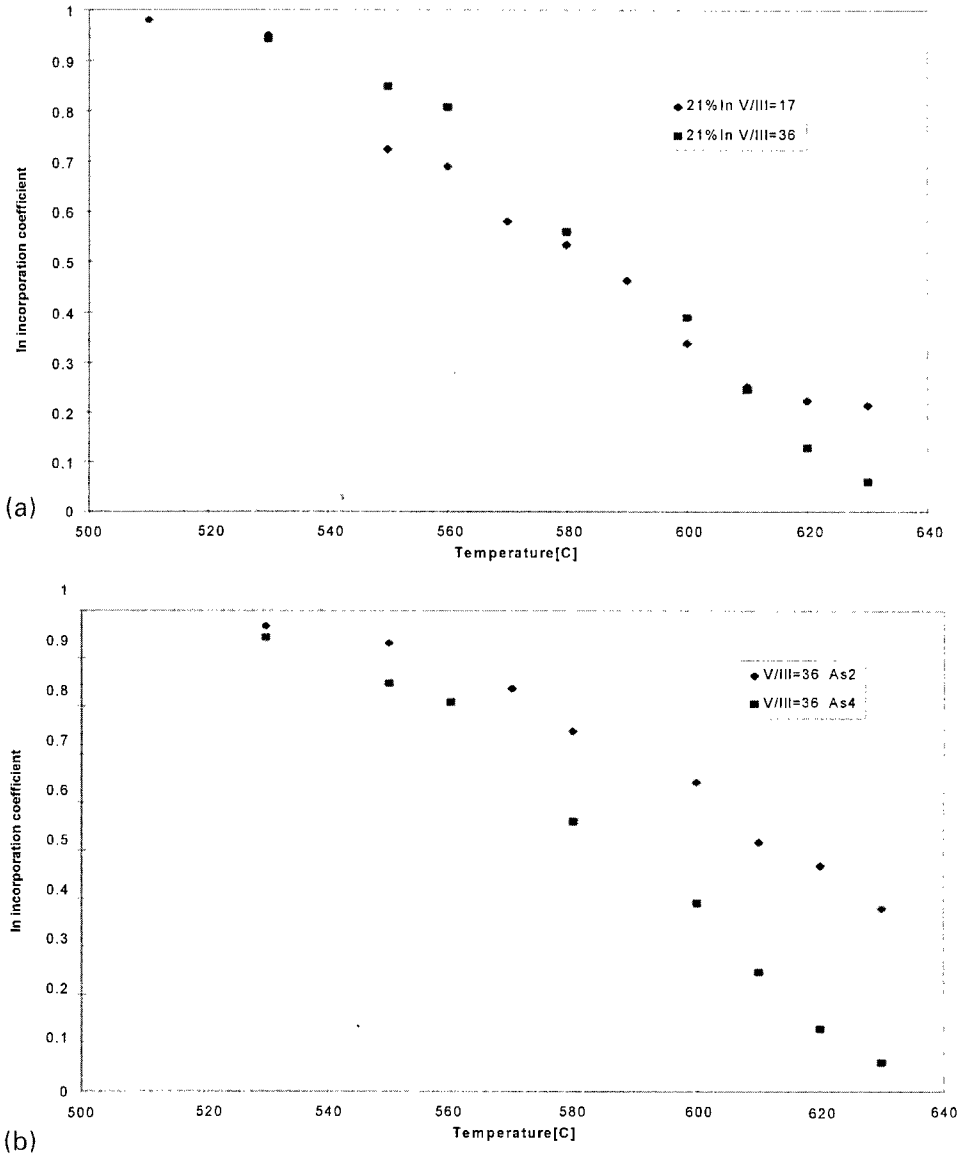

Fig. 3. Indium incorporation coefficient as a function of substrate temperature for low (~ 17 : 1) and high (~ 36 : 1) V/III ratio, in the presence of As_4 (a) and for V/III ratio (~ 17 : 1) for both arsenic species (b).

In addition, we observe little dependence of the activation energy on the indium composition in the growing InGaAs film. None of the spectra recorded for different indium compositions and the same V/III ratio show a significant variation of E_{A2}, although the measurements were taken for different but very similar InGaAs growth rates of 1.11 μm/h and 0.912 μm/h, respectively, for 5 and 21% indium. This result indicates that the link between strain and growth kinetics needed to exploit the SME approach will be found in surface mechanisms such as segregation and migration, rather than in indium desorption.

The integration of the area defined by the decay curve gives us information about the indium surface population (see Fig. 2). The average

population in the case of low V/III ratio (16 : 1, 20 : 1), given by area A, is found to be around 0.3 ML [13] (Fig. 2a) in the case of 21% In, for both arsenic species, and for 14% In with As_4. For the high V/III ratio case (36 : 1), the average population is given by area B (Fig. 2b). For 21% In, we have calculated a surface population of around 1.0 ML [13] and 0.5 ML, respectively, for As_4 and As_2. Evans et al., measure between 1.0 and 2.0 monolayers of segregated indium, independent of As_2 overpressure [7].

Finally, the steady-state part of the desorption spectra ($dN_s/dt = 0$) is used to calculate the indium incorporation coefficient α_{In}, defined by: $\alpha_{In} = 1 - F_D(In)/F_i$.

We compare in Fig. 3a the indium incorporation coefficient as a function of substrate temperature for high and low V/III ratio. For $T = 520°C$, α_{In} is very near unity. For higher temperatures, the incorporation coefficient decreases steadily.

For a higher V/III ratio of 36 : 1, α_{In} drops from 0.85 to 0.4 between 550°C and 600°C. The magnitude of the incorporation coefficient is greater for growth under a higher V/III ratio. However, in the presence of a low V/III ratio, the decrease of α_{In} with temperature is not as great as the decrease under a high ratio, which is in agreement with indium segregation studies [1, 14]. This results appears to be true for both As_4 and As_2. For high temperatures the situation seems to be reversed; for low V/III ratio, α_{In} stays around 0.3 because of the saturation phenomenon mentioned previously, whereas α_{In} continues to drop for high V/III ratio.

For a higher V/III ratio, the results show a higher indium incorporation coefficient and, concurrently, a higher indium surface population. This may appear contradictory but is not, since both the desorbed and incorporated fluxes, $F_D(In)$ and $F_I(In)$, are proportional to the indium surface population, N_S. The presence of a higher N_S does not automatically imply poorer incorporation.

When examining the interplay of the dynamics, the surface population, N_S, is apparently strongly dependent on the V/III ratio, while the activation energy for desorption is apparently independent of growth condition. Thus, it appears that the dominant mechanism controlling the observed differences in growth result from the varying surface population. Finally, as shown in Fig. 3b, a comparison of the incorporation coefficient curves for both arsenic species shows significantly greater indium incorporation for growth under As_2 for both low and high V/III ratios.

4. Conclusions

A DMS study of indium desorption during InGaAs growth by MBE has been presented for a wide range of growth conditions (substrate temperature,V/III ratio, arsenic species and In percentage). For low V/III ratio ($\sim 17 : 1$) two distinct desorption mechanisms were observed in the decay curve of the mass spectrometer data, whereas for higher ratio ($\sim 36 : 1$), only one mechanism was present. The fit of the decay curves give us a average value of 1.3 eV for one of the desorption mechanisms. This activation energy is found to be independent of both V/III ratio, arsenic species and indium composition. This result gives us the new directions to choose in order to fully exploit kinetics in our SME approach.

Additionally, we confirm that the indium incorporation is generally improved in the presence of high V/III ratio. The data also indicates that incorporation is probably controlled by the indium surface population, N_S, which depends significantly on the V/III ratio and As species. Indium incorporation is dramatically enhanced by the use of the arsenic dimer.

Acknowledgements

This work is supported by ARO/ARPA contract No. DAAH 04-95-1-0367

References

[1] K. Woodbridge, Appl. Phys. Lett. 60 (1992).
[2] C. Carter-Coman, A.S. Brown, R. Bicknell-Tassius, N.M. Jokerst, F. Fournier and D.E. Dawson, J. Vac. Sci. Technol. B 14 (1996).
[3] C. Carter-Coman, A.S. Brown, R. Bicknell-Tassius, N.M. Jokerst and M. Allen, Appl. Phys. Lett. 69 (1996).

[4] J.-P. Reithmaier, H. Riechert and H. Schlotterer, J. Crystal Growth 111 (1990) 407.
[5] K.R. Evans, C.E. Stutz, E.N. Taylor and J.E. Ehret, J. Vac. Sci. Technol. B 9 (1991).
[6] A.J. Spring Thorpe and P. Mandeville, J. Vac. Sci. Technol. B 6 (1988).
[7] K.R. Evans, R. Kaspi, J.E. Ehret and M. Skowronski, J. Vac. Sci. Technol. B 13 (1995).
[8] Y.C. Kao, F.G. Celii and H.Y. Liu, J. Vac. Sci. Technol. B 11 (1993).
[9] C.E.C. Wood and B.A. Joyce, J. Appl. Phys. 49 (1978).
[10] C.T. Foxon and B.A. Joyce, J. Crystal Growth 44 (1978) 75.
[11] Yu.O. Kanter, A.K. Gutakovsky, A.A. Fedorov, M.A. Revenko, S.V. Rubanov and S.I. Stenin, Thin Solid Films 163 (1988) 497.
[12] K. Radhakrishnan and S.F. Yoon, R. Gapalakrishnan and K.L. Tan, J. Vac. Sci. Technol A 12 (1994).
[13] The definition of one monolayer (1 ML) used for the calculations is the following: 1 ML = a ($In_xGa_{1-x}As$)/2, where a($In_xGa_{1-x}As$) is the lattice parameter in ångstrom.
[14] J. Nagle, J.P. Landesman, M. Larive, C. Mottet and P. Bois, J. Crystal Growth 127 (1993) 550.

ELSEVIER

Journal of Crystal Growth 175/176 (1997) 211–215

JOURNAL OF CRYSTAL GROWTH

A Monte Carlo study of gallium desorption kinetics during MBE of (1 0 0)-GaAs/AlGaAs heterostructures

K. Mahalingam[a,*], D.L. Dorsey[a], K.R. Evans[b], R. Venkatasubramanian[c]

[a] *Wright Laboratory, Materials Directorate (WL/MLPO), Wright Patterson AFB, Ohio 45433-7707, USA*
[b] *Wright Laboratory, Solid State Electronics Directorate (WL/AADP), Wright Patterson AFB, Ohio 45433-7323, USA*
[c] *Department of Electrical Engineering, University of Nevada, Las Vegas, Nevada 89154, USA*

Abstract

In situ desorption mass spectrometry studies (DMS) of AlGaAs/GaAs molecular beam epitaxy (MBE) at high substrate temperatures reveals a rich transient behavior in the Ga desorption signal during the formation of the AlGaAs-on-GaAs interface. In this study we develop Monte Carlo (MC) models for Ga desorption, in which the effects of the Al–Ga interaction strength and the inclusion of an Al–Ga surface exchange mechanism are investigated. The models which best describe the experimental observations are identified. The transients in Ga desorption rate at the AlGaAs-on-GaAs interface and the experimentally observed reduction in Ga desorption energy during growth of AlGaAs are explained in terms of the reduction in V/III flux ratio accompanying the opening of the Al shutter. The proposed effects of this reduction in V/III flux ratio are consistent with the results predicted by the different models.

PACS: 81.10.Aj; 68.45.Da; 68.35.Fx; 81.15.Hi; 81.05.Ea

Keywords: Monte Carlo models; Gallium desorption; Molecular beam epitxay

1. Introduction

In order to achieve smooth and abrupt interfaces, MBE of AlGaAs/GaAs is often performed at temperatures high enough to cause significant Ga desorption [1]. An understanding of Ga desorption behavior is extremely important as it affects both the growth rate and layer stoichiometry. The kinetics of Ga desorption during MBE of GaAs and AlGaAs have been studied extensively by a variety of experimental techniques, including reflection high energy electron diffraction (RHEED) [2], transmission electron microscopy (TEM) [3, 4], and desorption mass spectrometry (DMS) [5–8]. Recent in situ DMS [7, 8] have revealed significant differences in Ga desorption behavior between GaAs homoepitaxy and AlGaAs/GaAs heteroepitaxy. Upon opening the Al shutter, there is a sharp rise in the Ga desorption rate, followed by a gradual fall to a steady state value. Furthermore, relative to GaAs, a reduction in both the steady state Ga desorption rate and the activation energy

* Corresponding author. Fax: +1 513 255 4913: e-mail: mahalik@jane.ml.wpafb.af.mil.

0022-0248/97/$17.00 Copyright © 1997 Elsevier Science B.V. All rights reserved
PII S0022-0248(96)00853-6

for Ga desorption were observed for growth of AlGaAs. The observed variation in Ga desorption rate has important technological implications since it indicates a grading of the Al/Ga composition at the AlGaAs-on-GaAs interface.

In this study we develop a kinetic MC model [9, 10] to examine the possible mechanisms which could explain the above Ga desorption behavior. A strong candidate is the Al–Ga surface exchange, whose existence is supported by experimental evidence [11–14]. Other factors investigated include the effects of changes in V/III flux ratio and the influence of Al–Ga interaction energy. Based on predicted results, further details of their effects on surface stoichiometry and activation energy for Ga desorption are presented.

2. The model

The MC simulation procedure was developed previously to model cation desorption behavior during MBE of (1 0 0)-InAs and (1 0 0)-GaAs [15]. The MC algorithm adopted is similar to those used previously [9, 10]. However, an important difference is that the present model includes a temperature-dependent physisorption mechanism for cations in addition to adsorption, surface migration and desorption events. In this mechanism a cation arriving at a cation terminated site is allowed a fixed number (temperature dependent) of random jumps, determined by fit to experimental data, to find an anion terminated site; the cation desorbs if it is unsuccessful. This accounts for the finite surface residence time at high temperature. By including this mechanism, it was possible to obtain good agreement between predicted and experimental values for Ga and In desorption rates for a range of temperatures [15]. Also, the predicted dependence of the Ga desorption energy on V/III ratio for homoepitaxy of GaAs was in good quantitative agreement with experimental results [4].

In order to match growth conditions used in a recent experiment, MC simulations were performed for growth temperatures in the range 950–990 K and a V/III flux ratio of 5. The incident flux for Ga was 1.0 monolayer/s and that for Al 0.667 monolayer/s giving a nominal composition of $Al_{0.4}Ga_{0.6}As$. Simulations were performed on the (1 0 0) unreconstructed zinc-blende surface with a substrate size of 40×40, employing a solid-on-solid (SOS) model. The kinetic rates for deposition of Al, Ga and As were assumed to be equal to their respective fluxes. The rates for surface migration and desorption events were assumed to be of the Arrhenius form with configuration-dependent activation energies calculated in terms of the first and second nearest neighbor interaction energies, as in earlier MC models [9, 10]. The frequency factors and interaction energies for GaAs were taken from a previous study [15], and those for AlAs were determined from values for the cohesive energy [16]. The model parameters used were then: the frequency factors for diffusion and desorption are $R_{diff} = 10^{10}$/s and $R_{des} = 7.5 \times 10^{12}$/s, respectively; nearest neighbor interaction energies: $E_{Ga\text{–}As} = 0.85$ eV, $E_{Al\text{–}As} = 0.97$ eV; and second-nearest-neighbor interaction energies $E_{Ga\text{–}Ga} = 0.17$ eV, $E_{As\text{–}As} = 0.12$ eV and $E_{Al\text{–}Al} = 0.25$ eV.

In each simulation the Ga desorption ratio, defined as the fraction of incident Ga flux desorbed, was monitored. The deposition of Ga was governed by the physisorption rule, while Al, which has negligible desorption rate under conditions of this study, was allowed enough jumps to find an appropriate SOS site. The Al–Ga surface exchange was implemented by having Al atoms which arrive at Ga-terminated sites (by deposition or diffusion) replace the Ga atom. The ejected Ga atom then finds another site or desorbs, as per the physisorption rule.

3. Results and discussion

To develop a model that explains the experimental observations, we first examine the factors which account for the influence of Al on the Ga desorption rate. The Al–Ga exchange reaction can explain the initial rise in the Ga desorption rate upon opening the Al shutter, as the exchange reaction increases the surface concentration of Ga. However, the fact that the steady state Ga desorption rate during AlGaAs growth is lower than that during GaAs growth cannot be explained by this mechanism. Other factors which could explain this

include a decrease in the number of surface cation sites from which Ga can desorb due to the presence of Al on the surface and a higher interaction strength for Al–Ga compared to that for Ga–Ga. Based on these considerations we have examined two types of models; one which includes the Al–Ga exchange mechanism and another which excludes this mechanism. For each model, simulations were performed for the cases with $E_{Al\text{-}Ga} = E_{Ga\text{-}Ga}$ and $E_{Al\text{-}Ga} > E_{Ga\text{-}Ga}$.

The time evolution of the Ga desorption ratio predicted by the different models is shown in Fig. 1. For comparison the results obtained from experiment are also included. Note that for GaAs growth, inclusion of the Ga physisorption mechanism was required to match the experimentally observed steady state Ga desorption ratio. Fig. 1a shows results obtained from models which include the Al–Ga exchange mechanism, with different values for $E_{Al\text{-}Ga}$. All the models predict a sharp rise in the Ga desorption ratio accompanying the opening of the Al shutter, followed by a gradual decrease to a steady state. However, in contrast to experimental observations, the steady state Ga desorption ratio predicted by the model with $E_{Ga\text{-}Ga} = E_{Ga\text{-}Al} = 0.17$ eV is higher in AlGaAs than that for GaAs. On the other hand, results from the model with $E_{Ga\text{-}Al} = 0.21$ eV provide a better representation of the experimental data, although the predicted steady state Ga desorption ratio is higher than that obtained in experiment. Further analysis of the results from this model showed that good agreement with experiment is obtained when an Al–Ga exchange probability of 0.9 was used. Interestingly, in a previous study a probability of 0.98 was calculated for Ga–In exchange in InGaAs [12]. The value of 0.9 used is consistent since, based on bond energy arguments, the tendency for exchange is predicted to be In > Ga > Al.

The results obtained from models which exclude the Al–Ga exchange mechanism are presented in Fig. 1b. It is interesting to note that the model with $E_{Ga\text{-}Ga} = E_{Al\text{-}Ga}$ is able to describe both the sharp rise and gradual decrease in the Ga desorption ratio. The results also reveal that the Al–Ga interction

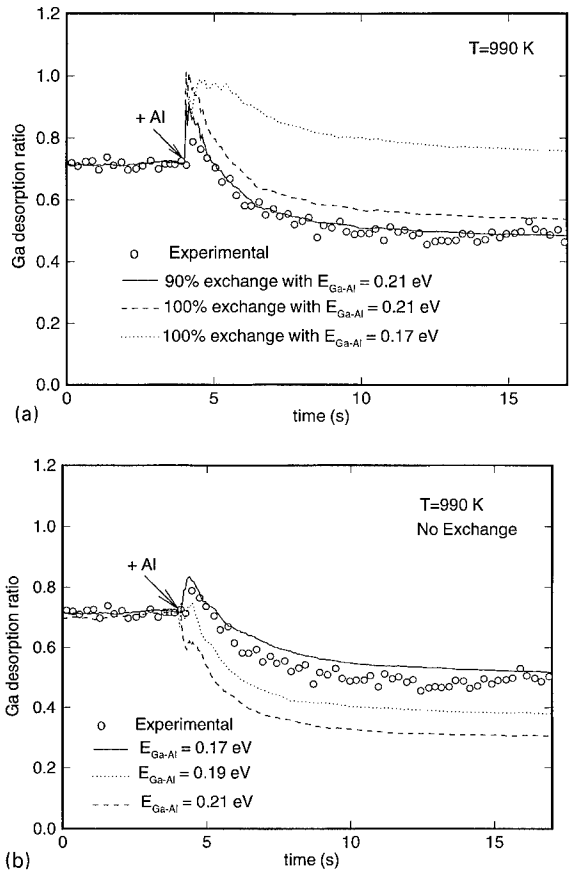

Fig. 1. Predicted Ga desorption ratio evolution using models which (a) include the Al–Ga surface exchange mechanism and (b) exclude the Al–Ga surface exchange mechanism.

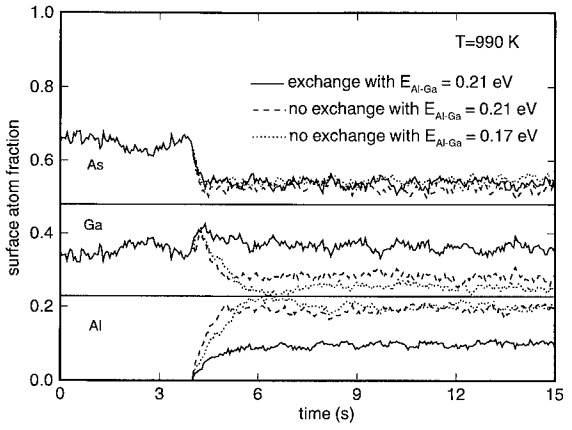

Fig. 2. Evolution of surface stoichiometry as predicted by the different models.

energy has a significant effect on the Ga desorption behavior. The sensitivity of the Ga desorption ratio to the magnitude of the Al–Ga interaction energy indicates that the sharp rise in the Ga desorption ratio must be due to an abrupt increase in the population of weakly bound Ga species when the Al shutter is opened. The only factor that can explain this situation is the reduction in V/III flux ratio accompanying the opening of the Al shutter, as surmised in an earlier study [8]. The gradual decrease in Ga desorption ratio can be attributed to the decrease in the number of surface cation sites from which Ga can desorb, as described earlier.

The proposed effects of change in V/III flux ratio on Ga desorption ratio may be verified by examining the time evolution of surface stoichiometry during growth. Fig. 2 is a plot of the Al, Ga and As concentrations of the surface versus time as predicted by the different models. It is clear that opening the Al shutter is accompanied by a sharp rise in the surface Ga concentration and a decrease in the surface As concentration. Following the sharp rise in Ga concentration, the models which exclude the Al–Ga exchange mechanism predict a gradual decrease in the surface Ga concentration with a corresponding increase in the Al concentration. Thus, the predicted trends are consistent with the desorption profiles shown in Fig. 1b, lending support to the argument proposed above. In contrast, the model which includes the exchange mechanism predicts a Ga surface concentration which rises sharply and remains at a higher level with no further decrease, as would be expected from its predicted desorption profile shown in Fig. 1a. The gradual decrease in the Ga desorption ratio despite a higher Ga surface concentration may be attributed to the gradual build up of the sublayer Al concentration having a stabilizing effect on surface Ga due to its higher interaction energy (0.21 eV).

Finally we examine the temperature dependence of the steady state Ga desorption during growth of GaAs and AlGaAs. A regression analysis of the experimental data, assuming Arrhenius kinetics for the Ga desorption rate, yielded an activation energy of 4.52 eV for GaAs and 4.15 eV for AlGaAs. The reduction in Ga desorption energy during growth of AlGaAs is illustrated in Fig. 3. As indicated in the figure, the temperature dependence

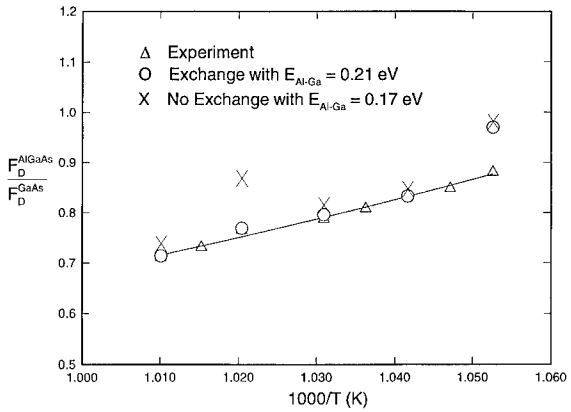

Fig. 3. Variation of the ratio of Ga desorbed from AlGaAs to that from GaAs versus the inverse of growth temperature. Solid line is an exponential fit to the experimental data.

could be well described by an exponential fit yielding a reduction in activation energy of 0.4 eV. A similar dependence was also observed in the results predicted by the different models. However, for clarity only results from those models whose predictions were close to the experimental data are included in Fig. 3. At first the reduction in Ga desorption energy in AlGaAs appears to contradict theory [17], since theory predicts that the effect of Al is only to reduce the Ga desorption rate and not the desorption energy. This apparent contradiction may be reconciled if the reduction in desorption energy is attributed to the reduction in V/III flux ratio and not to the addition of Al per se. This is consistent with theory [17], and has been reported in experimental studies [4].

4. Summary

Our MC simulation study of Ga desorption behavior during MBE of AlGaAs/GaAs heterostructures shows that the observations reported in experiment are best described by two models; one which includes an Al–Ga surface exchange mechanism with $E_{Al-Ga} > E_{Ga-Ga}$ and the other without the surface exchange with $E_{Al-Ga} = E_{Ga-Ga}$. The results from these models indicate that the transients in Ga desorption rate observed at the AlGaAs-on-GaAs interface, and the reduction in Ga desorption

energy during growth of AlGaAs can be explained in terms of the reduction in V/III flux ratio accompanying the opening of the Al shutter. An important implication of this result is that the transient in Ga desorption rate and the associated compositional grading of the AlGaAs-on-GaAs interface may be avoided by compensating for the decrease in V/III flux ratio by increasing the As flux when Al shutter is opened. In order to verify this prediction a simulation study employing a constant V/III flux is in progress.

Acknowledgements

We are grateful to Professor Stewart Harris for many useful discussions. This research was supported by Air Force contract F33615-94-C-5804 under the sponsorship of the Materials Directorate, Wright Laboratory, WL/MLPO, at Wright-Patterson Air Force Base, Ohio.

References

[1] W.T. Tsang, in: Semiconductors and Semimetals, Vol. 1.22, part A, Eds. R.K. Williardson and A.C. Beer (Academic Press, New York, 1985) p. 95.
[2] C.T. Foxon, in: Heterojunctions and Semiconductor Superlattices , Eds. G. Allen, G. Bastard, N. Boccara, M. Lannoo and M. Voos (Springer, Berlin, 1986) p. 27.
[3] A.H. Kean, C.R. Stanely, M.C. Holland, J.L. Martin and J.N. Chapman, J. Crystal Growth 111 (1991) 189.
[4] J.P. Reithmaier, R.F. Broon and H.P. Meier, Appl. Phys. Lett. 61 (1992) 1222.
[5] E.M. Gibson, C.T. Foxon, J. Zhang and B.A. Joyce, Appl. Phys. Lett. 57 (1990) 1203.
[6] J. Zhang, E.M. Gibson, C.T. Foxon and B.A. Joyce, J. Crystal Growth 111 (1991) 93.
[7] K.R. Evans, C.E. Stutz, D.K. Lorance and R.L. Jones, J. Vac. Sci. Technol. B 7 (1989) 259.
[8] K.R. Evans, C.E. Stutz, E.N. Taylor and J.E. Ehret, J. Vac. Sci. Technol. B 7 (1991) 2428.
[9] A. Madhukar and S.V. Ghaisas, CRC Critical Reviews of Solid State and Materials Sciences, Vol. 14 (CRC, Cleveland, 1988) p. 1.
[10] J. Singh and K.K. Bajaj, J. Vac. Sci. Technol. B 3 (1985) 520.
[11] R.E. Bachrach, J. Vac. Sci. Technol. 15 (1978) 1340.
[12] H. Yamaguchi and Y. Horikoshi, J. Appl. Phys. 68 (1990) 1610.
[13] T. Saitoh, M. Tamura and J.E. Palmer, Institute of Physics Conf. Vol. 141 (1995) p. 345
[14] T. Saitoh, A. Hashimoto and M. Tamura, Appl. Surf. Sci. 60/61 (1992) 228.
[15] K. Mahalingam, D. L. Dorsey, K. R. Evans and R. Venkatasubramanian, to be published.
[16] W.A. Harrison, Electronic Structure and Properties of Solids (Dover, New York, 1989) ch. 7, p. 176.
[17] R. Heckingbottom, J. Vac. Sci. Technol. B 3 (1985) 572.

ELSEVIER

Journal of Crystal Growth 175/176 (1997) 216–223

JOURNAL OF CRYSTAL GROWTH

Re-entrant behavior of 2D to 3D morphology change and 3D island lateral size equalization via mass exchange in Stranski–Krastanow growth: InAs on GaAs(0 0 1)

T.R. Ramachandran, R. Heitz, N.P. Kobayashi, A. Kalburge, W. Yu, P. Chen, A. Madhukar*

Departments of Materials Science and Physics, Photonic Materials and Devices Laboratory, University of Southern California, Los Angeles, California 90089-0241, USA

Abstract

Using in-situ, ultrahigh vacuum scanning tunneling and atomic force microscopy and ex-situ photoluminescence (PL) and PL excitation we show that the growth of highly strained InAs on GaAs(0 0 1) proceeds via a *re-entrant* behavior of the 2D to 3D morphology change. Quasi-3D clusters of heights 0.6–1.2 nm first appear at an InAs delivery (θ) of ~ 1.25 ML, only to disappear for $\theta \sim 1.3$ ML and reappear again at $\theta \sim 1.45$ ML, prior to 3D island initiation at ~ 1.57 ML. With increasing θ, an observed tendency of the 3D islands towards lateral size equalization is shown to be accompanied by mass exchange between the 2D and 3D surface features. Molecular dynamics simulations reveal a decreasing binding energy for atoms at island edges as a function of increasing island size and island–island interaction, thereby suggesting a role for atom detachment from larger islands in the size equalization process.

1. Introduction

The formation of coherent three-dimensional (3D) islands during highly strained growth [1–4] has been a key area of interest in recent years, especially for the Ge/Si [5, 6] and InGaAs/GaAs [7–14] material systems. This has partly been motivated by the intrinsic interest in understanding the nature of the 2D to 3D morphological transition in these systems. In addition, the fabrication of optically active InGaAs 3D island quantum dots (QDs) in GaAs and recent reports of lasing from InGaAs/GaAs structures containing InGaAs QDs [15] further motivates studies to unambiguously identify the origin of the optical features and the lasing. While a number of structural and optical studies have focused on the InGaAs/GaAs(0 0 1) system [7–14], the atomistic nature of the 2D cluster (1ML high, ~ 0.3 nm) to 3D island (typically ~ 2–4 nm high) transition in InAs/GaAs(0 0 1) is

* Corresponding author. Fax: +1 213 740 4333; e-mail: madhukar@mizar.usc.edu.

0022-0248/97/$17.00 Copyright © 1997 Elsevier Science B.V. All rights reserved
PII S0022-0248(96)00855-X

still not well understood. We therefore undertook a systematic in-situ ultrahigh vacuum (UHV) scanning tunneling microscope and atomic force microscope (STM/AFM) and ex-situ photoluminescence (PL) and PLE study of the molecular beam epitaxical (MBE) growth of InAs on GaAs(0 0 1) for InAs depositions, θ, from submonolayer to well-formed 3D islands prior to onset of coalescence, focusing on the nature of (i) the initial formation and (ii) the subsequent evolution of the 3D InAs islands. Our results show that quasi-3D InAs clusters ($\sim$ 0.6–1.2 nm high) appear and disappear well in advance of the regime of 3D island formation, reappear prior to 3D islands and subsequently *coexist* with 3D islands and 2D clusters. In addition, the 3D islands exhibit a natural tendency towards lateral size equalization via an accompanying mass exchange between the 2D and 3D features on the surface. These observations, revealing the atomistic nature of highly strained epitaxy for the first time, also show that MBE growth does not follow the hitherto held simple picture of the thermodynamic ground-state-based Stranski–Krastanow (SK) growth [2].

2. Experimental procedure

The details of the sample preparation are reported elsewhere [9]. All samples were grown via molecular beam epitaxy (MBE) on n^+-GaAs(0 0 1) $\pm$ 0.1° substrates using in-situ monitoring via reflection high energy electron diffraction (RHEED). InAs deposition was carried out at a rate of 0.22 ML/s with the substrate temperature T_s being 500°C and P_{As4} being 6×10^{-6} torr. The sample was allowed to cool down immediately following InAs deposition by shutting off power to the substrate heater, in order to examine the nature of InAs evolution as close as possible to the growth conditions without any intentional annealing or growth interruptions. Samples were transferred to the UHV interconnected UHV STM/AFM chamber for in-situ structural characterization. We note that samples for ex-situ optical studies were capped with GaAs grown by migration enhanced epitaxy (MEE) at T_s of 400°C [14].

3. Results and discussion

The main surface features observed in the structural studies are classified as follows: small (lateral size $\leqslant$ 20 nm) and large (lateral size $>$ $\sim$ 50 nm) 2D clusters (1 ML high), small and large quasi-3D clusters (2–4 ML high), and 3D islands (height $>$ 4 ML (typically 2–4 nm), lateral size $<$ $\sim$ 25 nm). The evolution of the surface densities of these features [16] with increasing InAs delivery is plotted in Fig. 1.

3.1. Re-entrant behavior of 2D → 3D morphology change

The evolution of the different structural features noted above is shown in the STM images of Figs. 2 and 3 for samples with increasing θ. At submonolayer depositions ($\theta \sim 0.87$ ML, Fig. 2a), the large-scale surface morphology is seen to consist of terraces separated by 1 ML high steps (marked S), with 1 ML deep holes (marked H) in the terraces that are a few tens of nm wide. The surface coverage

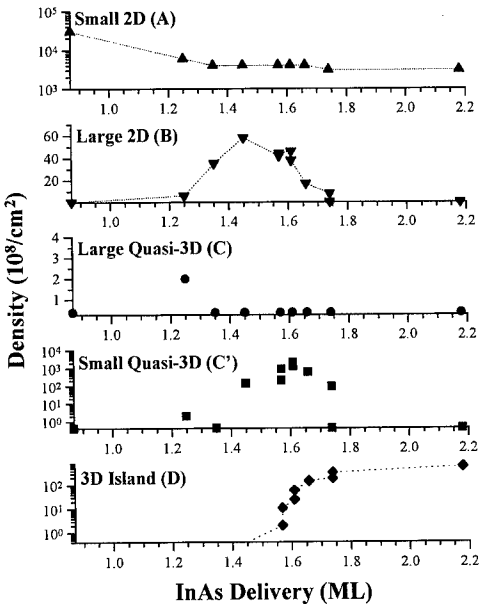

Fig. 1. Shows the density (in units of $10^8/cm^2$) of various InAs structural features on GaAs(0 0 1) as a function of InAs delivery (in ML) (dotted lines are a guide to the eye).

of these holes is ~ 20%, consistent with the InAs delivery. High-resolution images (Fig. 2b) show that the surface reconstruction (labeled R) is highly disordered in both InAs (terrace) and GaAs (hole) regions, with small groups of adatoms (small 2D clusters, marked A) on the surface. At $\theta \sim 1.25$ ML (Fig. 2c), the number of holes has decreased significantly, but the wetting layer is not yet complete as

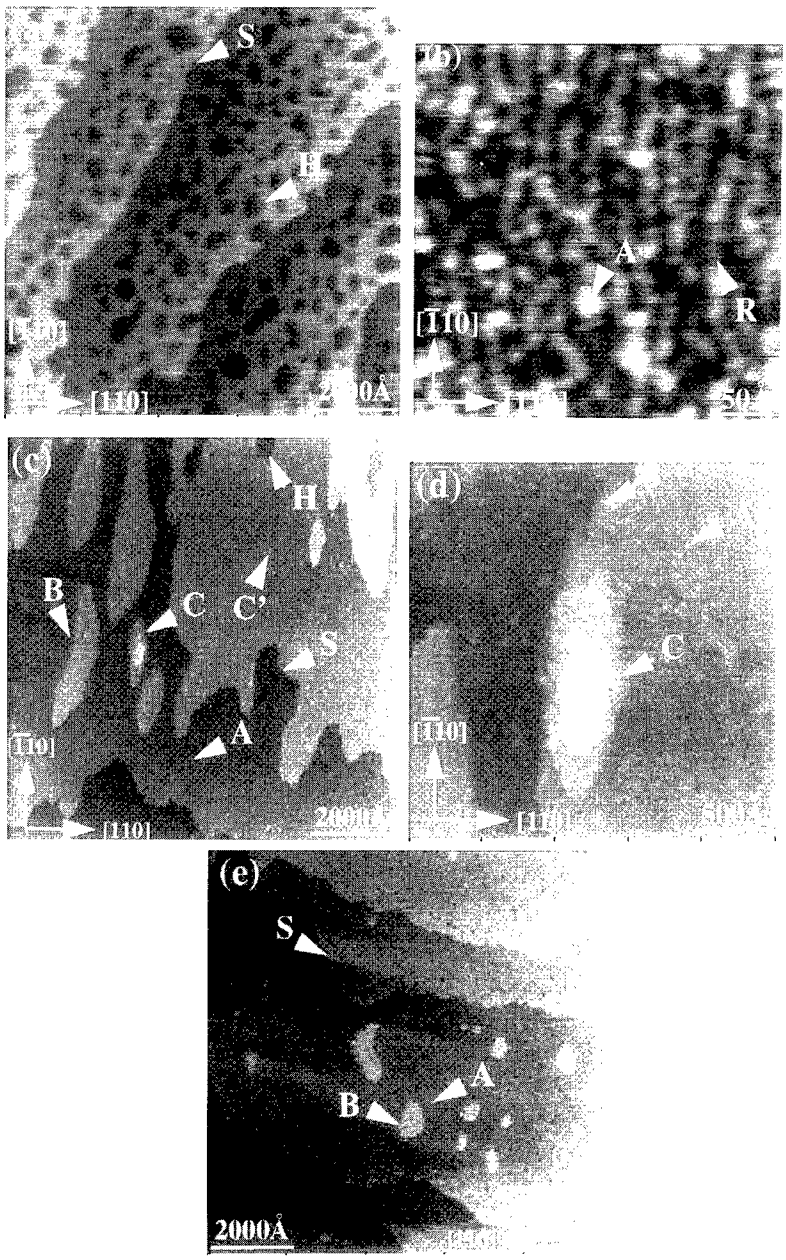

Fig. 2. UHV STM images for InAs depositions on GaAs (0 0 1) of (a), (b) 0.87 ML; (c), (d) 1.25 ML and (e) 1.35 ML. The labeling of the features in the figure corresponds to: A – small ($\leqslant$ 20 nm wide) 2D (1 ML high) clusters, B – large ($>$ ~ 50 nm wide) 2D clusters, C – large quasi-3D clusters, S – 1 ML high step edge, H – 1 ML deep hole, and R – rows of the surface dimer reconstruction. Note, in particular, the appearance of large quasi-3D clusters at 1.25 ML ((c) and (d)) and their absence at 1.35 ML (e) (see the text for details.)

evidenced by the continued presence of some ML deep holes (marked H). One of the new features seen at this stage are large 2D clusters (marked B) with lateral sizes in the range of several hundreds to thousands of angstroms. Strikingly however, there is also a significant density ($\sim 2 \times 10^8/\text{cm}^2$, Fig. 1) of small and large quasi-3D clusters (marked C′ and C, respectively in Fig. 2c). Note the distinct shape anisotropy (of $\sim$ 2–3) of the large 2D and quasi-3D clusters. The large quasi-3D clusters are laterally extended features with a multilevel morphology as seen more clearly in the higher-resolution image in Fig. 2d. Remarkably, the small and large quasi-3D clusters disappear as the InAs delivery is increased beyond $\sim$ 1.3 ML as seen, for example, in Fig. 2e at $\theta \sim 1.35$ ML. A completely 2D morphology is seen at this stage again, with small and large 2D clusters and a high density of small holes (H) in a yet incomplete InAs wetting layer.

As the InAs deposition is increased to 1.45 ML (Fig. 3a), *small* quasi-3D clusters (marked C′) reappear once again at a much higher density than before ($\sim 1.4 \times 10^{10}/\text{cm}^2$, Fig. 1), thus manifesting a re-entrant behavior of the 2D to 3D morphology change. At the same time, high-resolution images (Fig. 3b) show the disordering of the surface reconstruction to have decreased significantly over that at 0.87 ML. At $\theta \sim 1.57$ ML, the first 3D islands appear on the surface at a density of $\sim 2 \times 10^8/\text{cm}^2$, but importantly, they *coexist* with the small quasi-3D clusters as well as the small and large 2D clusters as shown in Fig. 3c (also see Fig. 1). For completeness, we note that even for InAs deliveries $>$ 1.57 ML until $\sim$ 1.74 ML, all the features observed at 1.57 ML are still present and only their relative densities change as shown in Fig. 1. Note in particular the extremely high density ($\sim 2 \times 10^{11}/\text{cm}^2$) of the small quasi-3D clusters at $\theta \sim 1.61$ ML.

PL and PLE studies confirm the initial appearance and subsequent disappearance of the large quasi-3D clusters prior to 3D island formation. As shown in Fig. 4, apart from the InAs wetting layer

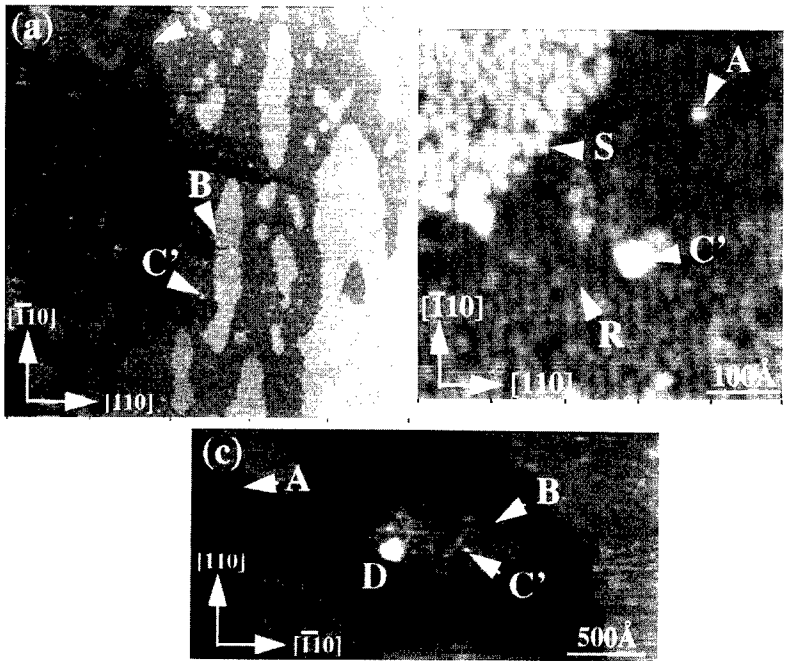

Fig. 3. UHV STM images for InAs depositions on GaAs(0 0 1) of (a),(b) 1.45 ML and (c) 1.57 ML. The labeling of features is as in Fig. 2, with the additional features shown here being labeled as follows: C′ – small quasi-3D clusters, D – 3D islands. Note, the presence of small quasi-3D clusters at 1.45 ML ((a) and (b)) prior to 3D island formation at 1.57 ML ((c)) (see the text for details).

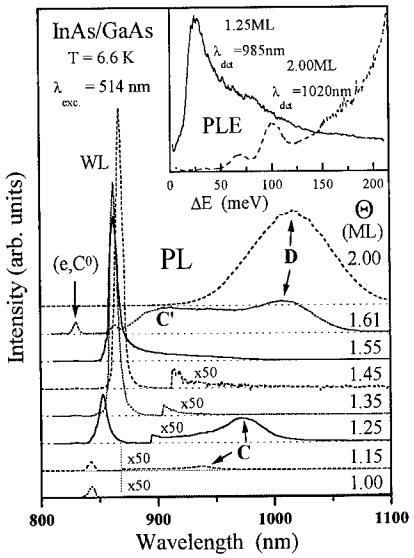

Fig. 4. PL and PLE (inset) spectra for various InAs depositions (θ) on GaAs(001). The labels C, C′ and D have the same notation as in Figs. 2 and 3. For the PLE spectra (inset), $\Delta E = E_{\text{excitation}} - E_{\text{detection}}$ (see the text for details).

peak (marked WL), luminescence in the range between 900 and 1000 nm is observed for InAs deliveries as low as $\theta \sim 1.15$ and 1.25 ML (marked C), but it vanishes for higher θ from 1.35 to 1.55 ML. PLE performed on the 1.25 ML sample with a detection wavelength of 985 nm (Fig. 4, inset), clearly indicates that the above PL is associated with a weakly confined state in a laterally extended quantum-well-like structure with a thickness > 2 ML. This behavior nicely fits the observation *only* at $\theta \sim 1.25$ ML of large quasi-3D clusters in STM, which are 2–4 ML high (i.e., 3–5 ML high with respect to the GaAs(0 0 1) substrate) with a lateral extension of > 50 nm.

The formation of quasi-3D clusters well in advance of the so-called "critical thickness" for 3D island formation ($\theta_c \sim 1.57$ ML for InAs/GaAs(0 0 1)) has been suggested to arise, in kinetic Monte–Carlo simulations of strained InAs/GaAs growth, via a strain-induced enhanced asymmetry in In upwards versus downwards interplanar migration rates [1]. The fact that small quasi-3D InAs clusters form *prior* to 3D islands and that even after the first 3D islands form at 1.57 ML, the density of the small quasi-3D clusters far exceeds the 3D island density (Fig. 1), suggests that the quasi-3D clusters mediate 3D island formation. In addition, at $\theta \sim 1.61$ ML, the small quasi-3D cluster average separation of ~ 22 nm (corresponding to $\sim 2 \times 10^{11}/\text{cm}^2$ density) is comparable to the lateral size of a typical 3D island. This implies that just beyond this stage, 3D island formation involves the merger of small quasi-3D clusters, further indicating the important role played by the small quasi-3D clusters identified in the present studies. Finally, we note that the coexistence of 3D islands not only with the small quasi-3D clusters but also with the small and large 2D clusters, is in contrast to the Stranski–Krastanow (SK) growth mode predicted by the equilibrium-energetics-based models of strained growth [2].

Once the InAs 3D islands form at $\theta \sim 1.57$ ML, their density (Fig. 1) initially increases rapidly and then saturates at $\sim 6 \times 10^{10}/\text{cm}^2$ at $\theta \sim 2.18$ ML. On the other hand, the density of the small quasi-3D clusters increases to a maximum at 1.61 ML as noted earlier, and then becomes insignificant beyond ~ 1.74 ML. The strong PL at ~ 900 nm for $\theta \sim 1.61$ ML (Fig. 4, label C′) we attribute to emission from the very high density of small quasi-3D clusters seen at this delivery. The dominant PL in the regime of well-formed 3D islands for $\theta > 1.61$ ML is centered around 1020 nm and extends down to 950 nm and lower (Fig. 4, label D). However, the nature of this PL process and that from the large quasi-3D clusters (label C, Fig. 4) is completely different in spite of the overlapping spectral region, as is obvious from a comparison of their PLE behavior (Fig. 4, inset). The PLE detected at 1020 nm for the 2.00 ML sample reflects the strong confinement of the involved carriers, consistent with the quantum box (QB) nature of the 3D islands [13, 14].

3.2. 3D island lateral size equalization and mass exchange

We have recently shown [9] that the 3D islands exhibit a natural tendency towards lateral size equalization as evidenced by an initial marked increase in their lateral size and size dispersion

followed by a subsequent narrowing and final stabilization of both. In order to obtain greater insight into this process, we have calculated, using the experimental data, the change in the volume of InAs material in the small quasi-3D clusters and 3D islands for a given incremental InAs delivery and have used this information to understand the comparative evolution of the 2D and 3D surface features with increasing InAs delivery. The results are summarized in Table 1 where it can be seen from the non-monotonic behavior of V[2D], the amount of InAs present in 2D form, that material exchange is occurring between the 2D and 3D features with increasing θ.

For 1.35 ML $\leqslant \theta \leqslant$ 1.57 ML, the amount of InAs in the 2D and 3D features (V[2D] and V[3D + Q3D]) both increase steadily indicating that the material from the flux is distributed between the 2D and 3D features with no indication of mass exchange between these features. This delivery range, as shown earlier (Figs. 2 and 3), corresponds to the formation of small quasi-3D clusters and the first appearance of 3D islands on the surface. In the delivery range 1.57 ML $\leqslant \theta \leqslant$ 1.61 ML, however, the delivered flux is insufficient to account for the increase in the volume of the 3D features and $\sim$ 0.10 ML worth of In has to leave the existing 2D clusters and incorporate in the 3D features, thereby decreasing the volume of the former. We note that this region corresponds to the increase in the quasi-3D cluster density to a maximum (Fig. 1), as well as the broadening of the mean lateral size and size distribution of the 3D islands due to their initiation and growth independent of other islands [9]. Remarkably, for 1.61 ML $\leqslant \theta \leqslant$ 1.66 ML, the total amount of InAs in 2D form as well as that in the 3D features have both stagnated or at best *increased* slightly (by $\sim$ 0.02–0.03 ML). This is because, firstly, the small quasi-3D cluster density is dropping rapidly and thus there is mass transfer from these clusters to 3D islands or 2D features. Secondly, this is the stage corresponding to the narrowing of the lateral size and size distribution of the 3D islands [9], and, as proposed earlier [9], it is possible that some material from the largest lateral size and height 3D islands is leaving them and moving to either 2D features or other 3D features. Although the island size distribution narrows and the quasi-3D cluster density drops significantly at this stage, we recognize that there is still a slight overall increase in the material in the 3D features (Table 1) due to the increase in the density of the 3D islands (Fig. 1). Thus, at this stage, the 2D clusters are not an active source of In for the 3D features but rather, may remain either passive or even act as a possible sink for In. As we go to the delivery range of 1.66 ML $\leqslant \theta \leqslant$ 1.74 ML, corresponding to the stage of island size stabilization concomitant with an increasing island density [9], the 2D clusters once again act as a source of In with mass transfer of $\sim$ 0.23 ML occurring from the 2D clusters to the 3D islands. At $\theta \sim$ 1.74 ML, the volume of material in the 3D islands (for all practical purposes) has reached $\sim$ 0.39 ML, with the material in the 2D features having reduced considerably from a value of $\sim$ 1.53 ML at the stage of first 3D island formation, to $\sim$ 1.35 ML. These results show that the evolution of the 3D islands

Table 1
Change in the InAs volume in the 3D and 2D features as a function of the InAs deposition amount θ, with $\theta \sim$ 1.35 ML being the starting reference

θ (ML)	1.35	1.45	1.57	1.61	1.66	1.74
$\Delta\theta$ (ML)	–	0.10	0.12	0.04	0.05	0.08
ΔV(3D) (ML)	–	0	0.01	0.07	0.08	0.23
ΔV(Q3D) (ML)	–	0.01	0.02	0.07	− 0.06	− 0.04
ΔV(2D) (ML)	–	0.09	0.09	− 0.10	0.03	− 0.11
V(2D) (ML)	1.35	1.44	1.53	1.43	1.46	1.35
V(3D + Q3D) (ML)	0	0.01	0.04	0.18	0.20	0.39

Note: The notation ΔX corresponds to the change in the quantity "X", where "X" can be θ, V(3D), V(Q3D) or V(2D), the latter three corresponding to the amount of InAs contained in the 3D islands, the small quasi-3D clusters, and the 2D features, respectively. ΔV(2D) is derived simply as $\Delta V(2D) = \Delta\theta - \{\Delta V(3D) + \Delta V(Q3D)\}$. Note the non-monotonic behavior of V(2D) (see the text for details).

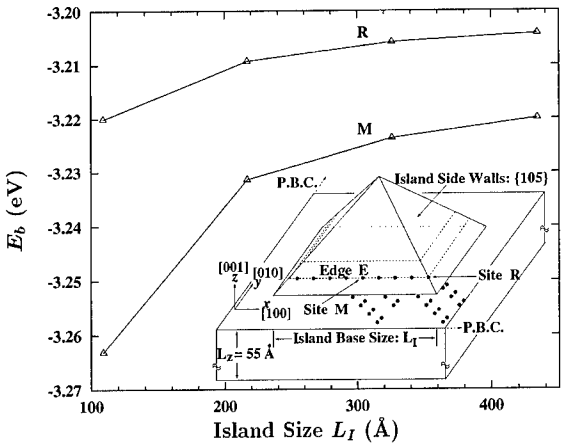

Fig. 5. Results of molecular dynamics simulations for Ge 3D islands on 1 ML Ge/Si (0 0 1). E_b is the binding energy of Ge atoms at the 3D island edge sites R and M shown in the inset (schematic). Note the systematic decrease in the magnitude of the binding energy with increasing island lateral size.

and their lateral size equalization is closely linked to a dynamic mass exchange between the 2D and 3D features on the surface.

Finally, in order to assess the importance of atom detachment processes from 3D islands [3, 9] in the island size equalization process, and in particular, to assess the plausibility of strain-field- and thus island-size- and separation-dependent atom detachment from 3D island edges [9], we have performed molecular dynamics simulations using 3D Ge islands on Si (0 0 1), for which the well-established Stillinger–Weber potentials are available. A key result that emerges from these simulations is that, as shown in Fig. 5, the binding energy of atoms at the edges of 3D islands decreases with increase in the lateral size of the islands due to the associated increasing compressive stress. This is expected to increase the probability of atom detachment from the edges of larger 3D islands and confirms the plausibility of the earlier proposed mechanism [9].

4. Conclusions

We have shown that during InAs/GaAs(0 0 1) heteroepitaxy, InAs quasi-3D clusters first form on the GaAs(0 0 1) surface for $\theta \sim 1.25$ ML, well in advance of the so-called "critical thickness" ($\theta \sim 1.57$ ML) for 3D island formation, disappear for 1.3 ML $< \theta <$ 1.45 ML and emerge again on the surface at $\theta \sim 1.45$ ML, prior to 3D island formation. This reveals a remarkable re-entrant behavior, unlike the usual descriptions of highly strained growth in terms of the SK growth mode. The small quasi-3D clusters appear to act as precursors to 3D island formation. In addition, once initiated, 3D island evolution is characterized by a dynamically evolving mass transfer between the 2D and 3D surface features, leading also to a tendency towards 3D island lateral size equalization. All the above observations are in contrast to predictions of current equilibrium-based models of strained growth. Molecular dynamics simulations show the importance of island-size and separation-dependent atom detachment processes from 3D islands, which may play an important role in island lateral size equalization.

Acknowledgements

This work was supported by the US AFOSR, ARO and ONR.

References

[1] S.V. Ghaisas and A. Madhukar, Proc. SPIE 944 (1988) 16; J. Vac. Sci. Technol. B 7 (1989) 264.
[2] C. Priester and M. Lannoo, Phys. Rev. Lett. 75 (1995) 93.
[3] C. Ratsch, P. Smilauer, D.D. Vvedensky and A. Zangwill, J. Phys. I France 6 (1996) 575.
[4] V.A. Shchukin, N.N. Ledentsov, P.S. Kopev and D. Bimberg, Phys. Rev. Lett. 75 (1995) 2968.
[5] D.J. Eaglesham and M. Cerullo, Phys. Rev. Lett. 64 (1990) 1943; Y.-W. Mo, D.E. Savage, B.S. Swartzentruber and M.G. Lagally, Phys. Rev. Lett. 65 (1990) 1020.
[6] J. Knall and J.B. Pethica, Surf. Sci. 265 (1992) 156.
[7] S. Guha, A. Madhukar and K.C. Rajkumar, Appl. Phys. Lett. 57 (1990) 2110; F. Houzay, C. Guille, J. M. Moison, P. Henoc and F. Barthe, J. Crystal Growth 81 (1987) 67.
[8] B.F. Lewis, T.C. Lee, F.J. Grunthaner, A. Madhukar, R. Fernandez and J. Maserjian, J. Vac. Sci. Technol. B 2 (1984) 419; C.W. Snyder, B.G. Orr, D. Kessler and L.M. Sander, Phys. Rev. Lett. 66 (1991) 3032; C.W. Snyder, J.F. Mansfield and B.G. Orr, Phys. Rev. B 46 (1992) 9551; A. Madhukar, Q. Xie, P. Chen and A. Konkar, Appl. Phys. Lett. 64 (1994) 2727.

[9] N.P. Kobayashi, T.R. Ramachandran, P. Chen and A. Madhukar, Appl. Phys. Lett. 68 (1996) 3299.
[10] J.M. Gerard, J.B. Genin, J. Lefebvre, J.M. Moison, N. Lebouche and F. Barthe, J. Crystal Growth 150 (1995) 351; D. Leonard, K. Pond and P.M. Petroff, Phys. Rev. B 50 (1994) 11687; A. Polimeni, A. Patane, M. Capizzi, F. Martelli, L. Nasi and G. Salviati, Phys. Rev. B 53 (1996) R4213.
[11] V. Bressler-Hill, S. Varma, A. Lorke, B.Z. Nosho, P.M. Petroff and W.H. Weinberg, Phys. Rev. Lett. 74 (1995) 3209; V. Bressler-Hill, A. Lorke, S. Varma, P.M. Petroff, K. Pond and W. H. Weinberg, Phys. Rev. B 50 (1994) 8479.
[12] Q. Xie, A. Madhukar, P. Chen and N.P. Kobayashi, Phys. Rev. Lett. 75 (1995) 2542.
[13] M. Grundmann, J. Christen, N.N. Ledentsov, J. Bohrer, D. Bimberg, S.S. Ruvimov, P. Werner, U. Richter, U. Gosele, J. Heydenreich, V.M. Ustinov, A.Yu. Egorov, A.E. Zhukov, P.S. Kopev and Zh.I. Alferov, Phys. Rev. Lett. 74 (1995) 4043, and references therein.
[14] Q. Xie, P. Chen, A. Kalburge, T.R. Ramachandran, A. Nayfonov, A. Konkar and A. Madhukar, J. Crystal Growth 150 (1995) 357.
[15] Q. Xie, A. Kalburge, P. Chen and A. Madhukar, IEEE Photon. Technol. Lett. 8 (1996) 965; D. Bimberg, N.N. Ledentsov, M. Grundmann, N. Kirstaedter, O.G. Schmidt, M.H. Mao, V.M. Ustinov, A.Yu. Egorov, A.E. Zhukov, P.S. Kopev, Zh.I. Alferov, S.S. Ruvimov, U. Gosele and J. Heydenreich, Jpn. J. Appl. Phys. 35 (1996) 1311.
[16] Typically $\sim 100\ \mu m^2$ ($10–20\ \mu m^2$) of area was imaged to extract density/structural information of various features for InAs deliveries < 1.57 ML ($\geqslant 1.57$ ML).

ELSEVIER

Journal of Crystal Growth 175/176 (1997) 224–228

JOURNAL OF CRYSTAL GROWTH

Heuristic rules for group IV dopant site selection in III–V compounds

R. Venkatasubramanian[a,*], Donald L. Dorsey[b], K. Mahalingam[b]

[a] *Department of Electrical and Computer Engineering, University of Nevada, Las Vegas, Nevada 89154, USA*
[b] *Materials Directorate, Wright Laboratory (WL/MLPO), Wright Patterson Air Force Base, Ohio 45433-7707, USA*

Abstract

The use of column IV dopants in III–V compounds is of great interest because they are easy to handle and in the case of Si, readily available in most molecular beam epitaxy (MBE) chambers. A column IV dopant can act as a donor or an acceptor or both depending on its size relative to the cation and anion sites, the substrate orientation and the growth conditions. In this article, we present heuristic rules for predicting group IV dopant site selection in III–V compounds based on the relative covalent radii of the dopant to the host lattice sites, types and relative numbers of surface dangling bonds and the growth conditions. Preliminary predictions show excellent agreement with available experimental data.

1. Introduction

The in situ doping of III–V compounds with the column IV elements, Si, Ge, and Sn during molecular beam epitaxy (MBE) is well established. Because of the possibility of occupying either a group III or group V lattice site, these dopants can act as donors, acceptors or both (resulting in compensation), depending on the specific material system and the growth conditions. While many aspects of the amphotericity of group IV dopants in III–V compounds are well known, a comprehensive description of site selection behavior of these dopants is not currently available. Such a description will allow the prediction of n-type and p-type column IV dopants for any III–V compound and also yield growth strategies for forcing a specific dopant to act as either a donor or an acceptor.

Various aspects of site selection behavior have been examined in the past. Madelung [1] developed a table of early experimental bulk growth results. Lilov [2] correlated electronegativities to solidification distribution coefficients, yielding a prediction of the sites occupied by impurities in the bulk crystal growth from the melt. Thermodynamic analysis of Heckingbottom [3], Hurle [3–7], and Hata et al. [8] have successfully predicted doping behavior of various elements in several III–V compounds. These approaches are not entirely adequate because they do not account for the influence of growth conditions and substrate orientations. Additionally, none of these approaches deal with all aspects of the problem.

* Corresponding author.

0022-0248/97/$17.00 Copyright © 1997 Elsevier Science B.V. All rights reserved
PII S0022-0248(96)00965-7

In this article, we report a set of heuristic rules that capture the experimental observations for column IV dopant in III–V MBE growth based on the relative covalent radii of dopant to host lattice atoms, substrate orientation and growth conditions. In Section 2, we state the rules and provide supporting arguments from existing experimental results. In Section 3, we present a detailed analysis of the rules by relating them to available data. Finally, we present conclusions in Section 4.

2. Heuristic rules for dopant site selection

Based on available experimental data, the most important factor for dopant site selection is the relative covalent radius of the dopant and the host lattice atoms. This leads to the following rule:

Rule 1 (Covalent radius). *Dopants atoms prefer to occupy the sublattice with larger covalent radius. If the dopant atom is larger than both sublattice sites, segregation of the dopant is likely. If the dopant atom is smaller than both the sublattice sites, the conduction type can be manipulated by varying the substrate orientation and conditions.*

The core of the rule (first sentence) has been known for some time. But the incorporation of the dopant at the larger site even when both sites are larger than the dopant is somewhat surprising. This contradicts macroscopic strain energy considerations which would predict the opposite behavior due to less strain energy. The reason for the behavior is unclear.

Rule 2 (Back bonding). *Dopants atoms incorporate with more ease at sites with fewer back-bonds to the underlying layer.*

A possible explanation for this observation is that the bond angle and length constraints make it difficult for the dopant atom to replace a host atom at a triple bonded site. Conversely, it is relatively easy for a dopant atom to be singly bonded to the surface. Double bonded sites are occupied by the dopant atom with medium difficulty.

Rule 3 (Site availability) *In III–V systems in which both cation and anion sites are suitable for dopant occupation, the ratio of donors to acceptors can be manipulated by changing the substrate orientation.*

Six types of surface sites are possible for the incorporation of atoms based on the back bonding. These are single-bonded III site, double-bonded III site, triple-bonded III site, single-bonded V site, double-bonded V site and triple-bonded V site. For a given surface, a particular combination of some of the six types of sites exist at a fixed ratio. For example, the (1 1 1)A GaAs surface has single-bonded As sites and triple-bonded Ga sites, whereas the (711)A surface has double-bonded Ga, double-bonded As and single-bonded Ga sites. For example, assuming that the electronic energies are similar for equal number back bonds at either a Ga or As site, and that Ga and As compete equally with Si for sites, the site in highest concentration on the surface is favored by Si (subject to Rule 2). This can lead to either n- or p-type doping with a possibility of compensation.

Rule 4 (Site competition) *In III–V systems in which both cation and anion sites are suitable for dopant occupation, the ratio of donor to acceptor can be manipulated using the growth conditions.*

The sites of the dominant flux species will be more efficiently occupied. Thus, the Si atoms will compete more effectively with the species of lower flux. Therefore, more Si will incorporate on the sites of the lower flux species.

3. Results and discussion

The consequences of Rule 1 are shown as a doping regime map for various III–V compounds in Fig. 1 for C, Si, Ge and Sn. For Si, the dotted lines through its coordinates split the map into three regimes I, II and III. The coordinates of the III–V compound in quadrant I and II will make Si acceptor and donor, respectively. If the coordinates of the III–V compound is in quadrant III, then the dopant will most probably segregate to the surface.

Based on Fig. 1, Si, Ge and Sn prefer to be n-type in all III–V compounds except for GaSb and AlSb. Si is amphoteric in the arsenides and antimonides, while Ge is amphoteric only in the antimonides. Sn will segregate in most of the III–V compounds except for GaSb and AlSb in which it is p-type. These observations are corroborated by the experimental data [8–15].

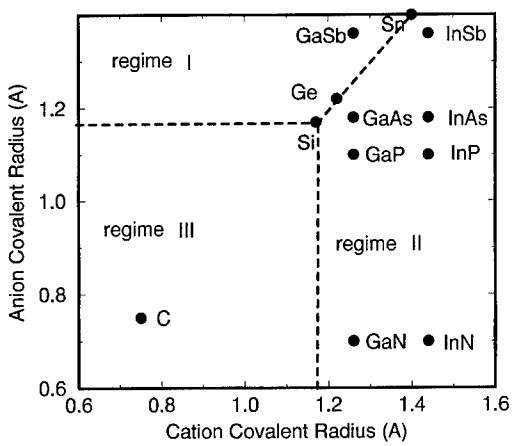

Fig. 1. Site selection regime plot for column IV dopants in III–V compounds.

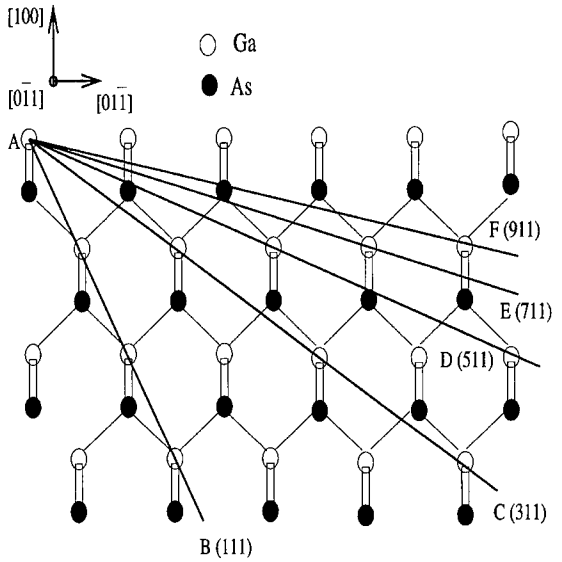

Fig. 2. Structure of (h11) planes of a zinc blende (e.g. GaAs) crystal as seen through [0 1 $\bar{1}$] projection.

The single exception to Rule 1 is C, which is predicted to be n-type, but is actually p-type in GaAs [16]. It has been postulated that the high electronegativity of carbon allows its occupation of group V sites only [2].

A classic example of Rule 2 is observed for GaAs where growth on (1 1 1)A and (1 1 1)B substrates result in p-type and n-type materials, respectively [17]. In the (1 1 1)A and (1 1 1)B orientations, Si is more stable at the singly bonded As and the singly bonded Ga sites, respectively. In (1 0 0) GaAs, both the Ga and As sites have two back bonds. The distribution of Si, therefore, depends on site availability which is dictated by the growth conditions.

To consider Rule 3, let us examine the (3 1 1)A, (5 1 1)A, (7 1 1)A and (9 1 1)A surfaces which are shown in Fig. 2 for typical GaAs growth conditions of anion to cation overpressure. The surfaces exhibit the following surface site patterns:

(311)A: $\underline{\text{DG SA}}$ DG SA DG SA... (1)

(511)A: $\underline{\text{DG DA SA}}$ DG DA SA DG DA SA...

(711)A: $\underline{\text{DG DA DA SA}}$ DG DA DA SA
$\overline{\text{DG DA DA SA}}$... (2)

(911)A: $\underline{\text{DG DG DA DA SA}}$ DG DG DA DA
$\overline{\text{SA DG DG DA DA}}$ SA...

where DG, DA and SA stand for double-bonded Ga, double-bonded As and single-bonded As, respectively, with the underlined set representing one period. The types of bonding sites and their ratios change with the indices of the plane. Using Rules 2 and 3, and noting that As dimer incorporation requires two As sites as neighbors, one can conclude that (3 1 1)A material should be p-type, while the others should be n-type for a flux ratio close to unity, which is in agreement with Ref. [17]. For (7 1 1)A, of the three As sites as neighbors, one of those sites is available for Si incorporation. Even though the (9 1 1)A surface has the same As configuration as (7 1 1)A, due to larger number of Ga sites, (7 1 1)A should be more compensated than either (5 1 1)A or (9 1 1)A, which is in agreement with Ref. [17]. Due to increased impurity scattering, the mobility should be smaller for (7 1 1)A than for (5 1 1)A or (9 1 1)A which is also in close agreement with Ref. [17].

In the GaAs(3 1 1)A [18], GaAs(3 3 1) [19] and GaAs(2 1 1)A [20] orientations, it has been shown that both n- and p-type materials can be realized by changing the flux ratio. In the (3 1 1)A and (2 1 1)A orientations, the As single-bonded sites are present

as nearest neighbors along the [0 1 $\bar{1}$] direction, even though such a configuration does not exist in the perpendicular direction on the surface. Si competes for sites with Ga for its double-bonded site and As for the single-bonded nearest-neighbor dimer sites. According to Rule 2, Si prefers As sites at flux ratio close to unity and hence the material is p-type. At high (anion to cation) flux ratios, As incorporates more efficiently in dimer sites along the [0 1 $\bar{1}$] direction and hence, Si competes with Ga for its double-bonded site. Hence the material becomes n-type. These observations are in agreement with Ref. [18].

Okano et al. [21] studied the doping behavior of Si in GaAs (1 1 1)A as a function of misorientation angle toward (1 0 0), flux ratio and temperature. They showed that the material changed from p-type to n-type with increasing misorientation angle and flux ratio. Based on the crystal orientation and bond configuration, the ratio of Ga to As sites R can be shown to be

$$R = \frac{1.155}{\tan\theta} \tag{3}$$

for a misorientation angle of θ. A misoriented substrate consists of Ga sites with triple bonds (TG) and double bonds (DG) and the As sites consist of single bonds (SA). The relative numbers of TG, DG and SA sites are not shown due to space limitations. According to Rule 2, the TG sites will be predominantly occupied by Ga. Therefore, Si competes only for the DG and SA sites. Combining the effects of site and flux ratios we define the dopant decision parameter (DDP) as

$$\mathrm{DDP} = \frac{\mathrm{SA}}{\mathrm{DG}} \frac{J_{\mathrm{Ga}}}{4J_{\mathrm{As_4}}}, \tag{4}$$

where factor 4 is required to convert the tetramer flux of As to a monomer flux. At DDP = 1 (critical value), the materials switches from p-type to n-type. The critical value will depend on relative sticking efficiencies of Ga and As, relative sticking efficiency of Si at a DG site to a SA site and the temperature. These factors are not considered here. A plot of DDP with misorientation angle is shown in Fig. 3 for flux ratios of 1.4, 3.3 and 5.0. The transitional orientation angles for flux ratios, 5.0, and 3.3 are found to be 2.2° and 2.9°, respectively, with an angle greater than 5° for a flux ratio 1.4 which is in close agreement with Ref. [21] at 600°C. At lower temperatures, the transition angle is expected to shift to lower values due to more efficient sticking of As as observed by Okano et al. [21]. These results are also in agreement with Shigeta et al. [22] and Kadoya et al. [23].

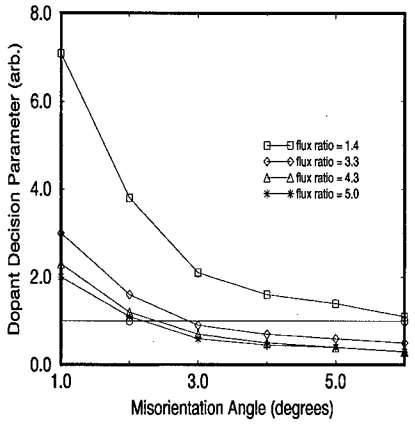

Fig. 3. Effect of misorientation angle and flux ratio on the dopant decision parameter.

A similar analysis of AlAs(1 1 1)A growth predicts that for misorientation angles greater than 2.5°, the film should be n-type which is in agreement with Yamamoto et al. [10]. The results of Uppal et al. [19] for Si doping of (3 3 1)A and (3 3 1)B GaAs can be explained satisfactorily using a similar analysis, but, this is omitted due to space limitations.

The rules presented and tested here are empirical, but based on physical considerations. These rules dictate the site occupation only and do not predict if the dopant is shallow or deep. These rules are general and are expected to be suitable for II–VI compounds also. Even though the focus of this work is MBE grown thin films, these rules may also apply to other vapor-phase techniques such as vapor-phase transport (VPT) and vapor-phase epitaxy (VPE). A judicious combination of thermodynamics and electronegativity considerations with the heuristic rules of this work is expected to be a powerful tool for predicting column IV dopant behavior in compound semiconductors.

4. Conclusion

We have developed heuristic rules for column IV doping of III–V compounds based on the covalent radii of the constituent atoms, crystallographic orientation of the surface and the flux ratio. These rules are empirically derived, but are based on physical considerations. We have applied them to several experimental reports and the agreement has been excellent.

Acknowledgements

One of the authors (R.V.) acknowledges the financial support provided through a visiting scientistship by the Materials Directorate of Wright Laboratory, USAF during Summer 1994.

References

[1] O. Madelung, Physics of III–V Compounds (Wiley, New York, 1964)
[2] S.K. Lilov, Chemtronics 5 (1991) 45.
[3] R. Heckingbottom, C.J. Todd and G.J. Davies, J. Electrochem. Soc. 127 (1980) 444.
[4] D.T.J. Hurle, J. Phys. Chem. Solids 40 (1979) 613.
[5] D.T.J. Hurle, J. Phys. Chem. Solids 40 (1979) 627.
[6] D.T.J. Hurle, J. Phys. Chem. Solids 40 (1979) 639.
[7] D.T.J. Hurle, J. Phys. Chem. Solids 40 (1979) 647.
[8] M. Hata, S.M. Lichtenthal and G.E. Stillman, Gallium Arsenide and Related Compounds, Vol. 129 (Bristol, Philadelphia, 1993) p. 507.
[9] J. Wagner, A. Fischer and K. Ploog, Appl. Phys. Lett. 62 (1993) 3482.
[10] T. Yamamotto, M. Inai, A. Shinoda, T. Takebe and T. Watanabe, Jpn. J. Appl. Phys. 32 (1993) 3346.
[11] S. Subbanna, H. Kroemer and J.L. Merz, J. Appl. Phys. 59 (1986) 488.
[12] C.A. Chang, R. Ludeke, L.L. Chang and L. Esaki, Appl. Phys. Lett. 31 (1977) 759.
[13] K.F. Longbach, S. Xin and W.I. Wang, J. Appl. Phys. 69 (1991) 3393.
[14] P.E. Thompson, J.L. Davis and M. Yang, J. Appl. Phys. 74 (1993) 6686.
[15] M. Oszwaldowski and T. Berus, Thin Solid Films 172 (1989) 71.
[16] T. Yamada, E. Tokumitsu, K. Saito, T. Akatsuka, M. Miyauchi, M. Konagi and T. Takahashi, J. Crystal Growth 95 (1989) 145.
[17] W.I. Wang, E.E. Mendez, T.S. Kuan and L. Esaki, Appl. Phys. Lett. 47 (1985) 826.
[18] W.Q. Li, P.K. Bhattacharya, S.H. Kowk and R. Merlin, J. Appl. Phys. 72 (1992) 3129.
[19] P.N. Uppal, J.S. Ahearn and D.P. Musser, J. Appl. Phys. 62 (1987) 3766.
[20] T. Takamori, T. Fukunaga, J. Kobayashi, K. Ishida and H. Nakashima, Jpn. J. Appl. Phys. 26 (1987) 1097.
[21] Y. Okano, M. Shigeta, H. Seto, H. Katahama, S. Nishine and I. Fujimoto, Jpn. J. Appl. Phys. 29 (1990) L1357.
[22] M. Shigeta, Y. Okano, H. Katahama, S. Nishine and K. Kobayashi, J. Crystal Growth 111 (1991) 284.
[23] Y. Kadoya, A. Sato and H. Kano, J. Crystal Growth. 111 (1991) 280.

ELSEVIER

Journal of Crystal Growth 175/176 (1997) 229–233

JOURNAL OF CRYSTAL GROWTH

Surface segregation of Si in δ-doped $In_{0.53}Ga_{0.47}As$ grown by molecular beam epitaxy

B. Vögele[a], C.R. Stanley[a,*], E. Skuras[b], A.R. Long[b], E.A. Johnson[c]

[a] *Department of Electronics and Electrical Engineering, University of Glasgow, Glasgow G12 8QQ, UK*
[b] *Department of Physics and Astronomy, University of Glasgow, Glasgow G12 8QQ, UK*
[c] *Blackett Laboratory, Imperial College of Science, Technology and Medicine, Prince Consort Road, London SW7 2BZ, UK*

Abstract

A study of Si spreading in δ-doped InGaAs grown lattice matched on InP by molecular beam epitaxy is reported. The layers were designed to distinguish between thermal diffusion and surface segregation as mechanisms for migration of the dopant atoms. Comparison of Shubnikov–de Haas data with self-consistent calculations shows that spreading occurs by surface segregation at substrate temperatures in the range 470–520°C and Si densities of $\leqslant 4.0 \times 10^{12}$ cm^{-2}; thermal diffusion is found to be negligible. A near ideal δ-doping profile can be maintained if a δ-doped layer is capped with as little as 3 monolayers of InGaAs grown at $\leqslant 470$°C before subsequent material is deposited at higher temperatures, up to ~ 520°C.

1. Introduction

Shubnikov–de Haas (SdH) measurements and self-consistent calculations (SCC) have been used to estimate the extent of Si migration in GaAs δ-doped structures grown by molecular beam epitaxy (MBE) [1]. The measured electron densities n_i ($i = 0, 1, 2, 3,...$) in the occupied subbands and the subband density ratio $n_{i=0}/n_{i=1}$ are compared with values predicted by SCC in which the dopant profile width w_{Si} is treated as a variable parameter to achieve a fit between theory and experiment. The combination of SdH and SCC can provide a comprehensive description of the electrical properties of the two-dimensional system including the individual subband densities, the subband mobilities as well as the dopant spreading. Alternative methods aimed at assessing the confinement of impurity atoms used for δ-doping include capacitance–voltage (C–V) profiling of the free carriers originating from the impurities [2] and direct measurement of the dopant concentration versus depth distribution by secondary ion mass spectrometry (SIMS) [3].

The combination of SdH measurements and SCC was used in previous studies of Si δ-doped InGaAs [4] grown lattice matched on InP in preference to C–V profiling which is limited by the generally low Schottky barrier height of metals on this ternary material. The inferred Si spreading was

* Corresponding author. Fax: + 44 141 330 6002; e-mail: c.stanley@elec.gla.ac.uk.

0022-0248/97/$17.00 Copyright © 1997 Elsevier Science B.V. All rights reserved
PII S0022-0248(96)00856-1

$w_{Si} \approx 40$ monolayers (ML) for a growth temperature T_s of $\sim 520°C$ and with Si areal densities $N_{Si} \leqslant 4.0 \times 10^{12}\ cm^{-2}$. When the δ-layer was deposited at $T_s \leqslant 470°C$ and covered by 20 ML of undoped material at the same substrate temperature, a near ideal δ-doping profile was created despite the subsequent growth of a 0.5 μm thick InGaAs cap layer at $T_s \approx 520°C$. These studies provide indirect evidence that the main mechanism causing the Si spreading away from the original doping plane at $T_s \approx 520°C$ is surface segregation. The validity of combining SdH measurements with self-consistent calculations was confirmed by intentionally confining the Si donors to a thin slab of known thickness, grown at $T_s \leqslant 470°C$ to eliminate spreading. The correspondence between the SdH and SCC results in this case was excellent when a uniform distribution of the dopants with width w_{Si} equal to the physical thickness of the slab was assumed.

In this paper, $In_{0.53}Ga_{0.47}As$ epitaxial layers δ-doped with Si and grown using novel procedures to separate the effects of dopant redistribution by thermal diffusion and surface segregation are described. It is shown that spreading occurs by surface segregation and that thermal diffusion of Si is negligible under the MBE growth conditions investigated. Spreading can be eliminated by capping the Si atoms with as little as 3 monolayers of InGaAs grown at $\leqslant 470°C$, before raising T_s to complete the deposition of the remainder of the structure at the optimum temperature for InGaAs, around 520°C.

2. Experimental procedures

2.1. MBE growth

The set of InGaAs δ-doped structures shown in Fig. 1 was grown on semi-insulating Fe–InP(1 0 0) substrates in a Varian 3″ Modular Gen II MBE system fitted with an arsenic cracker [5]. An As_2 flux of $\sim 1.9 \times 10^{15}$ molecules $cm^{-2}\ s^{-1}$ was used and the Ga and In fluxes were determined by RHEED intensity oscillations to ensure the correct ratio for lattice matching to InP and an InGaAs growth rate of 1.0 μm/h. The InGaAs surface was

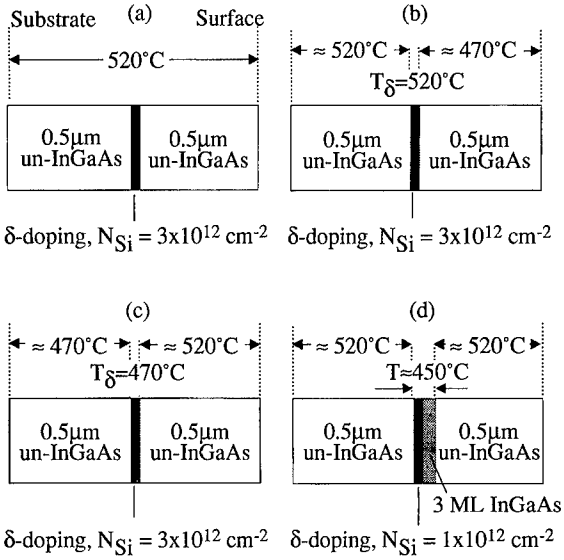

Fig. 1. Schematic diagrams of the set of samples used for the study reported here: (a) #B603; (b) #B684; (c) #B685; (d) #B737. The growth cycle for #B713 was similar to that for #B685, except that growth was interrupted for 15 min at $\sim 520°C$ after the δ-doping and before T_s was lowered to $\sim 450°C$ for the deposition of the 0.5 μm thick cap layer. Samples #B603, #B684 and #B685 have areal Si densities of $\sim 3.0 \times 10^{12}\ cm^{-2}$. The Si sheet densities of #B713 and #B737 are $\sim 2.5 \times 10^{12}\ cm^{-2}$ and $\sim 1.0 \times 10^{12}\ cm^{-2}$, respectively.

exposed to the As_2 flux throughout the growth of the structures, including the interrupts for the deposition of the Si δ-layers and during the time required to lower and raise T_s. Substrate temperatures were measured with an optical pyrometer. Additional information on the growth conditions was deduced from the surface reconstructions which changed from a (1×3) at $T_s \leqslant 470°C$, through to a (2×3) for $470°C \leqslant T_s \leqslant 500°C$ and a (2×4) for $T_s \geqslant 500°C$, all referred to the [1 $\bar{1}$ 0] azimuth. The Si furnace temperature was calibrated against both low magnetic field Hall and high magnetic field SdH measurements of the free electron density in a large number of uniformly doped GaAs and lattice-matched InGaAs layers.

The five samples discussed here are identified by the numbers #B603, #B684, #B685, #B713 and #B737. They form part of a larger series of InGaAs layers δ- and slab-doped with Si covering growth temperatures in the range ~ 420–$525°C$

and areal Si densities of $< 1 \times 10^{12}$ cm^{-2} to $\sim 1 \times 10^{14}$ cm^{-2} [6]. Layer #B603 (see Fig. 1a) was δ-doped with Si to a nominal sheet density of 3.0×10^{12} cm^{-2} and grown entirely at $T_s \approx 520$°C, including the interrupt for δ-doping. This sample provided a reference for the extent of Si migration in InGaAs grown under optimum conditions. The pair of layers #B684 and #B713, with nominal δ-doping concentrations of 3.0 and 2.5×10^{12} cm^{-2}, respectively, were grown with the following substrate temperature cycles to separate Si spreading towards the substrate from that migrating in the growth direction;

#B684 (Fig. 1b): 0.5 μm of un-InGaAs and δ-doping at $\sim$ 520°C; a pause of 300 s to lower T_s to $\sim$ 470°C; growth of a further 0.5 μm of un-InGaAs at $T_s \approx 470$°C.

#B713: 0.5 μm of un-InGaAs and δ-doping at $\sim$ 520°C; a 15 min growth interrupt with the substrate at $\sim$ 520°C; a pause of 300 s to lower T_s to $\sim$ 470°C; the growth of a final 0.5 μm of un-InGaAs at $\sim$ 470°C.

The only intentional change to the growth cycles of #B684 and #B713 was the inclusion in #B713 of a 15 min growth interrupt at $\sim$ 520°C after the δ-doping. For #B685, the temperature sequence applied to the growth of #B684 was reversed (Fig. 1c);

#B685: 0.5 μm of un-InGaAs and δ-doping at $\sim$ 470°C; a pause of 300 s to raise T_s to $\sim$ 520°C; growth of a further 0.5 μm of un-InGaAs at $T_s \approx 520$°C.

The key differences to note are that for #B684, growth of the 0.5 μm thick cap over the Si δ-doped layer was initiated at a relatively "low" temperature, whereas for #B685 the wafer temperature was "high" at the comparable stage of the cycle.

The final structure in the set, #B737 ($N_{Si} = 1.0 \times 10^{12}$ cm^{-2}), was grown with the aim of confirming that spreading is dominated by surface segregation with essentially no component arising from thermal diffusion. The growth cycle for #B737 was as follows (Fig. 1d);

0.5 μm of un-InGaAs at 520°C; a 300 s pause to lower T_s to $\sim$ 450°C; δ-doping and growth of 3 ML of un-InGaAs at $\sim$ 450°C; a further 300 s pause to raise T_s to $\sim$ 520°C followed by the deposition of 0.5 μm of un-InGaAs at this temperature.

2.2. Quantum transport measurements

SdH measurements were performed in the dark on Hall bars defined either by optical or electron beam lithography with a 3 : 1 length to width ratio. The magnetoresistance data were numerically differentiated, expressed in reciprocal magnetic field and frequency analysed by fast Fourier transform (FFT) techniques. The electron subband densities n_i ($i = 0, 1, 2, 3, \cdots$) are related to the frequencies v_i (in T) of the SdH oscillations by the expression $n_i = 2ev_i/h$ assuming unresolved spin-splitting, where e is the electronic charge and h is Planck's constant. For the same Si dopant density, narrower doping profiles lead to higher subband density ratios $n_{i=0}/n_{i=1}$ and lower mobilities for the electrons occupying the $i = 0$ energy state due to the increased physical proximity of the wave functions to the Si donors. Consequently, in order to resolve the 1.2 K SdH oscillations corresponding to the $i = 0$ subband within the 13 T upper limit of our superconducting magnet, the Si δ-doping densities were restricted to a maximum of $\sim 4.0 \times 10^{12}$ cm^{-2}.

3. Results and discussion

The total densities of electrons in all occupied subbands $\sum_i n_i$ and the subband density ratios $n_{i=0}/n_{i=1}$ from the Shubnikov–de Haas measurements and the self-consistent calculations are summarised in Table 1. Layer #B603 was grown entirely at 520°C with an intended Si doping density of 3.0×10^{12} cm^{-2} to provide a reference for the extent of spreading at the optimum InGaAs growth temperature. Four occupied subbands are observed in the FFT amplitude spectrum of this sample with a total carrier density $\sum_i n_i = 3.14 \times 10^{12}$ cm^{-2} and a subband density ratio $n_{i=0}/n_{i=1} = 2.160$. The Si spreading estimated from SCC assuming a uniform distribution of the Si atoms is $\sim$ 35 ML. Thermal diffusion would cause Si donors to migrate from the original doping plane both towards the substrate and in the growth direction to form a symmetrical profile. For surface segregation only, an asymmetric profile resulting from Si migration in the growth direction is expected.

Table 1
Summary of the total densities of electrons in all occupied subbands $\sum_i n_i$ and the subband density ratios $n_{i=0}/n_{i=1}$ from the Shubnikov–de Haas measurements with the corresponding values predicted by self-consistent calculations; in the SCC, a uniform distribution of Si atoms over a thickness w_{Si} is assumed, and w_{Si} is used as a fitting parameter

Sample no.	Nominal Si density ($\times 10^{12}$ cm^{-2})	$\sum_i n_i$ from SdH ($\times 10^{12}$ cm^{-2})	$n_{i=0}/n_{i=1}$ from SdH	$\sum_i n_i$ from SCC ($\times 10^{12}$ cm^{-2})	$n_{i=0}/n_{i=1}$ from SCC	Estimated spreading (ML)
B603	3.0	3.14	2.160	3.14	2.158	35
B684	3.0	3.45	2.662	3.44	2.623	2
B685	3.0	3.12	1.905	3.21	1.907	45
B713	2.5	2.24	2.642	2.30	2.644	2
B737	1.0	0.93	3.046	1.00	3.042	2

The growth cycle for layer #B684 allowed Si spreading towards the substrate to be differentiated from that in the growth direction. Since spreading is eliminated by growth at $T_s \leqslant 470$°C [4], any migration which occurred in #B684 must have been by thermal diffusion into the substrate during the time of ~ 16 s for δ-doping at ~ 520°C and the subsequent 300 s growth interrupt to decrease T_s to ~ 470°C. None could have taken place during the deposition of the 0.5 μm thick cap layer at ~ 470°C. The FFT amplitude spectrum for #B684 is shown in Fig. 2 together with that of #B685 for comparison. The tighter confinement of the Si atoms in #B684 compared with #B685 where the cap layer was deposited directly on to the dopants at ~ 520°C is confirmed by the higher frequency of its $i = 0$ peak (n_0(B684) > n_0(B685)), a shift of the $i \geqslant 1$ peaks to lower frequencies and an increase in the $n_{i=0}/n_{i=1}$ ratio. The estimated spreading is ~ 2 ML in #B684 and ~ 45 ML in #B685. Strictly, any thermal diffusion which might have occurred during the growth of a 0.5 μm thick cap layer at ~ 520°C was not completely mimicked in sample #B684. A further sample, #B713 was grown with a 15 min interrupt (equivalent to the growth of 0.25 μm of InGaAs at 1.0 μm/h) with the substrate at ~ 520°C before the final 0.5 μm of un-InGaAs was deposited at ~ 470°C. Comparison of the SdH and SCC data suggests that near ideal δ-doping was again achieved with an inferred spreading of ~ 2 ML.

The results for #B684 and #B713 show that diffusion of Si in InGaAs at temperatures around 520°C is negligible. Significant spreading of Si in InGaAs away from the δ-doped plane only takes place when the δ-layer is covered with additional material and the wafer temperature exceeds ~ 470°C (layers #B603 and #B685). This is compelling evidence for surface segregation.

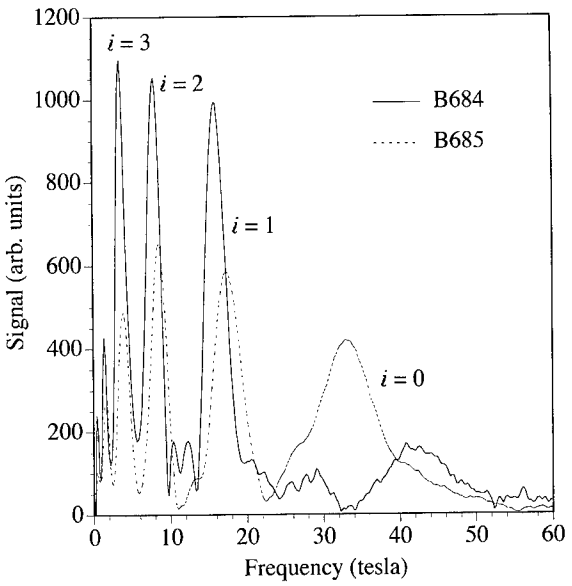

Fig. 2. FFT amplitude spectra for #B684 and #B685. The tighter confinement of the Si atoms in #B684 compared with #B685 is evident from the higher frequency of its $i = 0$ peak (n_0(B684) > n_0(B685)) and a shift to lower frequencies of the $i \geqslant 1$ peaks. The estimated spreading is ~ 2 ML in #B684 and ~ 45 ML in #B685.

The final layer in the set, #B737, was grown to demonstrate that the redistribution of Si atoms is indeed dominated by surface segregation. If Si had managed to penetrate through only 3 ML of InGaAs grown at ~ 450°C to a significant extent, then substantial spreading would have occured subsequently via surface segregation once the temperature had been raised to ~ 520°C and the growth of the 0.5 μm cap layer had been initiated. The SdH and SCC data for #B737 are summarised in Table 1; spreading of the Si atoms away from the original doping plane is ~ 2 ML, showing that thermal diffusion is absent and no significant redistribution by surface segregation has taken place.

4. Conclusions

It has been shown that surface segregation causes significant migration of Si δ-doping in InGaAs grown by solid source MBE at temperatures around 520°C. Spreading is eliminated for growth at $\leqslant 470$°C and diffusion is also negligible at temperatures up to ~ 520°C. Near-ideal Si δ-doping within InGaAs has been demonstrated simply by capping the dopants with a 3 ML thick layer of undoped material grown at $\leqslant 470$°C. Further material can then be grown at the optimum temperature around 520°C without the risk of smearing the dopant profile. We believe that this procedure can be used to advantage in optimising both the Si dopant profile and the electrical characteristics of InAlAs–InGaAs HEMT structures for shallow and high frequency devices.

Further work is required to determine if the model of kinetically limited surface segregation which accounts for the behaviour of Si in GaAs [7, 8] is applicable to Si in InGaAs. Also, the real distributions of Si atoms which result from growth at high temperatures need to be more accurately represented by asymmetric rather than uniform profiles in the self-consistent calculations.

Acknowledgements

This research programme has been supported by a grant, number GR/J/90718, from the Engineering and Physical Science Research Council. Technical assistance from J.R. Burns, R. Harkins, J. Cochrane and W. Reid is gratefully acknowledged.

References

[1] A. Zrenner, F. Koch and K. Ploog, Surf. Sci. 196 (1988) 671.
[2] E.F. Schubert, J.M. Kuo and R.F. Kopf, J. Electron. Mater. 19 (1990) 521.
[3] J.J Harris, J. Mater. Sci.: Mater. Electron. 4 (1993) 93 and references therein.
[4] M. McElhinney, E. Skuras, B. Vögele, M.C. Holland, A.R. Long, C.R. Stanley and E.A. Johnson, Appl. Phys. Lett. 68 (1996) 940.
[5] C.R. Stanley, M.C. Holland, A.H. Kean, M.R. Stanaway, R.T. Grimes and J.M. Chamberlain, Appl. Phys. Lett. 58 (1991) 478.
[6] E. Skuras, B. Vögele, M.C. Holland, A.R. Long, C.R. Stanley, M. McElhinney and E.A. Johnson, in preparation.
[7] R.B. Beall, J.J. Harris, J.B. Clegg, J.P. Gowers, B.A. Joyce, J. Castagné and V. Welch, Proc. Int. Symp. on GaAs and Related Compounds, Atlanta, Georgia, 1988; Inst. Phys. Conf. Ser. No. 96 (1989) 17.
[8] J.J. Harris, D.E. Ashenford, C.T. Foxon, P.J. Dobson and B.A. Joyce, Appl. Phys. A 33 (1984) 87.

ELSEVIER

Journal of Crystal Growth 175/176 (1997) 234–237

JOURNAL OF CRYSTAL GROWTH

Two-dimensional limitations when increasing the Si-concentration from δ-doping to thin Si-layers in GaAs

J.V. Thordson, T.G. Andersson*, G. Swenson, U. Södervall

Department of Physics, Chalmers University of Technology and Göteborg University, S-412 96 Göteborg, Sweden

Abstract

Silicon layers, embedded in GaAs extending from a low δ-doping concentration up to 6 monolayers (ML), were grown at 500°C, and in a δ-doped region at 580 and 630°C. The structures were mainly characterised by Hall effect measurements and secondary ion mass spectroscopy. For doping concentrations below 2×10^{12} cm^{-2}, the majority of the carriers were trapped. At 4 ML thickness, a relaxation of the Si-layer was detected which resulted in enhanced diffusion. Further, an assessment of diffusion as a function of growth temperature and doping concentration is made. Finally, a model is proposed to assess the minimum diffusion as a function of growth temperature.

1. Introduction

Delta-doping provides the ultimate doping profile. This facilitates the construction of the smallest possible devices which in turn means a decreased power consumption and a maximised device operation speed. In high electron mobility transistors (HEMT), this brings advantages like increased breakdown voltage [1], increased free carrier concentration in the conducting channel [1] and a decreased gate-to-channel distance, resulting in an increased transconductance [2]. Delta-doping superlattices could also have a future application in light emitting devices and light modulators [2, 3]. These applications of δ-doping make it interesting to investigate its limitations. One limit for the spatial extensions of the quasi two-dimensional electron gas (2-DEG) is the real distribution of silicon atoms from the doping layer. Another limitation is the maximum obtainable free carrier concentration. At δ-doping, maximum free carrier concentration is in the range of $(5\text{–}10) \times 10^{12}$ cm^{-2} for growth temperature $T_g = 500$°C and increases with temperature [4–6], probably due to the increased spread of the silicon atoms. Furthermore, it has been found that high doping concentrations in combination with high growth temperatures result in an excess migration of Si-atoms towards the surface as compared to the other direction. This results in an asymmetric δ-doping peak [7–9].

* Corresponding author. Fax: +46 31 772 3385; e-mail: f4bjt@fy.chalmers.se.

0022-0248/97/$17.00 Copyright © 1997 Elsevier Science B.V. All rights reserved
PII S0022-0248(96)00983-9

In this work we primarily report Hall effect and secondary-ion mass-spectroscopy (SIMS) measurements on silicon δ-doped GaAs structures from the 10^{11} cm^{-2} range up to the monolayer (ML) region at 500°C and in the δ-doping region at $T_g = 580$ and 630°C. In an attempt to describe the spread of the silicon atoms from the plane, we consider a mechanism where a certain percentage, f, of the Si-atoms are transported into the next GaAs-layer.

2. Experimental procedure

The structures were grown with a solid arsenic source in a Varian GEN II MBE system on semi-insulating (1 0 0)GaAs substrates. First, the GaAs-buffer layer was grown at 580°C. During the last 6 min of the buffer layer growth, the growth temperature was gradually changed to the temperature used during the δ-doping deposition. The silicon atoms were deposited from the dopant cell. After the silicon deposition the 100 nm thick GaAs cap layer was grown at the same temperature as the silicon layer. Our motivation for choosing these temperatures was to supplement earlier measurements at other temperatures. The structures were grown well inside the As-stabilised region, with a V/III flux ratio of ~ 60 at $T_g = 630$°C, and ~ 20 for the other growth temperatures. The silicon dopant source was calibrated by Hall effect measurements and an electrochemical capacitance–voltage profiler. The electrical characteristics were studied by Hall effect and the distribution by SIMS.

3. Results

At a doping concentration of $N_{2D} = 1.4 \times 10^{11}$ cm^{-2} and $T_g \leqslant 500$°C, we were not able to detect free carriers since the sample was too highly resistant. Furthermore, samples doped at $N_{2D} \leqslant 1 \times 10^{12}$ cm^{-2} gave a reduced relative carrier concentration as shown in Fig. 1. This is attributable to the fact that the shallow potential at low doping concentrations is easily emptied by internal electric fields due to the depletion close to

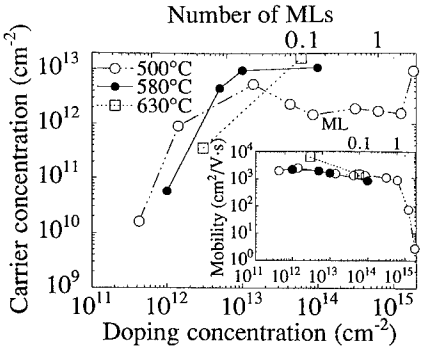

Fig. 1. Free carrier concentration and electron mobility (inset) as a function of the silicon doping concentration. A maximum is reached at $(5–10) \times 10^{12}$ cm^{-2}. The electron mobility decreases when the doping concentration is increased above 1×10^{12} cm^{-2}. After 1 ML thickness, the mobility falls faster until the samples become a highly resistant due to a relaxation at 4 ML.

the sample surface. After have been swept away, the electrons are trapped by surface states and deep levels. The maximum measured free carrier concentration was limited to 5×10^{12} cm^{-2} at $T_g =$ 500°C, arguably due to the incorporation of Si on As sites (autocompensation), donor–acceptor pairs (Si–Si pair formation), formation of Si–acceptor centres (Si–X centres) and formation of deep acceptor centres (DX-centres) [9–11]. With further coverage, the carrier concentration dropped somewhat but stayed fairly constant up to 2 ML, where the structures started to become degraded: electron mobility decreased when we increased doping concentration in the sub-ML range. At 2 ML, the mobility started to decrease much more quickly, probably due to a degradation of the structures. The films up to 3 ML of Si were strained and provided a streaky reflection high electron energy diffraction (RHEED) pattern. The relaxation occurred between 3 and 4 monolayers, as indicated by the fact that the (RHEED) pattern became spotty. At 4 ML, the sample was too highly resistant to obtain any conduction in the Hall effect measurements which is due to relaxation of the structure. Further indications of relaxation are provided by cross sectional transmission electron microscopy (XTEM) and X-ray diffraction (XRD) [13]. Relaxation giving a high defect density with reduced crystal quality in the cap layer results in an

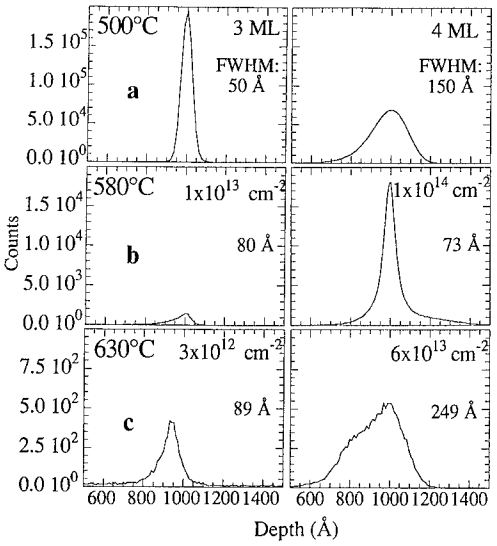

Fig. 2. Secondary ion mass spectra of the silicon content as a function of the sample depth. (a) Significant difference between the 3 and 4 ML Si layer thickness due to a relaxation of the structure in the 4 ML case. (b) Difference in the peak size is seen though the FWHM, ~75 Å, is still the same for the both samples. (c) The broadening of the silicon peak as a function of the doping concentration at high temperatures is illustrated. The broadening in the growth direction is much more pronounced in the high doping case.

enhanced diffusion of Si atoms into the surrounding layers, illustrated in Fig. 2a. The lattice relaxation at 4 ML thickness of silicon is in accordance with calculated critical layer thickness using atomistic Monte Carlo calculations [15].

Analysis by SIMS provided a clear dependence of the Si-layer peak width with the growth temperature. For $T_g = 580°C$, the full width at half maximum (FWHM) was 72–88 Å for a doping concentration in the range of 1×10^{12}–1×10^{14} cm^{-2} where we could not see any systematic dependence of Si-migration as a function of doping concentration seen in Fig. 2b. We can see in Fig. 2c that at $T_g = 630°C$, the broadening is explicitly dependent on the doping concentration. At the low doping concentration, a FWHM of ~75 Å is obtained instead of nearly 200 Å for layers above the solubility limit, as in our case, $N_{2D} = 6 \times 10^{13}$ cm^{-2}.

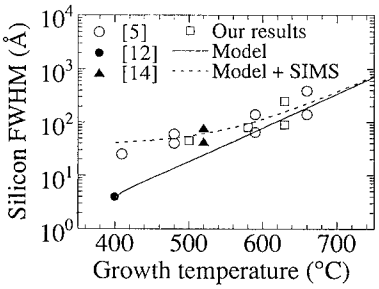

Fig. 3. The SIMS FWHM layer thickness is given as a function of growth temperature. Growth at 400°C gives an almost ideal layer [12]. The layer thickness also depends on doping concentration, particularly at higher growth temperatures [5]. Here the lower points represent low doping concentration (low 10^{12} cm^{-2}) and upper points (high 10^{13} cm^{-2}). The continuous line is a result from our model assuming a fraction of Si atom migrate into the next GaAs atomic plane. The broken line is the model plus 40 Å, taking the SIMS broadening into account. (○) [5]; (•) [12]; (▲) [14].

4. Discussion

Fig. 3 shows the silicon distribution thickness (FWHM) as a function of growth temperature. It illustrates our results and a set of measurements from references. As noted by Köhler et al. [5], there is a strong relation between the silicon distribution and both the growth temperature and doping concentration, especially for high temperatures. The lowest concentration (low 10^{12} cm^{-2}) gives the smallest spread and the highest doping concentration (low 10^{14} cm^{-2}) above the solubility limit gives the largest spread. The continuous line represents our model, described later. The line is adjusted to coincide with one monolayer thickness at 400°C [4]. The broken line shows the model plus 40 Å to account for the SIMS broadening. For $T_g < 600°C$, the FWHM is so small that a broadening contribution of the SIMS technique becomes significant.

If a fraction, f, of the atoms in the δ-doped plane migrate into the next neighbouring atomic plane, there will be a spatial distribution of Si-atoms as a result. Then the number of atoms in the plane i, is

$$N_i = \tfrac{1}{2} f^i N_0 (1 - f) \quad (1)$$

assuming there are N_0 atoms in the initial doping plane. The value of i, where the number of atoms

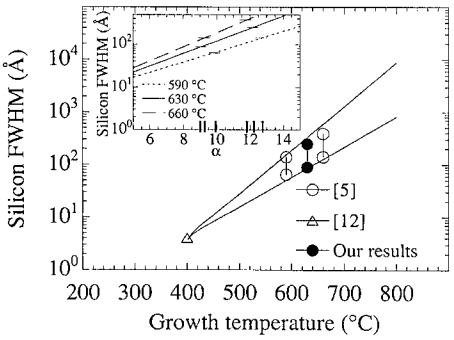

Fig. 4. The two lines in figure are the calculated values given by $\alpha = 9$ (lower) and 13 (upper). The inset shows the calculated FWHM with growth temperature and the constant α as parameters. The horizontal marks represent the experimental FWHM-values at the indicated temperatures.

has decreased to 50%, is given by $i = \ln(0.5)/\ln f$ and the corresponding thickness is $t = 2i5.65/2$, given the atomic migration is symmetric. There will be a declining concentration of the Si-atoms away from the doping plane which follows an exponential function as a relation to the growth temperature. Thus, the value of f is a function of temperature T, namely $f = 1 - \exp[g(T)]$. Since we normalised the migration to 400°C, where there is no observable increase of the thickness of the δ-plane [4]. We can write for $T_g > 400$°C,

$$g(T) = \alpha \frac{T - 400}{673}. \quad (2)$$

Here α is a coefficient which determines the fraction of the diffusion and the only constant describing how fast the migration will take place. In Fig. 3 the solid line is represented by $\alpha = 10$. In Fig. 4 results and graphs from two different α-values are presented. The inset, used as a guide for searching the appropriate α-values, shows the FWHM dependence as a function of the α-values, corresponding to measurements for $T_g > 550$°C. As shown in the figure, the smaller diffusion at a low concentration is given by $\alpha \approx 9$, indicating a lower limit of ~ 60 Å in the range 590–650°C for the low doping concentrations, [Si] $\sim (1-4) \times 10^{12}$ cm^{-2}, while the upper values from concentrations in high 10^{13} cm^{-2} range correspond to $\alpha \approx 12$.

5. Summary

At doping concentrations below 1×10^{12} cm^{-2}, the carrier concentration measured is lower than expected and a relaxation is seen between 3 and 4 ML. The silicon spread into GaAs is studied, and a model which fits diffusion as a function of temperature and growth temperature is demonstrated where we assume that a fraction of the amount of silicon diffuses into the next GaAs layer.

References

[1] E.F. Schubert and K. Ploog, Jpn. J. Appl. Phys. 24 (1985) L608.
[2] E.F. Schubert, J. Vac. Sci. Technol. A 8 (1990) 2980.
[3] G. Delgado, J. Johansson, A. Larsson and T. Andersson, IEEE Microwave Guided Wave Lett. 5 (1995) 198.
[4] T. Suzuki, H. Goto, N. Sawaki and H.I.K. Hara, Appl. Surf. Sci. 82/83 (1994) 103.
[5] K. Köhler, P. Ganser and M. Maier, J. Crystal Growth 127 (1993) 720.
[6] R. Rodrigues, P.S.S. Guimarães, J.F. Sampaio, R.A. Nogueira, A.T. Oliveira Jr, I.F.L. Dias, J.C. Bezerra, A.G. de Oliveira, A.S. Chaves and L.M.R Scolfaro, Solid State Commun. 78 (1991) 793.
[7] J.E. Cunningham, T.H. Chiu, B. Tell and W. Jan, J. Vac. Sci. Technol. B 8 (1990) 157.
[8] E.F. Schubert, H.S. Luftman, R.F. Kopf, R.L. Headrick and J.M. Kuo, Appl. Phys. Lett. 57 (1990) 1799.
[9] O. Brandt, G.E. Crook, K. Ploog, J. Wagner and M. Maier, Appl. Phys. Lett. 59 (1991) 2730.
[10] J. Maguire, R. Murray, R.C. Newman, R.B. Beall and J.J. Harris, Appl. Phys. Lett. 50 (1987) 516.
[11] R. Murray, R.C. Newman, M.J.L. Sangster, R.B. Beall, J.J. Harris, P.J. Wright, J. Wagner and M. Ramsteiner, J. Appl. Phys. 66 (1989) 2589.
[12] L. Hart, R. Murray, R.C. Newman, R.B. Beall and J.J. Harris, Appl. Phys. Lett. 50 (1987) 516.
[13] J.V. Thordson, P. Songpongs, G. Swenson and T.G. Andersson, J. Crystal Growth 150 (1995) 696.
[14] R.B. Beall, J.B. Clegg and J.J. Harris, Semicond. Sci. Technol. 3 (1988) 612.
[15] B.W. Dodson and P.A. Taylor, Appl. Phys. Lett. 49 (1986) 642.

ELSEVIER

Journal of Crystal Growth 175/176 (1997) 238–243

JOURNAL OF CRYSTAL GROWTH

Determination of $Al_xGa_{(1-x)}As$ composition: the MBE perspective

Z.R. Wasilewski[a,*], M.M. Dion[a], D.J. Lockwood[a], P. Poole[a], R.W. Streater[b], A.J. SpringThorpe[b]

[a] *Institute for Microstructural Sciences, National Research Council of Canada, Montreal Road, Ottawa, Ontario, Canada, K1A 0R6*
[b] *Nortel Technology[1], P.O. Box 3511, Station C, Ottawa, Ontario, Canada, K1Y 4H7*

Abstract

Although the $Al_xGa_{(1-x)}As$ alloy system has been extensively investigated, there are still considerable uncertainties in measuring the value of x. Here a new $Al_xGa_{(1-x)}As$ calibration structure, grown by molecular beam epitaxy, has been used to establish unambiguous alloy compositions. Such 'standard' $Al_xGa_{(1-x)}As$ layers were measured by high-resolution X-ray diffraction, photoluminescence, and Raman spectroscopy to determine the compositional variations of the measured physical parameters. The formulae provided give a reliable calibration base for other characterization tools. A detailed analysis of the X-ray results shows that Vegard's law does not hold for the variation of the $Al_xGa_{(1-x)}As$ lattice constant with x.

PACS: 61.10. – i; 62.20.Fe; 68.35.Dv; 68.55.Bd; 78.30 – j; 78.55. – m; 78.55.Cr

Keywords: AlGaAs; GasAs; Composition; MBE; X-ray diffraction; PL; Raman spectroscopy

1. Introduction

Of all the semiconductor materials used in the electronics industry, the $Al_xGa_{(1-x)}As$–GaAs alloy system is arguably second only to silicon in terms of its scientific and technological importance. As the properties of $Al_xGa_{(1-x)}As$ strongly depend on its aluminum content, it is not surprising that much effort has been put into establishing reliable ways of measuring it. Of all the characterization tools available, high-resolution X-ray diffraction (HRXRD), photoluminescence (PL), and Raman spectroscopy have proved to be the most popular due to their non-destructive character. HRXRD and PL are particularly useful when very high compositional resolution is needed. However, among the multitude of equations proposed over the last 20 years to relate observed peak positions to the aluminum content of the layer, many are mutually inconsistent. The increasing technological importance of $Al_xGa_{(1-x)}As$ has spurred renewed activity in the

* Corresponding author. Fax: +1 613 941 4667; e-mail: zbig.wasilewski@nrc.ca.

[1] Formerly Bell-Northern Research.

0022-0248/97/$17.00 Copyright © 1997 Elsevier Science B.V. All rights reserved
PII S0022-0248(96)01037-8

area. In spite of this effort, the divergence between different measurements has actually widened. The scatter of proposed AlAs material parameters needed for HRXRD interpretation is presently such [1–6] that the same layer can be assessed as having either 30% or 34% of aluminum content depending on the individual choice of parameters. In the context of molecular beam epitaxy (MBE) such scatter is unacceptable, since, if used as a feedback in growth calibration, it can in some cases lead to an error in the AlAs growth rate approaching 20%. In a more general context this uncertainty causes serious problems in establishing an effective device development loop: design → growth → fabrication → testing → design, particularly when some or all of the stages are contracted out.

The composition calibration and measurement scheme described in the present paper aims at providing a much needed common platform for both growers and users of epitaxial $Al_xGa_{(1-x)}As$ layers. A specially designed $Al_xGa_{(1-x)}As$ calibration structure, grown by MBE, has been used to establish unambiguous alloy compositions. Such 'standard' $Al_xGa_{(1-x)}As$ layers were measured by HRXRD, PL, and Raman spectroscopy to determine the compositional variations of the measured physical parameters. The structure design relies on the well established, yet unique, combination of three features of solid source MBE growth of $Al_xGa_{(1-x)}As$, namely (i) excellent crystalline quality of layers, (ii) excellent layer stoichiometry and (iii) unity sticking coefficient for both Ga and Al in the entire composition range [7]. We have ensured (i)–(iii) simultaneously by growing $Al_xGa_{(1-x)}As$ layers at 590°C, with 2.8–3.2 Å/s growth rates and with an As_2 overpressure only slightly higher than the minimum necessary to sustain As-stabilized reconstruction over the entire layer surface. Satisfying (ii) and (iii) means that the $Al_xGa_{(1-x)}As$ composition x is accurately given by $x = \Phi_{Al}/(\Phi_{Al} + \Phi_{Ga})$, where Φ_{Al} and Φ_{Ga} are the Al and Ga fluxes at the given location on the wafer, respectively. The excellent crystalline quality of GaAs and AlAs (i), along with (ii) and (iii), allows Φ_{Al} and Φ_{Ga} to be calculated accurately from the local growth rates of GaAs and AlAs layers embedded in the same structure as the $Al_xGa_{(1-x)}As$ layer. With this approach, only one factor may cause an error in the calculated composition of $Al_xGa_{(1-x)}As$, namely the possible deviation of Φ_{Al} and Φ_{Ga} from their actual values during the growth of the $Al_xGa_{(1-x)}As$ layer. This can be due to either poor flux stability or flux transients on opening the Ga or Al shutter to initiate GaAs or AlAs growth. The flux stability in our system over the time needed to grow the structures used here is better than 1% with a systematic drift due to the cell charge depletion of less than 0.3% (decrease of flux for Ga and increase for Al). The design of the effusion cells and their placement with respect to their shutters [8] gives flux transients on opening the Ga and Al shutters of less than 1.5%. The design of the calibration structures was such that the influence of these relatively small shutter transients on the measured growth rates was practically eliminated. The structures consisted of a 10 000 Å GaAs layer with 10 equally spaced 10 Å AlAs X-ray marker layers, followed by a 2 μm thick $Al_xGa_{(1-x)}As$ layer, and then a 4000 Å AlAs layer with 20 equally spaced 10 Å $Al_xGa_{(1-x)}As$ X-ray marker layers. The structures were grown on a 2000 Å GaAs buffer and capped with a 50 Å GaAs layer. The thicknesses are quoted for the wafer center. The periodic nature of the bottom and top layers used for sampling the GaAs and AlAs growth rates allowed the growth rates and the corresponding atomic fluxes to be measured locally, with a relative accuracy of better than 0.1%, using HRXRD. As the $Al_xGa_{(1-x)}As$ layers under investigation were sandwiched between such GaAs and AlAs 'rulers', their local X-ray signatures were measured at the same time as the local Ga and Al fluxes used to calculate the $Al_xGa_{(1-x)}As$ composition. Since the stability of the Ga and Al fluxes throughout the growth of the structure is crucial in this approach, we have performed high-precision SIMS measurements [8] of the structures studied. These measurements confirmed that the Ga and Al fluxes were stable within the accuracy of the measurement (better than 1%), giving an estimate of the maximum error for the derived local Al compositions of $\pm$ 0.0015. Three structures with such an 'internal' composition standard were grown for the purpose of the present study. Two of these were grown without substrate rotation and provided continuous $Al_xGa_{(1-x)}As$ compositional ranges of 0.28–0.40 and 0.60–0.72, as

well as GaAs and AlAs signatures in X-ray, PL and Raman experiments. One reference layer ($x = 0.154$) and a number of supplementary $Al_xGa_{(1-x)}As$, GaAs and AlAs layers were grown on rotating substrates. Full details of the X-ray, PL and Raman measurements and their analysis are given elsewhere [8]. Below we present the summary of our results for these three experimental techniques.

2. High resolution X-ray diffraction

The X-ray rocking curves were acquired with a Philips Materials Research Diffractometer in the five-crystal configuration using a four-crystal Ge(2 2 0) monochromator and Cu-Kα_1 radiation. All rocking curves discussed in the present paper were obtained at 293 K with the (4 0 0) symmetrical reflection.

Shown in Fig. 1 is the compositional dependence of the angular splitting $\Delta\theta$ between the Bragg peaks for the $Al_xGa_{(1-x)}As$ layer and the GaAs substrate measured in our experiments. The observed dependence can be described very well with a phenomenological second-order polynomial:

$$\Delta\theta(x) = 420x - 46.5x^2 \text{ arcsec},$$

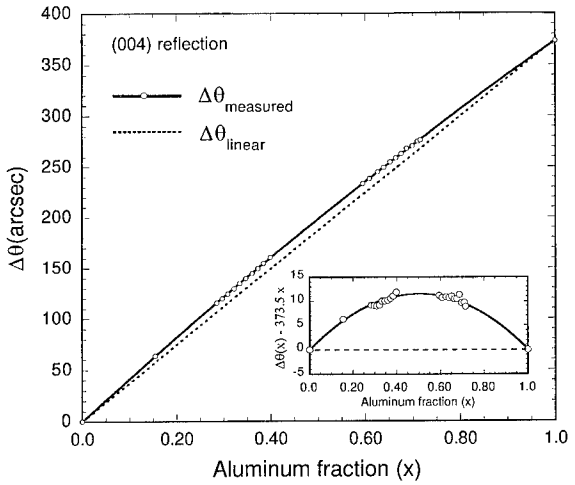

Fig. 1. AlAs–GaAs peak splitting, $\Delta\theta$, versus aluminum fraction, x. The inset shows the difference in peak splitting between the non-linear least-squares fit to the data and the linear relation.

with an R-factor of 0.99998 (least-squares algorithm fit). Note the very small scatter of the experimental points as illustrated by the R-factor being very close to one. All experimental points shown come from MBE layers grown on (1 0 0) GaAs semi-insulating (SI) vertical gradient freeze (VGF) substrates. We find that undoped GaAs MBE layers are lattice-matched to this type of substrate within 0.000022 Å. Thus for a thick $Al_xGa_{(1-x)}As$ layer (thicker than about 1.5 μm) $\Delta\theta \to 0$ for $x \to 0$. This is not the case for similar layers grown on n^+ VGF substrates where we find $\Delta\theta \to 5$–6 arcsec with $x \to 0$. The complete analysis of our X-ray results using a second-order approximation for $\Delta\theta$ [9] along with $a^{\circ}_{GaAs} = 5.65338$ Å for SI VGF GaAs substrates [10], and experimental values of the Poisson ratios for GaAs, $\nu_{GaAs} = 0.311$ [4, 6, 11], and AlAs, $\nu_{AlAs} = 0.325$,[2] gives the following expressions for the compositional dependence of the unstrained $Al_xGa_{(1-x)}As$ lattice constant $a^{\circ}_{AlGaAs}(x)$, and Poisson ratio $\nu_{AlGaAs}(x)$:

$$a^{\circ}_{AlGaAs}(x) = 5.65338 + 9.29 \times 10^{-3}(x - 0.134x^2) \text{ Å},$$

$$\nu_{AlGaAs}(x) = 0.311 + 0.014x .$$

The small quadratic term in the expression for $a^{\circ}_{AlGaAs}(x)$ demonstrates that *Vegard's law does not hold for the $Al_xGa_{(1-x)}As$ material system.* The above expression gives an AlAs free lattice parameter of 5.66143 Å at 293 K, or a value of 1.424×10^{-3} for the free lattice parameter mismatch between semi-insulating GaAs and AlAs, in good agreement with the powder diffractometry data [13, 14] and recent measurements performed on epitaxial AlAs layers [2]. However, in the case of commercially available X-ray rocking curve simulation software, Vegard's law is assumed in calculating the layer strain from the supplied layer composition. We find that correct lattice distortions (and corresponding rocking curves) are calculated with such programs, provided a different set of material parameters is chosen for AlAs, namely $a^{\circ}_{AlAs} = 5.66273$ Å

[2] As three independent recent evaluations of the AlAs Poisson ratio are available we choose its average value of 0.325 (0.322 ± 0.005 [2]; 0.324 ± 0.004 [1]; 0.328 ± 0.004 [12]) which lies within the error bars quoted in all three reports.

and $\nu_{AlAs} = 0.255$.[3] It should be stressed that the latter set has *only* a 'virtual' character, serving as a convenient intermediate stage connecting the layer composition x with the vertical lattice mismatch $\varepsilon_\perp$ between GaAs and $Al_xGa_{(1-x)}As$. When simulating rocking curves for the epitaxial layers grown on GaAs substrates mismatched with respect to the undoped MBE GaAs, a 'new' GaAs substrate material entry with the appropriate lattice parameters should be made in the program's library. Also, in order to avoid large errors in the layer composition, great care must be taken when interpreting rocking curves from doped layers or layers grown in conditions that do not guarantee stoichiometry. As pointed out in previous studies, many other precautions have to be taken to ensure a correct interpretation of rocking curves. These include (i) using full dynamical simulations for layers thinner than 1 μm [15], aluminum compositions lower than about 0.1, or multilayer structures; (ii) incorporating into the simulation an accurate value of the surface off-cut or collecting two rocking curves for azimuthal angle $\phi = 0°$ and $\phi = 180°$ [4, 6]; (iii) making sure that the layer is fully strained or supplementing the (0 0 4) symmetric rocking curve with a complete set of (3 3 5) asymmetric rocking curves [2, 12]; (iv) making sure that the parameters used are corrected for the measurement temperature (GaAs and AlAs lattice constants can be corrected by using published temperature coefficients of their respective lattice parameters [13]).

3. Low-temperature PL

Photoluminescence measurements were done using a grating spectrometer with a 0.2 meV energy resolution equipped with a liquid N_2-cooled CCD camera. The samples were mounted stress-free on the cold finger of the cryostat and kept at $T = (8 \pm 1)$ K. Very low excitation power densities, from 0.01 to 10 W/cm^2, were used for all measurements. For the optical measurements (PL and Raman) we use the structures described earlier along with their accurate compositional maps established during the HRXRD measurements. As in previous studies [16–20] we measured the dependence of the donor-bound exciton (D°, X) transition energy on the layer composition x. We find a purely linear variation of this energy for both direct, $x < 0.38$ (40 experimental points, R-factor of 0.9998), and indirect, $x > 0.40$ (46 experimental points, R-factor 0.9995) band-gap compositional ranges:

$$E^{\Gamma}_{(D^\circ,X)}(x) = 1.515 + 1.403x \text{ eV} \quad \text{for } x \in \{0,0.38\},$$

$$E^{X}_{(D^\circ,X)}(x) = 1.949 + 0.250x + \delta_D \text{ eV}$$

$$\text{for } x \in \{0.40,1\}.$$

The δ_D parameter in the second equation indicates that in this case many components may contribute to the (D°, X) transition [8]. These components most likely originate from the perturbation of the exciton binding energy by the short-range potential of the particular type of defect to which the exciton is bound (the so-called chemical shifts). The value of δ_D can be as large as 20 meV, depending on the defect type. The presence of such a correction makes layer composition determination difficult for the case of indirect band gap $Al_xGa_{(1-x)}As$, unless the defect responsible for the transition has been identified.

A number of precautions must be taken before a reliable layer composition can be deduced from the low-temperature PL spectrum, such as avoiding strain due to the sample mounting on the cold stage or avoiding excessively high laser pumping power. Also, the technique is accurate only when the donor-bound exciton transition can be identified positively in the spectrum. This is the case only for high-quality undoped $Al_xGa_{(1-x)}As$ layers, where the (D°, X) transition gives the narrowest line at the high-energy end of the PL spectrum.

4. Raman spectroscopy

The Raman scattering experiments were carried out at a temperature of 295 K in a quasi-backscattering geometry [21] with the incident light at an

[3] These values were calculated using the popular tangential approximation to connect the measured $\Delta\theta$ with the perpendicular strain in the layer [4, 6, 9]. If the more accurate second-order approximation [9] is used, the same value of the AlAs lattice parameter is obtained with a somewhat higher value of 0.256 for the Poisson ratio.

angle of 77.7° from the normal to the sample surface. The spectra were excited with 300 mW of 530.9 nm krypton laser light. The scattered light was analyzed with a Spex 14018 double monochromator under computer control and detected with a cooled RCA 31034A photomultiplier. The spectral resolution was $1.2\,\mathrm{cm}^{-1}$ in all of the measurements. The incident light was polarized in the scattering plane while the scattered light was recorded without polarization analysis. The frequencies of the Raman peaks were found to high accuracy using a computer search algorithm [22] and each spectrum was frequency-calibrated with respect to three reference points that covered the complete scan [the laser 'zero' position, the GaAs longitudinal optic (LO) phonon peak, and AlAs LO phonon peak].

As in previous studies [23, 24], we measured the dependence of the frequencies of GaAs-like and AlAs-like LO phonon modes in $Al_xGa_{(1-x)}As$ on the layer composition x. The Raman data versus Al fraction (total of 80 experimental points) are well represented by polynomial expressions. For the GaAs-like mode, a best fit (R-factor of 0.9998) was obtained with

$$\omega_{\mathrm{LO}}^{\mathrm{GaAs}}(x) = 290.2 - 36.7x\ \mathrm{cm}^{-1}.$$

For the AlAs-like mode, the best least-squares fit (R-factor of 0.9995) was obtained with

$$\omega_{\mathrm{LO}}^{\mathrm{AlAs}}(x) = 364.7 + 46.7x - 9.4x^2\ \mathrm{cm}^{-1}.$$

It is clear from the relatively small slopes of the measured dependencies, and the fact that it is difficult to normally maintain Raman spectrometer calibrations to better than $\pm 0.4\,\mathrm{cm}^{-1}$, that the compositional accuracy which can be obtained with this method is ± 0.01 at best. Although the accuracy is worse than that expected from properly carried out X-ray measurements or low-temperature PL, the technique is more robust as there is less possibility for misinterpretation of the data. Also, this technique, unlike X-ray or PL, can be used to derive compositions of very thin layers (less than 3 nm in thickness), without the need for significant corrections [25].

5. Conclusions

We have performed compositional studies of $Al_xGa_{(1-x)}As$ using HRXRD, low-temperature PL and Raman spectroscopy. The method of compositional calibration chosen relies only on the linearity of time and space measurements. In this way, possible errors in empirical or theoretical parameters and correction factors, and uncertainties in the instrument calibration, are eliminated. This reliable measurement of the layer composition, along with the very low scatter in the experimental points for all of the techniques used, gives the most accurate compositional dependences available to date.

The formulae provided should give a reliable calibration base for other important characterization tools, such as SIMS or ellipsometry. They should also allow many existing discrepancies in $Al_xGa_{(1-x)}As$ characterization, processing and modeling – all of which rely on knowing the correct $Al_xGa_{(1-x)}As$ composition – to be reconciled.

Acknowledgements

The expert technical assistance of H.J. Labbé in the Raman measurements is gratefully acknowledged.

References

[1] M. Krieger, H. Sigg, N. Herres, K. Bachem and K. Köhler, Appl. Phys. Lett. 66 (1995) 682.
[2] C. Bocchi, C. Ferrari, P. Franzosi, A. Bosacchi and S. Franchi, J. Crystal Growth 132 (1993) 427.
[3] Philips, PC-HRS Simulation Software and User Guide, Version 1.3 (Philips Electronics N.V., The Netherlands, 1993).
[4] M.S. Goorsky, T.F. Kuech, M.A. Tischler and R.M. Potemski, Appl. Phys. Lett. 59 (1991) 2269.
[5] K.H. Chang, C.P. Lee, J.S. Wu, D.G. Liu, D.C. Liou, M.H. Wang, L.J. Chen and M.M. Marais, J. Appl. Phys. 70 (1991) 4877.
[6] K. Tanner, A.G. Turnbull, C.R. Stanley, A.H. Kean and M. McElhinney, Appl. Phys. Lett. 59 (1991) 2272.
[7] E.M. Gibson, C.T. Foxon, J. Zhang and B.A. Joyce, Appl. Phys. Lett. 57 (1990) 1203.
[8] Z.R. Wasilewski, M.M. Dion, D.J. Lockwood, P. Poole, R.W. Streater and A.J. SpringThorpe, J. Appl. Phys. 81 (1997) 1683.

[9] M. Servidori, F. Cembali, R. Fabbri and A. Zani, J. Appl. Cryst. 25 (1992) 46.
[10] X. Liu, AXT Data, 1996.
[11] M. Grimsditch, R. Bhadra, I.K. Shuller, F. Chambers and G. Devane, Phys. Rev. B 42 (1990) 2923.
[12] R.P. Leavitt and F.J. Towner, Phys. Rev. B 48 (1993) 9154.
[13] M. Ettenberg and R.J. Paff, J. Appl. Phys. 41 (1970) 3926, and references therein.
[14] E. Estop, A. Izrael and M. Sauvage, Acta Cryst. A 32 (1976) 627.
[15] L. Tapfer and K. Ploog, Phys. Rev. B 33 (1986) 5565.
[16] T.F. Kuech, D.J. Wolford, R. Potemski, J.A. Bradley, K.H. Kelleher, D. Yan, J.P. Farrell, P.M.S. Lesser and F.H. Pollak, Appl. Phys. Lett. 51 (1987) 505.
[17] N.C. Miller, S. Zemon, G.P. Werber and W. Powazinik, J. Appl. Phys. 57 (1984) 512.
[18] G. Olegart, R. Schwabe, M. Heider and B. Jacobs, Semicond. Sci. Technol. 2 (1987) 468.
[19] G. Olegart, R. Mitdank and P. Heidborn, Semicond. Sci. Technol. 8 (1993) 1966.
[20] S. Adachi, J. Appl. Phys. 58 (1985) R1.
[21] D.J. Lockwood, M.W.C. Dharma-Wardana, J.-M. Baribeau and D.C. Houghton, Phys. Rev. B 35 (1987) 2243.
[22] J.W. Arthur, J. Raman Spectrosc. 5 (1976) 2.
[23] G.S. Solomon, D. Kirillov, H.C. Chui and J.S. Harris, Jr., J. Vac. Sci. Technol. B 12 (1994) 1078.
[24] N. Saint-Cricq, G. Landa, J.B. Renucci, I. Ardy and A. Muñoz-Yague, J. Appl. Phys. 61 (1987) 1206.
[25] E. Molinari, S. Baroni, P. Giannozzi and S.D. Gironcoli, in: Light Scattering in Semiconductor Structures and Superlattices, Eds. D.J. Lockwood and J.F. Young (Plenum, New York, 1991) p. 39.

ELSEVIER

Journal of Crystal Growth 175/176 (1997) 244–249

JOURNAL OF CRYSTAL GROWTH

Monitoring Ga and In desorption and In surface segregation during MBE using atomic absorption

Andrew Jackson[a,*], Paul Pinsukanjana[b], Larry Coldren[b], Arthur Gossard[a]

[a] *Materials Department, University of California, Santa Barbara, California 93106, USA*
[b] *ECE Department, University of California, Santa Barbara, California 93106, USA*

Abstract

The use of an atomic absorption flux monitor for measuring desorbing gallium and indium atoms during MBE is demonstrated. Several short InAs layers of known thickness were grown on a GaAs substrate. By desorbing these layers in a controlled substrate temperature ramping cycle, a calibration between the atomic absorption signal and desorption rate was determined. This calibration was then used to measure the desorption of excess indium that segregates to the surface during the growth of InGaAs for a range of In compositions. The atomic absorption signals were also measured for growth of GaAs and InGaAs at elevated substrate temperatures where the cation sticking coefficients are less than unity.

1. Introduction

Atomic absorption spectroscopy has recently been developed into a reliable and accurate in-situ monitor for measuring atomic beam fluxes of group III elements during MBE [1–3]. We have developed an atomic absorption optical-based flux monitor (OFM) capable of measuring growth rates accurately with a precision as high as 0.005 ml/s. By using the OFM signal for feedback control to operate the molecular beam shutters, we have achieved layer thickness control of better than 1%. This sensitivity allows us not only to monitor and control growth accurately, but also to observe desorbing fluxes of atoms from a heated substrate. In this paper we demonstrate in-situ monitoring of thermal desorption of indium and gallium atoms from a GaAs substrate.

Recently, line-of-sight mass spectrometry has been used to perform temperature-programmed desorption (TPD) analysis of surface-segregated indium from InGaAs [4]. This involves raising the substrate temperature after the growth of InGaAs which causes the excess surface indium to flash off. We have been able to perform TPD analysis using atomic absorption as an alternative to mass spectrometry. The desorption rate can be quantified by evaporating thin InAs films and correlating the thickness with the integrated atomic absorption signal. We have measured the surface-segregated

* Corresponding author.

0022-0248/97/$17.00 Copyright © 1997 Elsevier Science B.V. All rights reserved
PII S0022-0248(96)01232-8

indium population this way for several indium compositions.

We have also studied the growth of GaAs and InGaAs at high substrate temperatures where the sticking coefficient is less than unity. To monitor growth under these conditions, we need to understand better how the atomic absorption signal changes as the sticking coefficient drops. We have investigated the extent of this change by measuring absorption during growth at elevated substrate temperatures. We were also able to extract energy barriers for desorption from these measurements.

2. Experimental procedure

A more detailed description of the apparatus is given elsewhere [2]. The optical flux monitor (OFM) uses atomic emission lines from Al, Ga, and In hollow cathode lamps. The light from each of the three lamps is mechanically chopped at a different frequency and combined into a single beam using a trifurcating fiber bundle. This beam is then split into a reference beam and a probe beam, each coupled into an optical fiber. The probe beam passes through the growth chamber above the substrate and is then reflected back by a pair of flat mirrors. The returning probe beam is collected by another optical fiber which carries the beam to the signal detector. This dual pass configuration increases the measured absorption signal for a given flux. The signal is measured using a PMT and lock-in amplifiers. Another PMT measures the reference beam, which does not pass through the chamber, to account for lamp intensity drifts. A Macintosh Quadra 840AV computer is used for data acquisition.

The samples were grown on 2″ (1 0 0) semi-insulating GaAs substrates in a Varian Gen II MBE system. For the GaAs grown at elevated substrate temperatures, a 3″ wafer was used. The As_2 pressure was approximately 6.5×10^{-6} Torr throughout the experiments. Substrate temperature was measured using an optical pyrometer. The substrate was rotated at 20 rpm.

During growth, material is deposited on the ring-shaped region of the substrate holder surrounding the wafer. Upon heating, any material that desorbs from this ring would cause errors in the measured signal. To avoid this source of error, we used an EPI Uniblock with a stack of four ring-shaped molybdenum plates behind the front spring plate. These rings thermally insulated the front surface of the substrate holder, keeping temperatures below the range where significant desorption occurs. By comparing the difference in the measurements performed with and without the insulating rings, we verified that there was no significant desorption from the front of the insulated substrate holder.

3. Results and discussion

To calibrate the signal for growth, RHEED oscillations and atomic absorption were measured simultaneously. This calibration is not accurate for desorbing atoms, however, since the atoms leave the substrate in all directions, instead of in a nearly collimated beam. This creates a lower density of atoms and decreased atomic absorption when observing an outgoing flux instead of an incident flux. To calibrate the atomic absorption signal for desorbing atoms, InAs layers of a known thickness were desorbed by ramping the substrate through a controlled temperature cycle. The integrated absorption signal was then correlated with the total amount of InAs desorbed, assuming that the desorption rate is linearly proportional to atomic absorption. For small absorption values, a straight line is a very close approximation to the actual curve. Fig. 1 shows a typical desorption signal along with the substrate temperature ramping cycle. The calibration curve derived from measuring many of these peaks is shown in Fig. 2. Fitting these data with a straight line through the origin gives a desorption rate in monolayers/second of $r_{\text{desorption}} = (20.8)\gamma$, where γ is the atomic absorption. A desorbing flux absorbs only about 17% of the light of an equivalent incident flux during growth.

To observe indium segregation, InGaAs layers of several different compositions were grown at a substrate temperature of 524 ± 2°C. The layers were 30–40 monolayers thick so that the surface-segregating indium reached a steady-state value. GaAs

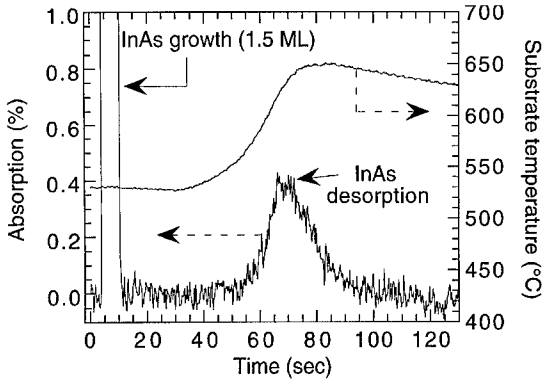

Fig. 1. Absorption signal during growth and desorption of 1.5 monolayers of InAs on GaAs. During growth, the absorption is about 6% which falls off scale on this plot. Substrate temperature as measured by optical pyrometry is also plotted. The small ripple in the substrate temperature measurement is due to the substrate rotation of 20 rpm.

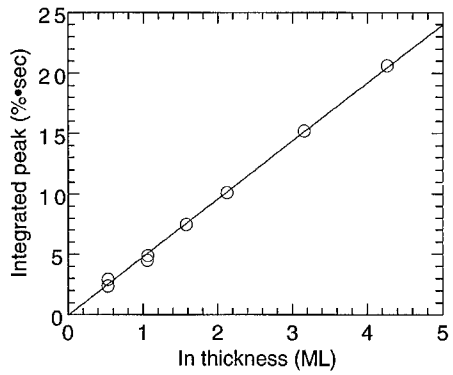

Fig. 2. Integrated indium desorption peak intensity vs. deposited InAs thickness. These data are used as a calibration between atomic absorption and desorption rate.

buffer layers 500 Å thick were grown between each of the InGaAs layers. After the growth of each InGaAs layer, the excess indium θ_{In} that segregates to the growing surface was desorbed using the same temperature ramping cycle that was used in the above calibration. Integrating the desorption peak gave the total desorbed indium for each composition. These data are shown in Fig. 3.

At an indium composition of $x = 0.22$ we measured a floating indium layer of 1.6 ML at 524°C. This agrees closely with previously measured

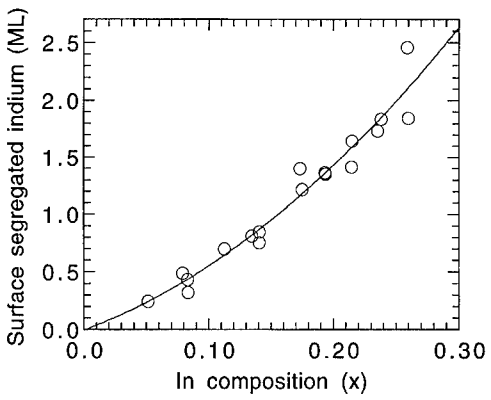

Fig. 3. Desorbed surface-segregated indium vs. composition x for $In_xGa_{(1-x)}As$.

values of 1.4 ML [5] at 520°C for $x = 0.23$ and 1.6 ML [4] at 530°C for $x = 0.22$.

The segregation ratio R can be calculated from the data in Fig. 3. The monolayer thickness of the surface-floating InAs $\theta_{In}(n)$ after n monolayers of growth, where x_0 is the nominal indium composition is [5]

$$\theta_{In}(n) = x_0 R(1 - R^n)/(1 - R). \quad (1)$$

For large n, the segregation ratio R is

$$R = \theta_{In}(n)/(x_0 + \theta_{In}(n)). \quad (2)$$

We have measured a composition-dependent segregation ratio at 524°C that ranges from 0.83 to 0.89 between $x = 0.05$ and 0.26. This is within the range of previously measured values [5–11] which range from about 0.7–0.9. Discrepancies among measurements could be due to many factors including substrate temperature and composition uncertainties. There are also probably variations due to the different measurement techniques. It is not clear, for example, if the desorbed indium during TPD includes only the surface InAs or if some In from the top one or two monolayers also diffuses to the surface and desorbs.

Another set of experiments was done to observe GaAs and InGaAs growth at elevated substrate temperatures where the sticking coefficients are less than unity. During growth, we cannot separately observe incident and desorbing atomic fluxes. Both fluxes contribute to the observed atomic

absorption. We can still, however, extract meaningful information about the sticking coefficients by either measuring RHEED and absorption simultaneously or by assuming a constant output flux from the effusion cell.

RHEED intensity oscillations and atomic absorption were measured simultaneously during the growth of GaAs over a range of substrate temperatures. The substrate was not rotated during this growth so that RHEED oscillations could be measured. At higher substrate temperatures, there are two sources of error in calculating the growth rate from the atomic absorption. As the substrate temperature is raised, some of the atoms re-evaporate, reducing the growth rate for a given incident flux. Additionally, the re-evaporating atoms increase the density of atoms in front of the substrate, raising the absorption. Fig. 4a shows a plot of the real growth rate (measured by RHEED) divided by the calculated growth rate (calculated from atomic absorption) over a range of substrate temperatures. Raising the substrate temperature to 640°C creates an error of about 1% in the calculated GaAs growth rate using the OFM. At typical growth temperatures (between 580 and 600°C) the error due to re-evaporating Ga atoms is negligible.

Fig. 4b shows an Arrhenius plot of these data. From the slope we calculated an activation energy for desorption of 3.3 ± 0.3 eV. We do not know the correlation between desorbing Ga flux and atomic absorption, but the energy barrier we calculated is insensititive to the absolute desorption rate. Our measurement agrees closely with the 3.4 eV calculated by Heckingbottom [12] for growth under As-stabilized surfaces and falls within the range of previously reported [13–19] experimental values (2.9–4.8 eV).

To observe indium sticking coefficients of less than unity, $In_{0.21}Ga_{0.79}As$ was grown on a 2″ GaAs(1 0 0) wafer at several substrate temperatures between 520 and 710°C. The composition ($x = 0.21$) and growth rate (1.23 ml/s) of the InGaAs was assumed to be constant throughout the experiment. The indium atomic absorption vs. substrate temperature is plotted in Fig. 5. At about 680°C the atomic absorption signal seems to level off, indicating that all of the indium is re-evaporating from the substrate. We can estimate the correlation between atomic absorption and desorption rate from these data by subtracting the absorption signal under unity sticking coefficient from the absorption signal where all of the indium is re-evaporating. We assume that growth rate and desorption rate are both linear with atomic absorption. Under unity sticking coefficient, the In growth rate is measured to be 0.264 ml/s. We assume that the cell output is constant so this value is also the maximum desorption rate of indium from the substrate at high temperatures. The desorption rate calculated this way is, $r_{\text{desorption}} = (20.2)\gamma$. This agrees closely with the slope of 20.8 previously calculated from integrating InAs desorption peaks.

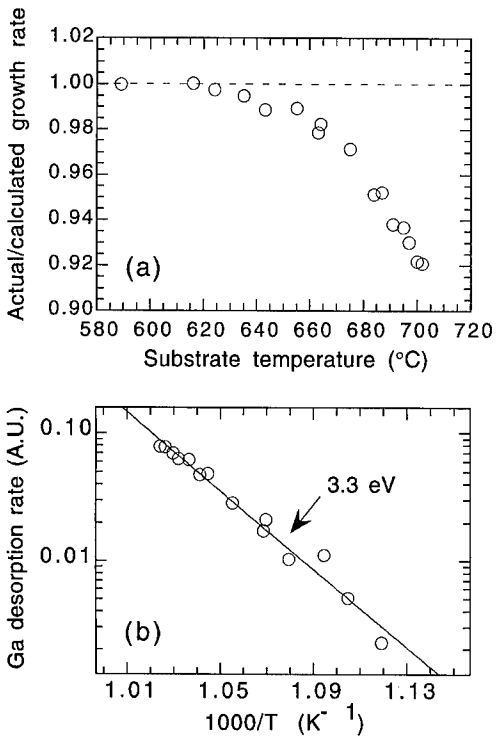

Fig. 4. (a) Actual growth rate as measured by RHEED divided by growth rate as calculated from atomic absorption. When Ga reevaporation occurs, the growth rate decreases and the atomic absorption increases. (b) Arrhenius plot of re-evaporation rate used to determine desorption activation energy.

The energy barrier for indium desorption from InGaAs should depend upon the indium composition. As the substrate temperature is raised, the composition changes and we do not see ideal

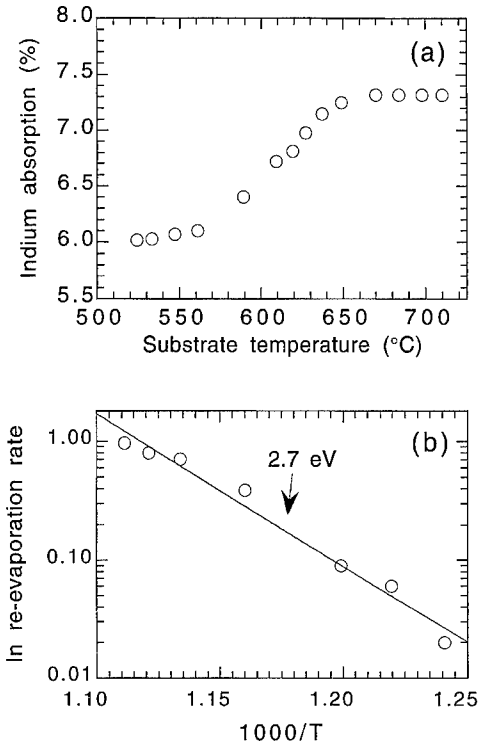

Fig. 5. (a) Indium atomic absorption during growth of $In_{0.21}Ga_{0.79}As$ at 1.23 ml/s. Above about 680°C the absorption signal saturates, indicating that all of the indium is re-evaporating. (b) Arrhenius plot of re-evaporation rate of indium. Slope indicates an energy barrier of 2.7 eV.

Arrhenius behavior. Over this entire temperature and composition range, the desorption activation energy is 2.7 eV (Fig. 5b). This falls within the range of previous measurements [13, 19–23] and is slightly greater than the 2.5 eV value [24] measured for the enthalpy of sublimation of indium.

4. Conclusion

We have demonstrated the use of an atomic absorption flux monitor for measuring desorbing Ga and In fluxes from a substrate in an MBE chamber. Although the absorption signal is lower for a desorbing flux than for an incident flux, the signal-to-noise ratio of the OFM is high enough to measure desorption of less than a single monolayer of InAs during about 45 s.

By monitoring desorbing fluxes, we have been able to measure surface-segregated indium using TPD analysis. We have also observed re-evaporation of In and Ga during growth at high substrate temperatures. Future work will include a study of Al, Ga, and In segregation and re-evaporation during the growth of the quaternary alloy, AlGaInAs, at high growth temperatures. This material is currently being investigated for use in diode lasers.

Acknowledgements

The authors would like to thank J. English for providing technical support during this experiment. This work is supported by DARPA under Optoelectronics Technology Center and the ULTRA program.

References

[1] S.A. Chalmers and K.P. Killeen, Appl. Phys. Lett. 63 (1993) 3131.
[2] P. Pinsukanjana, A. Jackson, J. Tofte, K. Maranowski, S. Campbell, J. English, S. Chalmers, L. Coldren and A. Gossard, J. Vac. Sci. Technol. B 14 (1996) 2147.
[3] C. Lu and Y. Guan, J. Vac. Sci. Technol. A 13 (1995) 1797.
[4] K.R. Evans, R. Kaspi, J.E. Ehret, M. Skowronski and C.R. Jones, J. Vac. Sci. Technol. B 13 (1995) 1820.
[5] H. Toyoshima, T. Niwa, J. Yamazaki and A. Okamoto, Appl. Phys. Lett. 63 (1993) 821.
[6] Y.C. Kao, F.G. Celii and H.Y. Liu, J. Vac. Sci. Technol. B 11 (1993) 1023.
[7] R. Kaspi and K.R. Evans, Appl. Phys. Lett. 67 (1995) 819.
[8] J.M. Moison, C. Guille, F. Houzay, F. Barthe and M.V. Rompay, Phys. Rev. B 40 (1989) 6149.
[9] K. Muraki, S. Fukatsu, Y. Shiraki and R. Ito, J. Crystal Growth 127 (1993) 546.
[10] J. Nagle, J.P. Landesman, M. Larive, C. Mottet and P. Bois, J. Crystal Growth 127 (1993) 550.
[11] H. Toyoshima, T. Niwa and J. Yamazaki, J. Appl. Phys. 75 (1994) 3908.
[12] R. Heckingbottom, J. Vac. Sci. Technol. B 3 (1985) 572.
[13] K.R. Evans, C.E. Stutz, D.K. Lorance and R.L. Jones, J. Vac. Sci. Technol. B 7 (1989) 259.
[14] A.H. Kean, C.R. Stanley, M.C. Holland, J.L. Martin and J.N. Chapman, J. Crystal Growth 111 (1991) 189.
[15] T. Kojima, N.J. Kawai, T. Nakagawa, K. Ohta, T. Sakamoto and M. Kawashima, Appl. Phys. Lett. 47 (1985) 286.
[16] J.P. Reithmaier, R.F. Broom and H.P. Meier, Appl. Phys. Lett. 61 (1992) 1222.

[17] A.J. SpringThorpe and P. Mandeville, J. Vac. Sci. Technol. B 6 (1988) 754.
[18] J.M. VanHove and P.I. Cohen, Appl. Phys. Lett. 47 (1985) 726.
[19] J. Zhang, E.M. Gibson, C.T. Foxon and B.A. Joyce, J. Crystal Growth 111 (1991) 93.
[20] T. Mozume and I. Ohbu, Jpn. J. Appl. Phys. 31 (1992) 3277.
[21] B. Goldstein and D. Szostak, Appl. Phys. Lett. 26 (1975) 685.
[22] K. Radhakrishnan, S.F. Yoon, R. Gopalakrishnan and K.L. Tan, J. Vac. Sci. Technol. A 12 (1994) 1124.
[23] J.P. Reithmaier, H. Riechert, H. Schlötterer and G. Weimann, J. Crystal Growth 111 (1991) 407.
[24] G.J. Macur, R.K. Edwards and P.G. Wahlbeck, J. Phys. Chem. 70 (1966) 2956.

ELSEVIER

Journal of Crystal Growth 175/176 (1997) 250–255

JOURNAL OF CRYSTAL GROWTH

Simultaneous in situ measurement of substrate temperature and layer thickness using diffuse reflectance spectroscopy (DRS) during molecular beam epitaxy

Y. Li, J.J. Zhou, P. Thompson, D. Pacheco, D.L. Sato, O. Arain, H.P. Lee*

Department of Electrical and Computer Engineering, University of California, Irvine, California 92717, USA

Abstract

Diffuse reflectance spectroscopy (DRS) is used for in situ measurements of temperature transient and temperature drift during MBE growth of AlAs/GaAs and InGaAs/GaAs layered structures. The experimental results are compared together with pyrometric interferometry (PI) measurement taken concurrently. Our results show that DRS is a viable method for in situ real-time monitoring of both substrate temperature and layer thickness.

Keywords: Diffused reflectance spectroscopy; In situ measurement; Temperature; Layer thickness

1. Introduction

In situ temperature and layer thickness measurements have always been integral parts of molecular beam epitaxy (MBE) technology development. Accurate monitoring of growth temperature is essential during MBE growth because the quality of epitaxial layers, growth rates and alloy composition are all dependent on growth temperature. The use of diffuse reflectance spectroscopy (DRS) for in situ temperature monitoring has been well established for GaAs substrate [1]. More recently, the method has been used for feedback control of GaAs growth at growth temperature between 500 and 600°C [2]. However, nearly all previous DRS experiments were focused on temperature measurement and were carried out on homoepitaxial GaAs growth.

In the present work, we explore DRS for (i) determination of Knudsen cell induced substrate heating over a wide temperature range between 200 and 600°C, (ii) simultaneous measurements of temperature drift and layer thickness during the growth of AlAs/GaAs layered structures, and (iii) the monitoring of surface morphology of $In_{0.18}Ga_{0.82}As$ on GaAs sample.

2. Experiment method

DRS measurement relies on nonspecular scattering of a spectroscopic probing light from the

* Corresponding author. E-mail: hplee@ece.uci.edu.

0022-0248/97/$17.00 Copyright © 1997 Elsevier Science B.V. All rights reserved
PII S0022-0248(96)01234-1

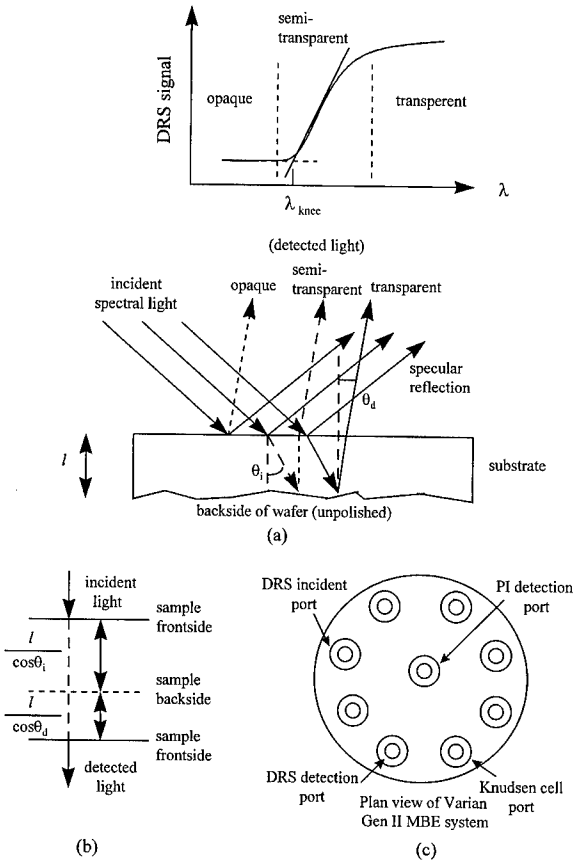

Fig. 1. The schematic of (a) the physical principle, (b) the equivalent folded structure transmission model, and (c) the measurement geometry in Varian Gen II MBE system. The optical paths of incident, specular reflected and diffused reflected light at the opaque, transparent and semi-transparent wavelengths are illustrated in part (a).

backside of the sample. In the present work, the scattering is provided by the backside of a single-polished GaAs wafer. The physical process and the equivalent transmission model (a folded structure) are shown in Fig. 1a and Fig. 1b, respectively. The working principle is very similar to that of the optical transmission measurement [3–6] but with two notable differences: (i) both the incident and the detection ports are located outside the chamber in front of the sample (at nonspecular angles), and consequently alleviate the technical difficulties of installing a light source at the backside of the substrate, and (ii) the detected probing light passes through the sample twice with a slight difference in path length. The measured DRS signal over the entire spectrum yields useful information on the sample temperature, layer thickness and surface morphology. From the cutoff wavelength (also known as knee wavelength, λ_{knee}) of the DRS signal (Fig. 1a), the band gap (Urbach edge) can be determined, from which the substrate temperature (T_s) is inferred [1]. As a temperature sensor using active light source, DRS has two major advantages over pyrometry: (i) it is capable of measuring much lower substrate temperature, and (ii) the measured data is unaffected by the background radiation in the growth chamber (such as the heated Knudsen cells in MBE). The DRS signal at the opaque wavelength is enhanced by the surface scattering of the sample and is therefore sensitive to the sample morphology. The DRS signal at the transparent wavelength, on the other hand, is sensitive to optical interference arising from layered structure, and can be used for real-time thickness and growth rate monitoring. However, the same optical interference effect also shifts λ_{knee} and causes undesirable oscillations in the temperature readout during the growth of layered structures. This complicates the measurement of true temperature change in the sample.

All growths are conducted in a Varian Gen II MBE system and the measurement geometry is shown in Fig. 1c. All samples used in this work consist of single-polished quarter of 2 in semi-insulating GaAs wafers. All wafers are indium-soldered to a 2 in molybdenum block. A commercial DRS system manufactured by Thermionics Laboratory (model DRS-1000) is used for the measurement. The DRS measured temperature is displayed in real-time after numerical processing of the spectroscopic data at the end of each scan (1060–1255 nm). The raw spectroscopic data for each scan is stored in a separate data file in an IBM PC. For the Varian Gen II MBE system, the DRS measured temperature exhibits negligible dependency on the relative positions between the incidence and detection port. In some cases, in situ narrow-band PI ($\lambda_m = 1048$ nm, $\Delta\lambda = 60$ nm) is also employed for simultaneous monitoring. A detailed description of the experimental setup for the PI apparatus can be found in Ref. [7]. All measurements were taken

without sample rotation in order to minimize uneven scattering from the sample block and the GaAs backside surface which has an anisotropic texture. Rotating the sample at 10–15 rpm causes an apparent fluctuation of DRS temperature of 5°C. This problem, however, is not intrinsic to the measurement technique itself. Using a backside diffuser on double-polished 2-in GaAs wafers, fluctuation of DRS temperature less than 1°C has been achieved for growth temperatures between 200 and 300°C [8].

3. Results and discussion

3.1. Knudsen cell induced temperature transient measurement

We have used DRS for in situ measurement of temperature transient arising from shutter opening of Ga and Si Knudsen cells at various T_s. Substrate heating induced by Knudsen cells has been observed previously from optical transmission [6], PI [9, 10], and DRS [1] measurements, but has not been systematically characterized over a wide temperature range. The results are shown in Fig. 2a and Fig. 2b. It can be seen that the temperature transient of Knudsen cell induced substrate heating becomes more significant at lowered T_s. We have also noticed that the time constants associated with the temperature transient become longer at lower temperature. The result is important for reproducible growth of low temperature (LT) GaAs and AlGaAs layers, where the exact growth temperature is difficult to determine accurately and reproducibly. We have also measured the double crystal X-ray diffraction (DCXRD) of the as-grown LT GaAs (≈0.75–1 μm) prepared at substrate temperatures between 200 and 300°C and the results are shown in Fig. 2c. The X-ray diffraction peak associated with LT GaAs layer appeared only at growth temperatures below 270°C. To our knowledge, this is the first time such a transition temperature has been identified. Given the fact that the stoichiometry of LT GaAs (and possible other III–V layers) is extremely sensitive to growth temperature, our results highlight the influence of Knudsen cell induced thermal loading on the structural properties of more complicated LT III–V layers such as GaA/AlGaAs superlattices, where switching of shutters are required.

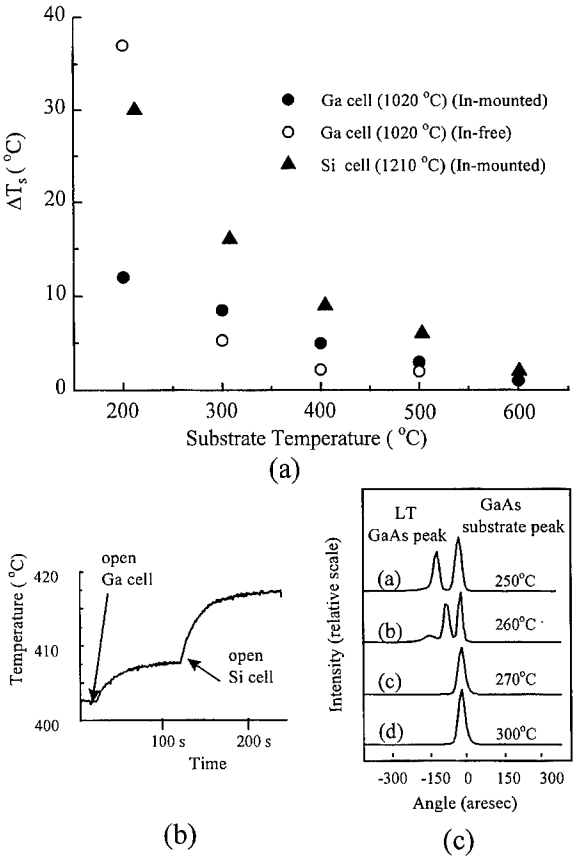

Fig. 2. Knudsen cell induced temperature and microstructural changes of LT GaAs layers versus growth temperature: (a) rise in temperature caused by the opening of the Si and Ga Knudsen cells for both In-soldered and In-free samples; (b) typical DRS measured temperature transient following the opening of Si and Ga shutters; and (c) X-ray diffraction of LT GaAs layers versus growth temperature.

3.2. Temperature drift of AlAs/GaAs layered structure

The growth of GaAs/AlAs on GaAs layered structures are also simultaneously monitored using DRS and PI. The results are shown in Fig. 3. The initial rise in T_s (label A of Fig. 3b) is attributed to the radiative heating of the sample following the

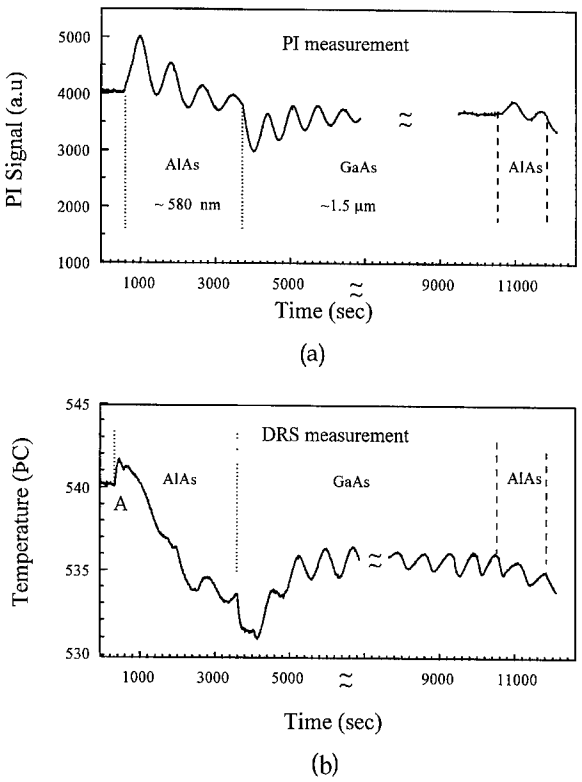

Fig. 3. Simultaneous measurements of PI (part (a)) and DRS temperature (part (b)) of thick GaAs/AlAs layered structure grown on GaAs substrate under constant thermocouple feedback control. The emissivity induced temperature drift is clearly evident. While the PI signal settles at a constant value after 1.5 μm of GaAs growth, the DRS measured temperature continues to oscillate. This is due to optical interference of the DRS signal near the knee wavelength.

opening of the Al Knudsen cell. The subsequent drift of substrate temperature during the growth of AlAs (decreasing T_s) and the GaAs overlayer (increasing T_s) is caused by the change of sample emissivity. Such temperature drift has also been noticed from previous PI measurements [9, 10]. It should be noted that the emissivity induced substrate temperature drift occurs even as the thermocouple reading remains constant. However, the DRS monitored temperature is hampered by the optical interference of the layered structures. Referring to Fig. 3, as the thickness of the GaAs overlayer exceeds 1.5 μm, the oscillatory PI signal settles at a steady-state value. The DRS temperature, on the other hand, exhibits a continuous quasi-periodic oscillation. Since PI probes the thermal radiation from the surface of the sample, optical interference vanishes when the thickness of GaAs overlayer exceeds the absorption length at the PI monitoring wavelength (estimated ≈ 1 μm for λ_m of 1048 nm). The constant PI signal in Fig. 3a is indicative that T_s has reached a steady-state value. In contrast, since the DRS signal transverse through the entire sample, optical interference near λ_{knee} does not attenuate with GaAs thickness. This results in an apparent temperature oscillation having a spatial period $\approx \lambda_{knee}/2n(\lambda_{knee})$, where $n(\lambda_{knee})$ is the refractive index of the growing layer at λ_{knee}. Using a recently developed DRS spectrum simulator (based on the transmission model shown in Fig. 1b) we have confirmed that the temperature oscillation is indeed caused by the optical interference effect [11]. Work is underway to quantify the amplitude of such temperature oscillations. For accurate monitoring of the actual temperature of a layered structure, it is important to develop a modified temperature extraction algorithm which can properly account for the interference effect.

3.3. *Interference of DRS signal in transparent wavelength*

We have also examined the evolution of the DRS signal versus time at fixed wavelength in the semi-transparent and transparent wavelength region from the time evolution of the DRS spectrum. The results are shown in Fig. 4a and Fig. 4b. These plots were retrieved from stored spectroscopic data files and therefore are not displayed in real time. At both semi-transparent and transparent wavelengths, a clear oscillation of the DRS signal versus time is observed. The signal oscillates with a spatial period $\approx (\lambda_m/2n(\lambda_m)) \cos\theta$, where θ is the angle of the effective optical path relative to the substrate normal. With proper modification of the data acquisition and storage procedure, such oscillating signal can be used for real-time thickness and growth rate monitoring of the growth process [12, 13]. A closer examination of the DRS signal at $\lambda = 1150$ nm shows a steady increase in the DC component during the growth of AlAs, followed by

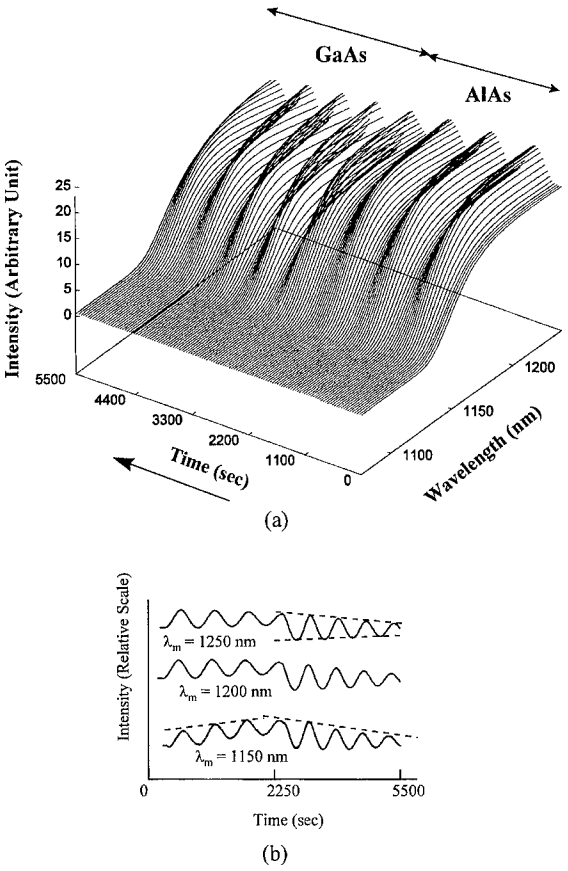

Fig. 4. Plot of DRS spectrum versus growth time for an GaAs/AlAs on GaAs layered structure. Part (b) highlights the DRS signal versus time at a fixed transparent wavelength. Such interference oscillation can be utilized for real-time layer thickness and growth rate monitoring. The asymmetrical envelope of DRS signal at 1150 nm reflects the change of sample temperature.

a decrease of the DC component during the growth of the GaAs layer (dashed line in Fig. 4b). This can be explained by a steady decrease and increase of T_s which occurred during the growth of AlAs and GaAs layers, respectively. As the temperature is decreased, λ_{knee} shifts towards shorter wavelength, and consequently results in higher DRS signal at wavelengths in the semi-transparent region. At the transparent wavelength of 1200 and 1250 nm, the envelope of the DRS signals exhibits a symmetrical attenuation during the growth of the GaAs layer. This phenomenon cannot be explained by the absorption of the GaAs layer. We suspect this to be caused by a loss of coherency of the probing light in the layered structure due to (i) a finite spread of wave vector at the incident and detection ports, (ii) the slight difference in the optical path of the folded structure, and (iii) nonuniformity of the layer thickness. The phenomenon is presently studied using the DRS spectrum simulator.

3.4. Surface scattering of InGaAs/GaAs layers

The evolution of DRS spectrum for $In_{0.18}Ga_{0.82}As$/GaAs sample and the corresponding monitored temperature are shown in Fig. 5. Enhanced absorption at longer wavelength due to epitaxial $In_{0.18}Ga_{0.82}As$ is clearly evident (see Fig. 5a). Except for the initial rise due to Knudsen cell heating, the substrate temperature changes only slightly (variation $<2.5°C$) during the entire growth process (see Fig. 5b). The result contradicts earlier reports on the growth of narrow-bandgap material on wide bandgap substrate where significant increase of substrate temperature has been measured from optical transmission measurement on In-free samples [4]. The discrepancy relates to the method in which the sample is mounted. For In-soldered sample, heat transfer to the sample remains unchanged when a narrower bandgap material is deposited. The only driving force for temperature drift originates from change of sample emissivity following the growth of $In_{0.18}Ga_{0.82}As$ layer. In contrast to AlAs on GaAs layer growth, the initial lowering of emissivity due to optical interference effect is partially balanced by increased radiation bandwidth from the $In_{0.18}Ga_{0.82}As$ layer which has narrower bandgap than GaAs. The DRS signal versus time at the opaque wavelength (1050 nm) shows a steady increase during the growth as shown in Fig. 5c. This is attributed to enhanced surface scattering of the relaxed $In_{0.18}Ga_{0.82}As$ layer. Post-growth DCXRD measurement confirms that the $In_{0.18}Ga_{0.82}As$ layer is indeed fully relaxed. The absence of a clear onset of increased DRS signal near the critical thickness is not clear at the moment [14]. We speculate that the sample is probably not oriented in a position for maximum detection of cross-hatch induced surface scattering.

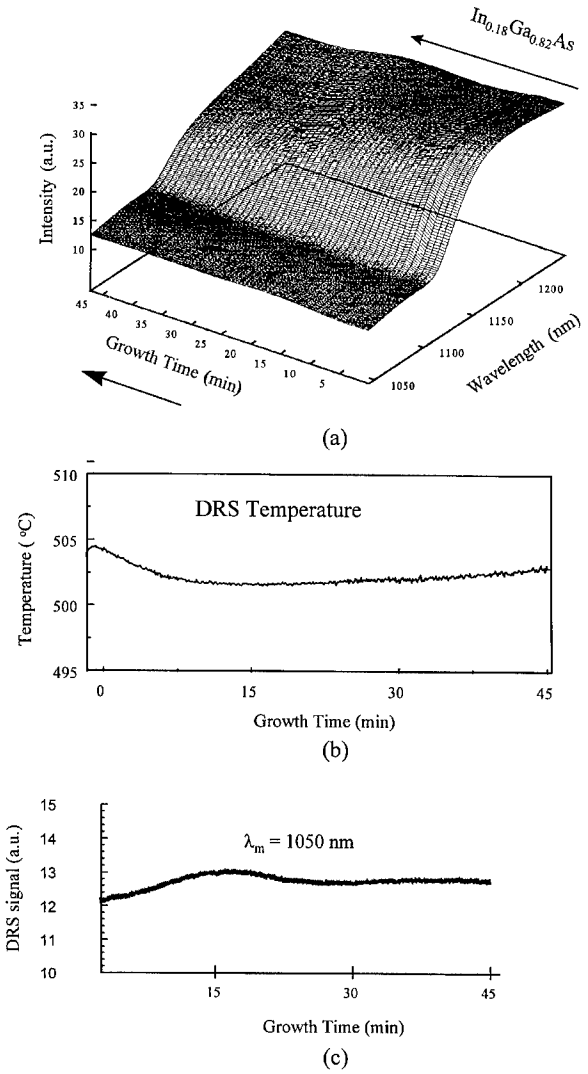

Fig. 5. DRS measurements for $In_{0.18}Ga_{0.82}As/GaAs$ layered structure: (a) DRS spectrum versus growth time, (b) the corresponding DRS measured temperature versus growth time, and (c) DRS signal at opaque wavelength ($\lambda_m = 1050$ nm) versus growth time. The increase in the DRS signal at $\lambda_m = 1050$ nm is attributed to enhanced surface scattering of the relaxed $In_{0.18}Ga_{0.82}As$ layer.

4. Conclusion

We reported the use DRS for simultaneous in situ measurements of substrate temperature, layer thickness and surface morphology during MBE growth of layered GaAs/AlAs and InGaAs on GaAs structures. The results show that with proper modification on existing data acquisition procedure, DRS has the potential to be a versatile in situ real temperature monitor for substrate temperature, layer thickness and surface morphology during the epitaxy process.

Acknowledgements

The project was supported by the UC MICRO Program and NSF Research Equipment Grant ECS-9500380.

References

[1] S.R. Johnson, C. Lavoie, T. Tiedje and J.A. Mackenzie, J. Vac. Sci. Technol. B 11 (1993) 1007; T.P. Pearsall, S.R. Saban, J. Booth and B.T. Beard, Jr., Rev. Sci. Instrum. 66 (1995) 4977.
[2] Z. Wang, S.L. Kwan, T.P. Pearsall, J.L. Booth, B.T. Beard and S.R. Johnson, Real-time noninvasive temperature control of wafer processing based on diffuse reflectance spectroscopy, presented at TMS Electronic Material Conf., University of California, Santa Barbara (1996).
[3] E.S. Hellman and J.S. Harrris, Jr., J. Crystal Growth 81 (1987) 38.
[4] B.V. Shanabrook, J.R. Waterman, J.L. Davis and R.J. Wagner, Appl. Phys. Lett. 61 (1992) 2388.
[5] J.A. Roth, T.J. de Lyon and M.E. Adel, Proc. Mater. Res. Soc., Vol. 324 (1994) 353.
[6] W.S. Lee, G.W. Yoffe, D.G. Schlom and J.S. Harris, Jr., J. Crystal Growth 111 (1991) 131.
[7] X. Liu, E. Ranalli, D.L. Sato, Y. Li and H.P. Lee, J. Vac. Sci. Technol. B 13 (1995) 742.
[8] Private communication with A. Jackson of University of California, Santa Barbara, USA.
[9] H.P. Lee, E. Ranalli and X. Liu, Appl. Phys. Lett. 67 (1995) 1824.
[10] F.G. Boebel, H. Moller, B. Hertel, H. Grothe, G. Schraud and St. Schroder, J. Crystal Growth 150 (1995) 54–61.
[11] D. Pacheco, J.J. Zhou et al., unpublished.
[12] H. Sankur, W. Southwell and R. Hall, J. Elecctron. Mater. 20 (1993) 1099–1104.
[13] K.P. Killeen and W.G. Breiland, J. Elecctron. Mater. 23 (1993) 179–183.
[14] F.G. Celii, Y.C. Kao, H.-Y. Liu, L.A. Files-Sesler and E.A. Beam, III, J. Vac. Sci. Technol. B 11 (3) (1993) 1014–1107.

ELSEVIER

Journal of Crystal Growth 175/176 (1997) 256–261

JOURNAL OF CRYSTAL GROWTH

Application of pyrometric interferometry to the in situ monitoring of $In_{0.52}Al_{0.48}As$, $In_{0.53}Ga_{0.47}As$, and quaternary alloy growth on InP substrates

R.M. Sieg*, R.N. Sacks, S.A. Ringel

Electronic Materials and Devices Laboratory, The Ohio State University, 205 Dreese Laboratory, 2015 Neil Avenue, Columbus, Ohio 43210-1272, USA

Abstract

The alloy system $In_{0.525}(Al_xGa_{1-x})_{0.475}As$, which is lattice-matched to InP, covers the technologically important wavelength range 0.8–1.6 μm, including the fiber optic communication wavelengths 1.3 and 1.55 μm. However, growth of these alloys on InP is complicated by the strong dependence of the lattice constant on In content, and would be improved by a convenient in situ method of growth monitoring. We consider the feasibility of extending the method of pyrometric interferometry (PI), whose utility is already established for $Al_xGa_{1-x}As$/GaAs, to $In_{0.52}Al_{0.48}As$, $In_{0.53}Ga_{0.47}As$, and general $In_{0.525}(Al_xGa_{1-x})_{0.475}As$ growth on InP. We find that PI provides useful information about changes in the growth rate and/or composition. The method works best for high Al content films (e.g. $In_{0.52}Al_{0.48}As$) due to the larger band-gap, and requires about 0.8 μm or thicker film growth for greatest accuracy. PI sensitivity is shown to be greater to changes in the In flux versus the Al flux. We determined the effective refractive index of $In_{0.52}Al_{0.48}As$ to be 3.515 for substrate temperature 500–550°C. The onset of In desorption as the substrate temperature is increased was also easily detected by PI.

1. Introduction

$In_{0.525}(Al_xGa_{1-x})_{0.475}As$ grown on InP provides a second lattice-matched alloy system which is compatible with conventional As-based solid source MBE, in addition to the $Al_xGa_{1-x}As$/GaAs system. $In_{0.525}(Al_xGa_{1-x})_{0.475}As$ heterostructures have several advantages over $Al_xGa_{1-x}As$/GaAs for electronic and photonic applications, including higher mobilities, larger attainable band offset, absence of D-X centers, and a band-gap range which includes the technologically important 1.3 and 1.55 μm wavelengths [1]. However, growth is complicated by the strong lattice constant compositional dependence of In-containing compounds. For example, reflection high-energy electron diffraction (RHEED) intensity oscillations on InP substrates cannot be used to determine simultaneously both the composition and the growth rate of $In_y(Al_xGa_{1-x})_{1-y}As$ grown on InP, as can be

* Corresponding author. Fax: +1 614 292 7596; e-mail: siegr@er4.eng.ohio-state.edu.

0022-0248/97/$17.00 Copyright © 1997 Elsevier Science B.V. All rights reserved
PII S0022-0248(96)00939-6

done for $Al_xGa_{1-x}As$ on GaAs. Instead, compositional and growth rate calibrations usually require ex-situ measurements such as double-crystal X-ray diffraction (DCXRD) or photoluminescence (PL). The increased difficulty in optimizing growth parameters makes some means of in situ detection of variations in growth rate and/or composition highly desirable. Pyrometric interferometry (PI) has been used for GaAs and $Al_xGa_{1-x}As$ [2–4] to monitor growth rate and composition during growth. In this article we investigate the applicability of PI to $In_{0.525}(Al_xGa_{1-x})_{0.475}As$.

2. Experimental procedure

All epitaxial growth was done in a Varian Gen II solid source MBE on 2 in (1 0 0) semi-insulating InP substrates. Growth rates were ~ 1 μm/h. Samples were mounted using In-free holders, and a sapphire backplate was used to minimize phosphorous outgassing from the back of the InP wafer. Growth temperatures were in the range 500–550°C except where noted. A relatively high dimeric arsenic flux was used (As_2/III BEP ratio $\sim$ 25:1), again to minimize any phosphorous outgassing. Hall mobility measurements indicated reasonable electrical quality of the ternary materials. For example, a Si-doped $In_{0.52}Al_{0.48}As$ film grown at 550°C gave $n = 4.3 \times 10^{16}\ cm^{-3}$ and $\mu_H = 926\ cm^2/V \cdot s$ at 297 K, and $n = 3.66 \times 10^{16}\ cm^{-3}$, $\mu_H = 981\ cm^2/V \cdot s$ at 77 K. The lack of carrier freeze-out implies a low concentration of deep levels, and in fact the Si doping efficiency was nearly identical to our epitaxial GaAs. The mobility values compare favorably with the published values [5, 6].

Initially, the lattice-matched $In_{0.53}Ga_{0.47}As$ composition was calibrated using DCXRD measurement of thick films. The In/Ga flux gauge sensitivity factor S was thus determined, and subsequently flux ratios were used for [In]/[Ga] calibration. Careful flux gauge measurements were found to reproducibly yield the lattice-matched condition within ~ 0.5 at% as verified by ex-situ DCXRD, as long as S was known to 3 significant figures. The $In_{0.53}Ga_{0.47}As$ growth rate was estimated from RHEED intensity oscillations for GaAs growth on a GaAs substrate by correcting for the additional group III flux due to the In beam (the same Ga flux is being used for both the GaAs and the $In_{0.53}Ga_{0.47}As$ layers) and the difference in unit cell volume:

$$R(In_xGa_{1-x}As) = \left(\frac{1}{1-x}\right)\left(\frac{a(x)}{a(GaAs)}\right)R(GaAs) = 2.3553R(GaAs), \quad (1)$$

where a is the lattice constant and R is the growth rate. The right-hand side applies for $x = 0.525$ and $a(x) = a(InP)$. Unity group III sticking coefficients and negligible desorption on both GaAs and InP substrates is assumed. Notice that the geometry correction involves the unit cell volume ratio. This is because all of the increase in the volume deposition rate must be taken up by the difference in the linear growth rate R. The Al flux was then calibrated for $In_{0.52}Al_{0.48}As$ by using RHEED intensity oscillations to obtain equal AlAs and GaAs growth rates on a GaAs substrate. The Al and Ga fluxes for the quaternary $In_{0.525}(Al_xGa_{1-x})_{0.475}As$ were similarly calibrated using the $Al_xGa_{1-x}As$ and GaAs RHEED growth rates to determine the $Al_xGa_{1-x}As$ growth rate and [Al]/[Ga] ratio. This procedure of combining RHEED on a sacrificial GaAs piece with beam flux rationing permits in-situ estimation of the composition and growth rate of lattice-matched $In_{0.525}(Al_xGa_{1-x})_{0.475}As$ assuming only a priori knowledge of the In/Ga flux sensitivity factor, thus minimizing the need for ex-situ DCXRD or PL calibration measurements. The $In_{0.525}(Al_xGa_{1-x})_{0.475}As$ growth rate calculated from RHEED was generally found to agree to $\sim 3\%$ with the more accurate ex-situ DCXRD measurements described next.

To determine more accurately the in-situ estimated growth settings, ex-situ DCXRD measurements were made of structures containing both thick layers and superlattices. Both $In_{0.525}(Al_xGa_{1-x})_{0.475}As/In_{0.52}Al_{0.48}As$ superlattices and $In_{0.525}(Al_xGa_{1-x})_{0.475}As$/GaAs superlattices were used for growth rate measurements. The latter structure uses very thin ($\sim$ 0.8–1.0 nm) GaAs layers and thicker ($\sim$ 50 nm) $In_{0.525}(Al_xGa_{1-x})_{0.475}As$ layers. We corrected for the strain reduction of the GaAs layer

thickness; however, due to the overall $In_{0.525}(Al_xGa_{1-x})_{0.475}As/GaAs$ thickness ratio, this amounted to less than a 0.25% correction in the $In_{0.525}(Al_xGa_{1-x})_{0.475}As$ growth rate. We found the strained $In_{0.525}(Al_xGa_{1-x})_{0.475}As/GaAs$ superlattices to be preferable because of greater X-ray contrast (6 periods were sufficient to obtain multiple strong satellite peaks, versus 25–30 periods needed for the lattice matched superlattice) and the need for only a single Al and Ga cell each (two Al cells are needed to grow the $In_{0.525}(Al_xGa_{1-x})_{0.475}As/In_{0.52}Al_{0.48}As$ structure if $x > 0$). For quaternary layers, we also used PL to verify the [Al]/[Ga] ratio using published $In_{0.525}(Al_xGa_{1-x})_{0.475}As$ calibration data [7, 8].

An IRCON narrow bandwidth ($\pm$ 30 nm) pyrometer with a center wavelength of 940 nm, viewing the substrate at normal incidence, was used to measure both the substrate surface temperature and the PI oscillations. The pyrometer was calibrated using the GaAs arsenic stabilized-to-gallium stabilized surface conversion temperature (585°C for an arsenic background pressure $< 1 \times 10^{-9}$ Torr) [9]. An absolute temperature error is expected due to the difference in emissivity between GaAs and InP or $In_{0.525}(Al_xGa_{1-x})_{0.475}As$, but the difference is shown in Section 3.3 to be no more than a few degrees celsius, and will certainly not affect the PI oscillation period. PI requires growth of a relatively thick layer (> 0.5 μm) which is sufficiently transparent at the pyrometer wavelength to permit multiple passes of radiation at the pyrometer wavelength. PI yields the growth rate $R = \lambda/(2Tn)$ where $\lambda = 0.94$ μm is the pyrometer free-space wavelength, T is the measured oscillation period, and n is the effective refractive index [3]. Conversely, to obtain the effective refractive index the composition and growth rate must be known. In this study we quantitatively determine n for $In_{0.52}Al_{0.48}As$.

3. Experimental results

3.1. Description of the observed PI oscillations

The pyrometer trace from a typical $In_{0.52}Al_{0.48}As$ PI calibration run is given in Fig. 1.

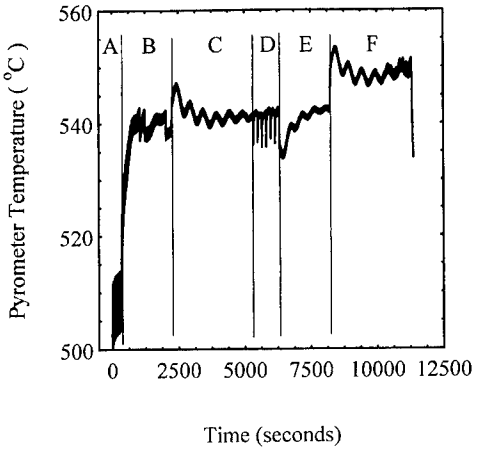

Fig. 1. Pyrometer trace for a typical $In_{0.52}Al_{0.48}As$ calibration run. Region A is prior to growth initiation, regions B and E are 500 nm $In_{0.53}Ga_{0.47}As$ layers, regions C and F are 800 nm $In_{0.52}Al_{0.48}As$ layers, and region D is a 6-period 40 nm $In_{0.52}Al_{0.48}As$/0.8 nm GaAs superlattice.

The structure contains two thick (800 nm) $In_{0.52}Al_{0.48}As$ layers for measurement of PI oscillations and composition by DCXRD, and a 6 period $In_{0.52}Al_{0.48}As/GaAs$ superlattice for the determination of growth rate by DCXRD. Several general observations can be made. Region A, which is prior to the initiation of growth, shows large pyrometer fluctuations during substrate rotation due to stray radiation from the open arsenic cell [10] and stray substrate heater radiation. The indium-free holders used for this work were of a new, modular design [11], and do not include the usual metal foil around the edge of the wafer. As a result, some heater radiation passes through the sapphire backplate around the perimeter of the 2 in InP wafer. The noise is greater than is usually observed when growing on GaAs, [11] because the lower substrate temperature greatly reduces the surface temperature "signal", thereby reducing the signal-to-noise ratio. To improve the situation, we grow a 500 nm $In_{0.53}Ga_{0.47}As$ buffer layer (region B). This deposition results in a significant rise in the substrate temperature as measured by the pyrometer, due to increased absorption of substrate heater radiation by the lower band-gap material [12, 13]. We have found $\sim$500 nm $In_{0.53}Ga_{0.47}As$ is adequate to block effectively the heater radiation escaping

through the exposed areas of the sapphire backplate. Region C, which is the first thick (800 nm) $In_{0.52}Al_{0.48}As$ layer, shows a greatly reduced noise level due to the effect of the $In_{0.53}Ga_{0.47}As$ buffer, as well as the higher surface temperature. An additional benefit of the $In_{0.53}Ga_{0.47}As$ buffer is stronger $In_{0.52}Al_{0.48}As$ PI oscillations. PI oscillations measured off the $In_{0.52}Al_{0.48}As/InP$ interface are $\sim 1°C$ peak-to-valley while PI oscillations from the $In_{0.52}Al_{0.48}As/In_{0.53}Ga_{0.47}As$ interface are $\sim 2°C$ peak-to-valley. We assume the improvement results from a larger refractive index step for the latter interface.

Regions C and F are 800 nm thick $In_{0.52}Al_{0.48}As$ layers. Strong oscillations are observed for both layers. The second $In_{0.52}Al_{0.48}As$ layer is grown atop a second 500 nm $In_{0.53}Ga_{0.47}As$ buffer. Notice that PI oscillations are also observed in the second $In_{0.53}Ga_{0.47}As$ buffer layer (region E), although they are weaker than those observed in the $In_{0.52}Al_{0.48}As$ layers. Both the $In_{0.52}Al_{0.48}As$ and the $In_{0.53}Ga_{0.47}As$ layer pyrometer traces show an overall envelope which is rising in the case of $In_{0.53}Ga_{0.47}As$ and falling in the case of $In_{0.52}Al_{0.48}As$. This correlates with what has been previously observed for $Al_xGa_{1-x}As$ [4], namely that growth of a smaller band-gap material on top of a larger band-gap material results in a rising envelope, while growth of a larger band-gap material on top of a smaller band-gap material results in a falling envelope. We speculate that these transients involve real surface temperature changes due to differences in layer absorption which correlates with band-gap, although the observed transients may instead be due to differences in surface emissivity. It has been shown previously [4] that apparent surface temperature transients make accurate PI rate measurements very difficult. While both $In_{0.52}Al_{0.48}As$ and $In_{0.53}Ga_{0.47}As$ show such transients, the larger band-gap of $In_{0.52}Al_{0.48}As$ makes the oscillations last longer, permitting more accurate determination of the oscillation period.

3.2. *Quantitative PI measurements of $In_{0.52}Al_{0.48}As$ films*

To extract an effective refractive index, we need to independently determine the composition and growth rate. We obtain these values from DCXRD measurements (and PL for quaternary compounds). Fig. 2 shows a DCXRD rocking curve of the same sample as shown in Fig. 1. Two features are observed. First, the presence of a single dominant peak, with a shoulder at smaller (more negative) angle implies that the lattice-matched composition has been obtained to within 0.5 at% indium. Second, the additional peaks, indicated in Fig. 2 by arrows, are the satellite peaks resulting from the 6 period 41.4 nm $In_{0.52}Al_{0.48}As$/0.8 nm GaAs superlattice. The superlattice period is obtained from these satellite peaks using the Bragg equation, and this period combined with the shutter times yields the growth rate. Averaging 3 similar runs (6 $In_{0.52}Al_{0.48}As$ layers in all) gave an effective refractive index for $In_{0.52}Al_{0.48}As$ of $n = 3.515 \pm 1\%$. In the case of $In_{0.53}Ga_{0.47}As$ the refractive index was found to be 3.836; however, between the apparent surface temperature rise and the strong absorption-related oscillation damping for $In_{0.53}Ga_{0.47}As$, typically only two usable PI oscillation periods were available and so the uncertainty is much larger. The effective refractive index for the composition $In_{0.525}(Al_{0.38}Ga_{0.62})_{0.475}As$ was measured to be 3.738, and the three $n(x)$ values are linear within the experimental error.

We next considered the ability of PI to detect changes in the growth parameters. Practically, this will usually involve an error in one of the group III

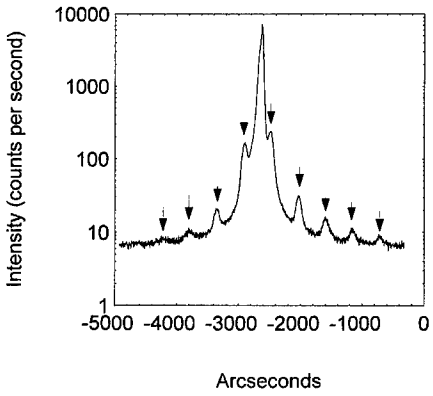

Fig. 2. DCXRD rocking curve for the same sample whose pyrometer trace is shown in Fig. 1. Superlattice satellite peaks are denoted by arrows.

Table 1
Sensitivity of PI oscillations to a 2% change in In composition; the percent change in period is versus the $x = 0.52$ composition for that growth run

Composition	Period (s) (% change)	Obtained by
0.50	425.6 (2.9%)	Al flux increased
0.52	438.0 (–)	–
0.54	456.6 (4.2%)	Al flux decreased
0.50	463.3 (4.6%)	In flux decreased
0.52	443.1 (–)	–
0.54	419.3 (5.7%)	In flux increased

fluxes, which will produce a change in both growth rate and composition. A change in the composition will in turn produce a change in the refractive index. Since the PI period is proportional to $1/(nR)$ where n is the refractive index and R is the growth rate, it is possible for the changes in n and R to cancel out. To investigate, we grew lattice-matched $In_{0.52}Al_{0.48}As$ and then varied the composition by $\pm$ 2%, as verified by ex-situ DCXRD. We did this first by changing the Al flux, and second by changing the In flux. The results are shown in Table 1. The change in oscillation period due to a 2% change in composition ranges from 2.9 to 5.7%, which is easily detectable in the case of a relatively thick ($\sim$ 0.8 μm or thicker) layer. We observe that PI is somewhat more sensitive to changes in the In flux versus Al flux changes. This is explained by noting that the refractive index of $In_xAl_{1-x}As$ increases with increasing x [14]. As a result, an increase in the In flux increases both n and R. In contrast, increasing the Al flux raises R but lowers n. Table 1 shows that in this case the change in growth rate dominates. We conclude that PI is sufficiently accurate to detect run-to-run changes producing a 2% change in composition, especially if the change is due to In flux variation.

3.3. Substrate temperature effects

An additional issue in the use of pyrometry for growth monitoring is the effect of substrate temperature. There are two aspects. First, the emissivity of $In_{0.525}(Al_xGa_{1-x})_{0.475}As$ is an unknown function of composition, although it is expected to be similar to other III–V compounds such as GaAs and InP. The effective emissivity of a given MBE system will also depend on factors such as the viewport transmissivity. Thus, we need to relate the measured pyrometer temperature to the actual substrate temperature. The second aspect is the effect of temperature on the refractive index. Usually, the temperature dependence of the refractive index is assumed negligible for small temperature variations [3], but this should be verified.

To examine these issues, we measured the $In_{0.52}Al_{0.48}As$ PI period as a function of substrate temperature. The data are shown in Fig. 3. Below $\sim$ 560°C the period is a constant within the experimental error. Above 560°C the period begins increasing rapidly. This corresponds to the onset of In desorption and/or reflection from the hot surface. Fig. 3 confirms two salient points. First, below the onset of In desorption the oscillation period is independent of temperature, indicating that the refractive index is indeed a weak function of temperature between 500°C and 550°C. Second, the data confirm that the temperature of $In_{0.52}Al_{0.48}As$ measured by pyrometry is fairly accurate. Literature values for the onset of In desorption vary from 535°C to 600°C [15–18]. Thus, the measured onset of In desorption at 560°C indicates that the pyrometer temperature is within $\sim$ 30°C of the actual surface temperature, when using an effective emissivity calibrated for GaAs. In practice, it is

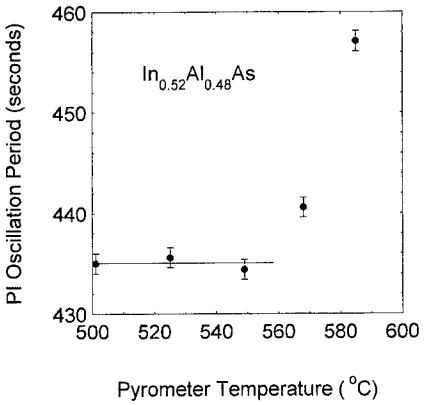

Fig. 3. Measured PI oscillation period of $In_{0.52}Al_{0.48}As$ versus the pyrometer surface temperature. Pyrometer temperature (x-axis) measured with the Al and In shutters closed.

usually desirable to grow at as high temperature as possible without introducing In desorption [15], and so a measurement such as shown in Fig. 3 will be sufficient to establish the optimal pyrometer growth temperature, regardless of any difference between the actual surface temperature and the pyrometer reading.

4. Conclusions

We have found that PI is a useful in-situ method for $In_{0.525}(Al_xGa_{1-x})_{0.475}As$ growth monitoring. As expected, it works best for high Al content films due to the larger band-gap, and a layer of ~ 0.8 μm or thicker must be grown to obtain maximum accuracy. An $In_{0.53}Ga_{0.47}As$ buffer layer significantly improves the measurement by reducing stray radiation effects and increasing the PI oscillation amplitude. A 2% change in $In_{0.52}Al_{0.48}As$ composition due to group III cell drift was easily detectable by PI. The sensitivity is greatest to fluctuations in the In flux, for which the changes in refractive index and growth rate are cumulative. As a result, PI provides a sensitive in-situ tool for detecting the onset of In desorption at higher surface temperatures. The technique does have some drawbacks, however. Due to the compositional dependence of the refractive index it is difficult to translate a deviation of the measured PI oscillation period into a corresponding change in growth rate and/or composition. In Fig. 3, for example, it is clear that In desorption begins at about 560°C. However, it is difficult to determine quantitatively the extent of In desorption above this threshold temperature from the PI data. Additionally, PI cannot measure absolute growth rates to better than a few percent due to uncertainty in the effective refractive index and slight variations in composition about the lattice-matched condition, and this accuracy level will be inadequate for many applications. We conclude that PI is most useful for monitoring drift in established growth conditions. Used in this mode, knowledge of the refractive index is unnecessary, and the main source of error is the accuracy with which the oscillation period can be measured (this can typically be determined to within a few seconds or better).

Acknowledgements

This work was supported in part by an NSF NYI award no. DMR-9458046 (SAR), by an Ohio Space Grant Fellowship (RMS) and by the Ohio State Center for Materials Research and Office for Research (RNS).

References

[1] P. Bhattacharya, Compound Semicond. 2 (1996) 35.
[2] A.J. Springthorpe and A. Majeed, J. Vac. Sci. Technol. B 8 (1990) 266.
[3] A.J. Springthorpe, T.P. Humphreys, A. Majeed and W.T. Moore, Appl. Phys. Lett. 55 (1989) 2138.
[4] R.N. Sacks, R.M. Sieg and S.A. Ringel, J. Vac. Sci. Technol. B 14 (1996) 2157.
[5] A. Ramam, S.J. Chua, G. Karunasiri and P.R. Vaya, J. Crystal Growth 156 (1995) 186.
[6] K.Y. Cheng and A.Y. Cho, J. Appl. Phys. 53 (1982) 4411.
[7] R.F. Kopf, J.M. Kuo and M. Ohring, J. Vac. Sci. Technol. B 9 (1991) 1920.
[8] T. Fujii, Y. Nakata, Y. Sugiyama and S. Hiyamizu, Jpn. J. Appl. Phys. 25 (1986) L254.
[9] L.P. Ramberg, J. Westin and T.G. Andersson, J. Vac. Sci. Technol. B 5 (1987) 1654.
[10] H.P. Lee, E. Ranalli and X. Liu, Appl. Phys. Lett. 67 (1995) 1824.
[11] R.M. Sieg, R.N. Sacks, P.N. Grillot and S.A. Ringel, J. Vac. Sci. Technol. A 14 (1996) 3283.
[12] B.V. Shanabrook, J.R. Waterman, J.L. Davies and R.J. Wagner, Appl. Phys. Lett. 61 (1992) 2338.
[13] F.G. Boebel, H. Möller, B. Hertel, H. Grothe, G. Schraud, St. Schröder and P. Chow, J. Crystal Growth 150 (1995) 54.
[14] J.-H. Baek, B. Lee, W. Choi, J.H. Lee and E.-H. Lee, Appl. Phys. Lett. 68 (1996) 2355.
[15] T.M. Brennan, J.Y. Tsao, B.E. Hammons, J.F. Klem and E.D. Jones, J. Vac. Sci. Technol. B 7 (1989) 277.
[16] E.G. Scott, D.A. Andrews and G.J. Davies, J. Vac. Sci. Technol. B 4 (1986) 534.
[17] K.R. Evans, C.E. Stutz, E.N. Taylor and J.E. Ehret, J. Vac. Sci. Technol. B 9 (1991) 2427.
[18] G.J. Davies, T. Kerr, C.G. Tuppen, B. Wakefield and D.A. Andrews, J. Vac. Sci. Technol. B 2 (1984) 219.

ELSEVIER

Journal of Crystal Growth 175/176 (1997) 262–266

JOURNAL OF CRYSTAL GROWTH

Use of optical fiber pyrometry in molecular beam epitaxy

K.G. Eyink*, J.K. Patterson, S.J. Adams, T.W. Haas, W.V. Lampert

Materials Directorate, Wright Laboratory, WL/MLBM, Wright-Patterson AFB, Ohio 45433-7750, USA

Abstract

In this work we will present results of experiments using optical fiber pyrometry (OFP) for the measurement and control of temperature in MBE. Examples of substrate temperature measurements using various OFP pyrometry modes will be given and compared to standard optical pyrometry, thermocouple readout, and spectroscopic ellipsometry (SE)). In another example, OFP has been integrated into a standard MBE effusion cell. The OFP measurement is considerably more sensitive than the usual thermocouple used in these applications and can give reproducible temperature resolution of $\pm 0.01°C$ at 800°C. This cell design has exhibited long term stability of $\pm 0.02°C$ when cell temperatures are controlled by OFP. This is about an order of magnitude better than what is typically available using thermocouples. In addition, because the OFP is measuring light from the crucible it does not depend on thermal contact to an insulator as does a thermocouple. We will present data showing the improved time response possible using the OFP control, in particular short term flux transient response. In addition, we will point out the robustness of the OFP sensor to cell failure modes such as crucible cracking and contamination.

Keywords: Molecular beam epitaxy; Process control; Temperature measurement; Knudsen (effusion) cell

1. Introduction

The measurement and control of temperature is very important in the practice of solid source MBE. Evaporation rates of materials from Knudsen source cells are very temperature sensitive [1]. Using, for example, Honig's equations and data for the vapor pressure of indium, one can see that a change in temperature of the In melt of $\pm 0.5°C$ will lead to a change in vapor pressure (and hence flux on the substrate) of $\pm 1\%$. This change can be very important when attempting to grow lattice-matched films such as InGaAs or InAlAs on InP substrates where composition control of 0.1% are desired. Control of source cell temperatures to $\pm 0.01°C$ would be highly desirable in these cases.

The measurement of substrate temperatures is of great importance [2–4] and has been the subject of many recent papers. For some materials systems such as GaAs(0 0 1), the epitaxial growth window may be very wide and substrate temperature measurement not so critical, whereas for materials such as GaAs(1 1 1)B [5] and InGaSb/InAs [6, 7] the growth window is very narrow. A variety of techniques have been developed to measure

* Corresponding author. Fax: +1 513 476 7788; e-mail: eyinkkg@ml.wpafb.af.mil.

0022-0248/97/$17.00 Copyright © 1997 Published by Elsevier Science B.V. All rights reserved
PII S0022-0248(96)00940-2

substrate temperatures including measurement of the substrate bandgaps by various transmission techniques [8, 9], diffuse reflectance [10], various forms of pyrometry [11–14], spectroscopic ellipsometry [15–17], etc. In a number of these cases the technology has progressed to the point that commercially available instruments exist.

In the current work we present data on the use of optical fiber pyrometry (OFP) for the measurement and control of both Knudsen cell and substrate temperatures. OFP is a form of pyrometry using a light pipe or lens system to collect light from the radiating body. The light collector is then coupled to a fiber optic cable which carries the signal to a measurement module. The advantages of this method are that losses through fiber optics can be very small and thus a remote, well-shielded, and low-noise detector system can be used. Commercially available versions of this technology exist which are capable of temperature sensitivities of 0.01°C when measuring from 300–1200°C. By contrast, MBE systems typically use Type C thermocouples which generate approximately 18 mV of output at 1000°C. Measurement sensitivities of 0.01°C would then require a voltage measurement accurate to 0.2 μV. In the electrically noisy environment of a typical MBE where SCR power supplies are typically used as heater power sources, this represents a considerable challenge. The OFP technique by contrast is essentially immune to this electrical interference.

2. Experimental procedure

The experiments described in this work were carried out in two MBE machines: a Varian Modular GEN II system and a Fison V80H MKII system. The GEN II system is primarily used for the growth of antimony-containing films. The Fison machine is used primarily for the growth of arsenides and was fitted with a variety of ports for optical sensors including sets of ports at close to the Brewster angle to allow for such measurements as spectroscopic ellipsometry (SE) on sample surfaces in situ to the growth process. The OFP module used in this work was a Model 100 instrument from Luxtron Corporation. Pyrometric and SE measurements were made though heated, strain-free windows.

Sample preparations for both GaAs and GaSb substrates were carried out using standard accepted techniques. An oxide desorption temperature of 585°C for GaAs and 550°C for GaSb was used as a temperature reference point. Oxide desorption was detected by RHEED utilizing a KSA 300 RHEED data detection and acquisition system. SE measurements were made using a Woollam M-44 system with associated software.

3. OFP-based Knudsen cell

The rationale for the construction of an optical sensor-based Knudsen cell was to overcome problems with the use of thermocouples mentioned earlier. In addition to the improved sensitivity and electromagnetic noise immunity already mentioned, the use of the light pipe with the OFP sensor module provides a high degree of robustness. The sapphire light pipe used is not affected by evaporants present in the system and unlike thermocouples, is not easily broken. In the event of a crucible breakage during operation, the light pipe can be rescued either by chemical cleaning or by mechanical cleaning. Finally, in the design discussed below, it is not necessary to remove the thermocouple, thus a redundant cell temperature measurement capability exists.

The cell used in this work was based on a standard EPI effusion cell design. The cell was remounted on a standard vacuum flange with a multiport adapter that allowed insertion of a light pipe. The light pipe accepts photons only within its numerical aperture. If too much distance exists between the light pipe and crucible, it may pick up light from the windings of the effusion cell and lead to erroneous readings, hence the light pipe must be in close proximity to the crucible. We used a spacing of approximately 0.1″.

The performance of the OFP-controlled cell is shown in contrast to that of a conventionally thermocouple-controlled cell in Fig. 1a and Fig. 1b. In the OFP controlled experiments the cell temperature was controlled by taking the output from the optical signal processing module and feeding this

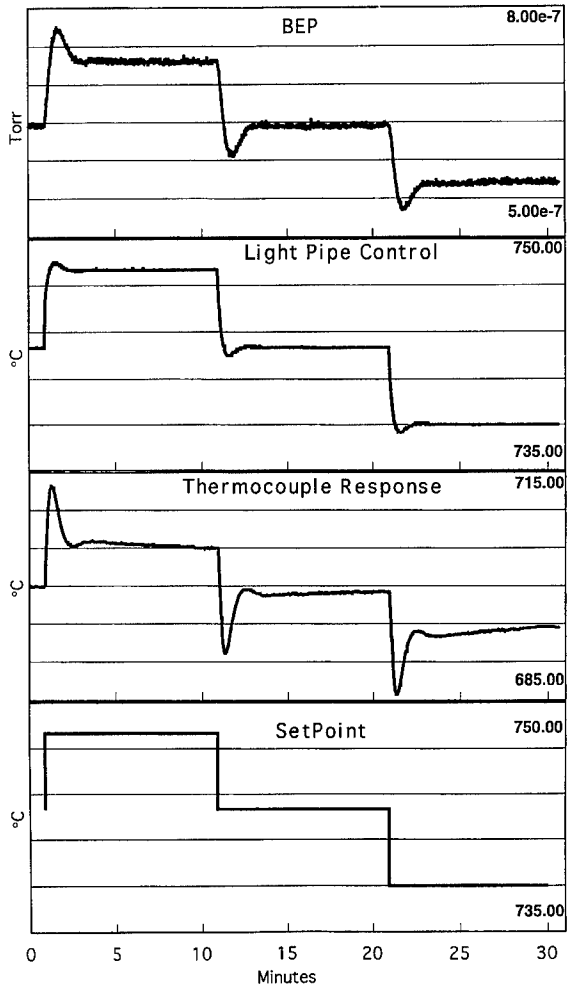

Fig. 1. Comparison of the performance of an In MBE effusion cell whose temperature was bumped up and down in ~ 5°C increments. The thermocouple, light pipe and thermocouple response were monitored with each change in set-point. The temperature of the indium cell was controlled by thermocouple (a) versus. OFP(b). The BEP signal was seen to tracked with the stability of the OPF response.

into a Eurotherm 905 temperature control module. This was done in order to retain PID control of the power supply. The experiments performed in this configuration were to step up and down the set point temperature of an In cell while monitoring the flux BEP (beam-equivalent pressure, from a flux gauge) from the cell, the thermocouple reading and the OFP reading. The experiments were performed for both thermocouple and OFP control.

Fig. 1a shows the results of these measurements for the case where the thermocouple is controlling the cell. The set point is first stepped up by 5°C then down by two 5°C increments. The results of this schedule can be seen in the top panel showing the BEP response. It is observed that BEP rises rapidly due to the stepped 5°C increase in set point, then continues a slow rise for approximately 10 or more minutes. Similarly when the set point is stepped down there is a rapid decline followed by a slower drift. This behavior may be due to the fact the thermocouple measures the temperature of an insulating body (PBN crucible) or to the direct heating of the thermocouple. Faulty PID settings are probably not the cause since a very flat and stable thermocouple reading was obtained with these settings. The PID values used in the experiments were set using the autotune feature of the Eurotherm 905 controllers. While they may not be optimum, they should be reasonably good. Interestingly, the OFP response mirrors very closely the BEP measurement. This is probably because the OFP, as we will show in the section on pyrometry, looks through the PBN crucible and is directly measuring the temperature of the cell contents. This, of course, is the most desirable method of controlling the flux from an effusion cell.

Reference to Fig. 1b shows the contrast when the cell is controlled by the OFP sensor. In this case the response to the step function increase or decrease is followed by the usual small over or undershoot followed by a very flat response. The BEP from the cell exactly mirrors this behavior. The thermocouple response, on the other hand, shows long-term drift presumably for the reasons stated above. Although the data are not yet quantitative, the signal-to-noise ratio of the cell temperature and BEP output are also improved with the OFP control by approximately 50–100%.

4. OFP substrate pyrometry

OFP pyrometry is similar to standard pyrometry but offers several advantages. The improved signal-to-noise ratio offers the possibility to trade off

improved temperature resolution (as good as 0.01°C under optimum conditions) for intensity (spot size being measured). In our case an optical telescope was used which accepted radiation from an approximately 1 mm diameter spot on the wafer and focused it into the fiber optic cable. Another advantage of the OFP pyrometry is in the signal processing and acquisition areas. The model used in this work allows for setting of the sensor sensitivity factor which allows for calibration at a known temperature. In addition, although not used in this work, it also allows for a polynomial fit of the emissivity with temperature which can also improve measurement accuracy over wide ranges. The model used in this work allows acquisition of radiation in three different wavelength regions: 0.8, 0.95 μm and a low-temperature detection band at 0.8–1.8 μm. The 0.8 and 0.95 μm detector can be used individually or in a ratio mode, the so-called two color pyrometry mode. The ratio method has the potential to overcome problems with emissivity changes and with coatings on windows [19]. We have found, however, that this two color pyrometer is of limited usefulness in III–V MBE both because the minimum measurable temperature is > 600°C and because we have observed a very slow buildup of coatings even on our heated windows that cannot be removed by heating as high as 600°C (presumably GaAs) that appears to preferentially absorb the 0.8 μm wavelength. This deposit does not appear to affect the 0.95 μm wavelength measurement appreciably.

In this work we have extended the work of Maracas et al. [17] to use an in situ spectroscopic ellipsometer (SE) to serve as a calibration standard for the various OFP pyrometry measurements. In the course of this work we did observe some significant errors in the SE temperature measurement if an incorrect model of the surface was used. SE requires a database of spectra [18] from known materials as a function of precisely determined temperatures as well as a precise model of the surface. Effects due to surface roughness, presence or absence of oxide layers, angle of incidence, etc. all must be accounted for. The software used to match SE spectra with temperature allows the match to include the best fit of all these variables or else allows fixing one or more of these variables. The statistics portion of this software shows a strong correlation with angle of incidence. Surface void fraction (essentially surface roughness) also has a strong effect on the apparent measured temperature. Variations of measured temperatures of up to 20°C could be calculated depending on the model to be fit. In this work we did not move the sample once aligned and hence kept the angle of incidence fixed as well as possible. This practice led to much more consistent results with typically 90% confidence limits of $\pm$ 2–3°C being calculated.

The desorption temperature of the oxide from GaAs surfaces is widely accepted as 585°C and the desorption is easily detected using the ellipsometric response. This gives a reference point to compare to the SE measurement. In making this measurement, however, it was found necessary to include a substantial surface roughness with a low void fraction for the oxide desorbed surface before growth. This is consistent with recent AFM observations made by Tomich et al. [20] on oxide desorbed GaAs surfaces. Following growth of a GaAs buffer layer the surface is found to be smooth and surface roughness equivalent of several monolayers are used to fit the SE data.

The comparisons of the SE with the OFP pyrometer are best illustrated with samples mounted by In bonding to a Mo holder. This is because the low-temperature measurement "sees" through the GaAs to the heater block and gives erroneous measurements. It should be noted, however, that the low-temperature detector can be used on InAs wafers and on GaSb substrates above about 200°C that are mounted on In free holders as the 1.8 μm radiation is above the band gap for these substrates and will not see the heater block. We should also note that a PBN or a sapphire diffuser plate used in the non-In bonded holder does not block the 0.8–1.8 radiation used by the low-temperature detector.

Table 1 gives a summary of a series of measurements on an In bonded GaAs wafer. Temperatures were set using the non-contact heater block thermocouple (T_{TC}) which reads considerably higher than the actual wafer temperature. Note that at T_{OX} (the point at which oxide begins desorbing, $\sim$585°) considerable surface roughness was needed

Table 1
Comparisons of temperature measurements made by spectroscopic ellipsometry (including some of the fitting parameters used) with various form of OFP pyrometry on GaAs wafers; various surface conditions of the GaAs wafer in the MBE system are indicated

T_{TC}	T_{SE}	Void (%)	Thickness (Å)	Angles	$T_{0.8}$	$T_{0.95}$	T_{LT}	Remarks
793	578	9.5	107.0	69.701	< 575	599	582	Oxide desorption begins
830	617	13	27	69.701	578–580	626	608	Complete oxide removal
793	585	14.2	24	69.701	< 575	598	580	After anneal
793	590	50	4.8	69.718	< 575	598	591	After 1 μm growth
840	627	50	4.43	69.701	595 ± 5	634	626	Temperature check
815	604	50	5.7	69.701	< 575	614	609	Temperature check
635	483	50	3.6	69.701	–	–	479	Temperature check

to fit the SE data. The T_{LT} (low-temperature detector) and $T_{0.95}$ (detection at 0.95 μm) measurements are in reasonable agreement at T_{OX} while the $T_{0.8}$ is out of range. After complete removal of the oxide layer, the T_{SE} fit still show considerable surface roughness. For the same T_{TC} the T_{SE} now reads 585° some 7° higher than before while the $T_{0.95}$ and T_{LT} are essentially the same. Following growth of about 1 μm of a GaAs smoothing layer, the T_{SE} now reads about 590° while the $T_{0.95}$ and T_{LT} read nearly the same as before. Other data points in Table 1 show the linearity of the measured temperatures by the various methods.

5. Conclusions

OFP can be a useful adjunct as a temperature measurement tool in solid source MBE. Its use in controlling the temperatures of effusion cells shows great promise. Its use in OFP pyrometry also shows some promise particularly if careful temperature calibrations are made to program emissivity as a function of temperature for particular samples. SE is useful for temperature measurements as well but care must be taken when fitting the data. SE also requires an appropriate data base for the materials systems of interest, but unfortunately such data is not available for a number of systems of interest.

References

[1] R.E. Honig, RCA Rev. XXIII (1962) 567.
[2] M. Nouaoura, L. Lassabatere, N. Berty and J. Bonnet, J. Vac. Sci. Technol. B 13 (1995) 83.
[3] S. Strite, M. Kamp and H.P. Meier, J. Vac. Sci. Technol. B 13 (1995) 290.
[4] S.L. Wright, T.N. Jackson and R.F. Marks, J. Vac. Sci. Technol. B 8 (1990) 288.
[5] M.Y. Yen and T.W. Haas, Appl. Phys. Lett. 56 (1990) 2533.
[6] J.L. Davis, R.J. Wagner, J.R. Waterman, B.V. Shanabrook and J.P. Omaggio, J. Vac. Sci. Technol. B 11 (1993) 861.
[7] B.V. Shanabrook, J.R. Waterman, J.L. Davis and R.J. Wagner, Appl. Phys. Lett. 61 (1992) 2338.
[8] E.S. Hellman and J.S. Harris, J. Crystal Growth 81 (1987) 38.
[9] B.V. Shanabrook, J.R. Waterman, J.L. Davis, R.J. Wagner and D.S. Katzer, J. Vac. Sci. Technol. B 11 (1993).
[10] M.K. Weilmeir, K.M. Colbow, T. Tiedje, T. Van Buuren and Li Xu, Can. J. Phys. 69 (1991) 422.
[11] S.L. Wright, R.F. Marks and W.I. Wang, J. Vac. Sci. Technol. B 4 (1986) 505.
[12] S.L. Wright, R.F. Marks and A.E. Goldgberg, J. Vac. Sci. Technol. B 6 (1988) 842.
[13] W.E. Hoke, P.S. Lyman and W.H. Labossier, J. Vac. Sci. Technol. B 5 (1987) 734.
[14] A.J. Spring Thrope, T.P. Humphries, A. Majeed and W.T. Moore, Appl. Phys. Lett. 55 (1989) 2138.
[15] D.E. Aspens, W.E. Quinn and S. Gregory, Appl. Phys. Lett. 56 (1990) 2569.
[16] H. Yao, P.G. Snyder and J.A. Woolam, J. Appl. Phys. 70 (1991) 3261.
[17] G.N. Maracas, J.L. Edward, K. Shiralagi, K.Y. Choi, R. Dropad, B. Johs and J.A. Woollam, J. Vac. Sci. Technol. A 10 (1992) 1832.
[18] Data Base provided by G.N. Maracas.
[19] J.W. Knope, presented at 1993 Utah Vacuum Symp.
[20] D.H. Tomich, N.Y. Li and C.W. Tu, presented at 1996 Electronic Materials Conf.

ELSEVIER

Journal of Crystal Growth 175/176 (1997) 267–272

JOURNAL OF CRYSTAL GROWTH

Measurement of MBE substrate temperature by photoluminescence

Y. Takahira, H. Okamoto*

Chiba University, Faculty of Engineering, 1-33 Yayoi-Cho, Inage-ku, Chiba 263, Japan

Abstract

A new method to measure the substrate temperature suitable for low-temperature growth MBE is presented, which utilizes photoluminescence from the substrate. Single optical fiber is used both to supply the excitation light from a laser to the substrate and also to gather the photoluminescence light from the substrate. An UHV flange with optical fiber feedthrough is used, which is bakable to a temperature 150°C and shows a negligible amount of vacuum leakage measured at a vacuum of 1×10^{-9} torr. In the experiment a GaAs-AlAs MQW wafer was used for the substrate because of its narrow PL spectral width. Differences in substrate temperature between a large wafer and a small wafer and between before and after starting the growth were measured by this method.

1. Introduction

In conventional MBE, the substrate temperature is measured by a thermocouple and/or by a pyrometer, both of which are inaccurate because the thermocouple is not in touch with the substrate nor with the Mo block, and because the pyrometer suffers from the ambient light such as room light and a light from an ionization gauge, thereby making it very difficult to measure accurately a low substrate temperature necessary for the low-temperature MBE growth (200–300°C). Lee et al. [1] reported another method using an infra-red spectroscopic technique to measure the temperature dependence of the band gap energy or the refractive index of the substrate. Both transmission and reflection modes of the measurement were proposed, which are free from any adjustable parameters such as emissivity and unaffected by window absorption or coating. The transmission mode is suitable for a non-In-bonded, radiatively heated substrate, thereby the substrate heater is used as the light source. But any change in current flowing through the heater will give rise to a change in the blackbody radiation spectrum of the heater. Ambient lights such as filaments of the RHEED gun and the ionization gauge will also give an error in the measured absorption or refractive index spectrum. The reflection mode of the refractive index measurement is suitable to the substrate mounted on a Mo block with or without In solder. But two viewing ports facing to the substrate are needed, and furthermore the refractive index is not well known at high temperature. An example of the measurement

*Corresponding author. Fax: +81 43 290 3442; e-mail: okamoto@tcom.tech.chiba-u.ac.jp.

0022-0248/97/$17.00 Copyright © 1997 Elsevier Science B.V. All rights reserved
PII S0022-0248(96)00876-7

showed that wavelength change corresponding to a temperature change by 100°C was comparable with the spectrum broadening of a transmission peak [1]. Then, Weilmeier et al. [2] developed the diffused reflectance spectroscopy, where a light incident on a specular front surface of the substrate transmits inside, reflects at the rear diffuse surface and is detected at an angle different from the specular reflection angle. The diffuse reflectance spectrum is determined by the band gap of the substrate, which is temperature sensitive. This method gives the substrate temperature very accurately ($\pm$ 1.5°C). However, it depends not only on the degree of roughness of the rear surface but also on the substrate thickness and front surface roughness. This method also requires two viewing ports [3–7].

In this paper, a new method is presented, which utilizes photoluminescence (PL) from the substrate. The measurement is based on a simple principle that the band gap energy $E_g(T)$ follows the relationship:

$$E_g(T) = E_g(0) - \alpha T^2/(T + \Theta),$$

where $E_g(0)$ is the energy gap at 0 K, and α and Θ are empirical parameters [8]. The PL measurement system is not unusual, except that an optical fiber is used through which an excitation laser light is introduced into the vacuum chamber and incident on the substrate. Photoluminescence light is also gathered into this fiber and supplied to the measuring system outside vacuum. An UV (ultra violet) silica fiber with core diameter as large as 400 μm is used to gather as much light as possible. A specially designed UHV flange with optical fiber feedthrough is used here, which exhibits negligible amount of vacuum leakage measured at 1×10^{-9} torr by a quadrupole mass spectrometer (QMS). In the experiment a GaAs/AlGaAs multiple quantum well (MQW) wafer is used for the substrate, because the full-width at half-maximum (FWHM) of the PL spectrum is as narrow as 10 nm at 20°C, which is only $\frac{1}{3}$ the wavelength change corresponding to the temperature change of 100°C.

2. Temperature measurement probe

The temperature measurement probe used here is shown in Fig. 1. It is composed of a substrate wafer mounted on a molybdenum block and an optical fiber. The fiber is introduced into vacuum through a flange and is movable to the direction perpendicular to the substrate surface. The edge of the fiber is in touch with the substrate surface in order to gather as much light as possible. We tried also a two fiber probe, with one of the fibers supplying the excitation laser light and the other gathering the PL light. Although this probe was a simple extension of the conventional PL measurement setup, alignment of the edges of two fibers was

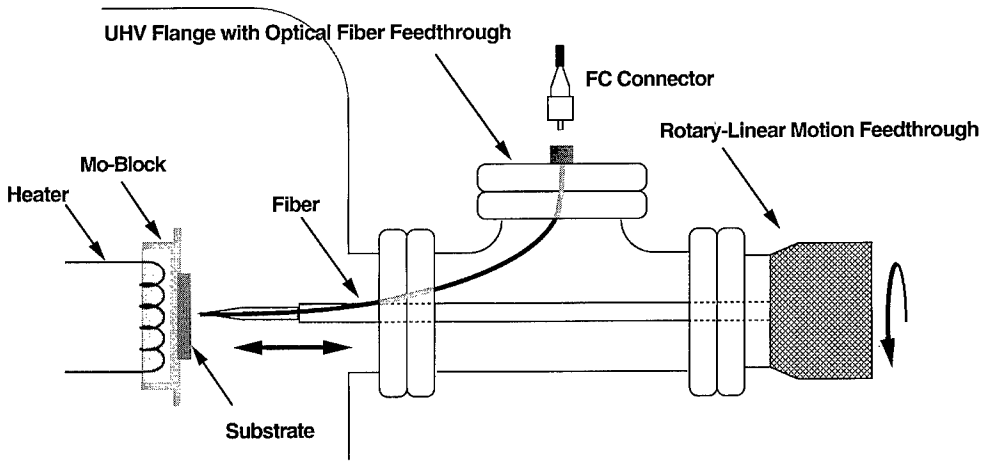

Fig. 1. Temperature measurement probe using an optical fiber.

extremely delicate in vacuum. Thus, we used the single fiber probe in this experiment.

An UV silica fiber (Sumitomo MS-04, step index fiber) is used here, whose core diameter is as large as 400 μm and optical transmission coefficient is more than 99%/m over the wavelength range 330–1200 nm. It is bakable upto 260°C. Plastic coating was removed near the edge of the fiber.

3. UHV flange with optical fiber feedthrough

Fig. 2 shows an UHV flange with an optical fiber feedthrough. Hermetic sealing is realized both by epoxy resin between the fiber and a ferrule, and by an o-ring between the ferrule and the flange. In the leakage test using He gas, no signal was detected by QMS under a vacuum of 1×10^{-9} torr. It is bakable nominally up to 150°C, and in our experiment the background pressure was less than 5×10^{-7} torr during baking at 200°C.

4. PL measurement setup outside vacuum

The conventional PL measuring setup must be modified in order to introduce both the excitation laser light and the PL light into a single optical fiber. This is realized by using a half mirror as shown in Fig. 3. However, the following two problems arise because the excitation laser light reflected at the substrate surface takes the same optical path as the PL light from the substrate and the intensity is much higher in the former than in the latter. Both of these problems may set the detection limit of the measurement system. One is that an optical low-pass filter which cuts down the excitation light emits photoluminescence in the relevant spectral range. In order to reduce this photoluminescence, the position of the filter must be changed from the usual one (just in front of the input slit of the monochrometer) to nearby the condenser lens as shown in Fig. 3. The other is the Raman scattered Stokes line of the excitation laser light passing through the optical fiber. Its peak

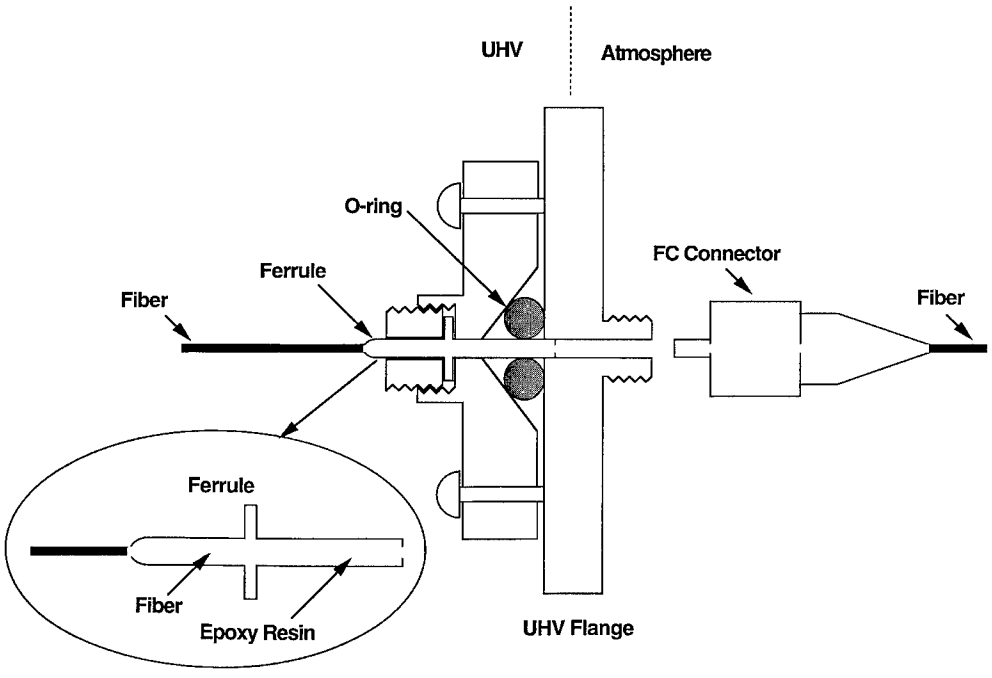

Fig. 2. UHV flange with optical fiber feedthrough.

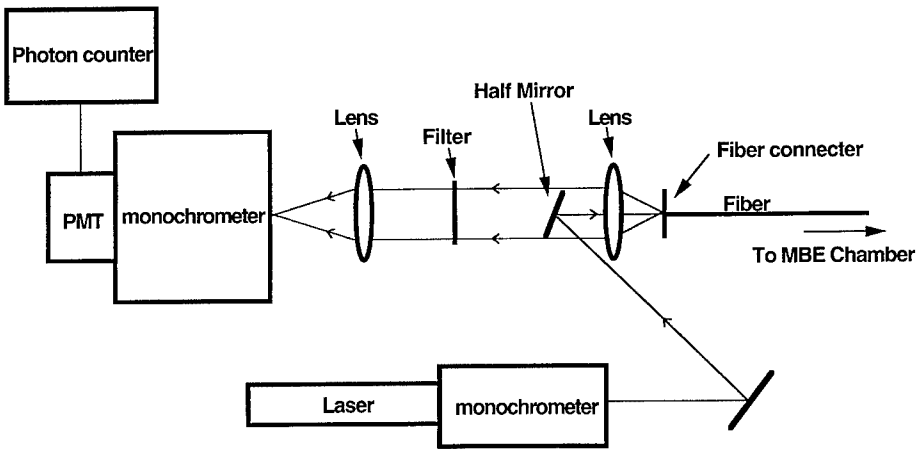

Fig. 3. photoluminescence measurement system using a single optical fiber.

wavelength depends on the laser wavelength, and its intensity depends on the length of the fiber. Although the Raman scattered light could not be reduced to a negligible level in the experiment here, subtracting it from the measured spectrum gave the desired PL spectrum from the substrate.

Since the PL peak from the substrate becomes weak and broad at high temperature as described later, reduction of the noise level of the measurement system is very important. To realize this, a high sensitivity photomultiplier tube (Hamamatsu R636-10) and a photon counter (Hamamatsu C5410) are used.

5. Substrate

As a substrate whose surface temperature is to be measured, two GaAs-based MQW wafers are used here. MQW-1 consists of 100 periods of GaAs(8.0 nm)–$Al_{0.3}Ga_{0.7}As$(10 nm), whose PL peak wavelength is 810 nm at room temperature (RT). MQW-2 consists of 100 periods of GaAs(7.0 nm)–AlAs(7.0 nm), whose PL peak wavelength is 790 nm at RT. Fig. 4 shows the temperature dependence of the PL peak wavelength. Solid and broken lines are the Varshni's empirical ones. Experimental data here deviates from the Varshni's line at a temperature higher than 250°C.

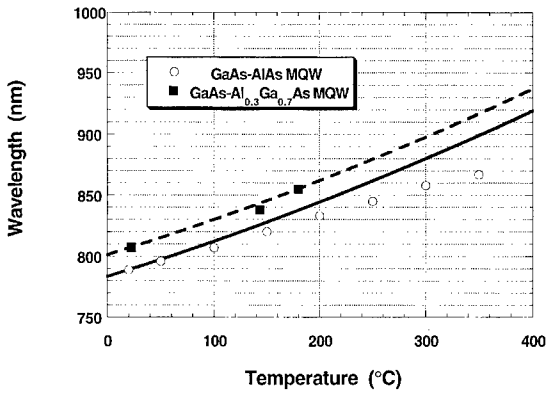

Fig. 4. Temperature dependence of PL peak wavelength of MQW wafers. The solid and broken lines are Varshni's empirical curves.

This is partly due to the reduction in splitting between the heavy-hole peak and the light-hole peak at high temperature. Although the MQW-1 is larger in PL intensity at RT by a factor of 3 or more than the MQW-2, reduction in the intensity and increase in the spectrum width at high temperature are more drastic in the MQW-1 than in the MQW-2. This is due to the difference in the barrier height. Therefore, the latter is used hereafter as a reference wafer. Its PL spectrum at different temperatures is shown in Fig. 5.

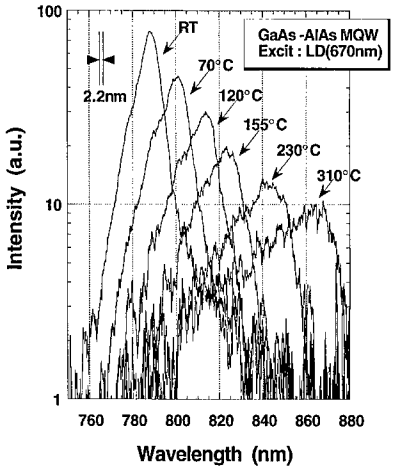

Fig. 5. Temperature dependence of PL spectrum of GaAs–AlAs MQW wafer.

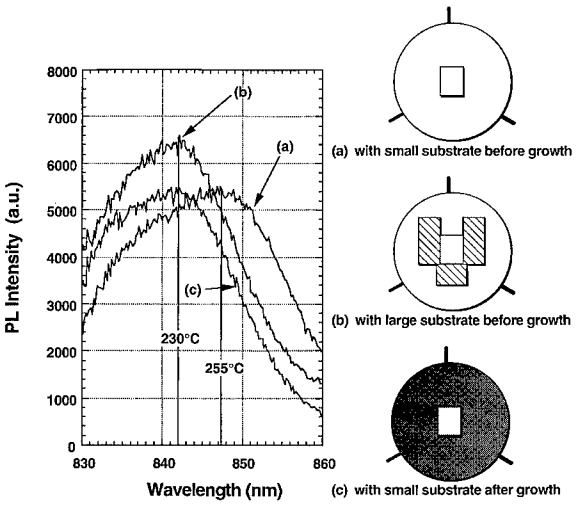

Fig. 6. Photoluminescence spectrum variation in three cases (a)–(c) shown in the inset, when the thermocouple temperature is kept constant.

6. Actual temperature measurement

In the conventional MBE, the substrate temperature is controlled by keeping constant the temperature of the thermocouple located behind the Mo block (thermocouple temperature, hereafter). Even so, the real surface temperature differs in each run if the size of the substrate differs. Furthermore, the surface temperature may change after starting the growth because the Mo block surface which was not covered with substrates becomes covered with Ga and As molecular beam adsorption, which changes the surface emissivity [1]. We measured these temperature differences by applying the present PL temperature measurement method.

Fig. 6 shows three PL spectra. Curve (a) is a spectrum from the small reference wafer on a clean Mo block when the thermocouple temperature was kept at a temperature which corresponds to a surface temperature at 255°C. Curve (b) shows a spectrum of the reference wafer in the case where additional three GaAs wafers $1 \times 1\,cm^2$ square were mounted on the same Mo block. Curve (c) shows a spectrum of the reference wafer, where only this wafer was on the same Mo block but its surface was covered with Ga and As adsorption due to a 1 μm thick GaAs MBE growth. All three spectra were obtained under the same thermocouple temperature. The result shows that the actual surface temperature in the case (b) and (c) is lower by 25°C as compared to the case (a).

7. Conclusion

A new measurement method of MBE substrate temperature was presented, in which an optical fiber probe is used to measure the photoluminescence peak wavelength, which is temperature dependent, of the reference wafer mounted along with the substrate. Mainly due to the flexibility and thinness of the optical fiber, only one UHV port is required in this method. This method does not rely on the measurement of PL intensity but on PL wavelength, so that it is essentially free from window absorption or fiber coating. It can also be used in real time during growth because the PL wavelength from the reference wafer is not affected by the overlayer, although PL intensity may be decreased. This method is essentially a non-contact method, and even if the optical fiber probe is in contact with the substrate, temperature disturbance is not serious because of the small thermal conductivity of the silica fiber. If the reference wafer is mounted at the center of a Mo Block, this

method can be used during rotation of the substrate. As a reference substrate, GaAs–AlAs MQW was used in the experiment. The surface temperature was measured up to 310°C. The maximum measurable temperature is limited by reduction in PL intensity and increase in its FWHM of the substrate. This limitation will be overcome if other MQW wafer of wide band gap material such as InGaP–InGaAlP or GaN–AlGaN is used. In the forthcoming paper, this temperature measurement method will be applied to the low-temperature MBE growth, where the quality of the grown film delicately depends on the growth temperature.

Acknowledgements

This work was supported by grands from the Asahi Glass Foundation, the Murata Science Foundation, and International Communication Foundation.

References

[1] W.S. Lee, G.W. Yoffe, D.G. Schlom and J.S. Harris, Jr., J. Crystal Growth 111 (1991) 131.
[2] M.K. Weilmeier, K.M. Colbow, T. Tiedje, T. van Buuren and L. Xu, Can. J. Phys. 69 (1991) 422.
[3] C. Lavoie, S.R. Johnson, J.A. Mackenzie, T. Tiedje and T. van Buuren, J. Vac. Sci. Tecnnol. A 10 (1992) 930.
[4] S.R. Johnson, C. Lavoie, T. Tiedje and J.A. Mackenzie, J. Vac. Sci. Tecnnol. B 11 (1993) 1007.
[5] S.R. Johnson, C. Lavoie, E. Nodwell, M.K. Nissen, T. Tiedje and J.A. Mackenzie, J. Vac. Sci. Tecnnol. B 12 (1994) 1225.
[6] T.P. Pearsall, S.R. Saban, J. Booth, B.T. Beard, Jr. and S.R. Johnson, Rev. Sci. Instrum. 66 (1995) 4977.
[7] J.A. Roth, in: Proc. 9th Int. Conf. on Moleculer Beam Epitaxy, California, August (1996) p. 10.1.
[8] Y.P. Varshni, Physica 34 (1966) 149.

ELSEVIER

Journal of Crystal Growth 175/176 (1997) 273–280

JOURNAL OF CRYSTAL GROWTH

Effect of substrate thickness, back surface texture, reflectivity, and thin film interference on optical band-gap thermometry

S.R. Johnson[a,*], T. Tiedje[b]

[a] *Center for Solid State Electronics Research, Arizona State University, Tempe, Arizona 85287-6206, USA*
[b] *Advanced Materials and Process Engineering Laboratory, University of British Columbia, Vancouver, Canada, BC V6T 1Z4*

Abstract

A model for the temperature-dependent shape of the absorption edge in GaAs is used to determine the effect of substrate thickness, back surface texture, and deposited dielectric films, on the temperature measurement accuracy, for both transmission and diffuse reflectance geometries of optical band-gap thermometry. A 5% change in substrate thickness, a 20% change in light scattering at the back of the substrate, or a 40% change in the residual absorption below the band edge all cause temperature errors of about 1°C. Band-gap thermometry is also sensitive to thin film interference during the growth of wide band-gap layers, which can cause the apparent temperature to oscillate. An algorithm is presented that uses the width of the knee in the spectrum to correct temperature errors caused by interference oscillations. This algorithm is suitable for real-time applications as the information needed to correct the knee position is obtained from the spectrum itself. The correction procedure is tested on data taken during growth of AlGaAs on GaAs. The interference oscillations in the deposited thin film reduced apparent temperature oscillations from about 1.5°C at 570°C to about 0.7°C (RMS).

1. Introduction

Substrate temperature is a critical parameter in determining the quality and composition of deposited layers in molecular beam epitaxy (MBE). Contact between the substrate and a temperature sensor is not practical or desirable because the sensor would cause perturbations in temperature or contamination of the substrate. Recently, several optical methods that infer substrate temperature from the band-gap of the substrate material have been developed. The two common implementations of optical band-gap thermometry are diffuse reflectance spectroscopy (DRS) [1–3] and transmission spectroscopy [4, 5]. In these methods the temperature of the substrate is inferred from the band-gap of the substrate material.

To determine the temperature accurately a spectral signature is needed that can be related to the band-gap and hence to the temperature. The point of inflection in the transmission spectra has been proposed as such a signature [5]. For maximum accuracy it is desirable to measure as close to the band-gap as possible because the absorption below the band-gap is more sensitive to material quality and doping density [6].

* Corresponding author.

0022-0248/97/$17.00 Copyright © 1997 Elsevier Science B.V. All rights reserved
PII S0022-0248(96)00889-5

The diffuse reflectance increases sharply in the wavelength region close to the band-gap as shown in Fig. 1. Two asymptotic lines are depicted in Fig. 1: *Line* 1 determined by linear extrapolation through the background at short wavelengths and *Line* 2, determined by linear extrapolation through the data points closest to the steepest part of the spectrum. The intersection of these two lines defines the wavelength of the bend in the spectrum which will henceforth be defined as the "knee" of the spectrum.

The knee region of the diffuse reflectance spectrum for GaAs can be fit by the following function:

$$y = y_0 + m_1(\lambda - \lambda_k) + m_2\lambda_a \ln\left[1 + \exp\left(\frac{(\lambda - \lambda_k)}{\lambda_a}\right)\right]. \tag{1}$$

In Eq. (1) $y_0 + m_1(\lambda - \lambda_k)$ is the linear background asymptote, *Line* 1, with slope m_1, $m_1 + m_2$ is the slope of the asymptote, *Line* 2, and the parameter λ_a determines how sharply the spectrum is bent at the knee. Eq. (1) characterizes the onset of transparency of the substrate with two parameters that are independent of the absolute intensity of the optical signal namely the position of the knee, λ_k, which is related to the band-gap energy of the substrate material and the width of the knee, λ_a, which is related to the width of the absorption edge of the substrate.

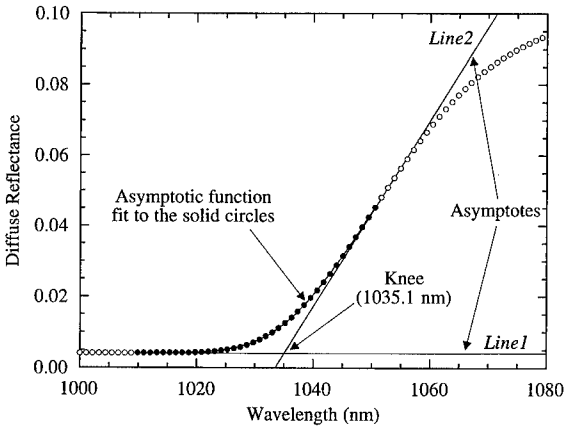

Fig. 1. Illustration of a fit of an asymptotic function to the knee region of the diffuse reflection spectrum, showing the position of the knee in the spectrum.

2. Sensitivity to substrate properties

The positions of the point of inflection and the knee are critical points in the spectrum that are related to temperature and are given by the maximums in the first and second derivatives of the spectrum. In the following analysis, we will consider the path of various light rays in the geometrical optics limit. Each ray will have an unique transmission spectrum and hence an unique energy at each critical point depending on its path length in the substrate. The fundamental ray has the highest intensity while the intensity of each subsequent ray decreases with each additional reflection inside the substrate. The total spectrum is given by the sum of the spectra of the individual rays. In this analysis, the position of a critical point in the total spectrum is written in terms of the position of the critical point of the fundamental ray plus a correction term. This correction term describes the difference between the position of the critical points of the total spectrum and the spectrum of the fundamental ray.

The diffuse reflection of light scattered at the back of the substrate [7] is

$$\mathrm{DRS} = f_e(1 - R)^2 \exp(-2\alpha d)[1 + y_s + y_s^2 + \cdots]. \tag{2}$$

The power series in y_s represents the fraction of light scattered from the textured back surface that survives to scatter again:

$$y_s = f_e R^2 \exp(-2\alpha d) + (1 - f_e)\exp[-2d\alpha(1 + \gamma)]. \tag{3}$$

Eq. (3) is derived from a model used to describe scattering and light trapping inside textured substrates [7], where γ is the scattering parameter that describes the width of the angular distribution of light scattered from the textured back surface of the substrate. The half-width at half-maximum of the distribution is about $67°\sqrt{\gamma}$. A polished surface will have γ equal to zero and for an ideal Lambertian scatterer γ will be one. f_e is the fraction of light scattered inside the escape cone of the substrate. For a polished surface f_e is one and the power series in y_s is the contribution of the higher-order rays to

the reflectance of a semitransparent slab; d is the substrate thickness and α is the absorption coefficient.

To determine the positions of the knee and the point of inflection of the spectrum, relative to the band-gap, the following analysis is done. The spectral dependence of an exponential term in Eq. (2) is described by $f = \exp(-x)$; where $x = a\alpha d$ is a dimensionless variable, and a is the total path length of the ray inside the substrate in units of the substrate thickness. The point of inflection and the knee of the spectrum of an individual ray (or each term in Eq. (2)) are given by the zero crossings of the second and third derivatives of f, respectively. The spectral dependence of the absorption coefficient, and hence x, is exponential for direct band-gap semiconductors such as GaAs [6]. To better represent the absorption characteristics of GaAs a constant absorption term $\alpha_0(T)$ is added. This term represents the slowly varying absorption below the band edge [6]. The resulting model for the spectral dependence of absorption is

$$\alpha(h\nu) = \alpha_g \exp\left(\frac{h\nu - E_g(T)}{E_0(T)}\right) + \alpha_0(T). \tag{4}$$

Where $E_0(T)$ is the width of the absorption edge (Urbach parameter), $E_g(T)$ is the optical band-gap [6], and α_g is absorption coefficient at the band-gap.

A critical point at energy E_c, has an absorption coefficient given by $\alpha_c = \alpha(E_c)$. By introducing a dimensionless parameter $a_c = a\alpha_c d - a\alpha_0 d$, the following relation between the energy of the critical point, the optical bandgap, and the Urbach parameter is obtained:

$$E_c(T) = E_g(T) - E_0(T)\ln\left(\frac{a\alpha_g d}{a_c}\right). \tag{5}$$

$a_c = 1$ at the point of inflection and $a_c = (3 + \sqrt{5})/2 = 2.62$ at the knee. The absorption coefficient at the critical points is $\alpha_c = a_c/ad + \alpha_0(T)$. The spectral positions of the inflection point and the knee for each ray depend on the bandgap energy, the band-gap absorption coefficient, the Urbach parameter, and the total path length of the ray inside the wafer. The critical points of an individual ray are independent of the subedge absorption, $\alpha_0(T)$, and the interface reflectivity. Also, the knee is $\ln(2.62)E_0 = 0.96E_0$ closer to the bandgap than the point of inflection, for both transmittance and reflectance.

The positions of the critical points are assumed to be given by a weighted average of the positions of the critical points of individual rays [7]. The position of a critical point of the total spectrum is given by the position of the critical point of the fundamental ray plus the shift $-\Delta_c E_0$, due to the contribution of the higher-order rays to the overall spectrum. The correction term Δ_c depends on the scattering parameter, the subedge absorption, the wafer thickness, and the wafer reflectivity [7]. The temperature dependence of the positions of the critical points of the spectrum are

$$E_c(T) = E_g(T) - E_0(T)\left[\ln\left(\frac{a_0\alpha_g d}{a_c}\right) + \Delta_c(T)\right], \tag{6}$$

where a_0 is the path length of the fundamental ray in units of substrate thickness. Since a_0 is one in transmission and two in reflection, the critical points are about $0.7E_0$ closer to the band-gap in transmission measurements.

Above room temperature the band-gap and Urbach parameter are linear in temperature with slopes S_g and S_0 [6], in which case the temperature shift associated with a shift in the critical points is approximately,

$$\Delta T \cong -\frac{1}{kS_g}\left[1 - \frac{S_0}{S_g}\ln(\alpha_g d)\right]\Delta E_c. \tag{7}$$

The temperature error associated with variations in the physical characteristics of the substrate from those of the calibration substrate, is determined from Eq. (7), where the temperature error for a 500 μm thick semi-insulating GaAs substrate, is $\Delta T = -1.8°\text{C/meV}\ \Delta E_c$. The temperature error due to differences in the physical properties of GaAs substrates from those of a 500°C, 500 μm thick, semi-insulating GaAs reference substrate, are given in Table 1. The back surface of the reference sample has a scattering parameter of 0.1. E_0 is 11.0 meV and α_0 is $3\ \text{cm}^{-1}$ for semi-insulating GaAs at 500°C [6].

Table 1
The temperature error associated with variations in the physical properties of a GaAs substrate from those of a 500 μm thick semi-insulating GaAs calibration substrate at 500°C with scattering parameter 0.1; for semi-insulating GaAs at 500°C the Urbach parameter is 11.0 meV and the subedge absorption coefficient is 3 cm^{-1}

Physical characteristics		Contribution of Δ_c		Temperature error	
Parameter	Value	Percentage of ΔT_p	Percentage of ΔT_k	ΔT_p (°C)	ΔT_k (°C)
d'/d	0.2	− 22	− 11	− 26	− 29
d'/d	1.05	− 36	− 17	0.71	0.83
a'_0/a_0	0.5	− 58	− 25	− 8.7	− 11.0
γ'/γ	0.8	100	100	− 1.5	− 0.9
γ'/γ	0.1	100	100	− 9.6	− 5.2
α'_0/α_0	1.5	100	100	− 2.2	− 1.2
R'/R	0.8	100	100	− 0.16	− 0.09

The first two columns of Table 1 give the ratio of the physical characteristics of the substrate to those of the reference substrate. Columns three and four list the contributions of the correction parameter to the temperature error as a percentage of the total error. Columns five and six list the temperature error caused by using the calibration curve for a 500 μm thick semi-insulating GaAs with scattering parameter 0.1 to determine the temperature of the substrate in question, using the inflection point and knee, respectively, to extract temperature.

The first line of Table 1 shows that the apparent temperature for a 100 μm substrate is 26°C cooler (at the inflection point) and 29°C cooler (at the knee), than the real temperature. The second line shows that the error associated with a 5% thickness variation, leads to a temperature deviation on the order of the sensitivity of the technique. The third line shows the effect of applying a calibration curve for reflection measurements to transmission data. Also shown in Table 1 are temperature errors for variations in the back surface scattering parameter with $\gamma'/\gamma = 0.8$ (scattering decreased by 20%) and for $\gamma'/\gamma = 0.1$ (scattering decreased 10×). These results show that small changes in the scattering at the back surface cause errors on the order of the sensitivity of the measurement but that large differences need to be calibrated for. The effect of increasing the wavelength independent absorption in the gap is also shown. This could be caused by additional deep level impurities in the substrate, for example.

During growth the reflectivity of the front surface of the substrate changes if the composition of the epilayer differs from the substrate. The reflectivity change shown in Table 1 is for a case where the refractive index of the epilayer is 3.0 compared to 3.5 for the substrate, such as for AlGaAs on GaAs. Variations in surface reflectivity have a negligible effect on the inferred temperature.

Variations in the spectral response of the measurement system, by window coating for example, also affect the position of the critical points. When the optical throughput, g, has slope I/E_s, the functional form of the spectra are

$$f \cdot g\,;\; g = 1 + \frac{(h\nu - E_c)}{E_s}. \tag{8}$$

The shift in the critical point for slope I/E_s in the optical throughput, to first order in E_0/E_s, is given by

$$a'_c = a_c\left(1 + a_s\frac{E_0}{E_s}\right), \tag{9}$$

where $a_s = 2$ at the inflection point and $a_s = 0.8$ at the knee. The inflection point is 2.4 times more sensitive than the knee to changes in the slope of the optical throughput. Typically, $|E_s| \geqslant 0.3$ eV for mirror/window coating during growth of GaAs based materials. The shifts in the critical points of spectrum due to variations in the optical throughput, for $E_s = -0.33$ eV, result in a temperature error of 1.3°C at the inflection point and 0.5°C at the knee, for the substrate in Table 1.

3. Correcting for spurious shifts in the position of the knee

In order to correct the knee for variations in the substrate, we need to relate the position and width of the knee to the physical properties of the substrate. When the background is zero Eq. (1) becomes

$$y(h\nu) = m_2 E_a \ln\left[1 + \exp\left(\frac{E_k - h\nu}{E_a}\right)\right]. \tag{10}$$

Furthermore, at the knee $y = -2\ln 2 E_a y'$ where y' is the derivative of the asymptotic function. Writing the total spectrum as a single ray $f = \exp(-x)$ with $f' = -x'f$, the position of the knee of the total spectrum is

$$E_k(T) = E_g(T) - \ln\left(\frac{a_0 \alpha_g d}{a_k}\right) E_0(T);$$
$$a_k(h\nu) = a_c\left[1 + a_s \frac{E_0(T)}{E_s}\right]\exp[-\Delta_c(T)]. \tag{11}$$

The width of the knee is related to the Urbach parameter by equating the fitting function divided by its derivative to the spectrum divided by its derivative, at the knee:

$$2\ln 2 E_a = \frac{1}{x'} = \frac{E_0}{a_k(h\nu)} \tag{12}$$

Solving Eq. (12) for $a_k(h\nu)$ and substituting this solution into Eq. (11), the knee of the total spectrum is

$$E_k(T) = E_g(T) - E_0(T) \left[\ln\left(\frac{a_0 \alpha_g d}{a_c}\right) + \ln\left(\frac{2\ln 2 a_c E_a(T)}{E_0(T)}\right)\right]. \tag{13}$$

The position of the knee relative to the knee of the fundamental ray is now written in terms of the width of the knee, E_a. The shift in the knee from multiple reflections and light trapping (Δ_c) and the shift in the knee due to spectral changes in the optical throughput ($1/E_s$), are sensed through the width of the knee. This is explained as follows: when the position of the knee shifts ΔE toward lower (higher) energies, due to changes in Δ_c and $1/E_s$, the position of the inflection point shifts about $2\Delta E$ toward lower (higher) energies, causing the width of the knee to broaden (narrow). Therefore, the width of the knee is a measure of spurious shifts in the position of the knee.

The position of the knee, $E_{k;cal}$ and the width of the knee, $E_{a;cal}$, are measured as a function of temperature for a given substrate in a calibration run. The position of the knee, E_k and the width of knee, E_a for a different substrate of the same material with different thickness or texture, are related to the calibration values (with extended subscript "cal") as follows:

$$E_k = E_{k;cal} + E_0 \ln\left(\frac{E_{a;cal} a_{0;cal} d_{cal}}{E_a a_0 d}\right). \tag{14}$$

Eq. (14) corrects for the shift in the knee due to differences between the substrate in question and the calibration substrate. These differences are substrate thickness, light trapping, optical throughput, and the path length of the fundamental ray (or measurement configuration). Variations in light trapping, and optical throughput are sensed through the width of the knee.

4. The effect of thin film interference during MBE growth

The growth of wide band-gap material such as AlGaAs on a smaller bandgap substrate such as GaAs, produces interference oscillations in the transmitted light. For reflection measurements, the fundamental ray passes through the overlayer two times, once in each direction. Transmission of the fundamental ray through the overlayer is given by

$$T_1 = \frac{(1 - R_1)^2 (1 - R_2)^2}{(1 + R_1 R_2 + 2\sqrt{R_1 R_2}\cos\delta)^2},$$
$$\delta = \frac{4\pi n_f d_f}{\lambda} = \frac{4\pi n_f d_f}{hc} h\nu, \tag{15}$$

where R_1 and R_2 are the reflectivities of the vacuum-epilayer interface and the epilayer-substrate interface, respectively and n_f is the index of refraction of the overlayer.

The diffuse reflectance spectrum from a substrate during the growth of a wide band-gap overlayer is

given by the product of T_1 and the spectrum from the substrate with no overlayer. This multiplicative term is analogous to the optical throughput of the system (Eq. (8)). The relationship between T_1, the optical throughput, g, and the slope of the optical throughput $1/E_s$ is

$$g = \frac{T_1}{\langle T_1 \rangle} \cong \frac{(1 - R_1R_2)^2}{(1 + R_1R_2 + 2\sqrt{R_1R_2}\cos\delta)^2}$$

$$\cong 1 - 4\sqrt{R_1R_2}\cos\delta\,;$$

$$E_s^{-1} = g' = 4\delta'\sqrt{R_1R_2}\sin\delta\,; \quad \delta' = \frac{4\pi n_f d_f}{hc}. \tag{16}$$

The interface reflectivities are $R_1 = r_1^2$ and $R_2 = r_2^2$ with $R_2 \ll 1$ and

$$\sqrt{R_1} \equiv \frac{n_f - 1}{n_f + 1};$$

$$\sqrt{R_2} \equiv \frac{\Delta n}{2n_f + \Delta n} \cong \frac{\Delta n}{2n_f}\left(1 - \frac{\Delta n}{2n_f}\right), \tag{17}$$

where $\Delta n > 0$ is the difference in the indices of the overlayer and substrate.

In this analysis absorption in the overlayer is neglected because the wide band-gap material is transparent in the wavelength region of interest and interference effects are considered only for the fundamental ray. This approximation is valid for wavelengths around the onset of transparency of the substrate, where the contribution to the intensity from higher-order rays is small. The interference oscillations cause the position and width of the knee to oscillate with an amplitude that increases with layer thickness. An expression for the oscillation in the width of the knee is derived from Eq. (11), Eq. (12), and Eq. (16), and shown below:

$$\lambda_a = \bar{\lambda}_a\left(1 - a_s\frac{E_0}{E_s}\right)$$

$$\cong \bar{\lambda}_a\left(1 - \frac{8\pi a_s E_0\sqrt{R_1}}{hc}\Delta n\left(1 - \frac{\Delta n}{2n_f}\right)d_f\sin\delta\right),$$

$$\bar{\lambda}_a = \frac{E_0\lambda_k^2\exp(\Delta_c)}{a_c(2\ln 2)hc\left(1 + a_\lambda\frac{E_0}{E_g}\right)} \cong \frac{E_0\lambda_k^2(1 + \Delta_c)}{a_c(2\ln 2)hc}. \tag{18}$$

The amplitude of the oscillations increase with the Urbach parameter, and the difference in the index of refraction between the overlayer and the substrate.

The oscillations in the width of the knee are observed during growth of a 4.2 μm thick $Al_{0.5}Ga_{0.5}As$ layer on a 450 μm thick semi-insulating GaAs substrate with a polished back surface, rotated at 0.5 Hz during growth. Variations in the layer thickness cause phase variations across the substrate which reduce the effects of thin film interference. The substrate heater is operated at constant power to maintain constant temperature. The knee region of the diffuse reflectance spectrum is fit to Eq. (1) at intervals of about 1 min. The width of the knee, λ_a, is shown in Fig. 2 as a function of layer thickness. The solid line in Fig. 2 is a fit of Eq. (18) to the data. The following parameter values are obtained from this fit:

$$\bar{\lambda}_a = 3.62 \pm 0.02\ \text{nm}, \quad \Rightarrow \Delta_c = 0.080,$$

$$\frac{\lambda_k}{2n_f} = 0.1733 \pm 0.0001\ \mu\text{m}, \quad \Rightarrow n_f = 3.32,$$

$$\frac{8\pi a_s E_0\sqrt{R_1}}{hc}\Delta n\left(1 - \frac{\Delta n}{2n_f}\right) = 0.026 \pm 0.002\ \mu\text{m}^{-1},$$

$$\Rightarrow \Delta n = 0.26. \tag{19}$$

From these values $R_1 = 0.288$, $R_2 = 0.0014$, and $n_s = 3.58$. The average substrate temperature during growth is 567.3°C ($\lambda_k = 1150.4$ nm). The inferred index for AlGaAs at 567°C and 1.15 μm is 3.32. This suggests the Al content is 44% [8], which is close to the $50 \pm 2\%$ concentration determined from the growth rates given by measurements of layer thickness using a scanning electron microscope. The index of refraction for the GaAs substrate at 567°C and 1.15 μm is 3.58 ± 0.05, where the uncertainty is a combination of the standard error [9] determined from the fit (0.02) and the uncertainty in the growth rate calibration (0.04). This value of the index of refraction for the GaAs substrate is close to the expected value of 3.68 for GaAs at 579°C [8]. The experimental value of $\Delta_c = 0.080$ is in agreement with 0.070 given by the model.

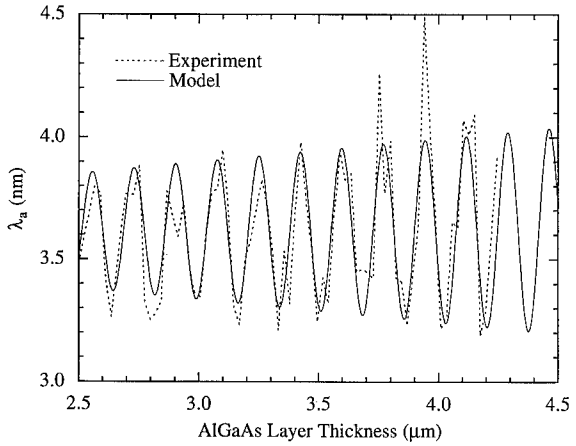

Fig. 2. Oscillations in the width of the knee during the growth of $Al_{0.5}Ga_{0.5}As$ on GaAs (dashed line).

The position and the width of the knee, during the growth of AlGaAs on GaAs, are compared in Fig. 3. As predicted, the position and the width of the knee oscillate in phase. The position of the knee also exhibits longer period fluctuations due to temperature drift in the substrate.

The data shown in Fig. 3 is used to determine the effectiveness of the algorithm given in Eq. (14), where spurious shifts in the knee are sensed by the width of the knee and corrected for. In this case the correction is in terms of wavelength, where the corrected position of the knee is iteratively given by

$$\lambda_k^{i+1} = \lambda_k^0 \left\{ 1 + \frac{\lambda_k^i E_0}{hc} \ln \left[\frac{\bar{\lambda}_a}{\lambda_a} \left(\frac{\lambda_k^0}{\lambda_k^i} \right)^2 \right] \right\}. \tag{20}$$

λ_k^0 and λ_a are the experimentally measured position and width of the knee, and $E_0 = 11.5$ meV at 567°C [6]. The temperatures given by the measured position of the knee (dashed line) and corrected position of the knee (solid line), are shown in Fig. 4. Also shown, is a smooth fit to the position of knee (broken line), which is assumed to represent the true temperature of the substrate. The root mean square (RMS) temperature fluctuations about the true temperature are 1.5°C for the measured knee and 0.7°C for the corrected knee.

5. Conclusions

A mathematical model has been developed for the optical transmission spectrum of GaAs in the wavelength region near the "knee" in the spectrum at the optical band-gap. In this model the temperature is given to first approximation by the position

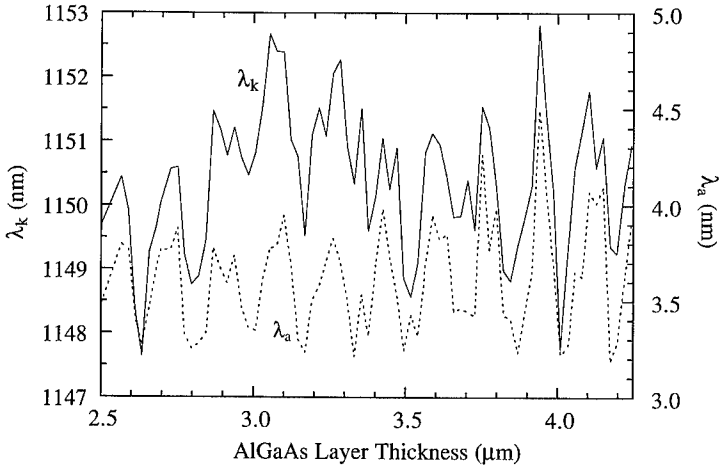

Fig. 3. The position of the knee (solid line) and the width of the knee (dashed line) during the growth of $Al_{0.5}Ga_{0.5}As$ on GaAs.

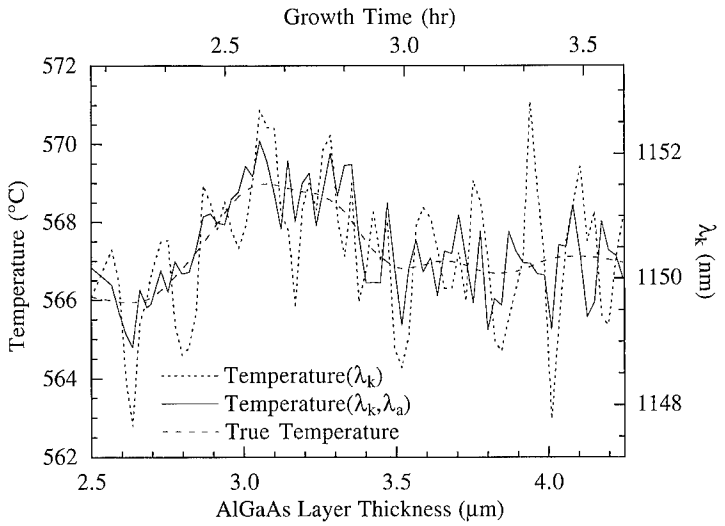

Fig. 4. Substrate temperature given by the position of the measured knee (dashed line), the position of the corrected knee (solid line), and the true temperature (broken line), during the growth of $Al_{0.5}Ga_{0.5}As$ on GaAs.

of the knee, while the width of the knee is used to correct for spurious shifts in its position due to the differences in the properties of the substrate or the measurement conditions from a reference configuration. This model is used in optical band-gap thermometry to correct for the effects of variations in the substrate thickness, measurement geometry, impurity content, back surface scattering, changes in optical throughput caused by window coating and interference oscillations due to a deposited film with a different index of refraction. We show that spurious temperature shifts caused by thin film interference can be reduced to the noise level of the measurement technique during the growth of AlGaAs on GaAs, by using both the position and the width of the knee of the spectrum to determine the temperature.

References

[1] S.R. Johnson, C. Lavoie, T. Tiedje and J.A. Mackenzie, J. Vac. Sci. Technol. B 11 (1993) 1007.
[2] S.R. Johnson, C. Lavoie, M.K. Nissen and T. Tiedje, US Patent No. 5,388,909 (1995).
[3] DRS-1000 data sheet, Thermionics Northwest, 231-B Otto St., Port Townsend, WA 98368.
[4] E.S. Hellman and J.S. Harris, J. Crystal Growth 81 (1987) 38.
[5] D.M. Kirillov and R.A. Powell, US Patent No. 5,118,200 (1992).
[6] S.R. Johnson and T. Tiedje, J. Appl. Phys. 78 (1995) 5609.
[7] S.R. Johnson, Optical bandgap thermometry in molecular beam epitaxy, PhD Thesis, University of British Columbia, (1995).
[8] George Maracas, Optical Constant Data Base for AlGaAs (1995).
[9] W.H. Press, B.P. Fannery, S.A. Teukolsky and W.T. Vetterling, Numerical Recipes (Cambridge University Press, New York, 1990) Section 14.4.

ELSEVIER

Journal of Crystal Growth 175/176 (1997) 281–285

JOURNAL OF CRYSTAL GROWTH

Real time in-situ thickness control of Fabry–Perot cavities in MBE by 44 and 88 wavelength ellipsometry

C.H. Kuo[a,*], M.D. Boonzaayer[a], M.F. DeHerrera[a], D.K. Schroder[a], G.N. Maracas[b], B. Johs[c]

[a] *Department of Electrical Engineering, Center for Solid State Electronic Research, Arizona State University, Tempe, Arizona 85287-6206, USA*

[b] *Motorola Phoenix Corporate Research Labs., 2100 E. Elliot Road, Tempe, Arizona 85284, USA*

[c] *J.A. Woollam Co., Inc., 650 J. St., Suite 39, Lincoln, Nebraska 68508, USA*

Abstract

We have demonstrated how to use the 44 wavelength ellipsometer for in-situ closed-loop feedback control of a molecular beam epitaxy in order to grow reproducible AlAs/GaAs Fabry–Perot cavities. Sample-to-sample reproducibility of the Fabry–Perot cavity mode position measured using normal incident reflection was better than 0.2% among six samples grown at different times and different growth conditions. This shows that a reproducible control of AlAs/GaAs layer thickness is achievable using the 44 wavelength ellipsometer. The new 88 wavelength ellipsometer includes UV wavelengths from 2770 to 4150 Å. The closed-loop in-situ control of Fabry–Perot cavity growth will be explained and the results from the two types of ellipsometers will be compared.

1. Introduction

Epitaxial growth techniques such as molecular beam epitaxy (MBE) and organometallic chemical vapor deposition (OMCVD) have been used to achieve heterostructure devices having complicated multilayer epitaxial structures. The strength of these epitaxial techniques is that alloy composition, thickness, and doping concentration can be reproduced on thickness scales of a few monolayers. Application of these techniques can be used in the growth of devices such as vertical cavity surface emitting lasers (VCSEL) and resonant tunneling diodes (RTD) [1].

Performance of such devices are affected by the epitaxial layer thickness variation. To achieve reproducible epitaxial layer thickness control of a complicated structure such as a VCSEL is a challenge in MBE growth. Several different techniques such as reflection mass spectrometry [2], desorption mass spectrometry [3], and laser-induced fluorescence [4] have been used to monitor group III or group V desorption from the substrate surface during the growth of epitaxial layers. With proper calibration, the real-time desorption flux

* Corresponding author. Fax: +1 602 965 0775; e-mail: chkuo@enuxsa.eas.asu.edu.

0022-0248/97/$17.00 Copyright © 1997 Elsevier Science B.V. All rights reserved
PII S0022-0248(96)01233-X

measurement can be used to monitor the epitaxial layer growth rate and composition.

Reflection high-energy electron diffraction (RHEED) is now a standard equipment in most MBE chambers. RHEED oscillation signal analysis is the most popular method of measuring epitaxial layer growth rate and, consequently, determining alloy composition. The disadvantage of the RHEED growth rate determination is that the oscillation signal is taken without substrate rotation. The growth rate can be very different when the substrate is rotating. The other disadvantage of RHEED is that it cannot account for the flux fluctuation when the shutter is opened. Real-time feedback control is not easy to implement using the techniques mentioned above.

Ellipsometry is becoming more popular ever since the work by Aspnes in the late 1970s [5]. The ellipsometry technique cannot only be used ex-situ to measure thickness and alloy composition, but can also be used in-situ to monitor and analyze data in real time for real-time feedback control. The ellipsometric data can be taken while the substrate is rotating at normal speed. This is an advantage over RHEED. When thickness information can be measured in real time in an MBE experiment, flux fluctuation does not affect the control of each epitaxial layer's thickness. Ellipsometry is becoming a useful technique for performing in-situ control during thin film growths in MBE experiments.

2. Experimental procedure

A detailed theory of ellipsometry can be found in Ref. [6]. The hardware necessary for implementing in-situ ellipsometric control of a MBE system is shown in Fig. 1. The growth chamber has two sets of optical ports whose axes coincide with the center of the wafer at angles of 75° and 60°. The 75° optical port configuration was used in the experiment since III–V epitaxial layers were grown.

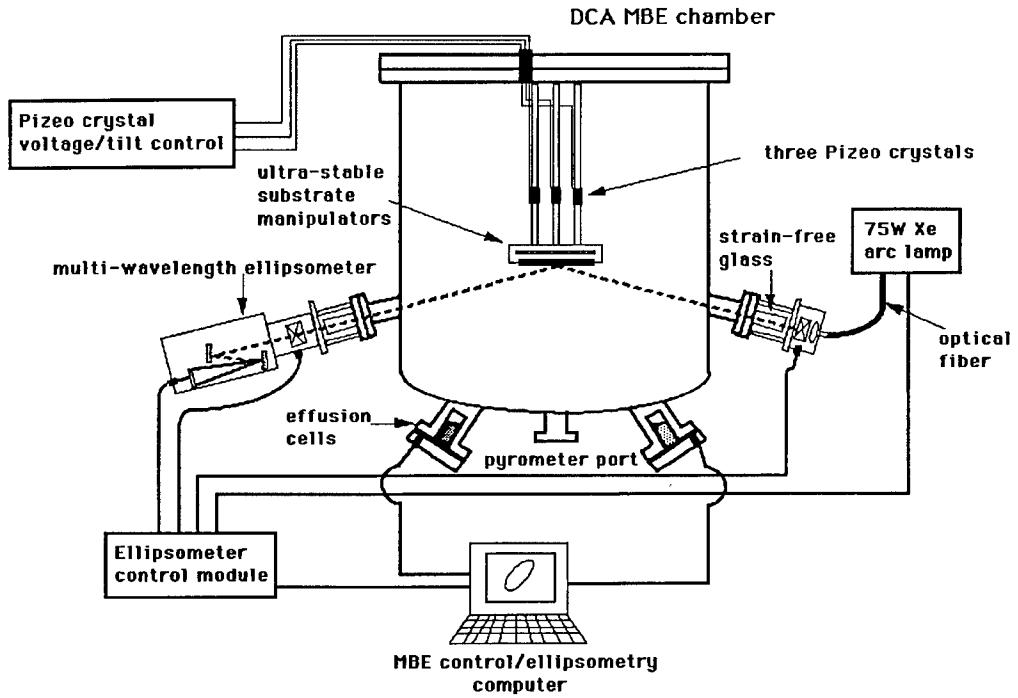

Fig. 1. Implementation of a MWE on a DCA MBE chamber.

The choice of 75°, which is close to the Brewster angle of III–V material, allows the ellipsometer to obtain the maximum sensitivity in monitoring epitaxial layer thickness during MBE growth. Both optical ports are equipped with a strain-free Bromco window to prevent birefringence effects from being introduced into the optical path. Since arsenic tends to stick to windows, both windows must be regularly heated to 300°C in order to desorb the arsenic coating to improve ellipsometric signal intensity.

During the growth of epitaxial layers, substrate rotation is necessary to ensure uniform epitaxial layer growth on the substrate. If the normal direction to the substrate surface is not parallel to the axis of the rotation, the reflected SE signal intensity on the detector will not be stable. Wobble of the substrate surface increases the error of the analyzed ellipsometric data. This, in turn, increases the uncertainty of analyzed epitaxial layer thicknesses and makes it more difficult to control layer thickness in real time to achieve a variation of less than 0.5%. To reduce the wobble of the substrate during rotation, sections of the three stainless-steel rods used to support the manipulator were cut off and replaced with piezo crystals. By externally adjusting the applied negative high voltages, the length of the three pizeo crystals can be changed by as much as 200 μm. Using this technique, changes in the incident angle due to wobbling of the substrate surface can be reduced from a typical variation of $\pm 0.2°$ to $\pm 0.02°$.

The multi-wavelength ellipsometers (MWE) (44 wavelengths ranging from 4150 to 7554 Å and 88 wavelengths ranging from 2770 to 7650 Å) by J.A. Woollam Co., can be used to obtain 44 or 88 wavelength ellipsometric data at the speed of 20 data points per second. MWE data is analyzed in real time to determine epitaxial layer thickness during epitaxial layer growth at the rate of 1 data point every 3 s. The analyzed thickness information is then passed to the MBE growth control program. The growth of a complicated quantum device structure is made feasible by determining epitaxial thicknesses during the thin film growth so that the MBE growth control program can control the shutter toggle times.

3. Results

Fabry–Perot cavities for use in vertical cavity surface emitting lasers (VCSEL) and electro-optic modulators were grown to demonstrate in-situ real-time MWE thickness control. Such structures consist of a one wavelength optical cavity between two dielectric mirrors. This particular structure was used to test MWE control of thick epitaxial layers because the position of the FP mode is very sensitive to a change in cavity thickness. Each mirror consists of alternating $\frac{1}{4}\lambda$ high and low index of refraction layers, known as distributed Bragg reflectors (DBR). This produces mirrors that have a high reflectivity at a selected wavelength band. High reflectivity is an indication of good thickness control in the DBR layers.

The FP cavity designed for this experiment consisted of a 10 period top mirror and a 10.5 period bottom mirror having AlAs/GaAs thicknesses of 822.2 and 679.4 Å, respectively. The GaAs 1λ FP cavity, nominally 2717.5 Å, was designed to have an FP mode at 970 nm.

In order to analyze ellipsometric data collected from MWE during epitaxial layer growth, the optical constants of AlAs and GaAs at growth temperature (i.e. 600°C) are needed. The bulk material optical constants of GaAs and AlAs [7] at growth temperature were obtained from our previous studies and used in this experiment to determine layer thicknesses in real time. Another important issue is that, in order to implement real-time control, the time required to obtain growth layer thickness information from complicated structures like DBRs had to be reduced. The virtual interface model [8] was used to reduce the data analysis from a complicated multi-phase model to a simple two-phase model (epitaxial layer/virtual substrate).

Six samples of 1λ FP cavities were grown under the control of the 44 wavelength ellipsometer in order to demonstrate the reproducibility of MWE thickness control. Samples 1–4 were grown over the period of one month using identical Al and Ga cell temperatures. No growth rate calibration was required before the growth of each FP cavity. The variation of FP modes between the four different samples was less than 2.1 nm, a difference of less than 0.3% in a 1λ GaAs cavity. The FP mode

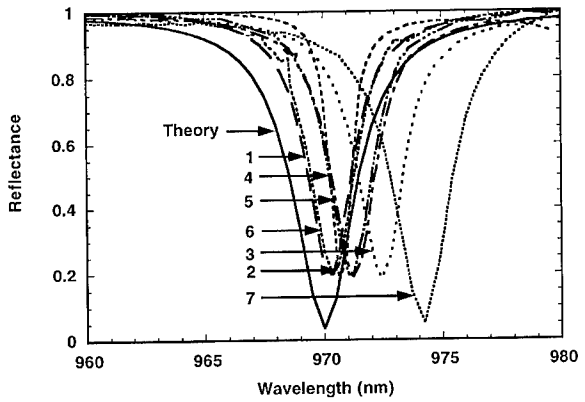

Fig. 2. Calculated normal incidence reflectance curve of a 970 nm FP cavity (labeled "Theory") superimposed with measured curves showing the FP modes from seven different samples.

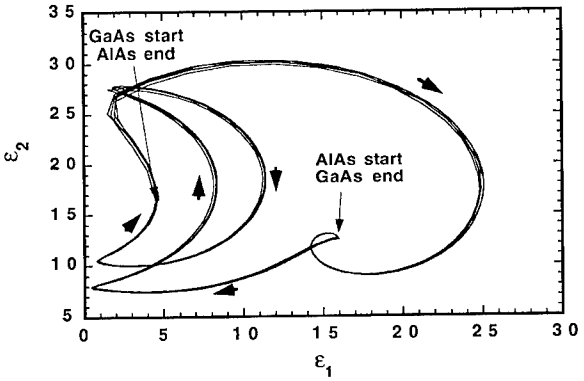

Fig. 3. Dynamical plot of 4150 Å in-situ ellipsometric data from 88 wavelength ellipsometer.

measured at the edge of the 2 inch wafers had a blue shift of about 5 nm compared to the center of the wafers. This indicates that the variation in layer thickness uniformity across the 2 in wafers was about 0.5%.

For sample 5, Al and Ga cell temperatures were perturbed during the growth of AlAs and GaAs layers. Since the thickness control program monitors epitaxial layer thickness information in real time, we did not expect the flux fluctuation to affect epitaxial layer thickness control. This is confirmed as shown in Fig. 2, where the FP mode from sample 5 is within the range of the earlier four samples. This indicates that calibrating the growth rate before the growth of binary epitaxial layers is not necessary in MWE thickness control experiments.

Sample 6 was grown with 1×10^{18} cm^{-3} Si doping in all the epitaxial layers. Since the virtual interface model is temperature-specific, temperature changes during the epitaxial layer growth cannot be taken into account. Also, the possible change of the epitaxial layer optical constants due to Si doping is not taken into account in data analysis. Nonetheless, the difference between sample 6 and the average FP mode from samples 1–4 is less than 0.1%. The effect of surface temperature changes due to Si shutter opening and Si doping can be neglected in in-situ DBR thickness control experiments.

Sample 7 was grown under the control of the new 88 wavelength ellipsometer to compare it with the 44 wavelength ellipsometer. The dynamical plot of the 10.5 period mirrors and thick GaAs FP cavity from the 4150 Å ellipsometric data is shown in Fig. 3. The periodic behavior of the dynamical plot is mainly due to the growth of optically thick GaAs layers. This is also a strong indication that the AlAs and GaAs layers were consistently reproduced. However, the FP mode from the 88 wavelength ellipsometry control was red-shifted 3 nm compared to the 44 wavelength ellipsometry control, as shown in Fig. 2. The source of the difference could be the low signal intensities of the long wavelengths from the 88 wavelength ellipsometer. This, in turn, will increasingly deteriorate the precision of layer thickness determinations as a layer grows thicker. More work will be done to compare the 44 and 88 wavelength ellipsometry controls.

4. Conclusion

Bulk material optical constants can be determined by MWE. These constants were used in real time to control the thickness of epitaxial layers used in Fabry–Perot cavity structures. Reproducibility of the FP mode position was better than 0.2% among four different samples grown at different times when controlled by the 44 wavelength

elliposmeter. The extended UV range of the 88 wavelength ellipsometer should give better composition determination for ternary layer FP cavity modes in the 850 nm range. The differences in FP cavity modes from 88 wavelength ellipsometry will be studied and ternary layer thickness control will be attemped at a later time. Bulk material optical constants can be used in closed-loop feedback control with MWE to increase the reproducibility of complex multilayer structures.

Acknowledgements

The authors would like to thank the Defense Advanced Research Agency for their support of AASERT grant No. DAAH0494G0363 and ULTRA grant No. MDA972-95-1-0016 as part of the Integrated Multi-Sensor Control Consortium, agreement No. MDA972-95-3-0046, between Hughes Research Laboratories, J.A. Woollam Company, Arizona State University, and The University of Colorado.

References

[1] F.G. Celii, Y.-C. Kao, A.J. Katz and T. Moise, J. Vac. Sci. Technol. A 13 (1995) 733.
[2] J.Y. Tsao, T.M. Brennan and B.E. Hammons, J. Crystal Growth 111 (1991) 125.
[3] K.R. Evans, R. Kaspi, C.R. Jones, R.E. Sherriff, V. Jogat and D.C. Reynolds, J. Crystal Growth 127 (1993) 523.
[4] C.H. Kuo, C. Choi, G.N. Maracas and T. Steimle, J. Vac. Sci. Technol. B 11 (1993) 833.
[5] D.E. Aspnes, Thin Solid Films 89 (1982) 249.
[6] R.M.A. Azzam and N.M. Bashara, Ellipsometry and Polarized Light (North-Holland, Amsterdam, 1977).
[7] C.H. Kuo, S. Anand, R. Droopad, Y. Choi and G.N. Maracas, J Vac. Sci. Technol. B 12 (1994) 1214.
[8] I.P. Herman, Optical Diagnostics for Thin Film Processing (Academic Press, New York, 1996).

ELSEVIER

Journal of Crystal Growth 175/176 (1997) 286–291

JOURNAL OF CRYSTAL GROWTH

Two-dimensional to one-dimensional mode change in GaAs molecular beam epitaxy revealed by in situ scanning electron microscopy

N. Inoue[a,*], Y. Kawamura[a], Y. Homma[b], J. Osaka[c], T. Araki[a], T. Ito[a]

[a] *Osaka Prefecture University, 1-2, Gakuencho, Sakai, Osaka 593, Japan*
[b] *NTT Science and Core Technology Laboratory Group, Musashino, Tokyo 180, Japan*
[c] *NTT LSI Laboratories, Morinosato, Atsugi, Kanagawa 243-01, Japan*

Abstract

Two-dimensional (2D) nucleation mode growth of GaAs molecular beam epitaxy is studied in detail by in-situ scanning electron microscopy. It is shown that the local growth mode changes from 2D mode to one-dimensional (1D) step propagation mode under a critical growth condition which causes mixing of 2D and 1D growth. The mechanism is discussed in terms of step interval homogeneization. Various intermediate 2D growth modes between pure 3D and 1D growths are observed depending on the growth condition. A 3D/2D/1D growth mode phase diagram is obtained.

1. Introduction

We have developed in-situ scanning electron microscopy (SEM) of GaAs molecular beam epitaxy (MBE) and shown that the actual growth process is inhomogeneous and unsteady compared to the simplified and ideal growth model [1]: For the two-dimensional (2D) growth mode, continuous nucleation was observed and delayed nucleation was found [2]. For post-growth annealing, competition of hole growth and shrinkage was found and anisotropic behavior was observed [3].

In the present study, the 2D nucleation mode is studied in detail. We show that the local growth mode changes from 2D to one-dimensional (1D) step propagation growth under a critical growth condition which causes mixing of 2D and 1D modes. Change of step interval and shape takes place simultaneously and is responsible for the local mode change.

There have been no reports on the phase diagram of 3D and 2D growth modes. Various intermediate 2D growth modes between pure 3D and 1D growths are observed depending on the growth condition. A 3D/2D/1D phase diagram is obtained.

* Corresponding author. Fax: + 81 722 52 1163; e-mail: inouen@riast.osakafu-u.ac.jp.

0022-0248/97/$17.00 Copyright © 1997 Elsevier Science B.V. All rights reserved
PII S0022-0248(96)00938-4

2. Experimental procedure

The experiment was done using an MBE-UHV SEM hybrid system. An ultrahigh vacuum scanning electron microscope (SEM) is mounted on an MBE system. A field emission electron gun of the cold cathode type is on top of the sample chamber, and an RHEED screen is at the bottom of it. A 25 keV electron beam was used both for SEM and reflection high-energy electron diffraction (RHEED) measurements. For in-situ SE imaging, the electron beam is directed downward to the sample surface at a glancing angle of 20–10°. The Ga and As_4 fluxes are incident upward to the sample surface. Scanning images are produced and stored on an image processor. They can be recorded on videotapes. RHEED measurements are done separately from the SE imaging at a grazing incidence of the primary electron beam.

Samples 8×8 mm^2 in size were cut from a GaAs (0 0 1) substrate misoriented 0.2° to the [1 1 0] direction which had nominal interstep spacing of about 80 nm. The sample was mounted using indium soldering on a silicon substrate. Sample heating was done by resistively heating the silicon substrate with direct current. The sample temperature was monitored with an infrared pyrometer. A smooth surface was prepared by a three-stage buffer layer growth. The 2D growths were performed at a substrate temperatures of around 600°C where the surface exhibited 2×4 reconstruction, and at various growth rates, for example, 1 ML per 40 s. High temperature and low rate were employed to make islands big enough to be clearly observed. SEM observation was performed with a resolution of about 5 nm and an observation rate of 1 frame per 80 s.

3. Results and discussion

3.1. 2D/1D mode change

Fig. 1 shows an example of morphology change with 2D–1D transition. The substrate temperature was 610°C and the growth rate was about 1 ML/50 s. Surface feature at the beginning of growth is shown in Fig. 1a. There are a few parallel dark lines on the upper half slightly declining to the right. They are the monolayer steps. These steps change direction downwards in the middle. The step shape was curved and smooth initially. The terraces bounded by these steps are numbered for clarity. On the real crystal surface the local terrace width is not uniform due to the surface undulation.

The growth was started when the electron beam was scanned at the top of Fig. 1a. In the middle, white small features appeared on the terraces as marked by the arrows. These are the monolayer islands. The islands were formed in three ways depending on the local terrace width: On the wide terraces like No. 7, island clusters appeared as marked by the triple arrows. On the relatively wide terraces like No. 2, the islands were formed in a line along the step as marked by double arrows. On the wide areas of relatively narrow terraces, the isolated island appeared as marked by the single arrows. In this figure, about 20 islands appeared on 5 terraces, Nos. 2, 4, 6, 7 and 8, among ten. Unfortunately, the 2D growth cycle was not so clear as compared to the one we reported previously [3]. There are no islands on the narrow terraces, which shows that the 1D step propagation growth occurs there. Therefore, the two growth modes coexist under a critical growth condition, as previously shown by RHEED measurements [4] and observed by SEM [1]. This is due to an inhomogeneity of terrace width introduced by surface undulation and step bunching during annealing before (and after) growth [5].

In Fig. 1b taken 80 s after Fig. 1a, the steps essentially preserved their location and shape. It is similar to the result of silicon growth on (1 1 1) surface where the step shape is preserved in the 2D growth mode [6]. Most islands appeared in the middle of the figure which suggests that the islanding stage of the growth cycle took place when the electron beam was scanned there. No clusters were observed in this figure.

In Fig. 1c, the clustering of islands took place on Nos. 2, 3 and 7 terraces. More than 20 islands were formed on 6 terraces. The step edges became zigzag apparently due to the coalescence of the islands to the steps as an example marked by the black arrow.

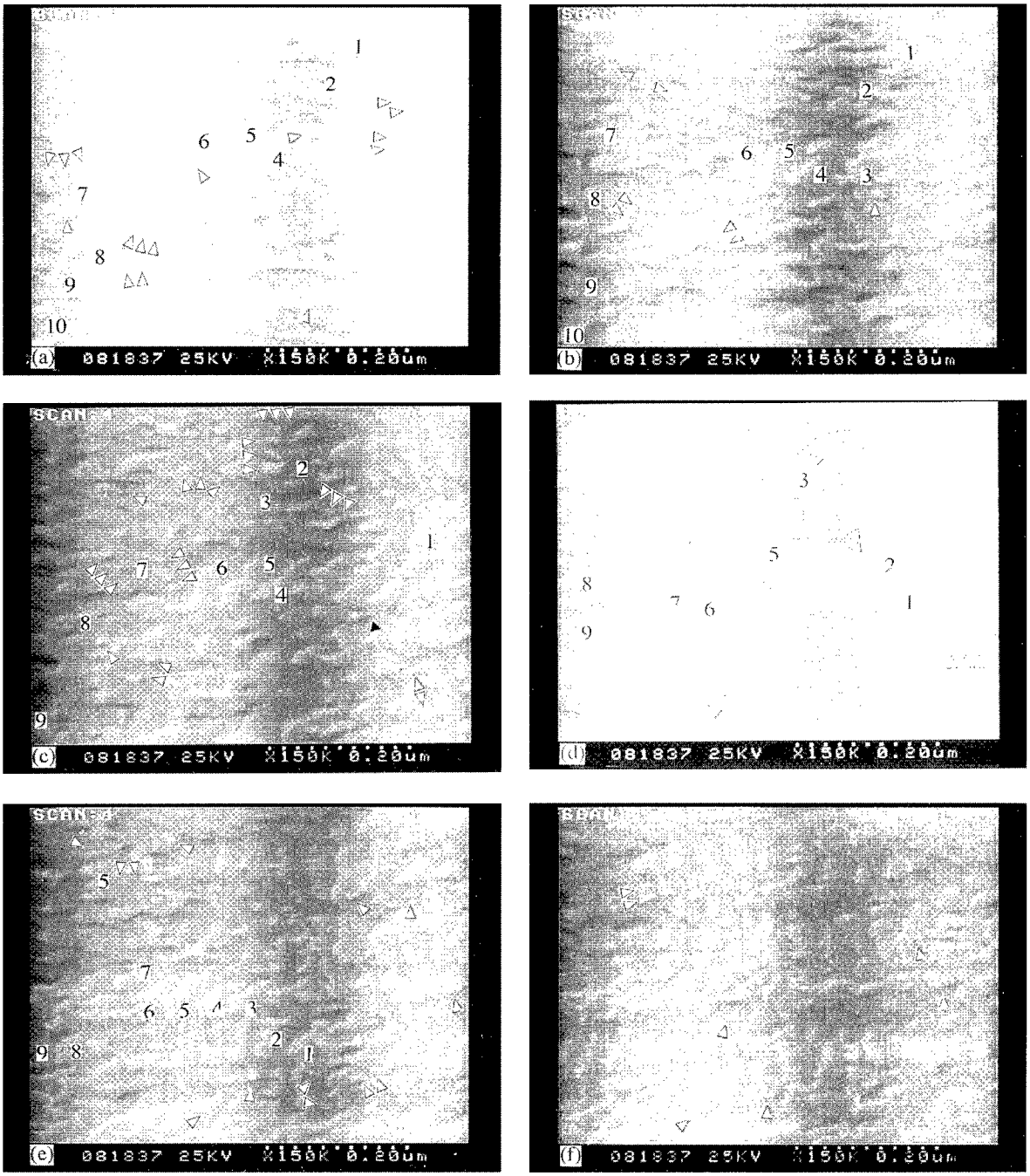

Fig. 1. SEM observation of morphology change. The substrate temperature was 610°C and the growth rate was about 0.02 ML/s. (a) beginning of growth, (b) 1 min, (c) 2 min, (d) 3 min, (e) 5 min, (f) 6 min. The image width is 0.45 μm. The images are foreshortened by a factor of 10 in the vertical direction due to the grazing incidence of the electron beam at 10° and image processing.

It is to be noted that, as the growth proceeded, island clustering became sparse as shown in Fig. 1d. At the same time the step shape began to change: There were no wide terraces except No. 3 and a new terrace appearing on the right side, and the steps became parallel and regular. These features show that the step propagation mode became dominant.

In Fig. 1e, the islands were formed separately in the upper and lower halves. Therefore, two growth cycles were observed during one scan. About 16 islands were formed on 7 terraces. Several new terraces (steps) appeared on the right sides (without numbers). Though the apparent island number is large, net number per cycle per terrace was decreasing. Steps became more parallel.

Finally, in Fig. 1f, only a few islands nucleated on the terraces. In almost all terraces, the growth mode changed to the step propagation. The step shape is macroscopically straight and parallel with small zigzags.

The 2D to 1D growth mode change and its cause is schematically illustrated in Fig. 2. The step interval was inhomogeneous initially (a) but regular (c) and parallel later. It is well known that the step bunching occurs during annealing before growth, which causes step interval nonuniformity as observed in Fig. 1a [5]. 2D and 1D growths take place on wide terraces as shown in (b), which is observed in the present experiment.

On the other hand, the step propagation growth causes the step ordering under some conditions as illustrated in (c) and observed here. One such mechanism is the Schwoebel effect [7]. This eliminated the wide terraces beyond the critical terrace size for 2D nucleation as illustrated in (d). As a result the local growth mode changed to 1D step propagation. The typical local terrace widths with and without islands was estimated from the figures to be 80 and 40 nm, respectively. Thus, the growth was done under the critical condition for the terrace width of about 60 nm. It is close to the nominal terrace width of 80 nm employed here. This is the reason why the 2D to 1D growth mode change occurred here. The disagreement of the observed critical terrace width from the nominal one is partially due to the grazing incidence of the electron beam.

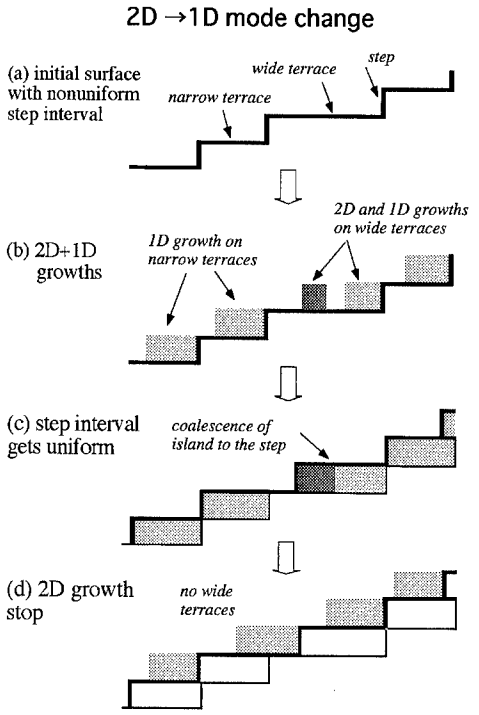

Fig. 2. A model for mechanism for the 2D–1D mode change.

3.2. 3D/2D/1D growth mode phase diagram

As shown above, the exploration of 2D growth mode should lead to boundaries to 1D or 3D growth mode. There have been no reports, however, on the phase boundary between the 3D and 2D growth modes. In this work various intermediate growth modes between pure 3D and 1D growths were observed by changing the growth condition as summarized in Fig. 3.

As for the boundary between 2D and 1D growths, 2D to 1D mode change is marked with the crosses in Fig. 3. This corresponds to the critical condition. The oblique line was the previous determination using STM [8]. The agreement is acceptable.

As for the boundary between 2D and 3D growth modes, it was found that an ideal 2D (2 level) growth is hardly observed, but the tendency to rough growth is usually observed. For example, a 2 level–3 level change occurs in a few layers

usually, due to the coexistence of monolayer-deep holes and islands. As the growth proceeds, the growth front spreads over multi levels [9], but the number of layers saturates at several layers [10] under a wide variety of growth condition as an example of SEM observation shown in Fig. 1d of Ref. [3]. They are shown by circles in Fig. 3.

In an extreme case, the multi-level growth changes into 3D growth, probably due to the preferential nucleation of islands on islands rather than on the terrace. They are shown by the squares in Fig. 3.

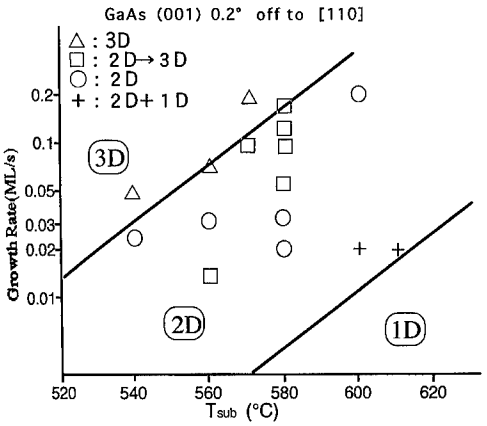

Fig. 3. 3D/2D/1D growth mode phase diagram with various 2D growths corresponding to RHEED behaviors.

At the lower temperatures or higher growth rates, though the formation of monolayer 2D islands was observed initially, recovery to the smooth surface (i.e., the growth cycle) was hardly observed and the surface got monotonically rough as an example shown in Fig. 4. This type of 3D growth is marked with triangles in Fig. 3. The boundary between 3D and 2D growths should be drawn on the squares. In the present study the line is drawn parallel to the boundary between 2D and 1D for simplicity. Detailed study on the various 3D growths will be reported separately.

4. Summary

In summary, the 2D nucleation mode is studied in detail by in-situ scanning electron microscopy. It is shown that the local growth mode changes from 2D to 1D step propagation growth under a critical growth condition of mixing of 2D and 1D growths. A growth model for such a mode change is proposed. Various intermediate growth modes between pure 3D and 1D growths were observed depending on the growth condition. A 3D/2D/1D growth mode phase diagram is obtained.

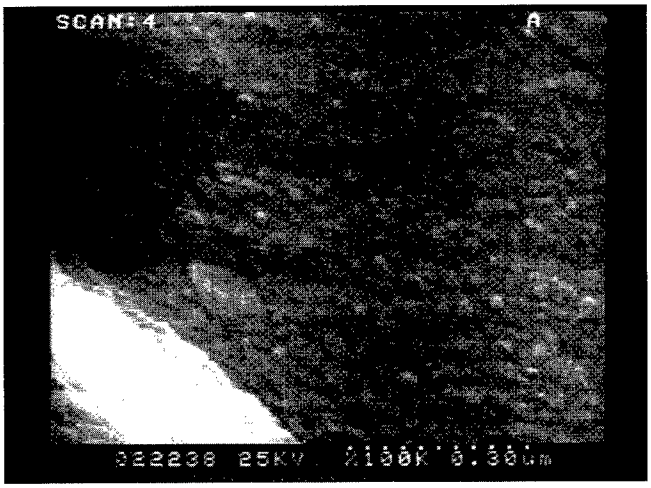

Fig. 4. An example of 3D growth. The substrate temperature was 540°C and the growth rate was about 0.05 ML/s.

Acknowledgements

The authors are grateful to Ryuta Sakai for help in sample preparation and to Saeko Ito for help in manuscript preparation, and the encouragement offered by Masafumi Yamamoto and Kosuke Ikeda is gratefully acknowledged. This study was partially supported by the Proposal-based Advanced Industrial Technology R&D Program of NEDO.

References

[1] N. Inoue, J. Crystal Growth 146 (1995) 334.
[2] J. Osaka, N. Inoue and Y. Homma, Appl. Phys. Lett. 66 (1995) 2110.
[3] N. Inoue, J. Osaka and Y. Homma, J. Crystal Growth 164 (1996) 88.
[4] T. Shitara, J. Zhang, J.H. Neave and B.A. Joyce, J. Appl. Phys. 71 (1992) 4299.
[5] T. Ide, A. Yamashita and T. Mizutani, Phys. Rev. Lett. B 46 (1992) 1905.
[6] M. Ichikawa and T. Doi, Appl. Phys. Lett. 50 (1987) 1141.
[7] R.L. Schwoebel and E.J. Shipsey, J. Appl. Phys. 37 (1966) 3682.
[8] N. Ionue, Adv. Mater. 5 (1993) 192.
[9] P.R. Pukite, C.S. Lent and P.I. Cohen, Surf. Sci. 161 (1985) 39.
[10] J. Sudijono, M.D. Johnson, M.B. Elowitz, C.W. Snyder and B.G. Orr, Surf. Sci. 280 (1993) 247.

ELSEVIER

Journal of Crystal Growth 175/176 (1997) 292–297

JOURNAL OF CRYSTAL GROWTH

In situ observation of MEE GaAs growth using scanning electron microscopy

Y. Homma[a,*], H. Yamaguchi[b], Y. Horikoshi[1,b]

[a] *NTT Science and Core Technology Laboratory Group, 3-9-11 Midoricho, Musashino-shi, Tokyo 180, Japan*
[b] *NTT Basic Research Laboratories, Atsugi-shi, Kanagawa 243-01, Japan*

Abstract

We have used in situ scanning electron microscopy (SEM) for real-time observation of migration enhanced epitaxy (MEE) processes. The surface morphology developed during MEE growth is either monolayer islands or monolayer holes depending on the amount of Ga supply per growth cycle. When island coverage is low, the islands disappear immediately after growth terminates, while the holes remain longer. Resulting surface roughness is much smaller than in molecular beam epitaxy even at a low substrate temperature. The present observations directly confirm enhancement of surface atom migration in MEE.

1. Introduction

Observing atomic level epitaxial processes in real time leads to a deeper understanding of nucleation and growth kinetics. We have demonstrated the potential and usefulness of in situ scanning electron microscopy (SEM) for direct imaging of molecular beam epitaxy (MBE) processes [1–4]. Secondary electron (SE) images of 2D-island nucleation and coalescence clearly showed the layer-by-layer growth in real space, and were correlated with the reflection high-energy electron diffraction (RHEED) intensity [4]. The main advantage of in situ SEM is that it can monitor growth processes without interruptions, i.e., surface quenching, which is still necessary for scanning tunneling microscopy (STM) for III–V compounds epitaxy.

In this paper, we apply in situ SEM to characterize migration enhanced epitaxy (MEE) of GaAs surfaces. In MEE, the surface migration of Group-III elements is enhanced by the alternate supply of Group-III and Group-V elements. As a result, a high-quality epitaxial layer can be grown at temperatures far below the MBE growth temperature range [5–7]. We compare the morphologies of GaAs(0 0 1) surfaces grown by MBE and MEE at 500°C [8]. This temperature is too low to grow high-quality GaAs epitaxial layers by MBE, but high enough for MEE growth. Lower temperatures were not chosen because the surface reconstruction would change to $c(4\times4)$, which is different from the (2×4) reconstruction normally used in MBE growth.

* Corresponding author. Fax: +81 422 59 3695; e-mail: homma@ilab.ntt.ca.jp.
[1] Present address: Waseda University, Okubo, Shinjuku, Tokyo 169-50, Japan.

0022-0248/97/$17.00 Copyright © 1997 Elsevier Science B.V. All rights reserved
PII S0022-0248(96)00880-9

2. Experimental procedure

In situ observations were performed using the ultrahigh vacuum SEM/MBE system reported previously [1]. The instrument is equipped with a field emission electron gun mounted on top of the sample chamber, in which gallium and arsenic effusion cells are installed. The electron beam energy was 25 keV, with a beam current of 0.1–0.3 nA. For SEM imaging, the sample stage was tilted 75° from the horizontal sample position, and the electron beam was directed downward to the surface at a glancing angle of 15°. The Ga and As_4 fluxes were directed upward to the surface at 31°.

An $8 \times 8\ mm^2$ sample, cut from a GaAs(0 0 1) substrate misoriented 0.2° toward the (1 1 0) plane, was mounted using indium soldering on a silicon substrate. The sample was heated by resistively heating the silicon substrate with direct current. Its temperature was monitored with an infrared pyrometer. After a buffer layer of GaAs was grown by MBE at 580°C, the comparative experiment between MBE and MEE was performed at 500°C. In MEE mode growth, the Ga and As shutters were opened alternately, while they were kept open during MBE growth. The As_4 pressure was about 1×10^{-5} Torr when the As shutter was open. It decreased to $\frac{1}{10}$–$\frac{1}{4}$ when the shutter was closed. The growth rate of GaAs was determined from the surface morphology oscillations observed by SEM when growing at a temperature of 580°C. The growth rate was typically 12–15 s per GaAs monolayer. The scanning rate for SEM imaging was 80 s per frame with an effective imaging time of 73 s. Thus, growth of 4–6 GaAs layers was imaged in one micrograph frame during growth. It should be noted that time-dependent morphology variations were superimposed on a normal SEM micrograph when the surface was imaged during growth or annealing.

3. Surface morphology in MBE

In the 2D-island nucleation mode of MBE, surface roughness develops during growth, because the nucleation–coalescence cycle does not occur in an ideal manner but in an out-of-phase one, so several levels of layers coexist [9]. Fig. 1 shows the surface morphology during MBE growth and after annealing for two different substrate temperatures. At 580°C, which is a normal temperature for MBE, the surface morphology oscillates clearly in the first three cycles as a result of nucleation and coalescence of 2D islands [image (a)]. However, the surface becomes rough due to accumulation of islands and holes. The step and terrace structure on the initial surface is buried in these multilayered islands. Nevertheless, the roughened surface easily recovers its initial smoothness after post-growth annealing. Image (b) is a 5 min annealed surface after growth termination. Steps consisting of one GaAs layer (monolayer) can be seen. Islands and holes developed during growth are incorporated into these steps and disappear.

On the other hand, at lower substrate temperature, 500°C, the morphology oscillation cannot be recognized during growth as shown in image (c), because surface diffusion is too low. Small Islands accumulate monotonically. Even after being annealed for a long time at this temperature, the surface did not recover its initial smoothness. Image (d) shows the surface after 10-monolayer (ML) growth followed by an 8 min annealing. Small islands coalesced to form 30–100 nm ones. Further annealing did not eliminate the islands. It was necessary to raise the substrate temperature to 550°C to anneal out these islands.

Thus, an atomically smooth surface is hard to grow without post-growth annealing when the 2D-island nucleation growth mode occurs. In the step propagation growth mode (so called step-flow mode), a well-defined step-terrace structure can be obtained during growth, but it requires a high substrate temperature or a low growth rate.

4. Surface morphology in MEE

In contrast to MBE, a fairly smooth surface can be obtained even at a low substrate temperature of 500°C in MEE. In Fig. 2, the surface morphologies are compared between the initial surface (a), and immediately after growth of 10 layers (b), and after annealing for 100 s (c). The initial surface shows monolayer steps, and a step bunch running from

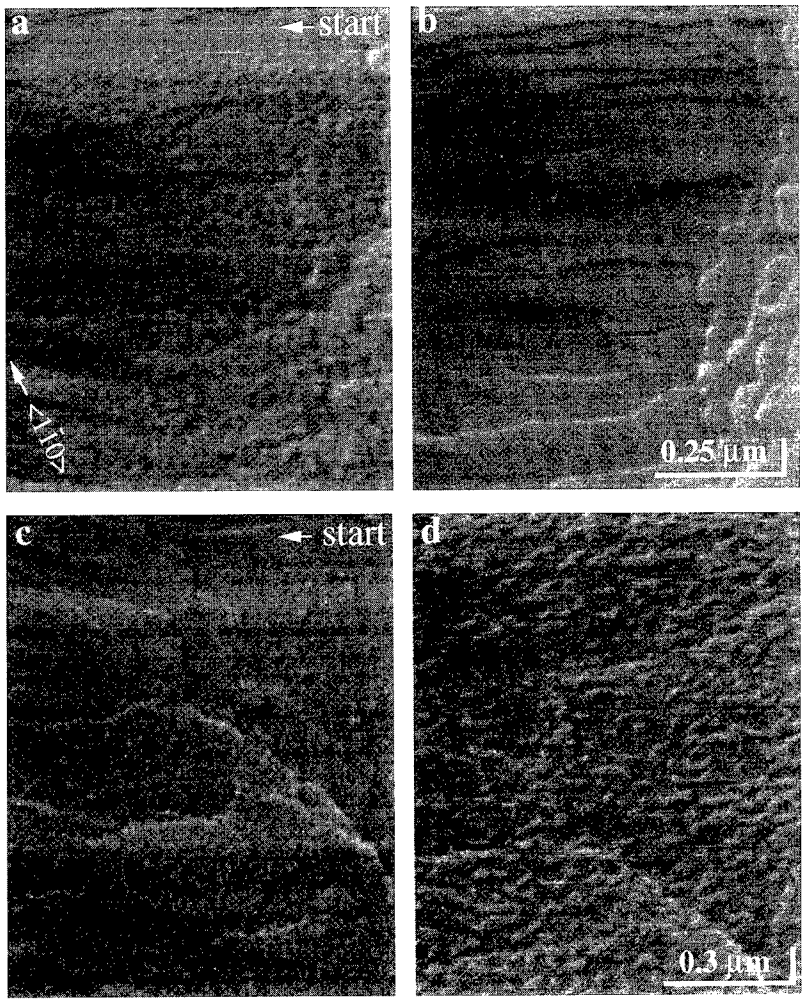

Fig. 1. SE images of MBE-grown GaAs(0 0 1) surface. (a) During growth at 580°C, (b) 5 min annealed surface at 580°C after MBE, (c) during growth at 500°C and (d) 8 min annealed surface at 500°C after MBE.

top left to middle right. During MEE growth, Ga and As were supplied alternately in amounts corresponding to 1 ML. For one cycle, the Ga shutter was opened for 11.5 s and the As shutter was opened for 3.5 s. Acquisition of image (b) started 15 s after the 10 cycles of Ga and As supply (i.e., 10-layer growth. SE images during growth are presented in Ref [8]). Bright spots are islands remaining on the surface. In spite of the existence of these islands, monolayer steps almost identical to the initial surface are seen. This is because the remaining islands are only a monolayer high, and their coverage is much smaller than unity. These islands are almost annealed out in the next image (c) taken 100 s after growth termination.

These results indicate that the surface diffusion is much greater in MEE than in MBE, so only monolayer-high roughness develops during growth. The surface diffusion of atoms from GaAs islands to steps during post-annealing should be the same for both MBE and MEE. The difference in recovery of surface smoothness is due to the height and density of islands; as discussed in the previous section, a high density of multilayered islands are formed in MBE.

It is not only islands but also holes that appear just after MEE growth. Fig. 3 shows SE images of the hole type morphology observed immediately after a 10-layer MEE growth. The top bright region in image (a) is the final period of Ga supply: the SE intensity increases with Ga coverage. Because of contrast enhancement, the image brightness is saturated in this area. In addition to some bright islands similar to those in Fig. 2, dark spots are seen. These are monolayer-deep holes. They are clearer in the next scan [image (b)] and are more resistant to elimination than islands. This is easily understood: eliminating a hole requires adatoms to be released from steps and to diffuse into the holes, while eliminating an island only needs adatoms to be released from the island. These holes remained for at least 5 min. It should, however, be emphasized that the remaining surface roughness is only caused by these monolayer-deep holes.

Whether islands or holes are formed depends on the amount of Ga supply in each cycle relative to the number of surface sites in a monolayer. Fig. 4

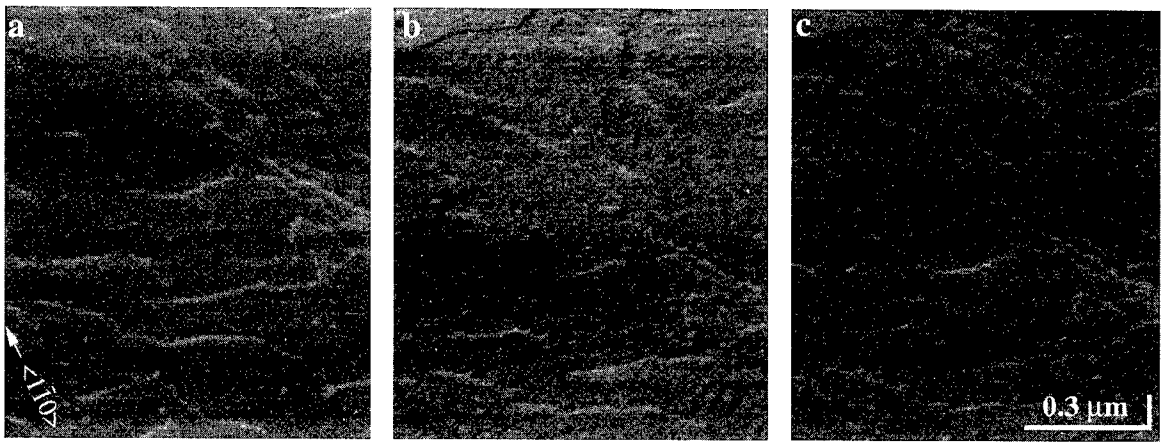

Fig. 2. SE images of MEE-grown GaAs(0 0 1) surface at 500°C. (a) Initial surface, (b) 15 s after 10-layer growth and (c) 100 s after growth.

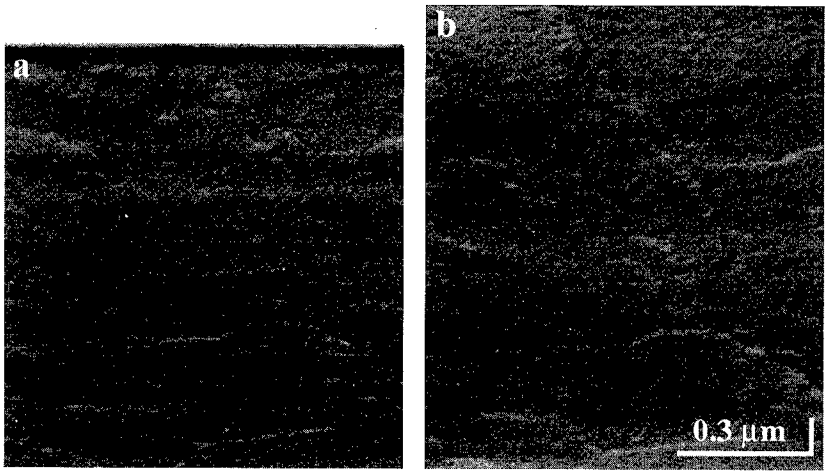

Fig. 3. SE images of MEE-grown GaAs(0 0 1) surface with holes on it. (a) Just after 10-layer growth and (b) 80 s after growth.

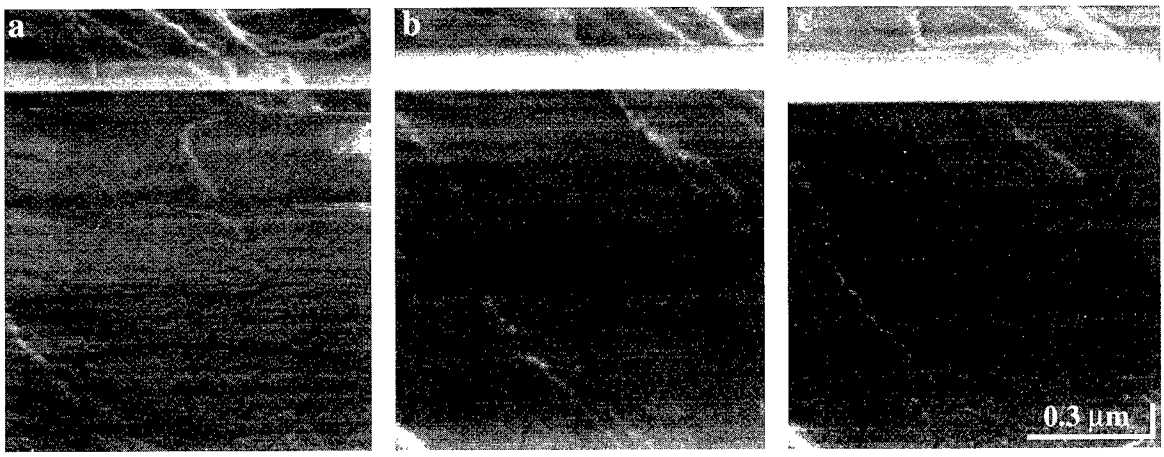

Fig. 4. Surface morphology of MEE-grown GaAs surface for different duration of Ga supply; (a) 5 s, (b) 6 s and (c) 7 s.

shows the surface morphology immediately after one cycle of MEE growth for different Ga supply periods. The bright band in each image corresponds to the Ga supply period. Since the shutters were controlled manually, after several cycles of MEE growth the error in the shutter opening time could accumulate. Therefore, the surface morphologies after just one cycle of growth were compared. Image (a) is for short Ga supply. Holes can be seen on the surface. Image (b) is for exact supply; no holes or islands are seen. Image (c) shows excessive supply causing island formation. There is some time delay before islands or holes become discernible. This delay might be because the islands are too small to be observed by SEM just after the first growth cycle; but they grow to a macroscopic size during annealing. Even during growth, almost no change was observed in the first two cycles, but then islands appeared in the third and later cycles [8].

As growth proceeds, island coverage increases and the size of islands or holes expands every cycle. This process was revealed by a previous RHEED study: if the Ga supply was not equal to the surface site number per unit area, N_S, the RHEED intensity oscillation showed beat-like modulation [6]. The beat frequency varied with the number of Ga atoms supplied per cycle, N_{Ga}. Thus, islands or holes equivalent to $N_{Ga} - N_S$ were formed every cycle and the surface recovered to a flat layer every $N_S/|N_{Ga} - N_S|$ cycles.

The present observations confirm by means of real-space images that surface migration during growth is significantly enhanced in MEE. Ga atoms supplied each cycle never stay on top of previously formed islands but move to edges of islands or in between them. Thus multilayer islands do not form, which causes the MBE surface to roughen.

5. Summary

Scanning electron microscopy was used for in situ observation of MBE- and MEE-grown GaAs surfaces. Secondary electron images observed in a surface sensitive condition clearly showed morphology due to nucleation and growth of 2D-islands. At 500°C, which is lower than the normal MBE growth temperature, a smooth surface with monolayer steps was obtained immediately after MEE growth, while the surface was roughened by random nucleation in MBE growth. On the MEE surface, holes or islands remained when the Ga supply was not equal to the monolayer coverage. However, the islands or holes are only a monolayer high (deep), and never develop a multilayered structure.

Acknowledgements

The observation of MBE surfaces were performed in collaboration with Dr. N. Inoue and Dr. J. Osaka, NTT LSI laboratories.

References

[1] Y. Homma, J. Osaka and N. Inoue, Jpn. J. Appl. Phys. 33 (1994) L563.
[2] N. Inoue, J. Osaka and Y. Homma, J. Crystal Growth 150 (1995) 107.
[3] J. Osaka, N. Inoue and Y. Homma, Appl. Phys. Lett. 66 (1995) 2110.
[4] Y. Homma, J. Osaka and N. Inoue, Jpn. J. Appl. Phys. 34 (1995) L1187.
[5] Y. Horikoshi, M. Kawashima and H. Yamaguchi, Jpn. J. Appl. Phys. 25 (1986) L868.
[6] Y. Horikoshi, M. Kawashima and H. Yamaguchi, Jpn. J. Appl. Phys. 27 (1988) 169.
[7] Y. Horikoshi, H. Yamaguchi, F. Briones and M. Kawashima, J. Crystal Growth 105 (1990) 326.
[8] Y. Homma, H. Yamaguchi and Y. Horikoshi, Appl. Phys. Lett. 68 (1996) 63.
[9] J. Sudijono, M.D. Johnson, M.B. Elowitz, C.W. Snyder and B.G. Orr, Surf. Sci. 280 (1993) 247.

ELSEVIER

Journal of Crystal Growth 175/176 (1997) 298–303

JOURNAL OF CRYSTAL GROWTH

A new in situ III–V surface characterization technique: chemical modulation spectroscopy

P.A. Postigo*, T. Utzmeier, G. Armelles, F. Briones

Instituto de Microelectrónica de Madrid (CNM-CSIC), Isaac Newton, 8 Parque Tecnológico de Madrid, E-28760 Tres Cantos, Madrid, Spain

Abstract

A new in situ technique for the study of the molecular beam epitaxy (MBE) growth process of III–V compounds based on the chemical modulation of the surface has been developed. In this technique, the anisotropic optical reflectivity is modulated by a periodic variation of the surface stoichiometry induced by using group V pulsed molecular beams. Pulses are produced by valved pulsed cells for group V elements (As, P, Sb) that we use for atomic layer molecular beam epitaxy (ALMBE) growth. The substrate is maintained at sufficiently high temperature in order to obtain rapid desorption of group V molecules from surface during flux interruptions, and the process is monitorized by reflection high energy electron diffraction (RHEED). Linearly polarized light, reflected at near normal incidence by the sample, is collected independently along one of the two principal axes of the crystal, [1 1 0] and [1 $\bar{1}$ 0]. This technique has been applied to the surfaces of epitaxial (1 0 0) layers of GaP, GaAs, GaSb, InP, InAs, and InSb grown by MBE. Spectra in the 1–3 eV range show well defined peaks for light polarized along [1 1 0] and [1 $\bar{1}$ 0] directions, parallel to group III and group V dimers, at specific energies for each compound.

PACS: 73.20. – r; 78.66.Fd

Keywords: In situ; Characterization; Optical; MBE

1. Introduction

Lot of work in optical characterization of growth processes during epitaxial growth has been done in the last two years. Reflectance difference spectroscopy (RDS) [1, 2] has been extensively used for the in situ characterization of semiconductor surfaces during or in stopped growth. Surface photo absorption (SPA) [3] has been also used for characterization during molecular beam epitaxy (MBE) [4, 5] growth. These kind of measurements usually are spectroscopic, but they also have been done at fixed wavelengths, using laser sources at photon energies near from the maximum of absorption of the surface group III dimers, for in situ control of growth processes [6] or stoichiometry [7, 8].

In this work, we report an in situ characterization of optical anisotropies in the near-normal-incidence reflectance spectra for two sets of semiconductor compounds, based on In and Ga:

* Corresponding author. Fax: + 34 1 806 07 01; e-mail: aitor@pinar1.csic.es.

0022-0248/97/$17.00 Copyright © 1997 Elsevier Science B.V. All rights reserved
PII S0022-0248(96)00942-6

GaP, GaAs, GaSb, InP, InAs and InSb. For this, we have developed an optical technique that measures the difference in the normal incidence reflectances between two surface coverage states, one that corresponds to a surface covered with group V element and the other corresponding to a surface after a rapid desorption of the group V element, leaving a surface nearly group III element stabilized. In this way, we produced a chemical modulation of the surface that allow us to obtain the difference between the reflectance spectra for light polarized along one specific direction, usually [1 1 0] and [1 $\bar{1}$ 0], and for light with energy values ranging from 1 to 3 eV. Finally, a simple calculation based on the determination of the transitions in a schematic molecule with a geometry similar to that of the dimers, has been done, and the results agree well with the general behavior of the experimentally observed results.

2. Experimental procedure

The experimental setup is schematically showed in Fig. 1. White light from a 50 W halogen lamp is focused by means of a lens and a plane mirror on the substrate placed in the MBE chamber, at near normal incidence. The reflected light passes through another lens and a quartz Rochon analyzer, being detected by a Si or GaInAs p-i-n photodiode in photoconductive mode placed at the plane of the exit slit of a 0.22 m monochromator. The current output is voltage converted and routed to a DC amplifier and the signal is recorded in a computer. Successive deposition and desorption of the group V element is obtained by means of pulsed valved cells for the group V elements and at sufficiently high substrate temperature as to permit rapid desorption of group V element from the surface. The corresponding surface reconstruction changes are monitorized by reflection high energy electron diffraction (RHEED). This modulation in the surface coverage produces a change ΔR in the intensity of the reflected light, $\Delta R = R_{III} - R_V$, that is represented normalized to the reflectivity R_{III}, $\Delta R/R = R_{III} - R_V/R_{III}$ in each polarization, [1 1 0] and [1 $\bar{1}$ 0]. Since the recorded signal is quite noisy, this process is repeated (about 20 times is sufficient) and the signal is averaged until mean quadratic standard deviation of ΔR is lower than a fixed value (usually 5%).

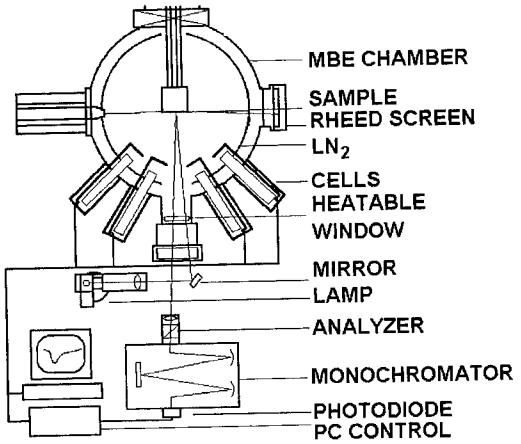

Fig. 1. Schematic representation of the experimental setup used.

Fig. 2 shows reflectance versus time for As_4 pulses over GaAs for different wavelengths in each azimuth. The beam equivalent pressure (BEP) of As_4 is 4×10^{-6} Torr and the pulse length is 0.3 s, with a constant substrate temperature of $T_s = 556°C$. The initial stage (As OFF) RHEED pattern corresponds to a (4×2) Ga-stabilized surface, and the initial level of reflected light intensity is arbitrarily fixed as R_{Ga}. When the As cell is open (As ON), the intensity of reflected light decreases to reach R_{As}, where surface saturation with As is achieved. A clear RHEED change is observed, showing a (2×4) diffraction pattern at this moment. The As_4 beam is then interrupted (As OFF) and desorption of As from surface occurs. The intensity of light increases exponentially with time until the initial level of intensity is recovered, and a RHEED (4×2) pattern is observed again. We define the increment in the reflectivity caused by the change in the coverage, ΔR, as $\Delta R = R_{Ga} - R_{As}$ and its normalized value, $\Delta R/R$, as $\Delta R/R = R_{Ga} - R_{As}/R_{Ga}$.

In this way, spectra in the energy range 1–3 eV were obtained for the two sets of compounds in each one of the two principal azimuths, [1 1 0] and [1 $\bar{1}$ 0]. We have grown epitaxial buffer layers on (1 0 0) oriented GaP, InP, and GaAs substrates.

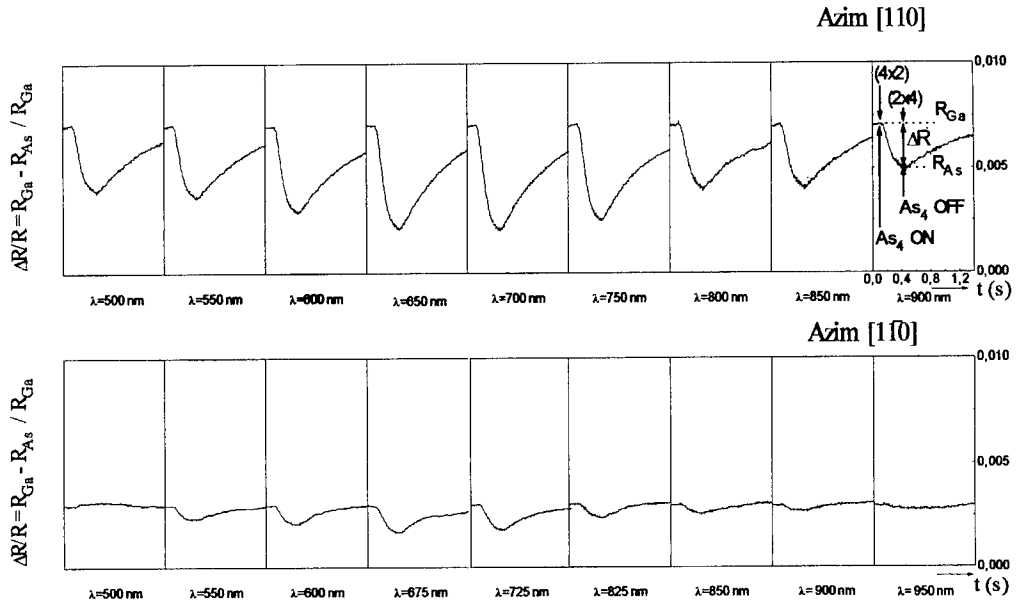

Fig. 2. Change in the reflectivity versus. time for different wavelengths and for both azimuths measured in GaAs. The signal for $\lambda = 900$ nm in the [1 1 0] azimuth is marked with the defined increment in the reflectivity, and with the changes in the reconstruction pattern observed during the measurement.

Table 1
Conditions for measurements

Composition	T_s (°C)	BEP (Torr)	$t_{on\ off}$ (s)	RHEED pattern change	
GaP	598	2.5×10^{-6}	0.5	(2 × 4)	(2 × 2)
GaAs	556	4×10^{-6}	0.3	(4 × 2)	(2 × 4)
GaSb	462	1.7×10^{-6}	0.5	(1 × 3)	c(2 × 6)
InP	370	2.5×10^{-6}	0.4	(2 × 4)	(2 × 1)
InAs	385	1.8×10^{-6}	0.3	(4 × 2)	(2 × 4)
InSb	310	1.8×10^{-6}	0.4	(4 × 2)	(1 × 3)

Buffer layers were sufficiently thick (~ 1 μm) so as to obtain a completely relaxed material. We have used atomic layer molecular beam epitaxy (ALMBE) [9] in the last 100 ML to enhance flat surface morphology. For the measurements, pulses of P_2 for GaP and InP, As_4 for GaAs and InAs, and Sb_4 for GaSb and InSb respectively, were used by means of valved-pulsed cells, usually employed for ALMBE growth. We have observed by RHEED that this temperatures provide a good desorption rate of group V molecules from the surface and assure the good quality of the sample. In Table 1 we summarized the change in reconstruction observed by RHEED when group V element is deposited or desorpted, the substrate temperatures used and the rest of measurement conditions.

3. Results

Fig. 3 shows the spectra for the Ga-based compounds, in which well-defined maxima appear in the [1 1 0] direction, parallel to Ga dimers at ~ 2.2, ~ 1.8, and ~ 1.2 eV for GaP, GaAs, and

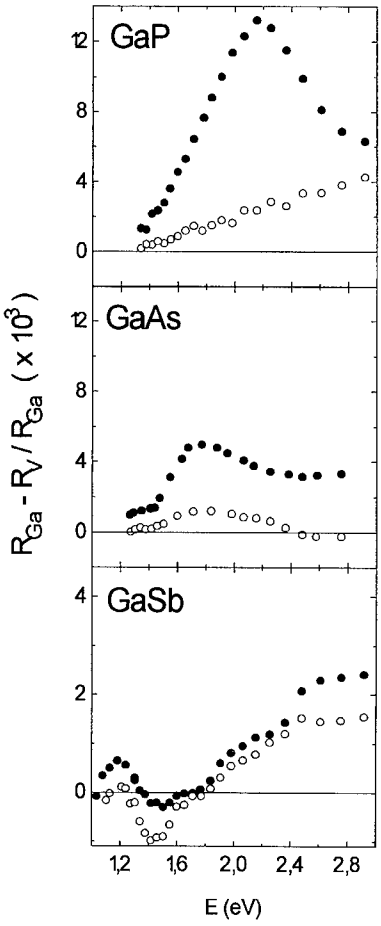

Fig. 3. Spectra obtained for the Ga-based compounds. Solid dots are for [1 1 0] azimuth whereas open dots are for [1 $\bar{1}$ 0].

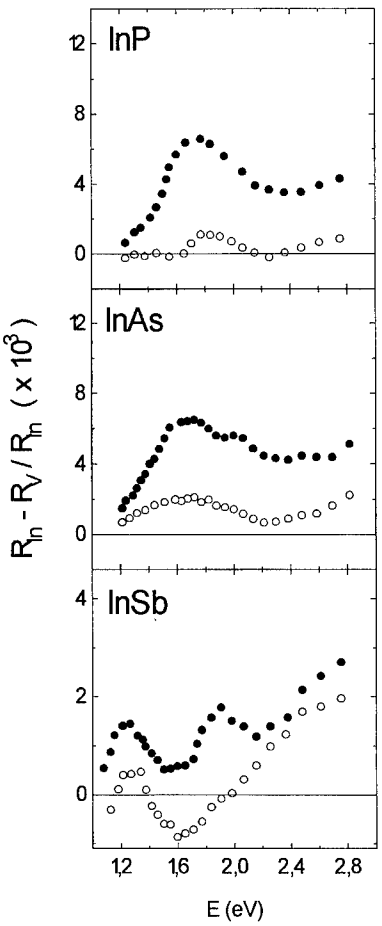

Fig. 4. Spectra obtained for the In-based compounds. Solid dots are for [1 1 0] azimuth whereas open dots are for [1 $\bar{1}$ 0].

GaSb respectively. Our technique establishes the difference of reflectivity between two surfaces, one covered by group III element and the other covered with group V element, respectively. In this polarization, and in the measured spectral range, group V element terminated surfaces are not expected to have abrupt optical features [10]. For these reasons, we assign the maxima to be due to transitions between occupied Ga-dimer bands and unoccupied dangling-bond bands at characteristic energies in each material. In the case of GaAs, the energy position agrees well with that observed by Aspnes et al. [11] at 1.8 eV and assigned to an optical transition between the occupied Ga-dimer and unoccupied dangling-bond bands [10]. In the [1 $\bar{1}$ 0] direction, that is parallel to group V dimers, the signal is much lower than in the [1 1 0] direction, and no clear features have been found except for GaSb, at an energy of $\sim$ 1.4 eV. This peak is assigned to a transition from the occupied lone-pair band to the unoccupied Sb dimer band.

Fig. 4 shows the spectra measured for InP, InAs and InSb. Clear peaks in the [1 1 0] direction appear at $\sim$ 1.7 eV for InP, $\sim$ 1.6 eV for InAs, and $\sim$ 1.2 eV for InSb all related with In-dimer transitions. Two peaks that are not observed for InP, appear in InAs at $\sim$ 2.0 eV and much more strongly in InSb at an energy of $\sim$ 1.9 eV, but only those at lower energies must be related to In-dimer absorption, according to the behavior of these kind

of transitions given by Harrison's rule [12]. For the [1 $\bar{1}$ 0] direction, clear peaks are also present, located at ~ 2.2 eV for InP and InAs, and at ~ 1.6 eV for InSb. Based on these assignments, we have done a simple calculation using a tight-binding (TB) model with interaction up to the first neighbors and an sp^3s^* basis. We have used in this calculation a schematic dimer molecule with a geometry similar to the surface atomic arrangement (see Fig. 5). The TB parameters at 0 K have been taken from Refs. [13, 14]. The results reproduce the correct tendency experimentally observed for the transitions in the [1 1 0] polarizing directions of the Ga and In-based compounds measured. Fig. 6 shows the experimental and calculated data for the energetic position of the transitions for each compound and on each direction versus the lattice parameter a. For InAs and InSb we have represented only the lower energy positions of the experimental peaks, but the calculation gives a strong probability for a near second transition in InAs and InSb as has been experimentally observed. The fact that the calculated points for the Ga-based compounds show higher energies than the In-based ones is probably due to not-been taking into account the temperatures of the measurements in the calculations, (from 150 to

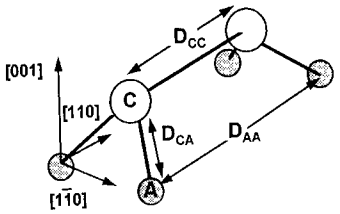

Fig. 5. Schematic representation of the molecule used for the calculation. The distance between anions D_{CC} is twice the covalent radii of the atomic element, and does not vary with the material. The distance between the anion and the cation is $D_{CA} = a\sqrt{3}/4$, and between anions, $D_{AA} = a\sqrt{2}/2$, where a is the lattice parameter of the compound.

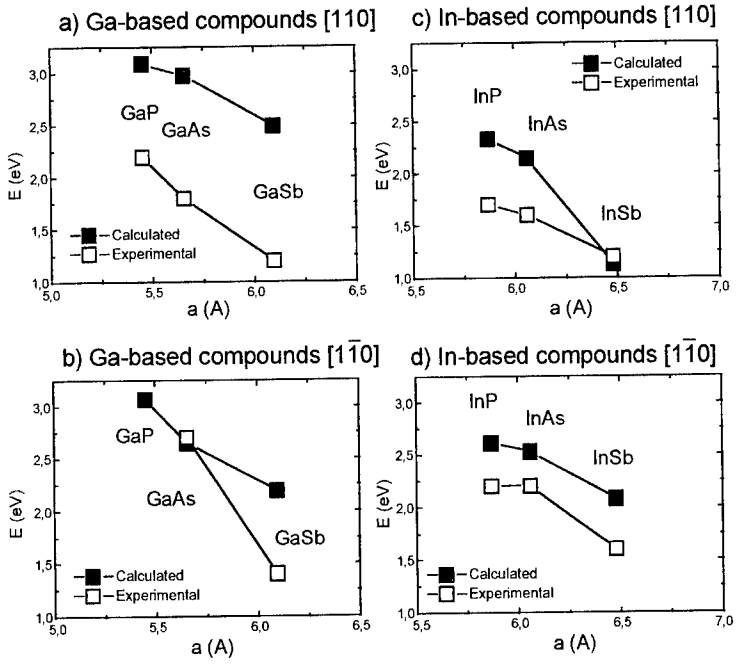

Fig. 6. The energies of the maxima experimentally obtained and the tight-binding calculated values as a function of the lattice parameter a. (a) and (b) are for the Ga-based compounds, and (c) and (d) for the In-based ones. The [1 1 0] direction is for the group III dimers whereas the [1 $\bar{1}$ 0] direction is for the group V dimers.

230°C higher for the Ga-based compounds). This simple calculation explains also the decrease in the intensity of the peaks as the lattice parameter increases.

4. Conclusions

We have observed the absorption energies of the Ga and In dimers in the compounds with their combinations with P, As and Sb, by means of a new optical in situ technique based on the chemical modulation of the surface. We have also observed the absorption for the group V dimers in these compounds, being located in the visible and near infra-red range of energies. Most of the transitions in these compounds have not been observed until now and in the case of GaAs agrees with the previous data. Finally, we have performed a simple tight-binding computation to try to reproduce the observed energies of the peaks for each compound, and the results are in good agreement with the data experimentally observed.

Acknowledgements

P.A. Postigo would like to thank Dr. Kunihiko Uwai for helpful discussions, and the support received from the Basque Government. This work has been partially supported by a MAT95-0966 Research Action.

References

[1] D.E. Aspnes, J.P. Harbison, A.A. Studna and L.T. Florez, Phys. Rev. Lett. 59 (1987) 1687.
[2] I. Kamiya, D.E. Aspnes, L.T. Florez and J.P. Harbison, Phys. Rev. B 46 (1992) 15894.
[3] N. Kobayashi and Y. Horikoshi, Jpn. J. Appl. Phys. 28 (1989) L1880.
[4] K. Uwai and N. Kobayashi, Appl. Phys. Lett. 65 (2) (1994) 150.
[5] K. Uwai and N. Kobayashi, Appl. Surf. Sci. 82/83 (1994) 290.
[6] R. Arès, C.A. Tran and S.P. Watkins, Appl. Phys. Lett. 67 (11) (1995) 1576.
[7] J. Jönsson, K. Deppert, S. Jeppesen, G. Paulsson, L. Samuelson and P. Schmidt, Appl. Phys. Lett. 56 (24) (1990) 2414.
[8] Y. González, L. González and F. Briones, J. Vac. Sci. Technol. A13 (1) (1995) 73.
[9] F. Briones, L. González and A. Ruiz, Appl. Phys. A 49 (1989) 729.
[10] D.E. Aspnes, Y.C. Chang, A.A. Studna, L.T. Florez, H.H. Farrell and J.P. Harbison, Phys. Rev. Lett. 64 (1990) 192.
[11] Y.C. Chang and D.E. Aspnes, Phys. Rev. B 41 (1990) 12002.
[12] W.A. Harrison, Electronic Structure and the Properties of Solids, (Freeman, New York, 1980).
[13] P.K. Larsen, J.F. van der Veen, A. Mazur, J. Pollmann, J.H. Neave and B.A. Joyce, Phys. Rev. B 26 (1982) 3222.
[14] P. Vogl, H.P. Hjalmarson and J.D. Dow, J. Phys. Chem. Solids 44 (1983) 365.

ELSEVIER

Journal of Crystal Growth 175/176 (1997) 304–309

JOURNAL OF CRYSTAL GROWTH

Electronic properties of monolayer steps on GaAs (0 0 1) surfaces studied by scanning tunneling microscopy

Kiyoshi Kanisawa*, Hiroshi Yamaguchi, Yoshiji Horikoshi[1]

NTT Basic Research Laboratories, 3-1 Wakamiya, Morinosato, Atsugi, Kanagawa 243-01, Japan

Abstract

The electronic properties of monolayer steps on $(2\times4)/c(2\times8)$ reconstructed GaAs (0 0 1) surfaces are studied by ultrahigh-vacuum scanning tunneling microscopy (UHV-STM). We quantitatively demonstrate that steps play the role of acceptor arrays by applying electron counting consideration to proposed structure models for monolayer steps. This suggestion is consistent with experimental results on vicinal GaAs (0 0 1) surfaces measured by STM. Energetical stability of the proposed monolayer step structures is theoretically explained. We found that the acceptors at the steps are equivalent to those at the kinks. We confirmed that the surface states responsible for surface Fermi level pinning are located at breaking points of coherent arrangement of semiconducting (2×4) unit cells on GaAs (0 0 1) surfaces.

1. Introduction

The properties of $(2\times4)/c(2\times8)$ reconstructed GaAs (0 0 1) surfaces are important because these surfaces are widely used for semiconductor growth by molecular beam epitaxy (MBE). On the surface, there are defects in coherent arrangement of (2×4) unit cells. These are mainly kinks in As dimer rows and monolayer steps. At the kink, the As dimer row moves over one As atom spacing along the [1 1 0] direction. Recently, each kink in the As dimer rows has been reported to act as a single-acceptor-type trap [1]. According to the report, they form to exactly compensate for space charges in the surface depletion region, and surface Fermi level is pinned at midgap. On the other hand, monolayer steps have been reported to behave as acceptors [2], but the relation between their acceptor nature and their precise structures is still unclear. Detailed investigation of the electronic character of a monolayer step is instructive for understanding not only the surface electronic state but also the MBE growth mechanism. In this paper, we studied the relation between the atomistic structures of monolayer steps on GaAs (0 0 1) surfaces and their electronic properties. For this purpose, we have proposed their microscopic structures. We have also applied the electron counting model to UHV-STM results of kink density on vicinal Si-doped GaAs (0 0 1) surfaces, and thus we have shown the coincidence between our theoretical suggestion and experimental

* Corresponding author. Fax: +81 462 40 4727; e-mail: kani@will.brl.ntt.co.jp.

[1] Present address: Faculty of Science and Engineering, Waseda University, 3-4-1 Ohokubo, Shinjuku, Tokyo, 169, Japan.

0022-0248/97/$17.00 Copyright © 1997 Elsevier Science B.V. All rights reserved
PII S0022-0248(96)00943-8

results by STM. Since the electron counting model has been explained in Refs. [3, 4], we will not repeat it here.

2. Experimental procedure

Si-doped n^+-GaAs layers were grown by MBE on GaAs (0 0 1) substrates exactly oriented and misoriented in the [1 1 1]A direction (A direction) and in the [1 1 1]B direction (B direction). Si concentrations of 4×10^{18} and $2\times10^{19}\,cm^{-3}$ were calibrated by secondary ion mass spectrometry. All doped Si atoms in the depletion layer are donors at these Si concentrations, and the surface electron densities are the same as those for kinks on exactly oriented surfaces [1]. After the growth, the surface was protected by an As passivation layer and transferred in air ambient to the UHV-STM system. The passivation layer was removed by annealing at temperatures up to 570°C in As flux to obtain a satisfactory (2×4) structure and to reproduce a (2×4) reconstructed reflection high-energy electron diffraction (RHEED) pattern. Then, the sample was quickly cooled down to room temperature maintaining the (2×4) RHEED pattern. Kink density measurement by STM was performed at a bias voltage of -3.5 V and a tunneling current of 0.06 nA.

3. Results and discussion

Fig. 1 shows STM images on n^+-GaAs surface of substrates misoriented 1° in the A direction and in the B direction, respectively. Si concentration in each epitaxial layer is $4\times10^{18}\,cm^{-3}$. The dark lines along the [1 $\bar{1}$ 0] direction are dimer vacancy rows, and the observed (2×4) unit cell is Chadi's (2×4) $\beta2$ structure [5]. The kink densities are $2.3\times10^{12}\,cm^{-2}$ for vicinal surfaces 1° off in the A direction, and $1.0\times10^{12}\,cm^{-2}$ for vicinal surfaces 1° off in the B direction. The kink density of the exactly oriented surface is $6.3\times10^{12}\,cm^{-2}$ at the same Si concentration, and this value is higher than those of vicinal surfaces. In addition, the kink density of a surface misoriented in the A direction is always higher than that of a surface misoriented in

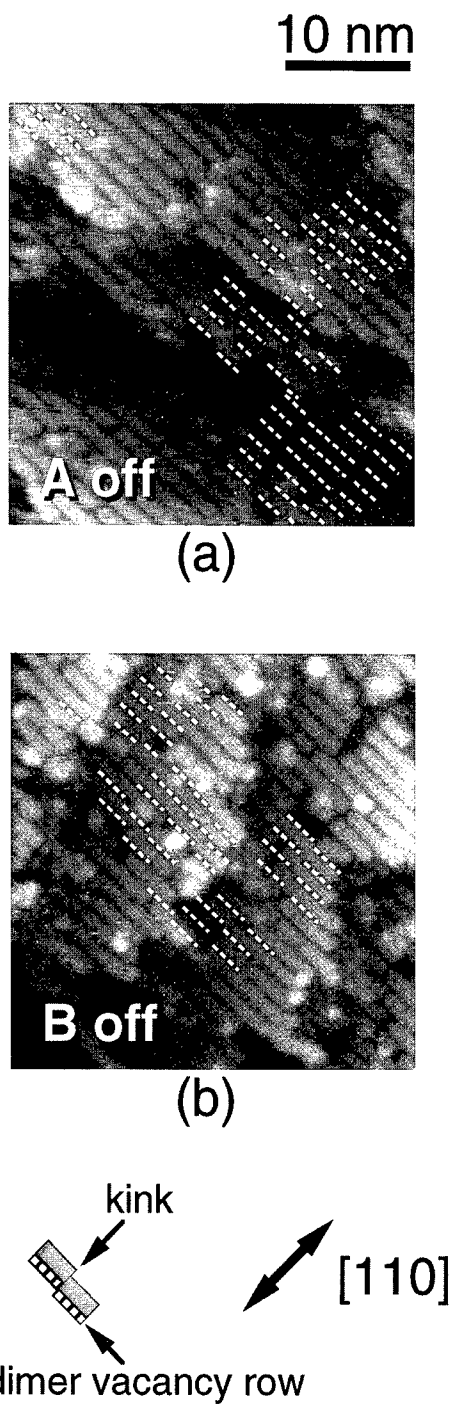

Fig. 1. STM images of vicinal GaAs (0 0 1) surfaces. Each area is 33 nm × 33 nm. Misorientation is 1° in (a) the A direction and (b) the B direction. Dotted lines are As dimer vacancy rows near the kinks in As dimer rows.

the B direction at the same misorientation angle. Other experiments reveal that larger misorientation angle induces lower kink densities. The high-resolution STM images at both an A step and a B step are shown in Fig. 2. The atomistic structure of (2×4) $\beta2$ unit is known as shown in the inset in Fig. 2, and each boundary of the (2×4) unit is resolved in the figure. Therefore, by maintaining relative As dimer positions between layers the same as those in the unit, we can determine atomistic configurations around steps, and they are superimposed as ball-and-stick models on STM images. Each rectangle drawn with broken lines indicates the unit structure for each step. There is no difference between the A step unit structures in the (2×4) area and the $c(2\times8)$ area. This is because the difference between them arises from parallel shift of (2×4) unit cells along A steps. On the other hand, two types of unit structures, type I and type II, appear for the B step as shown in Fig. 2b. The type is determined by the type of reconstruction at the B step. If the neighboring areas are of the same reconstruction area, consisting of either (2×4) or $c(2\times8)$ reconstruction, the unit structure is only type I. However, if the neighbors are different from one another, namely, one is (2×4) and the other is $c(2\times8)$, both type I and type II coexist at the B step.

We applied electron counting model to the proposed step structures. In Fig. 2, since the A step unit structure consists of 2 As dimers and 2 Ga dangling bonds, the unit of the A step has a

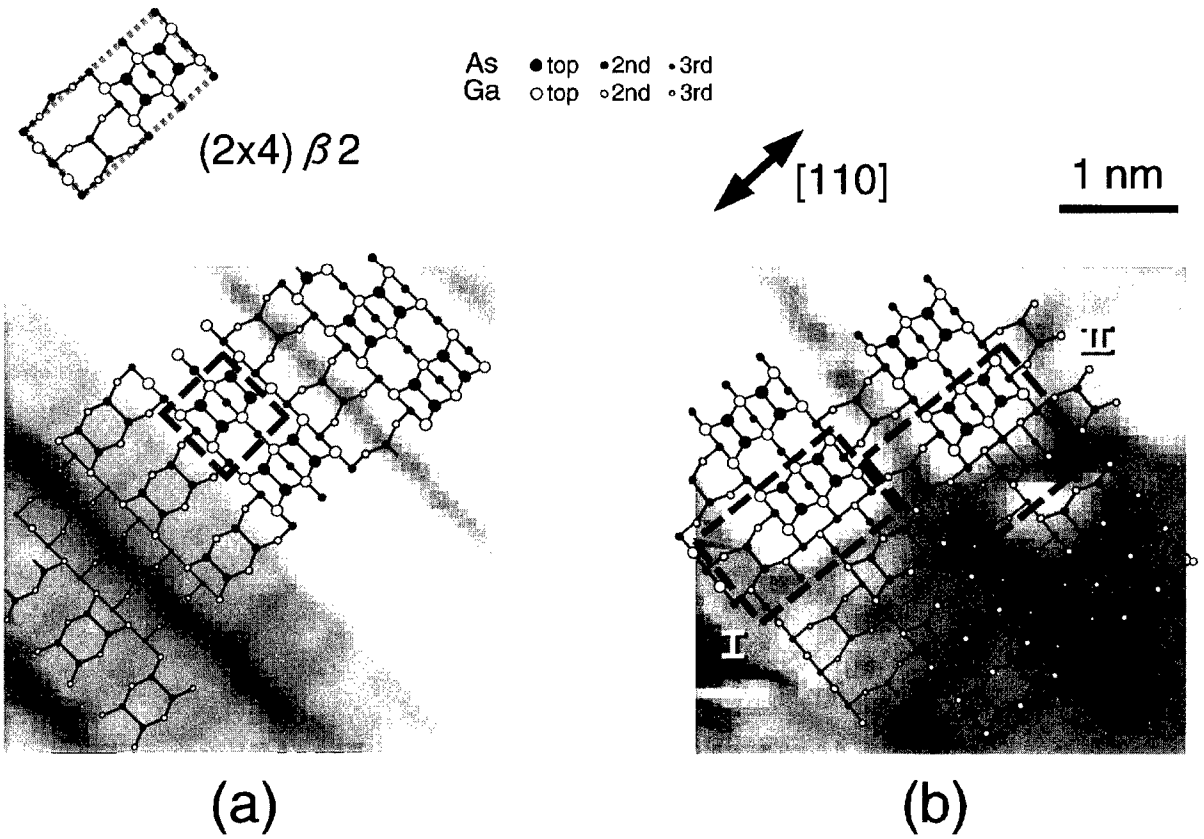

Fig. 2. High-resolution filled-state STM images of steps with structure models superimposed. Each area is 4.4 nm × 4.4 nm. Broken squares show unit structures of steps. Misorientation is in (a) the A direction and (b) the B direction. Inset is the structure of a (2×4) $\beta2$ unit cell.

deficiency of 0.5 electron (Fig. 2a). According to the same consideration, type I of the *B* step has a deficiency of 3 electrons, and type II of it has no deficiency at all (Fig. 2b). We mostly observed the type I structure at the *B* step through our STM observations. Therefore, we can predict that both *A* and *B* steps should play the role of acceptor arrays. Fig. 3a shows kink density as a function of misorientation of the substrate in the *A* direction. Horizontal lines L and H indicate the densities of surface electrons from the space–charge regions for corresponding Si concentrations. The estimated tendencies from the former electron counting consideration for each Si concentration explain the experimental results well. Fig. 3b shows kink density as a function of misorientation of substrates in the *B* direction. The experimental results are also consistent with the suggestion based on our structure models, if space–charge density is substantially higher than electron trap density at the step [6]. Moreover, STM measurement on surfaces with step bunching found that the acceptor-type trap density is constant for any area on the same sample surface, and it does not depend on step density. From this result, we found two electronic features. The first is that acceptors at steps are exactly equivalent to those at kinks in As dimer rows. Theoretically, we expect that this equality originates from the situation that all additional dangling bonds from As atoms at the kinks and the steps are very similar to each other. Zhang and Zunger calculated energies of surface structures by assembling each block of one or two atoms with defined energy and orbital geometry, resulting in very good agreement with results by total energy calculation based on local density approximation [7]. This suggests that electronic states of dangling bonds are governed by geometrical configuration of bonding orbitals with neighboring atoms. Since all As atoms with dangling bond have three bonding orbitals in mostly the same configuration, and each bond is crudely directed to the neighboring atoms at summits of a tetrahedron, each As dangling bond should have a mostly equivalent nature. The second is that surface acceptor density is dominated by electrons from space–charge regions depending on only donor concentration, if space–charge density is sufficiently higher

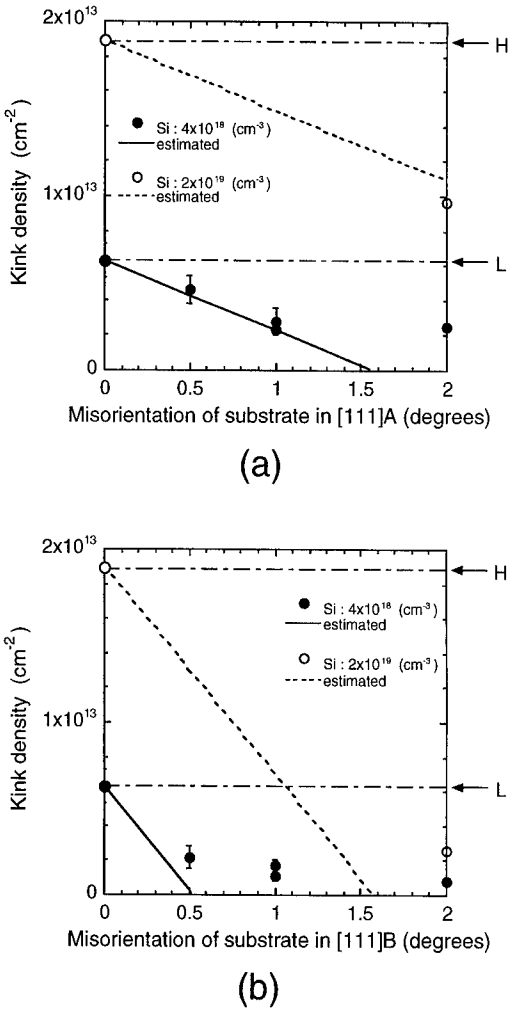

Fig. 3. Kink densities as a function of misorientation of substrates. Misorientation is in (a) the *A* direction ([1 1 1]*A*) and (b) the *B* direction ([1 1 1]*B*). Circles are experimental results by STM, and the solid and the broken lines are estimated results assuming the monolayer steps are acceptor-type surface traps. L and H indicate densities of electrons from space–charge regions of Si concentration $4\times10^{18}\,cm^{-3}$ (Si : Low) and $2\times10^{19}\,cm^{-3}$ (Si : High), respectively.

than step density. These features suggest that the surface Fermi level pinning is governed by the surface states induced by defects disturbing the coherency of the semiconducting (2×4) unit cell arrangement at monolayer steps and kinks in As dimer rows.

We will mention why acceptor-type step structures are mostly observed on vicinal n^+-GaAs (0 0 1) surfaces. Since the donor-type surface structure does not satisfy the electron counting model, it is unfavorable intrinsically. Forming the structure introduces an additional donor surface state, which contains an energetically higher electron in the antibonding p-like orbital [8], namely the partially occupied dangling bond of an electropositive element (Ga). This electron may be trapped by a hole and it contributes to the increase of the Fermi level. Thus, donor surface structure formation is expected to increase surface chemical potential very much. Additionally, the electron was originally in the bonding sp^3 hybrid orbital at the valence band before the structure formation. This means that the electron trap by a hole is electron transition between orbitals at the valence band, and energy gain by the transition may not decrease surface chemical potential very much. Finally, a donor-type surface structure may rather increase the surface chemical potential, and such a structure may scarcely exist on the surface unless some other factor, which contributes energy gain very much, is tied up. On the other hand, the acceptor-type surface structure again does not satisfy the electron counting model, and it is also energetically unfavorable. Forming the structure introduces additional acceptor surface state, which contains an energetically lower electron in the bonding s-like orbital [8], namely a partially occupied dangling bond of an electronegative element (As). Such a state can accommodate electron from the conduction band. Thus, if electron trap by the acceptor state decreases the total surface chemical potential, of high donor concentration n-GaAs for example, an acceptor-type structure can exist stably on the surface. This has been found by STM observation [1] and confirmed by donor concentration dependence of surface acceptor-type structure density on exactly oriented n^+-GaAs (0 0 1) surfaces [9]. Pashley et al. [10] followed their experiment and they showed that fundamental surface structures are semiconducting-type or acceptor-type with no evidence of donor-type structure formation even if at the high hole density p-type GaAs (0 0 1) surface. These experiments support our experimental results and suggestions on vicinal surfaces. Furthermore, our result is for monolayer steps on vicinal surface of n-type GaAs, but, from these considerations, unit step structures on undoped and p-type GaAs surfaces are expected to be the same as those we proposed. However, if the total energy difference between the two types of unit structures at B step is small, we can expect a difference in existing ratio of such two type units depending on Fermi level position.

4. Summary

We performed UHV-STM measurement to clarify the relation between the atomistic structures of monolayer steps and their electronic properties on $(2\times4)/c(2\times8)$ reconstructed vicinal GaAs (0 0 1) surfaces. We proposed unit structures of monolayer steps based on STM observation. A consideration of these proposed structures in terms of the electron counting model suggests that steps play the role of acceptor arrays, and this was confirmed by UHV-STM measurement. Experimental results show that acceptors at steps are equivalent to those at kinks in As dimer rows, and this is consistent with theoretical suggestion. We found that the number of surface acceptors is equal to the number of space–charge, if the surface electron density is substantially higher than step density. It was confirmed that surface Fermi level pinning is a result of electron capture by the surface acceptor states produced by structures which disturb the coherency of a semiconducting (2×4) unit cell arrangement at the steps and the kinks in As dimer rows. Energetical stability of proposed unit structures was also discussed and STM results were consistent with theoretical expectation.

Acknowledgements

We would like to thank Dr. Kenji Shiraishi for his helpful comments on the electron counting model and on the structural stability of surface atomic arrangement. We also thank Dr. Akihito Taguchi for his suggestions on the electronic structure of polar semiconductor surfaces.

References

[1] M.D. Pashley and K.W. Haberern, Phys. Rev. Lett. 67 (1991) 2697.
[2] S. Chang, L.J. Brillson, Y.J. Kime, D.S. Rioux, P.D. Kirchner, G.D. Pettit and J.M. Woodall, Phys. Rev. Lett. 64 (1990) 2551.
[3] W.A. Harrison, J. Vac. Sci. Technol. 16 (1979) 1492.
[4] M.D. Pashley, Phys. Rev. B 40 (1989) 10481.
[5] D.J. Chadi, J. Vac. Sci. Technol. A 5 (1987) 834.
[6] K. Kanisawa, H. Yamaguchi and Y. Horikoshi, Phys. Rev. B 54 (1996) 4428.
[7] S.B. Zhang and A. Zunger, Mater. Sci. Eng. B 30 (1995) 127.
[8] W.A. Harrison, Surf. Sci. 55 (1976) 1.
[9] H. Yamaguchi and Y. Horikoshi, Phys. Rev. B 53 (1996) 4565.
[10] M.D. Pashley, K.W. Haberern, R.M. Feenstra and P.D. Kirchner, Phys. Rev. B 48 (1993) 4612.

ELSEVIER

Journal of Crystal Growth 175/176 (1997) 310–316

JOURNAL OF CRYSTAL GROWTH

Evolution of short- and long-range order during Si incorporation on GaAs(0 0 1) observed by RAS and RHEED during MBE

L. Däweritz[a,*], K. Stahrenberg[b], P. Schützendübe[a], J.-T. Zettler[b], W. Richter[b], K.H. Ploog[a]

[a] *Paul-Drude-Institut für Festköperelektronik, Hausvogteiplatz 5-7, D-10117 Berlin, Germany*
[b] *Institut für Festkörperphysik, Technische Universität Berlin, D-10623 Berlin, Germany*

Abstract

The Si incorporation on GaAs (0 0 1) has been studied in real time by reflection high-energy electron diffraction (RHEED) and reflectance anisotropy spectroscopy (RAS) at conditions of enhanced adatom mobility. In the RAS spectra, besides resonances due to As and Ga dimers on the GaAs surface also features due to Si dimers in single and double layers as well as As dimers adsorbed on them are identified. The incorporation process is very complex due to Si-induced As desorption, combined incorporation of Si and As, and readsorption of As on (Si, Ga). At conditions of high adatom mobility (low As_4 pressure) a single Si layer is nearly completed before Si incorporation in a second layer takes place, whereas for reduced adatom mobility (high As_4 pressure) islanding with Si incorporation in a double layer is found in early growth stages.

PACS: 68.35.Fx; 61.14.Hg; 78.66.Fd; 81.15.Hi

Keywords: Molecular beam epitaxy; Gallium arsenide; Si-doping; Si-on-GaAs; Kinetics of interface formation; Surface reconstruction; Reflectance anisotropy spectroscopy; Reflection high-energy electron diffraction

1. Introduction

The incorporation of Si on GaAs(0 0 1) during molecular beam epitaxy has attracted considerable attention in view of its importance for delta (δ) doping [1] and as the first step of Si on GaAs heteroepitaxy [2]. Besides reflection high-energy electron diffraction (RHEED) as an established method for evaluating the structure of the growing surface, more recently reflectance anisotropy spectroscopy (RAS) is applied for monitoring the submonolayer heteroepitaxial growth [3]. These studies are usually performed at relatively high As coverages used in conventional δ doping. A strength of RAS is the capability to detect chemical bonding [4]. Atomic scale resolution scanning tunneling microscopy (STM) has also been used to study the deposition of Si under low- and

* Corresponding author. Fax: + 49 30 203 77 201; e-mail: daeweritz@pdi.wias-berlin.de.

0022-0248/97/$17.00 Copyright © 1997 Elsevier Science B.V. All rights reserved
PII S0022-0248(96)00854-8

high-temperature growth conditions [5–7]. In view of atomic ordering phenomena the incorporation at conditions of enhanced adatom mobility (high temperature, low As coverage) is of crucial importance. Such phenomena are observed in a relatively narrow substrate temperature range at a given As_4 pressure [8]. Due to complex adsorption–desorption processes it is difficult to quench in the actual surface configuration for STM studies. In this work, we study atomic processes during Si deposition at enhanced adatom mobility in real time by combining RHEED and RAS to detect the evolution of long- and short-range-order, respectively.

2. Experiment procedure

The initial surfaces were prepared by GaAs growth on 2° toward (1 1 1) Ga misoriented GaAs (0 0 1) substrates at conditions leading to a (2 × 4) reconstruction and to a step flow growth mode [8]. In comparative experiments the singular GaAs (0 0 1) surface was used to study the influence of misorientation steps on the Si incorporation. To ensure a high adatom mobility the Si was deposited with a flux of about 10^{11} atoms $cm^{-2}\,s^{-1}$ in pulses of 60 s duration and 180 s interruption (1 ML corresponds to ~ 90 min deposition) at a substrate temperature of 590°C. The As_4 beam-equivalent (BE) pressure was 1×10^{-6} Torr. Experiments on the Si incorporation at reduced adatom mobility were performed at an As_4 BE pressure of 5×10^{-6} Torr.

Real-time RHEED measurements were performed with the 15 keV electron beam in the [1 $\bar{1}$ 0] and [1 1 0] azimuth. The time evolution of the specular and fractional-order beams was analysed by using a system consisting of a video camera, video recorder and image processing unit.

For RAS measurements a system based on the standard design by Aspnes [9] was used. The monitored signal consisted of the real part of the reflectance anisotropy:

$$\Delta r/\bar{r} = 2(r_{[\bar{1}\,1\,0]} - r_{[1\,1\,0]})/r_{[\bar{1}\,1\,0]} + r_{[1\,1\,0]}).$$

RAS spectra were measured in the spectral range from 1.6 to 5.3 eV. To determine dynamic changes in the As surface dimer density during Si deposition the signal at 2.6 eV photon energy was monitored.

3. Results and discussion

3.1. Low adatom mobility

In Fig. 1 we show RAS spectra for pulsed Si deposition at conditions leading to low (a) and high adatom mobility (b). We first consider the case of the low adatom mobility (Fig. 1a) which is closer to conditions of conventional δ doping. The spectrum of the initial surface (thin solid line) is dominated by the transition at 2.6 eV due to As dimers with [1 $\bar{1}$ 0] bond direction and corresponds to the (2 × 4)β reconstruction [10]. During the deposition of 2.2 monolayers (ML) Si the whole spectrum shifts continuously to a lower level and a clear minimum at 2 eV due to Ga dimers with [1 1 0]

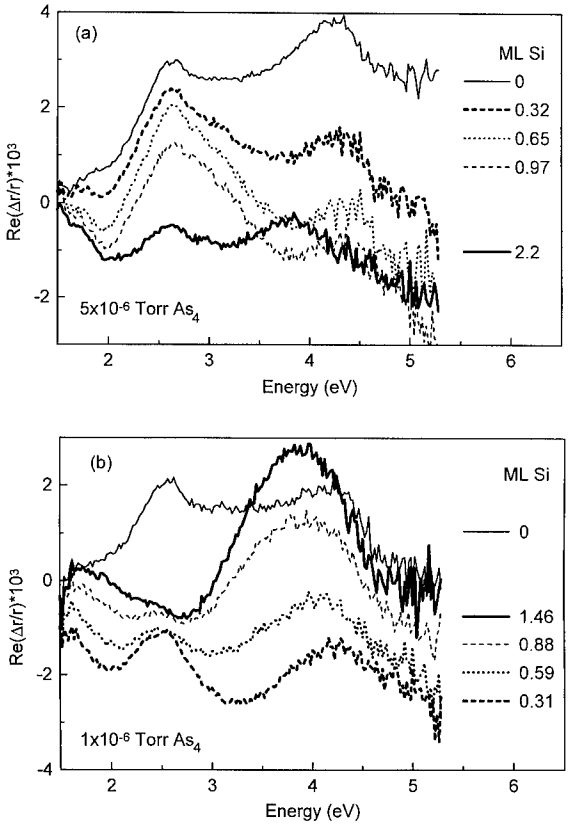

Fig. 1. RAS spectra taken at different Si coverages for pulsed Si deposition on vicinal GaAs(0 0 1) at 590°C. (a) low adatom mobility at $p_{BE}(As_4)$ 5×10^{-6} Torr; and (b) high adatom mobility at $p_{BE}(As_4)$ 1×10^{-6} Torr.

bonding direction [11, 12] appears, as expected for the gradual evolution of a Ga-rich surface. However, the clear 2.6 eV peak due to the As dimers persists indicating a separation into As- and Ga-terminated domains.

In a more complete interpretation of the spectra one has to include, besides As and Ga surface dimers, also other atomic configurations due to the incorporated Si atoms. Some of these configurations are illustrated in Fig. 2. Based on results of a recent study of the chemical bonding at the interface between Si and GaAs by synchrotron radiation photoelectron spectroscopy [13], we expect that on As-rich GaAs the Si bonds solely to As. Since theoretical treatment regarding RAS spectra for Si-on-GaAs to our knowledge is still missing, in a first approach we have to compare our experimental results with data for the bare Si (0 0 1) surface and for the Si (0 0 1) : As surface [14, 15]. Table 1 summarizes the known energetic positions of RAS features related to As and Ga dimers on GaAs (0 0 1), Si dimers on the bare Si (0 0 1) surface with (2×1) or (1×2) symmetry, and As dimers on the Si(0 0 1) : As surface with (1×2) or (2×1) symmetry. The 90° rotation between (2×1) and (1×2) reconstructed domains corresponds to the transition from a single to a double Si layer.

The drop in the high-energy part of the RAS spectrum in Fig. 1a can be explained by the assumption of a rather rough, anisotropic morphology. Another explanation is the coexistence of

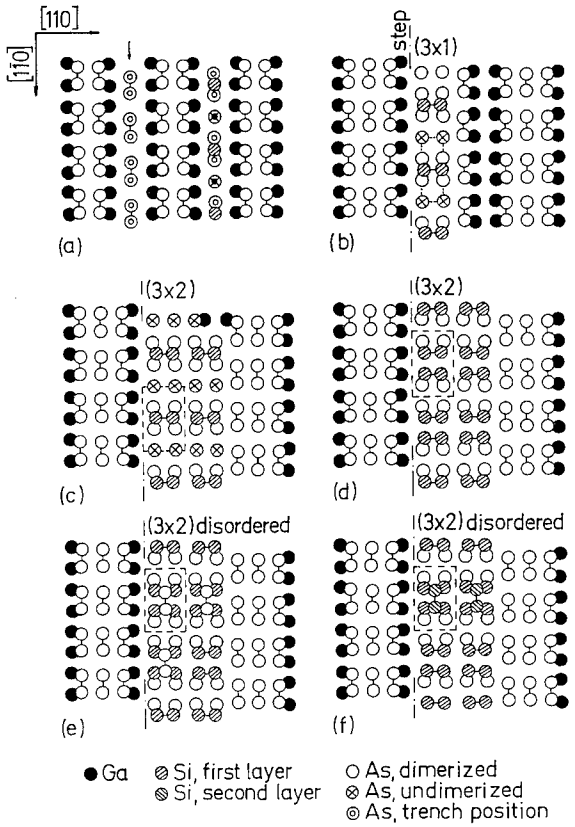

Fig. 2. Atomic configurations (a) for Si incorporation in a trench of the $(2 \times 4)\beta$ reconstructed surface, (b–d) during evolution of the (3×2) reconstruction, (e) for As adsorption on the (3×2) structure and (f) for Si incorporation in a second layer.

Table 1
Assignment of RAS features to atomic surface configurations for Si deposition on GaAs(0 0 1)

Configuration	Energy (eV)	Feature	Refs.
Ga_2	1.8–2.1	Dip	[11, 12]
$As_2(2 \times 4)$	2.6	Peak	[11, 12]
$Si_2(2 \times 1)$	~ 3	Dip	[14, 15]
	~ 4	Peak	
$Si_2(1 \times 2)$	~ 3	Peak	
	~ 4	Dip	
As_2 : Si (2×1)	~ 2.6	Dip	[15]
	~ 3.2	Peak	
	~ 3.8	Dip	
As_2 : Si (1×2)	~ 2.6	Peak	
	~ 3.2	Dip	
	~ 3.8	Peak	

Si (0 0 1) : As-(2 × 1) and Si (0 0 1) : As-(1 × 2) domains with an increasing concentration of the latter with increasing Si coverage. A closer inspection of the spectra reveals that, in accordance with this explanation, at a photon energy of ~ 3.2 eV with increasing Si coverage first a shoulder appears which changes to a minimum at a coverage of ~ 2 ML Si. The complementary behaviour is observed at a photon energy of ~ 3.8 eV with a change from a minimum to a maximum. This finding indicates that islands develop and locally a Si double layer is formed at relatively low coverages.

The formation of an island-like Si distribution at low adatom mobility becomes evident also from the RHEED data. As shown in Fig. 3, RHEED intensity linescans have been taken between the fundamental RHEED streaks and plotted as a function of time or Si coverage. Fig. 3d presents the plot taken in the [1 1 0] azimuth for the case of low adatom mobility. It is clearly seen that the half-order streak due to the (2 × 4) reconstruction of the initial surface splits into asymmetric third-order streaks. The splitting gradually increases until at a coverage > 1 ML symmetric third-order streaks due to a well-ordered (3 × 1) structure appear. This development of the final (3 × 1) structure via an asymmetric '3 × 1' structure has been discussed by Fahy et al. [16] in terms of a superperiodicity generated by the presence of a new type of domain in an otherwise ordered structure. These observations are consistent with a model of isolated Si atoms at very low coverages. At higher coverages Si clusters are formed whereby a Si double layer can develop in an early growth stage and As dimers are adsorbed on Si.

3.2. High adatom mobility

The Si incorporation mechanism changes drastically if the adatom mobility is increased by reducing the As_4 pressure. RHEED intensity linescan plots taken under such conditions in the [1 $\bar{1}$ 0] and [1 1 0] azimuth, respectively, are presented in Fig. 3b and Fig. 3c. The sequence of the reconstructions with increasing Si coverage is found to be (3 × 1), (3 × 2), (4 × 2), and an asymmetric '1x3' structure. The latter structure is derived from additional linescan measurements not shown in Fig. 3. It is important to note that in the transition range between the (3 × 2) and the (4 × 2) structures both phases coexist, i.e. separation into differently reconstructed domains takes place. The corresponding RAS spectra taken during Si deposition in this experiment with increased adatom mobility are shown in Fig. 1b. The spectrum of the initial surface corresponds now to a (2 × 4)α reconstruction [10]. It shows a clear peak due to As dimers with [1 $\bar{1}$ 0] bond direction. During deposition of 0.3 ML Si the whole spectrum shifts to a lower level

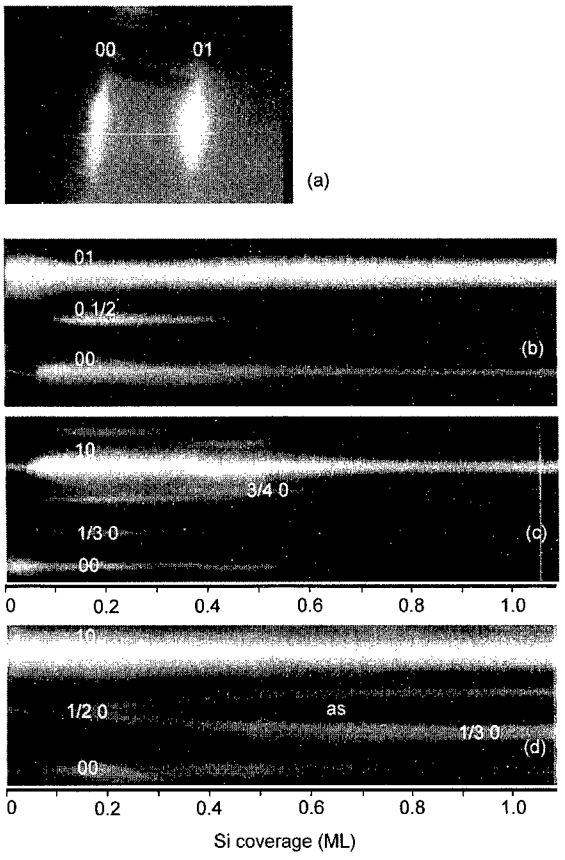

Fig. 3. Intensity linescans across the RHEED patterns as function of the Si coverage for pulsed Si deposition on vicinal GaAs(0 0 1); (a) illustration of the intensity recording along a line between the fundamental streaks; (b, c) plots for deposition at high adatom mobility in the [1 $\bar{1}$ 0] and [1 1 0] azimuth, respectively; and (d) plot for low adatom mobility in the [110] azimuth. Notice the coexistence of (3 × 2) and (4 × 2) reconstructed domains in (c).

and a clear minimum at ~ 2 eV due to Ga dimers with [1 1 0] bond direction appears, as expected for the evolution of a Ga-rich surface. As in the case of the more As-rich initial surface considered before, the clear peak due to the As dimers persists. It disappears, however, at coverages > 0.6 ML. This is consistent with the RHEED results (Fig. 3c) evidencing a clear separation into differently reconstructed domains. In marked contrast to the experiment with low Si adatom mobility, for coverages of > 0.3 ML Si the whole spectrum is shifted now again to a higher level and the minimum at 2 eV is gradually lost. This suggests that a combined incorporation of Si and As takes place and results in a smoothed surface again. Although the 2.6 eV peak degrades, the signal at this photon energy increases up to coverages of ~ 1 ML Si and then decreases, as will be shown later. At high Si coverages the interpretation of the 2.6 eV peak becomes complicated due the dominating peak at ~ 4 eV. This peak is caused by dominance of a bare single Si layer with Si dimers in [1 1 0] direction.

To study the influence of misorientation steps on the Si incorporation we have performed real-time measurements by RHEED and RAS for deposition on the exactly oriented and on the vicinal (0 0 1) surface (Fig. 4). The RAS signal recorded at 2.6 eV photon energy is most strongly affected by As surface dimers. The RHEED intensities of the specular beam and of the third- and half-order beams due to the (3 × 1) or (3 × 2) structure were monitored. Recordings of the fractional-order beams reveal that on the vicinal surface the (3 × 2) structure appears at lower Si coverages and evolves faster as compared to the singular surface [8]. This is also reflected in the behaviour of the specular beam. The rapid change in the specular beam RHEED intensity after deposition of ~ 0.1 ML on the vicinal surface (Fig. 4d) is typical for a system with rapid changes in strain and structure. This behaviour is quite different from that observed for the singular surface (Fig. 4c). Therefore, we conclude that the phase separation into metal-rich and As-rich domains is much stronger on the vicinal surface due to accumulation of Si atoms in the near-step-edge region.

From the RHEED and RAS monitoring including the RAS spectra we can deduce a Si incorporation model. The model has to start from the

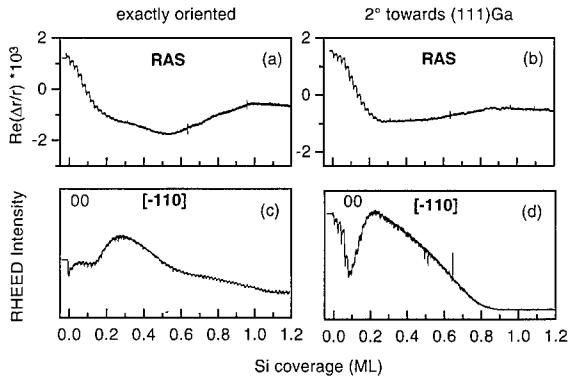

Fig. 4. (a, b) RAS transients and (c, d) recordings of the specular beam RHEED intensity in the [$\bar{1}$ 1 0] azimuth for Si deposition on vicinal GaAs(0 0 1) at high adatom mobility.

structure of the intial GaAs(0 0 1) surface. Recent STM studies [17] have revealed that at conditions leading to a (2 × 4)β reconstruction the unit mesh of the usually observed structure contains two As dimers on top and a third As dimer one monolayer lower in the trench (Fig. 2a). On such a surface Si can be incorporated into the trench by insertion into the As dimer bond. From Fig. 2a it can be seen that thereby As atoms marked by a cross can become undimerized and reevaporate. On the other hand, new adsorption sites for As dimers can be created if Si atoms are incorporated on two adjacent Ga sites in the trench.

In the following we concentrate on the case of high adatom mobility with a (2 × 4)α reconstruction of the initial surface. This structure contains second layer Ga atoms in the missing dimer trench [17]. Having in mind that Si bonds only to As as long as the surface structure is As stabilized, which requires a combined incorporation of As and Si atoms, a model with three As dimers per unit mesh is a good approximation for the following considerations. During Si deposition the half-order spots in the [1 $\bar{1}$ 0] azimuth appear at a slightly higher coverage than the third-order spots in the [1 1 0] azimuth, indicating that a (3 × 1) structure is the first stage in the development of the (3 × 2) reconstruction (Fig. 3b and Fig. 3c). As shown in Fig. 2b the ordered attachment of Si dimers in a row perpendicular to the dimer axis at any prefererred nucleation site, which can be a step, leads to

a (3×1) structure. Thereby the As atoms marked by a cross become undimerized and probably will reevaporate. A further attachment of Si dimers leads to a (3×2) symmetry with extended dimer rows (Fig. 2c). The reevaporation of undimerizesd As atoms exposes a row of Ga atoms that dimerize. This model is consistent with the 2 eV minimum in the RAS spectra and with the RAS-roughness signature. It provides also an alternative explanation for the Ga enrichment previously observed by Auger electron spectroscopy during Si deposition [18] that has been attributed to a Si–Ga exchange reaction [6]. The reduction of the As dimer density during the Si supply is evident from the decreasing 2.6 eV RAS signal (Fig. 4b). The pulsating behaviour of the signal reflects an ordering process with a destruction of dimers during the pulse and their partial reformation after flux interruption. In the ideal case, the structure considered in Fig. 2c would be completed at a coverage of 0.33 ML which is in good agreement with the coverages corresponding to the intensity maxima of the fractional-order RHEED beams. A (3×2) structure can be maintained if with increasing Si coverage Si dimers are incorporated between already existing dimer rows (Fig. 2d). This requires a combined incorporation of Si and As atoms. Once, however, two neighbouring Si dimers are created As atoms can condense on them as dimers (Fig. 2e) and/or a second Si layer with a 90° rotation of the dimer axis can nucleate (Fig. 2f). This and further completion of missing Si dimer rows leads to a degradation of the (3×2) reconstruction. Since the 2.6 eV signal is sensitive not only to As dimers on top of Ga but also on top of Si (see Table 1) we can also understand the characteristic changes in the slope of the RAS transients. In the case of the vicinal surface (Fig. 4b) an increase of the signal is observed at lower coverage as compared to the singular surface (Fig. 4a). This is expected for preferential Si incorporation at step edges, which allows the formation of the (3×2) structure with adjacent Si dimers (Fig. 2d) and As dimers on top of them (Fig. 2e) in an earlier growth stage. After completion of the first ML Si and beginning Si incorporation in a second layer one expects a 90° rotation of the As dimers in the top layer. In agreement with this the RAS curve changes the sign of the slope at a coverage of ~ 1 ML.

4. Conclusions

We have demonstrated that the atomic processes during incorporation of Si atoms on the GaAs (0 0 1) surface can be studied in detail by RHEED and RAS in real time. This is possible due to characteristic changes in short- and long-range order. The RAS spectra show resonances not only due to As and Ga dimers on GaAs (0 0 1) but also due to Si dimers and As dimers on top of Si. The incorporation mechanism critically depends on the As_4 pressure that influences the adatom mobility. At high As_4 pressure (low adatom mobility) Si clustering with incorporation into two layers occurs in an early growth stage. The pulsed Si supply at low As_4 pressure (high adatom mobility) promotes an ordered incorporation with a high completion of the first Si layer before the second Si layer nucleates. In a complex desorption–adsorption process the Si incorporation induces a phase separation into As-rich and Ga-rich domains at medium Si coverages. At higher coverages a readsorption of As takes place. These processes are influenced by misorientation steps of the vicinal surface.

Acknowledgements

The authors wish to acknowledge the support of the RHEED linescan measurements by Dr. W. Braun and the technical assistance of K. Hagenstein. This work was supported by the Deutsche Forschungsgemeinschaft (Sonderforschungsbereich 296).

References

[1] E.F. Schubert, J. Vac. Sci. Technol. A 8 (1990) 2980.
[2] O. Brandt, G. Crook, K. Ploog, R. Bierwolf, M. Hohenstein, M. Maier and J. Wagner, Jpn. J. Appl. Phys. 32 (1993) L24.
[3] D.A. Woolf, K.C. Rose, J. Rumberg, D.I. Westwood, F. Reinhardt, S.J. Morris, W. Richter and R.H. Williams, Phys. Rev. B 51 (1995) 4691.
[4] D.E. Aspnes, Mater. Sci. Eng. B 30 (1995) 109.
[5] A.R. Avery, D.M. Holmes, J.L. Sudijono, T.S. Jones, M.R. Fahy and B.A. Joyce, J. Crystal Growth 150 (1995) 202.
[6] A.R. Avery, J.L. Sudijono, T.S. Jones and B.A. Joyce, Surf. Sci. 340 (1995) 57.
[7] M. Wassermeier, J. Behrend, L. Däweritz and K. Ploog, Phys. Rev. B 52 (1995) R2269.

[8] L. Däweritz, H. Kostial, M. Ramsteiner, R. Klann, P. Schützendübe, K. Stahrenberg, J. Behrend, R. Hey, M. Maier and K. Ploog, Phys. Status Solidi (b) 194 (1996) 127.
[9] D.E. Aspnes, J.P. Harbison, A.A. Studna and L.T. Florez, J. Vac. Sci. Technol. A 6 (1988) 1327.
[10] J. Rumberg, J.-T. Zettler, K. Stahrenberg, K. Ploska, W. Richter, L. Däweritz, P. Schützendübe and M. Wassermeier, Surf. Sci. 337 (1995) 103.
[11] Y. Chang and D.E. Aspnes, J. Vac. Sci. Technol. B 8 (1990) 896.
[12] I. Kamiya, D.E. Aspnes, L.T. Florez and J.P. Harbison, Phys. Rev. B 46 (1992) 15894.
[13] S. Heun, M. Sugiyama, S. Maeyama, Y. Watanabe, K. Wada and M. Oshima, Phys. Rev. B 53 (1996) 13534.
[14] T. Yasuda, L. Mantese, U. Rossow and D.E. Aspnes, Phys. Rev. Lett. 74 (1995) 3431.
[15] L. Kipp, D.K. Biegelsen, J.E. Northrup, L.-E. Swartz and R.D. Bringans, Phys. Rev. Lett. 76 (1996) 2810.
[16] M.R. Fahy, M.J. Ashwin, J.J. Harris, R.C. Newman and B.A. Joyce, Appl. Phys. Lett. 61 (1992) 1805.
[17] A.R. Avery, C.M. Goringe, D.M. Holmes, J.L. Sudijono and T.S. Jones, Phys. Rev. Lett. 76 (1996) 3344.
[18] P.C. Zalm, P.M.J. Maree and R.I.J. Olthof, Appl. Phys. Lett. 46 (1985) 597.

ELSEVIER

Journal of Crystal Growth 175/176 (1997) 317–322

JOURNAL OF CRYSTAL GROWTH

A RHEED and STM study of Sb-rich AlSb and GaSb (0 0 1) surface reconstructions

P.M. Thibado[1], B.R. Bennett, B.V. Shanabrook, L.J. Whitman*

Naval Research Laboratory, Washington, DC 20375, USA

Abstract

The structure of AlSb and GaSb (0 0 1) surfaces prepared by molecular beam epitaxy has been studied with in-situ reflection high-energy electron diffraction and scanning tunneling microscopy. Under fixed Sb_4 flux, two AlSb reconstructions are observed with increasing temperature (and decreasing surface Sb : Al coverage): $c(4 \times 4)$, as observed for InSb, GaAs, AlAs, and InAs, and (1×3). In contrast, GaSb reconstructions observed with increasing temperature are: (2×5), (1×5), $c(2 \times 6)$, and (1×3). Whereas the (1×5), $c(2 \times 6)$, and (1×3) surfaces are composed primarily of Sb dimer rows on top of an Sb-terminated surface, the (2×5) surface is composed of Sb dimer rows on top of two layers of Sb (i.e. the surface is terminated by *three* Sb layers). We speculate that GaSb is unique in forming the $(n \times 5)$ reconstructions due to its excellent lattice match with trigonally bonded elemental Sb.

1. Introduction

There is an extensive effort to develop novel high-speed and optoelectronic devices utilizing the "6.1 Å" family of III–V compound semiconductors, InAs, GaSb, and AlSb [1, 2]. Because these devices are often based on short-period heterostructures, where the interfaces constitute a significant fraction of the total heterostructure volume, the structure and stoichiometry of the growth surface during interface formation is expected to have a significant impact on the ultimate device performance [2]. The structure of the growth front can affect the abruptness of a heterointerface in a number of ways. For example, the surface reconstructions may lead to anisotropic growth morphologies, thereby causing roughness at the heterointerface [3, 4]. In addition, the III/V stoichiometry of the reconstruction may lead to non-stoichiometric interfaces that cannot be compositionally abrupt [4, 5]. Hence, the development of smooth, abrupt interfaces requires a fundamental understanding of the structure of the III–V(0 0 1) surface reconstructions.

Given that 6.1 Å-based devices are generally grown under an As-or Sb-rich flux, the V-terminated reconstructions are the most important to understand. To date, the most intensively studied of the 6.1 Å compounds has been InAs. The As-terminated surface reconstructions of InAs(0 0 1)

* Corresponding author. E-mail: lloyd.whitman@nrl.navy.mil.

[1] Present address: Department of Physics, University of Arkansas, Fayetteville, Arkansas 72701, USA

0022-0248/97/$17.00 Copyright © 1997 Elsevier Science B.V. All rights reserved
PII S0022-0248(96)00982-7

mimic those of GaAs [5–8], with As dimer-based (2×4) and $c(4\times4)$ reconstructions. The Sb-terminated GaSb surface reconstructions have been less studied, although they are reported to include the Sb dimer-based "odd" reconstructions, (1×3), $c(2\times6)$, (1×5), and (2×5), as observed with reflection high-energy electron diffraction (RHEED) [5, 9–11]. It has been proposed that the (1×3) and (2×5) reconstructions are terminated with $1\frac{2}{3}$ and $2\frac{3}{5}$ layers of Sb, respectively, on a (1×1) Ga plane [12, 13]. Unlike InAs and GaSb, the structure of AlSb(0 0 1) has received little attention. To our knowledge, (1×3) and $c(2\times6)$ [but no $c(4\times4)$ or $(n\times5)$] reconstructions have been reported, and, as yet, no structural models have been proposed [5, 10, 11, 14]. In addition to the technological applications of GaSb and AlSb, these materials are of interest because they are a special pair of III–V compounds having very similar lattice constants (6.095 versus. 6.136 Å) but differing only by one element (a similar relationship exists for GaAs and AlAs). As such, they provide an opportunity to explore the role of elemental properties in determining surface reconstructions.

2. Experimental procedure

Experiments were carried out in an interconnected, multi-chamber ultrahigh vacuum (UHV) facility that includes a III–V semiconductor molecular beam epitaxy (MBE) chamber equipped with RHEED, and a surface analysis chamber equipped with a scanning tunneling microscope (STM). RHEED studies were performed on relaxed, thick films (>1 μm) of AlSb and GaSb grown on GaAs(0 0 1) substrates oriented to within 0.1° of (0 0 1). Surface reconstruction transition temperatures for a fixed Sb_4 flux were determined by either heating or cooling the substrate in 5°C increments through the transition region and recording the temperature at which the RHEED pattern changed. Substrate temperatures were determined by infrared transmission thermometry and are believed to be accurate to 10°C [15]. STM images of AlSb reconstructions were acquired on Si-doped (10^{17} cm^{-3}) thick films grown on n^+-GaAs(0 0 1) substrates at 550°C. These films were terminated with 10 nm of undoped AlSb grown at a reduced rate to eliminate Si contamination on the growth surface and produce large atomically well-ordered terraces. STM images of GaSb reconstructions were acquired on undoped films grown on p^+-GaSb(0 0 1) substrates at 500°C with frequent interrupts. STM samples were mounted on a custom-designed sample holder that mounts onto both a standard 5 cm diameter MBE sample block and the stage of a custom-modified commercial STM [16]. All STM images are displayed in gray scale and are uncorrected for thermal drift.

3. Results

The structural transitions between various Sb-rich surface reconstructions as observed by RHEED for AlSb(0 0 1) and GaSb(0 0 1) as a function of Sb_4 flux and substrate temperature are shown in Fig. 1. Both AlSb and GaSb exhibit a (1×3) RHEED pattern at high substrate temperatures. At lower temperatures, however, the surface reconstructions for these systems differ. We find that AlSb transitions to a $c(4\times4)$ structure, similar

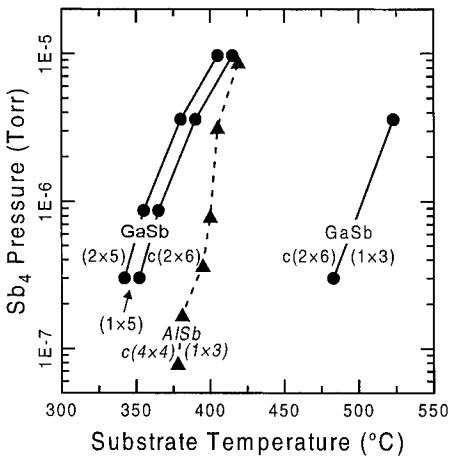

Fig. 1. Substrate reconstruction transition temperatures for AlSb and GaSb (0 0 1) surfaces as a function of incident Sb_4 beam equivalent pressure as observed with RHEED. The transitions for AlSb are indicated by triangles and those for GaSb by circles. The lines are drawn as guide to the eye. A pressure of 2.0×10^{-6} Torr corresponds to an Sb deposition rate of ~ 1 layer per second.

to the anion-terminated (0 0 1) surfaces of InSb, GaAs, AlAs, and InAs. Unlike AlSb, GaSb undergoes multiple reconstruction transitions with decreasing temperature: first from (1×3) to $c(2 \times 6)$, then to (1×5), and finally to (2×5). At still lower temperatures and/or higher Sb fluxes (not shown in Fig. 1) both AlSb and GaSb transition to three-dimensional, elemental Sb growth.

A high-resolution STM image of an AlSb(0 0 1)-(1×3) surface is shown in Fig. 2a. This surface appears to have a structure similar to what we and others [12] observe for GaSb(0 0 1)-(1×3). The model proposed for this reconstruction consists of a (1×1) plane of Sb with rows of Sb dimers on top, with the dimer rows spaced $3a_o$ apart [a_o is defined as the size of a (1×1) surface unit cell, 4.34 Å on AlSb]. The total Sb surface coverage for this model is $1\frac{2}{3}$ layers [12]. We attribute the zigzag nature of the rows and quasi-periodic kinking along the rows to buckling-like displacements of the dimers, which give the surface a more complicated structure than apparent from the observed diffraction patterns. An

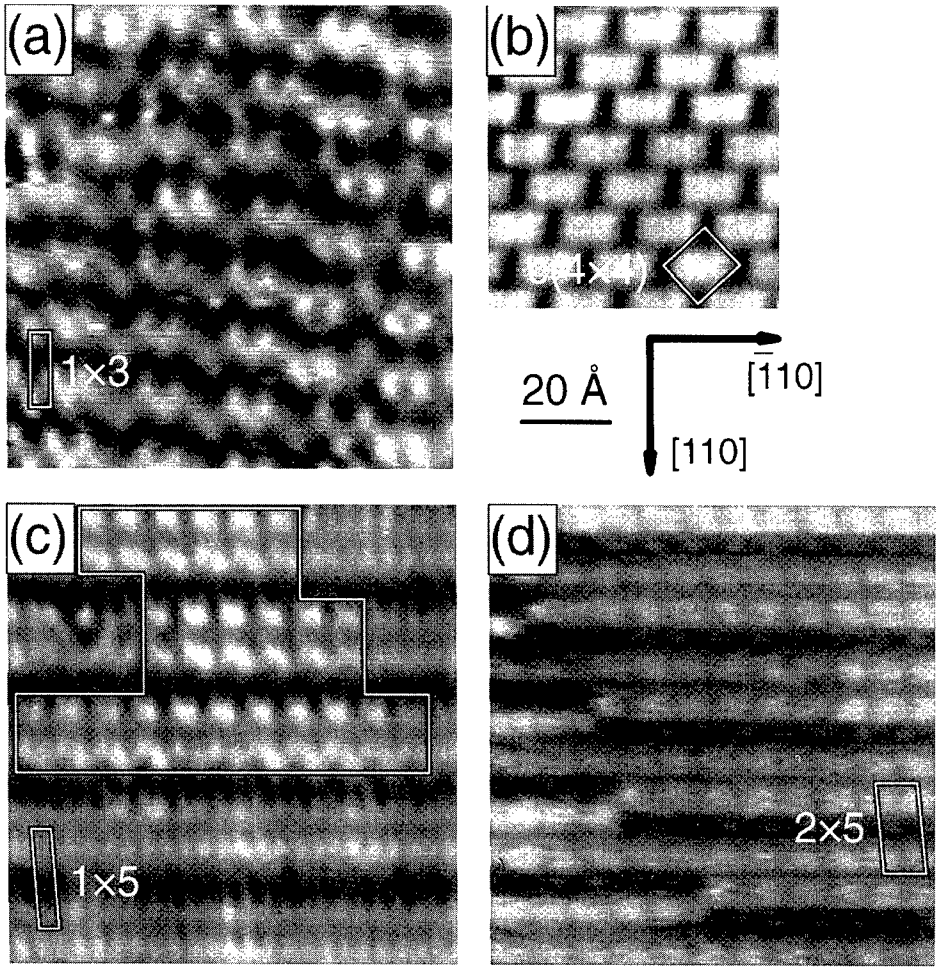

Fig. 2. Gray-scale STM images of AlSb and GaSb (0 0 1) surfaces; (a) AlSb(0 0 1)-(1×3), empty electronic states (3.0 V, 0.1 nA); (b) AlSb(0 0 1)-$c(4 \times 4)$, filled states (2.6 V, 1 nA); (c) GaSb(0 0 1)-$(1 \times 5)/(2 \times 5)$, filled states (2.4 V, 0.1 nA); a region with local $c(2 \times 10)$ symmetry is outlined; (d) GaSb(0 0 1)-(2×5), filled states (0.4 V, 0.1 nA). Primitive unit cells are indicated. The reconstructions refer to the symmetry observed in RHEED.

STM image of a well-ordered AlSb(0 0 1)-$c(4\times4)$ surface is shown in Fig. 2b. This surface consists of a brick-like structure similar to that seen on both GaAs(0 0 1)-$c(4\times4)$ and InSb(0 0 1)-$c(4\times4)$ [6, 17]. This reconstruction has been shown for the other surfaces to consist of a (1×1) plane of V-atoms with rows of V-dimers on top; every fourth dimer is missing along each row, with the missing dimers within adjacent rows shifted $2a_0$ apart (the total V-atom surface coverage is $1\frac{3}{4}$ layers) [6, 17].

An image of a mixed GaSb(0 0 1)-(1×5) and -(2×5) reconstructed surface is shown in Fig. 2c (the reconstruction notation refers to the symmetry seen with RHEED). The upper-central region of this image includes a brighter patch with a $(2\times5)/c(2\times10)$ reconstruction, whereas the rest of the image shows a (1×5) reconstruction. Although pure (1×5) and (2×5) regions were more typical, this region is shown because it allows a direct comparison between the two reconstructions. Focusing on the (1×5) region first, the structure consists of rows spaced $5a_0$ apart. Each row consists of pairs of elements spaced a_0 apart, with each element elongated along the [1 1 0] direction. When tunneling out of filled states closer to the Fermi level, a weak $2a_0$ periodicity is observed between the rows (not shown). This $2a_0$ periodicity may be either aligned or staggered from row to row, indicating that the "(1×5)" surface is actually a mixed $(2\times5)/c(2\times10)$ reconstruction. A model for this surface reconstruction is shown in Fig. 3a, consisting of a full plane of Sb with two adjacent rows of Sb dimers on top. Between the rows are rotated Sb dimers in the second layer, which may or may not be aligned across the rows [18]. The total Sb surface coverage is $1\frac{4}{5}$ layers. (Note that this structure is a simple extension of that proposed for the $c(2\times6)$ reconstruction [13], which consists of *single* Sb-dimer rows in the top layer separated by rotated second layer dimers.)

The (2×5) structures within Fig. 2c appear topographically higher than the (1×5), suggesting that there are additional Sb atoms on top. In addition, the periodic structures within the (2×5) rows are elongated at right angles to the dimers in the (1×5). These features are most simply explained by an additional layer of Sb-dimers adsorbed atop the (1×5) dimer rows [breaking the (1×5) dimer bonds]. The structure of the (2×5) reconstruction is shown more clearly in Fig. 2d. As observed in Fig. 2c, there are rows of dimer pairs along the $[\bar{1}\,1\,0]$ direction, with each pair of dimers spaced $2a_0$ apart. Under the tunneling conditions for this image, elongated maxima spaced $2a_0$ apart *between* the dominant rows are clearly visible, shifted $\sim\frac{1}{4}$ the distance between the maxima on the main rows. A domain wall-like structure produced by rows shifted a_0 along [1 1 0] is also observed in Fig. 2d. Note that shifts of a_0 along $[\bar{1}\,1\,0]$ of the maxima on both the dominant rows and the rows in between result in areas with local $c(2\times10)$ and (2×10) symmetry.

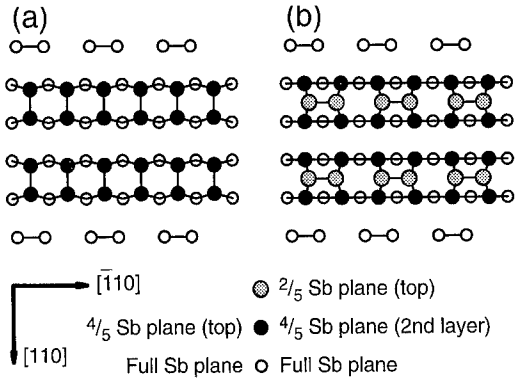

Fig. 3. Proposed structural models for GaSb surface reconstructions observed in RHEED as (a) (1×5), and (b) (2×5). The Sb planes are assumed to be separated by ~ 1.5 Å. Note that the Sb dimers in the second row of the "(1×5)" give this structure a (2×5) symmetry.

A possible structural model for the GaSb(0 0 1)-(2×5) reconstruction is shown in Fig. 3b. The model is a simple extension of the (1×5), consisting of additional Sb dimers on top of the Sb atoms that form the dimer rows of the (1×5) structure, making the total Sb surface coverage $2\frac{1}{5}$ layers. The simple structural differences between the (1×5) and the (2×5) may explain why the (1×5) exists for only a narrow temperature window (see Fig. 1) [9]. It is interesting to note that both of these reconstructions have more surface valence electrons than surface Sb bonds, in violation of the generally accepted "electron counting" model for III–V surface reconstructions [19].

4. Discussion

A different structural model for the (2×5) has been previously proposed by Sieger et al. based on RHEED and photoemission results [13]. Their model differs from ours in two respects. First, their model consists of rows of three dimers in the top-most plane, a structure inconsistent with our STM results. Furthermore, one would expect multi-layer Sb structures to be trigonally bonded [20, 21]. Whereas our model maintains a trigonally bonded environment for the top two planes of Sb, the previously proposed model only has the very top plane of Sb atoms trigonally bonded. The second difference between the two models is that their top Sb plane is bonded to a full plane of Sb, whereas our model has $\frac{4}{5}$ of a plane of Sb as indicated by the STM images. Hence, our models differ in overall Sb coverage: the previous model has $2\frac{3}{5}$ layers of Sb, while ours has only $2\frac{1}{5}$ layers. This difference, however, is within the uncertainty of the published photoemission analysis [22].

Beyond understanding the details of the atomic structure of these reconstructions, one surprising observation is that GaSb does not form the $c(4 \times 4)$ reconstruction common to all other III-Sb and III-As compounds. We believe that the unique GaSb surface reconstructions arise from a competition between adding multiple layers of Sb to the surface and the stress induced by the lattice mismatch between the resulting overlayers and the substrate. The principal source of this stress is expected to be the surface dimer bonds. For a single plane of Sb on a Ga-terminated GaSb(0 0 1) surface, an Sb dimer would result in the top Sb atoms moving from their (1×1) positions (4.3 Å apart) to a distance closer to the natural Sb–Sb bond length (2.9 Å), a 30% displacement. However, given that the lattice parameter of trigonally bonded elemental Sb (4.3083 Å) [21] is nearly equal to the size of the GaSb(0 0 1) bulk-terminated unit cell (4.3101 Å, 0.04% larger), the strain should be significantly reduced by forming a double surface layer of Sb, enabling the subsurface layer Sb to remain in bulk-terminated GaSb-like positions. The Sb atoms within each surface dimer can then be trigonally bonded (to two atoms in the second layer plus the other dimer atom; see Fig. 3a) in a configuration similar to that of elemental Sb. The match between these Sb structures and the GaSb substrate should be nearly perfect along the dimer row direction, resulting in dimer rows with very low strain along $[\bar{1}\ 1\ 0]$ that should act as an excellent template for another layer of (rotated) Sb dimers (Fig. 3b).

We speculate that AlSb(0 0 1) does not form the $(n \times 5)$ reconstructions due to the higher stress that continuous dimer rows would induce on this surface. AlSb has a slightly larger lattice mismatch with bulk Sb (0.70%), leading to more strained surface bonds. Furthermore, the stress associated with these strains will be proportionately greater because AlSb is stiffer than GaSb (for the same displacement, it takes 7% more energy to stretch Al–Sb bonds than Ga–Sb bonds) [23]. This stress may be reduced by periodically removing some of the Sb dimers along each row and allowing for local relaxation, i.e. forming the $c(4 \times 4)$ structure [24].

5. Conclusions

We have studied the structure of AlSb and GaSb (0 0 1) surfaces prepared by MBE with in situ RHEED and STM. Under fixed Sb_4 flux, two AlSb reconstructions are observed with increasing temperature (and decreasing surface Sb : Al coverage): $c(4 \times 4)$ and (1×3). In contrast, four different GaSb reconstructions are observed: (2×5), (1×5), $c(2 \times 6)$, and (1×3). Whereas the (1×5), $c(2 \times 6)$, and (1×3) surfaces are composed primarily of Sb dimer rows on top of an Sb-terminated surface, the (2×5) surface is composed of Sb dimer rows on top of two layers of Sb, i.e. it is terminated by *three* layers of Sb. We propose that GaSb is unique in forming the $(n \times 5)$ reconstructions due to its excellent lattice match with trigonally bonded elemental Sb combined with its lower stiffness compared with AlSb.

Acknowledgements

We thank T. Do for assistance with the GaSb wafer preparation and gratefully acknowledge technical discussions with J.R. Waterman, S.C. Erwin, and M.T. Sieger. This work was supported by

the Office of Naval Research and a Naval Research Laboratory/National Research Council Post-doctoral Fellowship (P.M.T.).

References

[1] T.C. McGill and D.A. Collins, Proc. 6th Int. Conf. on Narrow Band Gap Semiconductors, Eds. R.A. Stradling and J.B. Mullin (Institute of Physics Publishing, Bristol, 1993) pp. S1–S5.
[2] A.G. Milnes and A.Y. Polyakov, Solid-State Electron. 36 (1993) 803.
[3] V. Bressler-Hill, S. Varma, A. Lorke, B.Z. Nosho, P.M. Petroff and W.H. Weinberg, Phys. Rev. Lett. 74 (1995) 3209.
[4] P.M. Thibado, B.R. Bennett, M.E. Twigg, B.V. Shanabrook and L.J. Whitman, Appl. Phys. Lett. 67 (1995) 3578.
[5] M. Yano, H. Yokose, Y. Iwai and M. Inoue, J. Crystal Growth 111 (1991) 609.
[6] D.K. Biegelsen, R.D. Bringans, J.E. Northrup and L.-E. Swartz, Phys. Rev. B 41 (1990) 5701.
[7] J. Zhou, Q. Xue, H. Chaya, T. Hashizume and T. Sakurai, Appl. Phys. Lett. 64 (1994) 583.
[8] A.R. Avery, D.M. Holmes, J. Sudijono, T.S. Jones and B.A. Joyce, Surf. Sci. 323 (1995) 91.
[9] M. Yano, K. Yamamoto, T. Utatsu and M. Inoue, J. Vac. Sci. Technol. B 12 (1994) 1133.
[10] T.H. Chiu and W.T. Tsang, J. Appl. Phys. 57 (1985) 4572.
[11] S. Subbanna, J. Gaines, G. Tuttle, H. Kroemer, S. Chalmers and J.H. English, J. Vac. Sci. Technol. B 7 (1989) 289.
[12] G.E. Franklin, D.H. Rich, A. Samsavar, E.S. Hirschorn, F.M. Leibsle, T. Miller and T.-C. Chiang, Phys. Rev. B 41 (1990) 12619.
[13] M.T. Sieger, T. Miller and T.-C. Chiang, Phys. Rev. B 52 (1995) 8256.
[14] C. Chang, H. Takaoka, L.L. Chang and L. Esaki, Appl. Phys. Lett. 40 (1982) 983.
[15] B.V. Shanabrook, J.R. Waterman, J.L. Davis and R.J. Wagner, Appl. Phys. Lett. 61 (1992) 2338.
[16] L.J. Whitman, P.M. Thibado, F. Linker and J. Patrin, J. Vac. Sci. Technol. B 14 (1996) 1870.
[17] C.F. McConville, T.S. Jones, F.M. Leibsle, S.M. Driver, T.C.Q. Noakes, M.O. Schweitzer and N.V. Richardson, Phys. Rev. B 50 (1994) 14965.
[18] The low density of Sb dimers with (2×5) symmetry in the "(1×5)" structure as compared with those with (1×5) symmetry, their random alignment across the (1×5) dimer rows, and their height below the dimer rows all could contribute to making the 2×5 symmetry very difficult to observe in RHEED.
[19] P.M. Thibado, S.C. Erwin, B.R. Bennett, B.V. Shanabrook and L.J. Whitman, to be published.
[20] P.K. Larsen, J.H. Neave, J.F.v.d. Veen, P.J. Dobson and B.A. Joyce, Phys. Rev. B 27 (1983) 4966.
[21] R.W.G. Wyckoff, Crystal Structures (Wiley, New York, 1963) pp. 31–33.
[22] M.T. Sieger, private communications.
[23] R.M. Martin, Phys. Rev. B 1 (1970) 4005.
[24] J. Tersoff, Phys. Rev. B 45 (1992) 8833.

ELSEVIER

Journal of Crystal Growth 175/176 (1997) 323–327

JOURNAL OF CRYSTAL GROWTH

Effects of morphology on photoemission oscillation measurements during growth of resonant tunneling devices

J.J. Zinck*, D.H. Chow

Hughes Research Laboratories, Malibu, California 90265, USA

Abstract

Photoemission oscillations (PEO) are measured during the growth of InAs/AlSb/GaSb resonant tunneling diodes on (0 0 1) GaAs and (0 0 1) InAs substrates. PEO of the GaSb well are unresolved for growth on GaAs substrates but clearly observable for growth on InAs. AlSb barrier oscillations are observable on either substrate. The morphology of devices grown on GaAs is characterized by micron scale roughness whereas the devices grown on InAs are featureless on the same scale. Threading dislocations which terminate at the GaAs surface with a partial step are believed to influence the growth mode of GaSb but not AlSb due to the higher mobility of Ga in this system.

1. Introduction

The photoemission oscillation technique (PEO) [1] enables monolayer thickness measurements from a rotating substrate if the depositing layer grows in a two-dimensional (2D) layer-by-layer growth mode. PEO has been successfully used in situ to measure the barrier thicknesses of resonant tunneling devices (RTDs) grown by molecular beam epitaxy (MBE) [2, 3]. In particular, we have demonstrated that the correlation between theoretically predicted and experimentally measured peak current densities for InAs/AlSb RTD structures is higher when PEO is used to measure the barrier thicknesses than when these thicknesses are estimated using dead reckoning alone [3]. The largest perturbation of run-to-run device characteristics for the InAs/AlSb structure can usually be attributed to inadequate control of barrier thicknesses; however, for certain device configurations control of well thickness is also important. In particular, substituting GaSb for InAs as the RTD well material results in a system with a type II broken-gap band alignment where tunneling involves coupling between the InAs conduction and GaSb valence-band states [4]. In this device, it is desirable to control both the barrier and the well thicknesses.

In this paper we describe the measurement of photoemission oscillations during the MBE growth of InAs/AlSb/GaSb RTDs on both (0 0 1) GaAs ($\Delta a/a \approx 7\%$) and (0 0 1) InAs substrates. We have

* Corresponding author.

0022-0248/97/$17.00 Copyright © 1997 Published by Elsevier Science B.V. All rights reserved
PII S0022-0248(96)01043-3

correlated the oscillation behavior with the measurement of surface morphology of the devices by atomic force microscopy (AFM). In general, GaSb oscillation contrast is poor when the device is grown on GaAs but distinct and observable when InAs is used as the substrate. AlSb oscillations are observable on either substrate.

2. Experimental procedure

The MBE and PEO apparatus have been described in detail elsewhere [2, 5]. Briefly, the experiments were performed in a Fisons V80 MBE apparatus. A mechanically modulated 30 W deuterium lamp was used as the source of UV photons for PEO and was focused on the substrate at nominally normal incidence through a single element lens. Lock-in detection was used for the photoemitted electrons which were collected on a stainless steel ring concentric with the optical axis and biased at + 300 V. Atomic force microscopy measurements were performed under ambient conditions using a Quesant Instruments QScope operating in contact mode with a silicon nitride tip.

The InAs/AlSb/GaSb device structures grown on GaAs and InAs are shown in Fig. 1. Photoemission was monitored only during the growth of the AlSb barriers and GaSb well associated with each device.

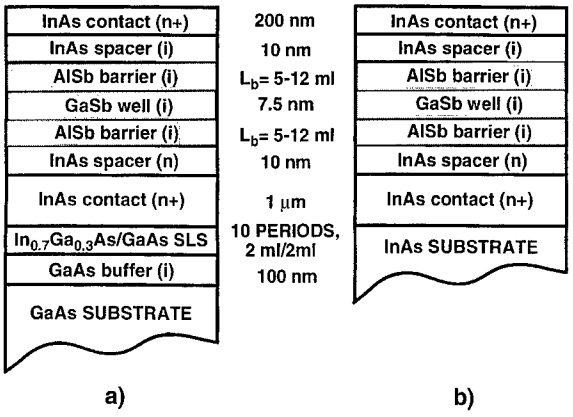

Fig. 1. Structure of the InAs/AlSb/GaSb RTD on (a) GaAs; (b) InAs.

The device recipes were identical, except a superlattice smoothing layer was included between the substrate and the InAs buffer layer for growth on GaAs. During growth of the barrier and well regions, represented by the shaded area of Fig. 1, the growth temperature was 450°C, and the AlSb and GaSb growth rates were 0.2 and 1.0 ml/s respectively. The MBE growth recipe included a 30 s Sb soak prior to the growth of AlSb and GaSb layers to smooth the surface for the PEO measurement. The substrate was rotated at 5 rpm.

3. Results and discussion

A comparison of the PEO from a GaSb well measured during RTD growth on GaAs and InAs substrates is shown in Fig. 2. GaSb well oscillations were weak or unresolved when the device structure was grown on GaAs substrates (Fig. 2a) but distinct and measurable for those grown on InAs substrates (Fig. 2b). A comparison of the PEO from an AlSb barrier measured during the RTD growth on GaAs and InAs substrates is shown in Fig. 3. In the case of AlSb, PEO are resolved on either substrate, with the oscillation contrast on InAs being arguably superior.

AFM images comparing an RTD structure grown on GaAs with a similar structure grown on InAs (as per Fig. 1) are shown in Fig. 4. The morphologies of the two surfaces are strikingly different. Despite the superlattice smoothing layer the surface of the device grown on GaAs is characterized by large-scale roughness on the order of a micron feature size. By comparison, the device grown on InAs is featureless when plotted on the same scale. Although the AFM measurements are performed on the top contact layer of the complete device, independent AFM measurements of InAs layers grown on (0 0 1) GaAs substrates have shown that this large scale morphology develops during the growth of the InAs buffer layer [6].

It is clear that the presence of large-scale morphology strongly influences the growth mode of GaSb under our conditions but has a much smaller effect on the growth mode of AlSb. We propose that the large-scale morphology and the effect on

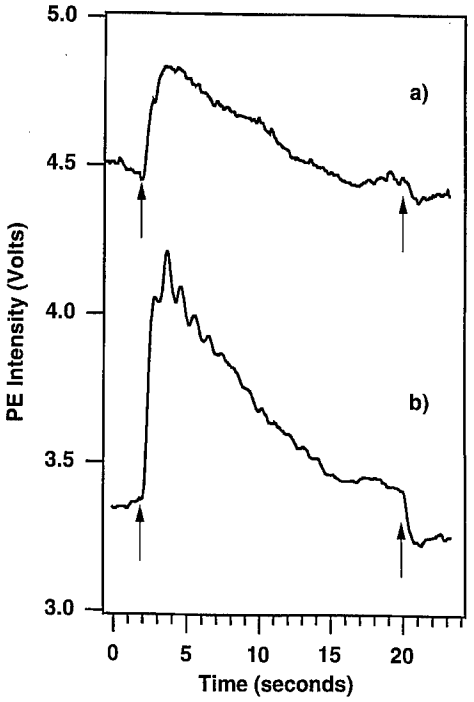

Fig. 2. PEO measured during the growth of a GaSb quantum well of an InAs/AlSb/GaSb RTD on (a) (0 0 1) GaAs; (b) (0 0 1) InAs. Arrows indicate Ga shutter actuation.

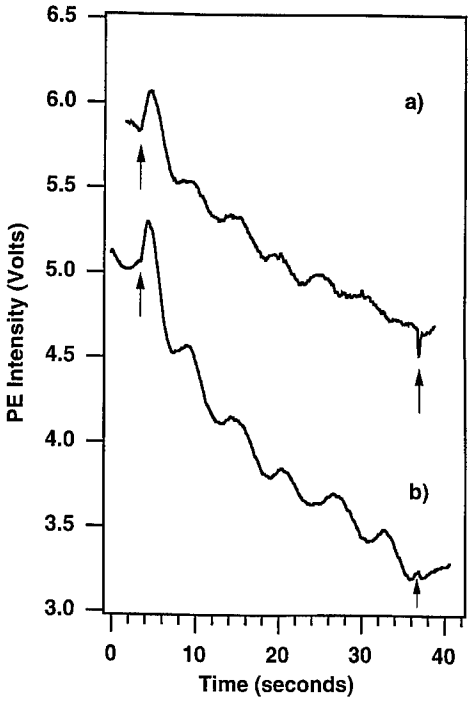

Fig. 3. PEO measured during the growth of an AlSb barrier region of an InAs/AlSb/GaSb RTD on (a) (0 0 1) GaAs; (b) (0 0 1) InAs. Arrows indicate Al shutter actuation.

the growth mode of GaSb are related to the presence of dislocations in the material as a result of the large lattice mismatch of the device material with the substrate. There have been a number of recent reports in the literature which identify unusual surface structure with the highly strained growth of GaSb and AlSb on GaAs [7, 8]. Kyutt et al. [9] have shown that the large lattice mismatch between GaSb and GaAs is accommodated by threading dislocations nucleating at the heterointerface and terminating at the surface with a mainly screw orientation and hence a partial step. It is reasonable to assume that an analogous mechanism for strain accommodation occurs with InAs on GaAs which has a similar lattice mismatch. Transmission electron microscopy measurements have shown that threading dislocations are present at a density of $10^8/cm^2$ in our devices grown on GaAs. The presence of dislocations which add additional step structure to the surface would accelerate the transition to step flow growth for the more mobile species in which case oscillations would not be resolved. This interpretation assumes that the mobility of Ga on GaSb will be higher than the mobility of Al on AlSb because of the difference in their respective bond strengths. The bond strength can be approximately represented by the cohesive energy which is reported as 1.7 for AlSb and 1.5 for GaSb [10]. In the case of the near lattice matched growth on InAs substrates, dislocations do not form, the morphology is smooth, and 2D island nucleation predominates over step flow as the growth mode for both AlSb and GaSb under our growth conditions.

4. Conclusions

During the growth of InAs/AlSb/GaSb RTD structures on (0 0 1) GaAs substrates large-scale surface morphology develops, in contrast to the growth of RTDs on (0 0 1) InAs substrates which

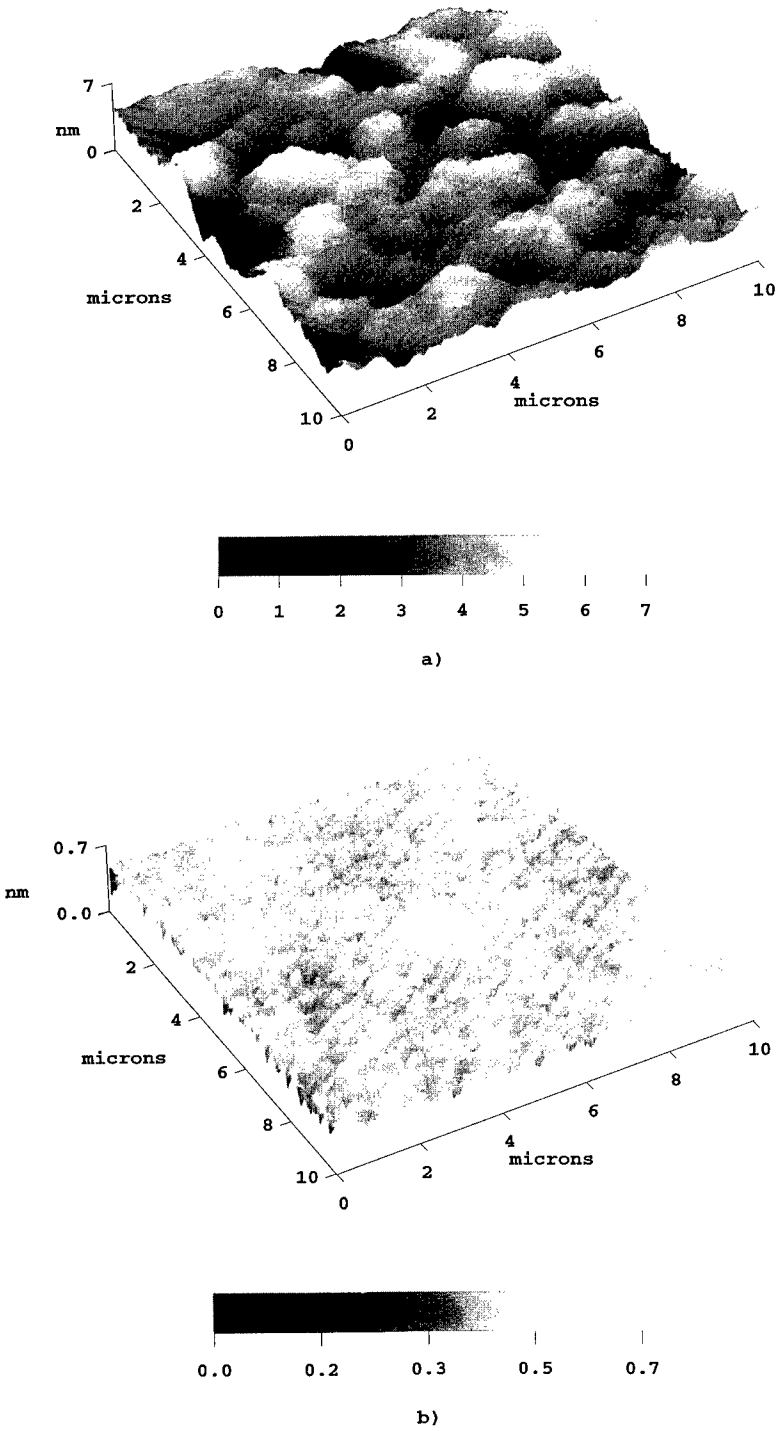

Fig. 4. Atomic force microscopy images of an InAs/AlSb/GaSb RTD grown on (a) (0 0 1) GaAs substrate; (b) (0 0 1) InAs substrate. Note the difference in vertical scales. When plotted with the same vertical scale, the device on (0 0 1) InAs is featureless.

remain relatively smooth. The growth mode of GaSb is different on these two substrates such that GaSb PEO are only resolved when InAs is used as the substrate. The presence of threading dislocations which terminate in a partial step are proposed as the cause of the GaSb growth mode change. AlSb PEO are relatively unaffected by the choice of substrate suggesting that the mobility of Ga is greater than Al under our conditions. The choice of GaAs versus InAs substrates has been reported to have only a small impact on (DC) RTD current–voltage characteristics [11], however, without the ability to control device layer thicknesses in situ, the achievable precision in device performance will be a limiting factor in high-speed circuit design. Understanding the development of surface morphology is critical if PEO is to be applied for in situ control of quantum device layers.

References

[1] J.N. Eckstein, C. Webb, S.-L. Weng and K.A. Bertness, Appl. Phys. Lett. 58 (1991) 2291.
[2] J.J. Zinck, D.H. Chow, J.N. Schulman and H.L. Dunlap, Appl. Phys. Lett. 68 (1996) 1406.
[3] J.J. Zinck, D.H. Chow and J.N. Schulman, J. Vac. Sci. Technol. B 14 (1996) 2163.
[4] M.S. Kiledjiaan, J.N. Schulman, K.L. Wang and K.V. Rousseau, Surf. Sci. 267 (1992) 405.
[5] J.J. Zinck and D.H. Chow, Appl. Phys. Lett. 66 (1995) 3524.
[6] J.J. Zinck, unpublished.
[7] B. Brar and D. Leonard, Appl. Phys. Lett. 66 (1995) 463.
[8] P.M. Thibado, B.R. Bennett, M.E. Twigg, B.V. Shanabrook and L.J. Whitman, J. Vac. Sci. Technol. A 14 (1996) 885.
[9] R.N. Kyutt, R. Scholz, S.S. Ruvimov, T.S. Argunova, A.A. Budza, S.V. Ivanov, P.S. Kopev, L.M. Sorokin and M.P. Scheglov, Phys. Solid State 35 (1993) 372.
[10] T. Soma, J. Phys. C: Solid State Phys. 11 (1978) 2669.
[11] E.R. Brown, S.J. Eglash, G.W. Turner, C.D. Parker, J.V. Pantano and D.R. Calawa, IEEE Trans. Electron. Dev. 41 (1994) 879.

ELSEVIER

Journal of Crystal Growth 175/176 (1997) 328–333

JOURNAL OF CRYSTAL GROWTH

Reflectivity difference spectroscopy study of thin film ZnSe grown on GaAs by molecular beam epitaxy

C.C. Kim[a,*], Y.P. Chen[a], M. Daraselia[a], S. Sivananthan[a], S.-C.Y. Tsen[b], David J. Smith[b]

[a] *Microphysics Laboratory, Department of Physics, University of Illinois at Chicago, Chicago, Illinois 60607, USA*
[b] *Department of Physics and Astronomy and Center for Solid State Science, Arizona State University, Tempe, Arizona 85287, USA*

Abstract

ZnSe films were grown on GaAs substrates with various growth conditions by molecular beam epitaxy (MBE). The optical anisotropy of the films was determined by reflectivity difference spectroscopy (RDS) during and/or after growth. Comparison of the in situ RDS data with spectroscopic ellipsometry (SE) data suggests that RDS could be utilized to determine film thickness, alloy composition and temperature during growth. The RDS spectra were also compared with results from transmission electron microscopy (TEM), X-ray double-crystal rocking curve (DCRC) and Hall measurements. Comparison with the Hall effect showed that the magnitude of the optical anisotropy is generally larger for higher carrier concentrations. Comparison with TEM results and the full-width-at-half-maximum measurements by DCRC reveals that: (i) the E_1 structure arising from the bulk spatial distribution (BSD) is correlated with film quality; (ii) the amplitude of the interference below E_0 provides a measure of the ZnSe/GaAs interface quality; and (iii) the large anisotropy above the band gap is correlated with surface roughness.

PACS: 78.20.Ci; 82.80.Ej; 61.16.Bg; 81.10.Bk

Keywords: RDS; SE; TEM; MBE; ZnSe

1. Introduction

Reflectivity difference spectroscopy (RDS) has been recognized for some time as a useful diagnostic tool because of its sensitivity to surface atomic and electronic structure. Much work has been carried out on the elemental and III–V systems [1–3], but little has so far been done on II–VI systems [4]. ZnSe-based alloys have received attention for their potential as laser diodes in the blue–green region of the spectrum [5]. The short lifetime of the laser diodes has been ascribed to poor interface quality arising from stacking faults, and to high dislocation densities. Thus, it would be useful to find a method of monitoring the interface quality and subsequent growth of these materials. In this paper, we show that RDS could be used, both during and after growth, to assess the quality of typical II–VI systems.

* Corresponding author.

0022-0248/97/$17.00 Copyright © 1997 Published by Elsevier Science B.V. All rights reserved
PII S0022-0248(96)01046-9

2. Experimental procedure

ZnSe films were grown on GaAs substrates by molecular beam epitaxy under various growth conditions, as described elsewhere [6]. The major growth variables were substrate preparation, growth temperature and cell temperature. The optical anisotropy for these materials was determined by ex situ and in situ RDS. The setup and data deduction procedures have been reported previously [7, 8]. The setup for the in situ RDS was similar to that used for the ex situ RDS, except that optical fibers were introduced in order to overcome the constraints imposed by the available space and location of the optical windows in the MBE chamber. For the (0 0 1) surface, the maximum optical anisotropy was obtained from the reflectivity difference $\Delta r/r_{0\,0\,1} = (r_{0\,1\,1} - r_{0\,\bar{1}\,1})/r_{0\,0\,1}$, with the polarization direction of the probing beam parallel to the sample [0 0 1] direction, where the subscripts refer to the crystal orientation. Experimental errors due to imperfection of the optical components, misalignment and electronic noise were further reduced by calculating the average

$$\left(\frac{\Delta r}{r}\right)_{av} \equiv \frac{1}{2}\left(\frac{\Delta r}{r_{001}} + \frac{\Delta r}{r_{0\bar{1}0}}\right). \quad (1)$$

3. Results and discussion

Many samples were characterized in this study, but we concentrate our attention here on six representative films which, for convenience, are labeled A to F. Fig. 1 shows the RDS data for Sample A, and the inset shows the optical dielectric function of ZnSe obtained from SE [9]. Comparison shows that the structure in the lineshape of the RDS data is related to the critical point structure at E_0, $E_0 + \Delta_0$, E_1 and $E_1 + \Delta_1$. These features are present in most samples although their magnitude varies from one film to another. The RDS data also show an interference pattern below the band gap with the same period as the structure in the SE data due to the Fabry–Perot effect in the film/substrate structure. The interference pattern as in the RDS data provides the information on thickness in similar fashion to the interference pattern in the SE

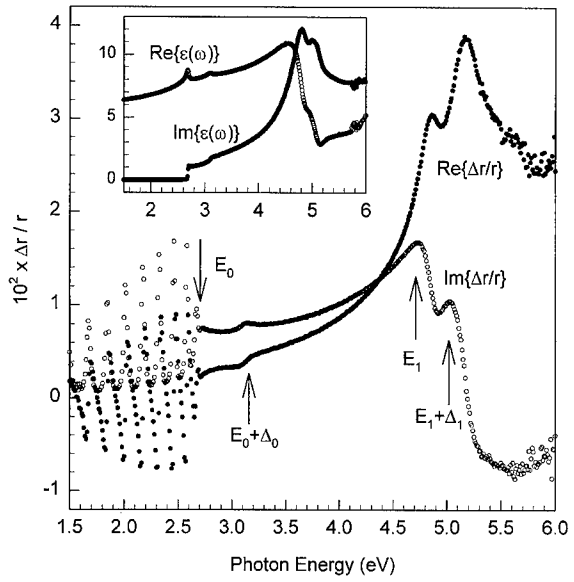

Fig. 1. RDS data for Sample A obtained using Eq. (1). Inset shows the optical dielectric function of ZnSe. Comparison shows that the RDS lineshape is similar to bulk optical dielectric function with critical point structures exaggerated.

data. Fig. 2 demonstrates this capability of in situ RDS for determining film thickness. This spectrum was taken at a wavelength of 600 nm during growth and shows the periodic change in $\Delta r/r$ with thickness. The simple formula $\Delta d = \lambda/2n$ for the peak-to-peak distance can be applied to obtain the growth rate, where d, λ, and n are the thickness, wavelength and refractive index, respectively. The value of n was obtained from the measured optical properties of ZnSe [9]. The accuracy of the thickness measurement depends primarily on the accuracy of the value used for n, and could be improved through calibration. The peak-to-peak amplitude decreases as the thickness increases, presumably due to a very small absorptivity below the bandgap.

Fig. 3 compares the RDS data from Sample A with those from Sample B. For clarity, only the real part is shown. The difference is rather drastic. The RDS data for Sample A show much larger anisotropy over the whole energy range above E_0 than those from Sample B. However, the derivative structure in the E_1 region is persistent in both data. The derivative structure in the E_0 region is even stronger for Sample B than that for Sample A.

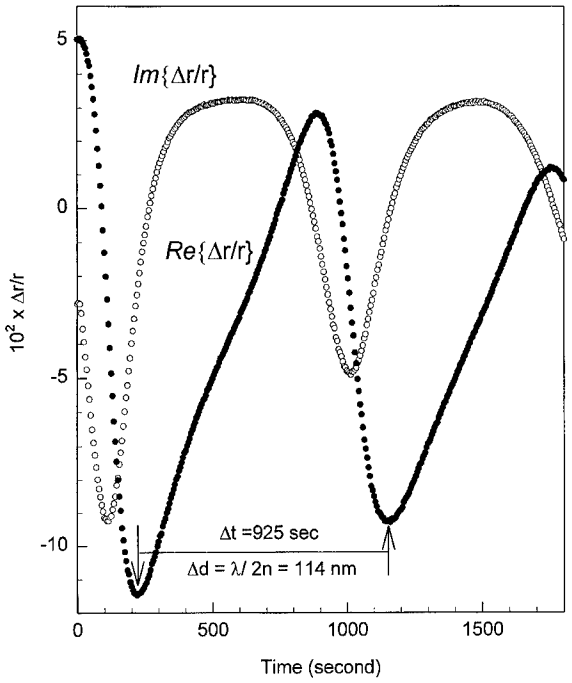

Fig. 2. In situ RDS signal at fixed wavelength, 600 nm, as a function of time.

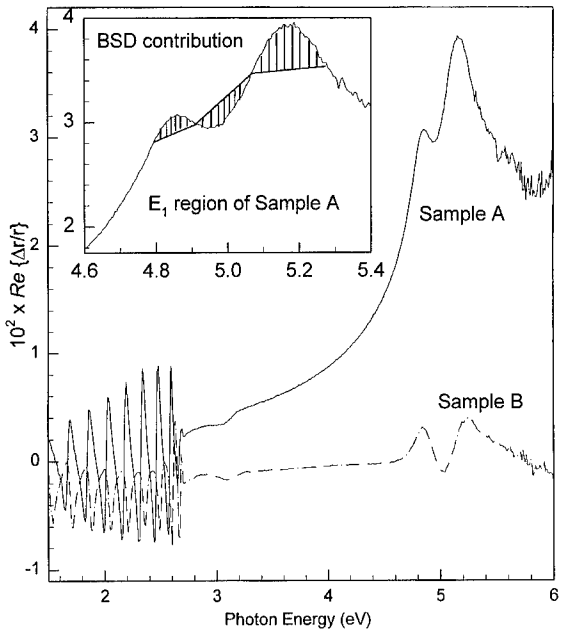

Fig. 3. Comparison of the real part of RDS for Sample A with that for Sample B. The schematic diagram in inset shows the method of calculating BSD contribution.

The corresponding SE data do not show such a large change. The drastic change in the RDS data clearly indicates that the RDS data depend more strongly than SE data on the sample quality. As discussed below, the RDS data are more sensitive to the surface morphology and interface quality determined by TEM, and the film mosaicity determined by the FWHM from DCRC.

The RDS lineshape is similar to the bulk optical dielectric function, but with the real and imaginary parts interchanged and with the critical-point structure exaggerated, as shown in Fig. 1. The difference were ascribed to three major contributions [10]: the surface local field (SLF), the bulk spatial distribution (BSD), and the surface roughness (SR). Previously, we adopted a fitting procedure in order to determine each contribution, using the SE data as a basis [8]. However, in this work, another approach was used to separate out these three contributions to the RDS data. For simplicity, only the real part of the RDS data was analyzed. The reason was that the linewidth of the BSD lineshape, as calculated from the SE data, is smaller than that of the RDS data, and also because the peak position of the BSD lineshape is more persistent than those observed in the RDS data. This made it rather difficult to obtain a consistent result for the strength of the BSD contribution by fitting. Therefore, we chose to calculate the area of the BSD contribution around the E_1 region, as depicted in the inset in Fig. 3. The SLF lineshape calculated from the SE data did not vary much, since the bulk dielectric function did not change much from one sample to another. On the other hand, the RDS data showed a large variation. Extracting the SLF contribution from the data and deducing the SR contribution in a consistent way was thus not simple. Moreover, it has been pointed out that large optical anisotropy values are primarily correlated with the surface roughness propagated from the strains in heteroepitaxial materials [11]. Thus, instead of separating the SLF and SR contributions and comparing them with other results, we calculated the average of the optical anisotropy between 1.5 and 6 eV, as presented in Table 1. The amplitude of the interference (AI) around 2 eV is also recorded in Table 1. From the nature of the RDS signal, this amplitude is reduced by

Table 1
Summary of experimental results for selected samples; the RHEED pattern at the growth start is designated by two-dimensional (2D) or three-dimensional (3D) growth; N is given in units of cm^{-3}; parameters obtained from RDS data are explained in the text: the amplitude of the interference (AI), BSD contribution in meV and average value of optical anisotropy (AOA); (–) means that measurement was performed, but the particular quantity was not determined

Sample	RHEED (at start)	N	TEM		RDS			d (nm)	FWHM (arcsec)
			Surface	Interface	AI	BSD (meV)	AOA		
A	2D	10^{18}	pp 8 nm	Smooth and flat	0.013	0.725	0.0122	1233	234
B	2D	10^{18}	pp 1.3 nm	Rougher than Sample A	0.006	0.754	− 0.0009	1098	218
C	2D	10^{16}	Relatively flat	Smooth and flat	0.005	0.000	0.0016	2825	144
D	2D	10^{19}	pp 3 nm	Relatively flat	0.004	1.178	0.0019	3385	156
E	3D	10^{18}	pp 2 nm	Rough	0.015	1.502	0.0035	643	–
F	3D		pp 2 nm	Rougher than Sample A	0.006	0.568	0.0022	751	–

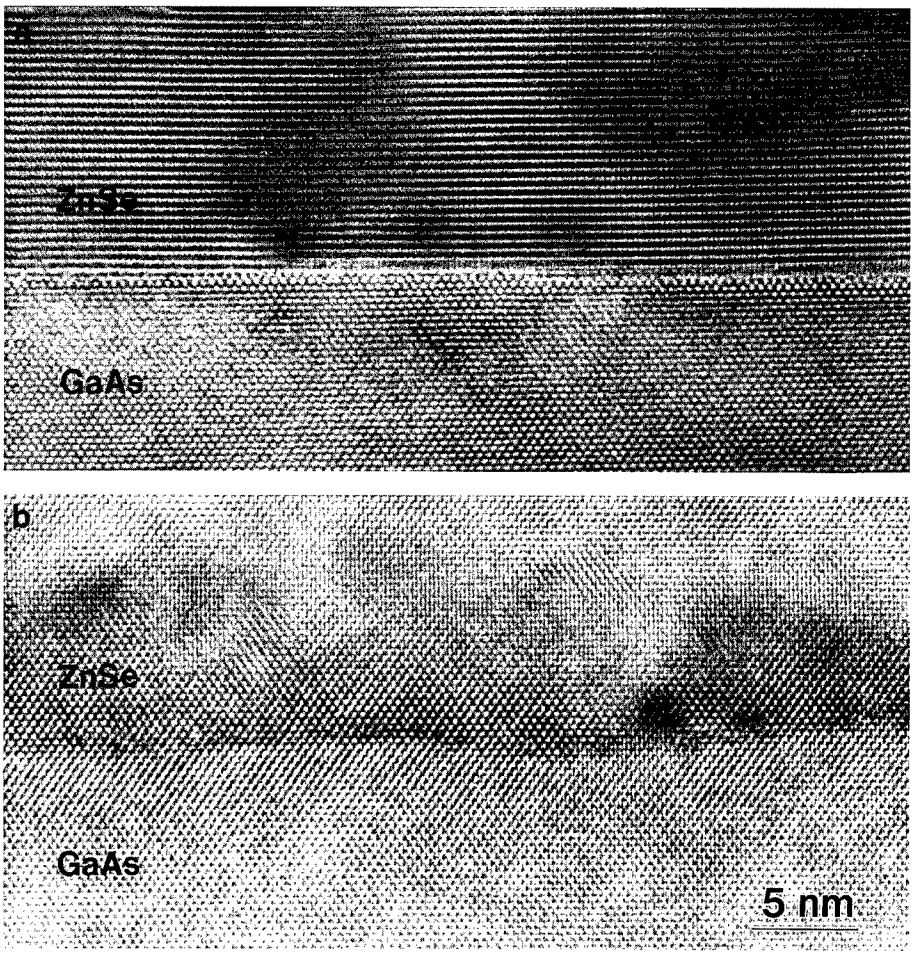

Fig. 4. Electron micrographs showing ZnSe/GaAs interface region: (a) Sample A and (b) Sample B.

absorption below E_0 and is enhanced by a large difference in the reflectivity at the interface. The contribution from the front surface is expected to be negligible based on the report that refractive index differences below the gap are on the order of 10^{-5} [12].

Table 1 summarizes results from the six selected representative samples. The table lists the growth quality at the start as determined by RHEED, the doping concentration (N) from Hall measurement, TEM results at the surface and interface, RDS results, the thickness (d) and the FWHM from DCRC. The TEM results summarize the average peak-to-peak amplitude for the surface and interface roughness. The BSD contribution around the E_1 region is related to other physical parameters such as the FWHM from DCRC, d, N and the TEM results. If d and N for two samples are in a similar range, the BSD contribution around the E_1 region is larger for the sample whose structural quality appears better from the FWHM of the DCRC and the TEM results. For example, the thickness and the FWHM for Sample A are slightly larger than that for Sample B, indicating that the structural quality of Sample B is slightly better than that of Sample A. This is also reflected in the BSD contribution in that the BSD contribution of Sample B is slightly larger than that of Sample A. The BSD contribution is also sensitive to the doping concentration. Samples C and D have similar structural quality in view of the FWHM of DCRC, but the BSD contribution of sample C is below the sensitivity limit, since its doping concentration is much less than that of sample D. The AI of Sample

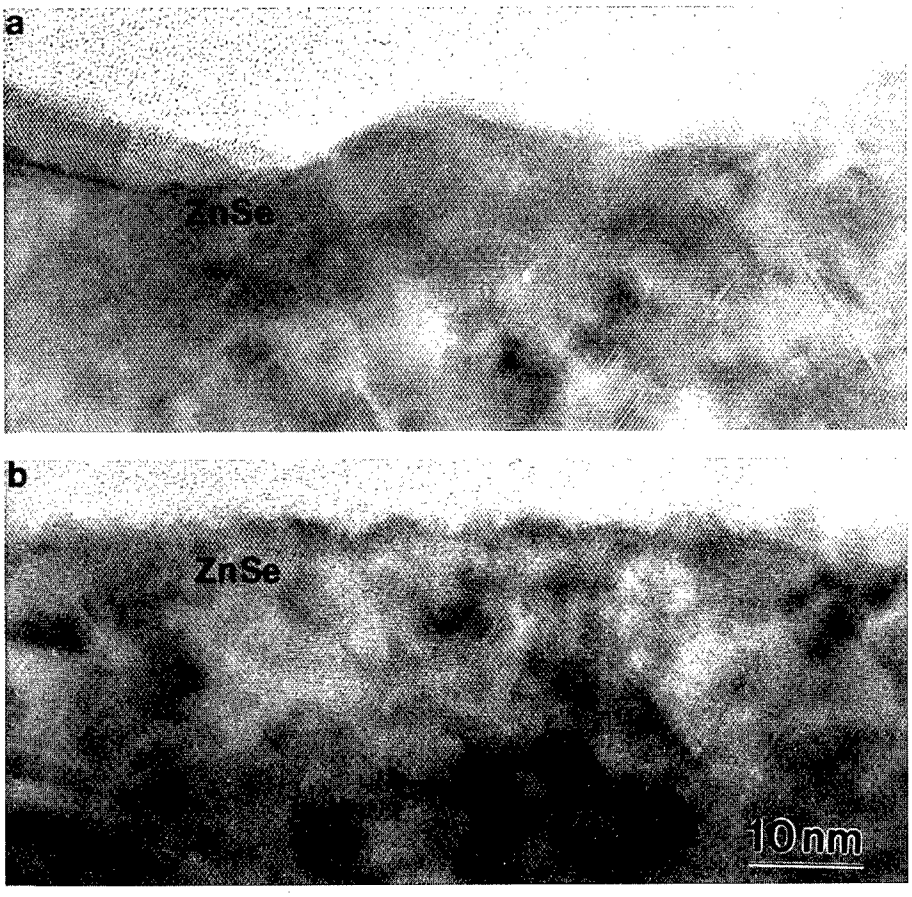

Fig. 5. Cross-sectional transmission electron micrographs comparing surface roughness: (a) Sample A and (b) Sample B.

A is larger than that of Sample B, and the TEM results show that the interface of Sample A is smoother than that of Sample B. This trend is also shown in Samples E and F. Thus, we believe that the value for AI could be related to the interface roughness. The micrographs in Fig. 4 compare the interface of Sample B with that of Sample A. Both show good quality layers without visible misfit dislocations, but the interface of Sample B is slightly rougher than that of Sample A. The average of the optical anisotropy (AOA) is larger for the sample with the rougher surface. For example, the large value of AOA for Sample A is due to the rough surface as shown by Fig. 5, whereas the TEM result for Sample B shows a very smooth surface. Another example is the comparison of E with F. Because these layers are thin, the DCRC were not strong enough to determine the corresponding FWHM. On the other hand, the BSD contributions for both samples showed that Sample E had better structural quality than Sample F, as also confirmed by the TEM results.

4. Conclusions

We have found that reflectivity difference spectroscopy as applied to the ZnSe/GaAs system was useful in deducing important physical parameters such as thickness and alloy composition, and for determining the surface, film and interface quality. A simple method was developed for analyzing the RDS to generate parameters which are valuable for comparison and correlation with the results of other types of sample probe. A complete analysis of the RDS data is in progress and will be published elsewhere.

Acknowledgements

This work was supported by internal funding of the Microphysics Laboratory at the University of Illinois at Chicago. Electron microscopy was conducted at the Center for High Resolution Electron Microscopy at ASU supported by NSF Grant DMR-93-14326.

References

[1] D.E. Aspnes, J.P. Harbison, A.A. Studna and L.T. Florez, Phys. Rev. Lett. 59 (1987) 1687.
[2] E. Colas, D.E. Aspnes, R. Bhat, A.A. Studna, J.P. Harbison, L.T. Florez, M.A. Koza and V.G. Keramidas, J. Crystal Growth 107 (1991) 47.
[3] D.E. Aspnes, Thin Solid Films 233 (1993) 1.
[4] H.H. Farrell, M.C. Tarmargo, T.J. Gmitter, A.L. Weaver and D.E. Aspnes, J. Appl. Phys. 70 (1991) 1033.
[5] R.L. Gunshor and A.V. Nurmikko, MRS Bulletin 20 No. 7 (1995) 15.
[6] B.J. Skromme, Y. Zhang, W. Liu, B. Parameshwaran, D.J. Smith and S. Sivananthan, Mater. Res. Soc. Symp. Proc. 326 (1994) 15.
[7] D.E. Aspnes, J.P. Harbison, A.A. Studna and L.T. Florez, J. Vac. Sci. Technol. A 6 (1988) 1327.
[8] C.C. Kim and S. Sivananthan, Mater. Res. Soc. Symp. Proc. 406 (1996) 319.
[9] C.C. Kim and S. Sivananthan, Phys. Rev. B 53 (1996) 1475.
[10] D.E. Aspnes, J. Vac. Sci. Techonol. B 3 (1985) 1138.
[11] B.R. Bennett, J.A. Delalamo, M.T. Sinn, F. Peiro, A. Cornet and D.E. Aspnes, J. Electon. Mater. 23 (1994) 423.
[12] D.E. Aspnes and A.A. Studna, Appl. Phys. Lett. 39 (1981) 316.

ELSEVIER

Journal of Crystal Growth 175/176 (1997) 334–339

JOURNAL OF CRYSTAL GROWTH

Real-time monitoring of RHEED using machine vision techniques

R.F. Kromann[a], R.N. Bicknell-Tassius[b,*], A.S. Brown[a], J.F. Dorsey[a], K. Lee[a], G. May[a]

[a] *School of Electrical Engineering, Georgia Institute of Technology, Atlanta, Georgia 30332-0250, USA*
[b] *Georgia Tech Research Institute, Georgia Institute of Technology, Atlanta, Georgia 30332-0250, USA*

Abstract

A RHEED system has been developed that allows real-time monitoring of RHEED information throughout a multilayer growth run with rotation. The machine vision system consists of high-speed image capture hardware coupled with digital signal processing software that allows the real-time extraction/analysis of the RHEED intensity and width signals from the noise induced by substrate rotation. This system has been used to investigate the oxide desorption process on GaAs substrates, along with the specular spot intensity and width variation during the growth of a set of InGaAs/AlGaAs single quantum well structures with systematically varied process parameters. A strong correlation of the specular spot intensity with growth parameters has been observed. It is also shown that the observed specular spot intensity can be used to predict the quality of the InGaAs quantum well structures.

1. Introduction

The reflection high energy electron diffraction (RHEED) technique has been widely applied to the study of molecular beam epitaxy growth kinetics. RHEED oscillations at the onset of growth have been used to both measure growth rates, and accurately determine alloy compositions and surface diffusion lengths [1]. The dynamics of the intensity oscillations have been recently employed to grow closely lattice-matched ternary alloys [2]. Not only have the dynamics of the specular spot intensity been used to obtain information about the growth kinetics but the profile of the specular beam has also been used to determine surface correlation lengths during the growth process [3]. One limitation of the RHEED technique is that, to date, it has been almost exclusively applied to non-rotating substrates due extrinsic effects such as substrate wobble, and intrinsic effects due to the complex variation of the specular spot intensity with azimuthal angle [4]. Thus, it has had limited application in real-time monitoring/control and the study of surface kinetics during growth of realistic device structures which are usually grown with rotation. Several approaches have been undertaken to allow the measurement of RHEED oscillations on rotating substrates during the initial stages of growth. These include: rotating at high speed

* Corresponding author. Fax: +1 404 894 4832; e-mail: rb91@prism.gatech.edu.

0022-0248/97/$17.00 Copyright © 1997 Published by Elsevier Science B.V. All rights reserved
PII S0022-0248(96)01184-0

(> 100 rpm) [5], specular spot tracking coupled with Fourier transform techniques [6, 7], and real time layer counting using digital signal processing techniques [7].

To date, little has been done to utilize RHEED for monitoring the material surface throughout the growth of an entire complex multilayer structure. It is important to study realistic structures due to coupling between the layers in such a multilayer structure. In the present work, a RHEED acquisition and analysis system has been developed that allows real-time monitoring and analysis of RHEED images throughout extended multilayer MBE growth runs in which the sample is rotated at standard rotation rates ($\sim$ 10 rpm).

As an initial application of this system, it was used to monitor and analyze the RHEED data from a set of 16 InGaAs/AlGaAs single-quantum well structures for which the growth parameters were systematically varied.

2. Experimental details

The structure investigated in the present work consisted of a 0.1 μm GaAs interface layer, a 0.5 μm AlGaAs buffer layer followed by a 75 Å InGaAs quantum well, which was capped by a 0.25 μm AlGaAs cap layer. All samples in this study were grown in a solid source Varian Gen II MBE system using solid As_4 as the arsenic species. Samples were grown on $\frac{1}{4}$ of a 2 in semi-insulating GaAs wafer that was etched in 5 : 1 : 1 $H_2SO_4 : H_2O : H_2O_2$ before being indium mounted on a standard molybdenum sample holder. The following factors were varied for the sixteen trial runs: oxide removal temperature from 580°C to 650°C, oxide removal time from 30 to 300 s, AlGaAs growth temperature from 580°C to 630°C, InGaAs growth temperature from 480°C to 520°C, interface interrupt time from 30 to 90 s and arsenic cell temperature from 325°C to 340°C (1×10^{-5} to 2×10^{-5} Torr). It is important to note that the RHEED pattern, as viewed by the MBE operator, indicated complete oxide removal for all the sixteen experiments.

The RHEED system consists of a 10 kV electron gun with the image captured with a video camera and digitized on a PCI high speed video capture card. The capture card acts as a PCI bus master and transfers the image array at very high speed directly to linearly mapped video display memory on a VGA video display card, also on the PCI bus.This configuration allows the transfer of a large amount of video data, about a one fourth of a megabyte for a standard NTSC image, without using any primary processor overhead, thereby eliminating a data transfer bottleneck that has historically prevented real time image analysis. Once in system memory, the image is then manipulated by the primary CPU while the next video frame is being digitized and stored.

To compensate for beam movement due to substrate wobble and other factors, the position of the centroid of each beam is tracked so that the measurement algorithm is always fixed on the beam. This tracking involves segmenting the image in order to separate beam pixels from background pixels in the vicinity of the last known position of the beam, and computing the row and column centroids of the connected portion of the non-background binary image at this last known position. The last known position is then updated, and passed to the measurement routines.

One complication in discriminating between the spot and the background is that the overall intensity changes by a factor of two or more over the entire multilayer growth run. Thus, a fixed threshold value for determining the cutoff between the brighter diffracted/reflected beams and the darker background is not a viable approach. The threshold intensity must be updated periodically using a local intensity histogram to account for the relative change in intensity with time. Fortunately, the rate of change in intensity is slow compared to the image sampling rate. Thus, the cutoff threshold can be held constant for a number of sampling periods before being updated. This is crucial to obtain rapid processing of the images.

The measured intensity of each spot being tracked is a normalized integral of the individual pixel brightness levels over a user selected area centered at the centroid of the spot. The area is a parallelogram with one set of sides aligned normal to the RHEED shadow edge and the other set of sides aligned with the vertical columns of the image. This geometry is chosen to allow selection of

a single spot/streak from a group of closely spaced spots while maximizing the area of integration without overlapping an adjacent spot.

Not only have the intensities of the beams been measured, but the widths of the beams were also determined. A narrower, more focused beam, indicates a large surface correlation length and a more uniform surface, while a less focused, wider beam corresponds to a more disordered surface with smaller surface correlation length. The width of a beam is measured by maximizing a cost function that favors a sharp gradient in intensity and a short distance from the center of the spot. The cost function is evaluated along a line passing through the center of the spot and parallel with the shadow edge. A technique such as that used by Collins et al. [6] in which a constant threshold is used to detect the edge of the spot is only applicable if the relative intensity of the whole image does not change significantly. In the case of monitoring over the whole duration of the growth run, however, the maximum and minimum intensities of the spots vary dramatically. During the growth of the GaAs buffer the diffuse background intensity is actually higher than the specular spot intensity during the AlGaAs layer, Thus, it is impossible to define a single constant threshold value that will discriminate the specular spot from the background throughout such multilayer structures.

A cost function technique was used instead of standard edge detection methods because in many cases the spots did not have a large enough brightness gradient to allow use of standard techniques [8, 9]. The cost function approach gives essentially the same results for sharp edges as the standard techniques, but for spots with a less steep gradient, this cost function approach gives a spot width equivalent to one which a human operator would choose. The full width at half maximum (FWHM) approach also fails to give consistently reasonable estimates of spot width, because in many instances the background intensity is so large and varied over the image that the FWHM technique gives a spot width many times bigger than the actual width.

The specular spot intensity and widths were measured at 10 Hz and then passed in real time through a tenth order Butterworth digital lowpass filter with a half power point of 0.1 Hz to remove changes in intensity due to factors such as rotation and wobble [10].

3. Results and discussion

The specular spot intensity as a function of time for a complete MBE growth run consisting of an AlGaAs buffer layer and a single InGaAs quantum well before any filtering is done is shown in Fig. 1. In this particular structure, the oxide was desorbed at 650°C for 300 s, the AlGaAs buffer layer was grown at 630°C, the InGaAs single quantum well was grown at a substrate temperature of 520°C, and an interrupt time of 90 s was used at each side of the quantum well. As can be seen, there is very little useful information readily available, because of the noise that is induced by the substrate rotation. However, the same data shows many significant features after low pass filtering, as shown in Fig. 2.

It was found that the relative difference in intensity between the specular spot and the diffusely scattered background is a good indication of the state of oxide desorption. Initially, when the oxide is largely intact, there is little, if any, diffraction. The majority of the illumination in the image is from diffuse scattering off the rough oxide surface. As the oxide desorbs, exposing the crystal lattice structure

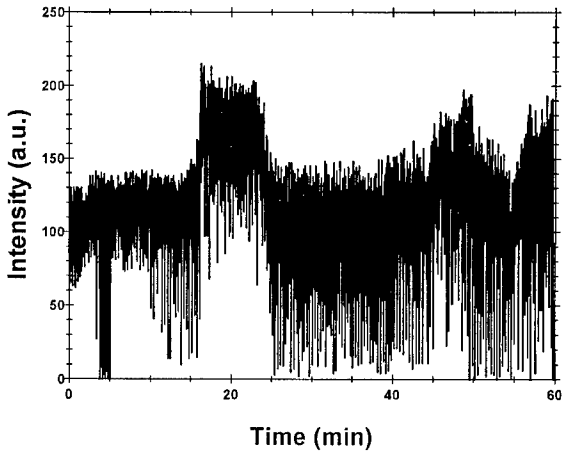

Fig. 1. Specular spot intensity during a 1 h MBE run while rotating the substrate at 10 rpm.

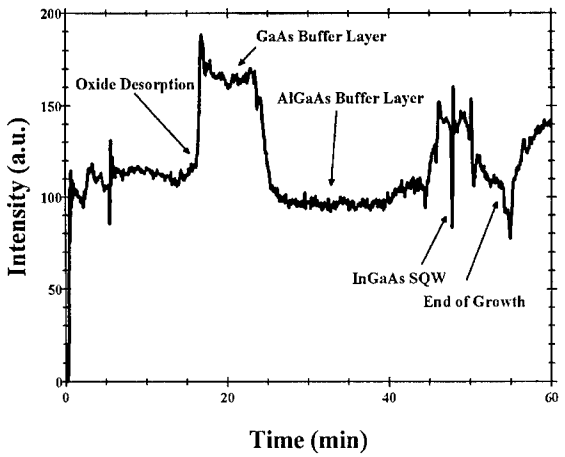

Fig. 2. Specular spot intensity during a 1 h MBE after being passed through a low-pass digital filter.

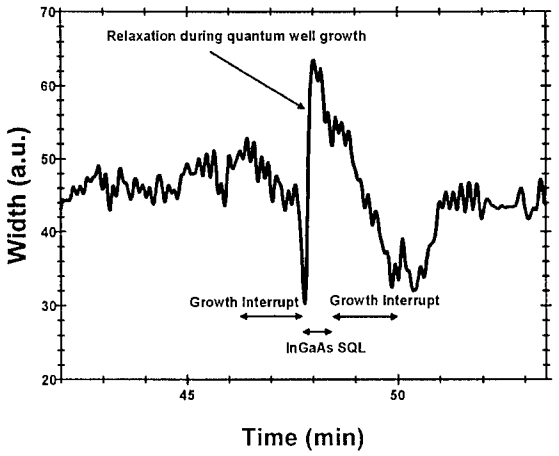

Fig. 3. Specular spot width during the growth of the single-quantum well.

to the electron beam, the familiar pattern of periodic spots and streaks emerges, with the spots and streaks getting progressively brighter as desorption progresses. Simultaneously the diffusely scattered background gets progressively dimmer. Thus, the peak intensity goes up while the background intensity goes down. Of great importance is the fact that there is a dramatic increase in the difference in these two intensities at the point where desorption is completed.

This difference between peak and background intensities represents a measurement of the extent of desorption, and thus provides a means of accurately determining when desorption has occurred. This, in turn, leads to shorter desorption cycles. In the standard approach, the substrate temperature is raised until the point where a bright and sharp RHEED pattern is observed, and, due to the subjective nature of the interpretation, this point may be significantly beyond the point at which desorption has actually completed. The information available from the real time machine vision system can reduce this ambiguity by providing a quantitative measure of desorption. The information can also prevent the desorption cycle from being cut short before desorption is complete. Thus, the impact of the real time machine vision is to shorten the desorption cycle, while producing more reliable results.

The width of the specular spot vs. time around the growth of the InGaAs quantum well is plotted in Fig. 3. It can be seen that during the first growth interrupt, the beam becomes narrower as the surface recovers to a smoother state. During the growth of the quantum well, the RHEED pattern change from narrow streaks to wider spots is a sign of strain relaxation, indicated by the increase in the specular spot width. The width then decreases as the specular beam gets sharp and narrow again with the surface smoothing associated with the second growth interrupt. This quantitative real time measure of the quality of the surface is a useful feedback tool for MBE growth.

Fig. 4 is a plot of specular spot intensity during the growth of the InGaAs quantum well. The qualitative shape of this filtered signal is consistent through all sixteen growth runs. It shows the recovery of the specular spot intensity during the periods of growth interruption as well as its variation during the growth of the quantum well while being rotated. The highest value of the specular spot intensity during the growth of the InGaAs quantum well, abbreviated as QWH (shown in Fig. 4) has been fit to a linear model, with the growth parameters as the independent variables. A number of the growth parameters were found to be statistically significant within a 95% confidence interval. QWH as a function of the substrate temperature

during the quantum well growth and the arsenic cell set point is plotted in Fig. 5. As can be seen the specular spot intensity is a strong function of both parameters. In this case the brightest specular spot was obtained for a substrate temperature of 450°C and an arsenic set point of 340°C. This is in agreement with previous reports on the growth of high quality InGaAs by MBE [11].

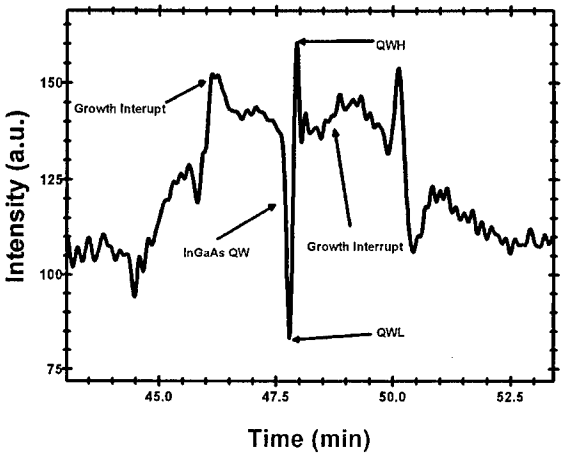

Fig. 4. Specular spot intensity during the growth of the single-quantum well.

Not only is there a strong correlation between the input growth parameters and the specular spot intensity during the quantum well growth, there are strong correlations between the low temperature photoluminescence and the specular spot intensity, as shown in Fig. 6. The inverse of the specular spot intensity (QWH) is plotted during the quantum well growth together with the FWHM of the InGaAs photoluminescence. These can be easily understood when one considers that the specular spot intensity is a measure of the surface roughness. Thus, when the interfaces are the smoothest the photoluminescence is the narrowest.

4. Summary

In summary, a machine vision system has been demonstrated that allows the quantitative real-time measurement of RHEED characteristics throughout the growth of multilayer device structures while rotating the substrate. A strong correlation of

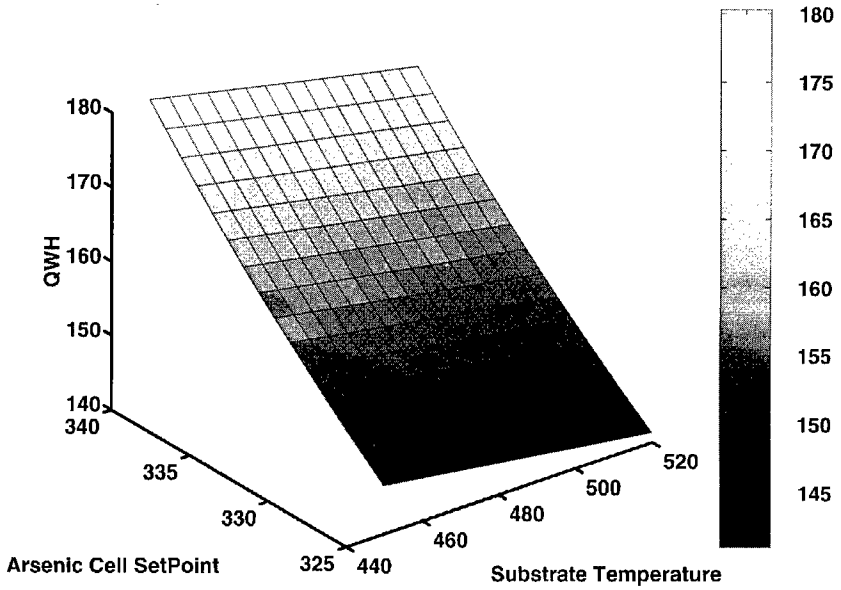

Fig. 5. Specular spot intensity before the growth of the InGaAs single-quantum well as a function of the substrate temperature and arsenic flux

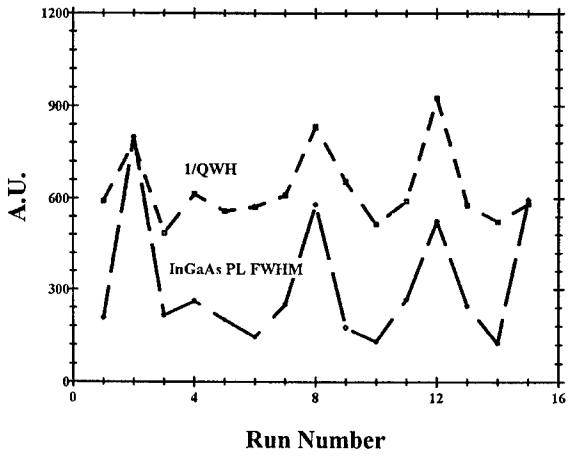

Fig. 6. Correlation between the specular spot intensity and the InGaAs SQW photoluminescence FWHM.

specular spot intensity during rotation with the growth parameters has been observed, for the first time. The specular spot has been correlated both with the growth parameters and with the low temperature photoluminescence spectra of the InGaAs quantum-well. Thus, this technique shows strong promise for real-time monitoring and control of advanced multilayer device structures grown by molecular beam epitaxy.

Acknowledgements

The authors wish to acknowledge support from the Advanced Technology Development Center (ATDC) of Georgia Institute of Technology.

References

[1] J.H. Neave, B.A. Joyce, P.J. Dobson and N. Norton, Appl. Phys. A 31 (1983).
[2] J.E. Cunningham, R.N. Pathak and W.Y. Jan, Appl. Phys. Lett. 68 (1996) 394.
[3] J.M.v. Hove, J. Crystal Growth 81 (1987) 13.
[4] J.H. Neave, B.A. Joyce and P.J. Dobson, Appl. Phys. A 34 (1984) 179.
[5] J.P.A.v. Wagt, J. James and S. Harris, J. Vac. Sci. Technol. B 12 (1994) 1236.
[6] G.W. Turner and A.J. Isles, J. Vac. Sci. Technol. B 10 (1992) 1784.
[7] D.A. Collins, G.O. Papa and T.C. McGill, J. Vac. Sci. Technol. B 13 (1995) 1953.
[8] G.A. Baxes, Digital Image Processing, Principles and Applications (Wiley, New York, 1994).
[9] G.W. Awcock and R. Thomas, Applied Image Processing (McGraw-Hill, New York, 1996).
[10] L. Thede, Analog and Digital Filter Design Using C (Prentice-Hall, Englewood Cliffs, 1996).
[11] P.R. Berger, K. Chang, P. Battacharya and J. Singh, J. Vac. Sci. Technol. 5 (1987) 1162.

ELSEVIER

Journal of Crystal Growth 175/176 (1997) 340–345

JOURNAL OF CRYSTAL GROWTH

In-situ BEEM study of interfacial dislocations and point defects

H. von Känel*, T. Meyer, H. Sirringhaus

Laboratorium für Festkörperphysik, ETH Zürich, CH-8093 Zürich, Switzerland

Abstract

Epitaxial $CoSi_2$/n-Si(1 1 1) interfaces have been studied by in-situ ballistic-electron-emission microscopy (BEEM) at 77 K. The scattering of hot electrons by individual misfit dislocations and point defects leads to significant contrast in the BEEM images, proving that interfacial defects of atomic dimensions can be probed by BEEM. The Schottky barrier height is not measurably affected by these defects. When present, grains of a metastable $CoSi_2$ phase with a defect-CsCl structure do, however, lower the barrier appreciably.

1. Introduction

The invention of ballistic-electron-emission microscopy (BEEM) by Kaiser and Bell [1] has made it possible to study electric transport across interfaces with a spatial resolution unattainable before. In BEEM the tip of a scanning tunneling microscope (STM) acts as the emitter injecting hot charge carriers into a metallic base. The base layer is kept thin, typically <10 nm, in order to allow a fraction of the injected current I_t to enter the semiconducting collector where it is measured as the BEEM or collector current, I_c. The configuration resembles thus the one of a point contact transistor with the exception that here the emitter can be moved across the sample just as in the usual STM operation. In the simplest case the metal base is deposited directly onto a uniform semiconductor, such that the injected carriers just have to surmount the Schottky barrier at the metal–semiconductor (m–s) interface in order to contribute to the collector current. More complicated heterostructures have been studied by BEEM as well, however, such as resonant tunneling diodes [2], metal–insulator–semiconductor (MIS) [3] and MOS structures [4].

Even though BEEM was designed to be a technique for studying buried interfaces, surface effects may contribute significantly to the variation of the collector current [5], such that operation in UHV is mandatory in order to attain the highest possible spatial resolution. Here we shall focus on epitaxial $CoSi_2$/Si(1 1 1) heterostructures fabricated by MBE. Misfit dislocations are shown to affect hot electron transport by leading to elastic scattering. They do not lead to a measurable change of the Schottky barrier height at the m–s interface. Barrier fluctuations do occur, however, when there are

* Corresponding author: Fax: +41 1 633 10 72; e-mail: vkaenel@solid.phys.ethz.ch.

0022-0248/97/$17.00 Copyright © 1997 Published by Elsevier Science B.V. All rights reserved
PII S0022-0248(96)00867-6

regions in which the crystal structure of the silicide deviates from the usual CaF_2 type. It has been shown recently that under certain conditions $CoSi_2$ may indeed assume a defected CsCl structure with vacancies on the cation sublattice [6, 7].

2. Experimental results and discussion

All $CoSi_2$ films were grown by standard MBE procedures [8, 9] on heavily As doped ($<0.004\ \Omega$ cm) 3 in Si substrates, after depositing first an undoped Si buffer layer with a thickness of typically 300 nm. Before growing the base for the BEEM measurements, the wafer was flipped and a thick (>10 nm) $CoSi_2$ layer was deposited on its back side, serving as an ohmic collector contact. The base thickness was chosen to be in the range 2–4 nm in order to ensure ballistic electrons to reach the interface [10]. In the case of $CoSi_2$/Si(111) films of this thickness can be grown coherently or partially relaxed. In order to avoid the (2×1) surface reconstruction present on strained films [11] the number of dislocations was maximized for the BEEM studies by adjusting the growth procedure accordingly. All BEEM experiments were carried out at 77 K, in a low-temperature STM situated in a UHV chamber attached to the MBE system.

2.1. Scattering by dislocations and point defects

The defect structure at $CoSi_2$/Si(1 1 1) interfaces has been studied extensively by transmission electron microscopy (TEM) [12]. The main defects of films annealed above 500°C are partial dislocations with Burgers vectors $\boldsymbol{b} = \frac{1}{6}a\langle 1\,1\,\bar{2}\rangle$ associated with interfacial steps. In topographic STM images these dislocations appear as faint surface corrugations resulting from their strain field (Fig. 1a). The simultaneously acquired BEEM image, taken at a tunneling voltage of $V_t = -1.4$ V and a tunneling current of $I_t = 20$ nA, is displayed in Fig. 1b. It is

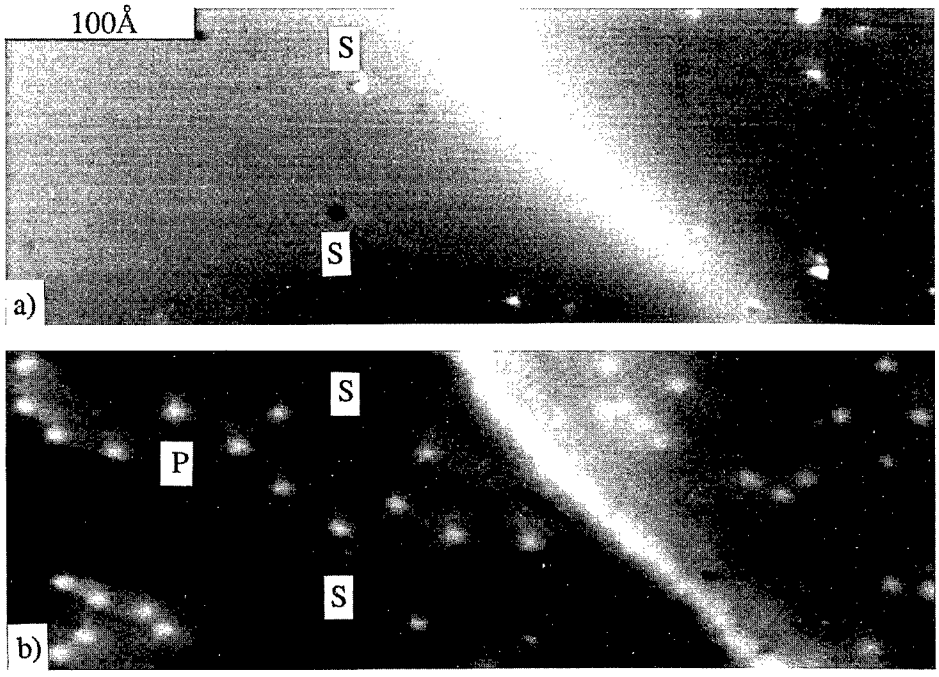

Fig. 1. (a) Topographic STM image obtained on a 3.2 nm thick $CoSi_2$ film on Si(1 1 1). The height of the dislocation induced corrugation is 0.06 nm. (b) BEEM image acquired simultaneously with the topography. The gray scale ranges from 0 to 160 pA. Tunneling parameters were: $V_t = -1.4$ V, $I_t = 20$ nA. *S* and *P* are surface and interface point defects, respectively

evident that the contrast in the BEEM image is far more pronounced than the topographic contrast, the collector current being enhanced by as much as 40% above the dislocation. In addition, the BEEM current exhibits the same kind of increase at certain point-like features which are not associated with surface defects, as can be seen by comparing with the topography image (Fig. 1a). It follows also from Fig. 1 that the dislocation appears much narrower in the BEEM image than in the topography image. This could be corroborated by taking cross-sections perpendicular to the dislocation line [13]. The smallest FWHM of a dislocation ever observed in a BEEM image was $\sim$0.8 nm, whereas in the topography it amounts to twice the film thickness in accordance with an elastic continuum model [11]. The width of the point-like features in Fig. 1b is of the same order of magnitude as the one of the dislocation.

Let us now discuss the origin of the BEEM contrast visible in Fig. 1b. As outlined in the Introduction, the nonuniformities of the BEEM current can be caused either by variations of the Schottky barrier height or by scattering processes. The barrier height follows immediately from the variation of the collector current I_c with the tunneling voltage V_t (ballistic-electron-emission spectroscopy or BEES). The Schottky barrier height at the $CoSi_2$/Si(1 1 1) interface was found to be $\Phi_b = 0.66 \pm 0.03$ eV both in the vicinity of a dislocation as well as far away from it, as long as the silicide has its normal fluorite structure everywhere. The contrast variations observed on a scale of nanometers must hence be due to elastic scattering at dislocation cores and at point defects. It has to be kept in mind that the angular distribution of the tunneling electrons is strongly forward focused, which should lead to low transmission across a perfect $CoSi_2$/Si(1 1 1) interface. The reason for this is indicated in Fig. 2 showing a projection of the constant energy surfaces of Si onto the interface Brillouin zone. Whereas hot electrons with a small parallel momentum $k_{\|}$ are primarily reflected back into the metal, this is no longer true if they undergo a scattering event, yielding the necessary large $k_{\|}$. While it is certain that the bright spots in Fig. 1b are due to scattering at point defects, the exact location of these cannot be determined

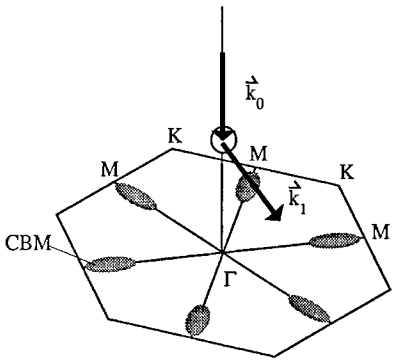

Fig. 2. Pictorial k-space representation of a scattering process allowing a hot electron to enter the off-centered conduction band minima at the $CoSi_2$/Si(1 1 1) interface.

experimentally at present. On the other hand, the dislocation line, which is *known* to lie at the interface, has an internal structure looking very much like a linear chain of similar point defects. It is likely therefore that the isolated spots are of the same kind. Of course, the point defects could also be trapped by the strain field of the dislocation. One argument in favour of interfacial point defects might be the electrical resistivity which was found to rise due to interfacial scattering only in films below $\sim$5 nm [14]. The ability to observe single point defects by BEEM depends very much on the structure and quality of the surface. Not only do surface defects give rise to contrast variations of the same size (Fig. 1b). Surface reconstructions were found to modify the tunneling distribution locally, again leading to large contrast changes and therefore masking any scattering effects taking place at the interface [5, 15]. On the other hand, variations of the Schottky barrier height are affected much less by these surface scattering effects.

2.2. Variations of the Schottky barrier height

As pointed out above, the Schottky barrier Φ_b at the interface between $CoSi_2$ with the fluorite structure and Si(1 1 1) was found to be unaffected by the commonly observed misfit dislocations of type $\boldsymbol{b} = \frac{1}{6}a\langle 1\,1\,\bar{2}\rangle$. In the past few years it has become increasingly evident, however, that, apart from its bulk stable fluorite structure, $CoSi_2$ can assume

other crystal structures which are stabilized by epitaxy [6, 7, 16]. The growth of $CoSi_2$ usually involves an annealing step typically at 600°C, which improves its electrical properties [8]. The anneal also causes most of the material to transform to the bulk stable phase. Grains of the defect-CsCl phase have, however, been observed in some films even after such an annealing [7]. A detailed account of this phase transition between epitaxially stabilized and bulk stable $CoSi_2$ phases will be given elsewhere [17]. Here we just discuss the BEEM results obtained on a film *known* from high-resolution transmission electron microscopy (HRTEM) to contain CsCl grains. The topography and corresponding BEEM image of such a film are shown in Fig. 3a and Fig. 3b, respectively. In the middle of

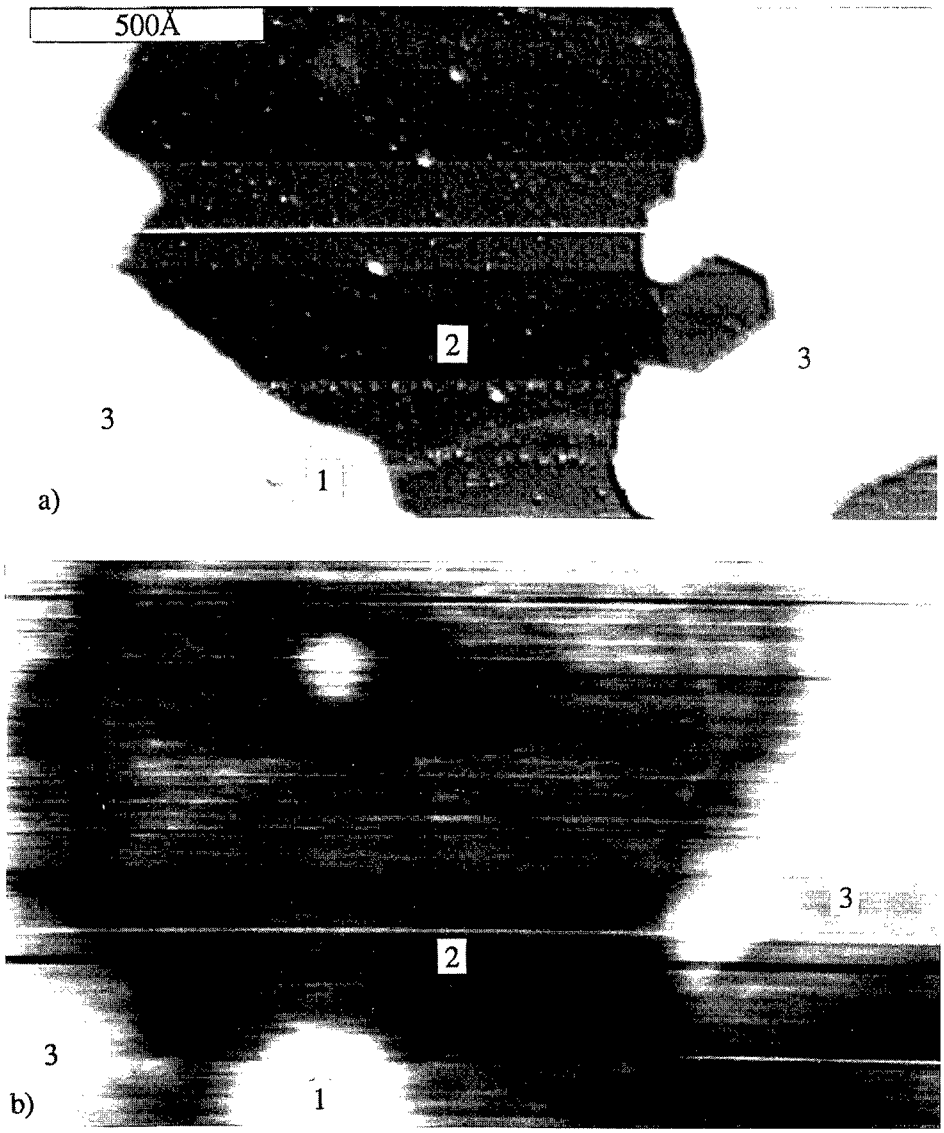

Fig. 3. (a) Topographic STM image of a 2.4 nm thick $CoSi_2$ film on Si(1 1 1), containing grains of the epitaxially stabilized defected CsCl phase in addition to the bulk stable CaF_2 phase. (b) Simultaneously acquired BEEM image. Tunneling parameters were: $V_t = -2$ V, $I_t = 5$ nA.

the topography image a large terrace can be seen (region 2) in which the BEEM current is nearly uniform. In a few nearly circular patches it is larger, however, by more than a factor of two (regions 1, 3). From spatially resolved BEES spectra it follows that the barrier height in region 2 is close to the normal value for this interface (0.66 ± 0.03 eV) (see Fig. 4). In the analysis we assumed a square law for the collector current I_c, according to Ref. [18]. In regions 1 and 3 the barrier is lowered to 0.4 and 0.5 eV, respectively. It is not possible to prove directly that the regions with a lower Schottky barrier really consist of material with a different crystal structure. We consider it to be very likely, however, that the CsCl grains found by cross-section HRTEM do correspond to those regions, since they could never be found in any of the samples exhibiting a uniform barrier.

The regions with a low barrier are large enough in order to analyse the I–V curves obtained on macroscopic diodes by the parallel conduction model [19]. The temperature dependence of the saturation current density I_s (not shown) revealed a lowering of the Schottky barrier height to $\Phi_b = 0.43 \pm 0.03$ eV in 11% of the active diode area, in good agreement with the BEEM experiments.

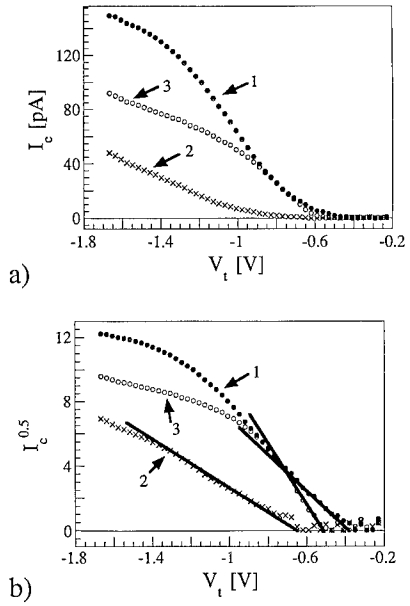

Fig. 4. (a) BEES spectra taken in the regions labeled 1–3 in Fig. 3. (b) Determination of the barrier height from the square root of the BEEM current.

3. Conclusions

In-situ BEEM experiments carried out at 77 K on epitaxial $CoSi_2$/n-Si(1 1 1) films have shown that the Schottky barrier height at this interface remains uniform as long as the $CoSi_2$ crystallizes with the bulk stable fluorite structure. In contrast, lower barriers are found in films containing grains of a metastable phase with the CsCl structure, characterized by random vacancies on the cation sites. The hot electron current across the silicide/Si interface exhibits large spatial variations even when the Schottky barrier is completely uniform. In the case of defect-free, unreconstructed surfaces these variations are entirely due to elastic scattering at dislocation cores and point defects. In favourable cases a spatial resolution below 1 nm has been attained, allowing isolated point defects to be imaged.

Acknowledgements

Financial support by Swiss National Science Foundation is gratefully acknowledged.

References

[1] W.J. Kaiser and L.D. Bell, Phys. Rev. Lett. 60 (1988) 1406.
[2] T. Sajoto, J.J. O'Shea, S. Bhargava, D. Leonard, M.A. Chin and V. Narayanamurti, Phys. Rev. Lett. 74 (1995) 3427.
[3] M.T. Cuberes, A. Bauer, H.J. Wen, M. Prietsch and G. Kaindl, Appl. Phys. Lett. 64 (1994) 2300.
[4] R. Ludeke, A. Bauer and E. Cartier, Appl. Phys. Lett. 66 (1995) 730.
[5] H. Sirringhaus, E.Y. Lee and H. von Känel, Surf. Sci. 331–333 (1995) 1277.
[6] C. Pirri, S. Hong, M.H. Tuilier, P. Wetzel, G. Gewinner and R. Cortès, Phys. Rev. B 53 (1996) 1368.
[7] H. von Känel, E. Müller, S. Goncalves-Conto, C. Schwarz and N. Onda, Appl. Surf. Sci. 00 (1996) 000.
[8] H. von Känel, Mater. Sci. Rep. 8 (1992) 193.
[9] R. Stalder, C. Schwarz, H. Sirringhaus and H. von Känel, Surf. Sci. 271 (1992) 355.

[10] E.Y. Lee, H. Sirringhaus, U. Kafader and H. von Känel, Phys. Rev. B 52 (1995) 1816.
[11] R. Stalder, H. Sirringhaus, N. Onda and H. von Känel, Surf. Sci. 258 (1991) 153.
[12] C.W.T. Bulle-Lieuwma, Appl. Surf. Sci. 68 (1993) 1.
[13] H. Sirringhaus, E.Y. Lee and H. von Känel, Phys. Rev. Lett. 73 (1994) 577.
[14] H. von Känel and G. Fishman, Phys. Rev. B 45 (1992) 3929.
[15] H. Sirringhaus, E.Y. Lee and H. von Känel, Phys. Rev. Lett. 74 (1995) 3999.
[16] S.-L. Zhang, J. Cardenas, F.M. d'Heurle, B.G. Svensson and C.S. Petersson, Appl. Phys. Lett. 66 (1995) 58.
[17] S. Goncalves-Conto, U. Schärer, E. Müller, H. von Känel, L. Miglio and F. Tavazza, unpublished.
[18] L.D. Bell and W.J. Kaiser, Phys. Rev. Lett. 61 (1988) 2368.
[19] I. Ohdomari and K.N. Tu, J. Appl. Phys. 51 (1980) 3735.

ELSEVIER

Journal of Crystal Growth 175/176 (1997) 346–351

JOURNAL OF CRYSTAL GROWTH

In situ STM characterisation of Ga^+ focused ion beam interactions with MBE grown GaAs(1 0 0)

S.J. Brown*, P.D. Rose, E.H. Linfield, D.A. Ritchie, V. Drouot, G.A.C. Jones

Semiconductor Physics Group, Cavendish Laboratory, University of Cambridge, Madingley Road, Cambridge CB3 0HE, UK

Abstract

Using an integrated fabrication facility consisting of molecular beam epitaxial growth chambers, a Ga^+ focused ion beam lithography system and an ultra-high vacuum scanning tunnelling microscope, we have studied, in situ, the interaction of high energy Ga^+ ions with the GaAs(1 0 0) surface. The ion beam dose was such that significant sputtering did not occur, but surface state changes were induced as observed with scanning tunnelling spectroscopy. We spatially identified electron traps induced in the surface state band gap as a result of ion beam irradiation, and also observed variations in their concentration in the ion beam profile. Nanometre scale regions were observed where monolayer sputtering had occurred, with the exposed layer taking on a $c(4\times4)$ surface reconstruction, as opposed to the (2×4) surface reconstruction of the un-irradiated surface.

PACS: 61.72.Vv; 61.16.Ch; 81.15.Hi; 81.05.Ea

Keywords: Ion beam implantation; Scanning tunnelling microscopy; Scanning tunnelling spectroscopy; Electron traps; Focused ion beam; Molecular beam epitaxy; GaAs

Focused ion beams (FIB) have extensive applications in III–V semiconductor device fabrication [1]. Of particular interest is the maskless process in which Ga^+ ions are implanted at high energy in order to damage thin doped GaAs layers [2]. This technique is well established and has been utilised during a molecular beam epitaxial (MBE) growth interruption to produce three-dimensionally patterned devices. For example, high electron mobility transistors have been fabricated where implanted regions of the backgate become highly resistive for areal doses $> 10^{13}$ ions cm^{-2} [3].

When an ion impinges on a surface its energy is dissipated through nuclear and electronic collisions. The results of nuclear collisions are target atom recoil, defect production and broken bonds. To determine the mechanism responsible for rendering a semiconductor insulating, free carrier concentration measurements have previously been performed on irradiated samples [4]. These experiments showed that compensating acceptors were introduced as a result of ion beam irradiation and it has been suggested that these acceptors could be attributed to the formation of Ga antisite defects

* Corresponding author. Fax: + 44 1223 337271; e-mail: sjb1013@cam.ac.uk.

0022-0248/97/$17.00 Copyright © 1997 Elsevier Science B.V. All rights reserved
PII S0022-0248(96)01185-2

(Ga_{As}). The measurements also show that n-type GaAs can be rendered non-conducting with doses less than the initial sheet doping level, suggesting that recoil atoms are involved in the process. Further studies, performed with deep level transient spectroscopy (DLTS) and *C–V* profiling, identified two electron traps induced in the band gap, situated 0.31 eV and 0.52 eV below the conduction band, as a result of Ga^+ FIB irradiation [2, 5].

Previous scanning tunnelling microscopy (STM) studies of ion interactions with a GaAs surface have concentrated on physical damage to the crystal structure [6]. However, the interaction of the impinging ion with the surface will also produce electrical and chemical changes. In this paper, we use STM and scanning tunnelling spectroscopy (STS) to characterise the irradiated surface and the spatial range of the induced damage. FIB irradiation is carried out at a sufficiently low dose that significant surface sputtering does not occur. The observed features are, therefore, more localised and electronic in nature.

The samples described in this paper were grown in a vacuum generator V80H molecular beam epitaxy (MBE) system on commercial, nominally flat, epi-ready GaAs(1 0 0) substrates. The wafers were initially thermally outgassed for 1 h at 450°C in a preparation chamber prior to being further outgassed in the growth chamber under an As overpressure for 20 min at 620°C, as measured with an optical pyrometer. A 1.0 μm layer of Si-doped n^+ GaAs was then grown on the substrate at a growth temperature of 600°C, to give a nominal carrier concentration of 10^{18} cm^{-2}. The wafer was next transferred in situ to the FIB chamber and irradiated with a variably spaced line pattern using 30 keV Ga^+ ions at a nominal line dose of 1×10^8 ions cm^{-1}. The beam was oriented normal to the surface and the full width half maximum spot size was approximately 200 nm. Wafers were finally transferred in situ to the ultra high vacuum scanning tunnelling microscope (UHVSTM). As all in situ transfers were performed under a vacuum of $< 10^{-10}$ mbar, atomic resolution was observed on all wafers, indicating that no significant surface contamination occurred during implantation and transfer. Typical STM tunnelling conditions were a constant current of 0.1 nA with sample biases ranging from + 1 to + 2 V.

STM topographic images of the surface typically exhibit faint image contrast outlining the irradiated lines, for example, Fig. 1a shows the ends of a series of FIB lines. Note that there is insignificant surface sputtering as the island mound morphology, typical of the GaAs(1 0 0) surface, is preserved. Smaller scale images (Fig. 1b) indeed show that there is no significant damage to the terrace and step edge morphology in regions irradiated by the ion beam. Fig. 1b does show that if there is any Ga cluster formation, it occurs along the edge of the ion beam implanted region. A corresponding 'current' image (a measure of the error signal in the STM feedback loop between the measured current and the asking current) also shows contrast (Fig. 1c), indicative of the change in surface states induced by the impinging ions. As the contrast in Fig. 1c is much greater than that in Fig. 1a, it appears that ion implantation changes the surface and/or near surface electronic structure rather than causing significant surface damage.

To investigate further the irradiated surface, current imaging tunnelling spectroscopy (CITS) [7] was performed at sample voltages between − 2 V and + 2 V. For this technique, the feedback loop is disabled at each imaging point during the acquisition of a topographic image. This keeps the tip-sample separation constant, and the current is measured for various applied biases. Spatial images of the electronic structure are therefore obtained for particular energies and the tip can be offset for each applied voltage to ensure an adequate dynamic range in the image.

Fig. 2 shows a series of CITS images for sample biases between + 250 mV and + 2 V, so electrons are tunnelling into empty surface states. Highly localised features are observed within the ion implanted region, however, as mentioned previously, the corresponding topographic image showed no significant disruption of the surface morphology. The most important aspect of these images is that tunnelling occurs within the surface state bandgap when the sample is biased at + 250 mV and + 500 mV (Fig. 2a and Fig. 2b, respectively). This increase in current signal in the exposed region is signified by bright localised features; while

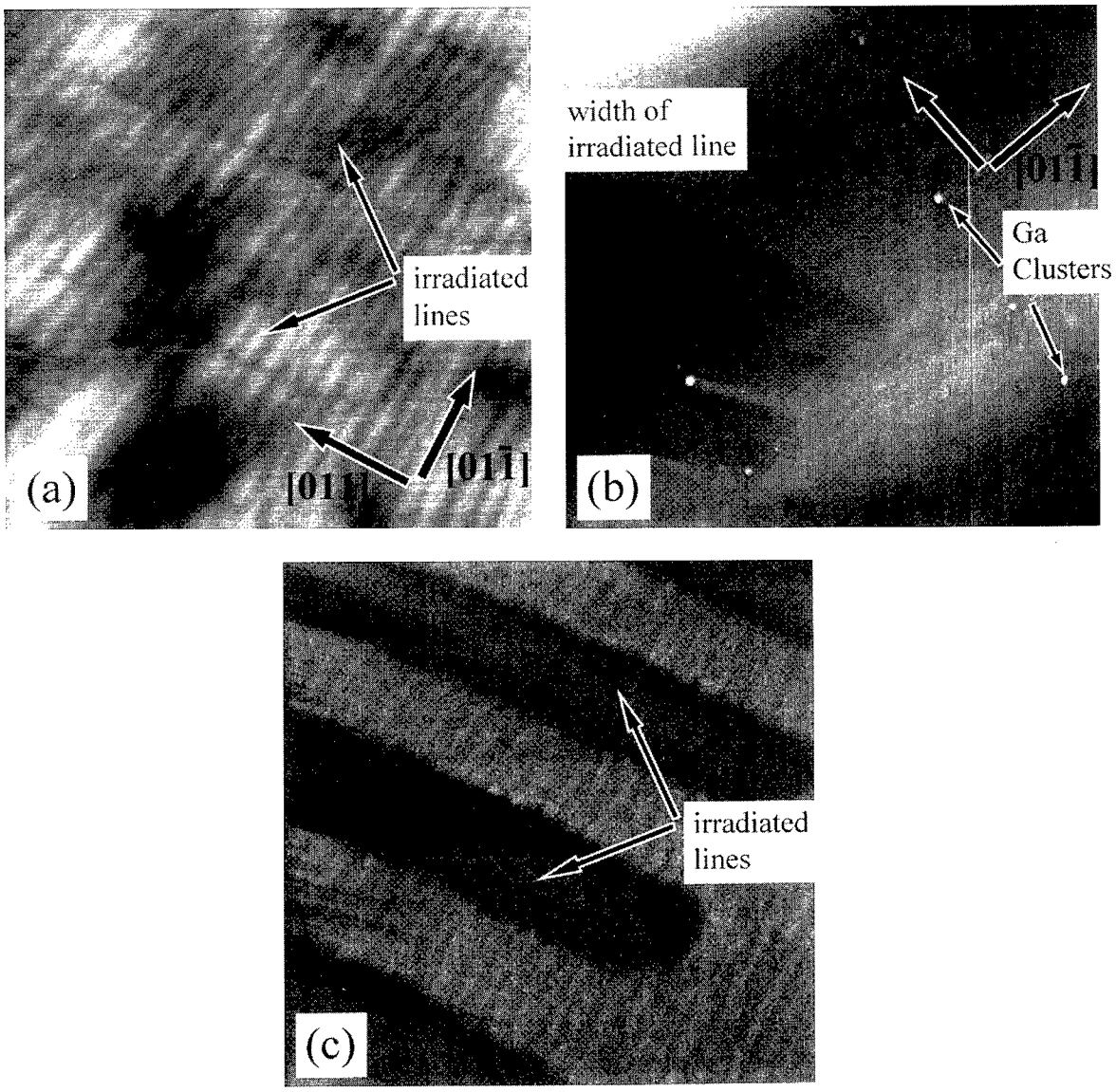

Fig. 1. (a) A 3.5 μm × 3.5 μm topographic image of a series of ion beam lines oriented in the [0 1 1] direction. Typical GaAs (1 0 0) island mound morphology is observed elongated in the [0 1 $\bar{1}$] direction. (b) A 600 nm × 600 nm topographic image showing the preservation of the step and terrace morphology in the irradiated regions. The ion beam has been scanned from top left to bottom right of the image. (c) Corresponding current image for Fig. 1a (refer to text for details).

tunnelling does not occur for these low biases in the un-irradiated region where the only contrast is due to small signal electronic noise. These results immediately suggest that electrically active defects have been induced in the bandgap by ion beam irradiation. The features are bright which is indicative of acceptor states below the conduction band that are being tunnelled into. Hence electron traps are associated with these induced defects. We do not believe the features are due to metallic clusters formed by the Ga^+ ion beam as they do not appear in CITS scans taken below $\sim +200$ mV, and there

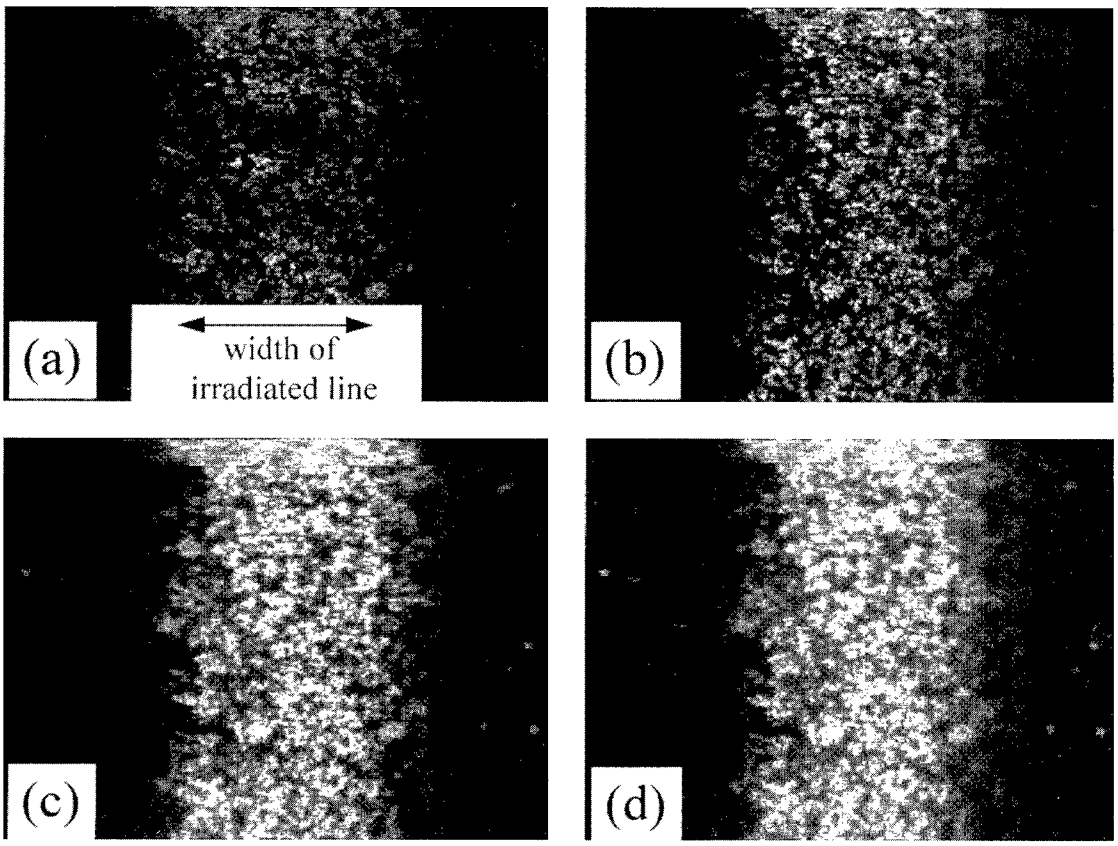

Fig. 2. CITS scans with sample biases of (a) 250 mV, (b) 500 mV, (c) 1500 mV and (d) 2000 mV. Scan area is 700 nm × 500 nm. The irradiated line is vertical in the image. The tip has been retracted from the surface by 5 Å for each I–V measurement.

is a bandgap observed in I–V curves taken above the features, as described below. Note that repeating the CITS scans reproduced exactly the position and concentration of the defect states. CITS images taken with negative sample biases show no significant contrast, suggesting that there are no full states from which tunnelling can occur.

The spread of electrically active defects away from the beam is particularly detrimental for submicron lithographic writing. We have noticed that electrically active defect sites are induced up to 300 nm from either side of the ion beam line. The diameter of the bright features observed in the irradiated regions is ~ 45 Å, which is several (2×4) unit cells in size. The large size of the feature could be due to numerous defect states caused by a single ion impact. It is unlikely to be due to a convolution of the STM tip apex, as several different tips produced the same result. Analysis of the number of features yields a concentration of approximately 2×10^7 cm^{-1}, which is almost an order of magnitude less than the implanted dose of 1×10^8 cm^{-1}. This discrepancy is almost certainly due to ion beam channelling, which is even more significant if we consider that some damage is induced by recoil atoms.

The variation in grey levels associated with the features observed in the CITS images indicates that the STM is observing states that lie at and below the first monolayer of the surface. This impression is reinforced by the fact that the concentration of features increases with applied bias. This confirms our view that contrast observed in the CITS images is not due to disruption of the surface lattice

structure. Rather, we are observing electrically active defects in the top few monolayers of the surface.

Information regarding the beam profile can be obtained from the spatial images of Figs. 1 and 2. The width of the electrically active region observed in Fig. 2 roughly corresponds to the FIB spot size ($\sim$ 200 nm). The ion distribution in the beam is expected to follow a Gaussian function, and a tail off in the concentration of defect sites can be seen on the edges of the profile, although it is difficult to determine its exact form.

Atomic scale images were performed both on and off the ion beam irradiated regions of the surface. For the un-irradiated surface, the reconstruction is (2 × 4) which is expected for GaAs(1 0 0) grown at these temperatures. However, where the surface has been irradiated (Fig. 3) there exists regions of both (2 × 4) and $c(4 \times 4)$ reconstructions. The $c(4 \times 4)$ reconstruction has previously been observed when a (2 × 4) reconstructed surface was slowly cooled to 300°C under As overpressure before the sample was quenched [8]. We are able, though, to quench our samples rapidly enough from growth temperature that the (2 × 4) reconstruction is reliably reproduced. Line profiles performed on Fig. 3 show that the $c(4 \times 4)$ regions lies $\sim$ 1.5 Å below the (2 × 4) reconstruction. This monolayer difference suggests that localised sputtering has occurred, however the sputtering yield is too high for single ion impacts, which is typically up to 10 atoms per ion. The exposed regions could be due to vacancies coalescing on the surface. The creation of the $c(4 \times 4)$ reconstruction is possibly due to localised heating as a result of thermal spikes in the crystal lattice produced by ion collisions, although their lifetime is quite short ($\sim 10^{-11}$ s).

To characterise the traps observed in the CITS scans more closely, differential I–V curves were performed on the electrically active defects observed in the CITS images, using a lock-in amplifier technique [9]. An average of the spectra is shown in Fig. 4, with the un-irradiated surface spectrum included for comparison. As expected the spectrum of the un-irradiated surface (Fig. 4a) shows no conductance within the surface state band gap. The band gap is approximately 1.4 eV and the Fermi level is pinned approximately mid-gap, which is typical for the n^+ GaAs(1 0 0) surface [10]. The

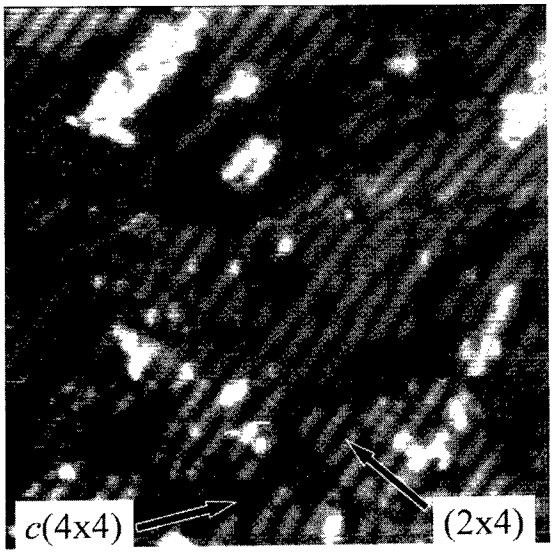

Fig. 3. A 100 nm × 100 nm scan on an irradiated area of the surface containing regions of both the (2 × 4) and $c(4 \times 4)$ surface reconstructions.

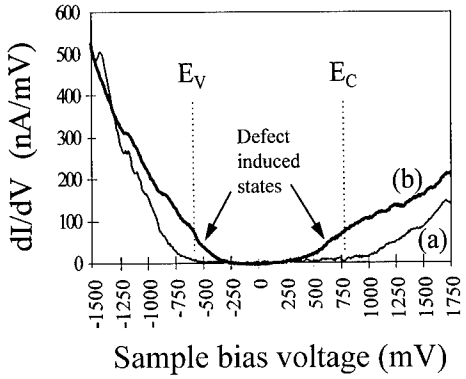

Fig. 4. (a) Conductance spectrum performed on an un-irradiated part of the surface showing the surface state band gap and (b) the conductance spectrum performed on the electrically active defect sites observed in the CITS images of Fig. 2.

tunnelling spectra performed on the irradiated regions of the surface (Fig. 4b) show a broad band of states lying below the conduction band edge. Again, the band gap is approximately 1.4 eV with the Fermi level pinned mid gap. The CITS results for Fig. 2a and Fig. 2b show that electrons are tunnelling into these states, and so are acceptor-like. It also appears in the spectrum that a small

band of donor-like states exists above the valence band. These states do not appear in the CITS scans performed at a negative bias, possibly because they are highly localised and not distributed like the defect induced acceptor states.

In this work, we have successfully used the STM to image ion beam irradiated surfaces. This suggests a new route to three dimensional nanostructure fabrication. Already we have used an MBE growth interruption to allow a buried conducting layer to be patterned to a resolution of 1 μm [11]. This work could be extended by using the STM to perform nanometre scale lithography in combination with implanted ion beam features.

In conclusion, we have characterised the surface electronic and structural changes induced by high energy ion beam irradiation. Surface sputtering does not occur at relatively low doses, however electrically active defects are created, producing electron traps within the surface state band gap. Spatial characteristics of the beam profile show that extended defects are created more than a beam width from the FIB line. Localised sputtering effects were observed as a result of ion beam impacts.

The authors are very grateful to Mark Welland of the University of Cambridge and Ian Wilson of The Chinese University of Hong Kong for valuable discussions. SJB also wishes to acknowledge the Institute of Physics and the British Vacuum Council for financial assistance in attending MBE IX, Malibu, USA, 1996. This work was partly funded by the ESPRC, UK.

References

[1] For a review, see: K. Gamo, Semicond. Sci. Technol. 8 (1993) 1118.
[2] H. Miyake, Y. Yuba, S. Namba and T. Shiokawa, J. Vac. Sci. Technol. B 6 (1988) 1001.
[3] E.H. Linfield, G.A.C. Jones, D.A. Ritchie and J.H. Thompson, Semicond. Sci. Technol. 8 (1993) 415.
[4] K. Nakamura, T. Nozaki, T. Shiokawa, K. Toyoda and S. Namba, J. Vac. Sci. Technol. B 5 (1987) 203.
[5] K. Gamo, H. Miyake, Y. Yuba, S. Namba, H. Kashahara, H. Sawaragi and R. Aihara, J. Vac. Sci. Technol. B 6 (1988) 2124.
[6] X.S. Wang, R.J. Pechman and J.H. Weaver, Appl. Phys. Lett. 65 (1994) 2818.
[7] R.J. Hamers, R.M. Tromp and J.E. Demuth, Phys. Rev. Lett. 56 (1986) 1972.
[8] D.K. Biegelsen, R.D. Bringans, J.E. Northrup and L.-E. Swartz, Phys. Rev. B 41 (1990) 5701.
[9] G. Binnig, K. Frank, H. Fuchs, N. Garcia, B. Reihl, H. Rohrer, F. Salvan and A. Williams, Phys. Rev. Lett. 55 (1985) 991.
[10] M.D. Pashley, K.W. Haberern and R.M. Feenstra, J. Vac. Sci. Technol. B 10 (1992) 1874.
[11] N. Iredale, E.H. Linfield, P.D. Rose, D.A. Ritchie, M. Pepper and G.A.C. Jones, Semicond. Sci. Technol. 12 (1997) 137.

ELSEVIER

Journal of Crystal Growth 175/176 (1997) 352–358

JOURNAL OF CRYSTAL GROWTH

MBE growth of highly reproducible VCSELs

Y.M. Houng*, M.R.T. Tan

Hewlett-Packard Laboratories, 3500 Deer Creek Road, Palo Alto, California 94304, USA

Abstract

Advances in the design of heterojunction devices have placed stringent demands on the epitaxial material technologies required to fabricate these structures. The increased demand for more stringent tolerance and complex device structures have resulted in a situation where acceptable growth yields will be realized only if epitaxial growth is directly monitored and controlled in real time. We report the growth of 980- and 850-nm vertical cavity surface emitting lasers (VCSEL's) by gas-source molecular beam epitaxy (GSMBE), in which the pyrometric interferometry technique is used for in situ monitoring and feedback control of layer thickness to obtain the highly reproducible distributed Bragg reflectors (DBR) for VCSEL structures. This technique uses an optical pyrometer to measure emissivity oscillations of the growing epi-layer surface. The growing layer thickness can then be related to the emissivity oscillation signals. When the layer reaches the desired thickness, the growth of the subsequent layer is initiated. By making layer thickness measurements and control in real-time throughout the entire growth cycle of the structure, the Fabry–Perot resonance at the desired wavelength is reproducibly obtained. The run-to-run variation of the Fabry–Perot wavelength of VCSEL structures is $< \pm 0.4\%$. Using this technique, the group III fluxes can also be calibrated and corrected for flux drifts, thus we are able to control the gain peak of the active region with a run-to-run variation of less than 0.3%. Surface emitting laser diodes were fabricated and operated CW at room temperature. CW threshold currents of 3 and 5 mA are measured at room temperature for 980- and 850-nm lasers, respectively. Output powers higher than 25 mW for 980-nm and 12 mW for 850-nm devices are obtained.

1. Introduction

Vertical-cavity surface-emitting lasers (VCSEL's) are of great interest for applications in optical communication, optical interconnects, and optical signal processing [1–5]. After more than 15 years of development, the VCSEL's have recently entered the early stages of volume production and have become a commercial and manufacturing reality. The VCSEL is a unique class of surface emitting lasers consisting of two distributed Bragg reflectors (DBR) sandwiching an active region. A typical VCSEL structure consists of more than 100 quarter-wave mirror layers and requires a relatively long period of time, 6–10 h, to grow this structure. For the device to perform properly, the thickness

* Corresponding author.

0022-0248/97/$17.00 Copyright © 1997 Elsevier Science B.V. All rights reserved
PII S0022-0248(96)00881-0

and alloy composition of all these layers have to be precisely controlled to less than 1% variation [6], in order to place the Fabry–Pérot resonance at the exact wavelength for lasing. Furthermore, the standing wave peak has to be placed on a very small gain region of ~ 240 Å and the material gain has to match with Fabry-Pérot wavelength. To maintain stable growth rate through such a long period of time, and to reduce the growth rate transients to less than 1% during the repetitive switching of constituents for the mirror stacks make the growth task rather difficult. In this paper, we present a simple in situ monitoring and control technique of using single narrow-band pyrometric interferometric measurements for the growth of highly reproducible 980- and 850-nm VCSEL wafers.

2. Experiment procedure

The epitaxial layers used in the present study were grown in a modified Varian Modular Gen II MBE chamber. Besides the standard high temperature effusion cells for providing group III sources of Al, Ga and In, it is also equipped with a high temperature (~ 975°C) hydride cracker for introducing AsH_3 for providing arsenic source and a low temperature (~ 150°C) gas injector for introducing p-type gaseous dopant source of carbon tetra bromide (CBr_4). The n-type dopant used in this study is Si produced by elemental Si in a high-temperature effusion cell.

The activation energy and the change of surface area of the melt due to depletion of the source material of the group III sources were periodically calibrated. This will ensure the precision pre-setting of the source temperatures for obtaining targeted values of growth rate and alloy composition in the daily growth operation. The information is also useful for adjusting source temperatures to compensate for long term source drifts.

The dual-filament cells fitted with a 125 cc straight-walled crucible and a conical crucible insert are used for Ga and In sources. It provides excellent thickness uniformity, low shutter-activation related flux transients, low defect densities and small source depletion effects. The dual-filament cells fitted with a 60 cc conical crucible is used for Al source. The Al cell is placed in a recessed position, where it is less sensitive to changes in the radiative shielding provided by the shutter, thus minimizing flux transient.

The 980-nm VCSEL's are bottom emitting structures typically consisting of 19.5 pairs of n-type $\lambda/4$ AlAs/GaAs Bragg mirror on the output face and 15 pairs of p-type AlAs/GaAs metal hybrid Bragg mirrors on the high reflectivity side. The one-λ cavity consists of two 60 Å InGaAs quantum wells (QW's) with 100 Å GaAs barriers and 1000 Å thick $Al_{0.3}Ga_{0.7}As$ on each side of the active region. The 850-nm VCSEL's are top emitting structures with 32.5 pairs of $\lambda/4$ n-AlAs/$Al_{0.2}Ga_{0.8}As$ Bragg mirrors on the high reflectivity side and 22 pairs of p-AlAs/$Al_{0.2}Ga_{0.8}As$ Bragg mirrors on the output face. The one-λ cavity consists of three 80 Å GaAs quantum wells with 100 Å $Al_{0.3}Ga_{0.7}As$ barriers and 840 Å thick of $Al_{0.5}Ga_{0.5}As$ on each side of the active region. The interface between GaAs and AlAs for 980-nm DBR or AlGaAs and AlAs for 850-nm DBR is digitally graded in 8 steps using a chirped short period superlattice. The GaAs/AlAs and AlGaAs/AlAs DBR stacks are uniformly doped to 1×10^{18} cm^{-3} except at the graded interface which is doped to 5×10^{18} cm^{-3}. A contact layer of p-type GaAs doped to 2×10^{19} cm^{-3} is added to provide non-alloyed ohmic contact for both 980- and 850-nm structures. The growths were performed at 520°C for 980-nm VCSEL's and 630°C for 850-nm VCSEL's, measured by an IR pyrometer, with a growth rate of 0.86 μm/h for AlAs, 1.25 μm/h for $Al_{0.2}Ga_{0.8}As$ and 1 μm/h for GaAs. The VCSEL structures were grown on an indium-free mounted 2″ diameter (1 0 0) n^+ GaAs substrate with a typical rotation rate of 25 rpm.

We use the interferometric technique for in situ monitoring and feedback control of layer thickness to obtain highly reproducible VCSEL structures. This technique uses an optical pyrometer to measure the periodic modulation in emitted light intensity of the growing epi-layer surface. This periodic modulation is due to changes in interference between light reflected from the top and bottom of the epilayer as the epilayer thickness changes. The

growing layer thickness can then be related to oscillation signal based on the model [7, 8]:

$$E_j = P_0 + \sum_i \left[P_i \left(1 - \left| \frac{r_j + r_{j+1} \exp(-i4\pi n_j d_j/\lambda_i)}{1 + r_j \cdot r_{j+1} \exp(-i4\pi n_j d_j/\lambda_i)} \right|^2 \right) \right], \quad (1)$$

where n_j is a complex refractive index constant; λ_i, the individual wavelength within the pass-band of the pyrometer; r_j, the reflection coefficient at the interface between the vacuum and the growing layer and r_{j+1} is the effective Fresnel coefficient of the underlying structure. P_i is a constant related to the substrate temperature and the signal conversion factor of the instrument at wavelength λ_i. P_0 is a constant related to a DC signal drift due to the apparent surface temperature variation caused by the background stray light such as opening and closing of high temperature effusion cells.

By monitoring the end-point intensity and phase of the signal one can only determine the optical thickness of the growing layer, but not the alloy composition. For monitoring and controlling the alloy composition we incorporated the amplitude monitoring [8] into the thickness monitoring technique, the precision control of both thickness and the alloy composition of AlGaAs layers can then be achieved.

The VCSEL structure data along with the growth conditions were then used to calculate the emissivity signal using Eq. (1) in the wavelength range of 0.92–0.96 μm. The simulated signals were then used as reference data during the actual growth run for in situ thickness monitoring and feedback control.

An IRCON Modline Plus V-series infrared pyrometer was used to monitor emitted radiation in a narrow range of wavelengths (0.92–0.96 μm) from the heated surface of the substrates through a heated viewport assembly [9]. The signal is then fed into a HP 382 computer for data acquisition and analysis in real-time. These measurements were performed with continuous substrate rotation and without any growth interruption. The pyrometer signal monitored during the growth of each layer was compared, in real-time, with the theoretical simulation data. Through a real-time computation algorithm, any deviation of the growth rate in the actual growth was then compensated by adjusting the closing time of the related group III source shutter, and the deviation of the alloy composition was compensated by adjusting the related source temperature, so the target layer thickness and alloy composition can be achieved.

The reflectivity measurements of the VCSEL wafers were made with a computer controlled spectrometer (SPEX 220M) and dual beam lock-in detection. The white light source is a tungsten lamp and the spectrometer selects the light from 600 to 1100 nm at 2 nm increments. The signal is normalized to a gold reference.

3. Results and discussions

As the activation energy and the rate of change of source melt are well calibrated, we are able to pre-set the cell temperatures, based on the previous day's data, to obtain desired growth rate and alloy composition accurately for daily operation as shown in Fig. 1. The data shown is the values for both GaAs growth rate and AlGaAs alloy composition obtained daily using the pyrometric interferometry technique in a span of 6 months between source recharges. The daily target value for GaAs is 1 μm/h, and the average values for 6 months is 1.0025 μm/h with a variation of $\pm$ 0.012 μm/h. The average daily increase in setpoint temperature to maintain 1 μm/h growth rate is $\sim$ 0.2°C/d. The target value for AlGaAs composition is 0.30 and the average value obtained is 0.294 $\pm$ 0.012. The average daily increase in Al setpoint temperature to maintain $x = 0.30$ is $\sim$ 0.5°C/d.

Although before each VCSEL growth run, a growth rate calibration [10, 11] was done to obtain the desired growth rates for both GaAs and AlAs, the reflectivity measurements of the 980-nm VCSEL wafers grown without the feedback control show that the center of the reflectivity stop band varied from run to run, variations as much as 50 nm have been observed, presumably due to flux instability during the growth. By making layer thickness measurements and control in real-time throughout the entire growth cycle of the structure, the Fabry–Pérot resonance at the desired

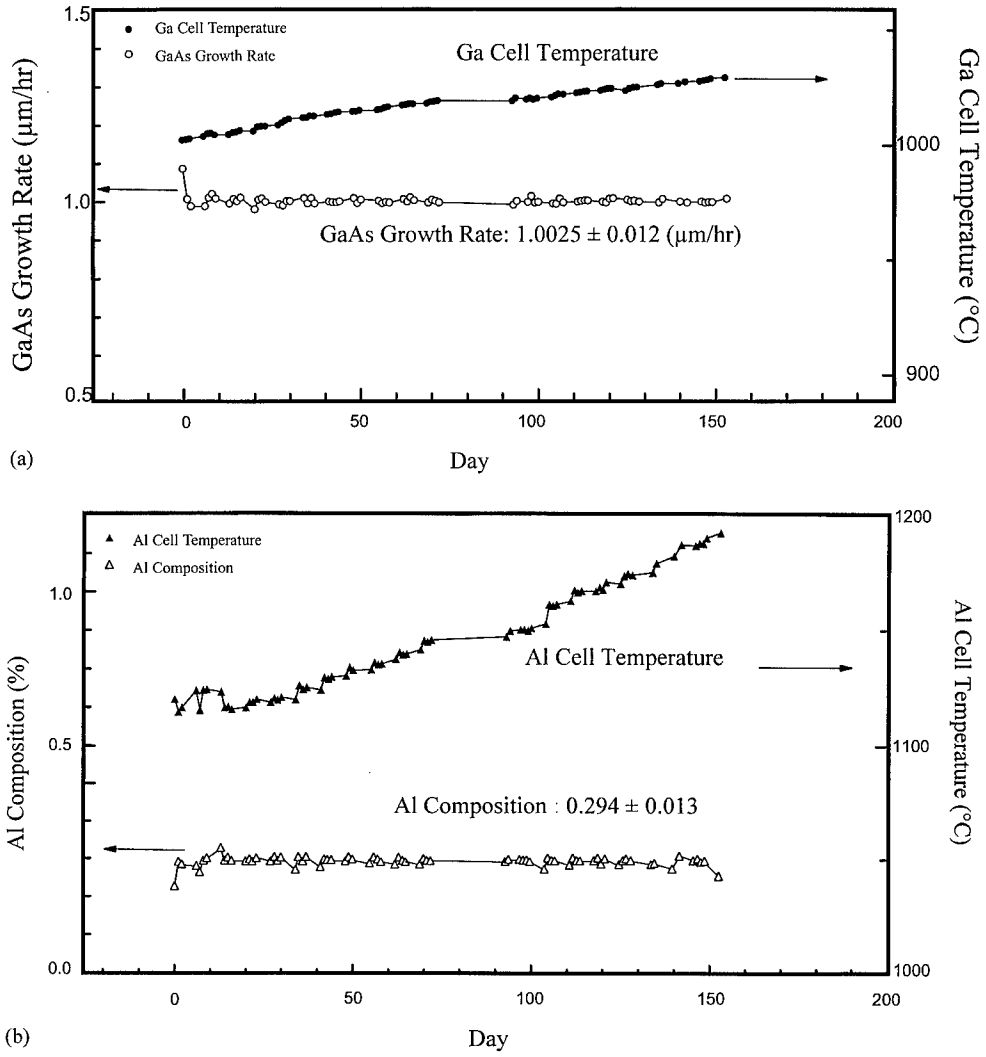

Fig. 1. (a) The daily pre-set temperature of Ga cell and the growth rate of GaAs grown and (b) the daily pre-set temperature of Al cell and the alloy composition of AlGaAs grown.

wavelength is reproducibly obtained. The reflectivity measurements (Fig. 2a) show for ten 980-nm VCSEL wafers grown in a span of more than 6 months with an identical structure, 15 pairs of p-type DBR and 21.5 pairs of n-type DBR stacks, have an average Fabry–Pérot resonance wavelength of 982 nm and a variation of $\pm$ 0.22%. Even with different number pairs of DBR and active region, the 980-nm VCSEL wafers have an average Fabry–Pérot resonance wavelength centered at 981 nm with a run-to-run reproducibility of $\pm$ 0.37% (Fig. 2b) and 850-nm VCSEL wafers have an average Fabry–Pérot resonance frequency centered at 851 nm with a run-to-run reproducibility of $\pm$ 0.38% (Fig. 3).

The gain peak is mainly determined by the alloy composition and thickness of the QW's. The thickness of the QW's are so thin that the growth time is

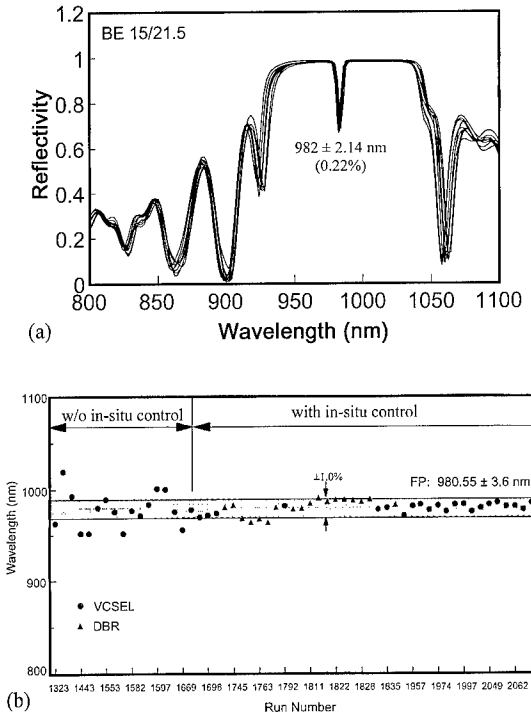

Fig. 2. (a) Reflectivity spectra of ten 980-nm bottom-emitting VCSEL wafers with 15 pairs of p-type DBR and 21.5 pairs of n-type DBR stacks grown using in situ feedback control and (b) the Fabry–Pérot resonance wavelength of 980-nm VCSEL wafers and the center wavelength of the reflectivity stop-band for DBR grown with and without in situ feedback control.

too short to be monitored and controlled using the current technique. However, with the in situ monitoring and control technique, the growth rates are well-calibrated during the growth of n-type DBR prior to the growth of QW's. Therefore, we are able to accurately control the QW structures and thus the gain peaks to less than $\pm$ 0.5% variations of 974.5 $\pm$ 2.4 nm (Fig. 4) and 848.3 $\pm$ 3.2 nm (Fig. 3) for 980-nm and 850-nm VCSEL wafers, respectively.

The gain media material qualities, InGaAs/GaAs QW's for 980-nm and GaAs/AlGaAs QW's for 850-nm VCSEL's, were evaluated with the threshold current density of the broad area edge emitting lasers fabricated from the VCSEL wafers. In a conventional VCSEL structure, undoped epilayers are used in the active region containing QW's. The typical threshold current density of our undoped InGaAs/GaAs QW's is ≤ 100 A/cm^2/QW, and as low as 46 A/cm^2/QW has been obtained. These values are comparable to the best reported value for the 980-nm lasers [12]. For 850-nm lasers with Al-containing QW's, however, the undoped active region yields relatively high threshold current, typically ≥ 300 A/cm^2/QW. We have found that by incorporating a controlled amount of carbon, $\sim 3 \times 10^{17}$ cm^{-3}, as a p-type dopant in the active region the threshold current density was drastically reduced to ~ 140 A/cm^2/QW [13].

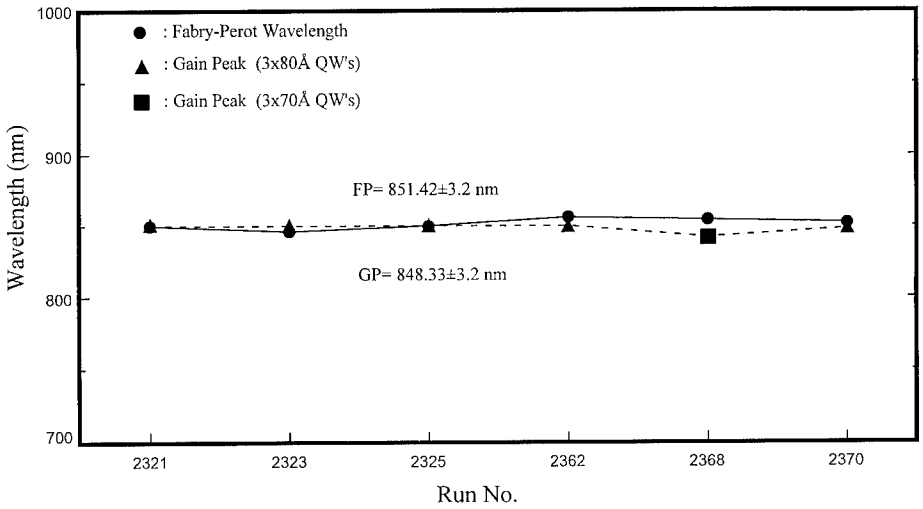

Fig. 3. The Fabry–Pérot resonance wavelength and gain peak of 850-nm VCSEL wafers grown with in situ feedback control.

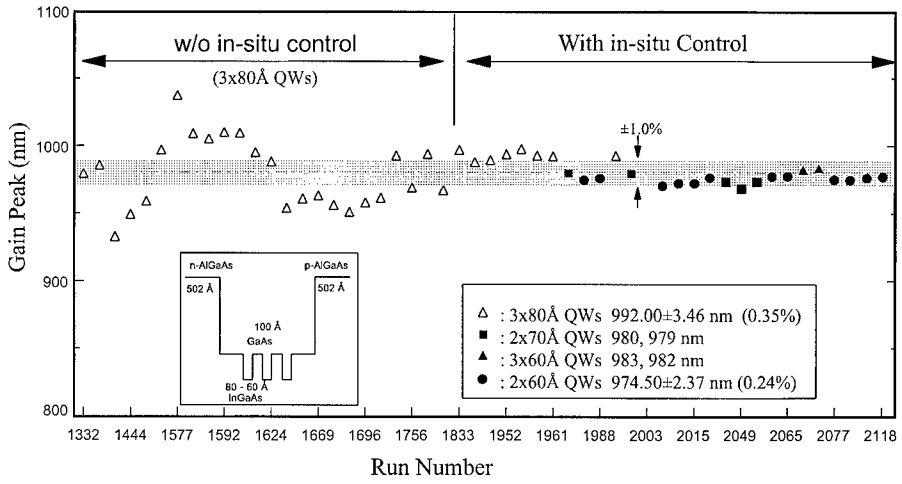

Fig. 4. The gain peak of 980-nm VCSEL wafers grown with and without in situ feedback control.

The VCSEL diodes were fabricated using a four level mask and proton isolation. After fabrication, the devices were mounted on a Cu heat sink. For 980-nm VCSEL, the CW threshold current of 3.0 mA was measured at room temperature for a 24 μm diameter laser. The turn-on voltage as low as 1.39 V was measured which is only 0.27 V above the InGaAs bandgap. The series resistance of the device is 20 Ω. Output powers higher than 25 mW are obtained from 24 μm diameter lasers. These devices had an external quantum efficiency higher than 26%. The 15-μm diameter 850 VCSEL's have a low threshold current of around 5 mA at a threshold voltage of 1.7 V and a series resistance of ~ 35 Ω. Output powers higher than 12 mw with an external differential efficiency higher than 32% are obtained.

Since our thickness monitoring and control technique is carried out on a continuously rotating wafer, the uniformity of the VCSEL structure is excellent. As shown in Fig. 5, the variation of the Fabry–Pérot wavelength across a 2-inch wafer is only ± 2 nm. Note that, this 0.2% uniformity variation is due to the variations of both thickness and composition across the 2″ wafer of those more than 1000 epilayers which constitute the VCSEL structure. Fig. 6a and Fig. 6b show the histograms of threshold-voltage and threshold-current distributions for a 980-nm VCSEL fabricated on a 2-in wafer. The average threshold voltage is 1.482 V with a standard deviation of 0.034 V, and the average threshold current is 3.99 mA with a standard deviation of 0.51 mA.

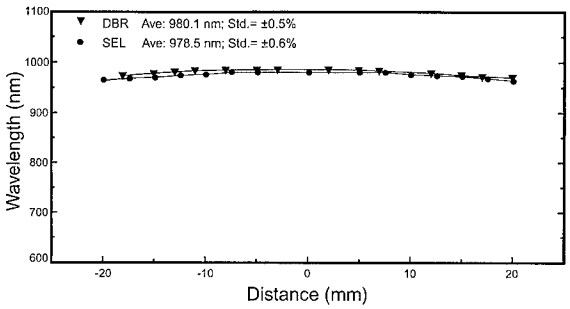

Fig. 5. Uniformity of the Fabry–Pérot resonance wavelength for a 2″ 980-nm VCSEL wafer.

4. Conclusions

In summary, we have demonstrated that using the pyrometric interferometry technique for in situ thickness monitoring and feedback control, of highly reproducible VCSEL structures can be grown by GSMBE. The reproducibility of the VCSEL structures with a variation of the

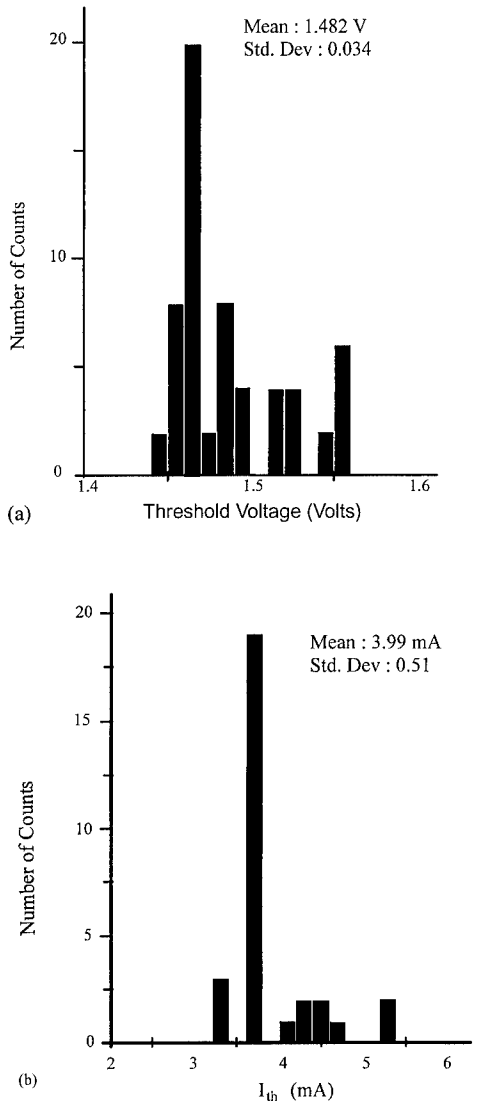

Fig. 6. (a) The histogram of the threshold voltages and (b) the currents of 29 devices tested across a 2″ 980-nm VCSEL wafer.

Fabry–Pérot wavelength of $\pm 0.4\%$ have been grown using this technique. Using this technique, the group III fluxes can also be calibrated and corrected for flux drifts, thus we are able to control the gain peak of the active region with a run-to-run variation of less than 0.3%. Surface emitting laser diodes were fabricated and operated CW at room temperature. CW threshold currents of 3 and 5 mA are measured at room temperature for 980- and 850-nm lasers, respectively. Output powers higher than 25 mW for 980-nm and 12 mW for 850-nm devices are obtained.

Acknowledgements

The authors would like to thank L. Martinez and M. Kanemura for their excellent technical support. We would also like to express our sincere thanks to G. Baldwin, R. Moon, W. Ishak, J.N. Miller, S.Y. Wang and K. Carey for their support and encouragement throughout this work.

References

[1] Y.H. Lee, B. Tell, K. Brown-Goebeler, J.L. Jewell and J.V. van Hove, Electron. Lett. 26 (1990) 710.
[2] C.J. Chang-Hasnain, J.R. Wullert, J.P. Harbison, L.T. Florez, N.G. Stoffel and M.W. Maeda, Appl. Phys. Lett. 58 (1991) 31.
[3] H.-J. Yoo, A. Scherer, J.P. Harbison, L.T. Florez, E.G. Paek, B.P. van der Gaag, J.T. Hayers, A. Von Lehmen, E. Kapon and Y.-S. Kwon, Appl. Phys. Lett. 56 (1990) 1198.
[4] B. Pezeshki, D. Thomas and J.S. Harris, Jr., Appl. Phys. Lett. 57 (1990) 1491.
[5] K.W. Hahn and D.W. Dolfi, SPIE Optoelectron. Interconnects and Packaging, Vol. CR62 (1996) pp. 393–404.
[6] J.L. Jewell, J.P. Harbison, A. Scherer, Y.H. Lee and L.T. Florez, IEEE J. Quantum Electron. 27 (1991) 1332.
[7] Y.M. Houng, M.R.T. Tan, B.W. Liang, S.Y. Wang, L. Yang and D.E. Mars, J. Crystal Growth 136 (1994) 216.
[8] Y.M. Houng, M.R.T. Tan, B.W. Liang, S.Y. Wang and D.E. Mars, J. Vac. Sci. Technol. B 12 (1990) 1221.
[9] D.E. Mars and J.N. Miller, J. Vac. Sci. Technol. B 7 (1989) 682.
[10] A.J. SpringThorpe and A. Majeed, J. Vac. Sci. Technol. B 8 (1990) 266.
[11] D.E. Mars, L. Yang, M.R.T. Tan and S.J. Rosner, J. Vac. Sci. Technol. B 11 (1993) 965.
[12] R.L. Williams, M. Dion, F. Chatenoud and K. Dzurko, Appl. Phys. Lett. 58 (1991) 1816.
[13] Y.M. Houng, M.R.T. Tan and S. W. Corzine, to be published.

ELSEVIER

Journal of Crystal Growth 175/176 (1997) 359–364

JOURNAL OF CRYSTAL GROWTH

Fabrication of InGaAs vertical-cavity surface-emitting lasers by molecular beam epitaxy on (4 1 1)A GaAs substrates and its room-temperature operation

Yoshihiko Hanamaki[a,*], Tetsuya Takeuchi[b], Nagaatsu Ogasawara[c], Yasuhiro Shiraki[a]

[a] *Research Center for Advanced Science and Technology (RCAST), The University of Tokyo, 4-6-1 Komaba, Meguro-ku, Tokyo 153, Japan*
[b] *Hewlett-Packard Labs. Japan, 3-2-2 Sakado, Takatsu-ku, Kawasaki-shi, Kanagawa 213, Japan*
[c] *Department of Electronics Engineering, University of Electro-Communications, 1-5-1 Chofugaoka, Chofu-shi, Tokyo 182, Japan*

Abstract

We investigated the optimum growth conditions for fabrication of a high-reflective distributed Bragg reflector (DBR) with extremely flat heterointerfaces on (4 1 1)A GaAs substrates by molecular beam epitaxy (MBE). A high-reflective DBR consisting of AlAs/GaAs was successfully fabricated under the investigated optimum conditions of 580°C with V/III (As_4/Ga) ratio of ~ 8. Using this high-reflective DBR, we succeeded for the first time in the optically pumped pulse operation of InGaAs vertical-cavity surface-emitting lasers (VCSELs) at room temperature on (4 1 1)A GaAs substrates with improved threshold characteristics compared to conventional (1 0 0) GaAs substrates.

PACS: 42.55.Px; 42.55.Sa

Keywords: MBE; (4 1 1)A GaAs substrates; VCSEL; Pulsed operation; Room-temperature operation

1. Introduction

Fabrication of atomically flat heterointerfaces is essential to achieve high performance of quantum devices such as resonant tunnel devices, optical modulators, surface-emitting lasers (VCSELs) and so on. Recently, molecular beam epitaxial (MBE) growth on (4 1 1)A GaAs substrates has been clarified to provide extremely flat interfaces in AlGaAs/GaAs quantum wells (QWs) [1, 2]. That is, $Al_{0.3}Ga_{0.7}As$/GaAs QWs grown on the (4 1 1)A GaAs substrates show very narrow photoluminescence (PL) lines at 4.2 K [1] and have extremely high uniformity of well thickness over a macroscopic region [2]. Such a flat interface is suitable for fabrication of a highly-reflective distributed Bragg reflector (DBR) used as the resonator mirror of VCSELs [3–5]. Moreover, the VCSELs on non-(1 0 0) surfaces are now attracting much attention both from the view points of device applications

* Corresponding author.

0022-0248/97/$17.00 Copyright © 1997 Elsevier Science B.V. All rights reserved
PII S0022-0248(96)00944-X

and scientific interests, since it can be expected not only to reduce the threshold of lasing action but also make it possible to control the polarization.

In this paper, we report on successful MBE growth of AlGaAs/GaAs QWs with extremely flat heterointerfaces for fabrication of VCSELs on (4 1 1)A GaAs substrates. We also report, for the first time, on room-temperature, pulsed operation of VCSELs on (4 1 1)A GaAs substrates fabricated under the investigated optimum growth conditions, whose threshold characteristics are better than on conventional GaAs(1 0 0) substrates.

Because the reflectivity of the DBR consisting of AlAs/GaAs multilayers is dominated by the flatness of heterointerfaces between GaAs and AlAs as well as their uniformity, as the first step of fabrication of VCSELs on (4 1 1)A GaAs substrates, the optimum growth condition, especially the growth temperature and V/III (As_4/Ga) ratio to achieve extremely flat heterointerfaces, was investigated using photoluminescence (PL) measurements of $Al_{0.3}Ga_{0.7}As$/GaAs quantum wells (QWs) grown on (4 1 1)A GaAs substrates.

The VCSEL used in our experiments was designed to emit approximately 980 nm light at room temperature. The 980 nm VCSEL is attracting wide attention for the possibility of realizing visible lasers in the 450–550 nm wavelength range in combination with second-harmonic generation (SHG) devices [6, 7]. The InGaAs/GaAs strained QWs were, therefore, chosen as the active region for our VCSEL. It is also expected for InGaAs/GaAs QWs that the threshold of lasing action can be reduced due to the strain effect.

2. Experimental procedure

Samples for PL measurements were prepared as follows. After the (4 1 1)A GaAs substrate was etched by the conventional method on the (1 0 0) GaAs substrates, the substrate was introduced into a growth chamber of a VG Semicon 80H MBE system. After the growth of a buffer layer consisting of a 3000 Å GaAs and GaAs(200 Å)/$Al_{0.3}Ga_{0.7}As$(200 Å) superlattice with 10 periods, AlGaAs/GaAs QWs with various well widths (30,40,55,75 and 100 Å) separated by 500 Å-thick layers were grown. The AlAs/GaAs superlattice was grown to examine the growth rate of GaAs and the composition of aluminum in AlGaAs by X-ray analysis. Growth temperature was varied from 520°C to 670°C and V/III ratio was changed between 2 and 10. Typical growth rates of GaAs and AlAs were 0.7 and 0.3 μm/h, respectively. PL measurements were performed at 7 K using an Ar^+ laser (488 nm) as an excitation source with excitation power of 2 mW.

The detailed VCSEL structure grown on the (4 1 1)A undoped GaAs substrate is shown in Fig. 1. It consists of three 65 Å $In_{0.2}Ga_{0.8}As$ quantum wells with 1343 Å GaAs barrier layers as active regions sandwiched by two AlAs/GaAs DBR (2λ-cavity). The layer thicknesses in the AlAs/GaAs DBR were designed to be one-quarter wavelength of the room-temperature exciton peak (980 nm) of the cavity, and they were nominally undoped. InGaAs single QWs on (4 1 1)A GaAs substrates with different well widths (20–100 Å) were grown in advance by fixing the indium composition at 20% at the growth temperature of 520°C. It was confirmed that the photoluminescence peak from the InGaAs QW with well width of 65 Å on (4 1 1)A GaAs substrates was around 980 nm at room temperature, and its peak intensity and full-width at half-maximum (FWHM) are improved in comparison

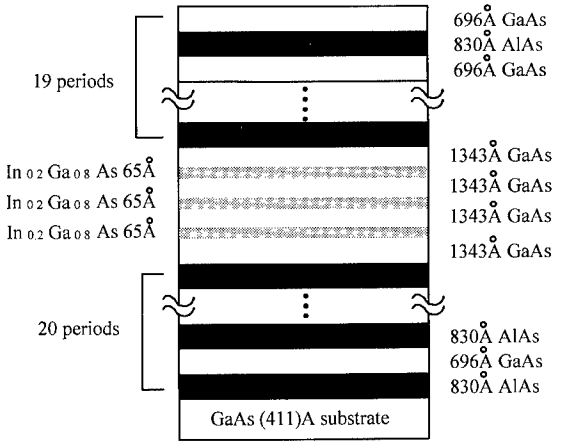

Fig. 1. Layer structure used for vertical-cavity surface-emitting laser (VCSEL) grown on (4 1 1)A GaAs substrate.

to QWs having the same structure on conventional (1 0 0) substrates, as shown in Fig. 2a.

After a 3000 Å buffer layer of GaAs was grown, a 20-period bottom DBR of alternating layers of AlAs (830 Å) and GaAs (696 Å) was grown under the optimum growth conditions for $Al_{0.3}Ga_{0.7}As$/GaAs QWs on (4 1 1)A GaAs substrates, that is, the growth temperature was 580°C and V/III ratio was ~ 8. Following the bottom DBR, the 2λ-cavity consisting of a series of three 65 Å $In_{0.2}Ga_{0.8}As$ active regions separated by 1343 Å GaAs barrier layers was grown. During 2λ-cavity fabrication, the growth temperature was kept at 520°C to prevent indium desorption and/or segregation. Finally, a 19-period top DBR identical to the bottom mirror was grown. The layer thicknesses were calibrated by X-ray diffraction on reference samples prior to growth.

The characterization of VCSEL was performed in the 800–1200 nm range by conventional reflection spectrum measurement and optical pumping at room temperature. Optical pumping of the VCSEL was carried out using a Styril 9M pulse dye laser as the excitation source pumped by a cavity-dumped mode-locked YLF laser at the repetition rate of 75.4 MHz. The sample was excited through the DBR with 5 ps laser pulses at 860 nm. The excitation pulse laser was focused on a spot with a diameter of about 20 μm and the average excitation power was varied from 10 to 100 mW (= excitation power density from 8.4 to 84 MW/cm^2) using ND filters. The luminescence was spectrally dispersed in a spectrometer and either detected in a time-resolved or integration mode at 955 nm.

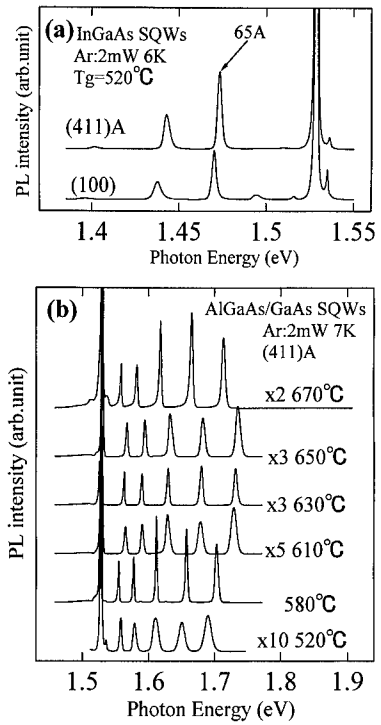

Fig. 2. Photoluminescence spectra from (a) $In_{0.2}Ga_{0.8}As$/GaAs QWs with L_w = 90,65,45,30 and 20 Å grown at 520°C on (4 1 1)A GaAs substrates. The V/III ratio was ~ 8. (b) $Al_{0.3}Ga_{0.7}As$/GaAs/ QWs with L_w = 100,75,55,40 and 30 Å grown at a temperature between 520°C and 670°C on (4 1 1)A GaAs substrates. The V/III ratio was ~ 8.

3. Results and discussion

Fig. 2b shows photoluminescence spectra from the $Al_{0.3}Ga_{0.7}As$/GaAs QWs with various well widths grown at various temperatures with V/III ratio of ~ 8. There was no significant difference in the luminescence intensity and the FWHMs of the luminescence peaks, when the V/III ratio was changed from 2 to 10 at the same growth temperature.

In Fig. 2b, six peaks corresponding to the QWs with different well widths and GaAs substrate are clearly observed. The most prominent feature is the very small line width of each luminescence peak of QWs grown at the temperature of 580°C. The line width of the luminescence peaks from QWs on (4 1 1)A GaAs substrates were smaller than that from QWs on (1 0 0) GaAs substrates which were simultaneously grown on the same Mo block, as shown in Table 1. Moreover, the reported FWHMs of PL lines from $Al_{0.3}Ga_{0.7}As$/GaAs QWs on (4 1 1)A substrates grown under almost the same growth condition as ours [1] are nearly equal to our results, or are wider in the case of 30 Å-wide QWs. It is also noteworthy that the integrated luminescence intensities of the QWs grown at the temperature of 580°C are the highest as seen in Fig. 2 and that they recover again above

Table 1
The FWHM values (meV) of each QW grown on (4 1 1)A and (1 0 0) substrates at 580°C

	FWHM (meV)					
	30 Å	40 Å	55 Å	75 Å	100 Å	GaAs sub.
(4 1 1)A	5.48	3.76	2.47	2.28	2.14	1.40
(1 0 0)	5.99	4.41	2.89	2.82	1.32	1.94

670°C. The luminescence intensity from $Al_{0.3}Ga_{0.7}As$/GaAs QWs on (4 1 1)A substrates was also found to be about 20% stronger than that of simultaneously grown QWs on (1 0 0) GaAs substrates. These results imply that effectively atomically flat heterointerfaces are realized in $Al_{0.3}Ga_{0.7}As$/GaAs QWs grown on (4 1 1)A GaAs substrates, especially at the growth temperature of 580°C with V/III ratio of ~ 8. The luminescence peaks from the QWs grown at temperatures of 520°C and 670°C shown in Fig. 2 are at slightly lower energies than those of QWs grown at other growth temperatures. This is probably due to the very small difference in growth rate and/or aluminum composition among these five samples.

The reflectivity spectrum of InGaAs VCSEL on (4 1 1)A GaAs substrate grown under the optimized condition described above is shown in Fig. 3. It is seen in this figure that a broad stop band with a bandwidth exceeding 90 nm is formed and that the peak reflectivity is nearly equal to the calculated maximum reflectivity of the mirrors (99.8%) [8]. The reflectivity of DBR on (4 1 1)A GaAs substrates is almost equal to or better than that on DBR on (1 0 0) GaAs substrates fabricated under the same growth conditions, as shown in the inset of Fig. 3. The resonance wavelength of VCSEL is 955 nm, which appears as the very small dip at the center of the high-reflective band in Fig. 3. The observed resonance mode wavelength (955 nm) is slightly different from the designed one (980 nm), which may be due to the small change in growth rate during MBE growth.

Fig. 4 shows the output spectra of the VCSEL on (4 1 1)A GaAs substrates under the different average excitation powers of the pulse dye laser. As shown in Fig. 4, the peak intensity increased drastically and the FWHMs decreased with increasing excitation power, indicating that the VCSEL on (4 1 1)A substrates has achieved the lasing action. This is the first report, to our best knowledge, on lasing of VCSELs on (4 1 1)A GaAs substrates. The

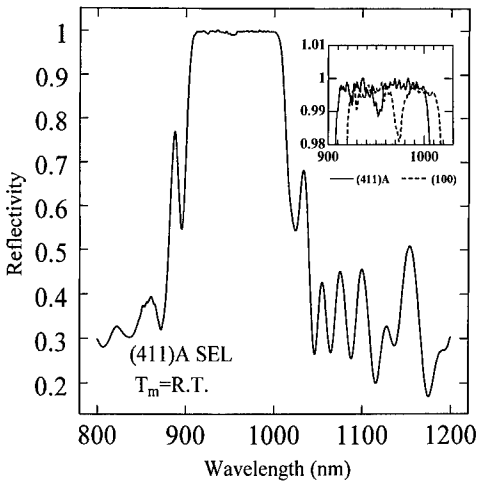

Fig. 3. The reflectivity spectrum of VCSEL grown on (4 1 1)A GaAs substrate.

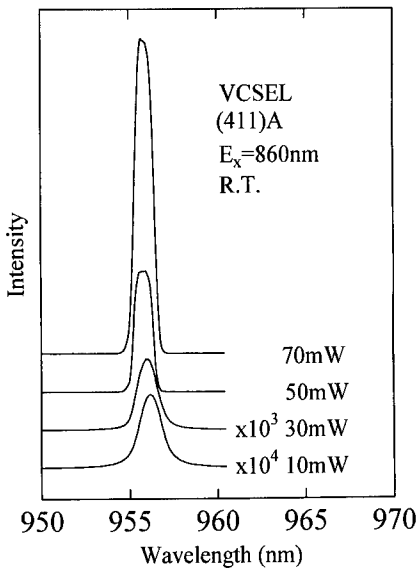

Fig. 4. The output spectra of the VCSEL on (4 1 1)A GaAs substrates under the different excitation powers of pulse dye laser.

peak wavelength of the lasing spectrum was around 955 nm. This wavelength corresponds to the resonance mode of cavity. The lasing action occurred in a shorter wave region than the luminescence peak. (956 nm) This blue shift may come from the change of the refractive indexes of GaAs and AlAs and/or the compensation of Piezo-electric field existing around the InGaAs/GaAs strained QW, due to high density of electrons and holes generated by optical pumping.

To evidence more clearly the lasing action of VCSEL on (4 1 1)A GaAs substrates, input–output characteristics were measured at the lasing wavelength. Fig. 5 shows the number of photons from VCSEL as a function of the average input power in a logarithmic scale. It is seen that the dependence has a clear step at certain excitation powers. This clear jump in the photon number definitely indicates lasing action [9, 10]. It is, therefore, seen that the threshold is 40 mW (34 MW/cm^2) and 60 mW (51 MW/cm^2) for VCSEL on (4 1 1)A and (1 0 0) substrates, respectively. It is remarkable that the threshold of lasing action is reduced by using (4 1 1)A substrates. In addition, the number of photons of VCSEL on (4 1 1)A substrate is larger in the spontaneous emission region but smaller in the stimulated emission region than that of VCSEL on (1 0 0) substrate. These experimental results may reflect the higher reflectivity of AlAs/GaAs DBR and the improved optical gain and optical confinement in InGaAs/GaAs active regions of VCSELs on (4 1 1)A substrates.

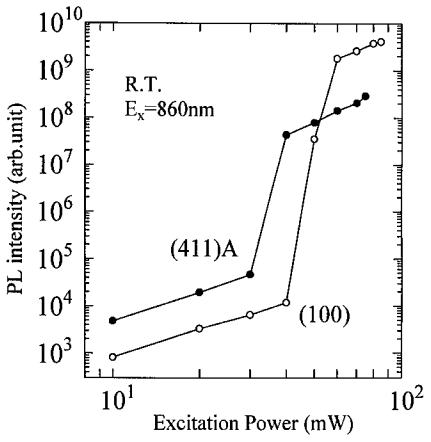

Fig. 5. Input–output characteristics of VCSEL on GaAs(4 1 1)A substrates and (1 0 0) substrates.

4. Conclusion

In conclusion, MBE growth of $Al_{0.3}Ga_{0.7}As$/GaAs QWs was successfully performed on (4 1 1)A GaAs substrates to achieve extremely flat heterointerfaces for fabrication of VCSELs. The optimum growth temperature clarified here was 580°C, and the influence of the V/III ratio was nominal. The $In_{0.2}Ga_{0.8}As$ VCSEL was fabricated on (411)A GaAs substrates for the first time under the above-mentioned growth conditions. Lasing action of the VCSEL structure was confirmed at room temperature by pulse optical pumping. Threshold excitation power density of lasing action was found to be about 40 mW (34 MW/cm^2) with an improved threshold characteristics compared to conventional GaAs(1 0 0) substrates. These results indicate that extremely flat heterointerfaces of AlAs/GaAs and InGaAs/GaAs are realized and that they can be used as a prominent DBR and active region of VCSELs.

Acknowledgements

The authors are thankful to R. Ito, H. Akiyama and Y. Watanuki for their encouragement and cooperation. They are also grateful to S. Ohtake for his technical support. This work was supported in part by a Grant-in-Aid for Scientific Research on Priority Area, "Quantum Coherent Electronics" from the Ministry of Education, Science and Culture.

References

[1] S. Shimomura, A. Wakajima, A. Adachi, Y. Okamoto, N. Sano, K. Murase and S. Hiyamizu, Jpn. J. Appl. Phys. 32 (1993) L1728.
[2] S. Hiyamizu, S. Shimomura, A. Wakajima, S. Kaneko, A. Adachi, Y. Okamoto, N. Sano and K. Murase, J. Vac. Sci. Technol. B 12 (1994) 1043.
[3] F. Koyama, S. Kinoshita and K. Iga, Appl. Phys. Lett. 55 (1989) 221.

[4] P.L. Gourley, T.M. Brennan, B.E. Hammons, S.W. Corzine, R.S. Geels, R.H. Yan, J.W. Scott and L.A. Coldren, Appl. Phys. Lett. 54 (1989) 1209.
[5] J.L. Jewell, A. Scherer, S.L. McCall, Y.H. Lee, S. Walker, J.P. Harbison and L.T. Florez, Electron. Lett. 25 (1989) 1123.
[6] S. Nakagawa, N. Yamada, N. Mikoshiba and D.E. Mars, Appl. Phys. Lett. 66 (1995) 24.
[7] N. Ogasawara, R. Ito, H. Rokukawa and W. Katsurashima, Jpn. J. Appl. Phys. 26 (1987) 1386.
[8] S.W. Corzine, R.H. Yan and L.A. Coldren, IEEE J. Quantum Electron. 27 (1991) 2086.
[9] R.J. Horowicsz, H. Heitmann, Y. Kadota and Y. Yamamoto, Appl. Phys. Lett. 61 (1992) 393.
[10] K. Ujihara, M. Osuge and M. Takaku, Jpn. J. Appl. Phys. 32 (1993) L1808.

ELSEVIER

Journal of Crystal Growth 175/176 (1997) 365–371

JOURNAL OF CRYSTAL GROWTH

Growth of vertical cavity surface emitting laser material on (3 1 1)B GaAs by MBE

D.E. Mars[a,*], S.J. Rosner[a], Y. Kaneko[b], S. Nakagawa[b], T. Takeuchi[b], N. Yamada[b]

[a] *Hewlett-Packard Laboratories, 3500 Deer Creek Road, Palo Alto, California 94304, USA*
[b] *Hewlett-Packard Laboratories, 3-2-2 Sakado Takatsu-ku Kawasaki-shi, Kanagawa 213, Japan*

Abstract

We report on the growth of VCSEL structures on (3 1 1)B GaAs substrates. For the growth of AlGaAs and AlAs, the best morphology and material quality were obtained for growth temperatures $> 650°C$. Surface morphology and mirror reflectivity degraded significantly at low growth temperatures ($< 600°C$). From low-temperature photoluminescence (LTPL), we found a "forbidden" temperature range for the growth of InGaAs quantum well-active regions on (3 1 1)B substrates between 540 and 560°C. Active region growth temperatures in this range showed low intensity, broad LTPL, and poor laser characteristics. Cross-section TEM measurements show poor homogeneity for material grown in this temperature range. At higher temperatures (580°C), In desorption is greatly increased, so $< 520°C$ was selected as the optimal growth temperature. Even with a non-optimized structure, the first reported VCSELs on (3 1 1)B were fabricated with a pulsed $J_{th} = 9\ kA/cm^2$ at $-40°C$ and 28 kA/cm^2 at room temperature. At $-40°C$, 10 nW of SHG blue light at 485 nm was detected under pulsed conditions, and 2 nW was detected under CW conditions and was visible to the naked eye. By improving the structure we obtained CW lasing at room temperature with 300 A/cm^2 as a broad area laser and 1.4 kA/cm^2 as a VCSEL. A maximum power of 0.55 nW at 490 nm was detected CW at room temperature.

1. Introduction

Yamada et al. [1, 2] have reported on a novel approach to realizing short-wavelength monolithic compact laser diodes. This is based on second-harmonic generation (SHG) inside a vertical-cavity surface-emitting laser diode (VCSEL). This type of device should emit coherent laser light at twice the frequency or half the wavelength of the fundamental laser light. The intracavity intensity of the fundamental light in a VCSEL is extremely high. This is very favorable for SHG since the conversion efficiency is proportional to the intensity of the fundamental light. In addition, GaAs and AlGaAs have relatively high second-order optical nonlinear coefficients.

One possible structure for an SHG-in-VCSEL device is shown schematically in Fig. 1. This structure differs from a typical VCSEL in two ways. First, we must grow on a substrate with an orientation

* Corresponding author. Fax: +1 415 857 2379; e-mail: dan_mars@hpl.hp.com.

0022-0248/97/$17.00 Copyright © 1997 Elsevier Science B.V. All rights reserved
PII S0022-0248(96)00882-2

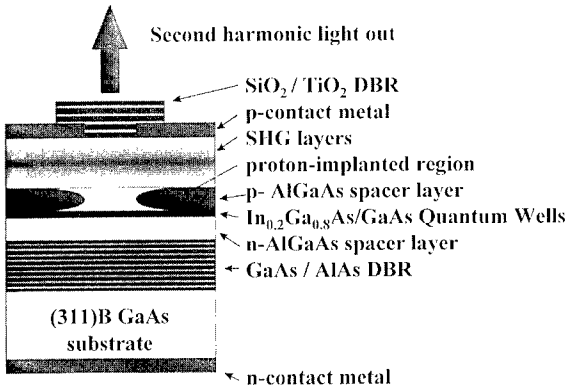

Fig. 1. Schematic diagram of a SHG in VCSEL device structure.

tilted away from (1 0 0) where the nonlinear optical coefficients are zero due to the crystal symmetry. Second, we incorporate layers within the cavity of the VCSEL optimized for the highest overall efficiency in converting fundamental light to second harmonic (SH) light. The first step in realizing an SHG-in-VCSEL device was to fabricate successfully VCSELs on a non-(1 0 0) orientation. We selected the (3 1 1)B orientation which still has a relatively large nonlinear optical coefficient though not as high as (2 1 1) or (1 1 1) and the B face can be effectively doped n-type with Si [3]. All of the work described here was using (3 1 1)B substrates with some comparisons to (1 0 0) substrates. Some of our early device results have been published elsewhere so that this paper will concentrate primarily on the growth and characterization of the epitaxial material.

2. Experiment procedure

The growths were done in a Varian Modular Gen II MBE system using all elemental sources. All the growths were done with non-In-bonded substrate holders. No chemical preparation was done on the substrates prior to growth. The wafers and blocks were baked in an auxiliary chamber at 500°C for 1 h. The substrate rotation rate was 30 rpm. Ga and In source furnaces were 125 cc cells designed with straight wall crucibles and tapered inserts to minimize shutter flux transients and to improve flux stability. The Al source furnace used a standard tapered 60 cc cell. Be was used as the p-type dopant and Si was used as the n-type dopant. Substrate temperatures were measured with an optical pyrometer through a heated viewport assembly to minimize coating due to As [4]. The same optical pyrometer was used for Ga and Al flux calibrations using interferometry [5, 6].

Nomarski optical microscopy was used to observe both surface roughness and macroscopic surface defects.

Low-temperature photoluminescence (LTPL) measurements were done with a liquid He cryostat with sample temperatures of 10–20 K. Excitation power was 5 mW focused onto the sample from an Ar-ion laser at 488 nm. A Ge detector was used to collect sample luminescence.

Specimens were prepared for transmission electron microscopy (TEM) by mechanical grinding and polishing to a thickness of less than 10 μm followed by ion beam thinning with 5 kV Ar^+ ions at low angle. Specimens were mounted on a liquid-nitrogen-cooled stage during ion thinning and final ion thinning was performed at incident angles less than 5°. Observations were performed in a JEOL 4000FX microscope operating at 400 kV.

3. Growth and characterization

There are many requirements for the growth of the VCSEL structures described in this work: (1) Just as in the case of in-plane lasers, the optical and electrical quality, of the material, particularly in the InGaAs quantum well-active region, must be sufficiently high. (2) As in the case of VCSELs grown on (1 0 0), the flux stability must be carefully controlled to within 1% for all of the group III sources [7]. (3) When we grow on (3 1 1)B substrates, we must maintain the excellent surface morphology and material quality that we observe on (1 0 0) substrates.

The starting substrate quality made a noticeable difference in the quality of the grown material. Our initial growths were on 2 × 4 cm pieces. Later another substrate vendor was able to supply us with 2 in diameter wafers. Both substrate mounting and

temperature measurement using pyrometry were greatly improved. The "epi-ready" polish of the second vendor gave superior surface morphology. Also, a substrate outgas temperature of higher than 650°C resulted in better surface morphology even though the minimum temperature needed to obtain a streaky RHEED pattern was unchanged.

Bose et al. [3] reported that Si doping on (3 1 1)B GaAs substrates results in n-type conductivity. To verify this, we grew Si-doped GaAs on both (1 0 0) and (3 1 1)B substrates simultaneously in the same growth. The growth temperature was 600°C and the target [Si] was $1 \times 10^{18}\,cm^{-3}$. Hall effect measurements showed that both samples were n-type and the carrier concentrations were within 3% of the target value.

Our procedure for growing VCSEL structures on (1 0 0) substrates is to grow the entire structure at the same substrate temperature to simplify the in-situ optical monitoring that we use during the growth [6]. This is usually at a temperature that is consistent with the InGaAs active region temperatures of 550°C or below. However, the same procedure on (3 1 1)B substrates resulted in a very rough and hazy morphology as shown in Fig. 2b. Increasing the growth temperature to 620°C improved the surface roughness, but there was a high density of morphological defects that are a few microns in size as shown in Fig. 2c. Increasing the growth temperature further to > 650°C resulted in specular surfaces with very low morphological defect density (Fig. 2d). At the higher growth temperature, the defects that remained were the classical oval defects that are commonly seen in MBE growth. Thus, for layers of AlGaAs or AlAs we found the best growth temperatures to be above 650°C.

In order to study the optical quality of the InGaAs active region on (3 1 1)B substrates compared to (1 0 0) substrates we grew special test

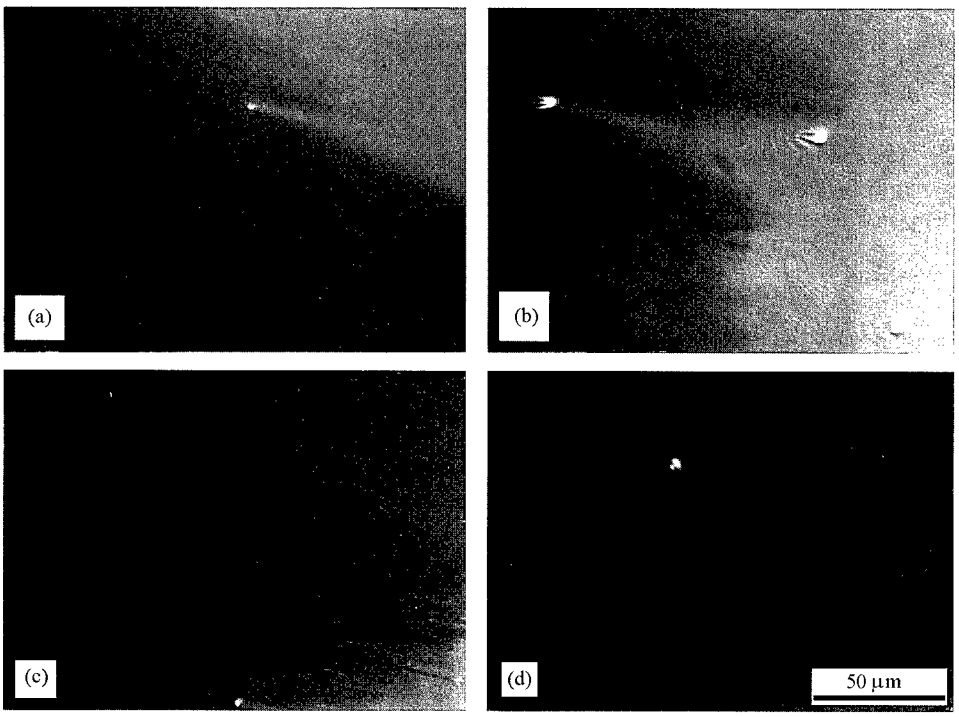

Fig. 2. Optical microscope photographs of surface morphology of VCSEL wafers grown at various temperatures on (1 0 0) and (3 1 1)B substrates: (a) (1 0 0), 520°C, (b) (3 1 1)B 520°C, (c) (3 1 1)B 620°C, 520°C for the InGaAs active region, (d) (3 1 1)B 650°C, 520°C for the InGaAs active region.

structures that included just the quantum well active regions. These were much simpler to grow than full VCSEL structures which take longer than 10 h to grow. The structure consists of 3 quantum wells of $In_xGa_{1-x}As$ with an In mole fraction of $x = 0.2$ and 80 Å thick, separated by 100 Å thick GaAs barriers. Fig. 3 shows the low-temperature photoluminescence measurements from four samples: growth temperatures of 520°C on (1 0 0), 520°C on (3 1 1)B, 550°C on (3 1 1)B, and 580°C on (3 1 1)B. The samples were grown in sequence within a two day period with identical source furnace temperatures. The only differences were the substrate orientation and the substrate temperature. The sample grown on (1 0 0) shows a single, narrow luminescence peak with a FWHM of 4.3 meV and is characteristic of the high quality of InGaAs that we observe on (1 0 0) substrates. The luminescence peaks from the samples grown at 520°C and 580°C on (3 1 1)B are fairly comparable to each other both in intensity and FWHM but are both inferior to the (1 0 0) case. Also, note the strong shift to shorter wavelength in the 580°C sample. This is due to the large decrease in In incorporation at the higher temperature. We also observed a variation in peak wavelength across the 2 in wafer that matched the known temperature nonuniformity of the substrate at 580°C. For the sample grown at 550°C there is a dramatic degradation in material quality. We observe multiple, broad peaks with low integrated intensity. Threshold current densities for lasers with active regions grown in this temperature region are very high. In separate experiments we have looked at active regions grown over a wide temperature range from 490°C to 580°C and have not seen this severe degradation in material quality on (1 0 0) substrates.

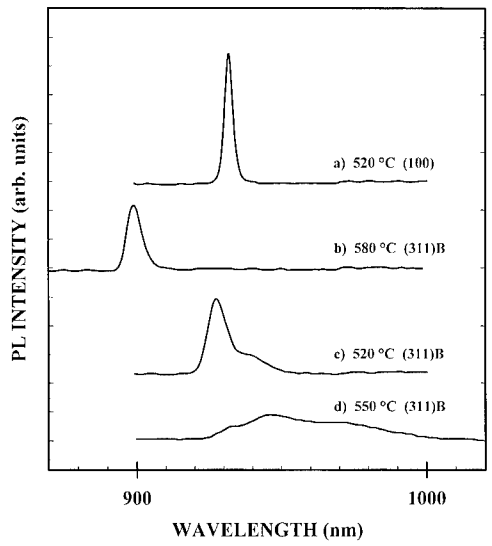

Fig. 3. Low-temperature photoluminescence spectra for InGaAs/GaAs multi-quantum well samples grown at various temperatures on (1 0 0) and (3 1 1)B substrates.

In order to understand further the poor optical quality of InGaAs quantum wells grown at around 550°C, we looked at the above set of four samples with cross-sectional TEM. The results are shown in Fig. 4. The 520°C, (1 0 0) and the 580°C, (3 1 1)B samples show relatively smooth, homogeneous interfaces between the InGaAs and GaAs layers. The 520°C, (3 1 1)B sample shows some degradation of the interfaces and in the LTPL measurements, there is a small increase in the FWHM. The 550°C, (3 1 1)B sample showed a very inhomogeneous active region with large variations in thickness and strain. The variations were so pronounced that clear imaging was not possible. Apparently at 550°C on (3 1 1)B the growth kinetics are such that the smooth, layer-by-layer growth is disrupted and there is some islanding of the InGaAs.

The LTPL and TEM results indicate that there is not much difference between the optical quality of the InGaAs quantum well region between the 520°C case and the 580°C case. But at 580°C we are in a temperature regime where the In incorporation is a relatively strong function of the substrate temperature and we are sensitive to run-to-run variations in growth temperature and nonuniform temperature profiles across a wafer. As a result we selected < 520°C as the optimal growth temperature for the active region. We have not yet seen LTPL characteristics on (3 1 1)B as good as that on (1 0 0).

We also compared a 100 Å GaAs barrier to a 200 Å GaAs barrier in multi-quantum well test structures with 60, 80, and 100 Å thick InGaAs quantum wells. The LTPL spectrum was markedly better in the sample with the thicker, 200 Å barrier:

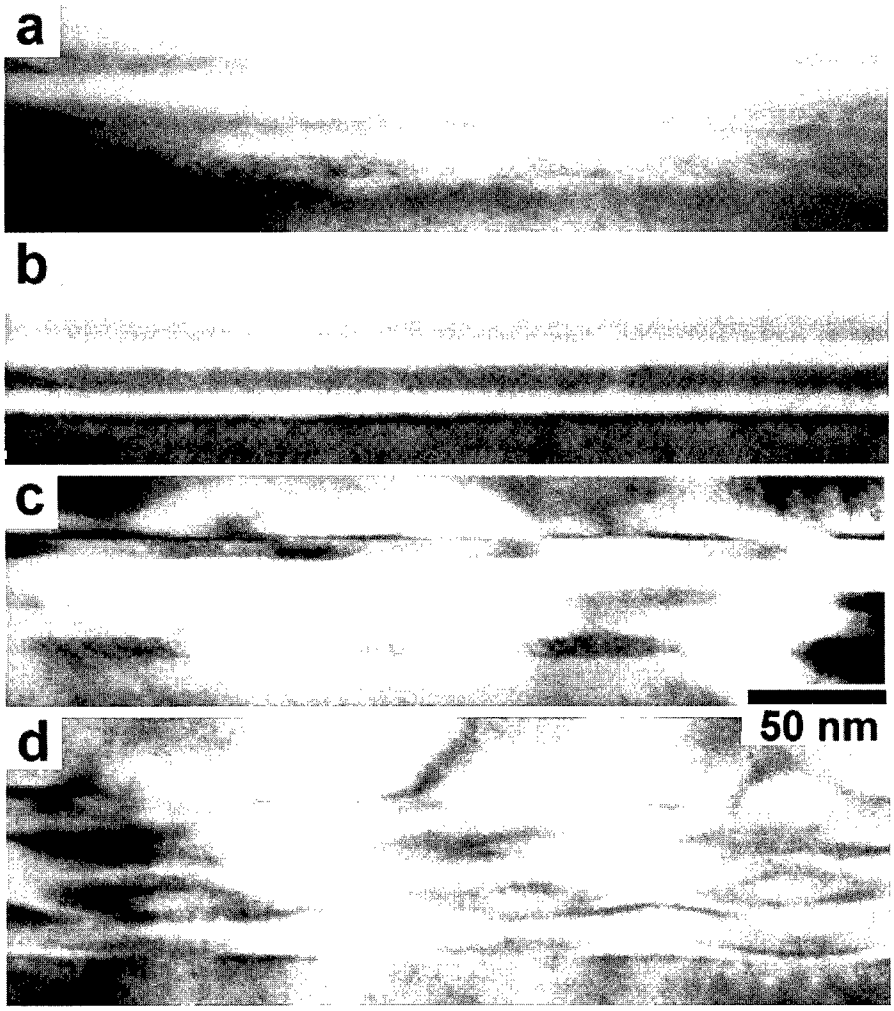

Fig. 4. Cross-sectional transmission electron microscope photographs of InGaAs/GaAs multi-quantum well test structures (same samples as Fig. 3): (a) (1 0 0), 520°C, (b) (3 1 1)B, 580°C, (c) (3 1 1)B, 520°C, (d) (3 1 1)B, 550°C.

For the widest well width of 100 Å, the FWHM was 47 meV for the 100 Å barrier compared to 5.6 meV for the 200 Å barrier. The integrated intensity was also about a factor of 2 higher with the 200 Å barrier compared to the 100 Å barrier. Cross-sectional TEM micrographs show inhomogeneous interfaces and evidence of islanding for the sample with 100 Å barrier widths, especially for the 100 Å thick well. Much smoother interfaces were observed in the sample with 200 Å barriers. The same structures grown on (1 0 0) with both 100 and 200 Å barriers show narrow, high-intensity peaks in LTPL.

Thus, our latest optimized structure for the active region is two 60 Å quantum wells of $In_xGa_{1-x}As$, $x = 0.20$, separated by a GaAs barrier that is 200 Å thick.

Our procedure for flux calibration and control is based on optical pyrometry and has been published elsewhere [6].

4. Device results

We have fabricated a VCSEL grown on an n-(3 1 1)B GaAs substrate and observed SH blue light for the first time [2]. It consists of a GaAs/AlAs semiconductor n-DBR bottom mirror, n-AlGaAs spacer layer, InGaAs/GaAs QWs, p-AlGaAs spacer layer, p-GaAs cap layer and a SiO_2/TiO_2 dielectric DBR top mirror. The top mirror has a high reflectivity at the fundamental wavelength but transmits SH light. This was our first SHG-in-VCSEL device and did not incorporate the optimized SHG layers but the p-GaAs cap and the p-AlGaAs spacer layers, to some extent, function as the SHG layers.

This VCSEL lases under pulsed operation at room temperature and lases under CW operation only at low temperature (130–270 K). The lasing wavelength of the fundamental light is 965 nm, and that of the SH blue light is 482 nm. The maximum CW output power of the fundamental and the SH light are 1.5 mW and 2.0 nW, respectively, at 135 K. More than 10 nW of SH light is observed under pulsed operation. Although the blue light output power is not very high, it is visible to the naked eye. Our simulations indicate that it can be improved to several hundred μWs by incorporation of an optimized GaAs/AlAs SHG layer structure [2]. To date, we have attempted two wafers that incorporate such layers and both have very high series resistance and did not lase.

Some recent device wafers that incorporate the optimized active region structure described at the end of Section 3 were processed and fabricated into VCSELs. The laser cavity is $6\lambda/n$ with thick AlGaAs as the top phase-matching layer. This thick AlGaAs is enough to confine the light and carriers in a broad-area, in-plane laser. The broad area J_{th} of this wafer was 350 A/cm^2. When processed into a VCSEL using a top dielectric mirror, the device lased CW at room temperature with a $I_{th} = 5$ mA for a 15 μm diameter device. The active area for current flow as defined by ion implantation was 21 μm. This corresponds to $J_{th} = 1.4$ kA/cm^2. The maximum fundamental power output at 981 nm was 40 μW at 20 mA. The maximum SH light output at 490 nm was 0.55 nW, also at 20 mA. The large difference between the broad area laser and the VCSEL threshold current density is being investigated. It may be related to a mismatch between the gain peak wavelength and the Fabry–Perot wavelength or other device processing parameters. Details of the processing and device characteristics will be reported elsewhere.

5. Conclusion

We have grown a number of wafers on (3 1 1)B substrates and found that the best VCSEL material is realized with (1) high-quality substrate material, (2) high substrate temperatures during oxide desorption before growth begins, (3) > 650°C growth temperature during Al-containing layers, (4) < 520°C growth temperature during InGaAs quantum well active region, and (5) thicker GaAs barriers between InGaAs quantum wells. The temperature range around 550°C for the active region should be particularly avoided due to inhomogeneous growth of InGaAs. 2 nW of blue SH laser light at 485 nm has been observed on a non-optimized VCSEL device. The best results on (3 1 1)B substrates to date are VCSELs that lase CW at room temperature with $J_{th} = 1.4$ kA/cm^2 and emit a maximum power of 40 μW at 981 nm and 0.55 nW at 490 nm.

Acknowledgements

The authors would like to thank Y.M. Houng, M.R.T. Tan, and S.Y. Wang for useful discussions on growth, laser design, and processing, D. Reed and M. Kanemura for technical assistance, and M. Wong for TEM sample preparation.

References

[1] S. Nakagawa, N. Yamada, N. Mikoshiba and D.E. Mars, Appl. Phys. Lett. 66 (1995) 2159.
[2] N. Yamada, Y. Kaneko, S. Nakagawa, Dan E. Mars, T. Takeuchi and N. Mikoshiba, Appl. Phys. Lett. 68 (1996) 1895.

[3] S.S. Bose, B. Lee, M.H. Kim and G.E. Stillman, J. Appl. Phys. 63 (1988) 743.
[4] D.E. Mars and J.N. Miller, J. Vac. Sci. Technol. B 7 (1989) 682.
[5] A.J. SpringThorpe and A. Majeed, J. Vac. Sci. Technol. B 8 (1990) 266.
[6] Y.M. Houng, M.R.T. Tan, B.W. Liang, S.Y. Wang and D.E. Mars, J. Vac. Sci. Technol. B 12 (1994) 1221.
[7] J.L. Jewell, J.P. Harbison, A. Scherer, Y.H. Lee and L.T. Florez, IEEE J. Quantum Electron. 27 (1991) 1332.

ELSEVIER

Journal of Crystal Growth 175/176 (1997) 372–376

JOURNAL OF CRYSTAL GROWTH

Molecular beam epitaxy of AlGaAsSb system for 1.55 μm Bragg mirrors

J.C. Harmand*, A. Kohl, M. Juhel, G. Le Roux

France Telecom/CNET, Laboratoire de Bagneux, 196 avenue Henri Ravera, B.P. 107, F-92225 Bagneux Cedex, France

Abstract

The growth of AlGaAsSb materials on InP substrate was carried out by elemental source molecular beam epitaxy (MBE). The control of group-V composition appeared complex. In order to minimize the fluctuations of group-V composition, its dependence on growth temperature, cracking of the group-V species, growth rate and Al/Ga ratio were evaluated. Then we focused on $AlAs_xSb_{1-x}$ and $Al_zGa_{1-z}As_ySb_{1-y}$ alloys with x and y allowing lattice matching to InP, and with z around 0.10 in order to have transparency at 1.55 μm. Pairing these alloys, we built up Bragg mirrors with the reflectivity centered at 1.55 μm. A mirror consisting of $20\frac{1}{2}$ pairs exhibited a reflectivity of 99.8% with a 200 nm stopband width. Doping studies of these materials demonstrated n- and p-type conductivities with carrier concentrations over 10^{19} cm^{-3} where Te and Be were, respectively, the n- and p-type dopants.

1. Introduction

The fabrication of vertical optical microcavities can be a key technology for a variety of photonic devices, including lasers, amplifiers, modulators and bistable switches. At the operating wavelength of 1.55 μm, the AlAsSb/AlGaAsSb Bragg stacks on InP substrates appear as good candidates to fabricate distributed Bragg reflectors (DBRs). The following advantages can be drawn: (i) lattice matching to InP (with the proper As/Sb ratio); (ii) transparency at 1.55 μm wavelength (for Al compositions higher than 10%); (iii) last but not least, high refractive index contrast attainable [1]. In spite of these advantages, only few attempts to realise these heterostructures on InP have been reported up to now [1–3]. Assuming a Vegard's law for GaAsSb and AlAsSb lattice parameters, the As composition must be 0.51 and 0.56, respectively, to match the InP lattice parameter. Liquid phase epitaxy was found to be inadequate to get these compositions [4] for which a miscibility gap was evidenced [5]. However, it was demonstrated that MBE can produce metastable layers with compositions inside the miscibility gap [6]. Here the composition control of these alloys grown by MBE is carefully examined, and high-reflectivity mirrors are reported.

* Corresponding author. Fax: + 33 1 42 53 76 32; e-mail: harmand@bagneux.cnet.fr.

0022-0248/97/$17.00 Copyright © 1997 Elsevier Science B.V. All rights reserved
PII S0022-0248(96)00883-4

2. Control of group-V composition

DBRs represent thick stacks with typical thickness of several μm. Hence a low lattice mismatch is required to prevent the generation of dislocations. In the AlGaAsSb alloys, the control of group-V composition is essential to reach a good lattice matching. In contrast to group-III elements, the sticking coefficients of group-V species are not unity. The solid phase group-V composition is therefore sensitive to most of the growth parameters. In addition, growth parameter fluctuations are emphasized by the relatively long growth times needed for these DBRs. Seeking a reduced sensitivity of the group-V composition on growth parameters, we investigated these dependences.

Our growth equipment was a solid-source MBE. The group-V sources were equipped with cracking tubes allowing to produce As_2 and Sb_2 fluxes. The experimental group-V mole fractions were deduced from As and Sb profiles obtained by secondary ion mass spectroscopy (SIMS) on samples where growth parameters were systematically varied in a single growth. The SIMS measurements were quantified with the support of X-ray diffraction on GaAsSb single layers which were used as calibration samples for the SIMS analysis.

Fig. 1 shows the influence of the growth temperature on the Sb mole fraction of AlAsSb and $Al_{0.1}Ga_{0.9}AsSb$ which are the material of interest for the 1.55 μm Bragg mirrors. No significant effect is evidenced up to 500°C. Above this temperature, Sb is preferentially desorbed for both alloys. A similar result was already reported for GaAsSb at a slightly higher temperature [7]. In order to be insensitive to substrate temperature fluctuations, we therefore used growth temperature lower than 500°C for the subsequent samples.

Then, we investigated the role of As and Sb cracker temperatures. Strong variations of group-V mole fractions were obtained in the solid as illustrated in Fig. 2. These variations clearly demonstrates that (i) the cracking is effective for arsenic and antimony. The efficiencies reach maximum values above about 800°C for both. It is believed that this temperature mainly allows to crack tetramers into dimers [8]. (ii) The cracked species are incorporated much more efficiently than the uncracked species. Fig. 2 shows that for arsenic as well as for antimony the composition after cracking is typically twice as before. This is consistent with a sticking coefficient which doubles when incoming species are dimers rather than tetramers. This observation meets the model of Foxon [9] where the As_4 sticking coefficient on GaAs has a maximum value of 0.5 against 1 for As_2. Because of this higher sticking coefficient, dimers were preferred to tetramers for the growth of the AlGaAsSb materials. With higher sticking coefficients, the group-V composition in the solid phase is expected to be less dependent on growth conditions. The cracker

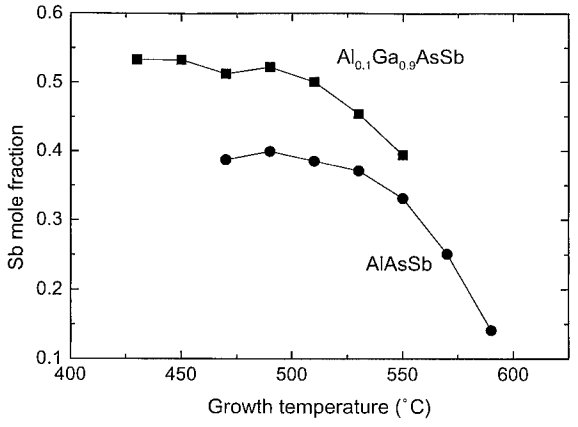

Fig. 1. Sb mole fraction in AlAsSb and $Al_{0.1}Ga_{0.9}AsSb$ versus the growth temperature. The incoming fluxes were fixed. The As and Sb cracker temperatures were 900°C.

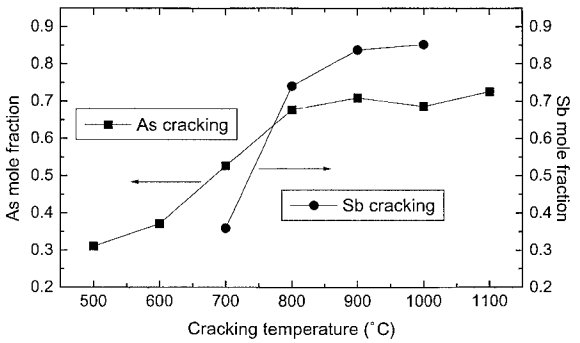

Fig. 2. As or Sb mole fraction in AlAsSb versus As or Sb cracker temperature, respectively.

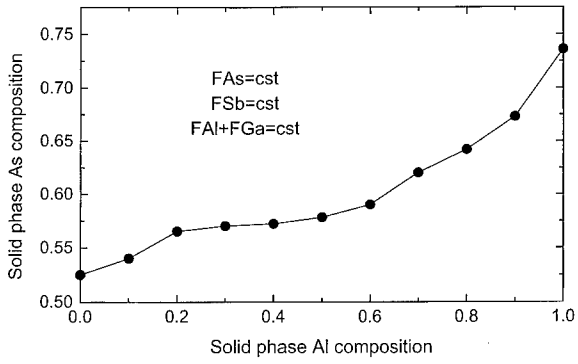

Fig. 3. As mole fraction in AlGaAsSb alloys versus the Al mole fraction. As and Sb fluxes were constant. The total group-III flux was fixed (constant growth rate) while the Al/Ga ratio was systematically varied.

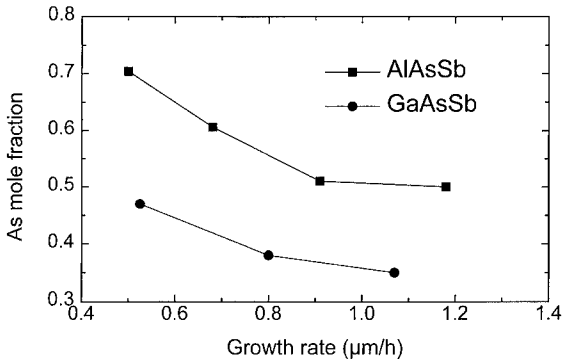

Fig. 4. Influence of the growth rate of GaAsSb and AlAsSb on their As mole fraction. As and Sb fluxes were fixed for each experiment (but different between GaAsSb or AlAsSb growth).

temperatures were fixed at 900°C to go beyond the region of lower cracking efficiencies.

In Fig. 3, the growth rate and the group-V fluxes were constant, but the Al/Ga ratio was varied. As one can see, at higher Al concentrations, more As is incorporated in the solid phase. This effect is partly usefull since for InP lattice matching, Al-rich alloys need a higher As mole fraction than Ga-rich alloys. However, the higher incorporation of As in Al-rich alloys is stronger than needed. An As mole fraction difference of 0.20 was measured between GaAsSb and AlAsSb while the lattice matching condition requires a difference of 0.05. This observation has an important consequence for the growth of AlGaAsSb/AlAsSb heterostructures: the lattice matching condition cannot be satisfied for both alloys at constant growth rate and group-V fluxes. Hence one has to change a group-V flux when switching from AlAsSb growth to AlGaAsSb growth. However, the solid-source MBE is not well suited to rapid and reproducible change of fluxes. Therefore this solution is not desirable for a DBR growth.

Another possibility to solve this problem was evidenced by investigating the influence of the growth rate on the group-V composition. Fig. 4 presents our observations for GaAsSb and AlAsSb. While As and Sb fluxes were constant, the group-III fluxes and therefore the growth rates were increased (however, in these experiments, the As and Sb fluxes were different for GaAsSb or AlAsSb growth). The consequence of increasing the growth rate is an Sb enrichment of the solid phase of each alloy. This behavior was also observed by Klem et al. [10].

The results of Figs. 3 and 4 can be summarized as follows: the group-V incorporation coefficient is affected by the group-III arrival rate and also by the group III species. With a careful adjustment of growth conditions, each effect can compensate the other: higher Al mole fractions need higher growth rates. To take full advantage of this possibility, two Al cells are required to adjust the Al mole fraction of each alloy independently of the growth rate. As a result, the lattice matching condition can be satisfied for the whole mirror while all the individual flux can be kept constant during the growth. This is favorable to the stability of the process.

Our observations on the influence of the growth parameters on the group-V composition in the solid can be qualitatively interpreted with thermodynamics. The group-V composition is driven by the competitive reactions between the incoming species. The free energies ΔG for the different reactions involved in the AlGaAsSb growth were calculated at 500°C from the database of Ref. [11]. The values are reported in Table 1, showing that the formation of arsenides is energetically more profitable than the formation of antimonides. This explains why the Sb is preferentially desorbed when

Table 1
Gibbs energies of the reactions involved in the AlGaAsSb growth

Growth reactions	ΔG (J/mol)
$Ga(g) + \frac{1}{2}As_2(g) = GaAs(s)$	− 282
$Ga(g) + \frac{1}{2}Sb_2(g) = GaSb(s)$	− 263
$Al(g) + \frac{1}{2}As_2(g) = AlAs(s)$	− 369
$Al(g) + \frac{1}{2}Sb_2(g) = AlSb(s)$	− 325

the growth temperature is raised, or when the V/III ratio is increased (decrease of growth rate). The difference of ΔG being more pronounced for the Al compounds, the As incorporation is even more favored when the Al/Ga ratio is increased, in agreement with our experimental results.

3. Mirror growth

We applied the optimized growth conditions discussed above to the growth of AlAsSb/AlGaAsSb mirrors. The refractive index of the materials were already evaluated in Ref. [1]. We found $n = 3.65$ for $Al_{0.13}Ga_{0.87}As_ySb_{(1-y)}$ and $n = 3.11$ for $AlAs_xSb_{(1-x)}$. Therefore, this material system has an index step of 0.54 which is among the highest ever reported for III–V compounds lattice matched to InP and transparent at 1.55 μm. A comparable value was reported for AlPSb/GaPSb system [12] which is also very attractive. However, the large difference of atomic radii involved in this system (P compared to Sb) is a priori not favorable to the growth.

Undoped quarter-wave stacks were realized for 1.55 μm wavelength. The reflectivity was measured on a Fourier transform infrared reflectometer. The experimental setup allows to measure a reference spectrum with one reflection on a reference mirror. Then the sample is placed on its holder and the reference mirror is moved to allow two reflections on the sample and one on the reference mirror with no optical adjustment of the source nor the detector. The square root of the ratio of the two spectra gives a quantitative measurement with an accuracy of ∓ 0.002. A first sample consisted of 15 pairs of $Al_{0.13}Ga_{0.87}As_ySb_{(1-y)}$ and $AlAs_xSb_{(1-x)}$

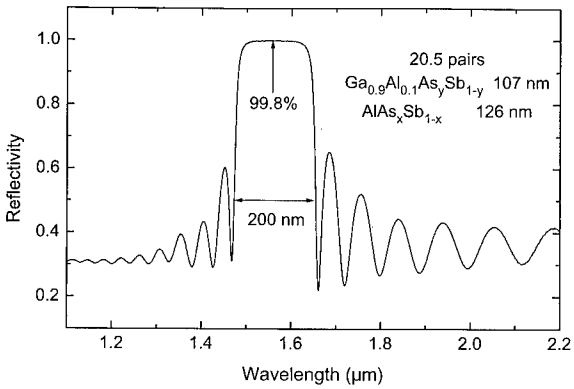

Fig. 5. Reflectivity spectrum of a $20_{1/2}$ pairs $Al_{0.1}Ga_{0.9}AsSb$/AlAsSb Bragg mirror.

plus an additionnal layer of $Al_{0.13}Ga_{0.87}As_ySb_{(1-y)}$ to prevent the strong surface oxidation in the air which is observed on $AlAs_xSb_{(1-x)}$. The photoluminescence of this sample was observed around 1.33 μm at room temperature. This confirms the transparency of the stack at 1.55 μm. The reflectivity is maximum at 1.58 μm with a value over 0.98 [1].

In a second sample, we increased the number of pairs to $20\frac{1}{2}$ and we slightly decreased the Al composition of the quaternary to 0.10. This yielded a maximum reflectivity of 0.998, as shown in Fig. 5. This value is in very good agreement with the predited value based on a calculation using the index values reported above. Moreover, this is typically the value required for vertical cavity surface emitting lasers. Moreover, these $20\frac{1}{2}$ pairs represent a total thickness of 4.8 μm. It is much less than the thickness of GaInAsP/InP or AlGaInAs/AlInAs distributed Bragg mirrors with a comparable reflectivity. The reduction of thickness is important to lower electrical and thermal resistances of the vertical device. In addition, small lateral size pixels would be more easily processed with a smaller height.

4. Doping studies

In order to inject current into vertical cavity structures, the doping of these materials is essential. We have studied both n- and p-type dopants. Silicon was first tested as the n-type source. The

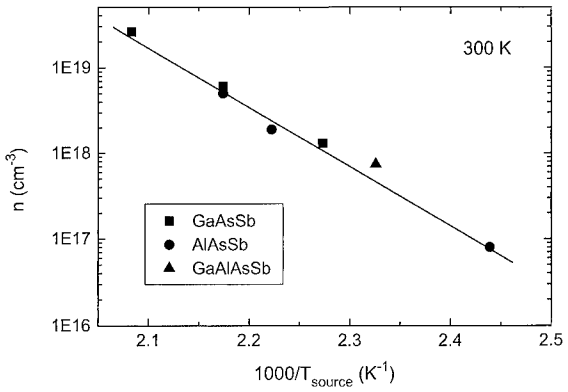

Fig. 6. Electron Hall concentrations in Te-doped GaAsSb, AlAsSb and AlGaAsSb samples versus the reverse of the dopant source (Sb_2Te_3) temperature.

Si-doped samples have all shown poor conductivities with a pronounced anisotropy. They were highly compensated, probably due to an amphoteric behavior of Si. Tellurium is a more common n-type dopant in the antimony-rich alloys. We loaded a Sb_2Te_3 source. Electrical measurements on Te-doped layers are reported in Fig. 6 versus the temperature of the Sb_2Te_3 cell. Electron concentrations in excess of 10^{19} cm^{-3} were obtained. These doping levels are high enough to fabricate a vertical laser (VCSEL). In addition, there is no evidence that the Te activity depends on the Al mole fraction since the experimental data in GaAsSb, AlGaAsSb or AlAsSb are roughly on a straight line. The room temperature electron mobilities were 560 cm^2 V^{-1} s^{-1} for GaAsSb doped at 1.3×10^{19} cm^{-3} and 80 cm^2 V^{-1} s^{-1} for AlAsSb doped at 9.4×10^{17} cm^{-3}. A Be source was used for p-type doping. Hole concentrations up to 4×10^{19} cm^{-3} were obtained. The hole mobility in AlAsSb was 9 cm^2 V^{-1} s^{-1} for a concentration of 1×10^{19} cm^{-3}. These doping results open the possibility of growing VCSEL structures with n- and p-type AlGaAsSb mirrors.

5. Conclusion

In spite of a difficult control of the group-V mole fraction, the AlGaAsSb material system is shown to be very attractive for fabrication of 1.55 μm Bragg mirrors on InP substrate. The group-V composition was found to be sensitive to growth temperature, cracking of group-V species, growth rate and Al/Ga ratio. These dependences are consistent with thermodynamics. The growth conditions of heterostructures were optimized to reduce the group-V composition fluctuations. The dependences on growth rate and on Al/Ga ratio were found to compensate each other. By a proper adjustment of growth rates, it was possible to grow AlGaAsSb/AlAsSb DBRs with fixed group-V fluxes. A reflectivity of 0.998 ∓ 0.002 is demonstrated at 1.55 μm on a DBR stack of $20\frac{1}{2}$ pairs which represents a thickness of less than 5 μm.

Acknowledgements

We thank R. Kuszelewicz for his skilled support for reflectivity measurements.This work was partially supported by the ACTS european project AC024.

References

[1] J.C. Harmand, F. Jeannès, G. Leroux and M. Juhel, Electron. Lett. 31 (1995) 1689.
[2] B. Lambert, Y. Toudic, Y. Rouillard, M. Gauneau, M. Baudet, F. Alard, I. Valiente and J.C. Simon, Appl. Phys. Lett. 66 (1995) 442.
[3] O. Blum, I.J. Fritz, L.R. Dawson, A.J. Howard, T.J. Headley, J.F. Klem and T.J. Drummond, Appl. Phys. Lett. 66 (1995) 329.
[4] C.G. Fonstad, M. Quillec and S. Garone, J. Appl. Phys. 49 (1978) 5920.
[5] J.R. Pessetto and G.B. Stringfellow, J. Crystal Growth 62 (1983) 1.
[6] C.A. Chang, R. Ludeke, L.L. Chang and L. Esaki, Appl. Phys. Lett. 31 (1977) 759.
[7] Y. Nakata, T. Fujii, A. Sandhu, Y. Sugiyama and E. Miyauchi, J. Crystal Growth 91 (1988) 655.
[8] Y. Rouillard, B. Lambert, Y. Toudic, M. Baudet and M. Gauncau, J. Crystal Growth 156 (1995) 30.
[9] C.T. Foxon, Acta Electron. 21 (1978) 139.
[10] J. Klem, D. Huang, M. Morkoç, Y.E. Ihm and N. Otsuka, Appl. Phys. Lett. 50 (1987) 1364.
[11] I. Ansara, C. Chatillon, H.L. Lukas, T. Nishizawa, H. Ohtani, K. Ishida, M. Hillert, B. Sundman, B.B. Argent, A Watson, T.G. Chart and T. Anderson, Calphad 18 (1994) 177.
[12] T. Anan, H. Shimomura and S. Sugou, Electron. Lett. 30 (1994) 2138.

ELSEVIER

Journal of Crystal Growth 175/176 (1997) 377–382

JOURNAL OF CRYSTAL GROWTH

Carbon delta doping in chemical beam epitaxy using CBr_4

T.B. Joyce[a,*], T.J. Bullough[a], T. Farrell[a], B.R. Davidson[b], D.E. Sykes[c], A. Chew[c]

[a] *Department of Materials Science and Engineering, The University of Liverpool, Liverpool L69 3BX, UK*
[b] *Interdisciplinary Research Centre for Semiconductor Materials, The Blackett Laboratory, Imperial College of Science, Technology and Medicine, Prince Consort Road, London SW7 2BZ, UK*
[c] *Institute of Surface Science and Technology, Loughborough University, Loughborough, Leicestershire LE11 3TU, UK*

Abstract

We describe the growth of carbon δ-doped GaAs by chemical beam epitaxy (CBE) using CBr_4 as the dopant during growth interrupts. Characterisation of the δ-doped samples using secondary ion mass spectrometry (SIMS) at a series of impact energies showed that the C was confined to a planar sheet less than 1 nm thick. This is in agreement with HRXRD measurements on C δ-doping superlattices. The results of SIMS profiling of layers with a range of interrupt times indicate that there is an initial surface coverage of C from CBr_4 of approximately 9×10^{12} cm^{-2} which increases relatively slowly during an extended interrupt.

1. Introduction

There is an increasing requirement for highly doped GaAs and $Al_xGa_{1-x}As$ in devices such as heterojunction bipolar transistors (HBTs) and distributed Bragg reflector (DBR) stacks. Carbon is well established as a p-type dopant in GaAs for HBT base layers because of its low diffusivity combined with the high active doping level [1]. There is considerable interest in carbon as a dopant in GaAs/AlAs or GaAs/AlGaAs DBRs for vertical cavity surface emitting lasers (VCSELs) [2]. The p-type dopants used in DBRs are typically Be in molecular beam epitaxy (MBE) and Zn in metal-organic vapour phase epitaxy (MOVPE). Neither are ideal dopants for DBRs because of the need for periodic doping, with a high doping level at the heterojunctions to smooth out the valence band discontinuities and a lower doping level where the optical field is high to minimise free carrier absorption [3]. Be doping in AlAs is difficult, particularly at the high levels required to achieve significant smoothing of the valence band discontinuities. The level of active dopants is uncertain and at the normal MBE growth temperature of around 580°C, significant degradation of the interface may occur. This degradation can be avoided by compromising on the Bragg structure, using Be-doped GaAs/$Al_{0.33}Ga_{0.67}As$ grown at about 480°C, but this requires the growth of a thicker DBR (typically 30 periods compared with 18 for GaAs/AlAs) with poorer thermal properties.

* Corresponding author. Fax + 44 151 794 4675; e-mail: tjoyce@liv.ac.uk.

0022-0248/97/$17.00 Copyright © 1997 Elsevier Science B.V. All rights reserved
PII S0022-0248(96)00957-8

A more attractive solution is to focus on a different dopant. Carbon acts as a p-type dopant in GaAs and AlAs and unlike Be it can be introduced at high levels and localised close to the AlAs/GaAs interface [1]. C is far more stable than Be or Zn during high-temperature processing, having a diffusion constant some three orders of magnitude lower [4]. C doping by MBE has proved difficult in the past, solid C sources tending to introduce O contamination or graphitic C, whereas CBE is an ideal technique for C doping using gaseous precursors [5, 6]. Using CBr_4 as the C source GaAs and AlAs can be doped at up to 5×10^{20} cm^{-3} under normal growth conditions with no adverse effects on material quality (Be doping in AlAs is limited to 6×10^{17} cm^{-3} at this growth temperature). Carbon-doped GaAs was found to be free of impurities such as O (seen when a C-filament doping source was used in MBE) or H–C_{As} compensation (seen in MOVPE material) [7]. At very high doping levels ([C] $> 10^{20}$ cm^{-3}) there is a reduction in the GaAs growth rate due to etching of the GaAs by Br species arising from the decomposition of CBr_4 [8]. Carbon doping in Al(Ga)As is similar to that in GaAs, whether using CBr_4 [5] or CCl_4 [9] there is little change in incorporation with Al fraction in AlGaAs. CBE also offers excellent control of layer composition, in particular the direct flux control available using vapour sources simplifies the growth of graded interfaces.

The use of delta-doping at the interfaces of DBRs, where a high concentration of the dopant is confined to a planar sheet in the high band-gap material, leads to a low series resistance [10]. In this paper we describe studies of carbon δ-doping in GaAs which demonstrate the localisation that can be achieved using CBE. True δ-doping requires a spread less than the spatial extent of the ground state wave function in the V-shaped potential well generated by the ionised impurities [11]. For p-type material the wave function spread is ≈ 30 Å [12] and so confinement of the acceptors to a sheet with a thickness of ≈ 10 Å or less is required for true δ-doping to be obtained. We have demonstrated that carbon δ-doping in GaAs grown by CBE can meet these conditions [13] and present further results in this paper.

2. Experimental procedure

All structures were grown by chemical beam epitaxy (CBE) in a VG V80H system configured for all vapour sources [14] with pressure control of flux through a fine orifice without the need for a carrier gas. Arsine which was thermally cracked in an injector cell was used as the group V source and triethylgallium (TEGa) was used as the group III precursor. The fluxes were held constant for all of these samples giving a V : III ratio of 10 : 1 (an arsine BEP of 2×10^{-4} mbar and a TEGa BEP of 2×10^{-5} mbar) and a growth rate of 1.1 μm/h at substrate temperatures in the range 500–600°C. Carbon dopant was introduced using CBr_4; C incorporation shows little dependence on substrate temperature or V : III ratio [15]. Carbon δ-doping was carried out using a growth interrupt; the highest practicable CBr_4 flux, which gave a BEP of 2×10^{-6} mbar, was introduced during an interruption in the TEGa flux. This CBr_4 flux would give a doping level of 3×10^{20} cm^{-3} if introduced during growth under these conditions.

Secondary ion mass spectrometry (SIMS) profiling was carried out using a Cameca ims 3f and the data quantified using implanted reference materials. Crater depths were measured using optical interference microscopy: layer thicknesses were cross-checked by cross-sectional transmission electron microscopy (TEM) and HRXRD.

HRXRD measurements were carried out using a Philips high-resolution X-ray diffractometer with a 4-reflection Ge220 monochromator using Cu $K\alpha_1$ radiation. The 400 Bragg reflection was measured along a $\langle 1\,1\,0 \rangle$ azimuth for all samples. Simulations using dynamical diffraction theory were performed assuming Vegard's law to be valid, giving a linear variation of strain with composition, and also assuming that all the carbon was present as isolated atoms occupying As lattice sites [13, 16]. The lattice parameter of "GaC" was calculated to be 4.688 Å (resulting in 17% strain) using tabulated covalent radii of the individual atoms.

3. Results and discussion

A nine period δ-doping superlattice (Table 1) was used for SIMS analysis of delta layer thickness

Table 1
Structure of the 9-period δ-doped sample, M601

	SIMS $[C]_A$ (10^{13} atoms cm^{-2})	
	Cs data	O data
50 nm undoped GaAs cap		
δ-C layer 1 (2 s interrupt)	1.40	1.23 (0.103)
100 nm undoped GaAs		
δ-C layer 2 (5 s interrupt)	1.47	1.33 (0.142)
100 nm undoped GaAs		
δ-C layer 3 (2 s interrupt)	1.30	1.13 (0.127)
100 nm undoped GaAs		
δ-C layer 4 (4 s interrupt)	1.50	1.275 (0.113)
100 nm undoped GaAs		
δ-C layer 5 (2 s interrupt)	1.32	1.14 (0.126)
100 nm undoped GaAs		
δ-C layer 6 (3 s interrupt)	1.49	1.24 (0.039)
100 nm undoped GaAs		
δ-C layer 7 (2 s interrupt)	1.28	1.16 (0.118)
100 nm undoped GaAs		
δ-C layer 8 (1 s interrupt)	1.14	1.16 (0.126)
100 nm undoped GaAs		
δ-C layer 9 (2 s interrupt)	1.29	1.20 (0.120)
250 nm undoped GaAs buffer		
C interface contamination	21	21 (by definition)
N^+ GaAs substrate		

Note: O data is averaged over a series of measurements, the standard deviation for each set of data is given in parentheses. These data were quantified against the C signal for the interface layer which was assumed to be constant for all O and Cs profiles.

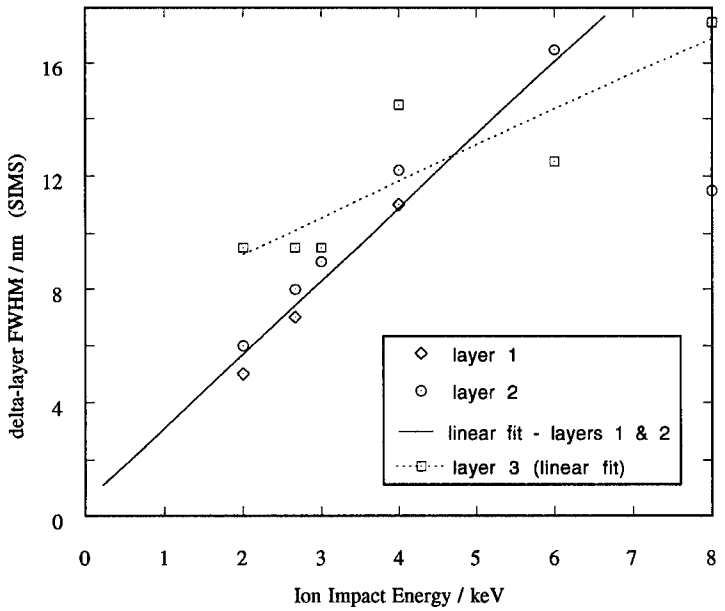

Fig. 1. Full width at half-maximum (FWHM) of SIMS profiles of three carbon delta layers as a function of ion impact energy. FWHM increases with energy and with layer depth, layers 1–3 were at depths of 50, 150 and 250 nm respectively.

and of areal carbon concentration $[C]_A$. SIMS resolution of a delta layer is limited by ion beam induced atomic mixing effects, which increase with ion beam energy and with profiled depth. Fig. 1 shows the influence of ion impact energy on the measured FWHM of the three topmost δ-layers of this sample (at depths of 50, 150 and 250 nm, respectively). The sample was sputter profiled using O^-, O_2^- and O_3^- ions at primary beam energies of 10.5 and 12.5 kV with an extraction voltage of

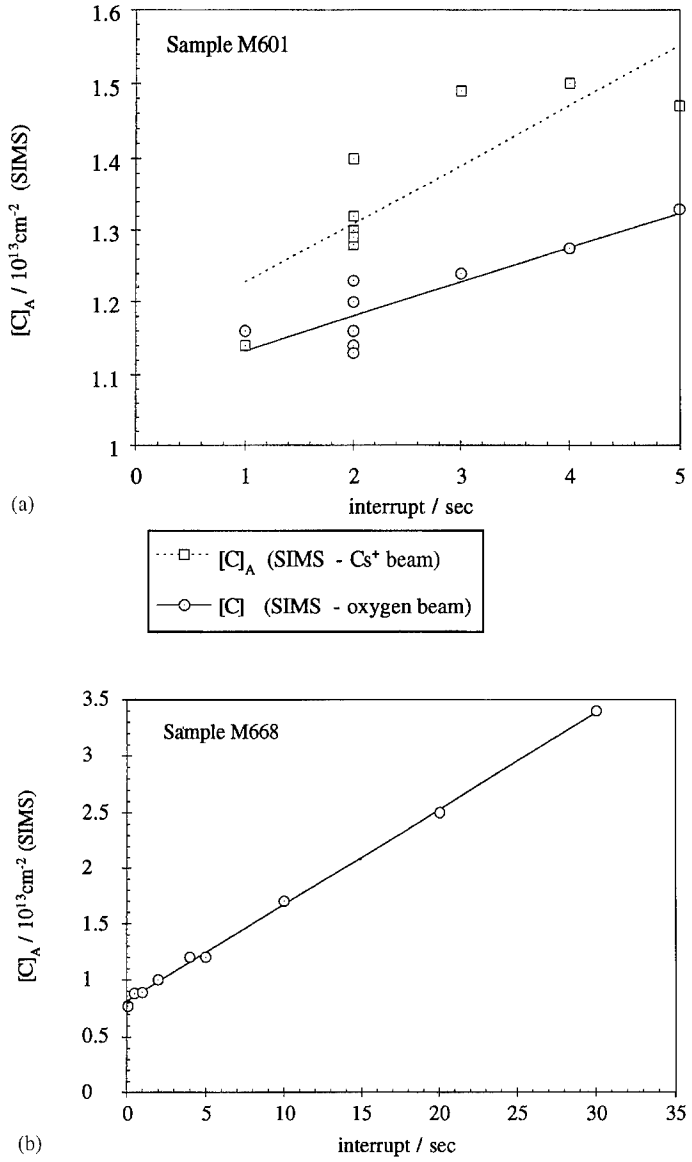

Fig. 2. Areal carbon concentration $[C]_A$ determined by SIMS for delta layers grown using CBr_4 introduced during various interrupt times. Data obtained profiling with Cs^+, O^-, O_2^- and O_3^- ions as described in the text. Sample M601 was a 9-period structure (detailed in Table 1), M668 was a 10-period sample with an extended range of interrupt times.

4.5 kV, to give ion impact energies in the range 2–8 keV. The deeper layers have a broader FWHM due to atomic mixing and surface roughening effects, particularly layer 3, while those measured at lower energy are sharper. The first layer has a FWHM of 5 nm at the lowest energy with a linear increase at higher energies. Lower ion impact energies are not easily achieved. Extrapolating the data set for layers 1 and 2 to zero impact energy suggests that the actual FWHM is less than 1 nm, which is in agreement with the results of HRXRD [13]. Only the data from layers close to the sample surface can be analysed in this way. The data for layers 3 and beyond show little dependence on impact energy as other SIMS induced profile distortions begin to dominate the measured delta layer widths.

Table 1 shows details of the nine period δ-doping superlattice and the results of SIMS analysis of areal carbon concentration $[C]_A$. To achieve a compromise between depth resolution and sensitivity to carbon the first analysis was performed at a slow sputter rate using Cs^+ primary ion bombardment and negative secondary ion detection, under these conditions the SIMS carbon background is about $5 \times 10^{17}\,cm^{-3}$. These data were quantified by calibration against ion-implanted standards and the value for $[C]_A$ derived by integrating the counts under the peak for each delta-doped layer. Broadening of the SIMS peak with depth gives a lower peak value but does not effect the value of $[C]_A$. The depth and the integrated signal for the interface contamination layer were then used to calibrate a second series of measurements which were taken using O^-, O_2^- and O_3^- ions as described above. The average values for these measurements are given; note that sputtering with oxygen gives improved depth resolution but lower sensitivity to carbon. Every alternate δ-layer was a reference layer with a 2 s interrupt so the variation of SIMS sensitivity and resolution with sputtered depth could be monitored; however, $[C]_A$ for the first layer is artificially high because of surface C contamination. No systematic variation in $[C]_A$ was found with layer depth or with primary ion species and energy.

As shown in Fig. 2a there is an approximately linear dependence of $[C]_A$ on interrupt time over the range studied but with a large offset term for zero interrupt. This would imply that there is an initial surface coverage of C from CBr_4 which increases relatively slowly during an extended interrupt. A second sample was grown with a range of interrupt times from 0.1 to 30 s. The results of SIMS profiling using 10 kV O_3^- ions are summarised in Fig. 2b. There is clearly a linear dependence on exposure time, with no evidence of saturation at higher coverage. This linear dependence appears to extend to times less than 1 s but the flux response is probably limited by pressure transients in the gas line rather than by valve switching. For both samples the value of $[C]_A$ for zero interrupt time is close to the calculated level of $8.5 \times 10^{12}\,cm^{-2}$ per monolayer for GaAs homogeneously doped at $3 \times 10^{20}\,cm^{-3}$, the expected level for these TEGa and CBr_4 fluxes.

SIMS values of $[C]_A$ are in reasonable agreement with those measured by other techniques. SIMS profiling using Cs^+ gave values between 1.3 and $2.0 \times 10^{13}\,cm^{-2}$ for a series of samples with a 2–3 s interrupt. As reported previously [13], HRXRD gave a value for $[C_{As}]_A$ of $1.5 \times 10^{13}\,cm^{-2}$ for a 50 period doping superlattice. IR absorption spectra showed a $[C_{As}]_A$ concentration of $1.1 \times 10^{13}\,cm^{-2}$ per δ-layer with no detectable hydrogen passivation, in agreement with Hall and ECV measurements of areal acceptor concentration of $1.1 \times 10^{13}\,cm^{-2}$ per δ-layer.

The C δ-doping superlattices grown for HRXRD analysis comprised 50 carbon δ-layers separated by 50 nm GaAs spacers. Comparison of measured and simulated HRXRD data for such a structure (sample M533, with C doping during 2 s growth interrupts) gave an excellent fit for a simulation which was obtained using a rectangular doping profile with an areal carbon concentration $[C_{As}]_A$ of $1.5 \times 10^{13}\,cm^{-2}$ and a thickness t_d of 5 Å [13, 16]. Decreasing t_d to one monolayer (2.8 Å) while $[C_{As}]_A$ was kept constant gave an equally good fit while increasing t_d to 10 Å with the same value of $[C_{As}]_A$ gave a slightly worse fit. Replacing the abrupt doping profile in the simulation with a triangular profile (linear spreading on both sides) showed that the spread of the δ-layers was less than 10 Å. To improve the fit a random period fluctuation of 2% was included in this simulation which broadened the satellite lines. Greater precision in

determining the δ-layer thickness would be possible only if more orders of satellites could be detected since it is the high-order satellites that result from abrupt interfaces [17].

4. Conclusions

We have demonstrated carbon delta-doping in GaAs grown by CBE. Areal C concentrations of up to 3.5×10^{13} cm^{-2} per delta layer were obtained using CBr_4 introduced during a growth interrupt. The results of SIMS profiling indicate that there is a rapid initial surface coverage of C from CBr_4 and a relatively slow increase during an extended interrupt. The delta layers were confined to a planar sheet less than 1 nm thick as measured by HRXRD and SIMS.

Acknowledgements

The authors would like to thank L. Hart and R.C. Newman for helpful discussions and to acknowledge the EPSRC for their financial support.

References

[1] T.H. Chiu, J.E. Cunningham, J.A. Ditzenberger, W.J. Jan and S.N.G. Chu, J. Crystal Growth 111 (1991) 274.
[2] M. Sugimoto, I. Ogaru, H. Saito, A. Yasuda, K. Kurihara, H. Kosaka and T. Numai, J. Crystal Growth 127 (1993) 1.
[3] M. Sugimoto, H. Kosaka, K. Kurihara, I. Ogaru, T. Numai and K. Kasahara, Electron. Lett. 28 (1993) 385.
[4] J. Nagle, R.J. Malik and D. Gershoni, J. Crystal Growth 111 (1991) 264.
[5] T.B. Joyce, S.P. Westwater, P.J. Goodhew and R.E. Pritchard, J. Crystal Growth 164 (1996) 371.
[6] C.R. Abernathy, Mater. Sci. Eng. R14 (1995) 203–254.
[7] M.J. Ashwin, B.R. Davidson, K. Woodhouse, R.C. Newman, T.J. Bullough, T.B. Joyce, R. Nicklin and R.R. Bradley, Semicond. Sci. Technol. 8 (1993) 625.
[8] T.B. Joyce, T.J. Bullough and T. Farrell, Appl. Phys. Lett. 65 (1994) 2193.
[9] C.R. Abernathy, S.J. Pearton, F. Ren, W.S. Hobson and P.W. Wisk, J. Vac. Sci. Technol. A 12 (1994) 1186.
[10] M.G. Peters, B.J. Thibeault, D.B. Young, A.C. Gossard and L.A. Coldren, J. Vac. Sci. Technol. B 12 (1994) 3075.
[11] E.F. Schubert, in: Doping in III–V Semiconductors, Cambridge Studies in Semiconductor Physics and Microengineering, Vol. 1 (Cambridge University Press, Cambridge, 1993) ch. 11.
[12] F.A. Reboredo and C.R. Proetto, Phys. Rev. B 47 (1993) 4655.
[13] B.R. Davidson, L. Hart, R.C. Newman, T.B. Joyce and T.J. Bullough, J. Crystal Growth 164 (1996) 383.
[14] T.B. Joyce, T.J. Bullough, P. Kightley, Y.R. Xing and P.J. Goodhew, J. Crystal Growth 120 (1993) 206.
[15] T.J. de Lyon, N.I. Buchan, P.D. Kirchner, J.M. Woodall, G.J. Scilla and F. Cardone, Appl. Phys. Lett. 58 (1991) 517.
[16] L. Hart, M.R. Fahy, R.C. Newman and P. Fewster, Appl. Phys. Lett. 62 (1993) 2218.
[17] L. Hart, P.F. Fewster, M.J. Ashwin, M.R. Fahy and R.C. Newman, J. Phys. D: Appl. Phys. 28 (1995) A154.

ELSEVIER

Journal of Crystal Growth 175/176 (1997) 383–386

JOURNAL OF CRYSTAL GROWTH

Strain compensation in highly carbon doped GaAs/AlAs distributed Bragg reflectors

A. Mazuelas*, R. Hey, M. Wassermeier , H. T. Grahn[1]

Paul-Drude-Institut für Festkörperelektronik, Hausvogteiplatz 5–7, D-10117 Berlin, Germany

Abstract

We use molecular beam epitaxial growth in order to synthesize strain compensated GaAs/AlAs-based distributed Bragg reflectors (DBR). The strain compensation is achieved by introducing carbon doping up to densities of about 2×10^{20} cm^{-3}. The residual strain with respect to the GaAs substrate can be reduced to less than 1×10^{-4}. X-ray topographs of the strain compensated DBRs showed no misfit dislocations, thus proving that the critical thickness for the formation of dislocations in strain compensated DBRs is much larger than in the undoped and Be-doped cases. X-ray reciprocal space mapping reveals a structural degradation of the DBR : C for thicknesses above 2.5 μm and the defect density is found to be much lower in AlAs : C than in GaAs : C. We study the effect of the strain compensation on the morphology and the optical reflectivity of the DBRs.

PACS: 61.10.Lx; 61.72.Vv; 68.55.Bd

Keywords: Strain compensation; High C doping; Distributed Bragg reflectors; Molecular beam epitaxy

1. Introduction

Distributed Bragg reflectors (DBRs) are a crucial part of complex optoelectronic devices such as vertical cavity surface emitting lasers (VCSEL). The DBRs must be rather thick (typically several micrometeres), which, altogether with the lattice mismatch results in the lattice relaxation by the formation of misfit dislocations degrading the structure [1]. Carbon acts as a p-type dopant in GaAs and AlAs. At the same time, it produces a strong contraction of the lattice [2]. Therefore, we have used carbon to produce highly doped p-type DBRs, which are simultaneously strain-compensated. We study the influence of the strain compensation on the structural quality of the layers, and on the optical reflectivity.

* Corresponding author: Fax: + 49 30 203 77 201; e-mail: mazuelas@pdi.wias-berlin.de.

[1] On leave from: Research Center for Quantum Effect Electronics, Tokyo Institute of Technology, 2-12-1 O-okayama, Meguro-ku, Tokyo 152, Japan.

0022-0248/97/$17.00 Copyright © 1997 Published by Elsevier Science B.V. All rights reserved
PII S0022-0248(96)00923-2

2. Experimental procedure

GaAs/AlAs-based DBRs layers were grown by soild source molecular beam epitaxy (MBE) on (0 0 1) GaAs substrate at a substrate temperature of 505°C and a beam equivalent pressure (BEP) ratio of 15 for GaAs. The growth rate was 1 μm/h for GaAs and 0.2 μm/h for AlAs. We used a resistively heated graphite filament as the carbon source. It was operated near its maximum power of about 570 W. The DBRs consist of 10 or 20 pairs of 82.7 nm AlAs and 69.6 nm GaAs for an operation wavelength of 980 nm. The doping level is about 2×10^{20} cm^{-3} in AlAs and 2×10^{19} cm^{-3} in GaAs. The X-ray diffraction (XRD) measurements were performed with a double- and a triple-crystal diffractometer using CuKα_1 radiation. The simulations of the rocking curves were performed using a fully dynamical model. The X-ray topographs (XRT) were obtained with a double-crystal camera equipped with a curvable Si monochromator [3]. The optical reflectivity was measured with a standard set up and by ellipsometry.

3. Strain compensation and critical thickness

In previous publications we reported on the best growth conditions for GaAs : C [4] and AlAs : C for a wide range of growth parameters. We also showed that the carbon incorporation in the lattice which results in a strong contraction of the average lattice parameter, can be used to compensate the strain in GaAs : C/AlAs : C DBRs [5]. The net reduction of the average strain due to the carbon doping can easily be seen in XRD rocking curves (Fig. 1). The shift of the zeroth-order peak is such that it overlaps with the substrate peak. This indicates that the strain has been totally compensated.

In the case of perfect strain compensation the critical thickness for the formation of misfit dislocations becomes (theoretically) infinitely large, since the misfit approaches zero. We measured double-crystal XRT in order to find out if the DBRs were strained or relaxed. Undoped DBRs do not exhibit any relaxation as long as there are only 10 periods of GaAs/AlAs layers with a total thickness of about 1.5 μm (not shown). However, for undoped, 20 period DBRs relaxation is clearly observed by the formation of misfit dislocations as shown in Fig. 2a. A similar relaxation is observed when Be doping is used [6]. When a large carbon-doping density is used in a 20 period DBR : C, no misfit dislocations are observed as shown in Fig. 2b. For the obtained residual strain (smaller than 1×10^{-4}) the theoretical critical thickness [7] is about 30 times larger than that of the undoped case.

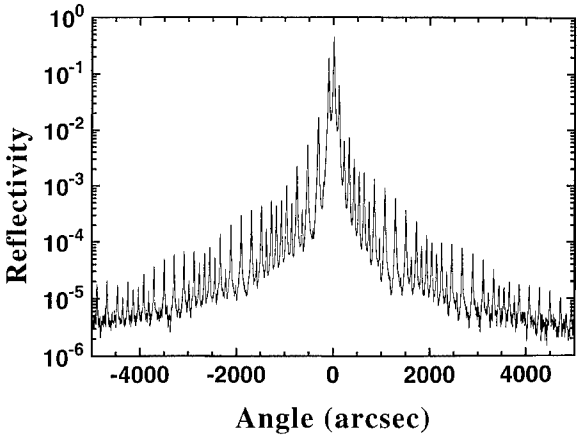

Fig. 1. Experimental rocking curves around the (0 0 2) reflection of a 20-pair GaAs : C/AlAs : C DBR, which is perfectly strain-compensated.

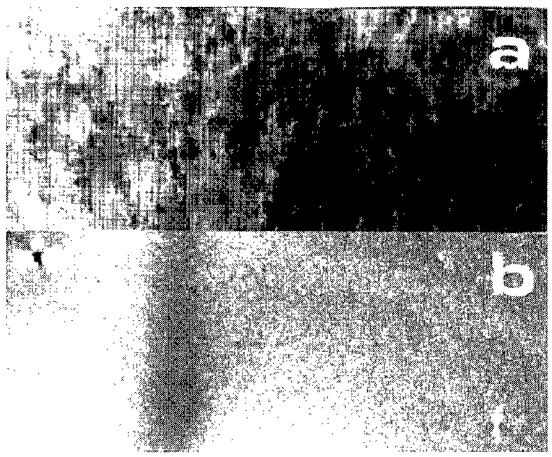

Fig. 2. X-ray topographs of two different 20-pair DBRs. While the undoped DBR in (a) contains a high density of misfit dislocations (relaxed), the highly doped strain compensated DBR : C in (b) is free of misfit dislocations (unrelaxed). Each image corresponds to an area of 5×2 mm^2.

Rocking curves of C-doped 20-pair DBRs repeatedly show broader satellite peaks compared to C-doped 10-pair DBRs. We performed reciprocal space mapping for these structures, and the results are shown in Fig. 3. For the 10-pair DBR : C (a), the peaks are sharp, both in the θ and Ω directions. However, for the 20-pair DBR :C (b), the peaks are clearly broadened. The experimentally observed peak broadening indicates a certian degradation of the crystalline quality, i.e., an increased spread of the microscopic tilting of the atomic planes. The measurement in the same sample of the (0 0 2) reflection (Fig. 1), which is a quasi forbidden reflection for GaAs and sensitive only to AlAs, showed that the structure is of high quality. This means that most of the crystalline defects are contained in the GaAs : C layer.

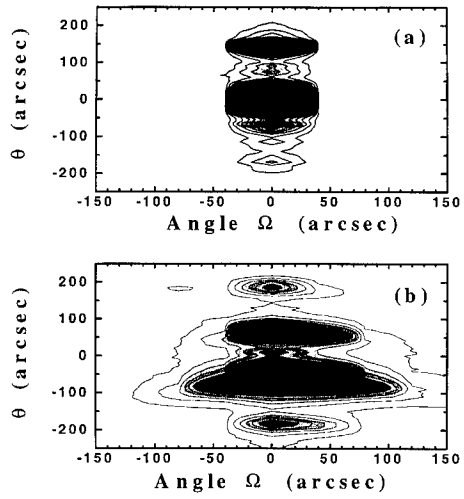

Fig. 3. Reciprocal space mapping of a doped 10-pair DBR : C in (a) and of a doped 20-pair DBR : C in (b). Broadening of the peaks is clearly observed in both, the θ and Ω, directions for the 20-pair DBR : C in (b).

4. Morphology and optical reflectivity

The surface morphology was studied by atomic force microscopy (AFM). Fig. 4 shows AFM images of two 20 pair DBRs. The images were recorded over an area of $3 \times 3\ \mu m^2$ in the constant force contact mode. The peak to valley values of the surface roughness are 17 nm for the undoped DBR (Fig. 4a) and 25 nm for the highly carbon doped DBR (Fig. 4b), while the root mean square (RMS) values are 1.2 and 3 nm, respectively. The comparison of these values should be done with care, since there are two different factors involved: the relaxation and the high doping. While the undoped DBR is relaxed, the doped DBR is unrelaxed, but contains a carbon concentration as high as $2 \times 10^{20}\ cm^{-3}$. This could explain the increase of the surface roughness compared to the undoped DBR.

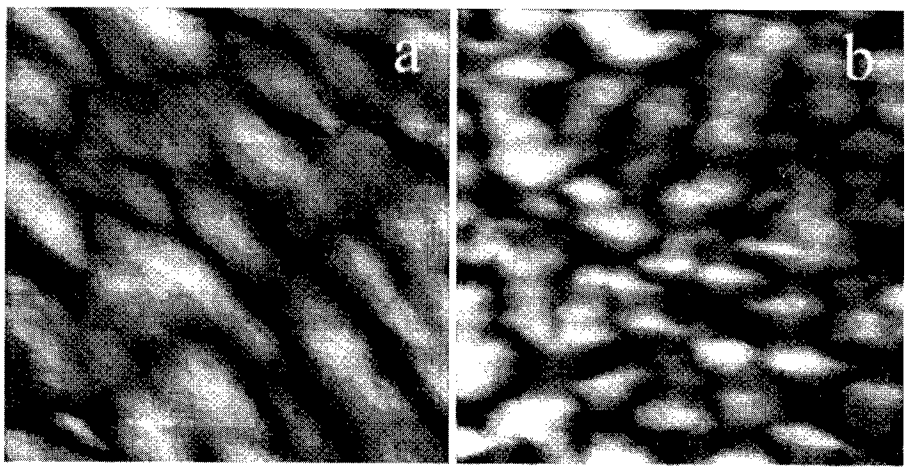

Fig. 4. AFM images of a 20-pair undoped GaAs/AlAs DBR (a) and a 20-pair highly doped GaAs : C/AlAs : C DBR (b). The grey scale covers the peak to valley value of 17 nm for (a) and 25 nm for (b). Each image corresponds to an area of $3 \times 3\ \mu m^2$.

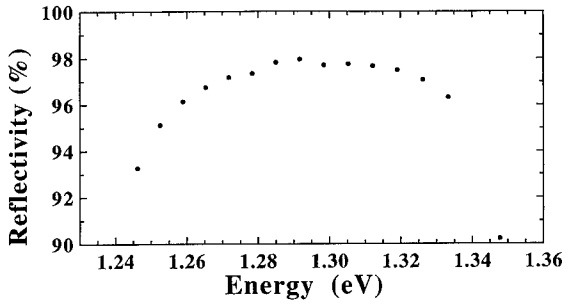

Fig. 5. Absolute optical reflectivity of a 20-pair highly doped strain compensated GaAs : C/AlAs : C DBR measured by ellipsometry. The energy scale is slightly shifted to higher energies due to the large angle of incidence.

The optical reflectivity was measured in a standard configuration in order to determine the stop band position, which was repeatedly in good agreement with the intended position, i.e., centered at 980 nm. This means that a good control of the quarter-wavelength layer thickness is obtained. The absolute reflectivity was measured by ellipsometry. We find that for the 10-pair strain compensated DBRs the absolute reflectivity is 93%, while for the undoped 10-pair case it is 96%. For the 20-pair strain compensated DBRs the absolute reflectivity was 98% (Fig. 5), only 1% lower than for the undoped 20-pair case. The lowering of the reflectivity can be explained by both, the larger interface roughening in these structures (as found by AFM) as well as by the interband absorption in highly doped material.

5. Conclusions

We have used MBE growth to synthesize strain compensated GaAs/AlAs DBRs. The strain compensation is obtained by high carbon doping and produces an increase of the critical thickness compared to the undoped case. We found that there is some structural degradation for thick DBRs. This degradation is related to defects in the GaAs : C layers, which is found to have a much higher defect density compared to the AlAs : C layers. The high carbon doping produces a slight degradation of the surface morphology as well as a slight reduction of the optical reflectivity.

Acknowledgements

We would like to thank M. Höricke for technical assistance, G. Jungk for ellipsometry measurements, B. Jenichen for support in the XRD measurements, and R. Nötzel for a critical reading of the manuscript. This work was supported in part by the Deutsche Forschungsgemeinschaft.

References

[1] B. Jenichen, R. Hey, M. Höricke and R. Köhler, J. Appl. Phys. 73 (1990) 2220.
[2] T.J. deLyon, J.M. Woodall, M.S. Goorsky and P.D. Kirchner, Appl. Phys. Lett. 56 (1990) 1040.
[3] B. Jenichen, R. Köhler and W. Möhling, J. Phys. E: Sci. Instrum. 21 (1988) 1062.
[4] H. Nörenberg, A. Mazuelas, K. Hagenstein, R. Hey and H.T. Grahn, Appl. Phys. A 62 (1996) 459.
[5] A. Mazuelas, H. Nörenberg, R. Hey and H.T. Grahn, Appl. Phys. Lett. 68 (1996) 806.
[6] R. Hey, A. Paraskevopoulos, J. Sebastian, B. Jenichen, M. Höricke and S. Westphal, in: Inst. Phys. Conf. Ser., Vol. 136, Eds. H.S. Rupprecht and G. Weimann (IOP, Bristol, 1994) p. 821.
[7] J.W. Matthews and A.E. Blakeslee, J. Crystal Growth 27 (1974) 118.

ELSEVIER

Journal of Crystal Growth 175/176 (1997) 387–392

JOURNAL OF CRYSTAL GROWTH

Improving the etched/regrown GaAs interface by in-situ etching using tris-dimethylaminoarsenic

N.Y. Li*, Y.M. Hsin, P.M. Asbeck, C.W. Tu

Department of Electrical and Computer Engineering, University of California at San Diego, La Jolla, California 92093-0407, USA

Abstract

In this study we have investigated, for the first time, the morphological and electrical properties of the in-situ etched/regrown interfaces of GaAs and $Al_xGa_{1-x}As$ using tris-dimethylaminoarsenic (TDMAAs) in a chemical beam epitaxy (CBE) chamber. The TDMAAs in-situ etching condition of GaAs is optimized according to the analysis of atomic force microscopy (AFM) and capacitance–voltage (C–V) carrier profiles. The TDMAAs etch rate of GaAs increases from 40 to 135 nm/h by increasing the substrate temperature from 550°C to 700°C, but the etched surface morphology of GaAs on a patterned substrate becomes rougher at higher etching temperatures. A smooth surface morphology of GaAs with an interface state density of 1.4×10^{11} cm^{-2} can be obtained at a lower in-situ etching temperature of 550°C. TDMAAs is shown to be an effective and promising precursor for in-situ etching of GaAs, thus providing a clean etched/regrown interface for novel device applications.

1. Introduction

As is well known, the presence of interface states at an etched/regrown interface or an epilayer/substrate interface is harmful for device performance. For example, in field-effect transistors (FET), these interface states usually increase the leakage current, resulting in a poor pinch-off characteristic and a lower breakdown voltage. Therefore, the interface-state density must be as low as possible to obtain excellent device performance. Today, multiple processes of ex-situ etching and passivation of semiconductor heterostructures are commonly used before regrowth to improve the performance of advanced electronic and optoelectronic devices, but one cannot expect a clean etched/regrown interface by these ex-situ processes due to possible contaminations from the atmosphere. Therefore, in-situ etching prior to regrowth would be very helpful for obtaining a clean etched/regrown interface. Recently, many research groups have reported studies of in-situ etching of III–V compounds using different gaseous sources. Mui et al. [1] reported high-quality etched/regrown GaAs interfaces using an in-situ Cl_2 etching process, but a complicated interlocking system of separate growth and etching chambers was used. Also Tappura et al. [2] reported that in-situ

* Corresponding author.

0022-0248/97/$17.00 Copyright © 1997 Elsevier Science B.V. All rights reserved
PII S0022-0248(96)00827-5

cleaning of GaAs surface in MBE using an atomic hydrogen plasma can obtain high quality interfaces. Tsang et al. [3] reported in-situ etching of GaAs and InP using $AsCl_3$ and PCl_3 prior to regrowth in the same chemical beam epitaxy (CBE) chamber; therefore, possible contaminations in the etched/regrown interface can be minimized. However, Cl_2 decomposed from $AsCl_3$ or PCl_3 is corrosive and may etch filaments in the growth chamber, so the long term use of $AsCl_3$ or PCl_3 could be a concern. Recently, Tateno and Kohama [4] and Hou et al. [5] found that gaseous carbon doping sources, such as CCl_4 and CBr_4, can etch GaAs and AlAs in organometallic vapor phase epitaxy (OMVPE), but carbon impurities dissociated from these doping sources during in-situ etching process would contaminate the etched/regrown interface. Therefore, an etching source that has no direct bonds to carbon and halogen (Cl and Br) would be highly desirable.

Tris-dimethylaminoarsenic (TDMAAs), with As directly bonded to N, is such a promising source. Since there are no As–H bonds, TDMAAs is expected to be less toxic than arsine (AsH_3) [6]. Due to the lack of direct As–C bonds, TDMAAs has also been successfully used in metalorganic molecular beam epitaxy (MOMBE)/CBE of (Al,Ga)As with a lower carbon incorporation [7–10]. Recently, Asahi et al. [11–13] and Tu et al. [14] found that TDMAAs has an etching effect on GaAs, but it is not clear whether the etched/regrown GaAs interface can be improved using TDMAAs. This characteristic should be realized if the TDMAAs in-situ etching technique is to be used for novel device applications. The purpose of this work is therefore to investigate the TDMAAs etched/regrown interfaces of GaAs and $Al_xGa_{1-x}As$. Our results demonstrate that clean etched/regrown interfaces and improved current–voltage (I–V) characteristics of etched/regrown p–n $Al_xGa_{1-x}As$ junctions can be obtained.

2. Experimental procedure

The in-situ etching and regrowth experiments were performed in a modified Perkin–Elmer 425B CBE system. TDMAAs was carried by hydrogen and transported into the CBE chamber through an ultrahigh vacuum leak valve. The H_2 flow rate was varied from 2 to 4 sccm to adjust the TDMAAs flux, corresponding to an As incorporation rate of 1.2 to 2.0 monolayer per second (ML/s), as determined from As-induced intensity oscillations of reflection high-energy electron diffraction (RHEED) on a Ga-rich GaAs surface. 250 nm-thick SiO_2 films were deposited on epi-ready semi-insulating (1 0 0) GaAs substrates as mask for determining the TDMAAs etch rate of GaAs at different substrate temperatures by scanning electron microscopy (SEM). A Dektak stylus profiler is also used to confirm the etch rate of GaAs obtained from SEM. The surface morphology and roughness were examined by atomic force microscopy (AFM).

Triethylgallium (TEGa), tertiarybutylarsine (TBA) or arsenic (As_4), and silicon tetrabromide ($SiBr_4$) or disilane (Si_2H_6) were used to regrow n-type GaAs epilayers on n^+ Si-doped (1 0 0) GaAs substrates, some of which were etched in-situ by TDMAAs. The regrowth temperature and V/III ratio were 510°C and 1.3, respectively. Here the V/III incorporation rate ratios were determined by group III- and group V-induced RHEED intensity oscillations [15]. The free carrier concentration of the regrown n-GaAs films was between 2×10^{17} and $3\times10^{17}\,cm^{-3}$. Capacitance–voltage (C–V) measurements using a HP-4284A LCZ meter were performed to measure the carrier profile for evaluating the quality of the etched/regrown GaAs interfaces.

3. Results and discussion

Patterned GaAs substrates with SiO_2 as the mask and unpatterned GaAs substrates, mounted side by side on the same Mo block, were exposed to the TDMAAs flux at substrate temperatures from 550°C to 700°C to calibrate the etch rate of GaAs, and investigate the TDMAAs etching effect on the surface morphology. The flow rate of the H_2 carrier gas for TDMAAs was kept at 4 sccm, and the leak valve setting, which was adjustable from 0 to 270, was fixed at 100 (a.u.) during the in-situ TDMAAs etching of GaAs. Substrate rotation ($\sim$6 rpm) was used to alleviate the effect of the directional nature

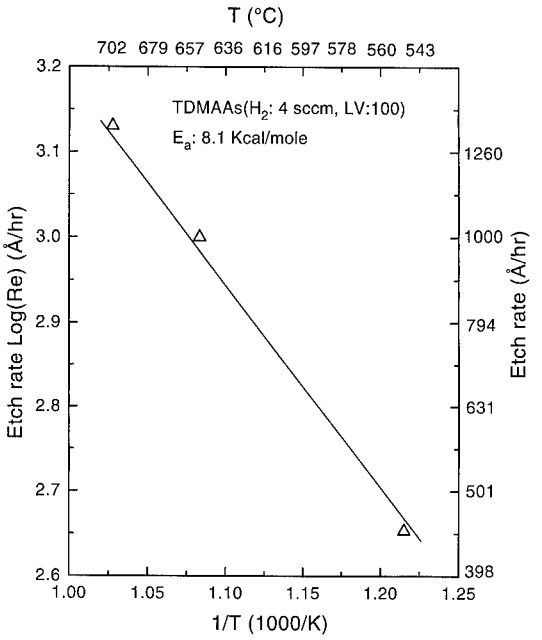

Fig. 1. The TDMAAs etch rate of GaAs as a function of substrate temperature. The H_2 flow rate for carrying TDMAAs was 4 sccm and the leak valve setting was 100.

of the TDMAAs flux. Fig. 1 shows the TDMAAs etch rate of GaAs as a function of etching temperature. The etch rate increases exponentially from 40 to 135 nm/h with an increasing substrate temperature from 550°C to 700°C. If the etching temperature is below 550°C, e.g. 500°C, the etch rate is too slow to be clearly measured in SEM. An activation energy (E_a) of 8.1 Kcal/mol is deduced from Fig. 1 and is very close to previous results (E_a = 7.4 Kcal/mol) reported by Villaflor et al. [12]. So far the exact etching mechanism using TDMAAs is still not clear, but it is possibly related to the amino species in TDMAAs [12–14].

Fig. 2 shows the etched GaAs surface morphology examined by AFM. On non-patterned GaAs substrates etched in the substrate temperature range 550–700°C, a very smooth surface morphology can be obtained, as shown in Fig. 2(a) (at 700°C for 1 hour). The root-mean-square (RMS) surface roughness over an area of 1 μm^2 of these samples is about 0.3 to 0.6 nm. The TDMAAs-exposed area of patterned GaAs substrates, however, shows a much rougher surface morphology, as shown in Fig. 2(b) for a 100-μm-wide stripe of a patterned GaAs substrate. This sample was etched at 700°C and has a RMS roughness of 10.2 nm. Lowering the etching temperature improves the surface morphology. At 550°C, the RMS roughness is 2.2 nm, as shown in Fig. 2(c), but it is still slightly rougher than that of non-patterned GaAs substrates. In our previous study using SEM [16], we also found the same phenomena. For the selective-area growth in the stripe opening of patterned GaAs substrates, the surface morphology is always textured, but that on non-patterned GaAs substrates is very smooth. Marx et al. [13] reported that lowering the TDMAAs/TEGa (V/III) ratio at a higher growth temperature of 650°C can improve the surface morphology of GaAs grown on non-patterned GaAs substrates. Therefore, we speculate that the much rougher surface observed on the stripe opening of patterned substrates is possibly due to the locally increased TDMAAs flux on the surface of small openings.

C–V measurements were performed on Au/n–GaAs Schottky diodes to study the electrical property of etched/regrown interfaces of GaAs with different sample preparations, as shown in Table 1. First, a 0.5-μm-thick *n*-type GaAs ($n = 2–4 \times 10^{17}$ cm^{-3}) buffer layer was grown with TEGa, As_4 and Si_2H_6 on an n^+ Si-doped GaAs (1 0 0) substrate ($n = 2–4 \times 10^{18}$ cm^{-3}) at 510°C. This sample was then taken out of the CBE chamber and exposed to air for one day. It was then divided into six pieces, labeled A, B, C, D, E, and F. Sample C is a control sample, which was etched 20 nm ex-situ by reactive-ion etching (RIE). It and Samples A and B were rinsed in acetone, methanol, and de-ionized water before being loaded into the CBE system. Prior to regrowth, Sample A was exposed to TDMAAs alone, and Samples B and C were exposed to an As_4 flux at 600°C to desorb the oxide layers. After oxide desorption Sample A was etched about 65 Å in-situ by TDMAAs (10 min exposure at 600°C). Sample D was exposed to a TBA flux at 600°C, and Samples E and F were exposed to TDMAAs at 650°C and 550°C, respectively. Here, the etched depth is estimated from Fig. 1. A 0.15-μm-thick *n*-GaAs ($n = 2–3 \times 10^{17}$ cm^{-3}) was regrown subsequently on these six samples to form the

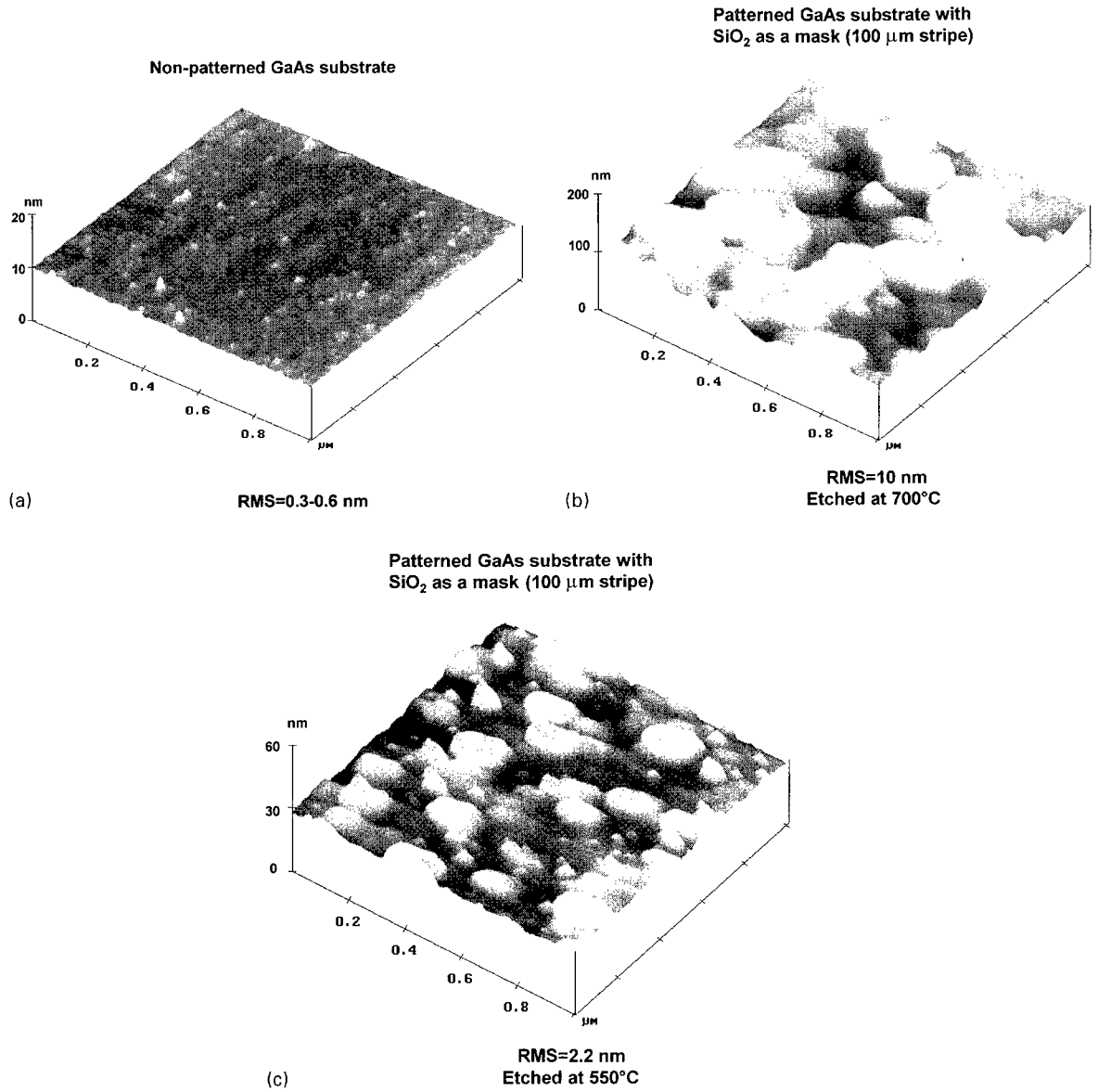

Fig. 2. AFM images of the TDMAAs etched GaAs surface (a) etched at 550–700°C on non-patterned GaAs substrates (RMS = 0.3–0.6 nm) (b) etched at 700°C (RMS = 10 nm) and (c) etched at 550°C (RMS = 2.2 nm) in 100 μm-wide stripes of patterned GaAs substrates.

etched/regrown interfaces. Finally a 150-nm-thick Au was evaporated to form Schottky contacts.

Fig. 3 shows C–V carrier concentration profiles around the etched/regrown interfaces of Samples A, B, C, and F. It is quite clear that the carrier depletion across the interface depends strongly on the sample preparation prior to regrowth. The interface-state densities (D_{int}) were estimated by integrating the carrier profiles, and they are 3.9×10^{11}, 1.1×10^{12}, and 2×10^{12} cm^{-2} for Samples A, B, and C, respectively. Sample C has the largest D_{int} due to damage from RIE etching. Sample A has the lowest

D_{int} among these three samples, indicating a clean interface can be achieved by the TDMAAs in-situ etching process, compared to the conventional oxide desorption process using As_4. The D_{int} in Sample B is about three times higher than that in Sample A. At first we suspect this high D_{int} is probably due to the impurities originating from the arsenic cell, but a similar result is obtained for Sample D ($D_{int} = 9.4 \times 10^{11}$ cm^{-2}), as shown in Table 1. Therefore, we confirm that these higher D_{int} are from residual impurities on the surface of GaAs during the ex-situ process, and they cannot be effectively removed during the conventional oxide desorption process.

The D_{int} of Sample A, however, is much higher than the result reported by Mui et al. [1] using an in-situ Cl_2 etching process ($D_{int} \geqslant 0.86 \times 10^{11}$ cm^{-2}). Therefore, several etching conditions were performed at different etching temperatures, etch rates and etch times to optimize the etched/regrown GaAs interfaces. As shown in Fig. 3 and Table 1, the carrier depletion across the interface is minimal ($D_{int} = 1.4 \times 10^{11}$ cm^{-2}) for sample F, etched at a lower in-situ etching temperature of 550°C for 20 min under a higher TDMAAs flux (flow rate of H_2: 4 sccm).

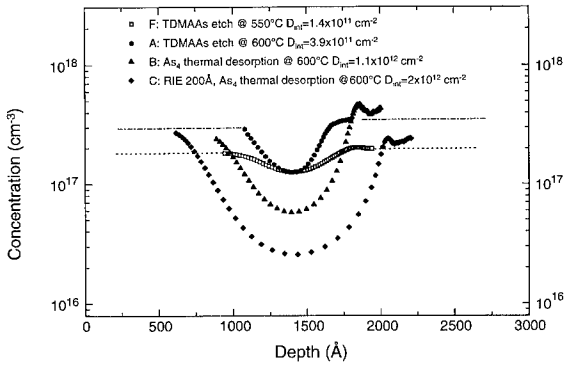

Fig. 3. *C–V* carrier profiles of four etched/regrown samples (Samples A, B, C and F) with different sample preparations.

AFM analysis mentioned above shows that the etched surface of non-patterned GaAs is very smooth (RMS = 0.3–0.6 nm) even at an etching temperature of 700°C. Therefore, surface roughness is not the origin of higher D_{int} at higher etching temperatures. Our best result obtained here, Sample F ($D_{int} = 1.4 \times 10^{11}$ cm^{-2}), is still slightly higher than Mui et al.'s result ($D_{int} \geqslant 0.86 \times 10^{11}$ cm^{-2}) [1]. We think the following reasons may contribute this higher D_{int}. Our previous study [17] reported that Si impurities were found by secondary-ion mass spectroscopy in CBE-grown undoped GaAs when the growth temperature is higher than 530°C using TDMAAs and TEGa. These Si impurities are possibly from the residual impurities in the TDMAAs source and might be deposited on the etched surface during in-situ etching process. Similar silicon accumulation at interrupted growth interfaces has been reported by SpringThorpe et al. [18] and Gary and Ebert [19] during molecular beam epitaxy. Kim et al. [20] have also observed that the use of a relatively low temperature during oxide desorption in OMVPE of GaAs can reduce the epilayer/substrate interface states. Therefore, in-situ etching of GaAs at higher temperatures such as 600°C and 650°C in this study might also introduce some background impurities, e.g. Si, C, on the etched surface, resulting in higher D_{int}. For regrowth applications the oxide desorption, in-situ etching and regrowth temperature must be kept

Table 1
Comparison of the interface state densities (D_{int}) of etched/regrown GaAs interfaces with different sample preparations prior to regrowth

Sample	Preparations prior to regrowth	D_{int} (cm^{-2})
A	TDMAAs etched at 600°C, H_2: 4 sccm, 10 min (~ 65 Å GaAs is etched)	3.9×10^{11}
B	As_4 flux at 600°C, 10 min	1.2×10^{12}
C	RIE (200 Å), As_4 flux at 600°C, 20 min	2.0×10^{12}
D	TBA flux at 600°C, 10 min	9.4×10^{11}
E	TDMAAs etched at 650°C, H_2: 2 sccm, 30 min (~ 250 Å GaAs is etched)	7.7×10^{11}
F	TDMAAs etched at 550°C, H_2: 4 sccm, 20 min (~ 150 Å GaAs is etched)	1.4×10^{11}

low but reasonable (400–550°C) to minimize the effect of dopant out-diffusion. Therefore, to obtain a reasonable etch rate and suitable etching temperature without degrading the device performance, we conclude that an in-situ etching temperature of GaAs at 550°C with an etch rate of 40 nm/h is the optimum etching condition in this study.

We have also applied this TDMAAs in-situ etching technique to improve the etched/regrown $Al_xGa_{1-x}As$ interface. Since the TDMAAs etch rate of GaAs is much faster than that of $Al_xGa_{1-x}As$ ($x \geqslant 0.25$) [21], a thin GaAs layer (50–150 Å) can be used as a cap layer on $Al_xGa_{1-x}As$. We first selectively in-situ etched away GaAs by TDMAAs at 550°C and then immediately regrew $p^+Al_{0.35}Ga_{0.65}As$ (2000 Å, $p = 8 \times 10^{19}\,cm^{-3}$) on an OMVPE-grown $Al_{0.25}Ga_{0.75}As$ layers (1700 Å, $n = 5 \times 10^{17}\,cm^{-3}$), thus eliminating the possibility of oxidation of $Al_{0.25}Ga_{0.75}As$ after etching. Compared to the epilayers directly regrown on $Al_{0.25}Ga_{0.75}As$ without the in-situ etching of GaAs, the in-situ etched/regrown $p^+Al_{0.35}Ga_{0.65}As/nAl_{0.25}Ga_{0.75}As$ junction has a much better I–V characteristics such as higher breakdown and turn on voltage. Details of this result will be reported elsewhere [22]. This result is consistent with the C–V results, indicating that TDMAAs is a suitable and promising source for obtaining clean etched/regrown interfaces of GaAs and $Al_xGa_{1-x}As$.

4. Summary

In this study, the TDMAAs etched/regrown interfaces are investigated and optimized. The TDMAAs etched GaAs surface morphologies are quite different between patterned and non-patterned GaAs substrates. We found that by lowering the in-situ TDMAAs etching temperature of GaAs, the etched/regrown GaAs and $Al_xGa_{1-x}As$ interfaces can be improved. The lowest D_{int} of $1.4 \times 10^{11}\,cm^{-2}$ reported in this study using TDMAAs is comparable to using other etching sources. Both C–V and I–V results demonstrate that TDMAAs is a suitable source in CBE for obtaining clean etched/regrown interfaces for novel device applications.

Acknowledgements

This work is supported by the US Air Force Wright Laboratory under Contract No. F33615-95-C-5441. N.Y. Li would like to thank D.H. Tomich and K.V. Smith for their help in operating the AFM.

References

[1] D.S.L. Mui, T.A. Strand, B.J. Thibeault, L.A. Coldren, P.M. Petroff and E.L. Hu, Inst. Phys. Conf. Ser. 141 (1995) 69.
[2] K. Tappura, A. Salokatve, K. Rakennus, H. Asonen and M. Pessa, Appl. Phys. Lett. 57 (1990) 2313.
[3] W.T. Tsang, R. Kapre and P.F. Sciortino, Jr., J. Crystal Growth 136 (1994) 42.
[4] K. Tateno and Y. Kohama, presented at 38th Electron. Mater. Conf., Santa Barbara, CA, 26–28 June 1996.
[5] H.Q. Hou, B.E. Hammons and H.C. Chui, presented at 38th Electron. Mater. Conf., Santa Barbara, CA, 26–28 June 1996.
[6] P. Gimmnich, A. Greiling, J.L. Lorberth, C. Thalmann, K. Rademann, G. Zimmermann, H. Protzmann, W. Stolz and E.O. Göbel, Mater. Sci. Eng. B17 (1993) 21.
[7] C.R. Abernathy, P.W. Wisk, D.A. Bohling and G.T. Muhr, Appl. Phys. Lett. 60 (1992) 2421.
[8] S. Salim, J.P. Lu, K.F. Jensen and D.A. Bohling, J. Crystal Growth 124 (1992) 126.
[9] K. Ishikura, A. Takeuchi, M. Kurihara, H. Machida and F. Hasegawa, Jpn. J. Appl. Phys. 33 (1994) L494.
[10] Y. Yoshida and M. Sasaki, J. Crystal Growth 150 (1995) 557.
[11] H. Asahi, X.F. Liu, K. Inoue, D. Marx, K. Asami, K. Miki and S. Gonda, J. Crystal Growth 145 (1994) 668.
[12] A.B. Villaflor, H. Asahi, D. Marx, K. Miki, K. Yamamoto and S. Gonda, J. Crystal Growth 150 (1995) 638.
[13] D. Marx, H. Asahi, X.F. Liu, M. Higashiwaki, A.B. Villaflor, K. Miki, K. Yamamoto, S. Gonda, S. Shimomura and S. Hiyamizu, J. Crystal Growth 150 (1995) 551.
[14] C.W. Tu, H.K. Dong and N.Y. Li, J. Crystal Growth 163 (1996) 187.
[15] H.K. Dong, S.C.H. Hung and C.W. Tu, Mater. Res. Soc. Proc. 340 (1994) 193.
[16] N.Y. Li, Y.M. Hsin, H.K. Dong, T. Nakamura, P.M. Asbeck and C.W. Tu, J. Crystal Growth 150 (1995) 562.
[17] H.K. Dong, N.Y. Li, C.W. Tu, M. Geva and W.C. Mitchel, J. Electron. Mater. 24 (1995) 69.
[18] A.J. Spring Thorpe, W.T. Moore, A. Majeed and R.W. Streater, J. Vac. Sci. Technol. B 11 (4) (1993) 1275.
[19] M.L. Gary and C.W. Ebert, J. Appl. Phys. 71 (1992) 3294.
[20] T.S. Kim, L.A. Files and L.K. Magel, Appl. Phys. Lett. 68 (1996) 2126.
[21] N.Y. Li, Y.M. Hsin, W.G. Bi, P.M. Asbeck and C.W. Tu, unpublished.
[22] Y.M. Hsin, N.Y. Li, C.W. Tu and P.M. Asbeck, Mater. Res. Soc. Proc. (1997), to be published.

ELSEVIER

Journal of Crystal Growth 175/176 (1997) 393–397

JOURNAL OF CRYSTAL GROWTH

Analysis of in-situ etched and regrown AlInAs/GaInAs interfaces

P. Chavarkar*, D.S.L. Mui, T. Strand, L.A. Coldren, U.K. Mishra

Department of Electrical and Computer Engineering, University of California, Mail Box 107, Santa Barbara, California 93106, USA

Abstract

We present the analysis of in-situ etched (using chlorine gas) and regrown AlInAs–GaInAs interfaces and the dependence of interface quality on etching temperature. Compared to GaAs-based materials, chlorine gas etching of In containing semiconductors like GaInAs and AlInAs requires higher etching temperatures (250–350°C) due to the low volatility of indium chloride which is a etch by-product. More important is the selection of an optimum etching temperature where the etch rates of both the group III etch by-products are equal. This is essential to achieve a smooth and stochiometric etched surface. The interface state density at the regrown interface depends on the morphology of the etched surface. A minimum surface roughness of 10 Å is obtained at 275°C, which also corresponds to low interface charge density of $4.52 \times 10^{11}/cm^2$ and mid-gap interface state density of $3 \times 10^{11}/cm^2$ eV at the AlInAs/GaInAs interface. The dependence of interface quality on the etched surface morphology is explained in terms of disorder-induced gap state (DIGS) model as proposed by Hasegawa and co-workers. A comparison of the regrown interface with as-grown AlInAs/GaInAs interface shows only a minor degradation, indicating the suitability of this technique for in-situ processing in the AlInAs/GaInAs/InP material system.

PACS: 71.55.Eq; 73.20. – r; 73.40.Kp; 81.15.Hi

Keywords: Molecular beam epitaxy; In-situ processing; Chlorine gas etching; Interface states; AlInAs/GaInAs

1. Introduction

Epitaxial regrowth has been used in the recent years for the fabrication of novel electronic and optoelectronic devices. It has also been used to improve the performance of existing devices and for monolithic integration of electronic and optoelectronic devices on the same substrate [1, 2]. This process often involves etching and selective area regrowth on previously grown epitaxial layers. In many cases a part of the device is regrown, thus making the regrown interface a performance-determining factor. It has been observed that carrier depletion occurs at this interface due to the presence of impurities and interface states [3, 4]. Also in the case of epilayers etched ex situ, oxidation of the exposed surface has to be prevented by suitable chemical passivation. This problem is

* Corresponding author. Fax: + 1 805 893 3262; e-mail: prashant@nemesis.ece.ucsb.edu.

0022-0248/97/$17.00 Copyright © 1997 Elsevier Science B.V. All rights reserved
PII S0022-0248(96)00934-7

aggravated in the case of regrowth on ternary semiconductors and Al-containing semiconductors as proper desorption of their oxides is difficult. An all in-situ etch and regrowth process is therefore required to achieve a high-quality regrown interface.

High electron mobility transistors (HEMTs) and heterostructure bipolar transistors (HBTs) fabricated in the AlInAs/GaInAs material system have shown superior performance compared to their GaAs-based counterparts. Further improvements in their performance by using epitaxial regrowth for surface passivation in HEMTs and for non-alloyed contacts to reduce parasitics in both HEMTs and HBTs is possible. To exploit the full potential of epitaxial regrowth, optimization of the interface quality of the etched-regrown interface in the AlInAs/GaInAs material system is necessary.

In-situ etch and regrowth of GaAs has been investigated before [5–7]. Saitoh et al. [8] have investigated the effects of in-situ growth interruptions on AlInAs/GaInAs interfaces by C–V characterization. Epitaxially regrown AlInAs/GaInAs HEMTs have been demonstrated previously, but the regrowth was done after selectively etching the existing epilayers to the InP substrate [9, 10]. The oxide on the etched InP substrate can be easily desorbed under arsenic overpressure before regrowth. However, this is not possible if the regrowth has to commence on a GaInAs or AlInAs layer. This problem can be solved by using an all in-situ etch and regrowth process. We have recently demonstrated a AlInAs/GaInAs HEMT with selective area AlInAs overgrowth for epitaxial passivation using an all in-situ chlorine gas etch and MBE regrowth process [11]. To the best of our knowledge, characteristics of in-situ etched and regrown AlInAs/GaInAs interfaces have not been investigated.

2. In-situ processing system

The all UHV etching and regrowth system used here consists of a dry etching chamber connected to a MBE growth chamber through a high-vacuum transfer tunnel. The base pressure of the dry etching chamber is 1×10^{-8} Torr. The chamber is equipped with a heater stage for thermal gas etching and an Evenson microwave cavity which can be used to crack the chlorine gas. The etching chamber is equipped with an Ar ion gun which can be used for ion-beam assisted etching. The Ar ions are generated by a hollow cathode–cathode ion source, the charging of the substrate in ion-beam-assisted etching is eliminated by the use of a neutralizer which supplies the same electron current as the Ar ion current. In-situ etch depth monitoring can be performed using He–Ne and He–Cd laser reflectance measurements. The substrate temperature is monitored using a thermocouple.

3. Chlorine gas etching of indium-containing semiconductors

Chlorine gas etching has been used extensively for in-situ etch and regrowth in GaAs-based materials [12, 13]. Chlorine gas etching of InP was first reported by Furuhata et al. [14]. Higher temperatures (compared to GaAs) are required for chlorine gas etching of indium-containing semiconductors due to the low vapor pressure of $InCl_3$ which is the by-product of the etching reaction and the desorption of which is the rate-limiting mechanism [15]. The optimum etching temperature for GaAs is 180°C, where higher temperatures ranging from 250°C to 350°C are required for GaInAs, AlInAs and InP. The selection of proper temperature for etching In-based alloys like GaInAs and AlInAs is critical as the desorption rates of $GaCl_3$ and $InCl_3$ in the case of GaInAs and $AlCl_3$ and $InCl_3$ in the case of AlInAs have to be equal. A difference in desorption rates would result in the surface being of varying composition and also increases the roughness of the etched surface. Reducing the surface roughness of the etched surface is essential to achieve a high-quality interface after subsequent molecular beam epitaxial regrowth.

Fig. 1 shows the variation of etch rates with temperature for GaInAs, AlInAs and InP. The chlorine gas flow rate is 3 sccm, and the chamber pressure is 8×10^{-5} Torr. The calculated activation energies for the etching rates are 9.22 kcal/mol for

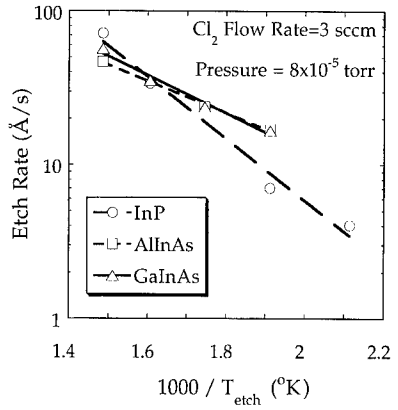

Fig. 1. Variation of etch rate with temperature.

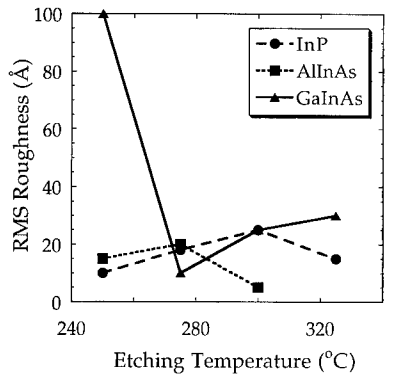

Fig. 2. Variation of etched surface roughness with etching temperature.

InP, 4.77 kcal/mol for GaInAs and 5.66 kcal/mol for AlInAs. The activation energy for InP is in the range as obtained by Furuhata et al. [14]. The etch rate of GaAs in this temperature range is constant. Hence, the activation energies for etch rates of GaInAs and AlInAs are expected to be lower than that of InP.

The surface roughness of the etched surfaces was measured using an atomic force microscope (AFM). Fig. 2 shows the variation of surface roughness with etched temperature for InP, GaInAs and AlInAs. The etch rates for GaAs and InP are equal for etching temperature of 275–280°C implying that the desorption rates of gallium and indium chloride etch by-products are equal at that temperature [14]. Therefore, a minimum surface roughness for GaInAs is expected at this etching temperature. This is indeed the case as seen from the plot in Fig. 2. The minimum surface roughness for AlInAs and InP is achieved at etching temperatures of 300°C and 250°C, respectively. As seen from Fig. 2 an unusually high surface roughness is observed for GaInAs layers etched at 250°C; this is probably due to presence of native oxide on the surface which acts as micromask and increases the surface roughness.

4. In-situ etch and regrowth

n-GaInAs layers doped $1 \times 10^{17}/cm^3$ with Si were grown on a n^+ GaInAs contact layer doped $1 \times 10^{18}/cm^3$ and lattice-matched to InP. The growth temperature was 510°C and the arsenic pressure was 1.3×10^{-5} Torr. The substrates were then transferred to the etching chamber through a UHV transfer tunnel. The GaInAs epilayers are etched using chlorine gas at temperatures ranging from 250°C to 325°C. The Cl_2 gas flow was 2.5 sccm and the pressure was 5×10^{-5} Torr. The substrates were then transferred back to the MBE growth chamber and n-AlInAs doped $1 \times 10^{17}/cm^3$ with Si is regrown at a temperature of 510°C. Also a control AlInAs/GaInAs structure was grown without any interruption for comparison. AuGe/Ni/Au ohmic contact was made to the n^+GaInAs and Ti/Au Schottky contact was made to AlInAs to fabricate AlInAs/GaInAs heterojunction capacitors. Fig. 3 shows the layer structure and schematic of the N–n heterojunction capacitor.

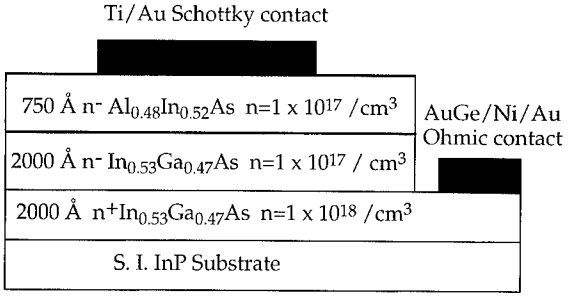

Fig. 3. Schematic of layer structure and N–n heterojunction capacitor.

5. *C–V* analysis of regrown AlInAs/GaInAs heterojunction

High-frequency capacitance was measured as a function of reverse bias using a CV analyzer. Apparent doping profile in n-GaInAs was extracted from the *C–V* curves. The AlInAs/GaInAs interface charge density was calculated by integrating the difference between the apparent doping and the actual doping as described by Kroemer et al. [16]. Table 1 lists the interface charge density for different etching temperatures.

An apparent increase in doping is observed near the interface which is due to the response of the interface states to the changing reverse bias. The interface state density distribution in GaInAs can be calculated by using the method described by Ikeda et al. [17]. Fig. 4 shows the interface state density distribution at the AlInAs/GaInAs interface for GaInAs layers etched at different temperatures. A midgap interface state density of $3 \times 10^{11}/cm^2$ eV is obtained for regrown AlInAs/GaInAs interface with GaInAs etched at 275°C.

The values of interface charge density and the mid-gap interface state density are comparable to values reported in the literature [8, 18, 19].

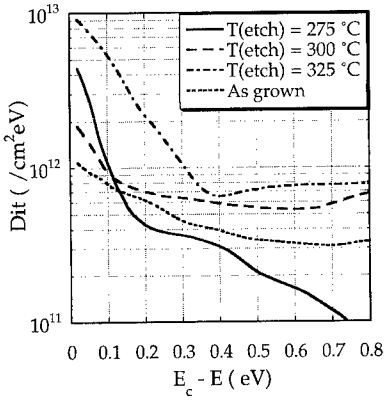

Fig. 4. Variation of interface state density distribution at the AlInAs/GaInAs interface with etching temperature.

Table 1
Variation of AlInAs/GaInAs interface charge density with etching temperature

GaInAs etching temperature (°C)	Interface charge density (cm^{-2})
275	4.52×10^{11}
300	6.14×10^{11}
325	1.92×10^{12}
As-grown AlInAs/GaInAs	4.14×10^{11}

6. Surface roughness and interface quality – the DIGS model

The presence interface states at the regrown interface can be explained in terms of unified disorder-induced gap state (DIGS) model as proposed by Hasegawa et al. [17, 20, 21]. According to the DIGS model, interface states are generated at the regrown interface due to the disordered region at the etched surface. Chlorine gas etching of GaInAs results in a rough off-stochiometric surface; subsequent regrowth on this surface creates a disordered region at the AlInAs/GaInAs interface. Thus, the interface state density depends on the morphology of the etched surface.

A minimum surface roughness of 10 Å is obtained at a etching temperature of 275°C, this also corresponds to minimum interface charge and mid-gap interface state density of $3 \times 10^{11}/cm^2$ eV in GaInAs as shown in Fig. 4. Fig. 5 shows the variation of fixed charge at the AlInAs/GaInAs interface and surface roughness of etched GaInAs

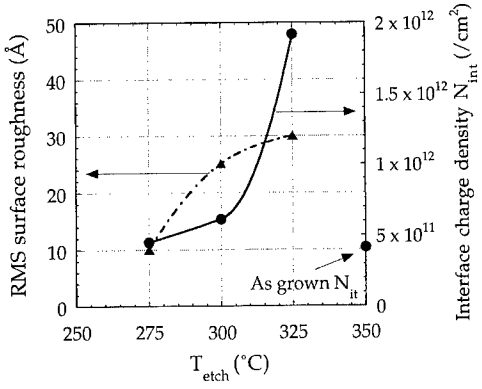

Fig. 5. Variation of surface roughness and AlInAs/GaInAs interface charge with GaInAs etching temperature.

surface with etching temperature. It can be seen that the interface charge density directly correlates with the surface roughness, validating the DIGS model for the regrown interface. Thus, the roughness of the etched surface and interface state density of the subsequently regrown interface are minimum when the desorption rates of both gallium and indium chloride etch by-products during etching are same. A comparison of the regrown interface with as-grown AlInAs/GaInAs interface shows only a minor degradation, indicating the suitability of this technique for in-situ processing in the AlInAs/GaInAs/InP material system.

7. Conclusion

We have demonstrated an in-situ etch and regrowth process in the AlInAs/GaInAs material system. The quality of the regrown interface depends critically on the etching temperature of GaInAs. Equal desorption rates of both Ga and In etch by-products are necessary to minimize surface roughness as the extent of disordered region at the regrown interface is directly proportional to etched surface roughness. The presence of interface states at the regrown interface can be explained in terms of the disorder-induced gap state (DIGS) model. In-situ etched and regrown AlInAs/GaInAs interfaces show only a minor degradation compared to as-grown interfaces.

Acknowledgements

The authors would like to thank John English for his technical support. This work was supported by QUEST and ARPA (Thunder and Lightning Project).

References

[1] D.C. Streit, D.K. Umemoto, K.W. Kobayashi and A.K. Oki, IEEE Trans. Electron Devices 42 (1995) 618.
[2] Y.C. Pao, J. Franklin and C. Shih, J. Crystal Growth 150 (1995) 1358.
[3] N.J. Kawai, C.E.C. Wood and L.F. Eastman, J. Appl. Phys. 53 (1982) 6208.
[4] Y. Imura, T. Shiraishi, H. Takasugi and M. Kawabe, J. Appl. Phys. 61 (1987) 2095.
[5] D. Biswas, P.R. Berger, U. Das, J.E. Oh and P.K. Bhattacharya, J. Electron. Mater. 18 (1989) 137.
[6] D.S.L. Mui, T.A. Strand, B.J. Thibeault, L.A. Coldren, P.M. Petroff and E.L. Hu, Proc. Int. Symp. on Compound Semiconductors, (1994) p. 291.
[7] N. Tanaka, I. Matsuyama and T. Ishikawa, Jpn. J. Appl. Phys. 33 (1994) 754.
[8] T. Saitoh, H. Tomozawa, T. Nakagawa, H. Takeuchi and H. Hasegawa, J. Crystal Growth 150 (1995) 96.
[9] R. Lai and P.K. Bhattacharya, J. Appl. Phys. 67 (1990) 4345.
[10] D.C. Streit, T.R. Block, A.-C. Han, M. Wojtowicz, D.K. Umemoto, K. Kobayashi, A.K. Oki, P.-H. Liu, R. Lai and G.I. Ng, J. Vac. Sci. Technol. B 13 (1995) 771.
[11] K. Kiziloglu, B.P. Keller, P.M. Chavarkar, X. Cao, S.P. DenBaars, and U.K. Mishra, Electronic Materials Conf. Abstracts, (1996) p. 13.
[12] E.M. Clausen, Jr., J.B. Harbison, L.T. Florez and B. Van der Gaag, J. Vac. Sci. Technol. B 8 (1990) 1960.
[13] H.G. Lee, R.J. Fischer, G.J. Zydzik and A.Y. Cho, J. Vac. Sci. Technol. B 11 (1993) 989.
[14] N. Furuhata, H. Miyamoto, A. Okamoto and K. Ohata, J. Appl. Phys. 65 (1989) 168.
[15] S.C. McNevin, J. Vac. Sci. Technol. B 4 (1986) 1216.
[16] H. Kroemer, W. Chen, J.S. Harris and D.D. Edwall, Appl. Phys. Lett. 36 (1980) 295.
[17] E. Ikeda, H. Hasegawa, S. Ohtsuka and H. Ohno, Jpn. J. Appl. Phys. 27 (1988) 180.
[18] R. People, K.W. Wecht, K. Alavi and A.Y. Cho, Appl. Phys. Lett. 43 (1983) 118.
[19] W.-P. Hong, J.-E. Oh, P.K. Bhattacharya and T.E. Tiwald, IEEE Trans. Electron Devices 35 (1988) 1585.
[20] H. Hasegawa and H. Ohno, J. Vac. Sci. Technol. B 4 (1986) 1130.
[21] H. Hasegawa, L. He, H. Ohno, T. Sawada, T. Haga, Y. Abe and H. Takahashi, J. Vac. Sci. Technol. B 5 (1987) 1097.

ELSEVIER

Journal of Crystal Growth 175/176 (1997) 398–403

JOURNAL OF CRYSTAL GROWTH

Selective area epitaxy of GaAs using very low energy Ga^+ focused ion beam deposition combined with molecular beam epitaxial growth

H.E. Beere*, J.H. Thompson, G.A.C. Jones, D.A. Ritchie

Cavendish Laboratory, Madingley Road, Cambridge CB3 0HE, UK

Abstract

A Ga focused ion beam (FIB) has been used to grow conducting n-type GaAs in areas defined by the FIB irradiation. A low energy (25–100 eV) mass separated $^{69}Ga^+$ FIB was supplied to a GaAs (1 0 0) substrate, simultaneously with Si and As_4 molecular beams. The FIB was rastered over a selected area of the substrate producing a square 200 μm × 200 μm mesa during growth. The 77 K Hall mobility and carrier concentration values of the grown GaAs layers showed that material quality improved as the ion energy was reduced from 100 to 25 eV. At 300 K a peak mobility of 2380 $cm^2\ V^{-1}\ s^{-1}$ at a carrier concentration of $2.5 \times 10^{17}\ cm^{-3}$ was achieved for the 25 eV ion grown sample.

1. Introduction

The selective area epitaxy of III–V semiconductor compounds could become an important technique in the preparation of complex integrated device structures such as opto-electronic integrated circuits. Molecular beam epitaxy (MBE) has proved very successful in producing high quality multilayered semiconductor structures, however it can only control the material composition in the growth (vertical) direction. Attempts at manipulating MBE into a selective area growth technique have utilized patterned oxide or elemental masks [1, 2] to define the selected region to be grown. This technique unfortunately limits the degree of sophistication attainable in device integration. Focused ion beam (FIB) technology, in contrast, offers a versatile maskless lithographic technique with high spatial resolution in the lateral plane. Hence the combination of these technologies (FIMBE) could provide an opportunity for an in-situ maskless selective area epitaxy technique capable of generating such complex device structures.

In III–V MBE growth, compound stochiometry can be achieved by an excess supply of the group V element during growth, since the sticking coefficient of the group V element depends only on the population of the group III element. Consequently, the flux rate of the group III element solely controls the growth rate of the semiconductor. Therefore replacing the conventional MBE group III matrix element source with a FIB source would

*Corresponding author. Fax: +44 1223 337271; e-mail: hcb1000@cus.cam.ac.uk.

0022-0248/97/$17.00 Copyright © 1997 Elsevier Science B.V. All rights reserved
PII S0022-0248(96)01028-7

facilitate the lateral selective area epitaxy of III–V materials.

Initial studies into the MBE growth of III–V compounds with ionized beam sources were carried out to improve the sticking coefficient of the group V element. Shimuzu et al. [3, 4] demonstrated the growth of GaAs and InP by supplying the group V species via an unfocused ion source. Epitaxial growth was achieved for incident ion energies < 300 eV and for growth temperatures above 200°C for GaAs and 300°C for InP, respectively. 4.2 K photoluminescence (PL) spectra of the GaAs films grown above 450°C and with an As^+ ion energy of 100 eV exhibited well-defined bound exciton structure indicating high quality films were obtained. Moreover the saturation of the PL intensity for films grown above 500°C suggests that any damage produced by the As^+ ion bombardment was annealed simultaneously during growth.

Similarly, Maruno et al. [5, 6] studied the growth of GaAsP and InP using an unfocused P^+ ion source. Again, for incident beam energies < 300 eV homoepitaxial growth was observed. The InP epilayers were doped unintentionally n-type and displayed comparable values of mobility and carrier concentration to InP grown by conventional MBE.

Recently, Pak et al. [7] have reported MBE growth of GaAs with a focused low energy Ga^+ (group III) ion source. Ex situ μRHEED measurements of the grown films showed single crystal epitaxy could be achieved for ion energies below 200 eV and for growth temperatures above 400°C.

For all these ionized beam growth experiments it was found necessary to employ ion energies of less than 300 eV. This is required to (i) minimise ion induced damage to the crystal and (ii) minimise the sputtering yield to ensure film growth is possible.

One exciting aspect of using ionized matrix element sources with MBE is their potential to allow technologically important improvements in semiconductor growth. The extra energy supplied to the wafer surface by low energy ion irradiation has allowed the growth of semiconductor crystals at reduced substrate temperatures [3, 5]. The capability to grow high quality MBE cystals at low temperatures would dramatically reduce diffusion related problems such as dopant redistribution and the surface segregation of alloys (e.g. In in InGaAs). Studies have also shown [3, 5] that surface roughness and defect levels can be improved by low energy ion irradiation during growth. These affects may lead to improvements in heterointerfaces for optical and electrical devices.

To date no literature has been presented on the effect of incident ion energy on the electrical properties of films grown from a focused ionized beam source. In this paper we present the preliminary results of the electrical characterisation of intentionally doped GaAs films grown with a Ga^+ FIB and MBE for various ion landing energies.

2. Experimental apparatus

To facilitate the use of a FIB with MBE growth a novel system has been developed by Thompson et al. [8]. It replaces a conventional thermal MBE source with a liquid metal ion source (LMIS) FIB located directly opposite to the sample on a standard MBE deposition chamber. To surmount the problem of focusing an ion beam in the required low energy regime retarding field optics were employed [9]. It has been demonstrated in earlier work [10] that this integrated arrangement does not interfere with or affect the conventional MBE growth of III–V compounds.

Fig. 1 shows a schematic diagram of the experimental apparatus. It consists of a VG MIG300 30 kV FIB column mounted perpendicular to the sample on the growth chamber of a VG V80H MBE machine.

The FIB column consists of a high brightness Ga LMIS, an 'electrostatic condenser' lens and an aperture below this lens to limit the beam current down the column. Since a Ga LMIS emits predominantly two singly charged isotropic species, $^{69}Ga^+$ ($\sim 60\%$) and $^{71}Ga^+$ ($\sim 40\%$), each with an energy spread of ~ 15 eV [11], an ion mass filter employing perpendicular electric and magnetic fields is used to select the more abundant, lower mass species. A second lens element is used for focusing, whilst finally an x–y deflection plate assembly is used to raster the beam over a selected area of the wafer. The above FIB column is a standard commercial design except that only MBE

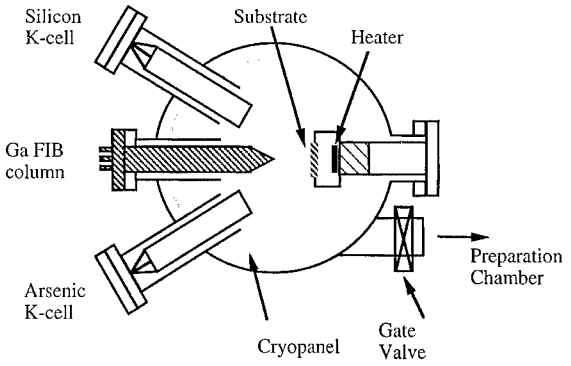

Fig. 1. A schematic diagram of the experimental apparatus showing the focused ion beam matrix element source attached to the growth chamber of an MBE machine.

compatible materials were employed in its construction, i.e. all insulators were ceramic and any hot stainless steel areas were replaced with molybdenum or tantalum components. To minimise contamination of the LMIS during growth the ion source is differentially pumped. With a growth chamber pressure of 2×10^{-7} mbar, a FIB column pressure of less than 1×10^{-9} mbar was achieved, thereby prolonging the operational lifetime of the LMIS.

To maximise the resolution of the FIB it is necessary to minimise the column's working distance (the distance from the end of the column to the sample) and to ensure the system is vibrationally isolated. Consequently, a growth chamber was chosen with high angled thermal sources ($\sim 35°$ from the normal to the sample), allowing line of sight access for the thermal beams to the sample with the FIB column in place. Vibration isolation of the system included the isolation of the cryopump from the growth chamber with bellow sections and the mounting of the system on an air support assembly.

The other important constituent of the system is a specially designed electrically isolated sample holder. This can be floated to a high voltage (up to 30 kV) to produce the ion beam's retarding potential as well as being used to measure the ion current incident on the sample. Consequently, the sample heater assembly is also floated to the retarding potential and is powered by a custom built power supply. To allow the optical alignment of the FIB on the sample the holder can be fully adjusted in both lateral and azimuthal planes.

3. Experimental procedure

The FIB was operated with a source ion energy of 20 keV at a working distance of 40 mm. Ion landing energies were varied from 100 eV down to 25 eV by changing the positive voltage applied to the sample from 19 900 V to 19 975 V, respectively, using a negative 0–2 kV power supply which was tied to the ion source voltage. The LMIS was operated with an emission current of 10 μA producing a beam current between 18–25 nA. The FIB beam diameter at 25 eV ion landing energy was measured to be approximately 50 μm although an estimated diameter < 30 μm was expected. The deterioration of the beam size was found to be associated with the vibration of the sample holder and has been subsequently eliminated with an internal vibration support mechanism.

All sample substrates were 25 mm × 25 mm squares of semi-insulating (1 0 0) GaAs. Samples were grown at a substrate temperature between 600°C and 620°C as measured by an optical pyrometer and an As to thermal Ga beam equivalent pressure ratio of 8–9 to 1. In order to allow lateral selective area epitaxy the substrate was not rotated during growth.

Prior to selective area growth using the FIMBE a 0.5 μm buffer layer of undoped GaAs was grown using only thermal molecular beam sources to provide a high-quality growth interface. The thermal Ga flux was then removed and replaced with a Ga^+ ion beam rastered over a 200 μm × 200 μm area, once per second. A thermal Si source was opened in unison with the Ga FIB thereby doping the growing selected GaAs area n-type. The Si thermal flux was set to provide a nominal doping concentration of 1×10^{18} cm^{-3} for an expected GaAs layer growth rate of ~ 0.5 μm h^{-1}. The duration of growth was approximately 2 hours to ensure 1.0 μm thick GaAs samples were grown.

4. Results and discussion

Fig. 2 shows Normarski micrographs of a film grown with a 25 eV ion landing energy, which is representative of all the ion beam grown samples detailed in this study. The sample demonstrates

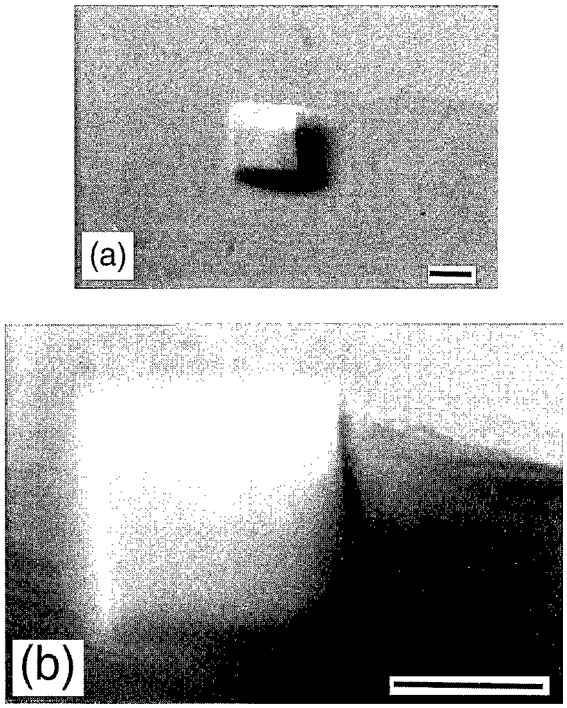

Fig. 2. Normarski micrographs at (a) ×50 magnification and (b) ×200 magnification of a selectively grown area of n-type GaAs, using a 25 eV Ga^+ rastered FIB simultaneously with Si and As_4 molecular beams. Marker represents 100 μm. The degredation of side wall definition in the top and bottom edges are attributed to vibration of the sample manipulator in the vertical plane.

selective growth over an area approximately 200 μm × 200 μm. The surface morphology of the film shows uniform, flat and defect free crystal growth. The selectively grown GaAs region appears trapezoidal in shape. This is believed to be a consequence of the sample being slightly off axis to the FIB scan field; however, it may also be the manifestation of an enhanced crystal growth mode and further investigation into this is to be undertaken. Also highlighted in Fig. 2 are darker (shadow) areas. This is believed to be the presence of a small component of the $^{71}Ga^+$ species in the FIB.

Depth profiles of all the samples, obtained by Dektak measurements, demonstrated that structures between 1.0 and 1.2 μm thickness with FWHM lateral dimensions of ~ 200 μm × 200 μm were grown. Sample growth rates were typically 0.5–0.6 μm h^{-1} which is consistent with the values calculated from the beam current measurements.

Electrical characterisation of the grown films was used to investigate the effects of ion beam growth on material quality. Sample processing began with the removal of the non-conducting Si layer deposited on the substrate surface in the region outside the FIB irradiation. This was carried out by conventional ex-situ optical lithography and wet etching techniques. The epilayer was then processed into a van der Pauw mesa for Hall resitivity measurements. Since the MBE growth chamber used in this experiment exhibits a p-type background doping level of 1.0×10^{15} cm^{-3} it is expected that the 0.5 μm undoped buffer layer would be completely depleted of carriers and therefore would not contribute to the conductivity of the ion beam grown layer. Sample assessment was carried out on an Oxford Scientific continuous flow He cryostat.

Fig. 3 plots the 77 K Hall mobility versus carrier concentration in the dark for samples nominally doped at 1.0×10^{18} cm^{-3}, with ion energies ranging from 100 to 25 eV. For comparison the result from a GaAs sample grown from a thermal Ga source under the same growth conditions is also shown. The solid and dotted lines indicate the theoretical mobility [12] calculated assuming a constant compensation ratio $(\gamma = N_D + N_A / N_D - N_A)$ of $\gamma = 2, 4$ and 19, respectively. The mobility of the thermally grown sample is situated on the $\gamma = 2$ line. This is expected and is due to the amphoteric nature of the Si dopant in GaAs. The mobility of the sample grown with an ion landing energy of 25 eV indicates a compensation ratio of $\gamma \sim 4$ which implies the layer is of good crystalline quality. For the samples grown with 50 and 100 eV ion energies the compensation ratio increases to $\gamma \sim 5$ and 17, respectively. Clearly a demonstrable improvement in material quality can be observed as the incident ion energy is reduced from 100 to 25 eV.

From this data, approximate values for the acceptor and donor concentrations can be estimated as a function of ion energy [12]. These results indicate that the electrical characteristics of the grown films were improved mainly due to the decrease in the acceptor concentration as the incident

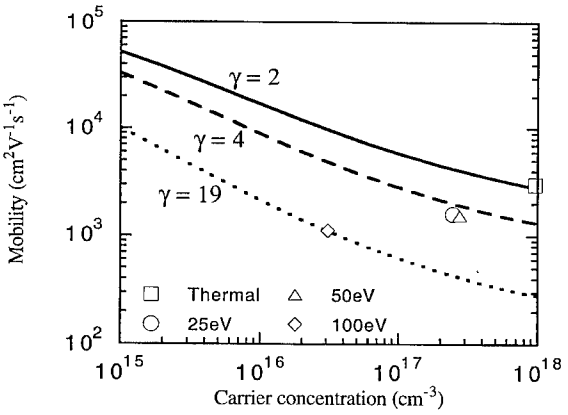

Fig. 3. The 77 K Hall mobility as a function of carrier concentration for ion beam samples grown with ion energies ranging from 100 to 25 eV and a conventionally grown GaAs sample. For comparison, the compensation ratios ($\gamma = N^+ + N^-/n$) equal to 2, 4 and 19 are plotted as lines on the graph.

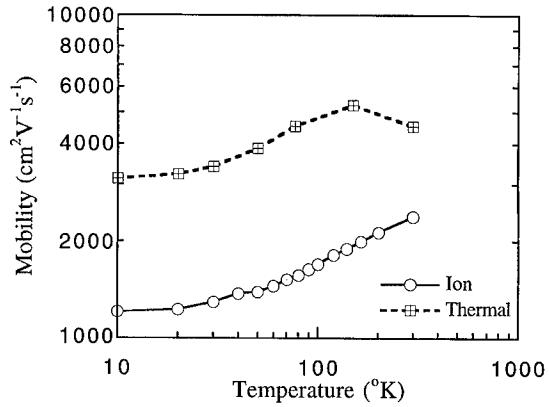

Fig. 4. Hall mobility versus temperature for the 25 eV Ga^+ FIB grown sample nominally doped at 1.0×10^{18} cm^{-3} with a thermal Si source (note the logarithmic axes). For comparison a conventionally grown MBE n-GaAs sample is also shown. Both samples maintain a free carrier concentration of 2.5×10^{17} cm^{-3} over the entire temperature sweep.

ion energy was reduced. The highest mobility achieved from an ion beam grown sample was 2380 cm^2 V^{-1} s^{-1} at a carrier concentration of 2.5×10^{17} cm^{-3} at 300 K for an incident ion energy of 25 eV.

Finally, the temperature dependence of the Hall mobility of the GaAs sample grown with a 25 eV ion energy is displayed in Fig. 4. The curve shows a monotonic reduction in mobility upon decreasing temperature from 300 to 10 K, whilst the free carrier concentration remained constant (within $\pm$ 5%) at 2.5×10^{17} cm^{-3} (not shown). For comparison the results from a thermally grown n-type GaAs sample with a free carrier concentration of 2.4×10^{17} cm^{-3} is also given. The mobility of the 25 eV ion grown sample is 2–3 times lower than the equivalent MBE grown sample. Furthermore, the ion grown sample does not exhibit the characteristic transition from the phonon to ionized-impurity dominated scattering regime at 100 K as observed in the thermally grown sample. This shows that the ion grown sample's mobility is dominated by ionized scattering centres within the crystal, and implies that there is ion-induced lattice damage in the grown film, even for a 25 eV ion landing energy. The nature of this ion-induced crystal damage is believed to be associated with acceptor defect complexes in the bulk.

The systematic improvement in material quality with decreasing incident ion energy suggests that the growth of high-quality GaAs comparable to conventionally grown MBE GaAs could be achieved by reducing the ionized beam energy below 25 eV. The combination of FIB and MBE has been shown to facilitate the maskless selective area epitaxy of GaAs and has the potential to be a growth technique capable of fabricating complex integrated semiconductor device structures.

5. Conclusions

For the first time conducting n-type GaAs has been grown using very low energy Ga^+ FIB deposition combined with MBE. The selective area growth of 200 μm × 200 μm GaAs structures was demonstrated using a Ga^+ FIB as a matrix element source. 77 K Hall resistivity measurements of the ion beam grown samples showed a systematic improvement in the material quality as the incident ion energy was decreased from 100 to 25 eV and demonstrated that the film quality approached that of conventionally grown MBE GaAs. The ability to grow selective areas of MBE quality GaAs should allow the growth of novel electronic structures.

Acknowledgements

Technical assistance was provided by D. Heftel, T. Jobson, E.H. Linfield, and P.J.A. Sazio. D.A.R. acknowledges support from the Toshiba Cambridge Research Centre. This work was also funded in part by the EPSRC, UK and the Defence Research Agency, Malvern, UK.

References

[1] W.T. Tsang, Semicond. Sci. Technol. 8 (1993) 1016.
[2] K.H. Gulden, X. Wu and J.S. Smith, Appl. Phys. Lett. 62 (1993) 3180.
[3] S. Shimizu, O. Tsukakoshi and S. Komiya, J. Vac. Sci. Technol. B 3 (1985) 554.
[4] S. Shimizu, O. Tsukakoshi and S. Komiya, J. Vac. Sci. Technol. B 3 (1985) 554.
[5] S. Maruno, Y. Morishita, T. Isu, Y. Nomura and H. Ogata, J. Electron. Mater. 17 (1988) 21.
[6] Y. Morishita, S. Maruno, T. Isu, Y. Nomura and H. Ogata, J. Crystal Growth 88 (1988) 21.
[7] K. Pak, I. Saitoh, N. Ohshima and H. Yonezu, J. Crystal Growth 140 (1994) 245.
[8] J.H. Thompson, G.A.C. Jones, D.A. Ritchie, E.H. Linfield, A.C. Churchill, G.W. Smith, M. Houlton, D. Lee and C.R. Whitehouse, J. Appl. Phys. 74 (1993) 4375.
[9] H. Kasahara, H. Sawaragi, R. Aihara, K. Gamo, S. Namba and M. Hassal Shearer, J. Vac. Sci. Technol. B 6 (1988) 974.
[10] J.H. Thompson, G.A.C. Jones, D.A. Ritchie, E.H. Linfield, M. Houlton, G.W. Smith and C.R. Whitehouse, J. Crystal Growth 127 (1993) 732.
[11] L.W. Swanson, G.A. Schwind and A.E. Bell, J. Appl. Phys. 51 (1980) 3453.
[12] D.L. Rode and S. Knight, Phys. Rev. 3 (1971) 2534.

ELSEVIER

Journal of Crystal Growth 175/176 (1997) 404–410

JOURNAL OF CRYSTAL GROWTH

Selective area chemical beam epitaxial regrowth of Si-doped GaAs by using silicon tetraiodide for field effect transistor application

Shigekazu Izumi*, Yoshitsugu Yamamoto, Tetsuro Kunii, Shinichi Miyakuni, Norio Hayafuji, Kazuhiko Sato, Mutsuyuki Otsubo

Optoelectronic & Microwave Devices Laboratory, Mitsubishi Electric Corporation, 4-1 Mizuhara, Itami, Hyogo 664, Japan

Abstract

Selective area regrowth of silicon-doped GaAs has been successfully achieved by chemical beam epitaxy (CBE) on dry etched trench structures. Abrupt doping-interface and excellent doping controllability have also been achieved by using a novel silicon dopant source of silicon tetraiodide (SiI_4). Metal-semiconductor field effect transistor (MESFET) and heterostructure field effect transistor (HFET) fabricated in this way with Ni/AuGe/Au alloyed contact metals on the Si-doped GaAs regrown layer reveal contact resistances as low as $3 \times 10^{-7}\ \Omega\ cm^2$ and perfect selectivity there being no polycrystalline growth on the dielectric mask film.

1. Introduction

Selective area epitaxy is one of the powerful techniques for various device fabrications. There are several papers showing a low contact resistance achieved using selective n^+-GaAs regrowth on the source and drain (S/D) regions of metal-semiconductor field effect transistor (MESFET), as well as GaAs/AlGaAs high electron mobility transistor (HEMT) grown by metalorganic chemical vapor deposition (MOCVD) [1, 2] and GaInP/GaAs HEMT grown by chemical beam epitaxy (CBE) [3]. CBE has been confirmed as a promising candidate for selective area regrowth [4, 5]. The most effective feature of CBE is that growth rate and material composition is independent of the aspect ratio of the mask area [6].

Si is one of the most commonly used n-type dopants for III–V compound semiconductors. Si_2H_6 has been mainly used for MOCVD and gas source molecular beam epitaxy (GS-MBE) [7–9], while the carrier concentration was limited to a maximum $1.4 \times 10^{18}\ cm^{-3}$ in CBE grown InP [9]. Controllability, especially at low doping level is also insufficient for device applications such as for the collector layer of heterojunction bipolar transistor (HBT). Relatively high Si doping efficiency and precise controllability has been obtained for InP and InGaAs growth by using silicon tetrabromide ($SiBr_4$) [10, 11] which has a relatively

* Corresponding author. Fax: +81 727 80 2694; e-mail: izumisg@hakobu.hoku.melco.co.jp.

0022-0248/97/$17.00 Copyright © 1997 Elsevier Science B.V. All rights reserved
PII S0022-0248(96)00874-3

weak Si-Br bond strength (87.9 kcal/mol [12]) that suggests the weak strength of Si-halogen (or others) bond is an inevitable item for Si-dopant source. Recently, silicon tetraiodide (SiI_4), which has weaker Si-I bond strength (70 kcal/mol [12]), has been successfully employed as a novel Si-dopant in CBE of GaAs and InP [13]. No precracking was necessary before supplying the SiI_4 with a helium (He) carrier gas. High electrical quality was ascertained for both of GaAs and InP with linear Si-doping controllability in the range from 2×10^{16} to 6×10^{18} cm^{-3} with a variation of less than 2% over a three inch diameter wafer.

In this paper, for the first time we show the CBE regrowth of n^+-GaAs S/D contact layer by using SiI_4 for MESFET and heterostructure field effect transistor (HFET).

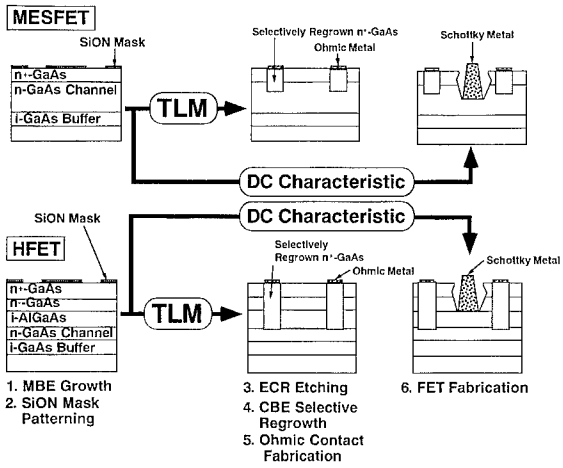

Fig. 1. Fabrication process and evaluation flows of MESFET and HFET.

2. Experimental procedure

Si-doped GaAs and Si-doped InP were grown by CBE on three inch diameter undoped GaAs and Fe-doped InP (1 0 0) substrates, respectively. The GaAs layer was grown with substrate in temperatures range between 510°C and 590°C and a growth rate of 0.65 μm/h by using triethylgallium (TEGa) and arsine (AsH_3), whilst the InP layer was grown at 460°C with a growth rate of 0.5 μm/h by using trimethylindium (TMIn) and phosphine (PH_3). The SiI_4 was supplied with a He carrier gas through a mass flow controller without any precracking. The Si-dopant used was 5N grade purity SiI_4. The boiling and melting points of SiI_4 are 288°C and 120.5°C, respectively [14]. Hall measurements have been performed at room temperature using the van der Pauw method to determine the net electron concentration and mobility. Secondary ion mass spectrometry (SIMS) with Cs^+ beams was performed to evaluate the Si-doping profile. Fig. 1 shows the process and evaluation flows of MESFET and HFET. The trenches were fabricated by ECR plasma etching with Cl_2/N_2 gases whose micro wave and RF power are 200 and 10 W, respectively. The surface to be regrown was cleaned by HCl solution for 2 min. Then thermal treatment was performed just prior to the regrowth for 5 min at 620°C under As_2 flux in CBE growth chamber. The 50 nm thick SiON (deposited by plasma CVD at about 300°C) film was used for the selective mask. Contact resistance was measured by the transmission line model (TLM) technique with exclusive patterns of Ni(10 nm)/AuGe(50 nm)/Au(250 nm) alloyed metals. The FETs whose gate length (L_g) and gate width (W_g) were 1.3 and 100 μm, respectively, were also evaluated by the DC characteristics. Gate metals for both FETs consist of Ti(150 nm)/Al(400 nm)/Mo(50 nm).

3. Results and discussion

3.1. Doping characteristics of SiI_4 for GaAs and InP

Fig. 2 shows the dependence of net carrier concentration and electron mobility for 5000 Å thick GaAs and 4500 Å thick InP on flow rate of SiI_4 diluted with He carrier gas. The net electron concentration increases from 2.0×10^{16} cm^{-3} (at 0.2 sccm) to 2.7×10^{18} cm^{-3} (at 10 sccm) for GaAs and from 3.7×10^{17} cm^{-3} (at 1 sccm) to 5.7×10^{18} cm^{-3} (at 10 sccm) for InP (the temperature of SiI_4 bubbler is fixed at 50°C). Linear Si-doping controllability has been confirmed for both of GaAs and InP by mass flow control system. The difference of Si incorporation efficiency between

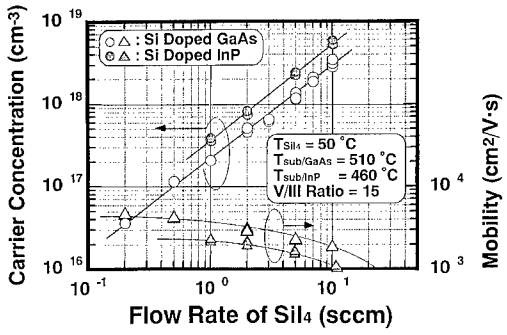

Fig. 2. Dependence of net carrier concentration and electron mobility in GaAs and InP on flow rate of SiI_4 diluted with He carrier gas. The temperature of SiI_4 bubbler was kept at 50°C.

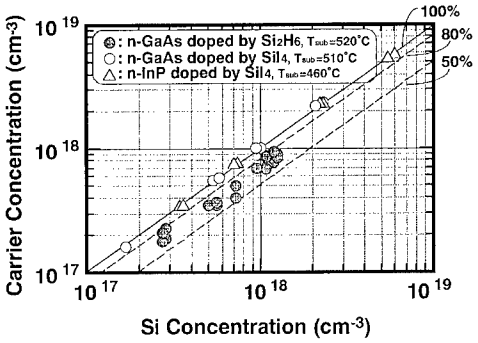

Fig. 3. Relation between carrier concentration and Si concentration in Si-doped GaAs by SiI_4, Si_2H_6, and Si-doped InP by SiI_4.

GaAs and InP at the same flow rate of SiI_4 is thought to be due to the machine's configuration. The maximum net carrier concentration obtained for GaAs and InP were 6.1×10^{18} and $1.7 \times 10^{19}\,cm^{-3}$ with the SiI_4 flow rate of 7 and 10 sccm, respectively when the temperature of SiI_4 bubbler was fixed at 60°C. Since the flow rate of SiI_4 in the present CBE system is controllable in the range between 0.2 and 10 sccm, the precise doping control can be achieved from 2×10^{16} to $2.7 \times 10^{18}\,cm^{-3}$ for GaAs, which is useable for the collector and emitter of AlGaAs/GaAs or InGaP/GaAs HBT, respectively. In addition surface is specular, even for the heavily Si-doped GaAs and InP. Electron mobilities of Si-doped GaAs layers by SiI_4 are comparable to these by elemental Si [15]. Those of InP layers are also comparable to those reported by Jackson et al. [10]. The net carrier concentrations of GaAs layers doped using SiI_4 are constant over the whole growth temperature range and V/III ratio range investigated, in contrast to doping by Si_2H_6 [13]. Growth rates for both of GaAs and InP are constant in a wide doping range, indicating that etching effect with iodine (*I*) radicals does not appear in this condition owing to a very low flow rate (high doping efficiency), resulting in the excellent uniformity. Furthermore, SiI_4 introduces no other impurities to GaAs and InP, such as iodine, oxygen and sulfur. The relationship between the carrier concentration and Si concentration in Si-doped GaAs by SiI_4, by Si_2H_6, and Si-doped InP by SiI_4 is summarized in Fig. 3. The electrical activation ratio of Si in SiI_4 for both of GaAs and InP is almost 100% in the whole range studied, while that in Si_2H_6 is 80% or less. The excellent doping characteristics are thought to be due to the weaker Si–I bond strength in SiI_4 (70 kcal/mol), which might promote an atomic Si formation and following Si incorporation into GaAs and InP, while Si_2H_6 contains a Si–Si and three Si–H bonds whose bond strength is stronger than that of Si–I bond.

3.2. Selective area regrowth for FET application

We first observed the selective area regrowth of n^+-GaAs contact region for various growth temperature. Fig. 4 shows the temperature dependence of poly-crystalline GaAs deposition on patterned SiON mask. Selective area regrowth for S/D GaAs contact region of MESFET and HFET by using SiI_4 with a concentration of $3 \times 10^{18}\,cm^{-3}$ has been successfully achieved on patterned trench structure fabricated by ECR plasma etching without any polycrystalline deposition on the dielectric mask film at relatively high growth temperature of 590°C, while previous reports showed that the selective regrowth on GaAs with SiO_2 was realized only at 600°C or higher by using TEGa [4, 5]. Sufficient low contact resistance as low as $3 \times 10^{-7}\,\Omega\,cm^2$ has been achieved with alloyed contact metals on Si-doped GaAs S/D surfaces of MESFET and HFET. DC characteristics of MESFET and HFET has been investigated. In

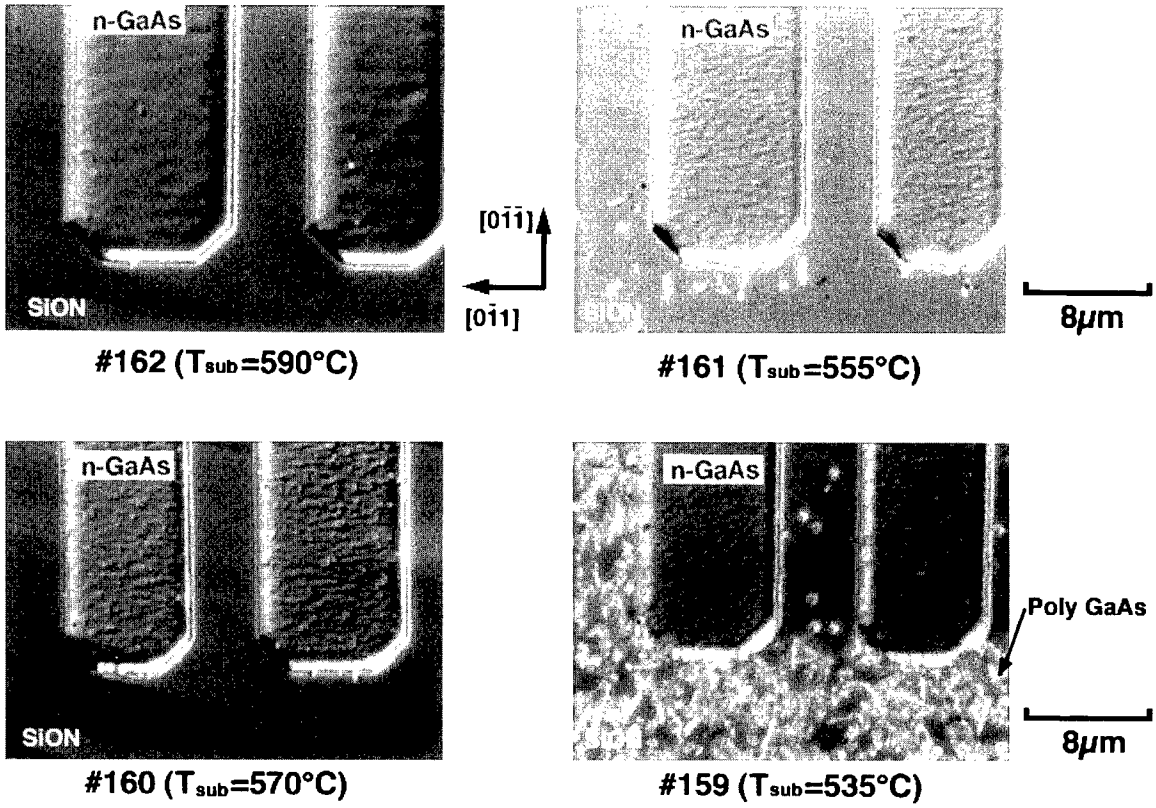

Fig. 4. Nomarski phase contrast photographs for selectively regrown n^+-GaAs region. Temperature dependence of poly-crystalline GaAs deposition on SiON mask is clearly seen.

spite of the same contact resistivity, HFET had no current flow between S/D (I_{DS}), although the normal current–voltage characteristics (I_{DS}/V_{DS}) is obtained for MESFET. Fig. 5a and Fig. 5b show cross-sectional SEM view of selectively regrown area for MESFET and HFET, respectively. Despite the fact that there is a little variation of the shape of regrowth area over a three inch diameter wafer, the trench of S/D region is well buried for MESFET. On the other hand, only the HFET structure reveals (3 1 1)A and (1 1 1)B facet formation in the [0 1 1] and [0 $\bar{1}$ 1] directions, respectively. This phenomenon suggests that revealed AlGaAs surface is easy to be oxidized and become a trigger for unexpected selectivity. The current flow was cut off by channel layer depletion due to the exposed surface. In order to bury the trench region perfectly, native oxide should be perfectly removed just prior to CBE regrowth by using every possible method, such as Cl etching, PCl_3 etching, ECR plasma etching, hydrogen radical beam irradiation and so on [3, 16–18].

4. Summary

Selective area regrowth of Si-doped GaAs has been successfully achieved on patterned trench structure fabricated by ECR plasma etching without any polycrystalline deposition on the dielectric mask film. SiI_4 has been used as a new Si-dopant source, which reveals excellent electrical quality with linear Si-doping controllability and high electrical activation in a wide range. Electrical activation

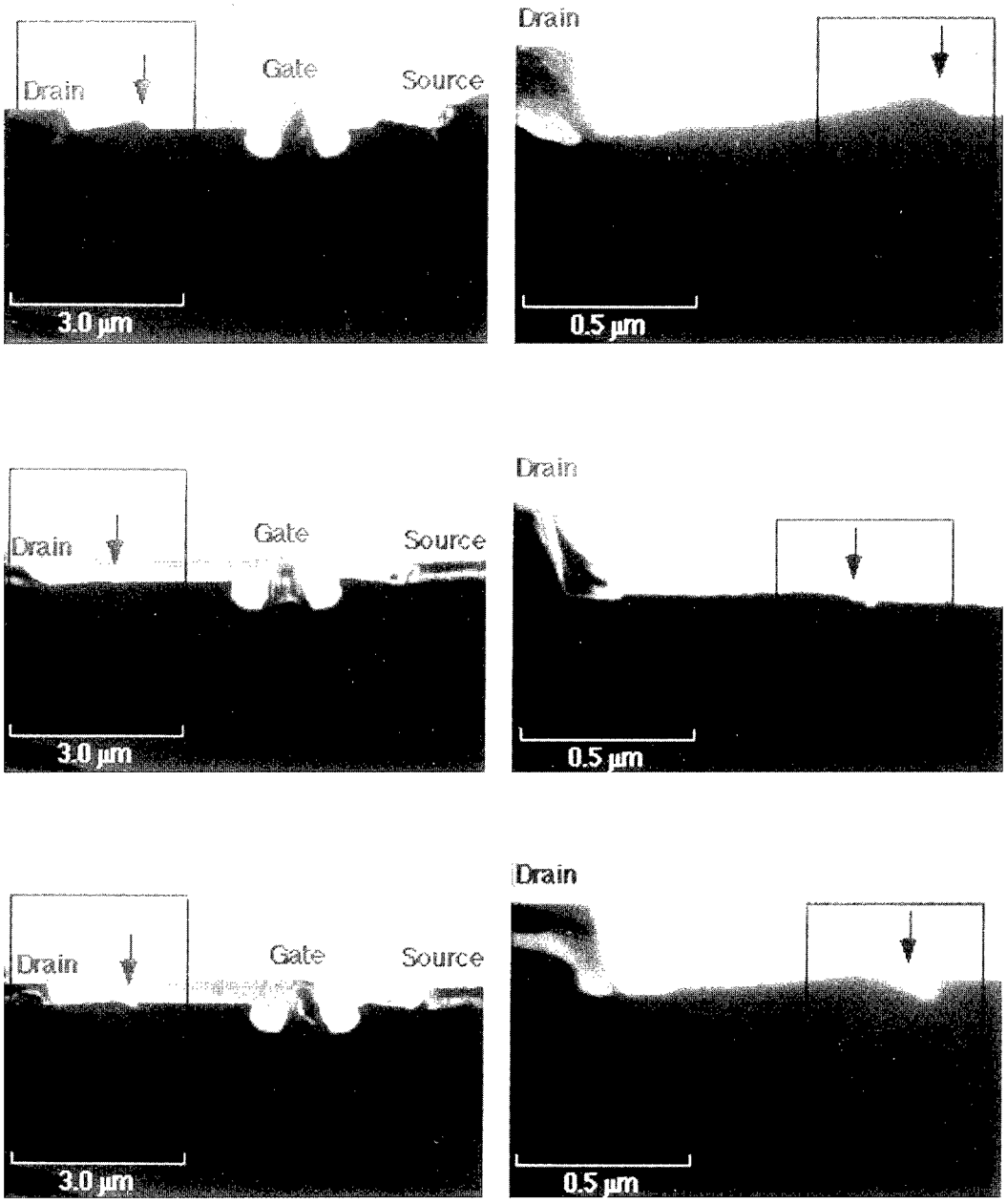

(a)

Fig. 5. Cross-sectional SEM view of buried selectively regrown layers. (a) S/D region of MESFET, (b) S/D region of HFET.

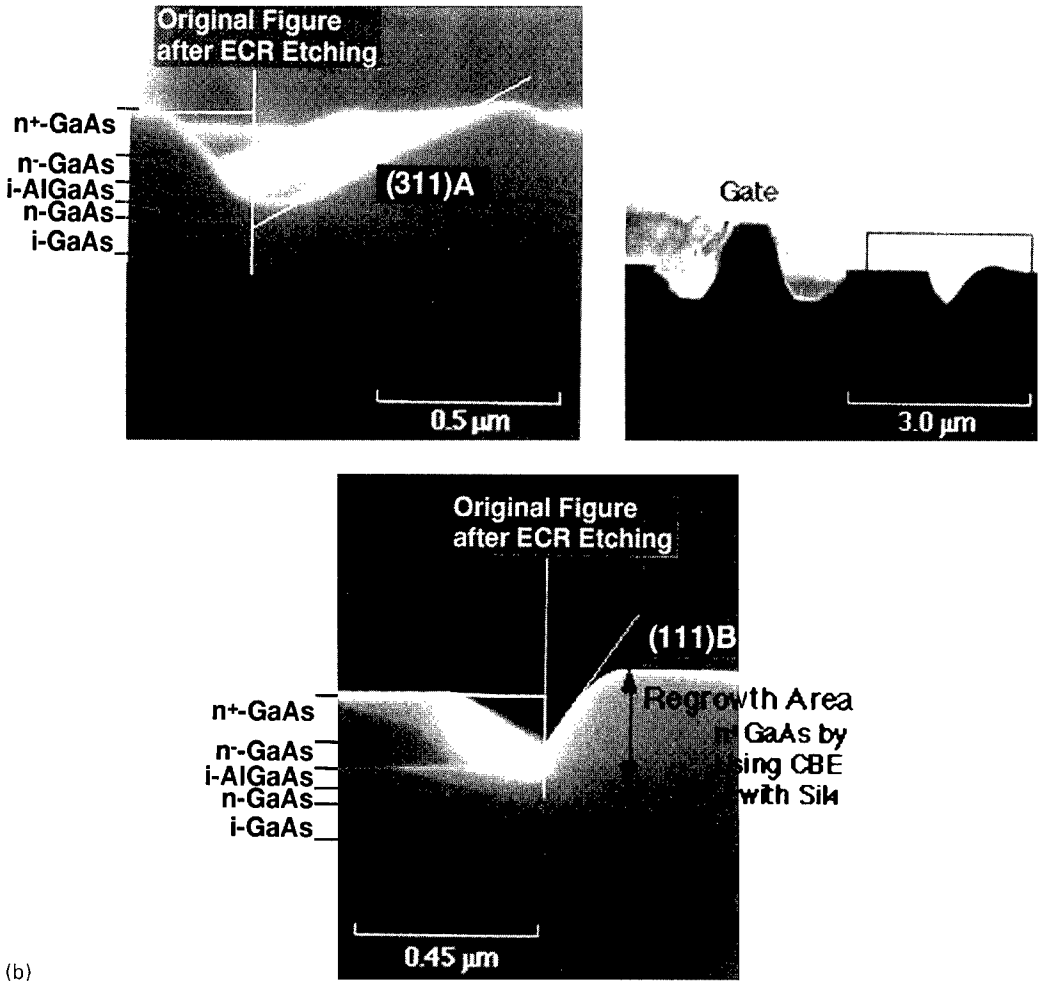

Fig. 5. (Continued)

ratio of Si in SiI_4 for both of GaAs and InP is almost 100% in the range studied, while that in Si_2H_6 is 80% or less. Sufficient low contact resistance as low as $3 \times 10^{-7}\,\Omega\,cm^2$ has achieved with Ni/AuGe/Au alloyed contact metals on Si-doped GaAs S/D surfaces. Preliminarily fabricated MESFET reveals the good I–V characteristics, although HFET operates not so well. The reason is thought to be due to the exposed AlGaAs surface which is easy to be oxidized and become a trigger for unexpected selectivity.

References

[1] S. Takatani, and J. Shigeta, IEEE-IEDM (1988) 692.
[2] A. Pavelski, P. Solomon, T.F. Kuech and M.A. Tischler, Appl. Phys. Lett. 64 (1990) 171.
[3] P. Bove, K. Ono, K. Joshin, H. Tanaka, K. Kasai and J. Komeno, J. Crystal Growth 136 (1994) 261.
[4] H. Heinecke, A. Brauers, F. Grafahrend, C. Plass, N. Putz, K. Werner, M. Weyers, H. Luth and P. Balk, J. Crystal Growth 77 (1986) 303.
[5] N. Furuhata and A. Okamoto, J. Crystal Growth 112 (1991) 1.
[6] H. Heinecke, J. Crystal Growth 136 (1994) 18.

[7] K. Kimura, S. Horiguchi, K. Kamon, M. Shimazu, M. Mashita, M. Mihara and M. Ishii, J. Crystal Growth 81 (1987) 276.
[8] M. Shimazu, K. Kamon, K. Kimura, M. Mashita, M. Mihara and M. Ishii, J. Crystal Growth 83 (1987) 327.
[9] H. Ando, N. Okamoto, A. Sandhu and T. Fujii, Jpn. J. Appl. Phys. 30 (1991) L1696.
[10] S.L. Jackson, M.T. Fresina, J.E. Baker and G.E. Stillman, Appl. Phys. Lett. 64 (1994) 2867.
[11] M.T. Fresina, S.L. Jackson and G.E. Stillman, Proc. Int. Symp. Compound Semiconds., San Diego (1994) p. 699.
[12] CRC Handbook of Chemistry and Physics, 72nd ed. (1991/1992) pp. 9–105.
[13] S. Izumi, N. Hayafuji, K. Ito, K. Sato and M. Otsubo, Appl. Phys. Lett. 68 (1996) 3102.
[14] Morton International, Inc., SiI_4 Material Safty Data Sheet.
[15] K. Ploog, in: Molecular Beam Epitaxy of III–V Compounds (Springer, Berlin, 1980) p. 73.
[16] W.T. Tsang, Semicond. Sci. Technol. 8 (1993) 1016.
[17] N. Kondo and Y. Nanishi, Jpn. J. Appl. Phys. 28 (1989) L7.
[18] H. Kizuki, N. Fujii, M. Miyashita, Y. Mihashi and S. Takamiya, J. Crystal Growth 146 (1995) 527.

ELSEVIER

Journal of Crystal Growth 175/176 (1997) 411–415

JOURNAL OF CRYSTAL GROWTH

MBE regrowth on AlGaInAs DFB gratings using in-situ hydrogen radical cleaning

H. Künzel*, J. Böttcher, A. Hase, H.-J. Hensel, K. Janiak, G. Urmann, A. Paraskevopoulos

Heinrich-Hertz-Institut für Nachrichtentechnik Berlin GmbH, Einsteinufer 37, D-10587 Berlin, Germany

Abstract

MBE regrowth on AlGaInAs surfaces structured with DFB gratings has been studied. As a crucial process, in-situ hydrogen radical processing established as a basic in-situ surface cleaning technique has been used, and appropriate process parameters have been evaluated. For an Al-content of $x_{Al} = 0.16$, adequate for waveguide layers in 1.55 μm laser structures, a short processing time of 5 min already leads to high-quality regrowth. Regrowth of InP on wet and dry etched AlGaInAs DFB gratings results in smooth and planar surfaces, with the planarisation of the growth front occurring within a thickness of 200 nm. The topography of the DFB gratings is neither affected by the hydrogen radical processing and the surface stabilisation procedure before regrowth nor by the MBE regrowth itself.

1. Introduction

1.55 μm DFB lasers represent key components for long wavelength fibre optic communication systems. Superior laser performance in terms of high temperature operation, high output power and speed as well as low chirp are expected from the implementation of $(Al_xGa_{1-x})_{0.48}In_{0.52}As$ (in the following referred to as AlGaInAs) quantum well lasers grown on InP substrates [1–3]. Such DFB lasers have been grown recently by MOVPE [3] and by a combination of solid source MBE and MOVPE [1] whereas until now a solely MBE-based fabrication has not yet been reported. A crucial step towards this aim is the successful development of an adequate regrowth procedure on DFB grating structures, which is the subject of the present work. The DFB gratings used in this study were formed in $Al_{0.16}Ga_{0.32}In_{0.52}As$ material, which corresponds to a commonly used composition of the wave guiding layer above the active quantum wells. As already previously reported [4, 5] in-situ cleaning using hydrogen radicals, H*, is the method of choice for the removal of the stable native oxide from AlGaInAs, particularly when thin layers are involved as no material is being removed in this process. In this study, the elaboration of suitable H* process conditions for the regrowth on $Al_{0.16}Ga_{0.32}In_{0.52}As$ DFB gratings will be addressed, and the impact of the stabilisation procedure before regrowth on the topography of the grating structures will be studied. The quality of the regrown layers will be described in terms of surface morphology and optical characteristics.

* Corresponding author: Fax: + 49 30 31002 558; e-mail: kuenzel@mails.hhi.de.

0022-0248/97/$17.00 Copyright © 1997 Elsevier Science B.V. All rights reserved
PII S0022-0248(96)00875-5

2. Experimental procedure

First order DFB grating structures were defined by a combination of e-beam lithography and either wet chemical etching, WCE, using a 4:1 mixture of citric acid and H_2O_2 (60 s) or dry etching with Ar/BCl_3 chemical assisted ion beam etching, CAIBE [6]. Test gratings were also made in GaInAs using CH_4/H_2 reactive ion etching, RIE.

Processed DFB grating structures and InP reference substrates were mounted side by side on Mo blocks using In solder. H* processing was performed prior to MBE regrowth in a separate cryo-pumped process chamber attached to a conventional solid source MBE system, without using any stabilising atmosphere (for further details cf. [4, 5]). After transfer of the cleaned wafers, the samples were heated up to the growth temperature, T_g, under a stabilising As_4 beam originating from a valved cracker cell. The calibration of the regrowth temperature was accomplished by means of the RHEED pattern of the reference InP sample by observation of the (2×4) to (4×2) transition of the surface reconstruction pattern. The simultaneous presence of a P_2 beam, necessary for the growth of InP and obtained from incongruent evaporation from a GaP source [7], was found not to induce any modification of the RHEED pattern during stabilisation.

Regrowth experiments were performed with InP using a P_2 beam from a GaP source [8] as well as with GaInAs or AlInAs using conventional sources at a growth rate of 1 μm/h. The growth temperatures were 440°C and 500°C for InP and GaInAs/AlInAs, respectively. The properties of the regrown layers were assessed using conventional characterisation tools: interference microscopy, scanning electron microscopy, SEM, and 300 K photoluminescence, PL.

3. Results

3.1. In-situ hydrogen radical cleaning of $Al_{0.16}Ga_{0.32}In_{0.52}As$ surfaces

Previous studies of H*-cleaning of $Al_{0.24}Ga_{0.24}In_{0.52}As$ demonstrated complete native oxide removal and reduction of surface contamination needed for high-quality regrowth [4]. In-situ Auger measurements carried out directly after H*-exposure of $(Al_xGa_{1-x})_{0.48}In_{0.52}As$ revealed an increase in cleaning efficiency with decreasing x_{Al} [9]. Thus, for $Al_{0.16}Ga_{0.32}In_{0.52}As$ the process time was reduced as compared to $Al_{0.24}Ga_{0.24}In_{0.52}As$, where a time of 25 min was found to be adequate. In order to qualify the H*-cleaning procedure for the $Al_{0.16}Ga_{0.32}In_{0.52}As$ material, we examined the optical properties of regrown GaInAs layers in terms of PL intensity, FWHM and temporal decay of the PL signal. In Fig. 1, the integral 300 K PL intensity of regrown GaInAs is depicted in dependence of the H* processing time, t_p, for a constant temperature of 350°C and a plasma power of 500 W. Data for GaInAs grown on $Al_{0.16}Ga_{0.32}In_{0.52}As$ without growth interruption are included as a reference. A strong increase of PL intensity is obvious to occur for shorter process times. The lower optical quality of the regrown material at increasing t_p may indicate that excess impurities are induced at the treated interface. This assumption is supported by the presence of donor-type accumulation at the interface, as detected by C/V-profiling [5]. The surface morphology appeared to be smooth down to $t_p = 5$ min in agreement with the high optical quality obtained, whereas further lowering of t_p resulted in an

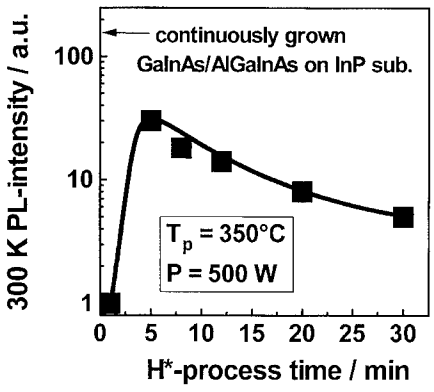

Fig. 1. 300 K PL intensity of MBE grown GaInAs on H*-treated $Al_{0.16}Ga_{0.32}In_{0.52}As$ in dependence of the process time in comparison to a continuously grown $Al_{0.16}Ga_{0.32}In_{0.52}As$/GaInAs structure.

increasing surface roughness of the regrown GaInAs along with a drastic decrease of the PL efficiency, which indicates incomplete removal of native oxide. Consequently, a constant process time of 5 min was applied throughout the MBE regrowth experiments on DFB grating structures.

A comparison of the 300 K PL data of the regrown and the continuously grown structure shows the optical quality to somewhat degrade in the case of growth interrupted and H*-treated GaInAs/AlGaInAs samples, indicating that residual impurities are still present at the treated interface. First results with an additional in-situ annealing under As following the H*-treatment not only led to a marked increase in PL intensity to values equivalent to those for continuously grown structures but also enhanced carrier lifetimes [10]. This result apparently points to a reversible change of the chemical nature of the H*-treated interface which may be due to the formation of any hydride layer at the H*-treated surface. On the other hand, the observed deficit in PL intensity seemingly has a small impact on device properties, as demonstrated on GaInAs/AlInAs quantum well laser structures incorporating one air exposed/H*-treated interface between the upper wave guiding $Al_{0.16}Ga_{0.32}In_{0.52}As$ and the AlInAs cladding layer. X-ray diffraction measurements showed that respective FWHM values were not affected by H* treatment, i.e. the FWHM of the AlInAs lower cladding layer remained constant within the measured range of 18–26 arcsec across the wafer [11]. In addition, the FWHM of the regrown AlInAs upper cladding amounted to 24 arcsec, which is the same as on a bare substrate. Device compatibility of the process was demonstrated by comparing the threshold current density of broad-area lasers made on continuously grown structures and those incorporating a growth interrupted interface. A minor discrepancy in the threshold density of at most 10% was found, meaning that the H*-process has no degrading effect [12].

3.2. Stabilisation procedure before MBE regrowth

Possible effects of the heating/stabilisation procedure before MBE regrowth on the topography of DFB gratings were studied with the help of first order (period: 240 nm) test gratings in GaInAs. These RIE-etched gratings exhibited a rather excessive height of 200 nm. The test gratings were subjected to the usual heating cycle up to a temperature of 500°C. The heat up time and the stabilising As_4 beam equivalent pressure were systematically varied between 20 and 120 min and 0.8×10^{-5} mbar and 2.4×10^{-5} mbar, respectively. After the heating/stabilisation procedure the samples were deloaded from the growth chamber and inspected by SEM. No influence of the heating/stabilisation parameters on the shape of the grating structures was detected, indicating that any pre-epitaxial desorption or redistribution of material can be excluded. As an example, Fig. 2 shows a cross-sectional SEM of the cleavage plane of such a test grating, overgrown with a 1.0 μm thick InP layer. In this particular case the grating structure was stabilised at a minimum As_4 flux and a prolonged heating time of 120 min before starting the InP regrowth. The complete preservation of the grating shape can be mainly attributed to the low temperatures involved in MBE growth. In agreement with earlier results [4], H* processing of AlGaInAs DFB gratings did not show any material removal from the horizontal and vertical planes of the gratings either.

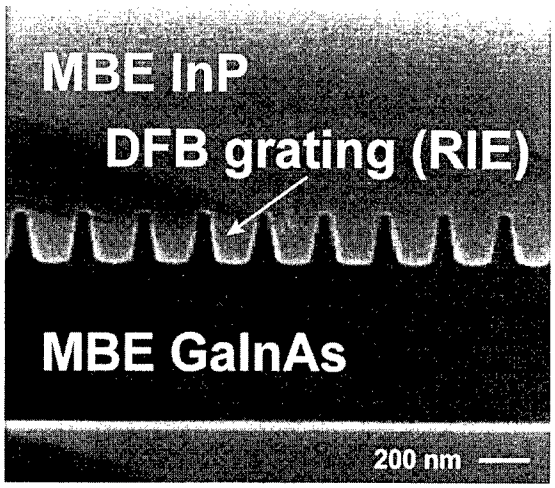

Fig. 2. SEM of the cleavage plane of MBE InP regrown on a DFB grating structure formed in GaInAs by RIE.

3.3. MBE regrowth on $Al_{0.16}Ga_{0.32}In_{0.52}As$ DFB gratings

Fig. 2 clearly shows that a flat surface finish can be obtained using MBE regrowth even for unusually high grating ridges. Complete planarisation was obtained for both GaInAs and $Al_{0.16}Ga_{0.32}In_{0.52}As$ grating structures irrespective of the applied etching technique. In contrary to InP, in the case of regrowth with GaInAs or AlInAs a rough morphology was observed despite an enhanced T_g of 500°C. SEM inspection of the cleavage plane additionally showed incomplete filling of the spacing between the ridges indicating insufficient lateral growth, probably being due to the reduced surface diffusion length of Al and Ga as compared to In. This finding is in contrast to earlier studies on GaAs-based DFB lasers, for which successful regrowth even with $Al_{0.3}Ga_{0.7}As$ material was reported [13], and may be attributed to the lower T_g applied in the case of InP-based materials.

In order to better reveal the MBE regrowth behaviour alternating 100 nm thick layers of undoped and Si-doped InP were deposited with an overall thickness of 1.5 μm. Prior to SEM inspection, the cleavage plane was selectively etched to reveal the individual InP/InP:Si interfaces and, hence, the evolution of the growth front. Fig. 3 shows a SEM micrograph of an InP-overgrown, wet chemically etched $Al_{0.16}Ga_{0.32}In_{0.52}As$ grating interface. The light lines in the regrown layer correspond to one InP/InP:Si period and demonstrate that after a nominal layer thickness of 200 nm complete planarisation is obtained. On the other hand, near the grating interface the growth rates appear strongly modified. From this it becomes obvious that lateral growth strongly prevails over vertical growth leading to a rectangular growth front and, thus, a fast infill of the DFB structure. From that point on, growth continues as on a planar surface. Basically, the same regrowth behaviour but with even further enhanced lateral growth rate was observed on trapezoidal shaped CAIBE etched AlGaInAs gratings.

As deduced from a systematic variation of the BEP(P_2/In) ratio, the growth conditions for successfully achieving perfect planarisation lie within a very narrow range. At $T_g = 420$°C smooth

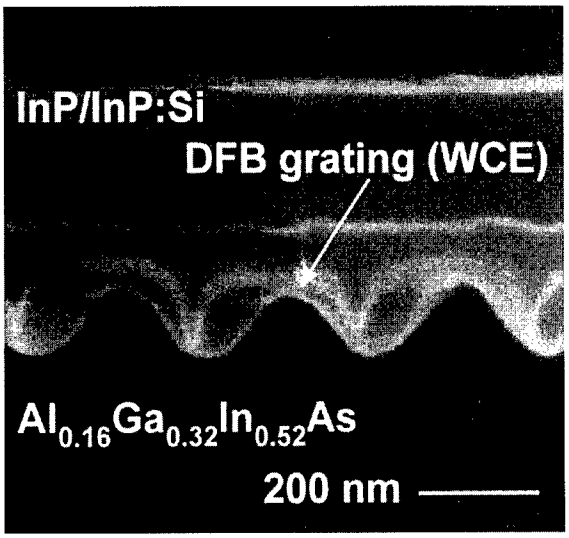

Fig. 3. SEM of the stained cleavage plane of a MBE i-InP/n^+-InP:Si layer structure regrown on a DFB grating structure defined in $Al_{0.16}Ga_{0.32}In_{0.52}As$ by wet chemical etching (WCE).

surfaces were obtained at a BEP(P_2/In) of 8. A reduction to BEP(P_2/In) = 6 results in group-V deficient growth in the grating area, whilst the material regrown on a planar surface still remaining smooth. This is attributed to the different growth planes involved in the initial stage of regrowth requiring higher BEP(P_2/In) ratios for P-stable growth in the grating area. An increase of BEP(P_2/In) towards a ratio of 10, on the other hand, again leads to a roughening of the surface in the grating area. This occurrence might reflect reduced surface diffusion lengths of the growth constituents which hinders smoothening of the growth front. However, outside the grating area the surface morphology remains perfect.

Application of growth conditions adequate for smooth regrowth on $Al_{0.16}Ga_{0.32}In_{0.52}As$ grating structures results in regrown material of high optical quality, as demonstrated by the 300 PL spectra of InP grown on a wet chemically etched grating (Fig. 4). Both, FWHM and peak intensity values approach those measured for InP grown on planar AlGaInAs outside the grating area (reference values). In addition, PL mapping on the grating area indicates a high lateral uniformity of the emission intensity. The variation amounts to

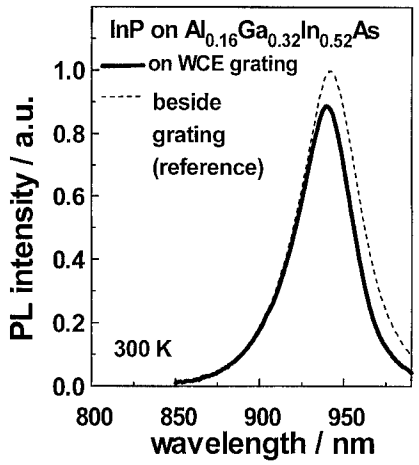

Fig. 4. 300 K PL spectra taken on MBE InP regrown on a DFB grating in $Al_{0.16}Ga_{0.32}In_{0.52}As$ (wet chemically etched) on top and beside the grating structure.

$\pm$ 5% of the mean value. For CAIBE etched gratings the PL intensity of the regrown InP was found to be reduced to approximately one-third of the reference value. This effect indicates some damage in the grating area generated during the dry etching process which, on the other hand, apparently did not affect the crystalline quality of the regrown material.

4. Summary

In summary, high-quality MBE regrowth of InP on $Al_{0.16}Ga_{0.32}In_{0.52}As$ gratings has been successfully achieved. As a prerequisite for single crystalline regrowth, hydrogen radical cleaning was applied for native oxide desorption. The heating/stabilisation procedure did not introduce any modification of the grating profile, irrespective of stabilisation conditions, due to the low temperature applied with MBE of InP-based layers. Regrowth of InP resulted in smooth surfaces. Complete planarisation within a layer thickness of nominally 200 nm, independent of the grating profile, was observed. The high optical quality reached with the regrowth process developed promises its successful application to 1.55 μm DFB laser structures based on AlGaInAs.

Acknowledgements

Part of this work was conducted under contract with Bosch-Telecom GmbH, Backnang. The authors would like to acknowledge J. Daleiden, IAF (Freiburg, Germany) for providing $Al_{0.16}Ga_{0.32}In_{0.52}As$ DFB gratings etched with CAIBE.

References

[1] H. Hillmer, R. Lösch, F. Steinhagen, W. Schlapp, A. Pöcker and H. Burkhard, Electron. Lett. 31 (1995) 1346.
[2] R. Bhat, C.E. Zah, M.A. Koza, B. Pathak, F. Favire, W. Lin, M.C. Wang, N.C. Andreadakis, D.-M. Hwang, T.P. Lee, Z. Wang, D. Darby, D. Flanders and J.J. Hsieh, J. Crystal Growth 145 (1994) 858.
[3] P.J.A. Thijs, T. van Dongen, J.J.M. Binsma and E.J. Jansen, Proc. 8th IPRM, Schwäbisch Gmünd, (1996), IEEE Catalog #96CH35930 Library of Congr. #96-75713#, p. 765.
[4] A. Hase, R. Gibis, H. Künzel and U. Griebenow, Appl. Phys. Lett. 65 (1994) 1406.
[5] H. Künzel, R. Bochnia, J. Böttcher, P. Harde, A. Hase and U. Griebenow, J. Crystal Growth 150 (1995) 18.
[6] J. Daleiden, K. Eisele, J.D. Ralston, G. Vollrath and F. Fiedler, Proc. 7th IPRM, Sapporo, (1995), IEEE Catalog #96CH35720 Library of Congr. #94-79424#, p. 632.
[7] T. Shitara and K. Eberl, Appl. Phys. Lett. 65 (1994) 356.
[8] H. Künzel, J. Böttcher, P. Harde and R. Maessen, J. Crystal Growth 175/176 (1997) 940.
[9] H. Künzel, A. Hase and U. Griebenow, Proc. 8th IPRM, Schwäbisch Gmünd (1996), IEEE Catalog #96CH35930 Library of Congres #96-75713, p. 408.
[10] A. Hase, H. Künzel, A. Moritz, J.S. Im and A. Hangleiter, unpublished results.
[11] H. Künzel, J. Böttcher, A. Hase, V. Hofsäss, C. Kaden and H. Schweizer, J. Crystal Growth 150 (1995) 1323.
[12] J. Böttcher, A. Hase, H. Künzel, A. Paraskevopoulos and G. Urmann, unpublished results.
[13] S. Noda, K. Kojima, K. Mitsunaga, K. Kyuma, K. Hamanaka and T. Nakayama, IEEE J. Quantum Electron. QE-23 (1987) 188.

ELSEVIER

Journal of Crystal Growth 175/176 (1997) 416–421

JOURNAL OF CRYSTAL GROWTH

Hydrogen radical surface cleaning of GaAs for MBE regrowth

T.M. Burke[a,*], E.H. Linfield[a], D.A. Ritchie[a], M. Pepper[a,1], J.H. Burroughes[b]

[a] *Cavendish Laboratory, University of Cambridge, Madingley Road, Cambridge CB3 0HE, UK*
[b] *Toshiba Cambridge Research Centre Ltd., 260 Cambridge Science Park, Milton Road, Cambridge CB4 4WE, UK*

Abstract

Modulation-doped GaAs/AlGaAs two-dimensional electron gas (2DEG) structures have been regrown on air-exposed GaAs buffer layers, at varying proximity to the regrowth interface. The degradation in 2DEG quality with decreasing separation from a hydrogen radical (H*) cleaned regrowth interface was found to be much reduced in comparison to that for a thermally cleaned interface. H* cleaning has allowed for the growth of a 2DEG lying only 50 nm from the regrowth interface with a mobility, after illumination, of 5.3×10^5 cm^2 V^{-1} s^{-1} at a carrier concentration of 4.2×10^{11} cm^{-2}. SIMS characterisation has been used to measure significant reductions in contamination at the regrowth interface at cleaning temperatures of 500°C. Cathodoluminescence data, measured for a 5 nm quantum well lying 30 nm from the regrowth interface, further indicate the improved growth morphology achieved following H* cleaning, in comparison to that achieved by thermal decontamination.

PACS: 61.55.Cf

Keywords: Cleaning; GaAs; MBE regrowth; Atomic nitrogen

1. Introduction

Ex-situ patterning of GaAs substrates combined with MBE regrowth provides a technique for the wafer scale production of novel three-dimensional structures [1, 2]. To exploit fully the length scales available through MBE growth in all three dimensions it is necessary to be able to regrow active layers in close proximity to the regrowth interface. The production of a clean, smooth regrowth interface therefore becomes essential [3]. Traditionally, contamination occurring at the interface following ex-situ processing, such as carbon and oxygen, has been removed by thermal desorption. Such cleaning requires temperatures in excess of ~ 600°C and can be of limited effect [4]. More recently, surface cleaning using a hydrogen radical (H*) beam has been shown to be a promising technique [5–8], being highly effective at temperatures as low as 400°C. This technique involves the reaction of incident hydrogen radicals directly with the contaminated surface layer and has been shown to result in a smoother, cleaner surface [9]. Lower

* Corresponding author. Fax: + 44 1223 337271.

[1] Also at: Toshiba Cambridge Research Centre, Ltd., 260 Cambridge Science Park, Milton Road, Cambridge CB4 4WE, UK.

0022-0248/97/$17.00 Copyright © 1997 Elsevier Science B.V. All rights reserved
PII S0022-0248(96)01029-9

temperature cleaning also results in reduced inter-diffusion of component species of patterned structures during decontamination. In this paper we present comparative results for a series of samples in which a two-dimensional electron gas (2DEG) has been regrown in close proximity to either a hydrogen or thermally cleaned interface. SIMS data, measured at the regrowth interface, is presented showing the significant level of contaminant reduction which occurs following H* cleaning at 500°C. Cathodoluminescence measurements highlight the improved morphology of the regrown layers achieved following such decontamination in comparison to that for thermally cleaned samples.

2. Experimental procedure

Carrier depletion at the regrowth interface was investigated using capacitance–voltage (C–V) measurements of a contaminated interface embedded in an n-type GaAs sample. A 2 μm GaAs buffer layer was grown, silicon doped at 1×10^{16} cm^{-3}. This sample was removed from the MBE system and cut into two halves. One-half was returned to the growth chamber without further treatment, the surface thermally decontaminated and further 1.5 μm of 1×10^{16} cm^{-3} n-type GaAs regrown. To simulate the surface of a photolithographically patterned mesa, photoresist was spun onto the surface of the second half, which was then ultrasonically cleaned in organic solvents and exposed to an oxygen plasma at 200 W for 1 min, to remove any traces of photoresist. On return to the MBE system, this sample was hydrogen radical cleaned at 500°C in a flux of 5×10^{15} cm^{-2} s^{-1} for 1 h and 1.5 μm of 1×10^{16} cm^{-3} n-type GaAs regrown. Measurement of a thermally cleaned 'patterned' interface was not carried out due to the risk of contamination of the MBE growth chamber during the production of such a sample.

To investigate the suitability of hydrogen radical cleaning for MBE regrowth, two sample sets were produced in which a two-dimensional electron gas was regrown on an air-exposed GaAs buffer layer. The GaAs buffer layers, nominally identical, were grown at a growth rate of 1 μm h^{-1} and a temperature of 630°C. All temperatures quoted were measured by infrared pyrometer. The two sets of regrown samples correspond to those in which the regrowth interface was either, A, thermally cleaned or B, hydrogen cleaned, respectively. Sample Sets A and B each comprise of three regrown wafers, the structure of which is given in Table 1. These structures were defined so as to give a two-dimensional

Table 1
Layer structures for regrown 2DEG samples

Sample			1	2	3
2DEG/regrowth interface separation			150 nm	75 nm	50 nm
Second growth					
Modulation doped structure	GaAs			10 nm	
	AlGaAs	Si doped 1×10^{18} cm^{-2}		40 nm	
	AlGaAs			20 nm	
Buffer layer structure	GaAs		105 nm	30 nm	25 nm
	AlGaAs		10 nm	10 nm	5 nm
	GaAs		5 nm	5 nm	5 nm
	AlGaAs		10 nm	10 nm	5 nm
	GaAs		20 nm	20 nm	10 nm
First growth					
Buffer	GaAs		1 μm	1 μm	1 μm

electron gas at varying proximity to the GaAs buffer layer/regrown layer interface (namely 150, 75 and 50 nm). To allow for subsequent cathodoluminescence measurements to be carried out on these samples, a GaAs quantum well (10 or 5 nm) was also incorporated into the growth schedule between the regrowth interface and the 2DEG. Each of the samples was regrown at a temperature of 630°C with the growth rate for GaAs of 1 μmh^{-1} and an AlGaAs mole fraction of 33%.

For the samples in Set A, thermal decontamination of the surface of the air-exposed buffer, carried out immediately prior to regrowth, consisted of heating the GaAs layer for 20 min in an excess arsenic pressure at a temperature of 650°C.

For the samples in Set B, prior to regrowth, the GaAs buffer layer was loaded into a dedicated decontamination chamber linked to the VG V80H MBE system via a UHV transfer tunnel. The decontamination chamber comprises of a VG Microtech SIMS300 quadrupole analyser for surface analysis and an Oxford Applied Research MPD21I RF radical source for surface cleaning. The base pressure of both the decontamination chamber and the transfer tunnel was 1×10^{-10} mbar.

To assess the level of contamination at the surface of the air-exposed buffer, static SIMS profiles were collected using an incident argon ion beam of energy 3.5 keV rastered over an area of 1 mm^2. The current at the sample during data collection was 1 nA. Following SIMS data collection, each of the Set B samples was cleaned in a hydrogen radical flux of 5×10^{15} cm^{-2} s^{-1} for 2 h. The chamber pressure during cleaning was constant at 4.6×10^{-4} mbar and each of the samples was cleaned at a pyrometer measured temperature of 500°C. Following cleaning, a second SIMS profile was taken of the hydrogen-treated GaAs surface to assess the level of contaminant reduction achieved. The sample was then immediately transferred to the MBE growth chamber and the modulation-doped structure regrown.

3. Results and discussion

Thermal decontamination of air-exposed GaAs surfaces results in a p-type layer at the regrowth interface. This can be seen from Fig. 1 which shows the carrier concentration versus depth profile for the n-type GaAs sample around the region of the thermally cleaned regrowth interface. From the data in Fig. 1, measured at room temperature, an interface state density of 7×10^{11} cm^{-2} is obtained for the thermally cleaned interface. Also shown in Fig. 1 is the corresponding profile for the hydrogen cleaned, 'patterned' n-type sample. This sample shows a reduced interface state density of 3×10^{11} cm^{-2}, significantly improved over that for an air exposed, thermally cleaned interface. These data therefore indicate the improved interface quality that can be achieved using hydrogen radical cleaning, even for patterned substrates.

In Fig. 2 the 2DEG carrier concentration and mobility of the thermally cleaned samples, Set A, are given as a function of 2DEG/regrowth interface separation. These data were measured at

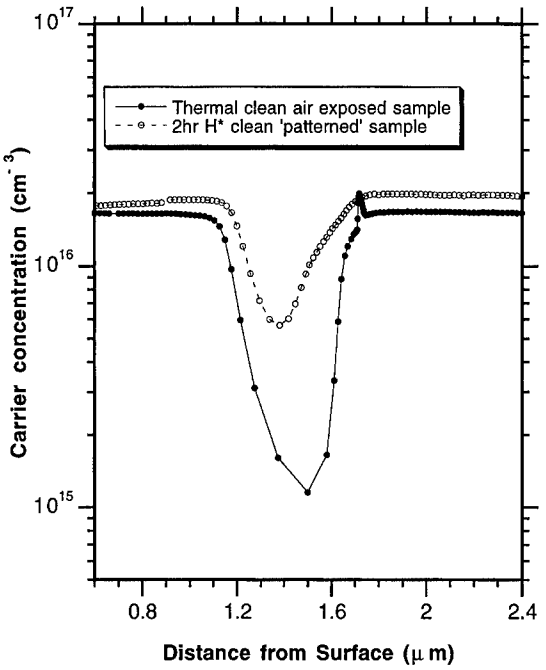

Fig. 1. Carrier concentration versus depth profiles for (nominally) 1×10^{16} cm^3, n-type GaAs samples around region of embedded thermally cleaned, air-exposed interface (dashed line, open circles) and hydrogen-cleaned, 'patterned' interface (solid line, filled circles).

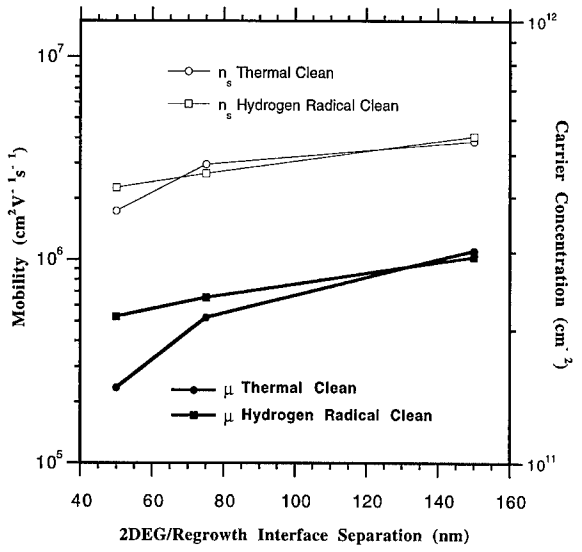

Fig. 2. Log carrier concentration n_s and mobility μ for hydrogen radical cleaned and thermally cleaned samples as a function of 2DEG separation from regrowth interface.

a temperature of 1.5 K, after illumination with a red LED. At a 2DEG/regrowth interface separation of 150 nm, the measured 2DEG carrier concentration and mobility corresponds to that for a standard 2DEG sample, grown during the same period, with the following structure: 1 μm GaAs buffer, 20 nm AlGaAs spacer, 40 nm AlGaAs Si doped at 1×10^{18} cm^{-2} and 10 nm GaAs cap, grown on an semi-insulating epiready substrate. However, as the 2DEG is brought into greater proximity with the regrowth interface depletion of the 2DEG carrier concentration can be observed due to the presence of the p-type region at the interface, falling to 3.7×10^{11} cm^{-2} at a separation of 50 nm. Also shown in Fig. 2 is the corresponding carrier concentration versus 2DEG/regrowth interface separation profile for the H* cleaned samples of Set B. For 2DEG/regrowth interface separations of 150 and 75 nm, the 2DEG carrier concentration for the H*-cleaned samples lie very close to that for the corresponding thermally cleaned sample. However, at a separation of 50 nm, the depletion of the 2DEG for the H*-cleaned samples is substantially reduced over that for the thermally cleaned samples, indicating a reduction in the internal field resulting from interface states and thus a reduced contaminant level at the H*-cleaned regrowth interface.

Also shown in Fig. 2 is the 2DEG mobility as a function of 2DEG/regrowth interface separation for both Set A and Set B samples. As the 2DEG carrier concentration falls, reduced screening of the 2DEG electrons from the scattering potential of the ionised donors in the AlGaAs, as well as any scattering due to the interface, will reduce the mobility of the 2DEG. The field due to the contaminated interface may also drive the electron wave function further towards the doped AlGaAs region, again increasing scattering of the 2DEG electrons. From Fig. 2 the 2DEG mobility for the thermally cleaned samples can be seen to degrade rapidly with the increasing proximity of the regrowth interface. This reduction may be enhanced by poor morphology in the region of the 2DEG, propagating from a rough interface. Previous studies have shown that thermal cleaning of GaAs results in a cleaned surface substantially rougher, on the atomic scale, than that achieved using hydrogen radical cleaning [10]. It can be seen from Fig. 2 that the mobility of the H*-cleaned samples is greater than the corresponding thermally cleaned samples at both 75 and 50 nm. Hydrogen radical cleaning of the regrowth interface has thus resulted in the production of a 2DEG lying only 50 nm from the regrowth interface with a low-temperature mobility, after illumination, of 5.3×10^5 cm^2 V^{-1}s^{-1} at a carrier concentration of 4.2×10^{11} cm^{-2}. This is a substantial improvement in 2DEG quality over that achieved by standard thermal decontamination.

For each of the thermally cleaned samples of Set A, population of the 2DEG was only possible following illumination. However, the hydrogen cleaned sample of Set B, having a 2DEG/regrowth interface separation of 50nm, gave a 2DEG in the dark with a low temperature mobility of 1.6×10^4 cm^2 V^{-1} s^{-1} at a carrier concentration of 1.2×10^{11} cm^{-2}. This result provides further evidence for the suitability of hydrogen radical cleaning for the regrowth of high-quality 2DEGs in close proximity to the regrowth interface.

This improvement in 2DEG quality may be related to the effective removal of contaminant species at the relatively low temperature of 500°C, following hydrogen radical cleaning. In Fig. 3

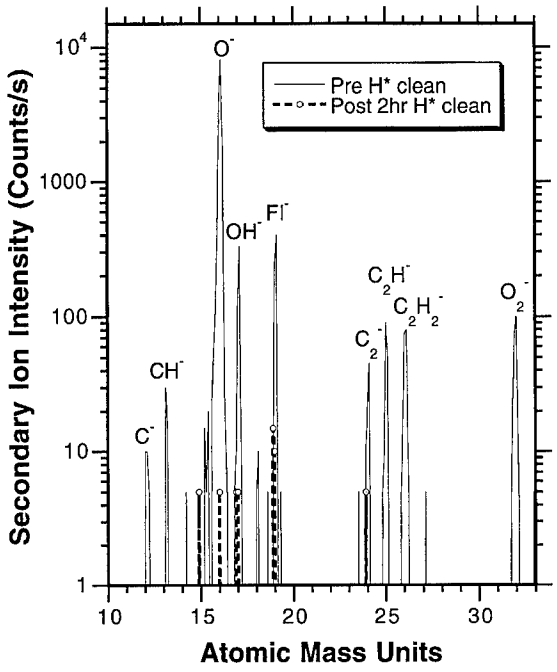

Fig. 3. Negative ion SIMS surface scans for air-exposed GaAs buffer layer showing oxygen and hydrocarbon contamination levels at the patterned regrowth interface before and after H* cleaning.

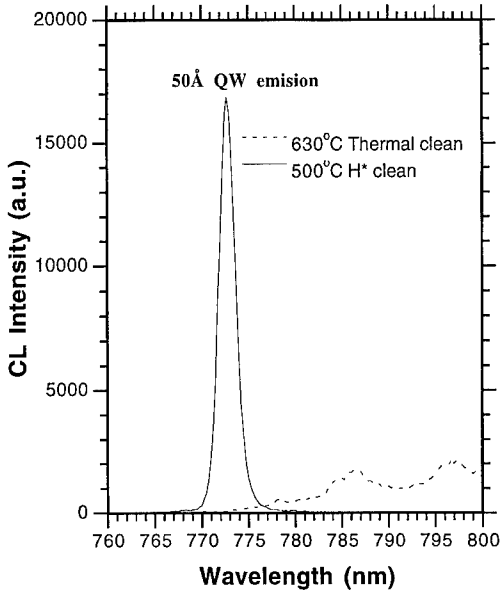

Fig. 4. CL emission from 50 nm quantum well, 30 nm from 500°C hydrogen radical cleaned (solid line) and 630°C thermally cleaned (dashed line) regrowth interface.

negative ion SIMS scans are given which were taken before and after hydrogen cleaning of the air-exposed GaAs buffer, on which the 50 nm separation 2DEG sample was regrown. Oxide levels at the surface are seen to be reduced by three orders of magnitude, below the detection level of the SIMS ($\sim 1 \times 10^{16}$ cm^{-3}). Hydrocarbon levels are also seen to be drastically reduced following the hydrogen cleaning procedure.

Fig. 4 shows cathodoluminescence (CL) scans for both the thermally and hydrogen-cleaned samples in which the 2DEG lies 75nm from the regrowth interface. The data given were measured at a beam energy of 10 keV, beam current of 100 pA and a sample temperature of 4.2 K. The region of the CL data shown relates to emission from the 5 nm quantum well, which lies 30 nm from the regrowth interface. For the hydrogen-cleaned sample a clear emission peak, due to the well, is observed at 772 nm, with a full-width half-maximum of 2 nm. In contrast, no emission is observed at this point for the thermally cleaned sample. A broad-low intensity feature, visible at $\sim$ 786 nm, may be due to emission from the quantum well in this sample, Stark shifted due to the high internal field resulting from the p-type regrowth interface. However, the substantial improvement in the growth quality in the near regrowth interface region, due to H* radical cleaning, is clearly evident from the data in Fig. 4. Surface CL emission scans, measured for the hydrogen-cleaned sample at 772 nm and for the thermally cleaned sample at 786 nm are shown in Fig. 5 and provide further evidence for the poor morphology associated with thermal cleaning of the regrowth interface in comparison to that achieved following H* cleaning.

H* cleaning had also been applied to the growth of resonant tunnelling devices, in which the regrowth interface lies between the collector and the double-barrier structure [11]. For thermally cleaned samples, the presence of contamination at the regrowth interface in these devices pins the Fermi level at the interface. The assymetry

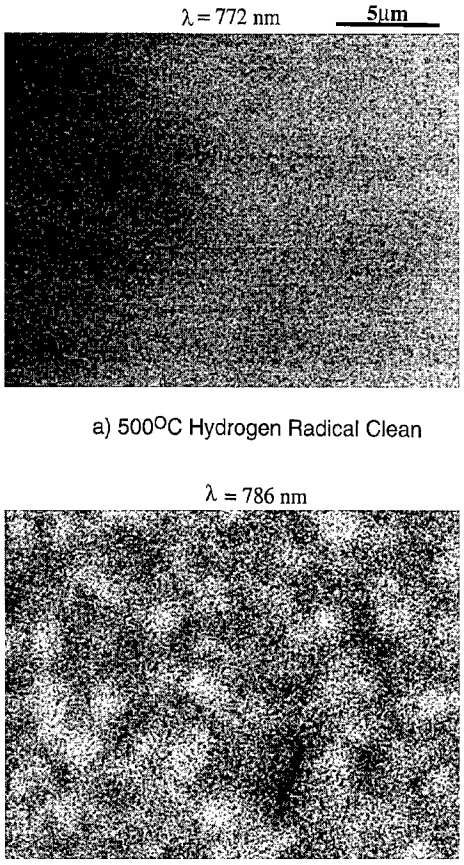

Fig. 5. Surface CL emission scans for 500°C hydrogen radical cleaned sample (measured at 772 nm) and 630°C thermally cleaned sample (measured at 786 nm) showing improved morphology after hydrogen radical cleaning.

introduced into the tunnelling structure by such pinning is reflected in an assymetric current–voltage curve for the device. H* cleaning of the regrowth interface has been found to restore the tunnelling characteristics to that for a similar tunnelling structure grown without the presence of a regrowth interface. H* cleaning of the regrowth interface has therefore substantially improved the operation of this device. This may be related to the improved quality which may be achieved at a patterned interface following such cleaning, as shown by the CV profiles in Fig. 1.

4. Conclusions

MBE regrowth of modulation-doped 2DEG structures on air-exposed GaAs buffers has been used to show the increased regrowth quality which may be achieved following hydrogen radical cleaning of the regrowth interface in comparison to standard thermal cleaning. SIMS data, collected before and after hydrogen cleaning, indicate the effective decontamination of the regrowth interface at temperatures of only 500°C. CL data, measured for a 5 nm quantum well lying 30 nm from the interface, show the improved morphology of the regrown layers following such hydrogen cleaning. These results highlight the suitability of hydrogen radical cleaning for the regrowth of sensitive device structures in close proximity to the regrowth interface.

Acknowledgements

We would like to thank L.L. Wang and S. Stevens for assistance in processing the samples. Work at the Cavendish Laboratory was supported by the EPSRC.

References

[1] R.J. Evans, T.M. Burke, J.H. Burroughes, M.P. Grimshaw, D.A. Ritchie and M. Pepper, Appl. Phys. Lett. 68 (1996) 1708.
[2] J.H. Burroughes, M.P. Grimshaw, M.L. Leadbetter, D.A. Ritchie, M. Pepper and G.A.C. Jones, J. Vac. Sci. Technol. B12 (1994) 1271.
[3] M.P. Grimshaw, D.A. Ritchie, J.H. Burroughes and G.A.C. Jones, J. Vac. Sci. Technol. B 12 (1994) 1290.
[4] S. Sugata et al., J. Vac. Sci. Technol. B 6 (1988) 1087.
[5] M. Yamada, I. Yuichi and T. Kiyoshi, Jpn. J. Appl. Phys. 31 (1992) L1157.
[6] M. Yamada and I. Yuichi, Jpn. J. Appl. Phys. 33 (1994) L671.
[7] E.J. Petit and F. Houzay, J. Vac. Sci. Technol. B 12 (1994) 1547.
[8] Y. Ide and M. Yamada, J. Vac. Sci. Technol. A 12 (1994) 1858.
[9] C.M. Rouleau and R.M. Park, J. Appl. Phys. 73 (1993) 4610.
[10] Y. Morishita, Y. Nomura, S. Goto, M. Yamada and Y. Katayama, Jpn. J. Appl. Phys. 34 (1995) L397.
[11] T.M. Burke, E.H. Linfiled, D.A. Ritchie, M. Pepper and J.H. Burroughes, to be published.

ELSEVIER

Journal of Crystal Growth 175/176 (1997) 422–427

JOURNAL OF CRYSTAL GROWTH

Novel $Ga_2O_3(Gd_2O_3)$ passivation techniques to produce low D_{it} oxide-GaAs interfaces

M. Hong*, J.P. Mannaerts, J.E. Bower , J. Kwo, M. Passlack[1], W-Y. Hwang, L.W. Tu[2]

Bell Laboratories, Lucent Technologies, 600 Mountain Avenue, Murray Hill, New Jersey 07974, USA

Abstract

Molecular beam epitaxy (MBE) has been extended to fabricate heterostructures of $Ga_2O_3(Gd_2O_3)$–GaAs. Two processes were used: (1) in situ approach in which the oxide molecules were deposited on freshly prepared GaAs (1 0 0), and (2) ex situ approach which comprises thermal desorption of native oxides of GaAs and subsequent $Ga_2O_3(Gd_2O_3)$ film deposition on GaAs (1 0 0) wafers all under ultra-high vacuum. A low interface recombination velocity S of 9000 cm/s equivalent to an interface state density D_{it} in the upper 10^{10} cm^{-2} eV^{-1} range has been inferred for the ex situ processed samples. In comparison, an interface recombination velocity of 4000–5000 cm/s and an interface state density D_{it} in the lower 10^{10} cm^{-2} eV^{-1} range were obtained for the in situ processed samples. The ex situ technique provides excellent passivation for GaAs wafers which may have been exposed to room air and/or processing environments during fabrication of devices such as FETs, HBTs, etc.

PACS: 68.55.Bd; 73.20.At; 73.40.Qv

Keywords: GaAs; Passivation; Low interface state density

1. Introduction

Low-power components are key to the widespread use of high-performance portable systems, such as cellular telephones, personal communicators, etc. At present, bulk Si CMOS offers significant advantages in terms of integration level and cost; however, drastic reductions in circuit speed of scaled bulk Si CMOS are anticipated as the power supply is scaled to 1 V or below [1]. Technologies using high mobility materials such as GaAs and related compounds would be a natural choice for low-power, high speed and high frequency devices. However, thermodynamically stable oxide-GaAs interfaces with low interface state density were not available and the fabrication of such heterostructures has remained one of the key challenges in the field of compound semiconductors during the last

* Corresponding author. Fax: + 1 908 582 2043; e-mail: mhw@bell-labs.com.

[1] Present address: Motorola Inc., Phoenix Corporate Research Laboratories, 2100 E. Elliot Road, Tempe, Arizona 85284, USA.

[2] Present address: Department of Physics, National Sun Yat-Sen University, Kaoshiung, Taiwan, ROC.

0022-0248/97/$17.00 Copyright © 1997 Elsevier Science B.V. All rights reserved
PII S0022-0248(96)01202-X

three decades [2]. Previous efforts include: (a) thermal, anodic, and plasma surface oxidation, (b) deposition of dielectric films, and (c) deposition of dielectric films after dry or wet surface treatments, which produced limited improvements of electronic properties of interfaces with $D_{it} \sim 10^{12}$ cm^{-2} eV^{-1} [2–5].

Approaches to overcome major sources of interface states should at least address the following aspects: (i) surface exposure and defects [6], (ii) thermodynamic instability [7], and (iii) intrinsic Fermi level pinning [8]. Experimentally, in order to overcome these major sources of interface states, first, it is required to achieve an atomically ordered and chemically clean GaAs surface before the deposition of the dielectric materials; therefore, ultra high vacuum is needed to minimize surface exposure, particularly to avoid oxidation. Any chemical reactions between the deposited species and GaAs surface must be excluded to achieve thermodynamic stability. Furthermore, there should be no introduction of GaAs gap states by the electronic structures of the deposited species.

In this paper we discuss the extension of MBE technique toward deposition of $Ga_2O_3(Gd_2O_3)$ molecules on GaAs. The new methods have provided the required ingredients for the implementation of thermodynamically stable, low D_{it} oxide-GaAs interfaces. Two different processes were used here in the preparation of GaAs surfaces for the oxide deposition: in situ, and ex situ approaches. For the in situ approach, a multiple-chamber MBE system [9] must be used, in which $Ga_2O_3(Gd_2O_3)$ was deposited on freshly grown GaAs epilayers with the growth of oxides and GaAs carried out in two separate chambers. There are transfer modules (under a ultra-high vacuum) connecting these two growth chambers. The in situ process, however, requires complex equipment and moreover, it is not readily applicable to electronic passivation of GaAs surfaces which were exposed to either processing environments and/or room air during device fabrication. The ex situ approach involves the deposition of $Ga_2O_3(Gd_2O_3)$ on thermally desorbed GaAs, all carried out in one UHV chamber. The latter technique provides efficient and thermodynamically stable insulator passivation of exposed GaAs surfaces for the first time.

2. Experiment

Here, we have used wafers consisting of a 1.5 μm thick n-type with a donor concentration of 1.6×10^{16} cm^{-3} GaAs epilayer grown by MBE on heavily Si doped (2×10^{18} cm^{-3}) GaAs (1 0 0) substrates. In the in situ approach, the wafers with the freshly prepared GaAs films were transferred under a vacuum of 6×10^{-11} Torr to the oxide chamber for deposition; Thus, no contamination or oxidation was incurred on the GaAs surface prior to the oxide deposition. An As-stabilized GaAs surface reconstruction of (2 × 4) was maintained. The background pressure of the oxide chamber was below 1×10^{-9} Torr.

For the ex situ process, the wafers were removed from the MBE chamber, exposed to room air for at least three days, and then put in the oxide chamber for deposition. Before the deposition of $Ga_2O_3(Gd_2O_3)$ molecules, the native oxides on the GaAs surface of the wafers were thermally desorbed with the substrate temperatures in the range of 580–600°C in the oxide chamber without As overpressure. Reflection high energy electron diffraction (RHEED) was used to monitor the process of native oxide desorption.

For both the in situ and ex situ approaches, $Ga_2O_3(Gd_2O_3)$ films were deposited by electron-beam evaporation of a single-crystal $Gd_3Ga_5O_{12}$ source at substrate temperatures in the range of 350–600°C. The single-crystal $Gd_3Ga_5O_{12}$ source material was chosen because of the unavailability of single crystal Ga_2O_3. Single crystal was preferred over the powder packed one due to the consideration of material purity.

Structural properties of the $Ga_2O_3(Gd_2O_3)$ films were investigated by transmission electron microscopy (TEM). Chemical composition profiles of the $Ga_2O_3(Gd_2O_3)$–GaAs heterostructures were studied by Rutherford backscattering spectrometry (RBS) and by X-ray photoelectron spectroscopy (XPS) [10]. Interfacial As 3d and Ga 3d core levels were acquired using a Perkin Elmer 5600 series XPS spectrometer equipped with a monochromatic Al K_α X-ray source. XPS depth profiling in chemical composition was performed in situ by Ar sputtering in a UHV chamber with a background pressure of 5×10^{-10} Torr. Electronic properties of

the ex situ fabricated $Ga_2O_3(Gd_2O_3)$–GaAs interface were investigated by standard steady-state photoluminescence (PL) measurements using an argon ion laser ($\lambda = 514.5$ nm).

3. Results and discussion

RHEED observation of the GaAs surface after the removal of the native oxides for the ex situ process shows no surface reconstruction; The RHEED pattern is not continuous, and is arrow-like in the nominal $4x$ direction (Fig. 1a). In comparison, a RHEED picture of the GaAs surface from the in situ process is shown in Fig. 1b. The surface reconstruction (2×4) and long streaky RHEED patterns observed on the in situ GaAs indicates an atomically ordered and smooth surface. From our previous study [9], chemically clean and contamination-free GaAs surface is easily obtained using the in situ process. The GaAs surface prepared by thermal desorption in the ex situ process would inevitably contain carbon, silicon, and oxygen, as was studied earlier [11, 12]. The surface contamination may contribute to the observation of no surface reconstruction on the ex situ GaAs. Furthermore, the discontinuous and arrow-like RHEED streaks are indicative of surface roughness and faceting.

The inferior surface properties of the ex situ prepared GaAs are believed to cause the higher recombination velocity and interface state density D_{it} as will be discussed later in the paper. The roughness, faceting, and no reconstruction on the ex situ GaAs surface, however, can be improved with the desorption of the native oxides performed under As overpressure. Moreover, an atomically smooth and chemically clean GaAs (as clean as

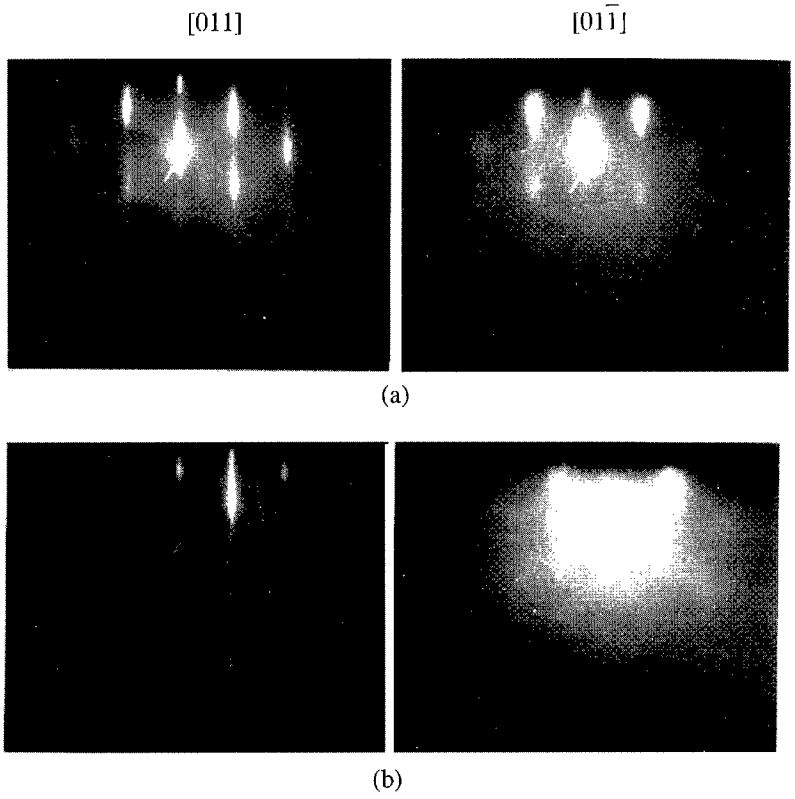

Fig. 1. (a) RHEED patterns along GaAs [0 1 1] and [0 1 $\bar{1}$] directions on GaAs (1 0 0) after native oxide desorption from an ex situ approach, and (b) RHEED patterns along GaAs [0 1 1] and [0 1 $\bar{1}$] directions on GaAs (1 0 0) from an in situ sample.

a surface of freshly grown GaAs) has been obtained using a dry etching method of H_2 electron cyclotron resonance (ECR) hydrogen plasma treatment followed by Cl_2 chemical etching [12].

RBS results for $Ga_2O_3(Gd_2O_3)$ on GaAs are shown in Fig. 2a and Fig. 2b for substrate temperatures of 360 and 550°C, respectively. Sticking coefficients of Ga_2O_3 and Gd_2O_3 on GaAs varies with substrate temperatures, with a higher coefficient for Gd_2O_3 at higher substrate temperatures. It is noted that the percentage of Gd_2O_3 in the oxide film is around 35% in Fig. 2b. A peak near channel 400, shown in Fig. 2b, is caused by the channeling effect on the GaAs epilayer. On the contrast, the Gd_2O_3 in the film prepared at lower substrate temperatures, such as the one shown in Fig. 2a, is negligibly small. A systematic study of Gd_2O_3 to Ga_2O_3 ratios as a function of substrate temperatures is now underway. The $Ga_2O_3(Gd_2O_3)$ films are amorphous as observed from TEM and in situ RHEED.

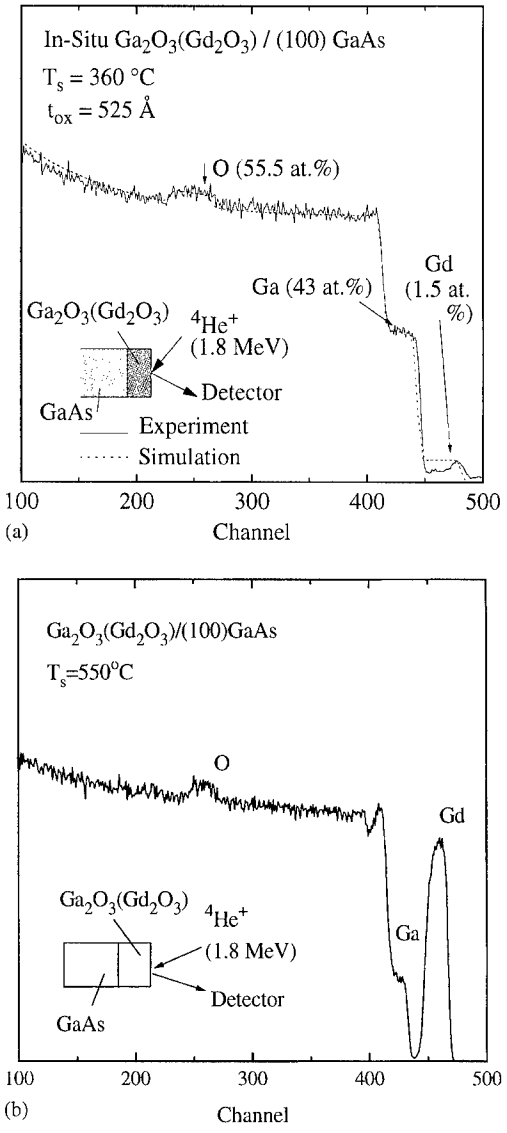

Fig. 2. RBS depth profiles for $Ga_2O_3(Gd_2O_3)$–GaAs structures, with substrate temperature during the oxide deposition at (a) 360°C and (b) 550°C.

The interfacial depth profiles of ex situ fabricated $Ga_2O_3(Gd_2O_3)$–GaAs structures studied by XPS are virtually identical to those obtained from in situ fabricated $Ga_2O_3(Gd_2O_3)$–GaAs interfaces [8, 10]. Chemical reaction products, in particular As_2O_3 and As_2O_5 are not detectable. Consequently, the chemical reaction $As_2O_3 + 2GaAs \rightarrow Ga_2O_3 + 4As$ ($\Delta G = -62$ kcal/mol) resulting in As formation and degradation of electronic interface properties is excluded. This is consistent with the prediction based on thermochemical phase diagrams [7] and is indicative of thermodynamic stability of the oxide–GaAs interface.

The internal quantum efficiency η has been measured over a wide range of incident light intensities ($1 \leqslant I_0 \leqslant 10^4$ W/cm^2) in order to infer the interface recombination velocity S. The technique is based on the relative weight of non-radiative and radiative recombination as a function of I_0 resulting in a unique curve shape of η versus I_0 for a specific surface recombination velocity S [13, 14]. This is demonstrated in Fig. 3 which shows the measured (triangles) and calculated (solid line) internal quantum efficiency η of ex situ fabricated $Ga_2O_3(Gd_2O_3)$–GaAs samples as a function of I'_0, where $I'_0 = T\ I_0$ with T being the optical transmissivity of the samples. Since the PL intensity is not measured in absolute units, the measured curves are rigidly shifted to the position of the calculated ones [15]. For the purpose of comparison, Fig. 3 also shows results typically measured on in situ fabricated $Ga_2O_3(Gd_2O_3)$–GaAs (squares, diamonds and circles) and conventional $Al_{0.45}Ga_{0.55}As$–GaAs interfaces (plus) [8]. The best fit of the simulations to the measurement data

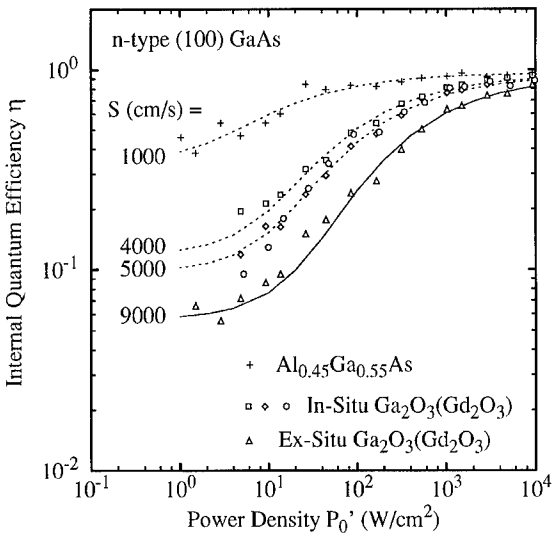

Fig. 3. Measured (symbols) and calculated (lines) internal quantum efficiency η of ex situ and in situ fabricated $Ga_2O_3(Gd_2O_3)$–GaAs samples and for conventional $As_{0.45}Ga_{0.55}As$–GaAs structures as a function of $I_0' = T I_0$. For in situ fabricated interfaces, diamonds, squares and circles represent results measured for $T_s = 360°C$, 550°C and 620°C, respectively.

has been obtained at $S = 9000$, 4000–5000, and 1000 cm/s for ex situ fabricated $Ga_2O_3(Gd_2O_3)$–GaAs, in situ fabricated $Ga_2O_3(Gd_2O_3)$–GaAs and conventional $Al_{0.45}Ga_{0.55}As$–GaAs structures.

Based on previously reported D_{it} in the low 10^{10} cm^{-2} eV^{-1} range as inferred from CV and GV characteristics for in situ fabricated $Ga_2O_3(Gd_2O_3)$–GaAs interfaces [8, 16], the estimated interface state density D_{it} observed at the ex situ fabricated $Ga_2O_3(Gd_2O_3)$–GaAs is in the upper 10^{10} cm^{-2} eV^{-1} range. The derivation of D_{it} at the ex situ fabricated interface is based on the linear relation between S and D_{it} [14]. The results reveal that excellent interface properties are also attainable for ex situ fabricated $Ga_2O_3(Gd_2O_3)$–GaAs interfaces. The simulation results shown in Fig. 3 have been obtained from calculated PL depth profiles using a self-consistent device model for semiconductor heterostructures [17].

Other oxide–GaAs heterostructures were also made using the in situ approach [18]. The interfacial depth profiles of these oxide–GaAs structures are similar to those obtained in the $Ga_2O_3(Gd_2O_3)$–GaAs interfaces using XPS, namely no observation of As_2O_3 and As_2O_5. However, the interface state density in the other oxide–GaAs is very high, in strong contrast to those observed in the $Ga_2O_3(Gd_2O_3)$–GaAs. It is, therefore, clear that in addition to (i) clean and atomically ordered GaAs surface and (ii) no As_xO_y at the oxide–GaAs interface, the attainment of low D_{it} also requires no introduction of GaAs gap states by the deposited oxides. The reason why low D_{it} is achieved in the $Ga_2O_3(Gd_2O_3)$–GaAs, but not in other oxide–GaAs heterointerfaces, is under investigation.

4. Conclusions

We have demonstrated the capability of the $Ga_2O_3(Gd_2O_3)$ deposition processes to provide excellent oxide–GaAs interface properties including low surface recombination velocity S and low interface state density. The ex situ process, in which S and D_{it} of 9000 cm/s and in the upper 10^{10} cm^{-2} eV^{-1} range were achieved, respectively, represents a significant development beyond the previously demonstrated in situ $Ga_2O_3(Gd_2O_3)$ deposition technique which produces oxide–GaAs interfaces with $S = 4000$–5000 cm/s and D_{it} in the low 10^{10} cm^{-2} eV^{-1} range [8]. We believe that the interface properties of the ex situ prepared GaAs can be further improved when an atomically smooth and chemically clean GaAs surface is obtained. The new ex situ deposition technique is compatible with GaAs device processing and will significantly improve existing GaAs based device technologies.

Acknowledgements

M. Hong and J.P. Mannaerts gratefully thank A.Y. Cho for his support and technical discussions. M. Passlack gratefully acknowledges support by the Deutsche Forschungsgemeinschaft.

References

[1] G. Schrom, C. Pichler, T. Simlinger and S. Selberherr, Solid State Electron. 39 (1996) 425.

[2] L.G. Meiners, D.L. Lille, J.F. Wagner, C.W. Wilmsen and R.W. Williams, Physics and Chemistry of III–V Compound Semiconductor Interfaces (Plenum, New York, 1985) chs. 1,3,4,6.
[3] J.S. Herman and F.L. Terry, Appl. Phys. Lett. 60 (1992) 716.
[4] C.J. Sandroff, M.S. Hedge, L.A. Farrow, R. Bhat, J.P. Harbison and C.C. Chang, J. Appl. Phys. 67 (1990) 586.
[5] A. Callegari, P.D. Hoh, D.A. Buchanan and D. Lacey, Appl. Phys. Lett. 54 (1989) 332.
[6] W.E. Spicer, I. Lindau, P. Skeath, C.Y. Su and P. Chye, J. Vac. Sci. Technol. 17 (1980) 1019.
[7] G.P. Schwartz, Thin Solid Films 103 (1983) 3.
[8] M. Hong, M. Passlack, D.Y. Noh, J. Kwo and J.P. Mannaerts, State-of-the-Art Program on Compound Semiconductors, The Electrochemical Society Proc. 96-2, Ed. F. Ren (1996) p. 36.
[9] M. Hong, J. Crystal Growth 150 (1995) 277.
[10] M. Hong, M. Passlack, J.P. Mannaerts, T.D. Harris, M.L. Schnoes, R.L. Opila and H.W. Krautter, Solid State Electron. (1996), to be published.
[11] A.Y. Cho and F.K. Reinhart, J. Appl. Phys. 45 (1974) 1812.
[12] M. Hong, R.S. Freund, K.D. Choquette, H.S. Luftman, J.P. Mannaerts and R.C. Wetzel, Appl. Phys. Lett. 62 (1993) 2658.
[13] O. Brandt, K. Kanamoto, M. Gotoda, T. Isu and N. Tsukada, Phys. Rev. B 51 (1995) 7029.
[14] R.K. Ahrenkiel and M.S. Lundstrom, Minority Carriers in III–V Semiconductors: Physics and Applications (Academic Press, Boston, 1993) ch. 2.
[15] O. Brandt, K. Kanamoto, M. Gotoda, T. Isu and N. Tsukada, Appl. Phys. Lett. 67 (1995) 1885.
[16] M. Passlack, M. Hong and J.P. Mannaerts, Solid State Electron. 39 (1996) 1133.
[17] M.S. Lundstrom and R.J. Schuelke, IEEE Trans. Electron. Dev. 30 (1983) 1151.
[18] M. Hong, M. Passlack, J.P. Mannaerts, J. Kwo, S.N.G. Chu, N. Moriya, S.Y. Hou and V.J. Fratello, J. Vac. Sci. Technol. 14 (1996) 2297.

ELSEVIER

Journal of Crystal Growth 175/176 (1997) 428–434

JOURNAL OF CRYSTAL GROWTH

Iodine-assisted molecular beam epitaxy

M. Micovic[a,*], D. Lubyshev[a], W.Z. Cai[a], F. Flack[b], R.W. Streater[c], A.J. SpringThorpe[c], D.L. Miller[a]

[a] *Electronic Material and Processing Research Laboratory, Department of Electrical Engineering, The Pennsylvania State University, University Park, Pennsylvania 16802, USA*

[b] *Department of Physics, The Pennsylvania State University, University Park, Pennsylvania 16802, USA*

[c] *Nortel Technology, Ottawa, Ontario, Canada,* K1Y4H7

Abstract

Iodine was introduced into our solid source molecular beam epitaxy chamber during the growth of GaAs and AlGaAs layers and strained-layer InGaAs quantum wells. Photoluminescence spectra of these samples taken at 4.2 K were compared to spectra from a series of test samples which were grown in the absence of iodine flux. We have observed a general improvement of the material quality of AlGaAs layers grown at substrate temperatures around and below 600°C since the introduction of iodine into our chamber regardless of whether an iodine flux impinged on the substrate during the growth process or not. Strong excitonic peaks with full width at half maximum of only 8 meV were observed in 4.2 K photoluminescence spectra of undoped $Al_{0.2}Ga_{0.8}As$ layers grown at substrate temperatures as low as 550°C using As_4. The epitaxial layers grown since the introduction of iodine are the brightest $Al_{0.2}Ga_{0.8}As$ samples that we have obtained from our molecular beam epitaxy system. These results suggest that the presence of iodine in a molecular beam epitaxy system can result in improved optical properties for AlGaAs. The 4.2 K photoluminescence spectra and secondary ion mass spectroscopy depth profiles also show that iodine preferentially removes Ga from AlGaAs layers during growth, resulting in layers with higher Al content.

1. Introduction

Aluminum-containing III–V compounds are sometimes considered difficult materials to grow epitaxially with electrical and optical qualities which are suitable for high-performance electronic and optoelectronic devices. For example, AlGaAs grown by solid-source molecular beam epitaxy (MBE) for optical devices such as lasers is usually grown at substrate temperatures near 700°C [1], which is higher than the typical growth temperatures for other III–V arsenides in MBE (450–600°C), and sufficiently high to cause significant dissociation of the AlGaAs layer and consequent loss of Ga [2, 3]. This loss of Ga is very sensitive to temperature, making composition control difficult. The high substrate temperature is also not compatible with the growth of InGaAs, which

* Corresponding author. Fax: +1 814 865 7065; e-mail: mxm249@psu.edu.

0022-0248/97/$17.00 Copyright © 1997 Published by Elsevier Science B.V. All rights reserved
PII S0022-0248(96)00818-4

dissociates rapidly at these temperatures, making the growth of high optical quality pseudomorphic InGaAs/AlGaAs heterostructures difficult. The use of dimeric arsenic or a low growth rate have been reported as means of achieving high quality AlGaAs at lower substrate temperatures [1–4] yet further improvements in technique would be welcomed.

We report here results of studies that suggest that the presence of iodine in a solid-source MBE system improves the quality of AlGaAs layers grown at relatively low substrate temperatures. We have shown in our previous work that iodine can be used for in situ etching of GaAs and InAs layers in MBE [5] and that the growth rates of GaAs, InAs, and AlAs are reduced when layers are grown in the presence of an iodine flux.

Although the growth of high-quality III–V semiconductor material by halide vapor phase epitaxy is well-known, there are few reports of the use of halides in a MBE system, and we know of no previous experiments using iodine to improve the quality of III–V materials during MBE growth. Several studies of etching of GaAs with iodine vapor have been reported previously [6, 7], but these were not done in an MBE growth chamber. Reports of the use of $AsCl_3$, $AsBr_3$, and PCl_3 for etching of GaAs and InP in chemical beam epitaxy (CBE) show that two-dimensional layer-by-layer material removal can be accomplished with halides [8, 9]. Use of CBr_4, which is also used as a C-doping precursor [10], for in situ etching in CBE has also been reported [11].

2. Experiment

Growth of all the epitaxial layers reported here was done in a Varian Modular GenII MBE system which is pumped only by a 400 l/s ion pump; we did not use the titanium sublimation pump except during the initial bakeout. The growth chamber is equipped with a UTI residual gas mass analyzer.

Gallium (7 N5 purity), aluminum (6 N purity), indium (7 N purity) and arsenic (7 N5 purity) [12] were sublimed from conventional pyrolytic boron nitride crucibles. As_4 was the arsenic species used for these layers, and the arsenic flux was 1.2×10^{-5} Torr at the ion gauge on our substrate stage (beam flux monitor). This arsenic flux is at the high end of the range that we normally use for GaAs growth. Growth rates were typically 2.8 Å/s for GaAs, 3.0 Å/s for AlGaAs and 3.3 Å/s for InGaAs. The substrate temperature was measured by a calibrated optical pyrometer. The substrate temperature was held constant during the growth of our structures, except for those structures containing InGaAs quantum wells. During the growth of the InGaAs quantum wells, the temperature was lowered to 500°C without a growth interruption, and then raised back to the original temperature (shown in Table 2) once growth of AlGaAs was resumed. Substrates were (1 0 0) semi-insulating GaAs, bonded with indium to standard substrate holders. Conventional MBE procedures were used for substrate preparation, degassing, and oxide desorption [13].

Iodine was delivered through an injection manifold (Fig. 1) which is also used to deliver CBr_4 to our chamber for carbon doping [10]. Briefly, iodine vapor in equilibrium at room temperature with solid iodine (5 N purity) [12] is delivered to a stainless steel run-vent manifold through a manual UHV leak valve (model 203, Granville-Phillips,

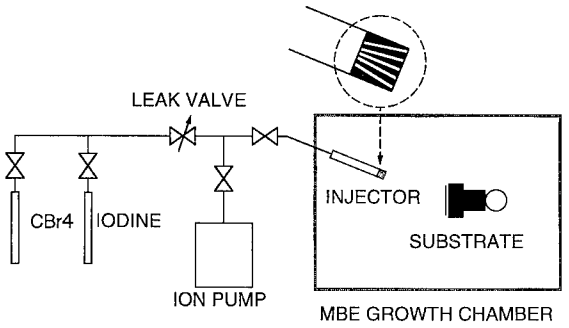

Fig. 1. Gas manifold and injector used to deliver iodine vapor to the substrate during MBE growth. The solid iodine is held at ambient temperature and the vapor is delivered to the MBE growth chamber through an UHV leak valve. An ion pump and valving provides a run-vent configuration. The injector nozzle comprises a piece of stainless steel rod drilled with many narrow holes to direct the gas flux to the substrate. The same manifold and injector are also used to deliver CBr_4 to the chamber for carbon-doping of GaAs and InGaAs.

Boulder CO). The flow of iodine to the MBE growth chamber is regulated by the leak valve and measured with the beam flux monitor. An unheated stainless steel nozzle with multiple drilled holes provides a collimated and uniform flux across a 3″ diameter area at the substrate holder. The maximum flux of iodine attainable is limited by the maximum conductance of the leak valve and the room-temperature vapor pressure of iodine (~0.3 Torr) to a beam flux monitor pressure of 1.0×10^{-6} Torr, which is the flux that was used for the experiments reported here. In our previous work [5] we found that this flux of iodine etches GaAs and InAs in a two-dimensional layer-by-layer mode at the etch rate of approximately 0.1 monolayer per second, determined from the period of the intensity oscillations of the specular spot of reflection high electron energy diffraction (RHEED) pattern. In the same study we observed that the growth rates of GaAs, AlAs, and InAs were reduced by approximately the same amount (0.1 monolayer per second) when the surface was exposed to this flux of iodine during growth. Results of that study also showed that iodine did not significantly etch grown AlAs layers for the experimental conditions explored.

Although our MBE system's growth chamber is pumped solely by a 400 l/s ion pump, the background pressure (measured outside the cold shrouds) during growth was dominated by arsenic and was not noticeably higher during iodine injection. Increases in pressure which occurred upon warming the liquid nitrogen-cooled shrouds were somewhat larger than without iodine use, but still could be handled by the ion pump.

We have grown a series of samples over a period of three months with and without iodine flux and have made photoluminescence measurements at room temperature and 4.2 K. Two identical structures were typically grown in consecutive runs using the same temperatures of MBE source ovens. The first structure was grown without iodine and the second was grown with iodine. We have compared the photoluminescence from this series of samples to samples having a similar structure which were grown prior to the introduction of iodine into our MBE system. Samples used for photoluminescence measurements had the layer structures shown in Table 1.

Photoluminescence spectra were obtained using a 0.75 m monochromator (Jobin Yvon) with 25 μm slit width and a photo multiplier detector. All

Table 1
Layer structures of epitaxial samples

Samples 2/96-1, 2/96-2	Samples 4/96-1, 4/96-2, 5/96-2	Samples 3/96-1, 3/96-2	Samples 10/94-1
100 Å GaAs	100 Å GaAs	100 Å GaAs	100 Å GaAs
500 Å $Al_{0.4}Ga_{0.6}As$	500 Å $Al_{0.4}Ga_{0.6}As$	500 Å $Al_{0.4}Ga_{0.6}As$	500 Å $Al_{0.4}Ga_{0.6}As$
		0.2 μm $Al_{0.2}Ga_{0.8}As$	0.18 μm $Al_{0.15}Ga_{0.85}As$
			300 Å GaAs
1 μm $Al_{0.2}Ga_{0.8}As$	0.5 μm $Al_{0.2}Ga_{0.8}As$	$3 \times \{$60 Å $In_{0.15}Ga_{0.85}As$ / 100 Å $Al_{0.2}Ga_{0.8}As\}$	$3 \times \{$60 Å $In_{0.15}Ga_{0.85}As$ / 100 Å GaAs$\}$
			200 Å GaAs
		0.19 μm $Al_{0.2}Ga_{0.8}As$	0.18 μm $Al_{0.15}Ga_{0.85}As$
0.1 μm $Al_{0.4}Ga_{0.6}As$	0.1 μm $Al_{0.4}Ga_{0.6}As$	0.1 μm $Al_{0.4}Ga_{0.6}As$	0.1 μm $Al_{0.4}Ga_{0.6}As$
1 μm GaAs	0.5 μm GaAs	0.75 μm GaAs	0.75 μm GaAs
0.1 μm $Al_{0.3}Ga_{0.7}As$	0.1 μm $Al_{0.3}Ga_{0.7}As$	0.1 μm $Al_{0.3}Ga_{0.7}As$	0.1 μm $Al_{0.3}Ga_{0.7}As$
$20 \times \{$20 Å AlAs / 20 Å GaAs$\}$	$20 \times \{$20 Å AlAs / 20 Å GaAs$\}$	$20 \times \{$20 Å AlAs / 20 Å GaAs$\}$	$20 \times \{$20 Å AlAs / 20 Å GaAs$\}$
GaAs substrate	GaAs substrate	GaAs substrate	GaAs substrate

samples except sample 10/94-1 were measured using both 632.8 nm HeNe and 325 nm HeCd laser light excitation with an estimated excitation power density of 1 W/cm^2. Spectra from the sample 10/94-1 were measured using only HeCd excitation. The spectra obtained with the two different excitation sources showed no significant differences in absolute and relative intensity of the observed photoluminescence lines. Secondary ion mass spectroscopy (SIMS) depth profiles were obtained with Cameca IV SIMS system.

3. Results and discussion

Two distinct peaks were observed in the 4.2 K photoluminescence spectra of all investigated AlGaAs layers grown after the introduction of iodine (see Fig. 2 for representative spectra). We attribute the higher energy sharp peak with the full width at half maximum (FWHM) of 8 meV to bound exciton recombination, while a broader peak located 20 meV below the excitonic peak with a FWHM of 20 meV is commonly attributed to carbon acceptor related luminescence [14–16]. The intensity of the higher-energy peak increases approximately linearly with excitation power density, while the lower-energy peak's intensity saturates at high excitation power density.

Fig. 2 compares the 4.2 K photoluminescence spectra of two samples which were grown after the introduction of iodine (4/96-1 and 4/96-2) to the spectrum of a sample (10/94-1) which is typical of AlGaAs grown before the introduction of iodine. The samples 4/96-1 and 4/96-2 grown after iodine introduction were grown at a substrate temperature of only 550°C. The strength and narrow line width (8 meV) of the exciton peak from both of these samples is remarkable for $Al_{0.2}Ga_{0.8}As$ grown using As_4 at such a low substrate temperature. Sample 10/94-1 was one of the brightest AlGaAs layers grown before the first introduction of iodine into the MBE chamber. Although it was grown at a substrate temperature of 640°C, the intensity of the photoluminescence signal of this sample was three orders of magnitude lower than that of sample 4/96-1 in a direct side-by-side comparison under the same excitation conditions. The

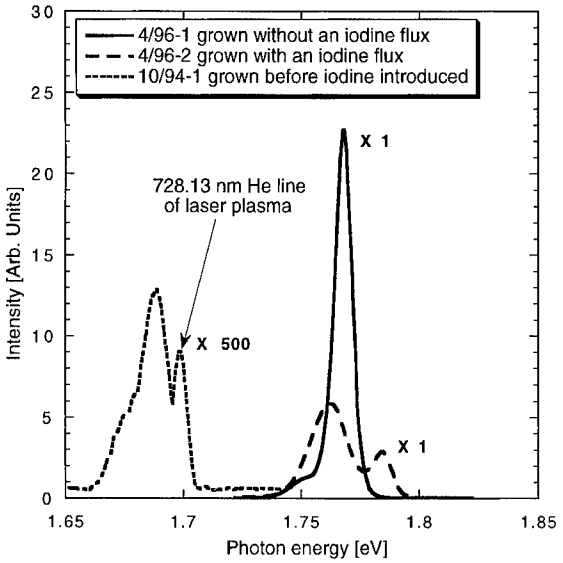

Fig. 2. Photoluminescence spectra at 4.2 K from samples grown before (10/94-1) and after (4/96-1, 4/96-2) the introduction of iodine into the MBE growth chamber. Sample 4/96-1 was grown without an iodine flux impinging on the surface, while sample 4/96-2 was grown with an iodine flux. Both were grown at a substrate temperature of only 550°C. We identify the higher energy peak of both samples as exciton-related, while the lower-energy peak is acceptor-related. A photoluminescence spectrum from one of the best AlGaAs layers grown at a substrate temperature of 640°C before the first introduction of iodine into the MBE chamber is shown for comparison (10/94-1). Excitation was with a He–Cd laser (λ = 325 nm) for all three samples. The peak indicated by the arrow is the 728.13 nm He line of the laser plasma.

intensity of sample 10/94-1 was also a factor of 50 lower than that of sample 3/96-2, which has a similar epitaxial layer structure to 10/94-1 and which was grown under iodine flux at a substrate temperature of 600°C.

Table 2 identifies the sample configuration, iodine flux during growth, substrate temperature, and AlGaAs peak intensity of the PL spectra at 4.2 K of samples grown for photoluminescence measurements after the introduction of iodine into our MBE system. In the initial series of experiments with iodine, the AlGaAs luminescence intensity of the samples grown under iodine flux was stronger than the luminescence intensity of the reference samples grown without iodine. During the period

Table 2
Comparison of the photoluminescence intensities from AlGaAs layers grown after the introduction of iodine into the MBE system; the features of the PL spectra are described in the text; sample configuration refers to Table 1; iodine fluxes measured by our beam flux monitor were 1.0×10^{-6} Torr whenever iodine was used; PL peak heights were measured using He–Ne laser ($l = 632.8$ nm) excitation of approximately 1 W/cm^2

Sample number	Configuration	Iodine during growth	Substrate temperature (°C)	4.2 K normalized acceptor-related intensity	4.2 K normalized exciton-related intensity
2/96-1	$Al_{0.2}Ga_{0.8}As$	No	620	5.4×10^{-2}	2.8×10^{-2}
2/96-2	$Al_{0.2}Ga_{0.8}As$	Yes	620	2.4×10^{-1}	4.8×10^{-2}
3/96-1	$Al_{0.2}Ga_{0.8}As$ + InGaAs QW	No	600	1.9×10^{-3}	2.0×10^{-2}
3/96-2	$Al_{0.2}Ga_{0.8}As$ + InGaAs QW	Yes	600	8.6×10^{-4}	4.0×10^{-2}
4/96-1	$Al_{0.2}Ga_{0.8}As$	No	550	3.0×10^{-2}	6.0×10^{-1}
4/96-2	$Al_{0.2}Ga_{0.8}As$	Yes	550	1.5×10^{-1}	7.4×10^{-2}
5/96-2	$Al_{0.2}Ga_{0.8}As$	Yes	640	1.1×10^{-1}	1.0

of experiments with iodine we observed that the quality (manifested in the intensity and linewidth of excitonic PL lines) of the AlGaAs layers grown without the intentional introduction of iodine had improved and exceeded that of the layers grown with iodine. We attribute this improvement to the presence of iodine residues in the MBE chamber. The presence of iodine residues was confirmed by the peak at atomic mass 127 in quadrupole residual gas mass analyzer spectra. This peak appeared after the first introduction of the iodine into the MBE growth chamber. The only natural isotope of iodine has an atomic mass of 126.9. We speculate that the iodine residues in the growth chamber act to remove impurities from the sources and/or chamber walls, or that residual iodine in the chamber reacts with impurities or point defects on the epitaxial layer surface, removing them before they are incorporated into the lattice, or that improvement is a result of both effects. We observed no iodine in SIMS depth profiles of our epitaxial material. The limit of sensitivity to iodine was about 10^{14}/cm^3 for GaAs and 10^{15}/cm^3 for $Al_{0.2}Ga_{0.8}As$.

We have taken no extraordinary steps in the operation of our MBE system to promote high-purity growth. On the contrary, we routinely grow material doped with CBr_4 to hole densities in the low- to mid-10^{19}/cm^3 range, and twice suffered a temporary ($\sim$1 h) air leak in the mid 10^{-7} Torr range during the months that iodine injections were done and these samples were grown, after which we did not bake the system.

We find that growth under an iodine flux increased the magnitude of the carbon acceptor-related peak in two of our samples pairs (see Table 2). The amount of carbon in these layers is below the detection limit for SIMS (about 4×10^{16}/cm^3 in $Al_{0.2}Ga_{0.8}As$), and we have not yet made electrical measurements to determine the hole density of this material. The source of carbon might be the manifold and injector used to deliver iodine to the growth chamber. During the period of iodine use, we also grew many epitaxial structures with layers heavily doped using CBr_4 injected through the same manifold. It is possible that the iodine flux contained traces of CBr_4 or other carbon-containing compounds picked up from the walls of the gas manifold and injector. Alternatively, the iodine charge could contain enough carbon to explain the increased acceptor luminescence, since it has a stated purity of only 5 N. Carbon incorporation could also be due to iodine-induced surface chemistry changes that enhance incorporation of background carbon.

The PL peaks of the AlGaAs layers grown with iodine were consistently shifted by 25–28 meV

toward higher energy with respect to the position of the peaks in the spectrum of reference samples grown without iodine (see Fig. 2). The shift in the peak position indicates that the Al content x is higher by approximately 0.02 in $Al_xGa_{1-x}As$ layers grown under iodine flux. Higher Al concentration in the layers grown under iodine flux was also confirmed by the SIMS depth profile measurements and double crystal X-ray diffraction measurements.

Fig. 3 shows the Al profiles obtained by SIMS from two samples grown one after the other for the same amount of time with the same temperatures for the MBE source ovens. Sample 2/96-2 was grown with an iodine flux, whereas sample 2/96-1 was grown without iodine flux. Both samples were grown at a substrate temperature of 620°C. It can be seen that the sample grown with iodine has thinner layers. The reduction of the layer thickness is consistent with a growth rate reduction of 0.1 monolayer per second, which we observed previously during the growth of GaAs, and AlAs layers

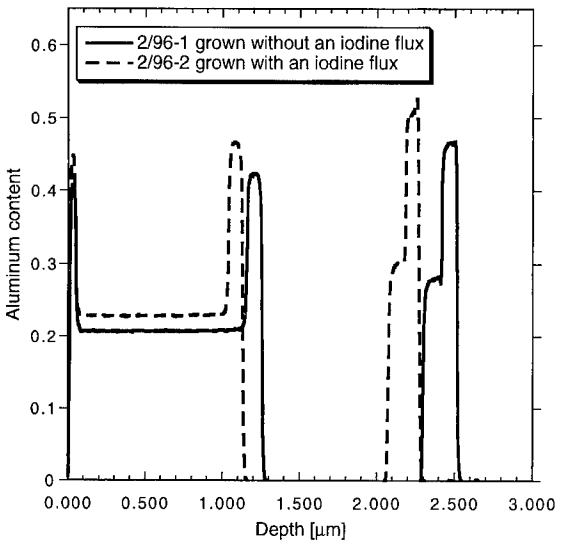

Fig. 3. SIMS profiles of the Al concentration from samples 2/96-1 and 2/96-2 grown one after the other for the same amount of time with the same temperatures for the MBE source ovens. Sample 2/96-2 was grown with an iodine flux of 1×10^{-6} Torr beam equivalent pressure, whereas sample 2/96-1 was grown without iodine flux. Both samples were grown at a substrate temperature of 620°C. For the sample grown with iodine, the Ga incorporation rate was lower, leading to thinner AlGaAs layers with higher Al concentration.

under the same iodine flux [5]. The observed increase in the Al concentration in AlGaAs layers grown under an iodine flux suggests that only the incorporation rate of GaAs is reduced by 0.1 monolayer per second while incorporation of AlAs is not affected by the iodine presence. The gallium and aluminum fluxes used during the AlGaAs growth corresponded to growth rates of 0.848 and 0.212 monolayers per second, respectively. The reduced incorporation rate of GaAs, due to iodine flux, would give an alloy with AlAs content of $x = 0.212/(0.748 + 0.212) = 0.22$, consistent with observed increase. The observation that the presence of iodine reduces the incorporation rate of only Ga during the growth of the ternary AlGaAs alloy does not conflict with our previous observation [5], that growth rates of binary GaAs and AlAs compounds were reduced by approximately the same amount when the growing surface was exposed to the same iodine flux. The results suggest that reactions of gallium with iodine that lead to Ga removal from the surface are thermodynamically more favorable than reactions that lead to the removal of aluminum, and that the total removal rate is limited by the availability of iodine.

Photoluminescence peaks from $In_{0.15}Ga_{0.85}As$ quantum wells grown under an iodine flux were shifted to lower energy compared to the peaks from the quantum wells grown without iodine. They were also lower in intensity. The observed red shift might be due to a higher concentration of In in the InGaAs layers grown under an iodine flux, but could as well be due to interface defects and impurities at the AlGaAs/InGaAs heterointerface. Further study is needed to determine the origin of the observed red shift.

Fig. 4 shows the 4.2 K PL spectra in the region of $In_{0.15}Ga_{0.85}As$ quantum well and GaAs buffer luminescence from sample 3/96-4, grown with iodine, and sample 3/96-3, grown without iodine. The height of the quantum well peak at 1.419 eV in the sample grown with iodine is about half the height of the similar peak observed in the sample grown without iodine. The peaks near 1.5 eV originate in the GaAs buffer, also grown with an iodine flux. The peak at 1.512 eV is due to excitons bound to shallow impurity levels, the line at 1.504 eV is due to point defect-bound exciton, and the line at 1.490 eV

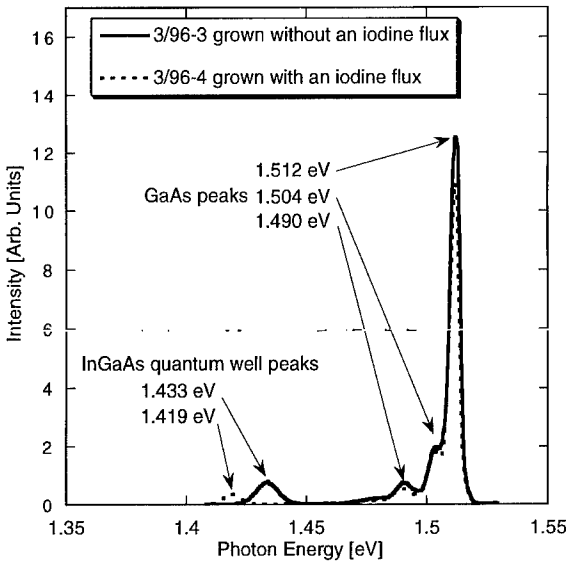

Fig. 4. Photoluminescence spectrum at 4.2 K of emission from the $In_{0.15}Ga_{0.85}As$ quantum wells and GaAs buffer of sample 3/96-4, grown with iodine, and sample 3/96-3, grown without iodine. The peak at 1.512 eV is due to excitons bound to shallow impurity levels, the line at 1.504 eV is due to defect-bound exciton, and the line at 1.490 eV is related to carbon acceptors. Excitation was with a He–Cd laser ($\lambda = 325$ nm).

is related to carbon acceptors [17]. The strong excitonic emission is indicative of good-quality GaAs.

4. Conclusions

We have observed a large increase in the intensity of photoluminescence emission from AlGaAs material which was grown in our MBE system during the period in which experiments with iodine-assisted growth were performed. We attribute this improvement to the presence of iodine residues in the molecular beam epitaxy chamber. We have grown high-optical-quality $Al_{0.2}Ga_{0.8}As$ exhibiting narrow excitonic luminescence at substrate temperatures as low as 550°C using As_4 in a solid source MBE system.

We have also observed growth rate reductions and composition changes in AlGaAs layers grown under iodine flux. Our results suggest that only the gallium incorporation rate is reduced when the AlGaAs layers are grown under iodine flux.

Acknowledgements

This work was supported in part by the National Science Foundation and the US Air Force, Rome Laboratory, through an SBIR contract with QED, Inc., Bethlehem, PA.

References

[1] M. Ilegems, in: Technology and Physics of Molecular Beam Epitaxy, Ed. E.H.C. Parker (Plenum, New York, 1985) pp. 110–114, and references therein.
[2] W.T. Tsang and V. Swaminathan, Appl. Phys. Lett. 39 (1981) 486.
[3] J.E. Cunningham, W.T. Tsang, T.H. Chiu and E.F. Schubert, Appl. Phys. Lett. 50 (1987) 769.
[4] M. Heiblum, E.E. Mendez and L. Osterling, J. Appl. Phys. 54 (1983) 6982.
[5] M. Micovic, F. Flack, R.W. Streater, A.J. SpringThorpe and D.L. Miller, Appl. Phys. Lett. 69 (1996) 2680.
[6] Kin-Chung Wong and Elmer A. Ogryzlo, J. Vac. Sci. Technol. B 10 (1992) 668.
[7] K. Jacobi, G. Streinert and W. Ranke, Surf. Sci. 57 (1976) 571.
[8] W.T. Tsang, T.H. Chiu and R.M. Capre, J. Crystal Growth 135 (1994) 377.
[9] T. Kaneko, P. Smilauer, B.A. Joyce, T. Kawamura and D.D. Vvedensky, Phys. Rev. Lett. 74 (1995) 3289.
[10] Kai Zhang, Wen-yen Hwang and D.L. Miller, Appl. Phys. Lett. 63 (1993) 2399.
[11] T.B. Joyce, T.J. Bullough and T. Farell, Appl. Phys. Lett. 65 (1994) 2193.
[12] Gallium (7N5 purity, Rhone-Poulenc, Morrisville, NJ); aluminum (6N purity, United Minerals and Chemical Corp., Lyndhurst, NJ)); indium (7N, Rasa Industries, Ltd., Tokyo, Japan, distributed by United Minerals and Chemical Corp., Lyndhurst, NJ); arsenic (7N5 purity, Furukawa Co., Tokyo, Japan, distributed by United Minerals and Chemical Corp., Lyndhurst, NJ); iodine (5N purity, Aesar/Johnson Matthey, Ward Hill, MA).
[13] J.D. Grange, in: Technology and Physics of Molecular Beam Epitaxy, Ed. E.H.C. Parker (Plenum, New York, 1985) p. 51–52.
[14] E.F. Schubert, E.O. Gobel, Y. Horikoshi, K. Ploog and H.J. Queisser, Phys. Rev. B 30 (1984) 813.
[15] G. Wicks, W.I. Wang, C.E.C. Wood, L.F. Eastman and L. Rathbun, J. Appl. Phys. 52 (1981) 5792.
[16] M. Mihara, Y. Nomura, M. Mannoh, K. Yamanaka, S. Naritsuka, K. Shinozaki, T. Yuasa and M. Ishii, J. Appl. Phys. 55 (1984) 3760.
[17] L. Pavesi, in: Properties of Aluminum Gallium Arsenide, Ed. S. Adachi (INSPEC, The Institution of Electrical Engineers, London, 1993) p. 248–249.

ELSEVIER

Journal of Crystal Growth 175/176 (1997) 435–440

JOURNAL OF CRYSTAL GROWTH

Passivation of misfit dislocations by atomic hydrogen irradiation in lattice-mismatched heteroepitaxy

Mikihiro Yokozeki*, Hiroo Yonezu, Takuto Tsuji, Naoki Ohshima

Department of Electrical and Electronic Engineering, Toyohashi University of Technology, 1-1 Hibarigaoka, Tempaku-cho, Toyohashi 441, Aichi, Japan

Abstract

We investigated the passivation effect of misfit dislocations in an $(InAs)_1(GaAs)_4$ strained short-period superlattice grown on GaAs with atomic hydrogen (H) by transmission electron microscopy and electron-beam-induced current. The misfit dislocations in the $\langle 1\,1\,0\rangle$ directions are generated at the heterointerface in order to accommodate the misfit strain. They were effectively passivated by atomic H irradiation during the growth and cooling processes. Furthermore, it was found that the misfit dislocation in the [1 1 0] direction was effectively passivated rather than that in the $[\bar{1}\,1\,0]$ direction. The desorption temperature of atomic H from the [1 1 0] misfit dislocation was higher than that from the $[\bar{1}\,1\,0]$ misfit dislocation. These phenomena could be attributed to the fact that the bonding strength of As-H is larger than that of Ga–H.

1. Introduction

Highly lattice-mismatched heteroepitaxies have been attracting considerable attention because of their promise for novel optoelectronic devices [1]. However, the three-dimensional growth (3D) occurs at the initial growth stage and threading dislocations are mainly generated in the lattice relaxation process of the 3D islands [2]. It has been well known that dislocations degrade the operating life of optoelectronic devices such as light-emitting diodes and laser diodes [3]. Thus, optoelectronic devices with a highly lattice-mismatched heteroepilayer have not been in practical use. It was a key issue to reduce the density of threading dislocations.

Recently, we have reported that the two-dimensional (2D) growth mode was kept and the threading dislocation density was effectively reduced by inserting multi-strained short-period superlattices (SSPSs) in the highly lattice-mismatched heteroepitaxial growth of GaAs-on-Si, InP-on-Si and InGaAs-on-GaAs [4–6]. However, misfit dislocations remain inevitably at the heterointerface in order to relieve the misfit strain. The degradation of optoelectronic devices could be caused by multiplication of the misfit dislocations under the minority carrier injection. Thus, the electrical passivation of the misfit dislocations is essential for optoelectronic devices with the heterointerface. It has been

* Corresponding author. Fax: +81 532 44 6757; e-mail: yokozeki@icg.eee.tut.ac.jp.

0022-0248/97/$17.00 Copyright © 1997 Elsevier Science B.V. All rights reserved
PII S0022-0248(96)00852-4

reported that the electrical activity of point defects and dislocations was reduced by hydrogen plasma irradiation in photoluminescence (PL), cathodluminescence (CL) and electron-beam-induced current (EBIC) measurements [7–10]. However, the nature of these dislocations has not been investigated.

Thus, we have investigated the passivation effect of the misfit dislocations by atomic H irradiation and the desorption temperature of atomic H from the misfit dislocations in the heteroepitaxy of $(InAs)_1(GaAs)_4$ SSPS-on-GaAs. As a result, it was clarified that the misfit dislocations were remarkably passivated by atomic H irradiation. The misfit dislocation in the [1 1 0] direction was effectively passivated, compared with that in the [$\bar{1}$ 1 0] direction. In addition, the desorption temperatures of atomic H differed with the directions of the misfit dislocations.

2. Experimental procedure

The GaAs(0 0 1) exactly oriented substrates were degreased and etched in a H_2SO_4 solution for 30 s at room temperature. The substrate was loaded into the growth chamber with a base pressure less than about 5×10^{-10} Torr in a molecular beam epitaxy (MBE) system. Then, it was heated at 630°C for 20 min under an As_4 beam in order to remove the thin oxide film on the substrate. A 200 nm thick GaAs buffer layer was grown at a substrate temperature of 580°C.

Then, the $(InAs)_1(GaAs)_4$ SSPS was grown on the GaAs(0 0 1) substrate at a growth temperature of 350°C. The density of misfit dislocations can be controlled by varying the number of the periods of the SSPS [11]. The periods were ranged from 45 to 65. Growth rates of InAs and GaAs composing the SSPS were about 6 and 2 s/ML, respectively. Fig. 1a illustrates a schematic drawing of a sample structure. The atomic H was irradiated for 30 min during the growth process and the cooling process, as shown in Fig. 1b. The same structures were also grown with molecular hydrogen (H_2) irradiation and without atomic H irradiation for comparison. In order to investigate the desorption temperature of atomic H from misfit dislocations, the samples

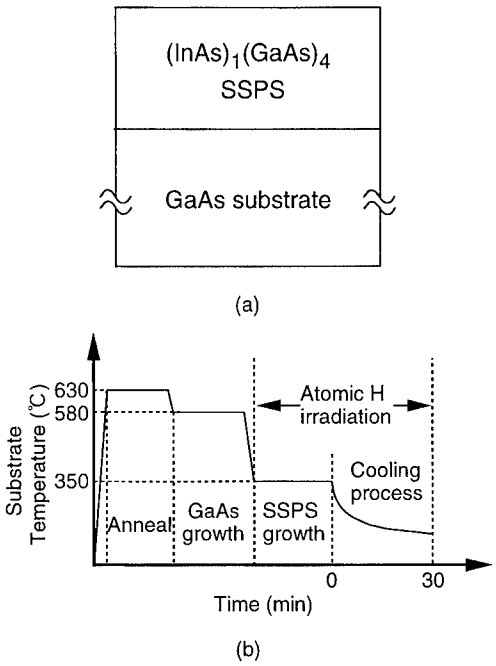

Fig. 1. A schematic drawing of a sample structure

with atomic H irradiation were annealed at the temperatures of 350°C, 420°C and 500°C for 60 min in pure N_2 atmosphere.

The atomic H was generated with a tungsten filament heated up to about 1800°C. The pressure of hydrogen was kept at 3×10^{-5} Torr. The surface reconstruction of the GaAs substrate was observed by reflection high-energy electron diffraction (RHEED) at an acceleration voltage of 25 kV. The passivation effect and the nature of misfit dislocations were evaluated by observing EBIC images at an acceleration voltage of 19 kV and by transmission electron microscopy (TEM) at an acceleration voltage of 200 kV, respectively. Specimens for TEM observation were prepared by mechanical grinding, followed by Ar^+ ion milling at an acceleration voltage of 4 kV.

3. Results

Fig. 2 shows RHEED patterns of the GaAs substrate with and without atomic H irradiation. The

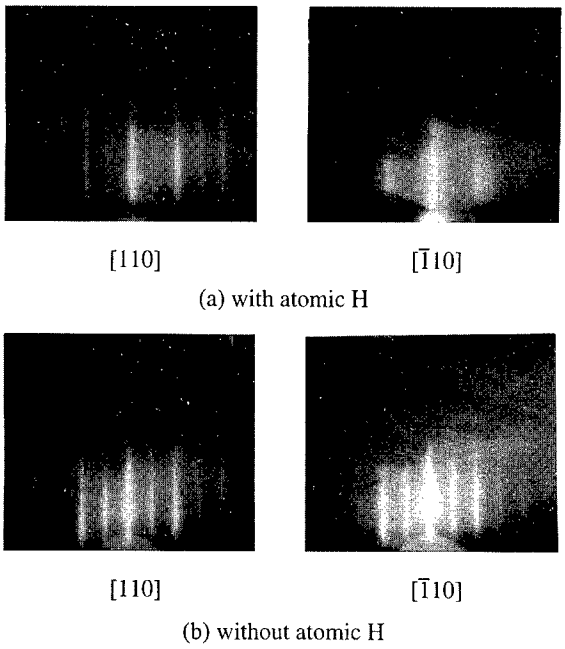

Fig. 2. RHEED patterns of GaAs(0 0 1) surface with (a) and without atomic H irradiation (b). The (2 × 2) pattern was changed to (2 × 4) one by atomic H irradiation.

surface reconstruction of the GaAs substrate was changed by atomic H irradiation. The (2 × 2) pattern formed with adsorbed excess As was changed to the (2 × 4) one. This phenomenon means that the atomic H reacts with surface atoms, possibly As, of the substrate.

Fig. 3 shows plan-view TEM images of the $(InAs)_1(GaAs)_4$ SSPS with 45 and 65 periods taken under $g_{\bar{2}\,2\,0}$ diffraction. The misfit dislocations in the [1 1 0] and [$\bar{1}$ 1 0] directions were observed along the heterointerface. The density of misfit dislocations increased with the increase of the SSPS periods. The densities of the [1 1 0] and [$\bar{1}$ 1 0] misfit dislocations were almost the same. It was reported that the density of misfit dislocations was almost equal in the two ⟨1 1 0⟩ directions in an InGaAs/GaAs system [12]. Most of the misfit dislocations were revealed to be the 60°-type dislocation by analysis with various diffraction conditions.

The EBIC images of the $(InAs)_1(GaAs)_4$ SSPS with 45 periods are shown in Fig. 4. Dark lines indicate unpassivated misfit dislocations. The dark

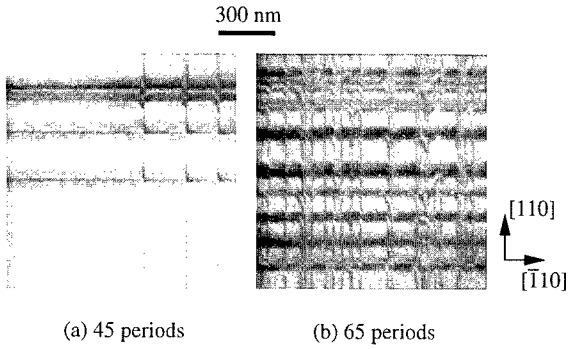

Fig. 3. Plan-view TEM images of the $(InAs)_1(GaAs)_4$ SSPS with 45 and 65 periods taken under $g_{\bar{2}\,2\,0}$ diffraction. The misfit dislocations at the heterointerface along the ⟨1 1 0⟩ directions were observed. The density of misfit dislocations was increased with the increase of the SSPS periods. Most of misfit dislocations were identified to be the 60°-type dislocation from various diffraction analyses.

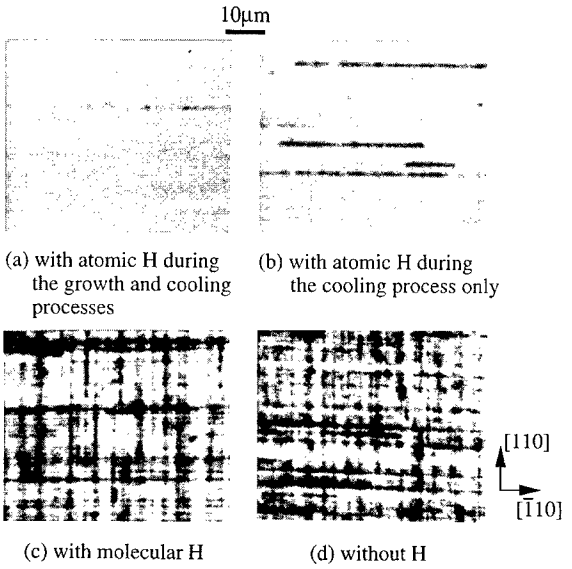

Fig. 4. EBIC images of samples of $(InAs)_1(GaAs)_4$ SSPS-on-GaAs with 45 periods. The dark line density was remarkably decreased by atomic hydrogen irradiation during the growth and cooling processes (a). The reduction is less effective for atomic H irradiation during cooling process only (b). No reduction occurred in H2 (c) and no hydrogen irradiation (d).

line density was remarkably decreased by atomic H irradiation during the growth and cooling processes, as shown in Fig. 4a. The reduction of the dark line density was less effective for atomic H

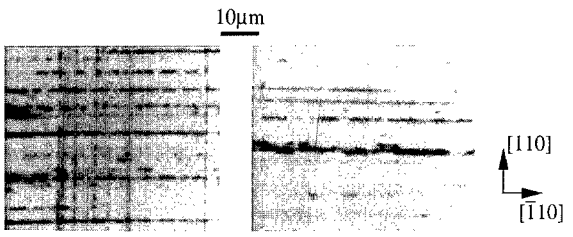

(a) 30 min (b) 60 min

Fig. 5. EBIC images of samples of $(InAs)_1(GaAs)_4$ SSPS-on-GaAs with 65 periods. The dark line density was reduced with the increase of irradiation time at low temperature.

irradiation during the cooling process only, as shown in Fig. 4b. On the contrary, no reduction was observed by H_2 irradiation during the growth and cooling processes, as shown in Fig. 4c. A lot of dark lines were observed in the sample without atomic H irradiation, as shown in Fig. 4d. It is apparent that the misfit dislocations were passivated by atomic H irradiation. It should be also noticed that the misfit dislocation in the [1 1 0] direction was passivated more effectively than the misfit dislocation in the [$\bar{1}$ 1 0] direction, as seen in Fig. 4b.

The time for atomic H irradiation was increased up to 60 min in the cooling process. The EBIC images of $(InAs)_1(GaAs)_4$ SSPS with 65 periods are shown in Fig. 5. The dark line density was decreased with the increase in irradiation time. In addition, the remaining dark lines of the $(InAs)_1(GaAs)_4$ SSPS with 65 periods in Fig. 5a were increased rather than those of $(InAs)_1(GaAs)_4$ SSPS with 45 periods, as shown in Fig. 4a.

We investigated the desorption temperature of atomic H which passivated the misfit dislocations. The EBIC images of annealed samples of the $(InAs)_1(GaAs)_4$ SSPS with 60 periods are shown in Fig. 6. There was no difference in the dark line densities between the sample annealed at 350°C (Fig. 6a) and nonannealed one. However, the dark line densities were increased by increasing the annealed temperature. The [$\bar{1}$ 1 0] dark line density was increased by annealing at 420°C, while the [1 1 0] dark line density was not changed, as seen in Fig. 6b. However, the densities of both the [1 1 0] and [$\bar{1}$ 1 0] dark lines were increased by annealing at 5 0 0°C, as seen in Fig. 6c. The densities of dark lines are summarized in the graph. It is obvious that the misfit dislocations were reactivated by high-temperature annealing and that the temperature at which atomic H desorbs from the [1 1 0] misfit dislocation was higher than that from the [$\bar{1}$ 1 0] misfit dislocation.

4. Discussion

Misfit dislocations are passivated by atomic H irradiation, depending on the irradiation time and substrate temperature. It should be noted that the misfit dislocations cannot be passivated by H_2 irradiation. Therefore, the passivation of misfit dislocations occurs by the adsorption of atomic H on dangling bonds of misfit dislocations [7].

The misfit dislocations were passivated more effectively during the growth and cooling processes than during the cooling process only. This means that the passivation of misfit dislocations occurs during the cooling process as well as the growth process. Therefore, the atomic H irradiation during the growth is effective for the passivation of the misfit dislocation as well as the enhancement of the two-dimensional growth mode [13].

The passivation efficiency is determined by the balance between the adsorption and desorption of atomic H. Therefore, the misfit dislocations could not be completely passivated by atomic H irradiation at high temperature. For effective passivation, it is necessary to irradiate atomic H at low temperature in order to suppress the desorption of atomic H. However, it is required to increase the irradiation time, as shown in Fig. 5, since the diffusion rate of atomic H is low at low temperature.

The misfit dislocation in the [1 1 0] direction was more effectively passivated than the misfit dislocation in the [$\bar{1}$ 1 0] direction, as shown in Fig. 4a, Fig. 4b and Fig. 5. Most of them were 60°-type dislocations. In III–V compound semiconductors, the [1 1 0] misfit dislocation has V-group atoms and the [$\bar{1}$ 1 0] misfit dislocation III-group atoms as their core for the shuffle set [14]. Therefore, the [1 1 0] misfit dislocation has dangling bonds of As atom and the [$\bar{1}$ 1 0] one has those of Ga atom. The passivation efficiency is determined by the bonding

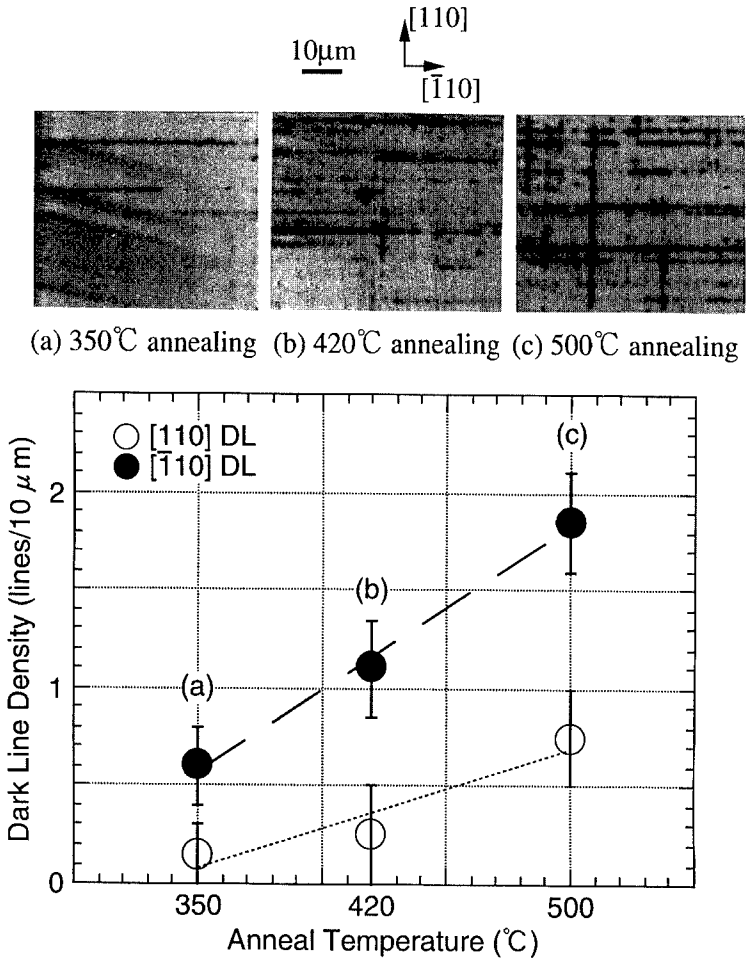

Fig. 6. EBIC images of the annealed samples of $(InAs)_1(GaAs)_4$ SSPS-on-GaAs with 60 periods. There was no difference in dark lines densities between annealing at 350°C (a) and no annealing. However, the [$\bar{1}$ 1 0] dark line density was increased by annealing at 420°C, while the [1 1 0] dark line density was not changed (b). Both densities of the [1 1 0] and [$\bar{1}$ 1 0] dark lines were increased by annealing at 500°C (c). The dark line densities were summarized as a function of annealing temperature in the graph.

strength. The bonding strength of As–H is known to be larger than that of Ga–H [15]. Thus, the desorption rate of As–H is higher than that of Ga–H in thermal equilibrium. It leads to more effective passivation for the [1 1 0] misfit dislocation than the [$\bar{1}$ 1 0] misfit dislocation.

It also results in the fact that the [$\bar{1}$ 1 0] misfit dislocation is reactivated by annealing at lower temperature, compared with the [1 1 0] misfit dislocation, as shown in Fig. 6.

Most optoelectronic devices are fablicated in wafer process with temperatures less than about 350°C. Thus, the atomic H irradiation could be applicable to novel optoelectronic devices with a lattice-mismatched heterointerface.

5. Conclusions

We investigated the passivation of the misfit dislocations by atomic H irradiation and the desorption temperatures of atomic H from the passivated misfit dislocations. As a result, it was clarified that the misfit dislocations can be effectively passivated

by atomic H irradiation during the growth and cooling processes. The passivation of the [1 1 0] misfit dislocation was more effective than that of the [$\bar{1}$ 1 0] misfit dislocation. The desorption temperature of atomic H from the [1 1 0] misfit dislocation was higher than that from the [$\bar{1}$ 1 0] misfit dislocation. These phenomena could be attributed to the fact that the bonding strength of As–H was larger than that of Ga–H. The passivation of the misfit dislocations by atomic H irradiation could be effective for realization of high-quality lattice-mismatched heterodevices.

Acknowledgements

The authors would like to thank Dr. J.K. Shin, Dr. K. Pak, Mr. K.J. Lee and Mr. Y. Fujimoto for valuable discussions. This work was partially supported by a Grant-in-Aid for Scientific Research on Priority Areas from the Ministry of Education, Science, Sport and Culture of Japan.

References

[1] I. Hayashi, Jpn. J. Appl. Phys. 32 (1993) 266.
[2] T. Kawai, H. Yonezu, D. Saito, M. Yokozeki and K. Pak, Jpn. J. Appl. Phys. 33 (1994) L1740.
[3] H. Yonezu, I. Sakuma, T. Kamejima, M. Ueno, K. Nishida, Y. Nannichi and I. Hayashi, Appl. Phys. Lett. 24 (1974) 18.
[4] Y. Takagi, H. Yonezu, T. Kawai, K. Hayashida, K. Samonji, N. Ohshima and K. Pak, J. Crystal Growth 150 (1995) 677.
[5] K. Samonji, H. Yonezu, Y. Takagi, K. Iwaki, N. Ohshima, J.K. Shin and K. Pak, Appl. Phys. Lett. 69 (1996) 100.
[6] T. Kawai, H. Yonezu, Y. Ogasawara, D. Saito and K. Pak, J. Appl. Phys. 74 (1993) 7257.
[7] S.S. Dosanjh, L. Hart, R. Nayak and B.A. Joice, J. Appl. Phys. 75 (1994) 8066.
[8] M.J. Matragrano, G.P. Watson, D.G. Ast, T.J. Anderson and B. Pathangey, Appl. Phys. Lett. 62 (1993) 1417.
[9] B. Chatterjee, S.A. Ringel, R. Sieg, R. Hoffman and I. Weinberg, Appl. Phys. Lett. 65 (1994) 58.
[10] V. Higgs and M. Kittler, Appl. Phys. Lett. 65 (1994) 2804.
[11] T. Kawai, H. Yonezu, D. Saito, M. Yokozeki and K. Pak, Jpn. J. Appl. Phys. 33 (1994) 5617.
[12] K.L. Kavanagh, M.A. Capano, L.W. Hobbs, J.M. Woodall, J.A. Stroscio and R.M. Feenstra, J. Appl. Phys. 64 (1988) 4843.
[13] M. Yokozeki, H. Yonezu, T. Tsuji, N. Ohshima and K. Pak, Jpn. J. Appl. Phys. 35 (1996) 2561.
[14] M.J. Matragrano, D.G. Ast, J.R. Shealy and V. Krishnamoorthy, J. Appl. Phys. 79 (1996) 8371.
[15] J.A. Kerr, in: CRC Handbook of Chemistry and Physics, 70th ed., Ed. R.C. Weast (CRC Press, Boca Raton, FL, 1989) p. F-197.

ELSEVIER

Journal of Crystal Growth 175/176 (1997) 441–446

JOURNAL OF CRYSTAL GROWTH

Formation of an n-GaAs/n-GaAs regrowth interface without carrier depletion using electron cyclotron resonance hydrogen plasma

Takaki Niwa*, Naoki Furuhata, Tadashi Maeda

Microelectronics Research Laboratories, NEC Corporation, 34 Miyukigaoka, Tsukuba, Ibaraki 305, Japan

Abstract

We report on the formation of a GaAs MBE regrowth interface without carrier depletion and contaminants using electron cyclotron resonance (ECR) hydrogen plasma. The mechanism for removing GaAs surface-contaminants such as Si, O, and C has been investigated to realize a contaminant-free regrowth-interface. Secondary ion mass spectroscopy (SIMS) analysis shows that Si and O contaminants result not only from adsorption when exposed to air prior to regrowth but also from the sputtering of the quartz liner in the ECR chamber during plasma treatment. These can be reduced to a level below the SIMS detection limit by lowering the hydrogen pressure to below 10^{-3} Torr, because sputtering can be suppressed. SIMS also reveals that the C contaminant can be removed at substrate temperatures above 400°C to a level below the SIMS detection limit. This was verified through thermal desorption spectroscopy (TDS) analysis. This is because the C contaminant is removed through transformation into CH_3 at substrate temperatures above 400°C. Furthermore, reflection high-energy electron diffraction (RHEED) observation, atomic force microscopy (AFM) and capacitance–voltage (C–V) measurements indicate that both structural and electrical damage induced by ECR plasma is completely eliminated at 500°C. Based on these methods, we are able to produce an undamaged and contaminant-free MBE regrowth interface on n-GaAs/n-GaAs for the first time.

1. Introduction

Contaminants adsorbed on a GaAs surface when the surface is exposed to air, especially C, O and Si, cause serious problems such as high contact resistance at the regrowth interface [1] or unstable device performance in GaAs FETs [2]. These contaminants could not effectively be removed by conventional thermal cleaning, thermal etching, HCl/H gas etching and Cl_2 gas etching prior to molecular beam epitaxial (MBE) growth [3–5]. The electron cyclotron resonance (ECR) hydrogen plasma treatment is superior to these cleaning treatments, because ECR hydrogen plasma can remove C to a level below the SIMS detection limit without seriously etching the GaAs surface, and this treatment can be handled in an ultra high vacuum chamber [6]. To apply the ECR hydrogen plasma treatment to the device fabrication process, the following conditions are required: (1) the

* Corresponding author. Fax: +81 298 50 1107; e-mail: niwa@uhl.cl.nec.co.jp.

0022-0248/97/$17.00 Copyright © 1997 Elsevier Science B.V. All rights reserved
PII S0022-0248(96)00960-8

complete removal of C, O and Si contaminants, (2) a flat surface after treatment, and (3) the complete elimination of ECR damage (elimination of carrier depletion).

Regarding contaminant removal, previous works reported that the C contaminant could be removed by using ECR hydrogen plasma, but that Si and O contaminants could not effectively be removed [7, 8]. Therefore, Cl_2 gas etching was necessary after the hydrogen plasma to remove these contaminants [8]. However, this treatment is difficult to apply to microscopic device-fabrication processes because Cl_2 gas excessively etches the surface being treated. Regarding a flat surface after treatment, previous work [6] indicated that reflection high-energy electron diffraction (RHEED) patterns after ECR plasma treatment at a substrate temperature as low as 300°C exhibited streaky (2×4) reconstruction. However, when the treatment time is longer than that at which a GaAs oxide layer is completely removed so that contaminants can be completely eliminated, the RHEED pattern after ECR plasma treatment at 300°C becomes spotty. Concerning the complete elimination of carrier depletion, there are no reports. Furthermore, it has not yet been clarified whether the ECR damage that causes the carrier depletion exists at the surface after ECR hydrogen plasma treatment.

In this paper, to obtain a carrier-depletion-free interface, we investigated the mechanism for removing C, O and Si contaminants. In particular, we clarify why O and Si contaminants are not effectively removed and how to remove these using only ECR hydrogen plasma treatment. Furthermore, under the hydrogen plasma condition of complete contaminant removal, the flatness of the GaAs surface after the plasma treatment is studied. Finally, we demonstrate a no carrier depletion regrowth interface using ECR hydrogen plasma treatment.

2. Experimental procedure

Experiments were performed in the UHV ECR chamber, connected to the MBE chamber by a transfer module. The samples were exposed to air for 1 month, after $8\times10^{16}\,cm^{-3}$ Si-doped GaAs had been grown on the GaAs (1 0 0) substrate by MBE. The sample surface was cleaned by hydrogen plasma in the ECR chamber without any other treatment, before the regrowth of $8\times10^{16}\,cm^{-3}$ Si-doped GaAs. The plasma treatment time was 20 min and microwave power was 200 W. During the plasma treatment, the sample surface was oriented toward the opposite side from the ECR source, that is, the backside direction of the sample was turned toward the ECR source. This was to prevent Fe and Mo contamination caused by sputtering the inner wall of the ECR chamber. The inner wall of the ECR source was covered with a quartz liner to further reduce Fe and Mo contaminants. In these treatments, Fe and Mo contaminants could not be detected by SIMS analysis. Regrowth was performed in the MBE chamber. The growth temperature and As pressure were 550°C and 1×10^{-5} Torr, respectively. The thickness of the regrowth layer was 0.34 μm.

The concentrations of C, O and Si contaminants at the regrowth interface were estimated by SIMS analysis. The detection limits of C, O and Si concentrations were 1×10^{17}, 2×10^{16} and $1\times10^{17}\,cm^{-3}$, respectively. The carrier concentration at the regrowth interface was evaluated by capacitance–voltages (C–V) measurement. The C–V measurements were performed with a Schottky diode structure. The diodes were formed by depositing 400 μm of Al on the surface of the sample and fabricating an ohmic contact of AuSn on the backside. The surface flatness was estimated by reflection high-energy electron diffraction (RHEED) observation and atomic force microscopy (AFM). Also, thermal desorption spectroscopy (TDS) analysis was performed in the ECR chamber to investigate the removal mechanism of the contaminants.

3. Results and discussion

3.1. Contaminant concentration

The dependence of C, O, Si contaminant concentrations at the regrowth interface on hydrogen pressure during ECR treatment is shown in Fig. 1. Si and O contaminants decrease with a decrease in the hydrogen pressure, while the C contaminant

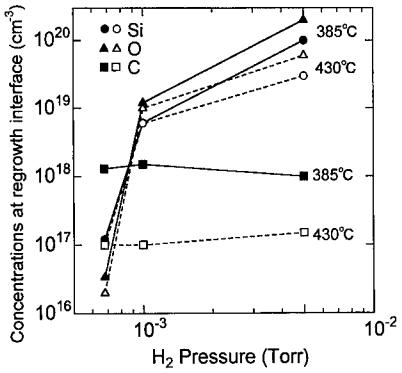

Fig. 1. Dependence of contaminant concentrations at regrowth interface on hydrogen pressure during plasma treatment. Contaminant concentrations were estimated by SIMS.

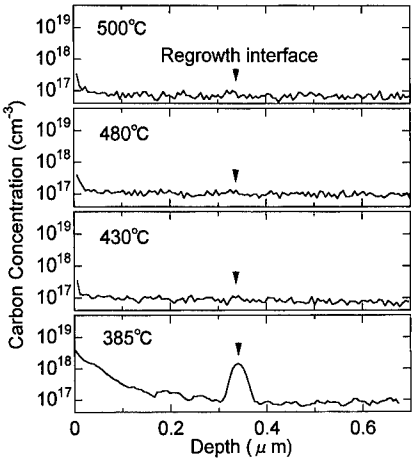

Fig. 2. SIMS profiles for a carbon contaminant near the regrowth interface cleaned by hydrogen plasma at various temperatures.

does not depend on hydrogen pressure. This tendency does not change at substrate temperatures between 385°C and 430°C. At a substrate temperature of 385°C and a hydrogen pressure of 1×10^{-3} Torr, O concentration is 1.2×10^{19} cm^{-3}, which is twice as large as the Si concentration of 6.1×10^{18} cm^{-3}. This reveals that high hydrogen pressure results in additional contamination due to sputtering the SiO_2 (quartz) liner in the ECR source except for the contamination when the surface is exposed to air. Actually, at a high microwave power of 500 W, the contaminant concentrations of Si and O are much larger than those at 200 W because of the higher sputtering rate of SiO_2. These Si and O contaminants are significantly reduced at hydrogen pressures below 1×10^{-3} Torr. At the lowest hydrogen pressure of 6.5×10^{-4} Torr to enable discharge, the contaminants can be removed to a level below the SIMS detection limit. This is due to the suppression of the sputtering by lowering the hydrogen pressure with sufficient hydrogen plasma density to remove the contaminants adsorbed prior to the plasma treatment.

The dependence of C contaminant concentration on substrate temperature is shown in Fig. 2. The regrowth interface is located at a depth of 0.34 μm. The quantity of the C contaminant at a substrate temperature of 385°C near the regrowth interface decreases at a peak concentration of 1×10^{18} cm^{-3} less than that when using conventional thermal cleaning (peak concentration of 10^{19} cm^{-3}) which is performed to maintain the substrate at a substrate temperature of 600°C for 5 min under an As pressure (shown in Fig. 4). However, carbon contaminant at the regrowth interface can effectively be removed at substrate temperatures above 430°C to a level below the SIMS detection limit.

To clarify the removal mechanism of the carbon contaminant, TDS analysis was performed in the ECR chamber for a GaAs surface after plasma treatment for 5 min. During this analysis, C, CH, CH_2, CH_3 and CH_4 ($m/e = 12$ to 16) gases were simultaneously monitored. The increment rate of the substrate temperature was 0.43°C/s. When the substrate temperature ranged from 100°C to 550°C, significant desorption peak for CH_3 could only appear as shown in Fig. 3. CH_3 gas desorbed at substrate temperatures above 400°C. This result indicates that the C contaminant on the GaAs surface reacting with hydrogen plasma produces CH_3, which can be removed from the GaAs surface at a substrate temperature of 400°C, according to the following equation:

$$C_{(\text{adsorption})} + 3H^* \rightarrow CH_{3(\text{adsorption})} \rightarrow CH_{3(\text{gas})},$$

at 400°C, (1)

where $C_{(\text{adsorption})}$ and H* are carbon contaminant on the GaAs surface and hydrogen radicals,

respectively. Therefore, substrate temperatures above 400°C result in a reduction of C contamination. The SIMS depth profile is shown in Fig. 4. The interface with conventional thermal cleaning, during which a substrate temperature is maintained at 600°C for 5 min, is located at 1 μm and the regrowth interface with hydrogen plasma treatment is located at 0.34 μm. The hydrogen pressure is 6.8×10^{-4} Torr and the substrate temperature is 500°C. The C, O and Si contaminants were completely removed at the regrowth interface with the hydrogen plasma treatment.

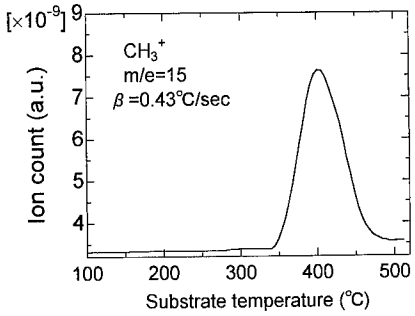

Fig. 3. TDS profile of CH_3^+ gas ($m/e = 15$) for the GaAs surface after hydrogen plasma treatment. The plasma treatment time was 5 min.

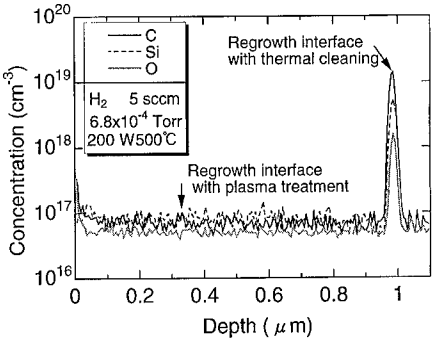

Fig. 4. SIMS depth-profile at the regrowth interfaces with plasma treatment (0.34 μm) and thermal cleaning (1.0 μm). The plasma treatment conditions were a hydrogen pressure of 6.8×10^{-4} Torr, a hydrogen flow rate of 5 sccm, a microwave power of 200 W, a substrate temperature of 500°C and a treatment time of 20 min. The thermal cleaning was held at a substrate temperature of 600°C for 5 min under As pressure.

3.2. Flatness of treated surface

The RHEED pattern after plasma treatment for 20 min is shown in Fig. 5. The RHEED pattern at a substrate temperature of 430°C is spotty, which indicates a rough surface. At a substrate temperature of 480°C, the RHEED pattern is streaky, which reveals an atomically flat surface. Moreover, at a substrate temperature of 500°C, a streaky $2\times$ reconstruction pattern can be observed, which proves that there is little structural damage on the treated surface. This is due to the elimination of ECR damage by thermal annealing at a substrate temperature of 500°C. The root-mean-square (RMS) roughness was evaluated by AFM for samples after plasma treatment for 20 min. The scan area is 0.5 μm × 0.5 μm. The RMS roughnesses at substrate temperatures of 430°C, 480°C, 500°C and 550°C are 34.1, 15.2, 9.6 and 35.4 Å, respectively. The increase in the roughness at 550°C is due to As desorption. These results reveal that a substrate temperature of 500°C produces the flattest treated surface during plasma treatment.

3.3. Carrier concentration

The carrier profile of C–V measurement is shown in Fig. 6. The regrowth interface is located at 0.34 μm. The carrier concentration at the regrowth interface is heavily depleted when plasma treatment is performed at a substrate temperature of 430°C. This depletion is caused by not only the acceptor due to the C contaminant but also the electron trap due to ECR damage. The acceptor concentration at the regrowth interface is calculated at 3.5×10^{11} cm^{-2} from the C–V profile. This concentration includes both the acceptor and electron trap concentration. The acceptor concentration due to the C contaminant is predicted at less than 1×10^{17} cm^{-3} from the SIMS analysis, which is evaluated at less than 1.8×10^{11} cm^{-2} (refer to the Appendix). The actual acceptor concentration due to the C contaminant is much less than 1.8×10^{11} cm^{-2} because the activation rate for the C contaminant is less than 100%. Therefore, the electron trap concentration due to ECR damage is estimated at much more than 1.7×10^{11} cm^{-2}.

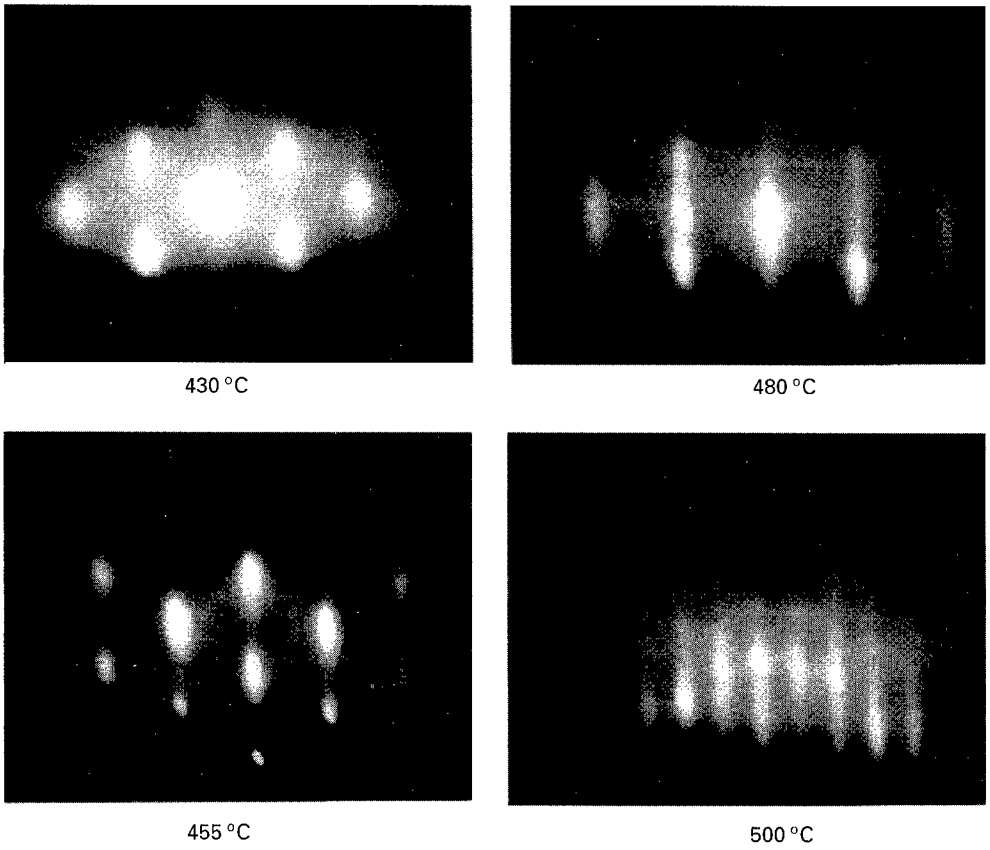

Fig. 5. RHEED patterns of the GaAs surface at room temperature after hydrogen plasma treatment. Substrate temperatures during plasma treatment were 430°C, 455°C, 480°C and 500°C.

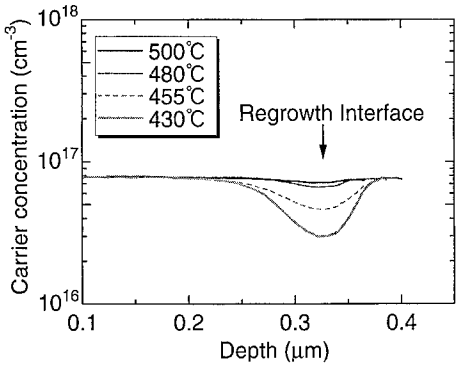

Fig. 6. C–V profile near n-GaAs/n-GaAs regrowth interface (0.34 μm) at various plasma treatment temperatures.

The carrier profile at a substrate temperature of 500°C is flat near the n-GaAs/n-GaAs regrowth interface, which proves there is little electrical ECR damage. Therefore, from the result of RHEED observation and C–V measurement, the structural and electrical ECR damage can be completely removed when the hydrogen plasma treatment is performed at a substrate temperature of 500°C.

4. Conclusion

We have demonstrated the elimination of carrier depletion and contaminants at the GaAs regrowth

interface by using ECR hydrogen plasma. The O and Si contaminants can be removed to a level below the SIMS detection limit by using ECR hydrogen plasma treatment at hydrogen pressures lower than 1×10^{-3} Torr. This is because a lower hydrogen pressure results in the suppression of additional Si and O contamination due to the sputtering of the quartz liner at the ECR source, and the contamination adsorbed prior to plasma treatment can be removed at an even lower hydrogen pressure. The C contaminant can be removed to a level below the SIMS detection limit by using the plasma treatment at substrate temperatures above 400°C. TDS analysis shows that substrate temperatures above 400°C result in the removal of CH_3 produced by hydrogen plasma and the C contaminant. As a result of *C–V* measurement, RHEED observation and AFM analysis, it was found that structural and electrical damage due to the ECR plasma is completely removed at a substrate temperature of 500°C. Therefore, by using ECR hydrogen plasma at a substrate temperature of 500°C and lower hydrogen pressures below 1×10^{-3} Torr, a carrier depletion-free regrowth interface can be realized. This technique will improve the electrical performance of devices with GaAs regrowth interfaces.

Acknowledgements

We would like to thank Mr. K. Kasahara and Dr. Y. Ohno for the calculation of the *C–V* profile. We also appreciate the useful discussions of Mr. H. Miyamoto and Mr. Tokushima. We wish to thank Dr. K. Honjo for his support and encouragement throughout our research.

Appendix

We evaluated maximum sheet concentration for the carbon contaminant at the regrowth interface when the concentration peak was below the SIMS detection limit. Generally, SIMS profile (F) is given by the convolution between the actual concentration profile (f) and the SIMS resolution function (g). In the case of the surface contaminants, f can be approximately written by Eq. (A.1):

$$f \approx a\delta, \tag{A.1}$$

where δ is a delta function and 'a' is the sheet concentration. In this case, SIMS profile can be rewritten as Eq. (A.2):

$$F \propto g \otimes f = ga, \tag{A.2}$$

where $\otimes$ is the convolution operator. Eq. (A.2) shows that the peak shape of the SIMS profile is not changed if the sheet concentration changes. When the C peak concentrations of the SIMS profile are 4×10^{19}, 4×10^{18} and 3×10^{18} cm^{-3}, C sheet concentrations are 6.4×10^{13}, 5.7×10^{12} and 5.3×10^{12} cm^{-2}, respectively in the experiments. From these results, a C peak concentration of 1×10^{17} cm^{-3} is estimated to be a sheet concentration of $(1.6 \pm 0.2) \times 10^{11}$ cm^{-2}. Therefore, the C sheet concentration below the SIMS detection limit (1×10^{17} cm^{-3}) is estimated to be less than 1.8×10^{11} cm^{-2}.

References

[1] A.Y. Cho and F.K. Reinhart, J. Appl. Phys. 45 (1974) 1812.
[2] K. Kasahara, K. Kunihiro, H. Nishizawa and Y. Ohno, Solid State Electron. 38 6 (1995) 1221.
[3] J. Saito, T. Ishikawa, T. Nakamura, K. Nanbu, K. Kondo and A. Shibatomi, Jpn. J. Appl. Phys. 25 (1986) 1216.
[4] J. Saito and K. Kondo, J. Appl. Phys. 67 (1990) 6274.
[5] H. Miyamoto, N. Furuhata, H. Hoshino, A. Okamoto and K. Ohata, Inst. Phys. Conf. Ser. 96 (1988) 47.
[6] N. Kondo and Y. Nanishi, Jpn. J. Appl. Phys. 28 (1989) L7.
[7] N. Kondo, Y. Nanishi and M. Fujimoto, Jpn. J. Appl. Phys. 33 (1B) (1994) L91.
[8] M. Hong, R.S. Freund, K.D. Choquette, H.S. Luftman, J.P. Mannaerts and R.C. Wetzel, Appl. Phys. Lett. 62 (1993) 2658.

ELSEVIER

Journal of Crystal Growth 175/176 (1997) 447–450

JOURNAL OF CRYSTAL GROWTH

High-temperature surface cleaning of AlGaAs without As flux for MBE regrowth

Kanji Iizuka[a,*], Kazuo Matsumaru[a], Toshimasa Suzuki[a], Yoshiyuki Takahira[b], Toshihiro Nishioka[b], Hiroshi Okamoto[b]

[a] *Nippon Institute of Technology, 4-1 Gakuendai, Miyashiro, Minami-Saitama, Saitama 345, Japan*
[b] *Chiba University, Faculty of Engineering, 1-33 Yayoi-cho, Inage-ku, Chiba 263, Japan*

Abstract

AlGaAs surfaces were cleaned by high-temperature heat treatment without As flux in a preparation chamber for regrowth of active layers by molecular beam epitaxy (MBE). Reflection high-energy electron diffraction from the cleaned AlGaAs surface showed a spotty pattern, but surface roughness observed by an atomic force microscope was smaller than the surface of cleaned GaAs. Auger electron spectroscopy showed that a cleaned surface was covered by Al, As and O_2. Surface sublimation measured by quadrupole mass spectroscopy during the heat treatment decreased drastically with increasing alloy composition x, suggesting that the cleaned surface consisted of AlAs or its oxide. Quantum well (QW) structures were grown on the cleaned surfaces and photoluminescence (PL) spectra were measured. Well-defined PL peaks corresponding to stacked single QWs (SQWs) with 500 nm thick buffer layer were obtained at 300 K, which were in contrast to the SQWs grown on the surface cleaned by the conventional method. The PL intensity was influenced strongly by the thickness of the buffer layer when it was thinner than 300 nm. GaAs passivation of the AlGaAs surface was effective for obtaining intense PL spectrum from the regrown SQWs.

1. Introduction

A novel surface cleaning method for GaAs substrates was proposed [1] which was very successful in molecular beam epitaxial (MBE) regrowth for fabricating an epilayer necessary for a distributed feedback (DFB) laser diode [2]. This cleaning procedure can be carried out in the preparation chamber at a temperature as high as 575°C without an As flux. Surface contamination was completely removed and furthermore, the cleaned surface maintained mirror-like smoothness. So, direct growth of high-quality GaAs/AlGaAs QW structures without any buffer layer on such surface was possible. By this high-temperature cleaning in the preparation chamber, the outgassing of oxygen and carbon monoxide from the molybdenum block during the temperature raising just before starting the MBE growth can be minimized. This is very beneficial to keep the growth chamber clean. On the other hand, surface cleaning of AlGaAs is usually more difficult

* Corresponding author. Fax: + 81 480 34 2941; e-mail: iizuka@nit.ac.jp.

0022-0248/97/$17.00 Copyright © 1997 Elsevier Science B.V. All rights reserved
PII S0022-0248(96)00891-3

because of high reactivity of aluminum. Goto et al. [3] reported that $Al_xGa_{1-x}As$ ($0 \leq x < 1$) could be etched by trisdimethylaminoarsine (TDMAAs) in a metalorganic MBE (MOMBE) chamber. The surface exposed to TDMAAs was cleaned, but it was also changed to an Al-rich surface by selective desorption of Ga atoms.

In this study, our high-temperature surface cleaning method is extended to the cleaning of an AlGaAs epilayer surface which was exposed to the atmosphere. The quality of the cleaned surface was characterized by reflection high-energy electron diffraction (RHEED), Auger electron spectroscopy (AES) and Atomic force microscope (AFM). GaAs/AlGaAs quantum well (QW) structures were grown over the cleaned surface and their photoluminescence (PL) spectra were also examined.

2. Experimental procedure

An $Al_xGa_{1-x}As$ (Al composition $x \leq 0.4$) epilayer was grown on GaAs (1 0 0) wafer mounted on Mo block with In solder. After taking out from vacuum after growth, the AlGaAs epilayer was immersed in deionized water and some oxide was formed on it. Then, the sample was put under heat treatment without an As flux in the preparation chamber which was evacuated to a pressure of 10^{-9} Torr. The treatment temperature was determined as 650°C from the critical point for selective sublimation of As atoms from the GaAs surface. Desorbed gases during the heat treatment were detected by a quadrupole mass spectrometer (QMS). In situ monitoring of surface crystallinity after cleaning was carried out by RHEED. Analysis of constituent elements of the cleaned surface was carried out by AES which was placed in the analysis chamber next to the growth chamber. AFM was also used to observe the cleaned surface and the root mean square (rms) of roughness was determined. In order to characterize the quality of the cleaned AlGaAs surface optically, GaAs/AlGaAs QW structures were grown on the cleaned AlGaAs surfaces with various thickness of GaAs buffer layer. PL from the QWs was measured at room temperature or at 50 K, using an Ar ion laser for excitation.

3. Results and discussion

3.1. Thermal cleaning of AlGaAs surface without As flux

High-temperature surface cleaning of an AlGaAs epitaxial wafer was performed in a preparation chamber at a temperature of 650°C. Fig. 1 shows RHEED pattern and AES spectrum of the AlGaAs surface after thermal cleaning. Although the surface looks mirror-like to naked eye inspection, RHEED shows a spot pattern. AES shows that oxygen remains on the surface, and formation of Al_2O_3 during the air exposure or under the thermal cleaning of the surface was suggested from the chemical shift of Al peak to lower-energy side by about 13 eV [4]. But carbon was desorbed from the surface. The dependence of the rms surface roughness on annealing temperature, obtained from AFM images, is shown in Fig. 2. The rms roughness of the AlGaAs surface did not depend on the cleaning temperature which is different from that of a GaAs surface. The QMS showed that the sublimation of Ga and As from the $Al_xGa_{1-x}As$ surface decreased

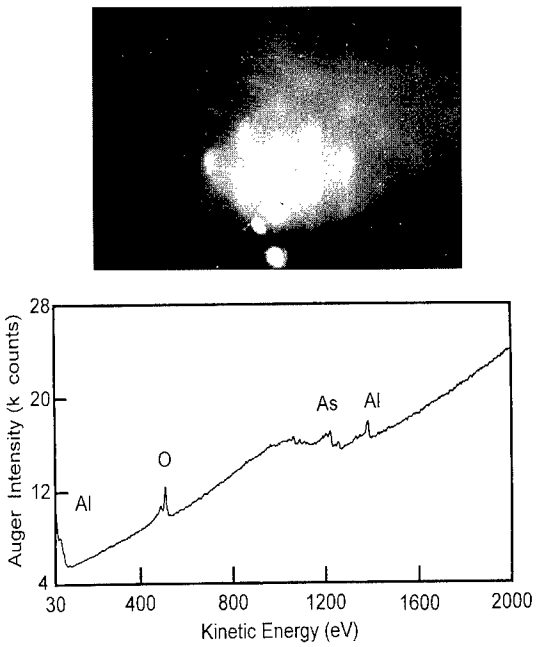

Fig. 1. RHEED pattern and AES spectrum of AlGaAs surface which was cleaned at 650°C without As flux.

drastically when the mole fraction x was increased from 0 to 0.3, as shown in Fig. 3. All desorbtion could be detected by the quadrupole head because it was placed in front of the cleaning AlGaAs surface. But Al peak was not measured accurately because Al peak (mass = 27) could not be resolved separately from carbon monoxide peak (mass = 28) in the present study. From the result of AES, the cleaned surface was found to consist of Al, As and O_2, so it could be considered that the surface was covered by AlAs or its oxide as a result of sublimation of the Ga–As pair from AlGaAs surface. This sublimation was dependent on mole fraction x with no sublimation when the surface was covered by thin AlAs layer. Therefore, surface roughness was independent of the cleaning temperature.

3.2. *Epitaxial growth of GaAs/AlGaAs QW structures on cleaned AlGaAs surfaces*

To further characterize the cleaned AlGaAs surface by PL, QW structures were regrown on the cleaned AlGaAs surfaces. The samples had stacked GaAs QWs 3, 4.5, 7 and 15 nm thick separated by 50 nm thick AlGaAs barriers grown on a GaAs buffer layer at a growth temperature of 670°C. This structure was grown on two AlGaAs surfaces cleaned by different procedure, i.e. on the surface prepared by high-temperature surface cleaning method without As flux at 650°C and on the surface cleaned by conventional method including flash annealing under As flux at 690°C. Fig. 4 shows PL

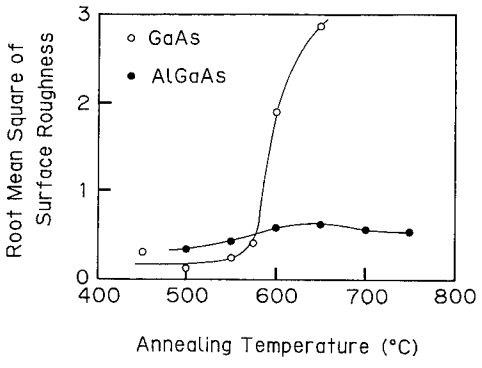

Fig. 2. Annealing temperature dependence of the root mean square of the surface roughness in AFM image.

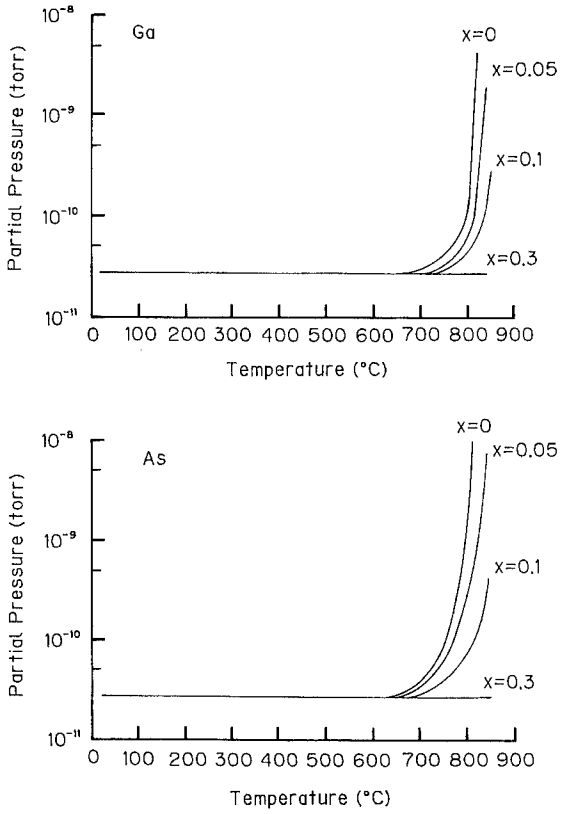

Fig. 3. Amount of sublimation of Ga and As from the surface as a function of cleaning temperature.

spectra from the samples which had 500 nm thick buffer layer. No resolved PL peak was obtained for the epilayer on AlGaAs surface prepared by conventional method. On the other hand, well-resolved PL peaks were observed even at 300 K for the epilayer grown on AlGaAs cleaned by the new method. This PL intensity depended on the thickness of the regrown GaAs buffer layer. The result of PL measurement at 50 K for the 20 ML thick SQW is summarized as a broken line in Fig. 5. When the buffer layer thickness decreased to less than 300 nm, PL intensity reduced drastically. In order to improve the quality of AlGaAs surface and to decrease the thickness of buffer layer, we tried to introduce a GaAs passivation layer which was grown on top of the first AlGaAs epilayer. This GaAs passivation layer was desorbed along with surface oxide during the heat treatment before the

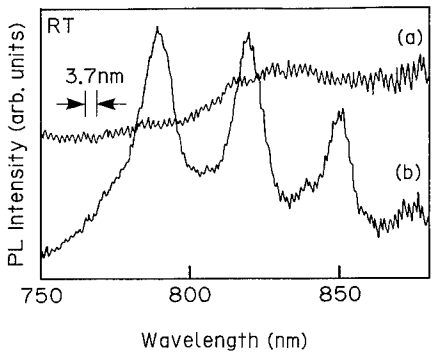

Fig. 4. PL spectra from the stacked SQWs regrown on cleaned AlGaAs with 500 nm thick AlGaAs buffer layer. (a) cleaned by conventional method. (b) cleaned by high-temperature surface cleaning method without As flux.

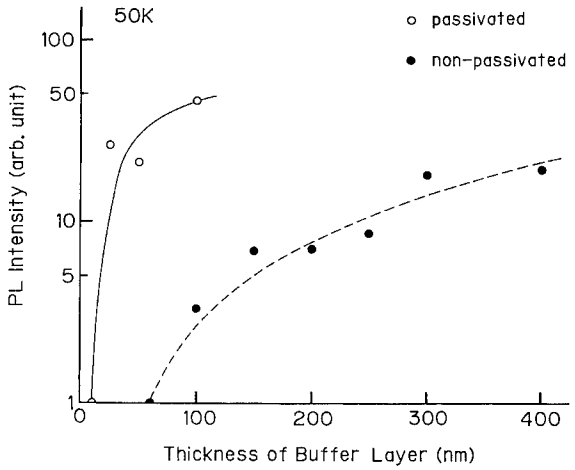

Fig. 5. PL intensity from SQW on cleaned AlGaAs surface which was passivated (open circle) or non-passivated (solid circle) as a function of thickness of regrown AlGaAs buffer layer.

regrowth. Passivation of the AlGaAs surface by GaAs layer was applied originally to the growth of cladding layer on the cleaned surface for the double-hetero (DH) laser structure fabricated by Tanaka et al. [5], and we here extended this concept to the growth of active layers on the cleaned surface. Thickness of the passivation layer was determined to be 100 nm from the data of GaAs sublimation during the high-temperature cleaning without As flux [1]. RHEED pattern from the passivated and cleaned AlGaAs surface was improved significantly to bright spotty one, and AES showed that Al_2O_3 formation was suppressed. The result of PL is shown in Fig. 5 by a solid line. Strong PL intensity was successfully obtained even when the thickness of buffer layer was as thin as 25 nm. This result indicates strongly that the protection of AlGaAs surface by GaAs passivation layer reduce remarkably the amount of residual oxygen on the cleaned surface.

4. Summary

The high-temperature heat treatment without As flux which was very successful as a new surface cleaning method of GaAs was applied to AlGaAs surface and the quality of the cleaned surface was examined. Although oxygen remained on the cleaned surface and RHEED showed a spotty pattern, the surface was still kept its mirror-like smoothness. Carbon was removed from the surface during the heat treatment. AFM revealed that cleaned AlGaAs surface had better flatness than the cleaned GaAs surface. Sublimation of Ga and As was drastically decreased with increasing the mole fraction x in $Al_xGa_{1-x}As$. PL spectrum from QWs grown on the AlGaAs surface cleaned by the present method suggested that the quality of the surface was much better than that cleaned by the conventional method with flash annealing. To obtain more clean surface, introduction of the GaAs passivation layer on AlGaAs surface was suggested. The high-temperature surface cleaning without As flux is an effective method to make AlGaAs surface with device quality.

References

[1] K. Iizuka, K. Matsumaru, T. Suzuki, H. Hirose, K. Suzuki and H. Okamoto, J. Crystal Growth 150 (1995) 13.
[2] Y. Takahira, T. Usami and Y. Matsushima, Tech. Dig. Optoelectron. Commun. Conf. '96 (1996) p. 406.
[3] S. Goto, Y. Momura and Y. Morishita, Jpn. J. Appl. Phys. 34 (1995) L533.
[4] H.H. Madden, J. Vac. Sci. Technol. 18 (1981) 677.
[5] H. Tanaka, M. Mushiage, Y. Ishida and H. Fukada, Jpn. J. Appl. Phys. 24 (1985) L89.

ELSEVIER

Journal of Crystal Growth 175/176 (1997) 451–458

JOURNAL OF CRYSTAL GROWTH

Fabrication and band alignment of pseudomorphic $Si_{1-y}C_y$, $Si_{1-x-y}Ge_xC_y$ and coupled $Si_{1-y}C_y/Si_{1-x-y}Ge_xC_y$ quantum well structures on Si substrates

K. Brunner[a,*], W. Winter[a], K. Eberl[a], N.Y. Jin-Phillipp[b], F. Phillipp[b]

[a] *Max-Planck-Institut für Festkörperforschung, Heisenbergstrasse 1, D-70569 Stuttgart, Germany*
[b] *Max-Planck-Institut für Metallforschung, Heisenbergstrasse 1, D-70569 Stuttgart, Germany*

Abstract

The structural and photoluminescence (PL) properties of several types of pseudomorphic $Si_{1-x-y}Ge_xC_y$ quantum well (QW) structures grown by solid-source molecular beam epitaxy on (0 0 1) Si substrates are described. Optimum $Si_{1-y}C_y$ growth takes place at a substrate temperature of about 550°C and a growth rate $\leqslant 1$ Å/s. Well-defined alloy layers with no defects or SiC precipitates are observed by transmission electron microscopy (TEM). Excitonic band edge related PL is emitted from $Si_{1-y}C_y/Si$ multiple QWs (MWQ). The band gap of strained $Si_{1-y}C_y$ is drastically reduced by about $\Delta E = -y \times 6.5$ eV. Reducing the width of $Si_{0.99}C_{0.01}$ layers results in a PL blueshift up to 45 meV which is attributed to the strong (weak) quantum well confinement of $\Delta(2)$ valley electron (light hole) states. The band alignment in $Si_{1-y}C_y/Si$ QWs is basically explained by the strain-induced shift of levels due to C incorporation. In $Si_{1-x-y}Ge_xC_y$ QWs, compressive strain caused by Ge is partially compensated by C and the band gap increases by $\Delta E = y \times 2.4$ eV. $Si_{1-y}C_y$ as well as $Si_{1-x-y}Ge_xC_y$ QWs give rise to spatially direct PL transitions. Closely spaced $Si_{1-y}C_y/Si_{1-x}Ge_x$ double quantum wells (DQW) give rise to spatially indirect PL recombination of $\Delta(2)$ electrons confined in the $Si_{1-y}C_y$ layers and heavy holes localized in the $Si_{1-x}Ge_x$ layers. The no-phonon transitions and the integrated PL intensity from thin DQWs are strongly enhanced compared to SQWs. In Hall transport studies, $Si_{1-y}C_y$ and SiGeC alloys on Si reveal electron and hole mobilities which are well comparable to Si and SiGe or even improved. C alloying provides a significant extension of the possibilities in band structure engineering of Group-IV semiconductors.

PACS: 73.20.Dx; 78.55.Hx; 81.10. – h

Keywords: Molecular beam epitaxy; Photoluminescence; Band alignment; $Si_{1-x}Ge_x$; SiGeC; Quantum well

* Corresponding author. E-mail: brunner@servix.mpi-stuttgart.mpg.de.

0022-0248/97/$17.00 Copyright © 1997 Elsevier Science B.V. All rights reserved
PII S0022-0248(96)00947-5

The multitude in materials and alloy systems of III–V semiconductors results in a high degree of freedom in band structure engineering. This fact and their good intrinsic optical and electrical properties have made possible several III–V devices which are not attainable by standard Si technology or SiGe heteroepitaxy. The first SiGe/Si devices which will reach industrial production are heterobipolar transistors, realized by a thin epitaxially grown pseudomorphic SiGe layer embedded in Si [1]. MOSFETs and some optoelectronic structures made from SiGe show good performance data but they are handicapped so far by the complicated structure design requiring thick relaxed buffer layers in order to adjust the strain of Si or SiGe layers on top of it [2–4]. Several years ago, a third group-IV element, carbon, was brought into play and the structural properties of $Si_{1-y}C_y$ and $Si_{1-x-y}Ge_xC_y$ layers on Si were very promising [5, 6]. Low-temperature epitaxy allows substitutional incorporation of C into an Si matrix for contents up to about 10%. The very small bond length of diamond compared to Si results in macroscopic tensile strain $\varepsilon = 0.35y$ within pseudomorphic $Si_{1-y}C_y$ on Si in agreement with Vegard's law. The lattice strain induced by C and Ge is of opposite sign. This fact and its consequences on electronic level splitting, band alignment, optical and electrical properties, and lattice strain relaxation imply that C may serve as a valuable counterpart of Ge in Si-based heteroepitaxy. The intention of this contribution is (a) to investigate the PL and electronic properties of pseudomorphic $Si_{1-y}C_y$/Si and $Si_{1-x-y}Ge_xC_y$/Si structures, (b) to get a first picture of the band alignments in such structures, and (c) to give an outlook on their advantages and limitations.

The samples studied here were deposited by solid-source molecular beam epitaxy on (0 0 1) n^--Si in a modified Balzers ULS 400 chamber. $Si_{1-y}C_y$ and $Si_{1-x-y}Ge_xC_y$ alloy layers are deposited at a typical growth rate of 1 Å/s at substrate temperatures $T_s = 500$–$600°C$ [7]. Si, Ge and C are supplied by an electron beam evaporator, an effusion cell, and a pyrolitic graphite filament sublimation source, respectively. Besides some aspects known from SiGe epitaxy, the design and performance of the high-temperature C source seems to be of great importance for the PL efficiency of samples. The filament is completely shielded by graphite and the source environment is efficiently cooled by water. Bright heat radiation of the cell and an increased CO and CO_2 background pressure are the main items which have to be addressed for optimum growth [7]. Each sample consists of a 20–30 period multiple layer structure which is embedded between a 400 nm buffer and a 50–100 nm cap layer of Si. Single QW (SQW) and double QW (DQW) assign periodically repeated SiGeC/Si and SiGeC/SiC/Si layer sequences, respectively. For PL measurements, the samples are excited by a 476 nm laser beam at 0.3 W/cm^2 power density. They are mounted on a cold-finger ($T = 8$ K) within a He-flow cryostat. PL spectra are detected by a single-grating spectrometer equipped with a cooled Ge detector in a standard lock-in technique.

MQW structures of about 0.5 μm thickness allow a very precise analysis of layer widths and Ge or C content by two-crystal high-resolution X-ray diffraction (XRD). Fig. 1 shows rocking curves of the zeroth- and first-order superlattice (SL) (0 0 4) reflection of different types of MQW structures with a period of about 240 Å as indicated in the figure. For a 33 Å $Si_{0.986}C_{0.014}$/210 Å Si MQW structure, a larger zeroth-order diffraction angle compared to the Si substrate indicates tensile

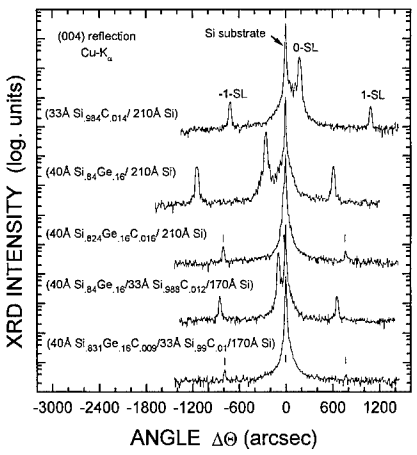

Fig. 1. High-resolution two-crystal X-ray diffraction curves of the (0 0 4) reflection from different multiple QW structures as indicated in the figure.

biaxial strain $\varepsilon = 0.50\%$ within the alloy layers. Compressive strain $\varepsilon = -0.64\%$ is observed for 40 Å $Si_{0.84}Ge_{0.16}$ QWs. The zeroth-order XRD peak of the $Si_{0.824}Ge_{0.16}C_{0.016}$/Si structure is shifted towards Si and indicates nearly complete strain compensation. A similar shift is observed for a 40 Å $Si_{0.84}Ge_{0.16}$/33 Å $Si_{0.988}C_{0.012}$/170 Å Si structure. The reduced average strain analyzed by XRD is attributed to a partial strain symmetrization with compressive and tensile strain in neighbouring layers. C alloying results in a nearly vanishing average strain for a 40 Å $Si_{0.831}Ge_{0.16}C_{0.009}$/33 Å $Si_{0.99}C_{0.01}$/170 Å Si structure. The zeroth-order SL peak coincides with the substrate peak and the weak first-order SL peaks are symmetrical to $\Delta\Theta = 0''$ (downmost curve in Fig. 1). Strain compensation in SiGeC and/or strain symmetrization in neighboring SiGe(C)/SiC layers should allow pseudomorphic growth of MQW and superlattice (SL) structures of large total thickness without lattice relaxation. TEM investigations show a high crystal quality of the different types of MQW structures without extended defects or SiC precipitates. As an example, Fig. 2a and b represent moderate and high-resolution TEM cross-sectional images of a 40 Å $Si_{0.84}Ge_{0.16}$/33 Å $Si_{0.988}C_{0.012}$/170 Å Si MQW structure. The TEM condiditons realized especially in Fig. 2b allow a clear distinction of the neighboring $Si_{0.84}Ge_{0.16}$ and $Si_{0.988}C_{0.012}$ alloy layers of opposite strain. A good layer homogeneity and interface quality are observed in all structures.

A PL spectrum from a 30-period (52 Å $Si_{0.99}C_{0.01}$/156 Å Si) MQW structure shown in Fig. 3 reveals similar features as known from $Si_{1-x}Ge_x$ QWs for $x < 20\%$. A no-phonon PL line (QW-NP) and its Si-like TO phonon replica line (QW-TO) as well as weaker TA and TO plus Γ phonon replica lines are observed at energies below the Si-TO phonon line originating from the Si layers (Si-TO). All these lines related to $Si_{1-y}C_y$ layers shift linearly down in energy with increasing C content by $\Delta E = -y \times 5.7$ eV. The PL lines shift to 45 meV higher energy for decreasing the $Si_{0.99}C_{0.01}$ layer width from 110 to 11 Å (see inset of Fig. 3). Both results prove that photoexcited carriers are localized to quantum-confined subband levels formed within the $Si_{1-y}C_y$. A detailed PL study and deformation potential calculations

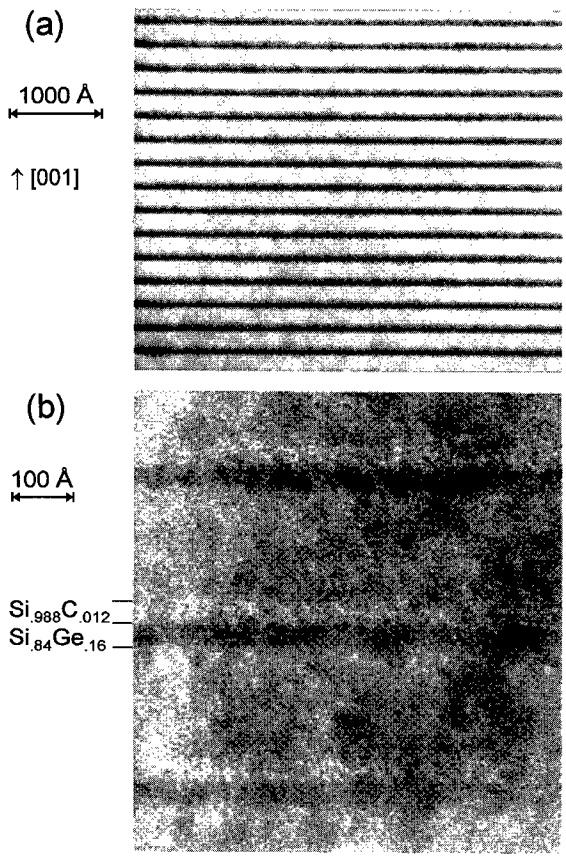

Fig. 2. Cross-sectional TEM micrographs with moderate (a) and high resolution (b) of a 25-period 40 Å $Si_{0.84}Ge_{0.16}$/33 Å $Si_{0.988}C_{0.012}$/170 Å Si DQW structure on (0 0 1) Si.

for the conduction (CB) and valence band edge (VB) energies in strained Si give evidence that the twofold degenerate Δ(2) electron states ($m = 0.92\ m_0$) oriented in growth direction are strongly and light hole (lh) states are weakly confined to the $Si_{1-y}C_y$ layers [8]. Fig. 4a shows the band edge shifts which are calculated using a simple Si deformation potential approach. We neglect intrinsic effects of C, but we regard only the influence of built-in biaxial strain $\varepsilon = 0.35y$ in $Si_{1-y}C_y$ on Si. Tensile strain splits and shifts electronic levels. Δ(2) states are strongly decreasing and lh states are slightly increasing in energy. They form the band edges and the observed low-temperature PL is attributed to spatially direct (type-I) transitions between these levels within $Si_{1-y}C_y$. The band gap

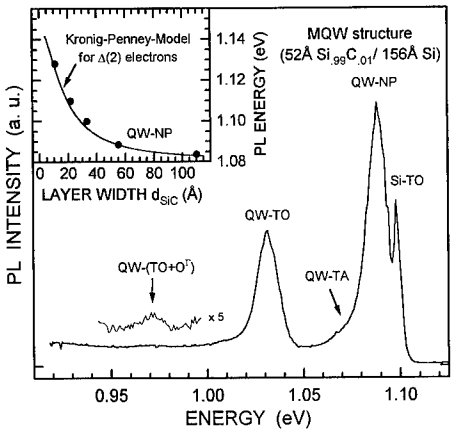

Fig. 3. PL spectrum observed from 52 Å $Si_{0.99}C_{0.01}$ QWs at $T = 8$ K. The PL lines observed originate from bulk Si (Si-TO) and from the alloy layers (QW-TO, QW-NP). The inset shows the NP PL energy depending on $Si_{0.99}C_{0.01}$ layer width. The solid line represents Kronig–Penney model calculations for electrons $m_{\Delta(2)} = 0.92m_0$ confined by $\Delta E_{CB} = -65$ meV.

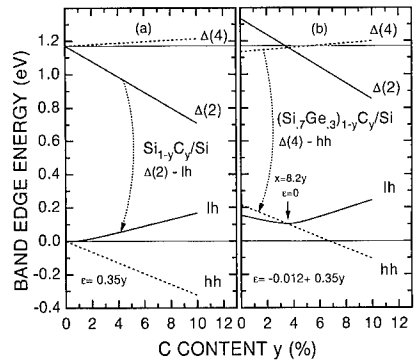

Fig. 4. Calculated band edge energies in strained $Si_{1-y}C_y$ (a) and $(Si_{0.7}Ge_{0.3})_{1-y}C_y$ (b) on (0 0 1) Si using a deformation potential approach. The energy shifts caused by strain and the band offsets due to Ge are taken into account. Any intrinsic influence of C is neglected.

reduction in $Si_{1-y}C_y$/Si deduced from PL $\Delta E = -y \times 6.5$ eV (including corrections for confinement shifts) is mainly attributed to strain effects. The intrinsic band gap of $Si_{1-y}C_y$ decreases by about $\Delta E_g = -y \times 1.5$ eV. This qualitatively agrees with tight binding model calculations considering microscopic relaxation of the Si–Si and Si–C bond lengths in unstrained $Si_{1-y}C_y$ alloys [9].

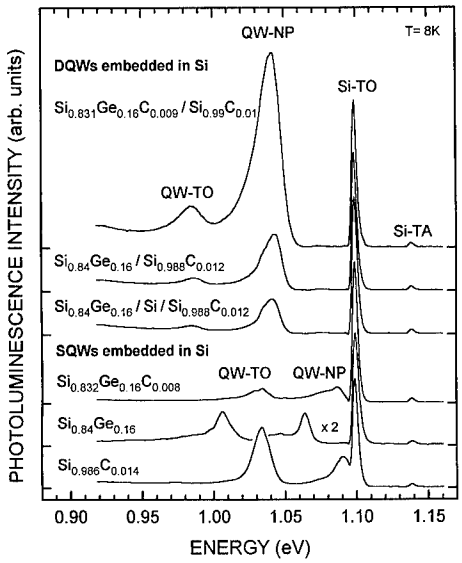

Fig. 5. Low temperature PL spectra of 25-period multiple layer structures containing SQWs and DQWs in an Si matrix. $Si_{0.84}Ge_{0.16}$ and $Si_{0.84}Ge_{0.16}C_y$ are 40 A, $Si_{1-y}C_y$ layers are 33 Å in width. The compositions are written in the figure. The excitonic no-phonon and TO-phonon PL lines originating from alloy layers are marked by QW-NP and QW-TO, respectively.

Recent studies on $Si_{1-x}Ge_x$/Si QWs ($x < 38\%$) have verified type I PL transitions of Δ(4) and heavy hole (hh) states localized within SiGe [10]. Starting from such a band alignment, as given in Fig. 4b for $x = 30\%$ (at $y = 0\%$), the strain-mediated influence of C on the SiGeC band edges is different from $Si_{1-y}C_y$. Compensation of strain induced by Ge and C reduces level splitting and opens the band gap by about $\Delta E = y \times 3.8$ eV. At a C content $y = x/8.2$, $Si_{1-x-y}Ge_xC_y$ layers are lattice matched to Si ($\varepsilon = 0$). Δ as well as lh and hh states should recover degeneracy. PL spectra from 40 Å $Si_{0.84}Ge_{0.16}$, 40 Å $Si_{0.832}Ge_{0.16}C_{0.008}$ and 33 Å $Si_{0.986}C_{0.014}$ SQWs are given in the lower part of Fig. 5, for comparison. The PL lines from $Si_{0.832}Ge_{0.16}C_{0.008}$ are about 20 meV higher in energy than the $Si_{0.84}Ge_{0.16}$ PL. The observed PL blueshift with C alloying $\Delta E_{SiGeC} = y \times 2.4$ eV agrees well with earlier results of Amour et al. [11]. All three SQWs emit NP and TO PL lines of comparable intensity. They are attributed to spatially direct transitions of excitons confined to the alloy layers.

The PL observed from DQW structures with $Si_{0.84}Ge_{0.16}(C_y)$ and $Si_{0.988}C_{0.012}$ layers in close proximity (see Fig. 2) reveal a different type of transition [12]. The PL energy in DQWs is lower than in all reference SQWs and depends on the Ge and C content of both layers (upper part in Fig. 5). The NP line is strongly enhanced in intensity compared to its TO replica and to SQW PL lines. A 40% intensity drop caused by separating the $Si_{0.84}Ge_{0.16}$ and $Si_{0.988}C_{0.012}$ layers by a thin 4 Å Si layer indicates the spatially indirect nature of PL from these novel DQW structures. Δ(2) electrons confined to the $Si_{0.988}C_{0.012}$ and hh states localized within the $Si_{0.84}Ge_{0.16}$ QWs emit strong no-phonon PL. The integrated intensity of DQW PL increases exponentially for decreasing layer widths $d_{SiGe} = 1.2d_{SiC}$, as shown in Fig. 6. The NP line is neglegibly weak in DQWs of 66 Å width, but at a width of 23 Å it is much stronger than the Si-TO line from all thick Si layers at the same energy $E = 1.10$ eV. This enhancement of PL concomitant with the PL energy shift is well described by model calculations of the confined band edge states and the squared overlap integral of wave functions. This overlap dominates the transition rate of spatially indirect PL from coupled DQWs [12].

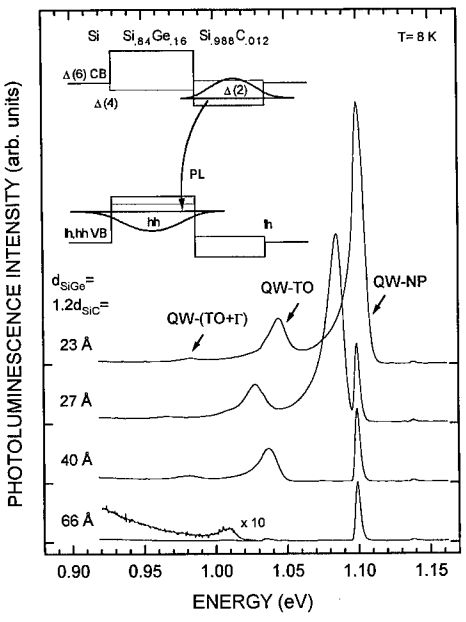

Fig. 6. PL spectra from $Si_{0.84}Ge_{0.16}/Si_{0.988}C_{0.012}$ DQW structures with varied layer widths $d_{SiGe} = 1.2d_{SiC}$ in Si. The spectra are plotted on the same intensity scale with offsets for clarity.

These experimental results promise further improvements in the optical properties of group-IV alloys using such DQW or SL structures. The enhanced NP PL intensity indicates a strong mixing of Δ(2) and Γ electron states which might be further improved in structures with larger Ge and C contents. Such structures with deep QWs for electrons and holes promise efficient capture, localization and luminescence emission of excited carriers and they offer an easier access to transition energies in the infrared wavelength range down to 1.55 μm. The energy and the efficiency of optical emission and absorption can be tuned by the composition, width and spatial distance of different alloy layers. From a technological point of view, the compensation or symmetrization of strain in SiGeC/Si, SiGe/SiC and SiGeC/SiC SLs and the resulting release of critical thickness limitations are very important. They should enable structures thick enough for waveguide or infrared detector applications.

Studying coupled SiGeC/SiC layers of a ternary alloy system also allows fundamental investigations of the CB and VB offsets in $Si_{1-y}C_y$ or SiGeC layers on Si, respectively. When the hh level, for example, is used as a fixed energy reference in the $Si_{0.84}Ge_{0.16}$ layer, the PL energy shift observed for increasing the C content of the neighbouring $Si_{1-y}C_y$ layer directly reflects the lowering of the Δ(2) electron state energy. The trend of the PL shift observed from 40 Å $Si_{0.84}Ge_{0.16}$/33 Å $Si_{1-y}C_y$ DQWs for $y \geqslant 0.8\%$ nearly matches that of isolated $Si_{1-y}C_y$ SQWs representing the shift of CB as well as VB levels, as shown in Fig. 7. This confirms qualitatively that the main part of band edge shifts in $Si_{1-y}C_y$/Si heterostructures is in the CB.

For a fixed Δ(2) level in $Si_{1-y}C_y$, additional C alloying of the SiGe layers results in a decreasing PL energy. This implies an increase of the SiGeC/Si VB offset with C alloying. It is in disagreement with capacitance voltage measurements indicating a reduced VB offset [13]. Confinement energy shifts caused by different potential barrier heights, a modified excitonic binding in DQWs, sample inhomogeneities and impurities may influence the

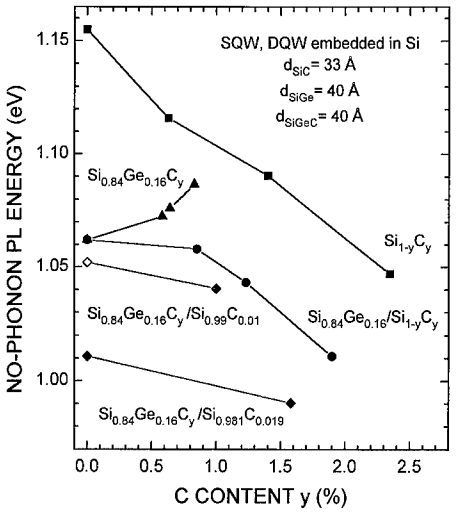

Fig. 7. Energy of the no-phonon PL line observed from $Si_{1-y}C_y$ and $Si_{0.84}Ge_{0.16}C_y$ SQW and from $Si_{0.84}Ge_{0.16}/Si_{1-y}C_y$ and $Si_{0.84}Ge_{0.16}C_y/Si_{1-y'}C_{y'}$ DQW structures versus C content y. Layers with (x = 16%) and without Ge are 40 and 33 Å in width, respectively.

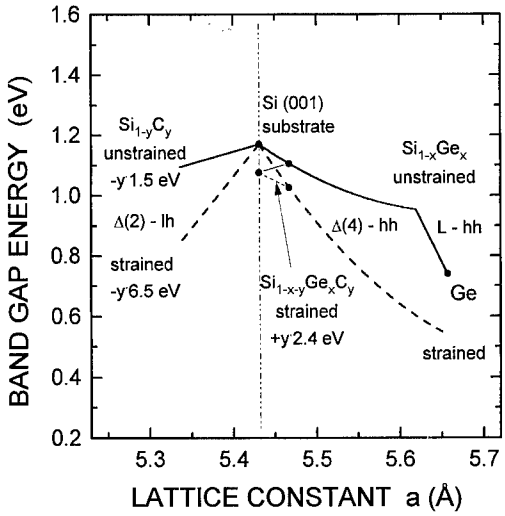

Fig. 8. Band gap in $Si_{1-y}C_y$, $Si_{1-x}Ge_x$ and $Si_{1-x-y}Ge_xC_y$ versus intrinsic lattice constant. The PL results from strained $Si_{1-y}C_y$ pseudomorphically grown on Si (0 0 1) are sketched by a dashed line. The band gap in unstrained $Si_{1-y}C_y$ is deduced from PL considering deformation potential calculations (solid line). SiGe data are taken from literature.

observed PL energy shifts plotted in Fig. 7. Nevertheless, we believe that comparison of similar structures with just the C content varied gives a reasonable qualitative insight into the band offsets in different SiGeC/Si heterostructures.

The band gap of alloys with type-I band alignment is analyzed more reliably by PL from SQWs. E_g is plotted versus lattice constant a_L for $Si_{1-y}C_y$, $Si_{1-x}Ge_x$ and $(Si_{0.84}Ge_{0.16})_{1-y}C_y$ alloys in Fig. 8. The Δ(4)-hh band gap in strained and unstrained $Si_{1-x}Ge_x$ was extensively investigated in recent years. The PL results from strained $Si_{1-y}C_y$ SQWs on Si reveal a shift of $-y \times 6.5$ eV from which an intrinsic band gap of about $E_g(Si_{1-y}C_y) = E_g(Si) - y \times 1.5$ eV is deduced applying Si deformation potential calculations. In the representation E_g versus a_L in Fig. 8, $Si_{1-y}C_y$ behaves similar to $Si_{1-x}Ge_x$. It should be noted, however, that the band gap as well as the lattice constant vary much stronger with C than with Ge alloying. Starting with a strained 40 Å $Si_{0.84}Ge_{0.16}$ layer, the band gap opens by about $y \times 2.4$ eV. This extrapolates to a band gap about 100 meV below that of Si for a $Si_{0.82}Ge_{0.16}C_{0.02}$ alloy which is lattice matched to Si. Exactly the same energy is estimated by assuming the same intrinsic band gap shift $E_g((Si_{0.84}Ge_{0.16})_{1-y}C_y) = E_g(Si_{0.84}Ge_{0.16}) - y(1.5$ eV) in Si and $Si_{0.84}Ge_{0.16}$ (thin solid line in Fig. 8). This seems to be reasonable for the Si-like Δ electron valleys in a dilute $Si_{1-x}Ge_x$ and we get a consistent picture of the $Si_{1-y}C_y$ and $Si_{1-x-y}Ge_xC_y$ band gaps within the studied composition range $x < 20\%$ and $y < 2\%$. PL was observed from thin 11 Å $Si_{1-y}C_y$ QWs with y up to 6.4% [7]. The influence of band gap energy, strain, quantum confinement, and layer quality at large y on the PL energy observed is yet not clarified.

Besides novel structures for optical applications, the strong influence of C on CB energy and the (partial) compensation of strain in SiGeC/Si heterostructures imply several new electronic structures. The fundamental transport properties of C alloys are studied on 0.5 μm thick pseudomorphic $Si_{1-y}C_y$ layers on Si which were homogeneously doped by P ($n = 2 \times 10^{17}$ cm^{-3}) or B ($p = 1 \times 10^{17}$ cm^{-3} at $T = 300$ K) [14]. For a C content $y = 0.4\%$, the electron and hole Hall mobilities $\mu_e = 600$ cm^2/V·s and $\mu_h = 180$ cm^2/V·s measured in Van der Pauw geometry at $T = 300$ K reach nearly the values observed from

MBE-grown Si reference samples. The mobility seems to be limited by scattering of charged dopant impurities, although the concentration of C exceeds that of P or B dopants by about 3 orders of magnitude. $Si_{1-y}C_y$ alloys represent a semiconductor material system which can be grown in high quality and whose fundamental properties (i.e. a large CB offset and a small in-plane mass $m_{\Delta(2)} = 0.2m_0$) promise novel n modulation-doped $Si_{1-y}C_y/Si$ structures with improved performance and without the need of thick relaxed buffer layers [15]. At low temperatures $T < 100$ K, however, an enhanced freeze-out of carriers is observed in $Si_{1-y}C_y$. This may indicate localization of carriers at local fluctuations in the alloy composition. The Hall mobilities at low temperatures are considerably higher in $Si_{1-y}C_y$ layers with low y than in Si [14, 15]. This may indicate enhanced mobilities which are expected for tensily strained Si due to smaller effective masses and reduced intervalley scattering rates [16–18]. An optimized layer and interface quality is required to rule out experimentally the merit of strain, the influence of C alloy scattering and the potential of $Si_{1-y}C_y/Si$ for MOS and MODFET devices.

In a different approach, C is used for strain reduction in Ge-rich SiGeC/Si structures to reduce the lattice mismatch. This increases the critical thickness for strain relaxation. An improved thermal stability of 7 Å $Ge_{0.964}C_{0.036}$ layers compared to Ge during thermal anneals at temperatures up to 750°C was demonstrated by XRD studies [19]. The Hall mobility at $T = 300$ K and 77 K in 80 Å $Si_{1-x}Ge_x/Si$ modulation doped p-channels grown at $T_s = 520$°C is shown in Fig. 9. A degradation of the mobility is observed for a Ge content $x > 40\%$. This is attributed to the strain relaxation and roughening of $Si_{1-x}Ge_x$ layers. Substitutional incorporation of C reduces strain from $\varepsilon = 2$ to 1.3% in a $Si_{0.49}Ge_{0.49}C_{0.02}$ layer. The recovery of the mobility $\mu_h = 185$ (2750) $cm^2/V \cdot s$ measured at $T = 300$ K (77 K) is attributed to an increased critical thickness > 80 Å for strain relaxation in $Si_{0.49}Ge_{0.49}C_{0.02}$. Very high hole mobilities are expected for strained Ge layers on Si [20]. No significant degradation of mobility by dilute C alloying but an improvement in layer stability is observed. This fact is an important step towards high mobility p-channels in pseudomorphic $Ge_{1-y}C_y/Si$ structures.

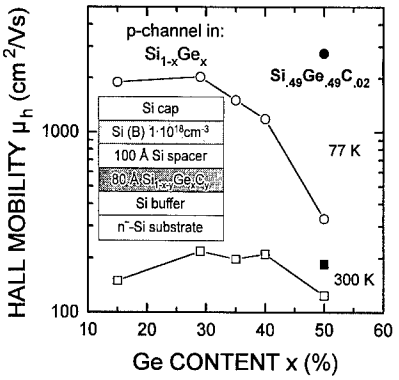

Fig. 9. Hall mobility of holes in modulation doped 80 Å $Si_{1-x}Ge_x$ layers with varied x and in a $Si_{0.49}Ge_{0.49}C_{0.02}$ layer measured in Van-der-Pauw geometry at $T = 300$ K and 77 K.

In summary, we have described the structural, optical and electrical properties of high quality $Si_{1-y}C_y$ and $Si_{1-x-y}Ge_xC_y$ alloy layers pseudomorphically grown on Si by MBE. Tensile strain $\varepsilon = 0.35y$ and a resulting strong lowering of the $\Delta(2)$ CB states are the main features of $Si_{1-y}C_y/Si$ heterostructures. The band gap reduction is of about $-y \times 6.5$ eV for $y < 2\%$. In 40 Å $Si_{0.84}Ge_{0.16}C_y$ QWs the band gap increases by about $y \times 2.4$ eV which is mainly due to strain compensation $\varepsilon = -0.04x + 0.35y$. The intrinsic band gap decreases with C alloying by about $-y \times 1.5$ eV. A similar shape of PL with comparable no-phonon and TO phonon line intensity supports a type-I band alignment for $Si_{0.84}Ge_{0.16}$, $Si_{1-y}C_y$, and $Si_{0.83}Ge_{0.16}C_{0.008}$ QWs. Coupled Si_{1-x-y} $Ge_xC_y/Si_{1-y}C_y$ QWs reveal strongly enhanced no-phonon PL lines originating from spatially indirect transitions of $\Delta(2)$ and hh levels confined to the $Si_{1-y}C_y$ and $Si_{1-x-y}Ge_xC_y$ QWs, respectively. Such multiple layer structures offer the possibility of fundamental studies on band alignments depending on composition. Several novel optoelectronic and electronic structures can also be designed with much higher flexibility using the SiGeC ternary alloy system.

The work has been supported financially by the Bundesministerium für Bildung, Wissenschaft, Forschung und Technologie. We gratefully acknowledge the support of K. von Klitzing.

References

[1] S.S. Iyer, G.L. Patton, J.M.C. Stork, B.S. Meyerson and D.L. Harame, IEEE Trans. Electron Dev. ED-36 (1989) 2043.
[2] K. Ismail, F.K. LeGoues, K.L. Saenger, M. Arafa, J.O. Chu, P.M. Mooney and B.S. Meyerson, Phys. Rev. Lett. 73 (1994) 3447.
[3] K. Ismail, J.O. Chu and B.S. Meyerson, Appl. Phys. Lett. 64 (1994) 3124.
[4] R. Zachai, K. Eberl, G. Abstreiter, E. Kasper and H. Kibbel, Phys. Rev. Lett. 64 (1990) 1055.
[5] S.S. Iyer, K. Eberl, M.S. Goorsky, F.K. LeGoues, J.C. Tsang and F. Cardone, Appl. Phys. Lett. 60 (1992) 356.
[6] K. Eberl, S.S. Iyer, S. Zollner, J.C. Tsang and F.K. LeGoues, Appl. Phys. Lett. 60 (1992) 3033.
[7] K. Brunner, W. Winter, K. Eberl and N.Y. Jin-Phillipp, Appl. Phys. Lett. 69 (1996) 91.
[8] K. Brunner, K. Eberl and W. Winter, Phys. Rev. Lett. 76 (1996) 303.
[9] A.A. Demkov and O.F. Sankey, Phys. Rev. B 48 (1993) 2207.
[10] D.C. Houghton, G.C. Aers, S.-R. Eric Yang, E. Wang and N.L. Rowell, Phys. Rev. Lett. 75 (1995) 866.
[11] A. St. Amour, C.W. Liu, J.C. Sturm, Y. Lacroix and M.L.W. Thewalt, Appl. Phys. Lett. 67 (1995) 3915.
[12] K. Brunner, W. Winter and K. Eberl, Appl. Phys. Lett. 69 (1996) 1279.
[13] K. Rim, S. Takagi, J.J. Welser, J.L. Hoyt and J.F. Gibbons, Mater. Res. Soc. Symp. Proc. 397 (1995) 327.
[14] K. Brunner, W. Winter and K. Eberl, Proc. 23rd Int. Conf. on Phys. of Semicond., Berlin, 1996 (World Scientific, Singapore, 1996), p. 1847.
[15] W. Faschinger, S. Zerlauth, G. Bauer and L. Palmetshofer, Appl. Phys. Lett. 67 (1995) 3933.
[16] M. Ershov and V. Ryzhii, J. Appl. Phys. 76 (1994) 1924.
[17] D.K. Nayak, J.C.S. Woo, J.S. Park, K.L. Wang and K.P. MacWilliams, Appl. Phys. Lett. 62 (1993) 2853.
[18] D.K. Nayak and S.K. Chun, Appl. Phys. Lett. 64 (1994) 2514.
[19] K. Brunner, K. Eberl and W. Winter, Mater. Res. Soc. Symp. Proc., Boston (1995), to be published.
[20] T. Manku and A. Nathan, IEEE Electron Dev. Lett. 12 (1991) 704.

ELSEVIER

Journal of Crystal Growth 175/176 (1997) 459–464

JOURNAL OF CRYSTAL GROWTH

MBE growth and structural characterization of $Si_{1-y}C_y/Si_{1-x}Ge_x$ superlattices

S. Zerlauth*, J. Stangl, A.A. Darhuber, V. Holý[1], G. Bauer, F. Schäffler

Institut für Halbleiterphysik, Johannes Kepler University Linz, Altenbergerstrasse 69, A-4040 Linz, Austria

Abstract

We report on the MBE growth and X-ray characterization of $Si_{1-y}C_y/Si_{1-x}Ge_x$ superlattices (SLs). The concentrations and thicknesses of the layers were chosen such as to get strain-symmetrized superlattices, lattice-matched to the Si (0 0 1) substrates. In-situ RHEED investigations showed increasing roughness during the growth of the $Si_{1-y}C_y$ layers and a smoothing effect of the subsequent $Si_{1-x}Ge_x$ layers. Further characterizations comprised double and triple axis X-ray diffraction, X-ray refraction (XRR), and atomic force microscopy (AFM). Dynamical simulations of the various X-ray configurations yielded the structural parameters of the SLs as well as information on the morphological and replication properties of the interfaces. With increasing carbon content we found an overall interface roughening concomitant with a significant decrease of the replication length. Lateral correlation length fits were compared with AFM-measurements, which give a more detailed picture of the interface morphology as long as the replication lengths are large.

PACS: 68.55.Bd; 68.65. + g; 68.35.Bs; 61.10.Lx

Keywords: MBE; Silicon; Germanium; Carbon; Superlattice; Interface roughness; X-ray defraction; AFM

The search for higher performance levels within a silicon-dominated world of electronic circuits has led to widespread interest in heterostructures based on group-IV semiconductors. Besides the Si/SiGe heterobipolar transistor, which is at the very brink of commercial availability [1], mobility enhancement by modulation doping [2], and band-structure engineering for optical applications [3] are major research targets.

Modulation doped n- and p-type Si/SiGe and Si/SiGe/Ge heterostructures with drastically increased carrier mobilities have been reported [4, 5]. For proper adjustment of the strain-dependent band offsets [6] concomitant with the use of Si substrates, strain-relaxed $Si_{1-x}Ge_x$ buffer layers are usually introduced between the substrate and the active layers. Although very successful on a laboratory scale [7], control of the buffer-mediated defect densities, and especially of threading

* Corresponding author. Fax: + 43 732 2468 650; e-mail: s.zerlauth@hlphys.uni-linz.ac.at.

[1] Permanent address: Faculty of Science, Masaryk University, Kotlárská 2, 61137 Brno.

0022-0248/97/$17.00 Copyright © 1997 Elsevier Science B.V. All rights reserved
PII S0022-0248(96)00931-1

dislocations, might become a problem for large-scale integration. The substitutional incorporation of a small percentage of carbon has been proposed as an alternative means of strain adjustment [8, 9], which might allow entirely pseudomorphic layer sequences: Since the covalent radius of Si is larger than that of C, but smaller than the one of Ge, the coherent $Si_{1-x-y}Ge_xC_y$/Si heterosystem allows the realization of both tensile and compressive in-plane strains. At a ratio $x/y \approx 8.5$ the Si lattice constant is preserved. If this ratio is maintained on the average, strain symmetrized $Si_{1-y}C_y$ /$Si_{1-x}Ge_x$ superlattices (SL) with unlimited overall thickness become possible, provided the individual layer thicknesses remain below the critical thickness for the generation of misfit dislocations [10]. This is an important feature especially for optical applications, where large enough active volumes are required.

Despite the obvious advantages of ternary $Si_{1-x-y}Ge_xC_y$ compounds, the available information on structural and electronic properties [11] are quite rudimentary, as yet. Of special concern is the almost negligible solubility limit of C in Si and Ge, concomitant with the existence of stochiometric SiC. This necessitates non-equilibrium (low temperature) growth techniques for the realization of useful C concentrations in the low percent range [12]. Interface morphology is another important topic for any kind of heterostructure, especially for lattice-mismatched heterosystems, where built-in strain can have a strong effect on the morphology of the growth front [13]. In the following we will restrict ourselves to an investigation of the interface roughness and replication of $Si_{1-y}C_y/Si_{1-x}Ge_x$ superlattices grown at temperatures between 400°C and 500°C by solid-source MBE. Because of the possible interference with future modulation doping experiments, no surfactants [14] were employed in this study.

Growth was performed in a two-chamber Riber-SIVA45 MBE machine with a base pressure of 10^{-10} mbar. Three electron beam evaporators for Si, Ge and C are employed, which are feedback-controlled by a common quadrupole mass spectrometer. 4″ Si(0 0 1) substrates with a miscut $< 0.25°$ were suspended in all-silicon mounts underneath a radiation heater made of pyrolitic graphite. The preparation steps comprised thermal desorption of the natural oxide at 900°C and the deposition of a 3000 Å thick buffer layer at 1–2 Å/s, which was grown during the cool-down ramp to the growth temperature of the subsequent ten-period $Si_{1-y}C_y/Si_{1-x}Ge_x$ superlattice (see Table 1).

Table 1
Growth and structural parameters of the ten-period $Si_{1-y}C_y/Si_{1-x}Ge_x$ superlattice samples; compositions and layer thicknesses are derived from X-ray rocking curves; T_s is the substrate temperature during the SL growth

Sample	y (%)	x (%)	d_{SiC} (Å)	d_{SiGe} (Å)	T_s (°C)
SG14	0	15	165	55	410
SGC18	1	16	116	57	410
SGC63	1.4	9.5	87	87	500
SGC21	2	15	84	95	410
SGC25	2.5	15	76	100	410

In a series of five samples (Table 1) the carbon content was systematically increased from 0% to 2.5%, whereas the Ge content was kept constant at 15% (except for sample SGC63 with $x = 9.5\%$). With increasing carbon content the thickness of the $Si_{1-y}C_y$ layers was reduced in order to stay within the critical thickness limitation for the individual layers. The thickness of the $Si_{1-x}Ge_x$ layers were adjusted properly in order to maintain strain symmetrization [10].

The surface was continuously monitored by reflection high-energy electron diffraction (RHEED), which revealed a clear (2×1) reconstruction during buffer growth. In agreement with previous reports [15], deposition of the $Si_{1-y}C_y$ layers led consistently to a spotty RHEED pattern, which recovered gradually during the growth of the subsequent $Si_{1-x}Ge_x$ layer. Generally, the RHEED pattern became more spotty with increasing number of periods, and this effect was more pronounced for $y > 1\%$. Under such conditions the RHEED patterns after the tenth period, although ending with a $Si_{1-x}Ge_x$ layer, were indicative of a rough (3D) surface.

The structural properties of our samples were determined by high-resolution X-ray diffraction (HRXRD) around the symmetric (0 0 4) reflex. In Fig. 1 we show rocking curves with increasing C concentration. The overlap of the zeroth order

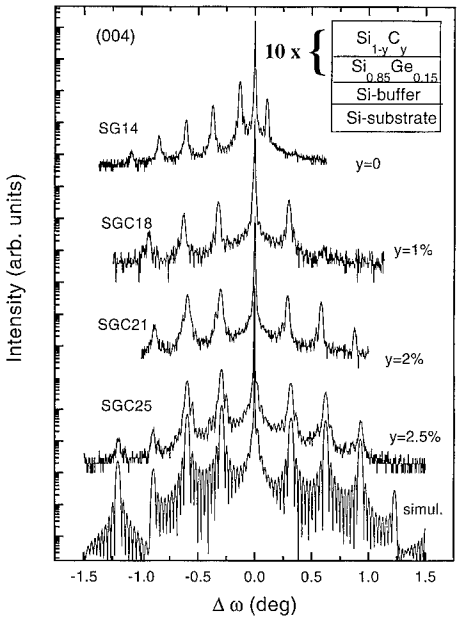

Fig. 1. HRXRD measurements of strain-compensated superlattices with different carbon contents and layer thicknesses, lattice matched to the silicon substrate. Also included is a simulation of the lowest curve.

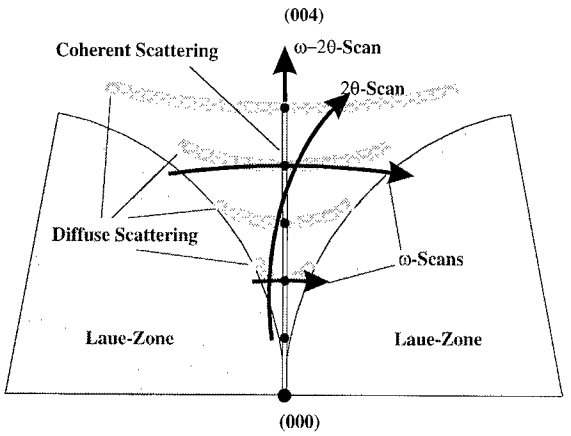

Fig. 2. The different XRR scan modes employed for the extraction of the lateral and vertical correlation length are schematically depicted in reciprocal space as bold arrows. Black dots mark the SL peaks in (0 0 1) growth direction, and the elongated, shaded areas adjacent to each peak are due to diffuse scattering. The Laue zones are not accessible experimentally in this regime.

SL signal with the substrate peak reveals almost perfect strain symmetrization for the samples with $y > 0$. The layer thicknesses and compositions in Table 1 were deduced from dynamical simulations that were fitted to the rocking curves. As an example, such a fit is included in Fig. 1 for sample SGC25. In addition, reciprocal space maps around the (0 0 4) and (2 2 4) reflex were recorded to make sure that the SLs are fully pseudomorphic. These experiments also showed that possible tilt angles of the epi-layer with respect to the substrate are very small (below 1/1000 degree), and that no indication of mosaicity exists in the samples.

To get further insight into the properties of the interfaces, XRR experiments were carried out at the OPTICS beamline at ESRF in Grenoble, and at the D4.1 beamline at Hasylab, Hamburg. For a concise characterization different geometries were utilized, which are schematically illustrated in Fig. 2. In a first configuration the intensity of the specular peak was recorded as a function of the incidence angle (ω–2θ scan). This scan is mainly used for deriving the overall root mean square (RMS) roughness σ_s of the SL interfaces [16, 17]. In another mode, the diffusely scattered intensity was measured, which is sensitive to the vertical and in-plane correlation of the interface morphology. The vertical correlation length Λ_n represents the replication of the interface morphology along the growth direction and is derived from non-specular 2θ scans, where the incidence angle ω is kept constant. Pure ω scans yield the in-plane correlation length Λ_p, as well as an RMS roughness σ_d. Generally, σ_s and σ_d are not identical, because the overall interface roughness can have contributions from the pure morphology and from interdiffusion of the alloys across the interface. The specular reflex (σ_s) is sensitive to both effects, whereas diffuse scattering is not affected by interdiffusion. Hence, σ_d is expected to be representative of the interface morphology, and should therefore be better suited for a comparison with atomic force micrographs. Fig. 3 shows XRR spectra and simulation curves of sample SGC25 in these three scan configurations. The upper panel depicts the specular ω–2θ scan, which reveals several orders of SL reflexes. Their spacing depends on layer thicknesses and compositions similar to the diffraction curves in Fig. 1. The attenuation of these peaks with increasing order is

a measure of σ_s, which is deduced from the fits. In the center frame a diffuse 2θ scan is shown, which consists of a sharp peak (specular reflex with $\omega = \theta$), and a number of smaller side maxima resulting from resonant diffuse scattering (RDS). The latter is caused by the correlation of the roughness profiles of different interfaces. The replication length Λ_n is deduced from fits to the shape of the RDS peaks, employing a distorted-wave Born approximation (DWBA) as described elsewhere [18, 19]. Since the height of the RDS peaks is also affected by other irregularities of the superlattice the fitted values listed in Table 2 should rather be read as a lower limit for Λ_n. Finally, the lowest frame in Fig. 3 shows ω scans through the two labeled peaks seen in the ω–2θ scan, and the fitted simulation curves for the extraction of Λ_p and σ_d. Because of problems with the calibration of the primary intensity, the error margins of the in-plane correlation lengths are rather large. A compilation of the interface parameters for two representative samples with $y = 1.4\%$ and 2.5% are listed in Table 2.

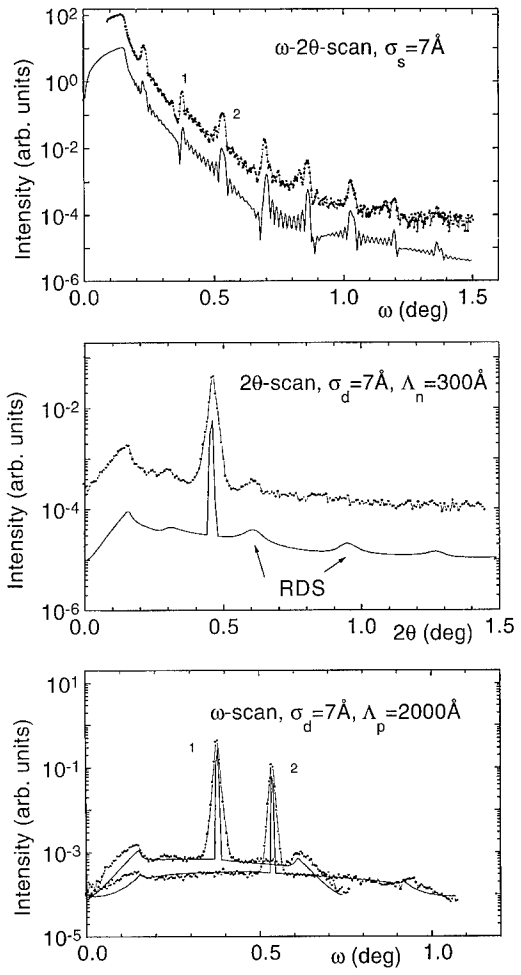

Fig. 3. ω–2θ scan, 2θ scan, and ω scan of sample SGC25. Both measured (points) and simulated (lines) curves are shown, which are off-set for reasons of clarity.

The most striking result of the XRR experiments is a systematic decrease of the replication length as y is increased. We get Λ_n values of 1200, 500 and 300 Å for carbon concentrations of $\leq 1.5\%$, 2% and 2.5%, respectively. Thus, while the Λ_n values at $y \leq 1.5\%$ are comparable to the thickness of the SL, a replication of the interface roughness is suppressed after less than two periods at $y = 2.5\%$. In connection with the aforementioned RHEED observations these results lead to the conclusion that the pronounced vertical replication found by several groups in $Si/Si_{1-x}Ge_x$ SLs [20, 21] is strongly disturbed in the presence of carbon-containing interlayers. Higher y, which enhance roughening of the $Si_{1-y}C_y$ layers according to RHEED, are obviously more effective in screening the replication process between subsequent $Si_{1-x}Ge_x$ layers.

The reduction of Λ_n with increasing y is accompanied by an overall increase of the interface roughness. The respective RHEED results are quantitatively confirmed by the σ values derived

Table 2
Interface parameters of two representative samples obtained by fits to the XRR measurements, and RMS roughness obtained by AFM measurements at the SL surface

Sample	y (%)	Λ_n (Å)	Λ_p (Å)	σ_s (Å)	σ_d (Å)	σ_{AFM} (Å)
SGC63	1.4	1200 ± 500	1900 ± 100	9 ± 2	4 ± 1	4 ± 2
SGC25	2.5	300 ± 100	2000 ± 1000	7 ± 1	7 ± 2	10 ± 2

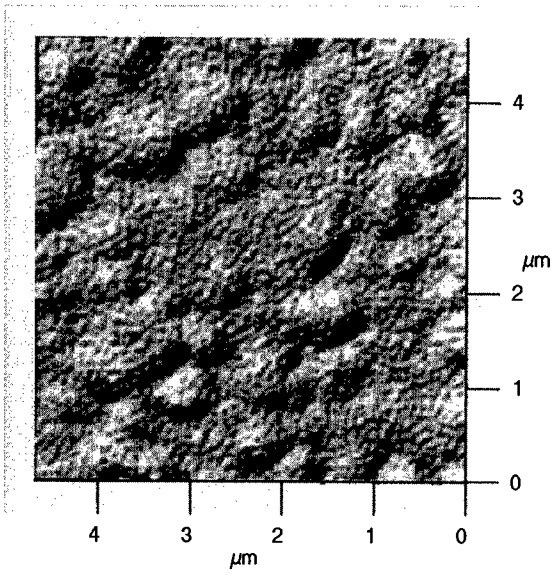

Fig. 4. AFM image of sample SGC63 containing hillock-like features superimposed on a short-length graininess.

from the XRR measurements, which yield a factor of two increase when y is increased from 1.4% to 2.5% (Table 2). But still, the fitted RMS roughness values of less than 10 Å appear rather small regarding the 3D appearance of the RHEED pattern at $y = 2.5\%$. We therefore performed AFM measurements at the surfaces of the two SLs listed in Table 2. Since the morphology of the topmost $Si_{1-x}Ge_x$ surface is probed, reasonable agreement between AFM and XRR RMS roughnesses is only to be expected for sample SGC63 ($y = 1.4\%$) with a replication length comparable to the thickness of the SL. In the case of sample SGC25 ($x = 2.5\%$), σ_{AFM} is expected to be larger than σ_d, since the XRR measurements average over all interfaces, with the lower-lying periods being smoother according to RHEED observations. In fact, we find good agreement between σ_{AFM} and σ_d for SGC63, but a significantly (30%) higher AFM roughness for SGC25.

Although restricted to the topmost layer, AFM yields additional information, because it provides a quantitative image of a several thousand μm^2 large portion of the surface. Fig. 4 shows an AFM image of sample SGC63, which clearly reveals a hillock-like structure with lateral spacing on the order of 1-μm, which is superimposed on a short-range graininess with a length scale of a few hundred to 1000 Å. In contrast, the XRR measurements yielded a Λ_p value of just about 2000 Å for this sample. This means that the hillock feature is outside the sensitivity window of XRR, which is basically determined by the divergence of the beamline. In addition, the AFM line scans can also reconcile the 3D RHEED patterns with the surprisingly small RMS roughnesses: Due to the large average spacing of the hillock features, modulation heights are on the order of 20 Å, which is sufficient to explain the RHEED observations, but still yields an RMS roughness of a mere 4 Å.

Even larger amplitudes are observed in the $y = 2.5\%$ sample (SGC25), which, however, lacked the long-range hillock features. In this sample we just found a short-range graininess, the length scale of which might be just within the error margins given for Λ_p.

In either case, the RMS roughnesses determined by XRR have to be treated with care, since they are not easily comparable to each other as long as the lateral correlation of a surface or interface is not well characterized. Also, it became clear that the limited length scale on which meaningful lateral correlation lengths can be derived from XRR measurements may require additional techniques, such as AFM, in order to get a complete picture.

In summary, we grew a series of strain-symmetrized, pseudomorphic $Si_{1-y}C_y/Si_{1-x}Ge_x$ superlattices with varying C content y, and characterized the interface properties by X-ray techniques. Upon increasing the carbon content from 0% to 2.5% the vertical correlation length Λ_n was found to decrease from a value comparable to the total thickness of the SL to a value comparable to a single-period length. Simultaneously, the RMS roughness increased by about a factor of two. According to AFM measurements the roughening is concomitant with a change of the interface morphology: With increasing carbon content long range features, which are tentatively attributed to strain induced growth phenomena at the $Si_{1-x}Ge_x$ surfaces, are suppressed by the $Si_{1-y}C_y$ interlayers.

Financial support by the FWF, GMe, and BMWVK (Vienna), and the opportunity to use

the OPTICS beamline in Grenoble and the D4.1 beamline at Hasylab, Hamburg, are gratefully acknowledged.

References

[1] Review: A. Schüppen and H. Dietrich, J. Crystal Growth 157 (1995) 207.
[2] Review: F. Schäffler, Solid State Electron. 37 (1994) 765.
[3] Review: H. Presting, H. Kibbel, M. Jaros, R.M. Turton, U. Menczigar, G. Abstreiter and H.G. Grimmeiss, J. Vac. Sci. Technol. 7 (1992) 1127.
[4] K. Ismail, M. Arafa, F. Stern, J.O. Chu and B.S Meyerson, Appl. Phys. Lett. 66 (1995) 842.
[5] U. König and F. Schäffler, IEEE Electron. Dev. Lett. EDL-14 (1993) 205.
[6] G. Abstreiter, H. Brugger, T. Wolf, H. Jorke and H.-J. Herzog, Phys. Rev. Lett. 54 (1985) 2441.
[7] Y.J. Mii, Y.H. Xie, E.A. Fitzgerald, D. Monroe, F.A. Thiel, B.E. Weir and L.C. Feldman, Appl. Phys. Lett. 59 (1991) 1611.
[8] K. Eberl, S.S. Iyer and F.K. LeGoues, Appl. Phys. Lett. 64 (1994) 739.
[9] W. Faschinger, S. Zerlauth, G. Bauer and L. Palmetshofer, Appl. Phys. Lett. 67 (1995) 3933.
[10] E. Kasper and F. Schäffler, in: Semiconductors and Semimetals, Vol. 33, Ed. T.P. Pearsall (Academic Press, Boston, 1990) p. 241.
[11] S.C. Jain, H.J. Osten, B. Dietrich and H. Rücker, Semicond. Sci. Technol. 10 (1995) 1289.
[12] A.R. Powell, K. Eberl, F.E. LeGoues, B.A. Ek and S.S. Iyer, J. Vac. Sci. Technol. B11 (1993) 1064.
[13] A.J. Pidduck, D.J. Robbins, A.G. Cullis, W.Y. Leong and A.M. Pitt, Thin Solid Films 222 (1992) 78.
[14] H.J. Osten, J. Klatt, G. Lippert and E. Bugiel, J. Appl. Phys. 74 (1993) 2507.
[15] P.O. Pettersson, C.C. Ahn, T.C. McGill, E.T. Croke and A.T. Hunter, Appl. Phys. Lett. 67 (1995) 2530.
[16] G. Parrat, Phys. Rev. 95 (1964) 359.
[17] L. Nevot and P. Croce, Rev. Phys. Appl. 15 (1980) 761.
[18] V. Holý and T. Baumbach, Phys. Rev. B 49 (1994) 10688.
[19] S.K. Sinha, E.B. Sirota, S. Garoff and H.B. Stanley, Phys. Rev. B 38 (1988) 2297.
[20] R.L. Headrick, J.-M. Baribeau and Y.E. Strausser, Appl. Phys. Lett. 66 (1995) 96.
[21] J. Tersoff, C. Teichert and M.G. Lagally, Phys. Rev. Lett. 76 (1996) 1675.

ELSEVIER

Journal of Crystal Growth 175/176 (1997) 465–468

JOURNAL OF CRYSTAL GROWTH

Why is a quantum-confined Stark shift absent in type-I strained $Si_{1-x}Ge_x/Si$ symmetric quantum wells?

Y. Miyake[a], J.Y. Kim[1,b], Y. Shiraki[b], S. Fukatsu[a,*]

[a] *Department of Pure and Applied Sciences, The University of Tokyo, 3-8-1 Komaba, Meguro-ku, Tokyo 153, Japan*
[b] *Research Center for Advanced Science and Technology, The University of Tokyo, 4-6-1 Komaba, Meguro-ku, Tokyo 153, Japan*

Abstract

We report on photoluminescence studies of the quantum-confined Stark effect (QCS) in strained $Si_{1-x}Ge_x/Si$ type-I quantum wells (QWs) with symmetric confinement potential. Application of a weak longitudinal electric field leads to an upward shift of the free-exciton peaks due to a field-driven decrease of the exciton binding energies arising from the shallow electron confinement of SiGe QWs. The existence of the masked QCS has been separately confirmed by observing prolonged luminescence decay times with increasing electric field. The insertion of an asymmetric potential does not fully restore the QCS redshift, indicating that an enhancement in the exciton binding energy is necessary to establish the QCS redshift.

PACS: 71.70.Ej; 78.55.Hx; 78.65. – s; 68.55.Bd

Keywords: Strained $Si_{1-x}Ge_x/Si$ quantum wells; Quantum-confined Stark effect; Exciton binding energy; Symmetric confinement potential

1. Introduction

Electrical control is a key feature in tuning semiconductor-based devices. There has been a surge in demand for developing optoelectronic devices utilizing electrically controlled optical phenomena based on quantum effects [1–3]. It is rather established that application of a DC electric field across a quantum-confined exciton leads to distinct electro-optic effects such as the quantum-confined Stark effect (QCS) [2–4]. Purely excitonic optical modulation by DC field has already been demonstrated for GaAs/AlGaAs. In view of this, the relatively small free-exciton (FE) binding energy, E_B, in GaAs, $\approx$ 4–8 meV [4], contrasts well with E_B = 15–30 meV of type-I SiGe strained quantum wells (QWs) [5]. A large E_B indicates that excitons are robust against the electric field, and therefore the QCS is expected to be more

* Corresponding author. Fax: + 81 3 5454 4311; e-mail: fkatz@srv.bme.rcast.u-tokyo.ac.jp.

[1] Permanent address: Semiconductor Physics Research Center (SPRC), Jeonbuk National University, Jeonju 561-756, South Korea.

0022-0248/97/$17.00 Copyright © 1997 Elsevier Science B.V. All rights reserved
PII S0022-0248(96)00932-3

pronounced. However, early attempts were not successful in identifying the QCS for "type-I SiGe/Si QWs" [6, 7]. Recently, we have found that the QCS is masked by the weakening of the free exciton under an electric field in type-I strained $Si_{1-x}Ge_x/Si$ symmetric QWs [5]. This basic limitation on the QCS in SiGe-based type-I QWs was shown to arise from the shallow confinement of the electrons.

In this paper, we further strengthen this observation by detailed experiments and discuss the possibility that the QCS redshifts would be restored by appropriate QW potential tailoring.

2. Experimental procedure

Strained $Si_{1-x}Ge_x/Si$ ($x = 0.18$) type-I QWs were grown by gas-source molecular beam epitaxy on nominally on-axis p-type Si(100) at 840°C using Si_2H_6 and GeH_4 [8]. The experimental setup for CW photoluminescence (PL) and decay time measurements is found elsewhere [9]. A DC longitudinal electric field was applied along the quantization axis through evaporated Al contacts for biased PL using an Ar^+ ion laser (3 mW) as the excitation source.

To justify the PL approach to the QCS, it should be noted that the QWs are made of an indirect-gap material and the absorption measurements are not straightforward in identifying the QCS due to their small oscillator strengths unlike direct gap materials. This is why we rely on relaxation process, i.e., PL, rather than absorption which requires much thicker layers. Besides this, the SQW is appropriate since a multiple QW geometry results in the strong coupling of the electron wave functions and the accumulated strain severely affects PL properties.

3. Results and discussion

As reported previously, the FE peaks in weakly biased PL spectra shift towards higher energies with increasing electric field, F(kV/cm), as opposed to the quadratic downward shift due to the QCS, $\Delta E_{QCS}(F) \propto F^2$ [5]. Such field-driven blueshifts were observed for all QWs. Reproduced in Fig. 1

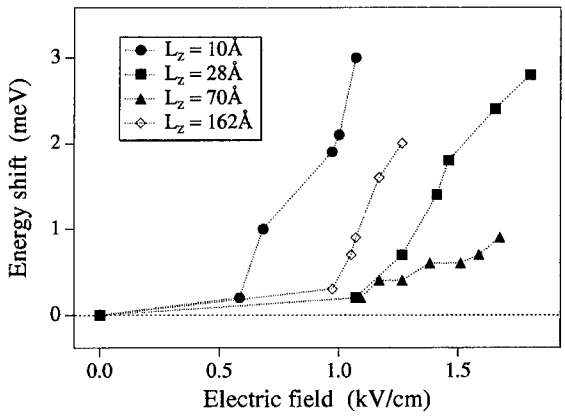

Fig. 1. PL peak shifts $\Delta E_{NP}(F)$ versus F(kV/cm) as a function of L_z taken at 23 K under an excitation power of 3 mW. Note that $\Delta E_{NP}(F)$ admits a minimum at intermediate L_z's.

are the F dependence of the no-phonon peak shifts, $\Delta E_{NP}(F)$, for various L_z. Clearly, the magnitude of $\Delta E_{NP}(F)$ at a particular F value admits a minimum at intermediate L_z's, i.e., the signature of two-dimensionally (2-D) confined FE [5, 9].

To a good approximation, $\Delta E_{NP}(F) = \Delta E_B(F) + \Delta E_{QCS}(F)$ where $\Delta E_B(F)$ is the field-driven shift of the exciton binding energy, E_B, i.e., the electrostatic energy of the electron–hole pair. Theoretically, $\Delta E_B(F) = E_B(0) - E_B(F) > 0$ and $\Delta E_B(F) \propto F^2$ for a type-I symmetric QW [5]. A more pictorial representation is that the electron and hole wave functions shift in opposite directions under F to give an elongated exciton orbit and therefore the Coulomb interaction is weakened.

Since $\Delta E_{NP}(F) > 0$ and $\Delta E_{QCS}(F)$ is always negative, it turns out that the sign of $\Delta E_{NP}(F)$ is determined by $\Delta E_B(F)$ while $\Delta E_B(F) > |\Delta E_{QCS}(F)|$. This scenario was confirmed by the variational calculations of E_B as functions of F and L_z taking account of appropriate $\Delta E_{NP}(F)$ [5, 10]. We found an almost perfect agreement between the calculation and experiment, and the 2-D confinement as observed in Fig. 1 was well accounted for by the calculation.

However, further consideration is obviously needed to justify the above discussion and for more correct interpretation of PL data. First of all, it is imperative to note that the band-to-band transition

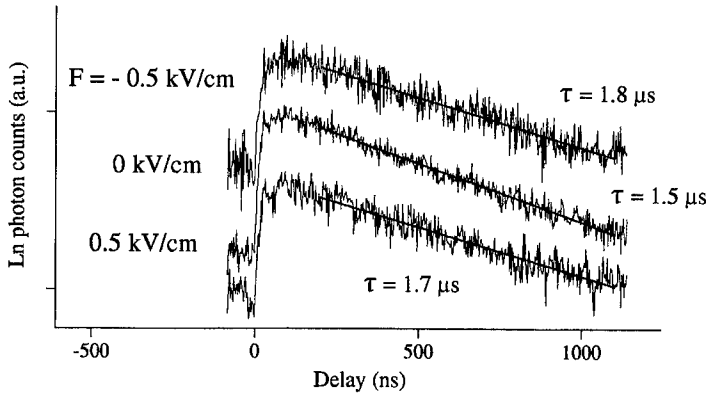

Fig. 2. PL decay transients of the 216 Å SQW for $F = -0.5$, 0, 0.5 kV/cm. Prolonged decay times confirm the existence of the underlying QCS.

lying higher in energy has not contributed to $\Delta E_{NP}(F)$. In fact, the observed $\Delta E_{NP}(F)$ (> 0) is of the order of 1 meV which is by an order of magnitude smaller than $E_B(0) > 15$ meV [5]. Therefore the contribution of the band-to-band recombination is unlikely.

It is of importance to confirm the underlying QCS which has been masked by $\Delta E_B(F)$. The existence of the QCS can be checked simply by monitoring a prolonged decay time of PL, $\tau(F)$, with reference to τ at zero field. This is true since the QCS can be traced back in phenomenological terms to a real space displacement of wavefunctions in opposite directions which would give a reduced overlap integral $S(F) < S(0)$ and hence $\tau(F) = \tau(0)(S(0)/S(F)) > \tau(0)$. The prolonged PL lifetimes at finite F values are demonstrated in Fig. 2 for the 216 Å SQW.

For biased PL, the choice of the excitation power, I_{ex}, is critical and the complexity arises due to carrier-induced effects under intense photopump. As a matter of fact, the $\Delta E_{NP}(F)$ depends on the excitation power, I_{ex}. The no-phonon peak energies for varied I_{ex} are summarized in Fig. 3. The gradual increase of the zero-field peak energy with increasing I_{ex} is attributed to two major effects, i.e., the band filling and the exciton weakening due to the carrier-induced screening. The applied F is also expected to be screened and accordingly the effective field strength sensed by FE decreases. All these

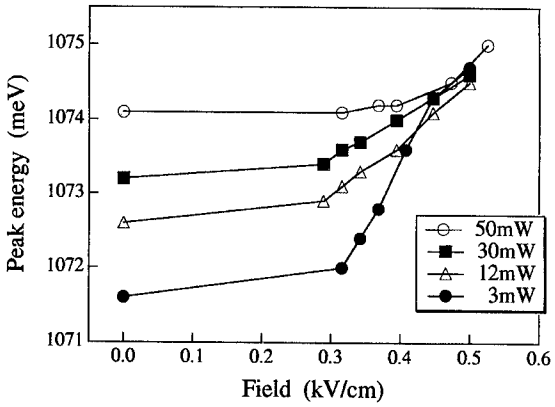

Fig. 3. $\Delta E_{NP}(E)$ versus F for the 27 Å SQW at different excitation powers. The data were taken at 23 K.

effects enter ΔE_{NP} and the net effect is a reduced $\Delta E_{NP}(F)$ with increasing I_{ex}. Therefore the ΔE_{NP} form should be modified as $\Delta E_{NP}(F, I_{ex}) = \Delta E_B(F(I_{ex}), I_{ex}) + \Delta E_{QCS}(F(I_{ex}))$. Thus an inappropriate I_{ex} obviously leads to significant departures from the calculated values and $I_{ex} = 3$ mW seems to be an optimum value.

We have explained the extreme susceptibility of SiGe FE to the electric fields as due to the small conduction band offset, ΔE_c [5]. Further studies on the F dependence revealed that there is no pronounced valence band effect and that at a given F,

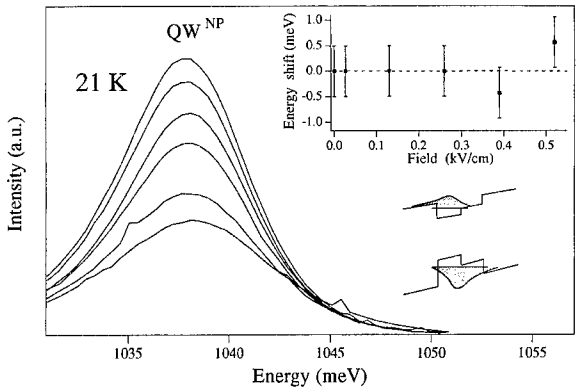

Fig. 4. 21 K biased PL spectra taken from a stepped QW having a 108 Å well ($x = 0.15$) with a 162 Å wide step ($x = 0.14$). The direction of the longitudinal electric field allows for the QCS redshift.

the almost constant red shifts are established at large ΔE_c since $\Delta E_B(F) \approx 0$ suggesting a fairly large E_B. By contrast, for $\Delta E_c < 30$ meV, *the QCS redshift cannot be obtained at all F values.* (At even higher F values, excitons are field-ionized.) This was checked on a series of $x = 0.35$ QWs where $\Delta E_c = 15$ meV. Thus we conservatively observe that the realistic $\Delta E_c = 7.7$ meV is too small to withstand F. More importantly, we conclude that $E_B = E_B(F, \Delta E_c)$ and $\Delta E_B(F)$ tends to zero as ΔE_c increases.

Aside from the condition $\Delta E_B(F) \approx 0$, one possible way of reducing the positive $\Delta E_{NP}(F)$ is the introduction of potential asymmetry since the first-order QCS occurs which is otherwise missing in a symmetric potential. An example is shown in Fig. 4 for a stepped QW consisting of a 108 Å well ($x = 0.15$) with a 162 Å wide step ($x = 0.14$). Apparently, $\Delta E_B(F)$ is suppressed by the ΔE_{QCS} increase whereas the data at high F values are not available due to field ionization. In this sense, we have not been much successful in restoring the QCS redshifts based on the potential asymmetry alone. Clearly, a large $E_B(0)$ in combination with the asymmetric potential will be the best way to eliminate $\Delta E_B(F) > 0$ and to restore the QCS redshift.

4. Summary

The exciton binding energy reduction due to the shallow electron confinement was clarified to be the origin of the field-driven blueshifts which mask the quantum-confined Stark redshifts in strained $Si_{1-x}Ge_x/Si$ symmetric type-I quantum wells. An enhanced exciton binding was pointed out to be necessary to establish the QCS redshift in addition to the potential asymmetry.

Acknowledgements

The authors gratefully acknowledge technical assistance from H. Sunamura and N. Usami. One of the authors (S.F.) acknowledges supports from Toray Science Foundation, Asahi Glass Foundation, Murata Science Foundation. This work was in part supported by a Grant-in-aid from the Ministry of Education, Science, Sports and Culture, Japan.

References

[1] W. Franz, Z. Naturforsch. 13a (1958) 484; L.V. Keldysh, Zh. Eksp. Teor. Fiz. 34 (1958) 1138.
[2] T.H. Wood, C.A. Burrus, Jr, D.A.B. Miller, D.S. Chemla, T.C. Damen, A.C. Gossard and W. Wiegmann, Appl. Phys. Lett. 44 (1984) 16.
[3] D. Delalande, J. Orgonasi, J.A. Berm, G. Bastard, M. Voos, G. Weimann and W. Schlapp, Appl. Phys. Lett. 51 (1987) 1346.
[4] D.A.B. Miller, D.S. Chemla, T.C. Damen, A.C. Gossard, W. Wiegmann, T.H. Wood and C.A. Burrus, Phys. Rev. B32 (1985) 1043.
[5] Y. Miyake, J.Y. Kim, Y. Shiraki and S. Fukatsu, Appl. Phys. Lett. 68 (1996) 2097.
[6] J.S. Park, R.P.G. Karnashiri and K.L. Wang, J. Vac. Sci. Technol. B 8 (1990) 217.
[7] H. Temkin, T.P. Pearsall, J.C. Bean, A. Logan and S. Luryi, Appl. Phys. Lett. 48 (1986) 963.
[8] S. Fukatsu, N. Usami, Y. Kato, H. Sunamura, Y. Shiraki, H. Oku, T. Ohnishi, Y. Ohmori and K. Okumura, J. Crystal Growth. 136 (1994) 315.
[9] S. Fukatsu, H. Akiyama, Y. Shiraki and H. Sakaki, J. Crystal Growth. 157 (1995) 1.
[10] G. Bastard, E.E. Mendez, L.L. Chang, and L. Esaki, Phys. Rev. B28 (1983) 3241; R.P. Leavitt and J.W. Little, Phys. Rev. B 42 (1990) 11774.

ELSEVIER

Journal of Crystal Growth 175/176 (1997) 469–472

JOURNAL OF CRYSTAL GROWTH

Sidewall faceting and inter-facet mass transport in selectively grown epitaxial layers on SiO_2-masked Si(1 1 0) substrates

Qi Xiang[a], Shaozhong Li[a], Dawen Wang[a,*], Kunihiro Sakamoto[a], K.L. Wang[a], Greg U'Ren[b], Mark Goorsky[b]

[a] *Device Research Laboratory, Department of Electrical Engineering, University of California, Los Angeles, Los Angeles, California 90095, USA*

[b] *Department of Materials Sciences and Engineering, University of California, Los Angeles, Los Angeles, California 90095, USA*

Abstract

The facet formation and inter-facet mass transport in selective epitaxial growth (SEG) of Si on SiO_2-masked growth windows aligned along [1 1 0] and [1 0 0] directions on Si(1 1 0) substrates by Si gas-source molecular-beam epitaxy were studied. For the sidewalls along the [1 1 0] baseline, both (3 1 1) and (1 1 1) facets were formed, while for the sidewalls along the [1 0 0] baseline, (1 0 0) facets were formed. Mass accumulation around the edges of the top surface was shown to be due to the inter-facet mass transport from the sidewall to top surfaces.

PACS: 81.15.Hi; 81.10 – h

Keywords: Facet; Selective epitaxial growth

The study of Si-based nanostructures is important as scaling-down efforts of integrated circuits continue. Selective epitaxial growth (SEG) of Si and SiGe on patterned Si substrates is an attractive technique for fabrication and integration of nanometer-scale devices. Epitaxial layers can be selectively grown on SiO_2-masked growth windows by gas-source molecular-beam epitaxy (GSMBE) [1–4] and chemical vapor deposition [5–8]. For SEG in nanometer-scale windows, facet formation and competition are important issues. Although some work has been directed to patterned Si(1 0 0) substrates [9], no SEG work has been attempted on other oriented substrates to our knowledge. The (1 1 0) orientation has several advantages. Among these are the high hole mobility and normal incidence inter-conduction subband transition which may find applications in infrared detectors [10].

In this paper, facet formation and inter-facet mass transport in SEG of Si on the SiO_2-masked Si(1 1 0) substrate were studied using GSMBE. We observed that for the sidewalls along the [1 1 0] baseline, both (3 1 1) and (1 1 1) facets were formed. For the sidewalls on the [1 0 0] baseline, however,

* Corresponding author.

0022-0248/97/$17.00 Copyright © 1997 Elsevier Science B.V. All rights reserved
PII S0022-0248(96)01217-1

only the (1 0 0) facet was observed. Mass accumulation around the edges of the SEG mesa top surface was observed and attributed to the inter-facet mass transport from the sidewalls to the top surface. There were obvious differences of mass accumulation around the edges of different sidewalls.

The SEG was performed on SiO_2 windows patterned on Si(1 1 0) substrates. The square windows with the edges along [1 1 0] and [1 0 0] directions were formed by etching the 100 nm SiO_2 layer on Si(1 1 0) substrates. A Si_2H_6 gas cell was used for the Si source. The system was evacuated by a turbomolecular pump and an ion pump and the base pressure of the growth chamber was 1×10^{-9} Torr. The residual gas was dominated by Si_2H_6, SiH_3, and H_2. The SEG of Si was carried out at growth temperatures ranging from 650°C to 875°C under a constant disilane flow rate of 3.0 sccm. Under these conditions, growth mechanism was controlled by surface kinetics. The pressure during epitaxial growth was 2.5×10^{-6} Torr.

In our previous work [9], we reported the facet growth of Si on an Si(1 0 0) substrate by SEG. The windows were patterned along the [1 1 0]. Sidewall facets were observed to evolve from the initial (3 1 1) to (1 1 1) facets and this evolution stemmed from different growth rates for the (1 0 0), (3 1 1) and (1 1 1) surfaces. In the present work, we report the experimental results on an Si(1 1 0) surface. An atomic force microscope (AFM) was used to analyze the grown mesa structures. Fig. 1a and Fig. 1b show the AFM line analyses of SEG mesa edges along the [1 0 0] and [1 1 0] directions. Typical (3 1 1) and (1 1 1) sidewall facets were observed for the [1 1 0] baseline, while for the [1 0 0] baseline (1 0 0) sidewalls were observed. For both cases, the mass accumulation around the edges of the top surface was observed. There were obvious differences of mass accumulation for sidewalls along different baselines.

The differences in the growth rate for different orientations and different growth conditions are important factors leading to faceting in SEG. In order to understand the mechanism during SEG, the growth rate for different orientations was studied experimentally for different growth conditions. Results are shown in Fig. 2. It is clear that the growth rate for the (1 0 0) direction is much higher than those for other surfaces and the growth rate for the (1 1 0) direction is the smallest at growth temperatures below 750°C. Growth rates for all the surfaces studied – (1 0 0), (3 1 1), (1 1 1), and (1 1 0) – increase rapidly until the temperature reaches 750°C, above which the growth rates saturate. The growth rate of (1 1 0) approaches that of the (3 1 1) surface at these higher temperatures.

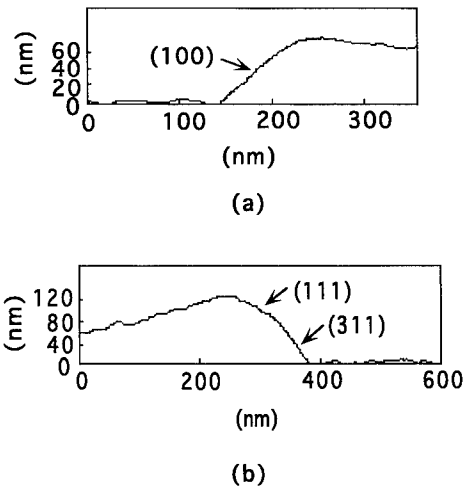

Fig. 1. AFM line analyses of grown SEG mesa edges: (a) along ⟨1 0 0⟩ direction; (b) along ⟨1 1 0⟩ direction.

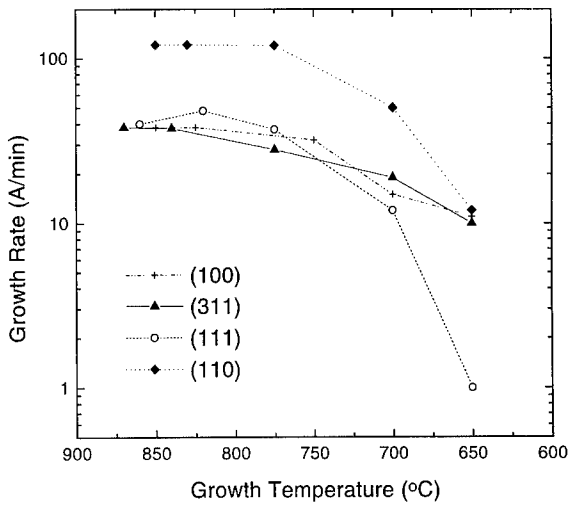

Fig. 2. Growth rate for different orientations of (1 0 0), (3 1 1), (1 1 1) and (1 1 0) with a disilane flow rate of 3 sccm.

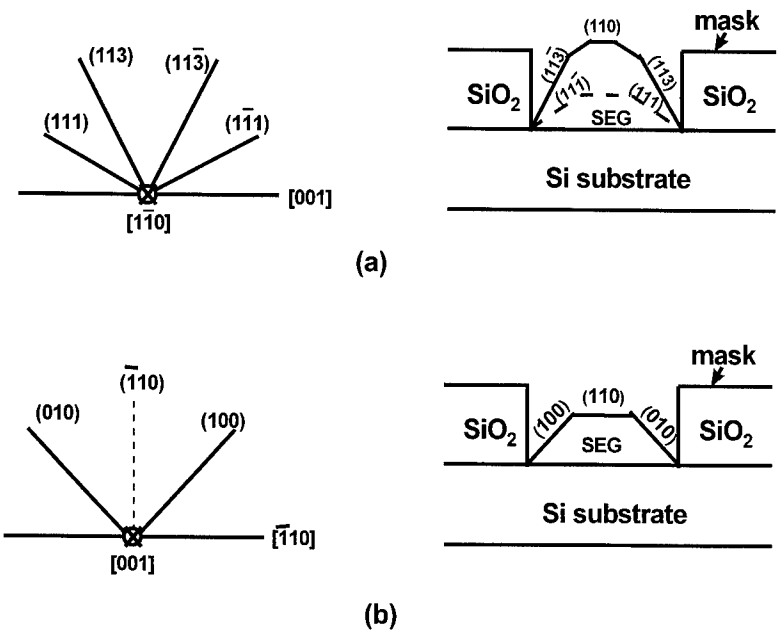

Fig. 3. Schematics illustrating possible facets for (1 1 0) substrate: (a) for alignment along ⟨1 1 0⟩, possible facets are (x x z) and lower indices are {1 1 1} and {1 1 3}, and (b) for alignment along ⟨1 0 0⟩, possible facets are (x y 0) and the low index is {1 0 0}.

The faceting of sidewalls and the mass accumulation arise from different surface energies and growth rates for (1 0 0), (1 1 0), (1 1 1) and (3 1 1). The free energy of the Si/SiO_2 interface is so high that Si deposited on it moves away from the SiO_2 to form sidewall facets. A model for SEG growth on windows was developed by taking both surface migration and free energy into consideration for the (1 0 0) Si surface [9, 11]. It is shown that in minimizing the total free energy, more than one facets are expected to appear as SEG proceeds. On (1 1 0) substrate, the possible low index facets are {1 1 1} and {1 1 3} for alignment along ⟨1 1 0⟩, while for alignment along ⟨1 0 0⟩, the possible low index facet is {1 0 0}, as illustrated in Fig. 3a and Fig. 3b, respectively. This is in agreement with our experimental results. In Fig. 1, the (3 1 1) and (1 1 1) sidewall facets were observed for the [1 1 0] baseline and for the [1 0 0] baseline, (1 0 0) sidewalls were observed. In addition, there is competition among different facets due to different growth rates. The fundamental principle for the facet competition is that the facet with a faster growth rate will be eventually replaced by the facet with a slower one. Thus, for the [1 1 0] baseline, the (3 1 1) facet will be eventually replaced by the (1 1 1) facet because of the slightly higher growth rate of the former.

The mass accumulation around the edges of the SEG mesa top surface is believed to be due to the inter-facet mass transport of Si from the sidewalls to the top surface during SEG growth. A similar phenomenon was observed in III–V growth on patterned substrates [12]. The driving force for the mass transport may be attributed to surface migration in minimizing the total free energy during the SEG growth. In other words, the mass transport will be directed to the energetically favored facet to minimize the total free energy. The surface free energies for the (1 0 0), (1 1 0), (1 1 1), and (3 1 1) orientation surfaces are 2.13×10^3, 1.51×10^3, 1.23×10^3 and 1.50×10^3 ergs cm^{-2}, respectively [13, 14]. In the present case, as illustrated in Fig. 4, because of the extremely high free-energy of the Si/SiO_2 interface, independent of the alignment of the growth windows, the mass transport from sidewalls to the mesa top dominates, thus we can see the mass accumulation on both ⟨1 0 0⟩ and ⟨1 1 0⟩ baselines on the Si(1 1 0) surface. For the ⟨1 1 0⟩

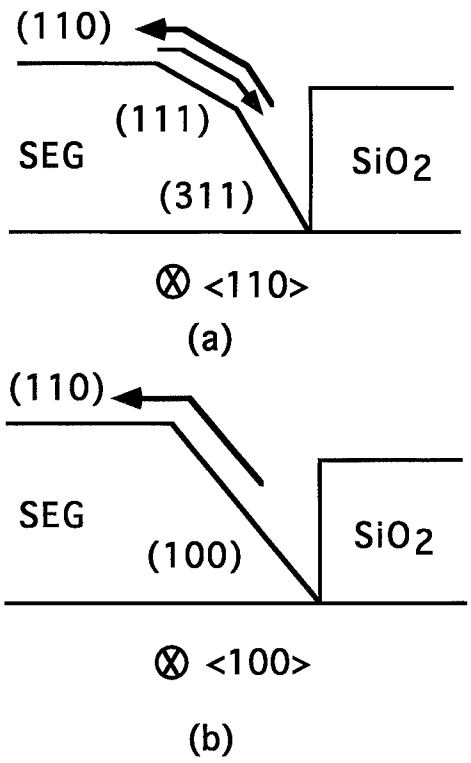

Fig. 4. Schematics illustrating inter-facet mass transport on the SEG growth: (a) for edges of sidewalls along [1 1 0] and (b) for edges of sidewalls along [1 0 0].

window alignment, the top surface free-energy is larger than that of the sidewall, thus the mass transport is reduced; for the ⟨1 0 0⟩ window alignment, the (1 1 0) top surface free-energy is smaller than that of the sidewall, thus the mass transport is enhanced. This is why we observed the obvious differences of mass accumulation for sidewalls along different baselines in Fig. 1.

In summary, facet formation and inter-facet mass transport in selective epitaxial growth (SEG) of Si on SiO_2-masked Si(1 1 0) were studied in gas-source molecular-beam epitaxy. The windows were patterned along the [1 1 0] and [1 0 0] directions on Si(1 1 0) substrates. For the sidewalls along the [1 1 0] baseline, both (3 1 1) and (1 1 1) facets were observed. For the sidewalls along the [1 0 0] baseline, only the (1 0 0) facet was observed. Mass accumulation around the edges of the SEG mesa top surfaces was attributed to the inter-facet mass transport from the sidewalls to the top surfaces. The faceting of sidewalls and the mass accumulation are attributed to different surface energies and growth rates for (1 0 0), (1 1 0), (1 1 1) and (3 1 1) surfaces.

Acknowledgements

This work was partially supported by SRC (Dr. W. Lynch) and NSF (Dr. L. Hess).

References

[1] K. Aketagawa, T. Tatsumi and J. Sakrai, Appl. Phys. Lett. 59 (1991) 1735.
[2] N. Usami, T. Mine, S. Fukatsu and Y. Shiraki, Appl. Phys. Lett. 63 (1993) 2789.
[3] Y. Utsumi, H. Akazawa, M. Nagase, T. Urisu and I. Kawashima, Appl. Phys. Lett. 92 (1993) 1647.
[4] Q. Xiang, K. Kim and K.L. Wang, J. Vac. Sci. Technol. 14 (1996) 1.
[5] D.B. Noble, J.D. Hoyt, C.A. King, J.F. Gibbons, T.I. Kamins and M.P. Scott, Appl. Phys. Lett. 56 (1990) 51.
[6] Y. Zhong, M.C. Ozturk, D.T. Grider, J.J. Wortman and M.A. Little-John, Appl. Phys. Lett. 57 (1990) 2092.
[7] M. Racanelli and D.W. Greve, Appl. Phys. Lett. 58 (1991) 2096.
[8] M. Hiroi and T. Tatsumi, J. Crystal Growth 120 (1992) 279.
[9] Qi Xiang, Shaozhong Li, Dawen Wang, Kang L. Wang, J. Greg Couillard and Harold G. Graighead, J. Vac. Sci. Technol. 14 (1996) 1.
[10] K.L. Wang and R.P.G. Karunasir, Semiconductor Quantum Wells and Superlatices for Long-Wavelength Infrared Detectors, Ed. M.O. Manasreh (Artech House, Norwood, MA, 1993).
[11] S. Li, Q. Xiang, Dawen Wang and K.L. Wang, J. Crystal Growth 157 (1995) 185.
[12] A. Madhukar, Thin Solid Films 231 (1993) 8.
[13] T. Aoyama, T. Ikarashi, K. Miyanaga and T. Tatsumi, J. Crystal Growth 136 (1994) 349.
[14] R.J. Jaccodine, J. Electrochem. Soc. 110 (1963) 524.

ELSEVIER

Journal of Crystal Growth 175/176 (1997) 473–476

JOURNAL OF CRYSTAL GROWTH

Enhancement of substitutional carbon incorporation in hydrogen-mediated pseudomorphic growth of strained alloy layers on Si(0 0 1)

G. Lippert*, P. Zaumseil, H.J. Osten , Myoengcheol Kim

Institute for Semiconductor Physics, Walter-Korsing-Strasse 2, D-15230 Frankfurt (Oder), Germany

Abstract

The reduction of strain in SiGe layers on Si substrate is possible by the substitutional incorporation of carbon into the SiGe lattice. The carbon incorporation depending on various growth parameters could be improved by an additional hydrogen residual atmosphere during MBE. Growth temperature in the range between 400°C and 550°C supports the amount of substitutional carbon in silicon.

PACS: 61.10. – i; 61.66.Dk; 64.75. + g; 68.10.Cr; 68.55.Bd; 68.60.Dv

1. Introduction

Layered systems based on group IV elements and heteroepitaxially grown on Si substrates extend the material variety for new device concepts in silicon microelectronic technology. $Si_{1-x}Ge_x$ layers on Si(0 0 1) substrates exhibit some severe limitations due to the lattice mismatch between silicon and germanium. Recently, carbon has been added to SiGe alloys to compensate the larger lattice constant of germanium compared to that of silicon.

One of the critical issues for further development and applications of strained C containing heterostructures is how to increase the amount of carbon incorporated on substitutional sites. This has a large impact on structural and electrical properties of these layers. An understanding of the factors limiting substitutional carbon incorporation is crucial in the heteroepitaxial growth of nonequilibrium materials, such as $Si_{1-y}C_y$ or $Si_{1-x-y}Ge_xC_y$ on Si(0 0 1) substrates. It is reported that the interstitial to substitutional carbon ratio is strongly influenced by the growth conditions, such as the growth temperature and Si growth rate [1].

2. Experimental procedure

The discussed layers were grown on Si(0 0 1) in a 4″ multichamber MBE system (DCA). Prior to the deposition, the wafers were H-passivated by wet cleaning. After this treatment they were loaded in

* Corresponding author. Fax + 49 335 5625 300; e-mail: lippert@ihp-ffo.de.

0022-0248/97/$17.00 Copyright © 1997 Elsevier Science B.V. All rights reserved
PII S0022-0248(96)00857-3

this UHV system (base pressure in the range of 10^{-11} mbar) within a few minutes. Silicon and germanium were evaporated from electron beam evaporators, and carbon was supplied by a pyrolytic graphite filament sublimation source. The substrates were heated from the backside by a graphite filament and the temperature was measured with a thermocouple.

X-ray measurements were carried out with a double crystal diffractometer (XRD) in parallel (n, – n) setting using 004 reflections and Cu Kα radiation for strain determination. Using simple linear interpolations between the lattice constants of SiC, Si and Ge and the appropriate relative concentration (Vegard's law) we can estimate the effective strain in the grown layers. Resulting from the measured strain, the substitutional content of carbon or germanium in silicon was determined.

Besides XRD, the total carbon and germanium concentrations of all samples were measured using secondary ion mass spectroscopy (SIMS).

To estimate the different film roughness, we used transmission electron microscopy (TEM).

3. Results and interpretation

The substitutional incorporation of carbon into the lattice of a growing silicon layer depends mainly on the relationship of surface mobility of the adsorbing species at the surface of the sample and the remaining time of the atoms on the surface itself. So far, the growth temperature and growth rate of the film [1] plays an important role to establish the structure of the growing lattice. Fig. 1 shows that either the reduction of the growth temperature and/or increase of the overall growth rate lead to an increase of the ratio of substitutional to interstitial carbon (Fig. 1). It gives a hint, that lower surface mobility of atoms and also reducing the time of their coverage by next coming atoms might assist the substitutional incorporation of carbon in silicon. However, this can also cause some deteriorations in crystal quality.

Strategies to change the surface kinetics by antimony as surfactant to smooth interfaces between Si and $Si_{1-y}C_y$ were successfully tested [2]. Introduction of hydrogen as a surfactant is expected to

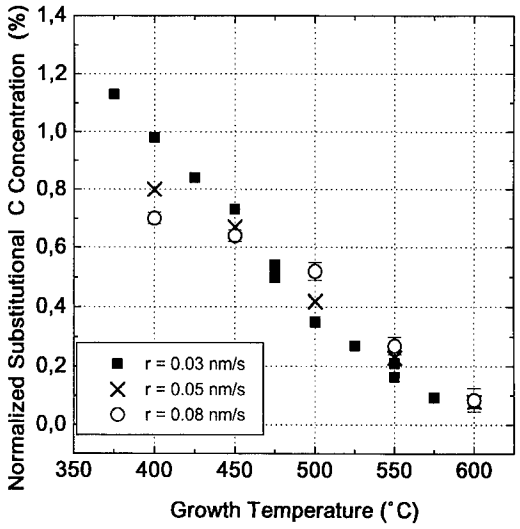

Fig. 1. Carbon incorporation versus growth temperature and growth rate of silicon for a constant carbon flux.

avoid a background doping. In SiGe, hydrogen was applied to sharpen Si/SiGe interfaces in a multiple quantum well [3].

H surfactant seems to be able to shift the window for a high substitutional to interstitial carbon ratio to process conditions suitable for good epitaxial quality. It is known that the presence of the so-called surfactant atoms on the surface during growth can drastically alter the growth kinetics. An application of carbon during growth of Si and $Si_{1-x}Ge_x$ is reported in Table 1.

The measured strain e is permuted to a strain equivalent to the content of germanium in silicon. It is shown that the strain reduction in strained silicon germanium layers is higher with lower growth temperature. This is caused by increasing substitutional incorporation of carbon with decreasing temperature of the sample. This incorporation was more prcisely investigated in [1].

The results discussed the influence of the growth rate of silicon on the incorporation of carbon is stressed in the table. Doubling the growth rate at 400°C leads to a strain reduction even at higher growth temperatures. Nevertheless, further heat up shows the known effect of decreasing strain reduction.

The introduction of carbon into a growing pure silicon layer shows that the stress alteration at these

Table 1
Strain reduction of $Si_{1-x}Ge_x$ layer on (0 0 1) silicon substrate due to substitutional carbon in epitaxial layer lattice total carbon concentration detected by SIMS about 2 at%; film thickness: 40–60 nm, constant carbon flux

Sample	Temperature (°C)	Growth rate (nm/s)	Ge-content (%)	Measured strain (as Ge %)	Strain difference (as Ge %)
C258	350	0.05	20	9	11
C259	350	0.05	33	18	15
C262	350	0.05	50	40	10
D208	400	0.1	20	3.5	16.5
C255	450	0.1	0	− 6.4	6.5
C254	450	0.1	20	15	5
C257	450	0.05	20	14	6
C256	450	0.1	20	13	7
C260	450	0.05	33	5.3	27.3[a]

[a] With hydrogen assistance.

growth parameters results mainly by carbon, which compensates the stress in the previous SiGe films.

The presence of hydrogen during the growth of SiGeC (*) shows the primary effect regarding stress reduction. The introduction of hydrogen as a surfactant enhances the growth perfection of the strain reduced layer (Fig. 2). Atomic hydrogen was supplied during MBE growth using a radio frequency (RF) source. The epitaxial layers were grown at a hydrogen pressure above 10^{-5} mbar.

The SIMS spectra on top of Fig. 2 shows the same level of carbon in the sample C251 and C252. On the contrary, X ray diffraction detected roughly a double of strain in C252 compared to C251. Both samples were deposited under the same growth conditions. The only difference is the background pressure of hydrogen during the growth process. In case of higher base pressure of hydrogen (C252), hydrogen assists the substitutional incorporation of carbon into the growing silicon lattice. The explanation of this effect should be the property of hydrogen as surfactant in silicon and silicon germanium. According to the literature [3] further investigations showed a smoother surface in case of application of hydrogen compared to the growth of SiGeC without hydrogen support.

Resulting from a couple of experiments at various pressure of hydrogen, we found that the maximum efficiency of hydrogen residual pressure is in the range higher than 10^{-5} mbar. In this range, activated hydrogen causes an additional increase of substitutional carbon in the lattice and results in a further strain reduction in the layer significantly.

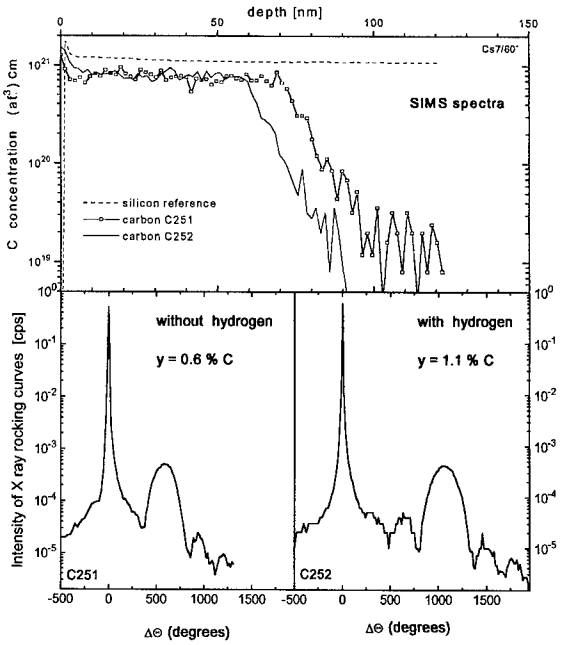

Fig. 2. SIMS profiles and X-ray rocking curves of two $Si_{1-y}C_y$ layers, grown at similar conditions ($d_{C251} = 77$ nm, $d_{C252} = 66$ nm; $T_{substrate} = 475$°C, growth rate = 6 nm/min) with and without hydrogen support.

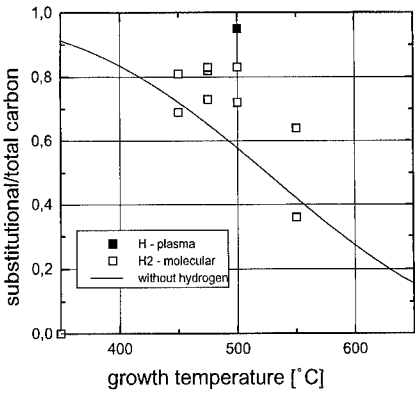

Fig. 3. Incorporation of carbon into the silicon lattice supported by different hydrogen residual pressure and at various growth temperatures.

The variation of the growth temperature influences the surface energetic conditions, which alter the mechanism of the surfactant and the surface mobility of the adsorbing atoms during film growth. Below 400°C hydrogen prevents an epitaxial growth of silicon and Si/Ge layers. Because of so much hydrogen (range: 10^{-5} mbar) the surface mobility of the atoms of the growing layer is too low to attain lattice positions and the film's growth is imperfect. At relevant deposition temperatures (400°C – 550°C) the carbon incorporation was significantly enhanced (Fig. 3).

Despite increase of the surface mobility of the atoms at the surface at temperatures higher than 600°C no hydrogen support for substitutional carbon incorporation compared to the growth without hydrogen is detected. These high temperatures weaken the chemical bond of hydrogen. It results in a lower surface coverage caused by higher desorption rate of hydrogen.

4. Conclusions

We found a significant enhancement of substitutionally incorporated carbon atoms in hydrogen-mediated growth compared to conventionally used growth in MBE.

At non-hydrogen assisted SiC alloy growth, an increasing growth temperature decreases the substitutional carbon incorporation into silicon. This effect is weak using hydrogen in the range of 400–550°C. At temperatures higher than 600°C hydrogen desorbs from silicon and carbon incorporation in silicon is in the same manner as without hydrogen.

The efficiency of hydrogen as a surfactant to alter the surface kinetics is relevant above 10^{-5} mbar residual pressure.

Finally, the atomic hydrogen compared to molecular hydrogen is much more efficient in the enhancement of substitutional carbon incorporation into the silicon lattice.

Acknowledgements

We are grateful for Dr. D. Krüger's careful cooperation to determine the absolute value of carbon by SIMS measurements. Special thanks to Dr. E. Bugiel for his help to characterize the structure of the grown layers by TEM.

References

[1] H.J. Osten, M.C. Kim, G. Lippert and P. Zaumseil, J. Crystal Growth 157 (1995) 405.
[2] P.O. Pettersson, C.C. Ahn, T.C. McGill, E.T. Croke and A.T. Hunter, Appl. Phys. Lett. 67 (1995) 2530.
[3] G. Otha, S. Fukatsu, Y. Ebuchi, T. Hattori, N. Usami and Y. Shiraki, Appl. Phys. Lett. 65 (1994) 2975.

ELSEVIER

Journal of Crystal Growth 175/176 (1997) 477–480

JOURNAL OF CRYSTAL GROWTH

New hydrogen desorption kinetics from vicinal Si(0 0 1) surfaces observed by reflectance anisotropy spectroscopy

J. Zhang[1,a,*], A.K. Lees[a], A.G. Taylor[2,a], M.H. Xie[a], B.A. Joyce[a], Z. Sobiesierksi[b], D.I. Westwood[b]

[a] *IRC for Semiconductor Materials, Blackett Laboratory, Imperial College of Science, Technology and Medicine, Prince Consort Road, London SW7 2BZ, UK*

[b] *Department of Physics and Astronomy, University of Wales, College of Cardiff, P.O. Box 913, Cardiff CF2 3YB, UK*

Abstract

Reflectance anisotropy (RA) from vicinal Si (0 0 1) surfaces is shown to be strongly influenced by the domain structure on the (2X1) + (1X2) reconstructed surface and by adsorbates such as hydrogen. Utilizing these adsorbate effects by monitoring the time dependence of RA from single domain vicinal surfaces, an accurate determination of surface hydrogen coverage can be made. We report a zeroth order coverage dependence of hydrogen desorption which is attributed to a desorption pathway incorporating a saturated and localised precursor state in which the diffusion/migration of surface hydrogen is not the rate limiting step.

PACS: 68.45.Da; 78.40.Fy; 81.15.Hi

1. Introduction

Reflectance anisotropy spectroscopy (RAS) [1], a surface sensitive diagnostic has been applied successfully to the study of Si and Ge surfaces [2] as well as many compound semiconductor surfaces. Recently, the authors have shown that RA from the Si (0 0 1) surface is strongly influenced by two parameters. First, changes in the relative domain coverage of the (1 × 2) and (2 × 1) surface reconstructions [3] demonstrated by the observation of RA oscillations during Si growth by gas source molecular beam epitaxy (GSMBE) on singular (0 0 1) surfaces. Second, adsorbates such as hydrogen dramatically modify the surface electronic structure and hence the RA response [4]. The latter effect provides an obvious opportunity for investigation of adsorbate concentrations. This is of particular interest to the Si epitaxy community since hydrogen is known to have a surfactant effect, has strong influence on the Ge surface segregation [5] and is a reaction by-product in chemical vapour deposition and GSMBE.

* Corresponding author. Fax: + 44 171 5946685; e-mail: jing.zhang@ic.ac.uk.

[1] Also at: Department of Physics, Imperial College, London, UK.

[2] Also at: Department of Chemistry, Imperial College, London, UK.

0022-0248/97/$17.00 Copyright © 1997 Elsevier Science B.V. All rights reserved
PII S0022-0248(96)00858-5

In this paper, we report detailed isothermal measurements of hydrogen desorption from vicinal Si (0 0 1) surfaces using RAS. The time dependent surface hydrogen coverage was monitored using changes in RA during desorption and reveals zeroth order desorption kinetics in contrast to existing studies on singular surfaces [6]. A new model is proposed to explain this unusual coverage dependence.

To ensure that changes in the RA are caused solely by the adsorption and desorption of surface hydrogen, the structural contribution to the changes in RA is eliminated by employing single domain vicinal Si (0 0 1) surfaces misorientated towards the nearest (1 1 1) plane. Under these conditions, growth proceeds by a step propagation mode, which eliminates the effect of domain coverage variation and retains a dominant single domain.

2. Experimental procedure

Experiments were performed in a GSMBE growth system described elsewhere [7], using a RA spectrometer similar in design to that of Aspnes [8, 9]. The vicinal Si (0 0 1) substrates misoriented towards (1 1 1) plane were cleaned by conventional wet chemical etching which produces a hydrogen teminated surface after the final HF dip. The samples were introduced in to the growth chamber via a vacuum interlock and preparation chamber and were outgassed at 200°C in the preparation chamber. Si buffer layers were grown at 750°C using disilane before any RA measurements. Surface hydrogen concentrations were generated from adsorption of atomic hydrogen produced from molecular hydrogen cracked on a hot tungsten filament or from the pyrolysis of silane (SiH_4) or disilane (Si_2H_6). This produces a monohydride phase, which also exhibit a (2×1) surface construction, throughout the temperature range used.

3. Results and disscussion

Fig. 1 illustrates the real part of the RAS obtained from the clean and hydrogen adsorbed vicinal Si (0 0 1) surfaces from the different sources, respectively. The largest spectral change observed on adsorption of hydrogen is the reduction in RA for photon energies below the E1 threshold at 3.1 eV. This is consistent with the removal of the Si

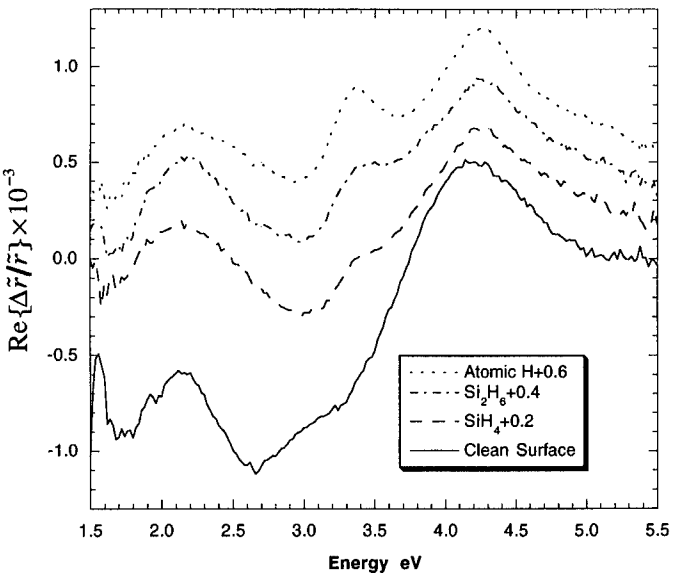

Fig. 1. RAS spectra of clean and hydrogen adsorbed (from atomic hydrogen, SiH_4 and Si_2H_6) on a Si (0 0 1) vicinal surface.

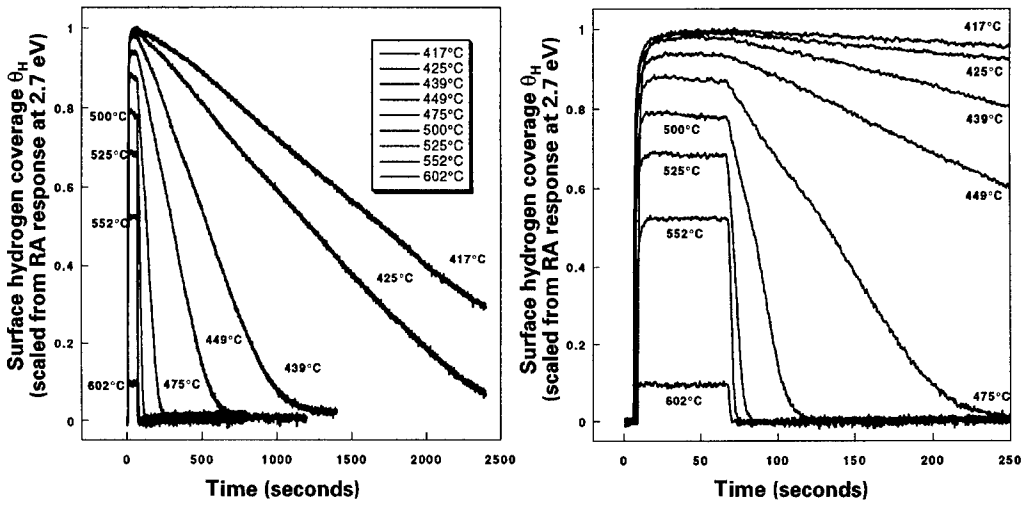

Fig. 2. Isothermal measurements of hydrogen desorption from vicinal Si (0 0 1) surfaces. The coverage is scaled from changes in RA response.

dimer dangling bonds by the formation of σ_{Si-H} bonds [4]. There are a number of reasons why one might expect the surface hydrogen concentration to be linear with respect to the change in RA. Hydrogen is known to form pairs on the Si dimer [10], and the surface is predominantly monohydride, so the change in RA at these energies is linearly proportional to the number of dangling bonds eliminated by hydrogen and hence surface hydrogen concentration.

The integrated change in RA response between 1.9 and 2.9 eV yields an accurate measurement of hydrogen coverage during growth and this is consistent with existing TPD measurements [11]. In situ isothermal hydrogen desorption measurements were carried out using changes in the RA response at 2.7 eV (the largest RA response below E1.) Fig. 2 shows the surface hydrogen coverage scaled from the RA response as a function of time and temperature. The early part of the decay exhibits a linear dependence of coverage with time, changing to an exponential like dependence as the coverage approaches zero. This observed linear dependence requires that the rate of desorption be independent of coverage itself, i.e. follows zeroth order desorption kinetics. This is contrary to previously reported first order hydrogen desorption kinetics made on nominally singular Si (0 0 1) [6].

Zeroth order kinetics dictate that a saturated precursor state must be involved in the desorption pathway. Under these conditions it is not the supply of atoms or molecules to this precursor state which is the rate limiting step, but rather the barrier to desorption from these states. Saturation of the precursor states can only be maintained if they are localised, existing in low and constant density. There are two possible mechanisms by which the precursor site density might be limited. The precursor sites could be associated with surface defects [12], but their density would be dependent on preparation methods and other parameters, so this is very unlikely. Alternatively, the precursor could be associated with surface steps, as in many cases of recombinative desorption from metals surfaces [13].

If our model is correct, the growth rate of an epitaxial layer should be dependent on the extent of misorientation in the temperature regime where there is a saturated hydrogen coverage. To test this hypothesis, Si layers were grown an substrates of two different misorientations at 501°C. The layer thickness measured by X-ray diffraction was found to be 20% greater for the 4°misoriented surface than for the nominally singular one. This confirms that a greater step density leads to a greater localized desorption site density and consequently a higher desorption rate and growth rate.

It is important to note that the existence of a step mediated desorption pathway does not preclude desorption from the terrace, and there is evidence to support this view. At low temperatures, the difference in desorption rate between surfaces with different step density (different misorientation) is quite large, with the higher step density giving rise to a larger rate. At higher temperatures, the differences become smaller as desorption from terraces increases its contribution to the overall desorption process. The balance between the two is then governed by the temperature, the density of precursor sites and the activation barriers for the two different desorption pathways. This is reflected in a small misorientation dependence in the activation energy obtained from the temperature dependence of the rate constant. Introduction of Ge also modifies the balance between the two possible desorption pathways as the Ge–H bond is expected to be weaker compared with that of Si–H. In this case, isothermal measurements of hydrogen coverage from SiGe alloy surface exhibit an exponential time dependence, consistent with desorption dominated by terrace sites.

4. Summary

We have demonstrated the potential of RAS as an in situ technique for kinetic studies. Zeroth order hydrogen desorption kinetics from a vicinal surface was observed and is explained in terms of a desorption pathway via a saturated localised precursor state.

Acknowledgements

This work is supported by the Engineering and Physical Science Research Council, UK under grant No. GR/J 97540.

References

[1] D.E. Aspnes, J. Vac. Sci. Technol. B 3 (1985) 1498.
[2] T. Yasuda, L. Mantese, U. Rossow and D.E. Aspnes, Phys. Rev. Lett. 74 (1995) 3431.
[3] A.R. Turner, M.E. Pemble, J.M. Fernandez, B.A. Joyce, J. Zhang and A.G. Taylor, Phys. Rev. Lett. 74 (1995) 3213.
[4] J. Zhang, A.G. Taylor, A.K. Lees, J.M. Fernandez, B.A. Joyce, D. Raisbeck, N. Shukla and M.E. Pemble, Phys. Rev. B 53 (1996) 10107.
[5] M.H. Xie, J. Zhang, A.K. Lees, J.M. Fernandez and B.A. Joyce, Surf. Sci. 367 (1996) 231.
[6] K. Sinniah, M.G. Sherman, L.B. Lewis and W.H. Weinberg, Phys. Rev. Lett. 62 (1989) 567.
[7] J. Zhang, A. Marinopoulou, J. Hartung, E.C. Lightowlers, N. Anwar, G. Parry, M.H. Xie, S.M. Mokler, X.D. Wu and B.A. Joyce, J. Vac. Sci. Technol. A 12 (1994) 1139.
[8] D.E. Aspnes, J. Vac. Sci. Technol. B 6 (1988) 1127.
[9] S.M. Scholz, A.B. Müller, W. Richter, D.R.T. Zhan, D.I. Westwood, D.A. Woolf and R.H. Williams, J. Vac. Sci. Technol. B 10 (1992) 1710.
[10] J.J. Bolland, Adv. Phys. 42 (1992) 129.
[11] M. Liehr, C.M. Greenlief, M. Offenberg and S.R. Kasi, J. Vac. Sci. Technol. A 8 (1990) 2960.
[12] Z. Jing, G. Locovsky and J.L. Whitten, Surf. Sci. 296 (1993) L33.
[13] S.L. Bernasek and G.A. Somorjai, J. Chem. Phys. 62 (1975) 3149.

ELSEVIER

Journal of Crystal Growth 175/176 (1997) 481–485

JOURNAL OF CRYSTAL GROWTH

Reduction of SiGe heterointerface mixing by atomic hydrogen irradiation during molecular beam epitaxy and its mechanism

Kiyokazu Nakagawa*, Yoshinobu Kimura, Masanobu Miyao

Central Research Laboratory, Hitachi Ltd., Kokubunji, Tokyo 185, Japan

Abstract

Ge surface segregation is a phenomenon in which Ge segregates to the epitaxial surface during MBE growth, and atomic hydrogen irradiation during MBE growth can reduce this phenomenon. To reveal the mechanism of both the phenomenon and the hydrogen irradiation effect, we have investigated the dependence of the phenomenon, with and without atomic hydrogen irradiation, on the Si growth rate, the substrate orientation, and the substrate temperature.

The segregated Ge concentration does not depend exponentially on the Si growth thickness and a second-order reaction as well as a first-order reaction is necessary to describe the Ge segregation phenomenon in Si. The segregation length on Si(1 0 0) is larger than that on Si(1 1 1). This difference in segregation lengths appears to be due to a difference in the number of segregation paths in different substrates. Atomic hydrogen irradiation does not change the potential of the two-energy-state model, but it does change the probability of the second-order reaction occurring. As a result, the segregation is reduced.

1. Introduction

Molecular beam epitaxy (MBE) is a powerful tool for forming abrupt heterointerfaces because its low-temperature growth process is thought to result in negligible effects of thermodynamic diffusion and intermixing at the heterointerface. It has been shown, however, that Ge segregates to the epitaxial surface during MBE growth [1, 2], which phenomenon inhibits the formation of abrupt heterointerfaces. A recent study using atomic hydrogen irradiation during MBE has shown that the surface segregation of Ge is significantly suppressed [3].

In this paper, we describe the dependence of the segregation phenomenon with and without atomic hydrogen irradiation on the Si growth rate, substrate orientation, and the substrate temperature to reveal the mechanism of both the segregation phenomenon and the hydrogen irradiation effect.

2. Experimental results and discussion

The Si MBE apparatus used was a Vacuum Generator V80 system with a base pressure of

* Corresponding author. Fax: + 81 423 27 7722; e-mail:k-nakaga@crl.hitachi.co.jp.

0022-0248/97/$17.00 Copyright © 1997 Elsevier Science B.V. All rights reserved
PII S0022-0248(96)00859-7

about 5×10^{-11} Torr. This system consists of an e-gun evaporator for Si deposition, an effusion cell for Ge deposition, and a quartz gas cell for hydrogen irradiation. The atomic hydrogen was formed by applying RF power to the gas cell. When the RF power was turned on, the ratio of atomic hydrogen to total hydrogen flow was nominally 0.5% and the remaining 99.5% of the flow was molecular hydrogen. The flow rate was controlled by using a mass flow controller. The growth chamber was evacuated by a 600 l/s turbo molecular pump and the pressure reached 2×10^{-5} Torr at the hydrogen flow rate of 2 cm^3/min. This flow rate corresponds to a molecular hydrogen irradiation rate of 20 monolayers (ML) /s on sample surfaces.

Si(1 0 0) and Si(1 1 1) substrates were precleaned by chemical treatment and a thin protective layer of oxide was formed. Next, each oxide layer was sublimated at 850°C for 20 min to obtain a clean surface. The substrate temperature was then lowered to 600°C and a 50 nm buffer Si layer was grown to provide a clean and smooth substrate surface. To study the segregation phenomenon on amorphous surfaces, a 50 nm buffer Si layer was deposited on Si(1 1 1) substrates at room temperature, and amorphous surfaces were formed. After that, about 1 ML of Ge atoms was grown on the Si surface at the same temperature. Then, undoped Si layers of various thicknesses were grown over the Ge surfaces at various growth temperatures with and without atomic hydrogen irradiation. In the case of amorphous surfaces, the Si overgrowth temperatures were below 250°C to prevent the surfaces from crystalizing. The Si deposition rate was varied from 0.05 to 0.3 nm/s.

The surface concentration of Ge atoms segregated on the overgrown Si surfaces was measured using X-ray photoelectron spectroscopy (XPS). The excitation was carried out with AlK_α having an energy of 1486.6 eV. The kinetic energy of the Ge(2p) photoelectrons was about 270 eV and their escape depth was less than 1 nm. The XPS signals of the 2p electrons observed here came mainly from the Ge atoms segregated on the Si surfaces. The XPS signal height of the Ge relative to that of the Si was confirmed as being proportional to the Ge surface concentration. In addition, the surface morphology and crystallinity were studied using reflection high-energy electron diffraction (RHEED).

Typical examples of the relation between segregated Ge concentration and Si-deposited thickness at a Si-deposition rate of 0.1 nm/s with and without atomic hydrogen irradiation are shown in Fig. 1. As we reported previously [3], the segregated Ge concentrations with and without hydrogen irradiation do not depend exponentially on the Si growth thickness in the region of high Ge concentration and a second-order reaction as well as a first-order reaction is necessary to describe the Ge segregation phenomenon in Si. The segregation length is defined as the Si-deposition thickness at which the Ge surface concentration becomes 0.1 ML ($\frac{1}{10}$ of the initial Ge concentration) at a Si-deposition rate of 0.1 nm/s. As shown in Fig. 2, the segregation phenomenon does not monotonically increase as the growth temperature increases; it reaches its maximum at 500°C with and without hydrogen irradiation.

The segregation length on Si(1 0 0) is larger than that on Si(1 1 1). As the growth temperature decreased, the segregation lengths on Si(1 0 0) and Si(1 1 1) substrates became constant at almost the same segregation length as that of the amorphous surfaces. The difference in the segregation lengths

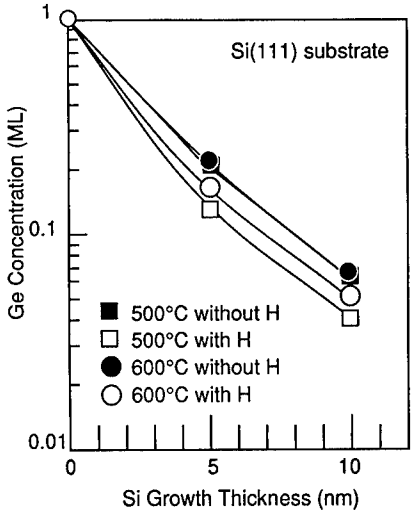

Fig. 1. Segregated Ge concentration as a function of Si overgrowth thickness with and without atomic hydrogen irradiation.

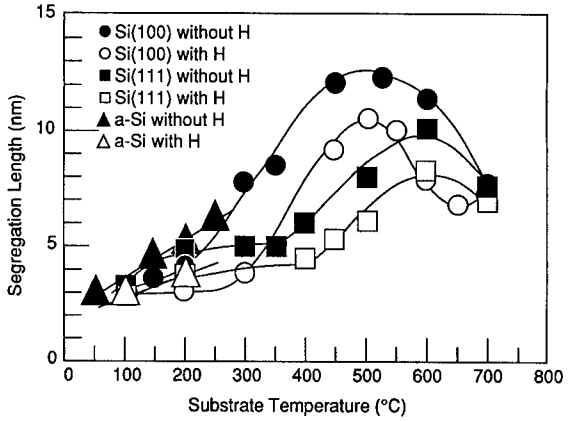

Fig. 2. Segregation length on Si(1 0 0), Si(1 1 1), and amorphous substrates with and without atomic hydrogen irradiation as a function of substrate temperature.

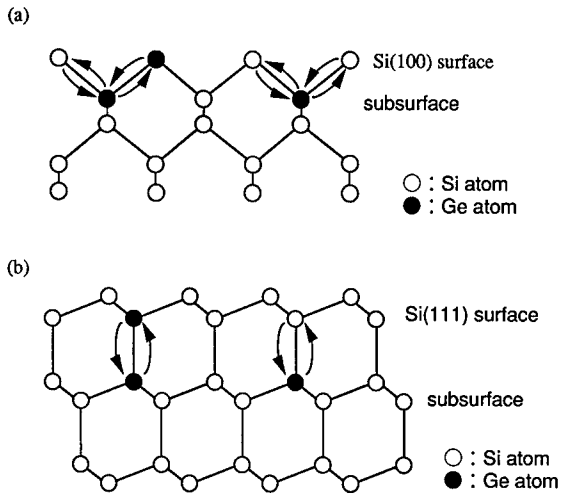

Fig. 3. Ge segregation paths of (a) Si(1 0 0) and (b) Si(1 1 1) substrates shown as cross-sections.

of the Si(1 0 0) and Si(1 1 1) substrates is considered to be due to the difference in the number of segregation paths in different substrates (Fig. 3). In the low-temperature range, however, the number of paths becomes the same due to the deterioration of crystal quality. The atomic hydrogen irradiation reduces the Ge surface segregation. The temperature at which the segregation length became constant was 50°C higher when hydrogen irradiation

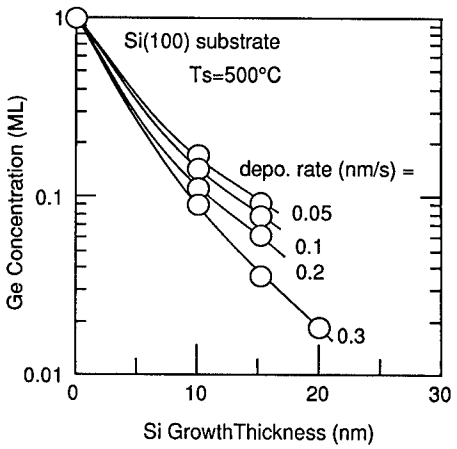

Fig. 4. Dependence of surface segregated Ge concentration on the Si deposition rate.

was used, regardless of the substrate orientations. This means that the hydrogen irradiation degrades the crystal quality possibly by reducing the migration of atoms on surfaces [3]. This irradiation effect becomes undetectable above 700°C. It appears that the thermal desorption of hydrogen from surfaces becomes larger at high substrate temperatures.

The increase of the Si deposition rate from 0.05 to 0.3 nm/s reduces the segregation phenomenon as shown in Fig. 4. This means that the jumping rate of Ge atoms for surface segregation is comparable with the Si growth rate.

The segregation phenomenon has been explained by the two-energy-state model [4, 5] and Fig. 5 shows the potential energy diagram for Ge. The energy of the surface state is lower than that of the subsurface state by an amount equal to E_b, and the Ge atoms jump over the potential barrier of E_a to segregate to the surface. From our studies on the dependence of the segregated Ge concentration on the Si growth thickness at high temperatures [2], the value of E_b is determined to be $\sim$0.28 eV [5].

In this case, the jumping probability r_f of Ge from the subsurface to the surface can be written as

$$r_f = v \exp(-E_a/kT), \quad (1)$$

and the jumping probability r_b of the reverse process from surface to subsurface can be written as

$$r_b = v \exp(-(E_a + E_b)/kT), \quad (2)$$

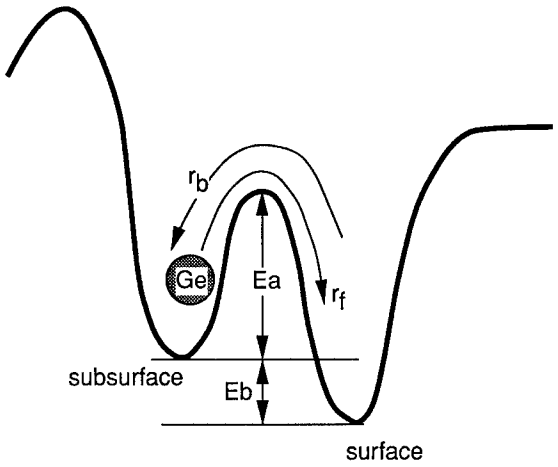

Fig. 5. Schematic illustration of an energy diagram of the two-energy-state model.

where ν is the frequency of attempts to jump over potential barriers. As the growth temperature increases, the reverse process denoted by r_b also increases and the surface segregation phenomenon is reduced. As a result, the segregation phenomenon reaches its maximum when the reverse process starts to become significant under high-temperature growth conditions. As mentioned above, the increase in the Si-deposition rate decreases the segregation as seen in Fig. 4, which means that the value of r_f is close to that of the Si-deposition rate.

In the model, the second-order reaction has been deduced using the following equations.

$$\frac{dn_1(t)}{dt} = -dr_b n_1(t)(1-n_2(t)) + dr_f n_2(t)(1-n_1(t)), \quad (3)$$

$$\frac{dn_2(t)}{dt} = -dr_b n_1(t)(1-n_2(t)) + dr_f n_2(t)(1-n_1(t)), \quad (4)$$

where $n_1(t)$ is the Ge occupant ratio of the surface layer, $n_2(t)$ is that of the subsurface layer, and d is the number of segregation paths; i.e., d is 2 on the Si(1 0 0) surface and 1 on the Si(1 1 1) surface, as shown in Fig. 5. The first terms of Eqs. (3) and (4) represent the rates of Ge jumping from the surface to the subsurface, and the second terms represent those from the subsurface to the surface. That is, these rates are assumed to be proportional to both the Ge occupant ratio of one layer ($n_1(t)$ or $n_2(t)$) and the Ge empty ratio of the other layer ($1-n_2(t)$ or $1-n_1(t)$). The term $n_1(t)\,n_2(t)$ of Eqs. (3) and (4) represents the second-order reaction. In the real system, since the segregated Ge atoms move around on the surface, the effective empty ratio of the surface is larger than $1-n_1(t)$, and this term can be written as $1-R\,n_1(t)$ instead of $1-n_1(t)$, where R is a number between 0 and 1. Thus, Eqs. (3) and (4) should be modified to the following Eqs. (5) and (6):

$$\frac{dn_1(t)}{dt} = -dr_b n_1(t)(1-n_2(t)) + dr_f n_2(t)(1-n_1(t)), \quad (5)$$

$$\frac{dn_2(t)}{dt} = -dr_b n_1(t)(1-n_2(t)) + dr_f n_2(t)(1-n_1(t)). \quad (6)$$

As can be seen in Fig. 1, hydrogen irradiation affects the second-order reaction instead of the first-order reaction which is observed in the range of low Ge surface concentrations. This means that the hydrogen does not change the energy E_a or E_b of Eq. (1) or Eq. (2), but changes the terms of $n_1(t)\,n_2(t)$ of Eqs. (5) and (6), i.e., the value of R. We believe that the atomic hydrogen adsorbs surfaces and limits the surface migration of atoms, and the reduced surface migration increases R. We have solved Eqs. (5) and (6) using fitting parameters of $E_a = 0.12$ eV, $E_b = 0.28$ eV, $\nu = 20$/s, $d = 2$ for the Si(1 0 0) surface, $d = 1$ for the Si(1 1 1) surface, $R = 0.4$ without hydrogen irradiation, and $R = 1$ with hydrogen irradiation. The results are shown in Fig. 6. It should be pointed out that ν is much smaller than the Debye frequency of about $1 \times 10^{12}\ s^{-1}$. The small value of ν is necessary to reproduce the experimental results of the Si-deposition rate dependence in Fig. 3 and the substrate orientation dependence in Fig. 2. We do not know the exact meaning of R yet, but the hydrogen effect can be reproduced fairly well by introducing the

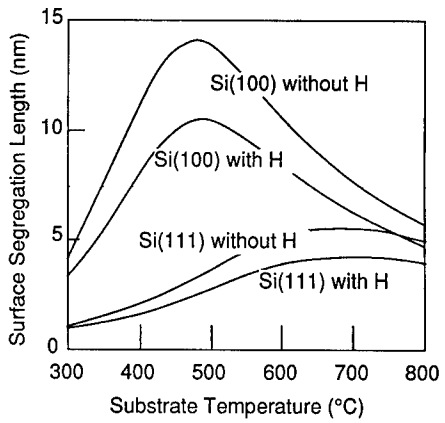

Fig. 6. Result of a simulation based on the two-state model. In the simulation, the decrease in the segregation lengths of Si(1 0 0) to Si(1 1 1) is due to fewer exchange paths along the bonds. The decrease in length caused by hydrogen irradiation is due to an increased incorporation ratio of Ge–Ge pairs into Si.

parameter R. We are now conducting a detailed study on this question.

3. Summary

We have investigated the dependence of Ge surface segregation, with and without atomic hydrogen irradiation on the Si growth rate, substrate orientation, and substrate temperature. We have obtained the following results.

(1) The segregation length on Si(1 0 0) is larger than that on Si(1 1 1).

(2) The segregation decreases when the Si growth rate increases from 0.05 to 0.3 nm/s.

(3) The atomic hydrogen irradiation reduces the Ge surface segregation but causes deterioration in the crystal quality.

(4) The atomic hydrogen irradiation does not change the potential of the two-energy-state model, but it does change the probability of the second-order reaction occurring.

Acknowledgements

We thank our coworker Takeshi Ikezu for his expert technical assistance with MBE.

References

[1] S.S. Iyer, J.C. Tsang, M.C. Copel, P.R. Pukite and R.M. Tromp, Appl. Phys. Lett. 54 (1989) 219.
[2] K. Nakagawa and M. Miyao, J. Appl. Phys. 69 (1991) 3058.
[3] K. Nakagawa, A. Nishida, Y. Kimura and T. Shimada, Jpn. J. Appl. Phys. 33 (1994) L1311.
[4] J.J. Harris, D.E. Ashenford, C.T. Foxon, P.J. Dobson and B.A. Joyce, Appl. Phys. A 33 (1984) 87.
[5] S. Fukatsu, F. Fujita, H. Yaguchi, Y. Shiraki and R. Ito, Mater. Res. Soc. Symp. Proc. 220 (1991) 217.

ELSEVIER

Journal of Crystal Growth 175/176 (1997) 486–492

JOURNAL OF CRYSTAL GROWTH

Control of composition and crystallinity in the molecular beam epitaxy of strain-compensated $Si_{1-x-y}Ge_xC_y$ alloys on Si

E.T. Croke[a,*], A.T. Hunter[a], C.C. Ahn[b], T. Laursen[c], D. Chandrasekhar[c], A.E. Bair[c], David J. Smith[c], J.W. Mayer[c]

[a] *Hughes Research Laboratories, Inc., 3011 Malibu Canyon Rd. RL63, Malibu, California 90265, USA*
[b] *California Institute of Technology, Pasadena, California 91125, USA*
[c] *Arizona State University, Tempe, Arizona 85287, USA*

Abstract

In this paper, we present a mass-spectrometry-based approach to the control of C concentration during molecular beam epitaxy (MBE) of $Si_{1-x-y}Ge_xC_y/Si$ superlattices. High-resolution X-ray diffraction, ion beam analysis, and transmission electron microscopy (TEM) were used to characterize composition and crystallinity in a series of superlattices for which the average strain condition was designed to range from biaxial compression to biaxial tension. For each sample, secondary ion mass spectrometry and Rutherford backscattering spectrometry confirmed that the average composition of each $Si_{1-x-y}Ge_xC_y$ layer was constant during growth. However, TEM revealed strain contrast variations within the $Si_{1-x-y}Ge_xC_y$ layers, leading to the conclusion that the presence of C on the wafer surface leads to laterally inhomogenous incorporation of C (and possibly Ge). TEM also showed that all samples were essentially free of extended defects except for short microtwins observed in the tensile-strained sample, that originated in the $Si_{1-x-y}Ge_xC_y$ layers and terminated in the Si layers directly above.

1. Introduction

Novel growth techniques such as molecular beam epitaxy (MBE) and chemical vapor deposition (CVD) have recently been shown to be suitable for producing high-quality alloys of Si, Ge, and C and therefore offer increased flexibility in the control of strain and electronic structure in Group IV heterostructures. These materials promise improved compatibility of Group IV heterojunction electronics with the processing environments currently available for Si CMOS. There are now compelling examples which suggest that circuits employing semiconductor heterostructure devices are potentially faster and less power-consuming than those employing homojunction devices alone. The lack of a well-developed lattice-matched material compatible with advanced Si processing has limited the wide-spread use of these devices in Si-based circuits, or has limited the performance advantage attainable because of stability limits. For

* Corresponding author. Fax: +1 310 317 5485; e-mail: croke@madmax.hrl.hac.com.

0022-0248/97/$17.00 Copyright © 1997 Elsevier Science B.V. All rights reserved
PII S0022-0248(96)00860-3

example, the performance of Si bipolar transistors has been improved by adding a built-in electric field to the base using a graded $Si_{1-x}Ge_x$ layer [1]. However, only a limited amount of Ge can be incorporated before devices degrade by strain relaxation during thermal processing. Furthermore, while $Si_{1-x}Ge_x$ strained to Si has a useful valence band offset, the conduction band offset is not large enough to produce significant electron confinement [2]. The ability to create thermally stable devices with band offsets larger than can be achieved with $Si_{1-x}Ge_x$ would greatly increase the performance advantage of circuits using Si-related heterostructure devices.

Alloys of Si, Ge, and C are expected to provide enhanced flexibility in the design of such structures since the $Si_{1-x-y}Ge_xC_y$ alloy system allows for the adjustment of strain relative to Si. Assuming that Vegard's law is valid, the lattice constant of relaxed $Si_{1-x-y}Ge_xC_y$ should attain a value between that of diamond and that of germanium; thus, for $Si_{1-x-y}Ge_xC_y$ alloys with a Ge to C ratio of approximately 8 to 1, material with a lattice constant exactly equal to Si is expected. The resulting material should therefore be stable with respect to strain-driven misfit dislocation formation and compatible with higher processing temperatures as compared with $Si_{1-x}Ge_x$ alloys of the same Ge concentration. To realize the potential of this ternary system, excellent control of composition is needed (as for any ternary semiconductor system), as well as concentrations of C and Ge high enough to provide significant band offsets with respect to Si. While techniques to control the composition of films containing Si and Ge have been well established by CVD and MBE growth techniques; control of C composition in such films remains the subject of extensive research.

To our knowledge, Furakawa et al. [3] first reported growth of $Si_{1-x-y}Ge_xC_y$ alloys in a United States Patent granted in 1989. Since then, considerable work has been done, notably by IBM [4–6] and others [7–13], to understand the growth conditions under which high-quality $Si_{1-x-y}Ge_xC_y$ can be grown and what its properties are, both structurally [4–10] and optically [11–13]. Most of the previous work dealt with very thin (typically <10 nm) layers with low carbon content. Here, we report studies of thicker layers (~ 25 nm) with C concentrations exceeding 1% and focus on their structural quality including the microscopic detail and its relevance to growth kinetics.

Preliminary estimates of band offset indicate that C concentrations up to approximately 5% are needed to make lattice-matched materials with useful band offsets with respect to Si [3, 14]. Previously, we reported [15] that, for C concentrations in excess of 1%, the growth of $Si_{1-y}C_y$ produced a rough surface, as evidenced by spottiness in Reflection High-Energy Electron Diffraction (RHEED) patterns observed during growth. As long as the $Si_{1-y}C_y$ layer thickness did not exceed a certain critical value (found to be strongly dependent on C concentration), growth of the subsequent Si layer smoothed the surface and the structures remained relatively defect-free. At still higher concentrations and thicknesses, RHEED revealed evidence of twinning and the material became highly defective. For $Si_{1-x-y}Ge_xC_y$ superlattices, the observed roughening and defect formation occurs at lower C concentration. The use of less than a monolayer of Sb as a surfactant [15] leads to improved morphology and much more abrupt interfaces between $Si_{1-y}C_y$ layers and Si than can be achieved without the use of Sb. This technique has recently been applied to $Si_{1-x-y}Ge_xC_y$ layers as well. While this development represents substantial progress, detailed studies of growth in the absence of Sb are still valuable. Our aim is to understand the C-related mechanisms that lead to poor morphology better and to understand further the basic growth mechanisms inherent to MBE, as well as explore the possibility of achieving good morphology at even higher C concentrations than possible with Sb alone.

In this paper, we discuss progress towards reproducibly depositing superlattices of $Si_{1-x-y}Ge_xC_y$ and Si. By growing a series of $Si_{0.9-y}Ge_{0.1}C_y$/Si superlattices, we show that our method of controlling the C flux can be successfully used to produce high-quality crystalline structures with strain configurations ranging from compressive, to lattice-matched, and finally to tensile, as the substitutional C concentration is increased from about 1% to 1.7%. We show that the films are crystalline, and analyze layer thickness and composition using

high-resolution X-ray diffraction (HRXRD), Rutherford backscattering spectrometry (RBS), and C-resonance backscattering. By analysis of secondary ion mass spectrometry (SIMS) data, the C and Ge contents are shown to be uniform from layer to layer within the superlattice. Transmission electron microscopy (TEM) has been used to analyze defect structure in the films, and a contrast is visible in the $Si_{1-x-y}Ge_xC_y$ layers that may be attributable to variations in the rate at which C is incorporated laterally across the wafer surface. This contrast seems to depend on the rate at which C is deposited, rather than the average strain. Finally, at higher C concentrations, microtwins are observed that originate in the alloy layers and, in some cases, terminate in subsequent Si layers.

2. Experimental procedure

Samples were prepared in a Perkin–Elmer (Model 430S) Si MBE system, capable of co-depositing Si, Ge, and C from electron beam evaporators onto heated Si substrates. Solid, high-purity graphite (<5 ppm ash) was inserted into the 40 cm^3 hearth of one of the evaporators and served as the source of C. Tuned to 24 amu (C_2), a residual gas analyzer (RGA) located directly above the C source provided a quantitative measure of the C flux. The signal from the RGA was compared with a previously calibrated setpoint value depending on the desired C flux and used to control the power to the electron gun. A cutout in the C shutter allowed the flux to be continually monitored and the electron gun to be controlled, regardless of whether the shutter was open or closed, eliminating transients that might otherwise occur as the shutter opened. A series of $Si_{1-y}C_y$/Si superlattices were grown at 450°C and analyzed by HRXRD to determine C concentration as a function of RGA setpoint for fixed Si flux, thereby generating a calibration curve used during growth of the $Si_{1-x-y}Ge_xC_y$ alloys.

The sample set chosen for this study consisted of 4 $Si_{1-x-y}Ge_xC_y$/Si superlattices (denoted "Calib", A, B, and C), which were composed of alternating layers of $Si_{1-x-y}Ge_xC_y$ and Si grown at 450°C. The Ge composition in each sample was chosen to be roughly 10%. The samples were prepared on 5 in. (1 0 0) Si substrates (p-type, 0.01–0.02 Ω-cm) which were degreased ex situ in tetrachloroethane, acetone, methanol, and deionized water followed by a 15 s etch in 5% HF. In situ cleaning consisted of heating the samples to 730°C to drive off adsorbed hydrogen or (in the case of sample C) exposure to a 0.1 Å/s Si flux at 875°C for 60 s. The C concentrations in each sample were deliberately chosen to vary about what is required to achieve a perfect lattice match with the Si substrate (sample B) and thus ranged between 0 and a few atomic percent.

3. Composition analysis

We used several different techniques to measure superlattice composition and layer thickness. Table 1 summarizes the results of our analysis for the four different samples. The biggest discrepancy is between the C content determined from RBS and SIMS which measure the total C, and that determined from HRXRD, which primarily measures the substitutional fraction.

HRXRD was used to measure the superlattice period and average strain. For the sample "Calib,"

Table 1
Composition and layer thicknesses for the superlatices used in this study [$Si_{1-x-y}Ge_xC_y$/Si superlattice sample set (10 periods each)]

Sample	HRXRD				TEM		RBS		SIMS
	t_{Si} (nm)	t_{SiGeC} (nm)	Ge (%)	C (%)	t_{Si} (nm)	t_{SiGeC} (nm)	Ge (%)	C (%)	C (%)
Calib.	33.3	23.9	10.6	0.0	34.0	22.0	11.2	0.0	< 0.06
A	33.3	23.9	10.4	1.0	32.6	22.5	11.0	1.2	1.3
B	38.1	27.0	9.2	1.1	34.6	28.0	8.5	1.3	1.6
C	34.1	24.5	10.1	1.7	30.9	24.5	10.1	2.3	2.4

grown without C, these data together with the shutter opening and closing times were sufficient to determine the Si and Ge fluxes, and therefore the Ge composition and individual superlattice layer thicknesses. For the samples A, B, and C, there were three unknown fluxes. The composition and thicknesses listed in the table were then determined with the additional assumption that the Ge flux was the same for these samples as it was for the calibration sample. We have found from previous experience that the Ge is our most stable source, and the assumption of constant Ge flux for depositions close to one another in time is usually justified.

Analysis of TEM images provided measurements of the layer thicknesses. The magnification was determined directly from the images by counting Si lattice planes within the Si layers. The perpendicular lattice constant used was that of bulk Si, since the electron micrographs indicated that the films were coherently strained to the underlying Si substrates.

Standard 2 MeV He^{2+} was used for probing Si and Ge, whereas 4.3 MeV He^{2+} C-resonance backscattering probed the C component. These ion backscattering techniques were used to measure the average Ge and C concentrations in the films, since the composition of the individual layers of the superlattice could not be resolved. To obtain the C and Ge content of the $Si_{1-x-y}Ge_xC_y$ layers from the average content of the superlattice, the thickness of the individual layers as obtained from the TEM analysis was used.

Finally, SIMS analysis was performed with a Cameca IMS 3f using a 10 keV Cs^+ primary beam. The analysis is based on the negative secondary ion yield. A thick layer of $Si_{1-x-y}Ge_xC_y$ which had been characterized by Elastic Recoil Detection and C-resonance backscattering provided a reference for quantifying the C content.

4. Results

4.1. HRXRD

(0 0 4) HRXRD rocking curve spectra were obtained from each sample in order to measure the composition and thickness of the superlattice layers. CuK_α radiation was selected using a Ge four-crystal monochromator and collimated onto each sample. The spectra generally consisted of a substrate peak and several sharp, evenly spaced peaks corresponding to the superlattices. By measuring the relative angular position of the zeroth-order peak and the substrate peak, an accurate determination of the average strain in the superlattices was obtained. Together with the average spacing of the superlattice peaks and the shutter opening and closing times, an accurate calibration of the Si and Ge fluxes was obtained from the sample "Calib". Assuming that the Ge flux could be held constant from run-to-run (confirmed by growing three such calibration samples on consecutive days), the Si and C fluxes were calculated from the spectra for each of the samples (A–C) that contained C. The spectra from these samples are shown in Fig. 1. The results confirm that the C concentrations span the range necessary for achieving perfect lattice match to the substrate. Sample A is compressively strained, since the zeroth-order peak appears at a lower angle than that of the substrate while sample C is under tension. For sample B, the C and Ge fractions are balanced so that the zeroth-order peak overlaps that of the substrate and thus it is lattice-matched. Confirmation of the assignment of the zeroth-order superlattice peak was obtained by comparing the results with simulation.

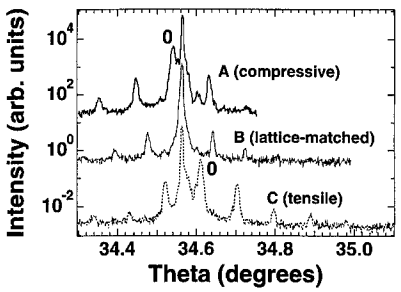

Fig. 1. HRXRD data obtained from samples A–C. The angular position of the zeroth-order superlattice peak (indicated) increases with respect to the substrate, indicating that the strain condition of the superlattices ranges from compressive (sample A) to lattice-matched (sample B) and finally, to tensile (sample C).

4.2. SIMS

SIMS was used to examine the uniformity of C and Ge within our epitaxial films. Fig. 2 shows the concentration of Si, Ge, and C for sample B as a function of distance from the outer surface of the layer. The depth scale was calculated from sputtering time using the superlattice period determined by HRXRD. The concentration scale was calculated using values for the average C and Ge composition obtained from RBS data. The top, or last deposited material consisted of 200 nm of pure Si. The ten periods of the superlattice are evident in the modulation of the concentrations from 200 to 800 nm into the film. The rounding of the concentration profiles is indicative of the depth resolution of the SIMS technique caused by non-uniform sputtering of the superlattice as depth profiles are made. Both the C and Ge concentration show a slight change in amplitude through the superlattice. The peak Ge concentration increases from 8.0% to 9.0% from the bottom to the top layer of the superlattice, and the C increases from 1.2% to 1.4%. Since the change in amplitude is monotonic, fairly linear and small, we attribute the variation to a slight increase in roughening as the film is sputtered. The actual uniformity of the Ge and C is likely to be better than the small variation seen in the SIMS profile.

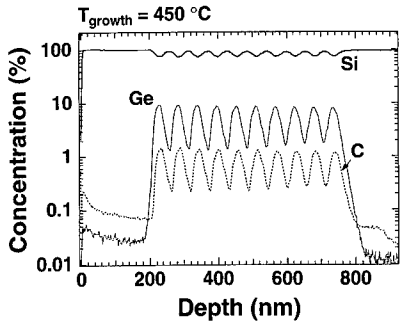

Fig. 2. SIMS profile showing film concentration as a function of depth from the top surface of sample B. The ten periods of the superlattice are evident in the region from 200 to 800 nm (the top 200 nm consists of a pure Si capping layer). The rounding of the composition modulation, and the slight decrease in modulation amplitude with depth are attributed to the roughening caused by the sputtering used to obtain the depth profile.

4.3. Electron microscopy

Each of the samples were analyzed for defects through the use of cross-sectional TEM. No defects were observed in the sample "Calib" and the layers appeared uniform in composition and pseudomorphic with the Si substrate. Samples A and B were of good crystalline quality with no extended defects observable (defect density $<10^7\,cm^{-2}$). A cross-sectional TEM micrograph taken from sample B (lattice-matched) is shown in Fig. 3. The figure shows that for the case of Si grown on $Si_{1-x-y}Ge_xC_y$, the interfaces were less abrupt than in the case of $Si_{1-x-y}Ge_xC_y$ grown on Si. These observations are consistent with RHEED which showed spotted patterns (indicative of rough surfaces) during $Si_{1-x-y}Ge_xC_y$ growth and streaked patterns (indicative of smooth surfaces) during Si growth. The marked difference in interface abruptness observed here is also consistent with the HRXRD spectra shown in Fig. 1 in that only 1–2 orders of superlattice satellite peaks are observable whereas several more orders can generally be seen in samples containing more abrupt interfaces.

Fig. 3 also reveals contrast within the $Si_{1-x-y}Ge_xC_y$ layers, indicative of intralayer strain variations which are attributed to possible phase separation at the growing surface. This contrast was also observed in samples A and C, although to a lesser extent in A, and to a greater extent in C. Since the strain contrast is observed more strongly for sample B (zero average strain) than for sample A (compressively strained), we conclude that it is more closely correlated with C concentration than with average strain. It appears that, at least on a local scale, there is a tendency for C (and perhaps also Ge) to cluster and precipitate into the growing film. As indicated earlier, the local strain contrast was even more pronounced in the tensile-strained sample (sample C) than in either samples A or B, and microtwins were visible along $\{1\,1\,1\}$ planes originating in the $Si_{1-x-y}Ge_xC_y$ layers and terminating in the Si layers directly above. Since the XRXRD and SIMS measurements disagree, it is surmised that a large fraction of the total C in this sample must be incorporated interstitially. A correlation between defect formation and the drop in the percentage of substitutional C is thus noted.

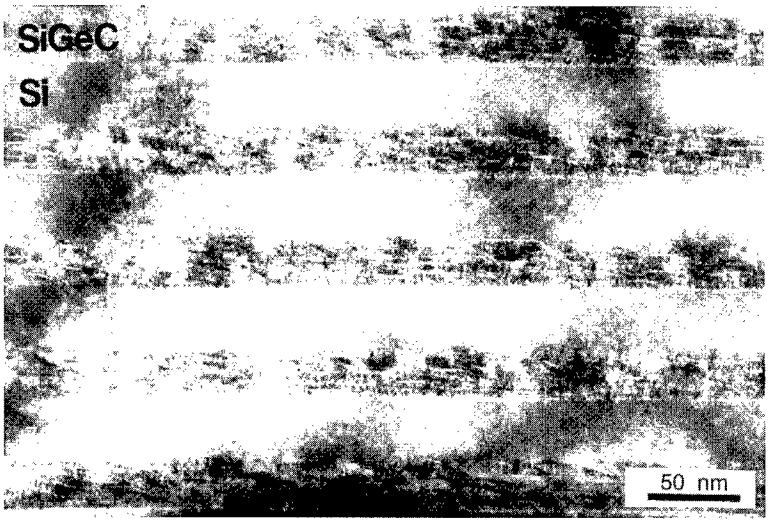

Fig. 3. Cross-sectional electron micrograph of lattice-matched sample B. Local strain contrast is visible within each $Si_{1-x-y}Ge_xC_y$ layer.

5. Conclusion

Superlattices of $Si_{1-x-y}Ge_xC_y$ and Si were grown and characterized through the use of a mass-spectrometry-controlled electron beam source of C. HRXRD, RBS, and SIMS analytical techniques were used to measure the Ge and C concentration and layer thicknesses for four $Si_{0.9-y}Ge_{0.1}C_y$/Si superlattices. The concentrations and thicknesses agreed closely except for the sample containing the highest C concentration, in which we presume a significant non-substitutional C component must be present. HRXRD and SIMS demonstrated the superlattices to be uniform in composition from the first period to the last, with little variation from period to period. The HRXRD data also show that the mass-spectrometry-controlled method of depositing C can be used to grow samples with a range of strain conditions varying from compressive to lattice-matched to tensile for fixed Ge concentration. Lastly, TEM images of the samples show that they were free of extended defects except for the tensile-strained sample containing the highest concentration of C in which microtwins were observed. Areas of modulated strain contrast within the $Si_{1-x-y}Ge_xC_y$ layers were observed in all three C-containing samples. This modulation appeared to depend primarily on C concentration, rather than average strain since even the lattice-matched sample showed this effect. The contrast is apparently due to a lateral inhomogeneity in the incorporation rate of the constituents due to the presence of C on the wafer surface during growth.

Acknowledgements

The authors gratefully acknowledge the fine technical assistance of D. Courtney for performing the X-ray characterization discussed here and the partial support of the Defense Advanced Research Projects Agency, monitored by Lt. Col. Gernot Pomrenke under Contract Number MDA972-95-3-0047. Electron microscopy conducted at the Center for High Resolution Electron Microscopy at Arizona State University was supported by NSF Grant DMR-93-14326.

References

[1] D.L. Harame, J.M.C. Stork, B.S. Meyerson, K.Y.-J. Hsu, J. Cotte, K.A. Jenkins, J.D. Cressler, P. Restle, E.F. Crabbé, S. Subbanna, T.E. Tice, B.W. Scharf and J.A. Yasaitis, IEDM Tech. Dig. 71 (1993).

[2] C.G. Van de Waal and R.M. Martin, Phys. Rev. B 34 (1986) 5621.
[3] S. Furakawa, H. Etoh, A. Ishizaka and T. Shimada, US Patent No. 4885614 (1989).
[4] K. Eberl, S.S. Iyer, J.C. Tsang, M.S. Goorsky and F.K. LeGoues, J. Vac. Sci. Technol. B 10 (2) (1992) 934.
[5] K. Eberl, S.S. Iyer, S. Zollner, J.C. Tsang and F.K. LeGoues, Appl. Phys. Lett. 60 (1992) 3033.
[6] K. Eberl, S.S. Iyer and F.K. LeGoues, Appl. Phys. Lett. 64 (1994) 739.
[7] H.J. Osten, E. Bugiel and P. Zaumseil, Appl. Phys. Lett. 64 (1994) 3440.
[8] Z. Atzmon, A.E. Bair, E.J. Jaquez, J.W. Mayer, D. Chandrasekhar, D.J. Smith, R.L. Hervig and McD. Robinson, Appl. Phys. Lett. 65 (1994) 2559.
[9] J. Mi, P. Warren, P. Letourneau, M. Judelewicz, M. Gailhanou, M. Dutoit, C. Dubois and J.C. Dupuy, Appl. Phys. Lett. 67 (1995) 259.
[10] S. Bondar and J.L. Regolini, J. Vac. Sci. Technol. A 13 (5) (1995) 2336.
[11] P. Boucaud, C. Francis, F.H. Julien, J.-M. Lourtioz, D. Bouchier, S. Bondar, B. Lambert and J.L. Regolini, Appl. Phys. Lett. 64 (1994) 875.
[12] A. St. Amour, C.W. Liu, J.C. Sturm, Y. Lacroix and M.L.W. Thewalt, Appl. Phys. Lett. 67 (1995) 3915.
[13] K. Brunner, K. Eberl, W. Winter and N.Y. Jin-Phillipp, Appl. Phys. Lett. 69 (1996) 91.
[14] R.A. Soref, J. Appl. Phys. 70 (1991) 2470.
[15] P.O. Pettersson, C.C. Ahn, T.C. McGill, E.T. Croke and A.T. Hunter, Appl. Phys. Lett. 67 (1995) 2530.

ELSEVIER

Journal of Crystal Growth 175/176 (1997) 493–498

JOURNAL OF CRYSTAL GROWTH

Stratified suspension of highly ordered Si nanoparticles in SiO_2 created by Si MBE with oxygen co-implantation

Yukari Ishikawa[a], N. Shibata[a], S. Fukatsu[b,*]

[a] *Japan Fine Ceramics Center, 2-4-1 Mutsuno, Atsuta-ku, Nagoya 456, Japan*
[b] *Department of Pure and Applied Sciences, The University of Tokyo, 3-8-1 Komaba, Meguro-ku, Tokyo 153, Japan*

Abstract

A new class of non-dispersive Si nanoparticle (SNP) system has been created on Si(1 0 0) wafers by low-energy oxygen co-implantation during Si MBE. Ordered, highly oriented Si nanoparticles embedded in SiO_2 with dimensions $d = 4$–100 nm are observed. Transmission electron microscopy shows that SNPs are oriented preferentially to [1 0 0], indicative of epitaxial growth of SNP as compared to conventional dispersive SNPs. Individual SNP is confirmed to be a single crystal and exhibits unusual habits with (1 0 0) and (1 1 1) facets. Broad visible luminescence bands are observed at room temperature.

PACS: 68.55.Bd; 68.55.Ln; 61.16.Bi; 68.35.B

Keywords: Highly oriented Si nanoparticles; Oxygen co-implantation; Si MBE; SiO_2

1. Introduction

Establishing a realistic device made of Si and allied compounds is a cornerstone issue in the field of optoelectronics. Recently, dielectric suspensions of Si and Ge fine structures of nanodimensions have attracted much interest due to their unique optical properties. In particular, visible light emission capability of Si nanoparticles (SNP) in SiO_2 at room temperature holds promise in the context of efficient Si-based light emitter fabrication [1–9].

The problems which arise when dealing with Si nanoparticles in SiO_2 fabricated by conventional techniques such as gas-evaporation, co-sputtering, and Si implantation are (1) the dispersive character of nanoparticles that are randomly distributed in SiO_2 without preference of crystal orientation and (2) the meager controllability over the particle dimensions [1–9]. Within the perspective of optoelectronic application, it is desirable to develop a technique which allows an ordered arrangement and control over the feature size to make use of the potential of SNP.

* Corresponding author. Fax: + 81 3 5454 4311; e-mail: fkatz@srv.bme.rcast.u-tokyo.ac.jp.

0022-0248/97/$17.00 Copyright © 1997 Elsevier Science B.V. All rights reserved
PII S0022-0248(96)00914-1

In this paper, a novel architecture of Si nanoparticles is described by using Si MBE hybridized with multiple oxygen co-implantation. An ordered, highly oriented Si nanoparticles are created and arranged in a layered manner. Visible light emission approaching the quantum confined regime was observed at room temperature.

2. Experimental procedure

Low-energy oxygen ion implantation during Si MBE [10] (LOI-MBE) was performed to create highly ordered and oriented SNPs on an n-type doped Si(1 0 0). LOI-MBE was originally developed for silicon-on-insulator (SOI) technology [10]. O^+ions at 25 kV were generated by an ECR ion source with a sector magnet. Maskless implantation was performed during MBE to an areal dose of 2×10^{17} cm^{-2}. A quality Si surface for MBE was obtained during the course of and even after oxygen implants with a 2×1 reconstruction on the top Si.

Alternate Si/SiO_2 bilayers were created by Si MBE, oxygen ion implantation, and annealing. Simultaneous implantation during MBE was performed for comparative purposes. Finally, extended ex situ annealing at 1280°C for 2 h was performed for both cases. Si nanoparticles are formed at this step. The Si growth rate was 1–2 Å/s with an e-gun and the substrate temperature was 700°C throughout. The layer thickness was measured by transmission electron microscopy (TEM).

3. Results and discussion

While standard SOI wafers carry a single buried oxide layer created either by implants/annealing or bond-and-etch-back, LOI-MBE is capable of producing a stack of Si/SiO_2 bilayers of extended period, $n = 2$–4. Si/SiO_2 stacks are promising for electrical isolation and optic application such as waveguides and mirrors using the refractive index step at Si/SiO_2 [11].

However, Si/SiO_2 bilayer morphologies are significantly modified by multiple LOI-MBE with $n = 5$ or more. As shown in Fig. 1a, LOI-MBE with $n = 5$ generates Si nanoparticles. Faceted Si polyhedra suspended in SiO_2 are identified. A magnified TEM picture (Fig. 1b) of a 160 Å SNP shows (1 1 1) and (1 0 0) habits. Single- crystalline character is confirmed by selective area diffraction shown in Fig. 1c. Laterally extended Si islands are also seen. Importantly, SNPs are slightly displaced from parent Si layers. The top Si is a large slab extending more than 400 nm. Thus the first grown four Si slabs have transformed to SNPs.

There sometimes appeared Si islands suspended in the SiO_2 even for $n = 2$ and 3. Such Si islands are created by excess oxygen dose. These are distinguished from SNPs since these islands are larger than SNP. However, such Si islands are as highly oriented as SNPs are. Therefore this highly oriented character seems to share the same origins with SNPs.

Simultaneous LOI-MBE with co-implantation was also examined. We obtained similar SNP of comparable dimensions arranged in a layered geometry while SNP orientation was slightly misoriented as compared to nearly ordered SNPs formed by co-implants followed by Si MBE.

It is also noted in Fig. 1 that the particle dimensions have a distribution. The particle dimension statistics of SNPs was taken by densitometry of a cross-sectional TEM image over more than 200 SNPs. The cumulative numbers of SNPs are plotted for vertical and lateral directions in Fig. 2. Note the log-scale. These distributions are reasonably fitted by lognormal distribution functions [12] of the form $1/(\sqrt{2\pi} \ln \sigma)\exp(-\ln(x/\bar{x})^2/\ln \sigma^2)$ with standard deviation of $\sigma = 1.5 \pm 0.1$ nm and the mean value of $\bar{x} = 21 \pm 2$ nm. Thus, we see that the morphologies of SNPs for $x < 50$ nm are isotropic and the formation kinetics have reached thermal equilibrium.

The arrow of the upper panel of Fig. 2 shows that there is a vertical dimension cutoff at 40 nm, whereas there is no ceiling over the lateral width. These indicate that the ceiling of the SNP height is precisely controlled by the parent Si thickness, t_{Si}. Therefore the vertical feature size is controlled simply by choosing the parent Si thickness. Although the width is not strictly limiting, it is spontaneously set almost the same as the height due to isotropic morphology for $x < 40$ nm. Such a controllability

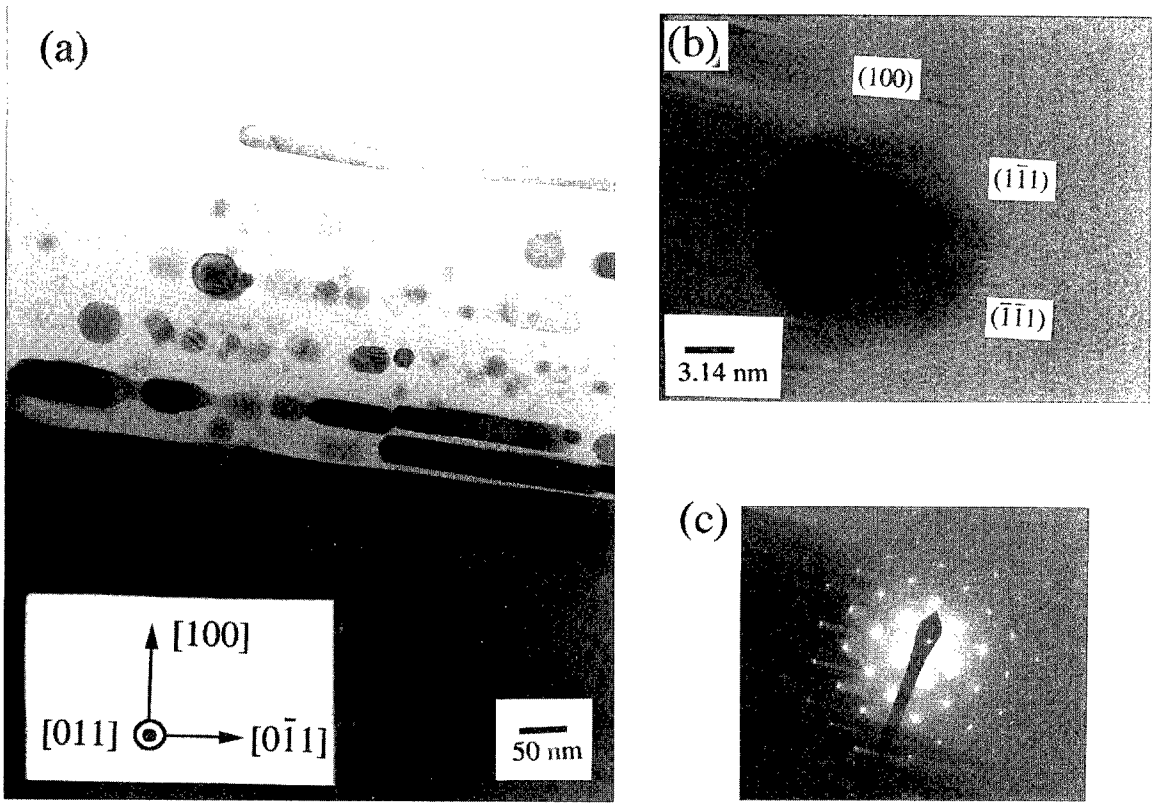

Fig. 1. TEM cross-sectional images of a stratifid SiO_2 suspension of highly-ordered, oriented 2-D SNPs ($n = 5$) (a). Note the well-defined facet morphologies on Si islands and SNPs. A higher magnification of a 160 Å SNP (b). (c) Selective area diffraction pattern of the SNP.

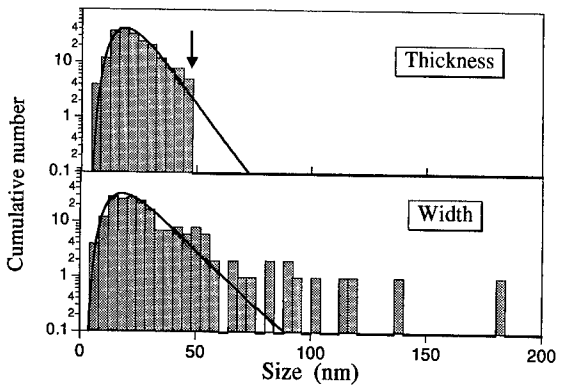

Fig. 2. Feature-size distributions taken over more than 200 SNPs by densitometry of a TEM cross-sectional image. Note that the height ceiling is 40 nm as indicated by the arrow.

distinguishes the LOI-MBE from dispersive SNPs. In the latter, feature sizes must be controlled via particle ripening kinetics. Thus the SNP formation based on LOI-MBE offers a better control of particle dimensions and even allows for a layered geometry [1–9].

Truncated silhouettes of SNPs projected onto (1 1 0) planes as seen in bright-field image of Fig. 1b indicate well-defined (1 1 1) and (1 0 0) facets. Such unusual crystal habits are more clearly identified in the lattice imaging of a SNP with a diameter of 150 Å as shown in Fig. 3. Note the SNP has been created by simultaneous LOI-MBE. The {1 1 1} planes at a separation of 0.314 nm are seen. Each SNP retains well defined (1 0 0) and (1 1 1) facets while (1 1 0) facets are apparently missing, although

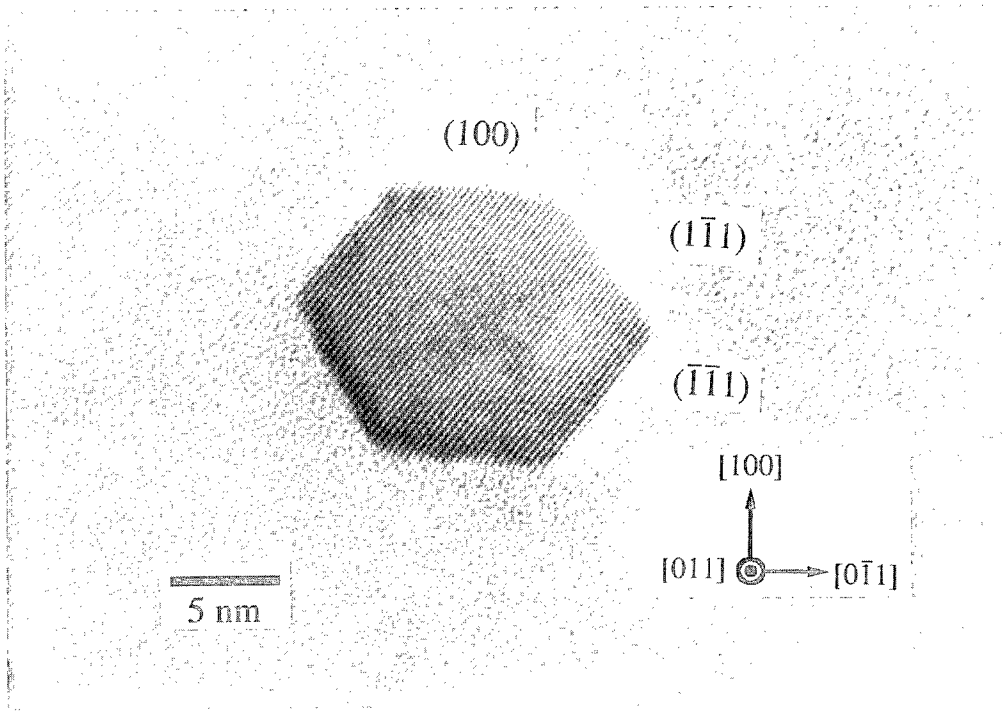

Fig. 3. A higher magnification of a SNP with 150 Å diameter. Note the SNP has been created by simultaneous LOI-MBE. {1 1 1}-planes as well as (1 1 1), (1 0 0) equivalent facets are identified. The (1 0 0) facets are parallel to the substrate-epitaxy interface.

the [1 1 0] habit is expected for the thermodynamic morphology of Si fine particles that is an icositetrahedron with (3 1 1) and (1 1 1) facets [13]. The different crystal habits indicate a modified formation energetics for LOI-MBE-grown SNPs. In addition, the lognormal distributions suggest that the SNP formation involves processes analogous to coalescence. In contrast, standard dispersive SNP formation is believed to occur through migration and crystallization from a supersaturated solution. However, oxygen migration rather than Si migration and subsequent oxidization of Si are likely to control the SNP formation.

Importantly, the presence of (1 0 0) facets indicate that SNPs and Si islands retain epitaxial relationship with Si(1 0 0) substrate. The (1 0 0) crystal habits remain coherent throughout the SNPs in support of the highly-oriented character of SNPs. In addition, Moiré fringes are seen in Fig. 1a. These indicate a slight rotation of (1 1 1) and (0$\bar{2}$ $\bar{2}$) planes about [0 1 1] by a few degrees, further supporting the oriented SNPs argument.

The visible PL bands observed at room temperature have provided the impetus for the previous studies on SNPs [1–9]. As a matter of fact, red band PL and blue-to-red bands were observed from the islanded and SNPs, respectively, as shown in the left panel of Fig. 4. A HeCd laser was used as the excitation. The red PL bands is centered at 6300 Å flanked by a small shoulder at 5500 Å, while split bands are observed at 4500 Å and 7600 Å for SNPs. There is clear correspondence between the broad band features for $n = 3$–5 except the 4500 Å (2.7 eV) band in the SNP sample. In view of the size distribution, it is expected that the 4500 Å-band is a signature of the 6300 Å-band blue-shifted by quantum confinement. However, the PL origins of these bands have not been fully accounted for. Visible PL bands bear a close similarity to the electroluminescence spectra taken from Si-enriched SiO_2 [14]. For the red bands, since there are Si slabs with a large area, the Si/SiO_2 interface state may provide a radiative pathway for $n = 3, 4$. For the blue emission of SNPs, although the 2.7 eV

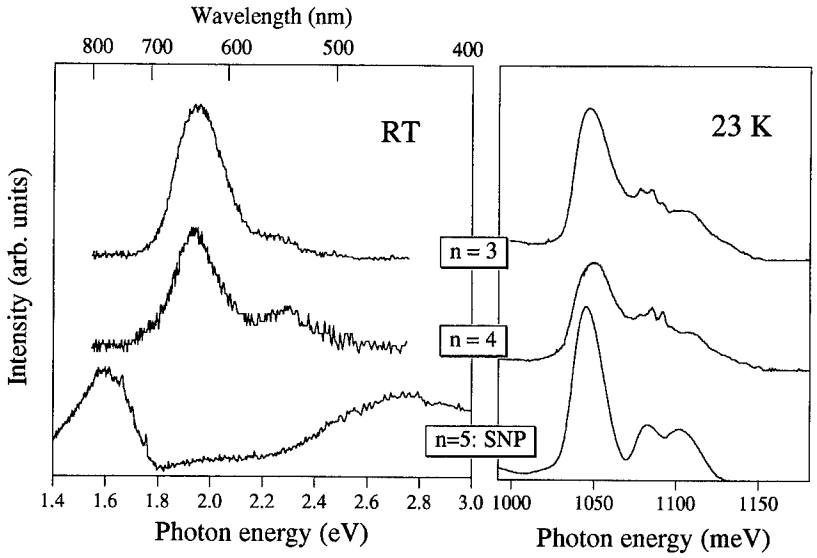

Fig. 4. Left; Room-temperature visible band PL spectra of Si/SiO_2 bilayer stacks of $n = 3, 4$ and highly oriented $SNPs/SiO_2$ ($n = 5$). Right; Low-temperature near-infrared PL spectra of Si/SiO_2 bilayer stacks of $n = 3, 4$ and highly oriented $SNPs/SiO_2$ ($n = 5$).

band [15] is known to be excited by two-photon absorption process when the ultraviolet is used, the oxygen-defect-mediated emission is unlikely. Since the SNPs are annealed at high temperatures, these defects will be eventually annealed out. However, impurity-mediated recombination is not ruled out. Low-temperature PL was taken as a check for optically active defect states as shown in the right panel. However, there was no deep level bands observed while a slight modulation of the spectra was identified around 1080–1120 meV. This may have correlation with the development of visible bands at room temperature. Further study is now in progress to identify the PL origins.

4. Summary

In summary, a stratified suspension of highly-ordered, highly oriented SNPs in SiO_2 was created by multiple low-energy oxygen ion implantation during Si MBE. SNPs hold epitaxial relationship with underlying Si(1 0 0) substrate while exhibiting (1 1 1)- and (1 0 0)- crystal habits as confirmed by TEM. Visible luminescence bands from SNPs were observed at room temperature.

Acknowledgements

One of the authors (S.F.) would like to acknowledge Toray Science Foundation, Asahi Glass Foundation, and Murata Science Foundation. This work was in part supported by a Grant-in-Aid for Scientific Research from the Ministry of Education, Science, Sports and Culture, and a Corning Research Grant.

References

[1] L.N. Dinh, L.L. Chase, M. Balooch, L.J. Termiinello and F. Wooten, Appl. Phys. Lett. 65 (1994) 3111.
[2] D. Zhang, R.M. Kolbas, P.D. Milewski, D.J. Lichtenwalner, A.I. Kingon and J.M. Zavada, Appl. Phys. Lett. 65 (1994) 2684.
[3] H. Takagi, H. Ogawa, Y. Yamazaki, A. Ishizaki and T. Nakagiri, Appl. Phys. Lett. 56 (1990) 2379.
[4] M. Rückschloss, B. Lnadkammer and S. Veprek, Appl. Phys. Lett. 63 (1993) 1474.
[5] S. Tong, X. Liu and X. Bao, Appl. Phys. Lett. 66 (1995) 459.
[6] H. Morisaki, H. Hashimoto, F.W. Ping, H. Nozawa and H. Ono, Appl. Phys. Lett. 64 (1993) 2977.
[7] Y. Maeda, N. Tsukamoto, Y. Yazawa, Y. Kanemitsu and Y. Masumoto, Appl. Phys. Lett. 59 (1992) 3168.

[8] T. Shimizu-Iwayama, S. Nakao and K. Saitoh, Appl. Phys. Lett. 65 (1994) 1814.
[9] Y. Kanemitsu, Phys. Rev. B 49 (1994) 16845.
[10] Y. Ishikawa and N. Shibata, Appl. Phys. Lett. 61 (1992) 1543.
[11] R. Soref, IEEE Proceedings 81 (1993) 1687; S. Fukatsu, J. Mater. Sci. 6 (1995) 341.
[12] C.G. Granqvist and R.A. Buhrman, J. Appl. Phys. 47 (1973) 2200.
[13] M. Stavola, J.R. Patel, L.C. Kimerling and P.E. Freeland, Appl. Phys. Lett. 42 (1983) 73.
[14] D.J. DiMaria, J.R. Kirtley, E.J. Pakulis, D.W. Dong, T.S. Kuan, F.L. Pesavento, T.N. Theis and J.A. Cho, J. Appl. Phys. 56 (1984) 401.
[15] R. Tohmon, Y. Shimogaichi, H. Mizuno, Y. Ohki, K. Nagasawa and Y. Hama, Phys. Rev. Lett. 62 (1989) 1388.

ELSEVIER

Journal of Crystal Growth 175/176 (1997) 499–503

JOURNAL OF CRYSTAL GROWTH

Characterization of mismatched SiGe grown on low temperature Si buffer layers by molecular beam epitaxy

K.K. Linder*, F.C. Zhang , J.-S. Rieh , P. Bhattacharya

Solid State Electronics Laboratory, Department of Electrical Engineering and Computer Science, University of Michigan, Ann Arbor, Michigan 48109-2122, USA

Abstract

Several types of buffer layer structures, including superlattice and step-graded layers, have been employed to reduce the threading dislocation in SiGe epitaxial layers. A new technique, using a 0.1 μm thick Si buffer grown at 450°C by molecular beam epitaxy, provides the best results. For a 0.5 μm thick $Si_{0.85}Ge_{0.15}$ layer, the dislocation density is $\leqslant 10^5$ cm^{-2}. Hall measurements indicate an improvement in the hole mobility of a 1 μm thick Boron doped $Si_{0.7}Ge_{0.3}$ layer. A SiGe/Si heterojunction bipolar transistor has been fabricated exploiting the low temperature Si buffer. Transmission electron microscopy of the structure does not indicate any evidence of threading dislocations.

PACS: 68.55.Bd

Keywords: LT-Si buffer; Threading dislocation density; TEM; DLTS

1. Introduction

SiGe/Si heterostructures offer both high carrier mobilities and cutoff times for both field effect and bipolar transistor technologies [1–4]. One of the obstacles to the production of defect-free SiGe epitaxy layers is the generation of dislocations caused by strain relaxation at the substrate/epitaxy layer interface. Threading dislocations formed in the SiGe layer degrade material quality resulting in poor device performance [5, 6]. Several authors have proposed a variety of methods for reducing the number of threading dislocations, including superlattice and step-graded layers [7–13]. However, many of the studies resulted in dislocation densities which were too high for high-performance device applications ($\geqslant 10^7$ cm^{-2}). Well defined lithography would not be possible for such structures because of their thickness. Furthermore, considerations for producing defect-free high Ge composition alloys – which, theoretically, would greatly improve the carrier transport properties of the device – were neglected [14].

* Corresponding author. Fax: + 1 313 763 9324; e-mail: klinder@engin.umich.edu.

0022-0248/97/$17.00 Copyright © 1997 Elsevier Science B.V. All rights reserved
PII S0022-0248(96)01004-4

In this study, we have investigated the reduction of threading dislocations in high Ge composition alloys using several strained superlattice (SPLS) and step-graded layer structures. We have also investigated the use of a low temperature Si (LT-Si) buffer, which dramatically reduces the threading dislocation density in SiGe/Si heterostructures.

2. Experimental procedure

We used (1 0 0)-oriented, p^+ Si wafers with resistivities of 0.005–0.02 Ω cm. The samples were grown by gas-source molecular beam epitaxy (MBE) using a three-chamber RIBER-32 system. Pure Si_2H_6 was maintained at a constant flow rate of 14 sccm while the solid Ge source temperature varied between 1140–1250°C. For each of our samples, an initial 0.1 μm thick Si buffer was grown at 700°C to minimize defects at the substrate/epilayer interface. A 1 μm thick layer of $Si_{0.4}Ge_{0.6}$ was then grown followed by single or multiple 20 period SPLS regions (50 Å Si/186 Å $Si_{0.25}Ge_{0.75}$) and a 0.5 μm thick $Si_{0.4}Ge_{0.6}$ cap layer, each at 570°C. The average lattice constant of the SLS is equal to that of $Si_{0.4}Ge_{0.6}$. The entire heterostructure is undoped. For comparison, a sample consisting of a single 1 μm $Si_{0.4}Ge_{0.6}$ layer on a 0.1 μm thick Si buffer layer was also grown.

For our LT-Si study, an initial 0.1 μm thick Si buffer was grown followed by a 0.1 μm thick LT-Si layer, grown at 450°C. A 0.5 μm thick layer of $Si_{0.85}Ge_{0.15}$ was then grown at 570°C. For comparison, a sample consisting of a 0.1 μm thick Si buffer layer followed by a 0.5 μm thick $Si_{0.85}Ge_{0.15}$ layer was also grown. Bright field cross-section

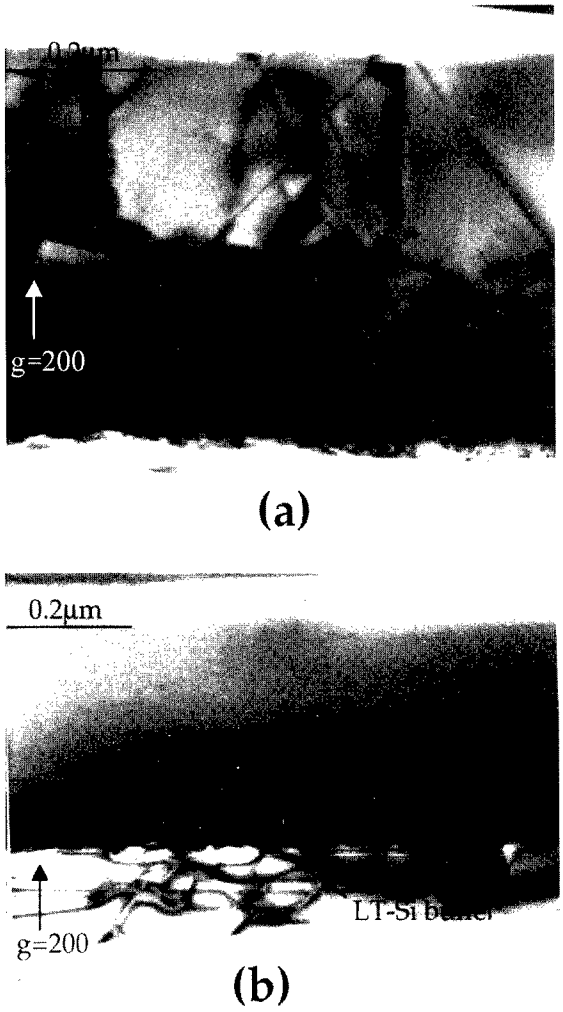

Fig. 1. Bright field (2 0 0) cross-section TEM image of 0.5 μm thick $Si_{0.85}Ge_{0.15}$ grown on (0 0 1) Si (a) without and (b) with LT-Si buffer.

Table 1
Threading dislocation spacing and density measured by planed-view and cross-section TEM

Sample description	Dislocation spacing (cm)	Dislocation density (cm^{-2})
Bulk $Si_{0.4}$ $Ge_{0.6}$(control)	9.2×10^{-6}	1.83×10^{10}
Structure with single SLS	2.0×10^{-5}	7.33×10^{9}
Structure with triple SLS	2.1×10^{-5}	6.42×10^{9}
Step-graded heterostructure	1.2×10^{-5}	8.13×10^{9}
Structure without LT-Si buffer layer	–	7.56×10^{9}
Structure with LT-Si buffer layer	–	$\leqslant 10^{5}$

(2 0 0) and plan-view (0 2 2) transmission electron microscopy (TEM) using a JEOL 2000-FX microscope was used for dislocation analysis. High resolution lattice imaging was also performed using a JEOL 4000-EX microscope.

3. Results and discussion

Cross-section TEM (XTEM) micrographs suggest that some amount of dislocation filtering takes place in the samples with the SPLS structure.

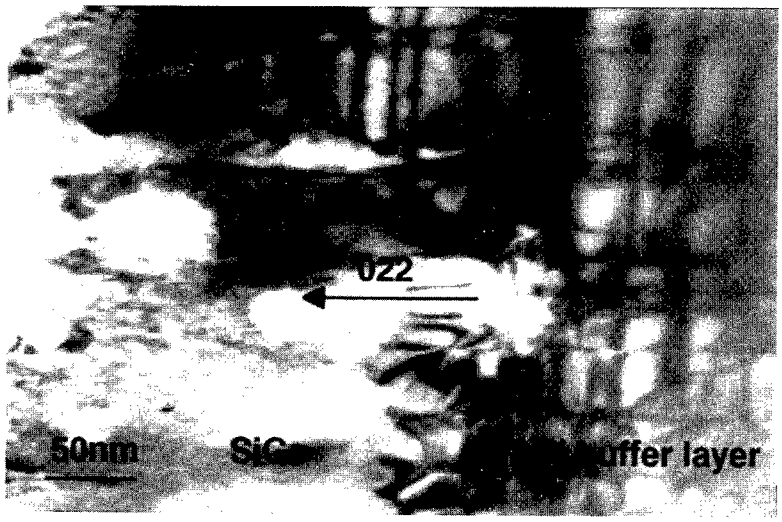

(a)

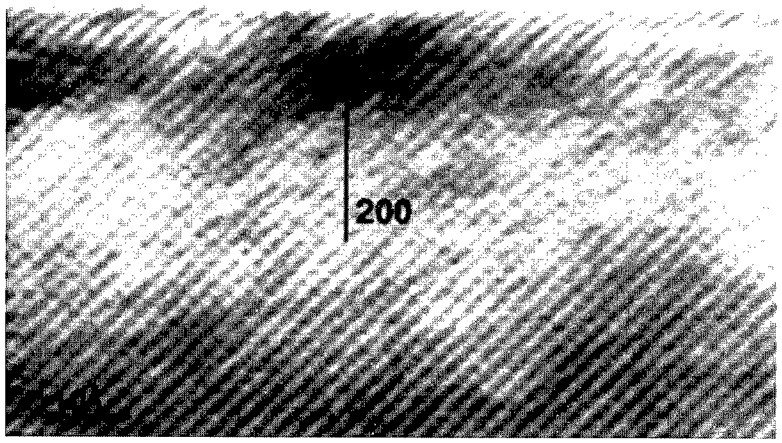

(b)

Fig. 2. (a) Bright field (0 2 2) plan-view TEM image of 0.5 μm $Si_{0.85}Ge_{0.15}$ grown on LT-Si buffer, and (b) high resolution lattice imaging of LT-Si buffer.

A comparison of the average threading dislocation density and spacing for the different types of samples, obtained from plan-view imaging, is given in Table 1. While some reduction in the threading dislocation density is obtained by using superlattice or step-graded buffer layers, it is still too high for practical applications (10^9 cm^{-2}).

XTEM micrographs of heterostructures without and with the LT-Si buffer layer, as shown in Fig. 1 and Fig. 1b, respectively, reveal that most or all of the threading dislocations are contained below the SiGe/LT-Si interface. This indicates that the threading dislocation density is at most 10^5 cm^{-2} in the $Si_{0.85}Ge_{0.15}$ layer. In the sample without the LT-Si buffer, the dislocations propagate into the alloy layer. The plan-view TEM image of the sample, shown in Fig. 2a, indicates the presence of a dislocation network at the SiGe/LT-Si interface. Lattice imaging of the LT-Si region is shown in Fig. 2b. Additionally, we have grown SiGe/Si HBTs with a relaxed 1.1 μm $Si_{0.85}Ge_{0.15}$ collector region on an LT-Si buffer-layer. There is no evidence of dislocations in the entire active region of the device. The 1.1 μm mismatched layer exceeds the critical thickness of 0.4 μm obtained from previous experimental values having the same Ge composition [15]. High performance n-channel SiGe/Si field effect transistors, exploiting the LT-Si buffer layer, are currently under investigation [16]. Both the $Si_{0.85}Ge_{0.15}$ layer and the collector region of the HBT are grown at normal substrate temperatures and both have thicknesses exceeding the critical thickness. It is, therefore, fair to assume that the alloy layers in both structures are relaxed, although it was not confirmed whether they are completely relaxed. The TEM micrographs show clear evidence of the dislocations being trapped in the LT-Si layer or being bent towards the substrate.

Double-crystal X-ray diffraction of the $Si_{0.85}Ge_{0.15}$ layer indicate a reduction in the width (FWHM) of the rocking curve corresponding to the alloy peak from 450 arc seconds to 371 arc seconds with the incorporation of the LT-Si buffer layer. Hall measurements were performed at room temperature on 1 μm $Si_{0.7}Ge_{0.3}$ layers grown with and without the LT-Si buffer layer. The samples were boron doped at $3.4 \pm 1.8 \times 10^{17}$ cm^{-3}. Ohmic contacts were made from indium dots annealed at

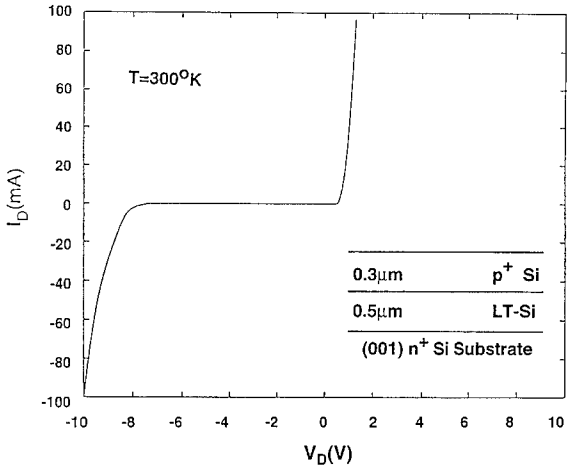

Fig. 3. Current-voltage characteristics of LT-Si diode. The diode structure is shown in the inset.

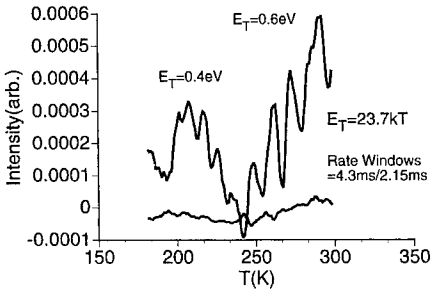

Fig. 4. DLTS spectra of LT-Si diode.

400°C for 10 min. Hole mobility improved from 160 ± 18 cm^2 V^{-1} s^{-1} to 200 ± 2.5 cm^2 V^{-1} s^{-1} by incorporating the LT-Si buffer layer. Deep level transient spectroscopy (DLTS) measurements were made on n^+(Si) -n^-(LT-Si) -p^+(Si) homojunction diodes as shown in Fig. 3. The LT-Si layer was grown at 450°C without doping and the $p^+(1 \times 10^{19}$ cm$^{-3})$ layer was grown at 570°C. Very weak DLTS signals were observed as shown in Fig. 4, signifying a very low density of deep levels. We estimate that the peaks correspond to traps with densities $\sim 10^{12}$ cm^{-3}. Accurate measurements could not be made for several rate windows. The trap activation energy, E_T, corresponding to the two peaks at 195 K and 290 K was estimated from the empirical relation, $E_T = 23.7$ kT. Using

this equation, $E_T = 0.4$ eV and 0.6 eV for the two levels was observed. The low trap density is expected in undoped epitaxial Si.

Several authors have reported the reduction of dislocation densities in InAlAs/InP, nitride and SiGe technologies using amorphous, low-temperature, and polycrystalline buffer layers [17–20]. The mechanism for threading dislocation reduction using LT-Si buffer layers is still under investigation. We believe the LT-Si layer contains a large number of defects because of the low temperature growth. Any dislocations generated from strain relaxation at the SiGe/Si interface are released in the LT-Si layer and become trapped at the defects.

4. Conclusions

In conclusion, several types of buffer layers have been studied to reduce the threading dislocation density in SiGe/Si heterostructures. A thin LT-Si buffer layer virtually eliminates any threading dislocations from propagating in the SiGe epitaxy layer. SiGe/Si n–p–n HBTs have been grown and fabricated for the first time incorporating the LT-Si buffer layers.

Acknowledgements

The authors would like to thank Dr. J. Mansfield and Hal Estry for their assistance with TEM. The work is supported by the Air Force Office of Scientific Research under Grant F49620-95-1-0013 and by an AASERT Fellowship (AFOSR) under Grant F49620-94-0404.

References

[1] K. Ismail, S.F. Nelson, J.O. Chu and B.S. Meyerson, Appl. Phys. Lett. 63 (1993) 660.
[2] K. Ismail, J.O. Chu and B.S. Meyerson, Appl. Phys. Lett. 64 (1994) 3124.
[3] A. Pruijmboom, J.W. Slotboom, D.J. Gravesteijn, C.W. Fredriksz, A.A. van Gorkum, R.A. van de Heuvel, J.M.L. van Rooij-Mulder, G. Streutker and G.F.A. van de Walle, Electron. Dev. Lett. 12 (1991) 357.
[4] K.D. Hobart, F.J. Kub, N.A. Papanicoloau, W. Kruppa and P.E. Thompson, J. Crystal Growth 157 (1995) 2115.
[5] K. Ismail, B.S. Meyerson and P.J. Wang, Appl. Phys. Lett. 58 (1991) 2117.
[6] K. Ismail, F.K. LeGoues, K.L. Saenger, M. Arafa, J.O. Chu, P.M. Mooney and B.S. Meyerson, Phys. Rev. Lett. 73 (1994) 3447.
[7] P.M. Mooney, J.L. Jordan-Sweet, J.O. Chu and F.K. LeGoues, Appl. Phys. Lett. 66 (1995) 3642.
[8] M.A. Lutz, R.M. Feenstra, F.K. LeGoues, P.M. Mooney and J.O. Chu, Appl. Phys. Lett. 66 (1995) 724.
[9] J.H. Li, V. Holy, G. Bauer, J.F. Nützel and G. Abstreiter, Appl. Phys. Lett. 67 (1995) 789.
[10] F.K. LeGoues, B.S. Meyerson and J.F. Morar, Phys. Rev. Lett. 66 (1991) 2903.
[11] R. Hull, J.C. Bean, R.E. Leibenguth and D.J. Werder, J. Appl. Phys. 65 (1989) 4723.
[12] G. Kissinger, T. Morgenstern, G. Morgenstern and H. Richter, Appl. Phys. Lett. 66 (1995) 2083.
[13] F.K. LeGoues, Phys. Rev. Lett. 72 (1994) 876.
[14] J. M. Hinckley, PhD Thesis, University of Michigan, Ann Arbor, 1990.
[15] E. Kasper, H.-J. Herzog and H. Kibbel, Appl. Phys. 8 (1975) 199.
[16] J. Welser, J.L. Hoyt and J.F. Gibbons, Electron. Dev. Lett. 15 (1994) 100.
[17] H. Chen, L.W. Guo, Q. Cui, Q. Hu, Q. Huang and J.M. Zhou, J. Appl. Phys. 79 (1996) 1167.
[18] J.M. Fernandez, J. Chen and H.H. Weider, J. Vac. Sci. Technol. A11 (1993) 889.
[19] S.D. Kim, J.A. Trezza and J.S. Harris, J. Vac. Sci. Technol. B 13 (1996) 1526.
[20] E. Scheid, L.K. Kouassi, R. Henda, J. Samitier and J.R. Morante, Mater. Sci. Eng. B 17 (1993) 185.

ELSEVIER

Journal of Crystal Growth 175/176 (1997) 504–508

JOURNAL OF CRYSTAL GROWTH

Hybrid MBE growth and mobility limiting factors of *n*-channel Si/SiGe modulation-doped systems

A. Yutani*, Y. Shiraki

RCAST, The University of Tokyo, 4-6-1 Komaba, Meguro-Ku, Tokyo 153, Japan

Abstract

We studied a novel MBE technique for growing strained-Si relaxed $Si_{0.8}Ge_{0.2}$ *n*-channel modulation-doped structures and found evidence for the interface roughness scattering in this system for the first time. Combination of gas-source MBE and solid-source MBE provided high quality modulation-doped structures with mobility of 50 000 $cm^2/V\,s$ and carrier density of $3 \times 10^{11}/cm^2$ at 25 K. The systematic study of the well-width dependence of the mobility clarified that the mobility is determined by the interface roughness when the thickness is in the range of 10–50 Å.

PACS: 73.50; 73.61

Keywords: Si; SiGe; Modulation-doped systems; Regrowth; Interface roughness

1. Introduction

Strained silicon/relaxed silicon–germanium (Si/SiGe) heterostructures are attracting a great deal of interest as Si-based novel materials used for high-speed *n*-channel modulation-doped (MOD) field-effect transistors (FETs) and mobilities up to 3000 $cm^2/V\,s$ at room temperature [1] and 500 000 $cm^2/V\,s$ at 0.4 K [2] have been reported so far. For growing such MOD structures, MBE is widely used owing to its high controllability. However, several problems are pointed out with respect to the integrity of structures fabricated by MBE. In the case of gas-source MBE (GSMBE) which generally provides high crystallinity, the memory effect of the dopant gas causes introduction of unintentional ionized impurities into the channel, resulting in a reduction of the mobility. On the other hand, solid-source MBE (SSMBE) possesses high doping controllability but provides relatively poor crystallinity, and the Ge and dopant atoms are known to segregate to the surface. To avoid these problems, we propose the combination of these two MBE methods, i.e., channel regions are grown by GSMBE and the carrier supply layers on the channel are grown by SSMBE.

In addition, although the well-known "graded buffer" technique has drastically reduced the dislocation density [3], the measured mobilities are still lower than expected [4]. This suggests that other

* Corresponding author. Fax: +81 3 3481 4509; e-mail: yutani@photonics.rcast.u-tokyo.ac.jp.

0022-0248/97/$17.00 Copyright © 1997 Elsevier Science B.V. All rights reserved
PII S0022-0248(96)01005-6

scattering processes rather than the scattering by threading dislocations dominate the mobility. In particular, interface-roughness scattering is thought to be important and Gold [5] and Monroe et al. [4] calculated mobilities limited by this scattering. However, experimental evidence of this effect has not been reported yet.

In the first part of the present paper, the combination of GSMBE and SSMBE is demonstrated to provide high-quality MOD structures. The cleaning method for regrowth and formation of δ-Sb doping layers are discussed in particular. In the second part, the influence of the interface roughness on the mobility is clarified by a systematic study on the well-width dependence of the mobility of the MOD structures.

2. Experimental procedures

Schematic structure of the samples is shown in Fig. 1. Si substrates used were p-type, (1 0 0)-oriented 5–10 Ω cm wafers. After cleaning in $H_2SO_4 : H_2O_2 = 2 : 1$ solution, they were dipped in 2.5%-HF solution to remove the oxide, and introduced immediately into the GSMBE chamber. 1.1 μm-thick graded buffer (Ge content: $0 \rightarrow 0.2$), 1 μm-thick uniform $Si_{0.8}Ge_{0.2}$ buffer, Si channel and 200 Å-thick $Si_{0.8}Ge_{0.2}$ spacer layers were successively grown. Si_2H_6 and GeH_4 were used as the source gases. The buffer layers were grown at 740°C in Sb doping experiments and at 620°C in the mobility experiments, where the latter gave better surface morphology. Channel and spacer layers were grown at 740°C in all experiments.

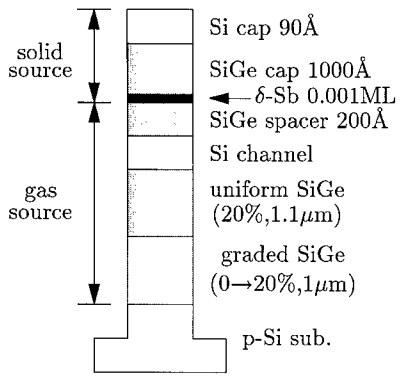

Fig. 1. Sample structure grown for the present study.

The wafers were then transferred to the solid-source MBE through the air within 5 min, and δ-Sb supply and cap layers were successively grown. The Sb dose ranged from 1 to 10^{-3} ML. In the mobility experiments the dose was set at 10^{-3} ML because, as shown later, this was optimal. The emission current of the electron gun (e-gun) for Si evaporation was kept constant during the deposition of the δ-doped layer and the substrate was always grounded. The cap layers were grown by solid-phase epitaxy (SPE), where Sb atoms as well as $Si_{0.8}Ge_{0.2}$ layers were deposited at room temperature and then annealed at 600°C for 10 min, or grown at a low temperature of 350°C to avoid Sb segregation.

3. Regrowth on gas-source MBE-grown $Si_{0.8}Ge_{0.2}$ surfaces

As mentioned, the samples prepared for this study were exposed to the air before the solid-source growth. If the surface is pure silicon, the following regrowth is known to be able to be performed without significant contaminations since the GSMBE-grown Si surface is passivated by hydrogen [6]. In the present case, however, the surface is $Si_{0.8}Ge_{0.2}$, and hydrogen passivation has not been clarified to be effective like the case of pure Si surfaces.

Fig. 2a shows the reflection high-energy electron diffraction (RHEED) pattern of an "as-loaded" sample into the SSMBE chamber. The pattern is streaky 1×1, indicating that the $Si_{0.8}Ge_{0.2}$ surface is contaminated.

It was found, however, that this contamination can be easily removed by a simple heat treatment at 700°C for 2 min in ultra-high-vacuum (UHV) as shown in Fig. 2b. The pattern is seen to change to 2×1 streaky pattern which is well known as the reconstructed clean (1 0 0) surface. Once this pattern appeared, it did not change during the successive growth. According to this result, all the samples were heated at 700°C for 15 min in the following experiments.

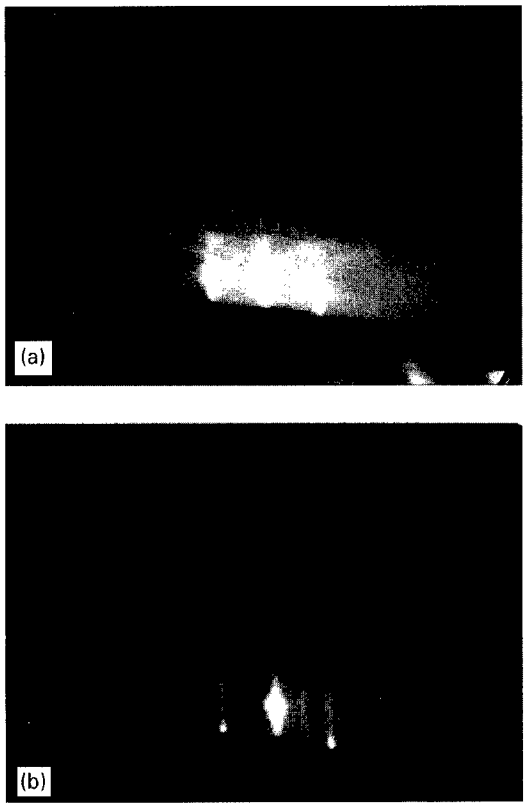

Fig. 2. RHEED images of the regrowth surface. (a) the pattern of "as-loaded" surface, (b) the pattern after a heating treatment at 700 °C for 2 min.

Fig. 3 shows the δ-Sb dose dependence of the mobility and the carrier density measured at 77 K, where channel width was fixed at 200 Å. It is seen that the carrier density decreases and the mobility increases with decreasing Sb dose. When the e-gun is on, the mobility shows the highest value of $\sim 18\,000\ \mathrm{cm^2/V\,s}$ around 10^{-3} ML, but the electron gas was not formed below 10^{-3} ML.

It is remarkable in this figure that the carrier density with e-gun on is larger than that of the e-gun off case, showing that the e-gun significantly affects the doping efficiency even though Si is not evaporated. Delage et al. observed an increase of carrier density with the electron irradiation and indicated that the molecule cracking effect due to the electrons enhanced the dopant incorporation [7]. It is well known that stray electrons are irradiated on the growing surface even if the Si flux is

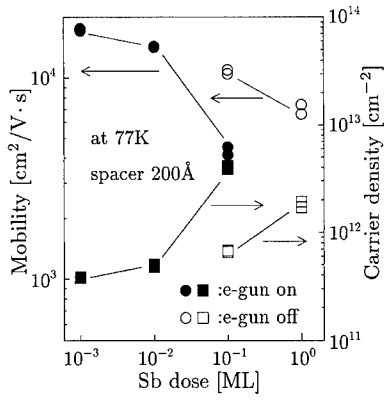

Fig. 3. Sb dose dependence of the mobility and carrier density.

shut and, therefore, the stray electrons may enhance cracking reaction of Sb_4 molecules and increase the carrier concentration.

4. Transport properties: influence of the interface roughness

The temperature dependence of the mobility of $Si_{0.8}Ge_{0.2}$ structures is shown in Fig. 4, where δ-Sb dose is fixed at the optimal value of 0.001 ML and the channel width, W, was varied from 200 to 13 Å. It is seen that the mobility decreases with decreasing channel width. When W is thicker than 53 Å, the mobility monotonically increases with decreasing temperature. On the other hand, when W is thinner than 40 Å, the mobility shows a peak and then decreases with decreasing temperature.

The maximum mobility of $50\,000\ \mathrm{cm^2/V\,s}$ is obtained at 25 K while the carrier density is about $3 \times 10^{11}/\mathrm{cm^2}$, indicating that the growth method employed here provides high-quality MOD structures.

The strong dependence of the mobility on the well width suggests that the interface roughness scattering is important in this system. In order to estimate the temperature dependence of the mobility limited by this scattering, calculations were performed using Matrix element deduced by Sakaki et al. [8] and screening factors derived by Stern [9, 10] and Maldague [11]. The results are shown in Fig. 5, where it is seen that the calculation well

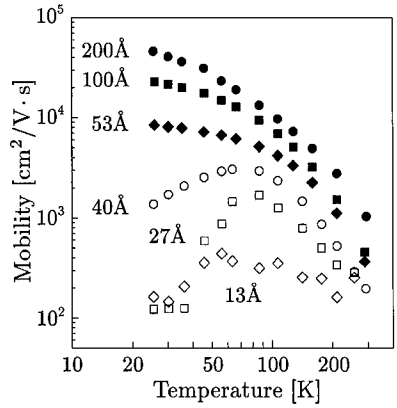

Fig. 4. Temperature dependence of the Hall mobility.

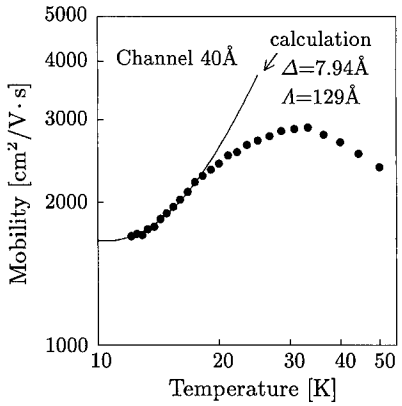

Fig. 5. Measured mobility and calculated interface-roughness-limited mobility of a 40 Å sample.

reproduces the measured data at low temperatures. By fitting parameters to several samples,vertical mean roughness, Δ, and lateral correlation length, Λ, were found to be 6.5–8.0 and 120–130 Å, respectively. These parameters are different from Feenstra et al.'s recent results obtained by atomic force microscope (AFM) [12]. This may be due to the different growth condition of their samples.

It should be noted that the Hall voltage of the samples with extremely narrow well width showed a drastic drop and large fluctuation at low temperatures, suggesting that the electrons are localized in this temperature range. It was also found that the conductivity of these samples follows the $T^{-1/3}$ dependence rather than the activation-type temperature dependence. This indicates that two-dimensional variable range hopping governs the conduction in these samples with extremely thin channels.

5. Conclusion

Strained Si/relaxed SiGe modulation-doped structures were grown by "hybrid MBE", namely, a combination of gas-source MBE and solid-source MBE, and experimental evidence of the interface roughness scattering was observed for the first time. This novel MBE technique provided samples with mobilities up to 50 000 $cm^2/V\,s$ and carrier densities of $\sim 3\times10^{11}/cm^2$ at 25 K, which indicates that this method is extremely promising to fabricate various types of high-quality SiGe/Si heterostructures. Systematic study on the channel width dependence of the electrical properties revealed that the mobility of this system is governed by the surface roughness when the channel thickness is in the range of 10–50 Å.

Acknowledgements

The authors would like to thank Dr. K. Nakagawa and N. Usami for fruitful discussions, and S. Ohtake for technical supports. A part of this work was supported by a Grant-in-Aid for Scientific Research on Priority Area, "Ultimate Integration of Intelligence on Silicon Electronic Systems", from the Ministry of Education, Science and Culture.

References

[1] S.F. Nelson, K. Ismail, J.O. Chu and B.S. Meyerson, Appl. Phys. Lett. 63 (1993) 367.
[2] K. Ismail, M. Arafa, F. Stern, J.O. Chu and B.S. Meyerson, Phys. Rev. Lett. 73 (1995) 3447.
[3] B.S. Meyerson, K.J. Uram and F.K. LeGoues, Appl. Phys. Lett. 53 (1988) 2555.
[4] D. Monroe, Y.H. Xie, E.A. Fitzgerald, P.J. Silverman and G.P. Watson, J. Vac. Sci. Technol. B 11 (1993) 1731.

[5] A. Gold, Phys. Rev. B 35 (1987) 723.
[6] Y. Kato, S. Fukatsu, N. Usami and Y. Shiraki, Appl. Phys. Lett. 63 (1993) 2414.
[7] S. Delage, Y. Campidelli, F. Arnaud d'Avitaya and S. Tatarenko, J. Appl. Phys. 61 (1987) 1404.
[8] H. Sakaki, T. Noda, K. Hirakawa, M. Tanaka and T. Matsusue, Appl. Phys. Lett. 51 (1987) 1934.
[9] F. Stern, Phys. Rev. Lett. 18 (1967) 546.
[10] T. Ando, A.B. Fowler and F. Stern, Rev. Mod. Phys. 54 (1982) 437.
[11] P.F. Maldague, Surf. Sci. 73 (1978) 296.
[12] R.M. Feenstra, M.A. Lutz, F. Stern, K. Ismail, P.M. Mooney, F.K. LeGoues, C. Stanis, J.O. Chu and B.S. Meyerson, J. Vac. Sci. Technol. 13 (1995) 1608.

ELSEVIER

Journal of Crystal Growth 175/176 (1997) 509–513

JOURNAL OF CRYSTAL GROWTH

Effect of Hydrogen on the growth kinetics of Si(0 0 1) during GSMBE from disilane

Kazuki Mizushima[a,*,1], Dimitri D. Vvedensky[a], Pavel Šmilauer[b], Andrew Zangwill[c], Jing Zhang[d], Bruce A. Joyce[d]

[a] *The Blackett Laboratory, Imperial College, London SW7 2BZ, UK*
[b] *HRLZ, KFA Jülich, D-52425 Jülich, Germany*
[c] *School of Physics, Georgia Institute of Technology, Atlanta, Georgia 30332, USA*
[d] *Interdisciplinary Research Centre for Semiconductor Materials, Imperial College, London SW7 2BZ, UK*

Abstract

The effects of hydrogen on the growth kinetics of Si(0 0 1) during gas-source molecular-beam epitaxy from disilane are investigated with kinetic Monte Carlo simulations. The growth model includes the surface decomposition of disilane, which requires four mobile and reactive surface species: Si, H, SiH_2 and SiH_3. Based on recent reflectance anisotropy measurements, the desorption of hydrogen is presumed to occur preferentially from step edges. Below approximately 400°C (where the model allows surface reactions to occur) the accumulation of surface hydrogen is found to prevent growth, but for temperatures above 600°C, where the surface lifetime of the hydrogen is relatively short, we find no significant differences in the overall growth features in comparison with a solid-source (no hydrogen) growth model of Si(0 0 1). At intermediate temperatures, where surface hydrogen atoms are present but do not prevent growth, we find a higher density of smaller islands and rougher propagating step edges in comparison with those of the solid-source model. Anisotropic morphological features, which are characteristic signatures in the solid-source model, are suppressed by the surface hydrogen atoms in the gas-source model.

PACS: 68.45.Da; 81.05.Cy; 81.10.Aj; 81.15.Hi

Keywords: Hydrogen; Silicon surface; Growth kinetics; Monte Carlo simulation

1. Introduction

The growth kinetics of silicon during gas-source molecular-beam epitaxy (GSMBE) from hydride sources such as silane (SiH_4) and disilane (Si_2H_6) are considerably more complex than those during solid-source molecular-beam epitaxy (MBE) because the surface chemical reactions produce several mobile and reactive species, including hydrogen [1, 2]. Several studies have addressed the effect of surface reactions and the presence of hydrogen on the growth rate [1, 3–7], but there have been comparatively few investigations of the

* Corresponding author.
[1] Permanent address: Central Research Institute, Mitsubishi Materials Corporation, 1-297 Kitabukuro-cho, Omiya, Saitama 330, Japan.

0022-0248/97/$17.00 Copyright © 1997 Elsevier Science B.V. All rights reserved
PII S0022-0248(96)00990-6

surface morphology [5, 8, 9]. Most studies are based on reaction sequences that release silicon and hydrogen from the precursors, but exclude surface migration and the site-specific interactions that are required to model surface morphology.

In this paper we will describe a new kinetic Monte Carlo model for the GSMBE of Si(0 0 1) that includes a decomposition pathway of disilane together with the migration and reaction kinetics of the pertinent surface species. The model is then applied to investigate the morphological differences of the growing surfaces in comparison with that of a solid-source (no hydrogen) model for the epitaxial growth of singular and vicinal Si(0 0 1) surfaces.

2. Kinectic Monte Carlo model

A kinetic Monte Carlo (KMC) model for the growth kinetics of Si(0 0 1) during GSMBE from disilane requires a reaction sequence which releases the Si and H atoms from the precursor. In some cases, such as the decomposition pathways of disilane, more than one mechanism has been identified in the literature [8] and more than one mechanism might be important in the overall decomposition rate, depending on the growth conditions. In our KMC model, we have assumed one primary pathway for the overall reaction:

$$Si_2H_6(gas) + 2Si^* \rightarrow 2SiH_3, \quad (1)$$

$$SiH_3 + Si^* \rightarrow SiH_2 + H, \quad (2)$$

$$2SiH_2 \rightarrow H - Si - Si - H + H_2\uparrow, \quad (3)$$

$$2H \rightarrow 2Si^* + H_2\uparrow, \quad (4)$$

where Si* denotes a Si-terminated surface site and the upward arrow denotes desorbed H_2. The growth kinetics are modeled with the four species appearing in these reactions (Si, H, SiH_2 and SiH_3) and includes the reactions (1)–(4), the anisotropic diffusion of each species, different sticking energies for *A* and *B* (single-atomic-height) step edges [10], and the effects of dimerization.

The substrate is assumed to have a simple cubic structure with neither vacancies nor overhangs (the solid-on-solid criterion [11]). The reaction sequence above is implemented as follows. Reaction (1): Growth is initiated by the random adsorption of Si_2H_6 at a rate determined by the flux. Two adjacent Si-terminated sites are required for Si_2H_6 to adsorb dissociatively as two SiH_3 fragments. Thus, the *arrival rate* at a given Si-terminated lattice site is proportional both to the flux and the number of its Si-terminated nearest neighbors. Reaction (2): If there is a nearest-neighbor Si-terminated site, the SiH_3 groups instantaneously [8] decompose into SiH_2 and H. Reaction (3): Two nearest-neighbor SiH_2 groups instantaneously transform into a hydride structure, indicated by H–Si–Si–H, while the other two H atoms desorb to the gas phase (as H_2). We assume that this hydride decomposes instantaneously into Si and H, so that there are no individual mobile monohydride species (SiH) in our model.

The desorption of hydrogen in Reaction (4) is modelled by appealing to recent reflectance anisotropy measurements [12], which show that the desorption kinetics follow a *zeroth-order* dependence on hydrogen coverage, in contrast to the widely accepted *first-order* dependence obtained mostly from singular (0 0 1) surfaces. The *zeroth-order* kinetics suggest the preferential desorption of hydrogen from pre-existing sites, in this case step edges, and that the surface diffusion of hydrogen to these sites is not the rate limiting step of the desorption process [13]. We assume that the H atoms located either at a step edge or at a nearest-neighbor site to a H atom at a step edge stay at these sites and form a precursor state prior to desorption. This rule produces an effective lateral interaction between H and Si step edges (see below). We have used an energy barrier for molecular desorption from this precursor state of 1.0 eV [14].

The reaction scheme (1)–(4) must be supplemented by the migration kinetics of the surface species produced by the reactions. The migration of each surface species is taken as a nearest-neighbor hopping process whose rate is given by $k(T) = k_0 \exp(-E_D/k_BT)$, where k_0 corresponds to an adatom vibrational frequency ($k_0 = 2k_BT/h$), E_D is the hopping barrier, T is the substrate temperature, k_B is Boltzmann's constant, and h is Planck's constant. The hopping barrier is comprised of a term from the substrate, E_S, and contributions from lateral nearest neighbors, $E_{N\|}$ and

$E_{N\perp}$, where $\parallel$ and $\perp$ indicate the directions that are parallel and perpendicular to dimer rows in the same layer, respectively. Hopping is permitted only onto Si-terminated sites.

For the surface migration of atomic H, we use values of E_S of 1.8 and 1.3 eV, respectively, for hopping parallel and perpendicular to the *underlying* dimer rows [15]. However, to avoid the proliferation of parameters, we use one value of E_S for Si, SiH_3 and SiH_2, which we take to be that for Si, $E_S = 1.0$ eV [16, 17], although, in fact, the surface migration of the radicals is generally expected to be faster than adatoms [18]. The anisotropic lateral interactions between migrating Si atoms are assigned the values $E_{N\parallel} = 0.5$ eV and $E_{N\perp} = 0.1$ eV. There is no lateral interaction between individual H and Si *adatoms*, but there is an effective lateral interaction between H and Si step edges, as described above.

The effect of dimers is taken into account with an additional barrier energy for the hopping of a Si atom which is initially part of a dimer. The value of this barrier is taken as $E_{dimer} = 0.85$ eV and, for simplicity, the alignment of dimer rows is prescribed by an odd–even rule similar to that used by Elswijk et al. [19]. The breaking of an underlying Si dimer by Si adatoms is taken into account by removing the contribution of E_{dimer}. Thus, the total hopping barrier of a Si adatom is given by $E_D = E_S + n_{\parallel}E_{N\parallel} + n_{\perp}E_{N\perp} + E_{dimer}$, where $n_{\parallel}$ and $n_{\perp}$ denote the numbers of lateral Si neighbor atoms parallel and perpendicular to dimer rows in the same layer, respectively.

The simulations reported in the next section were carried out on 200×200 lattices with a flux of 1 ML/s. The simulations were monitored by following the evolutions of the step density, relative domain coverage, the surface coverage of each surface species, as well as direct imaging of the surface morphology. In this paper, we will focus only on the latter two indicators and reserve a more detailed discussion of our results for a future publication.

3. Results and discussion

Fig. 1 shows the surface coverages of each species during growth at 400°C together with the concentration of Si-terminated sites on the terrace and at the step edges. The accumulation of SiH_2 and SiH_3 is not significant at this temperature nor even over the temperature range 300–600°C, since the model requires only that sites be available for the decomposition to occur. The reactions can, of course, be refined to include a temperature-dependence in the decomposition rate. Fig. 1 indicates that the accumulation of hydrogen on the surface increases with time until all terrace and step-edge sites are saturated, which prevents further growth. Thus, in this temperature/flux regime, the rate-limiting step for surface growth is the desorption of hydrogen, as expected.

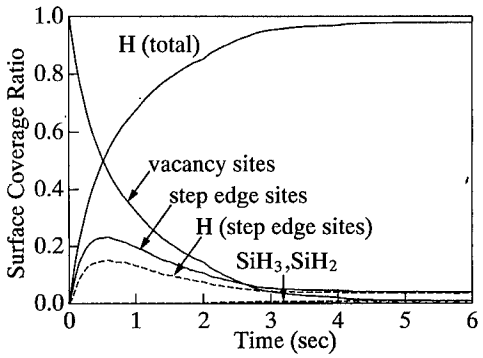

Fig. 1. The surface coverages of each species during growth at 400° and the concentration of Si-terminated sites on the terrace and at the step edges, with both of the latter showing the accumulation of hydrogen.

From the standpoint of understanding the effect of hydrogen kinetics on the growth of Si(0 0 1), the most interesting temperature range in this study is 500–600°C. There is a small amount of hydrogen present on the surface but growth still proceeds in a layer-by-layer manner (as indicated by oscillations in the step density). The morphologies of singular and vicinal surfaces produced by our GSMBE model are shown for comparison with those produced by a solid-source MBE model under the same growth conditions in Fig. 2. We consider the singular surfaces first. The morphologies produced by the solid-source MBE model exhibit the usual highly anisotropic islands extending along the direction of the dimer row [20, 21]. The corresponding morphologies produced by the

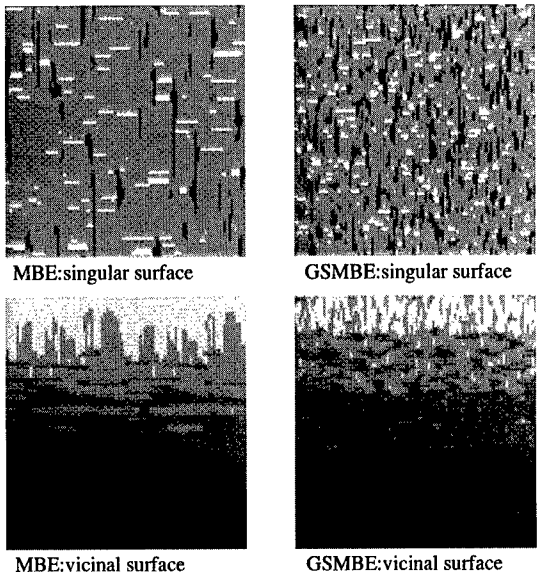

Fig. 2. Morphologies of surfaces after 1 s of growth at 550°C on singular and vicinal surfaces with the GSMBE and solid-source MBE models.

GSMBE model are different from these in two important respects: there is a larger number of smaller clusters and these clusters are not as anisotropic as in the solid-source MBE morphology. Both of these features are in qualitative agreement with the scanning tunnelling microscopy measurements of Vasek et al. [9]. We conclude from these morphologies that one important effect of the hydrogen is to block the growth front, i.e., the *B*-type step edges, which thereby increases the adatom density on the terraces which, in turn increases the likelihood of additional islands forming.

The morphology produced by the solid-source MBE model for vicinal Si(0 0 1) shows the characteristic alternation between roughness and smoothness of the step edges due to the alternating dimer orientation at these step edges [10]. This has a marked effect on the growth of the surface, with growth occuring preferentially at *B* steps [20, 21], and suggests that the attachment rate is larger in the direction perpendicular to the dimer bond axis [22]. Comparing this morphology with that produced by the GSMBE model shows that both types of step edges are rougher than in the solid-source MBE morphology and that the anisotropy of the surface features has again been reduced by the presence of the hydrogen. Thus, one of the main effects of the hydrogen is again seen to be preferential adsorption at step edges. This inhibits the propagation of steps by reducing the attachment of migrating Si atoms, which therefore increases the Si adatom concentration on the terraces.

To examine these conclusions in more detail, we performed additional simulations in which hydrogen atoms were in turn placed selectively at *A* and *B* steps. At a temperature of 550°C no distinguishable differences were found between the morphologies obtained with this procedure and those obtained with the GSMBE model. At lower temperatures, the density of islands was increased in both cases, but with the hydrogens reducing the attachment rate of Si at *B* steps, the anisotropy of the islands was correspondingly reduced. Thus, in light of the experiments of Vasek et al. [9], we conclude that the site-blocking at *B* step edges is one important effect of hydrogen on the morphology of Si(0 0 1) during GSMBE from silane or disilane.

Acknowledgements

We thank J.M. Fernández and A. Lees for helpful discussions. K.M. is grateful for the help of T. Kawamura. This work was supported in part by a NATO Collaborative Research Grant.

References

[1] S.M. Gates, C.M. Greenlief, S.K. Kulkarni and H.H. Sawin, J. Vac. Sci. Technol. A 8 (1990) 2965.
[2] Y. Suda, D. Lubben, T. Motooka and J.E. Greene, J. Vac. Sci. Technol. A 8 (1990) 61.
[3] S.M. Gates and S.K. Kulkarni, Appl. Phys. Lett. 58 (1991) 2963.
[4] S.M. Gates and S.K. Kulkarni, Appl. Phys. Lett. 60 (1992) 53.
[5] S.M. Mokler, W.K. Liu, N. Ohtani, J. Zhang and B.A. Joyce, Surf. Sci. 275 (1992) 16.
[6] S.M. Mokler, N. Ohtani, J. Zhang and B.A. Joyce, Surf. Sci. 275 (1992) 401.
[7] W.K. Liu, S.M. Mokler, N. Ohtani, C. Roberts and B.A. Joyce, Surf. Sci. 264 (1992) 301.

[8] Y. Wang, M.J. Bronikowski and R.J. Hamers, Surf. Sci. 311 (1994) 64.
[9] J.E. Vasek, Z. Zhang, C.T. Salling and M.G. Lagally, Phys. Rev. B 51 (1995) 17207.
[10] D.J. Chadi, Phys. Rev. Lett. 59 (1987) 1691.
[11] J.D. Weeks and G.H. Gilmer, Adv. Chem. Phys. 40 (1979) 157.
[12] J. Zhang, A.K. Lees, A.G. Taylor, M.H. Xie, D. Raisbeck, B.A. Joyce, Z. Sobiesierski and D.I. Westwood, to be published.
[13] There is some, albeit indirect, evidence for the recombinative desorption of H_2 from step edges on Si(0 0 1) from a scanning tunneling microscopy study of the pyrolysis of Si_2H_6 on Si(0 0 1) [8], which show a significantly reduced surface hydrogen concentration in the vicinity of step edges.
[14] This desorption barrier is somewhat lower than the value of ≈ 2.0 eV typically quoted. It must be borne in mind, however, that in models such as this we first estimate the relative rates of reactions before attempting the more ambitious task of obtaining absolute rates by comparisons with experiments. The 1.0 eV barrier is required to obtained appreciable desorption and might be a reflection of the fact the barriers for some of the other rates are incorrect in absolute terms.
[15] A. Vittadini, A. Selloni and M. Casarin, Surf. Sci. 289 (1993) L625.
[16] Y.-W. Mo, J. Kleiner, M.B. Webb and M.G. Lagally, Phys. Rev. Lett. 66 (1991) 1998.
[17] G. Brocks, P.J. Kelly and R. Car, Phys. Rev. Lett. 66 (1991) 1729.
[18] T. Shitara, T. Kaneko and D.D. Vvedensky, Appl. Phys. Lett. 63 (1993) 3321.
[19] H.B. Elswijk, A.J. Hoeven, E.J. van Loenen and D. Dijkkamp, J. Vac. Sci. Technol. B 9 (1991) 451.
[20] A.J. Hoeven, J.M. Lenssinck, D. Dijkkamp, E.J. van Loenen and J. Dieleman, Phys. Rev. Lett. 63 (1989) 1830.
[21] Y.-W. Mo, B.S. Swartzentruber, R. Kariotis, M.B. Webb and M.G. Lagally, Phys. Rev. Lett. 63 (1989) 2393.
[22] C. Pearson, M. Krueger and E. Ganz, Phys. Rev. Lett. 76 (1996) 2306.

ELSEVIER

Journal of Crystal Growth 175/176 (1997) 514–518

JOURNAL OF CRYSTAL GROWTH

Visible light emission from MBD-grown Si/SiO_2 superlattices

S.V. Novikov[a,*], J. Sinkkonen[a], O. Kilpelä[a], S.V. Gastev[b]

[a] *Electron Physics Laboratory, Helsinki University of Technology, Otakaari 7A, FIN-02150 Espoo, Finland*
[b] *A.F.Ioffe Institute, 194021 St. Petersburg, Russian Federation*

Abstract

Si/SiO_2 superlattices were grown by MBD using in situ oxidation by RF-plasma source. Room temperature photoluminescence (PL) was observed in the spectral range 1.9–2.3 eV. PL spectra show blueshifts due to the quantum confinement of the energy states in ultrathin silicon layers.

PACS: 68.65. + g; 78.66.Jg

Keywords: Si; SiO_2; MBE; Superlattices; Photoluminescence

Silicon-based, light-emitting devices (LEDs) are very attractive for optoelectronic applications. For example, the integration of silicon LEDs with silicon microelectronics could lead to reliable and inexpensive optical displays and optical interconnections. Until recently, however, it has not been possible to obtain efficient room-temperature luminescence from silicon. The discovery of the bright luminescence from electrochemically etched porous silicon [1] has increased research efforts aimed at fabricating efficient silicon-based LEDs. Because the emission wavelength does not show the size dependence typical of quantum confinement, the most recent model for this luminescence supposes the existence of oxygen-related surface localized defects which take part in the light emission [2]. Recently, the luminescence from Si/SiO_2 superlattices, grown by ex situ oxidation of thin Si layers, was reported [3]. In this case a strong dependence of the band gap and the emission wavelength on the Si layer thickness was observed, indicating the quantum confinement effect in this structure. However ex situ oxidation does not take full advantage of MBDs capability for ultra-clean processing, due to the possible contamination of the surface during the exposure of the sample to the atmosphere. Here we report the fabrication of fully in situ molecular-beam deposition (MBD) grown Si/SiO_2 superlattices, which have luminescence in the visible range. Using in situ RF-plasma source for oxidation allows one to eliminate the waiting time for loading the wafers into the deposition chamber after ex situ oxidation. It also offers more precisely controlled conditions for the oxide growth.

* Corresponding author. Fax: +358 0 460 224; e-mail: novikov@elfys4.hut.fi.

0022-0248/97/$17.00 Copyright © 1997 Elsevier Science B.V. All rights reserved
PII S0022-0248(96)00915-3

A modified VG Semicon V80M molecular beam epitaxy (MBE) system is used for the growth of the Si/SiO_2 superlattices. A plasma activated gas cell (Oxford Applied Research MPD-21) is used as the oxygen source. One-fourth of the 76 mm diameter (1 0 0)-oriented silicon wafer is cleaned using Si beam-assisted thermal desorbtion of the native SiO_2 layer after standard chemical treatment [4]. This cleaning procedure allows one to obtain a very smooth surface. The surface roughness as measured by atomic force microscopy (AFM) is less than 2 nm at 1 μm scan. The Si surface is oxidized at room temperature. Oxygen mass flow rate during the oxidation is 4.0 sccm which roughly corresponds to a pressure of 3×10^{-5} mbar inside the growth chamber. Typical power input to the RF-coil is 260 W. The growth time is 10 min which results in a SiO_2 thickness of 1.0 nm. Amorphous silicon layers, of thickness ranging from 1.5 to 6.0 nm, are deposited at room temperature with a growth rate of 0.07 nm/s. Part of the samples are grown with an additional flux of H-atoms during the Si deposition for passivation of dangling bonds in amorphous silicon. This flux is generated by the RF-plasma source with a typical H_2 flow rate 5.0 sccm and RF-power input of 400 W. The samples for transmission measurements are grown on the fused silica substrate. The samples have been characterized using ellipsometry, RHEED, transmission electron microscopy (TEM), AFM, X-ray diffraction (XRD), photoluminescence (PL) and transmission spectroscopy.

The cross-sectional TEM image using Jeol 2010 200 kV microscope taken of a six-period Si/SiO_2 superlattice with Si layer thickness 4 nm and SiO_2 thickness 1.0 nm is shown in Fig. 1. The Si and SiO_2 layers are white and dark regions, respectively. The layers are smooth and uniform in their thickness. The interface between Si and SiO_2 is abrupt.

The optical band gap is determined from optical absorption $\alpha(h\nu)$ data using the extrapolation of $(\alpha h\nu)^{1/2}$ from $h\nu$ to zero-ordinate i.e. the constant-n form of the Tauc law [5]:

$$(\alpha n h\nu)^{1/2} = \text{const.}(h\nu - E_g). \quad (1)$$

In Fig. 2 the absorption spectra in $(\alpha h\nu)^{1/2} - h\nu$ coordinates are shown. According to Ref. [3], the

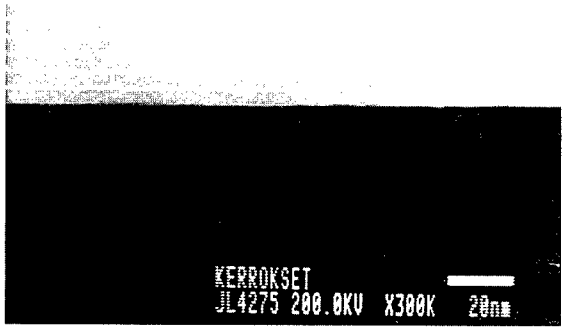

Fig. 1. Cross-sectional bright field transmission electron micrograph of the superlattice which consists of 6 Si layers (dark bands) and 7 SiO_2 layers (light bands).

energy gap E for one-dimensionally (1D) confined Si is given by

$$E(\text{eV}) = 1.60 + 0.72d^{-2}, \quad (2)$$

where d is the amorphous silicon layer thickness in nm. However, the absorption edge position for samples grown on fused silica substrates. (Figs. 2 and 3) is in good agreement with the formula

$$E(\text{eV}) = 1.12 + 0.72d^{-2}. \quad (3)$$

The value of the band gap energy (1.12 eV) in this case corresponds to crystalline silicon. So probably we have polycrystalline or nanocrystalline silicon layers in the superlattice, although XRD and RHEED show diffuse halo image, which is typical of the amorphous film. TEM image with atomic resolution (Fig. 4) also does not show any crystalline particles inside silicon films.

The room temperature PL spectra of superlattices are measured using the 488 nm (2.5 eV) line of argon laser excitation, a double monochromator and a photomultiplier. The PL peak energy position in our case is considerably higher than those reported in Ref. [3] (Fig. 3). An additional difference from Ref. [3] is that we have found a broad PL peak at 650 nm (1.9 eV) in the thickness range $d = 3$–6 nm (Fig. 5). This exceeds the value of 1.60 eV reported in Ref. [3] for thick amorphous silicon films. For thickness more than 3.0 nm, according to Eq. (2) the influence of quantum

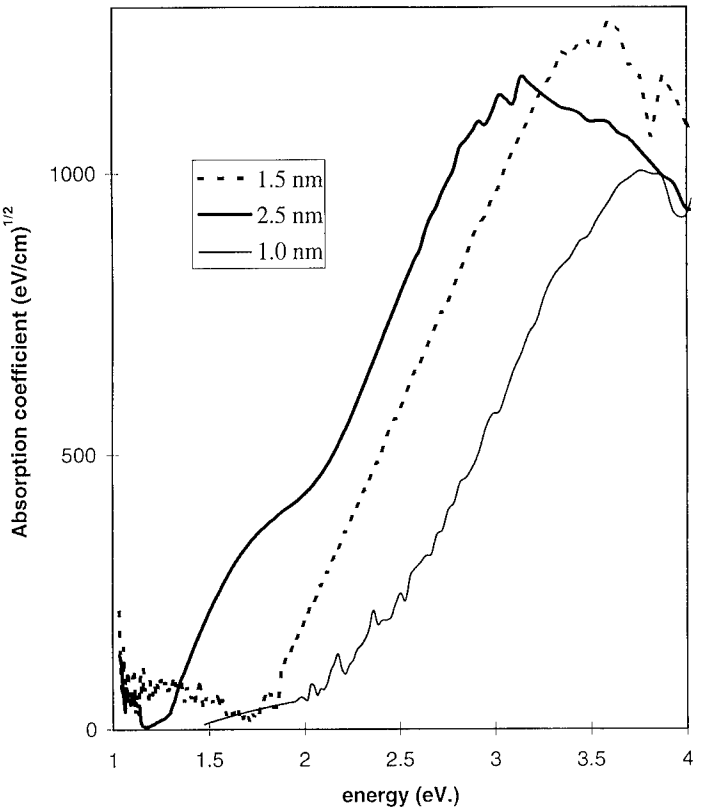

Fig. 2. Absorption spectra of the Si/SiO_2 superlattices grown on the fused silica substrate with different thickness of a-Si layers (the thickness is shown on the insert). The thickness of SiO_2 layers is 1 nm.

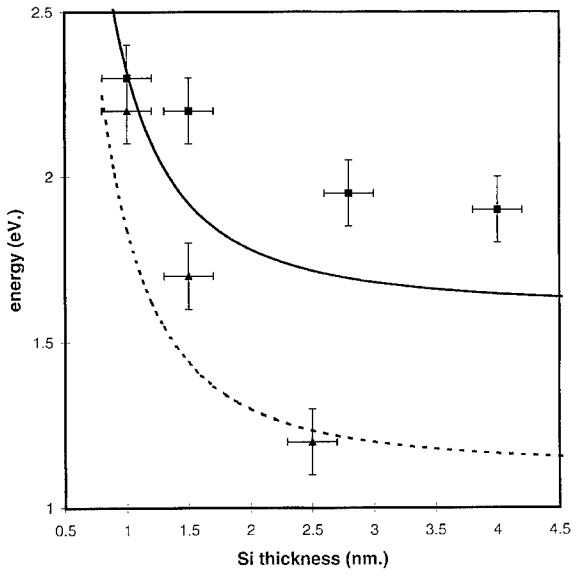

confinement on the peak energy is very weak. The intensity of PL depends on the total Si thickness in the superlattice. Thus, in this case, the luminescence is a property of the silicon layer. The increase of the luminescence energy to 1.9 eV could be explained by oxygen related defects. Our samples in difference from [3] may have a higher oxygen content in the silicon layers because the silicon growth and the oxidation were carried out in the same chamber with a 30–60 min waiting between oxidation and Si growth. In porous silicon it was reported [2, 6] that oxygen related defects such as non-bridging oxygen

Fig. 3. The photoluminescence peak energy (squares) and absorption edge energy (triangles) in Si/SiO_2 superlattices as a function of Si layer thickness. The solid and dashed lines are the fits obtained by effective mass theory with $E_g = 1.6$ and 1.12 eV, respectively.

hole centers (NBOHC) are the main source of the PL. Two forms of NBOHC exist in porous Si. The first form is stabilized by hydroxyls, such as Si–O···H–O and has been shown to red-shift with decreasing hydrogen content. The second NBOHC is Si–O· form. It has no wavelength shift due to hydrogen. Because the spectral position of the PL peak from our samples grown under a flux of H-atoms does not change, we can expect these centers to be of Si–O· form [5]. In the silicon layer thickness range 1–2 nm the luminescence peaks are more narrow and blue-shifting up to 530 nm (2.3 eV) as shown in Fig. 5. The peak energy shift is consistent with Eq. (2). Thus, we are observing quantum confinement of the energy states. The PL peaks have a long wavelength tail in the range 600–700 nm. It shows that the luminescence from defects is still existing, but its intensity reduced because the total Si thickness in this case is low.

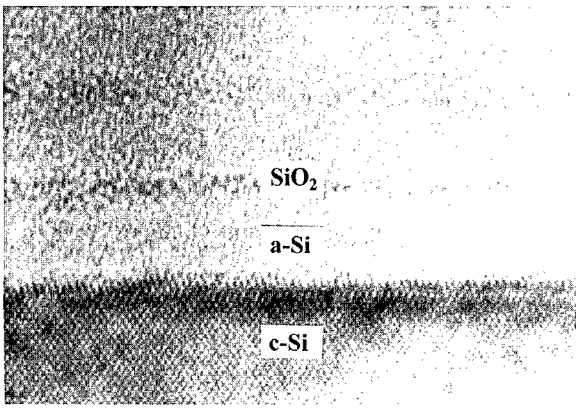

Fig. 4. High resolution transmission electron micrograph of the a-Si/SiO_2 superlattice on c-Si substrate.

In conclusion, the room temperature PL in the range 540–650 nm was observed from the Si/SiO_2 superlattices grown using in situ oxidation. The oxygen-related defects in silicon is the main cause for PL from superlattices with silicon thickness

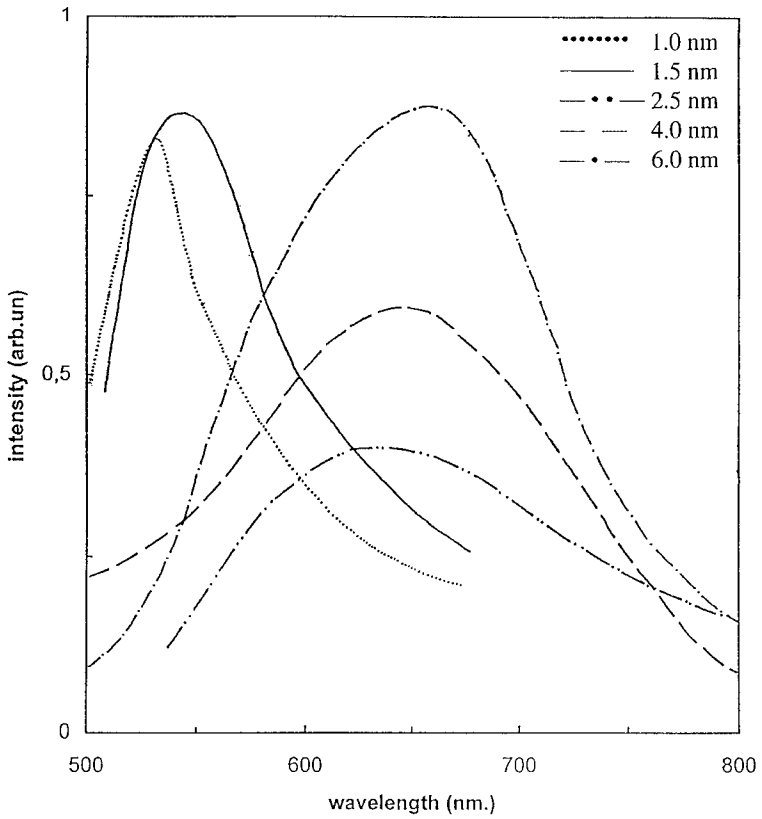

Fig. 5. Photoluminescence (PL) spectra of the Si/SiO_2 superlattices with different thickness of a-Si layers (the thickness is shown in the insert). The thickness of SiO_2 layers is 1 nm.

more than 2.0 nm. In the Si layer thickness range 1–2 nm the luminescence arises from the quantum confined energy states in the ultrathin silicon layers.

We would like to thank Dr. J. Laurila for making TEM analysis.

References

[1] L.T. Canham, Appl. Phys. Lett. 57 (1990) 1046.
[2] L.N. Skuja and A.R. Silin, Phys. Status Solidi (a) 56 (1979) K11.
[3] Z.H. Lu, D.J. Lockwood and J.-M. Baribeau, Phys. Rev. Lett. 76 (1996) 539.
[4] J. Lundsgaard Hansen, S.Yu. Shiryaev and E.V. Thomsen, J. Crystal Growth 157 (1995) 317.
[5] T. Tiedje, B. Abeles, P.D. Persans, B.G. Brooks and G.D. Cody, J. Non-Cryst. Solids 66 (1984) 345.
[6] S.M. Prokes, IEEE J. Selected Topics Quantum Electron 1 (1995) 1140.

ELSEVIER

Journal of Crystal Growth 175/176 (1997) 519–523

JOURNAL OF CRYSTAL GROWTH

Luminescence study on Ge islands as stressors on $Si_{1-x}Ge_x/Si$ quantum well

E.S. Kim[a,*], N. Usami[a], H. Sunamura[a], S. Fukatsu[b], Y. Shiraki[a]

[a] *Research Center for Advanced Science and Technology (RCAST), The University of Tokyo, 4-6-1 Komaba, Meguro-ku, Tokyo 153, Japan*
[b] *Department of Pure and Applied Sciences, The University of Tokyo, 3-8-1 Komaba, Meguro-ku, Tokyo 153, Japan*

Abstract

Photoluminescence (PL) study on lateral bandgap modulation in a $Si_{1-x}Ge_x/Si$ quantum well induced by self-assembled Ge islands which act as stressors is carried out. It is confirmed that excitons are confined in the modulated quantum structure (MQS) in compressively strained regions induced by the Ge islands. Redshift of PL peaks from MQSs does not show a monotonic change but complicated behavior, i.e., it increases up to $Q = 3.7$ ML and saturates above $Q = 4.1$ ML after once retrogressing with the increase in the Ge coverage. The results are explained in terms of elastic deformation due to Ge stressors and lattice relaxation in the Ge islands.

PACS: 78.55.Ap; 68.65. + g

Keywords: SiGe; Photoluminescence; Self-assembled islands; Lateral bandgap modulation; Stressor

1. Introduction

In SiGe/Si heterostructures, which are now being extensivly studied aiming at making a breakthrough in the present Si technology [1], strain resulting from the difference in the lattice constant between epilayers and substrates plays an important role. Quantum well (QW) and superlattice structures involving coherent strain are known to add strain-related effects to material properties [2]. On the other hand, Ge islands on Si substrates resulting from Stranski–Krastanov (SK) growth are indispensably associated with incoherent strain, i.e., an inhomogeneous strain distribution [3, 4] which brings about different effects from those of uniform strain. The inhomogeneous strain distribution generates lateral band gap modulation when Ge-rich islands are formed on Si substrates with buried QW structures [5]. The lateral band gap modulation realizes low-dimensional structures [6], and makes it possible to tailor the band structure.

In this paper, we report a photoluminescence (PL) study on the lateral confinement structures

* Corresponding author.

0022-0248/97/$17.00 Copyright © 1997 Elsevier Science B.V. All rights reserved
PII S0022-0248(96)00991-8

induced by self-assembled Ge islands which act as stressors on an underlying $Si_{1-x}Ge_x$/Si QW. The Ge layers are known to initially grow layer by layer and then grow in three-dimensional mode leading to the formation of the self-assembled islands as Ge coverage increases [3, 7]. This growth process deserves to attract much interest as a method to fabricate effective stressors. Therefore, we have studied how stressor effects appear at the changeover of the growth mode and proceed with the increase of the coverage. One of the noteworthy results is that the redshift of PL peaks due to stressors does not show a monotonous increase but an anomalous behavior as Ge coverage increases.

2. Experimental procedure

Samples were grown by gas source molecular beam epitaxy (Daido Hoxan VCE-S2020) on (1 0 0)-oriented p-type Si wafers with resistivity of 5–10 Ω cm. Disilane and germane were supplied as source materials. The Si wafers were loaded into a chamber after dipping in 2.5% diluted HF for about 30 s, and were heated at 850°C for 10 min to desorb hydrogen as well as the remaining oxide. At first, a 4000 Å Si buffer was grown, followed by a 34 Å strained $Si_{0.82}Ge_{0.18}$ QW at 740°C. Next, a Si spacer of 300 Å and a Ge top layer were grown at 700°C. The Ge coverage, Q, was varied in the range from 2 to 15 ML. Surface morphology of the Ge layers was examined by atomic force microscopy (AFM). The low-temperature PL spectra were measured in a standard lock-in configuration. An Ar^+ laser with 514.5 nm wavelength for the excitation and a liquid-nitrogen-cooled Ge detector for the detection were used. Time-resolved PL was measured in time-correlated photon counting mode with a photomultiplier.

3. Results and discussion

Fig. 1 shows the PL spectra of samples with Ge coverage of $Q = 3.3$ ML and without Ge, $Q = 0$ ML, under low excitation intensity. The sample with $Q = 3.3$ ML is seen to give rise to new peaks as indicated by solid arrows at around 1048 and 990 meV. We can readily identify the new peaks as no phonon (NP) transition and transverse-optical phonon (TO) replica which are redshifted from the corresponding peaks of the coherently strained $Si_{0.82}Ge_{0.18}$ QW [8]. This shift is caused by modulated quantum structures (MQSs), i.e., strain-induced lateral confinement structures in the QW due to the Ge islands. The new peaks are not observed up to 3.0 ML but seen to abruptly set in from 3.3 ML. That is, the appearance of the new peaks means that the Ge islands are formed and the changeover of growth mode occurred at this coverage.

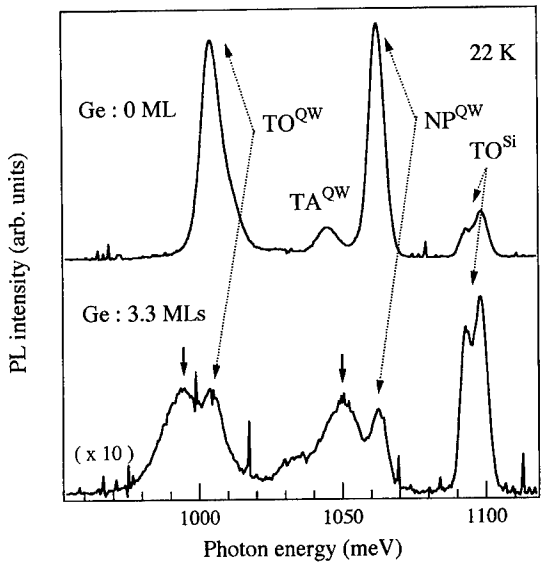

Fig. 1. PL spectra of samples with 3.3 ML of Ge coverage and without Ge. Solid arrows indicate new peaks from modulated quantum structures induced by the Ge islands.

Fig. 2 displays the surface morphology images of Ge layers observed by AFM. The Ge islands are observed from $Q = 3.3$ ML, which just agree with the result of PL measurements. The images are $2 \times 2\ \mu m^2$ in size, and it is seen that the density of the islands increases as Q increases. The size of the Ge islands is roughly 100–200 nm in diameter and 20–30 nm in height, according to AFM measurement.

Fig. 3 shows the PL spectra as a parameter of Ge coverage. We can see that the peaks from quantum

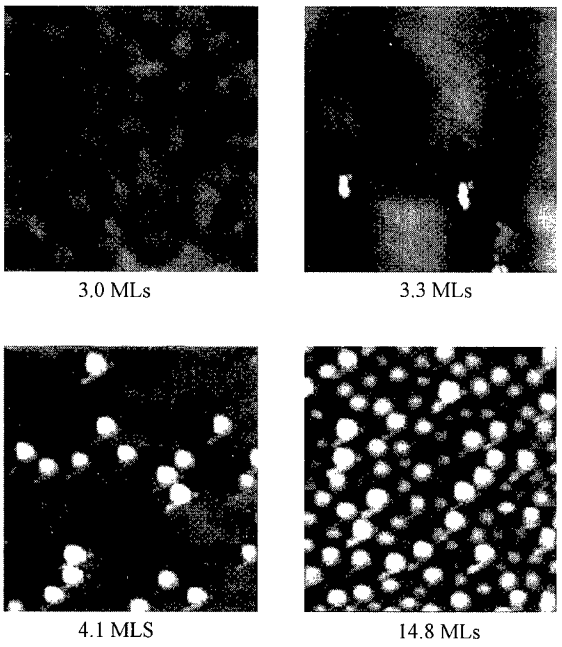

Fig. 2. AFM images of the surface morphology of Ge layer at various Ge coverage. The images are $2 \times 2\ \mu m^2$ in size.

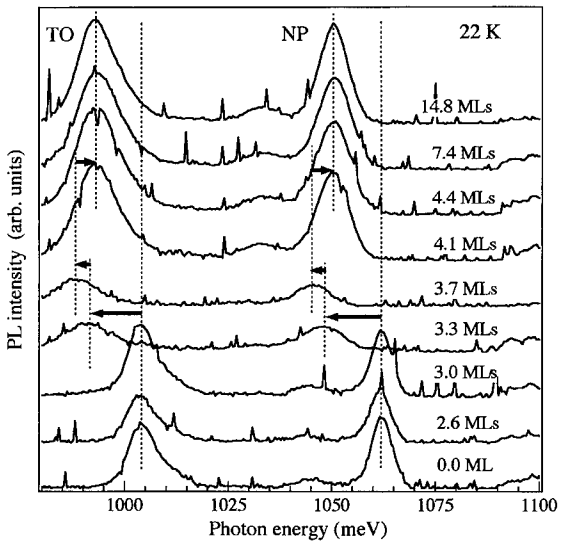

Fig. 3. Shift of the PL peaks with the increase of the Ge coverage. At 3.3 ML of Ge coverage the peaks begin to redshift. The redshift increases upto 3.7 ML, however, at 4.1 ML returns to higher energy side and remains constant.

structures (QW or MQSs), i.e., NP and TO peaks, are almost constant for $Q \leqslant 3.0$ ML. At 3.3 ML the peaks are observed to be abruptly redshifted and the redshift increases up to about 17 meV at 3.7 ML. However, above 4.1 ML the redshift is seen to decrease to about 12 meV and to be constant in spite of the increase of Q. The redshift of the peak energies well correlates with the Ge island formation and the changeover of growth mode of Ge on Si from two-dimensional to three-dimensional is seen to set in at 3.3 ML. This result is very close to the result of the growth mode changeover observed by the measurement of PL from the Ge islands itself in Ref. [7].

At the early stage of the Ge growth on Si, Ge grows layer by layer and the layer becomes compressively strained. At about 3.3 ML coverage, strain relaxation in the Ge layer is considered to occur by forming Ge islands without introducing misfit dislocations. This causes elastic deformation in the Ge islands as well as in the underlying structures [3]. In the underlying structures, i.e., in the Si spacer and the SiGe QW, the elastic deformation generates local tensile strain under the center part of islands and local compressive strain under the vicinity of the edge part of the islands.

Under the center part of islands, the amount of the compressive built-in strain of the QW is decreased by being compensated by the tensile induced-strain, while the Si spacer and buffer without built-in strain are deformed by the tensile induced-stress. In this case, the band line-up of the SiGe/Si QW should be type II according to the calculation in order to radiate the NP line at lower energies than the samples without Ge layers [9]. On the other hand, under the vicinity of the edge part of the islands, the compressive built-in strain of the SiGe QW is enhanced and the Si spacer and buffer receive the compressive strain. Then the band line-up is to be type I to redshift the NP peak energy. In order to clarify which part actually gives rise to lateral confinement effects, we applied external stress to the QW sample without any Ge layers. As shown in Fig. 4, for the compressive external stress, all PL peaks of the QW were observed to be redshifted, whereas for the tensile external stress they were observed to be blueshifted. Thus, the redshift of our samples are regarded as coming from the

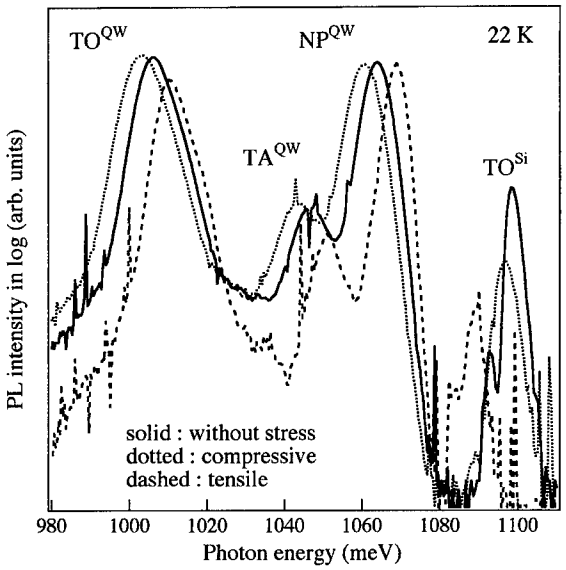

Fig. 4. PL spectra of the SiGe/Si QW under external stresses. The peaks are seen to be redshifted when the external stress is compressive, while they are blueshifted when the external stress is tensile.

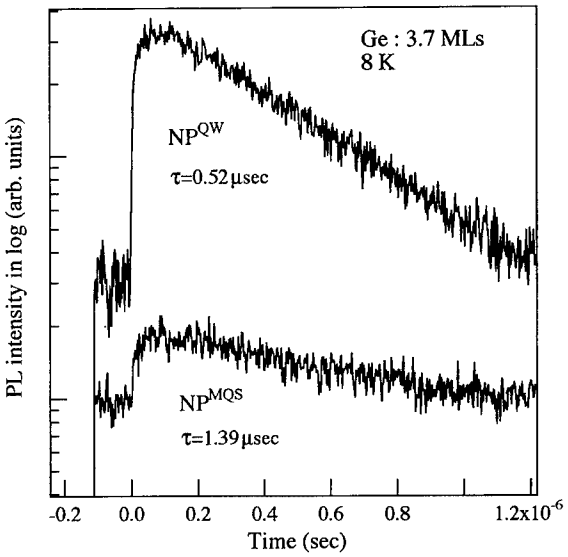

Fig. 5. Luminescence intensity decay profiles of the NP peaks of the QW and the MQS. The letter, τ, means the decaying time constant of the luminescence intensity.

compressive strained underlying layer. That is, a potential valley of the MQS is formed under the vicinity of the edge part of the island like a doughnut-shape, which differs from the case of other materials [10, 11]. In order to quantitatively estimate the energy shift, more information of island shape and dimensions is necessary.

Fig. 5 shows transient change of the NP peak intensities of the QW and the MQS. The intensity of the MQS decays more slowly than that of the QW, although the MQS is considered to have lower dimensionality than the QW. This suggests that the life time is determined by the non-radiative recombination process and that exciton localization is enhanced in the MQS. Localization may prevent carriers from being captured into non-radiative centers [12, 13]. Further studies are needed to clarify the dimensionality of the MQS.

The redshift is enhanced by the increase of the induced-strain up to 3.7 ML. When Q is increased from 3.7 to 4.1 ML, the redshift is seen to decrease abruptly. One of the possible explanations of this decrease is the interaction between the Ge islands. Although induced-strain of a single island itself is considered to increase with increasing Q, when the distance between the islands is shortened due to the increase of the number of islands, the interaction may take place and the induced strain is compensated by each other. This may result in the decrease of the redshift. For the constancy of the redshift above 4.1 ML, the saturation of the lattice relaxation of the Ge islands is considered to be responsible and the partially relaxed lattice constant may maintain up to $Q = 14.8$ ML.

However, the strain interaction between Ge islands is very complicated and does not seem to fully explain the observed tendency. The behavior rather suggests such a phase change as the change in Ge island shape or other natures of the islands. Misfit dislocations, however, are not responsible here, because no dislocation related peaks are observed and the luminescence efficiency does not decrease. To clarify the reason, more detailed studies are necessary.

4. Conclusions

We have systematically investigated the strain effects induced by self-assembled Ge islands grown

on strained SiGe/Si quantum well (QW) as a function of the Ge coverage. It was confirmed that the Ge islands act as stressors on SiGe/Si QW and that the redshift of PL peaks originates from the modulated quantum structures (MQSs) formed in the compressively strained region under the vicinity of the edge part of the Ge islands. The redshift, reflecting the strain effects, showed a complicated behavior, that is, it increases up to $Q = 3.7$ ML and saturates above $Q = 4.1$ ML after once restoring. Full understanding of the strain effects induced by Ge island stressors and the definition of the dimensionality of the MQS need further investigations for practical applications.

Acknowledgements

The authors are grateful to Daido Hoxan for developing the gas-source molecular beam epitaxy system. They would like to acknowledge H. Akiyama and H. Sakaki for time-resolved PL setup. They also would like to acknowledge H. Yaguchi for his fruitful discussion and S. Ohtake for his technical support. This work was supported in part by a Grant-in-Aid for Scientific Research on Priority Area, "Quantum Coherent Electronics" from the Ministry of Education, Science and Culture, and E.S. Kim acknowledges the Foundation For C&C Promotion.

References

[1] R.A. Soref, Proc. IEEE 81 (1993) 1687.
[2] F.H. Pollak, in: Semiconductors and Semimetals, Vol. 32, Ed. T.P. Pearsall (Academic Press, New york, 1990) p. 17.
[3] D.J. Eaglesman and M. Cerullo, Phys. Rev. Lett. 65 (1990) 1934.
[4] S. Christiansen, M. Albrecht, H.P. Strunk and H.J. Maier, Appl. Phys. Lett. 64 (1994) 3617.
[5] N. Usami, H. Sunamura, T. Mine, S. Fukatsu and Y. Shiraki, J. Crystal Growth 150 (1995) 1065.
[6] K. Kash, J. Lumin. 46 (1990) 69.
[7] H. Sunamura, N. Usami, S. Fukatsu and Y. Shiraki, Appl. Phys. Lett. 66 (1995) 3024.
[8] J. Weber and M.I. Alonso, Phys. Rev. B 40 (1989) 5683.
[9] E.S. Kim, N. Usami and Y. Shiraki, unpublished.
[10] Z. Xu and P.M. Petroff, J. Appl. Phys. 69 (1991) 6564.
[11] I.-H Tan, R. Mirin, V. Jayarman, S. Shi, E. Hu and J. Bowers, Appl. Phys. Lett. 61 (1992) 300.
[12] S. Fukatsu and Y. Shiraki, J. Crystal Growth 150 (1995) 1025.
[13] C. Weisbuch and B. Vinter, in: Quantum Semiconductor Structures (Academic Press, New York, 1991) p. 215.

ELSEVIER

Journal of Crystal Growth 175/176 (1997) 524–527

JOURNAL OF CRYSTAL GROWTH

The growth and luminescence of SiGe dots

H. Chen, X.G. Xie, W.Q. Cheng, Q. Huang*, J.M. Zhou

Institute of Physics, Chinese Academy of Sciences, Beijing 100080, People's Republic of China

Abstract

It is found that the SiGe alloy self-organizes into uniform quantum dots embedded in the Si layer during the growth of a strained SiGe/Si superlattices on a Si(0 0 1) substrate by molecular beam epitaxy. The energy of photoluminescence from the quantum dots is higher than that of the indirect band gap of Si, and the luminescence intensity of the quantum dots exceeds that of a quantum well by three orders of magnitude.

1. Introduction

There has been an enormous amount of work aimed at the realization of optical elements exploiting strained SiGe/Si quantum wells [1–3]. Despite these extensive efforts, Si-based optics has yet remained an exclusive goal. It has been proposed that zone-folding effects might create a quasidirect band gap in short-period Si/Ge atomic-layer superlattices, leading to the possibility of efficient radiative recombination [4, 5]. The reported PL spectra from such structures are very controversial, however [6]. The quantum dots can be defined by using high-resolution lithography combined with dry etching [7], leading to a higher luminescence yield. Unfortunately, these procedures inevitably result in a deterioration of the crystal quality. Recent reports of self-organized formation of quantum wires and disk semiconductor structures [8, 9] have attracted considerable interest as a means of overcoming these difficulties. Moreover, with the optimization of growth conditions, their size may be well controlled into the quantum region. The most well-known example is the Stranski–Krastanov (SK) growth of InGaAs on GaAs [10, 11]. These 3D islands are known to have quantum dot characteristics with unique optical properties. The strained SiGe/Si system, which is expected to play an important role in monolithic integration of Si-based optoelectronic devices, is another prominent example of SK-class growth [12–14]. The structure of the vertical self-organization of SiGe quantum dots is investigated by several researchers [15–17]. Photoluminescence (PL) from SiGe islands has been observed recently by several authors. In this article, we report that SiGe self-organized quantum dots can be formed when Si/Ge short-period superlattices are grown on Si substrates by molecular beam epitaxy. We also found strong photoluminescence at an energy higher than the band gap of Si.

* Corresponding author. Fax: + 86 010 2551205; e-mail: ghuang@aphy02.iphy.ac.cn.

0022-0248/97/$17.00 Copyright © 1997 Elsevier Science B.V. All rights reserved
PII S0022-0248(96)01218-3

The intensity is two orders of magnitude higher than that of a SiGe/Si quantum well.

2. Experiment

The structures were grown on Si(0 0 1) substrates in a VG Semicon V80S MBE system and were investigated by reflection high-energy electron diffraction (RHEED) in situ. The growth rates were 0.06 nm/s for the Si layers and 0.04 nm/s for Ge layers. The growth procedure of the sample was as follows: a 200 nm Si buffer layer was grown at 800°C, followed by one, two and five periods of Si(8 ML)/Ge(4 ML) superlattice for samples A, B and C, respectively, grown at a temperature of 800°C, and concluded by a 100 nm Si cap layer grown at 800°C. The growth interruption time between each layer was 20 s.

Specimens were prepared for both planar-view and cross-sectional TEM by mechanically thinning the specimen to about 20 μm, followed by ion milling to electron transparency. The TEM observations were made by H-9000AF at 300 kV.

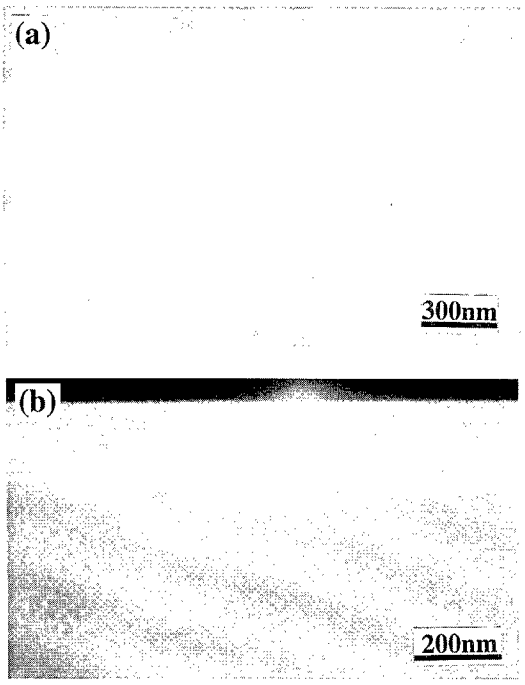

Fig. 1. (a) Planar-view bright field TEM image of sample C. (b) The (0 0 4) dark field image of the cross-section of sample C.

3. Structure and photoluminescence of SiGe quantum dots

From RHEED investigations, we found that the diffraction lines in the RHEED pattern become a little wider at the end of the first Ge layer growth, which indicates the formation of small coherent islands, and then become finer during the next Si-layer deposition. During the subsequent Si/Ge superlattice growth, the diffraction lines become wider gradually and sharp facet diffraction lines begin to appear. This implies the coherent islands of Ge become larger.

The planar-view TEM image for sample C, shown in Fig. 1a, reveals an array of well-ordered dots on the (0 0 1) plane. The size of the dots is about 100 nm, and the separation between two dots is about 100 nm. The alignment of the dots suggests a strong positional correlation during the formation process. The formation and composition of the dots is clarified by the (0 0 4) dark field image of the cross-section of sample C shown in Fig. 1b, which is composed of SiGe islands with a diameter of 100 nm, embedded in a Si matrix with a thickness of about 20 nm. The height of our quantum dots is much greater than that of others reported before.

Fig. 2 shows the photoluminescence (PL) spectrum of sample C at 80 and 300 K. For excitation the blue (488 nm) line of an Ar^+ laser was used with an excitation power of 10 mW. It is interesting to find that only one PL peak appears at the wavelength around 1 μm for both samples at 80 K. The peak position is at 995 nm and corresponds to the energy 1.24 eV, which is higher than the indirect band gap (1.15 eV at 80 K) of Si. By increasing the temperature from 80 to 300 K, the photoluminescence peak due to the quantum dots shifts to a lower energy, and as expected, the intensity decreases by two orders of magnititude. We also found that the PL intensity of the quantum dots is two orders of magnitude higher than that of SiGe/Si quantum wells at 80 K. Taking into account the filling factor, i.e., the coverage of the SiGe containing the quantum dot structures, the

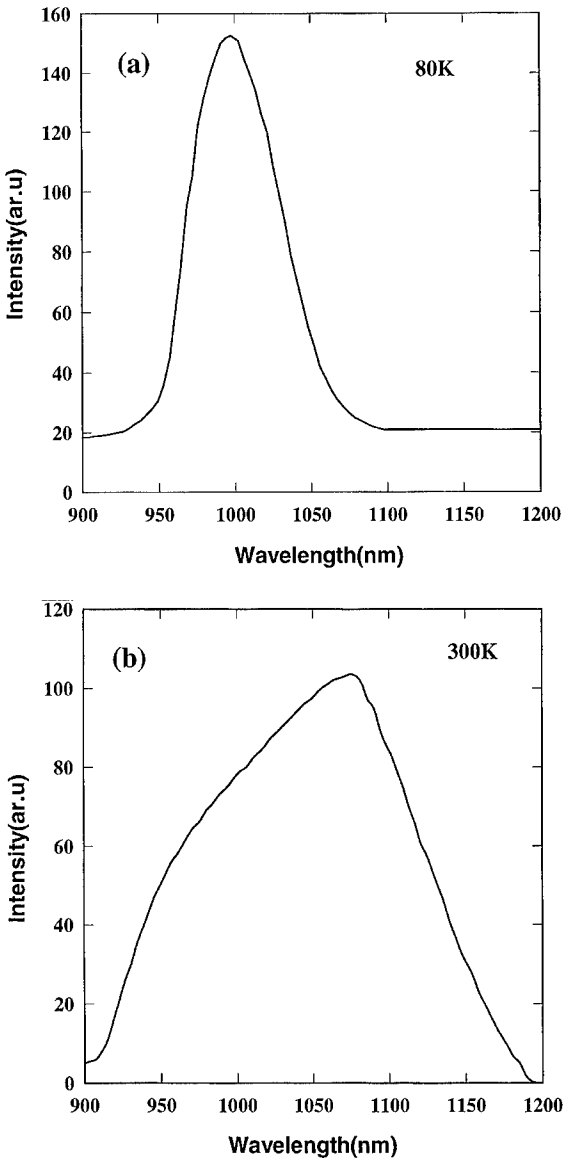

Fig. 2. (a) and (b): 80 K and room-temperature (300 K) photoluminescence of the sample C, respectively.

luminescence of dots seems to exceed that of the quantum well by more than three orders of magnitude. From these photoluminescence measurement results, we confirm that the PL peak from the quantum dots is the NP peak and the TO peak from quantum dots cannot be seen.

4. Band gap conversion in SiGe system

Fig. 3 shows the photoluminescence (PL) spectrum of quantum dots at 80 K. There are three peaks in PL spectrum from sample A, shown in Fig. 3a: one is the transverse-optical (TO) phonon peak with the energy of 1.09 eV from the Si substrate,

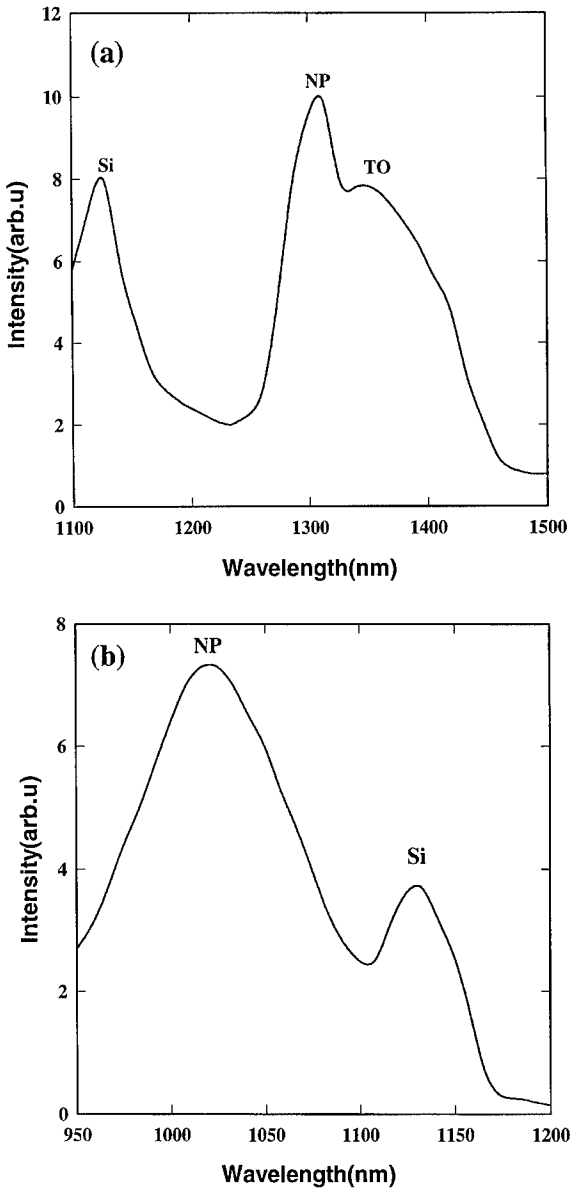

Fig. 3. (a) and (b): 80 K photoluminescence of samples A and B, respectively.

the other is no-phonon (NP) assisted peak with the energy of 0.95 eV from the Ge quantum well, the third one is the TO peak from the Ge quantum well. The results agree with a previous report [12]. The photoluminescence is from the indirect band gap of the Ge quantum well. There are two peaks from the sample B, shown in Fig. 3b. It is interesting to find that the NP peak increases from 0.95 to 1.21 eV, where the TO peak disappears. It should be noted that the energy of the peak from SiGe layer is higher than the indirect band gap (1.15 eV at 80 K) of Si. We also found that the PL intensity of quantum dots is twice that of the quantum well in sample A. Only one PL peak from quantum dots can be seen from sample C, and the TO peak from Si disappears (shown in Fig. 2a). We also found that the PL intensity from sample C is two orders of magnitude higher than that of Ge/Si quantum wells, suggesting very efficient light emission from the quantum dots.

5. Conclusions

It is found that the SiGe alloy self-organizes into uniform quantum dots embedded in the Si layer during the growth of a strained Si/Ge short period superlattice on a Si(0 0 1) substrate by molecular beam epitaxy. Transmission electron microscopy was used to confirm the existence of the quantum dots and to estimate its spatial distribution. The size of the dots is about 100 nm, the height is about 20 nm, and the separation between them is about 100 nm. The energy of photoluminescence from the quantum dots is higher than that of the indirect band gap of Si, and the luminescence intensity of the quantum dots exceeds that of a quantum well by three orders of magnitude. The band gap conversion in SiGe system is confirmed by the photoluminescence measurements.

References

[1] J.C. Sturm, H. Manoharan, L.C. Lenchyshyn, M.L.W. Thewalt, N.L. Rowell, J.-P. Noël and D.C. Houghton, Phys. Rev. Lett. 66 (1991) 1362.
[2] D. Dutartre, G. Brémond, A. Souifi and T. Benyattou, Phys. Rev. B 44 (1991) 11525.
[3] K. Terashima, M. Tajima and T. Tatsumi, Appl. Phys. Lett. 57 (1990) 1925.
[4] H. Okumura, K.S. Miki, K. Misawa, T. Sakamoto and S. Yoshida, Jpn. J. Appl. Phys. 28 (1989) L1893.
[5] R. Zachai, K. Eberl, G. Abstreiter, E. Kasper and H. Kibbel, Phys. Rev. Lett. 64 (1990) 1055.
[6] U. Schmid and N.E. Christensen, Phys. Rev. Lett. 65 (1990) 2610.
[7] Y.S. Tang et al., J. Electron. Mater. 24 (1995) 99.
[8] R. Nötzel, J. Temmyo and T. Tamamura, Nature 369 (1994) 131.
[9] R. Nötzel, N. Ledentdov, L. Däweritz, M. Hohenstein and K. Ploog, Phys. Rev. Lett. 67 (1992) 3812.
[10] S. Guha, A. Madhukar and K.C. Rajkumar, Appl. Phys. Lett. 57 (1990) 2110.
[11] H. Sunamura and Y. Shiraki, Appl. Phys. Lett. 65 (1995) 953.
[12] Y.-W. Mo, D.E. Savage, B.S. Swartzentruber and M.G. Lagally, Phys. Rev. Lett. 65 (1990) 1020.
[13] A.J. Pidduck, D.J. Robbins, A.G. Cullis, W.Y. Leong and A.M. Pitt, Thin Solid Films 222 (1992) 78.
[14] M.A. Lutz, R.M. Feenstra, P.M. Mooney, J. Tersoff and J.O. Chu, Surf. Sci. 316 (1994) L1075.
[15] T.S. Kuan and S.S. Iyer, Appl. Phys. Lett. 59 (1991) 2242.
[16] L. Vescan, W. Jïger, C. Dieker, K. Schmidt, A. Hartmann and H. Lïth, Mater. Res. Soc. Symp. Proc. 263 (1992) 23.
[17] J. Tersoff, C. Teichert and M.G. Lagally, Phys. Rev. Lett. 76 (1996) 1675.

ELSEVIER

Journal of Crystal Growth 175/176 (1997) 528–531

JOURNAL OF CRYSTAL GROWTH

Characterization of homoepitaxial SiC layers

J. Schmitt[a,*], T. Troffer[a], K. Christiansen[a], M. Schadt[a], S. Christiansen[b], R. Helbig[a], G. Pensl[a], H.P. Strunk[b]

[a] *Institut für Angewandte Physik, Universität Erlangen-Nürnberg, Staudtstrasse 7, D-91058 Erlangen, Germany*
[b] *Institut für Werkstoffwissenschaften-Mikrocharakterisierung, Universität Erlangen-Nürnberg, Cauerstrasse 6, D-91058 Erlangen, Germany*

Abstract

An n-type 3C-SiC MBE layer is grown on an off-oriented p-type 6H-SiC substrate with alternating supply of gas sources at a growth temperature of 1100°C. The crystalline quality of the 3C-SiC layer is characterized by high resolution transmission electron microscopy and the electrical properties of this layer are investigated by a series of analytical techniques (current–voltage measurement, capacitance–voltage measurement, deep level transient spectroscopy).

PACS: 68.55.Bd; 81.15.Ef; 73.61.Le

1. Introduction

Silicon carbide is a promising wide band gap semiconductor and crystallizes in varios polytypes. Cubic 3C- and hexagonal 4H- and 6H-SiC are favored when used in combination with electronic devices. However, the mechanisms for the selection of a specific SiC polytype during growth is not understood yet, although there exist some recipes how to grow a particular polytype from the vapor phase [1]. The MBE technique is an appropriate tool to study the formation of polytypes, as it provides a defined control of the growth parameters. Several authors have already described the deposition of SiC layers by MBE [2, 3]. In this paper, we report on the growth of a 3C-SiC layer on a 6H-SiC substrate and on the analysis of its structural and electrical properties.

2. MBE process

For the MBE growth, we used an Al-doped 6H-SiC (0 0 0 1) substrate (CREE) with an off-axis orientation of 3.5° towards (1 1 $\bar{2}$ 0). The Al concentration in the substrate is determined by the capacitance-voltage technique to be equal to $(6 \pm 1) \times 10^{17}$ cm^{-3}. Prior to the MBE process, the substrates were polished with diamond paste (minimum grain size of 0.25 μm) and oxidized in dry oxygen at 1120°C for 36 h to clean the surface. The oxide was etched off with HF.

* Corresponding author. Fax: + 49 9131 858423; e-mail: mpap05@rzmail.uni-erlangen.de.

0022-0248/97/$17.00 Copyright © 1997 Elsevier Science B.V. All rights reserved
PII S0022-0248(96)00994-3

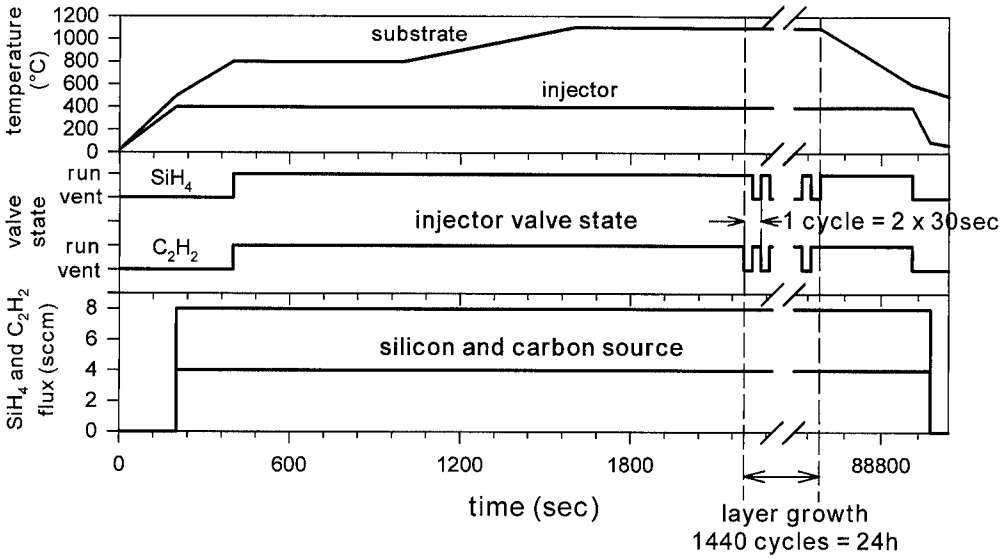

Fig. 1. Growth parameters used for the investigated 3C-SiC MBE layer. The temperature of the injector, valve states of the injector and gas fluxes are schematically sketched as a function of growth time.

The SiC layer was grown using gas sources with an alternating supply of silane SiH_4 and acetylene C_2H_2. The substrate temperature was kept at 1100°C during growth. The gas injector carrying both matrix gases was set to 400°C. Fig. 1 shows the temperature and gas flow program of the MBE growth. The growth procedure consists of several steps (see Fig. 1). First the substrate and injector temperature are increased to 800°C and 400°C, respectively. At 800°C both matrix gases are switched from vent mode, where the flux is stabilized, to run mode. In a final step, the substrate temperature is ramped up to the growth temperature of 1100°C. After 10 min of temperature stabilization under gas flow the alternate supply of the matrix gases starts. Each cycle consists of a 30 s SiH_4 supply with C_2H_2 switched off followed by a 30 s C_2H_2 supply with SiH_4 switched off (see Fig. 1). After 1440 cycles (=24 h growth time) both gases stay switched on and the substrate temperature is ramped down to 600°C.

No growth was observed supplying both matrix gases simultaneously, whereas the alternate supply of the gases showed a growth rate of 3.6 SiC double layers per cycle. In order to achieve a film thickness of at least 1 micron, which is necessary for electrical measurements, we chose a growth period of 1440 cycles.

3. High resolution transmission electron microscopy (HRTEM)

HRTEM investigations were performed to characterize the crystalline quality and to identify the polytype of the grown epitaxial layer. We used a Philips CM 300 UT, operated at 300 kV (point to point resolution of 1.72 Å). The cross sectional specimen were prepared by conventional mechanical grinding and dimpling, followed by ion milling with Ar^+ to electron transparency in a Gatan duomill (operated at 4 kV, 1 mA, 13° incidence, nitrogen cooling stage). The high resolution micrograph in Fig. 2 proves that the grown epilayer consists of the 3C polytype. A sharp transition can be observed between the 6H polytype of the substrate to the 3C polytype of the epilayer. The 3C polytype, however, is twinned; the frames indicate regions in twin orientation with the arrows marking the twin boundary in between. An analysis of the diffraction

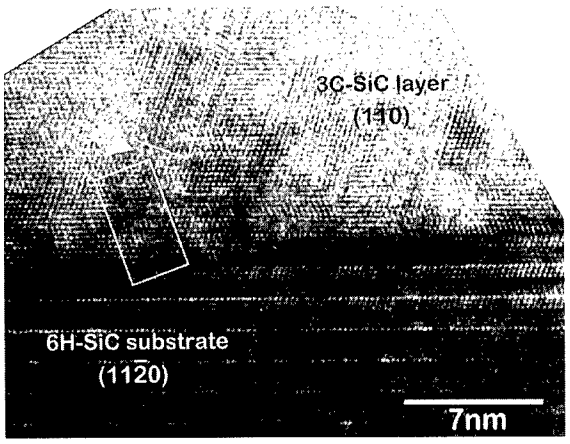

Fig. 2. High resolution transmission electron micrograph (HRTEM) of a 3C-SiC MBE layer grown on an Al-doped 6H-SiC substrate. The substrate surface is 3.5° off-axis oriented. The arrow and white frames mark a twin.

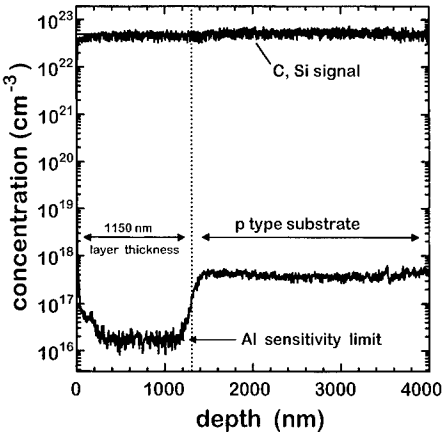

Fig. 3. Si, C and Al SIMS profiles of the 3C-SiC MBE layer grown on an Al-doped 6H-SiC substrate. The Al level in the epitaxial layer is given by the ^{27}Al sensitivity limit of the SIMS system. The thickness of the MBE-grown layer is obtained from the increase of the ^{27}Al concentration.

pattern shows that the incident beam is parallel to the (1 $\bar{1}$ 2 0) zone axis in the 6H polytype and to the (1 1 1) zone axis in the 3C polytype, respectively. Due to the fact that the 6H polytype is not continued into the epilayer, we assume that the surface mobility of adatoms is low and a two dimensional nucleation takes place on the terraces.

4. Secondary ion mass spectroscopy (SIMS)

The thickness of the layer was determined by secondary ion mass spectroscopy (SIMS) using an ATOMIKA A-DIDA 3000 instrument. Fig. 3 depicts the C, Si and Al depth profiles obtained with a 12 keV O_2^+ primary ion beam and a beam current of 500 nA resulting in a sputter rate of 33 nm/min. The Si and C signal serve as a reference. The low ^{27}Al level in the MBE layer represents the sensitivity limit of the SIMS system; the real concentration of ^{27}Al is probably much lower. The increase of the Al concentration at a depth of approximately 1.15 μm indicates the transition from the MBE layer to the substrate. Thus the thickness of the MBE layer determined from the ^{27}Al profile is (1.15 ± 0.1) μm and agrees within the error bar with the value of (1.29 ± 0.05) μm determined with a surface step profiler at the edge of the sample, where it was clamped during the growth process.

5. Electrical characterization

The 3C-SiC MBE layer was characterized by means of current–voltage (I–V) and capacitance–voltage measurements (C–V) as well as by deep level transient spectroscopy (DLTS). We prepared ohmic contacts (Ø = 0.3 mm) by evaporating Al onto the layer surface and heating the sample to 950°C. Schottky contacts (Ø = 0.4 mm) were fabricated by depositing nickel. I–V and C–V characteristics indicate n-type conductivity of the 3C-SiC MBE layer with a net donor concentration of $(2 \pm 1) \times 10^{16}$ cm^{-3}. We assume that nitrogen, which acts as a shallow donor in silicon carbide, is the prevailing impurity in our epitaxial layer.

DLTS measurements were conducted in the temperature range from 150–700 K applying a reverse bias of −7 V, a filling pulse bias of −1 V and a filling pulse width of 30 ms. The DLTS system used is described in [4]. The measured DLTS spectrum is displayed in Fig. 4; it consists of two peaks labeled T1 and T2. The ionization energies ΔE(T1), ΔE(T2), electrical capture cross sections σ(T1), σ(T2) and concentrations N(T1), N(T2) obtained

Table 1
Concentration N, ionization energy ΔE and capture cross-section σ of levels T1 and T2 as obtained from an Arrhenius plot are listed. The temperature dependence of the capture cross-section is assumed to be either $\sigma \propto T^0$ or $\sigma \propto T^{-2}$

	N (10^{15} cm^{-3})	ΔE (meV)		σ (cm^{-2})	
		$\sigma \propto T^0$	$\sigma \propto T^{-2}$	$\sigma \propto T^0$	$\sigma \propto T^{-2}$
T1	5.2 ± 0.7	680 ± 7	750 ± 7	$(8.9 \pm 1.2) \times 10^{-17}$	$(6.6 \pm 1.2) \times 10^{-16}$
T2	1.7 ± 0.4	895 ± 16	988 ± 16	$(4.3 \pm 1.4) \times 10^{-17}$	$(3.2 \pm 1.4) \times 10^{-16}$

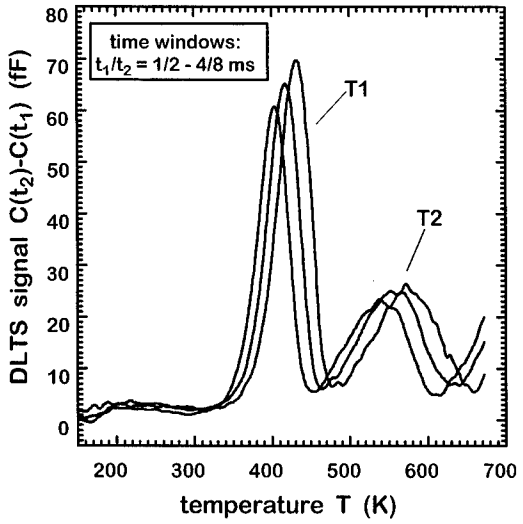

Fig. 4. DLTS spectra of the 3C-SiC MBE layer. Two deep levels T1, T2 are observed; the trap parameters are summarized in Table 1.

from an Arrhenius plot analysis are listed in Table 1. Because of the fact that the temperature dependence of the capture cross section is not known, we assumed the following two cases for the evaluation of ΔE and σ: $\sigma \propto T^0$ (multi-phonon capture) or $\sigma \propto T^{-2}$ (cascade capture process).

At the present stage, the chemical nature and microscopic structure of the T1 and T2 defects are not known. In order to decide whether T1 and T2 are donor- or acceptor-like, we conducted double correlated DLTS (DDLTS) measurements. It turns out that the ionization energy ΔE(T1) decreases with increasing applied electric field indicating that center T1 acts as a donor. The peak height of level T2 is too small to get any reliable information from a DDLTS analysis.

6. Summary

An n-type 3C-SiC MBE layer was grown on a p-type 6H-SiC substrate at a growth temperature of $T = 1100$°C by using alternating gas supply (SiH_4, C_2H_2). The growth rate was 50 nm/h. In order to achieve step controlled growth, it seems that the growth temperature has to be above 1100°C. Double positioning boundaries are observed in the MBE layer. DLTS spectra reveal two deep levels.

Acknowledgements

This work was supported by the German Bundesministerium für Bildung, Wissenschaft, Forschung und Technologie (BMBF).

References

[1] T. Yoshinobu, M. Nakayama, H. Shiomi, T. Fuyuki and H. Matsunami, J. Crystal Growth 99 (1990) 520.
[2] N. Kuroda, K. Shibahara, W.S. Yoo, S. Nishino and H. Matsunami, Extended Abstracts, 19th Conf. on Solid State Devices and Materials, Tokyo (1987) 227.
[3] L.B. Rowland, R.S. Kern, S. Tanaka and R.F. Davis, Appl. Phys. Lett. 62 (1993) 3333.
[4] K. Hölzlein, G. Pensl, M. Schulz and P. Stolz, Rev. Sci. Instrum. 57 (1986) 1373.

ELSEVIER

Journal of Crystal Growth 175/176 (1997) 532–540

JOURNAL OF CRYSTAL GROWTH

II–VI light-emitting devices based on beryllium chalcogenides

F. Fischer*, G. Landwehr, Th. Litz, H.J. Lugauer, U. Zehnder, Th. Gerhard, W. Ossau, A. Waag

Physikalisches Institut, EP III, Am Hubland, D-97074 Würzburg, Germany

Abstract

Beryllium chalcogenides are semiconductors with a large band gap. They have a higher-degree of covalent bonding than all of the other II–VI compounds. The bond energies of BeTe, BeSe and BeS are comparable to those of GaN. Due to their band gaps and their lattice constants they can be incorporated in quaternary mixed crystals which are lattice matched to GaAs. The hardness of II–VI materials containing beryllium offers new possibilities to enlarge the lifetime of laser diodes, emitting in the green and blue spectral range. First light-emitting diodes (LEDs) with beryllium as a constituent have been produced on GaAs substrates by molecular beam epitaxy (MBE). Double heterostructure devices were realized with quantum wells either of BeZnSeTe, ZnSe or BeZnSe. Special ohmic contacts consisting of BeTe–ZnSe graded superlattices were employed. Although for the first devices the growth conditions were not optimized, the lifetime at typical operating currents was very promising.

Keywords: Be-chalcogenides; Laser diode; Light emitting diodes

1. Introduction

Since the first demonstration of blue–green-emitting lasers on the basis of ZnSe by Haase et al. [1], rapid progress has been made in the improvement of the devices. The first lasers allowed only operation at 77 K and had a rather short lifetime. However, DC operation at room temperature was achieved soon and the lifetime steadily increased to more than 100 h [2].

A similar development occurred with the GaAs lasers before their lifetime exceeded 10 000 h. The first devices were simple diodes with excessive threshold current densities [3]. The introduction of the heterostructure principle by Kroemer [4] marked a significant progress and the first DC operation was achieved in 1980 by Alferov et al. [5] and by Hayashi et al. [6]. It took several years to get lifetimes which allowed technical applications. It was soon recognized that the origin of the degradation was nonradiative recombination at dark line defects. A similar situation holds for the ZnSe-based lasers at present. It has become clear that nonradiative recombination at defects in the active zone is limiting the lifetime. Systematic efforts to

* Corresponding author. Fax: + 49 931 888 5142; e-mail: fischer@physik.uni-wuerzburg.de.

0022-0248/97/$17.00 Copyright © 1997 Elsevier Science B.V. All rights reserved
PII S0022-0248(97)00127-9

reduce the density of extended defects led to a steady increase of the lifetime. However, the situation for ZnSe-based lasers differs somewhat from that in GaAs, because the II–VI devices usually are grown by heteroepitaxy on GaAs substrates. It became clear that stacking faults existing at the interface GaAs–ZnSe have a tendency to grow during operation and that an increase in dislocation and stacking fault density is eventually limiting the active life of a ZnSe laser diode. The density of defects at the interface also depends on the dislocation density of the GaAs substrate. The increase in lifetime of ZnSe lasers from a few seconds to more than 100 h resulted mainly from the use of substrates with a dislocation density of less than 10^3 cm^{-2} and an optimized growth start of the subsequent ZnSe layers. If dark line defects were the only reason of degradation, a very substantial increase of the lifetime had to be expected at such low dislocation densities. It turned out however, that the lifetime did not increase according to the expectations [7]. Consequently, other defects or defect complexes had to be invoked.

In this situation, we were looking for another approach. It is well-known that due to the ionicity of the chemical bond in II–VI semiconductors, these materials are relatively soft compared to materials with covalent bonds like silicon. Employing II–VI compounds with a larger percentage of covalent bonding than ZnSe should result in harder materials and a reduced mobility of extended defects. Recently, Verié has checked the possibility of using harder wide gap II–VI materials for optoelectronic devices. He came to the conclusion, that beryllium chalcogenides are promising in this respect due to their pronounced covalent bonding and due to their small bond length. Because practically no experimental data on the mechanical rigidity of BeTe and BeSe as well as BeS were available, the suitability of beryllium chalcogenides as a constituent of II–VI optoelectronic devices was estimated theoretically on a semiempirical basis [8]. A relation linking the shear modulus with the covalency was obtained, making use of the LCAO-based model of Harrisson [9]. It is predicted that the shear modulus of BeS is higher than that of GaAs and that the shear modulus of BeTe and BeSe will be considerably larger than that of ZnSe.

Only very few data on the basic properties of Be-compounds are available in the literature [10]. But it turned out that the beryllium chalcogenides are interesting for light-emitting diodes (LEDs) and for laser diodes (LDs) as well also for other reasons. These materials have lattice constants, which allow to grow thin films lattice matched to GaAs. The large band gap of BeSe makes it possible, to grow heterostructure lasers in which the band gap of the material in the cladding layer is large enough to facilitate operation in the blue spectral range. It is well-known that one of the problems with the ZnSe-based lasers with ZnMgSSe waveguides is the limitation in p-type doping of alloys with more than 20% Mg. The large band gap of BeSe requires only relatively small Be and Mg contents of quaternary BeZnMgSe barrier layers in order to achieve sufficient carrier confinement at room temperature.

Motivated by the above considerations, we began to grow beryllium chalcogenide structures by molecular beam epitaxy (MBE) [11]. The properties of MBE grown thin films and quantum well structures have been investigated by a variety of characterization methods and the first LEDs with a rather long lifetime have been demonstrated [12]. It turned out that due to the close matching of the lattice constants of BeTe, GaAs and ZnSe it has been possible to grow epilayers and quantum well structures of rather high perfection. Also, it has been shown, that BeTe can be very heavily p-type doped, allowing a novel contact structure with high crystalline quality. In passing, it should be mentioned that beryllium chalcogenides are also suitable for producing quantum well structures with properties very interesting for basic semiconductor physics [13]. In the following, we shall present data on beryllium chalcogenide structures and devices. These novel materials have been produced and investigated in our group during the last 12 months. The progress has been very encouraging.

In the last few years LEDs and LDs based on the III–V compound GaN have been realized. LEDs grown by metal organic chemical vapour deposition (MOCVD) on sapphire substrates with bright emission in the blue or green spectral range are produced commercially in large numbers at present. The first operation of a GaN laser was reported by Nakamura et al. [14]. Although the

first devices operated at low-temperature in the pulsed mode, steady progress has been reported and continuous operation has become possible in the meantime. The success of the GaN devices has several reasons, one of them being the considerable hardness of this material. In the following, it will be pointed out that beryllium chalcogenides have a bond strength comparable to that of GaN. Therefore, incorporating beryllium in II–VI devices should allow to overcome the existing lifetime problems. The competition between ZnSe and GaN is far from being over. One should also keep in mind that devices made from different materials usually complement each other.

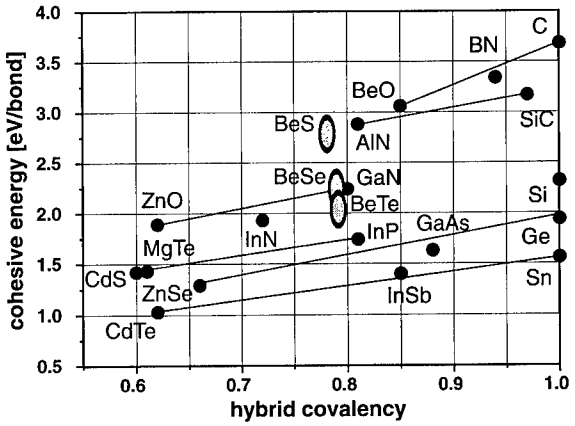

Fig. 1. Bond energy (cohesive energy) versus hybrid covalency for various binary semiconductors (from Ref. [9]). The lines indicate an empirical rule for isoelectronic compounds.

2. Experimental procedure

The epitaxial layers and devices which will be discussed subsequently, have been grown in a Riber 2300 four chamber system. GaAs substrates were overgrown by an epitaxial buffer layer. Elemental Be, Se, Te, Mg, Cd and Zn effusion cells have been employed. For n-type doping zinc iodine has been used. p-type doping was achieved by a plasma-activated nitrogen source. Usually, a substrate temperature of 300°C was chosen. Reflection high-energy electron diffraction (RHEED) has been intensively used to investigate the growth in situ. A 35 kV electron gun with a computerized detection system based on a CCD camera has been employed. Photoluminescence at 2 K and high-resolution X-ray diffraction (HRXD) served to characterize the specimens. Electrical measurements have been performed with a HP4145B semiconductor parameter analyzer at 300 K.

3. Results and discussion

3.1. Binding energy

The bond strength of binary semiconductor compounds is expected to correlate with the degree of covalency. This can be seen in Fig. 1, where the cohesive energy per bond (bond energy) has been plotted versus the hybrid covalency. The latter term is used following Harrisson [9]. Plotting the cohesive energy versus the hybrid covalency, one finds that both quantities are linearly related for isoelectronic compounds. This means that binary compounds with a same total number of electrons show a scaling behavior. Therefore, one can use Fig. 1 to estimate the bond energy of beryllium chalcogenides by making use of their theoretically calculated covalencies. This was done for BeS, BeSe and BeTe. All other values shown for the cohesive energy per bond were experimentally determined and were taken from Ref. [9]. One can recognize in Fig. 1, that the bond energies of the beryllium chalcogenides are significantly larger than those obtained for the II–VI compounds CdTe and ZnSe. It should be noted that GaN has almost the same hybrid covalency as BeS, BeSe and BeTe and that its bond energy is hardly different from that of the Be-compounds. It should also be noted that the bond strength of GaAs is below that of the beryllium chalcogenides.

Experimentally, the high bond energy of beryllium chalcogenides can be demonstrated by measuring the desorption of the compound in vacuum. The influence of the desorption can be determined by measuring the dependence of the growth rate of a binary compound as a function of substrate temperature [15]. With increasing substrate temperature the desorption exponentially increases, thereby decreasing the growth rate. The RHEED

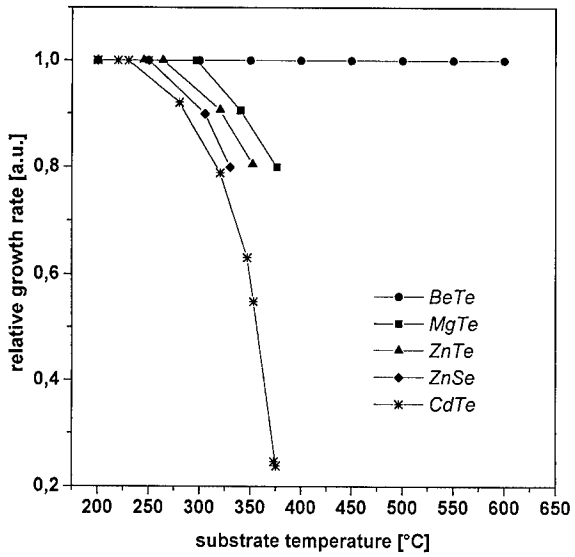

Fig. 2. MBE growth rates of II–VI compounds: for BeTe no significant onset of desorption at high substrate temperatures can be observed.

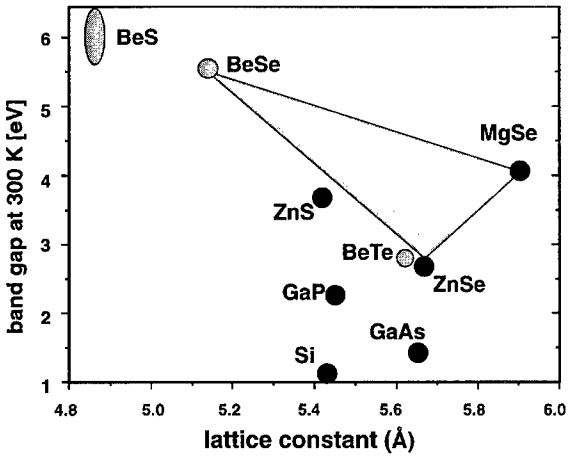

Fig. 3. Energy gap versus lattice constant for binary Be-chalcogenides.

oscillation technique has been used to measure the growth rate of BeTe as a function of substrate temperature. Due to the relatively good lattice matching of BeTe to the GaAs substrate (0.47%), well-pronounced and long-lasting RHEED oscillations can be observed in general. In Fig. 2, the growth rate of BeTe has been plotted as a function of the substrate temperature and the results are compared with that of the conventional II–VI semiconductors like CdTe, ZnSe and ZnTe. For the whole range of substrate temperatures used, the growth rate of BeTe stays constant. This indicates that desorption does not play a role even for substrate temperatures of up to 550°C. Therefore, the molecular beam epitaxial growth of BeTe is compatible to that of GaAs, and BeTe-GaAs heterostructures can be fabricated even at the high substrate temperatures typical for the growth of high-quality GaAs. In contrast to that, the growth rate of the conventional II–VI compounds decreases due to the desorption at much lower substrate temperatures, demonstrating that the bond energy of BeTe is high compared to that of the conventional II–VI compounds.

3.2. Defect generation

Another important property of beryllium chalcogenides is the fact that quaternary compounds can be lattice-matched to both GaAs and Si. This can be seen in Fig. 3, where the band gaps of conventional II–VI semiconductors as well as beryllium chalcogenides have been plotted versus their lattice constants. The position of the beryllium chalcogenides in the band gap–lattice constant plot opens some new possibilities: ZnS with its smaller lattice constant as compared to GaAs is in general used in quaternary ZnMgSSe for the fabrication of blue–green laser diodes. ZnS can now be replaced by BeSe which can be combined with MgSe for lattice matching to GaAs. In this way only the incorporation of 3 metals – Be, Mg and Zn – has to be controlled. The sticking coefficient of the 3 metals is high and relatively independent of the substrate temperature, resulting in a precise control of the lattice parameter for the quaternary BeMgZnSe. Experiments showed that n-type doping of quaternary BeMgZnSe by iodine can easily be achieved for electron concentrations exceeding 10^{19} cm^{-3} [16]. However, the situation is different for the case of p-type doping. As in ZnMgSSe [17], we see a decrease in p-type doping levels as the band gap of the quaternary BeMgZnSe is increased. However, the absolute limits have not been determined

yet. Doping with nitrogen goes along with the incorporation of point defects which can dramatically enhance interdiffusion as it has been shown in CdTe-based superlattices [18]. Usually, it is not possible to dope wide gap II–VI compounds strongly n-type as well as p-type. For instance, ZnSe can be readily n-type doped, but p-type doping causes difficulties. Whenever the nitrogen concentration is increased to enhance the hole density beyond $10^{18}\,cm^{-3}$, the hole concentration decreases. This is usually attributed to the generation of compensating defects. The creation of donors due to addition of acceptors has been dubbed 'self-compensation'. It was shown by Mandel [19] that the effect of self-compensation can be at least qualitatively understood by taking into account the band-gap energy and the enthalpy of the formation of a vacancy $\Delta H_M^{vac} = \Delta H_{MN} - E_r \approx 2E_{cohesive}$. The expression ΔH_M^{vac} is the formation enthalpy of a neutral vacancy and ΔH_{MN} corresponds to the standard molar enthalpy of the mixed crystal MN. E_r is the so-called relaxation energy of the vacancy and is neglected for our purposes [19]. It was shown that ΔH_{MN} is essentially twice the cohesive energy $E_{cohesive}$. Thus, one can roughly judge the tendency of a semiconductor mixed crystal towards self-compensation by comparing the ratio of the band gap and the formation enthalpy of a neutral vacancy $E_g/2E_{cohesive}$. For our considerations we use the cohesive energy per bond derived from Fig. 1. However, we do not consider the formation of a charged vacancy which would be a more realistic approximation. Nevertheless, the ratio $E_g/2E_{cohesive}$ can be considered as a rough estimation of the self-compensation 'boundary' [19]. In Fig. 4, the ratio $E_g/2E_{cohesive}$ has been plotted versus the covalency of the bonding (from [9]) for some binary semiconductor compounds. Unfortunately, the band gaps of BeSe and BeS are not known very precisely. In preliminary studies we determined the optical band gap of BeSe to be 5.6 eV but there are indications, that an indirect gap at around 4.4 eV can exist [11]. We did not investigate BeS, therefore, the literature values [10] were used. From the values $E_g/2E_{cohesive}$ for BeSe and BeS (Fig. 4), which are close to unity, one can conclude that the tendency of BeS and BeSe towards self-compensation is not negligible. In contrast to that BeTe seems to have a low probability to generate vacancy correlated defects. From that point of view the generation of vacancy-correlated compensating defects in n- and p-type BeTe could be very different from other II–VI semiconductors.

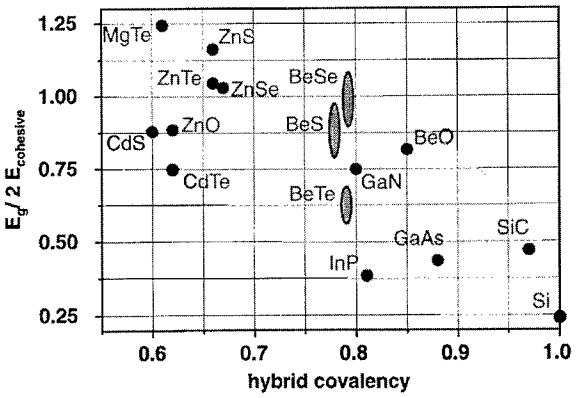

Fig. 4. Estimation of the tendency towards the generation of compensating vacancy defects according to Ref. [19]. Explanations are given in the text.

3.3. Electrical contacts using BeTe

In our first studies on Be–VI compounds it turned out that BeTe can play a key role in the fabrication of light emitters. The valence band offset between this binary and ZnSe was measured by photoluminescence (PL) to be about 0.9 eV [11], very similar to that in ZnTe/ZnSe. Thus, the absolute valence band energy nearly coincides with the valence band of GaAs. Therefore, the device architecture of light-emitting devices can be based on two schemes, which are shown in Fig. 5. In Fig. 5a, the substrate is p-type GaAs with an adjacent BeTe/ZnSe superlattice providing hole injection. Fig. 5b shows a variation of the conventional ZnMgSSe laser diode grown on a n-type GaAs substrate. In our case, Be-alloys and a BeTe/ZnSe pseudograding are used instead of ZnTe/ZnSe as p-type contact. In the following, the main components of these devices will be discussed in detail. One major advantage of BeTe is the possibility of high p-type doping, which is discussed in Ref. [20]. Together with the high valence band energy, which has already been expected by Mensz [21] and

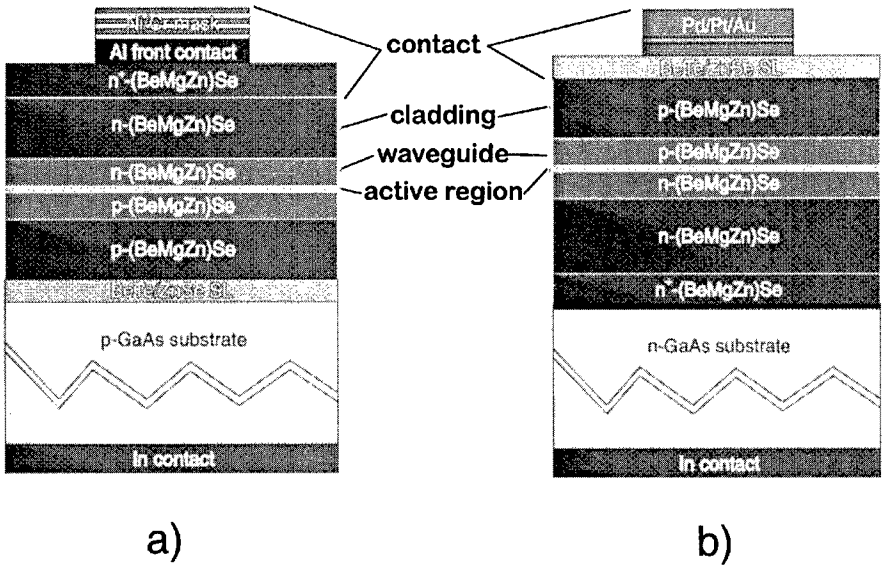

Fig. 5. Proposed structures of laser diodes based on Be-compounds (a) on p-GaAs and (b) n-type GaAs substrates.

Dandrea et al. [22], BeTe can easily replace ZnTe in p-type digital contacts to ZnSe based layers. Hence, it can provide an appreciable improvement of the structural quality of the graded gap contact sequence. BeTe is usually grown under Te-rich conditions with VI : II ratios of about 4 to 20. In this regime, one can obtain well-pronounced and long-lasting RHEED intensity oscillations indicating a smooth layer-by-layer growth mode. At optimum growth conditions thick BeTe layers can be fabricated with excellent surface morphology which can be seen in sharp RHEED patterns as shown in Fig. 6. For the growth of BeTe/ZnSe heterostructures the conditions have to be carefully adjusted in order to get smooth interfaces. At a substrate temperature of 300°C one can observe a degradation of the RHEED patterns, if Se impinges onto the 2×1 reconstructed Te-rich surface of BeTe. We attribute this to the repulsion of Te by Se atoms, which leads to an inhomogeneous distribution of Be–Te and Be–Se bonds at the interface. Both the competition between Se and Te as well as the high sticking coefficient of Be have consequences on the growth of BeTe/ZnSe heterostructures: before the growth of ZnSe on BeTe a Zn flux can be applied to the Te-rich BeTe surface in order to reduce the Se–Te exchange reaction. On top of the ZnSe layer a Zn-rich surface can be prepared by an additional Zn flux ($c(2 \times 2)$ reconstruction) which is followed by the growth of BeTe again.

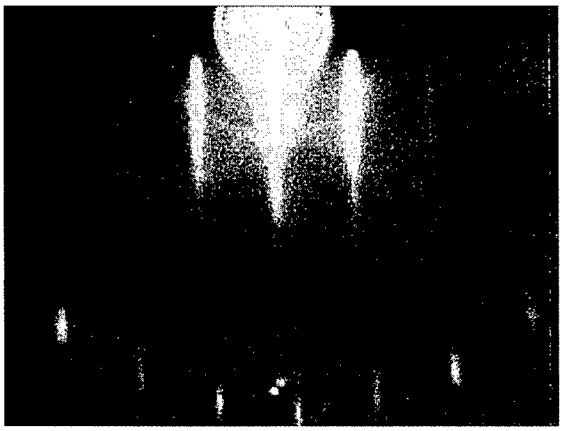

Fig. 6. [1 1 0] RHEED patterns of the Te-rich BeTe surface (35 keV).

In first experiments the application of a thin BeTe layer as a buffer layer on GaAs seems to reduce the grown-in stacking fault density in ZnSe-based materials. The reason for that could be

the prevention from Se reaching the clean GaAs surface where it can nucleate a lattice defect [23].

3.4. New materials for the active region

Using mixed crystals containing Be for the active layer the rigidity of this region will be increased. Recently, Law et al. [24] improved the lifetime of a blue–green ZnMgSSe laser diode by using a quaternary ZnCdSSe quantum well (QW) in the active zone, instead of a ternary ZnCdSe QW. They attribute this effect to a reduced growth of dark line defects, which can be interpreted in terms of a reduced defect mobility. By the use of Be-compounds, it is possible to tailor the optical as well as the lattice properties like rigidity and stress. Thereby, the lattice hardening effect is expected to be significantly stronger than in conventional II–VI alloys. For exploiting the properties of new materials like BeZnSeTe or BeZnCdSe, it has to be guaranteed that the electrical confinement will still be sufficient if the concentration of Be as a constituent of the active material is increased. In Fig. 7 the PL spectra of thin layers from (a) ZnCdSe (70 Å quantum well), (b) BeZnCdSe (70 Å quantum well), (c) lattice-matched BeZnSeTe (1 μm epilayer), and BeTe/ZnSe superlattices with various period widths (spectra (d) and (e)) have been plotted. For the BeZnCdSe QW the luminescence energy is shifted by 94 meV with respect to the ZnCdSe QW.

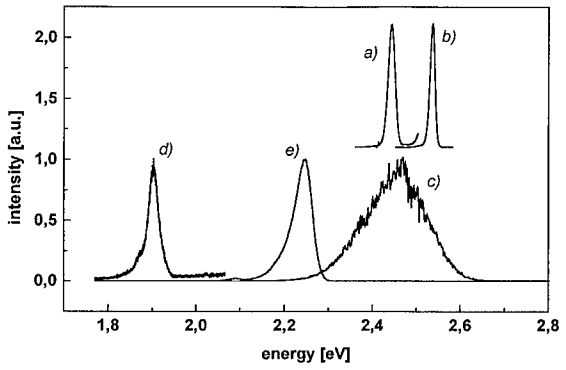

Fig. 7. PL spectra (2 K) derived from (a) ZnCdSe QW, (b) BeZnCdSe QW, (c) BeZnSeTe epilayer, (d) BeTe/ZnSe superlattice (period 300 Å) and (e) BeTe/ZnSe superlattice (period 39 Å). All spectra are normalized to their maximum.

The amount of Cd is equal in both QWs. The Be content of about 3% inside the QW was kept the same as in the BeZnSe barriers, which can be the material for the optical waveguide in a laser diode. The material BeZnSeTe can also be used for the light emitting zone in a LED or laser diode. Due to a pronounced bowing which is observed in this system, the emission line can be shifted over a wide range. In Fig. 7 one can see the PL spectrum of a BeZnSeTe layer. It exhibits a relatively broad line shape with a maximum at 2.46 eV. The concentration of Be and Te was chosen to match the GaAs substrate (8.4% Be, 9.5% Te as measured by wavelength-dispersive X-ray analysis WDX). For a better control of the composition BeTe/ZnSe superlattices (SL) can be considered for the device design. By adjusting period width and layer thicknesses, the miniband energies for electrons and holes can be varied. The type II transition between BeTe and ZnSe allows to tune the luminescence line between 1.9 and about 3 eV [25]. In Fig. 7 the spectrum (d) is shown for a BeTe/ZnSe superlattice with a wide period (100 Å BeTe, 200 Å ZnSe) which is nearly lattice-matched to the GaAs substrate. In that case, the spectrum is dominated by the intensive type II transition at 1.9 eV. Decreasing the period of the SL from 300 to e.g. 39 Å (13 Å BeTe, 26 Å ZnSe) the luminescence line shifts to 2.249 eV (spectrum (e)). Major advantage of that technique is the easy control of composition and energy by digital alloying and the introduction of high Be concentrations into the QW region.

3.5. Light emitting diodes based on BeMgZnSe

The first LED structures have been grown by MBE on p-type GaAs substrates according to the sketch in Fig. 5a. For the quantum well BeZnSeTe (LED1), ZnSe (LED2) and BeZnSe (LED3) have been used. For LED1 no waveguide layers have been used. In the case of LED2 and LED3 the waveguide consists of 100 nm BeZnSe and BeMgZnSe with low Mg and Be content, respectively. All cladding layers were made from BeMgZnSe with a band gap of about 3.0 eV at room temperature. The n-type contact was made with Al [16]. In Fig. 8 current–voltage (IV) characteristics of LEDs have been plotted. One can see a steep

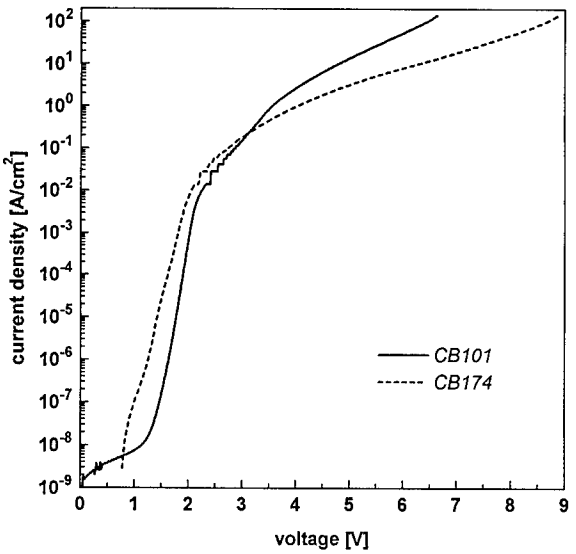

Fig. 8. Current–voltage characteristics of BeMgZnSe-LED structures at room temperature under cw excitation.

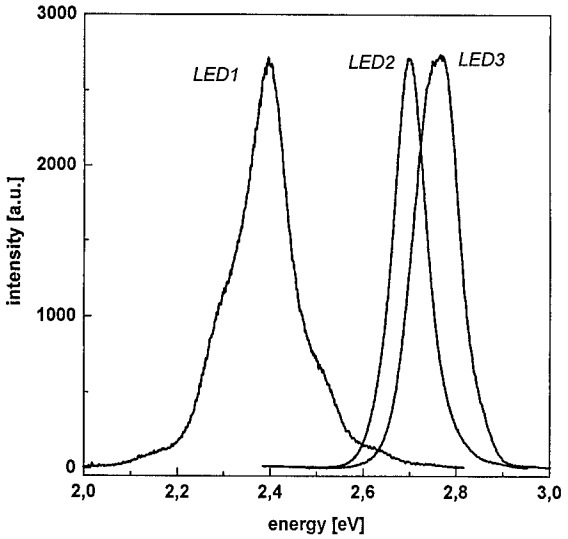

Fig. 9. Electroluminescence spectra of light emitting diodes. LED1: BeZnSeTe QW active region, LED2: ZnSe QW, LED3: BeZnSe QW. All spectra are normalized to their maximum.

increase of the current under low forward bias which can be attributed to recombination-controlled current. At bias voltages exceeding 3 V the series resistance seems to become dominant. The spectra of the LEDs (Fig. 9) have been measured under cw excitation at room temperature at moderate current densities of 15 A/cm^2. LED1 shows a broad emission line with a maximum peak at 2.41 eV. The emission of LED2 and LED3 have a maximum at 2.68 and 2.74 eV, respectively. All LEDs show bright luminescence in the vicinity of the nontransparent Al contact. For the optical measurements only the light from the edge of the contact pad was collected, thus, it is not reasonable to present any value of the external efficiency yet. Concerning the device lifetimes of LEDs, first experiments have been carried out on LED3. At moderate current densities (15 A/cm^2) a slow decay of the light output can be observed over a long time. Extrapolated exponential time constants of this decay to reach $\frac{1}{2}$ of the initial output have been determined to be in the range of 4000 h. At current densities exceeding 100 A/cm^2 a catastrophic degradation was observed after several hours. From scanning electron microscopy this can definitely be ascribed to the degradation of the metal pad which was attached by a contact needle. Therefore, the design of the LED structures has to be improved in order to investigate the real mechanism of degradation.

4. Conclusion

The potential of beryllium chalcogenides for the development of blue–green light emitters has been demonstrated. It turned out that quaternary mixed crystals of the composition BeZnMgSe can be produced in high-quality with high-precision. The first results obtained for light emitting devices have been very encouraging. The main task for the future will be the optimization of the growth conditions and the device design as well as the realization of laser diodes, based on this novel class of II–VI semiconductors.

5. Note added in proof

The first laser diodes containing beryllium have been realized in the meantime [26].

Acknowledgements

The authors gratefully acknowledge the support from the Bundesministerium für Bildung und Forschung, Bonn and the Bayerische Forschungsstiftung, München and they also want to thank P. Wolf-Müller, N. Hemmrich, V. Hock and K. Schüll for their help during sample preparation. The authors are grateful for the support by the Volkswagen Stiftung (F.F.) and the Deutsche Forschungsgemeinschaft (Th.L.).

References

[1] M.A. Haase, J. Qui, J.M. dePuydt, H. Cheng, Appl. Phys. Lett. 59 (1991) 1272.
[2] A. Ishibashi, J. Crystal Growth 159 (1996) 555.
[3] R.N. Hall et al., Phys. Rev. Lett. 9 (1962) 366.
[4] H. Kroemer, Proc. IEEE Conf. 51 (1963) 1782.
[5] Zh. Alferov et al., Fiz. Tech. Pol. 4 (1970) 1826.
[6] Hayashi et al., Appl. Phys. Lett. 17 (1970) 109.
[7] A. Ishibashi, M. Ukita, S. Tomiya, in: M. Scheffler, R. Zimmermann (Eds.), 23rd Int. Conf. on the Physics of Semiconductors, Berlin, vol. 4, World Scientific, Singapore, 1996, p. 3155.
[8] C. Verie, in: B. Gil, R.-L. Aulombard (Eds.), Semiconductor Heteroepitaxy, World Scientific, Singapore, 1995, p. 2145.
[9] W. Harrison, Electronic Structure and the Properties of Solids, Dover, New York, 1989.
[10] W.M. Yim, J.P. Dismukes, E.J. Stofko, R.J. Paff, J. Phys. Chem. Solids 33 (1972) 501.
[11] A. Waag, F. Fischer, H.J. Lugauer, Th. Litz, J. Laubender, U. Lunz, U. Zehnder, W. Ossau, Th. Gerhard, M. Möller, G. Landwehr, J. Appl. Phys. 80 (2) (1996) 792.
[12] A. Waag, F. Fischer, H.J. Lugauer, Th. Litz, J. Laubender and G. Landwehr, Int. Symp. on Blue-Light Emitting Diodes and Lasers, Chiba, 1996.
[13] U. Lunz, M. Keim, G. Reusher, F. Fischer, K. Schuell, A. Waag and G. Landwehr, J. Appl. Phys. 80 (1996).
[14] S. Nakamura, Proc. Physics and Simulation of Optoelectronic Devices IV, SPIE 2693 (1996) 29.
[15] Th. Litz, H.J. Lugauer, F. Fischer, U. Zehnder, U. Lunz, Th. Gerhard, H. Ress, A. Waag and G. Landwehr, EMRS Spring Meeting, Strasbourg, 1996.
[16] F. Fischer, J. Laubender, H.J. Lugauer, Th. Litz, A. Weingärtner, U. Zehnder, Th. Gerhard, W. Ossau, K. Schüll, A. Waag and G. Landwehr, EMRS Spring Meeting, Strasbourg, 1996.
[17] K. Kondo, H. Okuyama, A. Ishibashi, Appl. Phys. Lett. 64 (1994) 3434.
[18] S. Tatarenko, T. Baron, A. Arnoult, J. Cibert, M. Grün, A. Haury, Y. Merle d'Aubigné, A. Wasiela and K. Saminadayar, J. Crystal Growth 175/176 (1997) 682.
[19] G. Mandel, F.F. Morehead and P.R. Wagner, Phys. Rev. 136 (1964) A826; G. Mandel, Phys. Rev. 134 (1964) A1073.
[20] H.-J. Lugauer, F. Fischer, Th. Litz, A. Waag, U. Zehnder, W. Ossau, Th. Gerhard and G. Landwehr, EMRS Spring Meeting, Strasbourg, 1996.
[21] P.M. Mensz, Appl. Phys. Lett. 64 (16) (1994) 2148.
[22] R.G. Dandrea, C.B. Duke, Appl. Phys. Lett. 64 (16) (1994) 2145.
[23] W. Spahn, H.R. Reß, K. Schüll, M. Ehinger and G. Landwehr, J. Crystal Growth, to be published.
[24] K.K. Law, P.F. Baude, T.J. Miller, M.A. Haase, G.M. Haugen, K. Smekalin, Electron. Lett. 32 (4) (1996) 345.
[25] H.J. Lugauer, Th. Litz, F. Fischer, A. Waag, Th. Gerhard, U. Zehnder, W. Ossau and G. Landwehr, J. Crystal Growth 175/176 (1997) 619.
[26] A. Waag, F. Fischer, K. Schuell, T. Baron, H.-J. Lugauer, Th. Litz, U. Zehnder, W. Ossau, Th. Gerhard, M. Keim, G. Reuscher and G. Landwehr, Appl. Phys. Lett. 70 (1997) 280.

ELSEVIER

Journal of Crystal Growth 175/176 (1997) 541–545

JOURNAL OF CRYSTAL GROWTH

Molecular beam epitaxial growth of lattice-matched $Zn_xCd_yMg_{1-x-y}Se$ quaternaries on InP substrates

L. Zeng[a,*], A. Cavus[a], B.X. Yang[a], M.C. Tamargo[a], N. Bambha[b], A. Gray[b], F. Semendy[b]

[a] *CUNY Center for Advanced Technology (CAT) on Photonic Materials and Applications, Center for Analysis of Structures and Interfaces (CASI) and Department of Chemistry, City College-CUNY, New York, New York 10031, USA*

[b] *IR Optical Technology OFS, Army Research Laboratory, Fort Belvoir, Virginia 22060, USA*

Abstract

We report the molecular beam epitaxial (MBE) growth of lattice-matched $Zn_xCd_yMg_{1-x-y}Se$ quaternaries on InP substrates having a wide range of band gaps. The composition and, thus, band gap and lattice constant, can be accurately controlled by adjusting the group II fluxes. By optimizing the growth condition and incorporating of a III–V buffer layer, we have grown very high-quality quaternary layers. Our best lattice-matched samples exhibit double crystal X-ray rocking curves with full-width-at-half-maximum (FWHM) about 460 arcsec and photoluminescence line widths about 60 meV at 77 K for a band gap of 2.8 eV. These materials can be used for the fabrication of lattice-matched semiconductor lasers that can emit throughout most of the visible range, from yellow to blue.

1. Introduction

Wide band gap II–VI compounds have potential applications as blue–green light emitters. Currently, reported blue–green lasers [1–4] are based on heterostructures of ZnSe-based alloys grown on GaAs substrates. Pseudomorphic structures are obtained by using ZnMgSSe and ZnSSe lattice-matched to the GaAs substrate as the barrier and wave-guiding layers, respectively. A thin, strained $Zn_{0.8}Cd_{0.2}Se$ quantum well layer is used in the active region, and a ZnSe/ZnTe graded superlattice is used to obtain ohmic contacts to the top p-cladding layers. Using this material system, Sony Corporation [4] has succeeded in fabricating a blue–green laser diode with a room temperature cw operating lifetime in excess of 100 h, showing that significant improvements have been achieved.

However, the performance of the devices is still not adequate. Some of the issues that remain to be solved before practical devices are realized are the defects originating at the II–VI/III–V interface possibly due to the influence of sulfur and selenium on the GaAs substrates [5], p-doping [6], the presence of strain in the active layer and the formation of misfit dislocations in the contact layers due to the large lattice-mismatch between ZnTe and the rest of the structure. Therefore, it is of interest to

* Corresponding author.

0022-0248/97/$17.00 Copyright © 1997 Published by Elsevier Science B.V. All rights reserved
PII S0022-0248(96)00873-1

explore other wide band gap II–VI materials that may be used to design entirely lattice-matched structures that also meet the band-structure requirements of this complex device.

Recently [7–9], we reported the growth and properties of $Zn_xCd_yMg_{1-x-y}Se$, a new quaternary materials system that can be used in the design and fabrication of blue (visible) lasers. These lattice-matched quaternary layers encompass a wide range of band gaps, from 2.18 eV to above 3.5 eV, enabling the growth of device structures that can emit throughout most of the visible range [8]. By growing these on InP substrates, entirely lattice-matched heterostructures can be obtained. The use of InP substrates also allows the growth of a symmetrically strained ZnSe/ZnTe superlattice for the ohmic contact, eliminating the formation of misfit dislocations in the contact layer. These features are expected to improve the overall material quality and the performance of the laser structure.

In this paper, we report the molecular beam epitaxial (MBE) growth and properties of high-quality lattice-matched $Zn_xCd_yMg_{1-x-y}Se$ quaternaries with a wide range of compositions. We investigate the relationship between the growth parameters and the material properties such as lattice mismatch and band gap. By optimizing the growth condition and incorporating a III–V buffer layer, we have grown high-quality layers with double crystal X-ray rocking curve full-width-at-half-maximum (FWHM) $\sim$ 460 arcsec and 77 K photoluminescence (PL) line widths of about 60 meV for a band gap of 2.8 eV. Further improvements in crystalline quality may be achieved by modification of the nucleation process.

2. Experimental procedure

The layers were grown by molecular beam epitaxy (MBE) in a Riber 2300P system which includes a III–V chamber and a II–VI chamber connected by UHV. InP (1 0 0) substrates having defect densities of $\sim 10^3$ cm^{-3} were obtained from Sumitomo Electric. Prior to use, the substrates were etched in $H_2SO_4 : H_2O_2 : H_2O$ (4 : 1 : 1) for 1 min. Oxide desorption of the InP substrate was performed by heating with an As flux inpingent on the InP surface [10]. The best results were obtained by heating quickly to $\sim$ 500°C, once the oxide is removed we adjust the temperature to the growth temperature of the III–V buffers. It is expected that 1 or 2 strained monolayers of InAs may form during this step. A lattice-matched InGaAs or InP buffer layer ($\sim$ 200 nm) was grown on the InP substrate, then the substrate with the buffer layer was transferred to the II–VI chamber in vacuum to grow the ZnCdMgSe quaternaries. Growth was performed under Se-rich conditions with a beam equivalent pressure (BEP) ratio of the group-VI to group-II fluxes of $\sim$ 4. The growth was initiated at growth temperature of 170°C, and after 1 min of growth, the temperature was raised to the optimum growth temperature of 270°C without interruption [9]. After the growth of the quaternary for 1 h; a thin ($\sim$ 10 nm) ZnCdSe layer was grown as a cap layer to protect magnesium from oxidation. The quaternary layer thickness ranged from 0.4 to 0.8 μm for the different quaternary compositions.

In these experiments, the equivalent beam flux of Zn was fixed to about 2×10^{-7} Torr and the Cd flux was changed so that the Cd to Zn (Cd/Zn) flux ratio would vary from $\sim$ 0.5 to 2.2. Flux measurements of Mg could not be performed accurately with our chamber geometry so we adjusted the Mg flux by controlling the Mg cell temperature, which was varied from 245°C to 280°C.

The layers were characterized by low-temperature photoluminescence (PL) at 10 and 77 K using the 325 nm line of a He–Cd laser, the excitation power is 0.25 mw for 10 K and 1.5 mw for 77 K. Lattice mismatch was determined by single-crystal X-ray diffraction and crystalline quality was assessed in a few samples using double-crystal X-ray rocking curves. The surface morphology was observed with a Nomarski microscope. The thickness was measured using a Philtec sectioner.

3. Results and discussion

Fig. 1 shows the percent lattice mismatch of the quaternary layer to InP ($\%\Delta a/a$) as a function of Cd/Zn flux ratio used during growth for various Mg fluxes. The zero mismatch position is indicated in the figure by a dashed-line. The solid

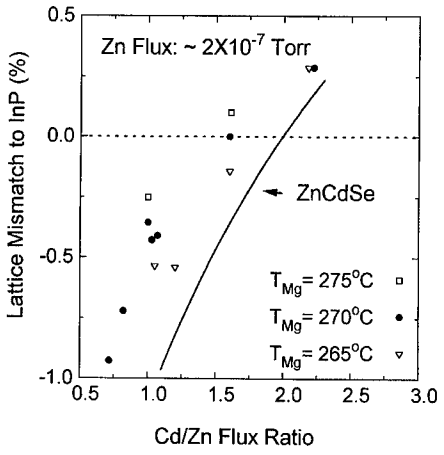

Fig. 1. Dependence of Cd to Zn flux ratio on the lattice-mismatch of ZnCdMgSe layers grown on InP with various Mg fluxes. The dashed line indicates the lattice matched conditions. The solid line shows the dependence for ZnCdSe.

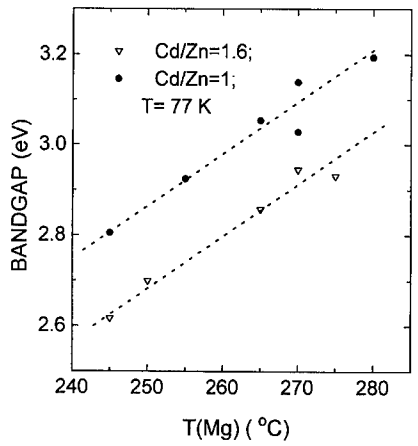

Fig. 2. Dependence of quaternary band gap on Mg cell temperature (flux) for two Cd to Zn flux ratios. The Zn flux is kept costant at 2×10^7 Torr.

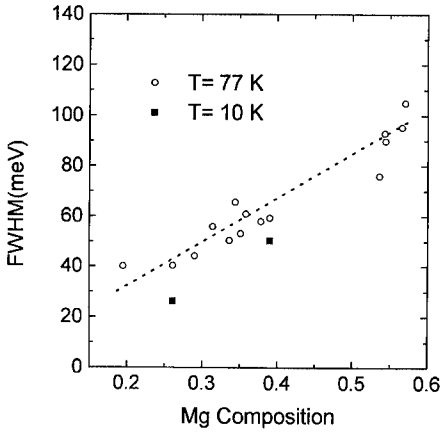

Fig. 3. Variation of the 77 K photoluminescence line width (FWHM) as a function of Mg cell temperature (flux). Two data points measured at 10 K are also shown (squares).

line represents the empirical fit to the ZnCdSe ternary. For Cd/Zn = 2 which is the condition for ZnCdSe lattice-matched to InP, changing the Mg flux does not affect the mismatch very much, but it is always greater than 0, and the layers tend to have spotty RHEED patterns. Therefore to obtain lattice-matched quaternaries we must reduce the Cd/Zn ratio: in order to incorporate more Mg and get higher band gaps, one must lower the Cd/Zn ratio further.

Fig. 2 shows the dependence of the quaternary band gap on Mg flux for two different Cd/Zn flux ratios both of which are less than 2. The band gap energy was estimated from the photoluminescence spectra at 77 K. A comparison between the PL emission wavelength and photoreflectance signals for several samples confirmed that the PL spectra are in fact dominated by bandedge emission. For the band gap estimates we did not account for any exciton binding energy at 77 K. We feel that this will not have a significant influence on our results. For Cd/Zn = 1, changing the Mg temperature from 245°C to 275°C causes the mismatch to change from -0.7% to -0.2% and the band gap to change from 2.6 to 2.9 eV. For this Cd/Zn ratio, in order to get less mismatch and higher band gap, one must increase the Mg flux further. However, when we increase the Mg temperature above 280°C, the layer quality degrades. When the Cd/Zn flux ratio is about 1.6, if we change the Mg temperature from 245°C to 280°C, the mismatch changes from -0.2% to 0.1%, and the band gap changes from 2.8 to 3.2 eV. At this flux ratio, for small changes in mismatch we can obtain a wide range of band gaps, making it useful for the laser design.

Fig. 3 shows the relationship between the FWHM of the PL measured at 77 K and the Mg composition in the solid for layers having a mismatch range from -1% to 0.2%. The Mg compositions $(1 - x - y)$ in the solid were calculated

from the PL and X-ray data by constructing a mathematical expression to describe the relations between the band gap, lattice constant of the quaternary and its composition, based on the known ZnCdSe function and assuming linear dependencies for the ZnMgSe and MgCdSe ternary boundaries. Similar calculations have been reported previously for ZnCdSeTe [11]. From the figure, we find that the PL FWHM increases linearly with increasing Mg composition and independently of the mismatch. Thus, we conclude that the large widths are not caused by defects resulting from a large mismatch. One possible explanation for the broadening of the PL peak with Mg fraction is possible compositional non-uniformities for high Mg compositions. From observations during growth, we note that it is very difficulty to grow $Zn_xCd_yMg_{1-x-y}Se$ quaternaries with Mg compositions higher than 0.6, because the RHEED pattern tends to be spotty. When the Cd/Zn flux ratio is either too low (less than 1) or too high (greater than 2), one needs to incorporate a large amount of Mg in the quaternaries to keep the layers well lattice-matched and with high band gaps; and the growth is difficult. So we conclude that the best Cd/Zn flux ratio to use should be around 1.6. Two PL FWHM data points taken at 10 K are also shown in Fig. 3. Even for high Mg composition, ~ 0.4, the FWHM at 10 K is about 50 meV which is significantly lower than the reported value of 100 meV [12] for quaternaries of the same composition.

The relationship between the Cd/Zn composition ratio in the solid and the Cd/Zn flux ratio used during growth is shown in Fig. 4 for samples grown with different Mg cell temperatures. The Cd and Zn compositions are calculated the same way we calculated Mg composition. We note that the calculated Cd/Zn ratio is proportional to the measured Cd/Zn flux ratio which suggests that incorporation of Mg does not affect the sticking efficiency of Zn and Cd. Taking advantage of this observation we have grown ZnCdSe ternary and ZnCdMgSe quaternary layers under the same growth conditions (including the growth time, Zn and Cd fluxes, etc.), and used the thickness difference between the ZnCdSe and ZnCdMgSe layers (i.e., the difference in growth rate) to estimate the Mg composition. Table 1 compares the calculated Mg composition based on our mathematical expression with the Mg composition estimated from thickness. Good agreement (better than 10%) between the two values was observed.

With the optimum growth conditions and with the incorporation of a III–V buffer layer, we have grown very high-quality ZnCdMgSe quaternaries. Fig. 5 shows the 77 K PL spectra for two of our

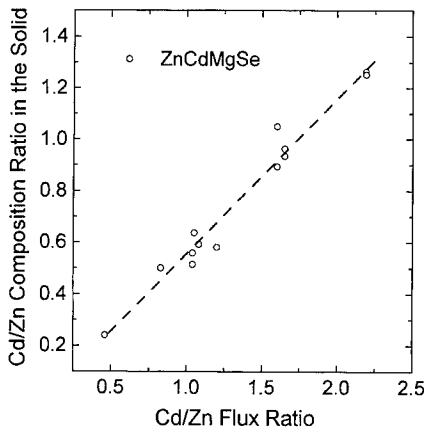

Fig. 4. Relationship between the Cd to Zn composition ratio in the solid, calculated as described in the text, to the experimental Cd to Zn flux ratios.

Table 1
Comparison of the calculated Mg composition in the layer and measured Mg composition, as described in the text

Sample	Mg composition	
	Calculated	Measured
1	0.57	0.62
2	0.47	0.53
3	0.43	0.45
4	0.39	0.43
5	0.5	0.52

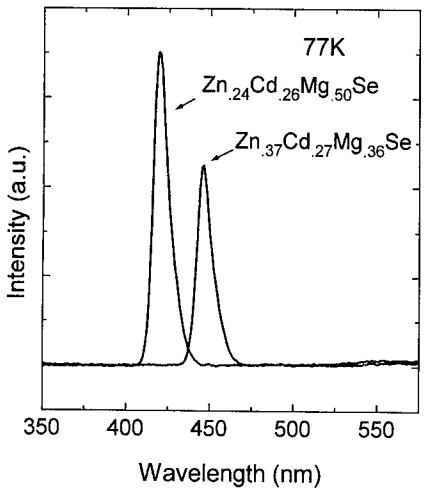

Fig. 5. Photoluminescence spectra at 77 K for two $Zn_xCd_yMg_{1-x-y}Se$ layers grown on InP substrates with InP buffer layers.

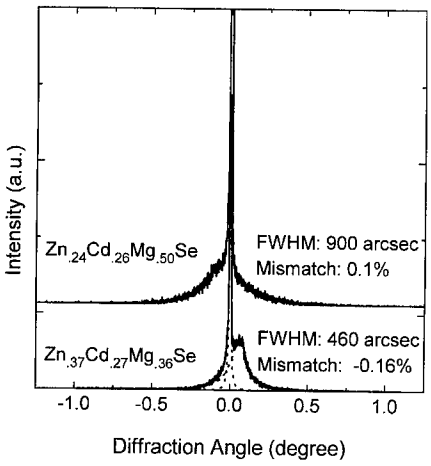

Fig. 6. Double crystal X-ray rocking curves for two $Zn_xCd_yMg_{1-x-y}Se$ layers grown on InP substrates with InP buffer layers.

samples, having band gaps of 2.8 and 3.0 eV. The PL data shows that the quaternaries have very strong and narrow band edge emission peaks without any significant deep-levels. The double crystal X-ray rocking curves, shown in Fig. 6, exhibit FWHM of about 460 and 900 arcsec, respectively. Preliminary results suggest that further improvements in the crystalline quality can be achieved by using a ternary ZnCdSe buffer layer.

4. Conclusions

We have investigated the growth conditions of ZnCdMgSe quaternaries and have obtained relationships that allow the determination of the appropriate group II fluxes needed to grow lattice-matched layers with band gaps varying over the entire range of the quaternary system. Using these conditions we have grown high-quality lattice-matched quaternary layers having band gap up to 3.1 eV. These materials have applications in the design and fabrication of lattice-matched wide band gap II–VI emitters (lasers and LEDs) that can be designed to emit throughout the visible range.

Acknowledgements

The support of the National Science Foundation through grant number ECS93-20415 is gratefully acknowledged.

References

[1] J.M. Gaines, R.R. Drenten, K.W. Haberbern, T. Marshall, P. Menz and J. Petruzzello, Appl. Phys. Lett. 62 (1993) 2462.
[2] N. Nakayama, S. Itoh, T. Ohata, K. Nakano, H. Okuyama, M. Ozawa, A. Ishibashi, M. Ikeda and Y. Mori, Electron. Lett. 29 (1993) 1488.
[3] A. Salokatve, H. Jeon, J. Ding, M. Hovinen, A.V. Nurmikko, D.C. Grillo, J. Han, L. He, R.L. Gunshor, G.C. Hua and N. Otsuka, Electron. Lett. 29 (1993) 2192.
[4] Compound Semiconductor, March/April, 1996 p. 7.
[5] S. Guha, B.J. Wu, H. Cheng and J.M. dePuydt, Appl. Phys. Lett. 63 (1993) 2129.
[6] Y. Ichimura, K. Kishino, M. Satake, M. Kuramoto and A. Yoshida, Proc. 8th Int. Conf. on Molecular Beam Epitaxy, Vol. B10-4, Osaka (1994) p. 278.
[7] M.C. Tamargo, A. Cavus, L. Zeng, N. Dai, N. Bambha, A. Gray, F. Semendy, W. Krystek and F.H. Pollak, J. Electron. Mater. 25 (1996) 259.
[8] A. Cavus, L. Zeng, M.C. Tamargo, N. Bambha, F. Semendy and A. Gray, Appl. Phys. Lett. 68 (1996) 3446.
[9] N. Dai, A. Cavus, R. Dzakpasu, M.C. Tamargo, F. Semendy, N. Bambha, D.M. Hwang and C.Y. Chen, Appl. Phys. Lett. 66 (1995) 2743.
[10] K.Y. Cheng, A.Y. Cho, W.R. Wagner and W.A. Bonner, J. Appl. Phys. 52 (1981) 1015.
[11] M.C. Tamargo, M.J.S.P. Brasil, R.E. Nahory, R.J. Martin, A.L. Weaver and H.L. Gilchrist, Semicond. Sci. Technol. 6 (1991) A8.
[12] T. Morita, A. Kikuchi, I. Nomura and K. Kishino, J. Electron. Mater. 25 (1996) 42.

ELSEVIER

Journal of Crystal Growth 175/176 (1997) 546–551

JOURNAL OF CRYSTAL GROWTH

Surface preparation of ZnSe substrates for MBE growth of II–VI light emitters

W.C. Hughes, C. Boney, M.A.L. Johnson, J.W. Cook, Jr., J.F. Schetzina*

Department of Physics, North Carolina State University, P.O. Box 8202, Raleigh, North Carolina 27695-8202, USA

Abstract

This paper describes substrate surface preparation techniques used in the development II–VI light emitting diode and laser diode structures on high-quality, bulk ZnSe substrates supplied by Eagle-Picher Industries. The use of ZnSe substrates eliminates many of the problems associated with lattice mismatch in heteroepitaxy of II–VI light emitters on GaAs substrates. However, defects still form during nucleation of an epitaxial layer on ZnSe substrates because of surface roughness, contamination, and defects. We have employed a variety of wet chemical etches, vacuum anneals, plasma treatments, and characterization techniques such as RHEED, Auger electron spectroscopy, and SEM studies to improve the ZnSe substrate surface prior to MBE film growth. A combination of hydrogen plasma exposure and annealing was found to be the most effective way to remove contaminants from ZnSe substrates but less than optimum homoepitaxial quality showed that the surface preparation is more complex than simply cleaning the polished surface. Since polishing can leave residual damage in the form of near-surface defects, the top layer of these substrates was removed by reactive ion etching with BCl_3. Parameters were chosen such that this etch was homogeneous and smoothed the ZnSe surface. Etch pit density measurements revealed that the polish-induced damage to ZnSe extended up to about 5 μm deep. A dramatic improvement in the characteristics of blue/green light emitting devices was observed for devices grown on ZnSe substrates from which this damaged layer had been removed. This surface preparation procedure has led to the brightest and longest lasting II–VI green LEDs made in the world today.

1. Introduction

Many demonstrations have recently been made of both light emitting diodes and laser diodes grown from ZnSe-based materials on both GaAs and ZnSe substrates. However, full commercialization of this technology will not be possible as long as high defect densities limit device lifetimes. While advances have been made in extending the lifetime by improving the quality of the heterointerface in ZnSe-based devices grown on GaAs, in other material systems the best quality films are always grown homoepitaxially.

The development of high-quality ZnSe substrates at Eagle–Picher Industries in Oklahoma has led to an improvement in homoepitaxial films and devices. Dislocation densities in these bulk crystals is now as low as 10^3 cm^{-3}. At North Carolina State,

* Corresponding author. Fax: + 1 919 5157667; e-mail:jan_schetzina@ncsu.edu.

0022-0248/97/$17.00 Copyright © 1997 Elsevier Science B.V. All rights reserved
PII S0022-0248(96)01022-6

we have demonstrated that molecular beam epitaxy (MBE) on these substrates can lead to improved LED properties such as lower threshold current, higher quantum efficiency, and longer lifetime. Further improvement depends upon the elimination of defects arising at the interface between the substrate and the film which are possibly caused by the homoepitaxial nucleation. These defects can be reduced by eliminating contamination, surface roughness, and defects in the substrate itself.

Wet cleaning and thermal annealing techniques have either not been sufficient to remove carbon and oxygen or have been too destructive for use in preparation of ZnSe substrates for MBE growth. Br/methanol solutions of varying strengths can remove the native oxide from ZnSe surfaces but either do not remove carbon or add carbon to the surface [1]. Furthermore, this etch has been found to roughen the surface of ZnSe in some cases. Similar contamination has been observed from other acid treatments and additional contamination with Cl or S was seen in some cases.

Contamination control is not a new field, and much of what has been learned from the surface preparation of Si and GaAs can be used on ZnSe. Oxygen and nitrogen can be removed from Si by dipping in HF [2, 3]. This does contaminate the surface further with carbon, but this can be removed by exposing the substrate to a hydrogen-containing plasma in a UHV system. This plasma cleaning also passivates the surface by hydrogen termination. Similar techniques have been used to remove contaminants on other semiconductors. This includes the use of atomic hydrogen generated in an rf plasma to clean GaAs used for ZnSe heteroepitaxy [4], and 6H–SiC [5] and GaN [6] surfaces for the MBE growth of GaN. Green light-emitting diodes have been grown on ZnSe substrates which were hydrogen cleaned by the University of Florida [7].

In this study, we have optimized the cleaning of ZnSe substrates using plasmas by observing the Auger electron spectra, RHEED patterns from the surface before and during growth, and the defect density and device characteristics of structures grown on the substrates. We cover not only the growth of homoepitaxial ZnSe, but also lattice-matched quaternary compounds containing magnesium, tellurium, and sulfur.

We have also considered the necessity of removing a layer of polishing-induced damage in the first few microns of the substrate. Since polishing can leave behind a smooth surface covering a layer of increased defect density, a technique was devised to remove the top 5 μm of the substrate without roughening the surface. We sought a correlation between the depth of material removed and the etch pit density of the substrate and characteristics of devices grown on these substrates.

2. Wet etching and annealing

The ZnSe substrates were sawed and polished into smooth, flat surfaces by Eagle–Picher Industries and degreased with a standard technique prior to MBE growth. The substrates were then loaded into a multichamber MBE growth system equipped with a RHEED gun for in situ surface analysis. The sample could be transferred in ultra-high vacuum to an analysis station, where Auger electron spectroscopy was performed.

RHEED images taken from the surface of an as-received substrate show diffuse streaks indicative of a smooth surface coated with a native oxide (Fig. 1a). Vacuum annealing at 550°C leads to a slight improvement in the RHEED pattern (Fig. 1b). However, the Auger spectrum showed that the annealing removed all the chlorine from the degrease but only a small amount of the oxygen or carbon (Fig. 2a and Fig. 2b). Higher temperature anneals could remove more oxide but at the cost of thermally etching and roughening the substrate.

Several substrates were wet etched and/or preheated before film growth. These treatments remove oxygen but not carbon from the surface of ZnSe. However, films grown on these substrates did not show high quality and contained large numbers of defects which led to reduced device lifetimes.

A related method of removing oxide is the sulfidization of the surface. This method has been shown to improve heteroepitaxial growth rates when used on GaAs substrates [8]. The ZnSe substrates were pretreated with ammonium sulfide to strip away native oxides and terminate the surface

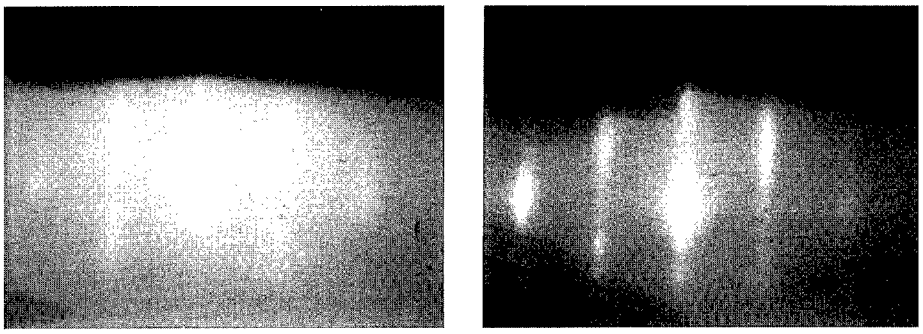

Fig. 1. (a) RHEED pattern from the surface of a bulk ZnSe substrate as loaded into the growth chamber after a degrease with TCE, acetone, and methanol. (b) RHEED pattern from the same sample after annealing in vacuum at 550°C for 10 min.

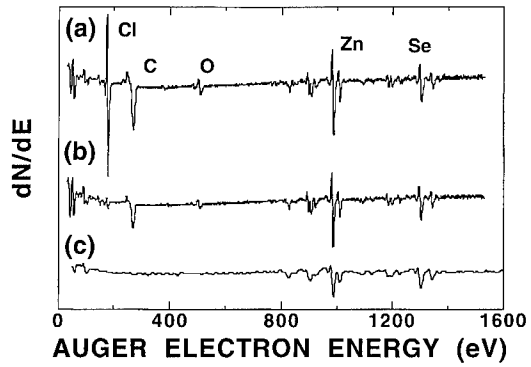

Fig. 2. Auger spectra of bulk ZnSe substrates (a) after a standard degrease with TCE, acetone and methanol; (b) after subsequent vacuum annealing at 550°C for 10 min; (c) after exposure to 325 W, 5×10^{-4} Torr hydrogen plasma at 200°C.

with sulfur. Again, there was no improvement in film quality and device lifetimes remained low so this technique was abandoned.

3. Hydrogen plasma cleaning

Hydrogen plasma cleaning experiments were performed in the MBE growth chamber using an Oxford applied research MPD21 rf plasma source located approximately 10 in from the substrate surface. In order to ignite the hydrogen mixtures of hydrogen with argon or helium were sometimes used.

A series of experiments were performed to determine the best plasma exposure time and sample temperature for removing carbon and oxygen. Since hydrogen can also be used as an etchant for ZnSe or other II–VI's with reactive ion etching [9–11] in which hydrogen removes Se by forming the highly volatile H_2Se. Therefore, to avoid depleting our surface of selenium, we must be careful to avoid conditions of high ion energy and flux which are useful in etching. This can be done by using lower power in a remote plasma source.

We found that a pressure measured at the substrate of $1x10^{-4}$ Torr, rf power of 325 W, and substrate temperature of 200°C were the best parameters for oxygen and carbon removal without surface roughening. An Auger spectrum taken of the surface of ZnSe after cleaning showed almost complete removal of oxygen and a large reduction in carbon (Fig. 2c). RHEED images (Fig. 3a) showed a slightly more diffuse, streaky pattern after cleaning than from an identical substrate without plasma cleaning (Fig. 1a). After preheating, the RHEED pattern was much sharper and evidence of a (2x1) surface reconstruction was observed (Fig. 3b). Surface reconstruction was not seen in the substrate which had not been plasma cleaned (Fig. 1b).

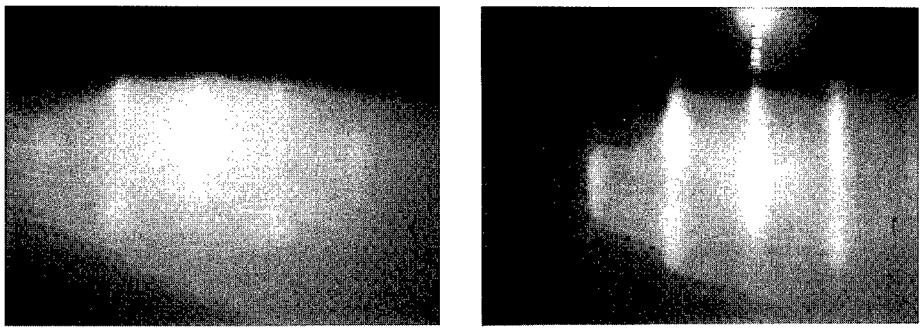

Fig. 3. (a) RHEED pattern from the surface of a bulk ZnSe substrate after exposure to 325 W, 5×10^{-4} Torr hydrogen plasma at 200°C. (b) RHEED pattern from the same sample after annealing in vacuum at 550°C for 10 min.

The quality of the MBE growth reveals the true usefulness of these substrates. Despite more impressive RHEED patterns and Auger spectra, the plasma cleaned substrates do not produce defect-free films. The films grown on substrates which were exposed to the plasma exhibit a higher defect density. Hillock densities observed by optical microscopy in the film grown on the cleaned substrate are higher by two orders of magnitude. SEM imaging shows dark spots indicative of defects that have been correlated with reduced device lifetime.

Experiments were also performed on ZnSe substrates used for the growth of the sulfur-containing, quaternary alloys used for blue laser diodes. Similar results were observed in which substrates cleaned with the hydrogen plasma appeared better in terms of cleanliness and smoothness, but did not produce better quality films.

An additional technical difficulty was observed when attempting to clean substrates in the growth chamber of an MBE system designed for quaternary growth. Upon heating the sulfur furnace, a large increase in background pressure was seen probably due to the reaction of the hydrogen from the cleaning process with the sulfur. Not only did this lead to an extended delay while waiting for the sulfur source to outgas, but it also caused large instabilities in the group VI flux during growth. Although a valved source was used to control the sulfur flux, this instability created difficulties when trying to adjust the critically important stoichiometry of the layers needed for a heterostructure such as a laser diode.

4. Reactive ion etching using BCl_3

It is believed that even a clean surface is insufficient for high-quality homoepitaxy because of numerous dislocations at the surface caused by the polishing of the substrate. As-polished substrates appear smooth when viewed under an optical microscope. However, this smoothness does not reveal the truly defective nature of the underlying material in which etch pit densities greater than 10^6 cm^{-2} can be seen (Fig. 4a) These defects are believed to be related to the polishing of the surface since the bulk material has been determined to have dislocation densities of the order of 10^3 cm^{-2} by high resolution X-ray methods. If this damaged layer could be removed without roughening the surface, the number of dislocations which propagate across the substrate film interface could be greatly reduced.

To remove this damaged layer, substrates were etched in a Plasma-Therm Batch-Top reactive ion etching system. This system uses a capacitively coupled plasma generated over a 7 in. diameter susceptor plate. BCl_3 was used as an etchant since it has been shown to be effective for patterning ZnSe films on GaAs [12]. Substrates were analyzed before and after dry etching for smoothness and

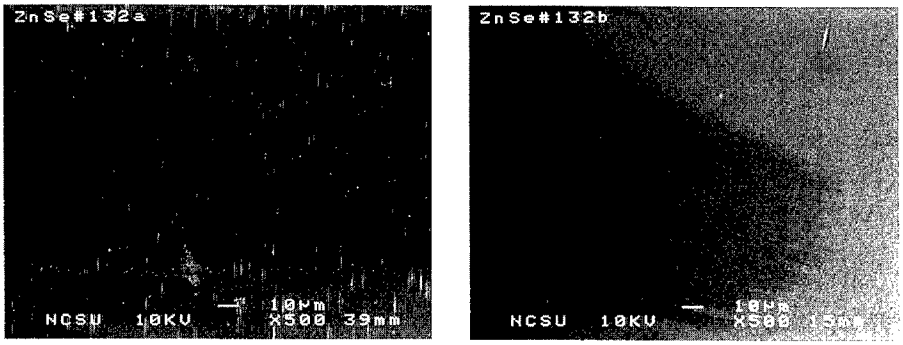

Fig. 4. .Scanning electron micrographs of etch pits in the surface of ZnSe after etching in 0.4% Br/methanol. (a) As-polished substrate. (b) Substrate after reactive ion etching to remove 5 μm of polishing-damaged material.

cleanliness. The defect densities in both the substrates and films were determined by etch-pit density measurements using a solution of 0.4% Br/methanol as described in the literature [13].

Various parameters were tested to determine the optimum conditions for etching the surface of ZnSe using BCl_3. Plasma powers from 50 to 250 W, pressures from 5 to 50 mTorr, and BCl_3 flow rates from 5 to 30 sccm were used. At higher powers and lower pressures, surface roughening was observed due to the large self-bias generated. Likewise, at low flow rates surface contamination and roughening were observed, most likely because of redeposition of etch products. An etch rate of 100 Å/ min was measured for etching done at 150 W, 10 mTorr, and 20 sccm.

Samples were etched to varying depths to determine the dislocation density as a function of depth. (Fig. 5) It can be seen that the density drops off dramatically in the bulk of the material to the residual level of about 10^3 cm^{-2}. Fig. 4b shows the low-etch pit density observed on the surface of a sample etched to a depth of 5 μm. A similar correlation was seen between the hillock density on the surface of epilayers grown on these substrates and the etch depth. Etch-pit densities in these epilayers are similar to those of the substrates; that is, the film replicates the quality of the substrate.

As might be expected, this reduction in defect density has led to a noticeable improvement in device performance. LEDs grown on substrates which were etched to remove the damaged layer had longer lifetimes, lower threshold voltages, and higher brightness than those grown on unetched substrates. Green LEDs with lifetimes greater than 5000 h and external quantum efficiencies of 6.9% have been produced. These are the brightest green LEDs in the world today.

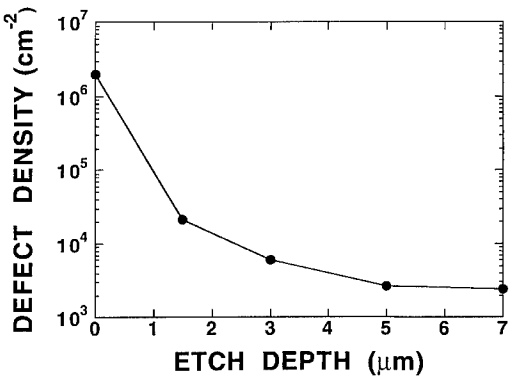

Fig. 5. Dislocation density as a function of depth in ZnSe substrates. Density determined by etch-pit density.

5. Conclusions

We have observed that oxygen, carbon, and chlorine contamination can be removed from the

surface of ZnSe by exposure to a remote hydrogen-containing plasma and vacuum annealing. This procedure generates surfaces nearly free from impurities and with atomic scale smoothness as measured by RHEED. However, cleaning alone is insufficient to completely prepare the substrate surface for MBE growth. While the substrate surface may be less chemically contaminated after hydrogen cleaning, there are still defects remaining from the polishing which will propagate up into the epilayer unless removed. It is possible that the problem of these defects are even exacerbated by the hydrogen-plasma exposure.

An example of this is the additional difficulty experienced with the growth of sulfur-containing compounds. An obvious conclusion is that the hydrogen plasma clean cannot be done in the same chamber where there is a growth of sulfur-containing material. This chemical compatibility may also influence other chalcogenides and lead to Se depletion of the surface of the substrate. This chemical incompatibility may be a significant technical barrier to be overcome for the use of hydrogen-containing plasmas to clean II–VI substrates for homoepitaxial MBE growth.

Our work has shown that the fundamental problem is not the removal of contaminants, but the removal of the dislocated layer up to 5 μm deep remaining from the polishing of the substrate. We have found that reactive ion etching with BCl_3 can be used to remove this layer without adding any additional roughness to the surface. Using this technique, surfaces with dislocation densities similar to the bulk of the crystal can be produced. The chemical contamination of the surface due to the RIE can easily be removed by either vacuum annealing or hydrogen-plasma exposure to ensure a clean, smooth, and low dislocation-density surface on which to grow a homoepitaxial layer. This preparation technique has been used to produce high-brightness, long-lasting green and blue light emitting diodes.

References

[1] J.L. Melendez and C.R. Helms, J. Elctrochem. Soc. 141 (1994) 1973.
[2] B. Anthony, L. Breaux, T. Hsu, S. Banerjee and A. Tasch, J. Vac. Sci. Technol. B 7 (1989) 621.
[3] H. Hirayama and T. Tatsumi, Appl. Phys. Lett. 54 (1989) 1561.
[4] C.M. Rouleau and R.M. Park, J. Appl. Phys. 73 (1993) 4610.
[5] M.E. Lin, S. Strite, A. Agarwal, A. Salvador, G.L. Zhou, N. Teraguchi, A. Rockett and H. Morkoc, Appl. Phys. Lett. 62 (1993) 702.
[6] W.C. Hughes, W.H. Rowland, Jr., M.A.L. Johnson, Sz. Fujita, J.W. Cook, Jr., J.F. Schetzina, J. Ren and J.A. Edmond, J. Vac. Sci. Technol. B 13 (1995) 1571.
[7] M.H. Jeon, L.C. Calhoun and R.M. Park, J. Electron. Mater. 24 (1995) 177.
[8] Yi-hong Wu, Yoichi Kawakami, Shizuo Fujita and Shigeo Fujita, J. Crystal Growth 111 (1991) 757.
[9] M.A. Foad, C.D.W. Wilkinson, C. Dunscomb and R.H. Williams, Appl. Phys. Lett. 60 (1992) 2531.
[10] K. Ohtsuka, M. Imaizumi, H. Sugimoto, T. Isu and Y. Endoh, Appl. Phys. Lett. 60 (1992) 3025.
[11] S.J. Pearton and F. Ren, J. Vac. Sci. Technol. B 11 (1993) 15.
[12] E.M. Clausen, Jr., H.G. Craighead, L.M. Schiavone, M.C. Tamargo and J.L. deMiguel, J. Vac. Sci. Technol. B 6 (1988) 1889.
[13] M. Shiraishi, S. Tomiya, S. Taniguchi, K. Nakano, A. Ishibashi and M. Ikeda, Phys. Status Solidi (a) 152 (1995) 377.

ELSEVIER

Journal of Crystal Growth 175/176 (1997) 552–557

JOURNAL OF CRYSTAL GROWTH

Reduction of extended defects in II–VI blue–green laser diodes

T.B. Ng[a], C.C. Chu[a], J. Han[a,1], G.C. Hua[a], R.L. Gunshor[a,*], E. Ho[b], E.L. Warlick[b], L.A. Kolodziejski[b], A.V. Nurmikko[c]

[a] *School of Electrical and Computer Engineering, Purdue University, W. Lafayette, Indiana 47907-1285, USA*
[b] *Department of Electrical Engineering and Computer Science, Massachusetts Institute of Technology, Cambridge, Massachusetts 02139, USA*
[c] *Division of Engineering, Brown University, Providence, Rhode Island 02912, USA*

Abstract

Early blue/green laser diodes based on ZnSe exhibited room temperature, continuous wave (cw) lifetimes of the order of a minute. Similar to the history of (Al,Ga)As lasers, the source of the degradation was the presence of extended crystalline defects. The dominant extended defects in the early room temperature cw lasers originated as stacking faults generated at the ZnSe/GaAs heterovalent nucleation event, and exhibited densities of the order of 10^6 cm^{-2}. In this paper a procedure is described which will reduce the density of such extended defects to the mid to low 10^3 cm^{-2} over a 3 in diameter wafer.

1. Introduction

Since the successful demonstration of room temperature continuous wave (cw) ZnSe-based injection laser diodes emitting in the blue–green region [1, 2], extending the laser lifetime has been a critical challenge. Early cw ZnSe-based lasers had lifetimes typically of the order of a minute. Degradation studies using electroluminescence (EL) microscopy revealed the formation of triangular dark defects in the laser stripe region. Plan-view transmission electron microscope (TEM) imaging of the degraded lasers identified the dark regions to consist of patches of dislocation networks developed at the quantum-well region during lasing [3]. The dislocation networks appeared to be nucleated at threading dislocations originated from stacking faults. Complexes of defects consisting of stacking faults nucleated in a range of depth up to 120 nm above the II–VI/GaAs interface [4], and their associated threading dislocations, are the most commonly observed extended defects present throughout the separate confinement heterostructure (SCH) laser structures. A quantitative correlation of the grown-in structural defect density with the laser diode cw lifetime has been suggested by Ishibashi [5], similar to the (Al,Ga)As experience. Currently, laser diodes with cw lifetimes between 1 and 3 h are reported to generally have a defect density of between 5×10^4 to 1×10^5 cm^{-2}. There is a recent report from SONY of a lifetime of more than 100 h from a particular device for which the defect density is less than 10^4 cm^{-2} [6].

* Corresponding author.

[1] Present address: Sandia National Laboratories, Albuquerque, New Mexico 87185-0601, USA.

0022-0248/97/$17.00 Copyright © 1997 Elsevier Science B.V. All rights reserved
PII S0022-0248(96)01024-X

The presence of stacking fault/dislocation complexes appears to be associated with the heterovalent nucleation of ZnSe on GaAs, since extended defects originating from the subsequent II–VI/II–VI (for example cladding/wave guiding) heterointerfaces have not been observed provided that growth conditions are appropriate. Studies of the initial nucleation of ZnSe on GaAs epilayers had shown that variation of the growth mode from a two-dimensional (2D) layer-by-layer growth to a 3D island mode can be achieved by modifying the stoichiometry of the starting GaAs surface [7, 8]. The latter has often led to the generation of extended structural defects during the coalescence of incoherent island surface. Reports on the nucleation behavior of ZnSe on GaAs, though not directly linked to the control and suppression of extended defects, include observations of the tendency of GaAs to react with column VI cations (Se and S) and led to subsequently a 3D nucleation [9, 10], the employment of Zn irradiation to promote 2D nucleation [11], and the use of migration-enhanced epitaxy (MEE) to improve the structure quality and extend the critical thickness [12]. In this paper we investigate the ZnSe/GaAs heterovalent nucleation in relation to defect generation, and describe the means for a consistent reduction in the density of the extended defects into the mid to low $10^3\ cm^{-2}$ range over a significant portion of a 3 in wafer.

2. Experimental procedure

A Perkin–Elmer 430 molecular beam epitaxy (MBE) system with separate II–VI and III–V growth chambers was used for all the epitaxial growth. The need for a III–V chamber is due to the previous observation that the use of a GaAs buffer layer grown on the GaAs substrate prior to the II–VI epitaxy improves the surface for ZnSe nucleation by burying the effects of chemomechanical polishing, residual surface contaminants, and sometimes surface damage due to thermal oxide desorption from the substrate [13], while at the same time allowing for the control of the surface stoichiometry of the GaAs prior to nucleation [14]. About 0.25 μm of GaAs buffer layer was grown on a 3 in epi-ready AXT GaAs substrate with a specified etch-pit-density (EPD) of less than $300\ cm^{-2}$. After the GaAs epitaxy, samples were annealed at 600°C under an As_2 flux to improve the surface smoothness, before being transferred under ultra-high vacuum to the II–VI chamber for the ZnSe-related epitaxy.

The growth of ZnSe-based separate confinement heterostructure (SCH) laser diodes begins with a nominally 200 Å thick ZnSe layer nucleated on the n-GaAs buffer layer. The next layer typically consists of approximately 1500 Å of ZnS_xSe_{1-x} ($x \approx 6$–7%; same for all references to ZnSSe henceforth). The purpose of the ZnSSe layer is to aid electron injection into the lower $Zn_{1-y}Mg_yS_xSe_{1-x}$ ($y \approx 7\%$; $x \approx 14\%$; same for all references to ZnMgSSe henceforth) cladding layer [15]. Since TEM studies have shown the extended defects to be nucleated at or near the ZnSe/GaAs interface, it was envisaged that test structures consisting of a ZnSe nucleation layer followed by a 1 or 2 μm ZnSSe growth were adequate for a systematic study of nucleation conditions to explore means to minimize defect densities. The same nucleation techniques were then employed for laser structures. Although paired stacking faults bounded by Shockley partial dislocations formed by far the dominant character of the extended defects observed in our ZnMgSSe-based laser structures, a variety of other types of extended defects, all manifestations of phase indecision [16] in stacking sequence at the II–VI/III–V interface have been observed. In the case of the ZnSSe test structures, the most common defects as observed by TEM have been identified as microtwins [4]. Paired Shockley-type and single Frank-type stacking faults have also been observed.

While plan-view TEM has been a crucial technique in identifying defect types and their characteristics, as an estimator of defect density it quickly loses its accuracy when the defect density drops below $10^6\ cm^{-2}$, mainly due to the limited area imaged. An etch pit decoration technique using bromine–methanol etchant was proposed as a way to reveal dislocations in ZnSe and ZnSSe [17]. However, the same formula (0.04% Br at 0°C) failed to work on ZnMgSSe epilayers due to the appearance of a rough surface morphology after etching. A modified etch involving a 1–2 s dip in

a 2% Br–methanol solution at room temperature was employed to reveal the defects in ZnMgSSe-containing structures such as diode lasers [18]. Despite the presence of textured background after etching, distinct paired etch pits with consistent spacing indicative of Shockley-type stacking faults were revealed, in agreement with observations by TEM [3, 19]. EPD provides a reliable estimate for the defect density range from mid-10^6 to 10^2 cm^{-2}. In addition to EPD counts, cathodoluminescence (CL) and X-ray topography (XRT) were also employed as independent confirmations.

3. Results

In recognition of the existence of various extrinsic factors which a wafer is exposed to in the course of substrate preparation that could lead to nucleation of extended defects, it was found necessary to minimize the wafer handling steps which include wafer cleaving, chemical cleaning and indium mounting. Such external factors add additional uncertainties to the study and tend to mask the behavior related specifically to the ZnSe/GaAs heterovalent nucleation. The appearance of slip lines near and perpendicular to the GaAs wafer cleaved edges following simple thermal desorption of surface oxide, as well as the presence of surface GaAs dust attributed to chips formed both during cleaving and In-mounting, raised questions as to the influence of difficulties associated with wafer cleaving and indium mounting. Clearly, such factors would serve to mislead an investigation to explore the possibility of an intrinsic minimum defect density associated with the heterovalent nucleation chemistry. The Nomarski micrograph of a Br–methanol-etched ZnSSe epilayer surface where a quarter of the 2″ GaAs substrate was In-bonded to the molybdenum sample block is shown in Fig. 1. The initial defect density of around 10^6 cm^{-2} (Fig. 1a) was subsequently reduced to a level around 2×10^5 cm^{-2} through the use of a whole unbonded "epi-ready" 3″ GaAs wafer (AXT Inc., EPD < 300 cm^{-2}). However, EPD from high 10^5 to 2×10^6 cm^{-2} had been also occasionally observed without apparent reason. This somewhat poor reproducibility of a procedure simply based on the principle of minimum wafer handling pointed to the presence of other contributing factors.

The aforementioned studies of the effects of subjecting the surface to a Zn flux had led to the use of the procedure by several groups. The energetics between the elements involved posed little reason to expect the reaction of Zn with a GaAs surface, especially at the growth temperatures employed for

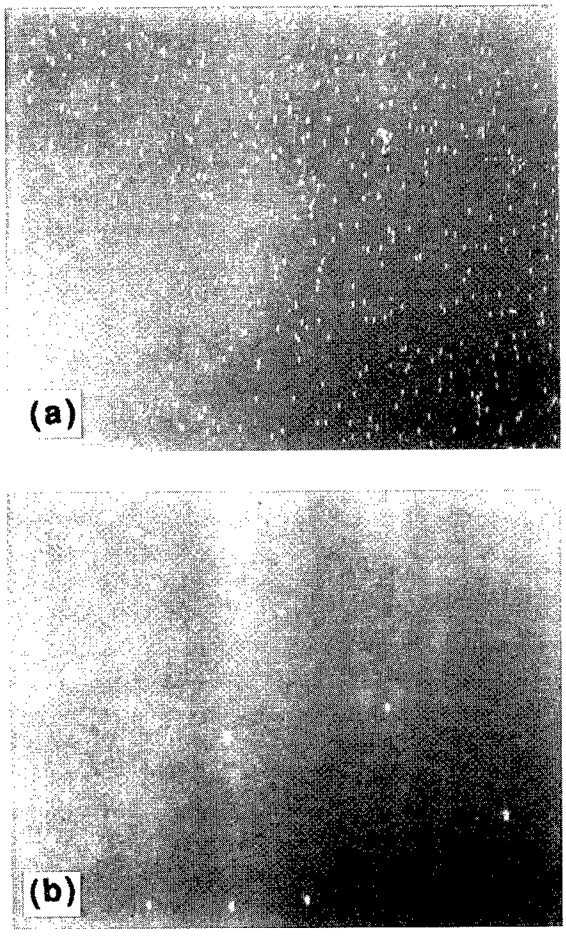

Fig. 1. Nomarski micrograph of the Br–methanol etched surfaces of (a) an early ZnSSe epilayer grown on an indium bonded block showing an EPD of about 1×10^6 cm^{-2}; the magnification is 400× and the viewing area is 272 μm × 210 μm; (b) a ZnSSe epilayer grown on indium-free block with Zn irradiation and MEE nucleation of ZnSe at 260°C showing an EPD of 6×10^3 cm^{-2}; magnification is 200× and the viewing area is 545 μm × 421 μm.

ZnSe growth. We nevertheless adopted the technique based on a speculation that the presence of a flux of Zn would tend to inhibit the reaction of the GaAs surface with Se and S, either from the background in the chamber or from "blow-by" from the imperfectly shuttered Se oven. Thus, when the GaAs is brought up to the orientation for growth, all the shutters are closed except for the Zn oven. The surface is then subjected to the Zn flux for an additional 60 s, followed by a "recovery" of 10 s during which the shutter is closed prior to a nucleation employing MEE.

The terminology of MEE is employed here to refer to the growth method of alternating the supply of anion and cation species to the growing surface, which does not necessarily result in enhanced migration [12]. Our initial investigation of the effect of using MEE on the density of extended defects was carried out at 300°C. Zn and Se fluxes were alternatively supplied for a complete monolayer coverage; the typical thickness of the MEE layer was determined by TEM to be about 35 Å. EPD measurements showed a defect density in the mid-10^4 cm^{-2}. Since a reduced growth rate and/or a higher growth temperature are known to lead to a surface roughening in other strained epitaxial systems, e.g. the case of InAs on GaAs, the substrate temperature was reduced to 260°C during MEE in an attempt to further suppress the tendency toward islanding. (It was also observed that there appeared to be a benefit from higher flux levels.) The result seen in Fig. 1b shows an EPD study indicating an average density, over the area of a 3″ wafer, to be in the low 10^4 cm^{-2} with certain regions into the mid-10^3 cm^{-2}. The same procedure was incorporated into the growths of SCH lasers. To complement the etching, a CL study was performed on several laser structures at MIT. Samples grown early in the study were compared to samples grown using the Zn irradiation and MEE nucleation. The CL emission was analyzed by a monochromator to ensure that emission from the quantum wells was measured. While many spots corresponding to nonradiative recombination show up in the early sample (Fig. 2a), a more recent structure appeared featureless over the area illuminated by the electron beam (Fig. 2b), consistent with the EPD study. XRT was performed on another SCH laser structure using a four-crystal Si monochromator, and (422) diffraction peaks were employed; the defect density over an imaged area of 0.8×0.5 mm^2 is around 4×10^3 cm^{-2}.

A number of models have been proposed to explain the formation mechanism of planar defects like stacking faults and microtwins. Planar defects have been shown to contribute little toward the relaxation of strain and are thus unlikely to be directly caused by the lattice mismatch in the heteroepitaxy [20]. However, there have been reports that stacking faults can be generated through the dissociation of misfit dislocations [21], and also by the coalescence of 3D nucleation islands [22], or through stacking errors of atoms depositing on the

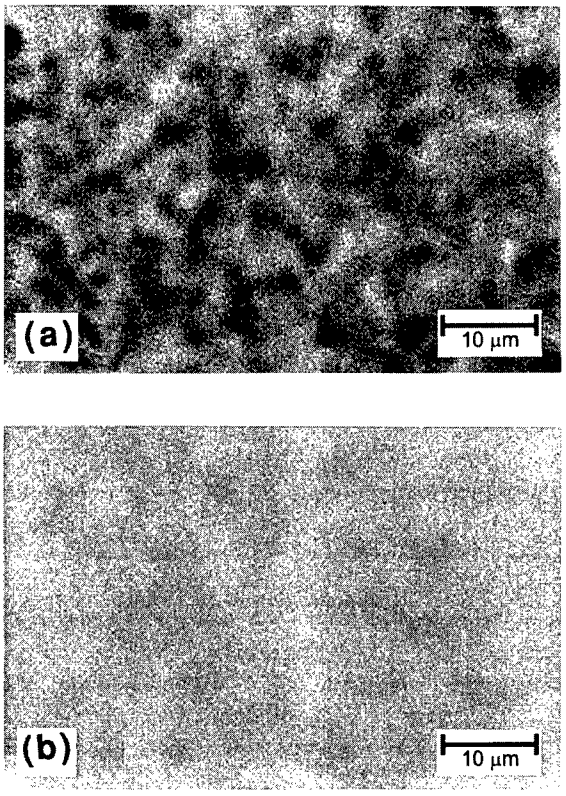

Fig. 2. Cathodoluminescence imaging with detection tuned to the quantum well emission of a ZnMgSSe-based SCH laser diode (a) grown by nucleation at 300°C without Zn irradiation and MEE; (b) grown by nucleation at 260°C with Zn irradiation and MEE. The area shown in each picture is 5×10^{-5} cm^2. The electron beam voltage used is 20 kV and probe current 30 nA.

facets of growth islands [20]. In our case, the dissociation of misfit dislocation is not likely to be the dominant cause of planar defects since the epilayers were pseudomorphic as confirmed by cross-sectional TEM. The observations that a lower growth temperature and a higher deposition rate reduce the defect density seem to imply a correlation between island formation and defect generation [20, 22].

At this stage, it was observed that some defects were associated with an anomalously high density and non-uniformity of surface morphological features such as oval defects on the as-grown GaAs buffer layers.We recently replaced the Ga crucible and subsequently noticed an even lower EPD on both the ZnSSe test structures and laser structures. Fig. 3 is a map of a 3 in wafer showing the values of etch pit densities. These results are consistent from growth to growth, and reveal densities of extended defects in the low to mid-10^3 cm^{-2} over most of a wafer. Nucleation experiments were also performed on a limited number of (2×4) reconstructed GaAs surfaces; the densities were found to be in the 10^3 cm^{-2} range over a large portion of the wafer, but in general were not as low as found for the normally $c(4 \times 4)$ samples.

A light emitting diode (LED) aging test under current injection condition comparable to the laser threshold (100 A cm^{-2}) has been conducted on a laser sample with these reduced defect densities [23]. LEDs were used due to their minimal required processing in order to avoid possible defects generated during the laser device fabrication steps. It was found that the LEDs degraded by a different mechanism, no longer related to the localized pre-existing extended defects. Instead, the active

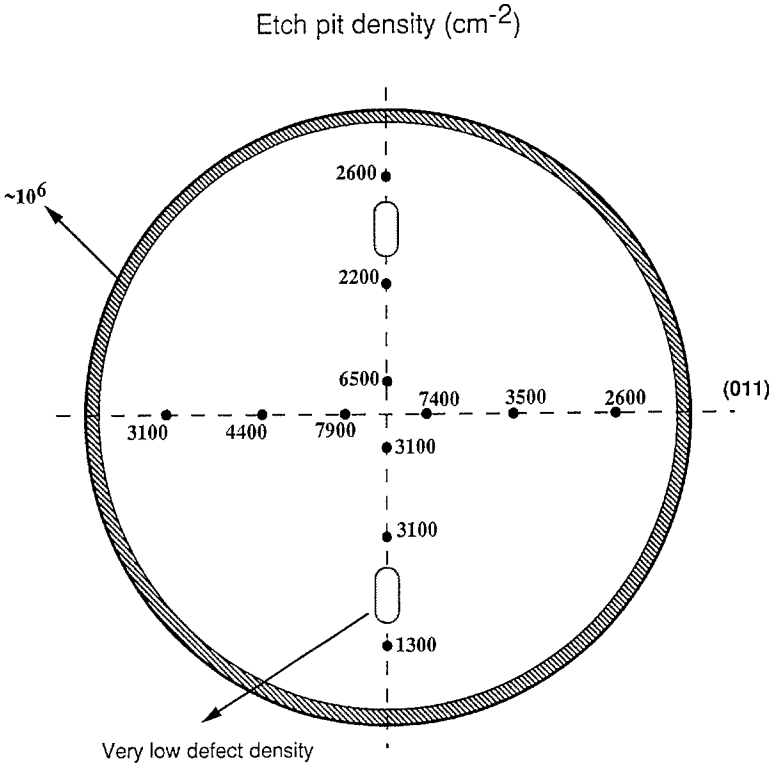

Fig. 3. Map of a sample showing the EPD at 12 spots across the 3 in wafer. The sample consists of a 1 μm ZnSSe epilayer grown on a $c(4 \times 4)$ GaAs surface with Zn irradiation and MEE nucleation at 260°C. The GaAs buffer layer had an improved surface morphology after a replacement of the Ga crucible.

quantum well appeared to degrade uniformly through some recombination enhanced defect generation/reaction (REDG/REDR) processes.

4. Conclusion

In conclusion, the defect densities which were observed to limit the lifetimes of early room temperature cw lasers, typically in the range of $10^6\,cm^{-2}$, are found *not* to be intrinsic to the ZnSe/GaAs heteronucleation process. A procedure is described in which the densities are consistently reduced to the low to mid-$10^3\,cm^{-2}$ over a 3 in wafer. At these densities the extended defects no longer appeared to be the limiting factor in determining the device lifetime; studies of laser structures are in progress. In our laboratory it now appears that the densities in the low $10^3\,cm^{-2}$ may be determined by the GaAs growth stage, and hence could be further reduced, possibly by the use of a more optimized Ga source oven.

Acknowledgements

The authors thank Yu Li for the X-ray topography result. The research was supported by NSF/MRG, AFOSR, ARPA/ONR, ARPA and NSF-MRSEC.

References

[1] N. Nakayama, S. Itoh, K. Nakano, H. Okuyama, M. Ozawa, A. Ishibashi, M. Ikeda and Y. Mori, Electron. Lett. 29 (1993) 1488.
[2] A. Salokatve, H. Jeon, J. Ding, M. Hovinen, A.V. Nurmikko, D.C. Grillo, L. He, J. Han, Y. Fan, M. Ringle, R.L. Gunshor, G.C. Hua and N. Otsuka, Electron. Lett. 29 (1993) 2192.
[3] G.C. Hua, N. Otsuka, D.C. Grillo, Y. Fan, J. Han, M.D. Ringle, R.L. Gunshor, M. Hovinen and A.V. Nurmikko, Appl. Phys. Lett. 65 (1994) 1331.
[4] G.C. Hua, D.C. Grillo, T.B. Ng, C.C. Chu, J. Han, R.L. Gunshor and A.V. Nurmikko, J. Electron. Mater. 25 (1996) 263.
[5] A. Ishibashi, IEEE J. Selected Topics Quantum Electron. 1 (1995) 741.
[6] S. Taniguchi, T. Hino, S. Itoh, K. Nakano, N. Nakayama, A. Ishibashi and M. Ikeda, Electron. Lett. 32 (1996) 552.
[7] M.C. Tamargo, J.L. de Miguel, D.M. Hwang and H.H. Farrell, J. Vac. Sci. Technol. B 6 (1988) 784.
[8] J. Qiu, Q.D. Qian, M. Kobayashi, R.L. Gunshor, D.R. Menke, D. Li and N. Otsuka, J. Vac. Sci. Technol. B 8 (1990) 701.
[9] D.R. Menke, J. Qiu, R.L. Gunshor, M. Kobayashi, D. Li, Y. Nakamura and N. Otsuka, J. Vac. Sci. Technol. B 9 (1991) 2171.
[10] B.J. Wu, H. Cheng, S. Guha, M.A. Haase, J.M. DePuydt, G. Meis-Haugen and J. Qiu, Appl. Phys. Lett. 63 (1993) 2935.
[11] L.H. Kuo, L. Salamanca-Riba, B.J. Wu, J.M. DePuydt, G.M. Haugen, H. Cheng, S. Guha and M.H. Haase, Appl. Phys. Lett. 65 (1994) 1230.
[12] J.M. Gaines, J. Petruzzello and B. Greenberg, J. Appl. Phys. 73 (1993) 2835.
[13] R.L. Gunshor, L.A. Kolodziejski, M.R. Melloch, M. Vaziri, C. Choi and N. Otsuka, Appl. Phys. Lett. 50 (1987) 200.
[14] J. Qiu, Q.D. Qian, R.L. Gunshor, M. Kobayashi, D.R. Menke, D. Li and N. Otsuka, Appl. Phys. Lett. 56 (1990) 1272.
[15] J. Han, Y. Fan, M.D. Ringle, L. He, D.C. Grillo, R.L. Gunshor, G.C. Hua and N. Otsuka, J. Crystal Growth 138 (1994) 464.
[16] B.J. Fitzpatrick, SPIE Proc. 2346 (1994) 192.
[17] A. Kamata and H. Mitsuhashi, J. Crystal Growth 142 (1994) 31.
[18] B.J. Fitzpatrick, private communication.
[19] J. Tanimura, O. Wada, T. Ogama, Y. Endoh and M. Imaizumi, J. Appl. Phys. 77 (1995) 6223.
[20] F. Ernst and P. Pirouz, J. Mater. Res. 4 (1989) 834.
[21] C. Frigeri, G. Attolini, C. Pelosi and A. Armigliato, Solid State Phenom. 32&33 (1993) 397.
[22] S. Guha, H. Munekata and L.L. Chang, J. Appl. Phys. 73 (1993) 2294.
[23] Y.K. Song, A.V. Nurmikko, C.C. Chu, J. Han, T.B. Ng and R.L. Gunshor, Electron. Lett. 32 (1996) 1829.

ELSEVIER

Journal of Crystal Growth 175/176 (1997) 558–563

JOURNAL OF CRYSTAL GROWTH

Optimized growth of lattice-matched ZnCdSe epilayers on InP substrates

A. Cavus[a,*], L. Zeng[a], B.X. Yang [a], N. Dai[a,1], M.C. Tamargo[a], N. Bambha[b], F. Semendy[b]

[a] *New York State Center for Advanced Technology on Ultrafast Photonic Materials and Applications, Center for Analysis of Structures and Interfaces and Department of Chemistry, City College of CUNY, New York, New York 10031, USA*

[b] *IR Optical Technology OFS, Army Research Laboratory, Fort Belvoir, Virginia 22060, USA*

Abstract

Ternaries and quaternaries of ZnCd(Mg)Se can be grown lattice-matched to InP substrates with band gaps spanning most of the visible range, having potential applications as visible light emitters. The quality of these materials is very sensitive to the surface preparation of InP substrates and the initiation of growth. In this paper, we report the details of the growth initiation of ZnCdSe epilayers on InP substrates. The composition of ternary alloy, and thus the lattice-mismatch to InP, was controlled by adjusting the Zn and Cd fluxes. A fast substrate deoxidation, followed by initial low-temperature growth results in two-dimensional growth and substantial improvements of ZnCdSe epilayers. These results along with observations on the use of InGaAs and InP buffer layers indicate that control of the interface chemistry is essential to obtain high-quality materials.

PACS: 81.05.Dz; 81.15.Hi

Keywords: Molecular beam epitaxy; II–VI/III–V heteroepitaxy

1. Introduction

Visible cw semiconductor lasers and light-emitting diodes (LEDs) may have many commercial applications in visible displays and optical data storage. Even though there are several materials being studied, ZnSe-based II–VI alloys have been successfully used to demonstrate blue-green cw injection lasers [1–6]. In current devices ZnMgSSe and ZnSSe epilayers grown lattice-matched to GaAs substrates are used as optical cladding and waveguiding layers, respectively. A strained ZnCdSe quantum well (QW) with about 1.7% mismatch to the GaAs substrate is being used as the active layer. The most successful method to form the ohmic p-type contact layer has been graded ZnSe/ZnTe superlattice structure [7]. Large lattice-mismatch between ZnTe and rest of the structure is a source of misfit dislocations in this layer.

* Corresponding author.

[1] Present address: Department of Physics, Fudan University, Shanghai 200433, People's Republic of China.

0022-0248/97/$17.00 Copyright © 1997 Elsevier Science B.V. All rights reserved
PII S0022-0248(96)01023-8

The strained QW active layer and the p-type contact layer may contribute to the degradation of these devices, which have maximum reported lifetimes of about 100 h [6].

Recently, we proposed to investigate a new series of wide band gap II–VI materials with possible use in cw semiconductor lasers and LEDs. We have successfully grown ZnCdSe and ZnCdMgSe epilayers lattice-matched to InP substrates [8–11]. In laser structures, ZnCdSe with a band gap of 2.2 eV can be used as the active layer, whereas ZnCdMgSe quaternary layers grown with various band gaps ranging from 2.2 to 3.7 eV maintaining lattice-matched compositions can be used as the optical cladding and waveguiding layers. A symmetrically strained ZnSe/ZnTe superlattice structure or a lattice matched ZnSeTe alloy can be used as the p-type contact layer. Thus, the laser structure including the active layer and the p-type contact layer can be grown entirely lattice-matched to InP by using these alloys. Another interesting feature of these structures is that because of the band-gap range of these materials, yellow, green, and blue luminescence emission can be obtained from the same materials by only varying the quantum well thicknesses [12].

However, as in ZnSe growth on GaAs, the quality of the ZnSe-based II–VI materials grown on InP is very sensitive to the surface preparation of the InP substrates. In this paper, we report the details of the growth conditions for lattice-matched ZnCdSe layers on InP substrates. We investigate the growth initiation procedure for these new materials and the quality improvements of the ZnCdSe epilayers grown directly on InP substrates obtained with optimized conditions. We also report preliminary observations on use of InGaAs and InP buffer layers to achieve further improvements.

2. Experimental procedure

The samples were grown in a Riber 2300P molecular beam epitaxy system equipped with conventional effusion cells for Zn, Cd, Mg, Se, $ZnCl_2$, and a nitrogen RF-plasma source. InP(1 0 0) substrates obtained from Sumitomo Electric were etched in $H_2SO_4 : H_2O_2 : H_2O$ (4 : 1 : 1) for 1 min prior to use.

As a result of our early studies [8–9], the growth conditions of ZnSe-based II–VI materials were initially set as follows: First, InP substrate was heated up to 200°C and then the As shutter was opened for surface passivation. The As flux used during the deoxidation, measured by a flux gauge placed in the substrate position, was about 1×10^{-5} Torr. After opening the As shutter, the substrate temperature was increased to 420°C and left at this temperature for about 20–30 min as the RHEED pattern became streaky and bright with a (2×1) reconstruction. We believe that this may be a disordered (or possibly Se-decorated) InP (2×4) surface. Later, the substrate temperature was lowered to 250°C and the As shutter was closed at this temperature, ending the deoxidation procedure. In order to obtain a two-dimensional nucleation our experiments indicated that it was necessary to start the growth of ZnCdSe on InP at a temperature lower than 270°C, which is the optimum growth temperature. Therefore, right after the deoxidation procedure the substrate temperature was set to 170°C. Once the substrate temperature was stabilized, the Zn, Cd and Se shutters were opened, and low-temperature initial growth was started. Within a couple of seconds, a clear II–VI (2×1) reconstruction was observed in the RHEED pattern. The initial growth temperature and the time period of the low-temperature growth were determined by a detailed study of various combinations. It was found that starting the growth at 170°C and remaining at this temperature for only 1 min results in a two-dimensional growth mode, supported by the presence of a streaky, bright (2×1) RHEED pattern. After this, the substrate temperature was increased to 270°C. It takes approximately 4 min in our system for the temperature to reach 270°C while growth continues. The rest of the growth was performed at 270°C. We will refer the growth conditions described as *early conditions* throughout the rest of the text.

In the present study, two changes were implemented regarding our growth technique that resulted in further improvements. One of these changes was in the deoxidation procedure, where the substrate was heated up to 500°C for only a few seconds. This gave us a clear (2×4) reconstruction on the InP before growth. The other change was the

interruption of the growth immediately after the initial low-temperature growth was performed at 170°C for 1 min. During the interruption, the substrate temperature was set to 270°C and then the growth was resumed. We will refer to the growth conditions with these changes as *improved conditions.*

3. Results and discussion

We have grown a series of near-lattice-matched 1 μm thick ZnCdSe epilayers directly on InP substrates, including lattice-matched layers. Fluxes were measured with an ionization gauge immediately before the growth. Fig. 1 shows the relationship between the ratio of the Cd flux (ϕ(Cd)) to the total group II flux (ϕ(Zn + Cd)) used during growth and the Cd fraction (y) in the grown $Zn_{1-y}Cd_ySe$ layer. The values of y were obtained from measured lattice mismatch by using known lattice constants for InP (5.8686 Å), ZnSe (5.667 Å), and CdSe (6.077 Å) [13] and assuming that the alloys are fully relaxed and that they follow Vegard's law. The dotted straight line represents the ideal case where the fraction of Cd in the fluxes (ϕ(Cd)/iϕ(Zn + Cd)) equal the fraction of Cd (y) in the epilayer. The non-linear relationship indicates that less Cd is incorporated than expected from the flux ratios. Thus, based on the data presented in Fig. 1, the sticking coefficient of Cd under our growth conditions is calculated to be 0.5 by assuming that Zn has unity sticking coefficient [14]. These data agree qualitatively with earlier data for ZnCdSe grown on GaAs substrates [15]. The lattice-matched composition $Zn_{0.51}Cd_{0.49}Se$ is obtained with a flux ratio ϕ(Cd)/ϕ(Zn + Cd) $\sim$ 0.67. The VI/II flux ratio was kept at about 4 to maintain group-VI rich growth conditions.

ZnCdSe epilayers on InP substrates with good surface quality were obtained under the growth conditions described as *early conditions.* Photoluminescence spectra of ZnCdSe epilayers grown with these conditions are shown in Fig. 2. Sharp and intense band edge emission with a full-width at half-maximum (FWHM) of 11 meV was obtained from 1 μm thick ZnCdSe epilayer as seen in Fig. 2a. This emission was accompanied by a broad second

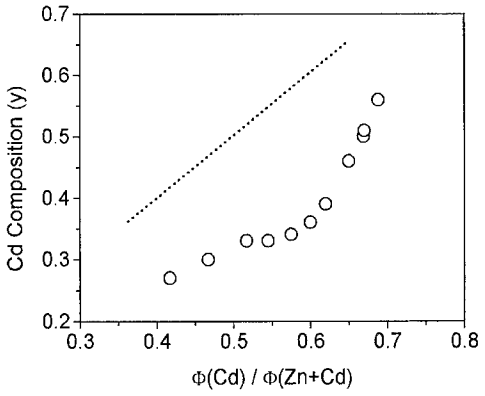

Fig. 1. Plot of Cd content (y) in $Zn_{1-y}Cd_ySe$ epilayers as a function of the ratio of Cd flux (ϕ(Cd)) to the total group II flux (ϕ(Zn + Cd)). The dotted straight line represents the ideal case where the fraction of Cd in the fluxes equals the Cd fraction in the epitaxial layer.

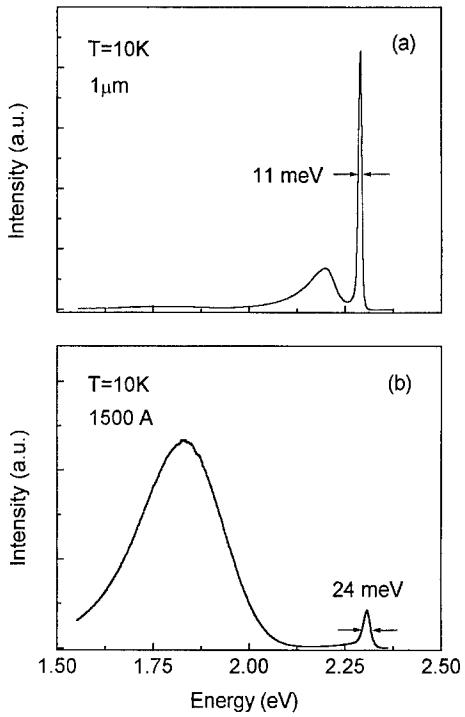

Fig. 2. Photoluminescence spectra at 10 K for (a) 1 μm and (b) 1500 Å thick ZnCdSe epilayer grown on InP substrates under the *early conditions.*

peak about 100 meV below the band gap, tentatively assigned to a donor–acceptor pairs [9] suggesting some impurities in the epilayer. A thin ZnCdSe epilayer was grown to investigate the quality near the II–VI/III–V interface. The PL spectrum of this 1500 Å thick ZnCdSe epilayer exhibits a strong deep level emission as shown in Fig. 2b. This suggests that the quality near the II–VI/III–V interface is poor.

To improve the quality of our layers two changes in the growth initiation procedure were implemented: First, the substrate was heated to 500°C quickly and kept there only for several seconds during the deoxidation and secondly, a growth interruption was included during the adjustment of the substrate temperature right after the initial low-temperature growth. The optical properties of ZnCdSe epilayers obtained with these *improved conditions* can be seen from PL measurements shown in Fig. 3. As seen in Fig. 3a, the FWHM of

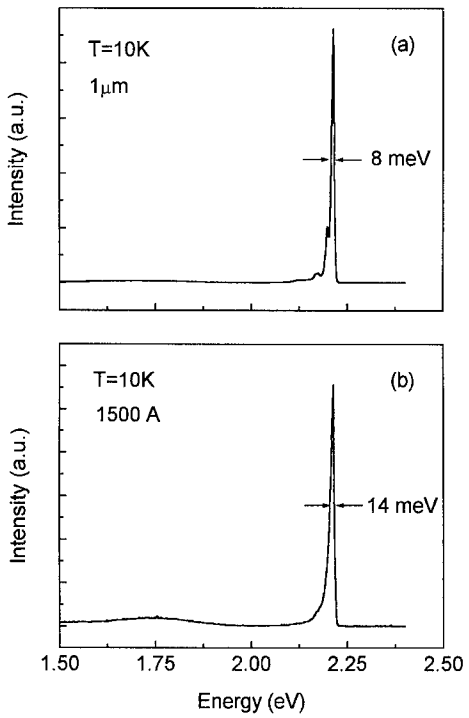

Fig. 3. Photoluminescence spectra at 10 K for (a) 1 μm and (b) 1500 Å thick ZnCdSe epilayer grown on InP substrates under the *improved conditions*.

band edge emission for 1 μm thick sample is reduced to 8 meV and the second peak ~ 100 meV below the band gap becomes much less pronounced, indicating improved optical quality in these epilayers. More dramatic enhancements were observed in the PL spectra from thin samples, where the deep level emission previously seen in the 1500 Å thick samples has almost disappeared, as seen in Fig. 3b. These PL spectra, especially from the thin samples, are clear indication of a better II–VI/III–V interface obtained with the *improved conditions*.

ZnCdSe epilayers were previously grown on GaAs substrates with various Cd compositions in the range between the two binaries ZnSe and CdSe [15]. Even though PL measurements of these samples exhibited efficient and narrow band-edge emission for the samples with low Cd content (~ 0.2), strong deep level emission was observed for the samples with higher Cd contents and large mismatch. These results emphasize the importance of lattice-matched growth for improved layer quality.

The difference in the crystalline quality between 1 μm thick samples grown with the *early* and the *improved conditions* can be seen clearly from single crystal X-ray rocking curve measurements, shown in Fig. 4. Layers having a slight lattice-mismatch of $\Delta a/a \sim -0.5\%$ were intentionally selected so that X-ray peaks from the epilayer and the substrate are easily seen. The characteristic X-ray data for a 1 μm thick ZnCdSe epilayer grown under *early conditions* exhibits unresolved $k\alpha_1$ and $k\alpha_2$ peaks as seen in Fig. 4a. FWHM of the X-ray peaks were determined from double-crystal X-ray rocking curves to be greater than 1000 arcsec. With the *improved conditions*, the single-crystal X-ray measurement of 1 μm thick sample shows well-resolved $k\alpha_1$ and $k\alpha_2$ peaks as seen in Fig. 4b. The double-crystal X-ray rocking curve measurements for a 1 μm thick ZnCdSe lattice-matched sample exhibited an X-ray peak with about 300 arcsec FWHM, as shown in Fig. 5. The lattice mismatch of this epilayer to InP substrate is about -0.07%.

The improvements in quality by the modifications of our growth conditions can be explained in part on the basis of the thermal stability of InP in comparison to GaAs. Growth of II–VI materials on GaAs substrates has been investigated previously

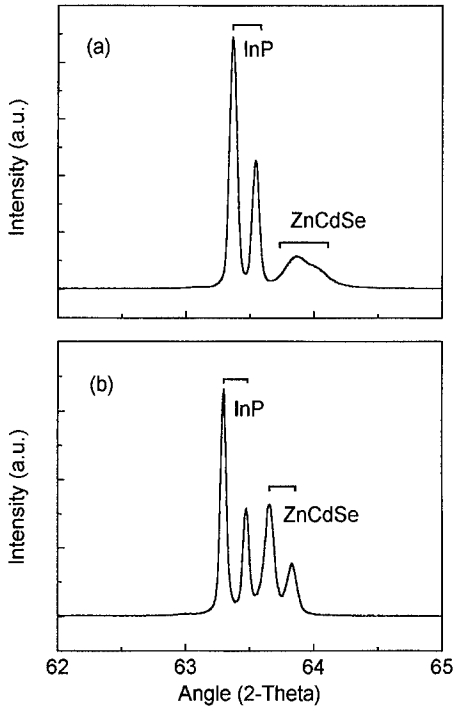

Fig. 4. Single-crystal X-ray rocking curve data for 1 μm ZnCdSe epilayers grown under (a) *early* and (b) *improved conditions*. The two peaks assigned to InP correspond to the $k\alpha_1$ and $k\alpha_2$ peaks. These peaks are well resolved for the ZnCdSe epilayer only in case (b). The lattice-mismatch in these epilayers is $\Delta a/a \sim -0.5\%$.

in detail. Deoxidation of GaAs substrates is performed at 600–620°C with (or without) As flux, followed by II–VI growth at around 270°C. Transition of the RHEED pattern from GaAs (2 × 4) to ZnSe (2 × 1) can be observed very readily. GaAs has a congruent evaporation temperature of 650°C [16], so that no substantial As loss is expected during the deoxidation. Since the oxide is removed around 600°C, the use of an As flux may be sufficient to protect the GaAs substrate and maintain As-rich surface conditions. In the case of InP the congruent evaporation temperature is 363°C [16]. So we must be concerned about the loss of P atoms from the InP surface during deoxidation when the substrate temperature is increased as high as 500°C. Once P has been lost, the excess In in the surface may react with Se to form various undesirable interfacial layers. The use of an As flux during the deoxidation is expected to minimize this

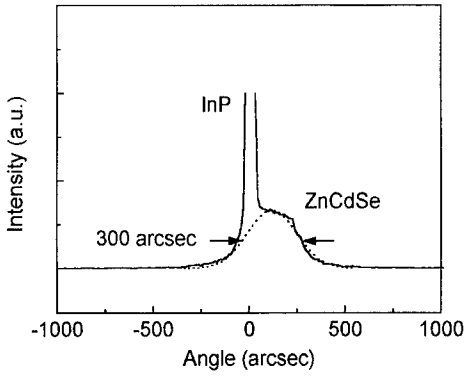

Fig. 5. Double-crystal X-ray rocking curve data for a near lattice-matched 1 μm thick ZnCdSe epilayer grown under the *improved conditions*. The mismatch in this epilayer is $\Delta a/a \sim -0.07\%$.

problem. Furthermore, faster heating during deoxidation produces a better interface because it is likely to reduce P loss and interactions with Se.

Other groups investigating the growth of ZnSe-based materials on GaAs substrates have concluded that interaction of Se with the substrate surface, forming Ga_2Se_3, reduces the epilayer and interface quality [17]. It is reasonable to expect that a similar interfacial compound such as In_2Se_3 may be forming at the InP/ZnCdSe interface. Steps that result in a suppression of this mixed III–VI layer, such as fast substrate heating and low initial growth temperature, are probably useful for improving the interface. Low initial growth temperature has recently been adopted in the growth of ZnSSe on GaAs for the reduction of stacking faults at the interface [18].

The second step in our *improved conditions* was the incorporation of a growth interruption while increasing the substrate temperature from the initial 170°C to the optimum growth temperature of 270°C. Growth was interrupted to avoid deposition at the low temperatures any longer than necessary. An additional effect of the growth interruption was observed from the RHEED pattern behavior indicating that the growth surface was becoming smoother during the interruption. Growth interruptions have been used in other materials systems as a means of smoothening the growth surfaces [19].

A way of improving the quality of the II–VI/III–V interface further is to first grow a III–V

buffer layer such as InGaAs and InP. Use of buffer layers is expected to provide a smoother and chemically more controlled surface resulting in improvements of the epilayer quality. Studies on the use of these buffer layers show very dramatic improvements in epilayer quality of ZnCdSe. Very narrow band-edge emissions were obtained in photoluminescence spectra, which exhibited FWHM of 3–5 meV and double-crystal X-ray measurements which gave line widths of 70–100 arcsec. TEM measurements on these samples also indicated dramatic reduction in the defect densities. Details of these further improvements for ZnCdSe epilayers grown on InP substrates with InP or InGaAs buffer layers have been reported elsewhere [20].

4. Conclusions

We investigate the MBE growth conditions for lattice-matched ZnCdSe epilayers on InP substrates. In particular, an optimized method for the treatment of InP(1 0 0) substrates and initiation of the growth for ZnSe-based II–VI compounds on these substrates is reported. Improved optical and crystalline quality were achieved by implementing a faster deoxidation step and a growth interruption right after the low-temperature initial growth of the II–VI epilayer. The improvements are attributed to reduced P loss from the substrate surface and reduced interaction of the substrate with Se by the faster deoxidation and to annealing and smoothening of the growth front by the growth interruption. Further improvements can be obtained with the use of III–V buffer layers such as lattice-matched InGaAs and InP.

Acknowledgements

The authors acknowledge the support of the New York Science and Technology Foundation through its CUNY Center for Advanced Technology on Photonic Materials and Applications, and the National Science Foundation (NSF) under cooperative agreement number RII-9353488 and the NSF grant number ECS-932045.

References

[1] M.A. Haase, J. Qiu, J.M. DePuydt and H. Cheng, Appl. Phys. Lett. 59 (1991) 1272.
[2] Z. Yu, J. Ren, B. Sneed, K.A. Bowers, K.J. Gossett, C. Boney, Y. Lansari, J.W. Cook, Jr., J.F. Schetzina, G.C. Hua and N. Otsuka, Appl. Phys. Lett. 61 (1992) 1266.
[3] W. Xie, D.C. Grillo, R.L. Gunshor, M. Kobayashi, G.C. Hua, N. Otsuka, H. Jeon, J. Ding and A.V. Nurmikko, J. Vac. Sci. Technol. B 10 (1992) 921.
[4] J.M. Gaines, R.R. Drenten, K.W. Haberern, T. Marshall, P. Mensz and J. Petruzzello, Appl. Phys. Lett. 62 (1993) 2462.
[5] N. Nakayama, S. Itoh, T. Ohata, K. Nakano, H. Okuyama, M. Ozawa, A. Ishibashi, M. Ikeda and Y. Mori, Electron. Lett. 29 (1993) 1488.
[6] S. Taniguchi, T. Hino, S. Itoh, K. Nakano, N. Nakayama, A. Ishibashi and M. Ikeda, Electron. Lett. 32 (1996) 552.
[7] Y. Fan, J. Han, L. He, J. Saraie, R.L. Gunshor, M. Hagerott, H. Jeon, A.V. Nurmikko, G.C. Hua and N. Otsuka, Appl. Phys. Lett. 61 (1992) 3160.
[8] M.C. Tamargo, N. Dai, A. Cavus, R. Dzakpasu, W. Krystek, F. Pollak, F. Semendy, N. Bambha, P. Boyd, D.M. Hwang and C.Y. Chen, SPIE 2346 (1994) 70.
[9] N. Dai, A. Cavus, R. Dzakpasu, M.C. Tamargo, F. Semendy, N. Bambha, D.M. Hwang and C.Y. Chen, Appl. Phys. Lett. 66 (1995) 2742.
[10] M.C Tamargo, A. Cavus, L. Zeng, N. Dai, N. Bambha, A. Gray, F. Semendy, W. Krystek and F. Pollak, in: Semiconductor Heteroepitaxy: Growth, Characterization and Device Applications, Eds. B. Gil and R.L. Aulombard (World Scientific, Singapore, 1995) p. 59.
[11] M.C. Tamargo, A. Cavus, L. Zeng, N. Dai, N. Bambha, A. Gray, F. Semendy, W. Krystek and F. Pollak, J. Electron. Mater. 25 (1996) 259.
[12] A. Cavus, L. Zeng, M.C. Tamargo, N. Bambha, F. Semendy and A. Gray, Appl. Phys. Lett. 68 (1996) 3446.
[13] N. Samarth, H. Luo, J.K. Furdyna, S.B. Qadri, Y.R. Lee, A.K. Ramdas and N. Otsuka, Appl. Phys. Lett. 54 (1989) 2680.
[14] F.S. Turco and M.C. Tamargo, J. Appl. Phys. 66 (1989) 1695.
[15] M.C. Tamargo, M.J.S.P. Brasil, R.E. Nahory, R.J. Martin, A.L. Weaver and H.L. Gilchrist, Semicond. Sci. Technol. 6 (1991) A8.
[16] J.D Grange, in: The Technology and Physics of MBE, Ed. E.H.C. Parker (Plenum, New York , 1985) p. 48.
[17] D. Li and M.D. Pashley, J. Vac. Sci. Technol. B 12 (1994) 2547; Z. Yu, S.L. Buczkowski, N.C. Giles, T.H. Myers, Appl. Phys. Lett. 69 (1996) 82.
[18] T.B. Ng, C.C. Chu, G.C. Hua, J. Han, R.L. Gunshor, E. Ho, E.L. Warlick, L.A. Kolodziejski and A.V. Nurmikko, J. Crystal Growth 175/176 (1997) 552.
[19] M. Tanaka and H. Sakaki, J. Crystal Growth 81 (1987) 153.
[20] E. Snoeks, L. Zhao, A. Cavus, L. Zeng, B. Yang and M.C. Tamargo, J. Crystal Growth, submitted.

ELSEVIER

Journal of Crystal Growth 175/176 (1997) 564–570

JOURNAL OF CRYSTAL GROWTH

Reducing the defect density in MBE-ZnSe/III–V heterostructures

E.L. Warlick, E. Ho, G.S. Petrich, L.A. Kolodziejski*

Research Laboratory of Electronics, Department of Electrical Engineering and Computer Science, Massachusetts Institute of Technology, Cambridge, Massachusetts 02139, USA

Abstract

The defect densities that are observed in 1 μm ZnSe films grown by molecular beam epitaxy on various III–V buffer layers are compared. Cathodoluminescence (CL) imaging has been used to provide a rapid and non-destructive method of characterizing the defect densities and was found to be in agreement with both etch pit density and transmission electron microscopy characterizations. We also examined the defect density of ZnSe epilayers grown on relaxed buffer layers of (In,Ga)P (lattice-matched to ZnSe) with the phosphide surface capped with eight monolayers of GaAs exhibiting various surface reconstructions. In this manner, the ZnSe/GaAs surface chemistry is maintained while simultaneously achieving a lattice-matched buffer layer to ZnSe. Films grown without special nucleation precautions on $c(4\times4)$-reconstructed GaAs were typically found to result in defect densities larger than 10^7 cm^{-2}. Using a Zn pre-exposure on (2×4)-reconstructed GaAs, the defect densities were decreased by over an order of magnitude. In this paper, the microstructural and optical properties of ZnSe on phosphide-containing III–V buffer layers will be described and contrasted to the more conventional ZnSe/GaAs heterostructure, using atomic force microscopy and CL.

Keywords: ZnSe; (In,Ga,Al)P; MBE; Nucleation methods; Defect density

1. Introduction

The need for compact, inexpensive, long-lived blue–green semiconductor injection lasers is driven by the advantages afforded by implementing a short wavelength laser in technologies utilizing high density optical recording. Currently, the two wide-bandgap material systems that promise to meet the aforementioned challenge are Zn chalcogenides-based II–VI materials and GaN-based III–V materials. In both cases, defect generation and control is at the forefront of the issues requiring investigation. Here, we explore the use of III–V phosphide-based (In,Ga,Al)P buffer layers, placed between the wide-bandgap ZnSe layer and the narrower-bandgap GaAs substrate. The phosphorus-containing III–V alloy enables one to vary the energy bandgap (and the lattice constant), suggesting that the large 1 eV valence band discontinuity present between the ZnSe and the GaAs substrate can be greatly reduced, thus facilitating hole injection [1]. A lattice-matched ohmic contact composed of III–V materials on a p-type III–V

* Corresponding author.

0022-0248/97/$17.00 Copyright © 1997 Published by Elsevier Science B.V. All rights reserved
PII S0022-0248(96)01175-X

substrate will offer an alternative to the use of a highly lattice-mismatched Zn(Se,Te) graded-layer ohmic contact [2]. Simultaneously, however, proper nucleation of the II–VI layer on the III–V surface is required to minimize defect generation, subsequently increasing both the luminescence efficiency and optical device lifetime [3].

A variety of phosphide-based III–V buffer layers have been grown by gas source molecular beam epitaxy (GSMBE) on GaAs substrates. These III–V layers were then used as epitaxial substrates for the ZnSe epilayers. To provide a lattice-matched II–VI/III–V interface, the alloy fraction of the phosphide-based buffer layer was varied to grade the in-plane lattice constant from that of the GaAs substrate to that of the ZnSe device layer [4]. A set of experiments was first carried out to study the nucleation of ZnSe on $c(4\times4)$- and (2×4)-reconstructed GaAs surfaces. To isolate the effect of lattice constant mismatch, this same II–VI/III–V interface chemistry was preserved on the phosphide-based lattice-matched III–V surface by the deposition of eight monolayers of GaAs exhibiting the selected $c(4\times4)$ or (2×4) surface reconstruction. The multitude of structures were monitored in situ using reflection high energy electron diffraction (RHEED), both before and after transferring the sample in vacuum from the III–V-dedicated reactor to the II–VI-dedicated reactor. The samples were further characterized ex situ by X-ray diffraction double crystal rocking curves, photoluminescence (PL), cathodoluminescence (CL), transmission electron microscopy (TEM), and atomic force microscopy (AFM). Confirmation of the defect densities was provided by wet chemical etching to illucidate extended defects intersecting the surface.

2. Experimental procedure

The ZnSe/III–V heterostructures were grown on epi-ready p+ GaAs (1 0 0) wafers. In all cases, a GaAs buffer layer was first grown at a substrate temperature of 600°C at 1 μm h^{-1} with an arsine flow rate of 1.0 sccm using an indium-free sample holder. For the ZnSe/GaAs heterostructures, the thickness of the GaAs epilayers was 0.75 μm. A 0.5 μm GaAs epilayer was grown for the samples containing an (In,Ga,Al)P buffer layer. These (In,Ga,Al)P layers were grown at 1 μm h^{-1} at a substrate temperature of 470°C with a phosphine flow rate of 3.0 sccm. The lattice constant of the (In,Ga,Al)P was graded from that of GaAs to that of ZnSe during the growth of the 4 μm thick relaxed buffer layer. Both (4 0 0) and (5 1 1) double crystal X-ray rocking curves were used to determine the in-plane and out-of-plane lattice constants.

In order to examine the effect of the GaAs surface reconstruction on the subsequent growth of the ZnSe, buffer layers were prepared that exhibited either a $c(4\times4)$ or a (2×4) surface reconstruction. After the growth of the buffer layer at 600°C, the surface exhibited an As-stabilized (2×4) reconstruction. As the substrate temperature fell below 530°C in an As flux, the (2×4) surface reconstruction changed to a $c(4\times4)$ reconstruction. This reconstruction remained stable even after the arsine flow into the chamber was terminated at 350°C. To prepare a buffer layer exhibiting a (2×4) reconstruction at room temperature, the substrate temperature and the As flux were simultaneously lowered after growth. The As flow was reduced to 0.1 sccm, which was sufficient to maintain the (2×4) reconstruction. As the sample temperature was lowered to 100°C, the arsine flow was terminated at 520°C. The RHEED pattern was closely monitored during this process.

To maintain the ZnSe/GaAs interfacial chemistry while studying the effects of the (In,Ga,Al)P buffer layers, a thin layer of GaAs was deposited onto the phosphide-containing surface. Eight monolayers of GaAs were grown at a substrate temperature of 470°C at a rate of two monolayers per shutter opening. Eight monolayers were required to provide the initial (2×4)-reconstructed GaAs surface. When the III–V growth was finished, the arsine flow and the substrate temperature were adjusted to create either a $c(4\times4)$- or a (2×4)-reconstructed GaAs surface cap.

The completed III–V buffer layers were then transferred in situ via an ultrahigh vacuum transfer chamber to the II–VI MBE reactor; the MBE chamber employs ultra-high purity (6N) Zn and Se as sources of the constituent species. The Zn and Se fluxes were measured with a water cooled quartz crystal monitor and the shutters closed prior to

introduction of the III–V buffer layer. The stability of the III–V-reconstructed surface was verified in the II–VI reactor by RHEED observations. The growth temperature for the experiments was determined by the use of a calibrated low temperature optical pyrometer and was approximately 290°C. During growth, optical pyrometer temperature oscillations were used to control the film thickness. The flux ratio, F_{Zn}/F_{Se}, was 0.7 in all cases. The surface Zn-to-Se stoichiometry was monitored with RHEED during growth.

The representative set of structures to be discussed in this paper are listed in Table 1. Each structure contains a 1 μm fully relaxed ZnSe epilayer. With the exception of sample C, the ZnSe growth was initiated with a 120 s Zn pre-exposure, directly followed by the opening of the Se source shutter. Sample A denotes a ZnSe epilayer grown on $c(4\times4)$-reconstructed GaAs, and sample B denotes a ZnSe epilayer grown on (2×4)-reconstructed GaAs. The second set of three samples involved the growth of ZnSe on a lattice-matched III–V buffer layer with 4 μm of relaxed (In,Ga)P, graded from the lattice constant of GaAs to that of ZnSe. In sample C, ZnSe was grown directly on (In,Ga)P by opening the Zn and Se shutters simultaneously. Samples D and E are ZnSe epilayers grown on graded (In,Ga)P buffer layers with $c(4\times4)$- and (2×4)-reconstructed GaAs caps, respectively. Zn pre-exposure of a $c(4\times4)$-reconstructed GaAs surface changed the surface to exhibit a (2×1) surface reconstruction; Zn pre-exposure of a (2×4)-reconstructed GaAs surface resulted in a (1×4) surface reconstruction.

The luminescence was evaluated at room temperature by CL employing a JEOL 840-A scanning electron microscope. The collection system employs an Oxford Instruments' MonoCL. The electron beam accelerating energy was 20 keV to insure full excitation of the 1 μm ZnSe epilayers [5]. Surface morphology was characterized in air by AFM using a Digital 3000 Nanoscope in the tapping mode. Threading dislocation estimates were determined by room temperature etch pit density measurements using a solution of 1% bromine in methanol to etch 250 nm of ZnSe.

3. Results and discussion

Initial growth experiments of ZnSe on lattice-matched (In,Ga,Al)P surfaces indicated the presence of an unexpectedly high density of dislocations. The origin of such a high density of defects is speculated to be due to surface chemistry and/or ZnSe nucleation conditions. Our initial effort examined the role of surface chemistry by using GaAs buffer layers with a $c(4\times4)$ or a (2×4) surface reconstruction. Fig. 1 shows atomic force micrographs of samples A and B. In the case of a ZnSe epilayer grown on a $c(4\times4)$-reconstructed buffer layer, a mean roughness (R_a) of 9 Å was measured over a 500 nm × 500 nm area, as shown in Fig. 1a. In contrast, the mean roughness from the 1 μm ZnSe epilayer grown on a (2×4)-reconstructed GaAs buffer layer was 7 Å, as seen in Fig. 1b. In other sets of similar films, the R_a values from the ZnSe epilayer grown on $c(4\times4)$-reconstructed GaAs were consistantly larger than the values measured from the ZnSe epilayer grown on (2×4)-reconstructed GaAs. Utilizing migration enhanced epitaxy (MEE) at the initial stage of heteroepitaxy resulted in the same conclusion that a (2×4)-reconstructed GaAs surface gives rise to a smoother ZnSe layer.

Table 1
Examples of ZnSe/III–V heterostructures under investigation

Sample	III–V buffer layer	GaAs reconstruction	Zn pre-exposure
A	GaAs	$c(4\times4)$	120 s Zn
B	GaAs	(2×4)	120 s Zn
C	Graded (In,Ga)P	NA	NA
D	Graded (In,Ga)P/GaAs cap	$c(4\times4)$	120 s Zn
E	Graded (In,Ga)P/GaAs cap	(2×4)	120 s Zn

A dramatic difference between the CL images of the ZnSe films grown on the $c(4\times4)$- and the (2×4)-reconstructed GaAs buffer layers was observed, as demonstrated in Fig. 2. The contrast in the CL images is due to variations in the amount of non-radiative recombination. The dark regions in the CL images have been attributed to threading dislocations which act as non-radiative recombination sites [6]. Fig. 2a and Fig. 2b show the CL images from samples A and B, respectively. Using CL, the defect densities of ZnSe grown on $c(4\times4)$-reconstructed GaAs buffer layers was estimated to be $7\times10^6\ cm^{-2}$, while the defect density of ZnSe grown on (2×4)-reconstructed GaAs buffer layers was estimated to be $9\times10^5\ cm^{-2}$. These defect densities were well correlated to the etch pit density (EPD) values of 10^7 and $10^6\ cm^{-2}$ for samples A and B, respectively. Characterization of the set of MEE-initiated samples did not demonstrate a noticeable difference in defect densities between the MBE and MEE growth of ZnSe on GaAs exhibiting a (2×4) reconstruction.

Thus, our studies suggest that the growth of relaxed ZnSe with a Zn pre-exposure on a (2×4)-reconstructed GaAs surface results in a lower threading dislocation density and a smoother surface than ZnSe grown on a $c(4\times4)$-reconstructed surface. Reduced defect densities in ZnSe epilayers grown on (2×4)-reconstructed GaAs agrees with other recent studies [7]. The complexity of the ZnSe/GaAs interfacial layer makes it difficult to isolate the reason for the reduced defect density in ZnSe grown on (2×4)-reconstructed GaAs surfaces compared to ZnSe on $c(4\times4)$-reconstructed

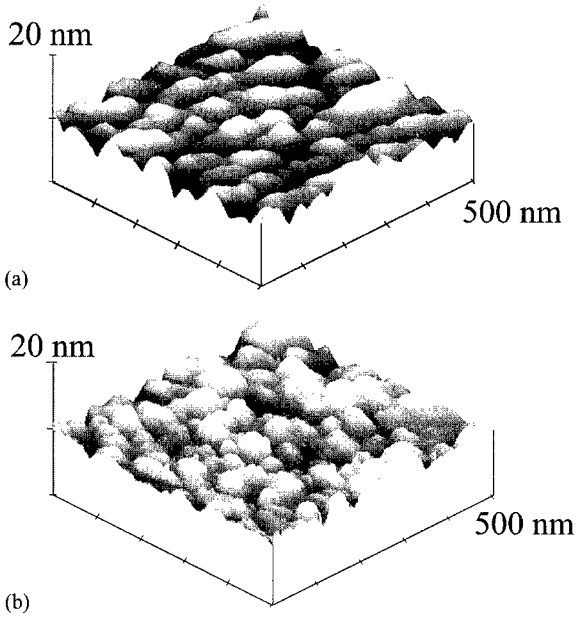

Fig. 1. Atomic force micrographs of 1 μm ZnSe films grown by MBE on (a) a Zn-exposed $c(4\times4)$-reconstructed GaAs buffer layer (sample A) and (b) a Zn exposed (2×4)-reconstructed GaAs buffer layer (sample B). The mean roughnesses in the 500 nm × 500 nm area were 9 and 7 Å, respectively.

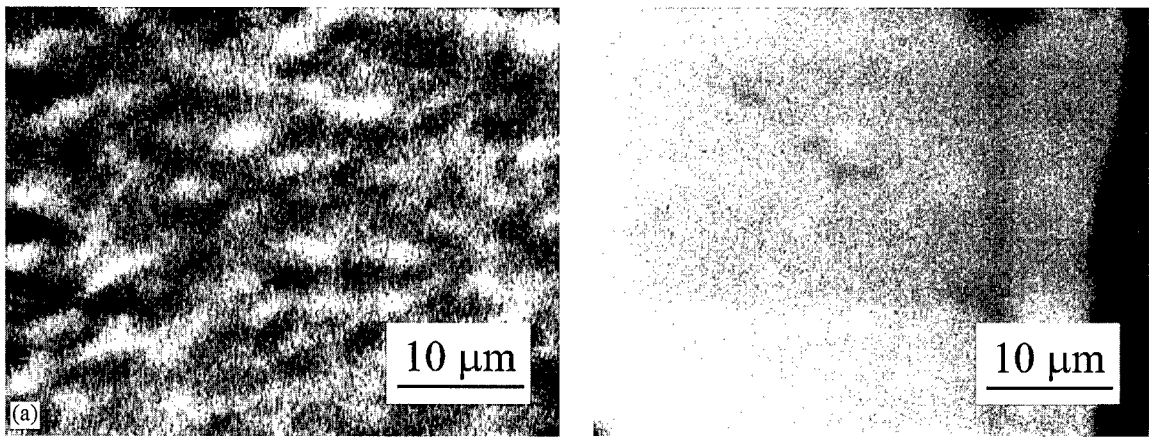

Fig. 2. The room temperature cathodoluminescence of 1 μm ZnSe films grown by MBE on (a) a Zn-exposed $c(4\times4)$-reconstructed GaAs buffer layer (sample A) and (b) a Zn-exposed (2×4)-reconstructed GaAs buffer layer (sample B). The defect density was estimated to be 7×10^6 and $9\times10^5\ cm^{-2}$, respectively. The electron probe parameters were: 30 nA, 20 keV. The magnification was 1700 times.

surfaces. A contributing factor for the difference is that a more charge neutral interface is formed on a (2×4)-reconstructed surface as opposed to a $c(4\times4)$-reconstructed surface. A completely charge neutral interface can be formed if the anion plane is 50% As and 50% Se. (2×4)-reconstructed GaAs has a 75% As surface coverage, which is lower than the 100% surface coverage of $c(4\times4)$-reconstructed GaAs [8]. MEE was also examined in response to recent reports which indicated an improvement in the ZnSe quality with the use of MEE for growth initiation [9]. We have not seen a noticeable improvement with this technique using the (2×4)-reconstructed GaAs surface, although further study is required before a definitive conclusion may be reached.

The insertion of the (In,Ga)P buffer layer between ZnSe and the GaAs substrate allows modification of the in-plane lattice constant to be matched to ZnSe. Fig. 3 shows the CL images of samples C, D, and E. The dark spots seen in Fig. 3a and Fig. 3b are due to threading dislocations, while the dark lines seen in Fig. 3c are due to misfit dislocations. The images taken of samples C and

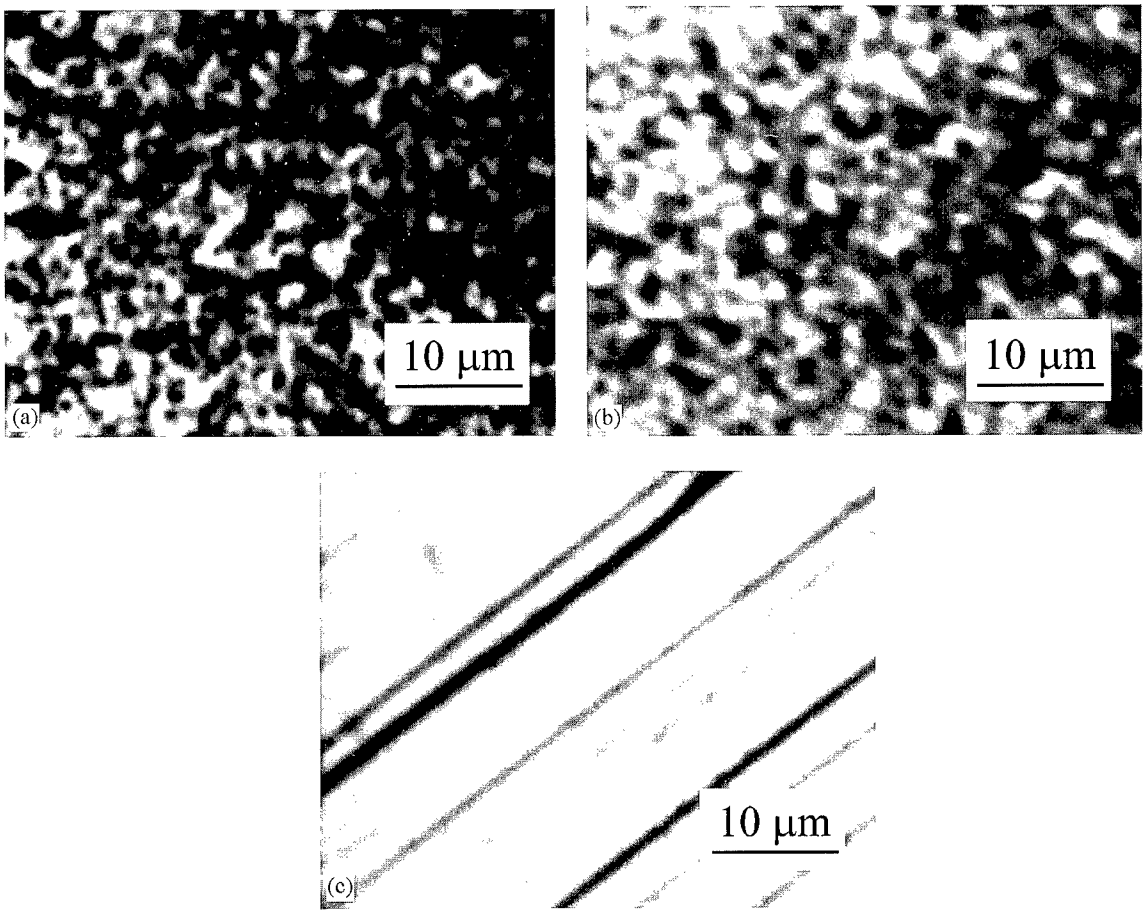

Fig. 3. The room temperature cathodoluminescence of 1 μm ZnSe films grown by MBE on 4 μm linearly graded (In,Ga)P buffer layers (a) without a GaAs layer between the (In,Ga)P and ZnSe (sample C), (b) with a Zn-exposed 8 monolayer, $c(4\times4)$-reconstructed GaAs layer between the (In,Ga)P and ZnSe (sample D) and (c) with a Zn-exposed 8 monolayer (2×4)-reconstructed GaAs layer between the (In,Ga)P and ZnSe (sample E). The (In,Ga)P lattice constant was graded from that of GaAs to that of ZnSe. The electron probe parameters were: 30 nA, 20 keV. The magnification was 1700 times.

D appear nearly identical to those of sample A. This suggests that the high dislocation density in these samples is due to poor nucleation and that the reduction of the lattice-match did not have a noticeable effect. The density of threading dislocations in these samples was estimated to be approximately $10^7\ cm^{-2}$, both from the CL images and from etch pit density measurements.

In contrast, an image of sample E primarily exhibits misfit dislocations with faint features due to various types of irregularities in the crystal lattice as shown in Fig. 3c. Since CL imaging shows enhanced contrast at misfit dislocations, these represent the dominant form of dislocations in this film. This suggests that the growth of ZnSe on (2×4)-reconstructed GaAs minimizes threading dislocations arising from the II–VI/III–V nucleation such that the lattice-match in sample E plays the primary role in the dislocation structure. The average spacing of the misfit lines in sample E is approximately 3 μm, indicative of the close lattice match [10] which is confirmed by X-ray diffraction measurements. CL and EPD both suggest a threading dislocation density of $10^6\ cm^{-2}$ in this sample. The remaining dislocations are speculated to arise either from the fully-strained pseudomorphic GaAs cap layer or from the relaxed III–V/III–V buffer layer.

Fig. 4 shows the results of the AFM characterization of the 1 μm ZnSe layer on various lattice-matched III–V epitaxial substrates. In Fig. 4a, ZnSe was nucleated by MBE on an (In,Ga)P surface by simultaneously opening the Zn and Se shutters. Although Fig. 3a shows a large percentage of non-radiative recombination in CL, the AFM results are very encouraging as the measured R_a value is about 4 Å, indicative of a very smooth growth front. The AFM result was not completely unexpected as RHEED intensity oscillations are routinely observed during the nucleation of ZnSe on phosphorus-containing III–V surfaces. In Fig. 4b and Fig. 4c, the AFM images are shown for ZnSe grown on GaAs caps exhibiting $c(4\times4)$ and (2×4) reconstructions, respectively. ZnSe grown on the (2×4)-reconstructed GaAs surface resulted in a much smoother ZnSe layer ($R_a \sim 3$ Å) as compared to ZnSe grown on the $c(4\times4)$-reconstructed GaAs surface ($R_a \sim 7$ Å).

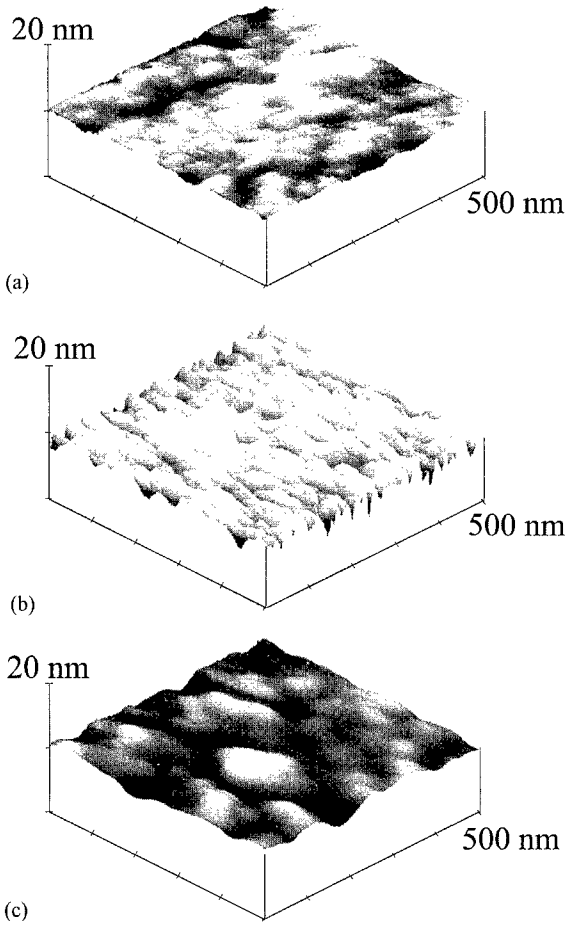

Fig. 4. Atomic force micrographs of 1 μm ZnSe films grown by MBE on 4 μm linearly graded (In,Ga)P buffer layers (a) without a GaAs layer between the (In,Ga)P and ZnSe (sample C), (b) with a Zn-exposed 8 monolayer, $c(4\times4)$-reconstructed GaAs layer between the (In,Ga)P and ZnSe (sample D) and (c) with a Zn-exposed 8 monolayer (2×4)-reconstructed GaAs layer between the (In,Ga)P and ZnSe (sample E). The (In,Ga)P lattice constant was graded from that of GaAs to that of ZnSe. The mean roughnesses values in the 500 nm × 500 nm areas were 4, 7, and 3 Å, respectively.

4. Summary

The nucleation study of ZnSe on $c(4\times4)$- and (2×4)-reconstructed GaAs surfaces identified the (2×4)-reconstructed surface as contributing to a lower density of extended defects and to a smoother overall surface. However, a 0.27% in-plane lattice constant mismatch is present, and also

contributes to the generation of defects due to plastic strain relief. To examine the role of lattice-matching, the surface chemistry, i.e. ZnSe on GaAs, was maintained, while the underlying in-plane lattice constant was varied. This was accomplished by the deposition of eight monolayers of GaAs on phosphorus-containing III–V buffer layers. Eliminating the lattice-mismatch by the use of (In,Ga,Al)P buffer layers shows a dislocation density of less than 10^6 cm^{-2} with the residual dislocations most likely originating in the relaxed but lattice-mismatched III–V epilayer. MEE was also examined in response to recent studies which indicated an improvement in the ZnSe quality with the use of MEE for growth initiation. We have not seen a noticeable improvement with this technique, although further study is required before a definitive conclusion may be reached.

The quality of the II–VI/III–V heterointerface has improved to enable a study of the electrical injection of holes from the p-type III–V layer into the p-type II–VI layer.

Acknowledgements

We would like to express our appreciation to E. Fitzgerald and J. House at MIT for discussions regarding CL and TEM. Our nucleation studies have also benefited greatly through our collaboration with J. Han and R.L. Gunshor at Purdue University. We gratefully acknowledge our sponsors: DARPA-University Research Initiative (Cont. No. 284-25041), the National Center for Integrated Photonic Technology (Cont. No. 542-381), and our ARO-Joint Services Electronics Program (DAAH-95-1-0038).

References

[1] K. Iwata, H. Asashi, J.H. Kim, X.F. Liu, S. Gonda, Y. Kawaguchi, A. Ohki and T. Matsuoka, J. Crystal Growth 150 (1995) 833.
[2] Y. Fan, J. Han, L. He, J. Saraie and R.L. Gunshor, Appl. Phys. Lett. 61 (1992) 3160.
[3] A. Ishibashi, IEEE J. Selected Topics Quantum Electron. 1 (1995) 741.
[4] K. Lu, J.L. House, P.A. Fisher, C.A. Coronado, E. Ho, G.S. Petrich and L.A. Kolodziejski, J. Crystal Growth 138 (1994) 1.
[5] T.N. Chin, Inst. Phys. Conf. Ser. 67 (1984).
[6] B.G. Yacobi and D.B. Holt, J. Appl. Phys. 59 (1986) R1.
[7] Z. Yu, S.L. Buczkowski, N.C. Giles and T.H. Myers, Appl. Phys. Lett. 69 (1996) 82.
[8] D.K. Biegelsen, R.D. Bringans, J.E. Northrup and L.-E. Swartz, Phys. Rev. B. 41 (1990) 5701.
[9] J.M. Gaines, J. Petruzzello and B. Greenberg, J. Appl. Phys. 73 (1993) 2835.
[10] C.H. Simpson and W.A. Jesser, Phys. Status Solidi (a) 149 (1995) 9.

ELSEVIER

Journal of Crystal Growth 175/176 (1997) 571–576

JOURNAL OF CRYSTAL GROWTH

Investigation of the structural properties of MBE grown ZnSe/GaAs heterostructures

I. Hernández-Calderón[a,*], E. López-Luna[a], J. Luyo[a], M. Meléndez-Lira[a], O. de Melo[a,1], P. Díaz[a,1], L. Hernández[a,1], J. Fuentes[a,1], R. León[a,1], H. Sitter[b]

[a] *Physics Department, CINVESTAV, Apdo. Postal 14-740, 07000 México, D.F., Mexico*
[b] *Institut für Experimentalphysik, Universität Linz, Linz, Austria*

Abstract

The results of photoluminescence and Raman spectroscopies, high resolution X-ray diffraction, and Auger electron spectroscopy are analyzed in terms of the structural properties of the ZnSe/GaAs(1 0 0) system as a function of film thickness and substrate temperature. The results of Raman spectroscopy and X-ray diffraction clearly show that the strain in the film is inhomogeneous and depends only on film thickness and not on growth temperature in the 285–325°C range. From these experiments a value of ~ 0.17 μm is inferred for the critical thickness of ZnSe on GaAs. Photoluminescence experiments sensitive to the ZnSe/GaAs interface reveal the presence of strain in the GaAs substrate. Analysis of the intensities of the LMM Auger transitions of Zn and Se indicate the formation of an interfacial layer with excess of Se, suggesting the formation of a pseudomorphic Ga–Se compound mixed with ZnSe at the interfacial region.

PACS: 61.10. – i; 68.35.Ct; 68.55.Vk; 78.30.Fs; 78.66. – w; 78.66.Hf

Keywords: ZnSe; ZnSe/GaAs heterostructures; Semiconductor interfaces; Auger; X-ray diffraction; Raman; Photoluminescence; Critical thickness

1. Introduction

The study of ZnSe/GaAs interfaces has attracted the attention of researchers since the last decade [1]. However, the recent increase in the investigation of the physical properties of ZnSe/GaAs heterostructures is noteworthy. One of the main reasons is that the improvement of their structural and chemical properties is of fundamental relevance for the elaboration of green–blue emission lasers based on ZnSe [2]. Recently, Sony reported a green laser with a lifetime larger than 100 h [3]. The noticeable improvement was attributed to the reduction of defect density from 10^6 to around $10^4\ cm^{-2}$. It needs to be further reduced to inhibit defect propagation during laser operation [4]. Wu and coworkers very recently reported that low defect

* Corresponding author. E-mail: ihernand@fis.cinvestav.mx.
[1] Permanent address: Faculty of Physics, University of Havana, Cuba.

0022-0248/97/$17.00 Copyright © 1997 Elsevier Science B.V. All rights reserved
PII S0022-0248(96)01215-8

density (less than 10^4 cm^{-2}) pseudomorphic ZnSSe and ZnSe layers can be grown on an As-rich GaAs buffer layer initially exposed to Zn [5]. Some of the intrinsic defects at the interface are caused by the chemical and structural differences between the GaAs substrate and the ZnSe film. The lattice mismatch produces biaxially compressed films which release the strain after reaching the critical thickness through the formation of misfit dislocations. It has also been shown that the charge imbalance at the ZnSe/GaAs interface can lead to 3D nucleation and interface roughening [6]. Interdiffusion and crystalline degradation can occur as a result of variations in the ZnSe stoichiometry near the interface [7]. The quality of the epilayers is strongly affected by initial growth conditions such as substrate preparation, growth temperature, and Zn to Se flux ratios [8]. Here, we report results on the investigation of the structural properties of ZnSe/GaAs(1 0 0) heterostructures grown by molecular beam epitaxy (MBE) by means of photoluminescence (PL) and Raman (RS) spectroscopies, high resolution X-ray diffraction (HRXRD) experiments, and Auger electron spectroscopy (AES).

2. Experimental details

The films were grown in a RIBER 32P MBE system. A series of epitaxial ZnSe films were deposited on semi-insulating GaAs(1 0 0) substrates at temperatures between 285 and 325°C. Prior to their introduction to the MBE chamber the substrates were chemically treated as described in Ref. [11]. The native oxide layer was removed by heating the indium glued substrate at about 550°C in ultrahigh vacuum (in the low 10^{-11} Torr range). The reflection high energy electron diffraction (RHEED) experiment of the annealed surface showed a (2×1) reconstruction pattern, indicating that residual Se from the background atmosphere reacted with the GaAs(1 0 0) surface [5, 9, 10]. The typical Zn/Se beam pressure ratio was ~ 0.3. The RHEED patterns confirmed the Se rich growth through the ZnSe(2×1) surface reconstruction. A typical growth rate of ~ 1 μm/h was employed [11]. The PL experiments were performed in a standard setup equipped with He–Ne and Kr–Ar lasers, a 0.5 m monochromator and a closed cycle He refrigerator. The Raman experiments were done with a double monochromator equipped with CCD detection and the 4880 Å line of an Ar laser. To verify the selection rules of RS we used a perfect backscattering $x(z, z)\bar{x}$ configuration; x, y, and z correspond to the $\langle 1\,0\,0\rangle$ crystal directions. The HRXRD experiments were done using CuK_{α_1} radiation and a four-crystal Bartels monochromator [12]. The AES spectra were taken in an analysis chamber connected through UHV to the growth chamber. The Auger spectra were measured immediately after growth of the films employing a MAC3 analyzer set to 2 eV resolution; the energy of the primary electrons was 3 keV.

3. Results and discussion

At room temperature (RT) the 0.26% lattice mismatch between GaAs ($a = 5.6532$ Å, RT) and ZnSe ($a = 5.6676$ Å, RT) gives place to biaxial stress at the interface. Most of the elastic deformation is accumulated in the ZnSe film, and it is customary to neglect the substrate deformation. A precise analysis of the strain must take into account the differences between the thermal expansion coefficients of ZnSe and GaAs, since in most cases the temperature of the sample during characterization or device operation is different from the growth temperature. A systematic analysis of the deformation, both in the substrate and in the films, is needed to have a better understanding of the interface strain. With the purpose of directly identifying the presence of substrate strain, we performed PL measurements sensitive to the GaAs surface. Fig. 1a shows the PL of covered and clean GaAs substrates. Since ZnSe is transparent to the 4880 Å photons (2.54 eV), we can easily reach the GaAs/ZnSe interfacial region. We observe a broad transition around 1.52 eV associated to excitonic transitions [13] and carbon impurities [14]. Transitions around 1.45 eV have been attributed to GaAs antisites [15] and those around 1.41 eV to Mn impurities [16]. There are additional transitions at lower energies, but here we are only interested in their energy shifts with film thickness. It is worth mentioning that the PL spectra taken

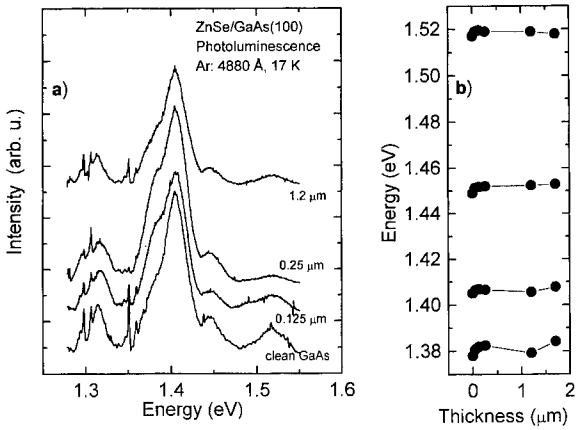

Fig. 1. (a) PL spectra of the clean and ZnSe covered substrates. (b) Energy shifts of the PL peaks of GaAs as a function of thickness of the ZnSe epilayer.

with the 6328 Å line of a He–Ne laser, which samples a larger GaAs volume than the 4880 Å line, exhibited sharper, stronger and much better resolved excitonic peaks than those of Fig. 1a, indicating that the uppermost interfacial region detected with the 4880 Å line has structural imperfections. At first glance the spectra shown in Fig. 1a could indicate that the substrate is not affected by the epilayer. However, a careful analysis of the PL peaks for samples with different thickness shows very small but noticeable and consistent energy shifts (see Fig. 1b). The general trend is an increase in energy with ZnSe film thickness up to around 0.2 μm and then a slight decrease. Considering the reduced magnitude of these changes, we realize this description may appear a bit imprecise, but as we will see later it can be understood in terms of the evolution of the strain in the substrate and the film before and after the critical thickness is reached and of the difference in the thermal expansion coefficients of ZnSe and GaAs.

As expected from high quality films, the RS experiments in the backscattering configuration, $x(z, z)\bar{x}$, did not show the TO phonon of the ZnSe film but a very weak TO signal from GaAs, indicating some degree of disorder at the interface. Fig. 2a shows the spectra of the films grown at 325°C; the

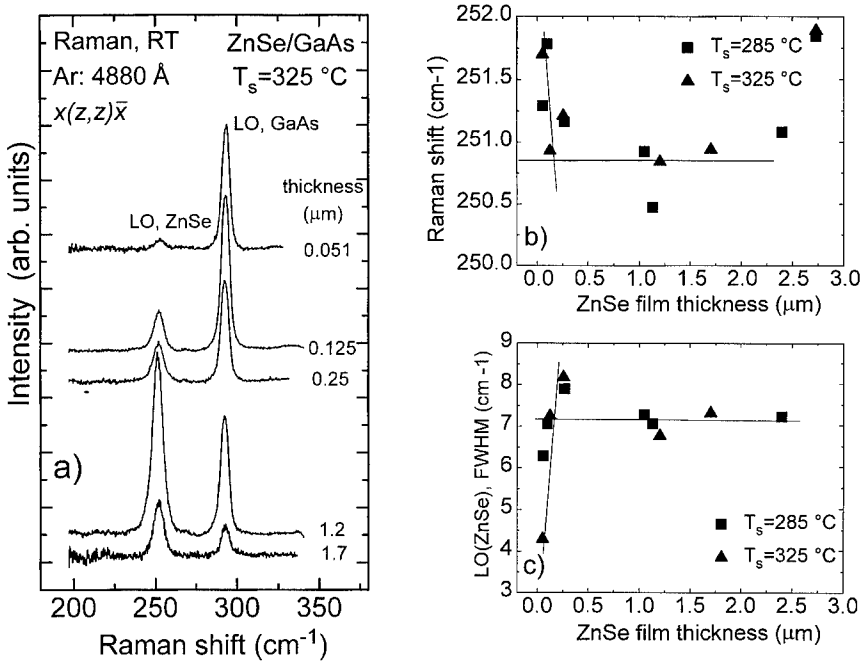

Fig. 2. (a) Raman spectra of ZnSe/GaAs heterostructures in a perfect backscattering configuration. (b) Changes in the energy of the LO phonon of ZnSe as a function of film thickness. (c) Changes in the FWHM of the LO phonon of ZnSe. The straight lines are just guides to the eye.

variations in intensity between the spectra are due to interference effects caused by different film thicknesses. Fig. 2b shows the observed shift in the energy of the ZnSe LO phonon and Fig. 2c the change in its full width at half maximum (FWHM) as a function of the ZnSe thickness. We observe that the LO peak moves towards lower energies up to around 0.17 μm and then remains at a value of 250.8 cm^{-1}. The total shift is around 1 cm^{-1}. A similar shift was observed between thin and thick ZnSe films grown by chemical vapor deposition [17]. In Fig. 2c we observe that the FWHM of the LO phonon increases from around 4 cm^{-1} for the thinnest film to around 8 cm^{-1} for the 0.25 μm thick ZnSe film; afterwards it remains at around 7 cm^{-1}. Looking at the straight lines (which are drawn just as a guide to the eye), we can describe the general behavior of the FWHM as an increase to around 0.18 μm and constant afterwards. Then, from the evolution of the LO energy shift and its FWHM, we can conclude that the changes depend on the thickness but not on the substrate temperature. These changes also indicate that the critical thickness (h_c) of ZnSe in GaAs(1 0 0) is around 0.17 μm. This value is consistent with previously reported values [18, 19]. The fact that the FWHM shows an important increase around h_c is an indication of the presence of structural disorder produced by the appearance of misfit dislocations which release the strain caused by the lattice mismatch. The observation in Fig. 2 that the average compressive biaxial strain of the ZnSe film is continuously reduced with increasing film thickness up to h_c, is a direct indication of nonuniform (or inhomogeneous) stress in the films, in agreement with previous results of Olego et al. [20].

In Fig. 3 we have summarized the results of HRXRD experiments. Fig. 3a presents the difference between the angle of the (0 0 4) reflection of ZnSe with respect to that of GaAs as a function of film thickness. We can see a very close similarity in the behavior of $\Delta\Theta$ and that of the LO phonon energy shown in Fig. 2a. Again, no dependence in the substrate temperature is observed. However, for HRXRD the changes reveal directly the modification of the (1 0 0) interplanar distance parallel to the substrate, indicating a value of h_c around 0.17 μm, consistent with the Raman measurements.

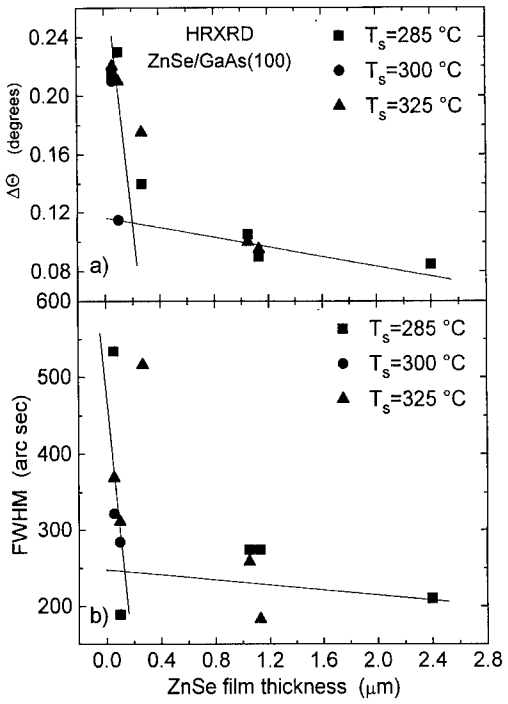

Fig. 3. (a) Difference between the angle of the (0 0 4) reflection of ZnSe and GaAs as a function of film thickness. (b) Changes in the FWHM of the (0 0 4) reflection of ZnSe as a function of film thickness. The lines are just guides to the eye.

The presence of residual strain is observed even for the thickest film. Fig. 3b shows the modification of the FWHM of the (0 0 4) reflection of the HRXRD patterns of the heterostructures. Analogous to the previous findings, we can see two types of behavior: a fast decrease up to around h_c and then a very slow decrease with thickness. Recent similar experiments by other groups show a variety of behaviors of the FWHM of the (0 0 4) reflection with ZnSe film thickness. Reichow et al. [21] found a continuous decrease of the FWHM with thickness of MBE deposited films, very close to our results. The report of Sou et al. [19] does not show a clear trend of the FWHM with film thickness in MBE deposited films. Lee et al. [17] found a reduction of the FWHM with film thickness of chemical vapor deposited films. Then, apparently the modification of the FWHM of the (0 0 4) reflection depends on the type and conditions of growth. In our case, we attribute the continuous decrease of the FWHM to

the improvement of the overall film structural quality with thickness. We start with a relatively rough substrate and the film becomes smooth with increasing ZnSe thickness. The apparent discrepancy between the conclusions from Fig. 2c and Fig. 3b is easily understood when we consider that Raman spectroscopy is very sensitive to the microscopic structure, while HRXRD is more sensitive to the average macroscopic structure of the films.

Based on the previous results it is easier to explain the shifts observed in PL in Fig. 1a. First, we have to consider the fact that the measurements were done at low temperature. Since the thermal expansion coefficient of ZnSe is larger than that of GaAs [22], after cooling to 17 K the situation will be reversed in relation to the one at growth temperature, the ZnSe film will be under biaxial tensile stress and the GaAs interfacial region will suffer biaxial compressive strain. The result is an increase in the band gap of GaAs with a maximum value just around h_c. The transitions observed in the PL spectra of Fig. 1 indicate this behavior. After h_c is reached most of the strain is released through the misfit dislocations and then the band gap energy of GaAs tends to decrease. Then, from the PL measurements we have obtained a direct indication of substrate strain.

We performed Auger experiments of the ZnSe/GaAs heterostructure as a function of ZnSe deposition of very thin films. Fig. 4 illustrates the ratio of the peak to peak intensities of the LMM transitions of Zn and Se from Auger derivative spectra. The intensities were measured at 5, 15, 30, 60 and 300 s deposition time. The typical growth rate of the films was ~ 1 μm/h (~ 2.8 Å/s); however, since growth conditions can change with film thickness we prefer to indicate a deposition time scale. From this figure is clear that the initial growth produces films with excess Se (or deficient in Zn). The stoichiometric regime is only reached around 30 s (around 60 monolayers, ML). The Zn/Se beam pressure ratio was maintained at ~ 0.3 for all the films during the whole growth, so the excess in Se with respect to Zn must be attributed to the chemical composition of the interfacial region. It is well known that the heating process employed to eliminate the native oxides of the GaAs substrate produces surfaces rich in Ga; even Ga clusters can be

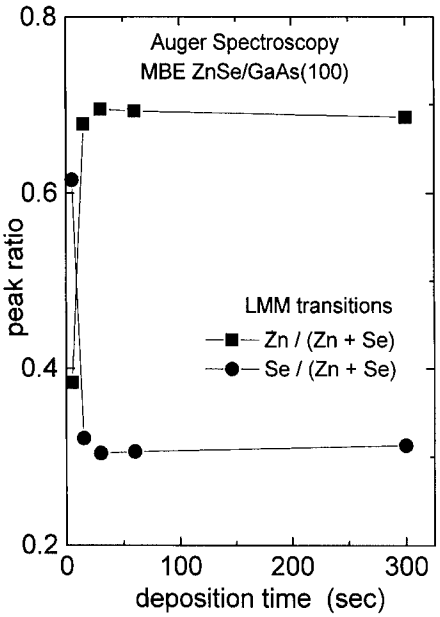

Fig. 4. Ratio of the peak to peak intensities of the LMM transitions of Zn and Se from Auger derivative spectra. The intensities were measured after 5, 15, 30, 60 and 300 s deposition time.

expected. We infer from the Auger data that an interfacial layer, which is a mixture of ZnSe and a Ga–Se compound, is formed during the first 30 s of growth. The possibility of formation of a pseudomorphic Ga_2Se_3 film has been mentioned frequently [1, 23–25] but it is still a matter of active discussion; however, our results point towards this direction. Another possibility could be the formation of a more complex pseudomorphic Zn–Ga–Se interfacial compound. The RHEED patterns show a clear transition between a spotty pattern at the beginning of the growth and a streaky pattern after around 20–30 s deposition. Additionally, the Auger spectra show the Ga and As transitions before 30 s deposition, afterwards no signal from the substrate can be detected. From all the previous discussions we can conclude that, under the growth conditions employed, the interfacial region is formed during the first 30 s of growth, which is the time needed to cover the whole substrate and also time needed to go from a 3D to 2D growth mode. It is unclear if this 30 s deposition time represents ~ 60 ML. The

initial growth can proceed at probably lower deposition rates, and could also vary as a function of substrate preparation. These results indicate that additional and systematic studies of the interfacial region are required to understand its nature and influence on the performance of ZnSe based devices.

4. Conclusions

We employed PL, RS, HRXRD and AES to investigate the structural properties of MBE grown ZnSe/GaAs heterostructures as a function of growth temperature and ZnSe film thickness. The presence of stress in the GaAs substrate was directly observed by PL. The results of RS and HRXRD show very good agreement and clearly indicate that the strain in the ZnSe film is inhomogeneous and depends on the film thickness, but not on the substrate temperature in the 285–325°C range. From these experiments we infer a value of 0.17 μm for h_c. From the analysis of the Auger spectra it is concluded that the interfacial region is composed of a mixture of a Ga–Se compound (probably Ga_2Se_3) and ZnSe. After the formation of this interfacial layer a stoichiometric regime is reached and the deposition proceeds in a 2D growth mode. We expect that these results will contribute to a better understanding of the ZnSe/GaAs interface. It is well known that important mechanisms of defect generation and propagation, that severely affect the performance of ZnSe-based green–blue emitting devices, take place in this interfacial region.

Acknowledgements

This work was partially supported by CONACyT (Mexico). M.M.L. thanks the OAS and NSF (grant DMR-9521507) for partial support. We thank A. Guillen, H. Silva, Z. Rivera and M. Guerrero for their kind technical assistance.

References

[1] D.-W. Tu and A. Kahn, J. Vac. Sci. Technol. A 3 (1985) 922, and references therein.
[2] M.A. Hasse, J. Qiu, J.M. DePuydt and H. Cheng, Appl. Phys. Lett. 59 (1991) 1272.
[3] Compound Semiconductors 2 (1996) 7.
[4] K. Nakano, S. Tomiya, M. Ukita, H. Yoshida, S. Itoh, E. Morita, M. Ikeda and A. Ishibashi, J. Electron. Mater. 25 (1996) 213.
[5] B.J. Wu, G.M. Haugen, J.M. Depuydt, L.H. Kuo and L. Salamanca-Riba, Appl. Phys. Lett. 68 (1996) 2828.
[6] M.C. Tamargo, R.E. Nahory, B.J. Skromme, S.M. Shibli, A.L. Weaver, R.J. Martin and H.H. Farrel, J. Crystal Growth 111 (1991) 741.
[7] G. Bratina, L. Vanzetti, A. Bonani, L. Sorba, J.J. Paggel, A. Franciosi, T. Peluso and L. Tapfer, J. Crystal Growth 159 (1996) 703.
[8] K. Menda, I. Takayasu, T. Minato and M. Kawashima, Jpn. J. Appl. Phys. 26 (1987) L1326; J.M. DePuydt, H. Cheng, J.E. Potts, T.L. Smith and S.K. Mohapatra, J. Appl. Phys. 62 (1987) 4756.
[9] H. Shigekawa, H. Oigawa, K. Miyake, Y. Aiso, Y. Nannichi, T. Hashizume and T. Sakurai, Appl. Phys. Lett. 65 (1994) 607.
[10] Y. Hirose, S.R. Forrest and A. Kahn, Appl. Phys. Lett. 66 (1995) 944.
[11] L. Hernández, M. Meléndez-Lira, O. de Melo, Z. Rivera and I. Hernández-Calderón, J. Vac. Sci. Technol. A 14 (1996) 2269.
[12] F. Heuzenberger, W. Faschinger, P. Juza, A. Pesek, K. Lischka and H. Sitter, Thin Solid Films 225 (1993) 265.
[13] V. Heim and P. Hiesinger, Phys. Status Solidi (b) 66 (1974) 461.
[14] G.B. Stringfellow, W. Koschel and F. Briones, Appl. Phys. Lett. 39 (1981) 581.
[15] L. Pavesi and M. Guzzi, J. Appl. Phys. 75 (1994) 4780.
[16] D.J. Ashen and P.J. Dean, J. Phys. Chem. Solids 36 (1975) 1041.
[17] C.D. Lee, B.K. Kim, J.W. Kim, S.K. Chang and S.H. Suh, J. Appl. Phys. 76 (1994) 928.
[18] Y.R. Lee, A.K. Ramdas, L.A. Kolodziejski and R.L. Gunshor, Phys. Rev. B 38 (1988) 13143.
[19] I.K. Sou, S.M. Mou, Y.W. Chan, G.C. Xu and G.K.L. Wong, J. Crystal Growth 147 (1995) 39.
[20] D.J. Olego, K. Shahzad, J. Petruzzello and D. Cammack, Phys. Rev. B 36 (1987) 7674.
[21] J. Reichow, J. Griesche, N. Hoffmann, C. Muggelberg, H. Rossmann, L. Wilde, F. Hennenberg and K. Jacobs, J. Crystal Growth 131 (1993) 277.
[22] T. Yao, Y. Okada, S. Matsui, K. Ishida and I. Fujimoto, J. Crystal Growth 81 (1987) 518.
[23] I. Suemune, K. Ohmi, T. Kanda, K. Yatake, Y. Kan and M. Yamanishi, Jpn. J. Appl. Phys. 25 (1986) 1827.
[24] D. Li, M. Gonsalves, N. Otsuka, J. Qiu, M. Kobayashi and R.L. Gunshor, Appl. Phys. Lett. 57 (1990) 449.
[25] A. Krost, W. Richter, D.R.T. Zahn, K. Hingerl and H. Sitter, Appl. Phys. Lett. 57 (1990) 1981.

ELSEVIER

Journal of Crystal Growth 175/176 (1997) 577–582

JOURNAL OF CRYSTAL GROWTH

ZnSe homoepitaxial growth on solid-phase recrystallized substrates

E. Tournié[a,*], P. Brunet[a], C. Ongaretto[a], C. Morhain[a], J.-P. Faurie[a], R. Triboulet[b], J.O. Ndap[b]

[a] *Centre de Recherche sur l'Hétéro-Epitaxie et ses Applications, Centre National de la Recherche Scientifique (CRHEA/CNRS), Rue Bernard Grégory, Parc Sophia Antipolis, F-06560 Valbonne, France*

[b] *Laboratoire de Physique des Solides de Bellevue, Centre National de la Recherche Scientifique (LPSB/CNRS), 1 Place Aristide Briand, F-92195 Meudon, France*

Abstract

We study the preparation, before homoepitaxy, of ZnSe substrates grown by solid-phase recrystallization. We show that an ex situ etch based on the Br_2 : HBr : H_2O solution provides a good quality surface. Further, we demonstrate that the in situ heat treatment plays a key role in the ZnSe nucleation. A Zn flux has to be impinging on the surface during heating if a 2D nucleation is to be obtained. This procedure allows to grow ZnSe homoepitaxial layers exhibiting superior optical properties with PL spectra dominated by the near-band edge emission, with negligible deep-level related and defect-related emissions.

PACS: 81.15.Hi; 61.14.Hg; 78.55.Et

Keywords: ZnSe; Homoepitaxy; MBE

1. Introduction

Molecular-beam epitaxy (MBE) of "blue-green" light emitters based on ZnSe and related compounds has up to now been developed mainly on GaAs substrates – available at low cost, large size and very high quality – because of the lack of substrate-quality ZnSe bulk material. However, this solution looks rather like makeshift because the necessary optimization of the heteropolar II–VI/III–V interface is extremely delicate. Consequently, in recent years serious efforts have been undertaken to improve the quality of ZnSe bulk material and significant progress has been achieved in terms of material purity [1–3] and structural quality [2, 4]. High-performance light-emitting diodes grown on ZnSe substrates are indeed emerging [5, 6].

Recently, we have demonstrated that solid-phase recrystallization (SPR) allows to obtain ZnSe single

* Corresponding author.

0022-0248/97/$17.00 Copyright © 1997 Elsevier Science B.V. All rights reserved
PII S0022-0248(96)00995-5

crystals of the highest quality currently achievable [7–9]. Line widths of the X-ray rocking curves lie in the 14–20 arcsec range. The low-temperature photoluminescence (PL) spectra are dominated by excitonic recombinations with negligible donor-acceptor pair (DAP) bands. More importantly no Cu-related deep-level emission is detected. In this work, we study the potential of these wafers for use as homoepitaxial substrates. We compare various substrate preparations. We show that both the ex situ and in situ preparations are critical to obtain a high-quality homoepitaxial growth. High-quality epitaxial layers exhibit PL spectra dominated by excitonic emission with negligible deep-level related and defect-related emissions.

2. Experimental procedure

For the growth of ZnSe single crystals by SPR, microcrystalline ZnSe boules, grown by chemical-vapour deposition at II–VI Inc., were annealed in the 1000–1100°C temperature range under Se-rich conditions for ~ 20 days. As a result large ($\sim 20\ cm^3$) single crystals were obtained. As-grown samples are highly resistive. More details on the growth procedure can be found in Ref. [7]. After growth, the boules were oriented along the [1 0 0] azimuth and cut into $1.5 \times 3 \times 0.2\ cm^3$ pieces. Each sample was then mechanically polished with alumina powder to a mirror-like finish. The samples were then further mechano-chemically polished (MCP) or chemically polished (CP) with various solutions and soldered with an In–Ga alloy on the Mo substrate-holders.

The homoepitaxial layers have been grown by solid-source MBE in a three-chamber system equipped with an in situ reflection high-energy electron diffraction (RHEED) set-up. The electron gun was operated at 20 keV. The growth temperature was ~ 280°C and the Se/Zn beam equivalent-pressure ratio ~ 2, i.e., the surface stoichiometry during growth was close to equilibrium as evidenced by the coexistence of both (2×1) and $c(2 \times 2)$ reconstructions. The growth rate was ~ 0.5 ML/s. As-grown samples have been characterized by low-temperature PL spectroscopy. The samples were mounted on the cold finger of a closed-cycle He cryostat regulated at 10 K. PL was excited by the 325 nm line of an He–Cd laser (excitation power $\sim 5\ W\ cm^{-2}$), and detected by a CO_2-cooled GaAs detector located at the exit of a 64 cm spectrometer.

3. Results and discussion

An additional reason why ZnSe homoepitaxy is not more popular is that the ideal surface preparation, a critical step in epitaxy, is not yet established. Various wet chemical etches based on $K_2Cr_2O_7 : H_2SO_4$ [10], $NH_4OH : H_2O_2$ [10, 11], Br_2-methanol [12], or a combination of them [13], have been proposed, but with only mitigated success. Dry etching using either BCl_3 gas [14] or a H_2 plasma [6] have also been implemented, this last technique apparently giving satisfactory results.

In this work, all mechanically polished ZnSe wafers have been first MCP with a $KMnO_4 : H_2SO_4$ solution. Then, they have been MCP and/or CP with various wet etches. The results have been compared in terms of RHEED patterns and PL properties.

When the substrate is further MCP and/or CP with a $K_2Cr_2O_7 : H_2SO_4$ solution, a weak RHEED pattern is already visible when introducing the sample into the growth chamber at 100°C. This pattern is invariably spotty and no improvement, beside an increase of the intensity, can be detected when heating up under a Se or Zn flux to the limit of substrate degradation (~ 550°C). The growth starts in a 3D mode and a streaky pattern appears after ~ 50 nm growth. The PL spectra are dominated by defect-related lines which reveal that this preparation procedure is not suitable.

When the ZnSe wafer is further CP with the $KMnO_4 : H_2SO_4$ solution, the RHEED pattern at the introduction in the growth chamber is either a spotty pattern or a modulated (1×1) pattern. In the former case, no amelioration can be seen when heating up the substrate. In the latter case, the streaks get longer and their intensity increase with the temperature. When heating up under a Zn flux, a faint $c(2 \times 2)$ reconstruction progressively emerges above ~ 400–450°C. When heating up under a Se

flux, on the other hand, a clear (3×1) reconstruction develops above 400°C (see the comment given below concerning this reconstruction). Both patterns remain unchanged either when heating up the substrate to degradation or when cooling down to the growth temperature. In both cases, the growth starts in a 3D mode and the RHEED returns to streaky after deposition of ~ 10 nm. The observed reconstructions are then the standard (2×1) or $c(2 \times 2)$ or a mixture of both, depending on the flux conditions [15]. The PL spectra taken from such-prepared samples reveal large inhomogeneities of the layer properties as well as a poor reproducibility from sample to sample. We show in Fig. 1 typical PL spectra taken from two different points of the same epilayer. These spectra are markedly different. Spectrum (a) is dominated by DAP bands, the position of which corresponds well to oxygen-related DAP [16]. A weak Y-line at 2.60 eV is also visible revealing the presence of extended defects [17]. Spectrum (b) on the other hand is dominated by the Y line. In both cases the near band-edge (NBE) emission is composed of free exciton (FX), neutral-donor bound-exciton (I_2), neutral-acceptor bound-exciton (I_1), deep-acceptor bound-exciton (I_1^{deep}) and defect-related (I_V^0) recombinations. The presence of intense Y and I_V^0 lines indicates that the epilayers contain a high density of extended defects [17], which should not be the case for homoepitaxial layers. The inhomogeneity of the PL properties leads us to conclude that the $KMnO_4:H_2SO_4$ solution produces either an inhomogeneous oxide or an oxide which desorbs non uniformly. In addition, the sample-to-sample variation can be attributed to the very poor stability of the solution. Although good results could occasionally be obtained, this etch thus does not appear to be suitable.

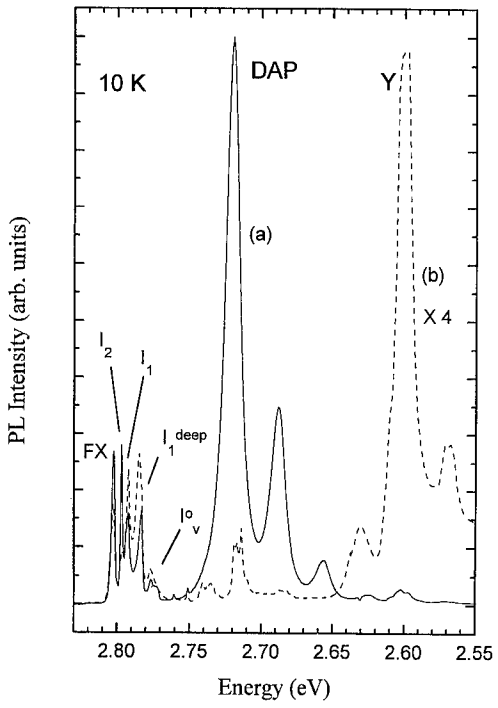

Fig. 1. PL spectra taken from two different points of a single ZnSe homoepitaxial layer. The ZnSe substrate surface had been MCP and CP with the $KMnO_4:H_2SO_4$ solution.

Finally, we have tested a third solution, namely $Br_2:HBr:H_2O$, which is often used to prepare the surface of InP substrates. After MCP with this solution the initial RHEED exhibits invariably a streaky, although dim and sometimes modulated, (1×1) pattern (Fig. 2a). A faint $c(2 \times 2)$ or a clear (3×1) reconstruction develops when heating above ~ 400–450°C under a Zn or Se flux, respectively. These patterns are stable when heating the substrate up to degradation or when cooling down to the growth temperature (Fig. 2b and Fig. 2c). When starting the growth the (3×1) reconstruction disappears immediately and the RHEED turns spotty (Fig. 3a). Streaks appear again after ~ 6 nm growth. On the other hand, when starting the growth the $c(2 \times 2)$ reconstruction leads to a continuous improvement of the RHEED pattern which remains streaky, if sometimes modulated (Fig. 3b). In both cases the classical reconstructions then develop.

Before turning to the PL properties of these layers we open a parenthesis to comment on the (3×1) reconstruction that we observe when heating the substrates under a Se flux. To our knowledge, this pattern has never been observed when growing homo- or heteroepitaxial ZnSe layers. On the other hand, it has been previously reported to develop when heating up ZnSe substrates before epitaxy [18]. This reconstruction disappears as soon as the growth starts. In addition, extensive annealing of ZnSe homo- or hetero-epitaxial layers under a Se

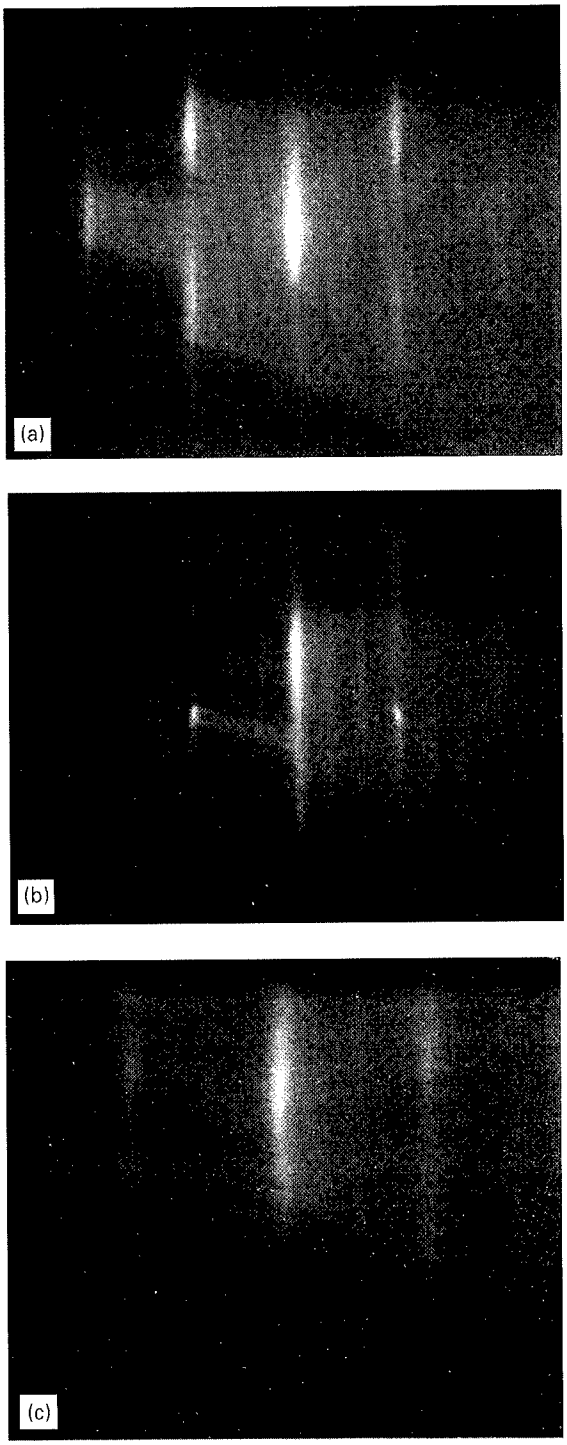

flux in the 400–500°C temperature range does not lead to a recovery of this reconstruction. We are thus inclined to attribute this reconstruction to adsorbates, probably stemming from the polishing procedures. Further work is necessary to clarify this point.

We believe that the different qualities of the RHEED patterns observed when starting the growth are directly linked to the pre-growth reconstructions. Starting from a (3×1) surface, a reorganization of the surface is necessary to evolve toward a classical reconstruction and results in the systematically observed transient spotty RHEED-pattern. On the other hand, since the $c(2 \times 2)$ reconstruction is a standard reconstruction for a ZnSe surface the growth on such a surface can start in a smooth 2D mode.

These initial stages of the MBE growth have also a dramatic impact on the PL properties of the layers. We show in Fig. 4 the PL spectra taken from homoepitaxial layers grown from (3×1) and $c(2 \times 2)$ starting surfaces. Both spectra are dominated by similar NBE emission which will be commented below. Important in our context is to compare the deep-level emissions. The spectrum of the layer grown from the (3×1) surface exhibits weak DAP bands as well as a pronounced Y line (Fig. 4a). The defect related I_V^0 line is also clearly detected. On the other hand, negligible DAP emission as well as Y line are detected when growth starts on the $c(2 \times 2)$ reconstruction (Fig. 4b). This is consistent with the fact that ZnSe grows initially in a 3D mode on the (3×1) surface and in a 2D mode on the $c(2 \times 2)$ surface. After 3D nucleation, extended defects are generated during island coalescence and give rise to the I_V^0 and Y lines in the PL spectra. These data reveal that the in situ heat

Fig. 2. RHEED patterns observed from a ZnSe MCP with the $KMnO_4:H_2SO_4$ and $Br_2:HBr:H_2O$ solutions in sequence; (a) at the introduction in the growth chamber a (1×1) reconstruction is observed ([1 1 0] azimuth); (b) after heating to 500°C under a Se flux and cooling down to growth temperature a clear (3×1) reconstruction is observed ([1 1 0] azimuth); (c) after heating to 500°C under a Zn flux and cooling down to growth temperature a weak $c(2 \times 2)$ reconstruction is observed ([1 0 0] azimuth).

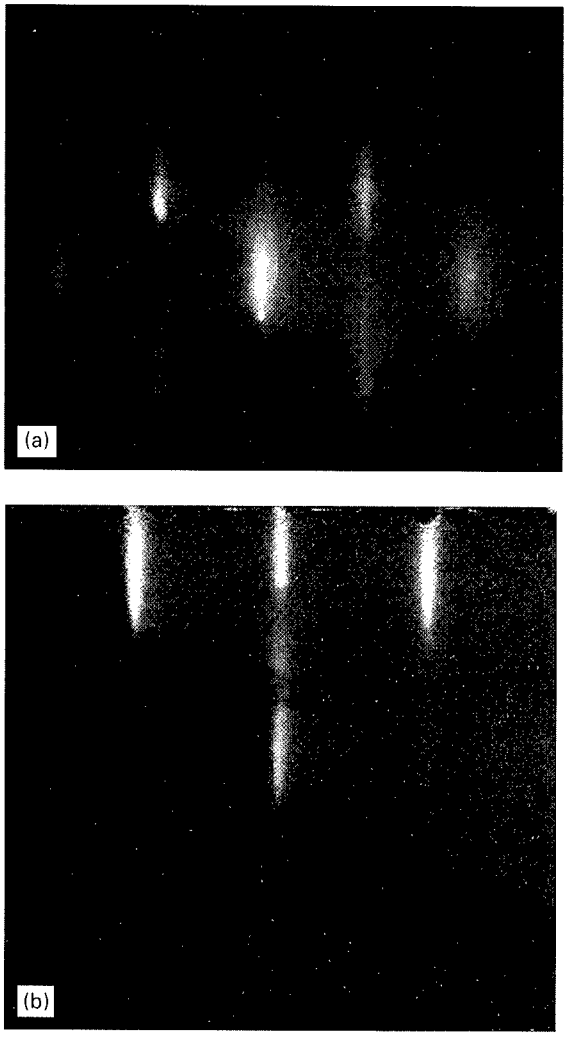

Fig. 3. RHEED pattern observed after 3 nm growth. The ZnSe substrate was MCP ex situ with the $KMnO_4:H_2SO_4$ and $Br_2:HBr:H_2O$ solutions in sequence. One sample was heated up in situ under a Se flux leading to a (3×1) reconstruction prior to growth (a), the other one was heated up in situ under a Zn flux leading to a $c(2 \times 2)$ reconstruction prior to growth (b).

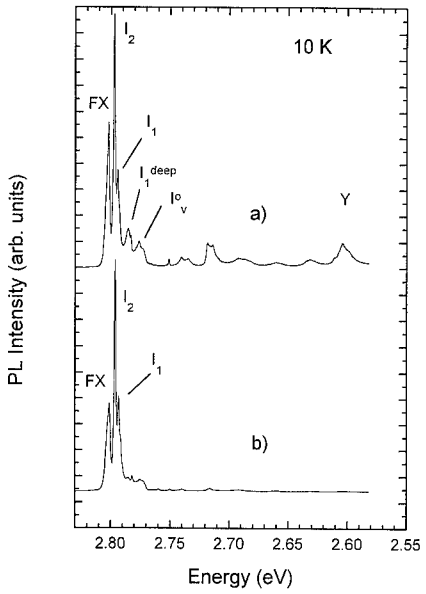

Fig. 4. PL spectra taken from two ZnSe homoepitaxial layers grown on substrates etched with the $KMnO_4:H_2SO_4$ and $Br_2:HBr:H_2O$ solutions in sequence. One sample was heated up in situ under a Se flux leading to a (3×1) reconstruction prior to growth (a), the other one was heated up in situ under a Zn flux leading to a $c(2 \times 2)$ reconstruction prior to growth (b).

treatment of the sample has a decisive effect on the quality of the homoepitaxial growth.

The NBE emission is dominated by a neutral-donor bound-exciton I_2, the free exciton FX and a neutral-acceptor bound-exciton I_1 recombinations (Fig. 4). We have shown by selective PL [19] that the impurities responsible for the I_2 line are Ga and In, most probably coming from the alloy used to mount the samples on the Mo substrate holders, and that Li diffusing from the substrate where it is the dominant impurity [8, 9] is responsible for the I_1 line.

These results thus indicate that preparing the ZnSe substrate by an ex situ etching with the $Br_2:HBr:H_2O$ solution followed by an in situ heat treatment under a Zn flux appears as a satisfactory, albeit not yet optimized, procedure to grow high-quality ZnSe homoepitaxial layers. In addition, our data provide further evidence that ZnSe single crystals grown by SPR are of sufficient high-quality to be used as substrates in epitaxy. We point out here that homoepitaxial growth proceeds much better than heteroepitaxial growth on GaAs substrates, as evidenced by the observation of much thinner streaks in the RHEED patterns and many more oscillations of the specular spot. Finally, we wish to stress that the PL spectrum displayed in Fig. 4b is among the best ever published for ZnSe homoepitaxial layers. The absence of defect-related lines, in contrast to recent reports [10–12, 20], is the

signature of a remarkable improvement of ZnSe homoepitaxial growth.

4. Conclusions

We have studied different preparations of the ZnSe surface before homoepitaxial growth. We have shown that an ex situ etch based on the $Br_2:HBr:H_2O$ solution provides a good quality surface. Further, we have shown that the in situ heat treatment plays a key role in the ZnSe nucleation. A Zn flux has to be impinging on the surface during heating in order to achieve a 2D nucleation. This procedure allowed us to grow ZnSe homoepitaxial layers exhibiting superior optical properties. This paves the way for the growth and study of ZnSe-based heterostructures aiming at preparing light-emitting devices.

References

[1] T. Taguchi, T. Kusao and A. Hiraki, J. Crystal Growth 72 (1985) 46.
[2] G. Cantwell, W.C. Harsch, H.L. Cotal, B.G. Markey, S.W.S. Mc Keever and J.E. Thomas, J. Appl. Phys. 71 (1992) 2931.
[3] K. Mochizuki, K. Masumoto, T. Yasuda, Y. Segawa and K. Kimoto, J. Crystal Growth 135 (1994) 318.
[4] P. Rudolph, K. Umetsu, H.J. Koh and T. Fukada, J. Crystal Growth 143 (1994) 359.
[5] D. B Eason, Z. Yu, W.C. Hughes, W.H. Roland, C. Boney, J.W. Cook, Jr., J.F. Schetzina, G. Cantwell and W.C. Harsch, Appl. Phys. Lett. 66 (1995) 115.
[6] M.H. Jeon, L.C. Calhoun and R.M. Park, J. Electron. Mater. 24 (1995) 177.
[7] R. Triboulet, J.O. Ndap, A. Tromson-Carli, P. Lemasson, C. Morhain and G. Neu, J. Crystal Growth 159 (1996) 156.
[8] E. Tournié, C. Morhain, G. Neu, J.-P. Faurie, R. Triboulet and J.O. Ndap, Appl. Phys. Lett. 68 (1996) 1356.
[9] E. Tournié, C. Morhain, G. Neu, M. Laügt, C. Ongaretto, J.-P. Faurie, R. Triboulet and J.O. Ndap, J. Appl. Phys. 80 (1996) 2983.
[10] M. Ohishi, K. Ohmori, Y. Fujii and H. Saito, J. Crystal Growth 86 (1988) 324.
[11] K. Menda, I. Takayasu, T. Minato and M. Kawashima, J. Crystal Growth 86 (1988) 342.
[12] R.M. Park, C.M. Rouleau, M.B. Troffer, T. Koyama and T. Yodo, J. Mater. Res. 5 (1990) 475.
[13] H. Wenisch, K. Schüll, D. Hommel, G. Landwehr, D. Siche and H. Hartmann, Semicond. Sci. Technol. 11 (1996) 107.
[14] K. Ohkawa, T. Karasawa and T. Mitsuyu, J. Vac. Sci. Technol. B 9 (1991) 1934.
[15] K. Menda, I. Takayasu, T. Minato and M. Kawashima, Jpn. J. Appl. Phys. 26 (1987) L1326.
[16] J. Chen, Y. Zhang, B.J. Skromme, K. Akimoto and S.J. Pachuta, J. Appl. Phys. 78 (1995) 5109.
[17] K. Shahzad, D.J. Olego and D.A. Cammack, Phys. Rev. B 39 (1989) 13016.
[18] J. Ren, D.B. Eason, Z. Yu, B. Sneed, J.W. Cook, Jr., J.F. Schetzina, N.A. El-Masry, X.H. Yang, J.J. Song, G. Cantwell and W.C. Harsch, J. Vac. Sci. Technol. B 12 (1994) 1262.
[19] E. Tournié, C. Morhain, C. Ongaretto, V. Bousquet, P. Brunet, G. Neu, J.-P. Faurie, R. Triboulet and J.O. Ndap, Mater. Sci. Eng. B, to be published.
[20] Y. Hishida, T. Toda, T. Yoshie, K. Yagi, T. Yamaguchi and T. Niina, Appl. Phys. Lett. 64 (1994) 3419.

ELSEVIER

Journal of Crystal Growth 175/176 (1997) 583–586

JOURNAL OF CRYSTAL GROWTH

MBE growth of n-type ZnSe and ZnS using ethylchloride as a dopant

Takashi Yasuda*, Bao-Ping Zhang, Yusaburo Segawa

Photodynamics Research Center (PDC), The Institute of Physical and Chemical Research (RIKEN), 19-1399 Koeji, Nagamachi, Aoba-ku, Sendai 980, Japan

Abstract

A new gas source n-type dopant, ethylchloride (EtCl), was used for MBE growth of ZnSe and ZnS. Carrier concentrations up to $3.2 \times 10_{18}$ and $3.5 \times 10^{17}\ cm^{-3}$ were achieved for ZnSe and ZnS, respectively. The use of the gas source dopant is advantageous in maintaining the MBE chamber.

PACS: 72.80.Ey

Keywords: ZnSe; ZnS; MBE; n-Type conductivity; Cl; Ethylchloride

1. Introduction

Recent progress on p- and n-type conductivity control of ZnSe-based II–VI compounds has facilitated the use of these compounds in blue–green laser applications [1, 2]. Nitrogen gas activated by an RF plasma cell is an efficient p-type dopant which can be introduced into the growth chamber through a variable leak valve [3, 4]. The source of the dopant gas can be separated completely from the vacuum chamber, which is advantageous in maintaining the MBE chamber. A solid source of zinc chloride ($ZnCl_2$), which is evaporated by a conventional Knudsen cell in the vacuum chamber, is used extensively as an n-type dopant. $ZnCl_2$ is an efficient n-type dopant for ZnSe. However, the relatively high vapor pressure of this source material limits the baking temperature of the chamber to about 100°C because the diffusion of $ZnCl_2$ in the MBE chamber contaminates the other sources. Therefore, considerable attention is necessary when utilizing $ZnCl_2$ during MBE growth.

In this study we used ethylchloride (EtCl), an alternate n-type dopant source. EtCl is a liquid source with high vapor pressure at room temperature and can be introduced into the chamber through a variable leak valve. The use of EtCl makes it possible to place the dopant source outside of the growth chamber and, therefore, enables a higher chamber baking temperature. In addition,

* Corresponding author. Fax: + 81 22 228 2010; e-mail: tyasuda@postman.riken.go.jp.

0022-0248/97/$17.00 Copyright © 1997 Elsevier Science B.V. All rights reserved
PII S0022-0248(96)00996-7

EtCl can be easily baked out due to its high vapor pressure. This new design also allows us to maintain the dopant source and the vacuum chamber separately.

2. Experimental procedure

ZnSe layers were grown by conventional MBE using high-purity zinc (6 N) and selenium (6 N) as sources. The growth was performed at 250°C with an equivalent beam pressure ratio (VI/II) between 3 and 5. High-purity elemental sulfur (6 N) was used for the ZnS growth. A specially designed cracker-effusion cell was used as the sulfur source [5]. The growth temperature was kept between 150°C and 190°C, and the VI–II beam equivalent pressure ratio ranged from 3 to 10.

GaAs(100) wafers were used as substrates for the growth of both ZnSe and ZnS. After organic solvent degreasing, the wafer was etched in a solution of Semicoclean 23 (Furuuchi) for 60 min. Prior to the growth, the wafer was thermally cleaned in the growth chamber at 600°C for 30–60 min to remove the oxide layer. A streaky RHEED pattern was observed after these preparations.

EtCl was introduced into the MBE chamber through a variable leak valve. The beam pressure was monitored by an ion gauge. No cracking was performed in this study. The EtCl stream was switched between a vent line and the MBE chamber by a computer-controlled air valve system, as shown in Fig. 1. This switching procedure prevented an inadvertent introduction of EtCl into the MBE chamber.

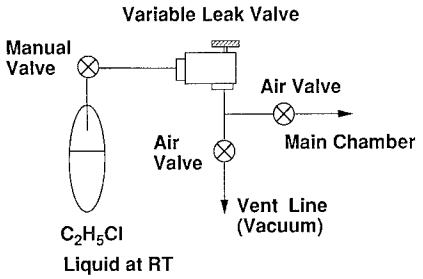

Fig. 1. Schematic diagram of gas lines for EtCl introduction.

The carrier concentration, resistivity, and mobility were measured using the Van der Pauw method at room temperature. Indium soldering was used to make ohmic contacts on both n-ZnSe and n-ZnS layers.

The photoluminescence was excited by a He–Cd laser (325 nm, 1.5 mW), and was detected by a photon counter with a cooled GaAs photomultiplier. The samples were immersed in liquid helium, which could be pumped below the λ point.

3. Results and discussion

To control the doping level of ZnSe, the Knudsen cell for $ZnCl_2$ must be operated accurately at a low temperature (below 200°C) because of its high vapor pressure. However, such low-temperature operation makes it difficult to maintain an accurate temperature for the commonly used Knudsen cell. In contrast, the beam pressure of EtCl can be maintained mechanically by using a variable leak valve, which is an established technique for introducing gas sources into an MBE chamber. Therefore, the extensive beam pressure range of EtCl was accurately achieved.

Fig. 2 shows the EtCl beam pressure dependence of the carrier concentration and the mobility of the Cl-doped ZnSe layers. When the beam pressure of EtCl was increased from 2.0×10^{-7} to 1.0×10^{-5} Torr, the carrier concentrations of the

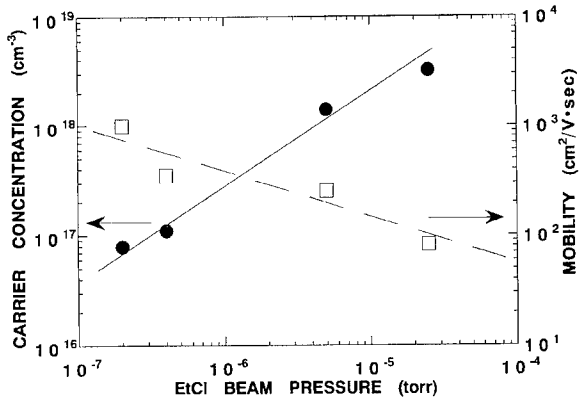

Fig. 2. The EtCl beam pressure dependence of the carrier concentration and the mobility of Cl-doped ZnSe layers.

ZnSe samples increased almost linearly from 7.9×10^{16} to 3.2×10^{18} cm^{-3}. The highest carrier concentration obtained in this study was limited by the achievable beam pressure of EtCl in the MBE system. An electron concentration of 1×10^{19} cm^{-3} can be achieved by the use of $ZnCl_2$ as an n-type dopant [6]; this value is higher than that obtained in this study. An increase of the Cl incorporation in ZnSe is essential to obtain samples with higher electron concentrations. The use of a thermal cracking cell will promote the decomposition of EtCl and enable us to obtain heavily doped ZnSe samples.

Fig. 3 indicates the low-temperature photoluminescence spectra of the Cl-doped ZnSe layers with different electron concentrations. The lightly doped sample exhibited a dominant excitonic emission at 2.795 eV, which agrees well with the donor bound exciton observed in ZnSe epitaxial layers grown on GaAs substrates. The spectral line shape broadened as the carrier concentration increased, and the peak position finally shifted to the higher energy side, due to the degenerate conduction band resulting from the highly incorporated Cl donors (Fig. 3c).

Orange deep emission from the Cl-doped ZnSe is known as a self-activated (SA) emission, which is a donor–acceptor (DA) pair transition between a shallow donor (Cl) and a complex of Cl and Zn-vacancy, which acts as a deep acceptor [7]. The increase of SA emission intensity is reflected by the high compensation ratio of Cl donors. However, in this study, even the heavily doped sample with 3.2×10^{18} cm^{-3} electrons exhibited intense edge emission but very weak orange deep emission, as shown in Fig. 4. This result indicates that the compensation of the doped donor in these samples is suppressed considerably under doping conditions using EtCl as a dopant source.

Cl-doping into ZnS is difficult compared to ZnSe. The optimum temperature of ZnS growth using an elemental sulfur as a group-VI source is lower than that of ZnSe growth because the sticking coefficient of sulfur is lower than that of selenium. When the ZnS layers were grown at 150°C, the maximum carrier concentration was 5×10^{16} cm^{-3}, which is low compared to Cl-doped ZnSe (Table 1). We suspect that the lower growth temperature of ZnS affected the decomposition rate of EtCl. When we increased the growth temperature to 190°C, the carrier concentration increased to 3.5×10^{17} cm^{-3} (Table 1), while the growth rate reduction was only 30%. Therefore, the primary reason for the increase in carrier concentration was the increase in the EtCl decomposition efficiency at a higher growth temperature.

MBE growth of ZnS has not been investigated extensively, therefore there are only a few reports

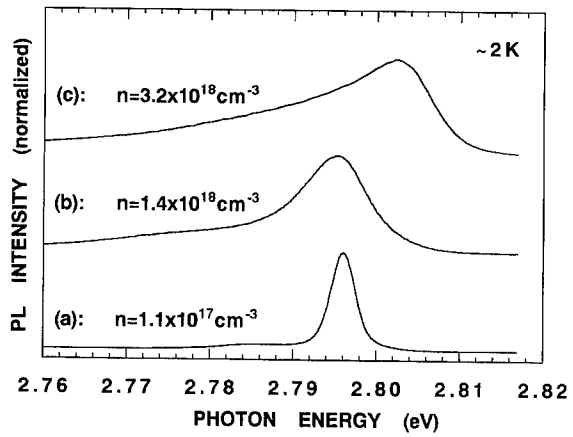

Fig. 3. Excitonic emission of Cl-doped ZnSe using EtCl as a dopant: (a) $n = 1.1 \times 10^{17}$ cm^{-3}; (b) $n = 1.4 \times 10^{18}$ cm^{-3}; (c) $n = 3.2 \times 10^{18}$ cm^{-3}.

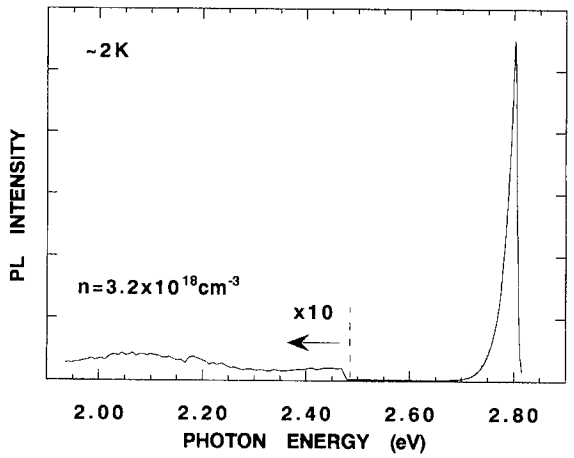

Fig. 4. Photoluminescence spectrum of heavily doped ZnSe : Cl.

Table 1
Electrical properties of Cl-doped ZnS layers

Sample no.	EtCl beam pressure (Torr)	T_{sub} (°C)	Carrier concentrations (cm^{-3})
334	9×10^{-8}	150	High resistivity ($\lesssim10^{16}$)
333	3×10^{-7}	150	High resistivity ($\lesssim10^{16}$)
332	5×10^{-7}	150	High resistivity ($\lesssim10^{16}$)
362	5×10^{-6}	150	3.5×10^{16}
429	1×10^{-5}	150	5.0×10^{16}
430	1×10^{-5}	190	3.5×10^{17}

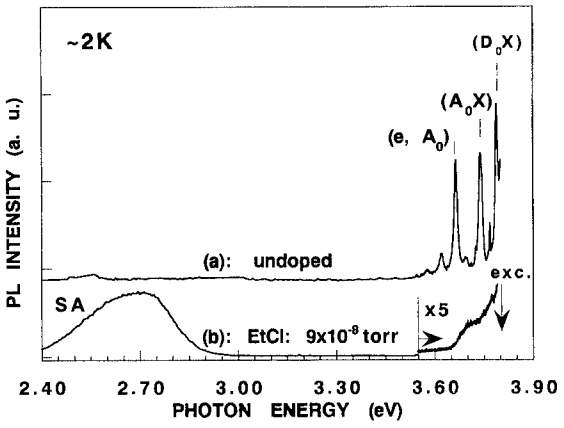

Fig. 5. Photoluminescence spectra of (a) undoped ZnS and (b) Cl-doped ZnS using EtCl as a dopant.

on n-type doping by MBE. The electron concentration of 10^{19} cm^{-3} was achieved for homo-epitaxial ZnS using an Al metal as a dopant [8]. However, the doping limit of group-III donors in ZnSe proved to be in the order of 10^{17} cm^{-3} [9]. Therefore, it is important to find an efficient group-VII dopant for ZnS, which can be used for ZnSe as well. The increase in carrier concentration is the key issue for utilizing EtCl as an n-type dopant. In this study, EtCl was introduced to the substrate without cracking; however, the use of a cracking cell for EtCl might be important in increasing the doping concentrations, as mentioned above.

The photoluminescence of undoped ZnS exhibited a dominant excitonic emission, such as a donor-bound exciton and an acceptor-bound exciton (Fig. 5a). However, even the lightly Cl-doped sample (#334) exhibited a dominant blue SA emission, resulting in a high compensation ratio of the Cl donor in ZnS (Fig. 5b). Further investigation into this compensation behavior is required to increase the doping level in ZnS.

4. Conclusions

EtCl was used as an n-type dopant source for ZnSe and ZnS during MBE growth. Carrier concentrations up to 3.2×10^{18} cm^{-3} for ZnSe and 3.5×10^{17} cm^{-3} for ZnS were successfully achieved. Using this liquid dopant source with high vapor pressure enables us to separate the dopant from the MBE chamber.

References

[1] M.A. Hasse, J. Qiu, J.M. DePuydt and H. Cheng, 49th Ann. Device Research Conf., Colorado (1991) p. IVA-7.
[2] Y. Morinaga, H. Okuyama and K. Akimoto, Ext. Abstracts 1992 Int. Conf. Solid State Devices and Materials, Tsukuba (1992) p. 707.
[3] K. Ohkawa, T. Karasawa and T. Mitsuyu, Proc. 6th Int. Conf. Molecular Beam Epitaxy, San Diego (1990) PIII-21; J. Crystal Growth 117 (1991) 375.
[4] R.M. Park, M.B. Troffer, C.M. Rouleau, J.M. DePuydt and M.A. Haase, Appl. Phys. Lett. 57 (1990) 2127.
[5] T. Yasuda, T. Yasui and Y. Segawa, J. Crystal Growth 159 (1996) 447.
[6] K. Ohkawa, T. Mitsuyu and O. Yamazaki, Ext. Abstracts 18th Conf. Solid State Devices and Materials, Tokyo (1986) p. 635.
[7] K. Era, S. Shionoya and Y. Washizawa, J. Phys. Chem. Solids 29 (1968) 1827.
[8] M. Kitagawa, T. Tomomura, A. Suzuki and S. Nakajima, J. Crystal Growth 95 (1989) 509.
[9] T. Niina, T. Minato and K. Yoneda, Jpn. J. Appl. Phys. 21 (1982) L387.

ELSEVIER

Journal of Crystal Growth 175/176 (1997) 587–592

JOURNAL OF CRYSTAL GROWTH

Growth mechanism of II–VI compound semiconductors by molecular beam epitaxy

Hiroyuki Okuyama*, Takayuki Kawasumi, Akira Ishibashi, Masao Ikeda

Sony Corporation Research Center, Fujitsuka 174, Hodogaya, Yokohama 240, Japan

Abstract

The basic model of MBE growth of ZnMgSSe at 275°C is considered. The net flux intensity is expressed by the product of the flux intensity and the maximum sticking coefficient for the cracked or heated beam flux. The surface of the crystal is divided into a surface covered with group II elements (surface II) and a surface covered with group VI elements (surface VI) and the adatom density is almost the same at surface II and surface VI. The desorption of these adatoms is expressed by considering the effect of cluster such as S_2 and Se_2. The desorption from the surface is disregarded because the growth temperature is low. The experimental composition and the growth rate of ZnMgSSe agrees with the values calculated using this theory and the tendency of these properties when the $c(2 \times 2)$ pattern is observed is different from the tendency when (2×1) is observed.

PACS: 68.22; 68.55; 81.10.B; 81.15

Keywords: ZnMgSSe; MBE; Adatom; Desorption; Cluster; RHEED

1. Introduction

The properties of II–VI compound semiconductors laser diodes (LDs) are improved and 100 h device lifetime was reported [1]. For further improvement, basic investigation in the crystal growth is necessary. The vapor pressure of group II and VI elements is relatively high, although that of II–VI compound semiconductor is relatively low. Thus, the mechanism of molecular beam epitaxy (MBE) growth of II–VI compound semiconductors may be different from that of III–V compound semiconductors [2–4], whose growth mechanism is similar to that of group VI semiconductors. In the crystal growth of II–VI compound semiconductors [5–7], we must consider the surface covered with group II elements and that covered with group VI elements. Although we can understand the basic mechanism of MBE growth of ZnSe from these works, many details are not yet clear. In this paper, we consider the basic model of MBE growth of ZnMgSSe. And we aim to establish the growth mechanism of II–VI compound semiconductors.

* Corresponding author. Fax: + 81 45 353 6905; e-mail: hokuyama@src.sony.co.jp.

0022-0248/97/$17.00 Copyright © 1997 Elsevier Science B.V. All rights reserved
PII S0022-0248(96)01179-7

2. Experimental procedure

ZnMgSSe films were grown on semi-insulated (1 0 0) GaAs substrates by MBE. The source materials were elemental Zn (6N), Se (6N), S (6N), Mg (6N). As the element S source, we used a valved cracking S cell. The evaporating temperature was 110°C. The growth temperature was 275°C. At present most II–VI LDs are fabricated at the growth temperature of 280°C [1]. The growth rate was measured in reference to an image of the cleaved facet which was taken using a scanning electron microscope (SEM). The composition x and y of $Zn_{1-x}Mg_xS_ySe_{1-y}$ were determined by electron-probe microanalysis (EPMA). Reflection high-energy electron diffraction (RHEED) was used to monitor the surface reconstruction pattern of each sample. When group-VI element (group-II element) flux is irradiated, a (2×1) ($c(2\times2)$) pattern is observed.

The beam flux intensity was estimated by measuring the mass of the deposition on a liquid-nitrogen-cooled (below 0°C) GaAs substrate. From a comparison between the flux intensity estimated from the mass of the elements and the beam pressure measured using a Bayard-Alpert (BA) ionization gauge, we obtained the sensitivity of the BA gauge in the following equation:

$$J_i(10^{15}\ \mathrm{cm}^{-2}\ \mathrm{s}^{-1}) = \chi P_i(10^{-6}\ \mathrm{Torr}), \tag{1}$$

where J_i is the flux intensity and P_i is the beam pressure measured by the BA gauge (i = Mg, Zn, S, Se). The inverse of the sensitivity (χ) of Mg, Zn, S, Se are estimated to be 1.8, 1.1, 0.7 and 0.5, respectively. Generally, BA gauge sensitivity is a function of the electron number/molecule [8]. The lower χ of an anion such as S and Se than that of a cation is explained by the effect of a cluster such as S_2 and Se_2.

3. Theory

In this paper we propose the following model:

(1) The net flux intensity is expressed by the product of the flux intensity from the effusion cell (J_i) and the maximum sticking coefficient (k_i). Generally, the sticking coefficient of cation (anion) increases with increasing flux intensity of anion (cation). We define the maximum sticking coefficient k_i as the limit of this sticking coefficient.

(2) The surface of the crystal is divided into a surface covered with group II elements (surface II) and a surface covered with group VI elements (surface VI) and the following equation applies:

$$\theta_2 + \theta_6 = 1. \tag{2}$$

Coverage of surface II (θ_2) and surface VI (θ_6) may correspond to the intensity of $c(2\times2)$ and (2×1), respectively. When the desorption is not large, the adatom density (n_i) is almost the same at surfaces II and VI because the adatom moves between surfaces II and VI [7].

(3) The incorporation of an adatom is proportional to n_i of group II (VI) elements and θ_6 (θ_2). Group II (VI) elements are incorporated on surface VI (II).

(4) The desorption of a cation such as Zn or Mg on surface II (VI) is proportional to n_i and θ_2 (θ_6). When the anion beam flux, which is a cluster beam, reaches the crystal surface, the adatoms may be dissolved to smaller clusters or atoms. The desorption of these adatoms on surface II (VI) is expressed by $D_{2i}n_i^{\gamma}\theta_2$ ($D_{6i}n_i^{\gamma}\theta_6$). The desorption rate on surface II D_{2i} is different from the desorption rate on surface VI D_{6i}.

(5) The desorption from the surface is expressed by $D_{s2}N_i\theta_2 + D_{s6}N_i\theta_6$ where $D_{s2}(D_{s6})$ is the desorption rate from surface II (surface VI), and N_i is the density of the atom sites. When the growth temperature is below 280°C, we observed that the reconstruction pattern of (2×1) ($c(2\times2)$) did not change to $c(2\times2)$ ((2×1)) during the time of 1 ML growth without beam irradiation. Thus, D_{s2} and D_{s6} is determined to be 0.

The following equations can be derived when these equations are applied to ZnMgSSe:

$$\mathrm{d}(n_i)/\mathrm{d}t = k_iJ_i - (D_{2i}\theta_2 + D_{6i}\theta_6)n_i^{\gamma} - p_in_i\theta_2 = 0 \quad (\mathrm{i} = \mathrm{S, Se}), \tag{3}$$

$$\mathrm{d}(n_i)/\mathrm{d}t = k_iJ_i - (D_{2i}\theta_2 + D_{6i}\theta_6)n_i - p_in_i\theta_6 = 0 \quad (\mathrm{i} = \mathrm{Mg, Zn}), \tag{4}$$

where D_{2i} and D_{6i} are the desorption rate of adatoms on surface II and surface VI, and p_i is the

incorporation rate of adatoms. In this paper, we use $\gamma = 2$ because we assume adatoms of S and Se dissolved at the surface desorb as clusters such as S_2 and Se_2 and because $\gamma = 1$ cannot explain the experimental results. Although S and Se (bulk) may desorb as another type of cluster such as S_2–S_8, Se_2–Se_8 at near RT, the species desorbed from the surface are assumed to be S_2 and Se_2 at 275°C. In steady state, the following equation applies:

$$N_i d\theta_6/dt = p_{Se}n_{Se}\theta_2 + p_S n_S \theta_2 - p_{Zn}n_{Zn}\theta_6 - p_{Mg}n_{Mg}\theta_6 = 0. \quad (5)$$

From these equations, the coverage θ_6 and the adatom density n_i can be calculated. We consider that both the group II element stabilized pattern $c(2\times 2)$ and the group VI element stabilized pattern (2×1) can be observed when the coverage is the same, $\theta_2 = \theta_6$. When θ_2 is nearly equal to 1, $c(2\times 2)$ is dominant. When θ_6 is nearly equal to 1, (2×1) is dominant. When both patterns are observed, the surface may be stoichiometric. The growth rate g ($cm^{-2}\,s^{-1}$) is expressed by the adatom incorporated, when the crystal is stoichiometric, as

$$g = p_{Zn}n_{Zn}\theta_6 + p_{Mg}n_{Mg}\theta_6 = p_{Se}n_{Se}\theta_2 + p_S n_S \theta_2. \quad (6)$$

The growth rate whose unit is μm/h is

$$G(\mu m/h) = g/6.26\times 10^{14}\times 2.83\times 10^{-4}\times 3600. \quad (7)$$

The mole fraction of Mg and that of S is expressed by the following equations:

$$x = p_{Mg}n_{Mg}/(p_{Mg}n_{Mg} + p_{Zn}n_{Zn}), \quad (8)$$

$$y = p_S n_S/(p_S n_S + p_{Se}n_{Se}) \quad (9)$$

4. Sticking coefficient of cracked S

To obtain the sticking coefficient, we fabricated ZnMgSSe under the same growth conditions except for the cracking temperature of the S cell, T_{crack}. The sticking coefficient was obtained from the growth rate, the composition and the beam flux intensity. When T_{crack} of the S cell is increased, the sticking coefficient of S decreased (Fig. 1). From Fig. 1, we see that the sticking coefficient of S is about 0.5 when the cracking temperature is 250°C. Although the sticking coefficient of S becomes higher at a higher group II flux intensity, the maximum sticking coefficient k_S is considered to be smaller than 1.

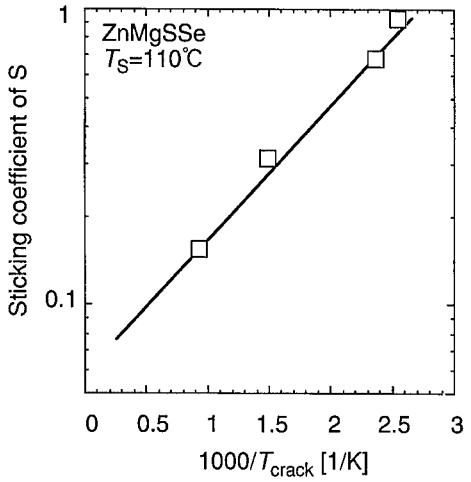

Fig. 1. Cracking temperature dependence of the sticking coefficient of S in ZnMgSSe.

In the first stage of the desorption of adatoms, the energy received from the cracking cell plays a crucial role. S clusters (S_k) are heated in the cracking zone at 250°C. At 800°C, the dominant species of S is S_2 from the analogy of ZnS [9], whose cell temperature is about 800°C, although the dominant species of S is S_2, S_3, S_4, S_5, S_6, S_8 when it is not cracked [9]. When dissolved S_k reaches the substrate, cracked S_k releases the excess energy, which increases the desorption rate and determines the maximum sticking coefficient. Thus, with increasing cracking temperature, the excess desorption caused by the excess energy increases and the sticking coefficient of S decreases. After S releases the excess energy, the desorption is determined by the same method as that of Se.

5. Determination of the growth parameters

The growth parameters in Eqs. (3) and (4) in Fig. 2 is determined in this section. First the maximum sticking coefficients k_i were determined. We

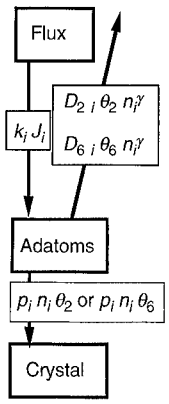

i	Zn	Mg	S	Se
k_i	1	1	0.65	1
$D_{2\,i}$	0.5	0.01	0	0
$D_{6\,i}$	0	0	0.4	0.15
γ	1	1	2	2
p_i	1	1	1	1

Fig. 2. Summary of the growth mechanism of ZnMgSSe. J_i is the flux intensity, k_i is the maximum sticking coefficient, D_{2i} is the desorption rate from surface II, D_{6i} is the desorption rate from surface VI, p_i is the adatom incorporation rate.

confirmed that the sticking coefficient of Zn (Se) is 1 when the flux intensity of Se (Zn) is about ten times larger than that of Zn (Se), as previously reported by Venkatasubramanian [7]. From this experiment and by analogy, k_{Zn}, k_{Se}, $k_{Mg} = 1$. Next, p_i (i: Zn, Mg, S, Se) were defined as 1. D_{6Zn}, D_{6Mg}, D_{2S} and D_{2Se} are considered to be zero because the growth temperature is low. This is further substantiated by the analogy between $D_{s2} = 0$ and $D_{s6} = 0$, because D_{6Zn} and D_{s2} are similar parameters because D_{s2} is the desorption of Zn and Mg on the second layer of S and Se and D_{6Zn} is the desorption of Zn on surface VI which is made from S and Se. Thus, to determine the other five parameters of Eqs. (3) and (4), about 15 samples of ZnSe, ZnSSe, ZnMgSe and ZnMgSSe were fabricated under various flux conditions and we applied the above theory to the experimental results of the growth rate G and the composition of Mg (x) and S (y), although we do not show the experimental data of ZnSe, ZnMgSe and ZnSSe. Figs. 3–5 show the comparison between the experimental x, y, G and the calculated ones of $Zn_{1-x}Mg_xS_ySe_{1-y}$. The experimental value of ZnMgSSe agrees with the value calculated using this theory and parameters D_{2Zn}, D_{2Mg}, D_{6S}, D_{6Se} and k_S. These parameters are shown in Fig. 2.

For group II elements, the composition and the growth rate can be explained because the desorption of Zn is larger than that of Mg. When the temperature is about 275°C, the vapor pressure of Zn is 1.2×10^{-3} Torr and that of Mg is $1\text{–}2 \times 10^{-5}$ Torr. When there is equilibrium, the desorption can be determined from the following equation:

$$P_e/(2\pi m k_B T)^{1/2} = n_e/\tau, \tag{10}$$

where P_e is the vapor pressure at equilibrium, k_B is Boltzman's constant, T and m are the substrate temperature and the mass of adatoms, n_e is the adatom density and τ is the time constant of the desorption. The ratio of the desorption rates D_{2Zn} and D_{2Mg} on surface II used in Eq. (4) is 50 : 1, which is almost the same as the ratio (50 : 1) obtained from Eq. (10). The reason is that Zn and Mg stick to surface II by the van del Waals force, which is the same force as the bond between the atoms of the elements. The relation between the desorption of S and Se ($D_{6S} > D_{6Se}$) is similar.

For group VI elements, it is important to consider the cluster. When clusters of group VI elements desorb on the surface, some atoms or some small clusters migrate, meeting to form larger clusters. Desorption of the anion is usually larger than the cation. It is curious that the desorption of Se ($D_{6Se}\,n_{Se}^{\gamma}$) is low although the vapor pressure of Se is very high. In our experimental results, both $c(2 \times 2)$ and (2×1) can be observed when ZnSe is grown and the ratio of the beam flux intensity of Zn to that of Se is 7 : 5. We assume that the desorption of Se becomes low when the adatom density is low and that the desorption of Se becomes large when the adatom density is very high.

6. Growth of ZnMgSSe

The samples of ZnMgSSe were grown under the growth conditions in which one flux intensity is varied and other three flux intensity are fixed. The value of the cracking temperature T_{crack} was 250°C. The surface reconstruction patterns were classified into A, where $c(2 \times 2)$ is dominant; B, where both $c(2 \times 2)$ and (2×1) is observed; and C, where (2×1) is dominant. Fig. 3 shows the Zn flux-intensity dependence of the composition, the surface pattern, and the growth rate. When C pattern is observed,

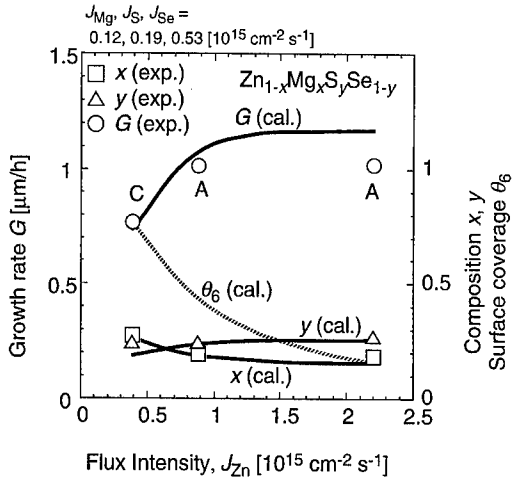

Fig. 3. Zn flux-intensity dependence of the composition of Mg (x), S (y), the surface coverage (θ_6) and the growth rate (G) of ZnMgSSe. The symbols show the experimental data (exp.) and the curves show the calculated value (cal.).

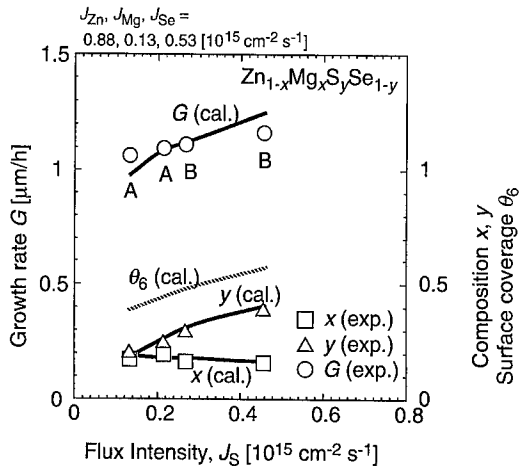

Fig. 4. S flux-intensity dependence of the composition of Mg (x), S (y), the surface coverage (θ_6) and the growth rate (G) of ZnMgSSe. The symbols show the experimental data (exp.) and the curves show the calculated value (cal.).

the mole fraction of Mg increases and that of S decreases and the growth rate decreases with decreasing Zn flux intensity. When A pattern is observed, the mole fraction of Mg and S and the growth rate remain almost constant with increasing Zn flux intensity. Fig. 4 shows the S flux-intensity dependence of the composition, the surface pattern, and the growth rate. When the S flux intensity increase, the surface reconstruction pattern changed from A to B. Under the growth condition in Fig. 4, the C pattern was not observed. The mole fraction of Mg decreases and that of S increases and the growth rate increases with increasing S flux intensity. Fig. 5 shows the Se flux-intensity dependence of the composition, the surface pattern, and the growth rate. When the Se flux intensity was increased, the surface reconstruction pattern changed from A to B. The mole fraction of Mg and S decreases and the growth rate increases with increasing Se flux intensity. When the flux intensity of Mg increases, the mole fraction of Mg and S increases, although this is not shown in the figure. From these results, the tendency of these properties when $c(2 \times 2)$ is observed are different from the tendency when (2×1) is observed.

The origin of the difference between the calculated value and the experimental value is con-

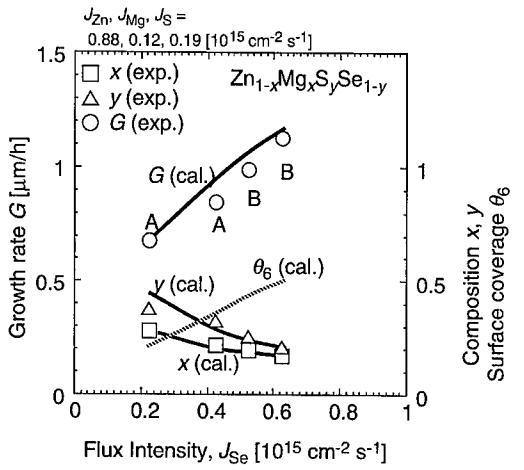

Fig. 5. Se flux-intensity dependence of the composition of Mg (x), S (y), the surface coverage (θ_6) and the growth rate (G) of ZnMgSSe. The symbols show the experimental data (exp.) and the curves show the calculated value (cal.).

sidered to be as follows. First, the relation between the flux intensity and the beam pressure is a difficult measurement because the mass of the flux is very small. Second, the desorption of Se is relatively large and that of S is relatively small if these adatoms of S and Se are desorbed as large clusters which include both S and Se. Third, the unevenness of the crystal surface and the free energy balance

may affect the growth. Fourth, the desorption from the surface may not be disregarded.

7. Conclusions

The basic model of MBE growth of ZnMgSSe at 275°C is considered. The composition and the growth rate of ZnMgSSe were measured. They are explained by a theory which assumes that the desorption rate of adatoms on surface II is different from that on surface VI and the effect of clusters is taken into consideration. The experimental composition, growth rate of ZnMgSSe agrees with the value calculated using this theory and the tendency of these properties when $c(2\times 2)$ is observed are different from the tendency when (2×1) is observed.

Acknowledgements

We would like to thank A. Hino, S. Kijima, M. Shiraishi, S. Taniguchi, S. Itoh, K. Nakano, Professor K. Akimoto, Dr. K. Kawai, Dr. J. Seto and Dr. T. Yamada for their encouragement during this work.

References

[1] S. Taniguchi, T. Hino, S. Itoh, N. Nakayama, A. Ishibashi and M. Ikeda, Electron. Lett. 32 (1995) 552.
[2] T. Shitara, E. Kondo and T. Nishinaga, J. Crystal Growth 99 (1990) 530.
[3] T. Nishinaga, J. Crystal Growth 146 (1995) 326.
[4] J.H. Neave, P.J. Dobson, B.A. Joyce and Jing Zhang, Appl. Phys. Lett. 47 (1985) 100.
[5] Z. Zhu, T. Nomura, M. Miyao and M. Hagino, J. Crystal Growth 96 (1989) 513.
[6] Z. Zhu, M. Hagino, K. Uesugi, S. Kamiyama, M. Fujimoto and T. Yao, Jpn. J. Appl. Phys. 28 (1989) 1659.
[7] R. Venkatasubramanian, N. Otsuka, J. Qiu, L.A. Kolodziejski and R.L. Gunshor, J. Crystal Growth 95 (1989) 533.
[8] T.A. Flaim and P.D. Ownby, J. Vac. Sci. Technol. 8 (1971) 661.
[9] J. Berkowitz and J.R. Marquart, J. Chem. Phys. 39 (1963) 275.

ELSEVIER

Journal of Crystal Growth 175/176 (1997) 593–597

JOURNAL OF CRYSTAL GROWTH

Hydrogen sulfide treatment of GaAs substrate and its effects on initial stage of ZnSe growth

Jun Suda*, Ryuji Tokutome, Yoichi Kawakami, Shizuo Fujita, Shigeo Fujita

Department of Electronic Science and Engineering, Kyoto University, Kyoto 606-01, Japan

Abstract

Hydrogen sulfide (H_2S) treatment of GaAs substrates was examined by means of in situ reflection high energy electron diffraction (RHEED) and ex situ atomic force microscope (AFM) observations. Its effects on initial stage of molecular beam epitaxy (MBE) of ZnSe were also investigated. According to the H_2S treatment conditions, an atomically flat surface with (4×3) reconstruction or a faceted surface with (2×6) reconstruction was obtained. Clear RHEED intensity oscillations over 40 cycles were observed just after starting the growth on the (4×3) surface, showing two-dimensional (2D) nucleation, i.e., layer-by-layer growth of ZnSe. Etch pit density (EPD) of the epilayer was about 2.5×10^6 cm^{-2}, which was much lower than that obtained by the ever applied ammonium-sulfide ($(NH_4)_2S_x$) treatment.

PACS: 81.60.Cp; 68.55.Bd; 68.55.Jk

Keywords: ZnSe; MBE; GaAs; Sulfur treatment

1. Introduction

Since it has been revealed that rapid degradation of ZnSe-based laser diodes is due to pre-existing stacking faults seeded at ZnSe/GaAs heterointerface, intensive studies have been done for reduction of the defects [1, 2]. Now it is commonly understood that the control of GaAs substrate surface and initial stage of growth of ZnSe is essentially important for high quality ZnSe/GaAs heteroepitaxy.

So far, thermal cleaning of GaAs substrate in a II–VI growth chamber without arsenic over pressure has generally been employed, but high vapor pressure of arsenic makes it difficult to control the surface stoichiometry. The surface usually became Ga-rich, which obstructed two-dimensional (2D) nucleation of ZnSe and resulted in high density (10^8–10^9 cm^{-2}) of the stacking faults.

As one of the solutions, a two chamber system is used to grow a GaAs epitaxial buffer layer and to control the surface stoichiometry precisely. Recently, it was reported that (2×4) As-stabilized GaAs surface followed by pre-irradiation of Zn brought 2D nucleation of ZnSe and very high

* Corresponding author. Fax: + 81 75 753 5898; e-mail: suda@kuee.kyoto-u.ac.jp.

0022-0248/97/$17.00 Copyright © 1997 Elsevier Science B.V. All rights reserved
PII S0022-0248(96)00997-9

quality ZnSe epilayers with the stacking fault density of 10^4 cm^{-2} [3, 4].

As other approaches, surface treatment techniques such as ammonium sulfide ($(NH_4)_2S_x$) treatment [5] and hydrogen plasma cleaning [6] have been proposed. These techniques, if they contribute to high quality ZnSe, are more handy and convenient, and will be applicable to regrowth of II–VI on patterned III–V layers for future novel opto-electronic integrated devices (OEIDs).

The $(NH_4)_2S_x$ treatment was shown to be effective for the improvement of photoluminescence (PL) spectra and full width at half maximum (FWHM) of X-ray rocking curves (XRCs) of ZnSe epilayers, but the fabricated laser devices degraded very rapidly. It was found that etch pit density (EPD) was still higher than 10^8 cm^{-2}, which can be attributed to the following: (i) The (2×1) surface obtained by the $(NH_4)_2S_x$ treatment is due to complete coverage of S on Ga, which can generate a lot of defects as has been observed for pre-irradiation of Se on Ga surface [3, 4]. (ii) The $(NH_4)_2S_x$ treatment results in rough GaAs surface due to etching effect [7], which is unfavorable for uniform nucleation at the initial stage of growth.

In this paper, we propose new in situ sulfur treatment technique by using hydrogen sulfide (H_2S). Its effects on initial stage of molecular beam epitaxy (MBE) of ZnSe and defect density of the epilayer are discussed.

2. Experimental procedure

Substrates used in the experiments were Zn-doped p^+-GaAs (0 0 1) just oriented wafers whose EPD was about 2×10^3 cm^{-2}. The substrates were prepared by the standard cleaning and etching procedures. Then, they were mounted onto a molybdenum holder by indium welding, and loaded into the exchange chamber immediately.

The main chamber is pumped by a diffusion pump with liquid nitrogen trap. It is equipped with Zn and Se Knudsen-cells, a H_2S gas-cell and a reflection high energy electron diffraction (RHEED) system. The background pressure is lower than 1×10^{-9} Torr after chamber baking.

The H_2S treatment was done under the H_2S environment pressure of 5×10^{-8} Torr. H_2S was supplied through the gas-cell without pre-cracking. It should be noted that due to high vapor pressure of H_2S, the H_2S partial pressure could not be reduced to lower than 5×10^{-9} Torr even after turning off the supply.

The treated substrate surface was characterized by in situ RHEED and ex situ atomic force microscope (AFM) observations. In order for the AFM observation, the substrate heater was switched off when desirable surface was obtained, then after cooling down to 300°C the sample was transferred to the exchanging chamber and measured by the AFM system in the air as soon as possible. It is thought that the surface morphology is basically unchanged during the cooling down and in the air.

Initial stage of MBE growth of ZnSe was evaluated by means of RHEED observations. ZnS_xSe_{1-x}/ZnSe heterostructures were grown on the H_2S treated GaAs substrates by gas-source MBE to evaluate quality of epilayers. Source materials were elemental Zn (6N) and Se (6N), and gaseous H_2S (4N). H_2S was pre-cracked by the gas-cell at 950°C. There was 20 min growth interruption between ZnSe and ZnSSe layers to increase the gas-cell temperature. During the interruptions, the growth surface stabilized by Se. The defect density was evaluated by EPD measurements using 0.24 vol% bromine-methanol at 0°C for 20 s [8, 9].

3. Results and discussion

3.1. H_2S treatment of GaAs substrate

Variations of in situ RHEED patterns and ex situ AFM images with the increase of substrate temperature under H_2S environment are shown in Figs. 1 and 2, respectively. Below 500°C, a halo pattern originated from the surface oxide layer was observed. Then, faint streaks began to appear with increasing substrate temperature. At about 590°C, the intensity of RHEED greatly increased and an arrow head-like spotty pattern appeared as shown in Fig. 1a. The surface oxide seems to begin to be

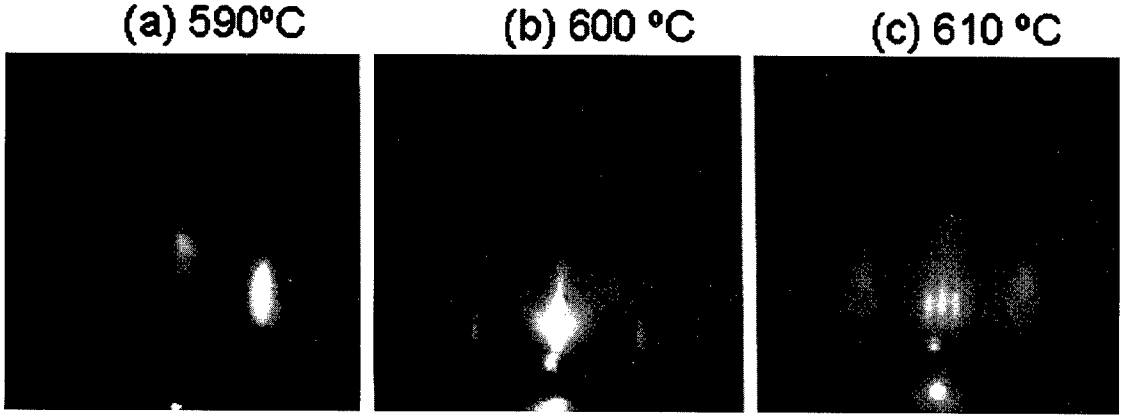

Fig. 1. Evolution of in situ RHEED patterns for [1 $\bar{1}$ 0] direction with increase of substrate temperature in H_2S environment. (a) Arrow head-like spotty pattern, (b) sharp streaks with (4 × 3) reconstruction and Laue zone reflection, and (c) arrow head-like streaks with (4 × 6) reconstruction.

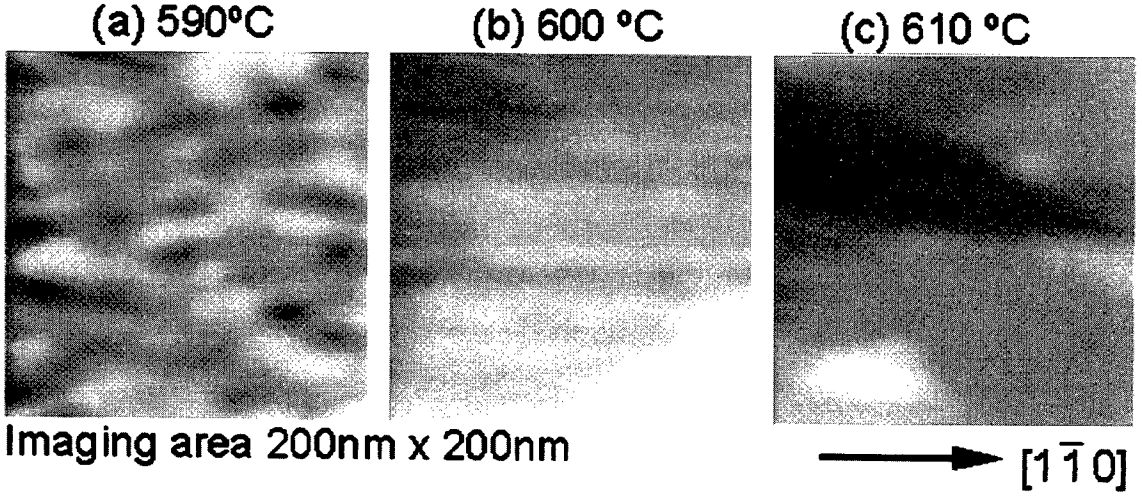

Fig. 2. Ex situ AFM images observed in the air for the GaAs surface corresponding to (a)–(c) in Fig. 1. (a) Wavy surface, (b) atomically flat surface with monolayer height steps, and (c) faceted surface with Ga-droplets.

desorbed at this temperature. The AFM images for this surface is shown in Fig. 2a. Wavy surface was observed due to partial oxide desorption.

After 10–20 s, the RHEED pattern changed into sharp streaks with (4 × 3) reconstruction as shown in Fig. 1b. Laue zone reflections were also clearly observed for [1 $\bar{1}$ 0] directions. Fig. 2b shows the AFM image for this surface. The surface was atomically flat with monolayer height (~3 Å) steps. Observation of Laue zone reflections may be due to such a high flatness. Obtaining such a flat surface only by annealing the GaAs substrate in H_2S environment is the new finding and will be useful not only for growth applications but also for other applications. The (4 × 3) reconstruction was known for GaAs thermally annealed with selenium irradiation [10–12], and was attributed to partially Se-adsorbed Ga-stabilized surface. The (4 × 3) reconstruction observed in our experiment may be the same kind of structure except for replacing Se

with S. As reported by previous works, the surface partially adsorbed by group VI elements can achieve charge neutrality at heterointerface [13]. In addition to that, high flatness of GaAs surface is also favorable for high quality ZnSe/GaAs heterointerface.

If the substrate temperature is further increased to 610°C, the RHEED pattern changed into arrow head-like streaks as shown in Fig. 1c. Although surface reconstruction seems to depend on H_2S pressure, (4×6)-like reconstruction which was assigned to Ga-stabilized surface was generally observed. If the substrate was cooled down to 300°C, the surface reconstruction changed into (2×6) [14]. This surface is thought to be really energetically stable S-terminated surface proposed by Tsukamoto and Koguchi [7]. Fig. 2c shows the AFM image for this surface. The surface was faceting, i.e., composed of small atomically flat domains with different height (~ 15 Å). Some protrusions (~ 40 Å height, shown as bright spots in the image) were also observed. Taking into account of the treatment temperature, 610°C, they seem to be Ga-droplets. For ZnSe heteroepitaxy, existence of Ga-droplets will affect quality of epilayers, because formation of Ga_xSe_y compound at the interface and/or Ga-diffusion to the epilayer are expected.

3.2. Growth of ZnSe

Fig. 3 shows RHEED specular spot intensity just after starting the MBE growth of ZnSe on the (4×3) or (2×6) GaAs surface prepared by the H_2S treatment. Before starting the growth, Zn flux was preirradiated for 10 s. Very clear intensity oscillations over 40 cycles were observed for the growth on (4×3) surface, showing 2D nucleation, i.e., layer-by-layer growth of ZnSe. To the best of our knowledge, this is the first observation of 2D initial growth of ZnSe directly onto GaAs substrates. In spite of clear RHEED intensity oscillations, RHEED patterns changed into rather diffuse streaks after starting the growth. It takes 10–20 s before the pattern changed into clear and sharp streaks.

Although RHEED oscillations over 40 cycles were observed for the growth directly onto GaAs substrates, only 15 cycle oscillations were observed for that onto ZnSe buffer layer stabilized by Zn or Se. It differs from the case of GaAs homoepitaxy.

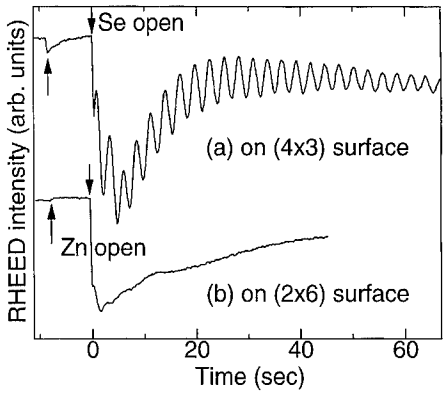

Fig. 3. Intensity oscillations of RHEED specular spot for just after starting growth of ZnSe on H_2S treated GaAs surfaces. (a) Clear intensity oscillation is observed for (4×3) surface and (b) no oscillation is observed for (2×6) surface.

Stabilization of GaAs surface by arsenic flux makes the surface flat, and clear RHEED intensity oscillations can be observed repeatedly by the stabilization.

On the other hand, no oscillations was observed for the growth on the (2×6) surface. The (2×6) surface is basically the same as (2×1) S-terminated surface except for existing one-missing dimer per six S-dimer cites [7]. In addition to the unfavorable nature of the (2×6) surface such as faceting and existing Ga-droplets, the surface stoichiometry similar to the (2×1) surface would be against 2D nucleation.

To evaluate defect density of ZnSe epilayer on the (4×3) surface, EPD measurements were done. The samples were $ZnS_{0.07}Se_{0.93}$ (2500–5000 Å)/ZnSe (300 Å) heterostructures. XRC of the structure was well fitted by the theoretical calculation. In other words, FWHM of ZnSSe is close to the theoretical value and many fringes due to interference in the structure were clearly observed. 4.2 K PL spectrum was dominated by free exciton emission and donor bound exciton emission. No deep-level emissions were observed. Fig. 4 shows a typical Nomarski micrograph of the etch pits. The EPD was about 2.5×10^6 cm^2, lower by two orders in magnitude compared to the $(NH_4)_2S_x$treatment. The reduction may be brought by 2D nucleation of ZnSe at the initial stage of growth due to the H_2S treatment of GaAs substrate. Further efforts by optimizing the growth sequence and/or the H_2S

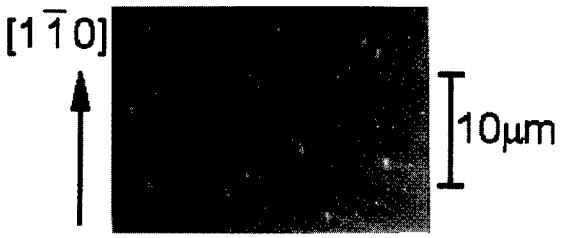

Fig. 4. Nomarski micrograph of ZnSSe surface etched by 0.24 vol% bromine–methanol solution at 0°C for 20 s. ZnSSe epilayer with ZnSe buffer layer is grown on (4 × 3) H_2S treated surface with pre-irradiation of Zn.

treatment conditions will lead to more reduction of the defects. It is necessary to determine the type of the defects in the layers by transmission electron microscope (TEM).

4. Conclusions

Atomically flat GaAs surface with (4 × 3) reconstruction was obtained by the H_2S treatment. Very clear RHEED intensity oscillations over 40 cycles were observed for the initial stage of growth of ZnSe on the (4 × 3) surface, showing 2D nucleation of ZnSe. EPD of the epilayer was about $2.5 \times 10^6\ cm^{-2}$, which was much lower than that obtained by the $(NH_4)_2S_x$ treament. Further optimization of growth and/or treatment conditions will bring lower EPD.

Acknowledgements

One of the authors (J.S.) is supported by Research Fellowships of the Japan Society for the Promotion of Science for Young Scientists. This work was partly supported by Grant in Aid for Scientific Research from the Ministry of Education, Science, Sports and Culture of Japan and also by the Hōsō Bunka Foundation (HBF).

References

[1] S. Guha, J.M. DePuydt, M.A. Haase, J. Qiu and H. Cheng, Appl. Phys. Lett. 63 (1993) 3107.
[2] G.C. Hua, N. Otsuka, D.C. Grillo, Y. Fan, J. Han, M.D. Ringle, R.L. Gunshor, M. Hovinen and A.V. Nurmikko, Appl. Phys. Lett. 65 (1994) 1331.
[3] L.H. Kuo, L. Salamanca-Riba, B.J. Wu, G. Hofler, J.M. DePuydt and H. Cheng, Appl. Phys. Lett. 67 (1995) 3298.
[4] L.H. Kuo, K. Kimura, T. Yasuda, S. Miwa, C.G. Jin, K. Tanaka and T. Yao, Appl. Phys. Lett. 68 (1996) 2413.
[5] Y.-H. Wu, T. Toyoda, Y. Kawakami, Sz. Fujita and Sg. Fujita, Jpn. J. Appl. Phys. 29 (1990) L144.
[6] C.M. Rouleau and R.M. Park, J. Vac. Sci. Technol. A 11 (1993) 1792.
[7] S. Tsukamoto and N. Koguchi, Appl. Phys. Lett. 65 (1994) 2199.
[8] A. Kamata and H. Mitsuhashi, J. Crytal Growth 142 (1994) 31.
[9] M. Shiraishi, S. Tomiya, S. Taniguchi, K. Nakano, A. Ishibashi and M. Ikeda, Phys. Status Solidi (a) 152 (1995) 377.
[10] N. Kobayashi, Jpn. J. Appl. Phys. 27 (1988) L1597.
[11] J. Qiu, Q.-D. Qian, R.L. Gunshor, M. Kobayashi, D.R. Menke, D. Li and N. Otsuka, Appl. Phys. Lett. 56 (1990) 1272.
[12] S. Takatani, T. Kikawa and M. Nakazawa, Phys. Rev. B 45 (1992) 8494.
[13] H.H. Farrell, M.C. Tamargo and J.L. de Miguel, Appl. Phys. Lett. 58 (1991) 355.
[14] J. Suda, Y. Kawakami, Sz. Fujita and Sg. Fujita, Jpn. J. Appl. Phys. 35 (1996) L1498.

ELSEVIER

Journal of Crystal Growth 175/176 (1997) 598–602

JOURNAL OF CRYSTAL GROWTH

Homogeneous and δ-doped ZnS:Mn grown by MBE

S. Schön*, M. Chaichimansour, W. Park, T. Yang, B.K. Wagner, C.J. Summers

Phosphor Technology Center of Excellence, Manufacturing Research Center, Georgia Institute of Technology, Atlanta, Georgia 30332-0560 USA

Abstract

An investigation is reported on the growth of homogeneously and δ-doped ZnS:Mn layers. Both undoped and Mn-doped ZnS thin films were grown by MBE and GSMBE using a sulfur overpressure. Photoluminescence measurements on undoped material indicated that high crystal quality was obtained, with band edge emission intensity several orders of magnitude higher than that from the self-activation peak, for a growth temperature of 180°C. Homogeneously doped ZnS:Mn films showed a maximum brightness at a Mn concentration of 3 mol% Mn before luminescence quenching was observed. The δ-doping technique was shown to quadruple the photoluminescence intensity compared to equivalently doped homogeneous material grown under the same conditions. The optimum distance between doping planes for a constant in-plane concentration was found to be 9–15 nm. SIMS studies of the diffusion behavior of Mn into the undoped ZnS layers revealed broad Mn peaks with a FWHM of about 10 nm.

1. Introduction

The wide bandgap compound semiconductor ZnS has many applications in optoelectronic devices. Manganese doped ZnS is used to fabricate AC- and DC-based electroluminescent flat panel display devices. The luminescence intensity strongly depends on the crystallinity, the nature of the luminescence center, its coordination in the crystal lattice and its concentration. Like most of the luminescent materials ZnS:Mn shows a reduction in the photoluminescent efficiency of Mn^{2+} ions as their concentration is increased beyond a critical value of approximately 1–2 mol% [1]. This concentration quenching is explained by the migration of the excitation among the centers and finally to a non-radiative or to a red or infrared emitting center. It is assumed that an excited Mn center can transfer energy to an unexcited one through a resonant non-radiative transfer process much faster than to a trap in form of a red, infrared or non-radiative center. The energy loss to a trap depends on the probability of finding a trap near the path of excitation. On one hand, it is suggested that this energy loss can depend on the growth technique by decreasing the concentration of defects [2]. On the other hand, the probability of finding a trap can be lowered by reducing the three-dimensional Mn coupling to a two-dimensional one by concentrating

*Corresponding author. Fax: +1 404 894 5073; e-mail: silke@bismarck.gtri.gatech.edu.

0022-0248/97/$17.00 Copyright © 1997 Elsevier Science B.V. All rights reserved
PII S0022-0248(96)00998-0

the Mn atoms in separate atomic layers (δ-doping) [3, 4].

In this paper we report the development of MBE coupled with or without a gas sulfur source to improve crystal quality, and the exploitation of the δ-doping technique to both change the coordination and coupling characteristics of Mn in the ZnS lattice. δ-doping is expected to confine the excitation energy transfer within separate two-dimensional planes and therefore suppress the three-dimensional coupling between Mn ions and non-radiative defects which cause luminescence quenching.

2. Experimental procedure

The ZnS:Mn films were grown by molecular beam epitaxy (MBE) on GaAs (1 0 0), glass/ITO and glass/ITO/dielectric stacks using a solid ZnS source. The gas sulfur precursor, t-butyl mercaptan $(C_4H_9)SH$ (t-BuSH) was precracked to $(CH_3)_3C$ (t-butyl) and SH at 700°C and used to provide an excess sulfur flux for some of the undoped and homogeneously doped films [5]. Substrate temperatures varied between 174°C and 250°C. Homogeneous doping was carried out for a range of Mn/ZnS flux ratios using a Mn solid source. δ-doping was achieved by depositing only Mn for a time period of 50 s periodically during the thin film growth. A Mn coverage of one atomic layer is expected. All δ-doped runs were performed using a constant Mn flux.

The doping concentration was determined by secondary ion mass spectroscopy (SIMS) using oxygen with a beam energy of 15 keV and a current of 50 nA at normal incidence. The sputter rate was 20 nm/min for the homogeneously doped samples and was reduced to 1.3 nm/min for the δ-doped samples. The ion concentration was analyzed every 5 s with a quadrupole analyzer. Different target voltages were applied to overcome charging problems for films grown on GaAs substrates. An electron beam was used for neutralizing the films grown on glass substrates. A homogeneously doped ZnS:Mn film with a Mn concentration of 0.5 wt% determined by RBS was used as a reference.

Photoluminescence measurements were carried out at both room temperature and 10 K using the 275 nm (4.51 eV) line from an argon ion laser. The PL signal was dispersed by a 1000M Spex monochromator and detected with a photomultiplier tube using the photon counting mode.

3. Results and discussion

Undoped ZnS thin films were studied by PL measurements to obtain optimum growth conditions. The ratio of the band edge (BE) emission peak to the self-activation (SA) peak was used to determine the crystal quality. Best results were achieved using a substrate temperature of 180°C. Fig. 1 shows the PL spectrum at 10 K of a 2.8 μm thick ZnS layer grown on GaAs (1 0 0). The intensity of the band edge emission peak is several orders of magnitude higher than the intensity of the self-activation peak indicating very high crystal quality. In contrast to previous studies this spectrum showed only a single, dominant defect [6]. The application of the sulfur precursor t-BuSH during growth lead to an improvement in the crystal quality by decreasing the number of sulfur vacancies but also reduced the growth rate. The optimum flux was found to be 0.25 sccm for a N_2 calibrated flow controller. A higher flux lead to an increased SA peak intensity. This was attributed to the HS on the

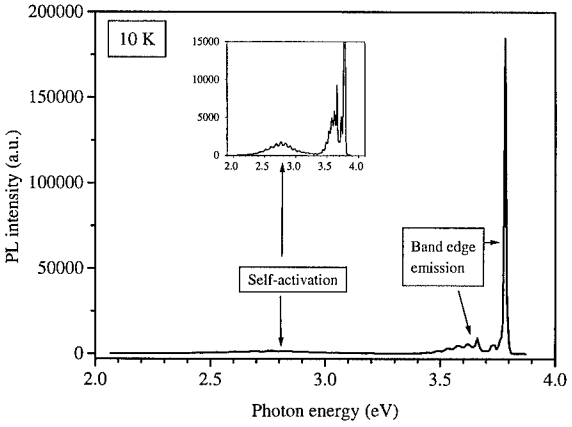

Fig. 1. Photoluminescence spectrum at 10 K of an undoped ZnS film grown on GaAs (1 0 0).

growth surface leading to a slight increase in the defect concentration. The application of precursors providing monomer sulfur to the growth surface is expected to have a greater influence. For the undoped ZnS films the application of t-BuSH lead to a small, but significant change in the PL intensity.

Similar to the results obtained on undoped ZnS films, investigations of homogeneously doped material revealed that the defect concentration in the crystalline film had an strong influence on the PL efficiency. The use of substrate temperatures higher than 180°C produced more defects as indicated by an increase in the SA peak intensity and a lower PL efficiency due to luminescence quenching. Fig. 2 shows the dependence of the PL intensity on the flux ratio Mn/ZnS for ZnS:Mn single crystal films grown on GaAs (1 0 0) at a substrate temperature of 180°C. Maximum luminescence was obtained at a Mn/ZnS flux ratio of 1.2% which corresponded to a Mn concentration of about 3 mol% and was higher than the observed 1–2 mol% reported by Thomas et al. [1]. ZnS:Mn films grown on glass substrates were polycrystalline with a strong ⟨1 1 1⟩ texture. They always showed brighter photoluminescence than the comparable films grown on GaAs (1 0 0) substrates due to multiple light reflections at the interface film/glass.

All δ-doped ZnS:Mn films were grown at a substrate temperature of 180°C with the same thickness of $d = 0.3$ μm to exclude differences in the PL intensity due to absorption effects. For a constant in-plane doping concentration the distance between planes was varied from 7 to 33 nm determined by dividing the film thickness by the number of doping planes. The total amount of Mn in the film was given by the product of the number of planes and the in-plane Mn concentration. Fig. 3 shows the normalized PL intensity that was obtained by dividing the total PL intensity by the number of δ-doped layers. The best luminescence was obtained for planes which were more than 30 nm apart. A decrease in PL intensity was observed for spacings less than 20 nm indicating the onset of three-dimensional coupling and luminescence quenching. The total PL intensity reached a maximum at a doping plane spacing of about 12 nm despite the fact that the concentration of Mn in the film was higher at lower spacings due to the higher number of doping planes. According to both curves the window for optimum δ-spacing was between 9 and 15 nm for the in-plane Mn concentration investigated.

The appearance of luminescence quenching due to three-dimensional coupling between the Mn^{2+} ions at distances less than 12 nm raises the question about the diffusion behavior of Mn in ZnS. Fig. 4 shows the SIMS depth profiles of two delta-doped ZnS:Mn films with a distance of 33 nm (9 layers) and 14 nm (24 layers) between the doping planes. In the film doped with 9 layers the peaks are clearly

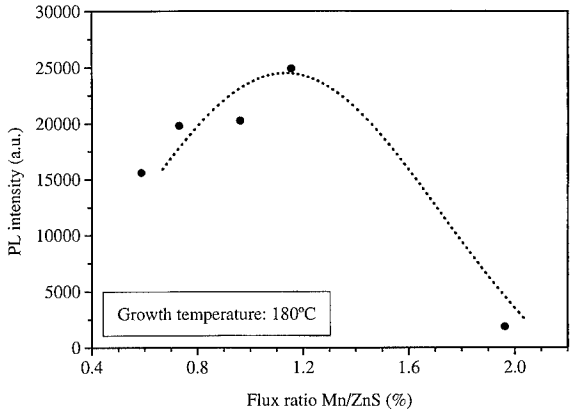

Fig. 2. Photoluminescence intensity of the yellow emission peak at 2.1 eV as a function of Mn/ZnS flux ratio for homogeneously doped ZnS:Mn grown on GaAs (1 0 0).

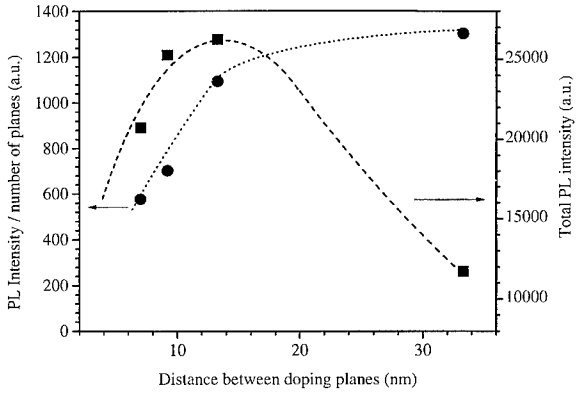

Fig. 3. Photoluminescence intensity of the delta-doped samples as a function of distance between doping planes (square – total PL intensity, circle – normalized PL intensity).

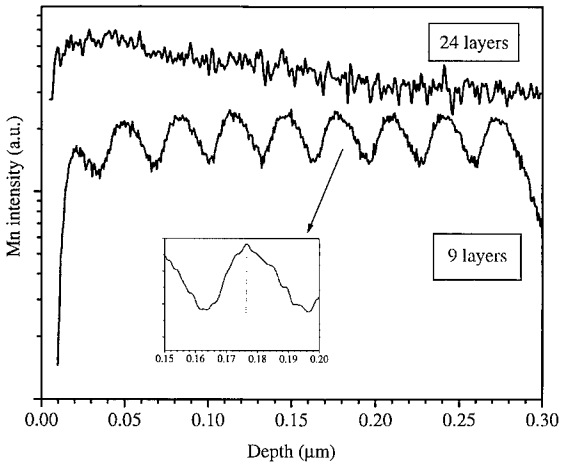

Fig. 4. SIMS depth profile for films with 9 and 24 layers of Mn.

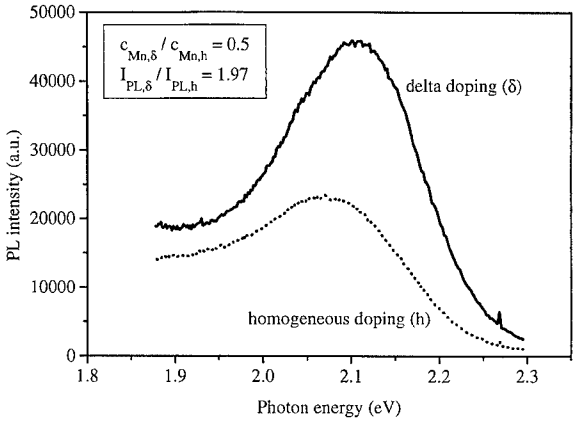

Fig. 5. Photoluminescence spectra at 300 K for homogeneously and δ-doped ZnS:Mn grown under the same conditions.

separated from each other in the SIMS depth profile. The broadness of the peaks indicates a diffusion into the undoped ZnS region. However, the influence of SIMS in terms of beam enhanced diffusion and the formation of manganese oxide MnO cannot be neglected. Studies indicated that the use of different primary beam incidence angles and lower energies did not offset the leading edge but did significantly affect the trailing edge of the Mn peaks. Thus, it was assumed that the asymmetry in the peak shape was an artifact of the SIMS method. Measurements with a xenon primary beam yielded asymmetric but narrower peaks. The full width of the half maximum of the Mn peaks was about 10 nm. A detailed report of these investigations will be given elsewhere [7]. For the ZnS:Mn film with a 14 nm distance between the doping planes the Mn peaks were superposed and could not be separated. Although the fact that the influence of beam enhanced diffusion and the formation of MnO has to be taken into consideration a remarkable amount of the Mn diffused into the undoped ZnS forming a homogeneous doped area which enabled three-dimensional coupling between the Mn ions and to red, infrared or non-radiative centers. The more closely spaced doping planes give higher doping. Luminescence quenching appears at a certain Mn concentration in this region causing a decrease in PL intensity even though a higher concentration of Mn ions was incorporated into the film due to the higher number of planes (see Fig. 3). It seems that a distance of about 10 nm between the doping planes was large enough to avoid three-dimensional coupling between the Mn ions and significant luminescence quenching.

In Fig. 5, the PL spectrum of a homogeneously doped ZnS:Mn film measured at room temperature is compared with that of a δ-doped sample grown at the same substrate temperature and flux ratio. The doping planes were 9 nm apart. Despite the fact that the δ-doped film had only half of the number of Mn ions, in comparison to the homogeneously doped film, the PL intensity was doubled. This clearly proves that the luminescence properties can be improved by the use of δ-doping technique.

4. Summary

It has been shown that both the improvement in the crystal quality and the application of the δ-doping technique leads to a significant increase in photoluminescence efficiency. Undoped ZnS films grown at very low substrate temperatures showed high crystal quality as reflected by the intensity of the band edge emission peak being several orders of magnitude higher than that of the self-activation

peak. A homogeneous Mn doping concentration of 3 mol% gave the highest photoluminescence intensity. Nevertheless, a quadrupling in brightness could be achieved by δ-doping, suggesting that this technique suppresses the photoluminescence quenching caused by three-dimensional coupling between the Mn ions.

Acknowledgements

The authors wish to thank Professor E.W. Thomas for his support of this work and for many helpful discussions. This work was supported by the German Academic Exchange Service (DAAD) and the Phosphor Technology center of Excellence PTCOE funded by Defense Advanced Research Projects Agency (DARPA) Contract No. MDA972-93-1-0030.

References

[1] C.B. Thomas, D. Sands, K.M. Brunson and H.S. Reehal, J. Elctrochem. Soc. 136 (1989) 1235.
[2] M. Katiyar and H. Kitai, J. Lumin. 4046 (1990) 227.
[3] A. Hunter and A.H. Kitai, J. Appl. Phys. 62 (1987) 4244.
[4] W. Tong, T.K. Tran, W. Park, S. Schön, B.K. Wagner and C.J. Summers, Proc. 1st Int. Conf. on the Science and Technology of Display Phosphors, San Diego, USA (1995), to be published.
[5] W. Tong, B.K. Wagner, T.K. Tran, W. Ogle, W. Park and C.J. Summers, J. Crystal Growth 164 (1996) 202.
[6] C.J. Summers, W. Tong, T.K. Tran, W. Ogle, W. Park and B.K. Wagner, J. Crystal Growth 159 (1996) 64.
[7] To be published.

ELSEVIER

Journal of Crystal Growth 175/176 (1997) 603–607

JOURNAL OF CRYSTAL GROWTH

Electrical characterization of engineered ZnSe–GaAs heterojunction diodes

Michele Lazzeri[a,*], Vittorio Pellegrini[a], Fabio Beltram[a,1], Marco Lazzarino[b,c], Jens J. Paggel[b,c,2], Lucia Sorba[b,c,3], Silvia Rubini[b,c], Alberta Bonanni[b,c], Alfonso Franciosi[b,c,4]

[a] *Scuola Normale Superiore and Istituto Nazionale per la Fisica della Materia, I-56126 Pisa, Italy*
[b] *Laboratorio Nazionale TASC-INFM, Area di Ricerca, I-34012 Trieste, Italy*
[c] *Department of Chemical Engineering and Materials Science, University of Minnesota, Minneapolis, Minnesota 55455, USA*

Abstract

Electrical characterization of ZnSe/GaAs n–p heterodiodes grown by molecular beam epitaxy under different Zn/Se flux ratios is reported. Large tunability of the band discontinuity at the heterojunction is shown by photocurrent measurements at low temperature with conduction-band offsets in the range 0.26–0.75 eV. Achievement of device-grade heterostructures with engineered offsets is shown under appropriate growth conditions.

PACS: 73.40. – c; 73.40.Lq; 79.60.Jv

Keywords: Diodes; Heterojuctions

1. Introduction

One of the most important tools of band-gap engineering is the tuning of energy-band discontinuities at heterojunctions. Several authors [1–4] attempted to achieve such tuning through the controlled introduction of impurities in the junction region.These efforts, however, have had limited impact on device applications. This is mostly because few results have been verified for heterojunctions incorporated in functional devices, and because the impurities used to change the local interface electrostatics [2] are poorly suited to device applications, since they are known to give rise to reliability problems (alkali metals), or deep levels (noble metals). Recently, however, owing to the growth of high-quality heterovalent heterostructures for optoelectronic applications, new avenues to achieve such tunability have become available

* Corresponding author.

[1] Also with Laboratorio Nazionale TASC-INFM, I-34012 Trieste, Italy.

[2] Present address: Philipps-Universität-Marburg, Fachbereich Physik, Renthof 6, D-35032 Marburg, Germany.

[3] Also with Instituto ICMAT del CNR, Monterotondo, I-00016 Rome, Italy.

[4] Also with Dipartimento di Fisica, Università di Trieste, I-34127 Trieste, Italy.

0022-0248/97/$17.00 Copyright © 1997 Elsevier Science B.V. All rights reserved
PII S0022-0248(96)00987-6

[5–8]. In heterovalent heterojunctions with polar orientation the band alignment should depend on the detail of the local atomic configuration achieved at the interface during growth [5–8]. Offset changes are therefore possible even in the absence of foreign impurities, provided that the growth kinetics can be exploited to obtain different interface configurations. A few applications of this technique have been recently demonstrated in heterojunctions – including ZnSe/GaAs – fabricated with heterovalent overlayers thin enough (2–3 nm) for the offset to be probed by photoemission spectroscopy [7, 8].

In this article, we report on the tunability of ZnSe/GaAs(0 0 1) heterovalent heterojunctions, which are essential elements of all recently demonstrated II–VI based solid-state blue–green lasers [9], in fully functional heterojunction diodes. We analyzed the current–voltage (I–V) and photo I–V characteristics of two sets of n-ZnSe/p-GaAs diodes fabricated by molecular beam epitaxy (MBE) with different interface compositions. Our results allowed us to determine the band discontinuity and the applicability of this technique to the fabrication of complete devices.

2. Experimental procedure

Samples were grown by solid-source MBE in a system that includes interconnected chambers for the growth of III–V and II–VI materials. We used GaAs(0 0 1) wafers, on which ZnSe layers were grown with a Zn/Se beam pressure ratio (BPR) of 0.1, 1, or 10. We employed two different growth methods to modify the local interface composition. In the first method, the whole II–VI overlayer was grown in Se-rich or Zn-rich conditions. Alternatively, the Se-rich or Zn-rich growth conditions were limited to a 2 nm-thick composition-control interface layer (CIL), the rest of the II–VI overlayer being grown with BPR = 1. The two methods have been shown to yield Se-rich (for low BPRs) or Zn-rich (for high BPRs) interface compositions under an essentially stoichiometric II–VI overlayer [8, 10].

Two sets of samples were grown. One set was used for the determination of the conduction-band offset ΔE_c via measurements of the tunneling current from photoinjected carriers, using a technique illustrated elsewhere in detail [11], and one set was used for I–V characterization. The latter samples were grown on p-type wafers and consisted of a 500 nm-thick GaAs layer grown at 580°C and doped $p = 3\text{–}4 \times 10^{16}$ cm^{-3}, followed by a 500 nm-thick ZnSe overlayer (including the CIL) doped with chlorine at $n = 3\text{–}4 \times 10^{16}$ cm^{-3}. A graded n^+ $Zn_{1-x}Cd_xSe$ region concluded the growth. The latter region was fabricated to promote the formation of ohmic contacts [12] which were realized by e-beam deposition of Al with no thermal treatment. Devices were fabricated by defining circular mesas (75 μm diameter) by standard photolithographic and wet etching techniques with removal of the entire II–VI epilayer around each mesa.

Samples used for photo I–V measurements differ in that the GaAs region adjacent to the ZnSe overlayer was limited to 10 nm and was grown on a $Al_{0.2}Ga_{0.8}As$ layer doped $p = 3\text{–}4 \times 10^{16}$ cm^{-3}. The compositional profile was chosen so that carriers could be photogenerated only in the thin GaAs layer near the interface using a low-power laser diode tuned at 1570 meV, i.e., above the GaAs band gap, but below the $Al_{0.2}Ga_{0.8}As$ band gap. This allowed us to avoid carrier generation far from the interface and possible transfer into GaAs satellite valleys before tunneling. All photo I–V measurements below 35 K were performed in a closed-cycle refrigerator in order to suppress thermally activated transport. More detail on the sample structure and experimental protocol can be found elsewhere [13].

3. Results

We measured the photo I–V characteristics at applied bias such that tunneling through the ZnSe-related triangular barrier is the dominant mechanism (i.e., in the range 12–20 V [13]). In the bias and temperature ranges of interest, electrons populate only the ground-state subband E_0. The functional dependence of the current on the applied bias can then be described by [14]

$$I = \alpha F_m^2 \exp[-B/F_m], \tag{1}$$

where $B = \frac{4}{3}(\sqrt{2m_e^*}/e\hbar)\phi_a^{3/2}$, $m_e^* = 0.14m_0$ is the ZnSe electron effective mass [15], α is a constant,

ϕ_a is the activation energy and F_m is the relevant electric field in the ZnSe layer. Since very low carrier densities were photogenerated, $\Delta E_c = \phi_a + E_0$. E_0 is a function of the electric field in the GaAs interface layer. The spatial dependence of the electric field across the entire structure was calculated solving Poisson's equation in the depletion-layer approximation and imposing the continuity of the displacement vector at the heterojunction interface [13].

In Fig. 1 we show representative semilog experimental plots of I/F_m^2 versus $1/F_m$ for diodes with ZnSe overlayers grown with BPR = 0.1 (top left) or 10 (bottom left) throughout, as well as diodes incorporating Se-rich (top right) or Zn-rich (bottom right) CIL. The solid lines are linear fits of the experimental data in the applied bias range where Eq. (1) holds [13, 14]. The slope of the fits yields B and, therefore, ΔE_c.

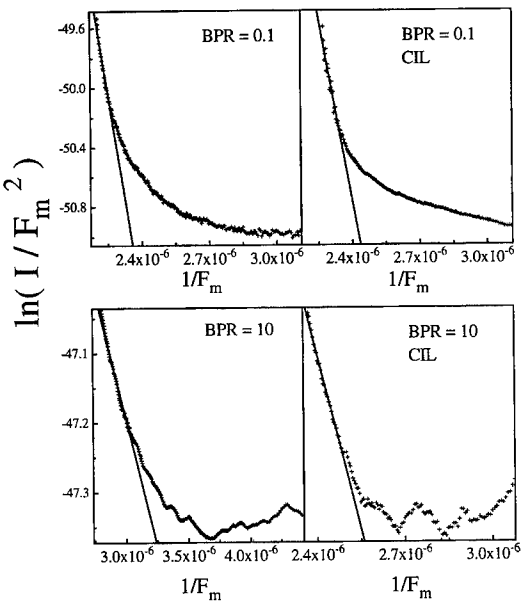

Fig. 1. Fowler–Nordheim plot of the photocurrent at low temperature and high applied bias for ZnSe/GaAs diodes incorporating Se-rich (top) or Zn-rich (bottom) interfaces. These were obtained by growing the ZnSe overlayer with Zn/Se beam pressure ratio (BPR) of 0.1 (top left) or 10 (bottom left) throughout, or by incorporating a thin composition control interfaces layer (CIL) grown in nonstoichiometric conditions (rightmost sections). Also shown is a least-squares fit of the data according to Eq. (1).

In Table 1 we summarize our findings for the conduction band discontinuity in all samples at 35 K (first column). The quoted experimental errors include both the uncertainty in the fitting

Table 1
Column one: Zn/Se beam pressure ratio (BPR) used for fabrication of ZnSe overlayers on GaAs, or for the composition control interface layer (CIL) in ZnSe/GaAs heterojunctions; column two: Measured conduction-band discontinuities; column three: Valence-band discontinuities ΔE_v as deduced from the experimental ΔE_c (this work) and the ZnSe/GaAs bandgap difference of 1301 meV; column four: ΔE_v as deduced from X-ray photoemission (XPS) data on thin overlayer samples; the quoted uncertainty in the XPS data correspond to the data scatter among several dozen thin overlayer samples [8, 10]

BPR	ΔE_c (meV)	ΔE_v (meV)	ΔE_v (XPS) (meV)
0.1	716 ± 45	585 ± 45	620 ± 70
1	361 ± 20	940 ± 20	850 ± 100
10	251 ± 10	1050 ± 10	1120 ± 80
0.1 CIL	751 ± 25	550 ± 25	580 ± 50
10 CIL	261 ± 10	1040 ± 10	1050 ± 50

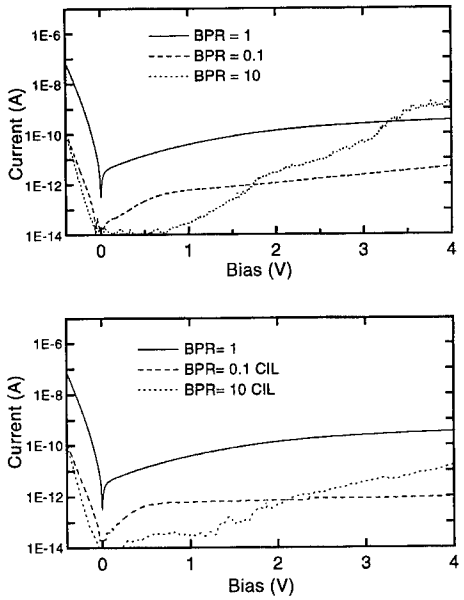

Fig. 2. Current–voltage characteristics at room temperature for representative diodes grown with different Zn/Se beam-pressure ratio BPRs. A given BPR were kept at the value indicated for the whole overlayer (upper panel) or for a 2 nm-thick interface layer (lower panel).

procedure and the scatter among the different individual devices measured. Samples grown with BPR = 1 yield $\Delta E_c = 361 \pm 20$ meV in agreement with values reported by other authors [16]. Conduction-band offsets in the range from 0.26 to 0.75 eV are observed in going from Zn-rich to Se-rich interfaces, proving both the efficacy of the offset modulation technique here exploited and the validity of the CIL concept in functional devices.

To study further the validity of the present approach for device fabrication, we also examined the *I–V* characteristics of a set of GaAs/ZnSe heterodiodes at room temperature (for the case of GaAs extending to the whole p-doped side). Fig. 2 shows our data for samples grown with the same BPR throughout the overlayer (upper panel) or incorporating an appropriate CIL (lower panel).

4. Discussion

Recent XPS studies which laid a background for the present work had indicated that the Zn/Se BPR employed during the early stages of interface fabrication determine the local interface composition and the band offset. Specifically, Nicolini et al. [8] presented the first X-ray photoemission spectroscopy (XPS) evidence of a valence band offset change in ZnSe–GaAs(0 0 1) heterojunctions involving 2–3 nm overlayers, discussed the variations in interface composition that correlate with the change, and examined theoretically the interface configurations that may account for offset tunability. Bonanni et al. [10] showed by XPS and photoluminescence spectroscopy that the growth conditions responsible for the change in interface composition and valence band offset can be restricted to the very early stages of interface formation, with a corresponding improvement in II–VI optical material quality.

All of the above results on the band alignment [8, 10] were obtained using heterostructures with ZnSe overlayers thin enough (2–3 nm) for the offset to be probed by XPS. The results in Fig. 1 are instead, to our knowledge, the first verification of a locally engineered heterojunction band offset in a fully functional device by transport methods. A quantitative comparison with the early XPS results in thin-overlayer samples can be made using the literature value of the ZnSe band gap to derive the valence band offsets from the conduction band offsets determined in Fig. 1. The resulting valence band discontinuities are listed in column two of Table 1, while the results obtained earlier by XPS [8, 10] are listed in column three. The agreement between the two sets of values is very satisfactory and suggests that the interface configurations responsible for band-offset tuning are sufficiently stable to withstand the fabrication stages required to go from the thin-overlayer samples to fully functional devices.

The results of Fig. 2 further support the possibility of exploiting the tunability of heterovalent heterojunctions in actual devices while pointing out some of the related limitations. The poorer structural quality of BPR = 10 overlayers, which contain a comparatively high density of stacking faults and dislocations [13, 17] manifests itself in Fig. 2 with the large leakage current (upper panel, dotted line), and is only marginally improved by the CIL technique (lower panel, dotted line). On the contrary, diodes fabricated with BPR = 0.1 (dashed line) show acceptable behavior and display good rectifying properties, particularly in the CIL case. The observed reduced reverse current as compared to the BPR = 1 control samples can be linked to the increased conduction-band discontinuity, which hinders the transfer of thermally generated electrons from the GaAs side into the ZnSe layer.

Diodes with engineered interfaces (dashed and dotted lines) do exhibit a somewhat degraded forward characteristics. Since heterostructures incorporating Se-rich CILs show extended defect densities substantially *lower* than those observed in the control samples [17], the most likely explanation is to be found in the presence of new *point* defects in the interface region leading to enhanced recombination at room temperature. Recent cathodoluminescence studies of ZnSe/GaAs heterojunctions [18] have shown that interfaces grown in Se-rich conditions are less stable against atomic interdiffusion and the formation of defect complexes involving substitutional Ga atoms. Systematic current–voltage studies in progress will address the relation between interfacial engineering and the final interface state density.

5. Conclusions

We have demonstrated that engineered band offsets can be observed and exploited in practical devices. In particular, reduction of the large valence-band offsets in ZnSe/GaAs heterojunctions can be obtained without degradation of the electrical properties of the heterojunction. This result may find an important applications in II–VI on III–V blue–green lasers since it should yield a reduced series resistance as a result of the improved hole injection in the active layer.

Acknowledgements

This work was supported in part by the US Army Research Office under Grants Nos. DAAH04-93-G-0206 and DAAH04-93-G-0319, and by CNR under the GaAsNET project.

References

[1] F. Capasso, A.Y. Cho, K. Mohammed and P.W. Foy, Appl. Phys. Lett. 46 (1985) 664.
[2] G. Margaritondo and P. Perfetti, in: Heterojunction Band Discontinuities: Physics and Device Applications, Eds. G. Margaritondo and F. Capasso (North-Holland, Amsterdam, 1987) 2.
[3] L.J. Brillson, in: Handbook on Semiconductors, Vol. I, Ed. P.T. Landsberg (North-Holland, Amsterdam, 1992) p. 281.
[4] A. Franciosi and C.G. Van de Walle, Surf. Sci. Rep. 214 (1996) 1.
[5] W.A. Harrison, E.A. Kraut, J.R. Waldrop and R.W. Grant, Phys. Rev. B 18 (1978) 4402.
[6] S. Baroni, R. Resta, A. Baldereschi and M. Peressi, in: Spectroscopy of Semiconductor Microstructures, Eds. G. Fasol, A. Fasolino and P. Lugli (Plenum, London, 1989) p. 251.
[7] G. Biasiol, L. Sorba, G. Bratina, R. Nicolini, A. Franciosi, M. Peressi, S. Baroni, R. Resta and A. Baldereschi, Phys. Rev. Lett. 69 (1992) 1283.
[8] R. Nicolini, L. Vanzetti, Guido Mula, G. Bratina, L. Sorba, A. Franciosi, M. Peressi, S. Baroni, R. Resta, A. Baldereschi, J.E. Angelo and W. Gerberich, Phys. Rev. Lett. 72 (1994) 294.
[9] See, for example: R.L. Gunshor and A.V. Nurmikko, Eds., II–VI Blue/Green Laser Diodes, Proc. SPIE 2346 (1994) 1.
[10] A. Bonanni, L. Vanzetti, L. Sorba, A. Franciosi, M. Lomascolo, P. Prete and R. Cingolani, Appl. Phys. Lett. 66 (1995) 1092.
[11] V. Pellegrini, A. Tredicucci, F. Beltram, L. Vanzetti, M. Lazzarino and A. Franciosi, J. Appl. Phys. 79 (1996) 929.
[12] M. Lazzarino, T. Ozzello, G. Bratina, L. Sorba and A. Franciosi, Appl. Phys. Lett. 68 (1996) 370.
[13] V. Pellegrini, M. Boerger, M. Lazzeri, F. Beltram, J.J. Paggels, L. Sorba, S. Rubini, M. Lazzarino, A. Franciosi, J.M. Bonard and J.D. Ganiere, Appl. Phys. Lett. 69 (1996) 3233.
[14] S.V. Meshkov, Sov. Phys. JETP 64 (1986) 1337.
[15] V. Pellegrini, R. Atanasov, A. Tredicucci, F. Beltram, C. Amzulini, L. Sorba, L. Vanzetti and A. Franciosi, Phys. Rev. B 51 (1995) 5171.
[16] S. Colak, T. Marshall and D. Cammack, Solid State Electron. 32 (1989) 647; D.J. Olego, Phys. Rev. B 39 (1989) 12743; Q.-D. Qian, J. Qiu, M. Kobayashi, R.L. Gunshor, M.R. Melloch and J.A. Cooper, Jr., J. Vac. Sci. Technol. B 7 (1989) 793.
[17] G. Bratina, L. Vanzetti, A. Bonanni, L. Sorba, J.J. Paggel, A. Franciosi, T. Peluso and L. Tapfer, J. Crystal Growth 159 (1996) 703.
[18] A.D. Raisanen, L.J. Brillson, L. Vanzetti, A. Bonanni and A. Franciosi, Appl. Phys. Lett. 66 (1995) 3301.

ELSEVIER

Journal of Crystal Growth 175/176 (1997) 608–612

JOURNAL OF CRYSTAL GROWTH

Molecular beam epitaxial growth of ZnSe(1 1 1) films on GaAs(1 1 1)B substrates and nitrogen doping

N. Matsumura*, T. Matsuoka, H. Shimakawa, J. Saraie

Department of Electronics and Information Science, Faculty of Engineering and Design, Kyoto Institute of Technology, Matsugasaki, Kyoto 606, Japan

Abstract

ZnSe films were grown on GaAs(1 1 1)B substrates by molecular beam epitaxy. The observation of reflection high-energy electron diffraction confirmed that the epilayers on both just and 10°-misoriented (1 1 1)B substrates consist of twins. The photoluminescence of the undoped epilayers showed defect-related Y-line emissions and deep emissions owing to the twins. Nitrogen was doped to the epilayers using an RF plasma cell. The photoluminescence spectra of the doped epilayers suggested that the nitrogen doping to ZnSe is enhanced using the GaAs(1 1 1)B substrates instead of the GaAs(1 0 0) substrates. We discussed the reason based on the bond number of the growing surface.

1. Introduction

In the molecular beam epitaxial (MBE) growth of ZnSe related compound semiconductors on GaAs substrates (1 0 0) surface has been usually used and other surfaces such as (1 1 1) surface were hardly used [1–4]. However, there is an attractive feature of (1 1 1) growth, that is, optical properties of strained-layer superlattice structure are modified by the piezoelectric effect and new optoelectronic devices are expected [5–7]. Another interest is the impurity doping to ZnSe(1 1 1) surface. The numbers of chemical bond of Zn and Se atoms to (1 1 1) surface are different from those on (1 0 0) surface, and consequently, the bond numbers of impurities which substitute for Zn or Se atoms are different from those to (1 0 0) surface. Therefore, we can expect the enhancement of doping efficiency by choosing suitable dopants.

In this paper, the properties of ZnSe(1 1 1) films grown on GaAs(1 1 1)B substrates by MBE and the results of nitrogen doping are reported. MBE growth of ZnSe films on GaAs(1 1 1)A substrates and nitrogen doping were already reported [4].

2. Experimental procedure

The substrates used were Cr–O doped just-oriented (within $\pm 0.5°$ misoriented) and 10°-misoriented GaAs(1 1 1)B toward [1 0 0] direction. In our previous study, we clarified that ZnSe films

* Corresponding author. Fax: + 81 75 724 7400; e-mail: matsumur@dj.kit.ac.jp.

0022-0248/97/$17.00 Copyright © 1997 Elsevier Science B.V. All rights reserved
PII S0022-0248(96)00988-8

grown on just-oriented GaAs(1 1 1)A substrates consisted of twins, but by using 10°-misoriented substrates single-crystalline films can be grown [4]. Therefore, we expected the same improvement in the films on 10°-misoriented GaAs(1 1 1)B substrates. For comparison, just-oriented GaAs(1 0 0) substrates were also used side by side. The substrates were thermally etched prior to the growth without As beam irradiation at 580°C for 2 min. The growth temperature was varied from 340 to 420°C (mainly 340°C). 6N–Zn and –Se were used as source materials. The effective pressure of the molecular beam was measured by a movable ion gauge at the substrate position, and corresponded to the molecular beam intensity of element VI and element II (J_{VI} and J_{II}) which was determined from the deposited quantity on liquid nitrogen-cooled GaAs [8]. The ratio of J_{VI}/J_{II} was mainly unity. Nitrogen from an RF plasma cell (Tech Science, RBS-30) was used as a p-type dopant [9]. The plasma power was varied from 0 to 100 W. The epilayers were characterized by surface morphology observed by Nomarski interference microscope, reflection high-energy electron diffraction (RHEED) at 4 kV, photoluminescence (PL) at 11 K using the 365 nm line of an ultrahigh-pressure Hg lamp as an exciting source and capacitance–voltage (C–V) measurement at 30 kHz using Au electrodes of ring-dot type (double-Schottky structure) on the epilayer surface.

3. Results and discussion

3.1. Undoped ZnSe(1 1 1) films

The surface of epilayers grown on GaAs(1 1 1)B substrates was mirror-like. The RHEED patterns of the (1 1 1)B epilayers grown on just- and 10°-misoriented substrates showed elongated spots and chevron plus streaks from the [2 1 1] azimuth of the incident electron beam, respectively. The twin spots were observed in the epilayers grown on both just- and 10°-misoriented substrates from the [0 $\bar{1}$ 1] azimuth. We grew ZnSe films under various growth conditions for obtaining twin-free crystals; with the J_{VI}/J_{II} ratio from 0.5 to 8, under the growth temperature from 340 to 420°C, with substrate surface treatment under Zn or Se beam irradiation just before the ZnSe growth, using ZnSe compound source for supplying hot Zn beam and Se_2 molecules and with ALE growth technique (alternating Zn and Se beam supply), expecting the migration enhancement of adsorbed atoms. But all films consisted of twins. On just-oriented (1 1 1)B substrate, adsorbed Zn atoms can take two kinds of orientations, which lead to the growth of twins similar to the growth on just-oriented (1 1 1)A substrates [3]. The RHEED patterns of the thermally etched just-oriented GaAs(1 1 1)B substrates showed elongated spots from the [2 1 1] azimuth. But the patterns of misoriented (1 1 1)B substrates showed chevron from the [2 1 1] azimuth and elongated spots from the [0 $\bar{1}$ 1] azimuth. The angle between adjacent edges of the chevron indicates that the surface consists of (3 2 1) or (3 3 1) facets. This is due to the thermal etching without As beam irradiation. While, in the thermal etching of GaAs(1 0 0) and (1 1 1)A substrates, streaks or elongated spots without chevron patterns were observed without As beam irradiation [3]. The growth of twins on the misoriented (1 1 1)B substrate seems to originate from the facets of the substrates, and the growth from the step edges of the misoriented surface may not be dominant, unlike the growth of twin-free epilayers on misoriented GaAs(1 1 1)A substrates [3].

Fig. 1 shows the PL spectra of undoped ZnSe epilayers grown on 10°-misoriented and just-oriented GaAs(1 1 1)B and (1 0 0) substrates. PL spectra of undoped ZnSe(1 1 1) epilayers on the just-oriented GaAs(1 1 1)B substrate showed defect-related Y-line [10, 11] and deep emissions. With the 10°-misoriented substrates, the emission intensity increased as indicated by the magnification factor in the figure and the exciton emissions appeared weakly, but the significant improvement in the PL spectra was not observed. While the PL spectra of the ZnSe(1 0 0) epilayers showed dominant strong exciton emissions with weak Y-line and weak deep emissions relative to the exciton emissions.

We reported that, in the PL spectra of ZnSe epilayers grown on 5°- or 10°-misoriented GaAs(1 1 1)A substrates, the strong exciton emissions, which were comparable with that of ZnSe(1 0 0), were observed [3]. These epilayers

were revealed to be twin-free by RHEED observation. But Y-line and deep emissions with weak exciton emissions were observed in the epilayers grown on the just-oriented GaAs(1 1 1)A substrates, which were similar to the PL spectra of the epilayers on GaAs(1 1 1)B substrates. The epilayers grown on the just-oriented GaAs(1 1 1)A substrates were revealed to consist of twins by RHEED observation [3]. These facts mean that the PL spectra of the ZnSe epilayers which consist of twins show the Y-line and deep emissions. It can be concluded that the twin boundaries of such crystals are the origin of defects and non-radiative centers.

3.2. N-doped ZnSe(1 1 1) films

Fig. 2 shows the PL spectra of the N-doped ZnSe(1 1 1) epilayers grown on the misoriented GaAs(1 1 1)B substrate under the various plasma powers. Y-line and deep emissions, which are dominant in the undoped epilayers, diminish and nitrogen-related emissions appear. The spectra of the N-doped ZnSe(1 0 0) epilayers grown in the same run as the ZnSe(1 1 1) epilayers are shown in Fig. 3 as references. The growth rates of the epilayers grown on the GaAs(1 1 1)B substrates were almost the same as those on the (1 0 0) substrates. Fig. 4 shows the net acceptor concentrations (Na–Nd) of the ZnSe(1 0 0) epilayers determined from the C–V measurement. It is clear that the acceptor concentration in the ZnSe(1 0 0) epilayers can be controlled

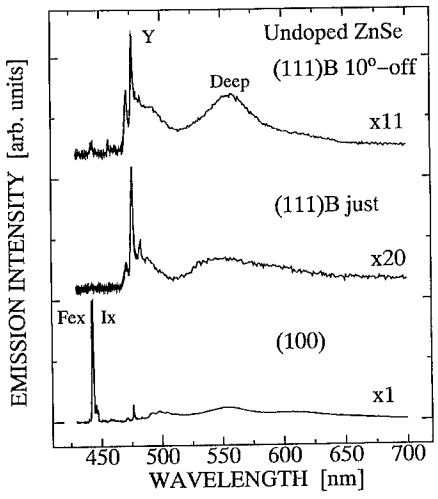

Fig. 1. PL spectra of undoped ZnSe(1 1 1) and (1 0 0) epilayers grown on GaAs(1 1 1)B and (1 0 0) substrates, respectively.

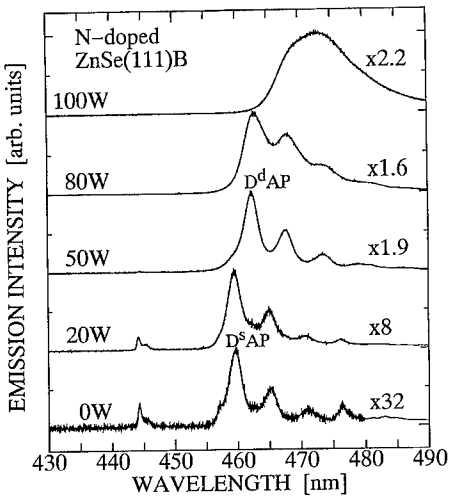

Fig. 2. PL spectra of N-doped ZnSe(1 1 1) epilayers grown on 10°-misoriented GaAs(1 1 1)B substrates with the various plasma input power.

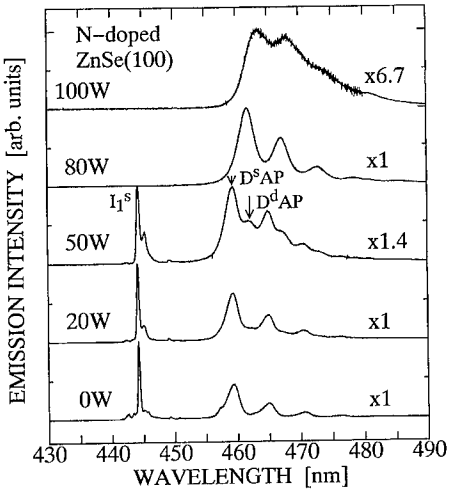

Fig. 3. PL spectra of N-doped ZnSe(1 0 0) epilayers grown on GaAs(1 0 0) substrates with the various plasma input power. The epilayers were grown in the same run as the ZnSe(1 1 1) epilayers.

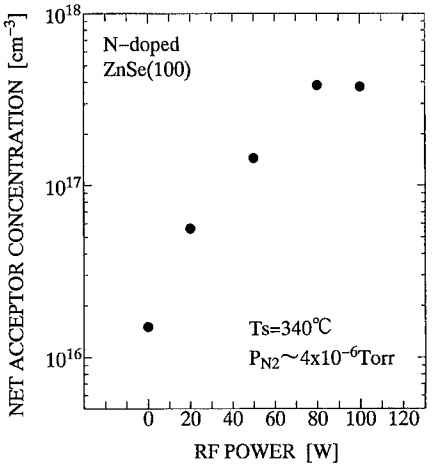

Fig. 4. Net acceptor concentrations (Na–Nd) of the ZnSe(1 0 0) epilayers determined from the C–V measurement as a function of the plasma power.

by the plasma power, that is, the concentration increases with increasing the plasma power. We have also tried the C–V measurement to obtain the net acceptor concentration of ZnSe(1 1 1) epilayers grown on GaAs(1 1 1)B substrates. But all the samples showed apparent high resistivity and the C–V measurements were not successful. This may be due to the presence of twin boundaries. The grain size was examined by chemical-etching technique using HCl as an etchant. The diameters of the grains were about 0.1–1 μm, which were observed with a scanning electron microscope. The gap between the dot and the ring of the double-Schottky electrodes was 40 μm. Therefore, many twin boundaries exist in the gap. The probable reason for difficulty in the C–V measurement is the existence of highly resistive barrier layers at the twin boundaries between the electrodes. Therefore, we compare the nitrogen doping properties of ZnSe(1 1 1) and (1 0 0) films by the PL spectra in the following.

When we compare the PL spectra with the net acceptor concentration in the (1 0 0) epilayers, generally reported results are observed. That is, in the epilayers with low acceptor concentration (below 10^{17} cm^{-3}), the PL spectra show dominant acceptor bound exciton emission (I_1^s) with shallow donor and acceptor pair emissions (D^sAP). With increasing the acceptor concentration, the D^sAP emissions diminish, the deep donor and acceptor pair emission (D^dAP) emerges and the intensity of I_1^s decreased. Under over doping condition at 100 W (compensated situation), the D^dAP emission broadens and the emission energy shifts to the lower-energy side owing to the reduction in the effective band-gap energy caused by the fluctuation of the conduction and valence band edge. The net acceptor concentration of this sample saturates as shown in Fig. 4. In the ZnSe(1 1 1)A epilayers grown on GaAs(1 1 1)A substrates, the relation between the net acceptor concentration and the PL properties, in which the Na–Nd values increased with increasing the intensity of D^dAP emissions, was also observed [4].

The PL spectrum of N-doped ZnSe(1 1 1)B epilayer prepared at 50 W showed D^dAP emissions, while that of the ZnSe(1 0 0) epilayer grown under the same run showed combination of the I_1^s and D^sAP emission, and D^dAP emission was minor. At a plasma power of 100 W, the red shift of the D^dAP emission of the N-doped ZnSe(1 1 1)B epilayer is more serious than that of the ZnSe(1 0 0) epilayer. If we assume that the relation between the net acceptor concentration and the PL spectrum in the (1 1 1)B epilayers is the same as that in the (1 0 0) epilayers, the enhancement of the nitrogen doping to ZnSe epilayers using GaAs(1 1 1)B substrates instead of GaAs(1 0 0) substrates is suggested by comparing the above mentioned PL spectra under the same conditions. However, it was not clear whether the maximum net acceptor concentration in the ZnSe(1 1 1)B films was larger than that in the (1 0 0) films, because of the unsuccessful C–V measurement in the (1 1 1)B films. A study of the confirmation of the doping enhancement by electrical measurements in twin-free ZnSe(1 1 1)B films remains to be done.

Now we discuss a probable reason of the enhancement of the nitrogen doping in the ZnSe(1 1 1) epilayers grown on GaAs(1 1 1)B substrates. The bond number of adsorbing nitrogen atoms on the Zn-exposed ZnSe(1 1 1)B surface is three and larger than the bond number of nitrogen atoms on the Zn-exposed ZnSe(1 0 0) surface (two). Therefore, the probable reason for doping enhancement is the increase in the sticking probability of

nitrogen on the ZnSe(1 1 1)B surface. This consideration is supported by our experimental results of the nitrogen doping in the epilayers grown on GaAs(1 1 1)A substrates [4]. The net acceptor concentration was small in the epilayers on GaAs(1 1 1)A substrates compared with that of epilayers on GaAs(1 0 0) substrates at the same nitrogen doping situation. The bond number of adsorbing nitrogen atoms on the Zn-exposed ZnSe(1 1 1) surface grown on GaAs(1 1 1)A substrate is one and smaller than that on the (1 0 0) surface, which brings the smaller sticking probability of nitrogen on (1 1 1)A surface.

If twin-free single-crystalline epilayers can be grown on GaAs(1 1 1)B substrates with thermal etching procedure under As beam irradiation or using (1 1 1)B family surfaces such as (2 1 1)B or (3 1 1)B surfaces, the enhancement of nitrogen doping in (1 1 1)B epilayers will be useful.

4. Conclusions

ZnSe films were grown on GaAs(1 1 1)B substrates by MBE. The observation of RHEED confirmed that the epilayers grown on both just- and 10°-misoriented substrates consist of twins. The growth of twins on the misoriented substrate seems to originate from the facets of the substrates owing to the thermal etching without As beam irradiation. The PL spectra of the undoped epilayers showed defect-related Y-line and deep emissions. It was concluded that the twin boundaries of the films are the origin of defects and nonradiative centers. Nitrogen was doped to the epilayers using an rf plasma cell. The net acceptor concentration of the (1 1 1)B epilayers could not be determined by C–V measurements owing to the presence of twin boundaries although that of the twin-free (1 0 0) epilayers could be determined. The comparison between the PL spectra of nitrogen doped (1 1 1)B epilayers and those of (1 0 0) epilayers suggested that the nitrogen doping to ZnSe films is enhanced using the GaAs(1 1 1)B substrates instead of GaAs(1 0 0) substrates. A probable reason for doping enhancement is the increase in the sticking probability of nitrogen on (1 1 1)B surfaces owing to the larger bond number of the adsorbing nitrogen atoms on the Zn-exposed ZnSe(1 1 1)B surface than that on the (1 0 0) surface.

References

[1] D.L. Smith and V.Y. Pickhardt, J. Appl. Phys. 46 (1975) 2366.
[2] T. Ohno, Y. Kawaguchi, A. Ohki and T. Matsuoka, Jpn. J. Appl. Phys. 33 (1994) 5766.
[3] N. Matsumura, K. Maemura, T. Mori and J. Saraie, Jpn. J. Appl. Phys. 34 (1995) L1114.
[4] N. Matsumura, K. Maemura, T. Mori and J. Saraie, J. Crystal Growth 159 (1996) 85.
[5] D.L. Smith and C. Mailhiot, Phys. Rev. 58 (1987) 1264.
[6] K.W. Goossen, E.A. Caridi, T.Y. Cheng, J.B Stark and D.B.A. Miller, Appl. Phys. Lett. 56 (1990) 715.
[7] B.C. Cavenett, P.J. Thompson, G.D. Brownlie, S.Y. Wang and K.A. Prior, in: Proc. Int. Symp. on Blue Laser and Light Emitting Diodes (Ohmsha, Tokyo, 1996) p. 277.
[8] N. Matsumura, M. Tsubokura, J. Saraie and Y. Yodogawa, J. Crystal Growth 86 (1988) 311.
[9] J. Saraie, K. Yamawaki, N. Matsumura and A. Ikehara, J. Crystal Growth 159 (1996) 334.
[10] S. Myhailenko, J.L. Batstone, H.J. Hutchinson and J.W. Steels, J. Phys. C 17 (1984) 6477.
[11] J. Saraie, N. Matsumura, M. Tsubokura, K. Miyagawa and N. Nakamura, Jpn. J. Appl. Phys. 28 (1989) L108.

ELSEVIER

Journal of Crystal Growth 175/176 (1997) 613–618

JOURNAL OF CRYSTAL GROWTH

Molecular beam epitaxial growth of ZnSe on GaAs substrates: influence of precursors on interface quality

C.C. Kim[a,*], Y.P. Chen[a], S. Sivananthan[a], S.-C.Y. Tsen[b], David J. Smith[b]

[a] *Department of Physics, Microphysics Laboratory, University of Illinois at Chicago, Chigago, Illinois 60607, USA*
[b] *Department of Physics and Astronomy and Center for Solid State Science, Arizona State University, Tempe, Arizona 85287, USA*

Abstract

The initial growth of thin ZnSe layers, grown on GaAs(0 0 1) using molecular beam epitaxy (MBE), has been studied using real-time reflection high-energy electron diffraction (RHEED), as well as X-ray double-crystal rocking curves (DCRC), reflectivity difference spectroscopy (RDS) and transmission electron microscopy (TEM). A noticeable difference in interface quality and growth was observed depending upon the initial precursor. Exposure to Se flux before growth led initially to three-dimensional growth, whereas exposure to Zn flux or no precursor led immediately to two-dimensional growth. X-ray DCRC and RDS confirmed that the overall sample quality was better with two-dimensional growth, and TEM observations were consistent with previous studies which have shown that initial three-dimensional growth is related to the formation of Ga_2Se_3 at the interface, leading to high densities of stacking faults and edge dislocations.

PACS: 81.10.Bk; 78.20.Ci; 61.14.Hg; 61.16.Bg

Keywords: MBE; Precursor; RHEED; X-ray; RDS; Interface

1. Introduction

ZnSe-based alloy systems have received much attention because of their potential as laser diodes in the blue–green region of the spectrum [1]. The success of p-type doping [2] and the first demonstration of green laser diodes [3] have stimulated the field. Rapid failure during device operation has, however, delayed the development of commercial applications [4]. The rapid failure has been ascribed to pre-existing defects such as stacking faults and point defects originating from the region of the interface. Recent research has focussed on improving the interface quality, which may increase device lifetime.

The ZnSe/GaAs interface is strongly influenced by the formation of mixed interfacial layers and misfit dislocations. One way to improve the interface quality is to optimize initiation of the ZnSe growth. Several groups [5–10] have reported on the initial growth mode of ZnSe on GaAs. Reichow et al. [8] found that the best quality ZnSe layer was achieved when the GaAs substrate was exposed to

* Corresponding author.

0022-0248/97/$17.00 Copyright © 1997 Published by Elsevier Science B.V. All rights reserved
PII S0022-0248(96)00999-2

Zn flux for 0.5 s prior to Se flux. Guha et al. [9] conducted more detailed studies and found that the initial growth mode could be characterized as three-dimensional (3D) mode, intermediate two-dimensional (2D), or 2D, as a result of exposing the GaAs surface to Se, Se + Zn, or Zn fluxes, respectively, prior to ZnSe growth. Furthermore, they found that the 2D growth mode at the beginning produced the best sample quality, with dislocation densities in the low 10^6 cm^{-2} range. Our current study using real-time RHEED has provided direct in-situ evidence on the influence of the precursor on growth initiation. Ex-situ characterization by X-ray DCRC, RDS and TEM also indicated that samples grown with the initial 2D growth mode had better quality, supporting previous conclusions. The cause of 3D growth with the Se precursor is tentatively ascribed to the formation of Ga_2Se_3 at the interface.

2. Experimental procedure

All ZnSe-based layers were grown in the Riber 2300 MBE system [11]. Elemental Zn and Se sources were used in growing ZnSe. Si-doped GaAs(0 0 1) substrates (Sumitomo) were prepared by conventional chemical cleaning and in-situ thermal oxide desorption. In-situ RHEED showed the expected bulk GaAs diffraction pattern and X-ray photoemission spectroscopy (XPS) of representative samples indicated that the surface was oxide-free (below the detection limit of 1.0%). ZnSe layers (1–3 μm thick) were then grown under Se-rich conditions on GaAs substrates without GaAs buffer layers. The growth temperature was nominally 310°C and the typical growth rate was about 1–1.5 Å/s. ZnSe growth was initiated after different surface treatments with Zn or Se flux prior to growth as follows:

(1) the GaAs substrate surface was only exposed to Zn or Se flux at the growth temperature for 1 s, 1 min and 10 min;

(2) the GaAs substrate surface was exposed to both Se and Zn flux at the growth temperature; and

(3) the GaAs substrate surface was exposed to either Zn or Se flux after thermal oxide desorption and during cooling of the substrate to the growth temperature.

Before and during growth, a K-space RHEED analysis system was used to monitor the growth. After growth, all samples were characterized by spectroscopic ellipsometry (SE), X-ray DCRC, TEM [12] and RDS [13, 14] .

3. Results and discussion

The differences between the initial growth modes are apparent from real-time RHEED patterns of the ZnSe(0 0 1) layers. Fig. 1 shows the patterns from the GaAs(0 0 1) substrates and the ZnSe(0 0 1) layers recorded at the growth temperature immediately before and during the initiation of ZnSe growth. For convenience, the samples corresponding to the columns from left to right are designated as Samples A, B, and C, respectively.

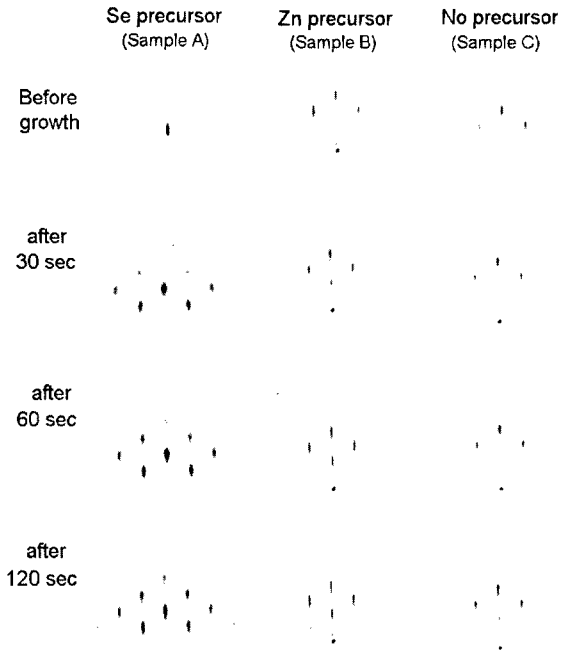

Fig. 1. RHEED patterns before and during the growth of ZnSe on GaAs substrates. The top row shows the patterns before initiation of growth, and the second, third and fourth rows show patterns at 30, 60, and 120 s after initiation of growth, respectively. The e-beam is along [1 1 0] direction.

The patterns were taken with the electron beam along [1 1 0].

When the GaAs substrate was exposed to Se flux for 1 min before Zn flux (Sample A), the growth mode was clearly 3D, as indicated by the spotty pattern in the first column. Even after 2 minutes, the RHEED pattern still remained spotty. The RHEED patterns usually turned to streaks after 10–30 min. Conversely, when the GaAs substrate was exposed to Zn flux for 1 min before growth (Sample B), the RHEED patterns remained streaky throughout growth, as shown by the second column in Fig. 1. These results are consistent with the experimental results reported by Guha et al. [9], where it was proposed that Se interacted with Ga to form Ga_2Se_3, which in turn led to the development of ZnSe islands. Our results suggest, however, that the coverage by Ga_2Se_3 is likely to be only on the order of a monolayer, since RHEED patterns at the onset of growth do not show any noticeable change.

To determine the duration of Zn treatment necessary for achieving 2D growth, we initiated ZnSe growth by opening the Zn shutter just 1 s before opening the Se shutter. The RHEED patterns still showed a smooth 2D start. Finally, ZnSe growth was initiated by opening Zn and Se simultaneously (Sample C). As shown by the third column of Fig. 1, the RHEED patterns remained streaky throughout the entire growth. The subtle differences between ZnSe growth with and without any Zn treatment, as observed by Guha et al. [9], was not observed in our experiment. This could be due to residual surface roughness, probably because the GaAs surface oxide was thermally desorbed without As flux.

Some ZnSe layers were grown on GaAs substrates with Zn or Se treatment immediately after oxide desorption, while the substrate was cooling to the growth temperature. Others were grown with 10 min exposure to Zn or Se flux. In all cases, when growth of ZnSe layers were initiated after Se treatment, RHEED patterns always showed initial 3D growth. The results are understandable, since they always involve exposure of Se flux to the GaAs surface at the growth temperature. At this temperature, the likely formation of Ga_2Se_3 would cause initial 3D growth [7, 10]. Conversely, when the GaAs substrate was exposed first to Zn flux, ZnSe layers tend to grow in a 2D mode. The duration of the exposure to the Zn flux, however, has some effect on initiation of growth of the ZnSe layers. RHEED patterns showed that prolonged exposure of the GaAs substrate to Zn flux tended to make the initiation slightly rough. After a period of 2 min, however, there was almost no difference in the RHEED patterns, regardless of treatment. The RHEED patterns for all layers showed smooth streaks with the Se (2×1) surface reconstruction, indicating a smooth growth front.

The microstructure of the samples grown with different treatments was characterized by TEM. Overall, the electron micrographs confirmed the differences between samples grown with different treatments as revealed by RHEED. Samples grown either with no treatment or with Zn treatment had better quality than those with Se treatment. For example, samples with Se treatment usually showed many stacking faults. Fig. 2 compares the interface

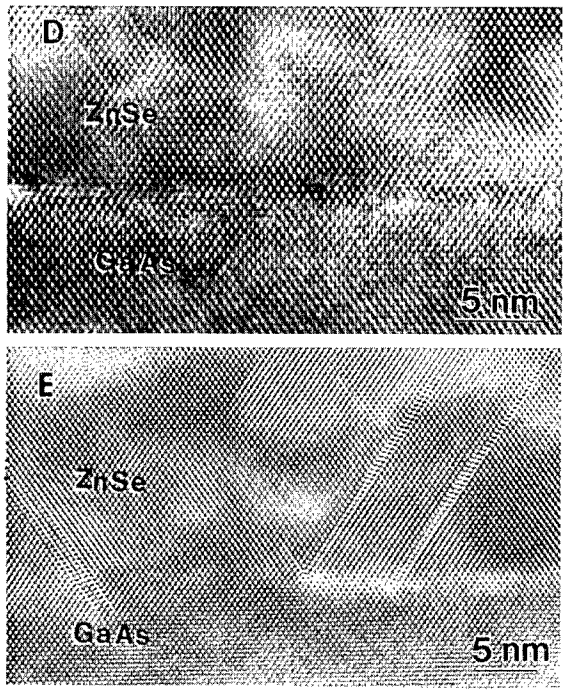

Fig. 2. TEM micrographs for Samples D and E. Sample D grown with Zn treatment shows better quality interface than Sample E grown with Se treatment. More stacking faults are observed in Sample D than Sample E.

of Sample D grown with the Zn precursor with that of Sample E grown with the Se precursor. Sample D shows a relatively smooth interface without any misfit dislocations visible in this region. On the other hand, Sample E grown with Se as the precursor shows a rough interface and some stacking faults that penetrate into the GaAs side. The greater defect density in this sample could well be caused by an intermixed phase such as Ga_2Se_3 at the interface which has a smaller lattice constant than either GaAs or ZnSe [7, 10].

The structural quality of the ZnSe layers was also characterized by X-ray DCRC. Fig. 3 shows a schematic diagram which relates the change of lattice constants to the shift of X-ray peaks. The out-of-plane and in-plane lattice constant for GaAs are designated by $a_\perp$ and $a_\parallel$, respectively. The out-of-plane and in-plane lattice constant for ZnSe are designated by $b_\perp$ and $b_\parallel$, respectively. The lattice constant of GaAs (5.6533 Å) [15] is smaller than that of ZnSe (5.6696 Å) [16]. According to these values, the peak-to-peak distance should be 386 arcsec. Under the ideal condition where coherent growth takes place, $b_\perp$ will increase and $a_\perp$ near the interface will decrease as illustrated by the dotted boxes. This leads to the further separation of ZnSe peak from GaAs peak as illustrated by the dotted curves. Fig. 4 shows experimental rocking curves from the (0 0 4) plane for Sample B: one with the X-ray source along [1 1 0], and the other after rotating the sample by 180°. Two measurements for each sample were performed to compensate for any misorientation of the ZnSe with respect to GaAs. GaAs peak from the substrate before growing ZnSe normally shows FWHM less than 30 arcsec. The doublet shown in this figure indicates that one peak

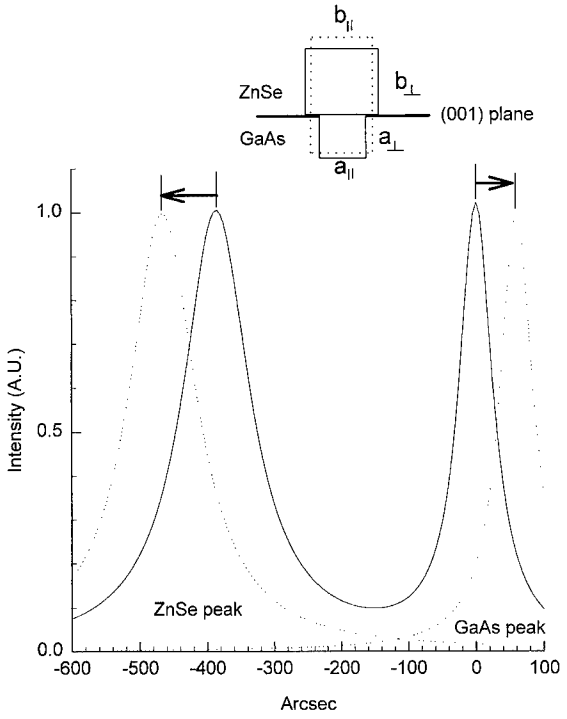

Fig. 3. Schematic diagram illustrating the relationship between the change of lattice constants and the shift of X-ray peaks which mimic diffraction from the (0 0 4) planes. The solid boxes represent the lattice constant for bulk ZnSe and GaAs, and the dotted boxes, for film ZnSe and GaAs. Likewise, the solid curve shows the X-ray peak from bulk ZnSe and GaAs and the dotted curve, from film ZnSe and GaAs.

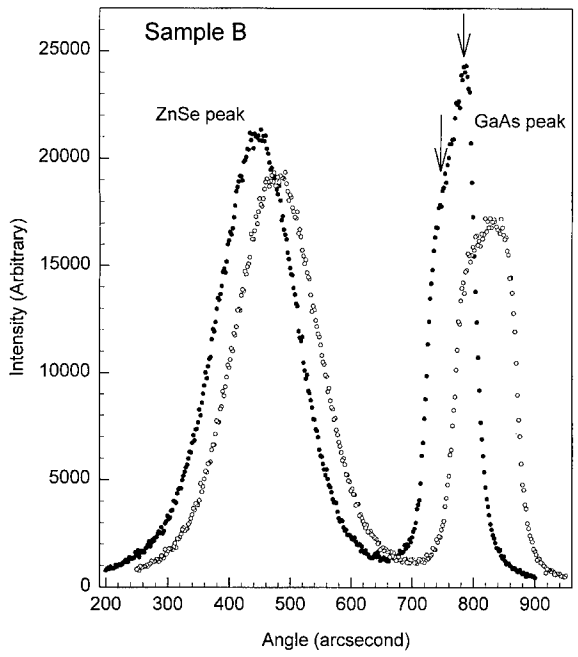

Fig. 4. X-ray DCRC for Sample B. One is taken with the X-ray beam along [1 1 0], the other, after rotating the sample by 180°. The average FWHM is 133 arcsec, and the average peak-to-peak distance is 339 arcsec.

may be from the bulk region and the other, from the region near the interface subjected to the larger strain. The average distance from ZnSe peak to GaAs peak for Sample B was 339 arcsec, where the average position of the GaAs doublet was used for the GaAs peak. The peak-to-peak distance for other samples was also similar to this value, which is always smaller than the expected value 386 arcsec. This indicates that (i) the literature value for ZnSe [16] is larger than the true value, or (ii) the lattice constant of film ZnSe is less than that of bulk ZnSe, implying the compressive strain even along [0 0 1]. Rocking curves for Sample A were similar to those for Sample B. But, the line shape of the GaAs doublet for the two samples was different in the sense that the stronger intensity for Sample B was at the position away from the ZnSe peak, with the weaker intensity at the position closer to the ZnSe peak, which was opposite to that for Sample A. Considering that the X-ray intensity is proportional to the number of planes having the same lattice constant, the line shape of the GaAs doublet for the two samples indicates that Sample B has more portion of coherent growth at the interface than Sample A. The average FWHM of ZnSe peak for Samples B and A was 133 and 143 arcsec, respectively, indicating that film ZnSe of Sample B is more ordered than that of Sample A. In relation to the RHEED patterns and TEM observations for these samples, the X-ray results again confirmed that better interface quality led to better structural quality.

The structural quality of film ZnSe for Sample D and E could not be determined by X-ray DCRC, since the thickness as determined by SE was only of the order 700 nm and the intensity of X-ray diffractometer was not strong enough to pick up the ZnSe signal. RDS was, however, able to determine the difference in the structural quality for thin samples. The setup and interpretation of RDS data are reported previously [14]. Fig. 5 shows RDS data for Samples D and E. The derivative-like structure around the E_1 region for Sample D is stronger than that for Sample E. The strength of the peaks, as shown by the arrows, is 0.011 and 0.004 for Sample D and Sample E, respectively. These results show that the structural quality of Sample D is better than Sample E, since it is proportional to the strength of the derivative-like structure [14].

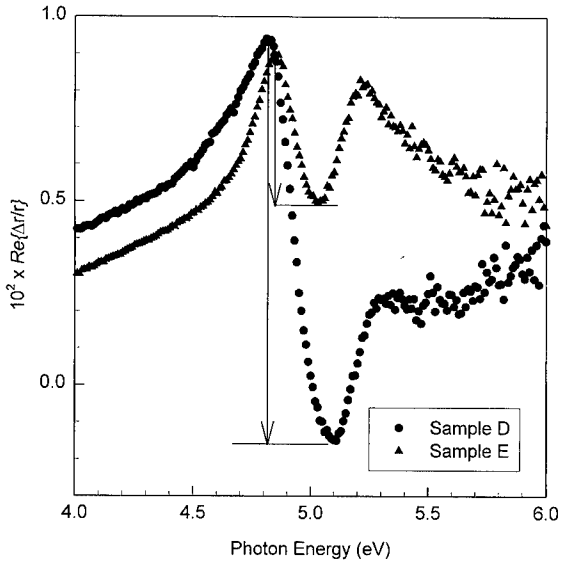

Fig. 5. RDS in the E1 region for Samples D and E. Sample D shows about three times stronger strength than Sample E.

4. Conclusions

The initial growth mode of ZnSe layers on GaAs(0 0 1) without GaAs buffer layers has been studied in detail using real-time RHEED images. ZnSe grown on GaAs substrates with Se as the precursor always showed a 3D growth mode, whereas layers grown with Zn as a precursor always showed the 2D mode. The duration of Zn exposure before growth was not critical although prolonged exposure somewhat roughened the surface. Thus, it is not necessary to prolong Zn exposure in order to ensure the 2D start. The TEM results indicated that samples exposed to Se treatment prior to growth form a defective interfacial region, possibly due to Ga_2Se_3, causing a high density of stacking faults and edge dislocations, originating from the vicinity of the interface. From X-ray DCRC FWHM, samples with Zn treatment were more ordered and coherent than those with Se treatment. RDS also indicated that better quality was associated with samples grown with Zn treatment.

Acknowledgements

We acknowledge internal funding from the Microphysics Laboratory at UIC. Electron microscopy was conducted at the Center for High Resolution Electron Microscopy at ASU supported by NSF Grant DMR-93-14326.

References

[1] R.L. Gunshor and A.V. Nurmikko, MRS Bull. 20 (1995) 15.
[2] R.M. Park, M.B. Troffer, C.M. Rouleau, J.M. DePuydt and M.A. Haase, Appl. Phys. Lett. 57 (1990) 2127.
[3] M.A. Haase, J. Qiu, J.M. DePuydt and H. Cheng, Appl. Phys. Lett. 59 (1991) 1272.
[4] S. Itoh and A. Ishibashi, unpublished.
[5] D.-W. Tu and A. Kehn, J. Vac. Sci. Technol. A 3 (1985) 922.
[6] M.C. Tamargo, J.L. DeMiguel, D.M. Hwang and H.H. Farrell, J. Vac. Sci. Technol. B 6 (1988) 784.
[7] J. Qiu, Q.D. Qian, M. Kobayashi, R.L. Gunshor, D.R. Menke, D. Li and N. Otsuka, J. Vac. Sci. Technol. B 8 (1990) 701.
[8] J. Reichow, J. Griesche, N. Hoffmann, C. Muggelberg, H. Rossmann, L. Wilde, F. Henneberger and K. Jacobs, J. Crystal Growth 131 (1993) 277.
[9] S. Guha, H. Munekata, L.L. Chang and W.C. Tang, J. Crystal Growth 127 (1993) 308.
[10] L.H. Kuo, K. Kimura, T. Yasuda, S. Miwa, C.G. Jin, K. Tanaka and T. Yao, Appl. Phys. Lett. 68 (1996) 2413.
[11] B.J. Skromme, Y. Zhang, W. Liu, B. Parameshwaran, D.J. Smith and S. Sivananthan, Mater. Res. Soc. Symp. Proc. 326 (1994) 15.
[12] D.J. Smith, S.C. Tsen, Y.P. Chen, J.P. Faurie and S. Sivananthan, Appl. Phys. Lett. 67 (1995) 11.
[13] C.C. Kim and S. Sivananthan, Mater. Res. Soc. Symp. Proc. 406 (1996) 319.
[14] C.C. Kim and S. Sivananthan, J. Crystal Growth 175/176 (1997) 328.
[15] J.B. Mullin, B.W. Straughan, C.M.H. Driscoll and A.F.W. Willoughby, Inst. Phys. Conf. Ser. 24 (1975) 275.
[16] J.K. Furdyna, J. Appl. Phys. 64 (1988) R29.

ELSEVIER

Journal of Crystal Growth 175/176 (1997) 619–623

JOURNAL OF CRYSTAL GROWTH

p-Type doping of beryllium chalcogenides grown by molecular beam epitaxy

H.-J. Lugauer*, Th. Litz, F. Fischer, A. Waag, T. Gerhard, U. Zehnder, W. Ossau, G. Landwehr

Physikalisches Institut, Experimentelle Physik III/MBE, Universitat Würzburg, Am Hubland, D-97074 Würzburg, Germany

Abstract

We have grown Be-chalcogenides for the first time by molecular beam epitaxy (MBE) on GaAs substrates. The lattice constants of both BeTe and BeSe are smaller than that of GaAs, therefore Be containing compounds such as (BeMg)Te or (BeZn)Se and (BeMgZn)Se are ideal candidates to replace ZnTe or Zn(SSe) and (ZnMg)(SSe) ternaries and quaternaries, respectively. In this contribution we present first results on the p-type doping of such layers using a modified nitrogen plasma source. The p-type dopability of BeTe as determined by van-der-Pauw measurements is comparable to that of ZnTe, free-hole concentrations of more than 1×10^{20} cm^{-3} have been reached. Heavily p-doped ternary (BeMg)Te or (BeMn)Te layers are obtained easily which are fully lattice-matched to GaAs. On the other hand, (BeZn)Se and (BeMgZn)Se ternaries and quaternaries seem to behave similar to their sulphur-containing counterparts, an increase of the band gap leads to a decrease of the free-hole concentration. Based on these results, we propose an alternative for the p-type doping of wide gap II–VI semiconductors. The small lattice mismatch of BeTe to GaAs allows to grow BeTe/ZnSe superlattices with excellent structural quality. We have calculated possible superlattice structures which should have an effective band gap comparable to or higher than ZnSe and at the same time are highly p-doped and almost lattice-matched to the GaAs substrate.

PACS: 68.55; 72.80.E; 73.60.F

Keywords: II–VI semiconductors; Beryllium chalcogenides; p-Type doping; Superlattice; MBE

1. Introduction

p-type doping is the key issue for the fabrication of laser diodes emitting in the short wavelength range. The first demonstration of ZnSe-based blue–green lasers [1] has been soon after the successful p-type doping of ZnSe with carrier concentrations of up to $p = 2 \times 10^{18}$ cm^{-3} by using plasma activated nitrogen as acceptor [2]. However, the p-dopability is decreasing with increasing band gap in the quaternary ZnMgSSe which is used for cladding layers in blue–green laser diodes. To

* Corresponding author. Fax. + 49 931 888 5142; e-mail: lugauer@physik.uni-wuerzburg.de.

0022-0248/97/$17.00 Copyright © 1997 Elsevier Science B.V. All rights reserved
PII S0022-0248(96)01000-7

reduce the leakage current in separate confinement heterostructures, a difference of at least 0.4 eV between the cladding layers and the active region is necessary [3]. Together with the band gap limit of the cladding layers of about 2.9 eV at which the p-type doping is still sufficient, continuous room temperature operation of such laser structures is possible only at wavelengths of more than about 490 nm.

With the introduction of Be containing II–VI semiconductors, a totally different approach for the p-doping can be considered. We suggest to use BeTe/ZnSe superlattices (SL) which can be highly p-doped due to the high p-dopability of BeTe, and at the same time are lattice matched to GaAs.

We present experimental results on the p-type doping of (BeMg)Te and (BeMgZn)Se with nitrogen, and calculate the effective band gap of the proposed ZnSe/BeTe superlattices depending on the thickness of the binary layers.

2. Experimental details

The structures have been grown in a RIBER 2300 four chamber system in a group VI rich regime at growth temperatures between 270°C and 300°C for ZnSe-based compounds and between 270°C and 400°C for (BeMg)Te. The growth rates have been chosen between 0.2 and 3 Å/s. Further details about the properties and growth of Be chalcogenides are published elsewhere [4]. For the p-type doping, a modified nitrogen plasma source (Oxford Applied Research) has been used which allows also the cracking of solid materials like arsenic by the plasma discharge [5]. However, for the samples presented here only nitrogen diluted with argon at different ratios has been used.

The net acceptor concentration of the Be chalcogenides has been determined by means of electrochemical capacitance–voltage (C–V) profiling (BIORAD PN4300) and mercury probe C–V profiling at lower concentration and Hall measurements in the van-der-Pauw configuration at higher concentrations. The band gaps have been determined by photoluminescence (PL) at 1.9 K and the structural quality of the thin films was checked by high-resolution X-ray diffraction (HRXRD) rocking curves employing a six-crystal diffractometer.

3. Results and discussion

3.1. p-type doping of Be chalcogenides

3.1.1. Tellurides

Te-based compounds like (BeMg)Te can be grown in excellent quality lattice-matched to GaAs substrates. The full width at half maximum (FWHM) of the rocking curve of the best film has been 24 arcsec for a 1 μm thick layer. At the same time the p-type doping level of (BeMg)Te using plasma activated nitrogen as acceptor is extremely high, free-hole concentration of $p = (1.2 \pm 0.3) \times 10^{20}$ cm^{-3} with a mobility of $\mu = 9.9 \pm 2.6$ cm^2/(V s) at 300 K have been determined by van-der-Pauw measurements. Together with the high structural quality this material is the ideal replacement for ZnTe : N which is commonly used in the ZnSe/ZnTe pseudograding on top of conventional ZnSe-based laser devices.

BeTe has roughly the same valence band position as GaAs [4], and in addition to the good lattice matching to GaAs it can also be used as pseudograding from p-type GaAs substrates to p-ZnSe for the use in inverted laser structures with the n-contact on top.

Finally, one can now even think of replacing the difficult and unstable nitrogen-plasma doping by arsenic doping in BeTe, since this element is a good choice in ZnTe, as reported before [5]. This is also a very promising point for the fabrication of light-emitting devices by MOVPE, because p-type doping is still a big problem with this technique. Especially the use of a BeTe/ZnSe superlattice as described below instead of a quaternary cladding layer may promote the fabrication of laser diodes by MOVPE.

3.1.2. Selenides

The structural quality of the Se-based ternaries and quaternaries (BeZn)Se and (BeMgZn)Se is also very high. We have reproducibly grown quaternary layers with a lattice mismatch lower than 0.1%, the FWHM of the rocking curves being under 25 arcsec

with a best value of 17 arcsec [4]. From these results we can conclude that Be is the ideal replacement this time of S, which – from the epitaxial point of view – is a rather inconvenient material because of its high vapour pressure, the strong temperature dependence of the sticking coefficient and its tendency to react with GaAs leading to defects at the III/V–II/VI-interface.

Concerning p-type doping the behaviour of the Be selenides is also similar to the sulphides. We have grown several N-doped quaternaries with different band gap energies, and above 3.0 eV the net acceptor concentration $N_A - N_D$ falls below 10^{16} cm^{-3}. Nevertheless, at lower energies of about 2.9 eV we have still measured $N_A - N_D = 2 \times 10^{17}$ by C–V profiling. More work has to be done to clarify whether these doping values are limited by similar compensation processes as compared to the ZnMgSSe : N system.

Further details about the p-type doping of Be chalcogenides are published in [6].

4. BeTe/ZnSe superlattices

The above results show that the p-type doping of the wide band gap selenides is still a problem. (BeMg)Te could be used for the p-type cladding layers in laser diodes, but the refractive index of this material is higher than that of ZnSe for wavelengths above about 450 nm, therefore the waveguiding properties of the laser structures would be distorted. On the other hand, this could be indeed a very interesting alternative for LEDs, where waveguides can be omitted. Here, we explore the possibility to use BeTe/ZnSe superlattices for the p-cladding. Since BeTe can be p-doped extremely high, the average doping level in such an SL should still remain very high, depending on the "dilution ratio" with ZnSe. Also the refractive index should be lower than that in ZnCdSe in these structures, which is an essential prerequisite for the usage as a cladding in laser diodes.

Fig. 1 shows the type II BeTe/ZnSe superlattice, i.e. ZnSe acts as a well in the conduction band and as a barrier in the valence band. Due to the type-II transition there is usually a local indirect absorption in such structures at about 1.8 eV at room temperature. To prevent this absorption, one has to calculate the suitable period widths of the superlattice at which the formation of minibands starts. These minibands can also have energies far higher than the type II-transition. The superlattice calculations have been performed by employing the envelope-function method in form of a standard Kronig–Penney model [7]. This model requires only a limited set of parameters, namely valence and conduction band offsets, respectively, and the effective electron and hole masses $m^*_{e,0}$ and $m^*_{h,0}$. Also the modest computing time needed is an advantage as compared to tight-binding, pseudopotential, orthogonalized plane wave methods, etc.

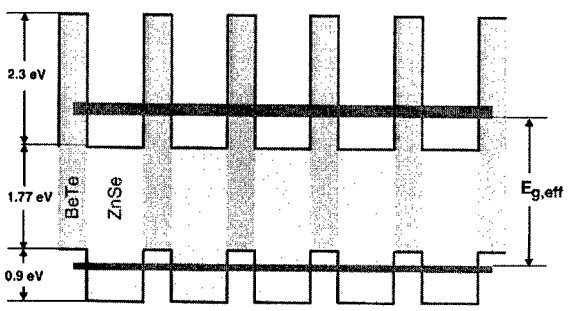

Fig. 1. BeTe/ZnSe type-II superlattice with minibands.

Table 1
Parameters used for the calculation of BeTe/ZnSe superlattices

	ZnSe	BeTe
Direct (indirect) band gap at RT (eV)	2.67	4.1 (2.8–2.9) [4]
Valence band offset to ZnSe (eV)	–	0.9
Lattice constant a_0 (Å)	5.668	5.622 [4]
Effective electron mass m^*_e/m_0	0.17 [8]	0.17
Effective hole mass m^*_h/m_0	0.65 [8]	0.65

If parameters were not known for BeTe, the values of ZnSe have been taken as a first approximation (see Table 1). Strain effects have been neglected, because both elastic constants and deformation potentials are unknown for BeTe until now and should differ significantly from other II–VI-materials, mainly due to the higher covalent bonding of this compound. An influence of the indirect

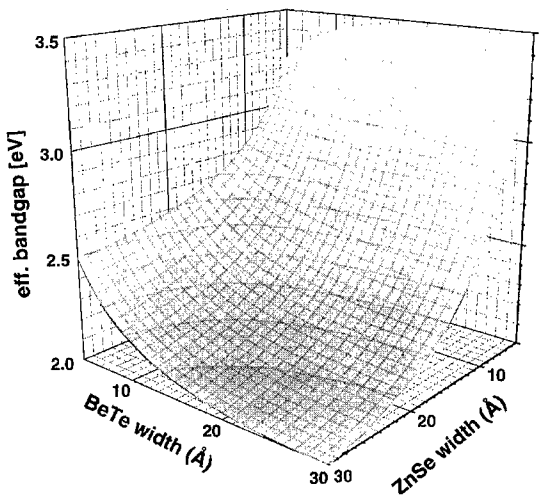

Fig. 2. Effective superlattice band gap $E_{g,eff}$ over BeTe and ZnSe width. The strong increase towards small ZnSe widths has its origin in the high confinement energy in the conduction band.

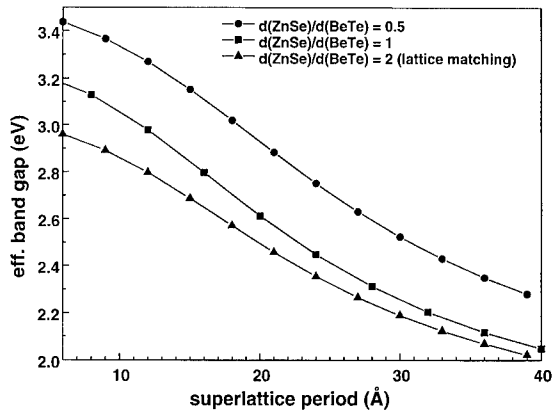

Fig. 3. The dependence of $E_{g,eff}$ on the superlattice period, for different thickness ratios $d_{ZnSe} : d_{BeTe}$.

gap of BeTe can be ignored, because the miniband energies in the conduction band of the SL lie below the indirect edge in the band structure of BeTe. This is the case for confinement energies in the conduction band not higher than about 1.2 eV. A disadvantage of this model is that it loses accuracy if we go to very small superlattice periods of a few monolayers, but nevertheless the feasibility of the proposed superlattice concept for the p-type doping can be checked. For finding a suitable combination of barrier and well thickness for a given effective band gap energy $E_{g,eff}$, the accuracy of the calculation is still high enough.

The dependence of $E_{g,eff}$ on the thickness of the BeTe and ZnSe layers is shown as an overview in Fig. 2. The biggest influence on the effective band gap comes from the confinement in the ZnSe conduction band quantum well, due to the high confinement energy and the lower effective mass of the electrons. The most important result is that $E_{g,eff}$ can indeed reach values of 2.9 eV and above by reducing the ZnSe thickness accordingly.

In Fig. 3 the dependence of $E_{g,eff}$ on the superlattice period for different thickness ratios $d_{ZnSe} : d_{BeTe}$ is displayed. To obtain an effective gap of, e.g. 2.7 eV and fulfil at the same time the lattice-matching condition to GaAs, appropriate values

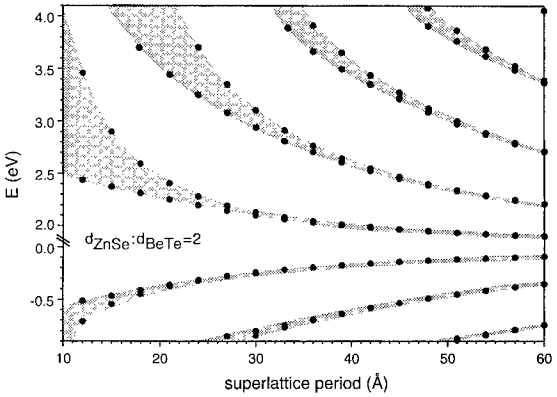

Fig. 4. Width of the minibands over superlattice period d. The thickness ratio of $d_{ZnSe} : d_{BeTe} = 2$ has been chosen to obtain lattice matching to GaAs.

would be around 12 Å for the ZnSe and 6 Å for the BeTe layer.

The width of the minibands over the superlattice period d is plotted in Fig. 4. For this calculation the ZnSe/BeTe thickness ratio has been chosen to obtain lattice matching to GaAs. A pronounced splitting of both minibands is seen only for values of d below 20 Å, which has again its origin in the high confinement energies for both conduction and valence band wells. This indicates that vertical transport under these conditions makes sense only for rather small periods.

5. Summary

Results concerning the p-type doping of Be chalcogenides have been presented. The possibility of using BeTe/ZnSe superlattices for the p-type doping of cladding layers has been examined by calculating the miniband structure in the frame of a standard Kronig–Penney model. This concept may circumvent the problems with the p-type doping of wide gap quaternary compounds like ZnMgSSe or BeMgZnSe. Experimental investigations to explore the feasibility of this concept are under way.

Acknowledgements

The authors want to thank P. Wolf-Müller and Th. Schuhmann for sample preparation, K. Schüll and V. Hock for metallisation and lithography, and A. Schönteich, R. Brauner and M. Fehn for keeping the MBE system running. The support of the Bundesministerium für Bildung und Wissenschaft, Forschung und Technologie (BMBF), the Deutsche Forschungsgemeinschaft (DFG) and the Bayerische Forschungsstiftung is gratefully acknowledged.

References

[1] M.A. Haase, J. Qiu, J.M. dePuydt and H. Cheng, Appl. Phys. Lett. 59 (1991) 1272.
[2] R.M. Park, M.B. Troffer, C.M. Rouleau, J.M. dePuydt and M.A. Haase, Appl. Phys. Lett. 57 (1990) 2127.
[3] A. Ishibashi, J. Crystal Growth 159 (1996) 555.
[4] A. Waag, F. Fischer, H.-J. Lugauer, Th. Litz, U. Zehnder, T. Gerhard, M. Möller and G. Landwehr, J. Appl. Phys. 80 (1996) 792.
[5] A. Kamata and H. Yoshida, Jpn. J. Appl. Phys. 35 (1996) L87.
[6] H.-J. Lugauer, A. Waag and G. Landwehr, J. Crystal Growth 161 (1996) 86.
[7] E.L. Ivchenko and G. Pikus, Superlattices and Other Heterostructures (Springer, Berlin, 1995) p. 73ff.
[8] P.M. Mensz, Appl. Phys. Lett. 64 (16) (1994) 2148.

ELSEVIER

Journal of Crystal Growth 175/176 (1997) 624–631

JOURNAL OF CRYSTAL GROWTH

Molecular beam epitaxy of BeTe on vicinal Si(1 0 0) Surfaces

Xiaochuan Zhou[1], Shan Jiang, Wiley P. Kirk*

NanoFAB Center, Engineering-Physics Building, Texas A&M University, College Station, Texas 77843-4242, USA

Abstract

BeTe was epitaxially grown on vicinal Si(1 0 0) substrates for the first time. Reflection high energy electron diffraction (RHEED) was used to study the initial growth mode and the surface structure. Transmission electron microscopy (TEM) was used to study the crystal quality. The material was grown on both bare and arsenic covered vicinal Si(1 0 0) surfaces. Smooth and well-ordered surface structures readily formed during the growth. Low stacking-fault densities were obtained in the BeTe epilayers. The potential applications of the new material are discussed briefly.

PACS: 81.15.Hi; 81.05.Dz; 81.05.Cy

1. Introduction

The growth of compound semiconductors on silicon substrates has been extensively studied as a means of integrating silicon-based electronic devices with compound-semiconductor-based optoelectronic devices [1]. Such studies were recently extended to the development of silicon-based quantum devices, in which silicon and compound semiconductors are both involved in bandgap tailoring [2]. The growth of II–VI compound semiconductors on Si(1 0 0) surfaces is unique because the interface charge problem can be eliminated by the use of a monolayer of group III or group V elements at the interface [3]. The use of an arsenic passivation layer was introduced by Bringans et al. for the purpose of growing ZnSe on Si(1 0 0) substrates [4]. We later used the arsenic passivation method to grow ZnS layers for the purpose of developing ZnS/Si double-barrier resonant-tunneling diodes, in which ZnS was used as a wide-bandgap tunneling barrier material [5, 6]. While the crystallinity of the ZnS and ZnSe layers was significantly improved by use of the arsenic passivation method, the problem of high stacking-fault densities in both layers remained. This has been attributed to the intrinsically low stacking-fault energies of ZnS and ZnSe materials [3]. We were, therefore, prompted to search for new semiconductor materials that have wide bandgaps, could be grown epitaxially on silicon substrates, and have high stacking-fault energies.

* Corresponding author. Fax: + 1 409 845 2590; e-mail: kirk@nanofab.tamu.edu.

[1] Present address: Electronics Manufacturing Laboratory, University of Michigan, Ann Arbor, Michigan 48105-2551, USA.

0022-0248/97/$17.00 Copyright © 1997 Published by Elsevier Science B.V. All rights reserved
PII S0022-0248(96)00911-6

The result of our search has focused on a group of beryllium-VI compound semiconductors, including BeS, BeSe, and BeTe. According to the literature, BeS, BeSe, and BeTe, all have zincblende crystal structures, with lattice constants of 4.8630, 5.1477, and 5.6269 Å, and bandgaps of 6.10, 4.50, and 2.7 eV, respectively [7–9]. Using a simple linear interpolation, we find that an alloy, $BeSe_{0.45}Te_{0.55}$, can be lattice matched to silicon with a bandgap of 3.51 eV. Therefore, the Be-VI compound semiconductors should make good candidates for our study.

Among the most important features of the Be-VI compound semiconductors is their low ionicities. According to Phillips [10], this group of compounds have the lowest ionicities among all II–VI compound semiconductors. As a matter of fact, according to the same reference, their ionicities are even lower than that of GaAs. In general, there is a strong correlation between the stacking-fault energy and the ionicity of III–V and II–VI compounds. For example, Takeuchi et al. [11] developed an empirical correlation between the stacking fault energy and the charge redistribution index of both II–VI and III–V compounds. The charge redistribution index measures the charge transfer accompanying the strain of the bond length and can be related to the Phillips' ionicity according to Phillips and Van Vechten [12]. Using Takeuchi's method, we calculated the stacking fault energies of the Be-VI compound semiconductors and plotted the results in Fig. 1 along with the experimental data of other II–VI and III–V compound semiconductors. According to this prediction, all three Be-VI compounds have high stacking-fault energies, which are interestingly even higher than that of GaAs.

The study of Be-VI semiconductors may also have an impact on the improvement of II–VI blue lasers [13]. The short lifetime problem of the present II–VI blue lasers arises from the ease with which crystal defects generate and propagate in ZnSe based materials [14, 15] and this is believed to be the result of the weak ionic chemical bonds [16]. The source of the dislocations in the ZnSe-based laser structures has been identified with stacking faults that originate at the ZnSe/GaAs interface regions [14]. The lower ionicities, stronger chemical bonds, and higher stacking-fault energies of the Be-VI semiconductors may help to strengthen the II–VI laser materials and to increase the lifetimes of the laser devices. This concept is supported by a recent theoretical study of lattice elastic rigidity of II–VI semiconductor materials [17].

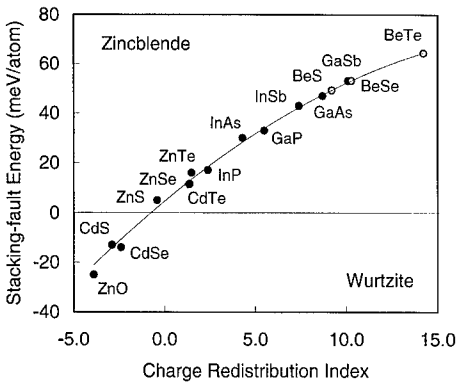

Fig. 1. Stacking fault energy of III–V and II–VI compounds. Solid dots are the experimental data, from Ref. [11], and open circles are the predicted values according to an empirical calculation method given in the same reference.

In this paper, we report initial results of molecular beam epitaxial growth and TEM studies of BeTe on vicinal Si(1 0 0) substrates.

2. Experimental procedure

Epitaxial growth was carried out in a Fisons VG-V80S MBE system. The system was equipped with an e-beam evaporator for silicon deposition and three effusion cells for Be, Te, and As sources. The MBE system was also equipped with a 15 keV RHEED system for surface structural studies and a Dycor M200 residual gas analyzer (RGA) for gas-phase composition analysis. The RGA was positioned in the line of sight of the substrate and had an orifice to confine the detection only to those atoms/molecules backscattered or desorbed from the substrate surface.

N-type vicinal Si(1 0 0) substrates with a 4° offcut towards [0 1 1] direction were used. The silicon

substrates were chemically cleaned using a peroxide cleaning procedure, which left surfaces covered with a thin layer of oxide formed in a $HCl : H_2O_2 : H_2O = 3 : 1 : 1$ solution [18]. The substrates were annealed in the MBE preparation chamber at 870°C for 20 min and then transferred into the growth chamber. A 1000 Å thick silicon buffer layer was grown on each substrate at a temperature of 620°C to produce a smooth starting surface. Double stepped surfaces were obtained by annealing the substrate at 870°C and then gradually lowering the temperature to room temperature. RHEED patterns of single-domain 2×1 reconstructed Si(1 0 0) surfaces were observed.

Arsenic deposition on the silicon substrates was performed by using the procedures described by Bringans et al. [19]. Single-domain Si(1 0 0) : As 2×1 and Si(1 0 0) : As 1×2 reconstructed surfaces were obtained by depositing arsenic at an As_4-beam partial pressure of 1.5×10^{-5} mbar and at substrate temperatures of 570°C and 0°C, respectively.

BeTe layers were grown in two steps. The first 50–100 Å thick layer was grown at a substrate temperature of 400°C and the remaining layer was grown at 500°C. The growth rate was 0.2–0.4 μm/h, and the Te_2/Be beam partial-pressure ratio was about 10. Since this work represents an initial effort, the growth conditions have by no means been optimized. The layer thickness and the growth rate was determined by using TEM. It was found that BeTe was somewhat air sensitive. After an extended exposure of a BeTe film to air, the film darkened in color. In order to protect the BeTe surfaces from contacting air, we deposited a 100–300 Å thick silicon-cap layer on top of the BeTe surface. According to the observation on Be-VI bulk materials by Yim et al. [8], BeSe and BeS are stable in air. Therefore, the formation of a ternary compound, such as BeSeTe and BeSTe, is expected to improve the stability in air.

Cross-sectional TEM samples were prepared by standard mechanical cutting, lapping and ion-milling procedures. To reduce the time of reaction with air, after ion milling, the samples were immediately transferred into a TEM system. All TEM micrographs were taken by using a JEOL 2010 microscope at 200 kV.

3. Results and discussions

3.1. BeTe growth on a bare Si(1 0 0) surface

RHEED was used to study the growth process. During the BeTe growth on a bare Si(1 0 0) 2×1 surface, the first 100 Å of the growth was deposited in island-growth mode, as characterized by spotty RHEED patterns. Although the island-growth mode can be partially attributed to the lattice mismatch between BeTe and the silicon substrate, the main reason is the unfavorable interfacial chemistry. It is likely that the formation of an interface dipole between Si(1 0 0) and BeTe(1 0 0) prevented the formation of an abrupt interface [20]. This was demonstrated in our previous study of ZnS growth on Si(1 0 0) surfaces [5]. While ZnS and silicon are almost lattice-matched, the initial deposition was characterized as island growth.

As the BeTe film grew thicker, from about 100 to 150 Å up, streaky 2×1 RHEED patterns became apparent, indicating the formation of a smooth and well ordered surface. These RHEED patterns are not shown here because they are very similar to the ones shown in Fig. 2c and Fig. 2d for a BeTe layer grown on a Si(1 0 0) : As 2×1 surface. The BeTe growth was conducted under a tellurium over-pressure condition, therefore the BeTe surface was tellurium rich and the 2×1 RHEED pattern was attributed to the formation of Te–Te dimers. We noted that the BeTe surface and the initial Si(1 0 0) substrate surface had the same 2×1 reconstruction. This indicates that the surface tellurium dimers have the same azimuthal orientation as that of silicon dimers on the substrate surface, both being parallel to the surface-step edges. Since, in silicon and zincblende crystal structures along the $\langle 1\,0\,0 \rangle$ directions, atoms in every two atomic layers have the same bond orientations, the atomic sequence at the BeTe/Si(1 0 0) interface must be –Si–Si–Be–Te–. In other words, the first layer on the Si(1 0 0) surface was beryllium. This is different from the interface structures of ZnS/Si(1 0 0) and ZnSe/Si(1 0 0), grown by molecular beam epitaxy. In those cases, due to the strong chemical adsorption of sulfur and selenium (group VI elements) on Si(1 0 0) surfaces, the first layers were dominantly sulfur and selenium [5, 4]. It is interesting to note that during our initial

growth of BeTe on a Si(1 0 0) surface, the tellurium shutter was actually opened first. The formation of Si–Be bonds implies a stronger adsorption of Be than Te on a Si(1 0 0) surface. A detailed study on the surface structure of Te adsorption on Si(1 0 0) 2×1 surfaces was performed by Higuchi et al. [21], who found that Te formed ordered phases up to one monolayer of coverage at 100°C. However, to our knowledge, no study of Be adsorption on Si(1 0 0) surfaces has yet performed.

3.2. BeTe growth on arsenic passivated Si(1 0 0) surfaces

On Si(1 0 0) : As 2×1 and Si(1 0 0) : As 1×2 reconstructed surfaces, BeTe growth exhibited a much improved initial growth mode, as compared with that on bare Si(1 0 0) 2×1 surfaces. Fig. 2(a), Fig. 2(b), and Fig. 3(a), Fig. 3(b) are the RHEED patterns of Si(1 0 0) : As 2×1 and Si(1 0 0) : As 1×2 surfaces, respectively. On a Si(1 0 0) : As 2×1 surface, the As–As dimers are parallel to the surface-step edges, while on a Si(1 0 0) : As 1×2 surface, the As–As dimers are perpendicular to the surface-step edges. On the two Si(1 0 0) : As surfaces, we observed similar BeTe growth behavior. During the first one or two monolayers of BeTe growth, the RHEED patterns became diffused and lost reconstruction lines. However, from the third monolayer (about 8 Å) up, the RHEED patterns became streaky and contained reconstruction lines, implying the formation of smooth and ordered BeTe surfaces. It is interesting to note that the BeTe growth on the Si(1 0 0) : As surfaces was neither in the Volmer–Weber growth mode (featured with initial three-dimensional growth) nor in the Stranski–Krastanov growth mode (featured with initial two-dimensional growth followed by the formation of three-dimensional islands). The diffused RHEED patterns at the very early stage of growth suggest that some initially adsorbed atoms do not occupy the exact epitaxial sites. However,

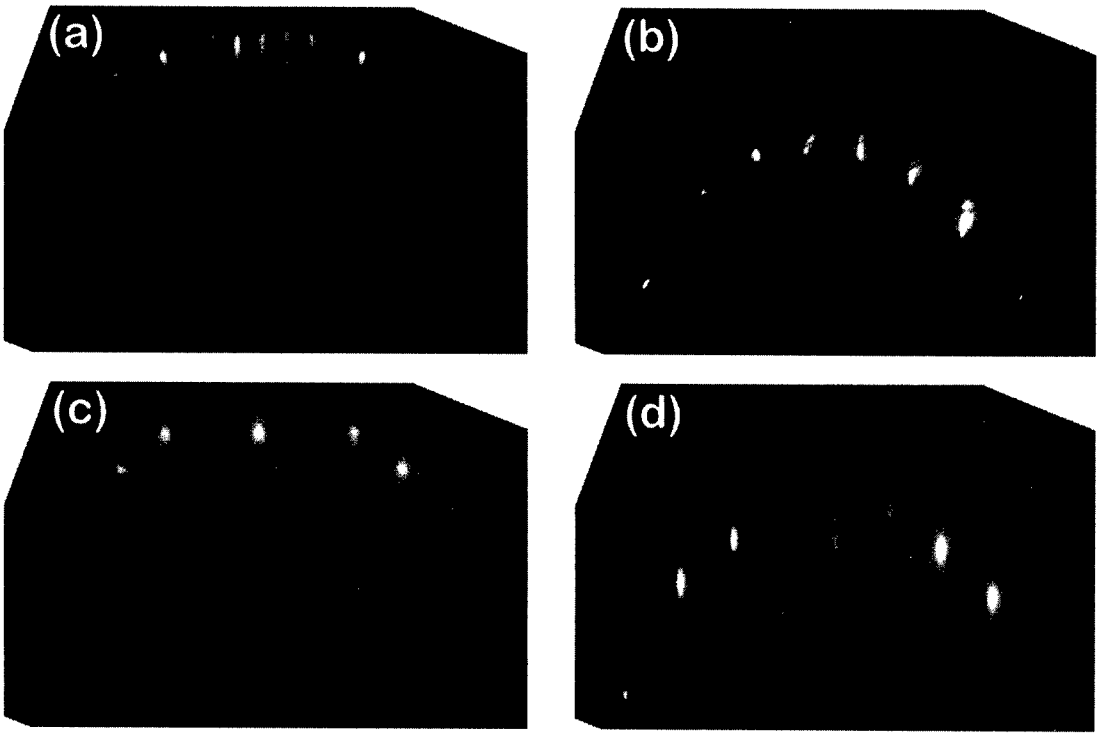

Fig. 2. RHEED patterns of a Si(1 0 0) : As 2×1 surface at (a) [0 $\bar{1}$ $\bar{1}$] and (b) [0 $\bar{1}$ $\bar{1}$] azimuthal directions, and of a BeTe 2×1 surface at (c) [0 $\bar{1}$ $\bar{1}$] and (d) [0 $\bar{1}$ $\bar{1}$] azimuthal directions.

the surface quickly became smooth and well ordered after adding just a couple of monolayers of BeTe to the surface, a similar phenomenon was observed in our study of ZnS growth on Si(1 0 0) : As surfaces. The exact growth mechanism is yet to be understood.

The layer thickness in the initial growth period, as given above, is an estimate, and was derived from the growth time and the average growth rate. However, by using a residual-gas analyzer in front of the substrate, we detected the desorption of beryllium from the substrate during the growth even at a low growth temperature of 400°C. This indicates that the sticking coefficient for Be is less than one. We also observed a higher beryllium desorption, as measured by the Be partial pressure, at the beginning of the growth. While the partial-pressure transient might be attributed to the temperature change in the beryllium effusion cell after the shutter opening, we leave open the possibility that the observation was due to a transient in the growth rate during the initial growth period. In any case, it is reasonable to expect a difference in the sticking coefficient of beryllium on a Si(1 0 0) : As surface as compared to a BeTe surface. Since we observed higher Be desorption in the initial growth period, the actual growth-mode transition from a somewhat disordered deposition into a planar epitaxial growth could have occurred at a BeTe thickness less than 3 monolayers.

Shown in Fig. 2c, Fig. 2d, Fig. 3c and Fig. 3d are the RHEED patterns of BeTe layers grown on the Si(1 0 0) : As 2×1 and Si(1 0 0) : As 1×2 surfaces, respectively. These RHEED patterns indicate the formation of BeTe 2×1 and BeTe 1×2 reconstructed surfaces on the two Si(1 0 0) : As surfaces. As mentioned earlier, the BeTe surfaces were terminated with tellurium dimers. For the same reason as explained earlier, we find that the BeTe layers have the same Te-bond orientations as those of initial arsenic atoms, regardless of starting with a Si(1 0 0) : As 2×1 or a Si(1 0 0) : As 1×2 surface.

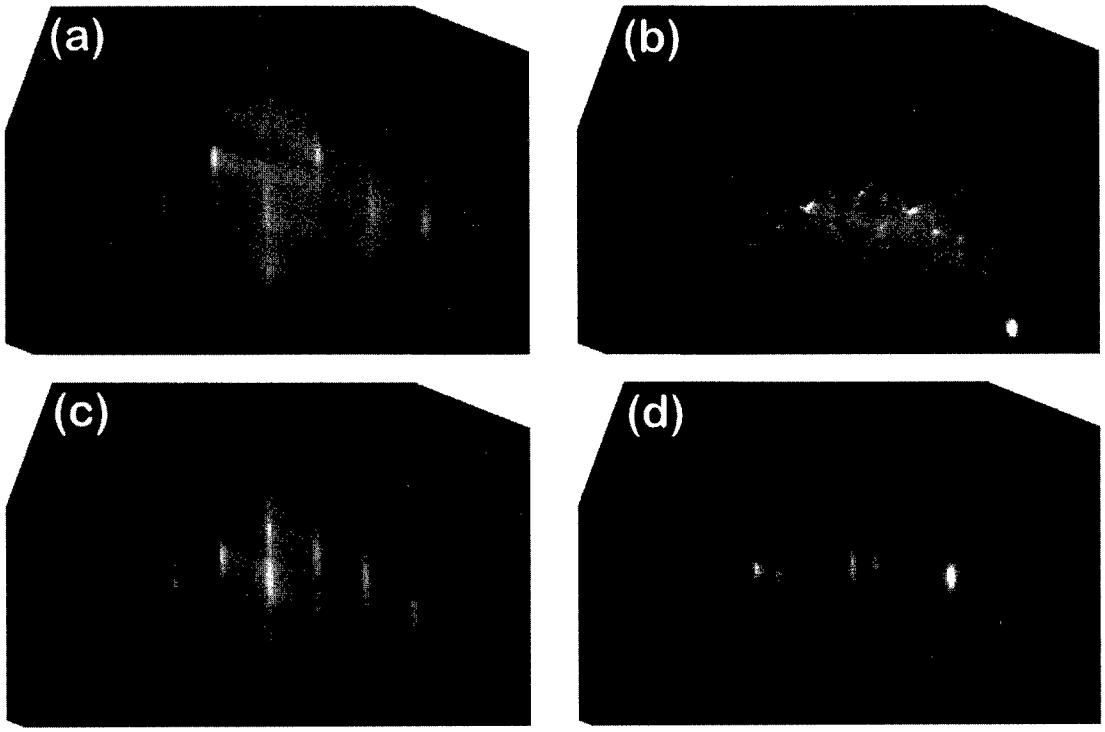

Fig. 3. RHEED patterns of a Si(1 0 0) : As 1×2 surface at (a) [0 $\bar{1}$ $\bar{1}$] and (b) [0 $\bar{1}$ $\bar{1}$] azimuthal directions, and of a BeTe 1×2 surface at (c) [0 $\bar{1}$ $\bar{1}$] and (d) [0 $\bar{1}$ $\bar{1}$] azimuthal directions.

Secondary-ion-mass-spectroscopy (SIMS) profile analysis of these samples revealed the arsenic remained at the interface between BeTe and silicon. Therefore, our RHEED results in Figs. 2 and 3 suggest an interface sequence of –Si–Si–As–B–Te–, for the BeTe layers grown on the Si(1 0 0) : As surfaces. According to an electron-accounting argument, all atoms in this interface structure are fully coordinated, therefore no interfacial dipoles are present and the structure is energetically stable [4].

When compared with the growth of ZnS, ZnSe, and GaAs on silicon surfaces, BeTe exhibited unique growth behavior of easily forming smooth surfaces. During the ZnS and ZnSe growth on Si(1 0 0) surfaces, even with the arsenic passivation layers, it was difficult to produce smooth enough surfaces for the observation of surface reconstructions by using RHEED [2, 22]. In the case of GaAs growth on silicon substrates, according to our experience, three-dimensional growth continues for several hundred to even a thousand angstroms before the surface becomes smooth. BeTe has about the same lattice mismatch that GaAs has on silicon substrates. However, for the BeTe growth on Si(1 0 0) : As surfaces, after only about three monolayers of growth, the epitaxial surface became smooth enough to observe the streaky RHEED patterns of a reconstructed surface. Even on a bare Si(1 0 0) surface, as discussed earlier, the BeTe epitaxial film became smooth within about 100–150 Å of growth.

3.3. TEM results

Fig. 4 shows a cross-sectional micrograph of a BeTe layer grown on a bare vicinal Si(1 0 0) substrate. In the BeTe/Si-substrate interface region, we observed relatively high densities of misfit dislocations "M" and stacking faults "S". The misfit dislocations were expected because of the large lattice mismatch of 3.6% between BeTe and Si. As for the stacking faults, most of them were annihilated within 150 Å. This thickness relates closely to our RHEED observation that island growth prevailed during the initial growth until about 100–150 Å. Most likely the stacking faults were formed at the peripheries of the islands when the islands collided with each other. Very few stacking faults extended to the upper surface of the 1300 Å thick BeTe layer. We also note that the crystal defect structure of the BeTe layer, shown in Fig. 4, is significantly different from that of ZnS and ZnSe layers grown on the same type of bare vicinal Si(1 0 0) surfaces [3, 4]. In both ZnS and ZnSe, the crystal defects were mostly microtwins lying exclusively in one of the two $\{1\,1\,1\}$ planes that are parallel with the surface-step edges. Although we observed the formation of microtwins in the BeTe layer, in high-resolution micrographs which are not shown here, we did not observe any anisotropy of the stacking faults and microtwins. This suggests a different nucleation mechanism occurred for the stacking fault formation. More importantly, the stacking-fault density in the upper portion of the BeTe layer, shown in Fig. 4, is about 2 to 3 orders of magnitude smaller than those in either ZnS or ZnSe layers of similar thickness grown on the same type of vicinal Si(1 0 0) surfaces.

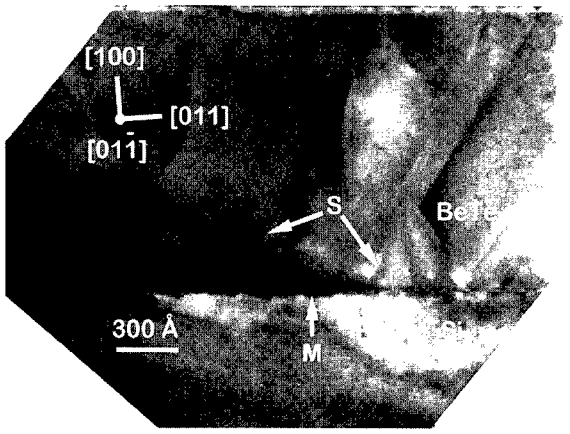

Fig. 4. Cross-sectional TEM micrograph of a BeTe layer grown on a bare vicinal Si(1 0 0) 2 × 1 surface. In the micrograph, arrows "S" point to stacking faults and arrows "M" point to misfit dislocations.

Fig. 5 shows a cross-sectional TEM micrograph of a BeTe layer grown on a Si(1 0 0) : As 2 × 1 surface. This layer showed even more improved crystal quality over the one grown on a bare Si(1 0 0) 2 × 1 surface. Very few stacking faults "S" can be observed in the region close to the epilayer/substrate interface. In this micrograph, we do not observe any stacking faults extending into or

emerging from the upper portions of the layer. The stacking fault density in a BeTe layer grown on a Si(1 0 0) : As 2×1 surface averages about one quarter to one tenth of that in the BeTe layer grown on a bare Si(1 0 0) 2×1 surface. This demonstrates the effectiveness of the arsenic passivation method. Our TEM study of a BeTe layer grown on a Si(1 0 0) : As 1×2 surface revealed similar crystal characteristics as the one shown in Fig. 5. We also compared the stacking fault density in the BeTe layers grown on Si(1 0 0) : As surfaces with that of ZnS layers of similar thickness grown on similarly prepared Si(1 0 0) : As surfaces [3]. We found about 100 times fewer stacking faults in the BeTe layers than in the ZnS layers. From Fig. 5 we also found that all the misfit dislocations "M" are confined to the epilayer/substrate interface with no threading dislocations observed, indicating a threading dislocation density below approximately 10^7 cm^{-2}.

The TEM results in Figs. 4 and 5 establish that BeTe has a low tendency to form stacking faults. This finding is consistent with our prediction of a high stacking fault energy for the material, as shown in Fig. 1. With the optimization of the growth conditions, further improvement of the crystal quality can be expected.

The demonstration of high-quality BeTe layers grown on Si(1 0 0) : As surfaces opens up the possibility for many applications. In addition to the ones mentioned in the introduction, the material can also be used as a template or as an interlayer for the epitaxial growth of other compound semiconductors on silicon substrates. According to our estimation shown in Fig. 1, BeSe and BeS also have high stacking fault energies. Therefore, it is reasonable to expect that high crystal-quality layers of the alloys of these Be-VI compounds can be grown epitaxially on silicon substrates. These alloy layers could then form the epitaxial templates of a wide range of lattice constants.

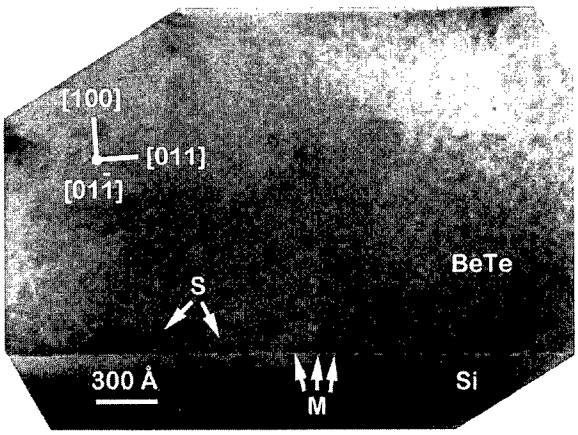

Fig. 5. Cross-sectional TEM micrograph of a BeTe layer grown on a Si(1 0 0) : As 2×1 surface. In the micrograph, arrows "S" point to stacking faults and arrows "M" point to misfit dislocations.

4. Conclusions

BeTe was shown to form high-quality epitaxial layers of low stacking fault densities on Si(1 0 0) substrates. On arsenic passivated Si(1 0 0) surfaces, a two-dimensional growth mode prevailed in the early growth stages in spite of a large lattice mismatch between BeTe and the silicon substrate. This study, therefore, provides a basis for the study of material fabrication and device development involving epitaxially grown Be-VI compound semiconductors.

Acknowledgements

This work was supported in part by Texas High Education Coordinating Board ARP-999903219, NSF ECS-9306293, and AFOSR/ARPA AF9620-96-C-0001. We are grateful to Robert Klima for his technical support. We acknowledge helpful discussions with Drs. R.D. Bringans of Xerox Corp. We acknowledge the Electron Microscopy Center of Texas A&M University for providing TEM facilities.

References

[1] R. Houdré and H. Morkoç, CRC Critical Rev. Solid State Mater. Sci. 16 (1990) 91.
[2] X. Zhou, S. Jiang, F. Li, G.F. Spencer, R.T. Bate and W.P. Kirk, in: Proc. 1995 IEEE Cornell Conf. on Adv. Concepts in High Speed Semi. Dev. and Circuits (1995) p. 498.

[3] L.T. Romano, R.D. Bringans, X. Zhou and W.P. Kirk, Phys. Rev. B 52 (1995) 11201.
[4] R.D. Bringans, D.K. Biegelsen, L.-E. Swartz, F.A. Ponce and J.C. Tramontana, Phys. Rev. B 45 (1992) 13400.
[5] X. Zhou and W.P. Kirk, Mater. Res. Soc. Symp. Proc. 318 (1994) 207.
[6] X. Zhou, F. Li, G.F. Spencer and W.P. Kirk, Mater. Res. Soc. Symp. Proc. 380 (1995) 3.
[7] W. Zachariasen, Z. Phys. Chem. (Leipzig) 119 (1926) 201; 124 (1926) 277, 440.
[8] W.M. Yim, J.P. Dismukes, E.J. Stofko and R.J. Paff, J. Phys. Chem. Solids 33 (1972) 501.
[9] R.L. Sarkar and S. Chatterjee, J. Phys. C 10 (1977) 57.
[10] J.C Phillips, Bonds and Bands in Semiconductors (Academic, New York, 1973).
[11] L. Takeuchi, K. Suzuki and K. Maeda, Phil. Mag. A 50 (1984) 171.
[12] J.C. Phillips and J.A. Van Vechten, Phys. Rev. Lett. 23 (1969) 1115.
[13] A. Waag. F. Fischer, H.J. Lugauer, Th. Litz, J. Laubender and G. Landwehr, Int. Symp. on Blue Light Emitting Diodes and Lasers, Chiba (1996).
[14] S. Guha, J.M. DePuydt, G.E. Hfler, M.A. Haase, B.J. Wu and H. Cheng, Appl. Phys. Lett. 63 (1993) 3023.
[15] S. Guha, J.M. DePuydt, M.A. Haase, J. Qiu and H. Cheng, Appl. Phys. Lett. 63 (1993) 3107.
[16] H. Morkoç, S. Strite, G.B. Gao, M.B. Lin, B. Sverdlov and M Burns, J. Appl. Phys. 76 (1994) 1363.
[17] C. Vèrié, in: Proc. Int. Conf. Semi. Heteroepitaxy, Montpellier, France (1995).
[18] R.C. Henderson, J. Electrochem. Soc. 119 (1972) 772.
[19] R.D. Bringans, D.K. Biegelsen and L.-E. Swartz, Phys. Rev. B 44 (1991) 3054.
[20] W.A. Harrison, E.A. Kraut, J.R. Waldrop and R.W. Grant, Phys. Rev. B 18 (1978) 4402.
[21] S. Higuchi and Y. Nakamishi, J. Appl. Phys. 71 (1992) 4277.
[22] R.D. Bringans, private conversation.

ELSEVIER

Journal of Crystal Growth 175/176 (1997) 632–636

JOURNAL OF CRYSTAL GROWTH

Blue-light emission from ZnSTe-based EL devices

I.K. Sou*, J. Mao, Z. Ma, W.S. Chen, Z. Yang, K.S. Wong, G.K.L. Wong

Department of Physics, Hong Kong University of Science and Technology, Clear Water Bay, Kowloon, Hong Kong

Abstract

We have demonstrated blue-light emission from ZnSTe-based electroluminescence (EL) devices. Photoelectroluminescence technique is used to study field-quenching effects on Te isoelectronic centers in undoped ZnSTe alloy. Heavy doping by Al in ZnSTe alloy is found to help reduce field quenching action and gives rise to much higher EL emission in ZnSTe : Al-based Schottky-barrier type structures. *I–V* characteristics and emission spectra reveal that a tunneling dominated mechanism is responsible for generating the carriers for impact excitation of the localized states associated with Te isoelectronic centers in these structures.

PACS: 73.40.Q; 85.30.H; 85.30.K; 81.15.H

1. Introduction

ZnS-based thin film electroluminescence (EL) devices are of growing interest because of their application for monochrome and full-color displays. [1] A well-known example is amber emitting ZnS : Mn thin film device initiated by Inoguchi and Mito. [2] ZnS : Te owns excellent bound-exciton photoluminescence properties attributed to the large difference in the electronegativity of Te (2.1) and Se (2.4), which results in efficient trapped-exciton recombination at Te isoelectronic traps [3–6]. The recent studies reported by Mach et al. [7] demonstrated that field quenching or even more likely impact ionization of the lower bound excitons by the energetic carriers occurs in the ZnS : Te system which implies that this system may not suitable for high-field EL applications. However, it does not rule out the potential use of Te isoelectronic centers as low-field EL emitters such as schottky-barrier and carrier-injection type of optoelectronic structures. In fact, Yu et al. [8] have reported the operation of a superbright-green-light-emitting diode (LED) based on ZnSeTe wells, the superior performance of which is attributed to the Te isoelectronic centers present in the active layers.

Recently, we reported the first successful molecular beam epitaxy (MBE) growth of $ZnS_{1-x}Te_x$ system with $0 \leqslant x \leqslant 1$ on both GaAs and Si substrates [9]. Very strong photoluminescence was observed in samples with x smaller than 10%. The color of the emitted light can be tuned from deep blue to

* Corresponding author. Fax: + 852 2358 1652; e-mail: phiksou@usthk.ust.hk.

0022-0248/97/$17.00 Copyright © 1997 Published by Elsevier Science B.V. All rights reserved
PII S0022-0248(96)01002-0

yellow by adjusting Te composition. Room temperature external quantum efficiency of about 4% has been achieved on epilayers as thin as 1000 Å. ZnSTe alloy enjoys the advantage that at 3% Te concentration, the alloy is perfectly lattice-matched with Si substrate. It also seems to have stronger thermal-mechanical strengths than those of ZnSe compound according to our photoluminescence and cathodoluminescence studies. Quite recently, we successfully demonstrated n-type doping of this alloy system using incorporation of Al during MBE growth [10]. Electron carrier concentration as high as 1.3×10^{19} cm^{-3} has been achieved.

In this work, we report the demonstration of blue-light EL emission from various ZnSTe-based metal–insulator–semiconductor (MIS) structures. The role of n-type doping in reducing field quenching of carriers bound to Te centers in the active layer is discussed. The mechanism of light emission from these structures is also investigated through their I–V and emission spectral characteristics.

2. Experimental procedure

The EL structures studied in this work are MBE-grown undoped and Al-doped $ZnS_{1-x}Te_x$ layers with x value chosen for blue-color emission ($\sim 1\%$). A VG V80H MBE system was used for the growth. Epi-ready semi-insulating GaAs(100) wafers with $2 \pm 0.1^\circ$ off toward $\langle 0\,1\,1 \rangle$ direction were used as substrates. Detailed growth condition and structural characterization have been described elsewhere [10, 11].

A 5×5 mm^2 piece is cut from each as-grown structure for device processing. A 200 Å thick Au layer was used to serve as a transparent electrode. It was deposited by RF sputtering technique on top of the as-grown structure. Array of square EL cells with area of 400×400 μm^2 was fabricated on each piece by standard photolithography together with wet chemical etching using Br–$C_2H_6O_2$ solution. The device wafer was then mounted on a copper sample holder using conductive silver ink for further optical and electrical measurements.

The EL cells were excited electrically using a Keithley 237 source measure unit. A sharp needle probe was used to make contact with the Au electrode. Photoexcitation was performed using a frequency-doubled output (wavelength = 395 nm, pulse width = 200 fs) of a Ti-sapphire laser. The luminescence spectrum was measured using a spectrometer and a charge coupled device.

3. Field quenching effect in undoped EL structures

In our earlier studies, structures of Au/undoped-$ZnS_{1-x}Te_x/n^+$-GaAs substrate are used with the thickness of the $ZnS_{1-x}Te_x$ active layer ranges from 0.5 to 1 μm. Fig. 1 shows the typical PL and EL spectra from a device based on these structures. The similarity between these two spectra indicates that the EL emissions are likely due to a trapped-exciton recombination at Te_n centers as in the case of PL emission. Mach et al. [7] observed that the EL spectrum is significantly redshifted compared to the PL spectrum of a ZnSTe layer with similar composition sandwiched between dielectrics of Al and Zr oxides prepared by E-beam evaporation. They argued that their observed emission was due to the excitons bound by Te_n ($n \geqslant 4$) while lower-bound excitons are destroyed by field action. The difference between our observations may be attributed to the better crystalline quality of our MBE-grown structures. In fact, the threshold field strength for our EL emission is about a factor of two lower than that for their structures. Thus the field quenching effect on the lower-bound excitons is less serious in our case.

However, similar to the Mach et al. observation, the EL emission from our undoped ZnSTe layer is much weaker than its strong PL emission. We believe that this is not due to impact ionization of the bound excitons by energetic carriers because in separate studies we reported earlier [12], the efficiency of cathodoluminescence from ZnSTe alloy is found to be as high as that of PL emission. We suspect that field quenching could be the main reason behind the poor EL emission obtained even in our MBE-grown structures. PL measurements under DC bias, the so-called photoelectroluminescence (PEL), were performed on the EL cells to further investigate the light emission characteristics. The range of applied bias used did not exceed the threshold for EL emission. Fig. 2 shows the

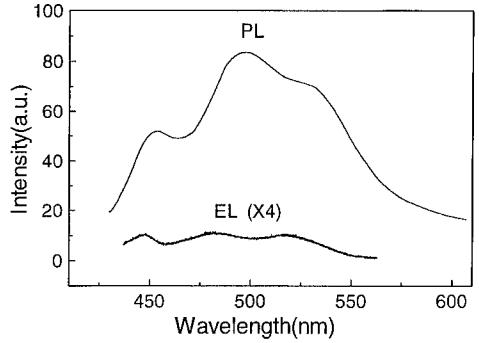

Fig. 1. PL and EL spectra of an undoped ZnSTe EL cell.

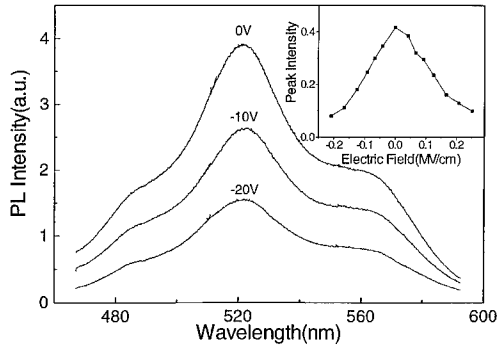

Fig. 2. PEL spectra of an undoped ZnSTe EL cell as a function of DC bias. The inset displays the PEL peak intensity versus applied electric field strength.

PEL spectra as a function of negative bias in which Au layer was connected to the negative electrode. One can see that a monotonous decrease in the PEL intensity occurs with increasing bias. Similar behaviors also appear when the EL cells are positively biased. The inset in Fig. 2 shows the change of peak intensity of the overall PEL spectrum as a function of bias, which shows that the monotonous decrease is nearly symmetric in both direction of bias. The fact that the whole spectrum changes nearly uniformly under bias indicates that the field quenching quite evenly attacks the different Te_n centers, in consistency with their EL emission described earlier. These results, unfortunately, still indicate that there is not much hope for developing ZnSTe as blue EL emitter in the high-field regime of conventional EL design.

4. Strong blue EL emission from doped-ZnSTe active layers

By incorporating Al during MBE growth, ZnSTe alloy with a few % of Te can be heavily doped to n-type. Detailed results of our doping studies have been described elsewhere [10]. Following successful n-type doping of ZnSTe alloy, we prepared several new EL structures. The first one (labeled #1) was fabricated on a p^+-type GaAs substrate and is shown in the inset of Fig. 3b. Strong blue EL emission with a few μW of output power can be detected at room light by naked eyes using 12 V DC excitation with Au being the negative electrode. Light emission can also be detected in the opposite bias direction though the intensity is at least an order of magnitude lower. Viewing under a microscope, the luminescence is uniformly distributed across the entire square EL cell. The measured EL spectrum of this structure is shown in Fig. 3a. It consists of a blue emission centered at 500 nm and

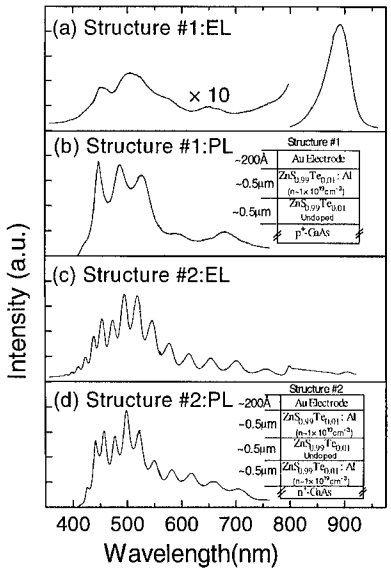

Fig. 3. PL and EL spectra of two ZnSTe : Al-based EL structures.

a rather strong infrared peak near 890 nm which is likely due to the carrier-injected emission from the p–n junction in the GaAs side of the II–VI/III–V interface. In order to understand the mechanisms behind the blue emission, we fabricated a similar structure (labeled #2) on an n^+-GaAs substrate as shown on the inset of Fig. 3d. The corresponding EL spectrum of structure #2 displayed in Fig. 3c only shows a blue emission peak centered at 500 nm. The non-existence of the infrared EL peak for structure #2 is expected since the p–n junction that appears in structure #1 is not present in this structure. It should be noted that the blue emission from structure #2 is as strong as that from structure #1 and also occurs only when the Au electrode is negatively biased. Measurements on structures similar to #1 and #2 but without the undoped ZnSTe layer still show similar transport and EL emission characteristics. It thus indicates that the undoped layer does not play much a role in these measurements. These observations imply that the blue emission is due more likely to localized states in the ZnSTe : Al layer that are impact-excited by hot carriers injected from the Au electrode. Fig. 3 shows that the PL spectra for both structures are very similar. Our earlier optical studies of Al-doped ZnSTe alloy show that Al dopant centers can also give blue luminescent states in ZnS matrix. A ZnS : Al EL structure similar to structure #2 but without Te incorporation was then prepared for comparison. The blue EL emission from this structure was found to be about an order of magnitude weaker than that from structure #2. These observations suggest that the efficient localized states in the ZnSTe : Al layer are mainly contributed by Te_n isoelectronic centers. It should also be noted that the relatively much higher EL efficiency in these new EL structures is a result of the fact that field quenching effect on Te centers in heavily n-type doped ZnSTe active layer is significantly reduced since no bias is applied to this conducting layer. This should be contrasted with the case for undoped ZnSTe active layers described in the previous section.

Room temperature *I–V* measurements were also performed on these structures to further investigate their light-emission mechanisms. The characteristics of structure #1 is made complicated by the existence of the additional p–n junction at the epilayer/substrate interface and thus is excluded in our discussion. The *I–V* curve recorded for structure #2 is displayed in Fig. 4. It does not resemble an ideal Schottky-barrier diode and show two distinct characteristics: (1) a large turn-on voltage is required even in the forward bias direction; (2) the diode conducts better in the reverse direction than in the forward direction. The large turn-on voltage possibly results from high contact resistance that exists between the needle probe and the Au electrode, as well as from the non-standard ohmic contact material used for the n^+-GaAs substrates. Since in our work the Au electrode is formed ex situ after the MBE-grown structures are exposed to atmosphere, a thin layer of oxide or other contaminants is expected to be present between the top epilayer and the Au electrode. An electron energy diagram including interfacial layer δ_{ox} and surface states, based on Bardeen's model [13], probably represents our EL structures better. Such a schematic drawing is shown in the inset of Fig. 4. The Al-doped ZnSTe layer in structure #2 is doped so heavily ($\sim 1 \times 10^{19}$ cm^{-3}) that the depletion layer width is sufficiently reduced and the field emission and tunneling field emission dominate the current flow. Rideout [14] has pointed out that in tunneling-dominated metal–semiconductor contacts, the ideality factor *n* should also appear in the reverse

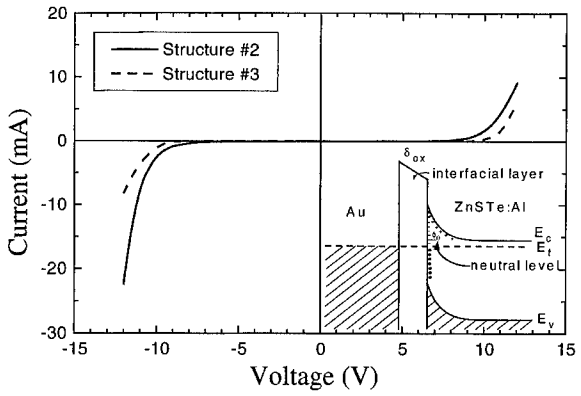

Fig. 4. *I–V* characteristics of EL structure #2 and #3. The inset shows the proposed electron energy diagram for these structures.

current term and the deviation of n from unity can be assumed to be mainly due to tunneling. The current–voltage relation can be expressed as [15]

$$I = I_s\left\{\exp\left(\frac{qv}{kT}\right) - \exp\left[\left(\frac{1}{n} - 1\right)\frac{qv}{kT}\right]\right\}.$$

For $n > 2$, this equation predicts that the diode conducts better in the reverse direction than in the forward direction. We believe that this offers a reasonable explanation for the similar I–V relation observed in our structure #2. Fig. 4 also displays the I–V relation for a structure labeled #3 which is similar to structure #2 except that the Al doping level is reduced to approximately 5×10^{18} cm^{-3}. The curve for structure #3 shows a more symmetric relation upon the two opposite bias directions. This result provides additional qualitative support for the above explanation.

In this work, we have not made much effort to optimize the efficiency of light emission from the Schottky-barrier-type EL structures discussed here. Significant improvement in performance can be expected if (1) a dielectric isolation is provided for each cell to reduce leakage current; (2) wire-bonding technique is developed for the Au electrode instead of needle probe touching to reduce contact resistance; (3) a standard Au/Ge/Ni alloy ohmic contact is employed for the n^+-type GaAs substrates; (4) optimization is performed as a function of the doping density and the thicknesses of the interfacial layer and the n-ZnSTe layers. Despite the lack of these efforts, plus the existence of extremely high density of misfit dislocations at the boundary between the GaAs substrate and the epilayer due to their large lattice mismatch, the best external quantum efficiency (EQE) of blue emission achieved in these structures is at mid 10^{-5} with up to a few μW of output power. Of course, the conventional p–n-junction-type LED structure will be much more efficient, an increase in EQE of more than three orders of magnitude than the current value can be expected for the optimal structure. Development of controlled p-type doping in ZnSTe alloy and its pseudomorphic growth on lattice-matched Si substrate are underway in our lab. The efforts along this direction represent important steps toward the practical application of ZnSTe-based structures as light-emitting devices that are integrated on Si.

5. Summary

Field quenching effects on Te isoelectronic centers in MBE-grown undoped ZnSTe alloy were studied. Following successful n-type doping using Al, strong blue emission from ZnSTe : Al-based Schottky-barrier-type EL devices has been demonstrated. Based on the analysis of I–V characteristics and emission spectra, the blue EL emission is believed to be resulted from impact-excited localized states associated with Te isoelectronic centers in the heavily doped active layer, where field quenching is significantly reduced. The hot carriers required for impact excitation are generated by a tunneling-dominated transport mechanism.

References

[1] R. Mach and G.O. Mueller, Semicond. Sci. Technol. 6 (1991) 305.
[2] T. Inoguchi and S. Mito, Electroluminescence, Topics in Applied Physics, Vol. 17 (Springer, Heidelberg, 1977) p. 222.
[3] G.W. Iseler and A.J. Strauss, J. Lumin. 3 (1970) 1.
[4] T. Fukushida and S. Shionoya, Jpn. J. Appl. Phys. 12 (1973) 549.
[5] W. Heimbrodt and O. Goede, Phys. Status Solidi (b) 135 (1986) 795.
[6] O. Goede, W. Heimbrodt, T. Lau, G. Matzkeit and B. Selle, Phys. Status Solidi (a) 94 (1986) 259.
[7] R. Mach, G.U. Reinsperger, G.O. Muller, B. Selle and G. Matzkeit, J. Crystal Growth 117 (1992) 1002.
[8] Z. Yu, W.C. Hughes, W.H. Roland, C. Boney, J.W. Cook, Jr., J.F. Schetzina, G. Cantwell and W.C. Harsch, Appl. Phys. Lett. 66 (1995) 115.
[9] I.K. Sou, K.S. Wong, Z.Y. Yang, H. Wang and G.K.L. Wong, Appl. Phys. Lett. 66 (1995) 1919.
[10] I.K. Sou, Z. Yang, J. Mao, Z.H. Ma, K.W. Tong and G.K.L. Wong, Proc. 10th Int. Conf. on Physics of Semiconductors, Berlin (1996).
[11] I.K. Sou, S.M. Mou, Y.W. Chan and G.K.L. Wong, Mater. Res. Soc. Symp. Proc. 340 (1994) 481.
[12] I.K. Sou, Y.H. Yeung, J. Mao, Z. Yang and G.K.L. Wong, Proc. 1st Chinese Optoelectronics Workshop, Taiwan (1995).
[13] J. Bardeen, Phys. Rev. 71 (1947) 717.
[14] V.L. Rideout, Solid State Electron. 18 (1975) 541.
[15] V.L. Rideout and C.R. Crowell, Solid State Electron. 13 (1970) 993.

ELSEVIER

Journal of Crystal Growth 175/176 (1997) 637–641

JOURNAL OF CRYSTAL GROWTH

Room-temperature continuous-wave operation of ZnSe-based blue–green laser diode grown by molecular beam epitaxy

Moon-Deock Kim*, Bong-Jin Kim, Min-Hyon Jeon, Jeong-Keun Ji, Sang-Dong Lee, Eun-Soon Oh, Jin-Suck Kim, Hae-Sung Park, Tae-Il Kim

Photonics Laboratory, Materials Sector, Samsung Advanced Institute of Technology, P.O. Box 111, Suwon 440-600, South Korea

Abstract

ZnSe-based II–VI laser diodes were grown by using molecular beam epitaxy (MBE) on GaAs(1 0 0) substrates. Continuous-wave, stimulated emission at room temperature was observed at a wavelength of 536.5 nm with a threshold current of 45 mA (642 A/cm^2) from a ZnCdSe/ZnSSe/ZnMgSSe single quantum well separate confinement heterostructure laser diode. A lifetime of 11 s was achieved when the defect density of laser diode structure was less than 10^5 cm^{-2}. Electroluminescence tests were conducted to find the origin of the defect generation at the laser diode structure. We monitored the generation of the dark line defects along $\langle 1\,0\,0 \rangle$ during the electroluminescence.

Keywords: ZnSe; ZnSSe; ZnMgSSe; LD

1. Introduction

Much effort has been devoted in recent years to studies on the wide-gap II–VI semiconductor heterostructures to realize blue–greenlaser diodes (LDs). In 1991, the first blue–green current injection LD was demonstrated under pulsed operation at 77 K by Hasse et al. [1]. Since then, several groups have demonstrated room-temperature continuous-wave (CW) operation of devices with emission at or near 520 nm using essentially identical structures [2–4]. In early February 1996, the Sony group had succeeded in fabricating a blue/green laser diode with a room-temperature CW operation with lifetime in excess of 100 h [5]. They used a separate confinement heterostructure (SCH) ZnCdSe single quantum well (SQW) with ZnSSe guiding layers and ZnMgSSe cladding layers lattice-matched on the GaAs substrate. However, there still remain several major obstacles to achieve a long-lived laser diode: the enhancement of p-type doping in ZnSe and ZnMgSSe, p-ohmic contact and the reduction or complete elimination of grown-in defects such as stacking faults which are believed to be sources for dark-spot defects (DSD). One way to reduce DSD is to use ZnSe substrates

* Corresponding author. Fax: + 82 331 280 9357; e-mail: mdkim@saitgw.sait.samsung.co.kr.

0022-0248/97/$17.00 Copyright © 1997 Published by Elsevier Science B.V. All rights reserved
PII S0022-0248(96)00989-X

for homoepitaxial growth, the other way is to use GaAs buffer layers. To reduce DSD, it is necessary to optimize the growth conditions of the II–VI/III–V interface [6]. We previously have reported CW operation of a blue–green LD at room temperature without GaAs buffer layer (DSD: $<10^6$ cm^{-2}) [7]. In this paper, we report an LD in which improved lifetime has been obtained owing to GaAs buffer layer. A GaAs buffer layer was essential for the growth of high quality II–VI epilayers on GaAs substrate. Also, we have investigated the degradation of LDs by applying electroluminescence (EL).

2. Experimental procedure

Laser diodes were grown on an n-type GaAs(1 0 0) substrate using a dual chamber molecular beam epitaxy, employing a Riber 32P MBE system. Zn(6 N), Se(6 N), Mg(6 N), Cd(6 N), Te(6 N), and ZnS(6 N) were used as molecular beam sources. The n- and p-type dopants were $ZnCl_2$ and atomic nitrogen generated by RF plasma source, respectively. The growth temperature was fixed at 280°C. After the growth of a GaAs : Si buffer layer on an n-type GaAs(1 0 0) substrate in a III–V chamber, the substrate was rapidly transferred via an ultra-high vacuum (UHV) transfer chamber into the II–VI growth chamber and the growth of ZnSe buffer layer was initiated. We believe that the rapid transfer preserves the (2×4) surface and prevents the interaction between the fresh GaAs surface with the background species in the II–VI growth chamber. A schematic diagram of our LD structure is shown in Fig. 1 and consists of a 30 nm thick ZnSe : Cl and 200 nm thick ZnSSe : Cl buffer layer, a 800 nm thick ZnMgSSe : Cl cladding layer, a 100 nm thick ZnSSe : Cl waveguiding layer, a ZnCdSe single QW, a 100 nm thick ZnSSe : N waveguiding layer, a 800 nm thick ZnMgSSe : N cladding layer, a 200 nm thick ZnSSe : N layer, a 100 nm thick ZnSe : N layer, a ZnSe/ZnTe multiple QW and a ZnTe : N contact layer. The n-ZnSe buffer layer (30 nm) was grown on top of GaAs buffer in order to keep GaAs buffer surface from sulfur attacks [8]. In addition, the thickness of ZnSe buffer is well

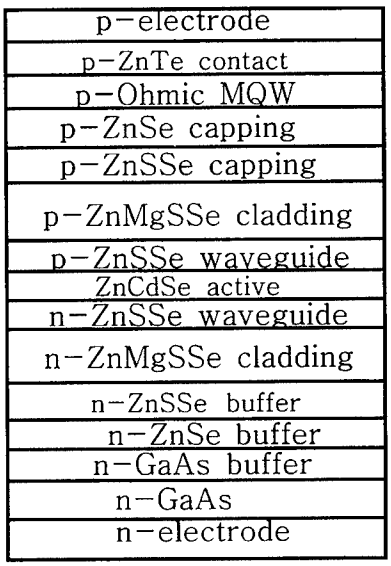

Fig. 1. Schematic of ZnCdSe/ZnSSe/ZnMgSSe SQW-SCH laser diode.

below the critical thickness. The free-electron concentrations of all n-type layers were found to be 1×10^{18} cm^{-3} by Hall effect measurements. The acceptor concentration of the ZnSe and ZnMgSSe layers were found to be 8×10^{17} and 7×10^{16} cm^{-3}, respectively. The p-type doping of ZnTe was conducted by using nitrogen free-radical generated by RF plasma source. The lowest free-hole concentration we achieved was greater than 10^{18} cm^{-3} and we had found it difficult to reduce the doping level further using our RF plasma system. Therefore, a modulation doping method was applied to decrease the p- type doping of ZnTe contact layer to $(1–3) \times 10^{18}$ cm^{-3}. The nitrogen concentration of the ZnTe layer affected the turn on voltage and the resistance of the structure [9]. The modulation doping for the ZnTe contact layer is composed of alternating undoped and doped layers for one pair of period and total 10 pairs were grown. The thicknesses of undoped and doped ZnTe layers are 3 and 1 nm, respectively. The free-hole concentration of the ZnTe : N was found to be 3×10^{18} cm^{-3} as shown in Fig. 2. The band-gap energies for the ZnCdSe and the ZnMgSSe were 2.43 and 2.95 eV at 11 K, respectively. The quantum well width of our

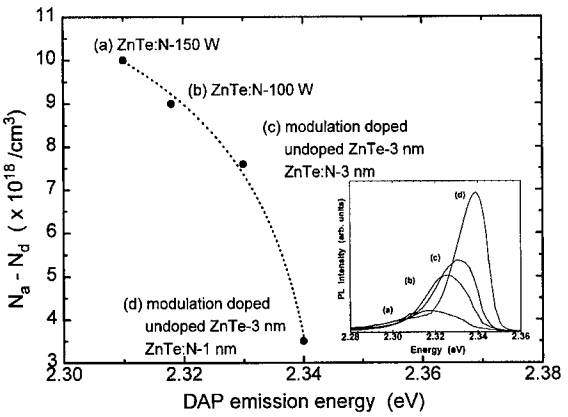

Fig. 2. The hole concentration of samples with various undoped ZnTe contact layer thickness and different RF plasma power. In the inset, the DAP emission spectra for samples grown by modulation doping and various RF plasma power are also shown.

LDs determined by cross-sectional transmission electron microscopy is 90 Å and the Cd mole fraction of the QW is about 33%.

3. Results and discussion

Fig. 2 shows the Hall effect data for samples with various undoped ZnTe contact layer thickness and different RF plasma power. The nitrogen background pressure in the chamber was kept as 1.2×10^{-6} Torr for all sample growth. As shown in Fig. 2, the hole concentrations of the p-ZnTe layers measured by van der Pauw method at room temperature ranged from 3×10^{18} to 1×10^{19} cm^{-3} in accordance with plasma power and undoped ZnTe thickness. The inset of Fig. 2 shows the donor–acceptor pair (DAP) emission spectra recorded by low-temperature photoluminescence for various samples. The DAP emission peaks were shifted to high-energy region as the nitrogen doping levels in the ZnTe contact layer were decreased. Therefore, we effectively reduced the free-hole concentration in the ZnTe layer by using modulation doping method (thicknesses of undoped/doped ZnTe: 30 Å/10 Å). The free-hole concentration was found to be 3.5×10^{18} cm^{-3} by Hall effect measurement, a low doping level for which we aimed [9].

A gain-guided laser devices were fabricated. The p-ZnSe/ZnTe multiple quantum well ohmic contact layer was chemically etched off to leave a 10 μm wide mesa stripe region. An insulating layer of polycrystalline ZnS was deposited on the open stripe region for reduction of the current path. This enhances the lateral optical confinement for the laser waveguide. Pd/Pt/Au metallic multilayer was evaporated as a p-electrode on the p-type ZnTe contact layer. Pd/Ge/Ti/Au metal serves as an n-electrode to the n-GaAs substrate. The wafer was cleaved into 700 μm long, and high reflectivity coating was made on the facets. The reflectivities were 70% for the front and 95% for the rear facet. The strips were then cleaved into 500 μm width pellets. The fabricated laser diodes were mounted p-down using indium on a copper block as a heat sink, with no additional cooling for the device.

Fig. 3 shows the light output against injection current (L–I) characteristics of this laser diode at room temperature measured under continuous mode of operation. The threshold current (I_{th}) of a laser diode without facet coating (Fig. 3a) under CW conditions was 75 mA. The voltage at lasing threshold was 8 V. After facet coating, the I_{th} was about 45 mA and corresponding threshold current density Jth was 642 A/cm^2.

The emission spectra taken at room temperature are shown in Fig. 4. The stimulated emission was observed at wavelength of 533.5 nm under pulsed operation and 536.5 nm under continuous operation, respectively. The shift in emission by 30 Å is believed to be due to heating in the SQW active region during device operation. The lifetimes of the tested lasers were 11 with output power 1 mW. After 11 s operation, however, the laser diode still operated in the LED mode. The defect density in the active layer for this diode was less than 10^5 cm^{-2} by etch-pit-density (EPD) measurement.

Fig. 5 shows EL image after turn on. This image was observed from the top surface through the 5 nm Au and 20 nm Pd film using a charge coupled device (CCD) video camera attached to an optical microscope. An indium metal pad was used as an n-electrode of the GaAs substrate. Electrical injection was provided by 100 μs pulses, the duty cycle

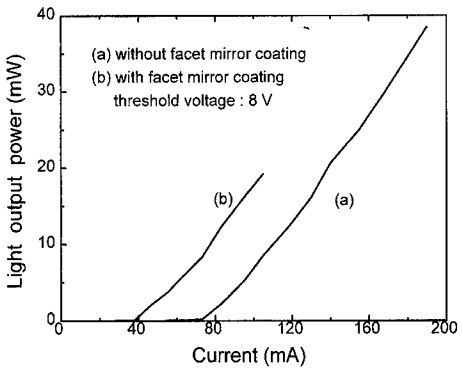

Fig. 3. *L–I* characteristics under continuous current operation of ZnCdSe/ZnSSe/ZnMgSSe SQW-SCH laser diode at room temperature without (a) and with (b) facet coating.

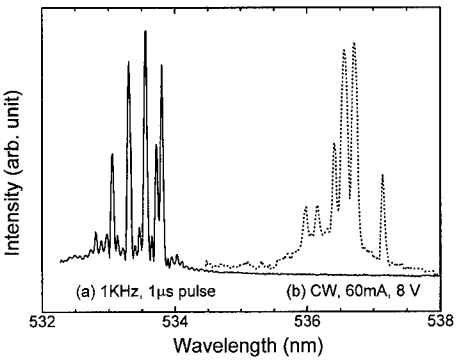

Fig. 4. Emission spectra of ZnCdSe/ZnSSe/ZnMgSSe SQW-SCH laser diode operating under pulsed and continuous wave.

ranging from 0.1% to 10% at room temperature. Fig. 5a shows an EL image of dark line defects 30 min after the power was turned on. At the beginning, the dark spots were formed at or near the facet coated region and propagated as a dark line into the stripe region along the ⟨1 0 0⟩ direction. Fig. 5b shows EL micrograph after 60 min. In this case, DLDs were clearly developed along the ⟨1 0 0⟩ direction. Fig. 5c is EL after 90 min with higher current density than used in Fig. 5a and Fig. 5b. The images were taken at duty cycle of 10% and current density of 642 A/cm^2. During this EL test, the length of the ⟨1 1 0⟩ DLDs did not change as indicated by 'L' in the figure. Small dark spots were also observed(see 'S' in the figure) just after turn on. In the next stage of degradation, the dark spots continue to propagate along ⟨1 0 0⟩. We believe that the formation of dark spots are the pre-existing defects such as stacking faults formed at the substrate/epilayer interface. As shown by using EL measurements, device degradation begins with the growth of DSDs, which become darker and spread out in the ⟨1 0 0⟩ direction during the test. Based on the etch-pit density and EL image analysis, the defect density of the LD structure was found to be about less than 10^5 cm^{-2}. Based on our EL test results, we believe that the relatively fast degradation of our LD (11 s of lifetime) seemed to be due to defects or microcracks created during bar-cleaving process during fabrication.

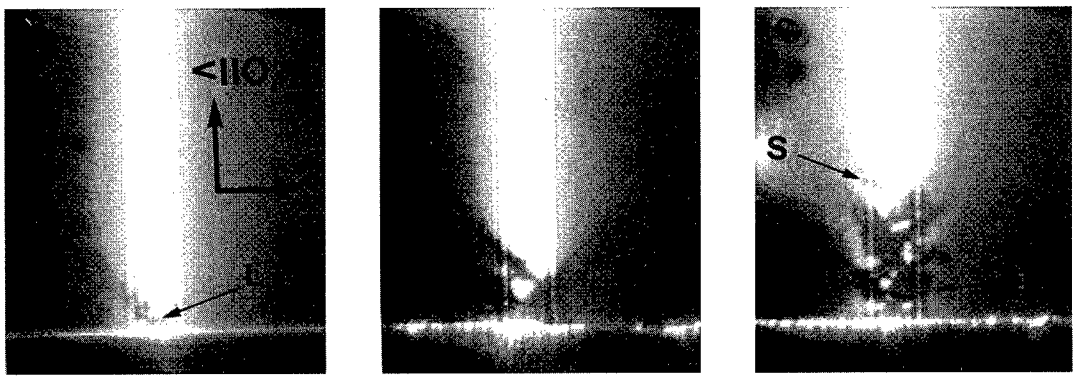

Fig. 5. Electroluminescence micrographs taken at 30 min (a), 60 min (b), and 90 min (c) after turn on are viewed from the top surface. Arrows marked L and S show ⟨1 1 0⟩ DLDs and dark spots, respectively.

4. Conclusions

We achieved the CW operation of blue–green quantum well laser diodes at room temperature with the emission wavelength of 536.5 nm. A threshold current of 45 mA was measured under CW operation for the ZnCdSe/ZnSSe/ZnMgSSe SQW-SCH structure. The lifetime of our laser diode was about 11 s with the output power of 1 mW. The longest lifetime published so far is 101 h by Sony. The relatively short lifetime is believed to be due to the growth related defects and defects generated from the cleaved facets. Dark spot defects were formed initially at or near the vicinity of the facet coated area and propagated into the stripe region. Dark line defects were eventually formed from the dark spot as time progressed along the $\langle 1\,0\,0 \rangle$ directions during current injection. Further research is in progress to reduce the grown-in defects such as stacking faults. We believe that the optimum growth conditions at the beginning of the growth (that is, initial ZnSe buffer layer growth on the GaAs buffer) is crucial for further reduction of defects. In addition, the careful fabrication is also extremely important for improving the lifetime of LD.

References

[1] M.A. Hasse, J. Qiu, J.M. DePuydt and H. Cheng, Appl. Phys. Lett. 59 (1991) 1272.
[2] C.T. Walker, J.M. DePuydt, M.A. Haase, J. Qiu and H. Cheng, Physica B 185 (1993) 27.
[3] N. Nakayama, S. Itoh, T. Ohata, K. Nakano, H. Okuyama, M. Ozawa, A. Ishibashi, M. Ikeda and Y. Mori, Electron. Lett. 29 (1993) 1488.
[4] A. Salokatve, H. Jeon, J. Ding, M. Hovinen, A.V. Nurmikko, D.C. Grillo, L. He, J. Han, Y. Fan, M. Ringle, R.L. Gunshor, G.C. Hua and N. Otsuka, Electron Lett. 29 (1993) 2192.
[5] Taniguchi, T. Hino, S. Itoh, K. Nakano, N. Nakayama, A. Ishibashi and M. Ikeda, Eletron. Lett. 32 (1996) 552.
[6] B.J. Wu, G.M. Haugen, J.M. DePuydt, L.H. Kuo and Salamaca-Riba, Appl. Phys. Lett. 68 (1996) 2828.
[7] M.-D. Kim, H.-S. Park, B.-J. Kim, J.-K. Ji, E.-S. Oh, S.-D. Lee, J.- S. Kim and T.-I. Kim, J. Korean Phy. Soc. 29 (1996) 403.
[8] S. Guha, B.J. Wu, H. Cheng and J.M. DePuydt, Appl. Phys. Lett. 63 (1993) 2129.
[9] A. Taike, M. Momose, M. Kawata, J. Gotoh, K. Mochizuki and S. Nakatsuka, Appl. Phys. Lett. 68 (1996) 388.

ELSEVIER

Journal of Crystal Growth 175/176 (1997) 642–646

JOURNAL OF CRYSTAL GROWTH

Growth and characterization of lattice-matched HgSe

L. Parthier*, H. Wißmann, S. Luther, G. Machel, M. Schmidbauer, R. Köhler, M. von Ortenberg

Institut für Physik, Humboldt-Universität zu Berlin, Invalidenstrasse 110, D-10115 Berlin, Germany

Abstract

HgSe layer on ZnTe and $ZnTe_{1-x}Se_x$ layers were grown by molecular beam epitaxy. The introduction of a GaSb substrate reduces the lattice mismatch drastically ($f = -0.11\%$) compared to GaAs ($f = -7.4\%$). By spatial variation of the Se content from $0.016 \leqslant x \leqslant 0.041$ the lattice constant of the buffer layer can be varied between that of the GaSb substrate and that of the HgSe layer. The different heterostructure systems were investigated by high-resolution X-ray diffraction to calculate the crystalline perfection and the strain behavior. A 150 nm HgSe layer pseudomorphically grown on a 145 nm $ZnTe_{0.964}Se_{0.036}$ buffer layer shows *pendellösung* thickness fringes indicating the high crystalline perfection of the structures, and has a FWHM of 84 arcsec. Only tensile strain is present in this structure. The carrier concentration and the mobility are calculated from Shubnikov–de-Haas oscillations in high magnetic fields up to 12 T. The best samples have a high mobility of up to 2.1×10^5 cm^2/V·s with a carrier concentration of 1.0×10^{17} cm^{-3} at 4.2 K.

PACS: 81.15.H; 81.05.E; 68.60.B

Keywords: Molecular beam epitaxy; Mercury selenide

1. Introduction

Mercury selenide is a semiconductor with interesting magnetic–optical properties. In technical applications undoped HgSe is used as p-contact for blue ZnSe-based devices [1]. The special modification of iron-doped HgSe is characterized by a donor level pinned to the Fermi energy ($N_{Fe} \geqslant 5 \times 10^{18}$ cm^{-3}) resulting in an extremely high carrier mobility especially favorable for low-dimensional structures. Also in combination with $Hg_{1-x}Mn_xSe$ layers ($x \leqslant 2\%$) a spin superlattice can be produced [2].

Up to now only few molecular beam epitaxial (MBE) grown HgSe structures have been reported [1, 3]. For these epitaxially grown HgSe layers, ZnTe buffers on GaAs substrates were used. However, the large lattice mismatch between ZnTe and GaAs ($f = -7.4\%$) requires a thick fully relaxed buffer layer (>2 μm) to reduce the high defect density generated at the interface. Despite the low mismatch of HgSe and ZnTe ($+0.29\%$) the crystal perfection of the HgSe layer is mainly limited by the defects and the residual strain of the buffer layer. Consequently, the reported minimum of the (0 0 4)

* Corresponding author. Fax: + 49 30 2093 7729; e-mail: parthier@albert.physik.hu-berlin.de.

0022-0248/97/$17.00 Copyright © 1997 Elsevier Science B.V. All rights reserved
PII S0022-0248(96)00993-1

rocking curve full width at half maximum (FWHM) for a HgSe layer of 220 arcsec is relatively broad for a strained layer (200 nm) as well as fully relaxed thick layer (2.3 μm) [3, 4].

In this paper we report on two fundamental improvements for the epitaxial growth of HgSe-based heterostructures. The first step is very simple but obvious, which is to replace the GaAs substrate by GaSb. In this way we reduce the lattice mismatch drastically ($f = -0.11\%$) and a smaller thickness of the buffer layer is sufficient, but the strain in the layer remains compressive. The second step is the complete fitting of the buffer to HgSe by the introduction of the ternary layer $ZnTe_{1-x}Se_x$. By spatial variation of the Se content from $0.016 \leqslant x \leqslant 0.041$, the lattice constant of the buffer layer can be varied between those of the GaSb substrate and the HgSe layer, corresponding to a change of the misfit from $+0.2\%$ up to zero compared to HgSe. Only tensile strain is expected in this case [5]. For an optimized heterostructure we have to consider the large difference of the thermal expansion coefficients $\alpha_{GaSb} = 6.2 \times 10^{-6}\,K^{-1}$, $\alpha_{ZnTe} = 8.19 \times 10^{-6}\,K^{-1}$, $\alpha_{HgSe} = 1.48 \times 10^{-6}\,K^{-1}$).

2. Experimental procedure

The epitaxial growth was carried out in a DCA 350 MBE system, specially designed for mercury evaporation and equipped with effusion cells for ZnTe, Zn, Se, and Hg. The layers were grown on undoped GaSb(0 0 1) substrates. Due to the small difference of about 120 K between melting point and oxide desorption temperature of GaSb without a Sb overpressure, the thermal desorption of the native oxide was optimized in a two-step annealing process at 300°C and 540°C. The substrate temperature was varied between 320°C and 350°C for $ZnTe_{1-x}Se_x$ and between 80°C and 120°C for HgSe. The growth process was monitored by RHEED. The (2×1) and $c(2 \times 2)$ surface reconstructions seen during the growth of ZnTe changed to a pure (2×1) reconstruction after the addition of Se, which indicated the transition from nearly stoichiometric to chalcogen-rich growth conditions. The composition of the ternary layers was controlled by the Se/Te flux ratio. The growth rate was determined in situ by RHEED oscillation and varied between 2.5 and 2.8 Å/s. The HgSe layers were grown with a Hg/Se ratio depending on the growth temperature ranging between 80 and 130. The layer thickness was measured at the cleaved edge by a scanning electron microscope, because a strong damping of the RHEED oscillation prevented an in situ analysis.

The grown layers were investigated by high resolution X-ray diffraction (HRXRD) with respect to the relaxation state and the crystalline perfection. The electrical properties were obtained from magnetotransport experiments, performed in DC field up to 12 T at 4.2 K, by an analysis of the Shubnikov–de Haas (SdH) oscillations.

3. Results and discussion

For the determination of the two lattice constants perpendicular and parallel to the growth direction we have measured the rocking curves of the symmetric (0 0 4) and the asymmetric (1 3 7) and (5 3 5) reflections. The lattice mismatch $f = (a_S - a_L)/a_L$ was calculated from the relaxed layer constant in the case of the buffer/substrate system. For the $HgSe/ZnTe_{1-x}Se_x$ system we put in the formula the fully relaxed buffer layer constant or the parallel lattice constant.

Four different buffer/substrate systems can be created for an HgSe top layer:

(i) HgSe/ZnTe/GaAs,
(ii) HgSe/ZnTe/GaSb,
(iii) $HgSe/ZnTe_{1-x}Se_x$/GaSb, $(0.016 \leqslant x \leqslant 0.041)$,
(iv) $HgSe/ZnTe_{1-x}Se_x$/GaSb, $(x > 0.041)$.

These heterostructures can be characterized as follows:

(i) ZnTe/GaAs – Large misfit ($f = -7.4\%$) required a thick buffer, which is compressively strained. The advantage of the low misfit to HgSe ($+0.289$, tensile strain) will be limited by high defect density of the buffer.

(ii) ZnTe/GaSb – Low misfit to substrate (-0.11%, compressive) and HgSe (tensile). These values allow to design a completely strained heterostructure HgSe/ZnTe/GaSb. We have determined

the critical thickness for ZnTe/GaSb to 296 nm (see Ref. [5]).

(iii) $ZnTe_{1-x}Se_x$/GaSb with $a_{GaSb} \geqslant a_{ZnTeSe} \geqslant a_{HgSe}$. The strain is always tensile. For a nearly matched Buffer to HgSe we obtained a critical thickness of 222 nm with respect to GaSb. An exact fitting at the growth temperature, considering the different thermal expansion coefficients, cannot be realized technologically, because of the strong dependence of the lattice constant on the Se content in the ternary buffer layer. The accuracy of the x value of about ± 0.0005 is very difficult to obtain. Therefore, we adjust a value between 0.020 and 0.035.

(iv) $ZnTe_{1-x}Se_x$ /GaSb with $a_{ZnTeSe} < a_{HgSe}$. The amount of the misfit is comparable to the last mentioned, but the strain changed from tensile (buffer) to compressive (HgSe).

For a further discussion it is necessary to consider the sign of the misfit, which leads to a different formation of misfit dislocations above the critical thickness. After [6] the most probable type of misfit dislocation in zinc-blende-type lattice is the 60° dislocation with a Burgers vector $\boldsymbol{b} = \frac{1}{2}a\langle 1\,1\,0\rangle$ and can be formed by two partial dislocations. One of these partial dislocations is parallel to the tensile strain field and therefore the nucleation barrier is low. This 90° dislocation has the Burgers vector of a stacking fault. Thus, due to a tensile strain stacking faults can be formed relatively easily as a result of the occurrence of only 90° partial dislocations. Compressive strain, however, will initially nucleate the 30° partial dislocations, which requires a higher activation energy. Immediately follows the nucleation of the 90° partial. These two dislocations create the perfect 60° dislocation resulting in the well-known dislocation network. Without the existence of threading dislocations the mechanism of dislocation and propagation is via half-loops, resulting in 60° dislocations at the interface for compressively grown structures.

Therefore, we can assume that the critical thickness for layers grown in compression is larger than the value for layers grown in tensile strain. On the other hand, the speed of propagation of the relaxation process in compressive strained layers is faster than in tensile strained layers due to the greater strain reduction by the creation of a 60° dislocation compared to a stacking fault. This corresponds to our results: we determined the so-called relaxation thickness parameter κ for ZnTe/GaSb ($f < 0$) to be 426 nm and for $ZnTe_{0.95}Se_{0.05}$/GaSb ($f > 0$) 1267 nm, whereas the critical thickness d_c is 296 and 222 nm, respectively (at $d = \kappa + d_c$, the relaxation state is about 63% of the full relaxation [5]). Furthermore, the FWHM in the (0 0 4) rocking curve of 140 arcsec for a 264 nm thick ZnTe layer and 100 arcsec for a 228 nm thick $ZnTe_{0.95}Se_{0.05}$ layer reflect a different strain behavior. The misfit dislocations have a greater strain field resulting in a broadening of the FWHM compared to stacking faults. In addition, the $ZnTe_{0.95}Se_{0.05}$ layer showed *pendellösung* interference fringes. Consequently, the structural perfection of HgSe top layer will be influenced by the different buffer systems with the same amount of misfit but opposite in sign. The (0 0 4) rocking curves for the individual structures are shown in Fig. 1. Only for complete tensile

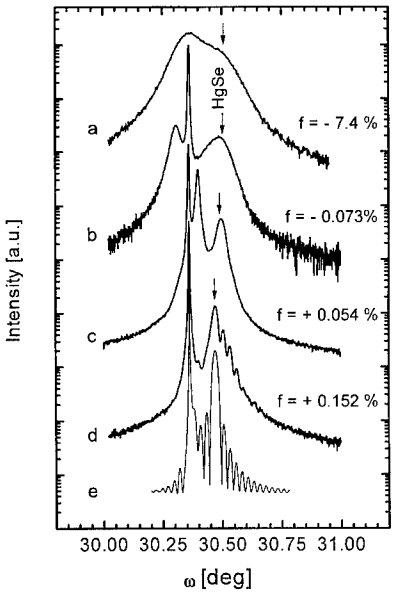

Fig. 1. Rocking curves of the (0 0 4) reflection for HgSe on different buffer systems: (a) 400 nm HgSe on 1.6 μm ZnTe/GaAs, (b) 200 nm HgSe on 225 nm ZnTe/GaSb, (c) 150 nm HgSe on 950 nm $ZnTe_{0.977}Se_{0.023}$/GaSb, (d) 150 nm HgSe on 150 nm $ZnTe_{0.964}Se_{0.036}$/GaSb, (e) simulation fit of (d). f means the misfit between buffer and substrate, the arrows indicate the HgSe layer.

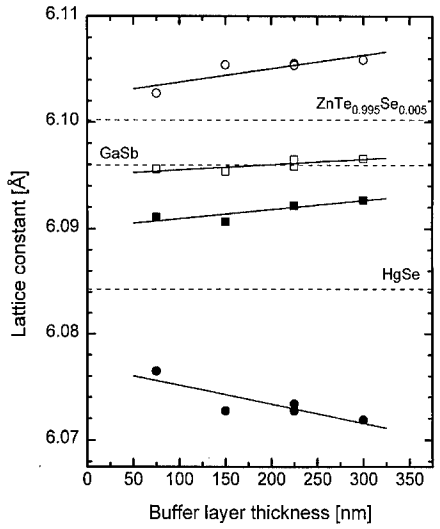

Fig. 2. Dependence of the lattice parameter of both HgSe and $ZnTe_{0.995}Se_{0.005}$ on the buffer layer thickness: (○) $a_\perp$ ZnTeSe; (□) $a_\parallel$ ZnTeSe; (●) $a_\perp$ HgSe; (■) $a_\parallel$ HgSe. The HgSe layer is kept constant at 200 nm.

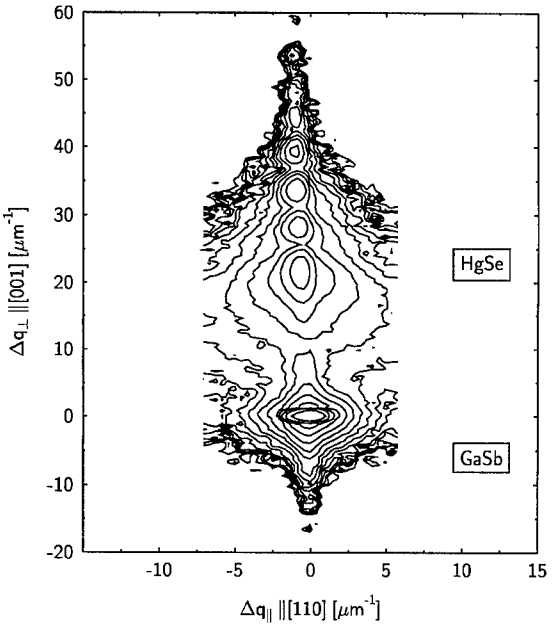

Fig. 3. Reciprocal space map of the (0 0 4) reflection of a 150 nm thick HgSe layer grown full pseudomorphic on $ZnTe_{0.964}Se_{0.036}$/GaSb (curve d in Fig. 1). $q_\parallel$ is the component of the scattering vector parallel to the surface, $q_\perp$ is parallel to the growth direction.

strained heterostructures (d – case (iii) in the listing above) we observed interference fringes for thin HgSe layers and complete pseudomorphic growth. The best FWHM was 84 arcsec for a 150 nm thick layer on a 145 nm thick $ZnTe_{0.964}Se_{0.036}$ layer, the calculated misfit +0.152% for the system buffer/substrate and +0.130% for the system layer/buffer. A 950 nm thick $ZnTe_{0.977}Se_{0.023}$ buffer, nearly matched to GaSb ($f = +0.05$), shows a smaller FWHM (58 arcsec), whereas the FWHM of 155 arcsec of the HgSe layer is larger (curve c). For case (ii), $f_{ZnTe/GaSb} < 0$ and $f_{HgSe/ZnTe} > 0$, the FWHM of HgSe does not exhibit a strong dependence on buffer layer thickness as expected ($\geqslant$230 arcsec) and is comparable to the best values published for very thick ZnTe/GaAs buffer [4]. A reason is illustrated in Fig. 2, where the dependence of both layer constants perpendicular and parallel to the interface on the buffer layer thickness is shown (the HgSe layer thickness has been kept constant). An increasing buffer thickness and nearly constant $a_\parallel$ results in an improved FWHM (430 to 142 arcsec). The increase in $a_\perp$ in the buffer and the decrease in $a_\perp$ in the HgSe layer are opposite to the expected behaviors. The ratio $a_\parallel/a_\perp$ of HgSe increased and therefore, the strain, which leads to only a slight improvement of the FWHM. In case (iv) – $a_{ZnTeSe} < a_{HgSe}$ –, i.e. tensile strain in the buffer and compressive in HgSe, the stacking faults in the buffer cause the creation of misfit dislocations without a nucleation barrier. For the same heterostructures (thickness and amount of misfit) the observed FWHM is about 50% larger compared to (iii).

Fig. 3 shows the reciprocal space map of the (0 0 4) reflection of a full pseudomorphically grown layer system on GaSb, 150 nm HgSe on 145 nm $ZnTe_{0.964}Se_{0.036}$ buffer (MS 543b, Fig. 1, curve d). It is clearly visible, that the orientation distribution is even slightly broadened for the HgSe layer main peak ($\Delta q_{\parallel 1/2} = 1.323\ \mu m^{-1}$) compared to the GaSb substrate ($\Delta q_{\parallel 1/2} = 1.24\ \mu m^{-1}$). This results from a very low dislocation density and no mosaicity can be concluded.

For the electrical characterization we performed transport measurements in high magnetic fields up to 12 T. The SdH oscillations were analyzed for the calculation of the carrier concentration as well as

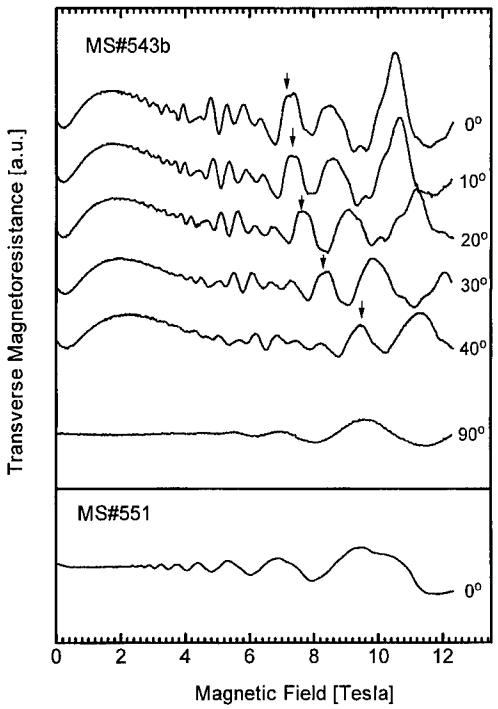

Fig. 4. Transverse magnetoresistance of two HgSe layers grown on ZnTeSe/GaSb at 4.2 K. The sample MS#551 has a 15 nm ZnTeSe cap layer. The arrows marked the shift of a Landau level.

the mobility. Fig. 4 shows the dependence of the transverse magnetoresistance on the magnetic field for two layers at 4.2 K. The Landau levels shift in tilted magnetic field B according to a cos θ dependence due to the decreasing perpendicular field component of B with respect to the layer axis (θ – angle between sample and B). The evaluation of the SdH-period for $\theta = 50°$ results in a carrier concentration of $n = 7.7 \times 10^{17}$ cm^{-3} (MS 543 sample) and $n = 6.5 \times 10^{17}$ cm^{-3} (MS 551). Furthermore, the sample MS 543 shows two additional periods at 0°, that disappear with increasing tilt angle in the Fourier analysis over $1/B$. This is a typically two-dimensional character of carriers in magnetic fields. The SdH period yields a carrier concentration of $n = 1.4 \times 10^{18}$ cm^{-3} and $n = 2.1 \times 10^{18}$ cm^{-3}. The same values were obtained for different structures. The MS 551 sample with a 15 nm ZnTeSe cap does not show this behavior. In conclusion we assume a band bending of the free HgSe layer surface resulting in a splitting into two subbands.

Acknowledgements

We acknowledge the financial support of the Deutsche Forschungsgemeinschaft (DFG), Sonderforschungsbereich 296 "Wachstumskorrellierte Eigenschaften niederdimensionaler Halbleiterstrukturen".

References

[1] S. Einfeldt, H. Heinke, M. Behringer, C.R. Becker, E. Kurtz, D. Hommel and G. Landwehr, J. Crystal Growth 138 (1994) 471.
[2] M. von Ortenberg, Adv. Solid State Phys. 31 (1991) 261.
[3] Th. Widmer, D. Schikora, C. Prott, B. Schöttker, K. Lischka, G. Machel, S. Luther and M. von Ortenberg, Semicond. Sci. Technol. 10 (1995) 1264.
[4] Th. Widmer, D. Schikora, G. Hendorfer, S. Luther, W. Jantsch, K. Lischka and M. von Ortenberg, Mater. Sci. Forum 182–184 (1995) 395.
[5] H. Wißmann, L. Parthier, P. Schäfer and M. von Ortenberg, 3rd Eur. Symp. on X-Ray Topography an High Resolution Diffraction, Palermo, 22–24 April 1996.
[6] J. Petruzello and M.R. Leys, Appl. Phys. Lett. 53 (1988) 2414.

ELSEVIER

Journal of Crystal Growth 175/176 (1997) 647–652

JOURNAL OF CRYSTAL GROWTH

p-Type doping with arsenic in (2 1 1)B HgCdTe grown by MBE

P.S. Wijewarnasuriya*, F. Aqariden, C.H. Grein, J.P. Faurie, S. Sivananthan

Microphysics Laboratory, Department of Physics (M/C 273), University of Illinois at Chicago, 845 W. Taylor St., Room #2236, Chicago, Illinois 60680, USA

Abstract

The results of arsenic incorporation in HgCdTe layers grown by molecular beam epitaxy (MBE) are reported. The incorporation into MBE-HgCdTe was carried out by a method called planar doping. Arsenic was successfully incorporated during the MBE growth as acceptors. Result suggests that most of the arsenic incorporates as an active acceptor at the MBE growth temperature. These findings are very promising for MBE-HgCdTe technology. Some layers show enhanced p-type mobilities with no carrier freeze-out at low temperatures. These results are very promising for in situ fabrication of infrared devices using HgCdTe material.

1. Introduction

The absence of a p-type in situ doping technique is one of the major stumbling blocks preventing the successful development of a truly MBE-based HgCdTe IRFPA technology. In HgCdTe, p-type doping can be controlled by Hg-vacancies and/or electrically active impurities. Hg-vacancy p-type MBE-HgCdTe single layers exhibit excellent electrical properties. In particular, lifetimes at 80 K are usually between 50 and 100 ns, which is considered to be very good for p-type HgCdTe with Cd composition ~22%. Both mobilities and carrier concentrations are excellent. Nevertheless, there has been an increasing emphasis on replacing native acceptor doping (Hg-vacancies) with extrinsic acceptor doping [1]. Precisely controlled extrinsic doping is very important for future high-efficiency multi-wavelength IRFPA device structures based on HgCdTe.

There are many problems to be solved in order to implement extrinsic doping in MBE technology to obtain p-type characteristics. The choice of dopant is crucial. Elements from groups I and V are potentially useful because they can act as acceptors in MBE-HgCdTe if they substitute metallic (column II) sites and nonmetallic (column VI) sites, respectively. Group I elements are favorable for p-type doping since they are easily incorporated into metallic sites during growth under optimum growth conditions. Among the group I elements, the incorporation of Li, Cu, Ag, and Au as p-type dopants in MBE-HgCdTe has been studied [2–4]. The high diffusivity of some of these elements in HgCdTe prevents their usefulness in FPA technology as p-type dopants [2, 3].

* Corresponding author.

0022-0248/97/$17.00 Copyright © 1997 Elsevier Science B.V. All rights reserved
PII S0022-0248(96)01230-4

In recent years, attention has been focused on arsenic as a p-type dopant due to its low diffusivity in HgCdTe [5–7]. In MBE growth, the primary goal is to obtain p-type doping at the growth temperature or after a low-temperature annealing in order to preserve the integrity of the structure. If a high-temperature annealing is required, MBE will lose the advantages associated with its low-temperature growth, i.e., the possibility of creating sharp intefaces. Arsenic should be incorporated during the growth at Te sites. But, MBE growth cannot occur under Hg-rich conditions, contrary to what can be achieved in LPE, MOVPE, or bulk growth. In MBE growth under Te-saturated conditions, it is not surprising that arsenic atoms (and antimony) incorporated during the MBE process have been found to act primarily as donors in as-grown materials [5–8]. This "intrinsic" difficulty in MBE explains why many approaches have been tried for achieving p-type doping in the MBE growth of HgCdTe using arsenic [9–16]. However, most of these approaches demand a high-temperature annealing ($>400°C$) in order to activate the arsenic.

In this paper we present results on arsenic incorporation in MBE-(2 1 1)B HgCdTe layers grown at the Microphysics Laboratory (MPL) at the University of Illinois at Chicago (UIC).

2. Experimental procedure

HgCdTe layers were grown in an ISA Riber 2300 MBE machine. The detailed growth technique has been reported previously [17]. The Cd composition and layer thickness were determined at room temperature by infrared transmission measurements. The Hall characteristics (carrier concentration and mobility) of the layers were measured by the van der Pauw technique for temperatures ranging from 300 to 23 K and with a magnetic field up to 1.0 T. Arsenic incorporation into HgCdTe layers was carried out by planar doping [19, 20]. In this method, periodically As shutter is open during the growth. During this time interval, HgCdTe growth is interrupted by closing Te and CdTe shutters. The mercury shutter is open all the time during the growth. This ensures that As is forced to react with mercury on the layer surface. The arsenic profiles in this study were performed at Charles Evans & Associates by secondary ion mass spectroscopic (SIMS) measurements using a CAMECA primary ion bombardment with a net impact energy of 14.5 keV.

3. Results and discussion

The electrical, material, and structural data of the arsenic planar-doped layers under study are summarized in Table 1. Fig. 1 shows the measured Hall characteristics versus reciprocal temperature of two layers with Cd composition of about 30%. Fig. 1a shows data for layer #124 and Fig. 1b shows data for layer #117. Layer #124 shows p-type characteristics below 50 K with a doping level of $2.5 \times 10^{17}\ cm^{-3}$ and a low-temperature mobility of $300\ cm^2/Vs$. Layer #117 shows p-type characteristics below 130 K with doping $1 \times 10^{15}\ cm^{-3}$ and a low-temperature mobility of $1000\ cm^2/Vs$ [18]. Layer #124 has a HgCdTe period of about 136 Å, and layer #117 about 42 Å. As can be seen in the figures, typical carrier freeze-out behavior is not observed as with Hg-vacancy doped HgCdTe. The carrier concentration and mobility are constant in the extrinsic temperature region.

For one sample with Cd composition in the MWIR region, we have observed the high hole mobility of $10^4\ cm^2/Vs$. This is an indication of possible 2D transport of holes. A similar trend is observed for higher Cd compositions. On the other hand, as the Cd composition decreases the layers show lower mobilities when compared to the higher Cd compositions. The observed temperature independence of the hole concentration confirms the conclusion of 2D transport since carrier freeze-out cannot occur in 2D transport systems [19]. In our planar-doping technique, the arsenic incorporates into HgCdTe as planar sheets. Due to the observed p-type character, the arsenic atoms must incorporate into nonmetallic sites and hence bond with either Cd or Hg atoms. Hence, holes from the arsenic atoms are transferred into the HgCdTe regions resulting in the separation of holes from the ionized arsenic scattering centers. This mechanism may provide the high mobility holes in the planar-doped HgCdTe system. Theoretical calculations

Table 1
Summary of the measured parameters of arsenic planar-doped MBE-$Hg_{1-x}Cd_xTe$ layers

Sample	x (%)	t (μm)	HgCdTe period (Å)	Hall characteristics as-grown	
				Doping (cm^{-3})	μ at low T ($cm^2/V \cdot s$)
106	38.0	19.3	193	1.0×10^{14}	1000
119	41.9	2.9	97	1.0×10^{15}	10000
117	32.9	4.2	42	1.0×10^{15}	800
124	31.7	4.5	136	2.5×10^{17}	300
101	24.2	4.5	096	6.0×10^{16}	250
1207	33.8	2.0	75	7.7×10^{16}	100

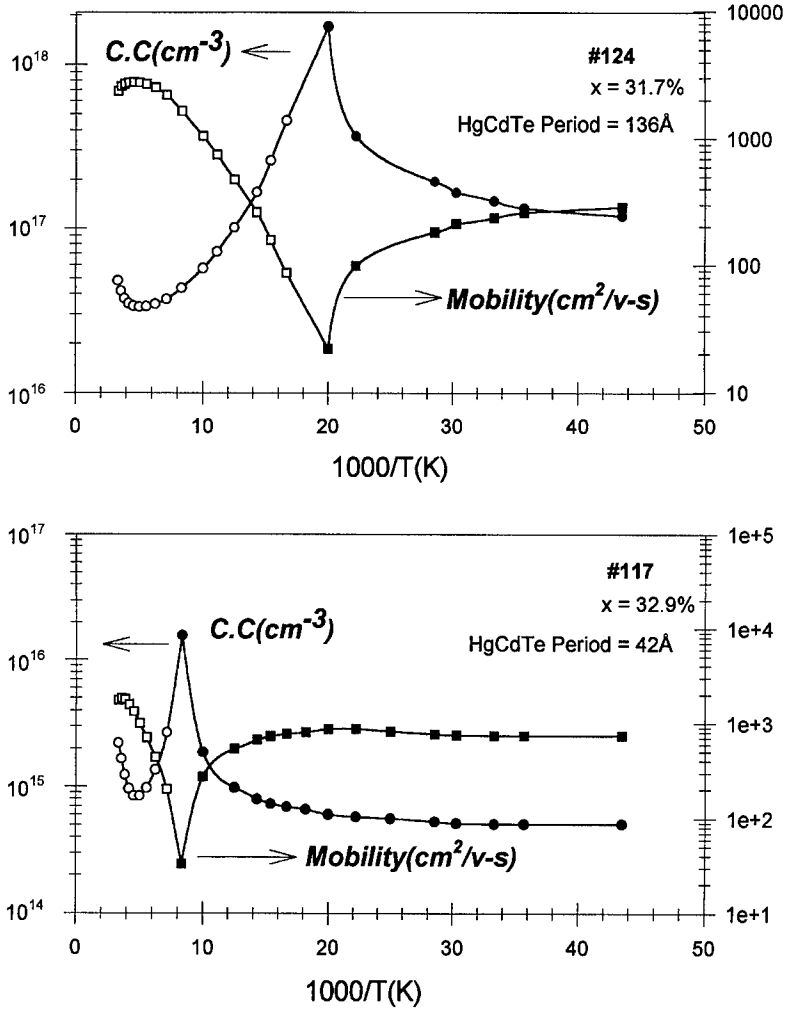

Fig. 1. Hall characteristics of as-grown arsenic planar doped layers: (a) $x = 31.7\%$ and HgCdTe period of 136 Å; (b) $x = 32.9\%$ and HgCdTe period of 42 Å. The open symbol (○) represents n-type conductivity, solid symbol (●) represents p-type conductivity. The data were taken at a magnetic field strength of 0.8 T.

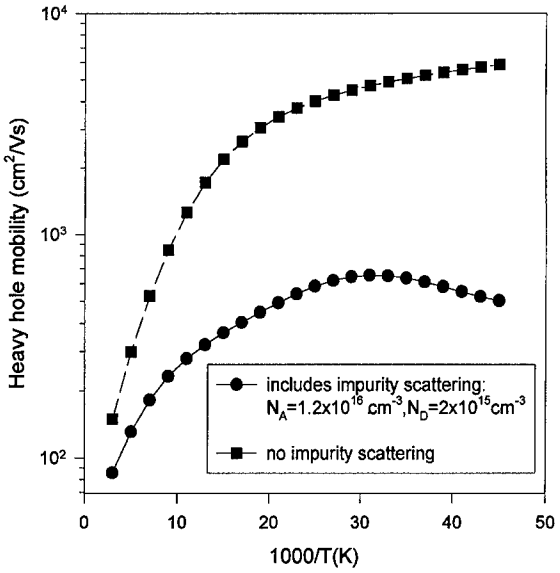

Fig. 2. Calculated heavy hole mobilities in a $x = 0.33$ sample of HgCdTe. One line describes the inclusion of impurity scattering, the other model modulation doping in planar-doped samples.

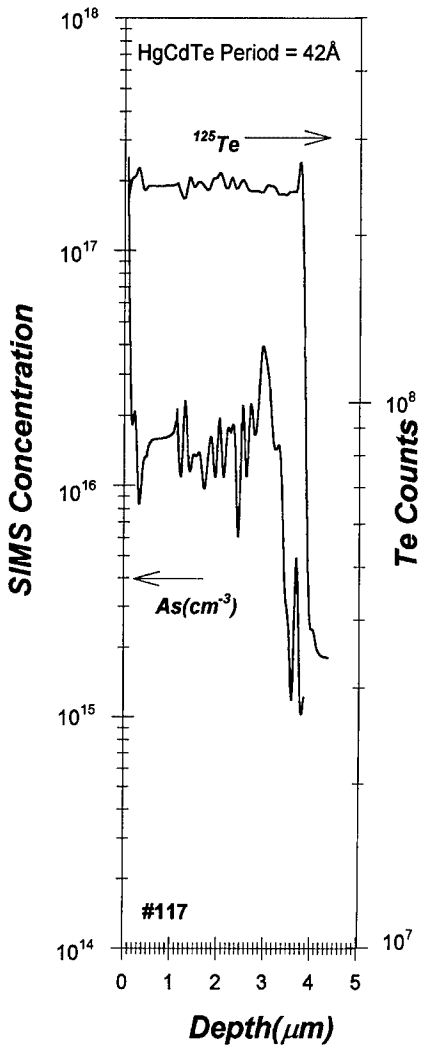

Fig. 3. SIMS profiles of arsenic and tellurium in as-grown arsenic planar doped MBE-HgCdTe (a) for layer #117.

plotted in Fig. 2 confirm that the observed hole mobilities can arise from such a modulation doping effect. A second reason for the high mobilities may be a decrease in the effective mass of the holes in the vicinity of the planar-doped regions. It is observed that as the Cd composition decreases the mobility enhancement diminishes. This may be due to the higher concentration of Hg vacancies acting as scattering centers.

Similar high mobility holes were observed by Arias and co-workers [21] in HgTe/CdTe superlattices (period 50–180 Å) with arsenic incorporated into CdTe during the MBE growth. Their SIMS result indicate that only a low percentage of arsenic atoms are electrically active at the growth temperature. After annealing at 250°C under Hg-saturated condition, they report that the conductivity of the layers remains p-type and with a higher acceptor concentration. The same approach has been employed by Han and co-workers [14]. In their studies, they observed no hole freeze-out at low-temperatures but no hole mobility enhancement.

We have annealed as-grown layers at 450°C followed by at 250°C under Hg-saturated conditions. As soon as layers were annealed, the high mobilities and constant carrier concentrations at low-temperature (2D properties) disappear. For layer #101, the doping level increased from 6×10^{16} to a low 10^{17} cm^{-3} level. This indicates less than 50% activation of arsenic during the MBE growth, assuming 100% electrical activity after annealing. SIMS analyses of the as-grown layers were carried out

to determine the percentage of active arsenic at the MBE growth temperature of HgCdTe. Fig. 3 shows the arsenic depth profile for as-grown layer #117. As evident from this graph, arsenic profiles are associated with peak structures and we believe that these are due to the periodic nature of arsenic concentration. High-resolution SIMS measurements need to be performed for further confirmation. As is evident from the ^{125}Te compositional profile, the interface between the substrate and the grown HgCdTe is very abrupt. For layer #1207, we have obtained doping level of 6.0×10^{16} cm^{-3} before annealing. After annealing at 450°C followed by at 250°C, measured doping level is 2×10^{16} cm^{-3}. We have obtained arsenic SIMS concentration of 5.0×10^{16} cm^{-3} on this layer indicating about 40% electrical activity.

We have also measured the minority carrier lifetimes in these arsenic planar-doped layers by the photoconductive decay technique. We have observed a lifetime of 4.3 μs at 80 K for sample #117. This sample has a Cd composition about 32.9% and p-type doping level of 1×10^{15} cm^{-3}. The measured lifetime value is in good agreement with values published in the literature [16]. These results demonstrate that the grown layers are of very high quality.

4. Summary

In this work, we report the results of arsenic incorporation in MBE-HgCdTe layers. The incorporation was carried out by a method called arsenic planar doping. In this method, arsenic atoms were successfully incorporated during the MBE growth as acceptors with doping up to 10^{17} cm^{-3}. SIMS measurements confirm the arsenic incorporation into MBE-HgCdTe layers. The Results suggest that most of the arsenic incorporates as an active acceptor at the MBE growth temperature. These findings are very promising for MBE-HgCdTe technology. The measured minority carrier lifetime in one of the samples ($x = 32.9\%$) is 4.3 μs at 80 K, indicating very good quality. This work confirms that arsenic can be used as an effective acceptor dopant at the MBE growth temperature of HgCdTe.

Acknowledgements

This work was funded by the Defense Advanced Research Projects Agency and monitored by the Air Force Office for Scientific Research under contract # F49620-91-C-0007 and was recently supported by the Air Force Wright Laboratories under contract No. F33615-95-C5424. Some of the layers were grown at EPIR Ltd.

References

[1] M.C. Chen, L. Colombo, J.A. Dodge and J.H. Tregilgas, J. Electron. Mater. 24 (1995) 539.
[2] P.S. Wijewarnasuriya, I.K. Sou, J. Kim, K.K. Mahavadi, S. Sivananthan, M. Boukerche and J.P. Faurie, Appl. Phys. Lett. 51 (1987) 2045.
[3] T.H. Myers, K.A. Harris, R.W. Yanka, L.M. Mohnkern, R.J. Williams and G.K. Dudoff, J. Vac. Sci. Technol. A 3 (1985) 1438.
[4] D.J. Peterman, M.L. Wroge, B.J. Morris, D.J. Leopold and J.G. Broerman, J. Appl. Phys. 63 (1988) 1951.
[5] M. Boukerche, P.S. Wijewarnasuriya, S. Sivananthan and J.P. Faurie, J. Vac. Sci. Technol. A 6 (1988) 2830.
[6] M.L. Wroge et al., J. Vac. Sci. Technol. B 4 (1986) 1306.
[7] T.C. Harman, J. Electron. Mater. 8 (1989) 191.
[8] P. Capper, J. Vac. Sci. Technol. B 9 (1991) 1667.
[9] M. Boukerche, S. Sivananthan, P.S. Wijewarnasuriya, I.K. Sou and J.P. Faurie, J. Vac. Sci. Technol. A 7 (1989) 311.
[10] H.R. Vydyanath, L.S. Lichtman, S. Sivananthan, P.S. Wijewarnasuriya and J.P. Faurie, J. Electron. Mater. 24 (1995) 625.
[11] S.H. Shin, J.M. Arias, M. Zandian, J.G. Pasko, L.O. Bubulac and R.E. DeWames, J. Electron. Mater. 22 (1993) 1039.
[12] J.M. Arias, S.H. Shin, J.G. Pasko, R.E. DeWames and E.R. Gertner, J. Appl. Phys. 65 (1989) 1747.
[13] R.L. Harper, S. Hwang, N.C. Giles, J.F. Schetzina, D.L. Dreifns and T.H. Myers, Appl. Phys. Lett. 54 (1989) 170.
[14] J.W. Han, S. Hwang, Y. Lansiri, R.L. Harper, Z. Yang, N.C. Giles, J.W. Cook, J.F. Schetzina and S. Sen, Appl. Phys. Lett. 54 (1989) 63.
[15] J.M. Arias, M. Zandian, J.G. Pasko, S.H. Shin, L.O. Bubulac and R.E. DeWames, J. Appl. Phys. 69 (1991) 2141.
[16] O.K. Wu, G.S. Kamath, W.A. Radford, P.R. Bratt and E.A. Patten, J. Vac. Sci. Technol. A 8 (1990) 1034.
[17] J.P. Faurie, S. Sivananthan and P.S. Wijewarnasuriya, SPIE Proc. 1735 (1992) 141.
[18] Layer #124 transition from n to p occurs at 50 K whereas for layer #117 at 130 K which has higher doping than layer #124. This is due to the following: $R_H \propto (n\mu_e^2 - p\mu_h^2)$.

[19] S. Sivananthan, P.S. Wijewarnasuriya and J.P. Faurie, 1993 Workshop on the Physics and Chemistry of HgCdTe, Extended Abstracts (1993) p. 7.
[20] S. Sivananthan, P.S. Wijewarnasuriya and J.P. Faurie, SPIE Proc. 2554 (1995) 55.
[21] J.M. Arias, S.H. Shin, D.E. Cooper, M. Zandian, J.G. Pasko, E.R. Gertner and R.E. DeWames, J. Vac. Sci. Technol. A 8 (1990) 1025.

ELSEVIER

Journal of Crystal Growth 175/176 (1997) 653–658

JOURNAL OF CRYSTAL GROWTH

High performance HgCdTe two-color infrared detectors grown by molecular beam epitaxy

R.D. Rajavel[a,*], D.M. Jamba[a], O.K. Wu[a], J.E. Jensen[a], J.A. Wilson[b], E.A. Patten[b], K. Kosai[b], P. Goetz[b], G.R. Chapman[b], W.A. Radford[b]

[a] *Hughes Research Labs., 3011 Malibu Cyn. Road, Malibu, California 90265, USA*
[b] *Santa Barbara Research Center, Goleta, California 93117, USA*

Abstract

High-performance in situ doped two-color detectors with the n–p–n architecture for the sequential detection of mid- and long-wave infrared radiation were grown by molecular beam epitaxy. These detector structures were twin-free, and exhibited narrow rocking curves ($\approx$ 45 arcsec) as determined by X-ray measurements. The near surface etch pit densities in these device structures were typically $(2–3) \times 10^6$ cm^{-2}. The structures were processed as mesas and their electrical properties measured. The spectral response of the mid-wave and long-wave diodes in the integrated detector were characterized by sharp turn-on and turn-off in both bands. Average R_oA values of 100 Ω cm^2 at 10.5 μm and 5.5×10^5 Ω cm^2 at 5.5 μm were measured at 77 K. These results are comparable to those of the best unispectral detectors and represents a significant milestone for MBE-grown HgCdTe two-color devices

Keywords: MBE; HgCdTe; In situ doped; Sequential; Two-color detector; Multispectral

1. Introduction

Devices capable of detection of two bands of infrared radiation are advantageous for military applications such as signature recognition, decoy identification and counter measure avoidance, as they provide an added dimension of contrast when compared to unispectral detectors. An integrated two color detector eliminates the need for a second focal plane array and thus offers advantages such as automatic pixel registration, lower cost and cooling requirements, and system complexity as compared to two independent detectors used for the same application [1]. $Hg_{1-x}Cd_xTe$ is the material of choice for the detection of mid-wave, long wave and very-long wave IR radiation, attributed to its band gap tunability and other desirable optical and electrical properties, and the ability to optimize performance at the desired temperature for the infrared band of interest [2].

Significant progress has been achieved in the molecular beam epitaxial (MBE) growth of devices

* Corresponding author. E-mail: rrajavel@msmail4.hac.com.

0022-0248/97/$17.00 Copyright © 1997 Published by Elsevier Science B.V. All rights reserved
PII S0022-0248(96)01200-6

such as unispectral p-on-n LWIR detectors [3, 4], since performance similar to the best devices demonstrated by the more established liquid phase epitaxy (LPE)-based production process [5] has been reported recently. This milestone is a consequence of sustained improvements in the quality of the HgCdTe films grown by MBE and in situ n- and p-type doping capability. Due to the flexibility in composition and doping control offered by vapor phase epitaxial growth techniques, MBE and metalorganic chemical vapor deposition (MOCVD) have been investigated for the growth of multispectral HgCdTe-based IR detectors [6, 7]. At Hughes, we have employed MBE for the growth of a variety of two-color detectors for the detection of radiation in the mid- and long-wave infrared (MWIR and LWIR) bands. This paper will focus on the growth and properties of integrated two-color detectors for the sequential detection of radiation in MWIR and LWIR bands. Results of electrical properties such as R_oA indicate that for the first time, the performance of HgCdTe-based two-color detectors is similar to that observed for unispectral detectors grown with the more established liquid phase epitaxial (LPE) growth process which is used for the commercial production of HgCdTe device.

2. Experimental procedure

The n–p–n devices were grown in a vacuum generator V80H MBE system equipped with Hg, Te and CdTe sources; the details of the growth conditions have been reported elsewhere [8]. The n–p–n device were grown on commercially available (2 1 1)B CdZnTe substrates, and its schematic is shown in Fig. 1. The alloy compositions of the n-type layer adjacent to the substrate (MWIR n-type) determines the spectral cut-off for the MWIR band and the composition of the final n-type layer (LWIR n-type) that is deposited on the p-type layer determines the cutoff of the LWIR band. As the alloy compositions determines the absorption wavelengths of the detectors, it is important to have precise control over the alloy composition. To determine the level of x-value control achieved by MBE, a series of LWIR layers were grown

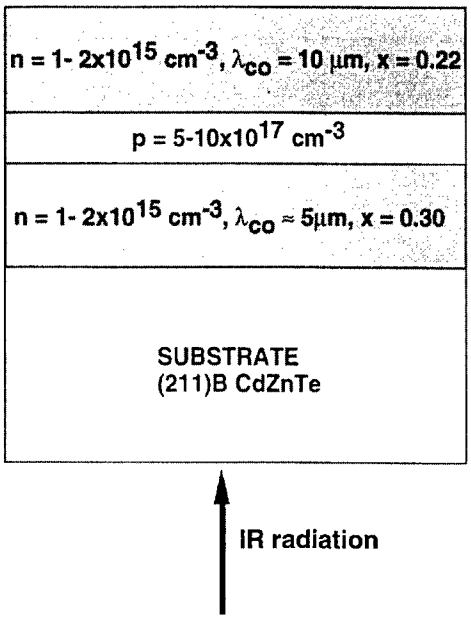

Fig. 1. Schematic of the n–p–n detector used for the sequential detection of MWIR and LWIR radiation.

independently, and analyzed by FTIR measurements to determine the alloy composition in the layers. A batch of n–p–n structures were grown and the crystalline qualities were evaluated using X-ray rocking curve and Θ–2Θ measurement, and wet chemical defect etch studies. The devices were fabricated as mesas and tested to determine the device properties and spectral response characteristics.

3. Results and discussion

3.1. Composition control

To determine the degree of run-to-run alloy composition control that can be achieved, a set of p-on-n LWIR $Hg_{1-x}Cd_xTe$ heterojunction detector structures were grown on 2.5×2.5 cm^2 substrates as reported previously [3]. A small lot of thirteen p-on-n layers were grown successively for this study. The alloy composition of the n-type (thickness = 7 μm) absorbing layer was determined from FTIR measurements using the equation

provided by Hansen, et al. [9]. The target composition for the $Hg_{1-x}Cd_xTe$ layer was $x = 0.225$, to provide a detector cutoff of 10 μm at 77 K. The average measured composition of the n-type $Hg_{1-x}Cd_xTe$ layers was $x = 0.226$, with a standard deviation of 0.003. Thus the level of x-value control demonstrated here enables us to grow detectors with the desired cut-off wavelengths to a precision better than ± 0.1 μm in the MWIR band and ± 0.2 μm in the LWIR band.

3.2. Electrical properties of p- and n-type HgCdTe layers

The main material property that determines the performance of the LWIR detector is the dislocation density in the LWIR n-type layer [10]. The structural quality (which is related to the dislocation density) of this layer is in turn strongly dependent on the underlying p-type layer as well as the MWIR n-type layer (see Fig. 1). Achieving good structural perfection with the desired electrical properties in the n-type MWIR layer that is first deposited onto the CdZnTe substrate is relatively straightforward. The growth parameters that have to be optimized are the substrate temperature and the Hg/Te flux ratio as these two parameters have a strong influence on the structural property. On the other hand, due to the high vapor pressure of Hg, and the tendency for compensation of acceptor impurities, in situ p-type doping has been a challenging issue. Thus achieving good structural perfection with desired levels of p-type conductivity in in situ doped layers are two pre-requisites for the growth of high-performance n–p–n two-color devices.

At Hughes we have developed a unique process that enables us to grow in situ doped p-type layers with good structural and electrical properties that are required for the growth of high-performance two-color detectors [3, 11]. To assess the electrical properties of in situ doped p-type layers, 4–6 μm thick MWIR-HgCdTe : As films were deposited on (2 1 1)B CdZnTe substrates. The samples were subjected to a post-growth Hg-anneal at 250°C to remove any Hg-vacancies in the films, which is a deep level impurity. Electrical contacts were made with Indium and variable temperature Hall effect

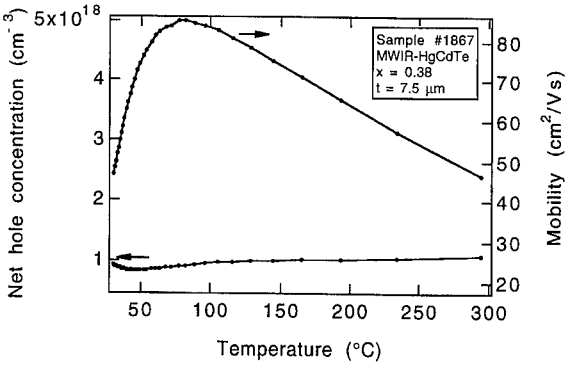

Fig. 2. Temperature dependence of the hole concentration and mobility for in situ doped MWIR-HgCdTe : As film. The electrical activity of the acceptor impurities is estimated at $> 60\%$.

and resistivity measurements were performed and the results are illustrated in Fig. 2. The HgCdTe films doped with As impurities by employing the in situ doping process exhibit classic p-type conductivity. The net hole concentration is in excess of 8×10^{17} cm^{-3} over the entire 300–25 K range. Due to the formation of impurity bands at doping levels exceeding 1×10^{17} cm^{-3}, the hole concentration in this heavily doped sample exhibits little dependence on temperature. As reported previously, the electrical activity in these in situ arsenic-doped films is expected to be greater than 60%, based on SIMS and Hall effect measurements [3]. The structural properties of the films will be discussed in the next section.

N-type conductivity in HgCdTe is obtained by doping the material with a group II or a group VII impurity. Indium is generally employed in MBE, and exhibits nearly 100% electrical activity at doping levels of 10^{15}– 10^{16} cm^{-3}. Hall effect and resistivity measurements were performed on MWIR-$Hg_{1-x}Cd_xTe$ ($x = 0.33$) layers and the variation in electron concentration and mobility is shown in Fig. 3. As expected, the electron mobility increases with decreasing temperature and reaches a maximum of 63 000 cm^2/(V s) at 30 K. The high mobility values measured in these films illustrates the background (unintentional) doping level is $< 7 \times 10^{14}$ cm^{-3}, as inferred from the net extrinsic electron concentration at 77 K.

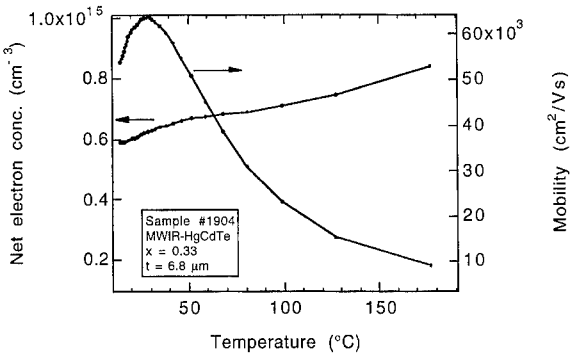

Fig. 3. Temperature dependence of the electron concentration and mobility for in situ doped MWIR-HgCdTe : In film.

3.3. Structural and electrical properties of n–p–n devices

After confirming the electrical properties (carrier concentration and mobility) in the individual n- and p-type layer, n–p–n structures illustrated in Fig. 1, were grown in one continuous growth process. The structural properties of the n–p–n were studies by X-ray diffraction and wet chemical defect etch measurements. X-ray rocking curve measurements of the (2 2 4) reflection utilizing a 3 mm $\times$ 0.5 mm beam of Cu Kα_1 X-rays from a Ge four-crystal monochromator were made to assess the crystalline quality of the epilayers. X-ray rocking curve scan of a representative two-color detector structure exhibited a FWHM of 47 arcsec and the width of the rocking curve is dominated by the top LWIR n-type layer, with some contribution from the underlying p- and n-type layers. X-ray Θ–2Θ measurements shows peaks that correspond to the (4 2 2) reflection and the absence of any (3 3 1)-related diffraction peaks indicates that the HgCdTe layer is twin-free, since such reflections arise when first-order twinning of a (2 1 1)-oriented layer, consisting of a 180°C rotation about the [1 1 1] twist axis, produces a (5 5 2)-oriented layer [12].

Besides X-ray characterization, the crystalline quality of the layers were also evaluated by wet chemical defect etch studies. The leakage current in a unispectral detector is strongly dependent on the dislocation density in the n-type absorbing layers, and it is desirable to minimize the dislocation density in the layers. For these two-color detector structures, the threading dislocation density at the near-surface region of the LWIR n-type layer was estimated through the use of a defect etch consisting of 80 ml H_20 : 10 ml HCl : 20 ml HNO_3 : 8.1 g $Na_2Cr2O_7 \cdot 2H_2O$ whose action is similar to that of other published HgCdTe (1 1 2)B defect etches [13]. The near surface etch-pit densities in these films ranged from 5×10^5 to 1×10^7 cm^{-2}, with a typical value of $(2–3) \times 10^6$ cm^{-2}. Step etch studies followed by etch pit density measurements indicate that the underlying p-type layers have etch pit densities that are similar to the near-surface values in the n-type LWIR layer. On the other hand etch pit densities in the n-type MWIR layers were consistently within $(5–10) \times 10^5$ cm^{-2}. Thus for this batch of n–p–n layers, the etch pit density in the top n-type LWIR layer was dependent on the etch pit density in the underlying p-type layer.

The n–p–n layers were fabricated as mesas and individual electrical contacts were made to the LWIR n-type layer and the MWIR n-type layer via the array common contact [14]. This device was operated in a sequential mode that does not require electrical contacts to the intermediate p-type layer. Depending on the bias applied to the contacts, the

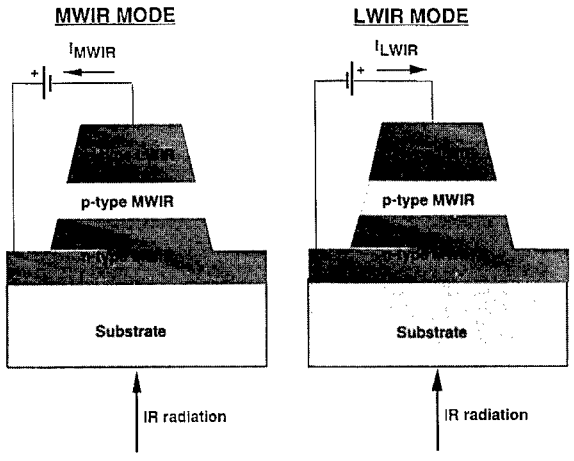

Fig. 4. MWIR and LWIR modes of operation of a sequential n–p–n two-color detector achieved by switching the bias.

MWIR or the LWIR diode can be activated for detection. As shown in Fig. 4, when a negative bias is applied to the LWIR n-type layer, the LWIR p–n junction is in forward bias, and behaves like a low resistance contact. In this mode, the MWIR p–n junction is in reverse bias, and the current that flows in the circuit is proportional to the MWIR photon flux. On the other hand, when a negative bias is applied to the MWIR n-type layer, the MWIR p–n junction is in forward bias, and behaves like a low resistance contact. For this mode of operation, the LWIR p–n junction is in reverse bias, and the current that flows in the circuit is proportional to the LWIR photon flux [6, 14]. In practice the bias for activating the MWIR and The LWIR diodes are chosen such that the current in the circuit in relatively independent of the voltage, but proportional to the optical generation rate. The I–V characteristics of this n–p–n structure with diodes measuring 50 μm × 50 μm are shown in Fig. 5, and are similar to that expected for diodes with this back-to-back configuration.

The spectral response of two-color detectors fabricated from sample #1690 were measured in a dewar at 80 and 40 K and the data are shown in Fig. 6. The average spectral response cut-off for the mid-wave diodes at 80 K is 5.5 μm. The longer wavelength radiation to which the MWIR n-type layer is transparent, produces the LWIR signal, whose average spectral response cut-off is 10.5 μm at 80 K for this sample. The measurements were made at zero bias for the MWIR diode and 150 mV for the LWIR detector. As expected, due to the narrowing of the band gaps at lower temperatures the spectral response of the MWIR and LWIR diodes are both shifted to the longer wavelength at 40 K.

One measure of two-color detector performance is the magnitude of R_oA (where R_o^{-1} is given by $[dI/dV]_{V=0}$ and A is the diode junction area) and this value is frequently compared with production LPE unispectral detectors with the same cut-off. In the case of these sequential diodes, the R_oA values generally represent components from both MWIR and the LWIR diodes. However R_rA (where $R_r^{-1} = [dI/dV]_{V=r\ V}$) values are a more meaningful measure of the figure of merit, since the high resistance of a reverse biased diode dominates the

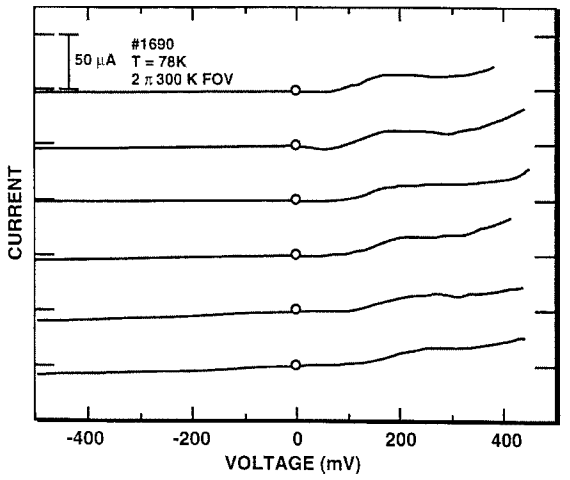

Fig. 5. I–V characteristics of n–p–n diodes measuring 50 μm × 50 μm.

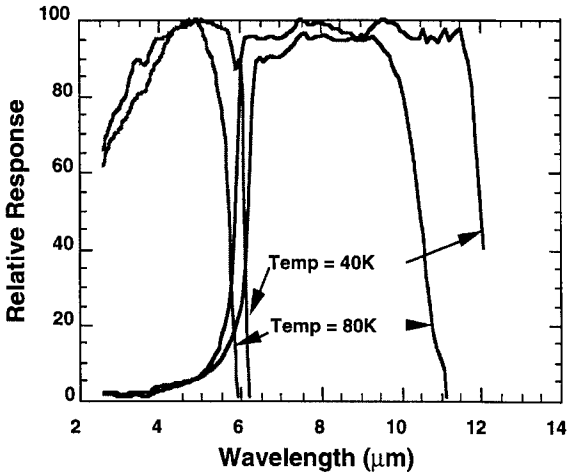

Fig. 6. Spectral response per watt of the MWIR (λ_{co} = 5.5 μm at 77 K) and LWIR (λ_{co} = 10.5 μm at 77 K) diodes.

forward bias characteristics of diodes in the back-to-back geometry. Based on R_oA and R_rA values measured for unispectral diodes, R_oA values for sequential two-color detectors can be estimated from their R_rA values. For a set of six LWIR diodes measuring 50 μm × 50 μm with a cut-off of 10.5 μm the average R_rA value was 3000 Ω cm^2 at 78 K at 0-fov (field of view), and the corresponding R_oA

value is estimated to be $> 100\,\Omega\,cm^2$. This value compares favorably with the best unispectral detectors operating at 10.5 μm, whose values range from ≈ 80 to $200\,\Omega\,cm^2$ [5]. The MWIR diode also exhibited LPE-trendline R_oA values of $5.5 \times 10^5\,\Omega\,cm^2$ at 77 K. Although the results presented here are from a mini-array of diodes, this is a significant milestone for MBE as R_oA values in two-color detectors is now equivalent to the best unispectral detectors. Currently work is underway for the development of an entire two-color focal plane arrays.

4. Conclusion

In situ doped sequential two-color detectors with the n–p–n architecture were grown by MBE, for the detection of MWIR and LWIR radiation. Narrow X-ray rocking curves with typical FWHM of 45 arcsec were measured. The layers were twin-free as determined from X-ray Θ–2Θ measurements. Near-surface dislocation densities as inferred from etch pit density measurements were typically $(2–3) \times 10^6\,cm^{-2}$. Electrical contacts were made to the MWIR n-type layer via the array common contact, and to the LWIR n-type layer at the top of the processed mesas. The spectral response of the MWIR and LWIR diodes in the integrated detector were characterized by sharp turn-on and turn-off in both bands. Average R_oA values of $100\,\Omega\,cm^2$ at 10.5 μm and $5.5 \times 10^5\,\Omega\,cm^2$ at 5.5 μm at 77 K were measured, and are comparable to the best unispectral detectors, which is a significant milestone for MBE-grown HgCdTe two-color devices.

References

[1] J.A. Wilson, E.A. Patten, G.R. Chapman, K. Kosai, B. Baumgratz, P. Goetz, S. Tighe, R. Risser, R. Herald, W.A. Radford, T. Tung and W.A. Terre, SPIE 2274 (1994) 117.
[2] D.A. Scribner, M.R. Kruer and J.M. Killiany, Proc. IEEE 79 (1991) 66.
[3] R.D. Rajavel, D.M. Jamba, O.K. Wu, J.A. Roth, P.D. Brewer, J.E. Jensen, C.A. Cockrum, G.M. Venzor and S.M. Johnson, J. Electron. Mater. 28 (1996) 1410.
[4] C.A. Cockrum, S.M. Johnson, P.G. Petrowoski, G.M. Venzor, R.D. Rajavel, J.E. Jensen, O.K. Wu, J.D. Benson, J.C. Brown, S.D. Phu and J.J. O'eill, Proc. IRIS Specialty Group on Infrared Detectors, NIST, Boulder CO (1996).
[5] T. Tung, L.V. DeArmond, R.F. Herald, P.E. Herning, M.H. Kalisher, D.A. Olson, R.F. Risser and S.J. Tighe, SPIE 1735 (1992) 109.
[6] E.R. Blazejewski, J.M. Arias, G.M. Williams, W. McLevige, M. Znadian and J. Pasko, J. Vac. Sci. Technol. B 10 (1992) 1626.
[7] M.B. Reine, P.W. Norton, R. Starr, M.H. Weiler, M. Kestigian, B.L. Musicant, P. Mitra, T. Schimert, F.C. Case, I.B. Bhat, H. Ehsani and V. Rao, J. Electron. Mater. 24 (1995) 669.
[8] R.D. Rajavel, O.K. Wu, J.E. Jensen, C.A. Cockrum, G.M. Venzor, E.A. Patten, P.M. Goetz, D. Leonard and S.M. Johnson, Mater. Res. Soc. Symp. Proc. 421 (1996) 335.
[9] G.L. Hansen, J.L. Schmit and Y.N. Casselman, J. Appl. Phys. 53 (1982) 7099.
[10] S.M. Johnson, D.R. Rhiger, J.P. Rosbeck, J.M. Peterson, S.M. Taylor and M.E. Boyd, J. Vac. Sci. Technol. B 10 (1992) 1499.
[11] O.K. Wu, D.N. Jamba and G.S. Kamath, J. Crystal Growth 127 (1993) 365.
[12] S.M. Johnson, J.B. Jones, W.L. Ahlgren, W.J. Hamilton, M. Ray and G.S. Tompa, Long Wavelength Semiconductor Devices, Materials and Processes, in: Mater. Res. Soc. Symp. Proc. Vol. 216, Eds. A. Katz, R.M. Biefield, R.L. Gunshor and R.J. Malik (Materials Research Soc., Pittsburgh, PA, 1991).
[13] J.S. Chen, US Patent No. 4 897 152.
[14] E.F. Schulte, US Patent No. 5 113 076.

ELSEVIER

Journal of Crystal Growth 175/176 (1997) 659–664

JOURNAL OF CRYSTAL GROWTH

Ellipsometric analysis of CdZnTe preparation for HgCdTe MBE growth

J.D. Benson*, A.B. Cornfeld, M. Martinka, J.H. Dinan, B. Johs, P. He, John A. Woollam

Night Vision and Electronics Sensors Directorate, 10221 Burbeck Rd., Ft. Belvoir, Virginia 22060-5806, USA

Abstract

An in-situ spectroscopic ellipsometer has been installed on a molecular beam epitaxy system to improve control of HgCdTe molecular beam epitaxy. Using the spectroscopic ellipsometer, in-situ analysis of substrate preparation, surface cleanliness and substrate temperature were monitored. These results were correlated with in-situ reflection high energy electron diffraction and Auger spectroscopy. A real time spectroscopic ellipsometric model was developed which determined the substrate temperature as well as the overlayer thickness.

Keywords: Molecular beam epitaxy; Spectroscopic ellipsometry

1. Introduction

$Hg_{1-x}Cd_xTe$ is an infrared detector material with significant military applications. Molecular beam epitaxy (MBE) is an advanced growth technique used to deposit $Hg_{1-x}Cd_x$ Te [1–3]. MBE is particularly useful for multi-layer growth necessary for novel 'smart' detectors [2, 3]. $Cd_{1-y}Zn_yTe$ is currently the substrate material of choice for high-performance long wavelength HgCdTe detectors. $Cd_{0.96}Zn_{0.04}Te$ is lattice matched to $Hg_{0.77}Cd_{0.23}$ Te (long wavelength detection) [4]. The preferred orientation of CdZnTe substrates for MBE growth is (2 1 1)B. This preference has been motivated by material quality and device performance results [5–7]. In the current state of the art MBE HgCdTe detector there is no buffer layer between the HgCdTe and CdZnTe. This makes the surface preparation extremely critical for proper heterojunction formation. An in-situ real-time vacuum compatible technique to determine surface contamination could have a significant impact on the critical startup growth of HgCdTe.

Ellipsometry is a widely used technique to determine semiconductor thin film optical constants [8]. It is a highly sensitive, nondestructive technique. Ellipsometry measures the change in the polarization of the light reflected from a surface. Two parameters, psi (Ψ) and delta (Δ) are measured by the ellipsometer. Physically, tan Ψ is the reflection coefficient amplitude ratio of the two orthogonal components of elliptically polarized light, and Δ is

* Corresponding author. Fax: + 1 703 704 1705; e-mail dbenson@nvl.army.mil.

0022-0248/97/$17.00 Copyright © 1997 Published by Elsevier Science B.V. All rights reserved
PII S0022-0248(96)01214-6

the change in phase difference between the two components. Spectroscopic ellipsometry measures these optical parameters as a function of several (in our case 88) wavelengths of light. Real-time analysis is now possible since the advent of powerful personal computers. State of the art spectroscopic ellipsometry with the accompanying analysis software can accurately measure in real time the thin film composition and surface chemistry of a wafer as it is being prepared for growth and during growth [9].

2. Experimental procedure

In-situ real-time spectroscopic ellipsometric data was acquired during MBE substrate preparation and growth of HgCdTe. The MBE growth was performed in a modified Fisons VG-80 chamber, upgraded to include ellipsometry viewports at a 75° angle of incidence with respect to the sample normal. A reduced wobble substrate rotation stage was also added to permit measurement during substrate rotation. This is necessary since the substrate is rotated during growth to enhance compositional uniformity. An 88 waveband ellipsometer over a 1.5–4.5 eV spectral range was used to acquire data. A Windows 95 based computer using an Intel Pentium processor controlled the ellipsometer; performed data analysis, and effected process feedback control. Further details of the ellipsometer hardware and software are given by Murthy [10].

Substrate preparation is an integral part of any vacuum deposition technique. A minimum amount of wafer handling was done in order to reduce contamination. CdZnTe wafers were soaked for 5 min in methanol, etched for 2 min in bromine methanol (0.3%), soaked for 5 min in methanol, rinsed in flowing deionized water, and blown dry with nitrogen. The wafer was clip-mounted on a substrate holder and installed as rapidly as possible in a fast entry vacuum port to minimize atmospheric contamination. The substrate was transferred into the load lock system and annealed overnight at 130°C.

MBE growth of HgCdTe took place by evaporating elements from the Hg, CdTe, and Te cells. The substrate was annealed at 340°C in-situ for 10 min and then reduced to the growth temperature of 180°C. These temperatures were measured by an optical pyrometer and controlled by a thermocouple. The substrates were 1.5 cm × 1.5 cm (2 1 1)B $Cd_{0.96}Zn_{0.04}Te$. Buffer layers were not grown on the substrate. The substrate was rotated at 6 rev/min during data collection. This rotation rate produced good lateral uniformity when the HgCdTe growth was initiated.

Reflection high-energy electron diffraction (RHEED) was carried out in-situ during the MBE CdZnTe surface preparation and during HgCdTe growth. A 10 kV electron gun at glancing angle of incidence was used.

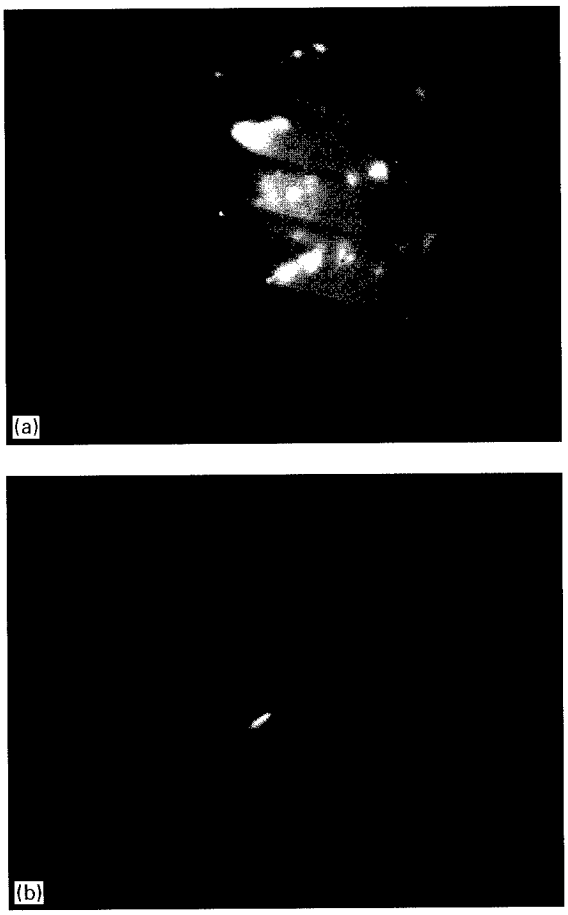

Fig. 1. (a) RHEED pattern for the CdZnTe wafer before thermal annealing in the MBE chamber; (b) RHEED pattern after in-situ annealing at 340°C for 10 min.

Auger spectroscopy was also used to determine the CdZnTe substrate preparation. Auger measurements were made on a PHI model 10-150. Although not in the MBE chamber, samples could be transferred to the Auger apparatus via an ultra-high vacuum transfer tube. The background pressure of the tube and analysis chamber is 1×10^{-9} Torr. The Auger electrons were measured in the differential mode $dN(E)/dE$ with a single pass cylindrical mirror analyzer with energy resolution $\Delta E/E = 0.6\%$. A 3 kV, 16 μA electron beam energy was used with a 1.5 V peak-to-peak modulation voltage. The scan rate was 2 eV/s. The elemental abundance was quantified using standard peak-to-peak amplitude measurements. These values were then multiplied by sensitivity factors measured from elemental Cd and Te.

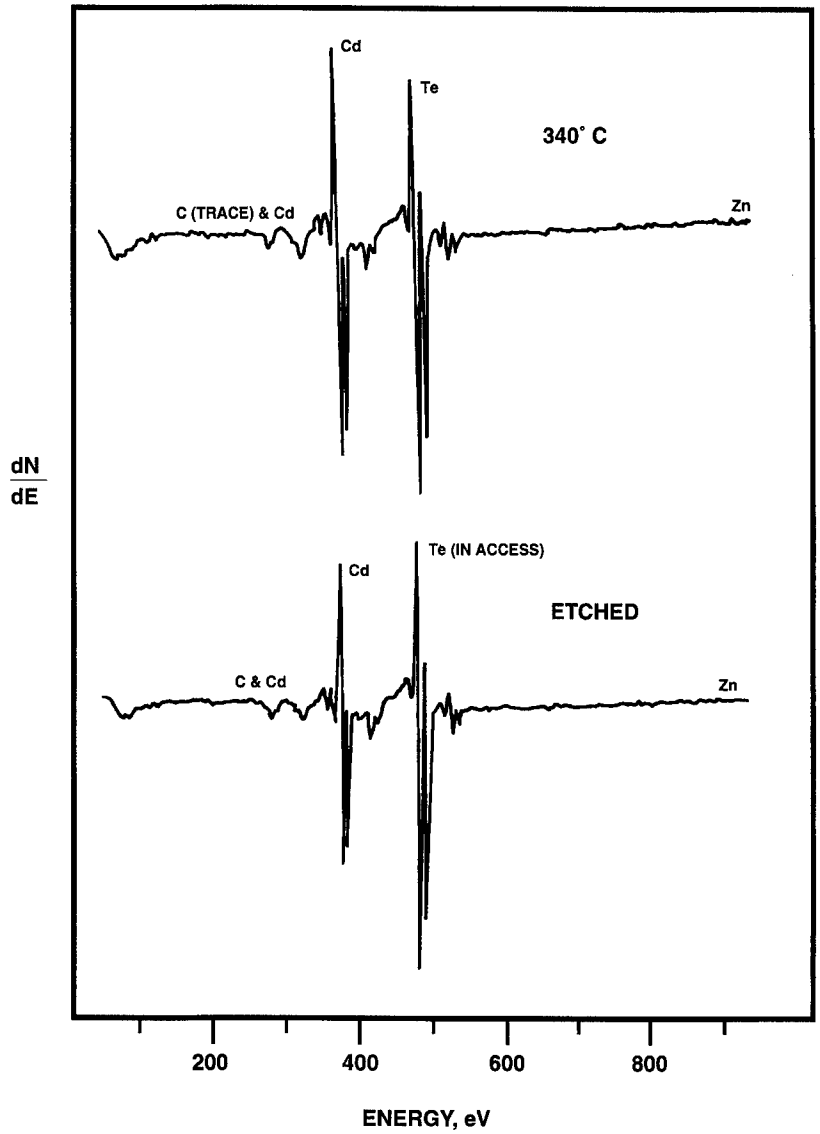

Fig. 2. Auger spectra of the initial etched surface, and the spectra obtained after in-situ annealing for 10 min at 340°C.

3. Results and discussion

Ellipsometric optical constants have proven very sensitive to oxide layers and etching reactions of II–VI compounds [8, 11–13]. This work investigates the ability of spectroscopic ellipsometry to determine changes in surface composition and cleanliness of CdZnTe as it is being prepared for MBE HgCdTe growth. To assure accurate spectroscopic optical constants for CdZnTe a very clean starting surface is necessary. A clip-mounted substrate was used to ensure the cleanliness of the CdZnTe surface. To determine if the CdZnTe substrate was clean, Auger and RHEED analyses were performed.

It is well known that CdZnTe wafers as prepared in a wet chemical environment have an adlayer of oxides and other contaminates including excess tellurium [14, 15]. This contaminate layer desorbs as the substrate is heated in vacuum. The temperature necessary for adlayer removal is approximately the congruent sublimation temperature (340°C) [16]. As seen in Fig. 1, RHEED indicated that the surface adlayer evaporated after 10 min MBE vacuum annealing at 340°C. To obtain more quantitative information with regard to surface contamination, Auger analysis was done on the same wafer and is shown in Fig. 2. Five and ten times increased sensitivity Auger spectra, not shown, were also collected up to an energy of 1300 eV. The initial surface, after the wet chemical treatment, is depleted in Cd and shows excess Te. After in-situ annealing for 10 min at 340°C the CdZnTe surface was clean except for some regions with a minor residual of carbon as shown in Fig. 2. This surface is nearly stoichiometric. Similar results of vacuum surface preparation of CdTe have been found by other authors [17–19].

In order to quantify the amount of contaminate left on the surface after MBE heating, a layer model was used to describe the Auger results [20]. The model of the homogeneous overlayer uses the relationship between concentration and normalized Auger signal from the surface layer combined with the attenuated normalized Auger signals from the substrate. Calculations are performed on a monolayer basis with numerical thickness incorporated at the conclusion. The model yields the composition and the total material detected in both the overlayer and substrate. This model determined that as the CdZnTe substrate was brought into the MBE chamber the contaminate overlayer was 2.2 Å thick (0.9 monolayers). The composition within the monolayer was Te = 84.7%, C = 13.3%, O = 1.5%, and Cl = 0.5%. After the 10 min 340°C in-situ anneal, 0.4 Å (0.16 monolayers) were present. The composition within the monolayer was Te = 88.3%, C = 7.3%, O = 4.4%, and chlorine was undetected.

The lack of temperature-dependent spectroscopic optical constants for CdZnTe complicates the ellipsometric analysis of the CdZnTe surface contamination. To determine these optical constants, a CdZnTe wafer mounted to the substrate holder using clips was heated in the MBE chamber. From 0 to 15 min the wafer was heated from

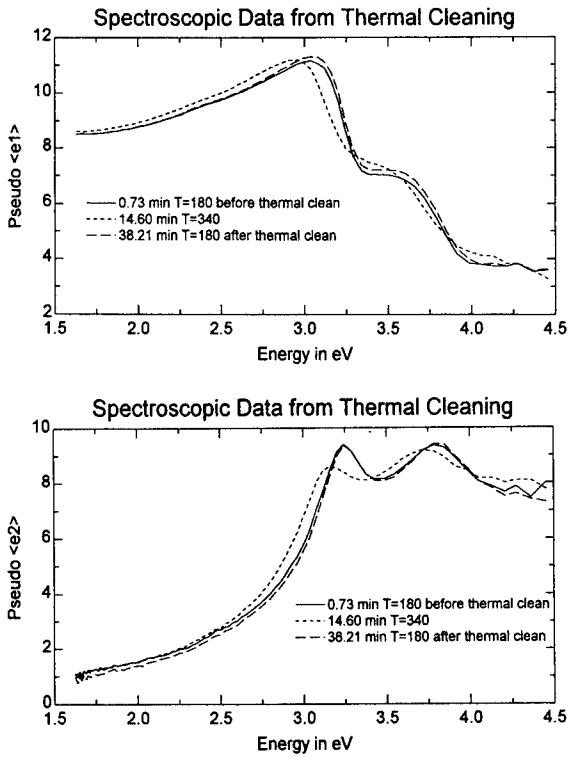

Fig. 3. Pseudodielectric constants ε_1 and ε_2 as for the CdZnTe wafer at three different times. At time $t = 0.73$ min the CdZnTe wafer is surface-contaminated and at approximately 130°C. At $t = 14.6$ min the overlayer has desorbed and the temperature is 340°C. At $t = 38.21$ min the overlayer is gone and the substrate temperature is 180°C.

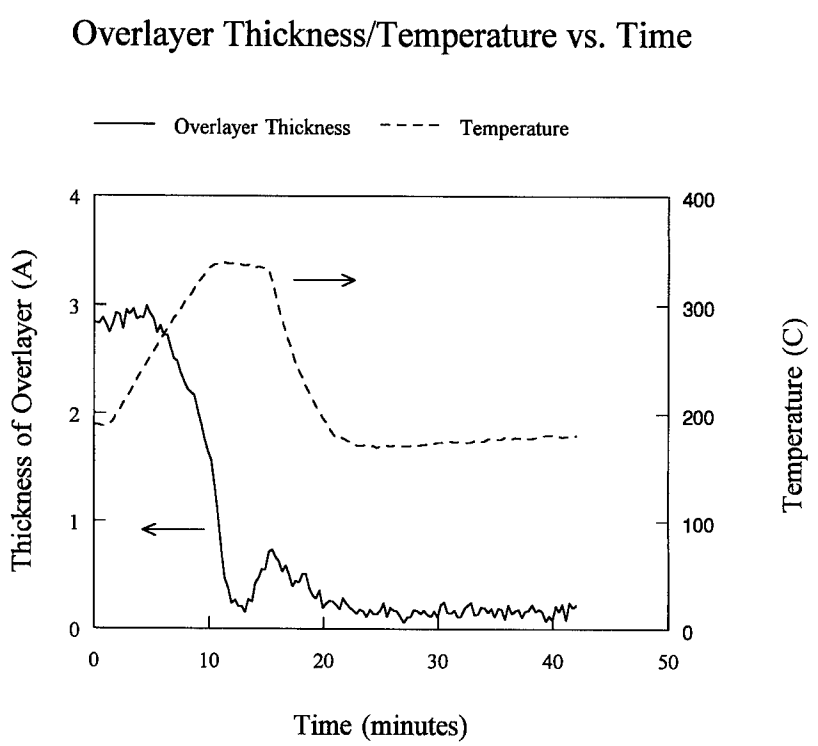

Fig. 4. Spectroscopic ellipsometric model of change in contamination overlayer thickness and CdZnTe wafer temperature as a function of time as the CdZnTe wafer is being increased to 340°C.

approximately 130°C to 340°C. During this time the overlayer desorbed. The substrate temperature was reduced to 180°C and allowed to stabilize at this temperature (15–42 min). Fig. 3 shows the spectroscopic data of all 88 wavelengths in three regions. At time $t = 0.73$ min at approximately 130°C the CdZnTe wafer is surface-contaminated. At $t = 14.6$ min the temperature is 340°C and the overlayer has desorbed. At $t = 38.21$ min the substrate temperature is 180°C and the CdZnTe wafer is clean and stoichiometric. From an analysis of Fig. 3 at times $t = 14.6$ and 38.21 min a temperature-dependent library of clean CdZnTe ellipsometric parameters was built. These data were then used to determine the contaminate adlayer thickness.

As determined from the above RHEED and Auger analysis, the contaminate overlayer thickness decreases as the CdZnTe substrate is heated in the MBE to 340°C. Using the temperature-dependent spectroscopic optical constants of clean CdZnTe determined above, the time period between 0 and 15 min was monitored for overlayer thickness. The change in overlayer thickness as a function of time and temperature was determined by an ellipsometric model [21, 22]. The result is shown in Fig. 4. As can be seen in this figure, the CdZnTe wafer starts with an overlayer thickness of approximately 3 Å. As the substrate temperature is increased to 340°C the overlayer thickness decreases to approximately 1 Å. This model also is in qualitative agreement with the in-situ Auger analysis done under the same conditions.

4. Conclusions

Spectroscopic ellipsometry has been used to monitor the preparation of CdZnTe substrates prior to HgCdTe MBE growth. Substrates were shown to contain surface contamination when brought into the chamber. As the CdZnTe

substrate was heated in the MBE chamber to 340°C, the contaminate adlayer desorbed. This surface preparation treatment was detected by the ellipsometer and confirmed by Auger and RHEED analysis. Spectroscopic ellipsometry is now routinely used as part of our start-up growth procedure.

References

[1] J.P. Faurie and A. Million, J. Crystal Growth 54 (1981) 582.
[2] E.R. Blazejewski, J.M. Arias, G.M. Williams, M. Zandian and J. Pasko, J. Vac. Sci. Technol. B 10 (1992) 1626.
[3] O.K. Wu, D. Rajavel, T.J. DeLyon, J.E. Jensen, C.A. Cockrum, S.M. Johnson, G.M. Venzor, G.E. Chapman, J.A. Wilson, E.A. Patten and W.A. Radford, Presented at SPIE Photonics West Conf., San Jose, CA, 31 January–2 February (1996), to be published.
[4] K. Hirata and O. Oda, Mater. Lett. 5 (1986) 42.
[5] R.J. Koestner and H.F. Schaake, J. Vac. Sci. Technol. 6 (1988) 2834.
[6] J.M. Arias, J.G. Pasco, M. Zandian, S.H. Shin, G.M. Williams, L.O. Bubulac, R.E. DeWames and W.E. Tennant, Appl. Phys. Lett. 62 (1993) 976.
[7] R.D. Rajavel, D. Jamba, O.K. Wu, J.A. Roth, P.D. Brewer, J.E. Jensen, C.A. Cockrum, S.M. Johnson and G.M. Venzor, J. Electron. Mater. 25 (1996), to be published.
[8] D.R. Rhiger, J. Electron. Mater. 22 (1992) 887.
[9] J.D. Benson, A.B. Cornfeld, M. Martinka, K.M. Singly, Z. Derzko, P.J. Shorten, J.H. Dinan, P.R. Boyd, F.C. Wolfgram, B. Johs, P. He and J.A. Woollam, J. Electron. Mater. 25 (1996), to be published.
[10] S. Dakshina Murthy, I.B. Bhat, B. Johs, S. Pittal and P. He, J. Electron. Mater. 24 (1995) 445.
[11] H. Arwin, D.E. Aspnes and D.R. Rhiger, J. Appl. Phys. 54 (1983) 7132.
[12] D.E. Aspnes and H. Arwin, J. Vac. Sci. Technol. A 2 (1984) 1309.
[13] H. Arwin and D.E. Aspnes, J. Vac. Sci. Technol. A 2 (1984) 1316.
[14] P.M. Amirtharaj and F.H. Pollak, Appl. Phys. Lett. 45 (1984) 789.
[15] R.D. Feldman, R.L. Opila and P.M. Bridenbaugh, J. Vac. Sci. Technol. A 3 (1985) 1988.
[16] J.D. Benson and C.J. Summers, J. Appl. Phys. 66 (1989) 5367.
[17] Y.-C. Lu, C.M. Stahle, R.S. Feigelson and J. Morimoto, J. Appl. Phys. 62 (1987) 4453.
[18] Y.S. Wu, C.R. Becker, A. Waag, R.N. Bicknell-Tassius and G. Landwehr, Semicon. Sci. Technol. 8 (1993) 293.
[19] Y. Luo, D.A. Slater and R.M. Osgood, Appl. Phys. Lett. 67 (1995) 55.
[20] C.C. Chang, in: Characterization of Solid Surfaces, Eds. P.F. Kane and G.B. Larrabee (Plenum, New York, 1978).
[21] G.N. Maracas, J.L. Edwards, K. Shiralagi, K.Y. Choi, R. Droopad, B. Johs and J.H. Woollam, J. Vac. Sci. Technol. A 10 (1992) 1832.
[22] C. Herzinger, B. Johs, P. Chow, D. Reich, G. Carpenter, D. Croswell and J. Van Hove, Mater. Res. Soc. Symp. Proc. 406 (1996) 347.

ELSEVIER

Journal of Crystal Growth 175/176 (1997) 665–669

JOURNAL OF CRYSTAL GROWTH

Molecular beam epitaxial growth of the CdMnTe/CdTe superlattices on (100) GaAs substrates

Mitsuaki Yano*, Kazuto Koike, Takeshi Furushou, Tokuo Yodo

New Materials Research Center, Osaka Institute of Technology, Asahi-ku Ohmiya, Osaka 535, Japan

Abstract

This paper deals with the molecular beam epitaxial growth of CdMnTe/CdTe superlattices on (100)-oriented GaAs substrates, focusing on the initial growth of CdTe film on the lattice mismatched substrate and on the interface sharpness of the superlattice. The growth condition was optimized using the in situ observed signals of reflection high-energy electron diffraction (RHEED) from the surface. In addition to the RHEED analysis, the film quality was examined by using scanning electron microscope, photoluminescence, and X-ray diffraction. Use of a sulfur-treated GaAs surface and a growth interruption at each interface under an irradiation of Te beam are proposed to improve the superlattice quality on the lattice-mismatched substrate.

1. Introduction

Diluted magnetic semiconductors (DMS) including transition metals (Mn, Fe, etc.) have attracted much attention among solid state physicists. Recently, samples with quantum structures consisting of alternating layers of DMS and non-magnetic semiconductors, like CdMnTe/CdTe, have been grown on GaAs substrates by molecular beam epitaxy (MBE) from the interests in fundamental physics [1] and device applications [2]. However, the film quality was not as good as that on lattice-matched substrates such as InSb [3] and CdZnTe [4], because of a large lattice mismatch (about 15%) between the CdMnTe films and the GaAs substrates.

In this paper, we first describe the optimized growth conditions for the CdTe films on (100)-oriented GaAs substrates. Subsequently, we report its application to high-quality CdMnTe/CdTe superlattices. We discuss their crystallographic and optical properties for various growth conditions.

2. CdTe films on GaAs substrates

In this experiment, CdMnTe/CdTe films on (1 0 0) GaAs substrates were grown from CdTe, Cd, Te and Mn source materials in K-cells in an MBE apparatus equipped with a 20 KeV reflection high-energy electron diffraction (RHEED) system. Typical beam equivalent pressures we used were

* Corresponding author. Fax: +81 6 957 2136; e-mail: yano@elc.oit.ac.jp.

0022-0248/97/$17.00 Copyright © 1997 Elsevier Science B.V. All rights reserved
PII S0022-0248(96)00968-2

2×10^{-7} Torr for CdTe, 7×10^{-8} Torr for Cd and Te, and 4×10^{-8} Torr for Mn. The growth rate was about 0.5 μm/h for CdTe films at 320°C.

Using the CdTe beam, both (1 0 0) and (1 1 1) CdTe films can be grown on (1 0 0) GaAs substrates. We found that the CdTe films always became (1 1 1) when the (1 0 0) GaAs substrate was covered with an As-stabilized surface, in agreement with the report by Kolodziejski et al. [5]. The (1 1 1) growth was highly controllable since the As-stabilized surface was easy to prepare by observing its characteristic RHEED patterns of (2×4) or (3×1) reconstructions. For the selective growth of (1 0 0) CdTe, on the other hand, we examined two different types of (1 0 0) GaAs substrates, covered with either a thin telluride or a thin native oxide layer, as suggested by previous works [6, 7]. The thin telluride layer, which had $(2\sqrt{3} \times 2\sqrt{3})$R30° reconstruction, was in situ prepared by heating the GaAs substrates in the Te beam at 580°C. To obtain the thin native oxide layer, on the other hand, the heating at 580°C was done without beam irradiation and was stopped when a faint (1×1) RHEED pattern appeared. We found that both types of substrates were effective to obtain (1 0 0) CdTe films. Control of the latter surface, however, was much more difficult compared to the former one since the (1 0 0) CdTe film easily became a mixture with (1 1 1) or polycrystalline unless the thickness of the oxide layer was appropriate.

In addition to these three types of substrates, we found for the first time that the selective growth of (1 0 0) CdTe was also possible on a S-treated (1 0 0) GaAs surface. This S-treated surface was prepared by using a GaAs substrate dipped in $(NH_4)_2S_x$ solution for 3 min. The excess S adatoms on the surface was removed in vacuum by heating up to 500°C just before the CdTe growth [8]. This selective growth method was found to be highly reproducible since we did not need other controlling factors to start the (1 0 0) growth. From the viewpoint of process reliability, we chose the following three different CdTe films to study the characteristics of initial growth, the (1 0 0) ones grown on the Te-irradiated and the S-treated substrates, and the (1 1 1) one grown on the As-stabilized substrate.

Due to the large lattice mismatch to GaAs, the CdTe films are highly strained during the initial growth. However, fast relaxation of the strained structure is desirable when we use the CdTe film as the buffer layer between the CdMnTe/CdTe superlattice and the GaAs substrate. In Fig. 1, we show the change of the lattice constant with the CdTe thickness. These data were measured by in situ monitored distances between the streaked elemental RHEED lines. Note that the lattice constant of CdTe in the [0 − 11] direction is about 15% larger than that of (1 0 0) GaAs. The data in Fig. 1 indicate that the coherent growth from the substrate is limited within the initial several monolayers due to the large lattice mismatch. When the film thickness exceeds the limit of coherent growth, a rapid relaxation is observed for the strained structure. It is seen from the figure that the fastest relaxation is realized on the S-treated substrate. The CdTe lattice constant on it becomes bulk value within the initial 5 nm growth. On the Te-irradiated and the As-stabilized surfaces, however, more than 50 nm growth is required to complete the relaxation. From these experimental data, we concluded that the (1 0 0) CdTe film on the S-treated GaAs is the most suitable one as the buffer layer.

In order to optimize the growth conditions, we checked the CdTe surface by RHEED. The RHEED pattern during growth was diffused (2×1) independent of the substrate temperature T_s. By

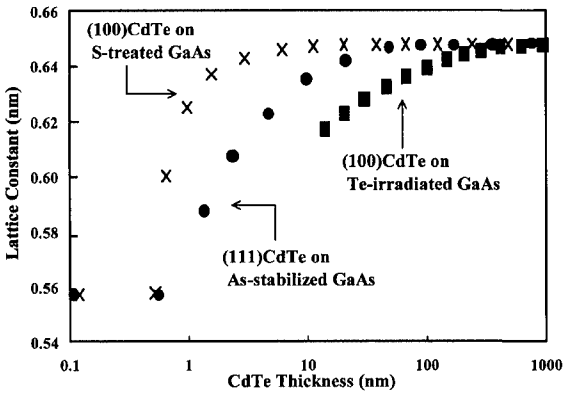

Fig. 1. Change of lattice constants with the thickness of CdTe film. Data are shown for the (1 0 0) CdTe growth on the S-treated and the Te-irradiated surfaces of (1 0 0) GaAs as well as the (1 1 1) CdTe growth on the As-stabilized surface of (1 0 0) GaAs.

interrupting the CdTe beam irradiation, however, the diffused pattern developed to $c(2\times2)$ at $T_s < 320°C$ and (2×1) at $T_s > 320°C$. To understand these reconstructions, we measured the dynamics of the reconstruction change under an alternating irradiation of Cd and Te beams. The inset of Fig. 2 shows the intensity change observed for $\frac{1}{2}$-order RHEED line in the [0 1 0] direction of the $c(2\times2)$ reconstruction on the CdTe surface after shutting the Te beam. The Te adatoms, which were accumulated during the Te beam irradiation, would stay on the surface for a while and then desorb to change the reconstruction from (2×1) to $c(2\times2)$, indicating the shift to a Cd-stabilized surface. The residence time of the adatoms decreased with the increase of the substrate temperature as shown by Fig. 2 in which the results for Cd adatoms are also summarized. Their activation energies were estimated to be 0.87 eV for Te and 3.0 eV for Cd on the (1 0 0) CdTe surface. These values are considerably different from the data $E_{Te} = 1.95$ eV and $E_{Cd} = 7.7$ eV Benson et al. reported [9] although the ratio E_{Cd}/E_{Te} is close to their value. The physical meaning of the difference is not clear yet. Fig. 2 indicates that the residence time of the Te adatoms becomes equal to that of the Cd adatoms at around $T_s = 320°C$, i.e., the stoichiometric composition is achieved on the CdTe surface.

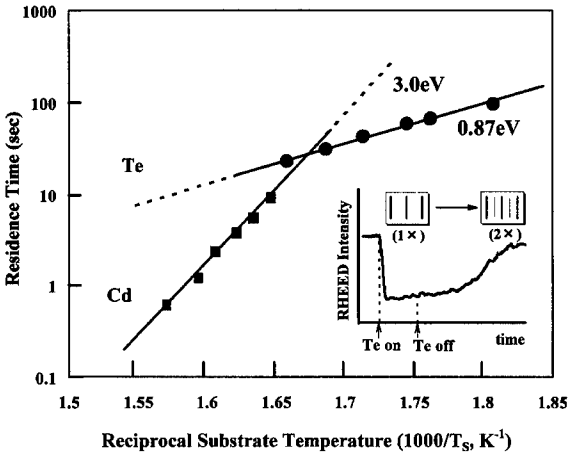

Fig. 2. The residence time of Te and Cd adatoms on a (1 0 0) CdTe surface as a function of the reverse substrate temperature.

Thus the optimum substrate temperature can be expected at $T_s = 320°C$.

In order to confirm this optimum substrate temperature, we observed surface morphologies of the (1 0 0) CdTe films using a scanning electron microscope (SEM) for T_s between 260°C and 360°C. The smoothest surface was obtained at around $T_s = 320°C$. This optimum substrate temperature was also confirmed by a photoluminescence (PL) measurement on these CdTe films. The emission due to the bound exciton became the strongest around at $T_s = 320°C$, indicating a superior quality of the film. At higher or lower substrate temperatures, the bound exciton peak intensity decreased and defect-related emissions increased. Thus, we grew the CdTe buffer layer at $T_s = 320°C$ in the following experiments.

3. CdMnTe films and CdMnTe/CdTe superlattices

Prior to the CdMnTe/CdTe superlattice growth, we grew CdMnTe films on a 400 nm thick CdTe layer by simply adding Mn and Te beams to the CdTe one. Single crystalline (1 0 0) CdMnTe films were obtained in the wide range of substrate temperature, from 260°C to 360°C. However, the growth rate, which was determined by a RHEED oscillation measurement, gradually became small at $T_s > 280°C$. This temperature dependence can be considered as the result of a selective reevaporation of CdTe in the films since their Mn composition became high in proportional to the decrease of the growth rate. Such a selective reevaporation may cause a surface segregation of Mn atoms when the CdMnTe growth is interrupted. Hence, a low substrate temperature is desirable for the superlattice growth. On the other hand, the CdMnTe surface became rough with decreasing the substrate temperature below 300°C. Thus our CdMnTe/CdTe superlattices were grown at $T_s = 300°C$ to reconcile these opposite aspects. The relatively low substrate temperature is also desirable to suppress the thermal diffusion of Mn atoms in superlattices [10].

Fig. 3 shows the RHEED oscillations observed for three different sequences of superlattice growth: (a) continuous growth, (b) growth only with interruptions at each heterointerface, and (c) growth

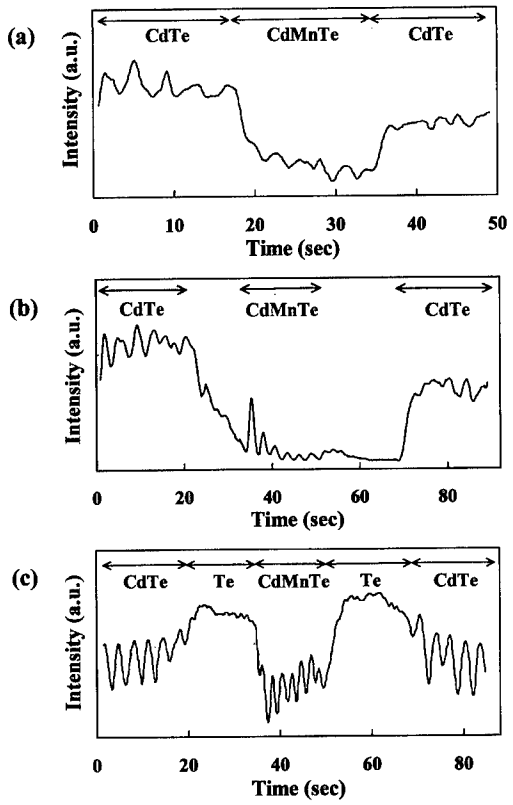

Fig. 3. RHEED intensity oscillations observed for different sequences of the CdMnTe/CdTe growth: (a) continuous growth; (b) only with growth interruptions at each interface, and (c) with interruptions under Te beam irradiation.

with interruptions under a Te beam irradiation. The interruption period is 15 s in (b) and (c). A rapid decrease is seen for (a) after the beginning of CdMnTe growth, suggesting surface roughness increases with the thickness. For (b), on the other hand, the oscillations during CdMnTe growth become clear although the intensity still damps rapidly. This improvement is probably due to the enhanced migration length of the surface adatoms. The weak oscillations during the interruption after CdTe growth may reflect a layer-by-layer reevaporation from the surface. As shown in Fig. 3c, however, this reevaporation was completely suppressed by the Te beam irradiation. Under this condition, the RHEED oscillations no longer damp but continue even after 50-period superlattice growth. From these results, we concluded that the growth interruption under the Te beam irradiation was effective to improve the interface sharpness. The effect of Te beam irradiation is to prevent the reevaporation of CdTe from the surface.

In Fig. 4, we show two PL spectra from differently grown 30-period $(Cd_{0.8}Mn_{0.2}Te)_{20}(CdTe)_{10}$ superlattices excited by an Ar ion laser (514.5 nm, 15 mW) at 12 K. The superlattice in sample (a) was grown continuously using a sequence similar to that in Fig. 3a. For sample (b), we introduced 30 s growth interruptions under the Te beam irradiation at each heterointerface. In both PL spectra, the major peaks at 1.75 eV were ascribed to the transition between electron and hole subbands in these superlattices in agreement with the calculation based on an envelope function model, and the second peaks at 1.86 eV were to the bound excitons in the thick underlying $Cd_{0.8}Mn_{0.2}Te$ layers. By comparing these major peaks, we can understand that the interface quality of the sample (b) is superior to the sample (a), which is consistent with the above-mentioned results by RHEED. The full width at half maximum (FWHM) is 18 meV for sample (b), indicating a high quality of the superlattice. Hence, our growth technique is effective to improve the superlattice quality on the lattice-mismatched substrate.

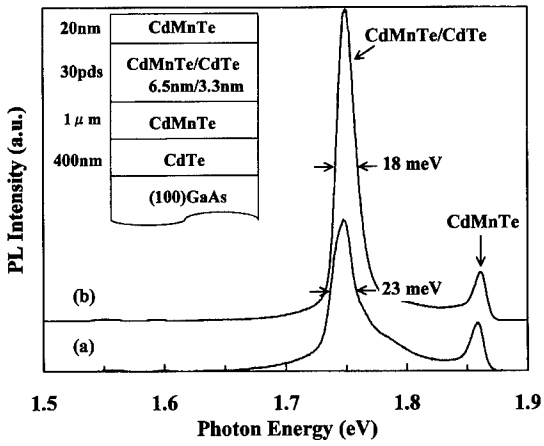

Fig. 4. 12 K PL spectra of two differently grown 30-period $(Cd_{0.8}Mn_{0.2}Te)_{20}(CdTe)_{10}$ superlattices: (a) grown continuously; and (b) with interruptions under Te beam irradiation.

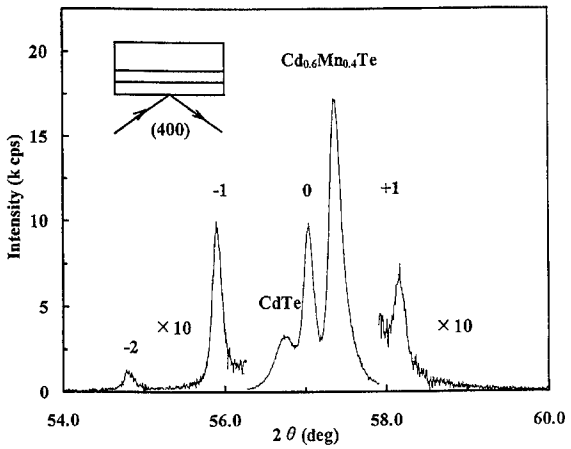

Fig. 5. A recorder trace of the θ–2θ scan of X-ray diffraction for a 30-period $(Cd_{0.6}Mn_{0.4}Te)_{20}(CdTe)_{10}$ superlattice on 1 μm $Cd_{0.6}Mn_{0.4}Te$/400 nm CdTe/(100) GaAs substrate. The peaks labeled 0, $\pm$ 1, 2 are satellites in the superlattice reflection.

In Fig. 5, we show a preliminary X-ray diffraction result from a 30-period superlattice of $(Cd_{0.6}Mn_{0.4}Te)_{20}(CdTe)_{10}$ on 1 μm $Cd_{0.6}Mn_{0.4}Te$/400 nm CdTe/(100) GaAs substrate. The superlattice was grown by the interruption technique with Te beam irradiation. The (400) reflection shown in Fig. 5 was measured by a conventional X-ray diffractmeter in the θ–2θ configuration using the $K\alpha_1$ line from a Cu target. The peaks at 57.3 and 56.8 are attributed to the diffraction lines from the $Cd_{0.6}Mn_{0.4}Te$ and CdTe underlying layers, respectively. The peak at around 57° is ascribed to the zeroth-order line and the other three small peaks to the $\pm$ 1 and 2 satellites in the superlattice reflection. These satellite peaks closely agree with the calculated angular positions of the structure; the measured superlattice periodicity is 9.4 nm and the corresponding value for the designed structure is 9.6 nm. The zeroth-order line locates between the peak from $Cd_{0.6}Mn_{0.4}Te$ and that from CdTe, which is reasonably understood by accounting the mean lattice constant of the superlattice. However, this result also indicates that the superlattice may be in the free standing state since its mean lattice constant is larger than the underlying thick $Cd_{0.6}Mn_{0.4}Te$ layer. This implies that further improvement is possible for the superlattice by reducing the Mn composition in the $Cd_{0.6}Mn_{0.4}Te$ underlying layer to have a lattice constant matched to the superlattice. A detailed X-ray analysis will be discussed elsewhere.

4. Summary

We studied the optimum MBE growth conditions of CdMnTe/CdTe films on (1 0 0) GaAs and succeeded to realize high-quality superlattices on the lattice-mismatched substrates. We propose that the S-treatment of GaAs substrate and the growth under stoichiometric condition at $T_s = 320$°C are useful to improve the CdTe quality and the growth interruption technique with Te beam irradiation is effective to grow CdMnTe/CdTe superlattice with sharp interface. The detailed superlattice analysis by X-ray diffraction is the subject of ongoing work on the diffusion of Mn atoms during growth.

Acknowledgements

The authors wish to thank Dr. M. Inoue, Dr. S. Sasa, and Dr. W. Jie for helpful discussions. This work was supported in part by a foundation from the Mitsubishi Kagaku Foundation for Scientific Research.

References

[1] J. Stankiewicz and A. Aray, J. Appl. Phys. 53 (1982) 3117.
[2] S. Datta, J.K. Furdyna and R.L. Gunshor, Superlattice Microstruct. 1 (1985) 327.
[3] B. Lvnn and J.J. Davies, Semicond. Sci. Technol. 5 (1990) 1155.
[4] W. Grieshaber, C. Bodin, J. Cibert, J. Gaj, Y. Merle, A. Wasiela and G. Feuillet, Appl. Phys. Lett. 65 (1994) 1287.
[5] L.A. Kolodziejski, T. Sakamoto, R.L. Gunshor and B. Datta, Appl. Phys. Lett. 44 (1984) 799.
[6] J.E. Angelo, W.W. Gerberich, C. Bratina, L. Sorba and A. Franciosi, J. Crystal Growth 130 (1993) 459.
[7] J.M. Ballingall, M.L. Wroge and D.J. Leopold, Appl. Phys. Lett. 48 (1986) 1273.
[8] Y. Wu, Y. Kawakami, S. Fujita and S. Fujita, J. Crystal Growth 111 (1991) 757.
[9] J.D. Benson, B.K. Wagner, A. Torabi and C.J. Summers, Appl. Phys. Lett. 49 (1986) 1034.
[10] D. Tönnies, G. Bacher, A. Forchel, A. Waag and G. Landwehr, Appl. Phys. Lett. 64 (1994) 766.

ELSEVIER

Journal of Crystal Growth 175/176 (1997) 670–676

JOURNAL OF CRYSTAL GROWTH

Elastic and plastic deformation in low mismatched $Cd_xHg_{1-x}Te/Cd_{1-y}Zn_yTe$

T. Colin*, T. Skauli, S. Løvold

Norwegian Defence Research Establishment, Division for Electronics, P.O. Box 25, N-2007 Kjeller, Norway

Abstract

We have measured, by X-ray diffraction, the deformation of uniform cadmium mercury telluride layers epitaxially grown on cadmium zinc telluride substrates with varying zinc concentration. It is then possible, within the same sample, to clearly identify elastic deformation in the regions of small lattice mismatch and plastic deformation in the regions with larger mismatch. The deformation has been analysed in a framework based on a stress relaxation model published by Fontaine et al. This analysis permits determination of the energies of formation of misfit dislocations. They have been compared with values obtained from ab initio models. From this comparison possible relaxation mechanisms are proposed. A clear dissymmetry is also observed between relaxation of tensile and compressive strain. Pre-relaxation dislocation movements are also detected by diffraction peak broadening. Possible reasons for these behaviours are discussed.

1. Introduction

In epitaxial structures used for infrared detectors, the required device thickness (around 10 μm for detection of the long wavelength infrared radiation) is well above the critical thickness if the lattice mismatch with the substrate is larger than 0.02%. $Cd_xHg_{1-x}Te$ (CMT) structures are therefore preferably grown on $Cd_{1-y}Zn_yTe$ (CZT) where the zinc concentration can be, in principle, adjusted to get perfect lattice matching with any composition in CMT. However, a perfect lattice match can be difficult to achieve in practice due to zinc segregation effects during bulk CZT growth [1, 2] leading to varying Zn concentration across wafers. This can be particularly drastic on the large-area CZT substrates, now commercially available. The mechanism and extent of strain relaxation needs therefore to be addressed. This is the goal of this article.

The method we have used here to determine the energy of formation of dislocation is by no means specific to the CMT/CZT heteroepitaxial system but relies only on the existence of substrates with varying lattice parameter. It could be applied to other epitaxial materials.

* Corresponding author. Fax: + 47 63 80 72 12; e-mail: thierry.colin@ffi.no.

0022-0248/97/$17.00 Copyright © 1997 Elsevier Science B.V. All rights reserved
PII S0022-0248(96)00986-4

2. Critical thickness and epilayer relaxation

Many models for critical thickness and strain relaxation have been published and are still under debate. This arises mainly from the difficulties of the ab initio models in describing correctly experimental results. Many authors have modified or developed other models in order to account for experimental observations. The supporting arguments are, either that the theoretical models predicts an equilibrium state while the deformation is only metastable [3], or that there is an additional nucleation barrier in the generation of dislocations which controls the relaxation [4].

For our low-mismatched heteroepitaxial system, we have generalized the energy equilibrium model of Fontaine et al. [5]. It was originally designed to account for measured critical thickness *and* relaxation in the low-mismatched CdTe/$Cd_{0.96}Zn_{0.04}Te$ system (lattice mismatch = 0.23%). The only fitting parameter in the model of Fontaine et al. is the linear energy of formation of dislocations (ξ_d). This has a clear physical meaning and can easily be compared to values measured or determined by other means, contrarily to some of the parameters used in other phenomenological models. The determined value of ξ_d can aid in identifying the relaxation mechanism. From observations made on CdTe/$Cd_{0.96}Zn_{0.04}Te$ it was concluded that the relaxation is governed by dislocation nucleation rather than by bending of threading dislocations and that the strain relief is not limited by the dislocation movement [5].

The model of relaxation and critical thickness is based on the minimalization of areal energy within the interface plane as the relaxation proceeds. It assumes that the deformation within the epilayer is tetragonal. Since our epilayers are grown on (2 1 1) we have generalized the model to low symmetry planes. We assume that the elastic deformation is isotropic in the growth plane and that the stress experienced by the layer is only related to misfit, and is exclusively in-plane. The calculation details are too extensive for this article and will be presented elsewhere [6].

The total areal energy is the sum of two terms: the areal elastic energy (A_e) due to the residual stress accumulated in the overgrown material, and the areal energy associated with the misfit dislocation network (A_d) once it has been created to release partially the stress.

$$A_e = K^{\parallel}_{hkl} e \varepsilon^2_{\parallel}, \tag{1}$$

where $K^{\parallel}_{hkl}$ is the elastic modulus relating the in-plane stress ($\sigma_{\parallel}$) to the in-plane strain ($\varepsilon_{\parallel}$) in the growth plane (hkl) and is dependent on the stress geometry. e is the layer thickness.

For (2 1 1) we calculated

$$K^{\parallel}_{211} = \frac{\sigma_{\parallel}}{\varepsilon_{\parallel}} = \frac{3(C_{11} + 2C_{12})\, C_{44}\, (11C_{11} - 11C_{12} + 2C_{44})}{4C^2_{11} + 4C_{11}C_{12} - 8C^2_{12} + 13C_{11}C_{44} - 7C_{12}C_{44} + 2C^2_{44}}, \tag{2}$$

where C_{ij} are the elastic stiffness constants of CMT [10], and

$$A_d = \sum_{i=1}^{n_d} \mathrm{Nd}_i\, \xi_d. \tag{3}$$

It is assumed that only one type of dislocation is active or at least predominant in strain release (in numerical calculations we assumed the predominance of 60° dislocations). ξ_d is the apparent linear energy of formation of these dislocations. It is an effective linear energy that takes into account all mechanisms required to create, and eventually move the dislocation towards the interface. n_d is the number of dislocation arrays able to release strain at the interface (for example, in the case of 60° dislocations aligned along [1 1 0], $n_d = 2$ for (1 0 0) while $n_d = 3$ for (1 1 1) and (2 1 1) growth planes).

Nd_i is the linear density of dislocations available for strain release in each array:

$$\mathrm{Nd}_i = \frac{2\,[(\Delta a/a) - \varepsilon_{\parallel}]}{n_d \quad b_{r,i}}, \tag{4}$$

where $(\Delta a/a)$ is the intrinsic lattice mismatch between the two materials, $b_{r,i}$ is the projection of the Burgers vector of the dislocations belonging to the ith array onto the interface plane perpendicularly to the dislocation line. In the case of growth on (2 1 1), there are, within each dislocation array, several possible Burgers vectors leading to different b_r projections and therefore different strain release efficiencies [6].

The condition for minimalization of the total areal energy all over relaxation leads to the invariant

$$\sigma_{\parallel} e = \frac{\xi_d}{n_d} \sum_{i=1}^{n_d} \frac{1}{b_{r,i}}. \tag{5}$$

Eq. (5) predicts a classical hyperbolic variation of the residual stress as the thickness of the epilayer is increased (the right-hand term of this equation is constant). This residual in-plane stress is dependent on the growth orientation through the term included in the summation sign and through n_d.

The critical thickness e_c can also be easily calculated because at that point the layer is at the onset of relaxation while the in-plane strain is still equal to the intrinsic lattice mismatch. One obtains

$$e_c = \frac{\xi_d}{n_d K^{\parallel}_{211}(\Delta a/a)} \sum_{i=1}^{n_d} \frac{1}{b_{r,i}}. \tag{6}$$

3. Deformation along the growth axis

In our experiments we determine by X-ray diffraction the apparent lattice parameter of the epilayer along the growth axis which is, whatever the deformation regime, given by

$$a_{\text{apparent}} = a_L(1 + \varepsilon_{\perp}), \tag{7}$$

$\varepsilon_{\perp}$ being the strain perpendicular to the surface. It can be related to the in-plane stress $\sigma_{\parallel}$ by the $K^{\perp}_{hkl}$ elastic modulus

For (2 1 1), we calculated

$$K^{\perp}_{211} = \frac{\sigma_{\parallel}}{\varepsilon_{\perp}} = \frac{-3(C_{11} + 2C_{12})\, C_{44}\, (11C_{11} - 11C_{12} + 2C_{44})}{8C_{11}^2 + 8C_{11}C_{12} - 8C_{12}^2 - 7C_{11}C_{44} + 19C_{12}C_{44} - 2C_{44}^2}. \tag{8}$$

Within the elastic deformation regime, the epilayer is fully strained on the underlying substrate ($\varepsilon_{\parallel} = \Delta a/a$). From Eqs. (2), (7) and (8) one obtains

$$a_{\text{apparent}} = a_L\left(1 + \frac{K^{\parallel}_{211}}{K^{\perp}_{211}}(\Delta a/a)\right) = a_L\left(1 + \frac{K^{\parallel}_{211}}{K^{\perp}_{211}}\left(\frac{a_S - a_L}{a_L}\right)\right). \tag{9}$$

In the plastic deformation regime, the epilayer lattice no longer follows the substrate lattice and dislocations are generated (or bent) to accomodate the difference of actual lattice parameter on each side of the interface. Combining Eqs. (5), (7) and (8) one obtains

$$a_{\text{apparent}} = a_L\left(1 + \frac{\sigma_{\parallel} e}{K^{\perp}_{211} e}\right) = a_L\left(1 + \frac{\xi_d}{n_d K^{\perp}_{211} e} \sum_{i=1}^{n_d} \frac{1}{b_{r,i}}\right). \tag{10}$$

4. Experimenal procedure

Epitaxial layers of $Cd_xHg_{1-x}Te$ ($0.2 < x < 0.5$) have been grown by Molecular Beam Epitaxy [8] on $Cd_{1-y}Zn_yTe$ ($0.02 < y < 0.04$) substrates. The relaxation state of epilayers is commonly measured by the separation of the X-ray diffraction peaks of the epilayer and its underlying substrate. However, in low

mismatch heteroepitaxial systems, for small elastic deformations, the overlapping of the diffraction peaks impedes a precise observation of their separation and, for unnegligible plastic deformation, the epilayer thickness is comparable to the probing depth of X-rays impeding a clear observation of the substrate diffraction peak. In order to overcome these problems we measured the substrate lattice parameter prior to growth. The deformation of the epilayer is then determined by correlating its apparent lattice parameter to the pre-recorded lattice parameter of the substrate measured at the same location.

The lattice parameters perpendicular to the wafer surface have been determined by the Bond method over the whole wafer area with a X-ray spot size of about 1 mm^2. Experimental details and related uncertainties (<50 ppm) are discussed in Ref. [2].

Our study has been specifically performed on CMT layers grown on CZT substrates with varying zinc concentration. It allows, within one sample, to clearly identify the different deformation regimes (elastic deformation in the regions of small lattice mismatch, plastic deformation in the regions with larger mismatch). The variations observed within the recorded data are then related to the varying lattice mismatch and not to changes of other parameters since the complete measurement is performed on a single wafer with uniform CMT composition and thickness (Cd mole fraction variations across 15 mm wafers <0.0003, thickness relative variation $<1\%$ as determined from room-temperature infrared transmission measurements, in-depth relative variations of Cd mole fraction $<1\%$ as determined by SIMS on 10 μm thick epilayers).

5. Results and discussion

Fig. 1 shows a deformation plot where the apparent epilayer lattice parameter along the growth axis is plotted against the underlying substrate lattice parameter. Two types of deformation regimes are easily discernible. In the elastic deformation regime the epilayer parameter varies in an opposite way to the substrate lattice parameter. In the plastic deformation regions the apparent epilayer lattice parameter is constant. They are well described mathematically by the present model.

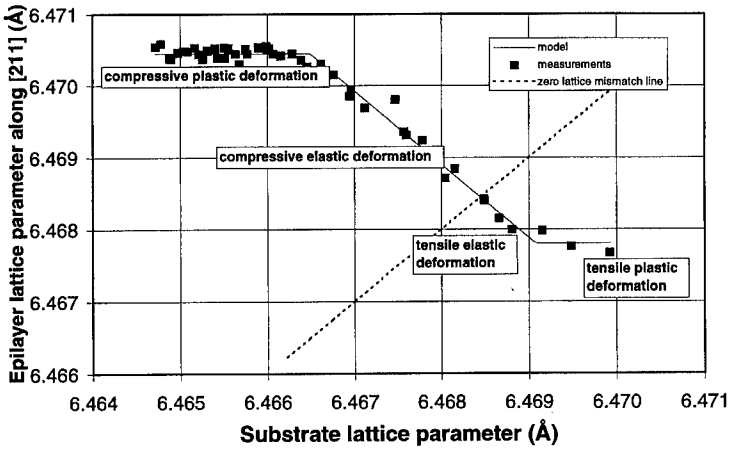

Fig. 1. Evolution of the lattice parameter along the [2 1 1] growth axis for a CMT epilayer ($x_{Cd} = 0.35$, $e = 7.9$ μm) as a function of the underlying CZT substrate lattice parameter. The measured data (dots) can be easily modeled (line) and show very clearly the transition between elastic and plastic deformation both in compressively and tensively strained material. Apparent energies of formation of misfit dislocations can be determined from the fit of the deformation curve in the two plastic deformation regions. In compression $\xi_d = 35.5 \times 10^{-9}$ J m^{-1}. In tension $\xi_d = 11.1 \times 10^{-9}$ J m^{-1}.

In the elastic deformation regime, as the substrate lattice parameter varies, the in-plane epilayer lattice follows its variations and consequently the apparent lattice parameter in the perpendicular direction (i.e along the growth axis) varies in the opposite way to roughly maintain the unit cell volume. This is well described by Eq. (9). No change in the published elastic stiffness constants of CMT [10] entering in $K^{\perp}_{211}$ and $K^{\parallel}_{211}$ is required to obtain a correct fit of the slope observed experimentally. This is particularly important to note because it confirms that this deformation regime is purely elastic (a progressive relaxation would reduce the apparent slope, a limited relaxation would produce a kink in the slope).

In the plastic deformation regime, the epilayer lattice can no longer follow the substrate lattice and dislocations are generated (or bent). The epilayer lattice parameter remains constant whatever the substrate lattice parameter, as stated in Eq. (10). This is a direct consequence of the $\sigma_{\parallel} e$ invariant stated in Eq. (5).

The line drawn in Fig. 1 is a fit of the adapted model (Eqs. (9) and (10)) to the recorded data. For this fit the unstrained CMT layer lattice parameter a_L is required and has been simply determined at the intersecting point between the deformation plot and the zero mismatch line. From the complete fit the energy of formation of the misfit dislocations in tensile *and* compressive deformation can be determined. Hu [7] has given an expression for the linear energy of a mixed dislocation starting from an ab initio calculation of critical thickness. From that we calculated for 60° dislocations in CMT a maximum value for ξ_d equal to 1.6×10^{-9} J m^{-1} which is almost a factor 7 below the lowest experimental value observed here (see Fig. 1 caption). It is therefore tempting to reject a simple extension of preexisting dislocations as the mechanism of relaxation and rather consider a mechanism where the nucleation of new dislocations is required, adding an energetic barrier to the linear energy calculated above. It is important to note however that the threading dislocation density would be large enough in CZT substrates to account by itself for the amount of relaxation experimentally observed (the required dislocation density for the maximum relaxation in Fig. 1 is 2.3×10^4 cm^{-2} to be compared with the specified substrate etch pit densities of 5×10^4 to 1×10^5 cm^{-2}).

Even if the tensile plastic deformation plateau is not perfectly defined due to the small number of experimental points, a clear dissymmetry can be seen between the relaxation of tensile strain and the relaxation of compressive strain. This has been observed on many other MBE samples. Dissymmetry effects in the CMT/CZT heteroepitaxy have already been reported by several authors using different growth techniques like LPE [1] and MOCVD [9]. Our observations are consistent with both works though based on slightly different measurements (determination of the onset of plastic deformation instead of measurement of X-ray diffraction peak broadening in the plastic deformation regions). The dissymmetry effect is then obviously not related to the growth technique and is most probably intrinsic to the heteroepitaxial system. However, precise studies of thermal expansion of CMT *and* CZT at elevated temperatures are required to ascertain that this dissymmetry effect is not purely due to the differential thermal expansion between substrate and epilayer.

Fig. 2 shows the evolution of the full width at half maximum (FWHM) of the epilayer (4 2 2) diffraction peak as a function of the substrate lattice parameter. A substantial broadening is observed in the compressive plastic deformation and is directly related to the presence of misfit dislocations, the density of which has been calculated from the deformation plot. One can note that the onset of broadening is located in the deformation regime near, but not exactly at the onset of relaxation. We assume that this is because the lowest values of FWHM in the elastic deformation regime are not limited by the intrinsic width of the diffraction peaks but rather related to mosaicity and residual lattice parameter variations in the measurement spot both convoluted with the beam divergence set by our monochromator [2]. This effect has been modeled in Fig. 2. A weaker broadening is observed in tension surprisingly before the onset of plastic deformation. This effect can be explained assuming that a limited number of dislocations located in the substrate or in the subgrain boundaries are released under tensile stress. The reason for not observing any substantial relaxation in the deformation plot would be related to the limited density of such dislocation (about 2×10^3 cm^{-2} in each possible dislocation array on (2 1 1) would be enough to account for the observations) and to their relative inefficiency in strain release (small b_{ri}). This is consistent with the assumption of these dislocations coming

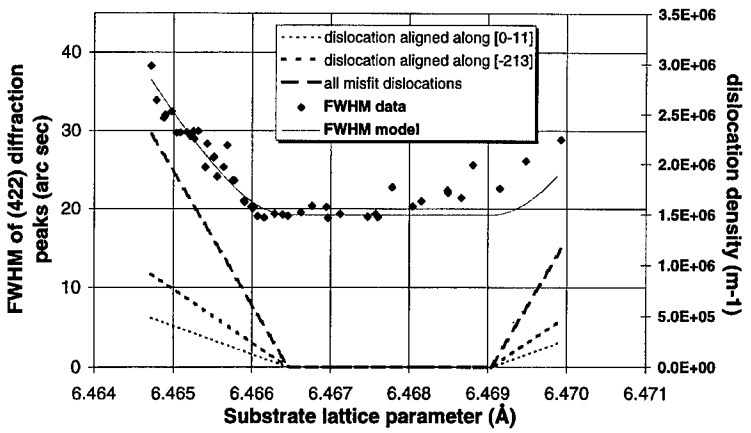

Fig. 2. Evolution of the full width at half maximum (FWHM) of the (4 2 2) diffraction peak of the CMT epilayer (dots) as a function of the underlying CZT substrate lattice parameter. The diffraction peak is recorded with a wide aperture detector by varying the angle of incidence of X-rays onto the sample. The density of misfit dislocations calculated from the deformation plot in Fig. 1 and the epilayer FWHM modeled from it are also shown.

from the substrate where Burgers vectors are randomly distributed over all allowed orientations contrarily to misfit dislocations which have Burgers vectors predominantly lying in the interface plane or close to it. The absence of such an effect under compressive stress is currently under investigation.

6. Conclusion

The use of X-ray diffraction on thick epilayers of cadmium mercury telluride deposited on nearly lattice-matched cadmium zinc telluride substrates with varying zinc content has permitted a detailed study of relaxation in this low-mismatch heteroepitaxial system. It has been clearly shown that there is only one relaxation mechanism within each relaxation domain. The use of a simple elastic and plastic deformation model adapted for low symmetry planes permits the determination of the apparent energy of formation of misfit dislocations in CMT. The values obtained are rather high and would suggest either that new dislocations are required to release the elastic strain or that the excess of energy is used to release the threading dislocations, already present in the material, from pinning sites like subgrain boundaries. As other workers, we observe an apparent dissymmetry in relaxation of tensile strain and relaxation of compressive strain. It is suggested that this behaviour is independent of the growth technique and instead specific to the material system. Nevertheless, a simple thermal differential effect cannot be completely ruled out as the main origin of this behaviour. There are some indications of the existence of dislocations with apparently lower energies of formation (possibly over a quite wide spectrum) but with limited density and only activated in tensile stress. Their low efficiency in strain release suggests that they could come from grain boundaries duplicated by the growth from the substrate into the epilayer or could come more directly from the substrate.

References

[1] S.P. Tobin, F.T.J. Smith, P.W. Norton, J. Wu, M. Dudley, D. Di Marzio and L.G. Casagrande, J. Electron. Mater. 24 (9) (1995) 1189.

[2] T. Skauli, T. Colin and S. Løvold, J. Crystal Growth 172 (1997) 97.
[3] B.W. Dodson and J.Y. Tsao, Appl. Phys. Lett. 51 (17) (1987) 1325.
[4] P.M.J. Marée, J.C. Barbour, J.F. van der Veen, K.L. Kavanagh, C.W.T. Bulle-Lieuwma and M.P.A. Viegers, J. Appl. Phys. 62 (11) (1987) 4413.
[5] C. Fontaine, J.P. Gaillard, S. Magli, A. Million and J. Piaguet, Appl. Phys. Lett. 50 (14) (1987) 903.
[6] T. Colin, T. Skauli and S. Løvold, to be published.
[7] S.M. Hu, J. Appl. Phys. 69 (11) (1991) 7901.
[8] T. Colin, D. Minsås, S. Gjøen and R. Sizmann, in: Compound Semiconductor Epitaxy, Eds. C.W. Tu, L.A. Kolodziejski and V.R. McCrary, Mater. Res. Soc. Proc. Vol. 340, San Francisco, CA (1994) p. 575.
[9] L. Sugiura, K. Shigenaka, F. Nakata and K. Hirahara, J. Crystal Growth 145 (1994) 547.
[10] J.C. Brice, in: EMIS Datareview Series No. 3-INSPEC (1987) 8.

ELSEVIER

Journal of Crystal Growth 175/176 (1997) 677–681

JOURNAL OF CRYSTAL GROWTH

A study of MBE growth and thermal annealing of p-type long wavelength HgCdTe

L. He[a,*], J.R. Yang[a], S.L. Wang[a], S.P. Guo[a], M.F. Yu[a], X.Q. Chen[a], W.Z. Fang[a], Y.M. Qiao[a], Q.Y. Zhang[b], R.J. Ding[b], T.L. Xin[b]

[a] *Epitaxy Research Center for Advanced Materials, National Laboratory for Infrared Physics, Shanghai Institute of Technical Physics, Chinese Academy of Sciences, 420 Zhong Shan Bei Yi Rd, Shanghai 200083, People's Republic of China*

[b] *Shanghai Institute of Technical Physics, Chinese Academy of Sciences, 420 Zhong Shan Bei Yi Rd, Shanghai 200083, People's Republic of China*

Abstract

The results of MBE growth and annealing of p-type HgCdTe are described in the paper. It is found that the surface morphology is sensitive to the growth temperature. HgCdTe epilayers showed excellent lateral uniformity in x-values as well as in thickness, relative deviations for x and thickness over a 2 in. wafer were found to be 0.18% and 2.19%, respectively. The hole concentrations in a range of $(1–2) \times 10^{16}$ cm^{-3} with hole mobilities higher than 600 cm^2 V^{-1}s^{-1} were obtained by p-annealing. MBE grown p-HgCdTe epilayers were successfully incorporated into 32×32 focal plane arrays detectors.

PACS: 81.15.Ef; 81.40.Ef; 78.66.Hf

Keywords: MBE; HgCdTe; Thermal annealing

1. Introduction

Molecular beam epitaxy (MBE) for HgCdTe has been demonstrated [1] to be a flexible technology for manufacturing infrared (IR) detectors. As compared to liquid phase epitaxy (LPE) which has been a relative mature technology dominating over today's HgCdTe industry, MBE technology is developing rapidly, specially in the recent years. The performance of IR focal plane arrays (FPAs) detectors made from MBE grown materials has reached a stage that it becomes comparable to those made from LPE materials [1]. In view of the future developments, because MBE technique has potential advantages of low temperature and UHV growth environment, flexibility in controlling compositions [1], availability of in situ growth of pn junctions [2], multilayered heterostructures [1, 2] and CdTe passivation layers [3], it is more promising for developing future detectors with sophisticated structures.

* Corresponding author. Fax: + 86 21 6324 8028; e-mail: lihe@fudan.ihep.ac.cn.

0022-0248/97/$17.00 Copyright © 1997 Elsevier Science B.V. All rights reserved
PII S0022-0248(96)01001-9

Availability of highly uniform p-type HgCdTe materials in both structural and electrical properties is essentially important for fabricating IR photovoltaic detectors based on n^+p architecture. The requirements for x-values uniformity and carrier concentration are very stringent. In concerns of reducing tunneling currents, avoiding the formation of surface depletion or inversion layers and raising minority carrier lifetime, a hole concentration of $\sim 10^{16}\,cm^{-3}$ is required [4]. In this paper, we describe our recent results on growth and characterization of p-type long wavelength (LW) HgCdTe materials.

2. Experimental procedure

HgCdTe epilayers were grown in a Riber 32P MBE system without intentionally doping on undoped semi-insulating GaAs (2 1 1)B substrates, which were mounted on Mo-blocks with Indium bonding. A CdTe buffer layer of around 3 μm in thickness was grown prior to the HgCdTe nucleation. The growth rate for HgCdTe was 2.5–3 μm/h with the growth temperature kept to be constant at 183 ± 2°C, monitored by an InSb IR pyrometer which was carefully calibrated before growth and interpreted by taking the effects of Febry–Perot oscillation and emissivity change into account. For some growth runs, an ellipsometer, attached to MBE chamber with an angle of approximately 70°, was used for in situ real-time monitoring of compositional variations. During growth the ellipsometer continuously generates the ellipsometric parameters Ψ and Δ at 44 wavelength channels varying with growth time, which are then fitted by an appropriate model to obtain angle of incidence, complex index of refraction, $n - ik$ with wavelength. x-values at each growth time is evaluated by fitting the obtained $n - ik$ to the standard data of $Hg_{1-x}Cd_xTe$ at 180°C with the x-value as variable.

IR transmission measurements were carried out by using a Fourier transformer spectrometer. P-type conductivity of samples was achieved by a post-growth p-annealing process. The Hall effect measurements were performed with the Van der Pauw geometry at different temperatures from 300 to 30 K, and at different magnetic field intensities from 0.1 to 4 kG. To minimize the influences of electrode size and symmetry on the measurement accuracy which are more pronounced in p-type materials [5, 6], a relatively larger size of $15 \times 15\,mm^2$ was employed for all the Hall measurements.

3. Results and discussion

3.1. Growth of HgCdTe

The surface morphology was found to be sensitive to the growth temperature. Fig. 1 compares the surface morphology of two samples, grown at different temperatures of 190°C (Fig. 1a) and 183°C (Fig. 1b) with the same flux (beam equivalent pressure) ratio of Hg to Te of 88. As it can be seen in Fig. 1a, the higher growth temperature results in voids with shapes like snowflakes in the surface. A SEM aided EDX compositional analysis indicated that the voids are due to lack of Hg in the growth front. As a contrast, the surface morphology was greatly improved by reducing the growth temperature to 183°C as shown in Fig. 1b.

Compositional reproducibility is a major issue of concern in developing HgCdTe MBE technology. In this work 12 samples with thicknesses of 10–12 μm were grown in a run to run base with a target x-value 0.23 of $Hg_{1-x}Cd_xTe$. An average x-value of 0.231 was obtained with a standard deviation (STDDEV) of 0.01 and a relative deviation (STDDEV/mean) of 4.33%. The result is not as good as those reported by Bajaj et al. [1], it is

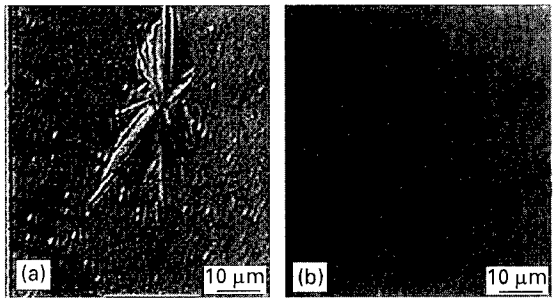

Fig. 1. Nomarski pictures of surface morphology of HgCdTe epilayers, grown at (a) 190°C and (b) 183°C.

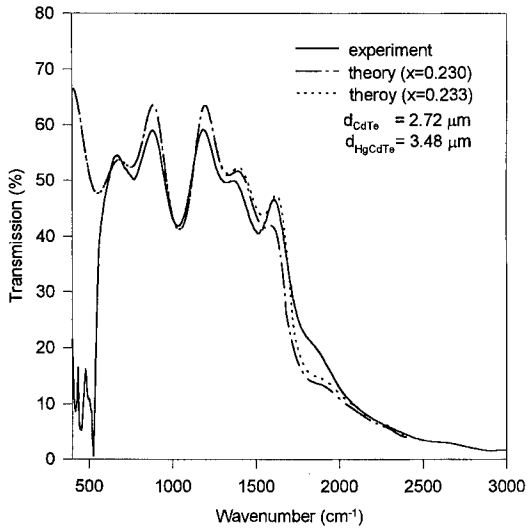

Fig. 2. A comparison between measured IR transmission curve and computer simulated curves. The experimental curve can be reproduced by assuming an x-value of 0.233 with thickness values for HgCdTe and CdTe buffer layer of 3.48, and 2.72 μm, respectively. The resolution in x-values of the computer simulation is also shown by the curve calculated assuming an x-value of 0.230. The same thickness parameters were used for the calculations.

believed that the deviation in x is caused by uncertainties in flux measurements, and can be further reduced by carefully refining the flux measurement procedures and improving the long-term stability of source ovens.

Due to the large lattice mismatch between GaAs substrate and HgCdTe epilayer, a high density of dislocations exists in HgCdTe epilayers. Our EPD study [7] showed a dislocation density of $(6–10) \times 10^6\ cm^{-2}$ for HgCdTe epilayers, and $\sim 4 \times 10^6\ cm^{-2}$ for CdTe buffer layers, which is in consistent with FWHM values of X-ray rocking curves of 70–90 arc sec. Similar results were also reported by the other workers [8]. It should be mentioned that because a high density of mismatch dislocations dominates over EPD values for all the samples, in this study no noticeable variation in EPD values was observed between samples grown at different temperature from 183°C to 190°C with the same Hg/Te flux ratio of 88.

3.2. Determination of x-values and thickness

To avoid the uncertainties in determining x and thickness parameters resulted from the multilayer interference in transmission curves, a computer simulation based on a simple model of multilayer interference was performed in an attempt to unambiguously determine these parameters. In the simulation, the relationships of reflectivity and absorption coefficient with x-value and wavelength [9, 10] are used with the x-value and the thickness as fitting parameters. The thickness deduced from the curve fitting was confirmed by cross-sectional observations of samples. The x-values obtained were found to be close to ($< \pm 0.004$) those deduced from the energy position at which the absorption coefficient reaches to 500 cm^{-1}. As shown in Fig. 2, the experimental curve can be fitted well with the simulated one. The reasons for the discrepancy in the transmission tail is not clear at the moment. However, it does not seem like to be due to the compositional grading in the growth direction. In fact, our results of real-time in situ ellipsometric monitoring of x-value variation showed that the x-values fluctuated within a STDDEV value of 0.004 to the average as the growth proceeded in a similar growth condition.

3.3. Lateral uniformity

Grown under the optimized condition, the epilayers showed excellent lateral uniformity in both composition and thickness. Fig. 3 shows an example of compositional and thickness distributions across a 2 in. HgCdTe sample. The transmission measurements were performed in 25 different locations (3 mm in diameter), which were distributed in concentric circles in the wafer numbered ascendingly from the wafer center (as #1) to the edge. The averaged x-value and thickness are 0.222 and 10.88 μm, respectively. The STDDEV for x-values is 0.0004, with a STDDEV for thicknesses of 0.238 μm were obtained. The relative deviations for x and thickness are 0.18% and 2.19%, respectively.

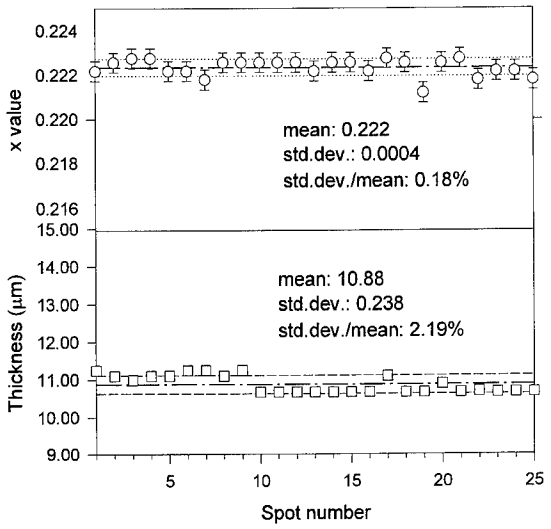

Fig. 3. Variations of x-values and thickness over a 2 in. HgCdTe epilayer.

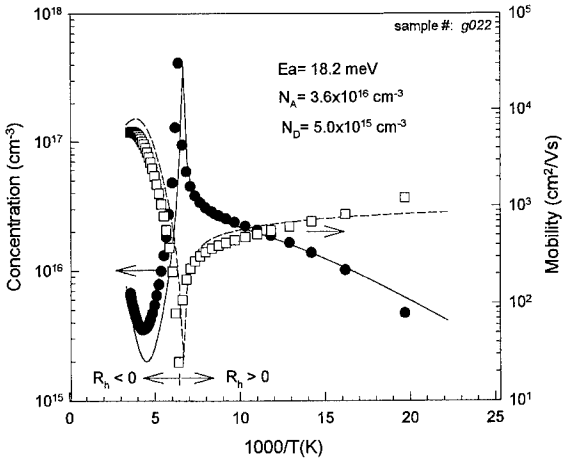

Fig. 4. Temperature dependencies of hole concentration and mobility, where solid circles represents measured concentration, and squares represents measured mobility. The theoretical values for hole concentration and mobility are shown as the solid and dashed lines, respectively.

3.4. Electrical properties

The as-grown LW samples were n-type. The typical electron concentrations and mobilities at 77 K were in ranges of low 10^{14} cm^{-3}, and high 10^4 to 10^5 cm^2 V^{-1}s^{-1}, respectively. The conductivity of as-grown samples was in situ annealed to p-type at 250°C for 12 h in the MBE growth chamber with a base pressure in the order of 10^{-9}–10^{-10} Torr. To prevent surface decomposition, a CdTe cap layer was grown on the annealing samples. This method takes the advantage of MBE technique, eventually eliminates any impurity contamination introduced by the ex situ annealing processes, such as isothermal annealing under Hg vapor in quartz ampoules, and easily handles annealing of large area samples. Destéfanis [11] found that vacuum annealing produced a homogeneous acceptor concentration inside their LPE grown HgCdTe. In this study, no surface morphological degradation and x-value change after the in situ annealing process were found. No magnetic field dependence of the Hall coefficients was observed at 77 K for the annealed samples, showing that a magnetic freeze-out condition is reached, which suggested that no electron components contribute to the Hall data at 77 K. The experimental temperature dependence of hole concentration and mobility obtained from the Hall measurement is shown in Fig. 4 together with the computer simulated curves. A model assuming single acceptor level and a uniform p-type layer was employed in the simulation [12]. As it can be seen in Fig. 4, no anomalous features [13, 14] originated from mixed conduction of n-type networks or layers can be found. Table 1 summaries Hall measurement results at 77 K for some of the annealed samples. The hole concentrations in a range of $(1–2)\times 10^{16}$ cm^{-3} together with hole mobilities higher than 600 cm^2 V^{-1}s^{-1} were obtained.

3.5. Device application

To confirm the device quality of the MBE grown materials, small scale 32×32 FPAs were fabricated with n^+p junctions formed by using Boron implantation (with a dose of $(0.5–1)\times 10^{14}$ cm^{-2} at 130 keV) into a p-type HgCdTe epilayer, which were interconnected to Si read-out chips by indium bumps. Examples of the thermal images at room temperature are shown in Fig. 5. The x-value of HgCdTe for this device is 0.24. The preliminary results showed that the average detectivity D^*_λ was approximately $(1–2)\times 10^{10}$ cm $\sqrt{\text{Hz}}$ W^{-1}, with an average $NE\Delta T$ value of less than 0.1 K. The aver-

Table 1
Electrical properties of p-type annealed samples measured at 77 K, 2 kG

Sample no.	Concentration (cm^{-3})	Mobility ($cm^2/V \cdot s$)	x-value
g09	1.67×10^{16}	653.0	0.234
g10	1.86×10^{16}	852.9	0.214
g15	1.25×10^{16}	1160.0	0.223
g16	1.14×10^{16}	866.0	0.222
g18	1.01×10^{16}	795.0	0.221
g19	1.48×10^{16}	696.8	0.231
g21	1.13×10^{16}	687.2	0.240
g22	1.57×10^{16}	690.1	0.238

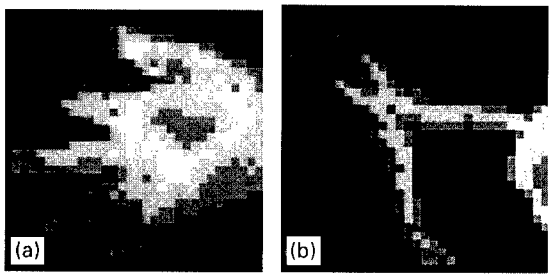

Fig. 5. Thermal images obtained from a 32×32 FPAs detector, where (a) is the picture of a human hand and (b) a pliers at room temperature.

age nonuniformity for responsivity is less than 12.5%. Obviously, the device performance still needs to be improved. One approach of doing this is to reduce the density of dislocations in HgCdTe layers arising from the lattice mismatch, which is known to shorten the lifetime of minority carriers [8].

4. Conclusions

We have studied MBE growth and annealing of HgCdTe epilayers. Small scale 32×32 FPAs were fabricated with n^+p junctions using MBE grown p-type HgCdTe.

It is found that the surface morphology is very sensitive to the growth temperature. The compositional reproducibility was studied in a limited number of samples with a target x-value of 0.23, a STDDEV for x-values of 0.01 deviated from an average value of 0.231 was obtained. The HgCdTe epilayers showed an excellent lateral uniformity in x-values as well as in thickness. Relative deviations for x-value and thickness over a 2 in. wafer were found to be 0.18% and 2.19%, respectively. Good electrical parameters were obtained by a p-type in situ vacuum annealing process. The hole concentrations in a range of $(1–2) \times 10^{16}$ cm^{-3} with high hole mobilities were obtained.

MBE grown p-HgCdTe epilayers were successfully incorporated into 32×32 FPAs detectors. The average detectivity D^*_λ was approximately $(1–2) \times 10^{10}$ cm $\sqrt{\text{Hz}}$ W^{-1}. A $NE\Delta T$ value of less than 0.1 K and an average nonuniformity for responsivity of less than 12.5% were obtained.

Acknowledgements

The authors would like to thank S.X. Yuan for stimulated discussions, J.B. Yu, M.R. Du and Y.R. Xu for technical assistance, Y.S. Gui, S.L. Guo and G.Z. Zhen for transport measurements.

References

[1] J. Bajaj, J.M. Arias, M. Zandian, J.G. Pasko, L.J. Kozlowski, R.E. DeWames and W.E. Tennant, J. Electron. Mater. 24 (1995) 1067.
[2] O.K. Wu, Mater. Res. Soc. Symp. Proc. 302 (1993) 423.
[3] L.O. Bubulac, W.E. Tennant, J. Bajaj, J. Sheng, R. Brigham, A.H.B. Vanderwyck, M. Zandian and W.V. McLevige, J. Electron. Mater. 24 (1995) 1175.
[4] E. Finkman and Y. Nemirovsky, J. Appl. Phys. 59 (1986) 1205.
[5] T.R. Lepkowski, R.Y. DeJule, N.C. Tien, M.H. Kim and G.E. Stillman, J. Appl. Phys. 61 (1987) 4808.
[6] M. Boukerche, P.S. Wijewarnasuriya, J. Reno, I.K. Sou and J.P. Faurie, J. Vac. Sci. Technol. A 4 (1986) 2072.
[7] J. S. Chen, US Patent No. 4 897 152.
[8] S.H. Shen, J.M. Arias, D.D. Edwall, M. Zandian, J.G. Pasko and E. DeWames, J. Vac. Sci. Technol. B 4 (1992) 1492.
[9] K. Liu, J.H. Chu, B. Li and D.Y. Tang, Appl. Phys. Lett. 64 (1994) 2818.
[10] J.H. Chu, B. Li, K. Liu and D.Y. Tang, J. Appl. Phys. 75 (1994) 1234.
[11] G.L. Destéfanis, J. Crystal Crowth 80 (1988) 700.
[12] K.K. Parat, N.R. Taskar, I.B. Bhat and S.K. Ghandhi, J. Crystal Growth 106 (1990) 513.
[13] M.C. Chen, S.G. Parker and D.F. Weirauch, J. Appl. Phys. 58 (1985) 1350.
[14] L.F. Lou and W.H. Frye, J. Appl. Phys. 56 (1984) 2253.

ELSEVIER

Journal of Crystal Growth 175/176 (1997) 682–687

JOURNAL OF CRYSTAL GROWTH

Nitrogen doping of Te-based II–VI compounds

S. Tatarenko[a,b,*], T. Baron[a], A. Arnoult[a], J. Cibert[a], M. Grün[a], A. Haury[a], Y. Merle d'Aubigné[a], A. Wasiela[a], K. Saminadayar[b]

[a] *Laboratoire de Spectrométrie Physique, CNRS et Université Joseph Fourier, Grenoble, B.P. 87, F-38402 St Martin d'Hères Cedex, France*
[b] *DRFMC/SP2M/PSC, CEA Grenoble, F-38054 Grenoble Cedex 9, France*

Abstract

We report on the doping properties of the II–VI Te-related compounds, ZnTe, CdTe and CdZnTe, CdMgTe and ZnMgTe, using two different nitrogen plasma sources. High doping levels are measured for ZnTe, slightly lower for CdTe (8×10^{17} cm^{-3}). Following the comparative study of nitrogen doping in these materials, we invoke the possible formation of nitride compounds as responsible for the large nitrogen amount incorporated in Mg-containing alloys. The formation of such compounds might be reduced by using appropriate growth conditions and doping levels in the 4×10^{17} cm^{-3} range are obtained in ternary and quaternary alloys containing Mg. Such doping levels allow the growth and the study of high-quality modulation-doped heterostructures.

PACS: 81.15.Hi; 68.55.Ln; 73.61.Ga

Keywords: Multilayers; Molecular beam epitaxy; II–VI semiconductors; Doping

1. Introduction

In the last few years, the development of blue light emitting laser diodes based on ZnSe has generated a large amount of studies on the nitrogen p-type doping of II–VI semiconductors. Among these materials, the tellurium-based compounds CdMgTe and ZnMgTe present an increasing interest [1]. In this paper, we present an extensive investigation on the nitrogen p-type doping of CdTe, ZnTe, CdZnTe, ZnMgTe, CdMgTe and the quaternary alloy CdZnMgTe as well as on the doping of related heterostructures.

2. Experimental procedure

The (0 0 1) MBE layers are grown on (0 0 1) $Cd_{0.96}Zn_{0.04}Te$ or $Cd_{0.96}Zn_{0.12}Te$ substrates by using CdTe, ZnTe, Cd, Zn, Te and Mg sources. A home-made electron cyclotron resonance (ECR) plasma source [2] and a Riber DC glow plasma source have been used in this study. As will be

* Corresponding author. Fax: + 33 2 76 88 50 97; e-mail: statarenko@cea.fr.

0022-0248/97/$17.00 Copyright © 1997 Elsevier Science B.V. All rights reserved
PII S0022-0248(96)01003-2

demonstrated, the DC glow source is particularly well adapted to obtain very high doping levels in ZnTe (10^{19}–10^{20} cm^{-3} range), but the residual nitrogen pressure in the chamber stays in the 10^{-4} Torr range during the MBE growth and the mastering of low doping levels is difficult. By contrast, with the ECR source we can maintain a lower residual pressure (in the 10^{-6} Torr range) in the MBE growth chamber and, by changing either the ECR power or the aperture between the cell and the growth chamber, the flux of doping species can be modulated allowing typical doping levels over the 10^{16}–10^{20} cm^{-3} range for ZnTe. Hence, by using the ECR cell it is not necessary to use the pulse doping method (repeated sequences of doped and undoped layers) which is necessary to obtain low doping levels with the DC source [3].

3. Results and discussion

3.1. ZnTe and CdTe doping

Concerning the doping of (0 0 1) ZnTe it is relevant to point out that doping levels as high as 10^{20} cm^{-3} have been achieved on continuously doped layers by using both types of cells. By using the ECR source much lower doping concentrations are obtained, thus it is possible to determine optically and electrically the acceptor ionization energy. Fig. 1 shows the temperature dependence of the hole concentration for two ZnTe layers, doped at 3×10^{18} and 10^{17} cm^{-3}, respectively. The acceptor ionization energy at infinite dilution deduced from such Hall measurements (plot of the Hall activation energy versus $(N_D)^{1/3}$, see Fig. 2 of Ref. [4]) and from photoluminescence spectra (fit of the photoluminescence line, see Fig. 4 of Ref. [4]) is 53.4 ± 1 meV.

Concerning (0 0 1) CdTe, continuously doped layers with doping levels of 8×10^{17} cm^{-3} have been obtained by using the ECR plasma source and a low growth temperature (220°C) under an excess of Cd. A hole concentration of 2.6×10^{17} cm^{-3} was previously reported by using an ECR plasma source [5]. With the DC glow plasma source the maximum doping level we achieved was 8×10^{16} cm^{-3} by use of pulse doping method [3].

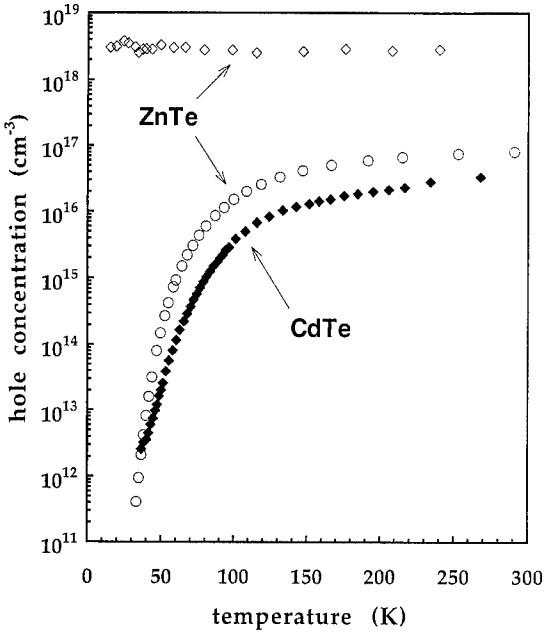

Fig. 1. Hole concentration versus temperature for two ZnTe and one CdTe layer doped with nitrogen.

Fig. 1 shows the temperature dependence of the hole concentration for a CdTe sample with a doping concentration of 3.4×10^{16} cm^{-3} at 300 K. From electrical and optical measurements performed on that sample an acceptor ionization energy of 57 ± 3 meV is found for the nitrogen in CdTe at infinite dilution [6].

The high nitrogen doping levels achieved in ZnTe allow to study the strains introduced in the doped layer and consequently to evaluate the length of the metal–nitrogen bond. From the light hole/heavy hole splitting in reflectivity measurements [7] of a heavily nitrogen doped ZnTe layer ($p = 3 \times 10^{19}$ cm^{-3}) grown on a (0 0 1) ZnTe substrate, a biaxial strain of about -4×10^{-4} is estimated. Such a value indicates the possibility to determine, by X-ray diffraction measurements, the length of the Zn–N bond by growing a superlattice constituted of alternately doped and undoped ZnTe layers (75/75 Å) [6]. The concentration of the holes in the doped parts is 3×10^{19} cm^{-3} while the total nitrogen concentration is about 9×10^{19} cm^{-3}. Fig. 2a shows the X-ray diffraction profile

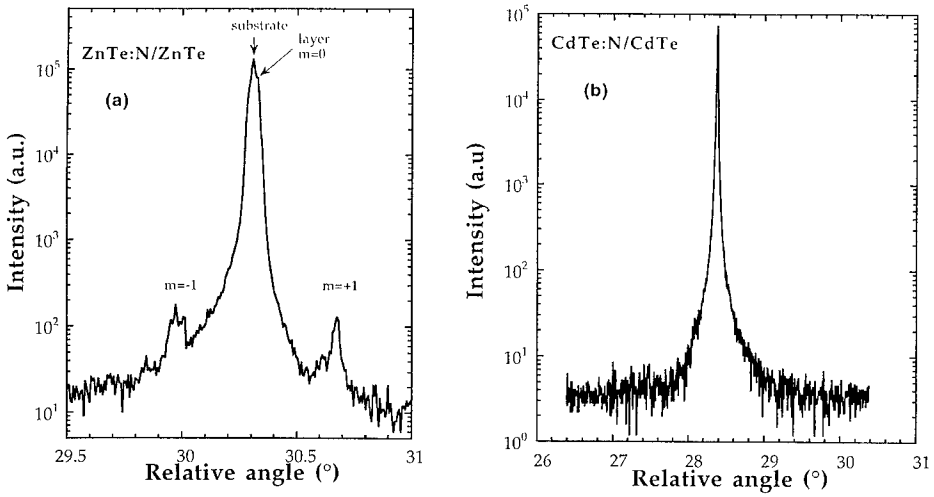

Fig. 2. X-ray diffraction rocking curves in the vicinity of the (0 0 4) reflection for, (a) a ZnTe : N/ZnTe (75 Å/75 Å) superlattice ($p = 3 \times 10^{19}$ cm^{-3}, [N] $= 9 \times 10^{19}$ cm^{-3}) grown on a (0 0 1) ZnTe substrate, (b) a CdTe:N/CdTe (100 Å/100 Å) superlattice ($p = 10^{16}$ cm^{-3}, [N] $= 10^{19}$ cm^{-3}) grown on a (0 0 1) CdTe substrate.

obtained for that structure. Clearly, two satellites peaks are observed due to the short period of the superlattice and due to the small lattice mismatch between the undoped ZnTe layers and the doped ones. From this profile, and using for the coherently strained ZnTe : N layer the same elastic coefficients as for undoped ZnTe, and a Vegard law, the length of the Zn–N bond is estimated to be (2.16 ± 0.05) Å in agreement with the theoretical estimation of Van de Walle and Laks (2.11 Å) from first principle calculations [8]. It is worth noting that in our estimation we use the carrier concentration and not the concentration of nitrogen atoms. If we use the total nitrogen concentration an improbable bond length of 2.5 Å is found. It can be concluded that only nitrogen atoms incorporated in active sites contribute to the decrease of the lattice parameter with respect to that of undoped ZnTe.

For a thin (3000 Å) CdTe layer with a high nitrogen content grown on a (0 0 1)CdTe substrate, a strain ($\varepsilon \approx -5 \times 10^{-4}$) was observed by reflectivity [7]. However, as shown in Fig. 2b, unlike in the nitrogen-doped ZnTe layers, no satellite peaks are observed in a heavily modulation-doped superlattice ([N] $= 10^{19}$ cm^{-3}), precluding any determination of the Cd–N bond length by this method. Following the assumption that only nitrogen atoms adsorbed in Te sites contribute to the reduction of the parameter, we have to take into consideration the low concentration of electrically active nitrogen atoms ($p = 10^{16}$ cm^{-3}) in these layers to explain the absence of a detectable superlattice structure. However, because the superlattice was grown at 300°C a strong diffusion of the nitrogen atoms in the matrix of CdTe and a possible degradation of the structural quality cannot be ruled out.

3.2. Doping of alloys

In the case of the CdZnTe and ZnMgTe alloys, using the DC glow plasma source at a substrate temperature of 300°C, a systematic decrease of the doping efficiency is observed as the Zn content decreases. This is illustrated in Fig. 3 in which the hole concentration is plotted as a function of the lattice parameter for different alloys all grown at 300°C. For the same cell operating conditions, SIMS measurements or nuclear reaction analysis show that the introduction of Cd in the matrix of ZnTe slowly decreases the incorporated nitrogen concentration, while the introduction of Mg increases it significantly [7] demonstrating the great affinity between Mg and N. Surprisingly, up to 6×10^{20} cm^{-3} nitrogen atoms can be incorporated

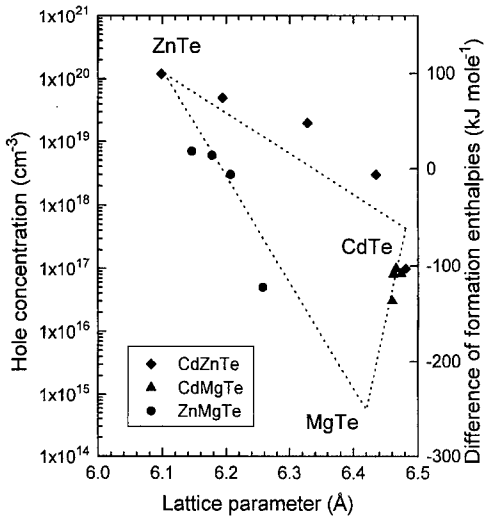

Fig. 3. Maximum hole concentrations versus lattice parameter for nitrogen-doped ZnMgTe, CdZnTe, and CdMgTe layers grown at 300°C and doped with a DC plasma source. The dashed line links the differences of formation enthalpies between A_3N_2 and ATe binary compounds (A = Cd, Zn, Mg).

in a layer of $Zn_{0.5}Mg_{0.5}Te$, but the doping level is only 5×10^{16} cm^{-3}. In the same way an increase of the nitrogen content with Mg concentration is observed in CdMgTe alloys together with a dramatic decrease of the doping efficiency (3×10^{16} cm^{-3} for 30% of Mg) as seen in Fig. 3.

In order to realize modulation-doped heterostructures, it is important to extend the previous doping limits in Mg-containing alloys. To this purpose, it is important to understand the compensation mechanisms in Te compounds. This subject is of current interest also in ZnSe for which different models have been proposed to understand the limiting factors in the doping [9]. In order to explain the fundamental trends of the doping of Te compounds, and particularly the differences observed in the nitrogen affinity of CdZnTe and ZnMgTe alloys (i.e., the increase of the nitrogen amount incorporated in Mg-related compounds [7, 10]) we invoke the possible formation of an A_3N_2 phase (A = Zn, Cd, Mg) resulting in a dramatic decrease of the solubility limit. Considering the formation enthalpy of ZnTe ($-\Delta H_F = 119$ kJ/mol) and of Zn_3N_2 ($-\Delta H_F = 20$ kJ/mol), the formation of the nitride is likely to occur only for a large N concentration. Differently, when comparing the formation enthalpy of CdTe and MgTe ($-\Delta H_F = 100$ and 210 kJ/mol, respectively) with those of the Cd_3N_2 and Mg_3N_2 compounds ($-\Delta H_F = 160$ and 460 kJ/mol, respectively), the formation of nitrogen compounds cannot be ruled out. The formation of such compounds might be a factor of decrease of the solubility limit of N in Cd and Mg containing materials. In Fig. 3 the evolution of the maximum doping levels measured at room temperature for CdZnTe, CdMgTe and ZnMgTe layers, grown at 300°C, is compared to the differences of formation enthalpies between ATe and A_3N_2 compounds. A correlation appears clearly between the maximum doping levels and the differences of formation enthalpies, which suggest that the A_3N_2 compounds might play a role in the nitrogen solubility limit. In addition, the fact that Mg_3N_2 is easier to form than Cd_3N_2 and Zn_3N_2 would favorably explain the differences in the amount of nitrogen incorporated in CdMgTe and ZnMgTe layers doped with the same cell conditions.

A possible way to block the formation of the A_3N_2 compounds is by limiting the desorption of the Te atoms from the growing surface. Desorption of Te dimers is observed for CdTe and MgTe at low temperature (250°C) while such a desorption is only observed above 390°C for ZnTe [11]. Hence, the formation of A_3N_2 compounds might be reduced by reducing the N_2 residual pressure and by decreasing the growth temperature. These conditions are realized by using the ECR plasma source and a low growth temperature (220°C). Then, doping levels as high as 4×10^{17} cm^{-3} have been achieved for CdMgTe alloys containing up to 30% of Mg. In addition, the same doping level was obtained in quaternary CdZnMgTe alloys (22% Mg and 7% Zn) grown at 240°C giving rise to layers showing excellent optical properties. It is worth pointing out that the previous values were obtained with a low nitrogen flux (small exit diaphragm on the ECR cell) and are probably not the highest achievable doping levels in these materials.

3.3. Doping of CdTe/CdZnMgTe heterostructures

Following the studies on the doping of the thick layers, the nitrogen doping of heterostructures has

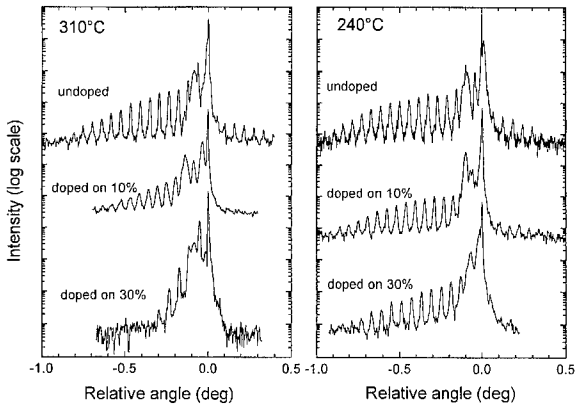

Fig. 4. X-ray diffraction profiles of $CdTe/Cd_{0.69}Zn_{0.08}Mg_{0.23}Te$ multiquantumwells (80 Å/780 Å) respectively grown at 240°C and 310°C. The samples are undoped, or doped ($p = 4 \times 10^{17}$ cm^{-3}) on 10% or 30% of the central part of the barriers.

been realized [12]. The electrical and structural properties of $CdTe/Cd_{0.69}Zn_{0.08}Mg_{0.23}Te$ (80 Å/780 Å) multiquantum wells doped in the barriers have been studied. Fig. 4 shows the X-ray diffraction profiles obtained on three samples grown at 240°C and three samples grown at 310°C. Sample (a) is nominally undoped, while in sample (b) 80 Å (i.e., 10%) at the center of each barrier is doped, and in sample (c) 240 Å (i.e., 30%) of each barrier is doped. X-ray diffraction analyses suggest the absence of a significant interdiffusion between the wells and the barriers when the structure is grown at low temperature (240°C) while an interdiffusion correlated to the presence of nitrogen is clearly observed for the doped samples grown at higher temperature (310°C). Furthermore, for layers grown at 240°C, capacitance-voltage (C–V) profiles confirm the localization of the nitrogen atoms in the barriers and the transfer of holes across the spacing layer into the quantum wells due to the significant valence band offset in the CdTe/MgTe system. Fig. 5 shows the C–V profile measured for a $CdTe/Cd_{0.69}Zn_{0.08}Mg_{0.23}Te$ multiquantum well structure doped on 30% of the barrier. The nominal structure is given for comparison with the experimental result. In order to get a uniform hole concentration in the quantum wells and to avoid band bending effect, the topmost barrier is thicker (2700 Å) and a part of it (370 Å) is doped. The C–V profile illustrates an equilibrium situation with, as expected, the transfer of a part of the holes coming from the first doped barrier towards the surface and

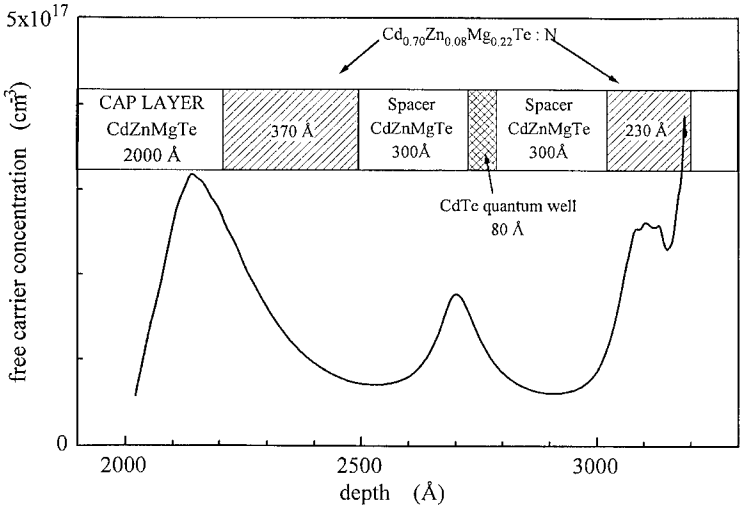

Fig. 5. Capacitance–voltage profile of a multiquantum well $CdTe/Cd_{0.69}Zn_{0.08}Mg_{0.23}Te$ doped in the barriers. The nominal structure is given as a reference.

into the quantum well. The presence of unionized acceptors in the second barrier is also clearly evidenced. The estimated density of 2D hole gas in the quantum well is in good agreement with the predictions using a simple model of the charge transfer in modulation-doped heterostructures. The realization of such structures has recently allowed the optical study of the 2D holes gas and the identification of the positively charged exciton (X +) for the first time in II–IV compounds [13].

4. Conclusion

High p-type doping levels have been obtained for ZnTe, CdTe as well as Mg containing alloys. The binding energies of nitrogen acceptor in ZnTe and CdTe are measured and the Zn–N bond length is determined. The formation of nitrides is proposed as a limiting mechanism, and growth at lower temperature is demonstrated as a way to achieve a higher doping in Te compounds. By using appropriate growth conditions, modulation-doped heterostructures have been successfully realized, opening the way to the study of their physical properties.

References

[1] A. Waag, H. Heinke, S. Scholl, C.R. Becker and G. Landwehr, J. Crystal Growth 141 (1994) 93.
[2] M. Grün, N. Sadeghi, J. Cibert, Y. Genuist and A. Tserepi, J. Crystal Growth 159 (1996) 284.
[3] T. Baron, S. Tatarenko, K. Saminadayar, N. Magnea and J. Fontenille, Appl. Phys. Lett. 65 (1994) 1284.
[4] M. Grün, A. Haury, J. Cibert and A. Wasiela, J. Appl. Phys. 79 (1996) 7386.
[5] S. Oehling, H.J. Lughauer, M. Schmitt, H. Heinke, U. Zehnder, A. Waag, C.R. Becker and G. Landwehr, J. Appl. Phys. 79 (1996) 2343.
[6] T. Baron, K. Saminadayar and N. Magnea, Appl. Phys. Lett. 67 (1995) 2972.
[7] T. Baron, N. Magnea, K. Saminadayar and S. Tatarenko, unpublished.
[8] C.G. Van de Walle and D.B. Laks, Solid State Commun. 93 (1995) 447.
[9] W. Fashinger, S. Ferreira and H. Sitter, Appl. Phys. Lett. 66 (1995) 2516 references therein..
[10] T. Baron, K. Saminadayar and S. Tatarenko, J. Crystal Growth 159 (1996) 271.
[11] S. Tatarenko, B. Daudin and D. Brun-Le Cunff, Appl. Phys. Lett. 66 (1995) 1773.
[12] A. Arnoult, J. Cibert and S. Tatarenko, unpublished.
[13] A. Haury, A. Arnoult, V.A. Chitta, J. Cibert, Y. Merle d'Aubigné, S. Tatarenko and A. Wasiela, Proc. 9th Int. Conf. on Superlattices, Microstructures and Microdevices, Liège (1996).